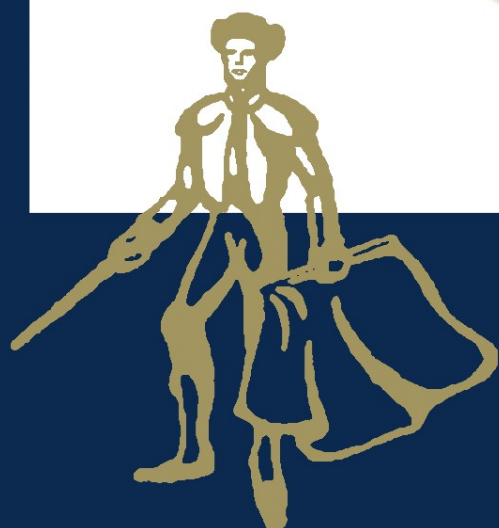


Srichand Hinduja
Lin Li
Editors

Proceedings of the 36th International

MATADOR

Conference



CD-ROM



INCLUDED

 Springer

Proceedings of the 36th International MATADOR Conference

Srichand Hinduja · Lin Li
Editors

Proceedings of the 36th International MATADOR Conference

Srichand Hinduja, PhD, CEng, FCIRP, FIMechE
Lin Li, PhD, CEng, FLIA, FCIRP, FIET

The University of Manchester
School of Mechanical, Aerospace
and Civil Engineering
Sackville Street
Manchester M13 9PL
UK

sri.hinduja@manchester.ac.uk
lin.li@manchester.ac.uk

ISBN 978-1-84996-431-9
DOI 10.1007/978-1-84996-432-6
Springer London Dordrecht Heidelberg New York

e-ISBN 978-1-84996-432-6

British Library Cataloguing in Publication Data
A catalogue record for this book is available from the British Library

Library of Congress Control Number: 2010930009

© Springer-Verlag London Limited 2010

Baytubes is a registered trademark of Bayer MaterialScience AG, 51368 Leverkusen, Germany, www.bayermaterialscience.com

Kistler is a registered trademark of Kistler Holding AG, www.kistler.com

MATLAB is a registered trademark of The MathWorks, Inc., 3 Apple Hill Drive, Natick, MA, 01760-2098 USA, <http://www.mathworks.com>

Mikron is a registered trademark of Mikron Holding AG, Biel, Switzerland, www.mikron.com

PTC and Pro/ENGINEER, are trademarks or registered trademarks of Parametric Technology Corporation or its subsidiaries in the U.S. and in other countries.

Apart from any fair dealing for the purposes of research or private study, or criticism or review, as permitted under the Copyright, Designs and Patents Act 1988, this publication may only be reproduced, stored or transmitted, in any form or by any means, with the prior permission in writing of the publishers, or in the case of reprographic reproduction in accordance with the terms of licences issued by the Copyright Licensing Agency. Enquiries concerning reproduction outside those terms should be sent to the publishers.

The use of registered names, trademarks, etc. in this publication does not imply, even in the absence of a specific statement, that such names are exempt from the relevant laws and regulations and therefore free for general use.

The publisher makes no representation, express or implied, with regard to the accuracy of the information contained in this book and cannot accept any legal responsibility or liability for any errors or omissions that may be made.

Cover design: eStudioCalamar, Figueres/Berlin

Printed on acid-free paper

Springer is part of Springer Science+Business Media (www.springer.com)

Proceedings of
The Thirty-Sixth International

MATADOR

Conference

Organising Committee

Professor S. Hinduja (*Co-Chairman*)

Professor L. Li (*Co-Chairman*)

Dr J. Atkinson

Dr R. Heinemann

Dr K. Kontis

Dr P. Mativenga

Dr J. Methven

Dr A. Pinkerton

Dr M. Sheikh

Dr Z. Wang

The University of Manchester
School of Mechanical, Aerospace and Civil Engineering

International Scientific Committee

Professor J C Aurich, University of Kaiserslautern, Germany
Professor S Blackburn, Birmingham University, UK
Professor M Brandt, RMIT University, Australia
Professor A Bramley, University of Bath, UK
Professor T H C Childs, University of Leeds, UK
Professor K C Fan, National Taiwan University, Taiwan
Professor F Z Fang, Tianjin University, China
Professor D K Harrison, Glasgow Caledonian University, UK
Professor B Hon, University of Liverpool, UK
Professor X Q Jiang, University of Huddersfield, UK
Professor F Klocke, RWTH Aachen, Germany
Professor J P Kruth, Katholieke University Leuven, Belgium
Professor M Kunieda, Tokyo University of Agriculture and Technology, Japan
Dr A Leacock, University of Ulster, UK
Professor M Leu, University of Missouri-Rolla, USA
Professor Y F Lu, University of Nebraska Lincoln, USA
Professor P Maropoulos, University of Bath, UK
Professor J A McGeough, University of Edinburgh, UK
Professor A Y C Nee, National University of Singapore
Professor R Neugebauer, Fraunhofer IWU, Germany
Professor J Ni, University of Michigan, USA
Professor B Rowe, Liverpool John Moores University, UK
Dr T S Sudarshan, Materials Modification Inc., USA
Dr J Summerscales, University of Plymouth, UK
Professor R Teti, University of Naples, Italy
Professor F Vollertsen, BIAS GmbH, Germany
Dr H Y Zheng, SIMTech, Singapore
Professor M L Zhong, Tsinghua University, China

Foreword

It gives us pleasure to introduce the Proceedings for the 36th international MATADOR conference. The Proceedings include 130 refereed papers from several countries on different continents, thus making this Conference truly international.

Since its inception in 1959, the MATADOR conferences have been held at various locations within the United Kingdom and overseas. The last conference was held in Taipei and this conference has reverted back to its “home” city, i.e. Manchester.

The MATADOR conferences in the 1960s dealt with metal working fundamentals in cutting, grinding and forming and the design of machine tools. Since those early days, new areas of research in manufacturing have emerged which therefore have become part of the conference’s scope as well. A substantial part of this conference is devoted to laser material processing especially recent developments in ultra-short pulse laser material processing, hybrid welding, fibre/disk laser applications and additive manufacturing. Other emerging areas that have been addressed in this conference include micro- and nano-manufacture, rapid manufacture, inspection of micro-parts, and sustainable and green engineering. The conference has continued to attract good quality papers from traditional areas such as metal cutting, forming, metrology and grinding.

We would like to express our gratitude to all the members of the Organising Committee and to those members of the International Scientific Committee who kindly refereed the papers. Our special thanks to Dr Robert Heinemann for preparing the Conference Proceedings and to Drs Roger Hannam and Nick Driver for proof reading and formatting the papers. Finally, we are indebted to Ms Janet Adnams and her team from ConferCare for organising this event.

We hope you find the papers interesting and stimulating.

Professors Srichand Hinduja and Lin Li
The University of Manchester, UK
2010

Contents

1 Bio- and Nanotechnology

1-1	Robust Control Strategy of Fluid Dispensing Process for Solid Freeform Fabrication of Tissue Engineered Hydrogel Scaffold M. Vlasea and E. Toyserkani	3
1-2	An innovative approach for the fabrication of highly conductive nanocomposites with different carbon H. K. F. Cheng, N. G. Sahoo, L. Li, S. H. Chan and J. Zhao	9
1-3	Analysis of local field enhancement including tip interaction for the application to nano-manipulation using FDTD calculations B. H. Liu, L. J. Yang, Y. Wang and J. L. Yuan	15

2 Forming

2-1	Numerical Simulation of the Four Roll Bending Process A. G. Leacock, D. McCracken, D. Brown and R. McMurry	21
2-2	Investigation on the Process Parameters and Process Window of Three-Roll-Push-Bending R. Plettker, P. H. Vatter, D. Vipavc, M. Cojutti and H. Hagenah	25
2-3	Casting of Aluminium Alloy Strip by Improved Single-Roll Caster K. Akitsu, T. Haga, S. Kumai and H. Watari	29
2-4	Casting of Al-Si-SiCp composite alloy strip by a vertical type twin roll caster H. Harada and T. Haga	33
2-5	Casting of aluminium alloy clad strip using a vertical type tandem twin roll caster R. Nakamura, T. Haga, S. Kumai and H. Watari	37
2-6	Micro-forming of aluminum alloy by cold rolling T. Haga, K. Inoue, H. Harada and R. Nakamura	41
2-7	Rapid shape measurement of micro deep drawing parts by means of digital holographic contouring N. Wang, C. v. Kopylow and C. Falldorf	45
2-8	Fracture Limits of Metal Foils in Micro Forming F. Vollertsen, Z. Hu, H. Wielage and L. Blaurock	49
2-9	A theoretical model for the velocity field of the extrusion of shaped sections taking into account the variation of the axial component P. Farahmand and K. Abrinia	53

2-10	A theoretical model for the material flow for the forward extrusion of complicated and non-symmetric sections M. Ghorbani and K. Abrinia	59
2-11	An Optimization Algorithm for Improving Combined Multi-Stage Deep-Drawing and Ironing Processes of Axisymmetric Components. Analysis and Experimentation F. J. Ramírez, R. Domingo and M. A. Sebastián	63
2-12	Nanofinishing Process for 3D Freeform Surfaces Using Ball End MR Finishing Tool A. K. Singh, S. Jha and P. M. Pandey	67
2-13	Pressure Distribution in Cold Rolling of Turbo-engine Thin Compressor Blades M. Sedighi and M. Mahmoodi	71
2-14	Determination of the duty cycle in thermoset pultrusion W. A. Khan and J. Methven	75
2-15	Development of New Press-Forming Process for a Screw-Threaded Fuel Filler Pipe N. Kamei, Y. Kawamura, T. Nagamachi and H. Watari	79
2-16	Roller Hemming: A New Simulation Model for the Automotive Industry A. Arroyo, I. Pérez, M. Gutierrez, J. Bahillo and H. Toja	83
2-17	Control of the uniformity of direct electrical heating for Rotational Moulding W. A. Khan and J. Methven	87

3 Grinding

3-1	High Efficiency Deep Grinding, an Application with conventional wheels A. D. L. Batako	93
3-2	Detection of High and Low Temperature in the Grinding Zone using Laser Irradiation Technique A. Mohammed, J. Folkes and X. Chen	97
3-3	Investigation of Influences of Wheel Speed on Root Geometrical Dimension of Gas Turbine Blade A. R. Fazeli Nahrekhalaji, M. Sohrabi and S. M. Izadi	101
3-4	Ultra-fine Finishing of Metallic surfaces with Ice Bonded Abrasive Polishing Process R. Mohan and N. Ramesh Babu	105
3-5	Plane surface grinding with application of Minimum Quantity Lubrication (MQL) L. M. Barczak and A. D. L. Batako	109
3-6	Study of the Behavior of Air Flow around a Grinding Wheel under the Application of Pneumatic Barrier B. Mandal, R. Singh, S. Das and S. Banerjee	113

4 Manufacturing Systems and Management

4-1	A cutting plane algorithm for solving single machine scheduling problems with uncertain sequence-dependent setup times S.H. Zegordi, E. Nikbakhsh and M. Modarres	119
4-2	A Knowledge-Based Engineering System for Assembly Sequence Planning Y. Y. Hsu, W. C. Chen, P. H. Tai and Y. T. Tsai	123

4-3	Product Family Modeling and Optimization Driven by Customer Requirements	
Y. Su	127
4-4	Transparency in Production by Monitoring the Condition of Molds, Dies and Machines	
R. Schmitt, M. Harding, A. Pavim and Y. Cai	131
4-5	Simulation Modelling of Product-Service Systems: the Missing Link	
S. Phumbua and B. Tjahjono	135
4-6	RFID Deployment at an Airport: A Simulation Study	
C. Saygin and B. Natarajan	139

5 Design and Structures

5-1	Failure knowledge based decision-making in product quality	
W. Dai, P.G. Maropoulos and X.Q. Tang	145
5-2	Predicting the End-Of-Life of Defence Electronic Systems at the Conceptual Design Stage	
W. M. Cheung, P. W. Griffin, L. B. Newnes, A. R. Mileham, R. Marsh and J. D. Lanham	149
5-3	Design of Multi-Span Microfixturing Cell for Parallel Assembly of Microparts Using Electrothermally Actuated Microclamps	
M. Vismeh, M. Hamed and P. Salimi	153
5-4	An Evaluation Method Based on Multiple Quality Characteristics for CNC Machining Center using Fuzzy Matter Element	
G. B. Zhang, J. H. Pang, G. H. Chen, X. L. Ren and Y. Ran	157
5-5	Design of a Meso-scale 3-axis Milling with Nanometer Accuracy	
K. C. Fan, F. J. Shiou, K. M. Pan, Z. Y. Ke, Y. J. Lin and K. J. Wu	161
5-6	A Novel Concept to Design Machine Tool Structures using Multifunctional Materials	
F. Aggogeri, A. Merlo and N. Pellegrini	165
5-7	Design Synthesis of a three legged SPS Parallel Manipulator	
A. Khalid and S. Mekid	169
5-8	Piezo-Metal-Composites as Smart Structures	
R. Neugebauer, L. Lachmann, W.-G. Drossel, S. Hensel, B. Kranz and M. Nestler	175
5-9	A Methodology for Engineering Design Change Management Using Modelling and Problem Solving Techniques	
G. Fei, J. Gao, O. O. Owodunni and X. Q. Tang	179
5-10	Modeling and Analysis of the strength of Adhesively Bond CFRP-Aluminium T-joints	
H. Cheng, K. F. Zhang and Y. Li	183

6 Metal Cutting

6-1	Modelling of Machine Tapping with Straight Flute Taps	
N. M. Chen and A. J. R. Smith	189
6-2	High Speed MQL Drilling of Titanium Alloy using Synthetic Ester and Palm Oil	
E. A. Rahim and H. Sasahara	193

6-3	Estimation of minimum chip thickness for multi-phase steel using acoustic emission signals A. J. Mian, N. Driver and P. T. Mativenga	197
6-4	Extension of a Simple Predictive Model for Orthogonal Cutting to Include Flow below the Cutting Edge G. P. Zou, I. Yellowley and R. J. Seethaler	201
6-5	Drilling Carbon Fiber Reinforced Plastics with Diamond Coated Carbide Cutting Tools Y. Karpas, N. Camuşcu, A. Kılıç, F. Sonat, B. Değer and O. Bahtiyar.....	205
6-6	Research on 3D Groove for Cutting Heat Distribution of Coated Carbide Milling Inserts Y. He, C. J. Li and J. H. Zhou.....	209
6-7	In-Process Monitoring and Prediction of Surface Roughness on CNC Turning by using Response Surface Analysis T. Somkiat, A. Somchart and T. Sirichan	213
6-8	Influence of Edge Beveling on Burr Formation in Face Milling of an Aluminium Alloy P. P. Saha and S. Das	217
6-9	Experimental Investigations on Drilling of Woven CFRP Epoxy Laminates: The Effect of Pilot-hole or Drill Chisel Edge on Delamination A. Faraz and D. Biermann	223
6-10	Modelling of hard turning: effect of tool geometry on cutting force Z.Y. Shi, Z.Q. Liu and C.M. Cao.....	227
6-11	Selection of optimal process parameters for gear hobbing under cold air minimum quantity lubrication cutting environment G. Zhang and H. Wei.....	231
6-12	The Formation of Adiabatic Shear Bands as a result of Cryogenic CNC Machining of Elastomers V. G. Dhokia S. T. Newman, P. Crabtree and M. P. Ansell	235
6-13	Analysis of process parameters in the micromachining of Ti-6Al-4V alloy S. I. Jaffery, N. Driver and P. T. Mativenga	239
6-14	Tool Orientation Effects on the Geometry of 5-axis Ball-end Milling E. Ozturk and E. Budak	243
6-15	On deposition and characterisation of MoS _x -Ti multilayer coating and performance evaluation in dry turning of aluminium alloy and steel S. Gangopadhyay, R. Acharya, A. K. Chattopadhyay and S. Paul.....	247
6-16	Novel Developments in Cutting and Grinding of Preheated Billets O. Mgaloblishvili, K. Inasharidze and M. Shvangiradze	251
6-17	Investigation of the Cutting Forces and Tool Wear in Laser Assisted Milling of Ti6Al4V Alloy S. Sun, M. Brandt, J. E. Barnes and M. S. Dargusch	255
6-18	Numerical Techniques for CAM Strategies for Machining of Mould and Die R. Ur-Rehman, C. Richterich, K. Arntz and F. Klocke.....	259

7 Welding

7-1	Net Shape Laser Butt Welding of Mild Steel Sheets R. M. Eghlio, A. J. Pinkerton and L. Li	267
-----	--	-----

7-2	Humping Modelling in Deep Penetration Laser Welding E. H. Amara	271
7-3	Keyholing or Conduction – Prediction of Laser Penetration Depth D. B. Hann, J. Iammi and J. Folkes.....	275
7-4	Dual Focus Nd:YAG Laser Welding of Titanium Alloys J. E. Blackburn, C. M. Allen, P. A. Hilton and L. Li	279
7-5	Product design for welding Antti Salminen, Jouko Kara, Marko Vattulainen, Aki Piironen.....	283
7-6	Studies on the Effect of Process Parameters on the Shear Performance of Joints of Aluminium Alloy Produced by Adhesive Joining, Spot Welding and Weld-Bonding M. D. Faseeulla Khan, D. K. Dwived and P. K. Ghosh	287
7-7	Influence of Electron Beam Local Annealing on the Residual Stresses for the joints with Electron Beam Welding of near α titanium alloy P. F. Fu, G. Fu, S. L. Gong, Y. J. Wang	293
7-8	Similar and Dissimilar Welding of Ductile Cast Iron M. El-Shennawy and A. A. Omar	297

8 Metrology

8-1	Recognition of Contact States in Robotized Assembly Using Qualitative Wavelet Based Features and Support Vector Machines Z. Jakovljevic and P. B. Petrovic	305
8-2	Linear Axes Performance Check on a Five-Axis Machine Tool by Probing an Uncalibrated Artefact T. Erkan and J. R.R. Mayer.....	309
8-3	A Holistic Approach to Quantifying and Controlling the Accuracy, Performance and Availability of Machine Tools P. Willoughby, M. Verma, A. P. Longstaff and S. Fletcher.....	313
8-4	Development of a Small 3-axis Angular Sensor for Real-time Abbé Error Compensation on Numerically Controlled Machine Tools K. C. Fan, S. M. Chen and S. Y. Lin.....	317
8-5	Micro-scale co-ordinate metrology at the National Physical Laboratory J. D. Claverley and R. K. Leach.....	323
8-6	Coating Thickness Measurement P. May and E. Zhou	327
8-7	Digital Alignment of a reconstructed Hologram for Measurement of Deterioration of Tools S. Huferath-von Luepke, T. Baumbach, E. Kolenovic, C. Falldorf and C. von Kopylow	331
8-8	Implementation of decision rules for CMM sampling in a KBE system B. J. Álvarez, E. Cuesta, S. Martínez, J. Barreiro and P. Fernández.....	335
8-9	Machine Vision System for Inline Inspection in Carbide Insert Production R. Schmitt, I. Scholl, Y. Cai, J. Xia, P. Dziwoki, M. Harding and A. Pavim	339

8-10	Assembly Tolerance Analysis including Flatness: Using Virtual Mating Plane T. Shuailong, Y. Jianfeng, L. Yuan and Y. Haicheng.....	343
8-11	Inspection of defects in CFRP-Foam Layered structure composite plates of aerospace materials using lock-in thermography L. Junyan, W. Song, W. Yang and W. Zhilan.....	347
8-12	Image Processing Methods for Online Measurement in Radial-Axial Ring Rolling H. Meier, J. Briselat, R. Hammelmann and H. Flick.....	355
8-13	Cognitive Production Metrology: A new concept for flexibly attending the inspection requirements of small series production T. Pfeifer, R. Schmitt, A. Pavim, M. Stemmer, M. Roloff and C. Schneider and M. Doro.....	359
8-14	The Metrology Enhanced Tooling for Aerospace (META) Framework O. C. Martin, J. E. Muelaner, D. Tomlinson, A. Kayani and P. G. Maropoulos.....	363

9 Rapid Prototyping

9-1	Application of 3D Printing for the Rapid Tooling of Thermoforming Moulds S. Junk, J. Sämman-Sun and M. Niederhofer.....	369
9-2	Printing Characteristics and Performance of Polymer Thick Film Inks for Direct Write Applications L. Hao, S. Raja, M. Sloan, R. Robinson, J. McDonald, J. Sidhu, C. Tuck and R. Hague.....	373
9-3	Effect of workpiece volume on statistically controlled rapid casting solution of aluminum alloys using three dimensional printing R. Singh and R. Singh.....	377
9-4	Using Additive Manufacturing Effectively: A CAD Tool to Support Decision Making P. C. Smith and A. E. W. Rennie.....	381
9-5	Dynamic strength and fracture toughness analysis of beam melted parts J. T. Sehrt and G. Witt.....	385
9-6	An additive method for photopatterning of metals on flexible substrates J. H. G. Ng, D. E. G. Watson, J. Sigwarth, A. McCarthy, H. Suyal, D. P. Hand, T. Y. Hin and M. P. Y. Desmulliez..	389

10 Green Engineering

10-1	An investigation of the EREE-based low carbon manufacturing on CNC machine S. Tridech and K. Cheng.....	395
10-2	Reduced Energy Consumption by Adapted Process Chains E. Brinksmeier, D. Meyer, M. Garbrecht, J.-W. Huntemann and R. Larek.....	401
10-3	Model-Based Predictive Consumption of Compressed Air for Electro-Pneumatic Systems P. Harris, G. E. O'Donnell and T. Whelan.....	405
10-4	Schottky Solar Cells Based on Graphene and Silicon X. M. Li, H. W. Zhu, K. L. Wang, J. Q. Wei, C. Y. Li and D. H. Wu.....	409
10-5	Variation of Engineer Performance and Emissions Using Ethanol Blends A. A. Abuhabaya and J. D. Feldhouse.....	413

11 ECM and EDM

11-1	EDM performance is affected by the white layer	
	J. D. Marafona	419
11-2	Development of a hybrid method for electrically dressing metal-bonded diamond grinding wheels	
	A. Sudiarmo and J. Atkinson.....	425
11-3	Robust Parameter Design and Multi-Objective Optimization of Electro-Discharge Diamond Face Grinding of HSS	
	G. K. Singh, V. Yadava and R. Kumar	429
11-4	Analysis of Non-limiting Current Resistance and Isopulse Power Supply for WEDM	
	C. J. Li, Y. F. Guo, J. C. Bai and Z. S. Lu	435
11-5	Some Aspects of Surface Integrity Study of Electro Discharge Machined Inconel 718	
	S. Rajesha, A. K. Sharma, Pradeep Kumar	439

12 Laser Technology – Cladding and Deposition

12-1	Advances in Direct Metal Deposition	
	J. Mazumder and L. Song	447
12-2	Effect of processing parameters in manufacturing of 3D parts through laser direct metal deposition	
	M. J. Tobar J. M. Amado, J. Lamas and A. Yáñez	451
12-3	A numerical investigation of powder heating in coaxial laser metal deposition	
	J. Ibarra-Medina and A. J. Pinkerton	455
12-4	Laser cladding of NiCr-WC metal matrix composites: dependence on the matrix composition	
	J. M. Amado, M. J. Tobar and A. Yáñez	459

13 Laser Technology – Bio and Micro System Processes

13-1	Wettability analysis of CO ₂ laser surface patterned nylon 6,6 samples soaked in simulated body fluid (SBF)	
	D.G. Waugh and J. Lawrence	465
13-2	Fast parallel diffractive multi-beam laser surface micro-structuring	
	Z. Kuang, D. Liu, W. Perrie, J. Cheng, S. P. Edwardson, G. Dearden and K. G. Watkins	469
13-3	Effect of different processing parameters of Ti:Sapphire femtosecond laser on human dental dentine	
	L. Ji, L. Li, H. Devlin, Z. Liu, D. Whitehead, Z. Wang, W. Wang and J. Jiao	473
13-4	Forming microchannels on a glass substrate by CO ₂ laser	
	Z. K. Wang, H. Y. Zheng, V. C. Tan and C. Y. Lam.....	477
13-5	Influence of pressure on aluminium plasma expansion produced by a nanosecond laser pulse: a numerical study	
	S. Aggoune, F. Vidal and E. H. Amara.....	481

14 Laser Technology – Powder Bed Processes

14-1	Consolidation behaviour and microstructure characteristics of pure aluminium and alloy powders following Selective Laser Melting processing P. G. E. Jerrard, L. Hao, S. Dadbakhsh and K. E. Evans	487
14-2	Influence of distortion on part accuracy of Indirect Metal Selective Laser Sintering K. Zakaria and K. W. Dalgarno	491
14-3	Surface Roughness Studies in Selective Laser Sintering of Glass filled Polyamide V. Srivastava, S. K. Parida and P. M. Pandey.....	495

15 Laser Technology – Forming

15-1	Finite Element Modelling of the Laser Forming of AISI 1010 Steel J. Griffiths, S. P. Edwardson, G. Dearden and K. G. Watkins	503
15-2	The effect of laser beam geometries on laser forming of sheet metal S. Jamil, M.A. Sheikh and L. Li	509
15-3	Towards Controlled 3D Laser Forming S.P. Edwardson, J. Griffiths, G. Dearden and K. G. Watkins	513

16 Laser Technology – Surface Modification

16-1	Fracture Toughness Modifications By Means of CO ₂ Laser Beam Surface Processing of a Silicon Nitride Engineering Ceramic P. P. Shukla and J. Lawrence	519
16-2	Surface oxygen diffusion hardening of TA2 pure titanium by pulsed Nd: YAG laser under different gas atmosphere C. Chen, M. Zhang, S. Zahng, Q. Chang and H. Ma	523
16-3	Investigation on the Key Techniques of Confined Medium and Coating Layer for Laser Shock Processing on Aeroengine Blade Z. Che, S. Gong, S. Zou, Z. Cao and Q. Fei.....	527
16-4	Improvement of Corrosion Performance of HVOF MMC Coatings by Laser Surface Treatment M. Rakhes, E. Koroleva and Z. Liu	531
16-5	Numerical and Experimental Studies on the Laser Melting of Steel Plate Surfaces I. A. Roberts, C. J. Wang, K. A. Kibble, M. Stanford and D. J. Mynors	535
16-6	Analysis of temperature distribution during fibre laser surface treatment of a zirconia engineering ceramic P. P. Shukla and J. Lawrence	539

17 Laser Technology – Micro and Nano Processes

17-1	WC Nano powder cold planting via laser shock peening onto aluminium/magnesium alloy surfaces M. Zhong, L. Lv, C. Dong, R. Zhu, H. Zhang and W. Liu	545
------	---	-----

17-2	Femtosecond laser induced two-photon polymerization of dielectric-loaded surface plasmon-polariton nanowaveguides Y. Li, Z. Liu, H. Cui, H. Yang and Q. Gong	549
17-3	Real-time control of polarization in ultra-short pulse laser micro-processing O. J. Allegre, W. Perrie, K. Bauchert, D. Liu, S. P. Edwardson, G. Dearden and K. G. Watkins	553

18 Laser Technology – Industrial Applications

18-1	Laser Inertial Fusion-based Energy (LIFE) - Developing Manufacturing Technology for low cost and high volume fusion fuel is critical to our future energy needs K. Carlisle and R. R. Miles	559
18-2	Initial Strategies for 3D RAP Processing of Optical Surfaces Based on a Temperature Adaptation Approach M. Castelli, R. Jourdain, G. McMeeking, P. Morantz, P. Shore, D. Proscia and P. Subrahmanyam	569
18-3	Wireless & Powerless Laser Welding Monitoring System G D'Angelo	573
18-4	System Design for Laser Assisted Milling of Complex Parts X. F. Wu, Y. Wang and H.Z. Zhang	577
18-5	Direct Laser Writing System of Mask for Integrated Photonics Devices S. Messaoud, A. Allam, F. Siserir, Y. Bouceta, T. Kerdja, D. Ouadjaout and T. Touam	581

19 Laser Technology – Welding

19-1	Direct Laser Welding for Al- Li Alloy Plate without the Cleaning of Surface Film C. Kai, Y. Wuxiong and X. Rongshi	587
19-2	Characteristics of keyhole and molten pool during laser welding of TC4 Ti-alloy D. Aiqin and C. Li	591
19-3	Typical Joint Defects in Laser Welding of Aluminium-Lithium Alloy J. Yang, S. Gang, X. Li, L. Chen and F. Xu	595

Robust Control Strategy of Fluid Dispensing Process for Solid Freeform Fabrication of Tissue Engineered Hydrogel Scaffold

M. Vlasea¹, E. Toyserkani²

¹ University of Waterloo, 200 University Ave. West, Waterloo, Ontario, Canada

² University of Waterloo, 200 University Ave. West, Waterloo, Ontario, Canada

Abstract. A recognized approach in tissue engineering is the design of biocompatible and bioresorbable 3D scaffolds that can be used as templates for growing neo-tissues. Depending on the target tissue, a range of hydrogel polymers may be used to construct anatomically accurate scaffolds using three dimensional solid freeform fabrication approaches. This paper focuses on the modeling, simulation and preliminary experimental verification of a robust real-time control protocol for a positive displacement fluid dispensing process to be used in the fabrication of hydrogel scaffolds with specified feature sizes and controlled internal architecture. The actual fluid dispensing process can be characterized as a non-linear time-varying system with a high dependency on fluid properties, which are often unknown and inherently non-linear. To develop a control paradigm, an approximate analytical model is used to estimate the fully developed laminar flow of an unknown fluid through a cylindrical geometry. Experimental data is used offline to estimate the model coefficients. The initial estimated model is used to develop a control scheme for tuning the hydrogel flow through the deposition nozzle. The developed control strategy is then experimentally tested to investigate and quantify the performance capabilities of the fluid dispensing process.

Keywords: Solid freeform fabrication, fluid dispensing control, scaffold design, tissue engineering.

1. Introduction

One of the main areas of interest in biomedical engineering is the development of artificial organs, tissues or compatible implants that can help patients overcome various medical conditions. This field is highly interdisciplinary, spanning knowledge from a broad range of areas such as engineering, medical, biological sciences, and ethics. Tissue engineering in particular focuses on developing a range of biological implants that can replace, ameliorate or regenerate the target damaged tissue [1]. One current area of research in tissue engineering is the design of biocompatible and bioresorbable scaffold implants [2] that can be seeded with cells cultured from the target patient to achieve a neo-tissue that can be used to replace the existing damaged or diseased tissue. The traditional approach in replacing tissue or organs is to use artificial materials,

prosthetics, donor autologous tissue grafts or organs to partially or fully replace the defect. The downside to these methods is the high risk of implant rejection, inflammatory responses and subsequent surgeries for implant replacement and readjustment [3]. These traditional methods also raise serious concerns over the morbidity of the donor site, the availability of donor healthy tissue to form an anatomically accurate graft as well as the availability of donor organs [4]. The scaffold approach offers the possibility of producing 3D anatomically accurate implants that can be seeded with the patients' own cells, thus avoiding the need for donor autologous grafts or transplant organs. The engineered scaffold, once implanted, will be gradually bioresorbed and replaced with healthy new tissue. Ideally, this methodology would offer minimal risk of graft rejection and follow-up surgery procedures since it uses the patient's own cultured cells.

Tissue engineered scaffold design has recently gained great momentum, as various research groups are exploring different approaches to build biocompatible scaffolds. Some of the most popular technologies in this field are Solvent Casting with Salt Leaching [5-7], Emulsion Freeze-Drying [8,9], Thermally Induced Phase Separation [10], Electrospinning of Nano-Fibres [11-13], and Direct Moulding [14, 15]. These methods may not accommodate for designing implants with high degree of control over localized pore morphology and porosity within the same scaffold structure [16]. Solid freeform fabrication (SFF), as an advanced layered manufacturing technique, offers the possibility of producing an implant with a highly controlled internal architecture in terms of pore spatial distribution, size, orientation, interconnectivity and varying layer characteristics. Such advantages are desirable for building structures that can support multiple tissue types within the same scaffold configuration [17]. There are various recently developed SFF techniques (Figure 1) that can be used to construct implants depending on the desired scaffold materials and the required part characteristics.

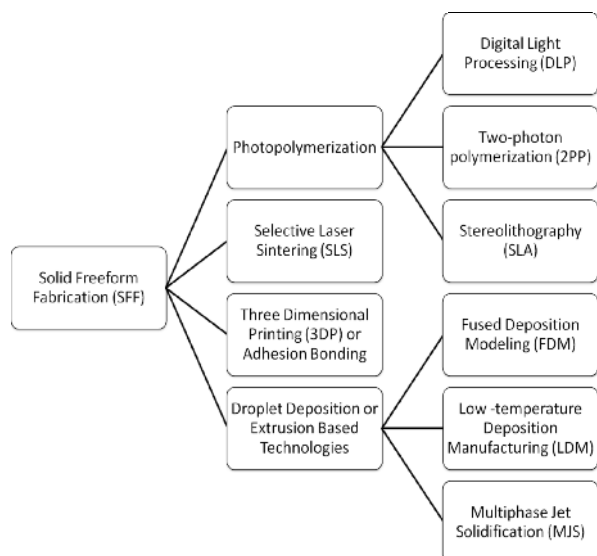


Fig. 1. SFF Classification

The purpose of this paper is to discuss a positive displacement fluid dispensing method for manufacturing of biocompatible and bioresorbable hydrogel tissue engineered scaffolds via Extrusion-Based SFF. The hydrogel scaffold is formed through a process called Fused Deposition Modeling (FDM) where the material is extruded through a heated nozzle. The deposition head is displaced in the x-y plane to produce one scaffold layer following a specific geometric path based on CAD data. The layer is then displaced in the z-direction, and a new layer can be built sequentially [18]. The molten material deposited onto each layer will soften the material deposited in the previous layer. Upon solidification, the two layers will be joined together [19]. The material is dispensed through the nozzle by the motion of a motor-actuated piston.

For this particular application, volumes of the liquid in the microliter range have to be delivered accurately. In this case, the actual fluid dispensing process can be characterized as a non-linear time-varying system with a high dependency on non-linear fluid properties. To develop a control paradigm, an approximate analytical model (i.e. grey model) is used to estimate the fully developed laminar flow of an unknown fluid through a cylindrical geometry. This model is then adapted to the particular fluid dispensing mechanism used for tissue scaffold manufacturing. Experimental data is collected and analyzed to establish the validity of the proposed model. The initial estimated model is used to develop an appropriate control scheme for controlling the hydrogel flow through the deposition nozzle. The developed control strategy is then experimentally tested to investigate and quantify the performance capabilities of the fluid dispensing process in terms of feature size, flow continuity and uniformity of the deposited hydrogel.

2. Apparatus

The hydrogel deposition system interprets CAD data pertinent to the part to convey layer characteristics to the deposition head. The required porosity, pore interconnectivity, distribution and size are translated into layer characteristics such as path trajectories, motion profiles and deposition flow characteristics. The deposition mechanism is driven by a motor-actuated piston. Figure 2 summarizes the system overview.

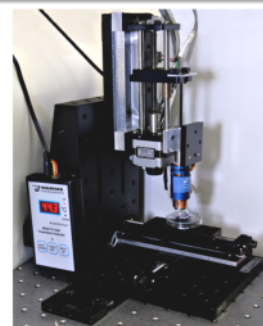
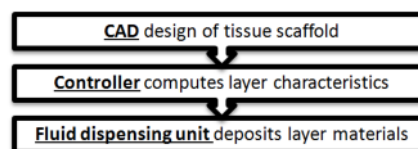


Fig. 2. System Overview

The fluid dispensing unit is temperature controlled. Ceramic deposition nozzles (1573-xx-437GM, Gaiser Tool Company, Ventura, US) have been adapted for this application to provide features as small as 50 μ m. Temperature control is achieved using a heating jacket (SWS10, Warner Instruments Inc., Hamden, US) with a feedback controller (TC-124, Warner Instruments Inc., Hamden, US). Motion feedback control has been achieved in LabVIEW (National Instruments, Austin, US) using the modular pump apparatus (70-2225 UL Modular Pump, Harvard Apparatus, Quebec, Canada). A load cell (FSG15N1A, Honeywell, Mississauga, Canada) was used to measure the weight of the fluid deposited.

Table 1 Dimensional Characteristics of Dispensing Unit

Description	Value
Dispenser piston diameter	D_p 3.26mm
Dispenser capacity	C 500 μ L
Needle length	L_n 10mm
Needle inner diameter	D_n 50 μ m-200 μ m
Hydrogel density	ρ 1005 kg/m ³
Hydrogel bulk modulus(at 44°C)	B 1.01E9Pa
Yield stress (at 44°C)	τ_0 58.08 Pa·s ⁿ
Consistency index (at 44°C)	K 207.70Pa

Table 1 lists the dimensional characteristics of the dispensing unit and fluid characteristics [28] as used in the modeling and experimental sections. The fluid used in these experiments is 2% agarose solution (courtesy of Mount Sinai Hospital, Toronto, Canada).

3. Modeling Approach

Successful control strategies rely on the appropriate understanding of the physical phenomena governing a system. Empirical, computational or analytical modeling are particular approaches used to achieve this goal. The complexity of the problem arises when dealing with fluid flows in the μL range, where fluid compressibility and fluid flow behaviour may significantly affect the resulting volumetric flow rate out of the dispensing nozzle [20]. The simplest approach is to assume that the fluid behaviour is strictly Newtonian as described by Vozzi et al [21], which render the flow equations quite simple. This assumption however may not be applicable to polymeric materials, where non-Newtonian effects need to be considered. To incorporate non-Newtonian effects, West et al [22] developed an empirical black-box model using autoregressive methods to model the volumetric output from a dispenser. Other empirical methods are described by Holsworth et al [23]. One of the major disadvantages to empirical methods is that the model needs to be re-evaluated if system parameters change. Non-Newtonian effects in fluid dispensing have also been modeled for time-invariant [24-26] and time-variant systems [27].

For the dispensing system considered in this study, it is assumed that the process is isothermal, fluid properties are time-independent and the flow is fully developed laminar throughout the dispensing barrel and needle. The analytical model used to approximate the dispensing process first considers the pressure build-up inside the syringe and then flow rate of fluid leaving the nozzle [25]. The model developed by Chen et al [25] is easy to adapt to this particular system and it is also relatively easy to implement in a programming environment. The following equation describes the pressure developed in the syringe for a compressible fluid under the assumption that non-Newtonian effects are neglected if the dispensing barrel is large enough [25]

$$A_p \dot{X} + Q = \frac{V_o - A_p X}{B} \dot{P} \quad (3.1)$$

where A_p is the piston area, X is the piston position, Q is the flow leaving the nozzle, V_o is the initial volume of fluid in the syringe and B is the fluid bulk modulus. The flow rate of fluid from the dispensing nozzle (Equation (3.3)) is developed by using the Generalized Power Law formulation (Equation (3.2)). [25] Equation (3.3) has been discretized and adapted to the dispensing mechanism used in this paper.

$$\tau = \tau_o + K\dot{\gamma}^n \quad (3.2)$$

$$\frac{Q(s)}{P(s)} = \frac{Q_u}{\rho L_n \frac{Q_u}{A_n} s + 1} \quad (3.3)$$

$$Q[k+1] = e^{-\frac{T_s A_n}{Q_u \rho L_n}} Q[k] + \frac{A_n}{\rho L_n} P[k] \quad (3.4)$$

In these equations, τ is the shear stress at the needle wall, τ_o is the yield stress, γ is the shear, K is the consistency index, n is the flow behaviour index, ρ is the fluid density and Q_u is the fluid flow in steady state under a unit pressure as described in [25, 20]. Figure 3 and Figure 4 show simulation results in terms of pressure build-up inside the barrel and mass flow rate leaving the nozzle at various piston actuation velocities. The appropriate fluid properties used for this simulation are described in Table 1 (for fluid temperature at 44°C).

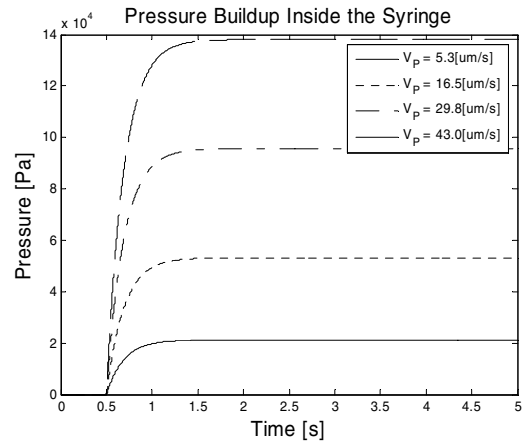


Fig. 3. Simulated barrel gage pressure vs. piston velocity

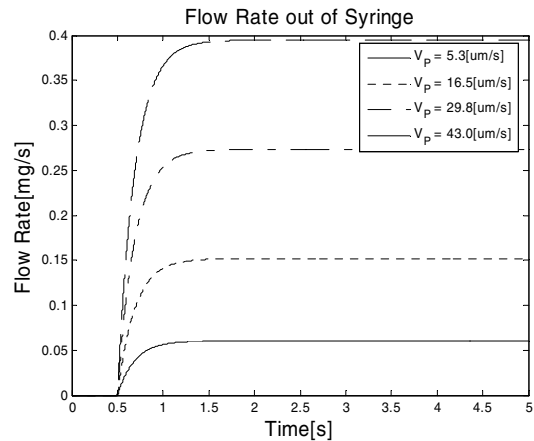


Fig. 4. Simulated nozzle flow rate vs. piston velocity

It can be seen that both pressure and flow have damped second order behaviours and have transient components. The system latency may produce significant errors if the system is required to have a fast response.

4. Experimental Model Validation

The model described in the previous section has not been validated to date. In this work, the model validation was carried out by injecting fluid under a range of piston velocities. The experimental and modeling test trials were conducted under the same geometrical and physical conditions summarized in Table 1. The results are summarized in Figure 5. The simulation data reflects the flow at steady state for each actuation velocity. The experimental flow is obtained measuring the weight of injected fluid at steady state over a period of 200 seconds. The fluid injection temperature was kept at 44°C. The experiment was conducted at room temperature. This result reflects the average flow and is considered to be equivalent to the steady state simulated flow.

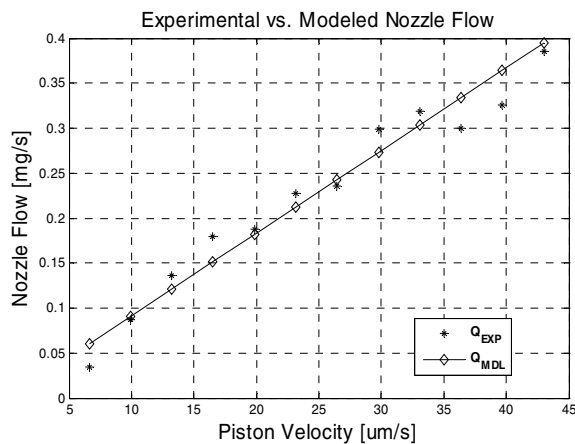


Fig. 5. Experimental vs. Modeling Results

The experimental results closely follow the same general trend as the simulated results. There are noticeable deviations when increasing the piston velocity past 35 $\mu\text{m/s}$. At higher piston velocities, the experimental results are noticeably smaller than the simulated results. When the fluid flow is higher, there is a greater chance of droplet accumulation on the nozzle; therefore some of the injected fluid mass will not be sensed by the load cell. Figure 6 illustrates an example of a deposition pattern that was deposited with a 200 μm nozzle. The agarose was stained with a green pigment. The tracks were deposited 1mm center-to-center distance apart.

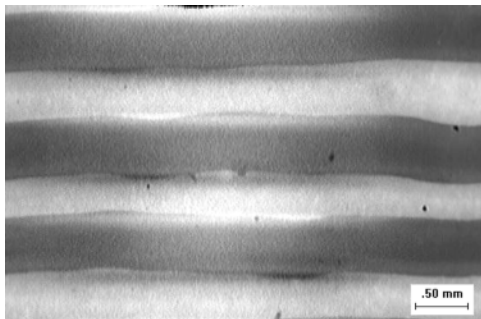


Fig. 6. Experimental deposition pattern

5. Future Control Strategy

Based on the proposed modeling approach, the fluid dispensing mechanism can be approximated to a second order system. Using this methodology, a simple PID controller can be utilized to enhance the capability of the system. A major difficulty arises because it is hard to close the control loop by using flow measurements. The proposed approach is to close the feedback loop using pressure sensor measurements. The idea is that flow control can be directly achieved through fluid pressure control. The proposed system will incorporate a small pressure sensor to close the control loop (EPIH-L1, Hoskin Scientific, Burlington, Canada). This system is currently under investigation. In a simple simulation, it can be seen from Figure 7 that the closed loop performance is enhanced over the open loop case. It is necessary to further investigate tuning capabilities and the experimental feasibility of using this control approach. This control strategy can be applied to other desired material such as collagen. The mechanical properties of the scaffold constructed using this system will be evaluated in terms of shrinkage, effect of temperature, humidity, and deposition patterns on mechanical strength and material integrity. The scaffolds will be evaluated in vitro to quantify the effect of this manufacturing approach on cell migration, cell attachment and proliferation.

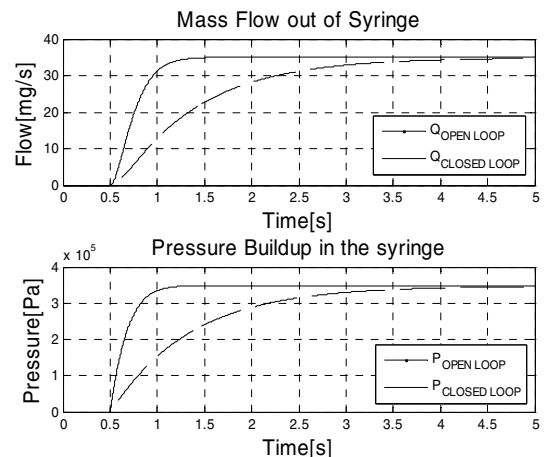


Fig. 7. Simulation results with controller feedback

6. Conclusions

The hydrogel dispensing process is a time-varying nonlinear system. The model describing the physical behaviour of the dispensing process can be successfully approximated using an analytical form by considering compressibility effects in the dispensing syringe barrel and non-Newtonian effects in the dispensing nozzle. The results from experimental results are conclusive with the described model. A proposed control methodology is to use pressure feedback measurements to improve the

system performance. The proposed PID control scheme is under further investigation to establish its feasibility and to fine-tune the control parameters.

References

- [1] Lagner R, Vacanti JP, (1993) Tissue engineering. *Science* 260:920-926
- [2] Vert M, Li MS, Spenlehauer G, Guerin P, (1992) Bioresorbability and biocompatibility of aliphatic polyesters. *J Mater Sci* 3:432-46
- [3] Gorbet MB, Sefton MV, (2004) Biomaterial-associated thrombosis: roles of coagulation factors, complement, platelets and leukocytes. *Biomaterials* 25: 5681-5703
- [4] Outerbridge HK, Outerbridge AR, Outerbridge RE, (1995) The use of a lateral patellar autologous graft for the repair of a large osteochondral defect in the knee. *Journal of Bone and Joint Surgery* 77-A:65-72
- [5] Mikos AG, Sarakinos G, Leite SM, Vacanti JP, Langer R (1993) Laminated three-dimensional biodegradable foams for use in tissue engineering. *Biomaterials* 14: 323-330
- [6] Kima SS, Pak MS, Jeon O, Choi CY, Kima BS (2006) Poly(lactide-co-glycolide)/hydroxyapatite composite scaffolds for bone tissue engineering. *Biomaterials* 27:1399-1409
- [7] Cao Y, Mitchell G, Messina A, Priced L, Thompson E, Penington A, Morrison W, O'Connor A, Stevens G, Copper-White J (2006) The influence of architecture on degradation and tissue ingrowth into three-dimensional poly(lactic-co-glycolic acid) scaffolds in vitro and in vivo. *Biomaterials* 27: 2854-2864
- [8] Wang M (2006) Composite Scaffolds for Bone Tissue Engineering. *American Journal of Biochemistry and Biotechnology* 2: 80-84
- [9] Sultana n, Wang M, (2008) Fabrication of HA/PHBV composite scaffolds through the emulsion freezing/freezing-drying process and characterisation of the scaffolds. *J Mater Sci: Mater Med* 19: 2555-2561
- [10] Wei G, Ma PX, (2004) Structure and properties of nano-hydroxyapatite/polymer composite scaffolds for bone tissue engineering. *Biomaterials* 25: 4749-4757
- [11] Yoshimoto H, Shina YM, Teraia H, Vacanti JP, (2003) A biodegradable nanofiber scaffold by Electrospinning and its potential for bone tissue engineering. *Biomaterials* 24: 2077-2082
- [12] Li C, Vepari C, Jin HJ, Kim HJ, Kaplan DL, (2006) Electrospun silk-BMP-2 scaffolds for bone tissue engineering. *Biomaterials* 27: 3115-3124
- [13] Shin M, Yoshimoto H, Vacanti JP, (2004) In Vivo Bone Tissue Engineering using mesenchymal stem cells on a novel electrospun nanofibrous scaffold. *Tissue Engineering* 10(1-2):33-41
- [14] Gomes ME, Riberio AS, Malafaya RL, Cunha AM, (2001) A new approach based on injection moulding to produce biodegradable starch-based polymeric scaffolds: morphology, mechanical and degradation behaviour. *Biomaterials* 22: 883-889
- [15] Soel YJ, Kim JY, Park EK, Kim SY, Cho DW, (2009) Fabrication of a hydroxyapatite scaffold for bone tissue regeneration using microstereolithography and molding technology. *Microelectronic Engineering* 86: 1443-1446
- [16] Leong KF, Cheah CM, Chua CK, (2003) Solid freeform fabrication of three-dimensional scaffolds for engineering replacement tissues and organs. *Biomaterials* 24: 2363-2378
- [17] Huttmacher DW (2000) Scaffolds in tissue engineering bone and cartilage. *Biomaterials* 21: 2539-2543
- [18] Dietmar W, Huttmacher DW, Sittinger M, Risbud MV, (2004) Scaffold-based tissue engineering: rationale for computer-aided design and solid free-form fabrication systems. *Trends in Biotechnology* 22(7):354-362
- [19] Yang S, Leong KF, Du Z, Chua CK, (2002) The Design of Scaffolds for Use in Tissue Engineering. Part II. Rapid Prototyping Techniques. *Tissue Engineering* 8(1):1-11
- [20] Chen SB, Zhang WJ (2003) Off-Line control of time-pressure dispensing processes for electronics packaging. *IEE Transactions on Electronics Packaging Manufacturing* 26(4): 286-293
- [21] Vozzi G, Previti A, Rossi D, Ahluwalia A, (2002) Microsyringe-based deposition of two-dimensional and three-dimensional polymer scaffolds with a well-defined geometries for application to tissue engineering. *Tissue Engineering* 8(6):1089-1098
- [22] West AA, Williams DJ, Hine CJ, (1995) Experience of the application of intelligent control paradigms to real manufacturing processes. *Proceedings of the Institution of Mechanical Engineers* 209:293-308
- [23] Holdsworth SD, (1993) Rheological models used for the prediction of the flow properties of food products: a literature review. *Trans Inst Chem Eng* 71(C3):139-179
- [24] Li HJ, Liu J, Chen CP, Deng H, (2007) A simple model-based approach for fluid dispensing analysis and control. *IEEE/ASE Transactions on Mechatronics* 12(4):491-503
- [25] Chen XB, Kai J, (2004) Modeling of positive-displacement fluid dispensing process. *IEEE Transactions on Electronics Packaging Manufacturing* 27(3):157-163
- [26] Chen XB, Ke H (2006) Effects of fluid properties on dispensing processes for electronics packaging. *IEEE Transactions on Electronics Packaging Manufacturing* 29(2):75-82
- [27] Chen XB, (2005) Time-dependent rheological behaviour of fluids for electronics packaging. *ASME Journal of Electronic Packaging* 127(4):370-374
- [28] Fernandez E, Lopez D, Mijangos C, Duskova-Smrckova M, Ilavsky M, Dusek K, (2007) Rheological and thermal properties of agarose aqueous solutions and hydrogels. *Journal of Polymer Science Part B: Polymer Physics* DOI 10.1002/polb21370

An innovative approach for the fabrication of highly conductive nanocomposites with different carbon

Henry Kuo Feng Cheng^{1,2}, Nanda Gopal Sahoo¹, Lin Li¹, Siew Hwa Chan¹, Jianhong Zhao²

¹ School of Mechanical and Aerospace Engineering, Nanyang Technological University, 50 Nanyang Avenue, Singapore 639798

² Singapore Institute of Manufacturing Technology, 71 Nanyang Drive, Singapore 638075

Abstract. A novel approach to the preparation of a super-conductive polymeric nanocomposite system with different carbon fillers is presented. The ternary composites of polyamide 6 (PA6) and conductive carbon black (CCB) and multi-walled carbon nanotubes (MWCNTs) were fabricated by a melt-mixing technique. The ternary nanocomposites with the high filler contents showed extremely higher conductivity compared with the corresponding binary polymer composites. The effects of CCB and MWCNTs at different compositions on the rheological, physical, morphological, thermal, mechanical, and electrical properties of the ternary nanocomposites have been studied systematically. A mechanism for the complementary effects of CCB and MWCNTs has been proposed.

Keywords: carbon black, carbon nanotube, electrical conductivity, nanocomposites, polyamides

1. Introduction

Carbon black (CB) is a material that has been widely used for many years as a reinforcing agent. Especially in the tyre industry, carbon black has been used in rubber as a reinforcing filler to improve mechanical properties.^[1, 2] Polymer-carbon black composites have higher electrical properties^[3-8] and higher strengths^[9-11] than those of their pure polymeric matrices. Nowadays, a special type of CB, conductive carbon black (CCB),^[8] is available and is added into polymers in order to achieve improvements in the thermal and electrical properties of polymers.

Carbon nanotubes (CNTs), since being first reported,^[12] are the most attractive fillers for polymer nanocomposites with superior properties. This is because of their unique properties and structure.^[13-16] However, due to their high surface energy, high aspect ratio and strong van der Waals force, CNTs have a great tendency to form agglomerates and this is the greatest challenge for the development of high performance polymer composites by uniformly dispersing CNTs into the polymers. Among the methods used to overcome this agglomeration problem, melt mixing is compatible with

current industrial practices. In this process, CNTs are mechanically dispersed into a polymer melt using a high shear force compounder.^[17]

From the literature,^[18-26] we know that it is very difficult to produce a polymer composite with a very high conductivity by adding a single type of filler such as CNTs or CCBs alone. In this study, we, therefore, are particularly interested in the fabrication of highly conductive polymer composites filled with both CNTs and CCB. In our approach to advanced conductive polymer composites, both multi-walled carbon nanotubes (MWCNTs) and conductive carbon black (CCB) were added into a polyamide6 (PA6) matrix. The effects of both MWCNTs and CCB in different compositions on the rheological, morphological and electrical properties of the PA6/CCB/MWCNT ternary composites have been examined. A complementary effect has surprisingly been found between MWCNTs and CCB in the polymer matrix, which endows the ternary composites with superior electrical and thermal properties.

2. Experimental work

2.1 Materials and sample preparation

Polyamide 6 (PA6) (Ultrad B36 LN 01) was purchased from BASF. The conductive carbon black (CCB, ENSACO 350G) was supplied by Timal. The properties of CCB supplied by the manufacturer were the density (135 kg/m³), particles size (45.0 nm), and volume resistivity (< 20.0 Ω-cm), respectively. The multi-walled carbon nanotubes (MWCNTs, Baytubes® C 150 HP) were purchased from Bayer Material Science. According to the manufacturer, the diameter, length, number of walls and bulk density were 5 - 20 nm, 1 ~ > 10 μm, 3 - 15 and 140 - 230 kg/m³, respectively.

Prior to mixing, the PA6, CCB and MWCNTs were dried at 60 °C for 12 hrs in a vacuum oven. Compounding for PA6/MWCNT, PA6/CCB and PA6/CCB/MWCNT composites was carried out in a HAAKE PolyLab, an internal mixer, equipped with two counter-rotating screws at 300°C and at a mixing speed of 30 rpm for 15 min. After being taken out from the mixer, the composites were molded into different shapes at 300 °C and an injection pressure of 60 MPa using a HAAKE MiniJet, a mini injection machine. The formulations and sample codes are tabulated in Table 1.

Table 1. The sample codes and formulations for the composites (in weight percentage)

Code	PA6	PB10	PN10	PB20	PN20	PBN10
PA6	100	90	90	80	80	80
CCB	-	10	-	20	-	10
CNT	-	-	10	-	20	10

2.2 Measurements

The rheological measurements were performed on a rotational rheometer (Anton Paar – Physica MCR301) with the samples of $\Phi 25$ mm x 1 mm. The experiments were carried out in a frequency sweep mode at 5% constant strain using parallel plates with a diameter of 25 mm at 300°C in dry nitrogen.

The surface morphology of the fractured samples was observed by scanning electron microscopy (SEM), after silver coating. The analysis was done using a JEOL JSM-5800 SEM.

Direct Current (DC) electrical conductivity measurements were carried out at room temperature using a probe station of four-pointed fixture (CASCADE – REL 4800) combined with a precision LCR meter (HP Agilent – 4284A). The applied voltage was varied from 0.01 to 1.00 V.

3. Results and Discussion

3.1 Effects of CCB and MWCNTs on rheological properties of PA6

Dynamic frequency sweep tests were used to explore the structure and network formation of the composites. The changes in complex viscosity (η^*) with respect to angular frequency for the pure PA6, the PA6/CCB, PA6/MWCNT and PA6/CCB/MWCNT composites at 300 °C are shown in Figure 1. The power law index for complex viscosity varies with the loading of carbon filler; details are listed in Table 2.

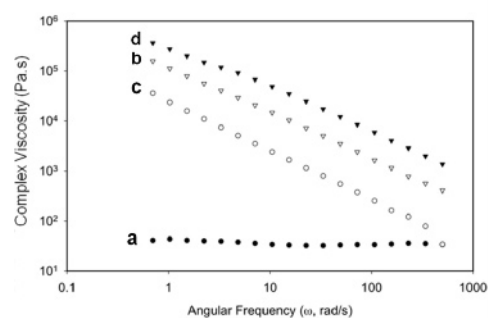


Fig. 1. Complex viscosity versus angular frequency for pure PA6, PBN, PB and PN composites at 300 °C, where: (a) PA6, (b) PBN10, (c) PB20 and (d) PN20.

Table 2. Power law index of complex viscosity, the slope of G' and G'' with respect to angular frequency for PB, PN, and PBN composites

Sample Code	Power law index of $\log \eta^*$ Vs $\log \omega$	Slope of $\log G'$ Vs $\log \omega$	Slope of $\log G''$ Vs $\log \omega$
PA6	0.03	1.572	0.958
PBN10	0.93	0.103	0.013
PB20	1.00	0.027	0.00
PN20	0.85	0.221	0.01

Over the range of angular frequency applied, the power law index for complex viscosity, η^* , increased with increasing carbon loading from $\omega^{0.03}$ for pure PA6 to $\omega^{0.93}$ for PBN10, $\omega^{1.00}$ for PB20 and $\omega^{0.85}$ for PN20. The power law index for pure PA6 is 0.03, which tells that the flow is almost a Newtonian one but the power law index increases as the carbon loading increase. These increases in power law show the flow behaviour changes from Newtonian to non-Newtonian. As was expected, the viscosities of the composites gradually increased with increasing carbon content which could be concluded to result from the formation of a dense MWCNT-CCB network in the polymer, as shown in Fig 1. From this figure, compared to the CCB-alone composite (PB20), the ternary composite (PBN10) has a higher viscosity but the viscosity of PBN10 is lower than that of the MWCNT-alone composite (PN20). This is probably due to MWCNT with a high aspect ratio could restrict the flow of the polymer chains in their molten state, while CCB with a spherical structure (in its powder-form) could have less effect. As a result, the mixture of the high aspect ratio MWCNT and spherical CCB results in the intermediate viscosity of ternary composites. On the other hand, the higher viscosity of MWCNT-alone composites increases the difficulty in dispersing MWCNTs into the polymer matrix, thus leading to a relative worse

dispersion than CCB in CCB-alone composites as is discussed in the following sections.

Similarly, addition of MWCNTs and CCB influences the frequency-dependence of the storage modulus (G') and loss modulus (G''), especially at low frequencies. Storage modulus and loss modulus versus angular frequency for pure PA6, PA6/CCB, PA6/MWCNT and PA6/CCB/MWCNT composites at 300 °C are shown in Figures 2 and 3, respectively. Over the range of angular frequency applied, pure PA6 tended to exhibit a typical terminal flow behaviour with the scaling properties of $G' \approx \omega^2$ and $G'' \approx \omega^1$ as ω was approaching 0 in accordance with the theory of linear viscoelasticity.^[27] But for all the composite samples, the dependence of G' on ω became smaller with increasing carbon loading. Thus, polymer chain relaxation in the composites was effectively controlled by the presence of carbon fillers. The decreases in the power law index, which is related to the dependency of G' on ω , with the loading of carbon fillers, are listed in Table 2.

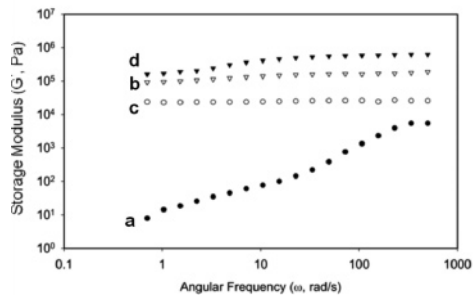


Fig. 2. Storage modulus versus angular frequency for pure PA6, PBN, PB and PN composites at 300 °C, where: (a) PA6, (b) PBN10, (c) PB20 and (d) PN20.

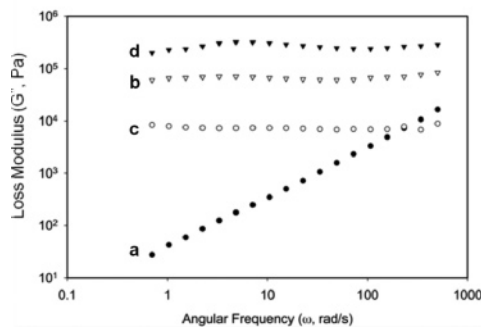


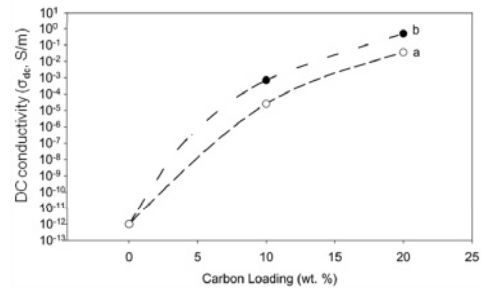
Fig. 3. Loss modulus versus angular frequency for pure PA6, PBN, PB and PN composites at 300 °C, where: (a) PA6, (b) PBN10, (c) PB20 and (d) PN20

The power law index for G' decreased with increase carbon loading from $\omega^{1.572}$ for pure PA6 to $\omega^{0.103}$ for PBN10, $\omega^{0.027}$ for PB20 and $\omega^{0.221}$ for PN20, respectively. The loss moduli of the composites exhibited a similar trend to the storage moduli. The frequency dependency of G'' also decreased from $\omega^{0.958}$ for pure PA6 to $\omega^{0.013}$ for

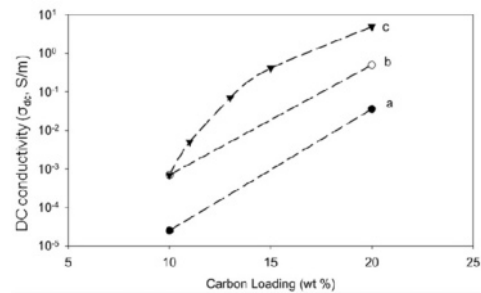
PBN10, $\omega^{0.001}$ for PB20, and $\omega^{0.01}$ for PN20, respectively. These decreases in the power law index of G' and G'' indicated a transitional behavior from a liquid-like to a solid-like viscoelastic flow. This phenomenon is mainly related to interactions between particles and network formation as the inter-particle distance decreases. This network significantly influenced not only rheological properties but also electrical ones of the composites, which is discussed in the following sections.

3.2 Electrical conductivity of PA6 induced by CCB and MWCNT

The comparison of DC electrical conductivity between PA6/CCB (PB) composites and PA6/MWCNT (PN) composites is as shown in Figure 4A. From this figure, PB20 has a conductivity of 0.5 S/m while PN20 has that of 0.04 S/m. So, it can be concluded that the composites with CCB alone have higher DC conductivity than those with MWCNTs alone although electrical conductivity of MWCNTs is higher than that of CCB.



(A)



(B)

Fig. 4. DC electrical conductivities for (a) PN composites, (b) PB composites and (c) PBN composites at different carbon loadings.

Surprisingly, when MWCNTs were added into the PA6 composite with 10 wt.-% CCB to make the ternary composites, there was another percolation leading to a significant improvement in the electrical conductivity of the resulting ternary composites. The comparison of conductivity among the three different composite systems is as shown in Figure 4B. The conductivity of the ternary composite (PBN5) is 0.4 S/m, which is 80 % of that of PB20 (0.5 S/m). This is 10 times higher than that of PN20

(0.04 S/m). At 20 wt.-% of carbon loading, the PBN10 (5 S/m) (the ternary composite with PA6, 10 wt.-% CCB and 10 wt.-% MWCNT) showed about 10 times higher in conductivity than PB20 (0.5 S/m) (the binary composite with PA6 and 20 wt.-% CCB) and about 125 times higher in conductivity than PN20 (0.04 S/m) (the binary composite with PA6 and 20 wt.-% MWCNT).

3.3 Enhanced electrical conductivity due to the formation of a conductive network from MWCNTs and CCB

CCB has the high surface energy and the relatively high conductivity while MWCNTs exhibit the high aspect ratio and excellent conductivity. Therefore, both CCBs and MWCNTs are outstanding candidates for the fabrication of conducting polymer composites. Figure 5 shows the FESEM micrographs of PN, PB and PBN composites. Referring to circles in Figure 5a, due to the agglomeration of MWCNTs resulting from the strong van der Waals forces of MWCNTs and high viscosity of MWCNT composite during the compounding process, MWCNT-based composites have a major drawback in conducting electricity. On the other hand, due to the inherent properties of CCB,^[8] it is possible for it to form a spider-like 3D network in the polymer matrix indicated by circles in Figure 5b. Then, according to Figure 5c, in the ternary composites of PA6, CCB and MWCNTs, CCB still can maintain its spider-like 3D structure (denoted by the circle A) while there are some MWCNT agglomerates (indicated by the circle B) in the composites. Moreover, there is interestingly observed a connection between the CCB network and MWCNT agglomerates (denoted by the circle C), which makes the network of the ternary composites more perfect and as a result, they have higher electrical conductivities.

According to Figure 4, it has been proved that the ternary composites have better conductivities than the binary composites. From these results, a possible mechanism explaining why the electrical conductivity of ternary composites is higher than that of their correspondent binary composites, is proposed in Figure 6. This proposed figure is an analytical sketch based on the FESEM micrographs from Figure 5. Although MWCNTs exhibit the high aspect ratio and high conductivity, MWCNTs tend to agglomerate themselves due to their strong van der Waals force and they are present as bundles in the polymer matrix as shown in Figure 5a (denoted by the circles). Therefore, we can conclude that it is extremely difficult for MWCNTs to form a conductive network as illustrated in Figure 6a. As a result, the composites with MWCNTs as fillers have lower conductivity. On the other hand, CCB has an ability to form a spider-like 3D network structure observed as the circles in Figures 5b and demonstrated in Figure 6b. However, the conductivity of CCB is limited due to their intrinsic feature. Thus, according to Figure 4B, ternary composites might be the best solution to

overcome these individual problems to obtain a complementary effect from MWCNTs and CCB, as shown in Figure 6c. As a result, the ternary composites showed much higher conductivity.

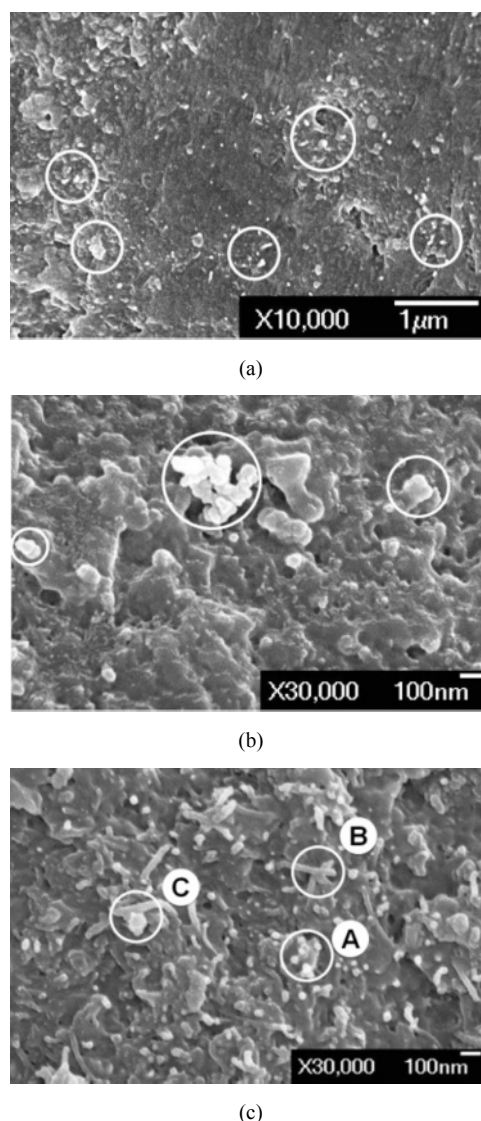
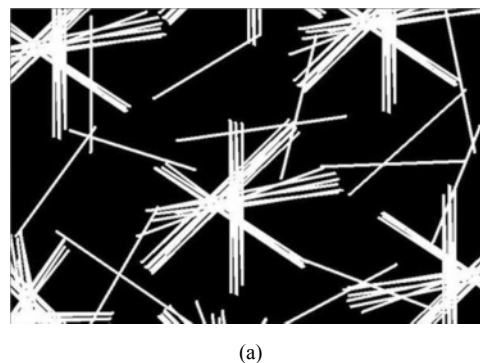


Fig. 5. FESEM micrographs of (a) PN 20, (b) PB 20 and (c) PBN10.



(a)

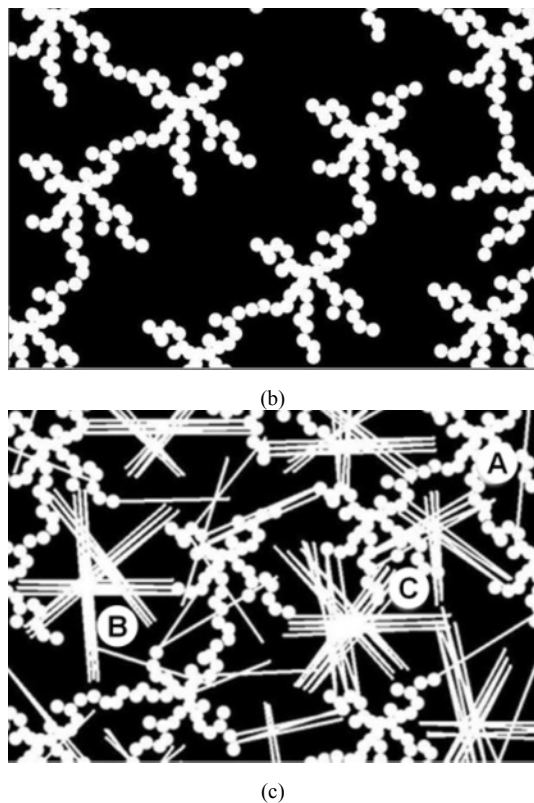


Fig. 6. Schematic diagrams for possible conductive mechanisms of (a) PN composites, (b) PB composites and (c) PBN composites.

4. Conclusions

In this work, a schematic mechanism has been proposed to explain why the properties of the ternary composite system are better than those of the binary systems. Therefore, our formulations will give an innovative idea to potential researchers in the fabrication of other composite systems with superior properties.

Acknowledgements

Authors want to express their sincere gratitude to Timcal Ltd. for providing the CCB used in this work. This work was supported by the A*STAR SERC Grant (0721010018), Singapore.

References

- [1] Wampler WA, Carlson TF, Jones WR, (2003) In *Rubber Compounding – Chemistry and Applications*; Rodgers B, Ed, Marcel Dekker, Inc.: New York, 239-84
- [2] Boonstra BB, (1967) *Journal of Applied Polymer Science*, 11:389-406
- [3] Lee CH, Kim SW, (2000) *Journal of Applied Polymer Science*, 78:2540-6
- [4] Ghofraniha M, Salovey R, (1998) *Polymer Engineering & Science*, 28:58-63
- [5] Lee GJ, Suh KD, Im SS, (1998) *Polymer Engineering & Science*, 38:471-7
- [6] Narkis M, Ram A, Flashner F, (1978) *Polymer Engineering & Science*, 18:649-53
- [7] Tang H, Liu ZY, Piao JH, Chen XF, Lou YX, Li SH, (1994) *Journal of Applied Polymer Science*, 51:1159-64
- [8] Gruenberger TM, Priese A, Van Bellinghen C, Grivei E, Ciallella C, Probst N, (2008) *Plastics & Rubber Singapore Journal*, 15:21-8
- [9] Grunlan JC, Gerberich WW, Francis LF, (2001) *Polymer Engineering & Science*, 41:1947-62
- [10] Kim DJ, Seo KH, Hong KH, Kim SY, (1999) *Polymer Engineering & Science*, 39:500-7
- [11] Koysuren O, Yesil S, Bayram G, (2006) *Journal of Applied Polymer Science*, 102:2520-6
- [12] Iijima S, (1991) *Nature*, 354:56-8
- [13] Lee CJ, Park J, Kang SY, Lee JH, (2000) *Chemical Physics Letters*, 326:175-80
- [14] Saito R, Dresselhaus G, Dresselhaus MS, (1998) *Physical properties of carbon nanotubes*; Imperial College Press: London
- [15] Ebbesen TW, (1996) *Journal of Physics and Chemistry of Solids*, 57:951-5
- [16] Treacy MMJ, Ebbesen TW, Gibson JM, (1996) *Nature*, 381:678-80
- [17] Andrews R, Jacques D, Minot M, Rantell T, (2002) *Macromolecular Materials and Engineering*, 287:395-403
- [18] Yoo HJ, Jung YC, Sahoo NG, Cho JW, (2006) *Journal of Macromolecular Science, Part B Physics*, 45:441-51
- [19] Sahoo NG, Jung YC, Yoo HJ, Cho JW, (2006) *Macromolecular Chemistry and Physics*, 207:1773-80
- [20] So HH, Cho JW, Sahoo NG, (2007) *European Polymer Journal*, 43:3750-6
- [21] Hou H, Ge JJ, Zeng J, Li Q, Reneker DH, Greiner A, Cheng SZD, (2005) *Chemistry of Materials*, 17:967-73.
- [22] Sen R, Zhao B, Perea D, Itkis ME, Hu H, Love J, Bekyarova E, Haddon RC, (2004) *Nano Letters*, 4:459-64.
- [23] Zhang WD, Shen L, Phang IY, Liu T, (2004) *Macromolecules*, 37:256-9
- [24] Lo'pez Manchado MA, Valentini L, Biagiotti J, Kenny JM, (2005) *Carbon*, 43:1499-505
- [25] Safadi B, Andrews R, Grulke EA, (2002) *Journal of Applied Polymer Science* 2002, 84:2660-69
- [26] Jun'ichi M, John MT, (2008) *Macromolecules*, 41:5974-77
- [27] Zhang Q, Fang F, Zhao X, Li Y, Zhu M, Chen D, (2008) *Journal of Physical Chemistry B*, 112:12606-11

Analysis of local field enhancement including tip interaction for the application to nano-manipulation using FDTD calculations

B. H. Liu¹, L. J. Yang¹, Y. Wang¹, J. L. Yuan²

¹ School of Mechanical and Electrical Engineering, Harbin Institute of Technology, Harbin, P. R. China

² School of Mechanical Engineering, Zhejiang University of Technology, Hangzhou, P. R. China

Abstract. Conventional optical tweezers rely on the field gradients near the focus of a laser beam which give rise to a trapping force towards the focus. However, the trapping volume of these tweezers is diffraction limited. Recently a promising method for nano-manipulation combining near-field optical tweezers and atomic force microscopy has been proposed. The light confinement in the vicinity of two nano-metric probes can produce strong gradient forces to trap and manipulate nano-scale particles at dimensions beyond the diffraction limit. In order to model this method, a finite difference time domain (FDTD) simulation enabling the calculation of the electromagnetic field in the vicinity of a metallic probe has been carried out for the first time in the context of near-field optical tweezers. For the case of nano-manipulating, a general model for the near-field simulation combining an actual optical fiber probe with a metallic probe under polarized laser irradiation is presented. The interaction between two near-field probes has been taken into account, and both near-field patterns of combined area and the dependence of field intensity have been analyzed. The simulations show that field enhancement and intensity profiles under the metallic probe strongly depend on the distance between the two probes, the incident angle of light, the polarization direction of incident light, the wavelength of the plane wave, and the permittivity of the probe material. The field intensity could be strong enough to manipulate nano-particles when the metallic probe is illuminated by an evanescent wave with high incident efficiency. Results of the FDTD calculations are found to be helpful for nano-manipulation.

Keywords: Evanescent field; Near-field optical tweezers; FDTD; Near-field optics; Field enhancement

1. Introduction

Nano-manipulation on a scale close to and beyond the resolution limit of light microscopy is needed for many modern applications. Shortly after the development of the mature optical tweezers manipulation technique, a number of groups began work on means of manipulating nano-particles with near-field tweezers [1-3]. For the three-dimensional manipulation of nano-particles, combined optical fiber probe-based near-field optical tweezers allowing for nano-manipulation together with a metallic probe of the atomic force microscope (AFM) is used.

Optical trapping by highly near-field enhancement has been investigated for the manipulation of nano-particles or other structures [4-7]. In the previous studies, a probe was not included in the calculations of the electric field near the tip of the metal-coated fiber probe because the major need is to find how the fiber probe enhances the field in near-field region. For combined nano-manipulation by metallic probe of AFM and optical fiber probe of near-field tweezers, the calculation of the electric field distribution formed in the combined area to find the field characteristics in terms of field enhancement is of interest. Currently, the near-field system when combining two kinds of probes is poorly understood, because the field changes drastically with the separation and the probe structures due to the strong electromagnetic interaction between the two probes [8].

In order to extend the interaction to optical fiber probes and metallic probes with optical fields for the practical application of manipulation, a general model for the near-field simulation for manipulating a combining of an actual optical fiber probe with a metallic probe under polarized laser irradiation is presented. Calculations were made to analyze the local field enhancement including tip interaction in the near-infrared region with the finite difference time domain (FDTD) method. This is a discrete straightforward calculation of Maxwell's electromagnetic equations [9]. Based on the calculations of the near-field distribution, the near-field patterns of combined area are described. In addition, the dependence of field intensity on the distance / separation between two probes, the incident angle, the polarization direction and the wavelength of the plane wave, and the permittivity of the probe material, are discussed.

2. Model of The Calculations

In order to find the maximum enhancement that is normalized to the excitation intensity at the surface, the field intensity distribution is measured in the plane of

polarization of the incident laser. Figure 1.a shows the configuration of a three-dimensional model for the near-field simulation combining an actual optical fiber probe with a metallic probe under polarized laser irradiation. An optical fiber probe at the wavelength of $\lambda = 632.8$ nm is located perpendicular to a conical probe made of copper with the conductivity of $\sigma = 5.8 \times 10^7$ S/m. The finite height of the metallic cone illuminated by the emitting evanescent wave of optical fiber probe is 600 nm with the radius of $a = 275$ nm, and the distance between the metallic probe and the optical fiber probe is 150 nm. The optical fiber probe used consists of a metal-coated waveguide that extends infinitely to the left and has a nano-wavelength aperture at the right cutting-off end. The waveguide is filled with homogeneous dielectric material with the relative permittivity of $\epsilon = 2.25$. The thickness of metal cover on the surface of probe with the diameter of $\Phi_1 = 700$ nm and the angle of $\theta = 90^\circ$ is 140 nm, and the conductivity of metal cover is assumed to be infinite. The aperture diameter $\Phi_2 = 200$ nm is used in the computation that is carried out in Cartesian coordinates, setting the aperture centre of the fiber probe as the coordinates origin. The excitation light polarized along axis y is incident on the probe giving the expression: $E = E_y \sin(2\pi ft) = \sin(2\pi ft)$. For the calculation, the configuration employed is placed in a volume discretized in mesh cells of $120 \times 178 \times 101$ shown in Figure 1.b, with space steps of $\Delta x = \Delta y = \Delta z = 10$ nm, and time step of $\Delta t = \Delta x / 2c$, where c is the light speed in vacuum. FDTD simulation that runs for tens of thousands of time steps is generally computationally intensive when high spatial precision is required, so a Intel Core 2 Duo 1.8GHz 2GB computer was used.

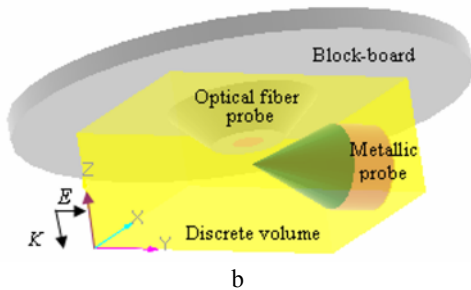
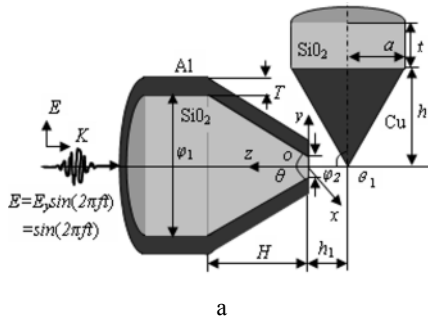


Fig. 1. a: three-dimensional configuration of a model system; b: the FDTD calculation model

3. Calculations and Analyses

For a particle in the vicinity of one probe, the magnetic field contribution to the force is found to be approximately two orders of magnitude lower than the electric field. Thus it mainly considers the distribution of the electric field intensity that affects the trapping force. The distribution of electric field shown in Figure 2.a reflects that the emitting wave spreads along all directions and decays quickly after exiting from the aperture, thus the clear diffraction of emitting light occurs in $x = 0$ plane. The near-field enhancement effect is apparent at the edge of aperture along axis y and at the metallic probe's tip. After the electric field reaching the outside of metal cover, the secondary near-field high enhancement appears in the angularity of the metal cover near the metallic probe because of point effect, while no clear near-field enhancement occurs in the other angularity away from metallic probe. The complicated near-field distribution in $x = 0$ plane will affect the manipulation of nano-particles.

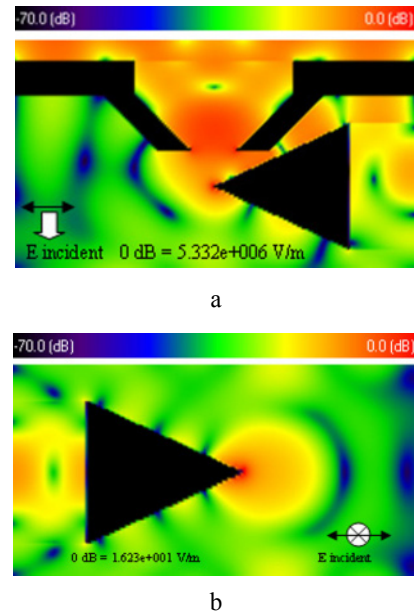


Fig. 2. a) FDTD simulated instantaneous field distributions in $x=0$ plane; b) field distributions in $z=-150$ nm plane

The metallic probe does not have an aperture or opaque coating surrounding the aperture but just the scattering point at the tip, so a large optical enhancement can be gained comparing the metal-coated fiber probe near the tip where the diameter of the probe is much shorter than the wavelength. It is found (in Figure 2.b) that the field is amplified at the probe tip, and is about 7 times higher than the incident field. The field enhancement of a metallic probe is caused mainly by the localized surface plasma mode excited at the tip of the probe by the evanescent field. The merit of field enhancement with an apertureless metallic probe has been successfully used for

photo fabrication of ultra-fine structures [10]. It may be also used for near-field optical nano-manipulation.

Seen from the simulation of the near-field distribution, the highly confined coupling evanescent fields present strong three-dimensional field gradients after adding the AFM metallic probe, resulting in the trapping capability of near-field optical tweezers increasing. If one particle is placed in the field gradients, it will inevitably be trapped to the extreme points of the near-field when the gradient force is strong enough to overcome the external interference. The three-dimensional nano-manipulation will be operated with adjustment of the distance between the optical fiber probe and metallic tip. When the distance is adjusted, the near-field of the metallic tip will naturally be different by virtue of the variation of perturbation between the optical fiber probe and the metallic tip. Let the incident angle $\theta_1 = 115^\circ$ and probe material be copper, giving a wavelength $\lambda = 632.8\text{nm}$, polarization direction $\varphi = 0^\circ$. The electric field relationship with the distance between the optical fiber probe and metallic tip is given in Figure 3. An intensity enhancement as high as 300 is predicted under the tip. The curve reveals that with increase of the distance, the field enhancement decreases rapidly. The curve indicates that the high intensity enhancement under metallic probe occurs only when it approaches the optical fiber probe in 0-100nm region. Therefore, it can be concluded that the near-field interaction between two probes is limited to a nanometer region, which means that the action range of the trapping force is about the radius of the aperture.

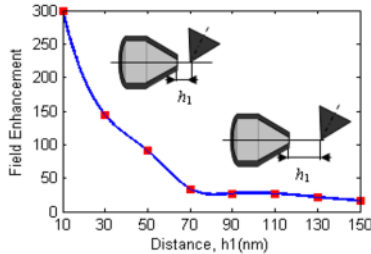


Fig. 3. Field enhancement as a function of distance (h_1)

The field intensity enhancement under the metallic probe is also dependent on the incident angle of the laser. Let the distance $h_1 = 150\text{nm}$, the probe material be copper, giving wavelength $\lambda = 632.8\text{nm}$, polarization direction $\varphi = 0^\circ$. The maximum enhancement of the near-field is given in Figure 4 for various incident angles. The relationship between the enhancement and the incident angle indicates that the field enhancement decreases gradually when the incident angle of the optical fiber increases or decreases from 90° . At the incident angle of 90° , the intensity enhancement profile has a high contrast and the tip of the metallic probe gets the highest enhancement. When the incident angle increases or decreases, the intensity enhancement decreases due to the mismatch between the metallic probe axis and the laser incident angle. At the same time, the secondary near-field

enhancement in the outside angularity of metal cover near the metallic probe decreases in this case, so it won't affect the manipulation of nano-particles so much because of the less complicated near-field distribution in $x = 0$ plane.

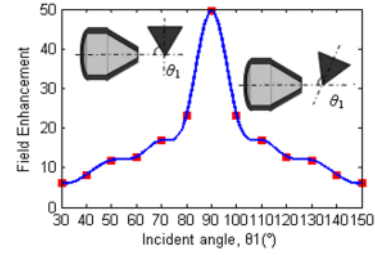


Fig. 4. Field enhancement as a function of incident angle (θ_1)

The degree of intensity enhancement by the metallic probe is also influenced by the polarization direction of the incident laser. Figure 5 shows the relationship between the peak enhancement and polarization angle letting the distance $h_1 = 150\text{nm}$ and probe material be copper, giving wavelength $\lambda = 632.8\text{nm}$, incident angle $\theta_1 = 90^\circ$. When the laser is p-polarized (i.e., $\varphi = 0^\circ$), maximum field enhancement can be expected at the tip of metallic probe. With increase in the laser polarization angle, the field enhancement decreases. This implies that the match between the polarization direction and probe axis is important for large optical enhancement in the near-field near a metallic probe. Due to the existence of birefringence in single-mode optical fiber with the variation of ambient temperature and stress, the polarization direction of incident laser may change randomly. For better nano-manipulation, it is important to avoid random polarization of the incident laser.

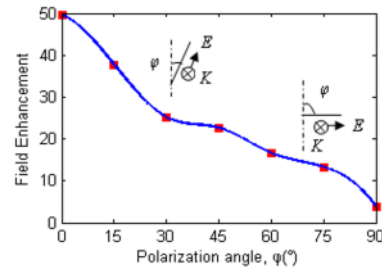


Fig. 5. Field enhancement as a function of polarization angle (φ)

Figure 6 shows the intensity distribution profiles of near-field under laser irradiation with different wavelengths. The lateral confinement of the field which decreases rapidly in the radial direction is believed to be the main reason for nano-manipulation observed experimentally. An intensity enhancement of 50 is predicted under the tip with a wavelength of 543.5nm , while the similar simulation with an input laser beam of 1523nm wavelength yields a much lower field enhancement of 3. This can be attributed to the fact that the "antenna-effect" which is prevalent at longer wavelengths is less dominant at visible wavelengths, and additional effects, such as tip-induced plasma oscillations, may

affect the field enhancement [11]. With the increase in the laser wavelength, the near-field region expands, thus the near-field region is frequency-dependent, and for higher enhancement, a shorter wavelength laser should be preferred. In view of the frequency-dependent field intensity, the trapping force would be affected by the wavelength of the incident laser. The particle can be trapped and approach the metallic probe for one wavelength, however, it is also possible to be repelled and escape from the probe for another wavelength. By the wavelength-dependent optical force, one can trap, move, and deposit the particle on a desired position on a nanometer scale.

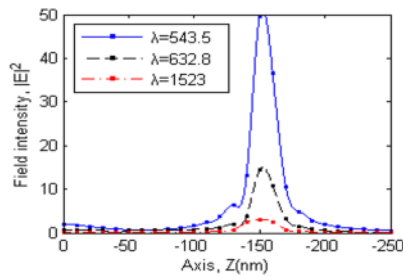


Fig. 6. Electric intensity distributions under the metallic probe with different laser wavelengths

The simulation was applied to different materials of metallic probe. Figure 7 shows the field intensity profiles in $y = 0$ plane calculated at the tip of probe using copper, gold and silicon materials. The local electric field is mainly oriented parallel to the probe axis, strongly localized below the tip and exhibits a higher enhancement. Under the copper tip there is strong enhancement, while under the gold tip, the enhancement is weak. This phenomenon can be explained by the finding that the resonance with the excitation light on the surface with good conductivity is much stronger than that on the surface with poor conductivity. In order to enhance the localized electric field effectively, the conductivity of the tip material should be high enough for exciting the plasma to increase the electric field intensity.

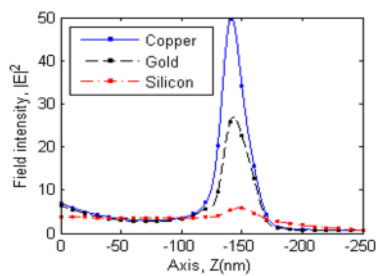


Fig. 7. Electric intensity distributions under copper, gold and silicon probes

4. Conclusions

In summary, a general model for the near-field simulation combining an actual optical fiber probe with a metallic probe under polarized laser irradiation is presented for the case of nano-manipulating. The electromagnetic field in the vicinity of a metallic probe is calculated to find the characteristics of it in terms of field enhancement in the context of near-field optical tweezers using the method of FDTD. With the combination of the metallic probe of AFM and the optical fiber probe of near-field tweezers, the tip interaction is taken into account when analyzing the electric field distribution of near-field optical tweezers for nano-manipulation. In virtue of the low emitting efficiency at the tip of optical fiber, the field enhancement at the tip of metallic probe seems to be not so high. However, the field intensity could be strong enough to manipulate nano-particles if the metallic probe is illuminated by an evanescent wave with high incident efficiency. Furthermore, the simulations show that field enhancement and intensity profiles under the metallic probe strongly depend on the distance between two probes, the incident angle of light, the polarization direction of incident light, the wavelength of the plane wave, and the permittivity of the probe material.

Acknowledgments

This project was supported by the National Natural Science Foundation of China (90923041), the 111 Project of China (B07018), and Open Foundation of the MOE Key Laboratory of Mechanical Manufacture and Automation of Zhejiang University of Technology (2009EP012).

References

- [1] Novotny L, Pohl DW, Hecht B, (1995) Scanning near-field optical probe with ultrasmall spot size. *Opt. Lett.* 20:970–972
- [2] Chaumet PC, Rahmani A, Nieto-vesperinas M, (2002) Optical trapping and manipulation of nano-objects with an apertureless probe. *Physical Review letters* 88:123601–1–4
- [3] Nieto-Vesperinas M, Chaumet PC, Rahmani A, (2004) Near-field photonic forces. *Phil. Trans. R. Soc. Lond. A.* 362:719–737
- [4] Tanaka M, Tanaka K, (1996) Boundary Integral Equations for Computer Aided Design of Near-Field Optics. *Electronics and Communications in Japan* 79:101–108
- [5] Wang KY, Zhen J, Huang WH, (1998) The possibility of trapping and manipulating a nanometer scale particle by the SNOM tip. *Optics Communications* 149:38–42
- [6] Novotny L, Bian RX, Xie XS, (1997) Theory of Nanometric Optical Tweezers. *Physical Review Letters* 79:645–648
- [7] Hong XG, Xu WD, Li XG, (2009) Field enhancement effect of metal probe in evanescent field. *Chinese Optics Letters* 7:74–77
- [8] Furukawa H, Kawata S, (1996) *Optics Comm* 132:170
- [9] Yee KS, (1966) *IEEE Trans. Antennas Propagat AP*–14:302
- [10] Jersch J, Dickmann K, (1996) *Appl. Phys. Lett.* 68:868
- [11] Ohtsu M, (1998) *Near-Field Nano/Atom Optics and Technology* (Springer, Tokyo)

Numerical Simulation of the Four Roll Bending Process

A. G. Leacock*, D. McCracken, D. Brown, R. McMurray
Advanced Metal Forming Research (AMFoR) Group, Nanotechnology & Advanced Materials Research Institute,
School of Engineering, University of Ulster, UK

Abstract. The traditional four roll bending process consists of a predetermined path for the workpiece with little or no compensation for material variability. This paper describes a prototype, modular four roll bending machine with extensive instrumentation that provides a means to compensate for the aforementioned variability. A Finite Element modelling methodology is presented and validated by comparison with force and curvature measurements from the machine. Excellent agreement was found between the experimental results and the modelled output for single curvature forming.

Keywords: Roll, Bending, Simulation

1. Introduction

Recent aircraft designs have illustrated that metallic fuselage structures will remain for the foreseeable future. The introduction of next generation Al-Li alloys has provided significant weight savings for these metallic structures. Nevertheless, due to material variability and serrated yielding, accurate manufacture of large single and double curvature fuselage panels from traditional Al-Cu and Al-Li alloys requires an alternative approach. Creep age forming has already been employed by Airbus in the production of the integrated wing sections of the new A380 [1]. Springback levels in this process are reported to be of the order of 80% [2,3]. The large tools, specialised autoclave, cold storage of components following solution heat treatment and long age times in excess of 20 hours reduce the flexibility and appeal of this process.

A more flexible and less costly alternative is provided by the roll bending process. Several machine configurations are available, including 2 roll[4], three roll[5,6] and four roll [5,6]. Many of the machines currently in use are manually controlled, whereby the radius is checked using a template [7]. The more modern machines use some form of CNC control, although this is generally based on a predetermined set of machine parameters. Mori [8] and Osakada [9] used fuzzy logic and Finite Element analysis to create a virtual closed loop control system. Experimental data confirmed the

suitability of the method in reducing flat regions and producing the desired curvature using two axis control of the top roll.

Yoon [12,13] proposed an incremental system for the rolling of double curvature components. The system used a single top roll and four spherical base supports. By varying the relative distances between these he was able to produce double curvature plates using an incremental rolling method. This system was later extended to include multiple rollers for the production of large double curvature plate components [14-16]. However, these systems lacked the instrumentation for closed loop 'in-process' control.

2. New Roll Bending System

The new roll bending machine was conceived in a modular form so that multiple modules could be combined into a Multi-Discrete-Roll-Bending (MDRB) system. A single module is illustrated in Fig. 1. Each module consist of four electromechanical actuators. Two actuators are co-axially located at the centre of the module, one at the top and one at the bottom. Two additional actuators pivot on parallel axes and are linked at the top to the lower actuator. The pivot and link combination avoids off-axis loading of the side rollers during a bending operation.

Each actuator contains an encoder for position control. A cylindrical roller (diameter 200mm) is mounted on the end of each actuator. The centre and side rollers each have an integrated dual axis load cell around which they rotate. The bespoke load cell is free from moments and provides a decoupled measurement of the load coaxial with and normal to the actuator motion. The centre roller also has a small curvature measurement device similar to that used by Hardt [10]. The drive roller provides the motion to pull the blank through the machine while pinched between the drive and centre rollers.

This unique, comprehensively instrumented system provides an excellent basis for the detailed validation of the four roll bending process simulation. The simulation and validation were designed with a view to future modelling and construction of multiple modules.

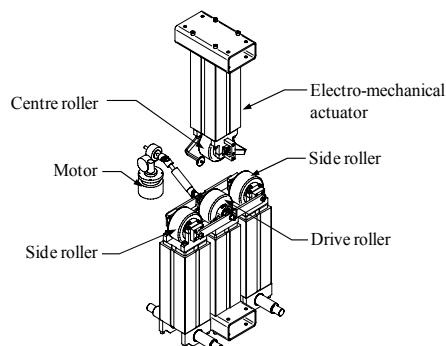


Fig. 1. Single MDRB system module configuration.

3. Simulation of MDRB system

The simulation of the process was performed using PAM-STAMP 2G. The forming process was modelling using the explicit solver while the springback was calculated using an implicit solver. In order to reduce the model run time and limit rigid-body rotation in the springback model, a symmetry plane was applied at the centre of the rollers. The rollers were modelled as undeformable rigid-bodies with centres of gravity located at the drive roller centre. Since the version of PAM-STAMP 2G used in this analysis was incapable of modelling multiple kinematics in a single body, the side rollers, and centre roller did not rotate with blank motion. To compensate, a frictionless contact is assumed throughout. The PAM-STAMP2G ‘accurate’ contact algorithm was used throughout all stages, with the blank as the slave in all cases. The 2024-O Alclad aluminium rectangular blank measured 600 mm by 50 mm by 2.54 mm and was initially assigned an element size of 17.5 mm. The Hill 1990 [17] yield criterion was used to represent the yielding behaviour, the calibration of which was performed using a numerical optimisation method in PAM-STAMP 2G. The corresponding model parameters used in the PAM-STAMP 2G material model 109 are listed in table 1. Material hardening was represented as a series of data-points derived from uniaxial data in the rolling direction.

It is normal practice to instantly apply a blank holder load when using shell elements. However, the boundary conditions in this model differed from the standard stamping force application in two important regards, a line contact between the blank and centre/drive rollers and the large proportion of unconstrained material in the blank. These differences together resulted in an instability in the pinch stage that was manifest as a

vibration in the blank and hence the roller loads. Through a simple sensitivity study it was possible to reduce the oscillations in the centre roller to acceptable levels.

Similar problems were encountered during the bending and rolling stages. Side roller 1 and 2 were rotated (Fig. 2(b)) about the driver roller centre using a sinusoidal velocity function during the acceleration and deceleration stages. A sinusoidal function was also used to control the rotation of the drive roller (Fig. 2(c)). These functions ensured that initial and final accelerations were zero and minimised the vibration in the blank between stages. The sinusoid RMS was adjusted until the blank vibration converged to a minimum value. A convergence study was also performed on the effect of blank and roller mesh densities on the blank vibration. A complete list of optimised boundary conditions is given in table 2.

3.1 Simulation results

The normal loads for each roller are illustrated in Fig. 3. Since the centre roller has a constant force applied throughout stages 1, 2 and 3, there is little change in this value, save for the oscillations noted during the rolling stage. These oscillations are common to all simulation force measures and can be attributed to the roller/blank line contact and the large unconstrained deformable blank. Similar effects have been noted by Shim et al. [14].

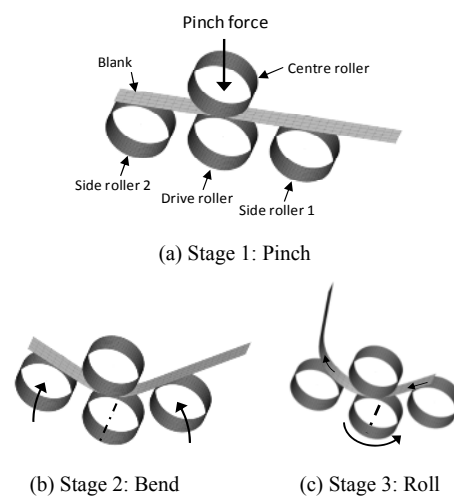


Fig. 2. Simulations stages for MDRB system

Although the drive roller force cannot be measured in the current machine, the simulation results are nonetheless informative. The drive roller force tends to reduce during the bending stage and then increase once rolling commences. The reduction is caused by a transfer of force during the bending process to the centre roller, ‘lifting’ both the centre roller and blank from the drive roller. The constant force boundary condition on the centre roller results in zero net change to the force in this roller. The force on drive roller then increases as the side

roller 2 (exit roller) force decreases from the onset of rolling (stage 3). The combined forces illustrate that the deformation process has changed from a four roll bending to a three roll bending process in which the centre roller bends the blank in a three point contact mode between the drive roller and the side 1 roller [18].

Table 1. Material model parameters for the 2024-O blank

Parameter	Hill 1990 Notation	Value
Density		2780 kg/m ³
Modulus		70 GPa
Poisson's Ratio		0.33
m	m	1.1390
α	σ_0/τ	2.1590
β	$-2a$	0.0257
γ	b	0.0485

Table 2. Optimised model boundary conditions

Parameter	Value
Pinch Force	250 N
Pinch force application time	10 ms
Average side roller speed	0.5 rad/s
Side roller rotation	0.384 rad
Average rolling speed	0.5 rad/s
Roller mesh size	4.0 mm
Blank mesh size	6.0 mm

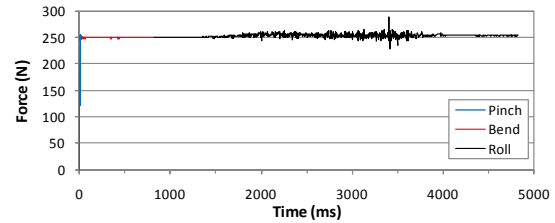
The oscillations in the normal roller force are greatest on side roller 2. For all the other rollers, the oscillations reduce at 3700 ms when the quantity of unconstrained blank material moving towards side roller 1 is reduced, whereas the oscillations in the side roller 2 remain significant throughout the process where the quantity of unconstrained blank material adjacent to side roller 2 is increasing.

4. Experimental validation of simulation

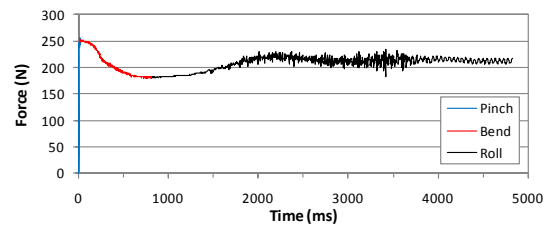
In order to determine the accuracy of the FE simulation a series of tests were conducted on the experimental system illustrated in Fig. 1. 2024-O Alclad aluminium rectangular blanks measuring 600 mm by 50 mm by 2.54 mm were removed from the parent material with the 600 mm dimension aligned with the rolling direction. These specimens, labelled S21-25 were then deformed using the stages described in Section 3.1.

The force-rotation plots for side rollers 1 and 2 are shown in Fig. 4 and 5 respectively. There is excellent correlation between the simulated and experimental forces, with only a slight deviation at approximately 0.075 rad. The reason for the deviation becomes clear when the heterogeneous nature of the Alclad alloy is considered. The outer 5% of the material thickness is constructed from a soft, commercially pure aluminium. The soft cladding is subjected to the highest tensile and compressive bending stresses during the forming process

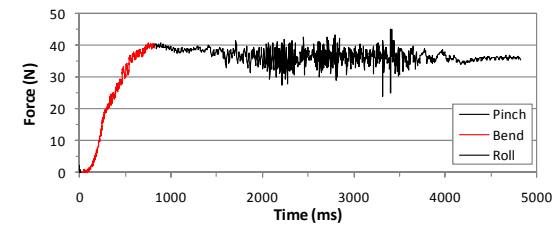
and will be the first region of the material to yield. The simulated material is a single homogenous representation of the complete alloy and will therefore tend to yield at a higher stress without the transition of the plastic/elastic interface from the soft cladding layer to the harder inner core material.



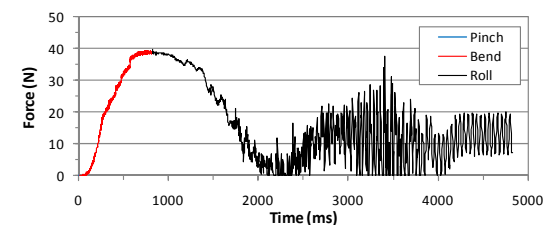
(a) Centre roller



(b) Drive roller



(c) Side roller 1



(d) Side roller 2

Fig. 3. Simulation results for normal roller loads: Pinch 0-10 ms, Bend 10-810 ms, Roll 810-4810 ms.

Additional bend angles of 6, 10, 14 and 18 degrees were used to extend the simulation validation. The final curvature predictions from the simulations, shown in Fig. 6, compare well with the experimental results. The deviations at the higher curvature values are thought to be caused by the aforementioned heterogeneity in the Alclad aluminium.

5. Conclusions

The difficulty in obtaining a stable model for the roll bending of large unconstrained blanks is clearly demonstrated. There is a complex interaction between simulation kinematics and model discretization, which must be balanced against reasonable model run times. A set of optimised simulation boundary conditions is presented. The results of this simulation were successfully validated by comparison with force and curvature measurements from an experimental roll bending machine. Slight deviations are apparent between the experimental and simulated results. However these can be attributed to the heterogeneous nature of the Alclad aluminium used in the validation.

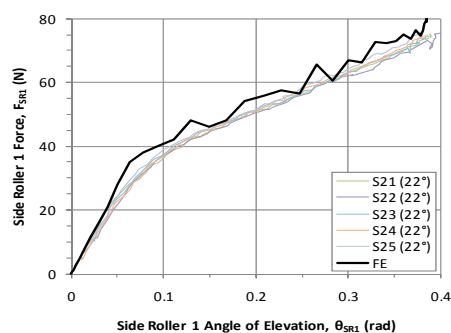


Fig. 4. Comparison of FE and experimental results for side roller 1 normal forces

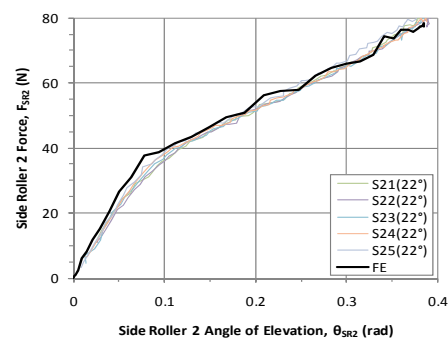


Fig. 5. Comparison of FE and experimental results for side roller 2 normal forces

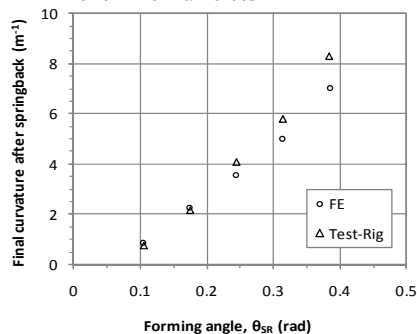


Fig. 6. Comparison of FE and experimental results for the unloaded curvature

References

- [1] Levers, A. 2003, Jumbo processes, *Manufacturing Engineer*. 82/3 :42-45.
- [2] Hibbert, L. 2004, Wing win situation [manufacture of wings for A380 superjumbo aircraft], *Professional Engineering*. 17/5 :28-30.
- [3] Ho, K. C., Lin J., Dean T. A. 2004, Modelling of springback in creep forming thick aluminum sheets, *Int.J.Plast.* 20/4-5 :733-51.
- [4] Finckenstein, E. v., Haase F., Kleiner M., Reil G., Schilling R., Sulaiman H. 1993, Roll bending of thin sheet metal parts on press brakes, *CIRP Ann.Manuf.Technol.* 42/1 :295-300.
- [5] Hua, M., Lin Y. H. 1999, Large deflection analysis of elastoplastic plate in steady continuous four-roll bending process, *Int.J.Mech.Sci.* 41/12 :1461-1483.
- [6] Hua, M., Lin Y. H., 1999, Effect of strain hardening on the continuous four-roll plate edge bending process, *J.Mater.Process.Technol.* 89-90/ :12-18.
- [7] Hua, M., Baines K., Cole I. M. 1999, Continuous four-roll plate bending: A production process for the manufacture of single seamed tubes of large and medium diameters, *Int.J.Mach.Tools Manuf.* 39/6 :905-935.
- [8] Mori, K., Yang G., Osakada K. 1995, Determination of optimal motion of tools in metal forming processes by controlled FEM simulation, *Int.J.Mach.Tools Manuf.* 35/6 :851-859.
- [9] Osakada, K., Yang G., Mori K. 1993, Determination of optimum forming path in three-roll bending by combination of fuzzy reasoning and finite element simulation, *CIRP Ann.Manuf.Technol.* 42/1 :291-294.
- [10] Hardt, D. E., Roberts M. A., Stelson K. A. 1982, Closed-loop shape control of a roll-bending process, *Transactions of the ASME.Journal of Dynamic Systems, Measurement and Control.* 104/4 :317-22.
- [11] Hale, M., Hardt D. E. 1987, Dynamic analysis and control of a roll bending process, *IEEE Control Syst.Mag.* 7/4 :3-11.
- [12] Yoon, S. J., Yang D. Y. 2003, Development of a highly flexible incremental roll forming process for the manufacture of a doubly curved sheet metal, *CIRP Ann.Manuf.Technol.* 52/1 :201-204.
- [13] Yoon, S. J., Yang D. Y. 2005, An incremental roll forming process for manufacturing doubly curved sheets from general quadrilateral sheet blanks with enhanced process features, *CIRP Ann.Manuf.Technol.* 54/1 :221-224.
- [14] Shim, D. S., Jung C. G., Seong D. Y., Yang D. Y., Han J. M., Han M. S. 2007, Process development and simulation for cold fabrication of doubly curved metal plate by using line array roll set, *AIP Conference Proceedings.* 908/1 :865-70.
- [15] Shim, D. S., Yang D. Y., Kim K. H., Han M. S., Chung S. W. 2009, Numerical and experimental investigation into cold incremental rolling of doubly curved plates for process design of a new LARS (line array roll set) rolling process, *CIRP Ann.Manuf.Technol.* 58/1 :239-242.
- [16] Shim, D.S., Yang D.Y., Kim, S.J., Chung, D.W., Han, M.S., Investigation of forming sequences for the incremental forming of doubly curved plates using the line array roll set (LARS) process. *Int.J.Mach. Tools Manuf.* In press. Manuscript accepted.
- [17] Hill, R., 1990, Constitutive modeling of orthotropic plasticity in sheet metals, *J.Mech.Phys.Solids*, 38/3-405-417.
- [18] Hua, M., Baines, K., Cole, I.M., 1995, Bending mechanisms, experimental techniques and preliminary tests for the continuous four-roll plate bending process. *J.Mat.Process Technol.* 48/1 - 4: 159-172.

Investigation on the Process Parameters and Process Window of Three-Roll-Push-Bending

R. Plettke¹, P. H. Vatter¹, D. Vipavc¹, M. Cojutti¹, H. Hagenah¹

¹ Chair of Manufacturing Technology, Egerlandstraße 13, 91058 Erlangen, Germany

Abstract. Three-roll-push-bending is a highly flexible method for the manufacturing of free-form bent tubes. The bending radius as target value is mainly determined by the position of the setting roll, defined by its axes P and Y. In industrial application the process design is carried out incrementally by trial-and-error. To avoid machine occupancy and to save expenditure of human labor, a lean offline process design is desirable. Furthermore, the technically possible parameter range is not fully used in common production processes. The machine's behavior should be investigated in the complete range to find the optimal choice of process parameters for each case. For a methodical process design a reliable data basis had to be gained about the resulting bending radius depending on the position of the rolls. To achieve this, a parameter study was run where samples were taken covering the entire theoretically feasible parameter range. To determine the influence of the roll position, the measured data have been approximated by thin plate splines. The new data covers a considerably enlarged process window, which proved to have yet unused regions featuring low scatter.

Keywords: Three-roll-push-bending, tube bending, parameter study, process design

1. Introduction

Tube bending is a common forming technology for tubular components up to a diameter of 70 mm. Tubes are used both as structural components and for the transport of fluids in nearly every industrial sector [1, 2]. Tubular components are mostly bent starting from straight pipe sections to the desired final shape. Bent pipelines frequently have a very complex geometry, the realization of which requires expensive production processes consisting of many manufacturing steps. Some widespread tube bending technologies, like for example rotary draw bending, have reached a high degree of reliability and robustness but suffer from a lack of flexibility, since only one constant radius can be bent in one forming operation with one toolkit depending on the outer diameter of the tube [3].

Three-roll-push-bending is a manufacturing method in which the tube is pushed through a die of variably positioned rolls. Depending on their position in the bending plane, different radii can be produced. The major advan-

tage compared to traditional processes is the possibility to realize arbitrary part geometries with one tool and within one forming step. By this the process chain can be shortened and a significant reduction of the manufacturing cost can be achieved. However, the process control employed is run based on empirical setup procedure requiring significant experimental effort and expenditure of time. A scientific investigation of the three-roll-push-bending process would allow a deep understanding of the forming process and a faster and more robust process design.

2. Three-Roll-Push-Bending Technology

In order to understand the terms used in the following paragraphs and to introduce some relevant concepts used throughout this study, a short description of the tool used for the experimental investigations is given in this section.

The bending tool consists of two holding rolls, the bending roll and the setting roll (Fig. 1). The bending roll and the front holding roll serve as a support for the transmission of bending moment and transverse force to the workpiece, whereas the rear holding roll stabilizes the process preventing lateral buckling of the tube. The setting roll can be moved on the bending plane by either rotating around the center of the bending roll (Y-axis) or translating in radial direction (P-axis). The positions of both axes are given in degrees, although the P-axis describes a linear movement. The feeding of the tube, which is operated by an electric driven spindle, is referred to as the C-axis of this machine.

The result of a forming operation is a two-dimensional tubular component whose geometry can be basically described by means of two parameters: the bending radius r , measured at the extrados, the magnitude of which is ruled by the preset position of the setting roll, and the bending angle α resulting from the feed length set (Fig. 2).

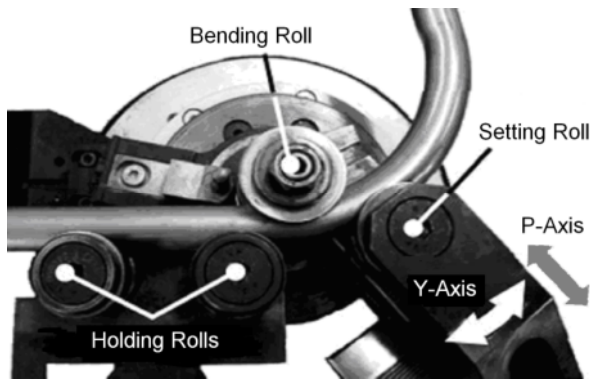


Fig. 1. Tool of a three-roll-push-bending machine.

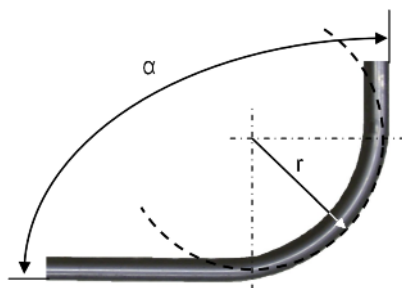


Fig. 2. Tube geometry described by radius and bending angle α measured at the extrados.

3. Process Design by Experiments

In industrial application, the process design is prepared by a series of experiments for each semi-finished product in which the resulting geometry is ascertained for several combinations of axis settings. To limit complexity, the P-axis is fixed to a certain value. The Y-axis is varied in a certain range. For the used P-values, the range the Y-values have to be varied in, is much smaller than the range the setting roll could be positioned in by the machine's design. The reason for this is that high values for Y and P would lead to a very small radius which causes damage in the semi-finished product. In these cases the tube cripples instead of following the course forced by the setting roll.

In the remaining range a series of experiments with different Y-values is carried out and the results are used to determine a so called characteristic line (Fig. 3). Even if the P-value has been slightly varied throughout various studies, the over all parameter range examined has been very small compared to the technically reachable range (Fig. 4). This is because for each desired bending radius an according parameter combination could already be found.

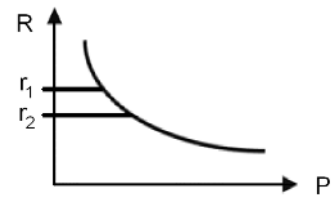


Fig. 3. Schematic characteristic line for constant Y.

4. Aims of Investigation

For an efficient automatic process design the need of a series of experiments for each variation of any parameter is dissatisfactory. A future process design system ought to know the process behavior throughout the complete reachable parameter range. Equipped with this information the system should not only predict the resulting geometry for a given parameter set, in the long run the system should be able to consider the scatter in different areas of the parameter range. As soon as deviations of the resulting geometry occur – e.g. due to the use of a new batch – new characteristic lines could be generated easily. A study was carried out pursuing several goals:

The first intention was to gather further experience about the extended parameter range beyond the one which has been used in industrial application so far. To achieve this, parameter combinations have been examined covering the entire possible parameter range. Thus, additional characteristic lines were generated. Additionally, the process boundaries were determined. In particular, a conception about the parameter combinations suitable for extremely small radii was obtained.

The second objective was to investigate the process behavior concerning scatter. The intention was to discover new areas with lower scatter than those which have been used so far.

5. Experimental design and set-up

To define the sample points for this parameter study the technically reachable parameter range was first restricted by areas in which a meaningful production could be ruled out in former experiments [4]. As shown in Fig. 4, area A could be excluded, because the setting roll does not have any contact with the tube at all or does only cause an elastic deformation. Earlier experiments have already shown that in area B this process leads to buckling of the workpiece, so this area can be excluded as well. Area C holds a certain risk of buckling, too, but for different reasons: the distance between bending roll and setting roll is too large and the force transmission onto the bent tube is almost perpendicular to the feeding direction. Furthermore the probability of collision between tube and parts of the tool rises. So this area is not interesting for applica-

tion and could be excluded as well. In area D the force transition is almost perpendicular towards the bending roll, which causes the tube to suffer significant ovalization. Additionally, the scatter is expected to be very high, as small deviations of the rolls, e.g. due to yielding of the die, lead to a different bending radius. The remaining area was divided on the Y-axis in steps of 5° and 65 sampling points were allocated approximately uniformly as shown in Fig. 4. The sample size was $n = 3$.

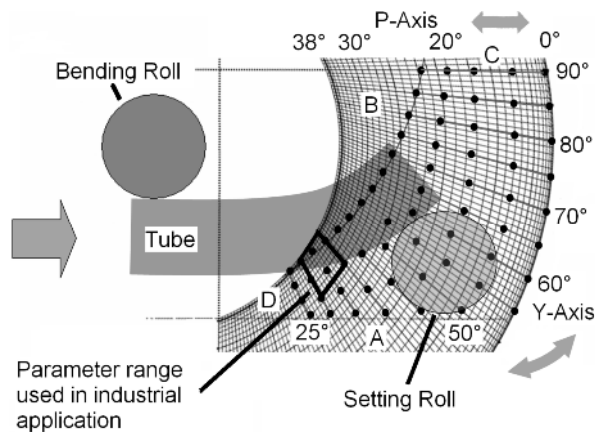


Fig. 4. Distribution of sampling points.

The semi-finished products used for the experiments were taken from one batch of carbon steel E235 with an outer diameter of 20 mm and 1 mm wall thickness. The tubes had been welded, calibration drawn and stress relieve heat treated. This kind of material is not commonly used in industrial manufacturing for cost reasons. The intention was to reduce scatter due to material variance. Investigations on material based scatter have to be carried out, here only the process was investigated.

The experiments were carried out on a machine by Wafios AG called BMZ 61. All tubes had been degreased with acetone and bent with 10% of the maximum process velocity. At 13 parameter combinations no proper manufacturing could be achieved. Their positions are marked in Fig. 6. The specimens were measured by the tactile measurement system Leitz PMM456 on the extrados.

6. Results and Interpretation

After measuring the specimens the data was imported in Origin8. The representation of the radius of each tube by the arc length showed an uneven section at the beginning of the bending progress and a section with a fairly constant radius later on (Fig. 5). The constant section was identified for each tube and fit by the Levenberg-Marquardt algorithm to retrieve the bending radius [5].

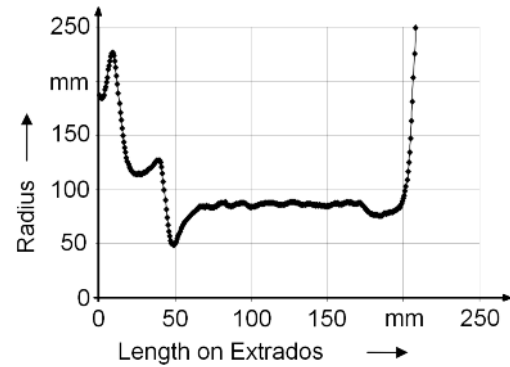


Fig. 5. Developing of radius on the extrados.

As can be seen in Fig. 6 most of the investigated areas proved to be suitable for production. At the inner arc of the chart, the tubes crumbled and did not follow the course given by the setting roll. This leads to an uncontrolled deformation of the semi-finished product and the tubes got destroyed. At the lower right corner of the parameter range the deformation was mostly elastic. Several specimens did not show any plastic deformation.

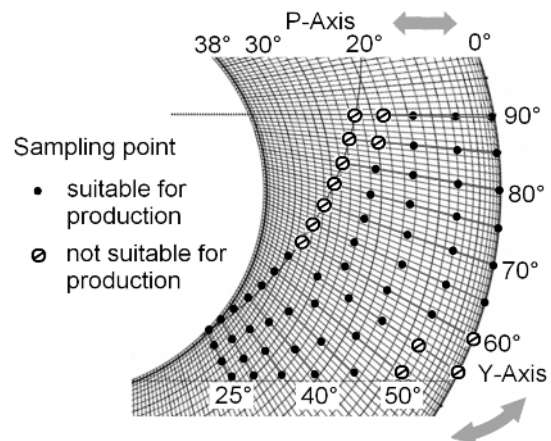


Fig. 6. Process boundaries as observed in experiments.

The characteristic lines have been approximated over the retrieved radii by thin plate splines. A few of them are plotted in Fig. 7.

The examination of the scatter corresponding to the used parameter combinations features a non-uniform effect (Fig. 8). But at closer reflection two main conclusions can be drawn. The first one is that small radii in general tend to more scatter than large ones. The highest value reaches a standard deviation of 3 mm at a bending radius of 120 mm. But still there are parameter combinations which allow a manufacture with a low standard deviation of about 0.3 mm which is just as good as the best combinations at large radii. This means that for small radii the parameters just have to be chosen more carefully.

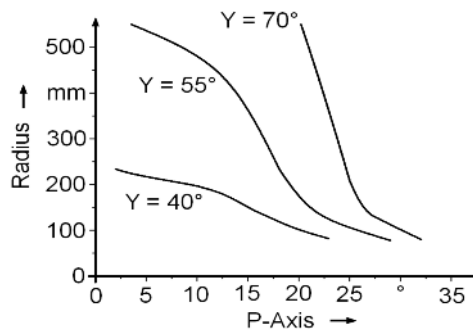


Fig. 7. Characteristic lines for several constant Y.

Large radii from 200 mm on have an average standard deviation between 0.5 mm and 1.0 mm. A reason for this could be that a bending of small radii causes much higher forces onto the die and an accordingly low yielding. Moreover, constant process results depend mainly on homogeneous material behavior. The inequality of the material could affect the spring-back behavior more than in the case of a light bending. Further investigation on this issue will be carried out.

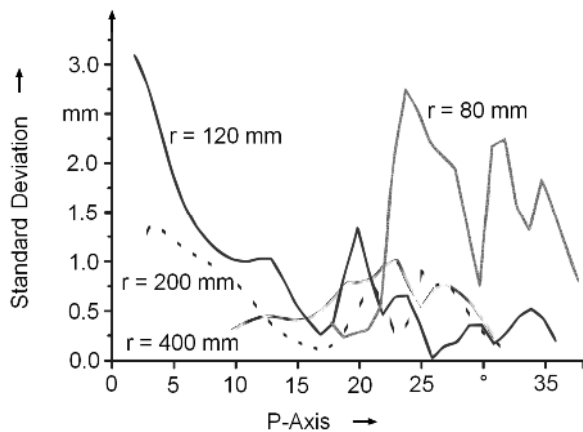


Fig. 8. Interpolated scatter for different radii.

The other observation to point out is that at a P-value of 15° to 20° there is a local minimum for almost any radius. It appears at $P = 20^\circ$ for a radius of 80 mm and moves slightly downwards to 15° for 400 mm when the radius increases. This may be interrelated with the angle of the force exposed by the tube onto the setting roll during the bending process. Earlier measurements already proved the existence of yielding [6]. As the mounting of the setting roll suffers a higher yielding in tangential direction than in radial direction, the affective angle of the force does provide an idea of the causes.

7. Summary and Outlook

This work investigated the tree-roll-push-bending process and the influence of the tool setting in P- and Y-axis coordinates. By means of a parameter study it covers the entire technologically feasible parameter range. The knowledge about the process boundaries has been expanded. The parameter ranges which lead to damage of the semi-finished products due to buckling could be identified, as well as the regions in which no plastic forming can be achieved. New characteristic lines have been approximated and can be utilized for a more flexible process design. Especially the knowledge gained about the scatter is considered very helpful. For both, small and large radii, parameter combinations with less than 0.3 mm standard deviation could be found. In general, the scatter showed to be lower for large radii than for small ones. But at careful parameter choice small radii can be bent just as precisely. The P-axis showed significant influence as the scatter turned out to be notably low at P-values between 15° and 20°. The minimum is displaced slightly depending on the bending radius. An explanation of the observed effects and the transfer of the gained knowledges will be objective of the future work.

In ongoing research the parameter study is expanded to a sampling size of $n = 5$ and additional sampling points will be added in interesting parameter ranges. A comparison with other tube dimensions will be carried out to proof the portability to different semi-finished products. Detailed research by the means of FE-simulation is in progress.

References

- [1] Von Finckenstein, E.; Adelfhof, A.; Haase, F.; Kleiner, M.; Schilling, R.: Biegen von Aluminium-Profilen. In: *Blech Rohre Profile* Vol. 40, No. 3 (1993), pp. 215-220.
- [2] Bettin, M.; Findeisen, V.; Hermans, J.: Gebogene Aluminium-Profil und Rohre im PKW-Bau. In: Siebert, K. (Editor): *Neuere Entwicklungen in der Massivumformung*. Oberursel: DGM-Informationsgesellschaft (1995), pp. 49-82.
- [3] Franz, W. D.: *Maschinelles Rohrbiegen: Verfahren und Maschinen*, VDI Verlag, Düsseldorf (1988).
- [4] Cojutti, M.; Vipavc, D.; Hagenah, H.; Merklein, M.: An Innovative Approach for the Process Design for Three-Roll Bending of Plain Tubular Components Proc. Proceedings of the International Congress on Efficient Rollforming. 14.10.2009-15.10.2009, Bilbao, Spain2009, 133-139.
- [5] Arnet, H.: *Profilbiegen kinematischer Gestalterzeugung*, Meisenbach Verlag, Bamberg (1999).
- [6] Merklein, M.; Hagenah, H.; Cojutti, M.: Investigations on Three-Roll Bending of Plain Tubular Components Proc. Proceedings of the 13th International Conference on Sheet Metal SheMet. 06.04.2009-08.04.2009, Birmingham, Großbritannien, Zuerich: Trans Tech Publications, 2009, ISBN 0-87849-336-0, 325-334.

Casting of Aluminum Alloy Strip by Improved Single-Roll Caster

Kazuya Akitsu¹, Toshio Haga², Shinji Kumai³ and Hisaki Watari⁴

¹ Graduate School of Osaka Institute of Technology 5-16-1 Omiya Asahiku Osaka 535-8585 Japan

² Department of Mechanical Engineering, Osaka Institute of Technology 5-16-1 Omiya Asahiku Osaka 535-8585 Japan

³ Department of Materials Science and Engineering, Tokyo Institute of Technology 4259 Nagatsuda Midoriku Yokohama city 226-8502 Japan

⁴ Department of Production Science and Technology, Gunma University 1-5-1 Tenjin kiryu city 376-8515 Japan

Abstract. A scribe was equipped to a single roll caster to improve the free solidified surface. The scribe contacted to the free solidified surface at the constant force. The some amount of semisolid layer at the surface was removed and the surface became flat. The scribe was made from the mild steel plate. The mild steel plate was covered by the insulator paper to prevent the cooling of the melt by the plate. The melt pool was made on the roll by the side dam plates, back dam plate and the scribe. Therefore, a tip or a nozzle was not needed. The AA5182 and AA6022 aluminum alloy strip were cast by single roll caster with scribe. The as-cast strips could be cold rolling. The microstructure of as-cast strip was not uniform at thickness direction. However, the microstructure became uniform after the cold rolling and the annealing.

Keywords: single roll caster, scribe, strip casting, roll casting

1. Introduction

The twin roll caster has advantages of the energy saving, low cost equipment and rapid solidification. The single roll caster like the melt drag process is more simple process than the twin roll caster. Therefore, the single roll caster is superior to the twin roll caster at the points the energy saving and low cost equipment. However, the single roll caster has disadvantage, too. It was unsoundness of the free solidified surface of the strip. If the procedure to improve the free solidified surface was devised, the single roll caster may become useful process. The single roll caster can be used for casting of the strip with no center line segregation. In the previous reports which described about the strip casting by the single roll caster, there were few reports about the equipment to improve the free solidified surface. In the present study, the scribe was devised and tried to improve the free solidified surface. The simplicity of the single roll caster was not influenced by the use of the scribe. The strip casting of AA5182 and AA6022 was tried using the scribe. The flow stress of AA5182 at semisolid condition of low solid fraction is not large. The flow stress of

AA6022 at semisolid condition of low solid fraction is large. It was thought that semisolid condition influence the condition of the scribed surface. The two kinds of alloys, which flow stress at semisolid condition is different, was chosen and tested. The cold rolling was operated on the as-cast strip, and ability of cold rolling was investigated. The microstructure was observed by the optical microscope. The bending test was operated on the cold rolled and T4-heat-treated AA6022 strip to investigate the difference of the free solidified surface and roll contact surface.

2. Experimental apparatus

2.1 Single roll caster

The schematic illustration of single roll caster is shown in Fig. 1. The melt drag is the typical single roll caster (ref. Fig. 1 (a)) [1, 2]. The process is very simple and the casting of the strip is very easy. The strip can be cast only by the pouring of the melt into the nozzle. The melt is solidified and the strip is dragged from the melt. The roll is not hot working like the twin roll caster. Therefore, the cooling method of the roll can be designed freely. For example, the shell of the roll can be thinner than that of the twin roll caster. In this way, the single roll caster has the advantages. However, the single roll caster has disadvantages too. The free solidified surface of the strip is not flat like the roll contact surface. The temperature of the cast strip by single roll caster is higher than that of the cast strip by twin roll caster. The strip is cooled at the roll bit in the twin roll caster. The most important problem of the single roll caster is unsoundness of the free solidified surface of the strip. In the present study, the improvement of the free solidified surface was tried by the scribe [3].

The single roll caster devised in the present study is shown in Fig. 1 (b). The melt pool was made on the roll by the two side dam plates, a back dam plate and a scribe. The melt pool was mounted on the top of the roll as the scribe was easily operated to attain the aim. If the low temperature casting is operated by the melt drag, there is tendency that the melt solidifies in the nozzle. In the process of Fig. 1 (b), the melt was directly poured on the roll, and the solidified metal did not remain on the roll. Therefore, the low temperature casting could be operated in the process of the present study. The scribe pushed the strip to the roll, and the contact condition between the strip and the roll became better than the melt drag.

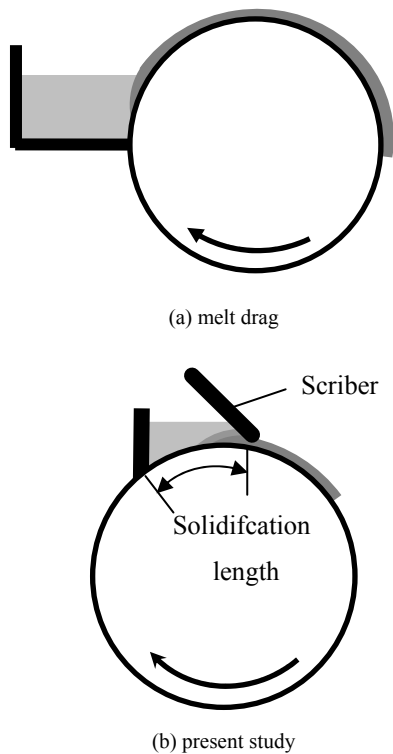


Fig. 1. Schematic illustration of the melt drag single roll process and the single roll process of the present study

2.2 Scriber

Schematic illustration around the scriber is shown in Fig. 2. The scriber was made from a mild steel plate, and the plate was coated by insulator paper. The insulator paper was used to prevent the decrease of the temperature of the molten metal. Moreover, the insulator paper was useful to protect the leak of the melt. The scriber was pushed to the roll direction at the constant load. The free solidified surface was in semisolid condition. The scriber scratches the some amount of the semisolid metal. The degree of the scratching was controlled by the dead weight. The strip was stuck by the scriber at the too heavy load. The scriber moved along the thickness of the solidified layer.

The scriber was supported by the fulcrum. The free solidified surface became flat after going through.

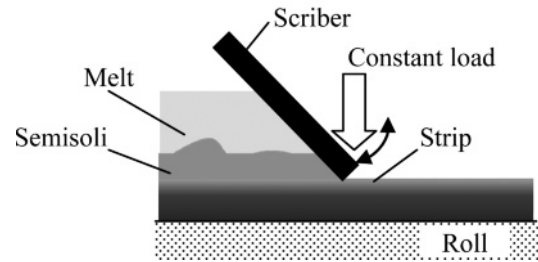


Fig. 2. Schematic illustration showing the around the scriber

3 Experimental conditions

The diameter of the roll was 1500 mm, and width was 50 mm. The roll was made from mild steel. The parting material was not used. The AA5182 and AA6022 aluminum alloys were cast. The melt temperature was 665, 680, 700 and 750°C. Roll speed was 20 m/min. The dead weight, which was used to push the scriber to the solid layer, was 0.5 kg.

4 Result and discussion

4.1 Effect of the load on the scribed surface

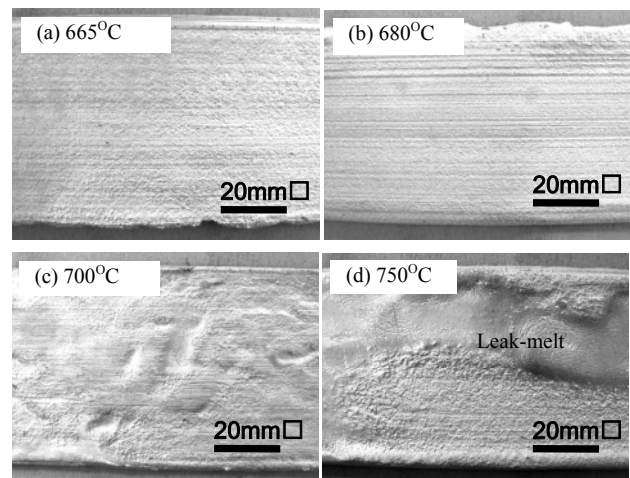


Fig. 3. Relationship between the melt temperature and scribed surface of AA6022 strip

The relationship between the melt temperature and scribed surface is shown in Fig. 3. The temperature of the molten metal influenced on the scribed surface.

The scribed surface became sound at the temperatures of 665°C and 680°C. The leak of the melt occurred at the temperatures of 700°C and 750°C. The thickness of the solidified layer might become uniform as the melt temperature became lower. Moreover, the condition of

semisolid metal was suitable for the scribing. Therefore, the leak of the melt did not occur at the temperatures of 665°C and 680°C.

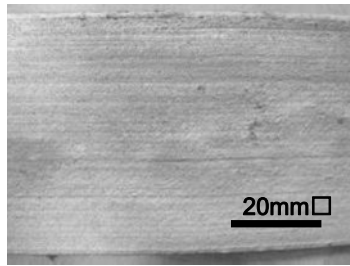


Fig. 4. Scribed surface of AA5182 strip. The melt temperature was 665°C

2.3 Cold rolling

The strip cast from the molten metal of 665°C was cold rolled down to 1mm after annealing at 430°C for 1 hour. The free solidified surface after cold rolling is shown in Fig. 5. The free solidified surface could be cold rolled and the roughness was improved. There was no difference between the roll contact surface and free solidified surface after cold rolling.

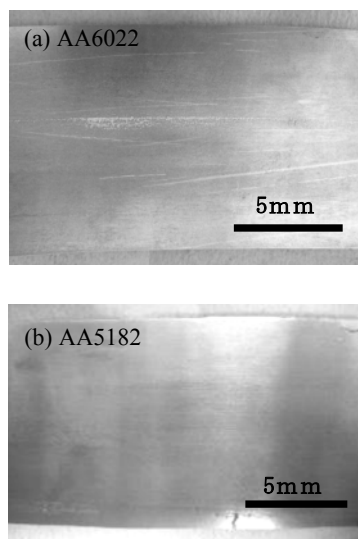


Fig. 5. Scribed surface of AA6022 and AA5182 strip after cold rolling. The melt temperature of casting was 665°C. The as-cast strip was annealed at 430°C for 1 hour, and strip was cold rolled down to 1 mm.

2.4 Microstructure

The microstructure of the cross section of the strip was observed by the optical microscope. The microstructure of AA6022 is shown in Fig. 6. The microstructure of as-cast strip was not uniform at thickness direction. The microstructure was as same as the microstructure of the strip cast by the high speed twin roll caster [4]. The

globular structure, which was typical structure of semisolid casting, was at free solidified surface. Some amount of the globular structure might be scribed by the scriber. The microstructure near the roll contact surface was dendrite structure. The microstructure after cold rolling and T4 treatment became almost uniform at the thickness direction. The strip was kept at 430°C for 1 hour and water-quenched as T4 treatment.

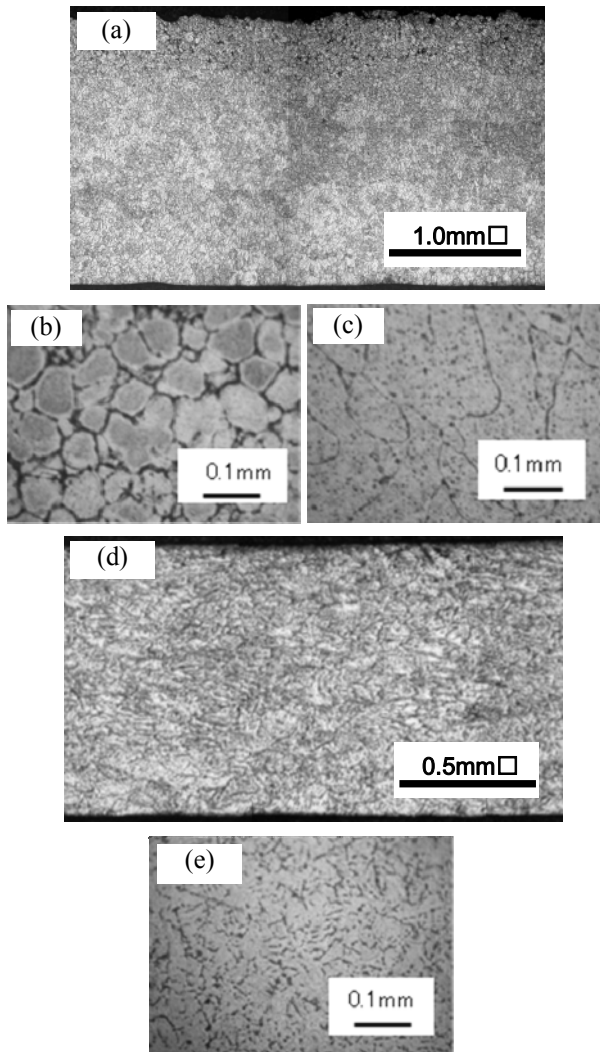


Fig. 6. Micro structure of cross section of AA6022. (a) as-cast strip, (b) near the free solidified surface of as-cast strip, (c) near the roll contact surface of as-cast strip, (d) after cold rolling down to 1 mm and T4 heat treatment of 430°C for 1 hour, (e) enlarged view of (d)

The microstructure of the cross section of AA5182 strip is shown in Fig. 7. The microstructure was not uniform at thickness direction. The grain was spherical and fine. The globular structure like semisolid casting was not existed near the free solidified surface. The globular structure might be scribed by the scriber. The porosity of the free solidified surface was less than the porosity at center area of the strip cast by the high speed twin roll caster.

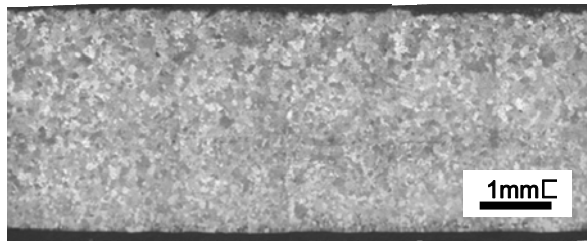


Fig. 7. Microstructure of the cross section of as-cast AA5182 strip

2.5 Mechanical property

The mechanical property of AA6022 strip was investigated by the 180 degrees bending test and the tension test. The bending direction and the result of the bending test were shown in Fig.8. The as-cast strip was cold rolled down to 1mm and was water cooled after keeping at 430°C for 1h. The 180 degrees bending test was operated after cold rolling and the heat treatment. There was no difference on the result of bending test between the free solidified surface and roll contact surface. This result showed that the free solidified surface could be improved up to the roll contact surface by the scribe and cold rolling.

The tension test was operated on the strip which was used for 180 degrees bending test. The tensile stress was 248 MPa, proof stress was 115 MPa and elongation was 32%. The proof stress was a bit less than conventional data. The cause of this was thought as below. The solid-solubility of Si was not enough. The solution temperature of 430°C was too low, and proof stress became low. The elongation was enough and this might show that there was no important defect on the free solidified surface.

3. Conclusions

The single roll caster equipped with a scribe was devised to improve the free solidified surface. The scribe was useful to improve the free solidified surface. It was thought that the free solidified surface was the same as the roll contact surface after cold rolling from the result of 180 degrees bending test. The casting of the strip using the single roll caster was easier than the twin roll caster, and the equipment cost of the single roll caster was lower than that of the twin roll caster. The single roll caster equipped with a scribe may be used instead of the twin roll caster.

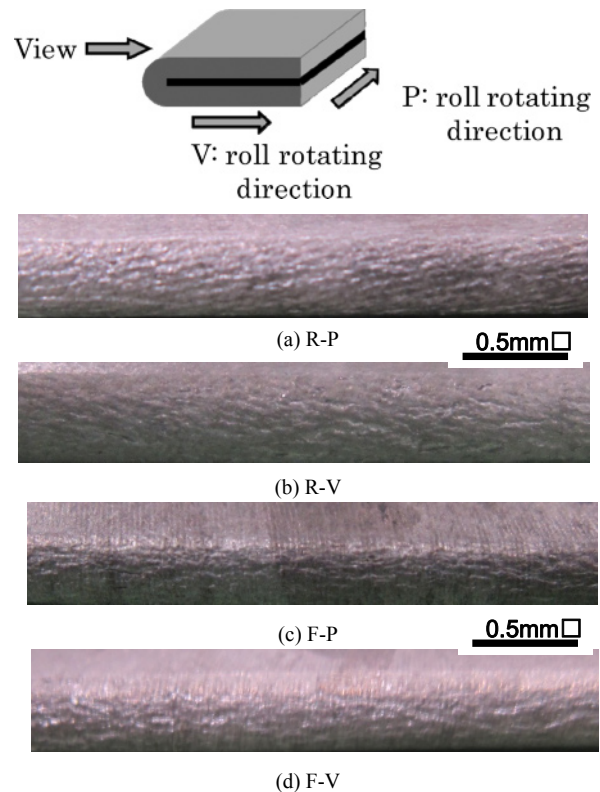


Fig. 8. Result of the 180 degrees bending test. "R" shows that roll contact surface was outer surface. "F" shows that free solidified surface was outer surface. "P" shows that bending direction was parallel to the casting direction. "V" shows that bending direction was vertical to the casting direction. The as-cast strip was cold rolled down to 1mm and was water cooled after keeping at 430°C for 1 h.

References

- [1] N.Toyama, H.Aho, H.Arai, H.Yoshimura: Tetsu-to-Hagane, Vol.71(1986), p.A245
- [2] D.B. Love, J.D. Nauman, Controlling the physical and mechanical properties of cast stainless steel band, Proceedings of the TMS International Symposium, Casting of Near Net Shape Products, 1988, 597-611.
- [3] T.Haga, M.Sawai, R.Nakamura, H.Watari and S.Kumai(2010) Mater.Sci. Forum, Castihg of clad strip by an unequal diameter twin roll caster, Vol. 633-642, p.413.
- [4] T.Haga, H.Watari, S.Kumai (2006) Archives of Materials Science and Engineering, High speed twin roll casting of Mg alloy strip by a vertical type twin roll caster, Vol.15, p.18.

Casting of Al-Si-SiC_p composite alloy strip by a vertical type twin roll caster

Hideto Harada¹, Toshio Haga²

¹ Graduate School at Osaka Institute of Technology, 5-16-1, Asahi-ku, Osaka city, Osaka, 535-8585, Japan

² Department of mechanical Engineering, Osaka Institute of Technology, 5-16-1, Asahi-ku, Osaka city, Osaka, 535-8585, Japan

Abstract: This study was aimed at investigating the casting of Al-Si-SiC_p composite alloy strip by a vertical type twin roll caster. Al-Si-SiC_p aluminum alloy has some useful advantages i.e., low thermal expansion, better thermal conductivity and wear resistance. Recently, a plate of Al-Si-SiC_p, with a thickness thinner than 1mm was required. A possibly useful process to make the thin plate was by hot rolling involving many passes. However, Al-SiC_p is hard and brittle, so hot rolling was readily applicable. An possible alternative, which also offered energy savings, was the roll casting of Al-Si-SiC_p strip using a vertical type high speed twin roll caster. The trials of the method are presented in this paper. The size of the twin rolls was $\phi 300 \times W100$. Roll-load was set low enough to prevent the strip sticking. Both of the rolls were water-cooled. The roll speed was operated at 60m/min and 90m/min. The solidification length of circumferential velocity at 90m/min was 60mm, and that of circumferential velocity 60m/min was 100mm. The Al-Si-SiC_p strip, about 3mm thick, was cast directly from the molten metal. The particles of SiC were dispersed uniformly. The as-cast Al-Si-SiC_p could be coiled because the product had superior ductility. The reason for this was that the eutectic Si of matrix aluminum alloy (Al-Si alloy) became fine and globular. Cold rolling could be used after 1-pass of hot rolling. The 1mm-thick Al-Si-SiC_p plate could be made by one-pass of hot rolling and 3-passes of cold rolling / annealing from as-cast strip. Process savings were attained. The width of Al-Si-SiC_p as-cast strip could be increased up to 600mm.

Keywords: Al-Si-SiC_p, casting, twin roll caster, composite alloy strip

1. Introduction

Recently, aluminium alloy strip is used as a stiffener for copper electronic circuit boards. Many electronic circuit boards are made from copper. The coefficient of linear expansion of aluminium alloy strip is higher than that of an electronic circuit board made from copper; therefore with copper and aluminum alloy strip there is a problem of separation. As a solution to resolve this problem, if an Al-Si-SiC_p composite of low expansivity having the same coefficient of linear expansion as copper could be used, then it was likely it could be used as a stiffener. The composite alloy is a metal matrix composite(MMC) that has high thermal conductivity and high rigidity. Therefore

an Al-Si-SiC_p composite stiffener and a copper electronic circuit board is a good match.

Al-Si-SiC_p alloy has low ductility that is less than 4%. If a slab is rolled over and over in conventional manufacturing by rolling to produce a thin strip, this makes for a high cost production process. And so the present study focused on a twin roll caster because it can make a thin strip directly from molten metal. It also requires low initial capital-investment spending and has low running costs. Vertical type twins roll casters overcome a disadvantage [1] of conventional twin roll casters which is low productivity. The present study investigates the casting of Al-Si-SiC_p composite alloy strip. We also attempt observation of internal tissue and possibility of cold rolling by as cast.

2. The Conventional Twin-Roll Caster

Fig. 1 shows the conventional twin-roll caster design and process operation. The conventional twin-roll caster is able to cast directly from molten metal to thin strip. The caster also needs only a low initial capital-investment. The caster shown uses parting material. The rolls are made from copper. The heat-transfer coefficient of this caster is 30W/mK. Roll surface velocity is 1~3m/min. A characteristic of this caster is cast high loading. It was difficult to make Al-SiC_p composite alloy strip using the conventional caster. The vertical caster has a number of advantages compared with the conventional one.

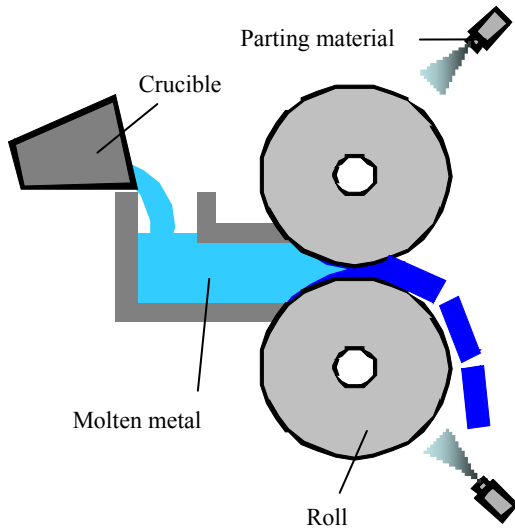


Fig. 1. A conventional twin roll caster

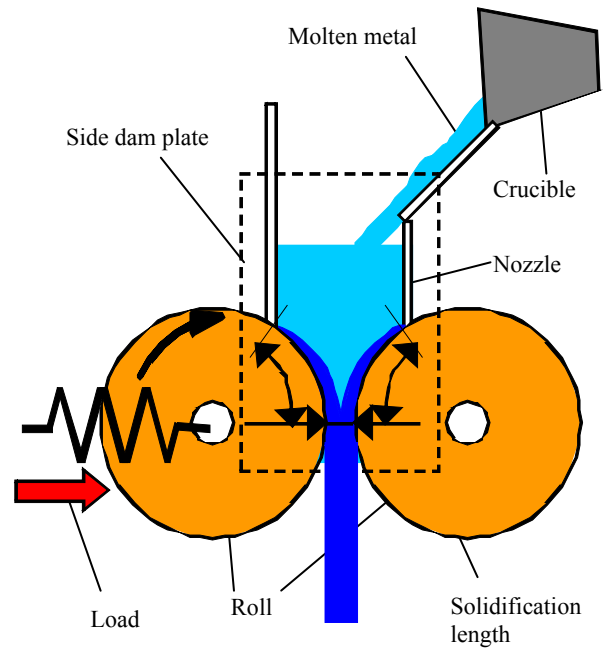


Fig. 2. A vertical type twin roll caster

3. The Vertical Type Twin-Roll Caster

A schematic illustration of the high-speed twin-roll caster is shown in Fig.2. The vertical-type twin-roll caster used was equipped with a nozzle and a cooling slope. The twin roll size was $\phi 300 \times W100$. Copper rolls were used. The coefficient of thermal conductivity is 390 W/mK . This was able to solidify molten metal rapidly as the cooling power of a roll was improved compared with a conventional twin roll caster using steel rolls. Therefore with this caster, it is possible to cast at high roll velocity and benefit from increased productivity. Thin sheet getting is anchored to the roll during the casting process with a high load. The roll was provided with a shape-forming load of 28.2 kN/mm by using a spring. The rolling load was very small. This small load means that hot rolling was not used [2]. Adjustment of sheet thickness did not use pressure, rather adjustment was made through roll velocity and solidification length. A casting nozzle was used to set the solidification strength precisely. The nozzle is set at the upside of the roll. This is to adjust the thickness of the freeze layer. Then heat insulating paper is pasted on to the nozzle and heat insulation cloth is bolt to side-dam-plate. The nozzle is useful to increase the hydrostatic pressure [3]. This leads to an improvement in heat transfer between the roll and the molten metal. The hydrostatic pressure prevents the path of solidification from clogging up. roll and the molten metal. The hydrostatic pressure prevents the path of solidification from clogging up.

4. Experimental conditions and specifications

Experimental conditions and specifications of the roll caster process are shown in Table 1. The metal was used, MC21MMC (metal matrix composite), which was developed by MC21-company. This matrix is A359. Table of ingredients of A359 is shown in Table 2. In the case of the steel roll used for the conventional twin-roll caster for aluminium alloy (CTRCA) [4] [5], parting material was used for preventing the strip from sticking to the rolls. (It does this by improving the heat transfer between molten metal and the rolls). In the case of the copper rolls, the strip did not stick to the rolls by virtue of their high coefficient of thermal conductivity and because the surface temperature did not increase so much. Therefore, the present study did not use parting material.

The roll velocities used were 60 m/min and 90 m/min . This is 15~45 times of the production rate of the conventional twin-roll caster for aluminium alloy (CTRCA). Having made a thin strip, the inside structure was observed by optical microscope. For comparisons, observations were also made of the ingot. This made by heat insulation casting mold having the same cooling velocity as DC casting. The present study investigated the possibility of rolling and attempted cold rolling of the specimen after annealing ($500^\circ\text{C}5\text{h}$) and as cast strip.

Table 1. Experimental conditions

Material	MC21MMC (Al-20%SiC _p)
Liquidus-line temperature [°C]	610
Molten metal amount [Kg]	2
Molten metal temperature [°C]	630
Solidification length [mm]	100, 60
Roll velocity [m/min]	60, 90
Initial roll gap [mm]	0.5
Initial load [kN]	28.2

Table 2. Table of ingredients (wt. %)

Si	Mg	Mn	Cu	Al
8.5-9.5	0.5-0.7	0.1	0.2	bal

5. Results and Discussions

Using the experimental conditions shown in Table 2, it was possible to produce a continuous thin strip of Al-20% SiC alloy. In the case of the experimental condition which is shown in Fig. 3.1 (and the Fig. 3.2 detail) in which roll velocity is 60m/min, it was possible to produce the continuous thin strip of 1.7mm thickness. In the case of 90m/min, much thicker strip of 1.2mm thickness could be produced.

The structure of the surface of a thin strip with the thickness of 1.2mm is shown in Fig. 3. Some brilliant brightness is seen at the surface. In case when the thin strip of 1.2mm in thickness, 100mm in width, and 2500mm in length was rolled into as rolled strip with roll velocity in 90m/min and it was noted that the coil could be made with inner most small diameter of 460mm, without any cracks. The as cast strip was wound at diameter 460mm and the surface condition is shown in Fig. 4.

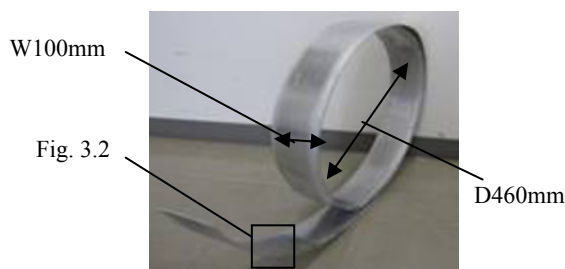
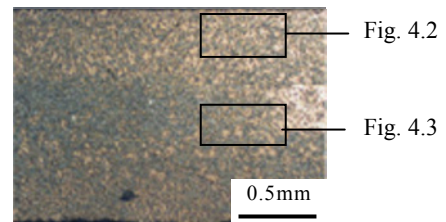
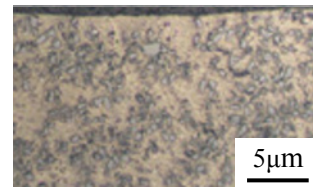
**Fig. 3.** Coil of Al-20%SiC alloy strip**Fig. 4.** Condition of the surface of as cast strip, thickness of this strip is 1.2mm.

Fig. 5 showed the inner structures of the thin strip prepared, namely, the whole area of the thin strip in the thickness direction and large magnifications of two areas near top surface, (Fig. 6), and the central region (Fig. 7). By examining the composition of the prepared thin strip, it is seen that there are many more SiC particles in the central region of the strip than at the top surface. This phenomena is the phenomena thought to be the reason.

**Fig. 5.** Structure of as cast Al-20%SiC_p**Fig. 6.** Structure of near top surface**Fig. 7.** Structure of central region

Inner structure of the thin strip formed by the vertical twin roll caster and by casting mold cast of heat insulating are shown in Fig. 8. The structure made by casting mold cast of heat insulating is seen to have better eutectic silicon. The structure made by a vertical type twin roll caster is seen not to have the better eutectic

silicon. Eutectic silicon was not forming, that mean was brought under review miniaturization by rapid solidification from molten metal.

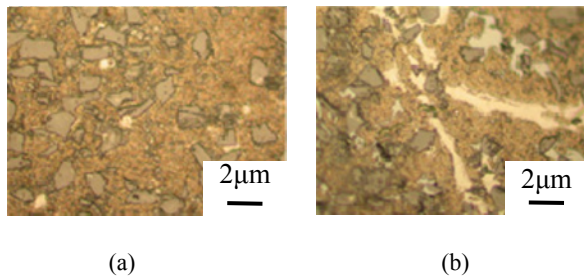


Fig. 8. (a) Inner structure of the thin strip formed by the vertical twin roll caster. (b) Inner structure of the thin strip formed by casting mold cast of heat insulating

The surface condition of the thin strip after cold rolling and that after annealing heat material are shown in Fig. 6. The thickness of the as cast strip was not uniform. The ends of the strip had variable thickness. The central part of strip thickness was uniform. Therefore, both ends of the strip were cut off and a central 25mm portion of uniform thickness was cold rolled. The As cast strip has a crack after cold rolling which is shown Fig. 9 (a). The ingot material was annealed but a subsidiary fracture was caused by cold rolling. However using the annealing material of the roll cast strip, cold rolling was possible, which is shown in Fig. 9(b). That reason is that miniaturization of eutectic Si by using copper roll and having high cooling power a vertical type twin roll caster made for rapid solidification of Al-20%SiC_p. Eutectic Si concerns rolling. Annealed material of thickness 1.7mm, manufactured using a roll velocity of 60m/min was able to be cold rolled twice to reduce it to 1mm.

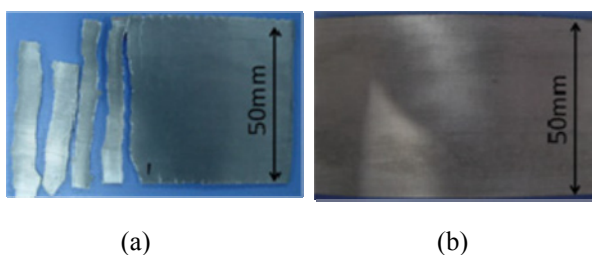


Fig. 9. (a) As cast strip has crack after cold rolling. (b) Cold rolling and that after annealing heat material

6. Conclusions

It was possible to manufacture Al-20%SiC_p by using a high speed vertical type twin roll caster. The addition of SiC-particles may not affect roll cast, nor its continuity. The strip became difficult to adhere when SiC-particles were added. The distribution of SiC-particles was not uniform in the thickness direction. Degree of SiC-particle's density tends to get too high in the strip thickness direction. It was possible to use cold rolling for annealed material. It was possible to roll the as cast to a coil of 460mm inside diameter. In the case of thin strip made by the vertical twin roll caster, eutectic Si became miniaturized compared with ingot material.

7. Suggestion for a New process

The present study suggests a new process for manufacturing thin strip. The reason is that cold rolling and the manufacture of coils are possible. It is possible to anneal as cast strip using a volume of metal in one treatment once it is made into a coil. It is then possible subsequently to continuous roll it as shown in Fig.10. This new process has the advantages that it is able to cut process flow, reduce cost and save space.

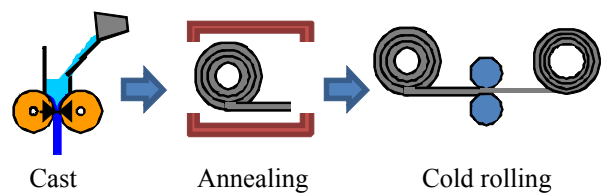


Fig. 10. Suggestion for a new process

References

- [1] T. Haga, (2003) *J.mater.process.Technol.*,140, 610-615
- [2] T. Haga, (2001) *J.mater.process.Technol.*,118:165-168
- [3] T. Haga, H. Inui, H. Sakaguchi, H. Watari, S. Kumai, (2007) *Journal of Achievemets in Materials and Manufacturing Engineering*, vol. 24:365-371
- [4] M. Yun, X. Yang, D.V. Edmonds, J.D.Hunt, P.M. Thomas, (1991) *CastMet*. Vol.4-2, p.108.
- [5] D.V. Edmonds, J.D. Huunt, (1991) *Extraction Refining and Fabrication of Light Metals*, CIM, Ottawa, p.257

Casting of aluminium alloy clad strip using a vertical type tandem twin roll caster

Ryoji Nakamura¹, Toshio Haga², Shinji Kumai³ and Hisaki Watari⁴

¹ Graduate School of Osaka Institute of Technology 5-16-1 Omiya Asahiku Osaka 535-8585 Japan

² Department of Mechanical Engineering, Osaka Institute of Technology 5-16-1 Omiya Asahiku Osaka 535-8585 Japan

³ Department of Materials Science and Engineering, Tokyo Institute of Technology 4259 Nagatsuda Midoriku Yokohama city 226-8502 Japan

⁴ Department of Production Science and Technology, Gunma University 1-5-1 Tenjin kiryu city 376-8515 Japan

Abstract. A roll caster to cast three layers clad strip was devised. In this process, two set of twin roll casters were set at the vertical tandem position. This vertical type tandem twin roll caster was assembled, and three layers clad strip was tried by this caster. The base strip was cast by the upper caster. The overlay strips were cast by the lower caster. The material of the base strip was AA8079. The material of the overlay strip was AA6022. The fabrication process of the three layers clad strip is as blow. The base strip was cast by the upper caster. This strip was drawn into the lower caster. When the base strip went through the roll-bite of the lower caster, the melt of the overlay strips was poured to the lower caster. Three layers clad strip could be cast by a vertical type tandem twin roll caster of the present study. The clad strip was made directly from the molten metals. From the result of the line analysis, the diffusion area between the base strip and the overlay strips was very narrow. The interfaces between the base strip and the overlay strips were clear and flat. It became clear that base and overlay strips were bonded firmly from the bending test.

Keywords: Twin roll caster, Three layers clad strip, Casting

1. Introduction

Recently, the energy saving in the factory is essential to protect the global warming. The process saving is very useful for the energy saving. The many process are needed to fabricate the clad strip in the conventional method. The single strip is made from the slab by the processes as below; homogenization, scrapping, hot rolling and cold rolling [1]. The cladding process is as below; track welding, pressure welding and rolling [1]. The clad strip was made by many processes than single strip. In this way, the clad strip was fabricated many processes. Therefore, the energy saving of fabricated the clad strip was required. In this study, the process to fabricate the clad strip from molten metal was devised. It is thought that the twin roll caster is useful for energy saving at the process to make the strip [2]. The reason is that the strip can be cast directly from the molten metal.

The vertical type tandem twin roll caster is devised by application of the twin roll caster. This makes that the interface of the clad strip can be formed by rolls. In the present study, the vertical type tandem twin roll caster for the clad strip was designed and assembled. Three layers clad strip was tried by the vertical type tandem twin roll caster. Conditions of the interface of this clad strip were investigated and as-cast strip was cold rolled.

2. Vertical type tandem twin roll caster

A vertical type tandem twin roll caster for the clad strip was designed and assembled. Figure 1 shows the schematic illustration of a vertical type tandem twin roll caster. The photograph of the vertical type tandem twin roll caster was shown in Fig. 2. This apparatus is composed of two vertical type twin roll casters. One of the vertical type twin roll casters was the upper position and the other of that was the lower position. The upper position of the vertical type twin roll was upper caster and the lower position of that was lower caster. The base strip was cast by the upper caster. The overlay strips were cast by the lower caster. The diameter of rolls is 200 mm. The material of rolls is copper. The width of rolls of the upper caster is 40 mm. The width of rolls of the lower caster is 50 mm. The width of rolls of the lower caster was wider than that of the upper caster. This mean is that the base strip is easy to go through the lower caster. The nozzle plate and the side dam plate were used at the upper and lower caster. The material of the nozzle and the side dam plate was the mild steel. The thickness of the nozzle and side dam plate was 3.2 mm. The liquidus line of the base strip is higher than that of overlay strips. This reason is that the base strip was remelted by the heat of the molten metal of the overlay strips when the liquidus line of the base strip was lower than that of overlay strips.

Advantages of the this caster is as blow. This clad strip is rapid solidification by copper rolls [3]. Many layers clad strip can be cast by increased the vertical type twin roll caster. The interface between strips is flat by formed rolls.

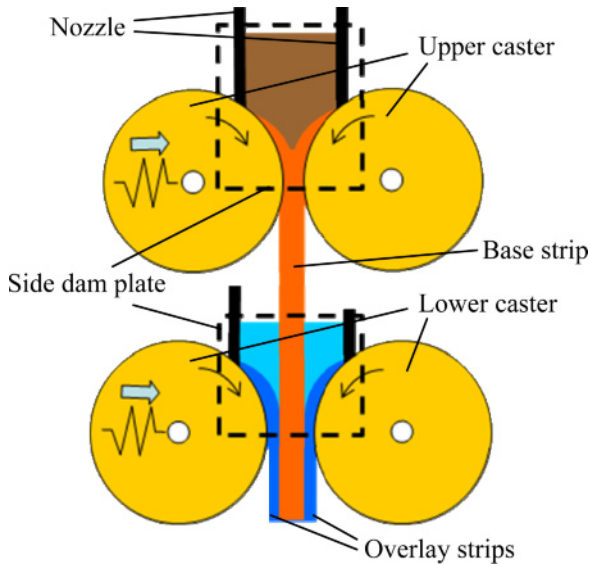


Fig. 1. Schematic illustration of a vertical type tandem twin roll caster

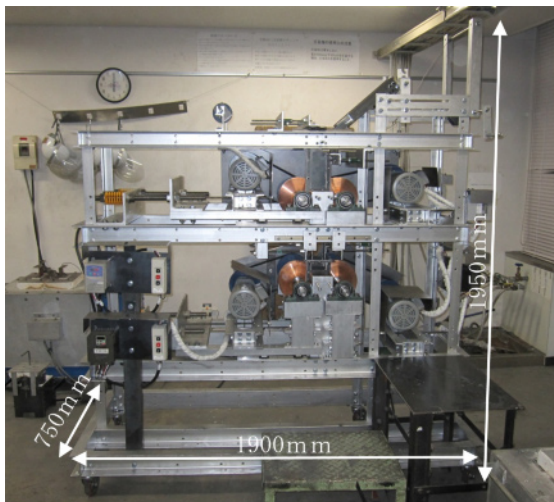


Fig. 2. Photograph of a vertical type tandem twin roll caster

3. Process of the connecting on a vertical type tandem twin roll caster

The process of the connecting on a vertical type tandem twin roll caster is shown in Fig. 3. Procedure of casting of three layers clad strip in this study is as below. The base strip is cast by the upper caster. When the base strip goes

through roll-roll gap of the lower caster, the molten metal of overlay strips is poured in the nozzle. The surface of the base strip contacts the molten metal of overlay strips. Therefore, the surface of the base strip is heated by the molten metal of overlay strips. Base strip and overlay strips were connected at the roll-roll gap. Important factors of the connecting between strips are temperature of the surface of base strip, the temperature of the molten metal of overlay strips and roll speed.

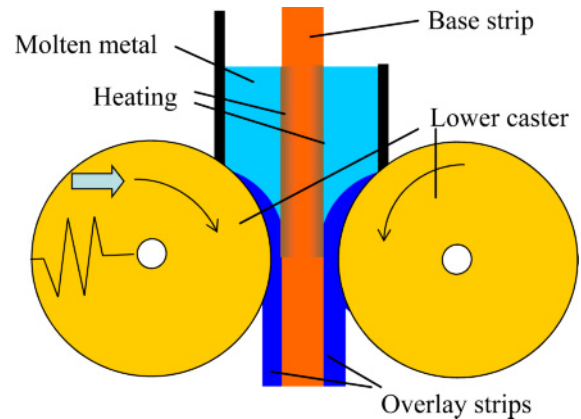


Fig. 3. Illustration of the connecting process

4. Experimental conditions

Table 1. Experimental conditions

Upper caster	Roll[mm]	Diameter: 200, width: 40, material: copper
	Material	AA8079
	Melt temperature[°C]	700
	Contact length[mm]	40
Lower caster	Roll[mm]	Diameter: 200, width: 50, material: copper
	Material	AA6022
	Melt temperature [°C]	670, 700, 750
	Contact length[mm]	80
Roll speed[m/min]		20, 30, 40

Experimental conditions are shown in Table 1. The diameter of rolls was 200 mm. The width of the upper caster was 40 mm and the width of the lower caster was 50 mm. The material of rolls was copper. The material of the base strip was AA8079 and the material of overlay strips was AA6022. The contact length of the upper caster

was 40 mm. The contact length of the lower caster was 80 mm. The melt temperature of the base strip was 700°C. The melt temperature of overlay strips was 670°C, 700°C and 750°C. The roll speed was 20 m/min, 30 m/min and 40 m/min.

5. Results and discussion

5.1 Surface of the clad strip cast

The roll casting of the clad strip was operated. The clad strip could be cast by this caster. Figure 4 shows the surface of three layers clad strip. There was not difference in three kinds of the roll speed. The thickness of the roll speed was 20, 30 and 40 m/min was about 5.0 mm, 4.5 mm and 3.8 mm respectively.

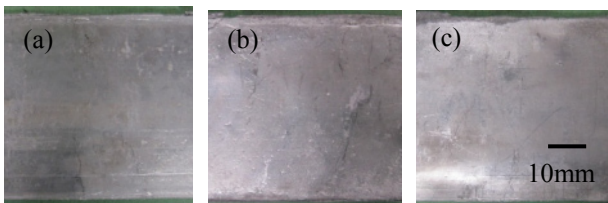


Fig. 4. Surface of three layers clad strip, (a) Roll speed was 20 m/min, (b) Roll speed was 30 m/min, (c) roll speed was 4 m/min

5.2 Effect of connecting conditions of the clad strip by roll speed

The cross sections of the clad strip of three kinds of roll speed were shown in Fig. 5. The cross section of three layers clad strip of Fig. 5(a) was cast at the roll speed was 20 m/min. When the roll speed was 20 m/min, the clad strip was not connected between the base and overlay strips. This reason is that the contact time of rolls of the upper caster is long. Therefore, the surface temperature of the base strip is low. This clad strip was not connected to be low at the surface temperature of the base strip. The cross section of three layers clad strip of Fig. 5(b) was cast at the roll speed was 30 m/min. When the roll speed was 30 m/min, the clad strip was connected between the base and overlay strips. The interface of this clad strip was clear and flat. This reason is that the interface between the base and overlay strips is flat to form at rolls. The cross section of three layers clad strip of Fig. 5(c) was cast at the roll speed was 40 m/min. When the roll speed was 40 m/min, the interface of this clad strip was diffused. This reason is that the roll contact time of molten metal of base strip is short and melt temperature of the overlay strips is high. Therefore, the base strip was remelted by the molten metal of overlay strips.

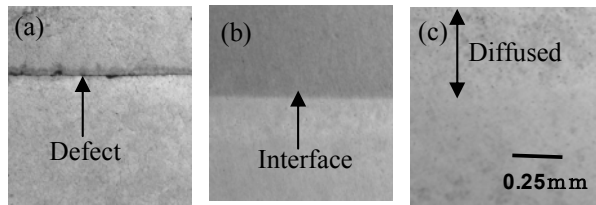


Fig. 5. The cross section of the clad strip. (a) non-sound the clad strip cast by the roll speed was 20 m/min. (b) sound the clad strip cast by the roll speed was 30 m/min. (c) non-sound clad strip cast by the roll speed was 40 m/min, this clad strip was diffused.

5.3 Effect of connecting conditions of the clad strip by melt temperature of overlay strips

The cross sections of the clad strip of three kinds of the melt temperature of overlay strips were shown in Fig. 6. The roll speed of the cross section of three kinds of the melt temperature was 40 m/min. The cross section of the clad strip of Fig. 6(a) was cast by the melt temperature of the overlay strips was 670°C. This clad strip of Fig. 6(a) was not connected between the base and overlay strips. This reason is that the melt temperature of overlay strips is low. The cross section of the clad strip of Fig. 6(b) was cast by the melt temperature was 700°C. This clad strip of Fig. 6(b) was connected. The interface between the base and overlay strips is clear and flat. The cross section of the clad strip of Fig. 6(c) was cast by the melt temperature of overlay strips was 750°C. This clad strip of Fig. 6(c) was diffused at the interface between the base and overlay strips. This reason is that the melt temperature of overlay strips is high. Therefore, the base strip was remelted by the melt temperature of overlay strips.

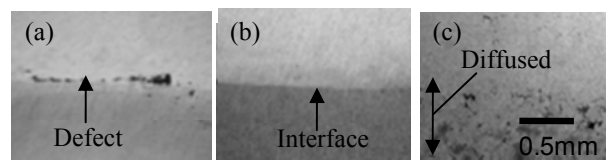


Fig. 6. Cross section of the clad strip cast by three kinds of melt temperature of overlay strips, (a) non-sound the clad strip cast by melt temperature of the overlay strips was 670°C. (b) sound the clad strip cast by melt temperature of the overlay strips was 700°C. (c) non-sound the clad strip cast by melt temperature of the overlay strips was 750°C.

5.4 Line analysis of the interface

Figure 7 shows the cross section of three layers clad strip. The interface of this three layers clad strip was clear and flat. The result of the line analysis of the clad strip around the interface is shown in Fig. 8. It is thought that diffusion zone of the Fe is very narrow. The clad strip could be made from AA8079 strip and AA6022 strip without mixed zone by this process.

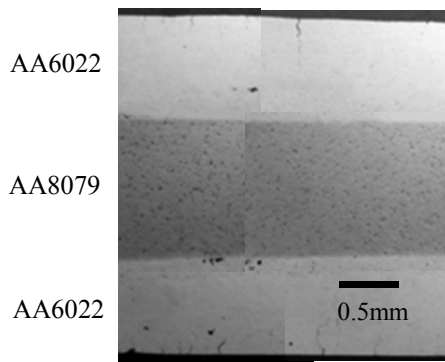


Fig. 7. The cross section of three layers clad strip at roll speed was 30 m/min

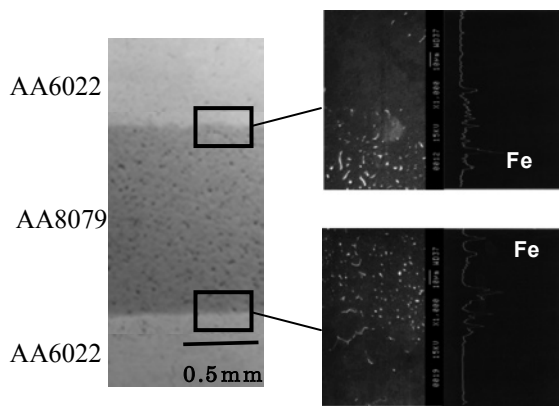


Fig. 8. Result of the line analysis of the clad strip around the interface

5.5 Cold rolling of three layers clad strip

The cross section of the clad strip after cold rolling is shown in Fig. 9. The as-cast strip was cold rolled down to 1 mm without annealing. If the joining is not enough, the crack occurs at the interface between the base and overlay strips. The crack did not occur at the interface between the base and overlay strips after cold rolled. The clad ratio of as-rolled strip was as same as that of as-cast strip.

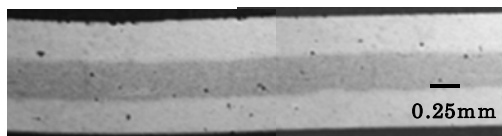


Fig. 9. Result of the cold rolled

5.6 Bending test

Figure 9 shows the cross section of three layers clad strip after the bending test. Three layers clad strip was bend continuously until broken. Result of the bending test, three layers clad strip was not peeled at the interface. It is

thought that three layers clad strip was joined firmly at the interface.

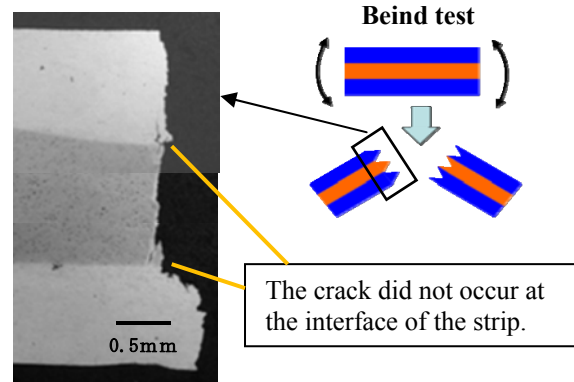


Fig. 10. The cross section of three layers clad strip after the bending test

6. Conclusions

The vertical type tandem twin roll caster to cast three layers clad strip was devised and assembled. The casting of three layers clad strip was tried using the vertical type tandem twin roll caster of the present study. Three layers clad strip could be casted by this caster. The interface between the base strip and overlay strips of this clad strip was very narrow. The as-cast strip could be cold-rolled down to 1 mm. The interface of this clad strip was not peeled by the bending test. This clad strip could be connected firmly. This process is very useful to save the energy to make three layers clad strip.

References

[1] T. Haga, R. Nakamura, S. Kumai, H. Watari, Clad strip casting by a twin roll caster, Archives of Materials Science and Engineering 37/2 (2009) p.p.117-124.
 [2] H. Watari, T. Haga, K. Davey, N. Koga, T. Yamazaki (2006) Effects of production parameters on characteristics of magnesium alloy sheets manufactured by twin-roll casting, Journal of Achievements in Materials and Manufacturing Engineering, Vol.16, p.p.171-176
 [3] T. Haga, H.Inui, H. Sakaguchi, H. Watari, S. Kumai, (2007)High speed twin roll caster for aluminum alloy thin strip, Journal of Achievements in Materials and Manufacturing Engineering, Vol.24, p.p.365-371

Micro-forming of aluminum alloy by cold rolling

Toshio Haga¹, Kouta Inoue¹, Hideto Harada¹ and Ryoji Nakamura¹

¹ 5-16-1 Omiya Asahi-ku Osaka city 535-8585, Japan

Abstract. In the present study, crystal aluminum alloy with fine grain was used for micro-forming. The micro-forming was tried on the melt spun Al-14mass%Si foil by cold rolling. The ability of micro-forming of a metallic alloy by cold forming was investigated. A V-shape die was used with depths of 1, 3, 5 and 10 μm . Rolling speed was 1 m/min. The as-cast foil was cold rolled and polished to make the surface smooth. The polished foil was annealed at 400°C before the micro-forming. The thickness of the foil used for micro-forming was 100 μm .

Keywords: micro-forming, melt spinning, aluminum alloy

1. Introduction

The metallic glass was used for the micro-forming [1-4]. The reason was that the metallic glass has good formability and smoothness of the surface at the micro-forming. The grain of the crystal alloy is usually too large against the die size for the micro-forming and the micro-forming is not easy. In the present study, crystal aluminum alloy with fine grain was used for micro-forming. The micro-forming was tried on the melt spun Al-14 mass%Si foil by the cold rolling. In the microforming of the metallic glass, forming speed was slow compared to macro-forming. The micro-forming of the metallic glass is operated at the temperature higher than the glass temperature T_g . In the present study, the rolling speed was near to that of the macro-forming. The micro-forming was operated at the room temperature. The ability of the micro-forming of the metallic alloy by the cold forming was investigated.

2. Experimental condition

Figure 1 shows a schematic illustration and photograph of the melt spinning process of the present study. This process is a nozzle pressing melt spinning method [5]. The specification and the experimental conditions of this melt spinning process are shown in Table 1. The property of the melt spinning of this study is the thickness of the foil. The foil cast by the conventional melt spinning or PFC (planer flow casting) is thinner than 0.05 mm. The

melt spinning in the present study can cast a foil of 0.2 mm thickness. Some devices were adopted to cast thicker foils. The gap of the slit-nozzle in this study was 1 mm (ref. Fig.1). The gap is usually 0.5 mm. The gap was wider than the conventional melt spinning to cast thick foils. The nozzle was inclined by 30 degrees against the roll surface to prevent the back break of the melt. The nozzle is usually perpendicular to the roll surface. The back break of the melt occurred easier as the nozzle-roll gap becomes wider. The tip of the nozzle is pressed against the foil. The roll contact surface flattens due to the pressing force. When the press load became too high, the foil started to stick to the nozzle-tip. The initial nozzle-roll clearance was 0.1 mm, and it increased to 0.2 mm during the casting as the foil lifted up the nozzle. The nozzle pressing made the better-heat-transfer condition between the strip and the roll. When the nozzle pressing was not operated, the foil was not cooled enough.

Al-Si alloy is conventional alloy for casting. Therefore, Al-Si alloy has good casting ability for melt spinning. Moreover, Al-Si alloy is reasonably cheap, and Al-12%Si is eutectic. The eutectic point shifts to the hyper side as the cooling rate increases. The Si content at eutectic was about 15 mass% at the roll contact surface of the foil when the foil was cast by the nozzle pressing melt spinning method. In eutectic condition, the grain size decreased. However, the free solidified surface was not sound when the Si content was higher than 15 mass%. In this reason, Al-14%Si, which was close to eutectic, was chosen in the present study. It is thought that the Al-14 mass%Si is hard enough to use the mold die of the resin as this alloy exhibits a good wear-resistance.

Figure 2 shows the processes of foil-casting, flattening of the surface of the foil and micro-forming by cold rolling. The roll contact surface of the as-cast foil was not flat. The unevenness of the surface is thought to be caused by the unevenness of the wetting condition between the molten metal and the roll. The surface of the as-cast strip was too rough to operate in micro-forming. Cold rolling using a Cr-plate roll was operated to flatten the surface. The as-cast foil was annealed for 4 hours at 250°C before cold rolling. The unevenness was improved

by cold rolling. However, the evenness was not sufficient for micro-forming yet. Therefore, buffing was operated on the surface of the as-rolled foil to improve the evenness. Annealing was done at 300°C and 400°C before the micro-forming. The micro-forming was operated on the surface after buffing at roll speeds of 0.5, 1.0 and 2.0 m/min respectively.

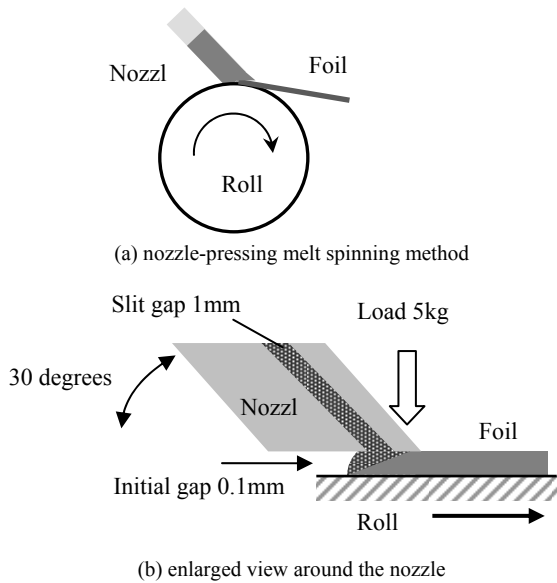


Fig. 1 Schematic illustration showing the nozzle-pressing method to cast the foil

Table 1 Specification and experimental conditions of nozzle-pressing method to cast the foil

Roll	material: copper diameter: 300 mm speed: 10 m/min
Nozzle-roll gap	initial: 0.1 mm
Specimen	Al-14mass%Si
slit nozzle	gap: 1.0 mm inclination angle: 30 degrees
nozzle pressing	50 N

Usually, stamping is used for micro-forming. However, cold rolling was chosen as the process for micro-forming in this study. In case of stamping, the contact condition is face-contact, whereas in rolling, the contact condition is line-contact. The load on the die in the case of of-line-contact is smaller than that of face-contact, which is a major advantage. In micro-forming, the forming speed is very slow (500 s/10 μm). The forming speed of the

rolling could be set much higher (0.08 s/10 μm) than that of stamping (press forming). The roll speed was set to 2 m/min, and rolling was carried out at conditions identical to those at cold working.

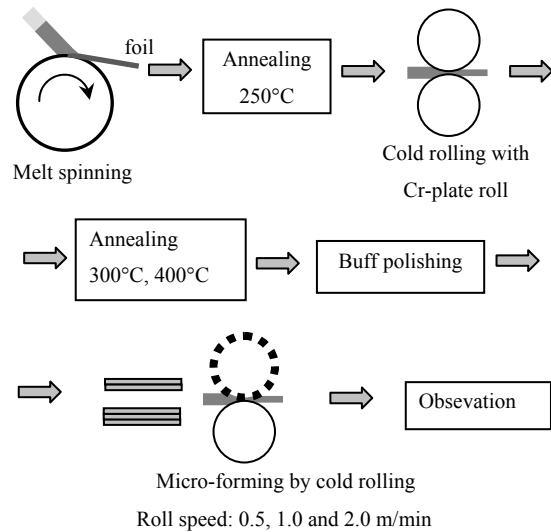


Fig. 2 Schematic illustration showing the process of foil-casting, flattening of the foil-surface and micro-forming by cold rolling.

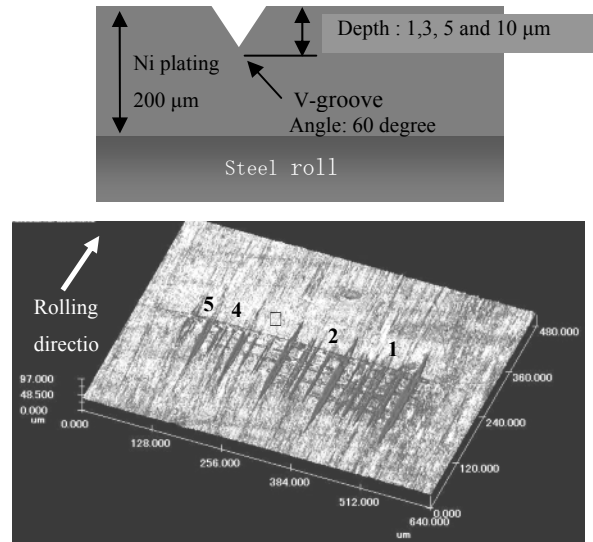


Fig. 3 Schematic illustration and LSCM image of V-groove die

A 200 μm-thick Ni plating was applied to the tip, and the V-grooves for the die were machined into the surface of this Ni plating. The tip was then attached to the roll. The angle of the V-groove was 60 degrees. The depth of the V-groove was 1, 3, 5, and 10 μm respectively, and the diameter of the roll was 70 mm.

The LSCM (laser scanning confocal microscopy) image of the V-grooves on the chip and their pattern is shown in Figure 3. There five areas are marked 1 to 5. The depths of the grooves were different in each area.

The directions of the grooves were rolling direction and lateral direction. The grooves were machined by FANUC ROBONANO α -OiB which is a 5-axis nano machine [6, 7].

The thickness of the strip after buff-polishing was about 0.1 mm. Setting the roll-bite clearance below 0.1 mm proved to be difficult. Therefore, two or three foils were superimposed when the micro-forming was operated by the cold rolling to prevent breaking of the grooves.

3. Result and discussion

The foil could be cast continuously, and the as-cast foil is shown in Fig. 4. The thickness of the as-cast foil ranges from 0.20 mm to 0.23 mm. The nozzle-pressing process was useful to reduce the air pocket on the roll contact surface of the foil compared to conventional melt spinning. However, many air pockets remained on the roll-contact surface of the as-cast foil. The air pocket could not be completely pressed by the nozzle-pressing. The nozzle-pressing process was useful to make the free solidified surface sound, too. The free solidified surface was not flat when the method except for the nozzle-pressing process was used. Moreover, the free solidified surface was not completely solidified at 0.2 mm-thick foil cast by other processes. The free solidified surface was completely solidified when the nozzle-pressing method was used. The heat transfer between the foil and the roll was improved by the nozzle-pressing. The foil flew off from the roll after having cooled sufficiently. The edges of the foil were linear and width of the foil was constant.

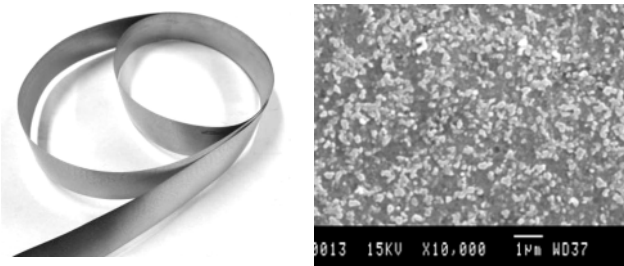
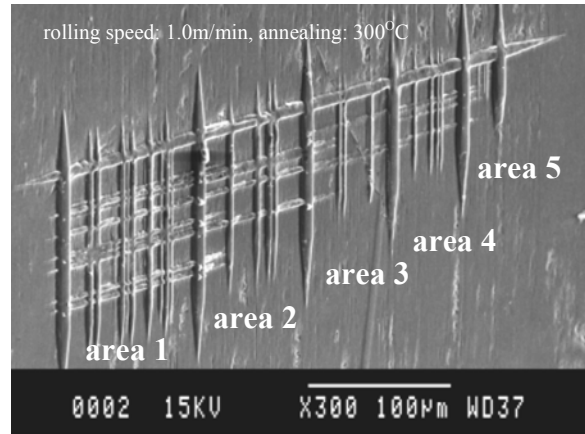
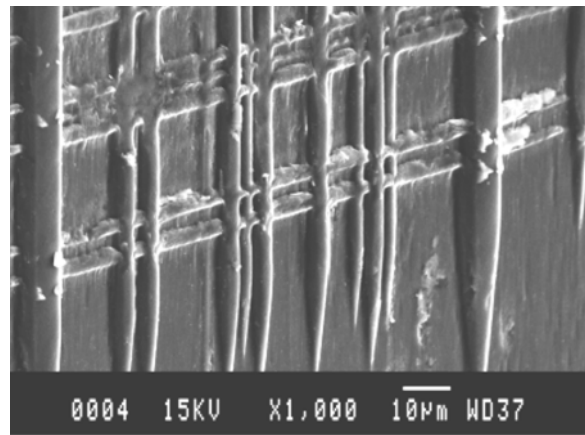


Fig. 4 The over view of the as-cast foil and microstructure near the roll-contact surface of the as-cast strip

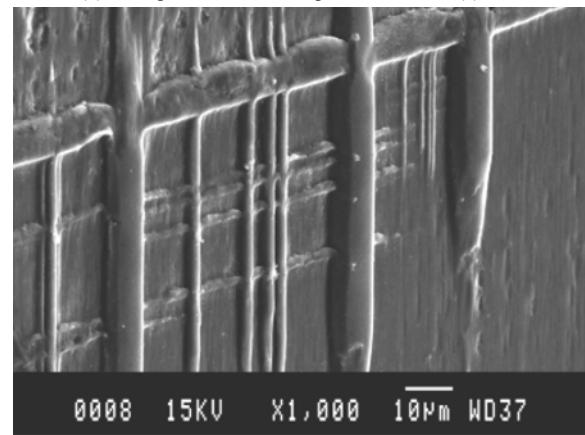
The microstructure of the as-cast foil is shown in Fig. 4, too. The area depicted in Fig. 4 is located 10 μm off the roll contact surface. The white particle is eutectic Si. The size of the eutectic Si was smaller than 0.4 μm . The picture shows the presence of primary Al, although primary Si cannot be detected, in spite of Al-14 mass%Si being hyper eutectic. The reason for this is believed to be that the eutectic point shifted to hyper side due to rapid solidification.



(a) Overview of micro-formed area



(b) Enlarged view of lower part of area 1 of (a)



(c) Enlarged view of area 4 and area 5 of (a)

Fig. 5 Result of micro-forming of Al-14 mass%Si foil by cold rolling at a speed of 1 m/min

This research explored cold rolling as well, and SEM images of the result of micro-forming are shown in Figures 5 and 6. The effects of annealing temperature, rolling speed and number of superimposed foils on micro-forming were investigated. The SEM image provides an overview of the micro-formed area. It is clear that micro-forming of Al-14%Si aluminum alloy by cold rolling was

not possible. The protrusion was formed in rolling direction. However, the height of the protrusion was low in lateral direction, indicating that the forming ability is affected by the direction. The protrusion in rolling direction was not drastically affected by the conditions of rolling speed, annealing temperature and the number of superimposed foils at the forming by grooves deeper than 3 μm . The forming of protrusions by 1 μm deep grooves was affected by the number of super imposed foils. When the two pieces of foils were superimposed, the protrusion could be formed by the 1 μm deep groove as shown in Fig. 6. When the 2 grooves of 1 μm depth were side by side without clearance, the protrusions were formed side by side.

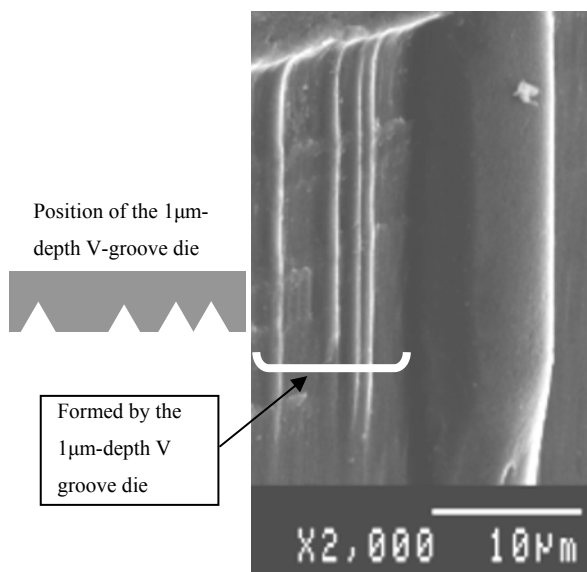


Fig. 6 Result of the micro-forming operated using the 1 μm -depth V-groove die by the cold rolling

The forming speeds were 0.08 s/10 μm , 0.04 s/10 μm and 0.02 s/10 μm , at roll speeds of 0.5 m/min, 1.0 m/min and 2.0 m/min. The forming speed represents the time it took to form a 10 μm high protrusion. In the conventional micro-forming of metallic glass, the forming speed is, for example, 500 s/10 μm . In this way, the forming time used in the present study was very short.

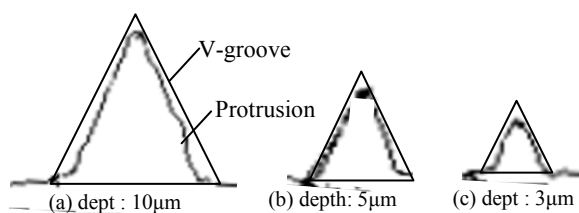


Fig. 7 Schematic illustration showing the relationship between V-groove and protrusion. The shape of the protrusion was measured using LSCM. The direction of the protrusion is in rolling direction.

The shape of the protrusion measured by the LSCM is shown in Fig. 12, and its height is provided in Table 2. The direction of the measured protrusion is in rolling direction. The V-groove was not filled by the metal. The width of protrusion was narrower than that of the V-groove. The foil was prolonged and the width of protrusion might become narrow. The difference between the depth of the V-groove and the height of the protrusion was less than 0.3 μm . It is thought that this result is sufficient.

Table 2 The height of the protrusion formed by the V-groove. The direction of the protrusion is in rolling direction.

Depth of V-groove	1 μm	3 μm	5 μm	10 μm
Height of formed metal	0.7 μm	2.8 μm	4.8 μm	9.7 μm

4. Result and discussion

Micro-forming was tried on the surface of a rapidly solidified Al-14 mass%Si crystalline foil by cold rolling. The angle of the V-groove was 60 degrees, with a depth of 1, 3, 5 and 10 μm . The rolling speed was 0.5, 1.0 and 2.0 m/min. With this rolling speed, the forming time for protrusions of 10 μm height was 0.08 s, 0.04 s and 0.02 s, respectively. The 1 m/min of rolling speed was better. Protrusions parallel to the rolling direction could be formed. The forming of the protrusion was better at the two pieces of imposed foils. This reason was not clear. The ability of micro-forming of crystalline aluminum alloy with a fine grain structure by cold rolling was demonstrated by this study.

References

- [1] Y. Saotome and A. Inoue, (1994) Superplastic microforming of microstructures, Proc.IEEE Micro Electro Mechanical System, Tokyo, 343-347.
- [2] Y. Saotome, T. Iijima, T. Zhang and A. Inoue, (2003) Microforming of metallic glasses with laser micromachined polyimide dies, J.Metastable and Nanocrystalline Materials, 15-16: 655-658.
- [3] Y. Saotome, S. Okaniwa, T. Zhang, A. Inoue, (2005) Nanofarming of metallic glass with nano-scale die fabricated by focused ion beam, *ibid.* 24-25: 291-294.
- [4] M. Ishida, H. Takeda, N. Nishiyama, Y. Shimizu, K. Kita, Y. Saotome, A. Inoue, (2005) Characterization of super-precision microgear made of Ni-based metallic glass, *ibid.* 1.24-25: 543-546.
- [5] T. Haga, M. Motomura, (1998) Casting of aluminium alloy thin strip by nozzle pressing single roll rapid solidification method, Trans. Japan Society of Mechanical Engineering 64: 390-396.
- [6] www.eengraving.com/machines/fanuc/pdf/FANUC_ROBOno_Alpha-OiB.pdf
- [7] www.fanucbulgaria.com/robonanos.html

Rapid shape measurement of micro deep drawing parts by means of digital holographic contouring

N. Wang, C. v. Kopylow and C. Falldorf

Dept. of Optical Metrology, BIAS GmbH, Klagenfurter Str. 2, 28359 Bremen, Germany

Abstract. An experimental approach is presented to rapidly measure the shape of a micro deep drawing part, which is based on a lensless Fourier-holographic contouring. The surface structure of the investigated object is dominated by the properties of the drawing process. Therefore, the statistical properties of the light scattered from the surface have been investigated and it is shown that digital holography is applicable in this case. Finally, experimental results which prove the big potential of digital holography in regards to inspection of micro parts are given. It is shown that the field of depth can be considerably enhanced by combining several reconstructions associated with different observation planes from a single measurement.

Keywords: Contouring, Digital Holography, 3D shape measurement, depth of focus, micro deep drawing parts

1 Introduction

Currently, the manufacturing of modern mass produced products has to be cost-effective. The cold forming process fulfills this requirement especially for the production of high quantities of micro parts. Fig.1 shows a commonly produced micro deep drawing part, which has dimensions of about 1mm width and 0.5mm height. It is seen, that this bowl-like metal part has a special shape and surface characteristic which depends on the deep drawing process.

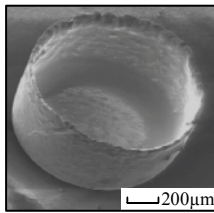


Fig. 1. Image of a micro deep drawing part obtained by means of a scanning electron microscope (SEM).

These micro parts are commonly fabricated at a high production rate and are liable to shape mismatches, fractures and other defects. Therefore, in order to control

the quality during the complex forming process, a fast and non-invasive measurement technique has to be used.

For this purpose, a large variety of already existing shape measurement approaches [1-7] might be considered. For example, the confocal microscope can provide precise inspection of micro objects with high accuracy. However, currently there are no commercially available solutions, which at the same time provide both a rapid and a non-invasive investigation of microscopic objects. One of the major problems is the limited depth of focus which is a common characteristic for any microscopic imaging technique. In the following paragraphs, it will be shown that digital holographic contouring [8] can solve this problem and therefore might be considered a valuable approach in regards to inline inspection of micro deep drawing parts.

1.1 Principle of Contouring by means of Multiple Illumination Directions

Contouring by means of multiple illumination directions is a well established method to measure the shape of a diffusely reflecting object [4,7,8]. Generally this technique is based on two sequentially recorded phase distributions of light, which are scattered by the object under test. Each recorded phase distribution is associated with a specific direction of illumination. If the geometrical setup parameters are known, the shape of the object can be calculated from the phase difference of the two phase distributions. In this section the scheme used to measure the shape of the micro part is briefly presented. (see Fig. 2). The method is based on the shifting of a point source from position S_1 to S_2 .

Firstly the distance between the object and the source point is assumed to be large compared with the dimensions of the object. In this case, the light incident on any point P at position $\mathbf{r}_P=(r_x, r_y, r_z)$ on the surface of the object can be described as a plane wave. Its phase $\varphi_{P,i}(\mathbf{r}_P)$ is given by:

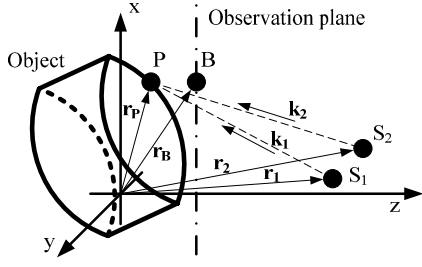


Fig. 2. Geometric model of contouring by means of multiple illumination directions: S_1 and S_2 indicate the positions of the light source. P is a point on the object and B a point on the observation plane. The distance between the object and the light source should be so large in comparison to the dimension of the object, that the light incident on point P can be regarded as a plane wave.

$$\varphi_{P,i}(\mathbf{r}_P) = \mathbf{k}_i \cdot (\mathbf{r}_P - \mathbf{r}_i), \quad (1)$$

where \mathbf{r}_i and \mathbf{k}_i denote the positions of the light source during the i -th measurement and the wave vector of the corresponding plane wave. Let it be further assumed that any point P on the surface can be associated to a specific point B in the observation plane. This is especially true for those parts of the image, on which the object appears to be in focus. The phase $\varphi_i(\mathbf{r}_B)$ at this observation point B is then given by:

$$\varphi_i(\mathbf{r}_B) = \varphi_{P,i}(\mathbf{r}_P) + \frac{2\pi}{\lambda} |\mathbf{r}_B - \mathbf{r}_P|. \quad (2)$$

The shape information of the object can be calculated from the phase difference of the phase distributions associated with two positions of the light source:

$$\begin{aligned} \Delta\varphi(\mathbf{r}_P) &= \varphi_1(\mathbf{r}_B) - \varphi_2(\mathbf{r}_B) \\ &= (\mathbf{k}_1 - \mathbf{k}_2) \cdot \mathbf{r}_P + c_0. \end{aligned} \quad (3)$$

Here, the constant c_0 only depends on the position of the light sources and the wave vectors rather than the shape information of the object. The phase difference is independent of the observation point but is directly related to the position of the point P on the surface of the object. When the differences of the wave vectors $\Delta\mathbf{k} = \mathbf{k}_1 - \mathbf{k}_2$ and their components $\Delta\mathbf{k} = (\Delta k_x, \Delta k_y, \Delta k_z)$ are introduced, the scalar product in Eq. 3 can be rewritten in the following form:

$$\Delta\varphi(\mathbf{r}_P) = \Delta k_x r_x + \Delta k_y r_y + \Delta k_z r_z + c_0. \quad (4)$$

Since the shape of the object is related to the coordinate r_z , the first two terms in Eq. 4 can be ignored when subtracting a phase ramp. This ramp can either be determined by the geometrical parameters of the setup or by a calibration process using a flat surface. According to this, if the angles of the illumination direction α_i are known and c_0 is set to be $c_0 = 0$, then we obtain:

$$\begin{aligned} \Delta\varphi_1(r_z) &= \Delta k_z r_z \\ &= \frac{2\pi}{\lambda} [\cos \alpha_1 - \cos \alpha_2] \cdot r_z. \end{aligned} \quad (5)$$

From this, the desired shape information of the object can be directly calculated by the height r_z .

1.2 System Setup

Here, digital holography is used in order to obtain the phase distribution of the light in the observation plane. In Fig. 3, a schematic Fourier-holographic setup for digital holographic contouring is presented. A micro deep drawing part, which has the same dimensions as the one shown in Fig.1, is the object under measurement. It is illuminated by a plane wave, provided by an optical fibre in the front focal plane of a collimating lens. The angle of the plane wave can be changed by either shifting the source point or the lens. A second fibre is located close to the object and provides a spherical reference wave. In order to capture the hologram arising from the superposition of the reference wave and the light scattered from the object, an analyzer (polarization filter) is located in front of the camera which equalizes the polarization states of the interfering wave fields. Considering the complex amplitude $U(\mathbf{r}_S) = A(\mathbf{r}_S) \cdot \exp[i\varphi(\mathbf{r}_S)]$ in the sensor domain $\{\mathbf{r}_S\}$, the hologram $H(\mathbf{r}_S)$ is given by [5]:

$$\begin{aligned} H(\mathbf{r}_S) &= |U(\mathbf{r}_S) + R(\mathbf{r}_S)|^2 \\ &= |U(\mathbf{r}_S)|^2 + |R(\mathbf{r}_S)|^2 + U^*(\mathbf{r}_S) \cdot R(\mathbf{r}_S) + U(\mathbf{r}_S) \cdot R^*(\mathbf{r}_S). \end{aligned} \quad (6)$$

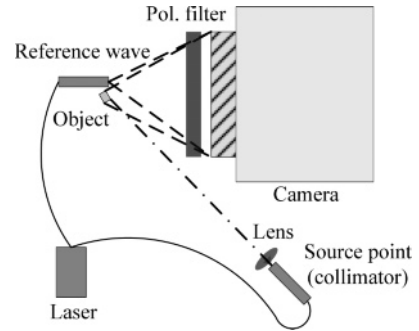


Fig. 3. Sketch of the setup

For the investigations, a dye-laser was used with a wavelength of $\lambda = 582\text{nm}$ and the sensor of the camera had 2452×2054 pixels with a size of $3.45 \times 3.45\mu\text{m}$. The distance between the object and the camera was set to be about 3cm, in order to obtain a suitable speckle size compared with the pixel size of the camera.

2. Experimental Results

Digital holographic contouring is a speckle technique. Therefore, an important prerequisite is that the speckle field is fully developed [9], e.g. that the surface scatters light in any direction rather than reflecting it like a specular surface. Since the surface characteristics of the object investigated depends strongly on the fabrication process of micro deep drawing, this important fact must be validated in preparation to the measurement. A common technique for verification of the statistical properties of fully developed speckles is the probability density distribution of the captured intensity which is given by [10,11]

$$P(I) = \frac{1}{I} \exp\left(-\frac{I}{I}\right). \quad (7)$$

The calculated probability density distribution of the measured intensity of the speckle field is given by Fig. 4. The dashed line shows the probability density function $P(I)$ as it is expected from Eq. 7. Comparing the curves, it is found that the measured probability density is in reasonable agreement with the theory. The remaining deviations arise because the physical speckle field has been convoluted by the sensitivity profile of the camera pixels. This has the effect of lowpass filtering and therefore reduces the probability for black and changes the statistics for small intensities as seen from the measured density distribution in Fig. 4 [12]. From the results, it can be concluded that digital holographic contouring should in principle be applicable to typical micro deep drawing parts such as the presented bowllike structure.

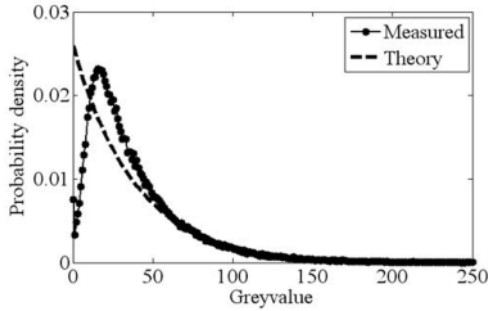


Fig. 4. Probability density function of the detected speckle field.

The captured holograms have been used to reconstruct the complex amplitude $U(\mathbf{r}_B^{(j)})$ of the wave field scattered by the object in four different observation planes ($j = 1, \dots, 4$) by extracting $U(\mathbf{r}_S)$ from Eq.6 by means of Fourier filtering and solving the Rayleigh-Sommerfeld diffraction formula [5]:

$$U(\mathbf{r}_B^{(j)}) = \int U(\mathbf{r}_S) \cdot \exp[i(\mathbf{r}_S - \mathbf{r}_B^{(j)})] d\mathbf{r}_S^{(j)}. \quad (8)$$

The differences $\Delta\varphi^{(j)} = \varphi_1(\mathbf{r}_B^{(j)}) - \varphi_2(\mathbf{r}_B^{(j)})$ of the corresponding phase distributions associated with the two illumination directions are exemplarily shown for two depths in Fig. 5.a and Fig.5.b. It is clearly seen that due to the limited depth of focus across a single reconstruction, both of the phase differences is partly corrupted by speckle decorrelation, which is marked by the white boxes.

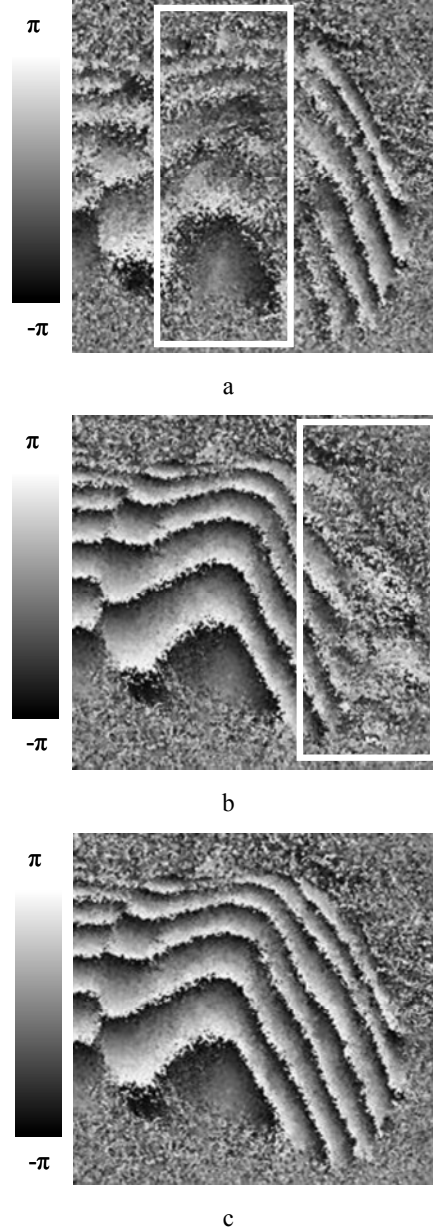


Fig. 5. The phase differences between the two phase distributions exemplarily (a) $\Delta\varphi^{(1)}$ in the lower, (b) $\Delta\varphi^{(4)}$ in the top observation plane and (c) a combined phase difference, obtained in only one Fourier-holographic measurement with two illumination directions. All distributions are sampled by 440×460 pixels.

In order to retrieve an undistorted phase difference for the whole micro deep drawing part, a combined phase difference was created manually from the parts which are not prone to decorrelation effects. The result of this procedure is presented in Fig. 5.c. To recover the shape from the combined phase difference, it has to be unwrapped, e.g. the discontinuous 2π -jumps arising from the sinusoidal nature of the phase have to be eliminated by adding multiples of 2π [13]. After subtracting the known phase ramp as mentioned in Section 2, the unwrapped phase values are inserted into Eq. 5. The result is shown in Fig.6.b. For comparison the reconstructed amplitude $A(\mathbf{r}_B^{(4)})$ in the top observation plane is shown by Fig.6.a.

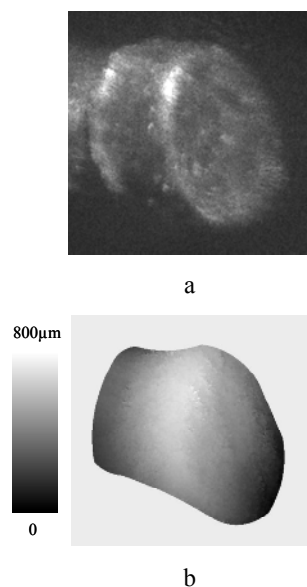


Fig. 6. (a) The reconstructed amplitude $A(\mathbf{r}_B^{(4)})$ in the top observation plane for comparison, and (b) the unwrapped phase map from the manually created phase difference after subtracting of phase ramp, which corresponds to the height of the object. All distribution are sampled by 440×460 pixels.

3. Conclusion

In order to measure the shape of a micro deep drawing part, an experimental approach has been taken which is based on a lensless Fourier-holographic contouring by means of two illumination directions. Using this scheme, the shape of the micro part was successfully captured. The advantages of the proposed method over the current state of the art are:

- this method is non-invasive, rapid and accurate for objects fabricated in a micro deep drawing process;
- this method provides an enhanced depth of focus in comparison with standard microscopic imaging techniques.

The investigations have shown that digital holographic contouring has big potential in regards to quality control and optical inspection of micro parts fabricated in a cold forming process.

Acknowledgement

The authors would like to thank Prof. R. B. Bergmann for valuable discussions. Further, we gratefully acknowledge the financial support by the DFG (German Research Foundation) within the frame of subproject B5 *Sichere Prozesse* of the SFB 747 (Collaborative Research Center) "Mikrokalumformen - Prozesse, Charakterisierung, Optimierung".

References

- [1] Takeda M, Yamamoto H, (1994) Fourier-transform speckle profilometry: three-dimensional shape measurements of diffuse objects with large height steps and/or spatially isolated surfaces. *Appl. Opt.* 33:7829-7837
- [2] Sansoni G, Corini S, Lazzari S, Rodella R, Docchio F, (1997) Three-dimensional imaging based on Gray-code light projection: characterization of the measuring algorithm and development of a measuring system for industrial applications. *Appl. Opt.* 36:4463-4472
- [3] Huang PS, Hu Q, Jin F, Chiang FP, (1999) Color-encoded digital fringe projection for high-speed three-dimensional surface contouring. *Opt Eng* 38 6:1065-1071
- [4] Kreis T, (2005) *Handbook of Holographic Interferometry: Optical and Digital Methods*. Weinheim, Wiley-VCH
- [5] Schnars U, Jueptner W, (2005) *Digital Holography: Digital Hologram Recording, Numerical Reconstruction, and Related Techniques*. New York, Springer
- [6] Chen F, Brown GM, Song M, (2000) Overview of three-dimensional shape measurement using optical methods. *Opt. Eng.* 39:10-22
- [7] Agour M, Huke P, Kopylow Cv, Falldorf C, (2009) Shape measurement by means of phase retrieval using a spatial light modulator. In *Proc. On Advanced Phase Measurement Methods in Optics and Imaging*, Locarno, Switzerland
- [8] Abramson N, (1976) Holographic contouring by translation. *Appl. Opt.* 15:1018-1022
- [9] Goodman JW, (1975) Statistical properties of laser speckle patterns. In: J.C. Dainty, Editor, *Laser Speckle and Related Phenomena*, Springer-Verlag:9-75
- [10] Kadono H, Asakura T, (1985) Statistical properties of the speckle phase in the optical imaging system. *J. Opt. Soc. Am. A* 2:1787-1792
- [11] Falldorf C, Osten W, Kolenovic E, (2003) Speckle shearography using a multiband light source. *Optics and Lasers in Engineering* 40:543-552
- [12] Osten W, (2000) Digital processing and Evaluation of Fringe Patterns in Optical Metrology and Non-Destructive Testing In: K.-H. Laermann (Ed.): *Modern Optical Methods in Experimental Solid Mechanics*, Springer Verlag Wien:289
- [13] Robinson DW, (1993) Phase unwrapping method. In: *Interferogram Analysis: Digital Fringe Pattern Measurement Techniques*:194-299

Fracture Limits of Metal Foils in Micro Forming

F. Vollertsen, Z. Hu, H. Wielage, L. Blaurock

BIAS – Bremer Institut für angewandte Strahltechnik GmbH, Klagenfurter Str. 2, 28359 Bremen, Germany

Abstract. The downscaling of manufacturing processes leads to a rise in new challenges in process design. Amongst these challenges is a decrease in the limiting drawing ratio observed in micro deep drawing of metal foils. Furthermore, fracture occurs at punch force levels well below those predicted by common equations. In this paper, it is proposed that these phenomena can be accounted for by non-uniformities in the flow behavior of the material due the large difference between grain sizes. The localized strains before fracture - as recorded by digital image correlation - of stretch formed aluminum foils are presented and the strain evolution is examined. Evidence to verify the working thesis is gathered by implementing the observed flow non-uniformities into a finite element simulation and comparing the computed results with the experimental ones.

Keywords: micro forming, material failure, material limits

1. Introduction

The process limit in micro sheet forming is usually mainly affected by material failure [1]. The layout of a process in order to achieve a required process capability value relating to material failure requires a precise knowledge of the real process conditions which lead to material failure in the form of cracks. Thus, a requested process capability can be reached concurrently with cost efficient material selection.

An indicator of the maximum formability of the material is the limiting drawing ratio. It is defined as the ratio of the maximum blank diameter that can be successfully drawn into a cup to the punch diameter without flange [2]. A major failure mode that prevents a blank from being successfully drawn into a cup is fracture near the cup bottom. In [3], process windows for micro and macro sheet forming were determined. A decrease in the limiting drawing ratio was observed in the micro deep drawing of metal foils. Furthermore Hu established [4] that fracture occurs below the theoretical force by bottom fracture. Therefore, experimental investigations in micro deep drawing with a punch diameter of 1 mm with aluminum (thickness 20 μm) were carried out. It was found that the maximum punch force ranged 50 % below the calculated force by bottom fracture.

In order to find an explanation for these phenomena, a closer look was taken at the forming limit behaviour of

micro stretch formed specimens. Therefore, this paper reports on forming experiments conducted on aluminum foils (AISI 1050A) with a thickness of 20 μm , and results of a finite element simulation of the strain behaviour of the stretch formed specimens.

2. Experiments

In order to analyze fracture limits of micro formed specimens, the forming method pneumatic bulge test was used. The set-up of the pneumatic bulge test is shown in Fig. 1. The specimen is fixed on the pressure hull by a drawing die. By adjusting the regulating valve, the internal pressure is raised till the specimen cracks. The pressure gauge measures the actual pressure in the cavity before the specimen cracks. The equivalent punch velocity is set to 0.4 mm/s. For the stretch-forming experiments, a die with a diameter of 6.4 mm was used.

All experiments were conducted using cold-rolled aluminum foil AISI 1050A which was fully annealed by the supplier to condition O. The cross-sections of the aluminum foils were investigated by optical microscopy and electron backscatter diffraction mapping.

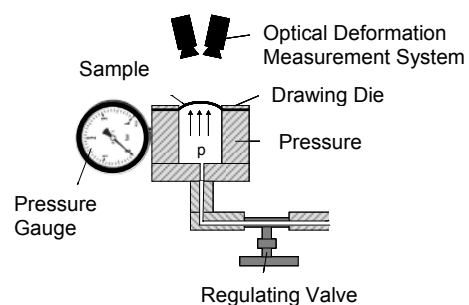


Fig. 1. Set-up of the pneumatic bulge test

The local strain on the specimen was measured using digital image correlation with an adapted optical deformation measurement system ARAMIS (GOM International AG). For correlation purposes, a fine gray-

scale pattern was applied to the blanks via a spray-painting process specially adapted to the accuracy requirements and fragility of the blank material. The uncertainty in displacement measurement is calculated to a typical value of 0.04 Pixel. With the pixel spacing of 6.8 μm , the displacement uncertainty therefore equals 0.03 microns. With a given computational domain for the discrete derivation Δx , the uncertainty of strain measurement can be calculated using [5]

$$\Delta\varepsilon = \frac{\Delta d}{\sqrt{2} \cdot \Delta x} \quad (1.1)$$

Equation 1.1 shows the impact of a chosen computational domain on the uncertainty of strain measurement. Maximizing the computational domain leads to a negligible uncertainty in strain measurement and a reduction in calculation time for the derivation. However, as a trade-off, the increased computational domain blurs localized strain differences. A computational domain of $\Delta x = 8$ Pixel was found to be a good compromise allowing the observation of local effects with a reasonable uncertainty of strain measurement of approximately 0.35 % engineering strain.

3. Results

3.1 Strain Distribution over Specimen

The strain at the position of fracture is usually larger than anywhere else in the specimen in a bulge test. Therefore, it is necessary to investigate the strain distribution on the specimen, especially before cracking occurs. For this purpose the pneumatic bulge test was first simulated using the program ABAQUS 6.9-2 to get a theoretical strain distribution for this test. In this simulation, the same conditions and the same material properties as in the experimental tests were applied. The simulated strain distribution is shown in Fig. 2a). The strain increases monotonically from the border to the center of the specimen. Theoretically, the fractures should occur in this range. Furthermore, major and minor strains show the same distribution pattern with identically values.

Using the method described in section 2, the strain distribution in the specimen in the pneumatic bulge test was acquired experimentally. One example is shown in Fig. 2b). Compared with the simulated results, the experimental strain distribution clearly shows a large difference. The strain is not distributed rotationally symmetric. Some separated islands show higher strains than the remaining material of the specimen. These local strain maxima are the starting points of the cracks. No crack showed the same major and minor strains.

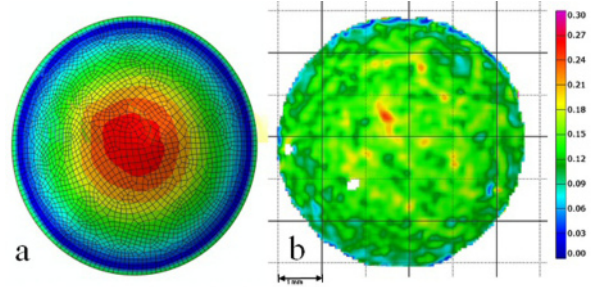


Fig. 2. Comparison of simulation and experiment for an aluminum specimen with a thickness of 20 μm , die diameter 6.4 mm, color scale: von Mises strain; a) FEM-simulation of pneumatic bulge test, load: 5 bar in 13 s, material data of tensile tests; b) effective strain of a pneumatic stretch formed specimen, last picture before crack

3.2 Fracture Distribution over Specimen

As a main indicator for the characterisation of fracture behaviour, the fracture distribution over the specimen was investigated. Therefore, fifteen 20 μm thick specimens, which were stretch formed by the pneumatic bulge test, were evaluated to determine the crack position on the specimen. Fig. 3 shows the position of the crack with respect to the direction of rolling. It can be seen that no preferred direction of cracking with respect to the direction of rolling can be identified.

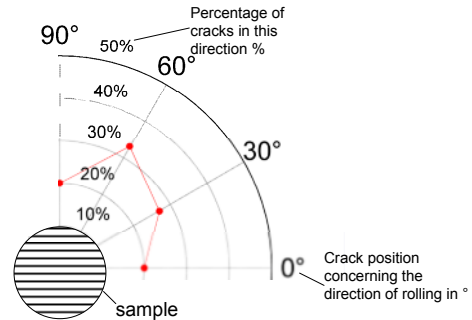


Fig. 3. Position of the crack with respect to the direction of rolling of 20 μm thick specimen

A frequency scale of the distance from the specimen center to the position of the fracture is displayed in Fig. 4. The graph reveals no normal distribution of the fracture distance. The fractures are distributed between boundary and center of the specimen. However, the frequency of fractures at the middle of the specimen (within a circle with a diameter of 1 mm) is the lowest, which is totally opposite to the theoretical prediction shown in Fig. 2a). This indicates that the conventional theory implemented in the model is not necessarily valid for the analysis of fracture behaviour of micro specimens. For a better control of the micro forming processes, an increase in understanding of forming behavior of micro specimens is required.

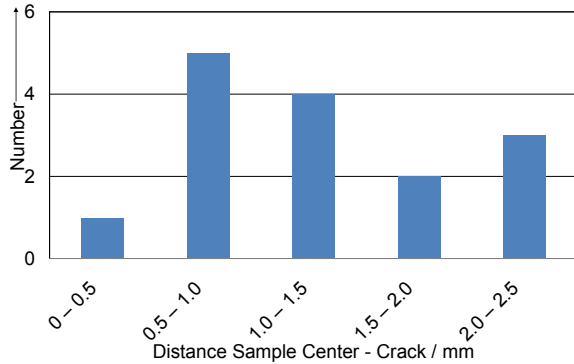


Fig. 4. Distribution of the distance of specimen center to crack on the specimen of 20 μm thick specimens

4. Discussion

4.1 Yield Strength Distribution over Specimen

Using ARAMIS, the local strain of the specimen in a pneumatic bulge test can be acquired. Since the geometrical parameters and the pressure in the cavity are known, the actual stress loaded locally on the specimen in bulge test can be calculated. Thus, a stress-strain curve can be produced for each spot of the specimen. Due to the non-uniform strain distribution (Fig. 2b) on the thin specimen in the bulge test, different stress-strain curves were produced for one specimen. As an example, Fig. 5 shows two different flow curves produced from one specimen. Curve B is for an element in the crack, which was not positioned in the middle of the specimen. Curve A is for a specimen element, which was not cracked. The flow stress of curve A is obviously higher than of curve B.

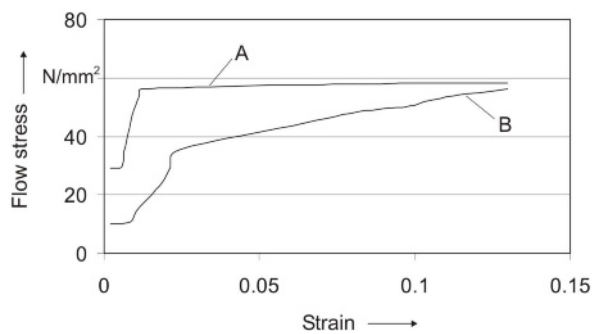


Fig. 5. Different flow curves of a specimen

In order to verify the influence of these different stress-strain curves on the fracture behaviour of thin specimens, the observed flow non-uniformities were implemented into a FEM-simulation for the bulge test with the program ABAQUS 6.9-2. The conditions implemented in the

simulation are shown in Fig. 6a), in which several regions with properties defined according to curve B in Fig. 5 were set. The rest of the specimen material was defined according to the curve A. The simulated strain of the specimen in bulge test is shown in Fig. 6b). A focused strain exists in the spot, whose property was defined according to the curve B, though its position is not in the middle of the specimen. This is similar to what was observed in the experiments and indicates that the non-uniform fracture behaviour of thin specimens is due to the non-uniform material strengths.

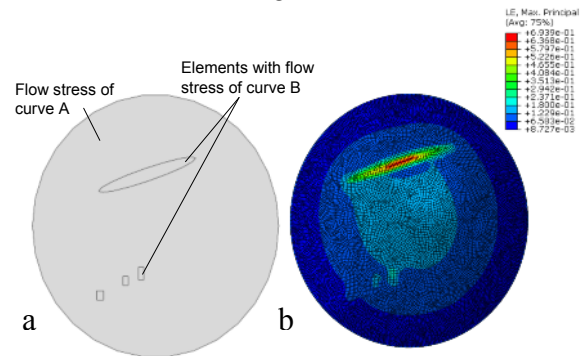


Fig. 6. FEM-Simulation conditions (a) and results for true strain behavior (b) for an Al99.5 specimen with a thickness of 20 μm

4.2 Grain Size Distribution over a Specimen

In order to find out the reason for the non-uniform strength of thin specimens, a closer look was taken at the material and its microstructure. Fig. 7 shows micrographs of the surface of a 20 μm (Fig. 7a) and a 0.4 mm (Fig. 7b) thick aluminum foil. In both cases, there are many big grains and some regions with quite small grains. Grains in different sizes have different flow behaviours. In the case of the 0.4 mm thick sheet, the difference between the big grains and the small grains is not as large as in the case of the 20 μm thick foil. This might be the reason for the extreme non-uniform strength of the thin specimen, which leads to a non-uniform fracture behaviour in micro forming processes.

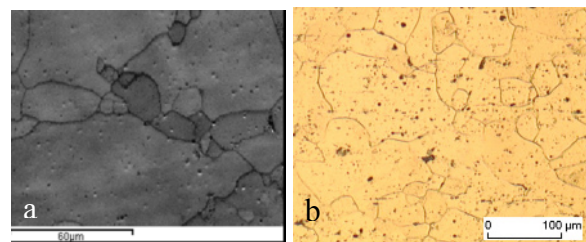


Fig. 7. Surface micrograph of: a) Material Al99.5, thickness 20 μm ; b) Material Al99.5, thickness 0.4 mm

5. Conclusion

Pneumatic bulge tests were carried out on aluminum foils with the thickness of 20 μm . Contrary to the expected concentric strain-pattern, a highly irregular local distribution of strain was observed on the specimens. Fracture occurred at random radial distances from the centerpoint of the specimens. One possible reason for this non-uniform fracture behavior was identified as non-uniformities in the flow behavior of the material due to the large difference between grain sizes. This was illustrated by a FEM-simulation.

Acknowledgements

The authors would like to thank the Deutsche Forschungsgemeinschaft (DFG) for their support within the Collaborative Research Centre 747 "Micro Cold Forming" (subproject B1)

References

- [1] Vollertsen, F., Blaurock, L., Einfluss der Umformgeschwindigkeit und der Messauflösung auf das Formänderungsverhalten in der Mikroblechumformung, Proceeding of 4th Kolloquium Mikroproduktion, Editors Vollertsen, F. et al., BIAS Verlag, ISBN: 978-3-933762-32-0, 243-252
- [2] Lange, K.: Umformtechnik - Handbuch für Industrie und Wissenschaft, Band 3: Blechbearbeitung, Springer-Verlag, Berlin (1990)
- [3] Hu, Z., Walther, R., Vollertsen, F., Influence of size effects on the process window for deep drawing, IDDRG 2009 International Conference, June 1-3 2009, Golden/USA, eds. B.S. Levy, D.K. Matlock and C.J. Van Tyne, ISBN 978-0-615-29641-8, 785-796
- [4] Vollertsen, F., Hu, Z., on the Drawing Limit in Micro Deep Drawing, Journal for Technology of Plasticity, Vol. 32 (2007), number 1-2, 1-11
- [5] Allais L, Bornert M, Bretheau T, Caldemaison D. Experimental characterization of the local strain field in a heterogeneous elastoplastic material. Acta Metall Mater 1994, 42(11), 3865–80, in: Orteu, J.-J.: 3-D computer vision in experimental mechanics

A theoretical model for the velocity field of the extrusion of shaped sections taking into account the variation of the axial component

P. Farahmand¹ and K. Abrinia¹

¹ School of Mechanical Engineering, College of Engineering, University of Tehran, Tehran, I.R.Iran,
Tel: +98 21 61114026 Fax: +98 21 88013029, Email: Cabrinia@ut.ac.ir

Abstract. A new formulation has been given which accounts for the variation of the velocity field in the axial direction in any section of the deforming region. The difference in the present formulation with previous ones is its generality and the improvements in the final results obtained by this method as compared with previous works. The main features in the new formulation are the initial and final velocity discontinuity surfaces which are defined by three dimensional curved surfaces. These surfaces are constructed using parametric B-spline curves which could be easily manipulated changing the shape of the velocity discontinuity surface and hence the deforming region. An upper bound on power has been obtained using the mentioned velocity field. Extrusion of polygonal shaped sections was analyzed using the present formulation and the results showed about 10 percent improvements over previous works data. Experiments were also carried out and good agreements were observed between experimental and theoretical results.

Keywords: Velocity Field, Discontinuity Surface, Forward Extrusion, Shaped Sections, Upper Bound, Experiment

1. Introduction

Velocity fields proposed for the upper bound analysis of the forward extrusion of shaped sections, by previous workers, have mostly assumed flat surfaces of velocity discontinuities at entry to and exit from the deforming region. This is obviously a deviation from reality and apart from causing the upper bounds to be further away from the real situation; this also meant that the prediction of material flow could not have been predicted properly using the previous solutions.

Early works on this subject could be found in paper by Nagpal and Altan [1] who introduced the idea of a dual stream function. Based on this concept they obtained a kinematically admissible velocity field on which the upper bound to the extrusion load was based. Yang and Lee [2] published an analysis of the three-dimensional extrusions of sections through curved dies using a conformal transformation technique. Extrusion of non-circular sections through shaped dies was

investigated by Gunasekara and Hoshino [3] who improved their results as compared to previous works. Chitkara and Abrinia [4] gave a generalized upper bound solution for the forward extrusion of shaped sections in which CAD-CAM mathematical relations were incorporated. Cleik and Chitkara [5] applied the upper bound method to off-centric extrusion of square sections. Abrinia and Bloorbar [6] presented a new improved upper bound solution for the extrusion of shaped sections using CAD techniques. Abrinia and Makaremi [7] gave a formulation for the extrusion of sections with larger dimensions than the initial billet. Wu and Hsu [8] gave account of a velocity field which incorporated the effect of the varying axial component of the velocity field. However in this paper a newly developed formulation has been presented for the kinematically admissible velocity field of the forward extrusion of circular to square section profile, accommodating the variation of the velocity in the axial direction. Due to the generality of the formulation, it could be applied to many shaped profiles.

2. Theory

In the present work the velocity profile has been formulated according to a more realistic case of Figure 1, where the entry and exit surfaces of the deforming region have been taken as curved surfaces. Clearly the amount of curvature for the entry and exit velocity discontinuity surfaces could be different. In fact these have been taken as optimization parameters for the upper bound formulation.

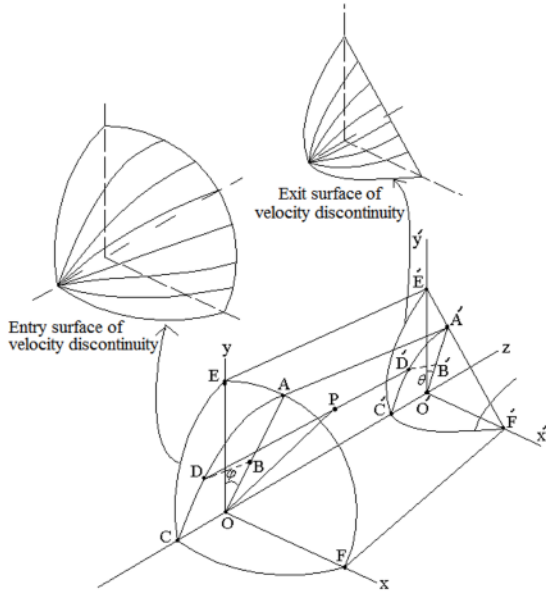


Fig. 1 Deformation zone of the forward extrusion of the shaped sections-velocity fields with varying axial components

Consider a particle of material moving towards the deforming region from the left side of Figure 1 and touching the velocity discontinuity surface at point D and then moving on a streamline DD' where it leaves the deforming region at D' . Then one can define the entry and exit surfaces of velocity discontinuities as follows.

$$Z = Z(u, \varphi) \tag{1}$$

$$Z' = Z'(O'B', \varphi') \tag{2}$$

Now points B and B' lie on lines OA and $O'A'$ respectively and are used to define the coordinates of points D and D' as general points on the curved velocity discontinuity surfaces. A general expression defining the streamline DD' could be defined as:

$$\vec{r}(u, q, t) = f(u, q, t)\vec{i} + g(u, q, t)\vec{j} + h(u, q, t)\vec{k} \tag{3}$$

where u, q and t are parameters related to the cylindrical coordinate system r, φ and z such that

$$0 \leq u = \frac{r}{R} \leq 1, \quad 0 \leq q = \frac{n\varphi}{\pi} \leq 1 \quad \text{and} \quad 0 \leq t = \frac{z}{l} \leq 1$$

Functions f, g and h define the x, y and z coordinate of any point in the deforming region. More details about these formulations can be found in earlier works by the author [6] and [7]. The Cartesian

coordinates of a general point P on any streamline such as DD' can be written as:

$$X = f(u, \varphi, t) = u(R \cos(\varphi)(1-t) + F_2 t) \tag{4}$$

$$Y = g(u, \varphi, t) = u(R \sin(\varphi)(1-t) + G_2 t)$$

$$Z = h(u, \varphi, t) = (1-t)Z + t(L + Z')$$

Hence equation (3) becomes:

$$r = u \left[\begin{matrix} (R \cos \varphi(1-t) + F_2 t)\vec{i} + (R \sin \varphi(1-t) + G_2 t)\vec{j} \\ + ((1-t)Z + t(L + Z'))\vec{k} \end{matrix} \right] \tag{5}$$

Now in order to determine the function $h(u, q, t)$ we have to define the initial and final discontinuity surfaces as in Figure 2.

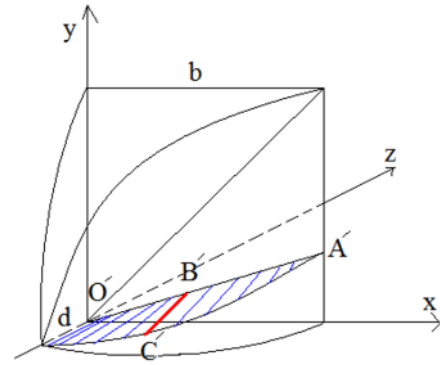


Fig. 2 Deformation region for the exit section

The initial velocity discontinuity surface (Figure 2) is defined by a parametric function. This function is influenced by various initial extrusion parameters. The function chosen to provide these properties is a **B-Spline** function. It is defined by four control points in an allowable region obtained using De Boor algorithm:

$$\begin{aligned} p_{i-3}(z) &= 0 \\ p_{i-2}(z) &= d/4 \\ p_{i-1}(z) &= 3d/4 \\ p_i(z) &= d \end{aligned} \tag{7}$$

Rotating the base function around Z-Axis covering the velocity discontinuity surface, the control points above Z axis would not change. Thus the cubic_B spline function is:

$$\begin{aligned} z(v) &= \frac{(1-v)^3}{6} p_{i-3} + \frac{3v^3 - 6v^2 + 4}{6} p_{i-2} \\ &+ \frac{-3v^3 + 3v^2 + 3v + 1}{6} p_{i-1} + \frac{v^3}{6} p_i \end{aligned} \tag{8}$$

Substituting for the control points from equation (7) into equation (8) we have:

$$z(v) = \frac{3v^3 - 6v^2 + 4}{6} \times \frac{d}{4} + \frac{-3v^3 + 3v^2 + 3v + 1}{6} \times \frac{3d}{4} + \frac{v^3}{6} \times d \quad (9)$$

Kinematically admissible velocity field

The velocity field formulation used here is very similar to that in [7] except that the axial component is formulated differently to accommodate its variation in each cross section. For the extrusion of a circular billet to a square section, considering that \bar{r} in equation (3) defines a general streamline (point p in figure (2)), the equation of the velocity vector for the same point on the streamline could be defined by:

$$V = \frac{1}{(V_x^2 + V_y^2 + V_z^2)^{\frac{1}{2}}} (V_x i + V_y j + V_z k) \quad (10)$$

The components of the velocity field are given by:

$$V_x = \frac{f_t}{h_t} V_z, \quad V_y = \frac{g_t}{h_t} V_z \quad \text{and} \quad V_z = M(u, q, t) \quad (11)$$

where the derivative of function f , g and h are derived from equations (4) and function $M(u, q, t)$ is obtained from the incompressibility conditions (see [7]). Once the velocity field has been obtained the strain rate and the upper bound on power are easily found using the equations given in [7].

3. Results and Discussions

The results for the extrusion of rectangular section from round billet are shown in Figure 3. The effect of reduction of area on the extrusion pressure is illustrated in this figure and it can be seen that the correct trend is predicted. It is also noted that higher reductions cause the optimum relative die length to increase.

Similar results for the extrusion of hexagonal sections are also shown in Figure 4 where the influence of friction on the extrusion pressure is shown. In these figures putting the friction factor equal to 1 gives the case for flat faced die extrusion and other values of friction factor are for bilinear dies with different lubrication and surface qualities.

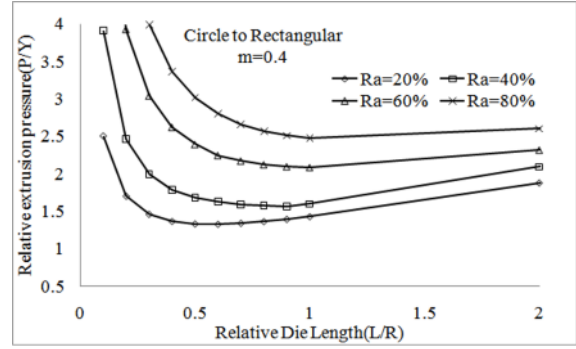


Fig. 3 Extrusion of rectangular section-effect of reduction of area on the relative extrusion pressure

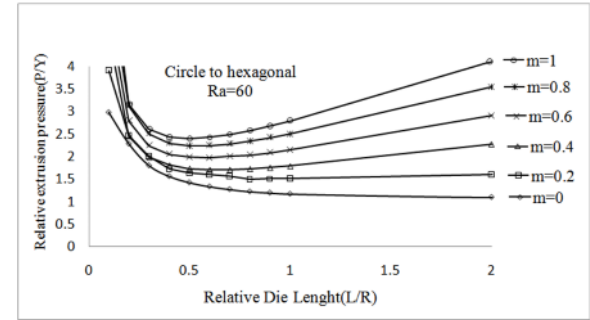


Fig. 4 Extrusion of hexagonal section-effect of friction on the relative extrusion pressure

As it was explained in the theory section, the shapes of the initial and final velocity discontinuity surfaces are controlled by parameters a and d so that smaller values for these parameters mean that the shape of the surfaces approach a flat plane. The effect of these parameters is shown in Figure 5. It can be seen from this figure that the smaller the value for the initial velocity discontinuity parameter, a , the smaller is the value for the extrusion pressure. This means that the initial velocity discontinuity surface must be flat. It is also seen from Figure 5 that the final velocity discontinuity parameter, d , influences the extrusion pressure, having an optimum value for a given set of conditions.

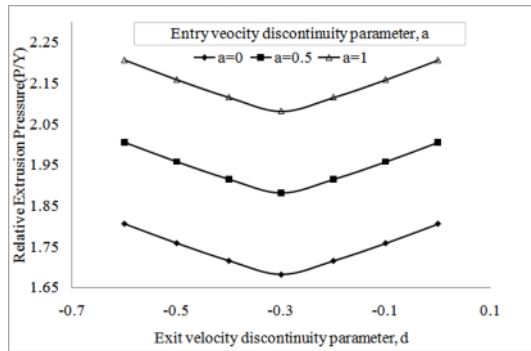


Fig. 5 Effect of initial and final velocity discontinuity parameters on the relative extrusion pressure

Since in this work the component of the axial velocity was taken to be varied in each cross section along the deforming region the velocity distributions of the axial component are given in Figure 6. The top figure shows the velocity distribution for different angular positions and at a certain position on the radial direction as shown. In the bottom figure the distribution is shown for different radial positions and a certain angular position.

Comparisons of results with previous work for the extrusion of square section from round billet are shown in Figure 7 and the extrusion of hexagonal section from round billet is shown in Figure 8. From Figures 7 and 8 it can be seen that the present results give lower upper bounds and are better when compared with previous results.

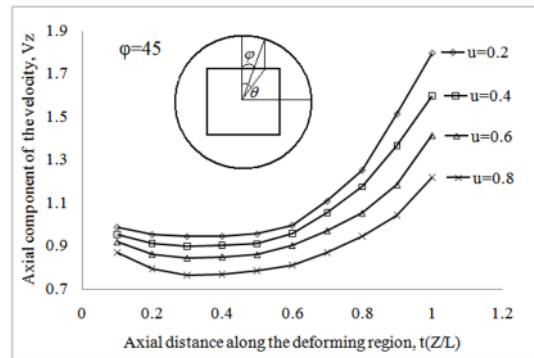
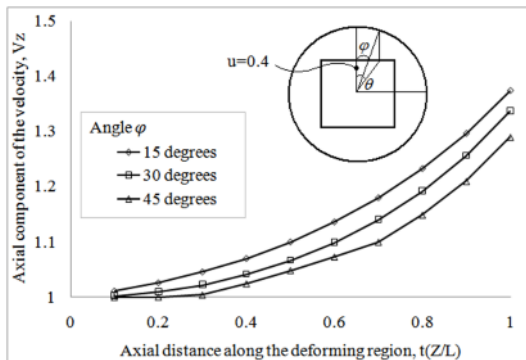


Fig. 6 Velocity distribution for the axial component of the material flow along the deforming region.

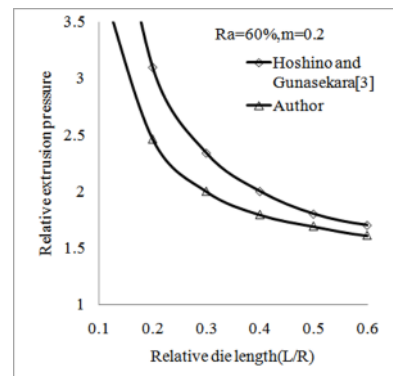


Fig. 7 Comparison of results with previous work for the extrusion of square profile

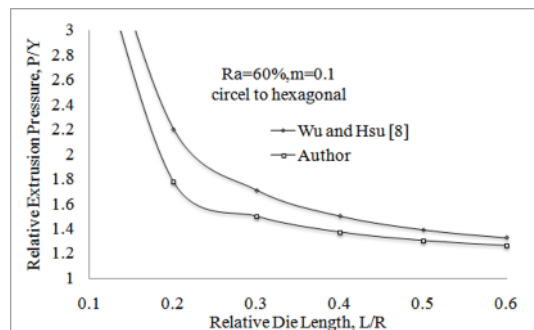


Fig. 8 Comparison of results with previous work for the extrusion of hexagonal profile

References

- [1] Nagpal V, Altan T, (1975) Analysis of the three dimensional metal flow in extrusion of shapes with the use of dual stream functions. 3rd. NAMRC Conference, Pa., Pittsburgh, 26-40.
- [2] Yang DY, Lee CH, (1978) Analysis of three-dimensional extrusion of sections through curved dies by conformal transformation. *Int.J.Mech.Sci.* 20(9) 541-552.
- [3] Gunasekara, JS, Hoshino S, (1980) Extrusion of non-circular section through shaped dies. *Annals of the CRIP VOL 29.*
- [4] Chitkara NR, Abrinia K, (1990) A generalized upper-bound solution for three-dimensional extrusion of shaped sections using CAD/CAM bilinear surface dies. 28th Int. Matador Conf.
- [5] Celik KF, and Chitkara NR, (2000) Application of an upper bound method to off-centric extrusion of square sections, analysis and experiments. *Int.J.Mech.Sci.* 42 321-345.
- [6] Abrinia K, Bloorbar H, (2000) A new improved upper bound solution for the extrusion of shaped sections using CAD techniques. *Proceedings of COMPLAS VI Conference-Barcelona, Spain.*
- [7] Abrinia K, Makaremi M, (2008) A New Three Dimensional Solution for the Extrusions of Sections with Larger Dimensions than the Initial Billet. *J.Mat.Proc.Tech.* 205, 259-271.
- [8] Wu CW, Hsu RQ, (2000) A universal velocity field for the extrusion of non-axisymmetric rods with non-uniform velocity distribution in the extrusion direction. *J. Mat. Proc. Tech.*, 97, 180-185.

A theoretical model for the material flow for the forward extrusion of complicated and non-symmetric sections

M. Ghorbani¹ and K. Abrinia²

¹ Graduate student, School of Mechanical Engineering, College of Engineering., University of Tehran, Iran

² Associate Professor, School of Mechanical Engineering, College of Engineering., University of Tehran, Iran

Abstract. In this paper A new generalized analysis for the forward extrusion of complicated and non-symmetric sections is presented. The new formulation is based on the concept that all points on the cross section of the initial billet map similar points on the final section of the extruded profile. As a typical nonsymmetric shape a U shaped section was chosen. The new formulation is more advanced over the previous models as regards the material flow. In previous models due to assumptions made for the sake of simplicity of the formulations, the flow of material was very far away from the reality of the problem. However in the present formulation the flow of the material in the theoretical model is much closer to the real problem than any previous works. Using the admissible velocity field obtained based on the present theoretical model, results were obtained which were in good agreement with experimental data. Also comparing the previous works with the present method improvements on upper bound values were observed.

Keywords: 3D nonsymmetric extrusion, Upper bound method, U shaped section.

1. Introduction

Extrusion is one of the most important metal forming processes due to its high productivity, lower cost and better mechanical properties. Forward extrusion of symmetric shapes has been a heavily worked research area during the past three decades. However extrusion of complicated components, especially ones with no axis of symmetry have rarely been touched by researchers.

The process is difficult to analyze due to the complexity of die shape and metal flow in the deforming region. Material flow is not contained in the radial plane along the die axis and this behavior results in unusual stress and strain fields. Therefore most of the attempts to predict metal flow behavior are based on simplifying assumptions.

Chitkara and Abrinia [1] developed a generalized method based on the streamline die design for analyzing

3-D extrusion which automatically gave an admissible velocity field for arbitrary sections. Abrinia and Bloorbar [2] presented their formulation for the solution to the three dimensional problem of the extrusion of shaped sections using a deforming region which unlike previous work did not consider the entry and exit to the deforming region as flat surfaces but rather as curved surfaces.

Chitkara and Celick [3] presented a method for the extrusion of U and I shaped sections through round billets, which was based on off-centric points. They investigated the optimum shape for designed extrusion dies and carried out some experimental tests to verify their theoretical results. Abrinia and Zare [4] gave a new formulation for the sections without an axis of symmetry.

Abrinia and Makaremi [5] developed a new formulation for the extrusion of a section with larger dimensions of initial billet. Davarzani and Abrinia [6] presented a method for the optimization of die shape for extrusion of round billet to L, I and C shaped sections.

In this paper a new formulation for the forward extrusion of U sections is presented. Comparison between new and former methods is presented. Also some experiments were carried out to verify the analytical results.

2. Deforming Region

In order to develop a theoretical solution, a deformation region for the extrusion of shaped section is defined as shown in Figure 1. The dimensions of the section shown are considered in parametric form to generalize the problem. As illustrated in Figure 2, the exit surface was divided so that the material flow could be modelled in a more realistic way with respect to previous works.

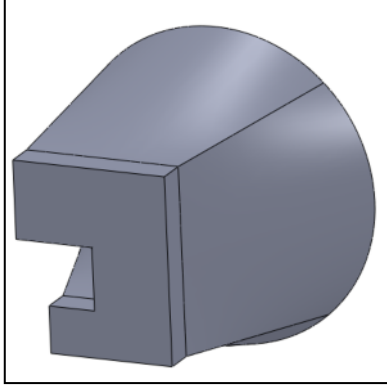


Fig. 1. Deformation Region for U-shaped section

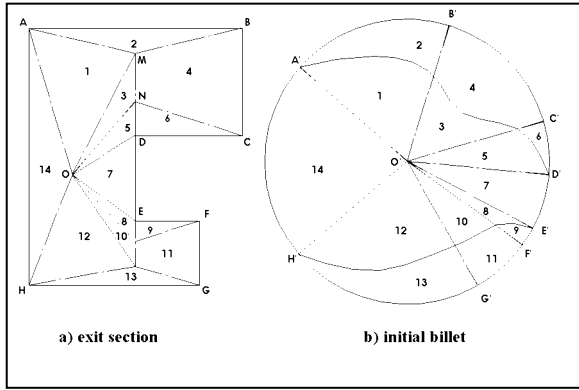


Fig. 2. Divisions for the extrusion of a U section
a) exit section b) corresponding initial billet

As shown in Figure 2, the exit section is divided so that whatever values the parametric dimensions assume, the number of divisions remains the same. Area O'A'B' in the initial billet is extruded to area OABM in the exit section and so on. Any point in the deforming region could be defined as the following vector:

$$r(u, q, t) = f(u, q, t)\hat{i} + g(u, q, t)\hat{j} + h(u, q, t)\hat{k} \quad (1)$$

where f, g and h define the positions of X, Y and Z coordinates respectively and u, q and t are dimensionless variables changing between 0 and 1 that are defined as follows:

$$u = \frac{r}{R}; q = \frac{\varphi}{2\pi}; t = \frac{z}{L} \quad (2)$$

By changing these variables any point in the deforming region can be defined.

Considering Eq. 1 cartesian coordinates of any arbitrary point in the deforming region can be written as:

$$\begin{aligned} f(u, q, t) &= uR \cos(2\pi q)(1-t) + Ft \\ g(u, q, t) &= uR \sin(2\pi q)(1-t) + Gt \\ h(u, q, t) &= Lt \end{aligned} \quad (3)$$

where F and G are x and y coordinates of the corresponding point on the exit section and are computed based on cross sectional area. All points on the exit cross section are defined by assigning values between 0 and 1 to u and q, and by assigning values between 0 and 1 to t all the point in the deforming region could be defined. For the case of bilinear dies h is only a function of t.

3. Velocity Field

The general velocity vector for any arbitrary point in the deforming region is given by:

$$\vec{V} = v_x i + v_y j + v_z k \quad (4)$$

A kinematically admissible velocity field based on the above deforming region is given by:

$$v_z = M(u, q, t); v_x = \frac{f_t}{h_t} v_z; v_y = \frac{g_t}{h_t} \quad (5)$$

where M is a function that is obtained by considering compressibility conditions.

Three dimensional incompressibility relation is given by:

$$\frac{\partial v_x}{\partial x} + \frac{\partial v_y}{\partial y} + \frac{\partial v_z}{\partial z} = 0 \quad (6)$$

By using the introduced velocity field and after some manipulation and integration of the compressibility equation the following equation is obtained for M:

$$M = \frac{C(u, q)}{(f_u g_q - f_q g_u) + \frac{h_q}{h_t} (f_t g_u - f_u g_t) + \frac{h_u}{h_t} (f_q g_t - f_t g_q)} \quad (7)$$

where C(u,q) is obtained from boundry condition at t=0:

$$c(u, q) = \left[(f_u g_q - f_q g_u) + \frac{h_q}{h_t} (f_t g_u - f_u g_t) + \frac{h_u}{h_t} (f_q g_t - f_t g_q) \right]_{t=0} \quad (8)$$

By defing M(u,q,t) velocity field is fully obtained through Eq. 5.

4. Upper bound solution

Upper bound value for extrusion power is given by:

$$J^* = W_e + W_i + W_f + W_x \quad (9)$$

where W_e the power due to the velocity discontinuity at entrance section is given by:

$$\begin{aligned} W_e &= \frac{\sigma_m}{\sqrt{3}} \iint_{S_e} \Delta V_e \, ds_e \\ &= \frac{\sigma_m}{\sqrt{3}} \iint_{S_e} \sqrt{v_x^2 + v_y^2 + (v_z - v_0)^2} \, ds_e \end{aligned} \quad (10)$$

W_x the power due to velocity discontinuity at exit section is given by:

$$\begin{aligned} W_x &= \frac{\sigma_m}{\sqrt{3}} \iint_{S_x} \Delta V_x \, ds_x = \\ &= \frac{\sigma_m}{\sqrt{3}} \iint_{S_x} \sqrt{v_x^2 + v_y^2 + \left(v_z - \frac{A_e}{A_x} v_0\right)^2} \, ds_x \end{aligned} \quad (11)$$

W_f the power due to friction between working material and die surface is given by:

$$\begin{aligned} W_f &= \frac{m \sigma_m}{\sqrt{3}} \iint_{S_f} \Delta V_f \, ds_f \\ &= \frac{m \sigma_m}{\sqrt{3}} \iint_{S_f} \sqrt{v_x^2 + v_y^2 + v_z^2} \, ds_f \end{aligned} \quad (12)$$

where m is the friction factor.

Finally W_i the power due to internal deformation is given by:

$$\begin{aligned} W_i &= \frac{\sigma_m}{\sqrt{3}} \iiint_V \hat{\epsilon} \, dv \\ &= \iiint_V \sqrt{(\hat{\epsilon}_x^2 + \hat{\epsilon}_y^2 + \hat{\epsilon}_z^2 + \hat{\epsilon}_{xy}^2 + \hat{\epsilon}_{zx}^2 + \hat{\epsilon}_{yz}^2)} \, dv \end{aligned} \quad (13)$$

Relative extrusion power is given by:

$$P/Y = \frac{J^*}{\pi R^2 v_0} \quad (14)$$

where v_0 is the velocity at the entrance section of the deforming region.

5. Results and Discussions

Results of relative extrusion power versus dimensionless length of the die (P/Y vs. L/R) for the friction factors of 0.2 and 0.4 for the U-shaped profile is indicated in Figure 3. As seen with increasing the friction factor the extrusion pressure is increased.

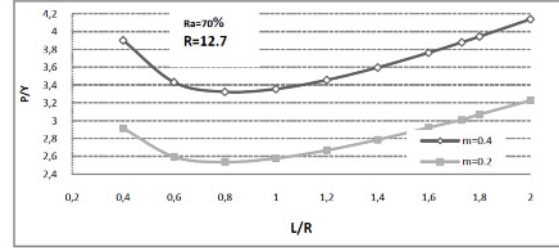


Fig. 3. Relative extrusion pressure for U-shaped section.

Comparison of results of the relative extrusion pressure against relative die length (P/Y vs. L/R) for the works of Chitkara and Ceilik [3], Davarzani and Abrinia [6] and the authors for the extrusion of the U-shaped section rod are shown in Figure 4. It can be seen that authors' results are lower than those obtained by others. For these samples the reduction of area is 70% ($Ra=70\%$), the billet radius is equal to 12.7mm and the friction factor is 0.4. Some experiments were carried out by Chitkara and Ceilik [3] for this die section with $L/R=1.73$ (see Figure 4).

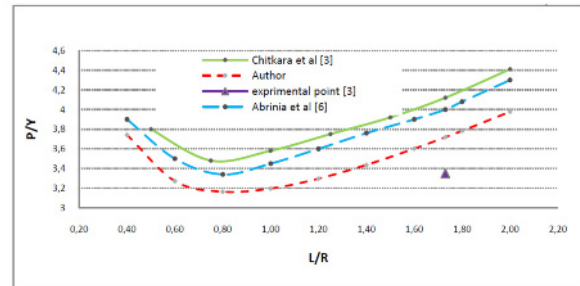


Fig. 4. Comparison of relative extrusion power vs. relative die length between references [3], [6] and author's results.

As shown the authors' results are much closer to the experimental results than the former method. Also seen is the optimum relative die length which is about $L/R=0.8$ in all methods. In Table 1, results of the present study have been compared with the results from references [3] and [6] and experimental results.

Table 1. Comparison of results for references [3] and [6] and authors' method with experimental data from [3].

	P/Y	Force
Author	3.58	58.2
Abrinia et al [6]	3.70	-
Chitkara et al[3]	4.01	-
Experiment [3]	3.35	54.5

Die position effects the results of relative extrusion pressure considerably so that optimizing the die position, gives a lower value for the extrusion pressure. The upper bound method has been used to find the optimum place for die position. Figure 5 shows the optimum position of the die as computed.

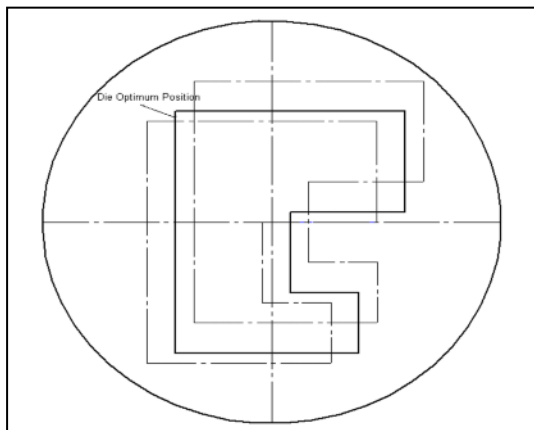


Fig. 5. Optimum die position

Figure 6 shows the relative extrusion pressure versus the die center distance from the billet center. Values of h_0 and v_0 are x and y distances between the billet center and the profile section's center of area respectively. As seen in this figure the profile center is not the optimum position of the die in this section. Optimum position of the die is at $h_0=0$ and $v_0=-0.4$.

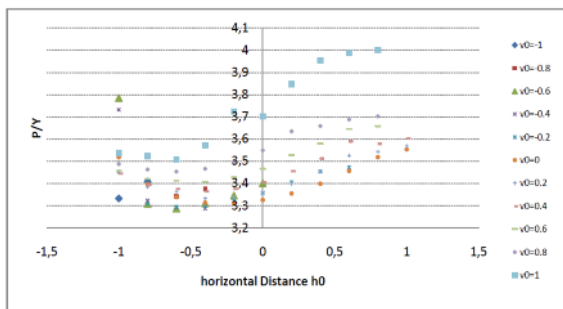


Fig. 6. Optimum die position

For further investigation on the validity of present method, results of upper bound are verified with experimental results of Chitkara and Ceilik [3]. Figure 7 shows extrusion force vs. displacement of ram.

Tellurium Lead is considered as working material and its stress-strain curve is given by [3]:

$$\bar{\sigma} = 32.1\bar{\epsilon}^{0.2} MN / m^2 \quad (5.1)$$

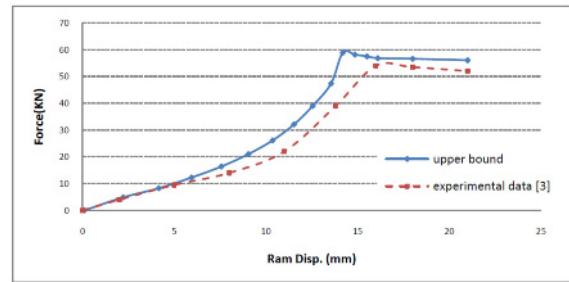


Fig. 7. Extrusion force vs. ram displacement

As shown in Figure 7, the inflexion point of the curve predicted by the upper bound method is to the left of the same point in experimental results. This is due to the fact that the ram displacement during the elastic deformation and filling of die cavity has not been considered in the theoretical method. Otherwise the results of the upper bound method are in good agreement with the experimental results.

References

- [1] Chitkara NR, Abrinia K, (1990) A generalized upper bound solution for three-dimensional extrusion of shaped sections using CAD-CAM bilinear surface dies. Proceedings of the 28th International Matador Conference, 417–24.
- [2] Abrinia K, Bloorbar H, (2000) A new improved upper bound solution for the extrusion of shaped sections using CAD techniques. COMPLAS VI Conf Barcelona, Spain.
- [3] Chitkara, NR, Ceilik KF, (2002) Extrusion of nonsymmetric U and I-shaped sections through ruled-surface dies. Int.J.Mech.Sci., 144, 217–246.
- [4] Abrinia K, Zare H, (2003) A new method of solution for the extrusion of sections with complexities. Proceedings of the 11th ISME Conference, Ferdowsi University, Mashhad.
- [5] Abrinia K, Makaremi M, (2008) An analytical solution for the spread extrusion of shaped sections” Int.J.Adv. Mat.Tech. 205, 257-259.
- [6] Davarzani H, Abrinia K, (2009) Comparison and optimization of forward extrusion of circular billet to non-symmetric L, C and I-shaped sections. Proceedings on Recent Advances in Materials, Processing and Characterization of the 12th Incama conference, Kalasalingam University, Tamilnadu, India.

An Optimization Algorithm for Improving Combined Multi-Stage Deep-Drawing and Ironing Processes of Axisymmetric Components. Analysis and Experimentation

Ramírez, Francisco Javier¹; Domingo, Rosario²; Sebastián, Miguel Angel²

¹ School of Advanced Computer Engineering, University of Castilla-La Mancha, Albacete, Spain

² Department of Manufacturing Engineering, National Distance University (UNED), Madrid, Spain

Abstract. A new optimization algorithm for combined processes of deep-drawing and ironing has been created in order to improve these types of axisymmetric components manufacturing procedures. The model provides a comprehensive analysis of those phenomena occurring in multi-stage processes of axisymmetric geometry workpieces. The scientific development starts out from works that provide LDR (limiting drawing ratio) solutions based on normal anisotropy value, strain hardening exponent and others parameters which have just been applied to the drawing and redrawing stages so far. The authors extend this work to the ironing stages, and also provide a global and integral scientific solution for the whole process. At the beginning the algorithm provides an initial solution which is afterwards optimized by means of objective functions and constraints. The resolution of the optimization process is carried out by a recursive function that minimizes the total time of the global process. The enhanced solution performs a significant reduction in time and costs of the process. The model allows the modification and correction of certain process variables in order to predict the impact of those that are not fully controllable. The final results are compared using experimental results obtained by the authors, so as to show the reliability of the complete solution.

Keywords: Optimization algorithm, Deep drawing, Ironing, Limiting drawing ratio, Aided system, Intelligent manufacturing.

1. Introduction

Industry requires developments to be more efficient and, in particular with regards to the deep-drawing procedures, where it is important to decrease the process times and costs. Thus, it is necessary to devise specific algorithms that will satisfy these needs. These algorithms should be based on a technological and scientific basis that will provide solutions capable of transferring to industries. The deep-drawing process has been analysed under this perspective but it is also convenient as a global model that considers all stages of the process (drawing, redrawing and ironing).

This paper presents a model, which provides a comprehensive analysis of those phenomena occurring in the multi-stage processes of axisymmetric geometry

workpieces. The scientific development departs from the works of Leu [1] and Sonis et al. [2] that provide LDR (limiting drawing ratio) solutions based on normal anisotropy value, strain hardening exponent and others, applied to the drawing and redrawing stages. The technological model proposed in [3, 4] has a scientific foundation based on the literature regarding the plastic deformation processes and, in particular about drawing [5, 6], redrawing [7] and ironing. This analysis allows for analyzing geometries of axisymmetric components, to manufacturing by a multi-stage deep-drawing process.

The literature has realised contributions in the drawing process of blanks [1,8]. The phenomena that has happened in this operation has been researched and, today, these phenomena and their equations are well known [9, 10]. However, the redrawing and ironing phenomena have received less attention [2, 11]. This work contributes to the definition and modelization of the drawing, redrawing and ironing process, together with a common focus of the drawing process, to analyse in general the three processes.

The technological model shows a quantitative and integrated analysis in a multi-stage deep-drawing process based on a scientific solution and real measurements. Also, the model permits a modification for some process variables to predict the influence on the results [12]. In addition, it is based on the definition of limiting conditions to guarantee the stability of the process. The simultaneous accomplishment of the limiting situations of each process (drawing, redrawing and ironing) allows for fixing a boundary to the values of each stage. This is the initial solution. The model permits the optimisation of the initial solution from several points of view: process total time, manufacturing cost, among others, such as punch and die wear, etc. This optimisation is based on the resolution of an algorithm by means of recursive functions, which explore all the possibilities of the process and it selects the more adequate. The algorithm is

supported by a software that provides an Aided System [13].

2. Initial solution

The technological model offers an initial solution, by means of the following output data:

- Characterization of drawing stage
- Characterization of redrawing stages
- Characterization of ironing stages
- Number of stages
- For each stage:
 - Exterior diameter, d_n
 - Length, l_n
 - Wall thickness, e_n
 - Drawing ratio, DR_n
 - Limiting thickness reduction, K_n
 - Drawing load, F_e

Moreover, the model supplies output data from stage m , that is the redrawing limiting stage or ironing limiting stage. It is the last stage; its operation assumes to exceed the final dimensions of the part (stage n). The parameters of this limiting stage will be used to realize the optimization. The model provides the following output data in relation to stage m :

- Exterior diameter d_m
- Length l_m (mm)
- Wall thickness e_m
- Drawing ratio DR_m (respect to stage n)
- Limiting thickness reduction ratio K_m (respect to stage n)
- Force F_e (N, respect to stage n)

3. Optimization process

The model is based on the minimization of the process total time, according to the following objective function:

$$F_o = \min t_e = \min \sum_1^n t_n \quad (1)$$

where: F_o is the objective function
 t_e is the process total time
 t_n is the process time in the stage n

The process time of the stage n is given by the expression:

$$t_n = \frac{1.1 \cdot l_{n-1} + L_{un} + l_n}{v_{an}} + \frac{L_{un} + l_n}{v_{en}} + \frac{1.1 \cdot l_{n-1} + L_{un} + l_n}{v_{sn}} \quad (2)$$

where: l_{n-1} is the part length in stage $n-1$
 L_{un} is the punch length in stage n
 l_n is part length in stage n
 v_{an} is the approach velocity of the press in the stage n

v_{en} is the ironing velocity in the stage n
 v_{sn} is the recovery velocity of the press in the stage n

Therefore, the technological model presents an optimization problem with an objective function and its constraints:

Objective function

$$F_o = \min t_e = \min \sum_1^n t_n = \min \sum_1^n \left(\frac{1.1 \cdot l_{n-1} + L_{un} + l_n}{v_{an}} + \frac{L_{un} + l_n}{v_{en}} + \frac{1.1 \cdot l_{n-1} + L_{un} + l_n}{v_{sn}} \right) \quad (3)$$

considering that:

$$l_n = \frac{s_n (d_o^2 - d_p^2)}{(D_n^2 - d_p^2)} \quad (4)$$

where: D_n is the optimised diameter in the stage n
 s_n is the bottom thickness in the stage n
 d_o is the blank diameter
 d_p is the punch diameter in the stage n

Constraints

The objective function has the constraint,

$$d_n \leq D_n \leq d_n (1 + \Delta DR_e) \quad (5)$$

where ΔDR_e is the drawing surplus ratio between the stages n and m , defined by the expression:

$$\Delta DR_e = DR_m - DR_n \quad (6)$$

The optimization requires a distribution between the stages 1 to n of the drawing ratio no used, ΔDR_e . This distribution is conditioned to the minimization of the process total time as the sum of each stage time. Thus, an improvement is achieved in each drawing stage. In this manner the optimized drawing conditions are separate of the maximum limits fixed by the initial drawing conditions.

The resolution of the recursive function is carried out according to values of all the possible diameters between d_n and $d_n(1+\Delta DR_e)$. The algorithm identifies which combination is the most suitable, and it selects the optimised diameter D_n in each stage, with the condition of satisfying the objective function: the combination of diameters must give as final result the minimum time of the process.

The algorithm permits to modify the velocity parameters in each press required in the ironing process: approach velocity of the punch towards part (v_{an}), ironing velocity (v_{en}) and recovery velocity of the punch in the direction of the initial position (v_{sn}). Accordingly, it is possible to realise a more adequate distribution of available presses in the facility.

Once the parameters are calculated and the optimized solution has been found, it is possible to determine the

process cost, considering the following costs of: raw material, workforce and electricity.

4. Algorithm resolution process

The algorithm performs the resolution in four phases:

- *Phase 1.*- Definition of incremental factor t , given by the following expression:

$$t = \frac{\Delta DR_e}{x_e} \tag{7}$$

where:

ΔDR_e is the surplus ratio of drawing

x_e is the number of time that the drawing surplus ratios is fractioned

- *Phase 2.*- Progressive increment of diameter of each process stage, from d_n to $d_n(1+kt)$, where k is a parameter that varies from 0 to factor x_e .

- *Phase 3.*- the resolution of the recursive function is based on obtaining all possible substages, by means of the modification of each stage diameters, from d_n to $d_n(1+\Delta DR_e)$.

- *Phase 4.*- Once defined all the possible diameters of each stage, the algorithm selects the arrangement that allows for the minimizing of the process total time.

5. Experimental results

The Aided System has allowed for the corroboration of this algorithm's integrity. Computational and experimental tests have been carried out on brass, in particular on UNS C26000 alloy. The dimensions of the parts are shown in Table 1. Figure 1 shows the part A obtained.

Table 1. Dimensions of parts

Dimensions (mm)	Part A	Part B	Part C
External diameter, d_n	98.5	150	150
Length, l_n	620	1800	600
Bottom thickness, s_n	13.5	4	4
Wall thickness, e_n	2	1	1



Fig. 1. Part of brass UNS C26000

Figure 2 expresses the calculation of the drawing ratio (DR) by means of the Aided System, while the algorithm is solved. Values for X_e , in operations of redrawing and ironing are given. Figures 3 and 4 show the results that have been observed and obtained in each stage, while the final part is processed. Data from diameters and lengths, in each stage, are shown. The results are coherent with the number of stages required in the process, according to the part geometry (see Table 2).

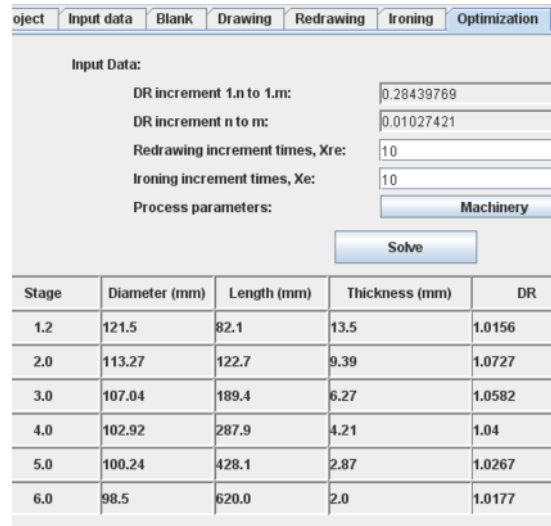


Fig. 2. Part of brass UNS C26000

Table 2. Number of stages

Number of stages	Part A	Part B	Part C
Drawing	1	1	1
Redrawing	1	3	1
Ironing	5	4	4

6. Analysis of results

The results and analysis obtained in this case shows that the system is capable of solving these types of geometries using operations of drawing, redrawing and ironing.

Further, the great potential of the system to optimize several process variables, improving the total process time and the total process cost on the process has also been demonstrated.

Regarding the obtained improvements (about the process total time and manufacturing costs), it is substantial in the majority of cases, although time and cost are not directly associated (see Figures 5 and 6). The application of this algorithm has caused a reduction in time process of between 10% and 16% and in manufacturing costs in the order of 3.28% and 8.26%.

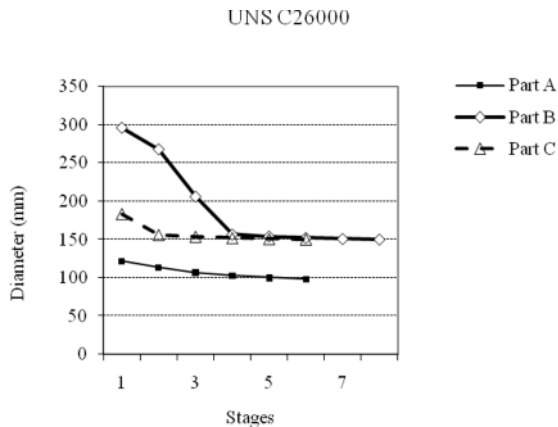


Fig. 3. Diameters in each stage (redrawing and ironing)

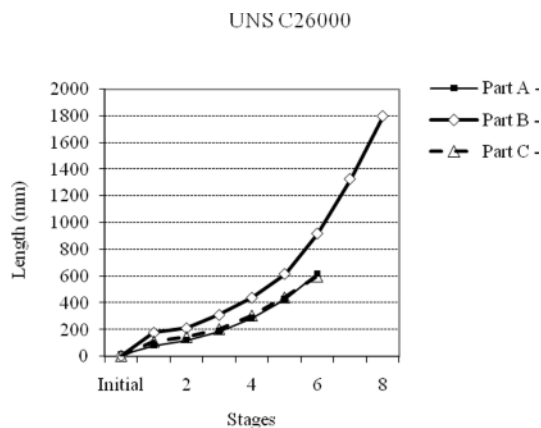


Fig. 4. Length in each stage

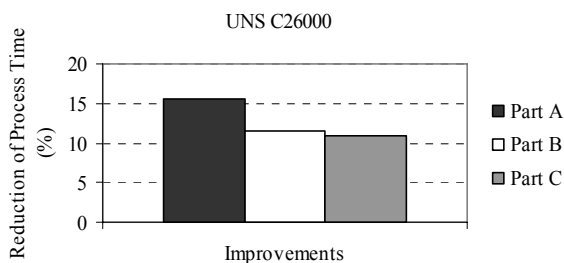


Fig 5. Improvements of time

7. Conclusions

This work presents an algorithm that allows the reduction of process time and costs in the manufacturing of axisymmetric components. Consequently, it is of industrial interest.

Currently, the authors are working on the improvement of this algorithm aiming to get a more efficient process, from a perspective of sustainable energy, and thus achieving an integral solution, based on scientific and technological basis.

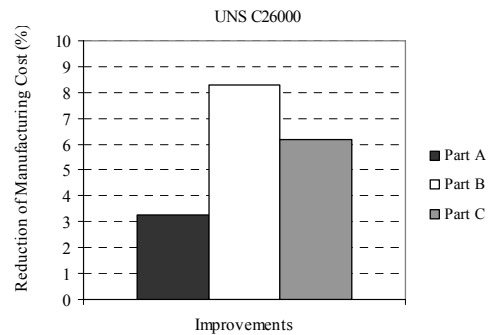


Fig. 6. Improvements of manufacturing costs (without raw material)

References

- [1] Leu DK. The limiting drawing ratio for plastic instability of the cup drawing process. *Journal of Materials Processing Technology* 1999; 86: 168-176.
- [2] Sonis P, Venkata N, Lal GK. On multistage deep drawing of axisymmetric components. *Journal of Manufacturing Science and Engineering* 2003; 125: 352-362.
- [3] Ramirez FJ, Domingo R. Application of an aided system to multi-step deep drawing process in the brass pieces manufacturing. *American Institute of Physics Proceedings* 2010, 1181: 370-379.
- [4] Ramirez FJ, Domingo R, Sebastian MA (2009) "Design of an Aided System to Optimise Times and Costs in Deep Drawing Process", *Proc. 2nd IPROMS International Researchers Symposium*, Vol 1, pp. 191-196.
- [5] Lange K. *Handbook of Metal Forming*. McGraw-Hill Book Company, 1985.
- [6] Kalpakjian S, Schmid SR. *Manufacturing, Engineering and Technology*. Prentice-Hall, 2007.
- [7] Chung SY, Swift SH. An experimental investigation into the re-drawing of cylindrical shells. *Proceedings Institute of Mechanical Engineering* 1975, 1B: 437-447.
- [8] Colgan M, Monaghan J. Deep drawing process: analysis and experiment. *Journal of Materials Processing Technology* 2003, 132: 35-41
- [9] Rahul K, Sanjay C. An improved model for predicting limiting drawing ratio. *Journal of Materials Processing Technology* 2005, 172: 218-224.
- [10] Agrawal A, Venkata N, Dixit PM. Determination of optimum process parameters for wrinkle free products in deep drawing process. *Journal of Materials Processing Technology* 2007, 191: 51-54.
- [11] Sebastian MA, Sanchez-Perez AM. *Diseño asistido por ordenador de los útiles para la embutición profunda de piezas cilíndricas huecas*. E.T.S.I.I, UPM: Madrid, 1980.
- [12] Padmanabhan R, Oliveira MC, Alves JL, Menezes LF. Influence of process parameters on the deep drawing of stainless steel. *Finite Elements in Analysis and Design* 2007, 43: 1062-1067.
- [13] Ramirez FJ, Domingo R, Sebastian, MA (2010) "Deep Drawing Tool for E-learning: A didactic approach for manufacturing engineering education", *Proc. IEEE International Conference EDUCON*, IEEE Education Society, Madrid, 14-16 April 2010. In edition.

Nanofinishing Process for 3D Freeform Surfaces Using Ball End MR Finishing Tool

Anant Kumar Singh, Sunil Jha and P.M.Pandey

Department of Mechanical Engineering, Indian Institute of Technology, New Delhi 110016, India
suniljha@mech.iitd.ac.in

Abstract. A new precision finishing process for nanofinishing of 3D freeform surfaces using ball end MR finishing tool is developed. The newly developed finishing process is useful to finish ferro magnetic as well as non-magnetic materials of 3D freeform surfaces using specially prepared magnetorheological polishing (MRP) fluid. The smart behaviour of MR-polishing fluid is utilized to precisely control the finishing forces, hence final surface finish. The existing MR finishing devices and methods are likely to be incapable of finishing of 3D freeform surfaces due to restriction on relative movement of finishing medium and work piece. In this newly developed finishing device, the ball end MR finishing tool is used for finishing of different kinds of 3D surfaces where there are no such limitations of relative movement of finishing medium and workpiece. It can finish the work surfaces as same as the machining of 3D freeform surfaces by CNC ball end milling cutter and open a new era of its applications in future. The developed process may have its potential applications in aerospace, automotive and molds manufacturing industries. A computer controlled experimental setup is designed to study the process characteristics and performance. Maxwell simulations were done on ferro magnetic as well as non ferro magnetic materials of 3D surfaces to observe the ball end shape of magnetic field intensity at the tip of the MR finishing tool.

Keywords: Magnetorheological fluid; MR polishing; strength of magnetic field; Magnetorheological (MR) finishing tool

1. Introduction

The traditional methods of finishing processes like grinding, lapping, honing etc. are labor intensive, comparatively less controllable for finishing operations in the manufacturing of precision parts. These processes generally employ a rigid tool that subjects the workpiece to substantial normal stresses which may cause microcracks and other defects resulting in reduced strength and reliability of the machined parts. Among these, finishing of complex 3D shapes and obtaining surface finish of nano-meter order on advanced materials is still a challenging task. To minimize the subsurface damage it is necessary to finish the materials under gentle conditions, i.e., by applying very low forces. The precise control of finishing forces is an important

consideration for fine finishing with close tolerances and without damaging surface topography.

In the last decade, many advanced fine finishing processes have been developed to precisely control the abrading forces such as Magnetic Abrasive Finishing (MAF) [1], Magnetic Float Polishing (MFP) [2], Magnetorheological Jet Finishing (MRJF) [3], Magnetorheological Abrasive Flow Finishing (MRAFF) [4], and Magnetorheological Finishing (MRF) [5] in which the magnetic field is used to control the abrading forces. But the applications of these processes are limited to specific geometries only such as concave, convex, flat and aspherical shapes due to restriction on relative movement of finishing medium and work piece. These are incapable of finishing of 3D intricate shaped surfaces.

To overcome the above mentioned problem a new precision finishing process for nanofinishing of 3D surfaces using ball end MR finishing tool is developed. The newly developed finishing process is useful to finish ferro magnetic as well as non-magnetic materials of 3D surfaces using specially prepared magnetorheological polishing (MRP) fluid. The MRP-fluid used is comprised of carbonyl iron powder particles and silicon carbide abrasives dispersed in the viscoplastic base of grease and heavy paraffin liquid; it exhibits change in rheological behaviour in presence of external magnetic field. This smart behaviour of MR-polishing fluid is utilized to precisely control the finishing forces, hence final surface finish. In this process a small hemi spherical ball end of MR polishing fluid is formed by indigenous setup and this ball is used to abrade/erode the material from work surface. The movement to the ball is provided by computer controlled 3-axis motion controller. This MR finishing ball may be visualized similar to ball end of a milling cutter movement on a 3 axis vertical CNC machine. The MR finishing tool tip of stiffened ball end of MR polishing fluid is likely to have very much flexibility to move over different kinds of 3D surfaces and it can finish the work surfaces as same as the machining of 3D surfaces by CNC ball end milling cutter

and open a new era of its applications in future. The developed process may have its potential applications in aerospace, automotive and molds manufacturing industries. A computer controlled experimental setup is designed to study the process characteristics and performance.

2. Design of New Magnetorheological Finishing Setup

The design of this setup is directed to improve methods and devices for magnetorheological finishing of work surfaces. A new magnetorheological finishing device for process of generating magnetically controlled ball end smart abrasive laden shape for finishing of 3D surfaces is developed which will be automated and become a part of manufacturing system.

The ball end MR finishing tool is used for finishing of different kinds of 3D surfaces. The MR finishing tool is positioned on a vertical slide (Fig.1) such that the tip of the MR finishing tool can approach the surface of a work piece. A pressurized MR fluid is supplied axially from the top end of the MR finishing tool and once the MR fluid reaches the tip of the MR finishing tool, the fluid forms a finishing segment with the help of a magnetic field available at the tip of the MR finishing tool. This stiffened ball end of MR fluid may be visualized similar to ball end of a milling cutter movement on a 3 axis vertical CNC machine. The stiffened ball end so produced is a semi-solid MR fluid that is used as a finishing medium. The movement of the stiffened ball end of MR fluid over 3D work surface is enabled by means of a computer. The stiffened ball end at the tip of the MR finishing tool performs the finishing operation over the work surfaces due to the relative motion as well as abrasion actions between the stiffened ball end of MR fluid and the work surfaces. There are likely to no limitations of relative movement between the finishing medium and the work surfaces as compared to existing MR finishing processes, because tool tip with stiffened ball end can move over almost any location of 3D work surfaces, and hence appropriate finishing of 3D surfaces is performed.

A partially schematic elevation view of a Magnetorheological (MR) finishing machine accordance with the present method of operation is shown in Fig.1. The device includes vertical oriented MR finishing tool which comprises concentrically inner core, electromagnet coil and outer core respectively (Fig. 2). The MR finishing tool is positioned vertically on a vertical Z-slide and is driven by a servo motor.

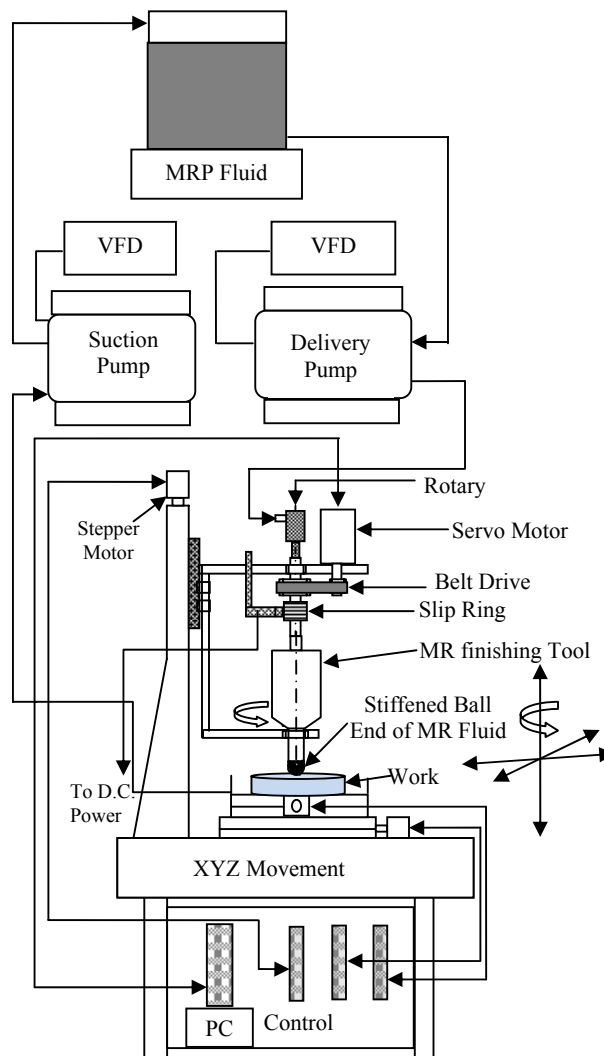


Fig. 1. Schematic of new magneto-rheological finishing machine setup

Three stepper motors are used for controlling the linear motion of X-Y-Z directions, where as the X - Y direction motion controllers are used for controlling horizontal linear motion of workpiece and Z motion controller is used for controlling vertical linear motion of MR finishing tool.

The electromagnet coil is designed to obtain maximum magnetic flux density of ~ 0.8 T at the tip of the MR finishing tool. A comparative study of different coil design parameters such as number of turns, wire gauge, number of layers, geometric factor and coil diameter was made before selecting the final coil parameters as: number of turns = 2000, maximum current = 5 A, copper wire gauge = 17 SWG, coil inner diameter = 20mm, outer diameter = 80mm and length = 80mm with the cores material is used as cold rolled annealed steel.

The means for supplying MR fluid comprises a storage tank (funnel) along with D.C. controlled stirrer, a delivery pump for supplying MR fluid from the storage tank to the MR finishing tool and a suction pump for recollecting the MR fluid from a finishing zone to the fluid storage tank. Both pumps are peristaltic pumps and an AC Variable Frequency Drive (VFD) is used to vary the speed of Peristaltic Pump (Fig.1).

The MR finishing tool depicting the formation of a stiffen ball end shape of MR polishing fluid in the direction of magnetic field at the tip of the tool as shown in Fig.2. Once the MR fluid reaches at the tip of the MR finishing tool, the magnetic carbonyl iron particles of MR fluid are aligned and formed a chain like structure along the magnetic field direction at the tip of the MR finishing tool and then the MR fluid becomes stiffened to a physical texture like a wet clay ball end shape and apparent viscosity along the direction of magnetic field becomes very high. The magnetic field strength can be controlled by controlling the magnetizing current in real time and hence controls the stiffness of the MR fluid.

The schematic representation of microstructure of abrasive and magnetic particles in the vicinity of workpiece surface is shown in the Fig.3. The magnetic force between iron particles encompassing abrasive grain provides bonding strength to it and its structures are just adjacent to the workpiece surface.

3. Electromagnetic Modeling for MR Finishing Tool

An electromagnetic model of MR finishing tool along with workpiece and MRP fluid has been developed as shown in the Fig.4. The current and number of turns to the electromagnet is assigned as 2A and 2000 turns. The material for electromagnet coil is copper of relative permeability 1.0. The assignments of material for the inner core as well as outer core are iron of relative permeability 4000. The relative permeability of MR fluid material properties is assigned as 4.

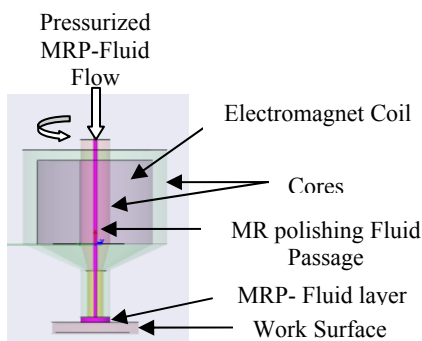


Fig. 4. Electromagnetic model of MR finishing tool

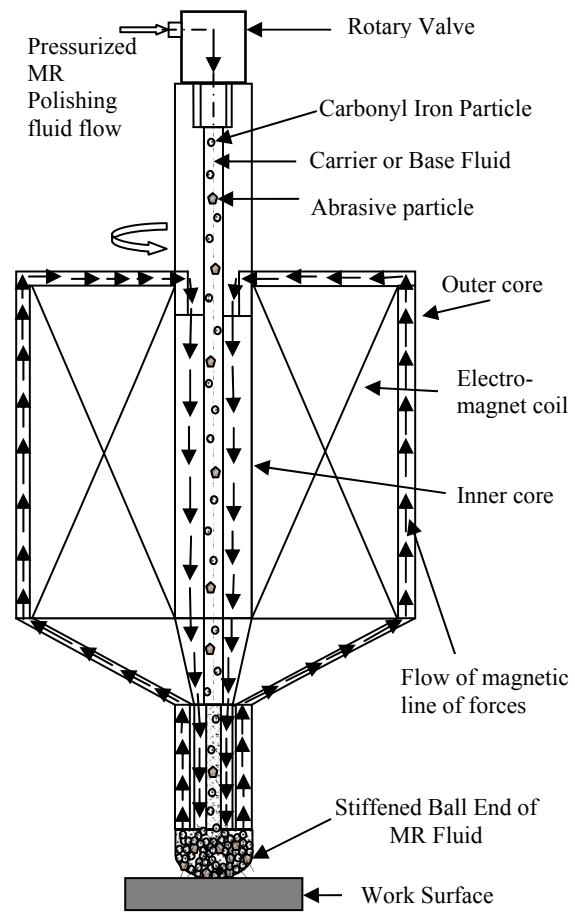


Fig. 2. Mechanism of formation of the stiffen ball end of MR polishing fluid at the tip of the tool.

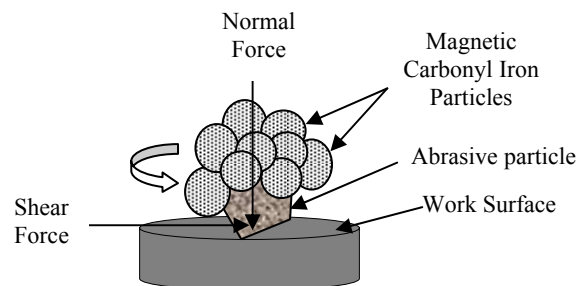


Fig. 3. Microstructure of abrasive and magnetic particles in the vicinity of workpiece surface

4. Results and Discussion

The magnetostatic simulation of developed model has been done using Maxwell software to check the shape of magnetic field generation at the tip of MR finishing tool. The working gap of 5mm is filled with MR polishing fluid between the tool tip and work piece surface.

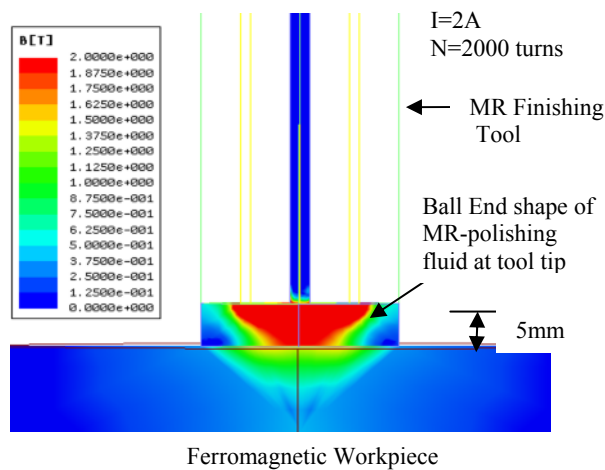


Fig. 5. The ball end shape of magnetic flux density generated at the tip of the tool for ferromagnetic work material

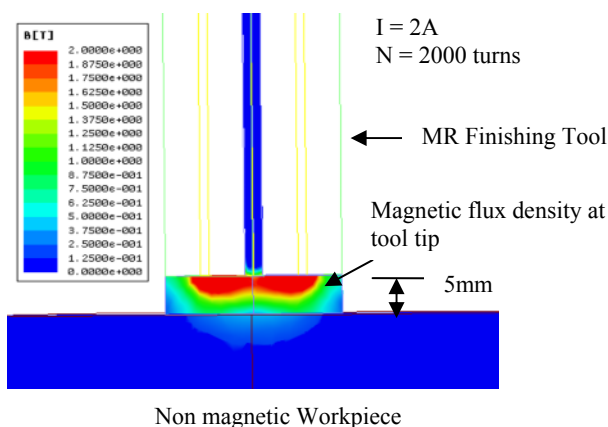


Fig. 6. The ball end shape of magnetic flux density generated at the tip of the tool for the non ferromagnetic material

4.1 Effect of Ferromagnetic Work Material on the variation of Magnetic flux density at the Tool Tip

The simulated result for ferromagnetic work material is shown in the Fig.5. The variation of magnetic flux density at the tip of the MR finishing tool is visualized similar to ball end cutter of a CNC milling machine. This ball end of MR fluid is used as finishing tool and when it rotates over the work surface, finishing takes place. Since this tool is having semisolid stiffened ball end, there is not much limitation of relative motions with respect to the different kinds of 3D work surfaces as compare to the existing MR finishing processes.

4.2 Effect of Non Ferromagnetic Work Material on variation of Magnetic flux density at the Tool Tip

The simulation result of variation of magnetic flux density with non ferromagnetic work piece material is shown in Fig.6. The magnetic lines of forces are not attracted towards the workpiece and it does not make very good shape similar to ball end of MR polishing fluid. This is because, almost all the magnetic line of forces are diverted from inner core to outer core and MR fluid becomes stiffened along these lines of magnetic forces only. Therefore, the present methods and devices are excellent for finishing of magnetic materials as compared to the non magnetic materials of work surfaces. It will take more number of cycles for finishing non magnetic work piece surfaces.

5. Conclusion

A new precision finishing process for 3D freeform surfaces using ball end MR finishing tool is developed. The newly developed finishing process is useful to finish ferro magnetic as well as non-magnetic materials of 3D freeform surfaces using specially prepared magnetorheological polishing (MRP) fluid. Magnetostatic simulation of the variation of magnetic flux density in the finishing region indicates clear formation of ball end finishing surface. The smart behaviour of MR-polishing fluid is utilized to precisely control the finishing forces, hence final surface finish.

References

- [1] Shinmura T., Takazawa K., Hatano E., Matsunaga M. (1990), Study on Magnetic Abrasive Finishing, Annals of CIRP 39/1:1325-328
- [2] Komanduri R(1996), On material removal mechanisms in finishing of advanced ceramics and glasses, Annals of CIRP 45/1: 509-514
- [3] Kordonski W and Shorey A(2007), Magnetorheological (MR) Jet Finishing Technology, Journal of Intelligent Material Systems and structures 18 :1127-1130.
- [4] Jha Sunil, Jain V.K(2004), Design and development of the magnetorheological abrasive flow finishing (MRAFF) process, International Journal of Machine Tools & Manufacture 44 :1019-1029.
- [5] Kordonski W.I., Jacobs S.D. (1996), Magnetorheological Finishing, International Journal of Modern Physics B 10:2857-2865.

Pressure Distribution in Cold Rolling of Turbo-engine Thin Compressor Blades

M. Sedighi and M. Mahmoodi

School of Mechanical Engineering, Iran University of Science and Technology, Tehran, Iran, Email:sedighi@iust.ac.ir

Abstract. In rolling processes, the material undergoes plastic deformation due to flow stresses caused by the roller pressure. In this paper, first, the process of cold rolling of compressor blades has been studied by means of experimental testing and computer simulation, and for the case of simulation, deformable rollers have been utilized. Then, during the rolling process, the pressure distribution on the blade's surface has been investigated. The results show that the pressure distribution is not assumed as a known common hill shape, but depends totally on the caliber section. Highest values of pressure are associated with areas close to the edges of the section which are affected by more reduction and stress and thus, the surface pressure distribution diagram changes to a saddle shape. The simulation experimental result are calculated and compared showing a good agreement.

Keywords: cold rolling, simulation, pressure distribution, compressor blade

1. Introduction

The process of cold rolling is one of the methods used for the manufacturing of blades and twisted sections. In this process, the very high plastic deformation of the work-piece material causes the rolling forces and pressures exerted by the rollers to be very large. The roller pressure exerted on the work-piece changes not only along the rolling direction, but also perpendicular to the rolling direction; or across the width of the preform. To evaluate the amount of pressure during ordinary longitudinal rolling process, Hockett [1] and Rows [2] have used the slab method and thus, have considered the assumption of plane strain and homogenous deformation. Shin [3], using the FEM, has studied the effects of rolling stages on the formation of the rolling forces and also the manners of stress distribution in the rolled products. Liu [4], by modeling the cold rolling of strips using the elastic/plastic finite element method, has revealed the maximum pressure around the neutral point and also the stresses outside the contact area. In the multi-stage rolling process of sections, Inoue [5] has utilized the finite element, and electron diffraction analysis to show how the effective strains are distributed in a particular section. Highest

strains appear at the corners or the edges of the section. How the flow stress is distributed in the rolled piece during various rolling stages has been investigated by Milenin [6]. According to him, the problems that arise in the finite element analysis of a multi-stage rolling process fall into two categories: First, is the problem of reconstructing the finite element network and transferring the material properties from one stage to the next; and the second is considering the conditions of strain hardening at various stages and the interactions between them. Komori[7], in his research on the ordinary rolling process, has used the FEM to study the ways of pressure distribution on the surface of the rollers and also the distribution of hydrostatic stresses in the material, and has applied it to the rolling of sections. In this paper, computer simulation has been applied in order to study the way that pressure is distributed on the surface of the preform during rolling, and the average value of this pressure has been determined. Furthermore, the average pressure has been measured through an experimental test and compared with the simulation results.

2. Evaluation of pressure in the rolling process

In rolling processes, the work material undergoes plastic deformation due to flow stresses caused by the pressure from the roller. Roll pressure along the path of contact comprises two portions: one is the pressure necessary to overcome the internal resistance of the work material against deformation, and the other is the necessary pressure to overcome the friction resistance between the rollers (or dies) and the work-piece. Pressure exerted by the roller changes along the path of contact with the plate and also across the width of the plate. It reaches its highest value in the mid section of the width and reduces to its lowest value along the edges of the plate. Each of the curves in Fig. 1 displays the roller pressure distribution along the rolling direction for a particular position across the width of the plate.

Curves pertaining to the mid section of the plate show a higher pressure compared to other locations. It could be said that in the middle portions of the plate, a kind of obstruction takes place and the requirements for the deformation of these regions entail that the pressure necessary for overcoming the flow resistance of the material should increase.

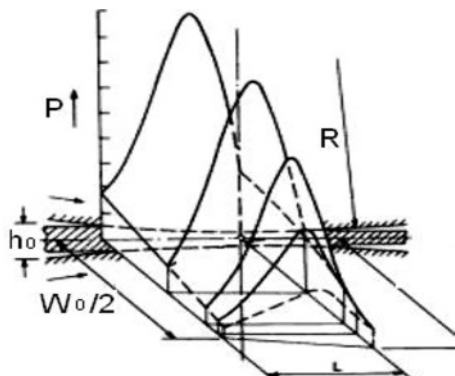


Fig. 1. Roller pressure distribution across the width of the plate[9]

In addition, friction along the mid section of the plate is more than that along the plate borders and as a result it causes an increase of pressure in this region. Considering pressure values along the longitudinal and lateral directions of the preform, a hill shape pressure curve could be envisioned.

All the mentioned conditions are associated with the longitudinal rolling process, a work-piece having an initially rectangular cross section, and rolls without dies attached. However, for cold rolling of sections such as blades where the material thickness and reduction across the width of the preform change, different conditions are involved in the investigation of pressure. In such cases, the maximum amount of pressure does not occur in the mid section of the preform, but depends on the shape of the section, although, like in longitudinal rolling, pressure values in the vicinity of the neutral point are the highest.

3. Experimental test

The material used for the rolling process is the Nickel-Chrome (Inconel 718) alloy which has a good strength and ductility. Properties of this material are listed in Table 1.

Table 1. Material properties of alloy Inconel 718

ρ (gr/cm ³)	V	E(GPa)	σ_y (MPa)
8.16	0.29	210	1200

To reduce simulation error and obtain closer results to the empirical ones, it is better to include in the simulation, properties of the same preform material which is used in

experimental testing. Therefore, several test samples are made and by conducting tensile tests, the stress-strain characteristics of the material are determined. Flat test samples are selected for the tensile tests. Plates out of which the test samples are made are nearly 1.7 mm thick. The British standards applied for making the test samples are (B.S.18 Part1: 1970, B.S.18Part 2, 3&4:1971)

The flow stress behaviour of the alloy is $\bar{\sigma} = 2005\bar{\epsilon}^{0.091}$.

The preforms are made by wire cutting method from a 2.0 mm thick plate. The material used for making the dies is steel D2 with UNS: T30402. A special cold rolling machine which forms blade-like sections such as compressor blades (with lengths of about 3 to 10 cm) is used for forming the material. The rollers are positioned horizontally under each other and the dies are fixed onto them. According to Fig. 2, the preform material is fed horizontally into the gap between the dies.

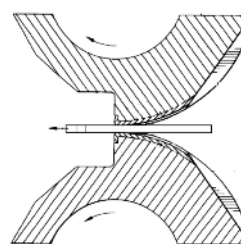


Fig. 2. Blade rolling through two dies

Before contact, the dies are adjusted relative to each other into a correct position. The lubricant used in the process is low-viscosity motor oil. The preform is first positioned by the help of two holes in it and fixed by a fixture. Then a hydraulic jack drives the piece in between the two dies. As the rollers rotate, the dies grab the work-piece and by deforming it, return the blade to the initial location. Angular velocity of the roller is 1.04 rad/sec and radius of the roller is 200 mm. the coefficient of friction in cold rolling with lubricating conditions has been chosen as 0.07. To examine the blade made by rolling, 5 points of the section with specific distances from the end of the blade are measured by the CMM. Fig. 3 shows the rolled blade in the initial stage of the process.

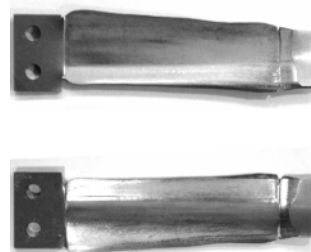


Fig. 3. the rolled blade in the initial stage of the process

4. Simulation of the process

The Abaqus software and the Dynamic/Explicit analysis have been used for the simulation of the rolling process. The element used for the preform is an 8-node linear brick (C3D8R) element and the structural technique is applied. Before applying a mesh to the work-piece, the process-related mesh sensitivity diagram is used to determine the suitable mesh size. Based on this diagram, the element with dimensions of 1 mm (relatively small mesh size) is selected. The element applied for the upper and lower dies is of a 4-node (R3D4) element type. Due to the elastic behavior effect of rollers and the apparatus structure under very large forces and pressure, the rollers have been designed to be deformable, as is shown in Fig.4.

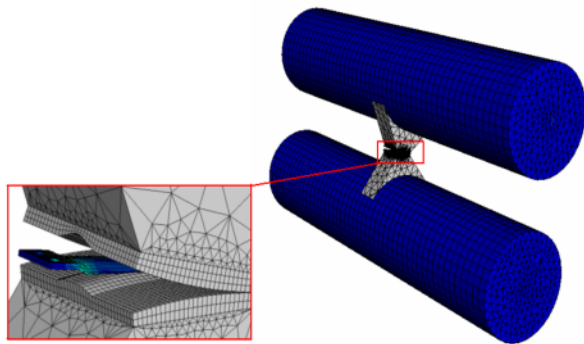


Fig. 4. Blade rolling by means of the dies set on the deformable rolls

With the help of the analysis provided by the software, the applied pressure could be investigated. In this case, pressure values in the elements existing on the contact surface area are computed and plotted.

5. Analysis of simulation and experimental test results

To evaluate the soundness of the devised simulation, the thickness parameter is considered. Table 2 displays the empirical and the simulated thickness values in the longitudinal mid section.

Table 2. The experimental and the simulated thickness values in the longitudinal mid section

Experimental thickness results (mm)	Simulated thickness results (mm)	Thickness reduction	Difference in experimental & simulated results (mm)
1.84	1.81	0.16	0.03
1.75	1.74	0.25	0.01
1.42	1.45	0.58	0.03
1.28	1.32	0.72	0.04
0.96	0.95	1.04	0.01

Based on the results, the estimated error is small and therefore, a good agreement exists between the results. Fig. 5 compares the rolled blades obtained from the experiment and the simulation.

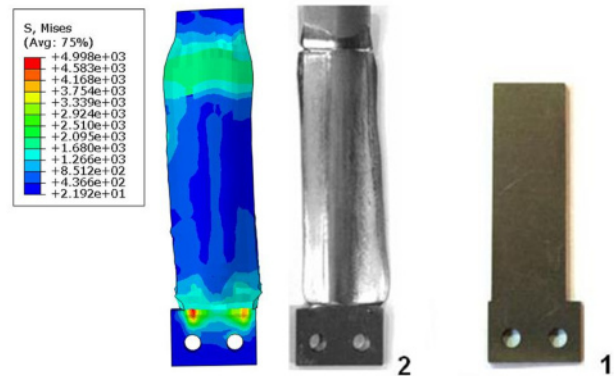


Fig. 5. 1) Preform with 2 mm thickness; 2) The rolled blades obtained from the experiment and the simulation

Pressure values have been determined from existing elements on the surface (contact region) of the blade. Fig. 6 shows the pressure distribution level resulting from these values. According to this figure, the pressure level forms a saddle shape where, due to more reduction in the two corner areas of the material, the pressures along the neutral lines assume maximum values.

In the middle portion, contrary to ordinary rolling process, because of the shape of section and less reduction, a pressure drop could be observed. According to the simulation, average pressure value at the neutral line is equal to 2028 MPa.

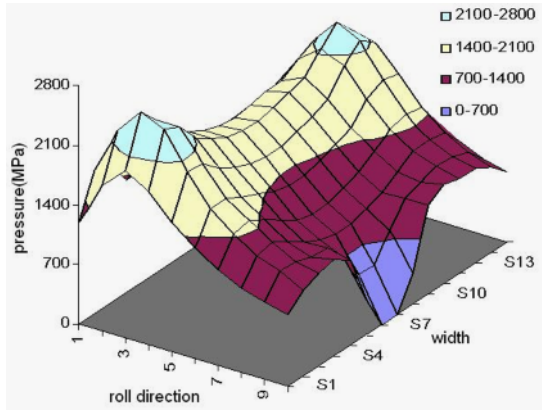


Fig. 6. Pressure distribution in cold rolling of the blade

In experiment, at the edge of the blade with severe reduction, the thickness is thinner than the middle of the piece and this leads to an increase of pressure in that region. One of the methods for determining the average pressure with the help of empirical test results is the use of forging method. In this way, the rolling process, regardless of the dynamic conditions, could be regarded as forging the piece between two jaws of a press machine. The average pressure formula is written as eq. (1):

$$P_m = 2\bar{K} \frac{h_m}{\mu l_d} (e^{\frac{\mu l_d}{h_m}} - 1) \quad (1)$$

The Von Mises yield criterion is shown by relation (2) [9]:

$$(\sigma_1 - \sigma_2)^2 + (\sigma_2 - \sigma_3)^2 + (\sigma_3 - \sigma_1)^2 = 2Y^2 = 6k^2 \quad (2)$$

The relation (2) is simplified as (3) [8]:

$$\sigma_1 - \sigma_3 = \Psi Y \quad (3)$$

In which Ψ is the obstruction coefficient of the material and defined as (4):

$$\Psi = \frac{2}{\sqrt{3 + \mu^2}} \quad (4)$$

whereas μ is defined as (5):

$$\mu = \frac{2\sigma_2 - \sigma_1 - \sigma_3}{\sigma_1 - \sigma_3} \quad (5)$$

Thus, the yield conditions of the material is simplified and $\Psi Y = 2K$ is considered as the yield stress of the material for that specific condition. Using the formulas, empirical results are determined according to Table 3. The computed pressure value through relation 5.1 is equal to 2500 MPa which is close to the average value obtained from the simulation (2028 MPa.)

Table 3. Calculated values via experimental results

ε_w	$\bar{\varepsilon}$	ψ	μ	l_d (mm)
0.11	0.5	1.12	0.07	13.2
h_0 (mm)	h_1 (mm)	h_m (mm)	ε_h	ε_l
2	1.22	1.61	-0.49	0.37

6. Conclusion

In this paper, pressure distribution on the surface of the preform in the cold rolling of blades and twisted sections has been investigated. For this purpose, the results obtained from experimental tests and computer simulations have been analyzed. According to these results, the pressure does not have a hill shape distribution pattern and depends entirely on the caliber section. Therefore, the highest values of pressure occur at areas close to the edges of the section which experience more reduction, friction, and stress, and as a result, a rather saddle shape pressure distribution pattern is formed. Also, the average pressure value calculated from the simulation shows a good correlation with the average pressure obtained from the theoretical relations and empirical results.

7. References

- [1] Hockett JT, (1960) calculation of rolling force using the Orawan theory, Trans. ASM, Vol 52: 675
- [2] Rows GW, (1977) Principles of industrial metal working processes, Edward Arnold
- [3] Shin W, Lee SM, Shivpuri R and Altan T, (1992) Finite-slab element investigation of square-to-round multi-pass shape rolling, Journal of Materials Processing Technology, Volume 33:141-154
- [4] Liu C, Hartley P, Sturgess CE, Rowe GW, (1985) elastic-plastic finite-element modeling of cold rolling of strip, International Journal of Mechanical Sciences, Volume 27:531-541
- [5] Inoue T, Yin F, Kimura Y, (2007) Strain distribution and micro structural evolution in multi-pass warm caliber rolling, Materials Science and Engineering, pp.114-122
- [6] Milenin AA, Dyja H, Mróz S, (2004) Simulation of metal forming during multi-pass rolling of shape bars, Journal of Materials Processing Technology, , pp.108-114
- [7] Komori K, Kato K, (2001) Analysis of stress distribution in caliber rolling by the energy method using finite-element division, journal of material processing Technology, pp.201-208
- [8] Moshksar MM, (2005) Fundamentals of rolling engineering, Iran, Shiraz university press
- [9] George ED, Howard A, Semiatin SL., (2003) Handbook of workability and process design

Determination of the duty cycle in thermoset pultrusion

Wajid Ali Khan¹, Jim Methven¹

¹ Manufacturing and Management Group, School of Mechanical Aerospace and Civil Engineering, The University of Manchester, Sackville Street, Manchester M60 1QD, United Kingdom

Abstract Pultrusion is an important process for the manufacture of thermosetting composites profiles of constant cross section. This work has shown experimentally and analytically the advantages of preheating the precursors to increase the line speed. The work was extended to quantify for the first time the duty cycle of a typical process. Heat transfer equations have been formulated to establish the temperature profiles within the heaters and the die and were solved using the implicit finite difference method.

Keywords Pultrusion, Duty Cycle, Pre-Heating, Specific Energy Consumption

1 Introduction

Pultrusion is the only continuous process for manufacture of composites based on thermosetting resins. It involves pulling a package of reinforcement (fibres and mats) from a storage creel through a bath of catalysed resin, then through a series of squeeze-out bushes and, finally, through a heated die wherein the resin cross-links and cures. The cured profiles are cut in length by a cut-off saw at the end of the line. Common thermosetting resins include unsaturated polyester, urethane acrylate, vinyl ester and epoxy while reinforcement includes glass, carbon, aramid and basalt.

The key to the process is the die: this is a split construction, typically 1m long with machined flat lands through which the die halves are bolted together. The mould must contain the prevailing internal pressure during the crosslinking and flow process. Typical pultrusion dies are heated by elements attached to the external mould surfaces and the temperatures are maintained in zones along the length of the die by PID controllers [1-4].

Much of the literature on pultrusion has focussed on the profile temperature and the extent of crosslinking of the material in the die [3, 12-17].

By contrast this work attempts to predict the duty cycle of the heaters in order to estimate the specific energy consumption of the process.

2 Analysis

Equation 1 gives the conservation of energy for conduction in the three co-ordinate directions with the source term (q) representing the rate of heat generation per unit volume of the crosslinking reaction. k is the thermal conductivity of the material.

$$\frac{\partial^2 T}{\partial x^2} + \frac{\partial^2 T}{\partial y^2} + \frac{\partial^2 T}{\partial z^2} + \frac{q}{k} = \frac{1}{\alpha} \frac{\partial T}{\partial t} \quad (1)$$

The reaction term, q can be expressed by the conversion of the precursors, α , and the total heat of reaction, Q_0 ,

$$q = Q_0 \frac{d\alpha}{dt} \quad (2)$$

The rate of conversion is given by the Kamal equation [17-20] in terms of the Arrhenius rate constants, k and the stoichiometry indices m and n . This is given here as equation (3)

$$\frac{d\alpha}{dt} = (k_1 + k_2 \alpha^m)(1 - \alpha)^n \quad (3)$$

Equation 1 was solved by the implicit finite difference method and Equation 2 integrated by the 4th order Runge Kutta method. The various parameters for the simulation are given in Table 1. The simulation was performed using MATLAB.

Table 1: Simulation Parameters

Reaction's Order, m	0.67
Reaction's Order, n	1.34
Arrhenius Coefficient	$A_1=1.04 \times 10^{13} \text{ sec}^{-1}$
Arrhenius Coefficient	$A_2=3.68 \times 10^8 \text{ sec}^{-1}$
Activation Energy	$E_1=124 \text{ kJ mol}^{-1}$
Activation Energy	$E_2=73.435 \text{ kJ mol}^{-1}$
Universal Gas Constant	$R=8.314 \text{ J mol}^{-1} \text{ K}^{-1}$
Thermal Conductivity	$k=10.4 \text{ Wm}^{-1}\text{K}^{-1}$
Specific Heat	$C=1010 \text{ KJkg}^{-1}.\text{K}^{-1}$
Density	$\rho=2101 \text{ kgm}^{-3}$
Line Speed	0.2-1.0 m/min
Profile Thickness	6.0 mm
Die Length	900 mm
Initial Temperature	25°C

The control algorithm for the heaters and duty cycle is based on a simple on/off control with the location of the control temperature at the interface between the die and the profile. If the profile temperature is below this set point temperature the heaters are on at full power and if the temperature falls below the control temperature then the heaters are off.

3 Simulation Results

Figures 1-4 are outputs from a simulation in which the die temperature is fixed at 180°C

Figure 1 and Figure 2 show, respectively, the axial temperatures and conversions at the surface of the profile for a range of line speeds. Figure 3 and Figure 4 show, respectively, the corresponding temperatures and conversions at the centre of the profile.

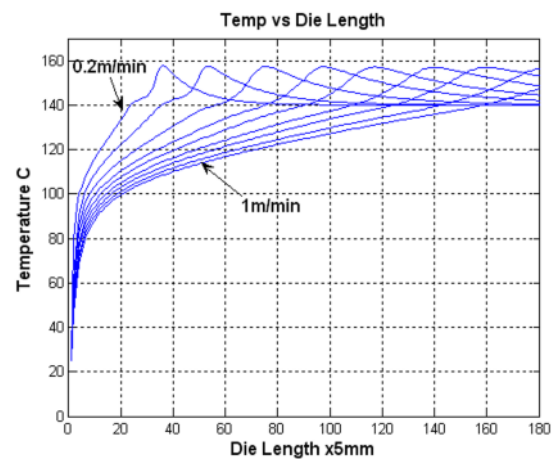
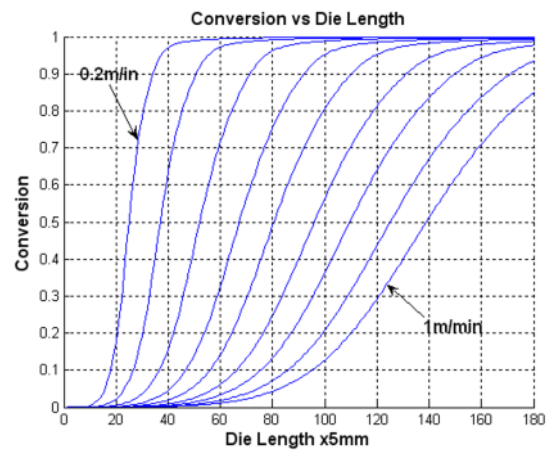
These results are in broad agreement with the reported literature [2, 5, 7, 9] and show for example, the relatively large characteristic peak exotherm at slow pulling speeds and the reduction in total conversion at higher speeds. Optimally, the peak temperature and peak conversion should coincide at the die exit.

Figure 5 and 6 are outputs from a simulation which includes the control algorithm. Here, the total power from the die heaters is 1200 W spread uniformly along the die and the control temperature is located at the

interface of the mould and profile. The temperature is set at 140°C.

Figures 5 show the cyclic variation in die temperature as a result of the simulated control algorithm.

As the precursor progresses through the die, heat is transferred from the die to the profile, causing the die temperature to drop, and this causes the heaters to switch on. As the profiles progress more the die, the temperature increases again as a result and due to the heat released by the crosslinking exotherm. The process repeats as shown in Figure 5 and establishes the so-called duty cycle.

**Fig. 1:** Temperature at the profile surface**Fig. 2:** Conversion at the profile surface

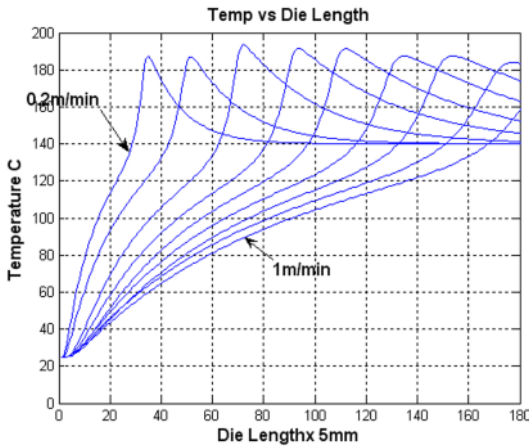


Fig. 3: Temperature at the profile core

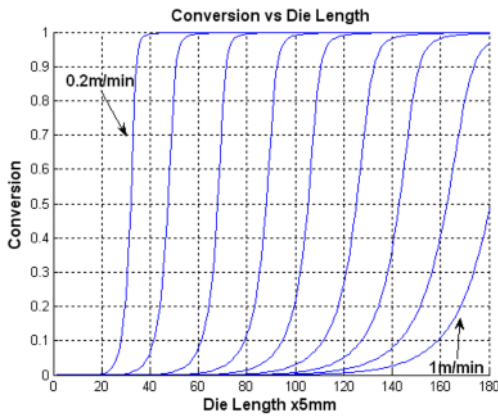


Fig. 4: Conversion at the profile core

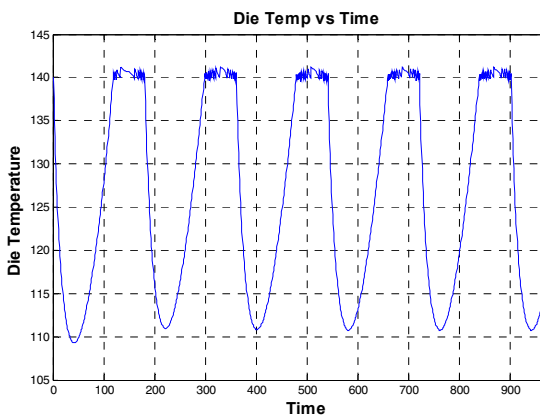


Fig. 5: Cycling of heater power

From Figure 6 the duty cycle shows an expected reduction as the process tends towards steady state.

However, taking the overall average from Figure 6, the duty cycle is around 30%-40%.

4 Experimental Measurements

The simulations were tested by experimental work at EXEL Composites, Runcorn, on a Pultrex machine.

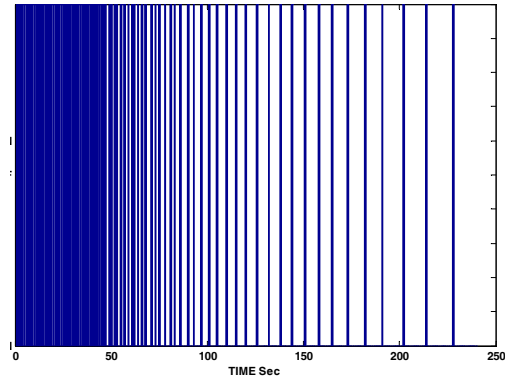


Fig. 6: Duty Cycle

For these experiments, the line speed was 0.55 m/min, the die length 1.2 m and the profile thickness was 3 mm

The power input to one of the die heaters was measured by passing one phase through the loop of a LEM PR-20 recording ammeter (Figure 7). The output from this was connected to an oscilloscope (CS4025).



Fig. 7: LEM PR 20 Current Meter

Since the oscilloscope was not a storage device and the duration of the recording quite long, the measurements were made by recording a video of the oscilloscope screen. The screen showed a blip when the power to the heaters was on this and a spot when the power was off. By recording a number of such sequences and digitising the resulting video an accurate time between the on and off states was obtained. From this the duty cycle could be calculated.

In fact these measurements showed a fairly constant duty cycle of around 30% which is in broad

agreement with the simulation. The oscilloscope set-up is shown in Figure 8.

5 Conclusions

This work has described the first simulation of the pultrusion process which takes account of the temperature control of the die heaters. The results are in fair agreement with experimental measurements but require further validation by organising an experiment from “cold”. This is difficult to organise.

Nonetheless the simulation has been used to predict the increase in line speed achieved by pre-heating the precursor (described elsewhere) and with some refinement such as a PID control algorithm is likely to prove extremely useful.

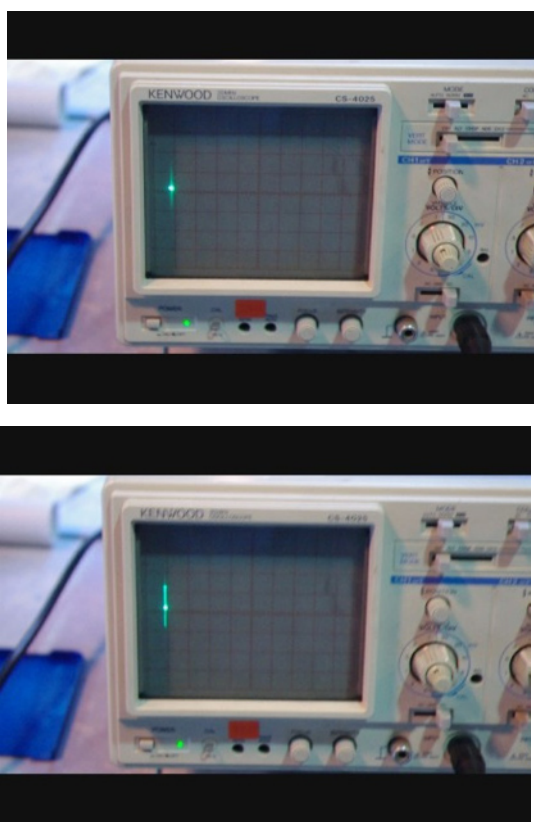


Fig. 8: Frame 1 (top) shows the power off and frame 25 (bottom shows the power on (see text))

6 References

- [1] J. M. Methven, S.R.G., A. Z. Abidin, Manufacture of Fiber-Reinforced Composites by Microwave Assisted Pultrusion. *Polymer Composites*, 2000. 21(4): p. 586-594.
- [2] Gibson L. Batch, C.W.M., Heat Transfer and Cure in Pultrusion: Model and Experimental Verification. *AIChE*, 1993. 39(7): p. 1228-1241.
- [3] Mariasun Sarrionandia, I.M., Stella Maris Moschiar, Maria Marta Redboredo, Analia Vazquez, Heat Transfer for Pultrusion of a Modified Acrylic/Glass Reinforced Composite. *Polymer Composites*, 2002. 23(1): p. 21-27.
- [4] Astrom, B.T., Development and application of a process model for thermoplastic pultrusion. *Composites Manufacturing*, 1992. 3(3): p. 192-197.
- [5] Xiao Lin Liu, I.G.C., Y.C. Lam, Simulation of heat transfer and cure in pultrusion with a general-purpose Finite element package. *Composite Science and Technology*, 2000. 60: p. 857-864.
- [6] Noha Hassan, J.E.T., R. C. Batra, A Heat Transfer Analysis of the Fiber Placement Composite Manufacturing Process. *Reinforced Plastics and*
- [7] C. Dispenza, A.A.P., P. Fuschi, Numerical simulations of the mechanical characteristics of glass fibre reinforced C-profiles. *Composite Science and Technology*, 2006. 66: p. 2980-2989.
- [8] Chin-Hsing Chen, C.-C.M.M., Pultruded Fibre-Reinforced Polyurethane Composites. III. Static Mechanical, Thermal, and Dynamic Mechanical Properties. *Composite Science and Technology*, 1994. 52: p. 427-432.
- [9] S. Paciornik, F.M.M., M.H.P. de Mauricio, J.R.M. d'Almeida, Analysis of the mechanical behavior and characterization of pultruded glass fiber-resin matrix composites. *Composite Science and Technology*, 2003. 63: p. 295-304.
- [10] Liqun Xu, Z.D., S. Li, L. James Lee. Computer Simulation of Resin Injection Pultrusion (RIP). in *Composites 2001*. 2001. Tampa, FL USA.
- [11] Shoujie Li, Z.D., L. James Lee, Herbert Engelen, Effect of Die Length on Pulling Force and Composite Quality in Pultrusion, The Ohio State University: Texas.
- [12] ANDREAS CARLSSON, B.T.A., Modeling of Heat Transfer and Crystallization Kinetics in Thermoplastic Composites Manufacturing: Pultrusion. *Polymer Composites*, 1998. 19(4): p. 352-359.
- [13] M. R. Kamal, S.S., Kinetics and Thermal Characterization of Thermoset Cure. *Polymer Engineering and Science*, 1973. 13(1): p. 59-64.
- [14] D. Lahlali, M.N., M. Dumon, Cure Kinetics and Modeling of an Epoxy Resin Cross-Linked in the Presence of Two Different Diamine Hardeners. *Polymer Engineering and Science*, 2005.
- [15] Kenny, J.M., Determination of Autocatalytic Kinetic Model Parameters Describing Thermoset Cure. *Applied Polymer Science*, 1994. 51: p. 761-764.

Development of New Press-Forming Process for a Screw-Threaded Fuel Filler Pipe

N. Kamei¹, Y. Kawamura², T. Nagamachi², and H. Watari²

¹ nobu1217edin@gmail.com, D.I.P., Inc Managing Director and Graduate School of Engineering, Department of Production Science and Technology, Gunma University, Japan

² Graduate School of Engineering, Department of Production Science and Technology, Gunma University, Japan

Abstract. The growing demand for lightweight products has been increased by the rapid development of automobiles in order to reduce fuel consumption. One of the keys to reduced fuel consumption is to utilize high-strength, light materials like stainless steel that are difficult to form due to their strength. This paper discusses the development of pressing technology that forms relatively high-strength stainless-steel pipe with surface screw threads. Our new press-forming process was tested to obtain accurate screw threads on stainless-steel pipe. A 3-D digitizer was used to measure the accuracy of pipes manufactured by the proposed pressing method. The proposed press-forming method decreases pipe thickness more effectively than conventional roll-forming technology. The maximum decrease in material thickness produced by conventional roll forming was 40%, but the maximum decrease in material thickness produced by our press-forming process was 20%. Stress and strain were clarified by using Finite Element Simulation to expand effectiveness of the new press forming technology.

Keywords: threads-forming, stainless pipe, press-forming process, finite element simulation

1. Introduction

Industries must produce green products to protect the global environment. In particular, the automotive industry needs to develop fuel-efficient cars, so weight-reduction is of great interest. The desire to reduce weight has shifted steel products to stainless steel, and the forming industry must deal with such materials [1, 2].

This paper discusses the forming of single threads on stainless-steel pipe. Roll forming has been used for single threads forming [3, 4]. However, roll forming tends to decrease material thickness and has inadequate forming accuracy because stainless steel is hard but brittle whereas steel is ductile [5-8]. Accordingly, this paper proposes our radically new method of press-forming single threads on stainless-steel filler pipe and documents its high accuracy that can not be achieved by roll forming as well as the greater decrease in material thickness.

2. Formed Product

This paper focuses on stainless-steel filler pipes that feed fuel from the filler neck to the fuel tank. The main material of the filler pipe has been STKM11A but has gradually transitioned to stainless steel, especially SUS436 [9]. The shape of the filler pipe screw is standardized by Japanese Industrial Standards (JIS D2501). SUS436 is a ferritic stainless steel and was used as a specimen.

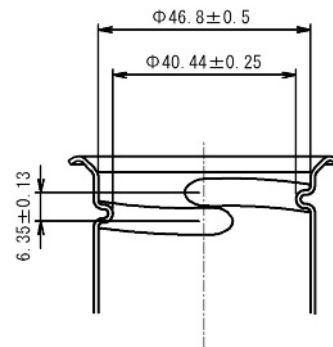


Fig. 1. Dimensions of filler pipe regulated by JIS D2501

2.1 Manufacturing Method

Roll forming is ordinarily used to form filler pipe threads. A forming roller presses the work and goes around it with a certain amount of pressure. Roll forming easily causes a local decrease due to a concentrated pressure at a point [10]. The authors clarified that the threads-forming process increases the material thickness in the beginning at a rate of 20% and later decrease it at a rate of 40% (Figure 2).

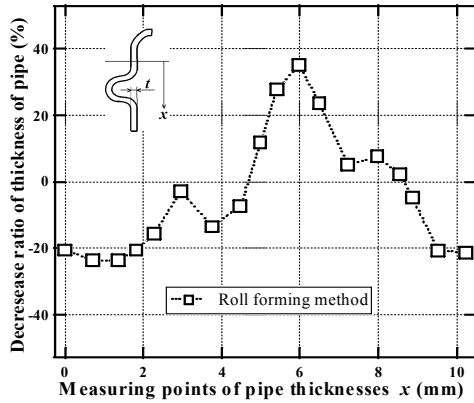


Fig. 2. Pipe thickness after roll forming

In order to resolve this, we developed a totally new press-forming process to form a pipe screw. Our press-forming process reduces the material load by using line pressure.

A new test machine has been developed based on a concept originated by D.I.P., Inc. Figure 3 illustrates the forming motion of the test machine. There are six dies outside of the specimen and three dies inside the specimen. First, odd numbered outer dies and inner dies press the trial pipe and return to the starting position. The inner dies then turn 60 degrees and move in an axial direction by the screw pitch (6.35 mm). Second, the even numbered outer dies and inner dies press the trial pipe, and all dies return to the starting position.

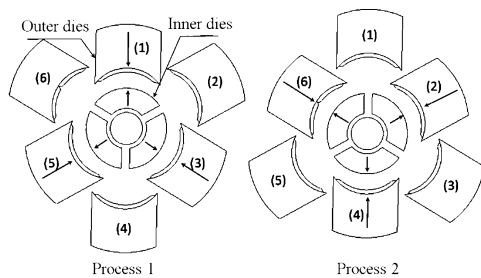


Fig. 3. Schematic illustration of manufacturing method

2.2 Estimating the Thickness of the Formed Specimen

The thickness of the specimen formed by the test machine was measured by a three-dimensional coordinate measuring system, UPMC 850/700 CARAT HSS made by Carl Zeiss.

Figure 4 plots the measurements by the three-dimensional coordinate measuring system. The local decrease of material thickness was a maximum 20%, which is an improvement compared to roll forming.

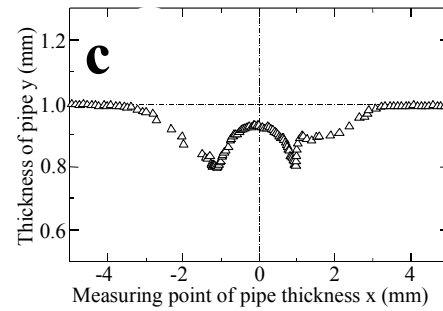


Fig. 4. Result of pipe thickness measurement

3. Three-Dimensional Finite-Element Simulation

A three-dimensional finite-element analysis was performed to determine the mechanism of local decrease of pipe thickness from the strain tendency. DEFORM 3D Ver.6.1 is adopted for the analysis. As an analytical parameter, there are 337,680 elements, the dies are fed at 10 mm/s, Poisson's ratio 0.3, Young's modulus 220, and the processes are divided by 40. Coulomb friction with a coefficient of friction of 0.12 is assumed in the analysis.

3.1 Strain of Analyzed Pipe

Figure 5 depicts the distribution of radial strain ϵ_r produced by process 2 in Figure 2 and analyzed by the finite-element method. In Figure 5, the sign of the radial strain ϵ_r differs between the inner forming area and the outer forming area. Accordingly, radial compressive strain ϵ_r is generated in the inner forming area (light area of Figure 5) whereas radial tensile strain ϵ_r is generated in the outer forming area (dark area of Figure 5). Starting points of threads-forming (dark area of Figure 5) generate tensile strain ϵ_r because the entire area is pressed by inner and outer dies.

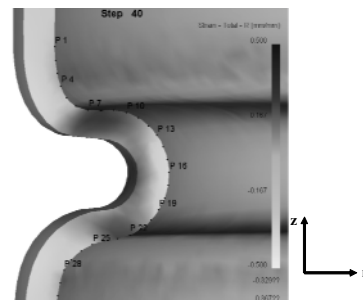


Fig. 5. Distribution of radial strain ϵ_r

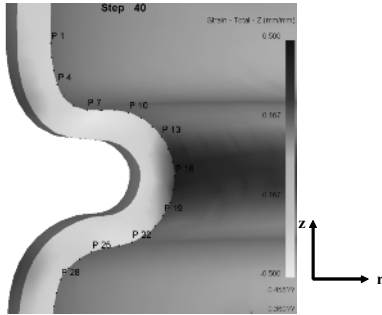


Fig. 6. Distribution of z-direction strain ϵ_z

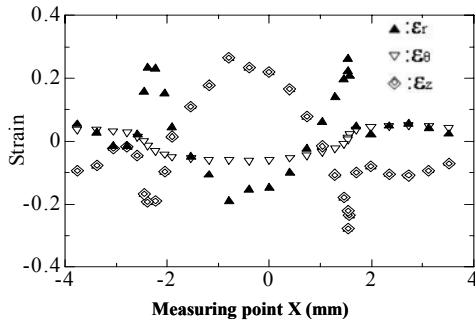


Fig. 7. Distribution of strain of inner forming area

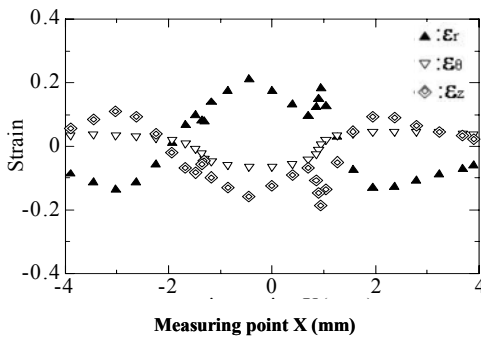


Fig. 8. Distribution of strain of outer forming area

Figure 6 illustrates the distribution of strain in the z-direction. The sign of strain distribution ϵ_z is opposite that of radial strain ϵ_r .

The radial strain ϵ_r , the z-direction strain ϵ_z , and the circumferential strain ϵ_θ that are compressive overall, ultimately have a significant effect on the distribution of the pipe thickness. Figures 7 and 8 graph the result of FEM strain analysis.

3.2 Thickness of analyzed pipe

Figure 9 compares the distribution of the material thickness determined by the experiment and that determined by finite-element analysis, which is measured as the distance between an outer point of a forming area and an inner intersection point of the normal line and the tangent line of point. The comparison reveals that the

local maximum decrease is generated at the starting points of the screw threads, not at the top of the screw threads [11]. The experiment indicates a 20% decrease, and finite element analysis, a 12% decrease.

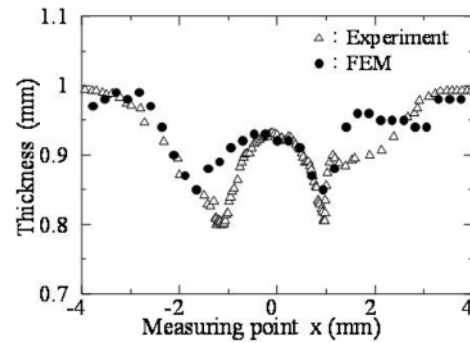


Fig 9. Distribution of thickness of the pipe

4. Discussion

This study confirmed that our press-forming process is superior to roll forming for making single threads on a stainless filler pipe. Notably at the top of screw threads, local decrease ratio is improved from 40% (Figure 2) to 10% (Figure 9). This is because roll forming locally presses the specimen at a point, on the other hand, our press-forming process reduces the material load by using line pressure (Table 1).

Table 1. Comparison between roll forming and press-forming

	Roll forming	Press-forming
Load type	Concentrated pressure at a point	Line pressure
Distribution of wall thickness	Nonuniformity	Uniformity
Contact pressure	High	Low

However, both of roll forming and our press-forming cause 20% wall decrease at the both sides of the beginning of the threads-forming. Figure 10 illustrates the amount of the strain of each area. The figure indicates that the absolute value of the amount of the strain is greater in the high wall decrease area, so it has a significant effect on the wall thickness after forming. In order to improve the decrease ratio more, the absolute value of the strain have to be reduced in the decrease area by studying the shape of inner die and outer die.

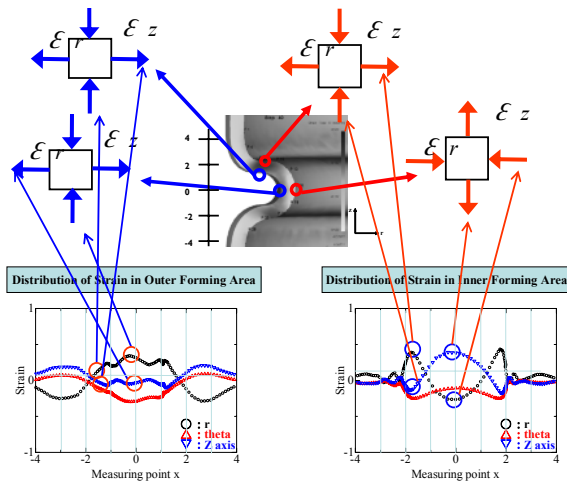


Fig. 10. distribution of strain of wall decrease area

5. Conclusion

This study confirmed that our press-forming process is superior to roll forming for making single threads on a stainless-steel filler pipe. Our press-forming process produces a local decrease in material thickness of around 20%, whereas roll forming yields a local decrease in material thickness of around 40%. The amount of the absolute value of the strain has a significant effect on the wall thickness after forming.

Furthermore, finite element analysis by DEFORM 3D revealed a correlation between the material thickness and the strain.

References

- [1] H. Hayashi and T. Nakawaga, Recent trends in sheet metals and their formability in manufacturing automotive panels, *Journal of Materials Processing Technology*, Volume 46 (1994), 455-487
- [2] M. Kleiner, S. Chatti, and A. Klaus, Metal forming techniques for light weight construction, *Journal of Material Processing Technology*, Volume 177 (2006), 2-7
- [3] V. Ivanov, Profiling of Rollers for Thread Rolling, *Journal of Materials Processing Technology*, Volume 59 (1996), 333-336
- [4] A. Gontarz, Z. Pater, and W. Weronki, Head forging aspects of new forming process of screw spike, *Journal of Materials Processing Technology*, Volume 153-154 (2004), 736-740
- [5] M. Salmani Tehrani, H. Moslemi Naeni, P. Hartley, and H. Khandemizadeh, Localized edge buckling in cold roll-forming of circular tube section, *Journal of materials Processing Technology*, Volume 177 (2006), 617-620
- [6] G. Nefussi, L. Proslie, and P. Gilormini, Simulation of the cold-roll forming of circular tubes, *Journal of Materials Processing Technology*, Volume 95 (1999), 216-221
- [7] S. Kalpakjian, *Manufacturing Processes for Engineering Materials*, Addison-Wesley Publishing Company 3rd Edition (1997), 122-125
- [8] T. Mori, and S. Kurimoto, Press formability of stainless steel and aluminum clad sheet, *Journal of Materials Processing Technology*, Volume 56 (1996), 242-253
- [9] M. Zhan, H. Yang, J. H. Zhang, Y. L. Xu, and F. Ma, 3D REM analysis of influence of roller feed rate on forming force quality of cone spinning, *Journal of Materials Processing Technology*, Volume 187-188 (2007), 486-491
- [10] H. Yan, H. Bi, and Z. Xu, Microstructure texture and grain boundaries character distribution evolution of ferritic stainless steel during rolling process, *Journal of Materials Processing Technology*, Volume 209 (2009), 2627-2631
- [11] Y. Abe, K. Mori, and O. Ebihara, Optimization of the distribution of wall thickness in the multistage sheet metal forming of wheel disks, *Journal of Materials Processing Technology*, Volume 125-126 (2002), 792-797

Roller Hemming: A New Simulation Model for the Automotive Industry

Amaia Arroyo¹, Iñaki Pérez¹, Marian Gutierrez¹, Jesús Bahillo² and Herman Toja²

¹ Labein-Tecnalia, Edificio 700, C/Geldo, Parque Tecnológico Bizkaia, 48160 Derio (Spain)

² Ingemat, S.A., Edificio 201, Parque Tecnológico Bizkaia, 48170 Zamudio (Spain)

Abstract. Hemming is used in the automotive industry to join two sheet metal panels by bending the flange of the outer panel over the inner one. In roller hemming process, a robot guides a small roller across the flange to fold a sheet onto itself or onto another sheet. The process is oriented to low volume automotive applications, providing a distinct advantage in manufacturing closures and subassemblies with developed flanges. The most important benefit of the roller hemming process is the flexibility to handle multiple product variations. Robotic roller hemming can be used to replace some flanging operation reducing overall investment costs. Robot roller hemming is a relatively new process, so nowadays there is no much fundamental process know-how available. The trial-and-error process is the most common way to achieve and maintain the right quality. To make a finite element analysis of the process can avoid this cost and time method. The work described in the paper is a development of a FE-simulation technique; which can accurately predict the geometry of the part before hemming, and also the required forces for the hemming operation. A complete 3D model was developed, considering the robot stiffness as well as the rotary of the roller, and the results were compared with experimental measurements for simple pieces (straight, convex and concave parts) showing a very good agreement.

Keywords: roller hemming, simulation, automotive industry

1. Introduction

Although the use of simulation tools is becoming increasingly important, the development and deployment does not affect all the processes forming alike. There are a wide variety of commercial softwares devoted specifically to forming processes such as hot and cold forging and sheet metal forming. However no specific commercial software for rotating incremental processes such as spinning, flow-forming or roller hemming has been developed so far, due to its complexity to be treated by finite element modeling. Due to the obvious interest generated by the possibility of having simulation tools to increase the understanding of these processes, the use of finite element software for general purpose (Abaqus, Marc.) tries to fill this vacuum.

The difficulty in suggesting strategies to adequately simulate the roller hemming has its origins in the very nature of the process. The process combines localized

deformation areas and very high roller speed. This cause the contact points between roller and material vary constantly throughout the process. The numerical simulation for this scenario is very complex, given the need to ensure the continuity of the forces of a nodal element to the next one throughout the whole process, for which a high number of iterations, and therefore a large time is required.

2. Process

In the automotive industry, hemming is used to join two sheet metal panels by bending the flange of the outer panel over the inner one. Currently in the industry there are basically two methods of mechanical hemming: the conventional mechanical hemming and the roller hemming (Figure. 1).

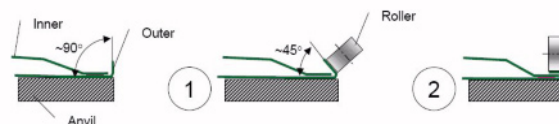


Fig. 1. Roller hemming process

The roller hemming process is generally carried out in three steps. The orientation (angle) of the roller changes in between the hemming steps.

The tensile state created during roller hemming process (non bending plane strain) with a component in the axis of folding, favors a smaller elongation of the grain in the deformed area and thereby delay the onset of shear bands and fractures compared with plain strain bending state achieved using the conventional hemming.

To perform and develop the FEM methodology three different geometries were selected, straight, concave and convex. The straight test was 800 mm length and the concave and the convex one had 250 mm radius. (Figure 2). The roller had a 62 mm diameter and a 28 mm depth.

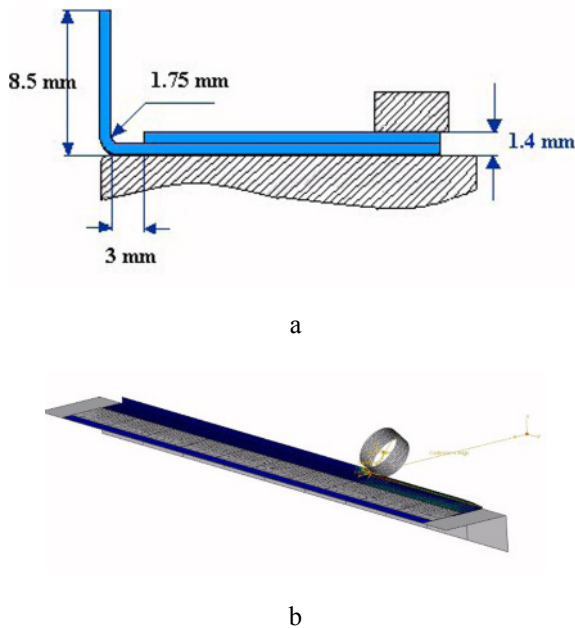


Fig. 2. a. Test dimensions; b. Straight model

There are many parameters to evaluate the hemming quality in terms of dimensions and surface aspects. In this study we have concentrated on only two dimensional parameters, the roll-in and the hemming height. The roll-in of the hem is defined as the distance between the outer radius of the hem and the original flange of the panel and the hemming height is the flange height obtained.

The material used for the model developed is a bake hardening mild steel, E220B with an isotropic hardening behavior and strain rate dependency.

3. Finite Element Model

There are many works that try to develop simulation models for FE hemming in an accurate and efficient way. Most studies conducted so far are 2D models to reduce the size of the model and the computing time. There are several defects due to the deformation (cracks and wrinkles), which can not be reproduced by 2D models. Consequently, it is necessary to perform 3D hemming simulations.

There are also numerous studies ([3]) that attempt to elucidate the question of whether it is more appropriate to use an implicit or explicit code to simulate the process of hemming. Large deformation, nonlinear problems, and restrictions on contact are relatively easy to implement on an algorithm explicit. With the explicit time integration scheme is possible to accelerate the simulation through the mass scaling factor (MSF), reducing the computation time sometimes at the expense of sacrificing some accuracy. To maintain an acceptable accuracy being monitored ratios of kinetic energy in front of internal

energy of deformable materials, and must be smaller than the 5% to minimize the dynamic effects and thereby guarantee a quasistatic process in a simulation of forming explicit.

Another cause of dispute is if it's possible to use shell elements in the hemming simulations. The hemming generates a radius of curvature of the exterior sheet metal whose order of magnitude is the same as its thickness, which makes the conditions for using this kind of theory elements are not met in this case according to the theory of Reissner-Mindlin. However, studies ([1], [2]) conducted comparisons with solid elements that would show that the shell is as appropriate or more.

Taking into account these considerations, the model described in this paper was constructed following the next premises: 3D model, explicit code, shell elements. Non-linear simulation with Abaqus explicit was used to model the process, and 4 nodes shell elements (S4R) were used to model the outer and inner panels and rigid shell elements (R3D4) to model the roller, the holder and the base.

Shell elements for deformable materials represent the middle surface of the thickness while shell elements for rigid ones represent the real surface of contact. Fine mesh was generated in the bent flange (3 shell elements in the radius) while coarse meshes were used for low deformation areas. The smaller element size used in the radius area was 1 mm with a 2:1 aspect ratio. For straight case for example 11750 elements were defined, 12249 nodes and a time increment of 5e-05 applying the mass scaling of 100.

In order to reproduce the movement and behavior of the roller as realistically as possible, a set of connector elements were modeled that conferred the movement, positioning as well as the rigidity of the roller.

The connector elements represent a kind of "arms" and "hinges" that help us define the complex movement of the roller. In addition they permit dynamic and cinematic outputs, being able to monitor in this way, movements and forces in local coordinate systems, such as the roller.

The connection type used in all cases of our model is an assembled connection consisting of two basic connections. The components of a basic connection affect either the translations or rotations of the second node in respect of the first one. Our connector's elements consist of a basic translational connection and a rotational one. To define local directions they are referred to the local axes created before. The kinetic behavior is defined by a "behavior" associated with components free of relative motion, enabling incorporate "springs and dampers".

4. Experimental Procedure

Experimental tests were performed in order to validate the simulation results of the straight model. To measure the forces on the robot arm that holds the roller, two

loading cells have been installed as seen in the image below. One loading cell is used to measure the load in the arm direction (normal force) and the other one in the movement direction (tangential or advance force). These loading cells had been calibrated before being used in the experiments.



Fig. 3. Roller hemming system

Different tests have been carried out, varying the robot speed from 1200 mm/s to 150 mm/s and with different number of roller passes, two or three, in order to see the differences in forces supported by the robot during the process as well as the final shape. The experiments were conducted by Ingemat S.A, corporate partner in the project.

5. Results and discussion

The way that simulations have been validated was comparing the forces supported by the robot and the ones obtained from simulation, normal and tangential forces. One of the most important variable of the process is the K elastic constant used in the definition of the rigidity of the robot because the normal force obtained in the simulation will be directly dependent on it. It was previously adjusted to a 350 N/mm with an experiment

Two simulations were carried out in order to validate the model. In the first case the roller initial position was exactly the nominal one, that is, the roller begins the movement leaned on the sheet. In the second case the initial position of the roller is 3.7 mm under the nominal one. Both cases were conducted at 1200 mm/s velocity of the roller and two passes of the roller were necessary. In Figure.4 there is a comparison between experimental and simulation forces for a straight case with a nominal position of the robot and another with 3.7 mm of offset of the roller from the nominal position.

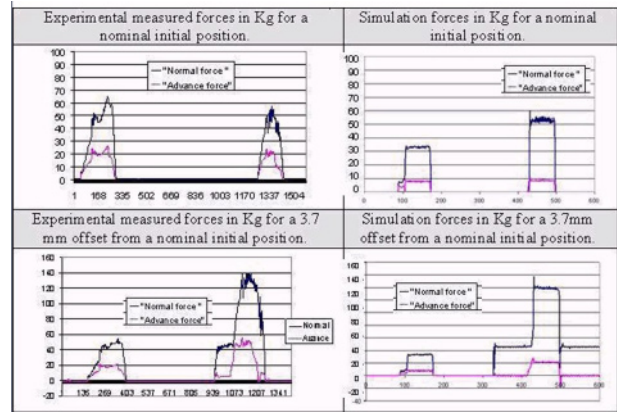


Fig. 4. Experimental and numerical forces in kg for straight case

Comparing the results obtained from Abaqus and the real ones from experiments there is a good agreement between them respect to forces. The simulation represents in a good manner the increment on forces due the offset of the roller.

The normal force is always higher than the tangential or advance one in both cases, simulation and experimental. The simulation gives values of the tangential forces lower that the experimental ones but for normal forces the agreement is better. This could be due to the fact that normal force is directly proportional to the elastic K value adjusted for the case and the tangential ones depends more on the friction. The friction value has not been evaluated in this study and a constant value of 0.2 has been used in all the simulations.

The normal forces in kg obtained in the simulation for the concave case with a velocity of the roller of 300 mm/s in the first pass and 600 mm/s in the second pass of the roller were the ones showed in the Figure.5

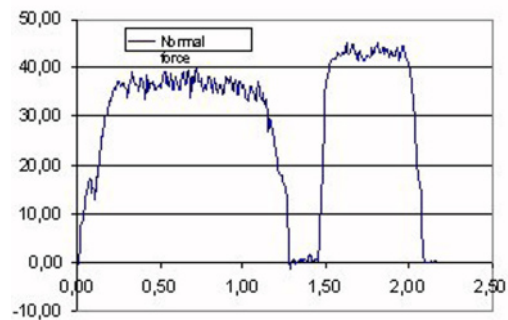


Fig. 5. Normal forces in kg for the concave format

Another analysis carried out to validate the model was the study of the dependency of the roll in and hem thickness with the initial bending radius. Similar simulations were conducted changing only the initial bending radius in a straight model. In Figure.6 there are showed both models; the left one has a 1.75 mm initial radius and the right one has a 0.3 mm inner radius.

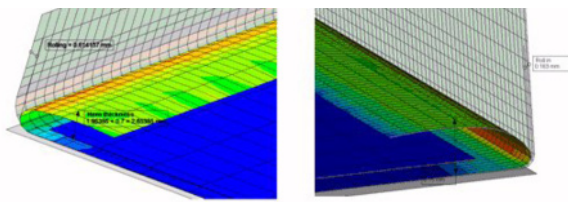


Fig. 6. Different initial bending radius

The values of the roll in and the hem thickness were measured in three points along the sheet and these are the averaged values of these measurements as it is showed in Table 1.

Table 1. Roll in and hem thickness depending on the bending radius and velocity of the roller

	Roll in (mm)	
Bending radius	1.75 mm	0.3 mm
V=225 mm/seg	0.61 mm	0.1627 mm
V=1200 mm/seg	0.62 mm	0.163 mm
	Hem thickness (mm)	
Bending radius	1.75 mm	0.3mm
V=225 mm/seg	2.66 mm	3.19 mm
V=1200 mm/seg	2.66 mm	3.15 mm

The developed model represents the tendencies of both variables in a good way, roll in and hem thickness depending on the inner radius maintaining the rest of conditions equal.

As well as the bending radius decreases the roll in and the forces also decreases and the hem thickness increases using the same conditions in both (rigidity of the robot). There is no big influence on these variables with respect to the velocity of the roller, but the inner radius influences the roll in, the hem thickness as well the force used to do it.

6. Conclusions

A complete model was developed to simulate the hemming of simple models: straight, concave, convex, considering the rigidity of the robot with good agreement between experiments and simulations.

The effects of the different variables of the process, velocity of the roller, rigidity of the roller, initial position of the roller, friction and initial bending radius were taken into account in the model.

This model is applicable to small models with planar and simple roller movements and it is possible to study the influence of the different variable in the forces, final geometry and also prediction of wrinkles.

References

- [1] Svensson M., Mathiasson K. (2002) "Three-dimensional simulation of hemming with the explicit FE-method" Journal of Materials Processing Technology Vol. 128, pp 142-154
- [2] Lange C., Felder E., Massoni E., Auger P., Nanji A. K.. (2000) "Hemming simulations with different element formulations and material models" IDDRG Conference Proceedings
- [3] Livatyali H., Muderrisoglu A., Ahmetoglu M. A., Akgerman N., Kinzel N. A., Altan T. (2000) "Improvement of hem quality by optimizing flanging and pre- hemming operations using computer aided die design" Journal of Materials Processing Technology Vol. 98 pp. 41-52

Control of the uniformity of direct electrical heating for Rotational Moulding

Wajid Ali Khan¹, Jim Methven¹

¹ Manufacturing and Management Group, School of Mechanical Aerospace and Civil Engineering, The University of Manchester, Sackville Street, Manchester M60 1QD, United Kingdom

Abstract: This work uses FE Analysis supported by experiment to establish the uniformity of mould heating in rotational moulding by the use of electrical heating elements placed in direct contact with the mould surface. This study is part of a larger project run by the Manufacturing and Management Group in The University of Manchester known as CHARM (Contact Heating Applied to Rotational Moulding), and which is supported by the DTI and Industry (DTI Reference J3530B with Haywood Rotomoulding, Rochdale and Tecni-Form, Stone).

Keywords: Rotational Moulding, Direct Electrical Heating, Cyclic Heating, Slip rings, Heat Distribution

1 Introduction

Rotational moulding (Rotomoulding) is a well established process for manufacture of large hollow parts from thermoplastics. A mould, made as a split shell, from cast aluminium or, more commonly nowadays, CNC machined aluminium is charged with thermoplastics powder and mounted on a mould carrier which is located at the extremity of the rotomoulding machine arm. The arm rotates about its long axis and the mould, in turn, rotates about its own (orthogonal) axis. The machine arm is moved into a gas-fired forced air oven and the temperature of the recirculating air inside the oven is controlled to typically around 300°C. At this temperature and under the biaxial rotation of the mould, the powder coats the inner surface of the mould and consolidates to a thin (typically less than 10mm thick) shell. At this point the arm is moved to a cooling station and the mould is allowed to cool before the part is removed. The process is relatively slow as a result of the poor heat transfer between the mould and the ambient air during both the heating and cooling stages and, typically, each of these operations can take around 20 minutes [1-6].

2 The CHARM Process

The CHARM process has been shown to reduce the Specific Energy Consumption (SEC) [7] of rotational moulding from more than 6 kWh/kg to less than 3 kWh/kg [8].

At the same time it changes the process from one of low capital, low skill and high running cost to one of higher capital, higher skill and lower running costs. The process is based on direct electrical heating via slip-rings [9].

Figure 1 shows a picture of the lab scale CHARM machine with the mould clamped on one of the rotating frames.

The mould (Figure 2) was CNC machined from solid aluminium by Finecut Graphics Designs, Poole. A closer view of one of the slip rings is shown in Figure 3

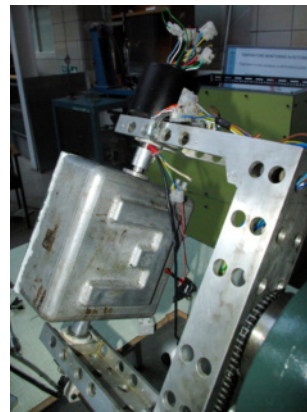


Fig. 1. Lab scale CHARM machine



The heaters are 200W, 12mm diameter cartridge devices (RS 376-1843) which are inserted into aluminium blocks. The blocks are attached by means of "strangle bands" (RS 171-938)

Fig. 2. Mould (300 mm by 300 mm by 80 mm deep) with Heaters attached

3 Analysis

Since the mould heaters are placed discretely on the mould surface (rather than conformal to it) the issue of control now becomes how to program a number of heaters to provide a uniform temperature on the mould surface.

This was modelled by mapping the mould wall to a simple square plate, measuring 300 mm on the side and 10 mm thick. (This is the same thickness as the mould).

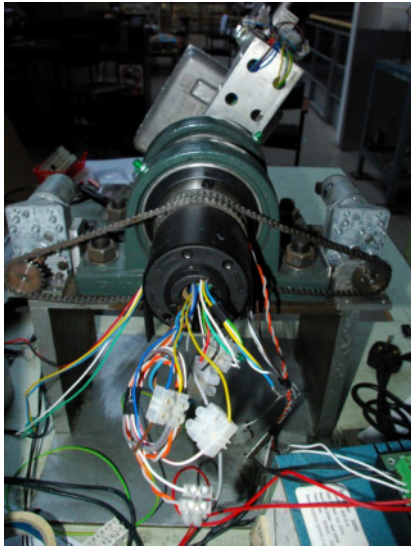


Fig. 3. Close-up of one of the slip rings

The specific heat capacity of the aluminium was $897 \text{ Jkg}^{-1}\text{K}^{-1}$ and the thermal conductivity $237 \text{ Wm}^{-1}\text{K}^{-1}$. The density was taken as 2700 kgm^{-3} . In this work the temperature dependence of these properties was ignored since the maximum temperature was less than 300°C [7]. The energy balance is given by

$$\int_V \rho \dot{U} dV = \int_S q dS + \int_V r dV \quad (1)$$

Here, V is the volume of solid material, with surface area S ; ρ is the density of the material, U is the material time rate of the internal energy, q is the heat flux per

unit area of the body, flowing into the body and r is the heat supplied externally into the body per unit volume. It is assumed that the thermal and mechanical problems are uncoupled in the sense that $U=U(\theta)$ only, where θ is the temperature of the material, and q and r do not depend on the strains or displacements of the body.

A Finite Element Thermal Model of the plate was generated using ABAQUS, using DC3D8, an 8 node linear heat transfer brick to mesh the plate.

3.1 Boundary Conditions

The heat conduction across the interface is assumed to be defined by

$$q = k(\theta_A - \theta_B) \quad (2)$$

Here, q is the heat flux per unit area crossing the interface from point A on one surface to point B on the other, θ_A and θ_B are the temperatures of the points on the surfaces, and k is the gap conductance.

The radiation heat flow per unit area between corresponding points is assumed to be given by

$$q = E[(\theta_A - \theta^Z)^4 - (\theta_B - \theta^Z)^4] \quad (3)$$

Here, θ^Z is the value of absolute zero temperature on the temperature scale being used, q is the heat flux per unit surface area crossing the gap at this point, from surface A to surface B, θ_A and θ_B are the temperatures of the two surfaces; and E is the gap radiation constant derived from the emissivity of the two surfaces. The convective heat transfer is defined by

$$q = h(\theta - \theta^0) \quad (4)$$

Here, q is the amount of heat transferred per unit area, h is the convective heat transfer coefficient and θ is temperature of the surface at a given time.

The heat loss to the environment (ambient temperature) is taken into account by using a surface film coefficient of $10 \text{ W/m}^2\text{k}$ [8-10]. For the initial step all the model surfaces, the internal and external air are at room temperature. The volume of the internal and external air is infinite and any turbulence in the air is ignored (free convection).

3.2 Thermal Loads

220 W heaters with the dimensions of the aluminium blocks which are shown in Figure 2 (75 mm by 65 mm by 5 mm) were used for the simulation and for the subsequent experimental measurements.

4 Results and Discussion

Simulations were carried using one, two, three and four heaters, which are distributed on the surface of the plate. Only a few of these results are actually shown here.

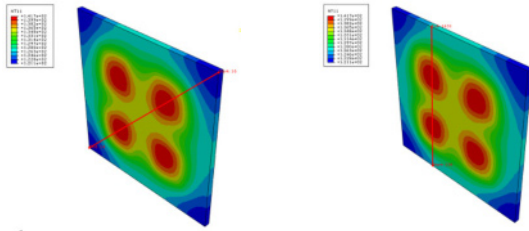


Fig. 4. Temperature Simulations and Paths 1 and 2 with all four heaters on for 5 minutes of heating

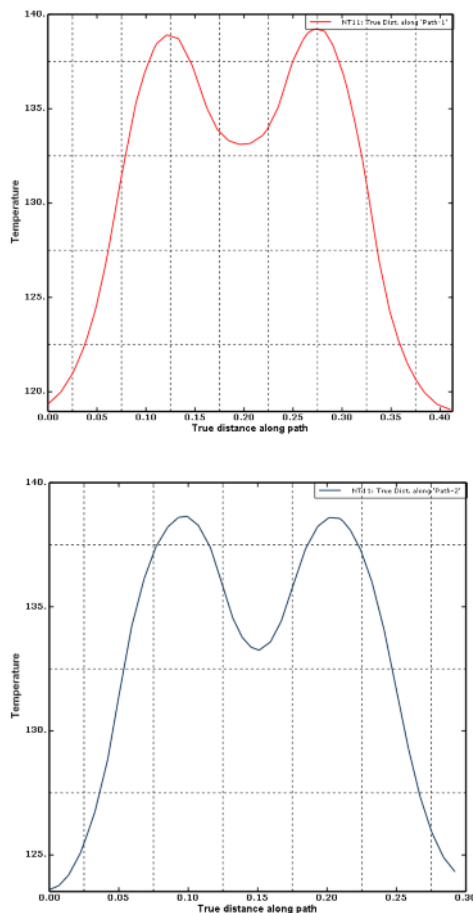


Fig. 5. Temperature variations along Path 1 (top) and Path 2 (bottom) for the simulations in Figure 4

It was noticed during these simulations that with one and two heaters being turned on continuously for five

minutes the temperature difference between the hottest and coolest point on the plate is about 20°C and with three and four heaters this temperature difference rises to about 25°C. By way of comparison a simulation of an impinging hot air jet was performed. This provides a simple model of the hot air heating in the traditional process. This model was created with a Fortran user subroutine, DFLUX, linked to the ABAQUS model. In this case the air jet moves in a defined rectangular path, with the same corners as shown in Figure 3 for the four heaters. The velocity of the moving jet was taken as 0.04 m/sec, so that the cycle is completed in 16 seconds.

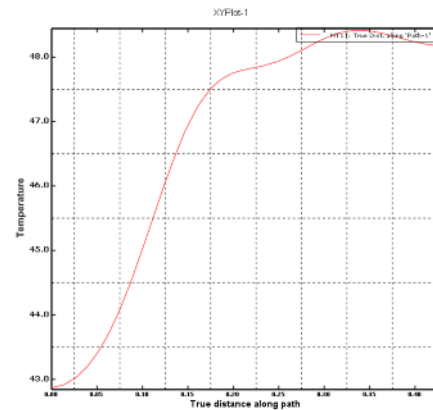


Fig. 6. Temperature variations along Path-1 with moving air jet

Using this information, an initial control regime based on the cycling of the electrical heaters was modelled. Here, the heaters are controlled to switch on and off in a prescribed and adjustable duty cycle and sequence.

Duty cycles of 20, 10, 5, 4 and 2 seconds were simulated and, as shown in Figure 6, the 2 second duty cycle showed a great improvement over that of the fixed (always on) regime.

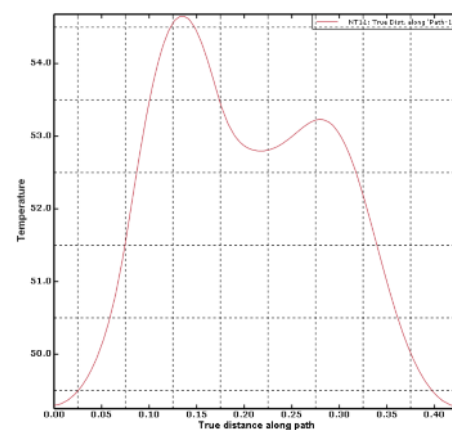


Fig. 7. Temperature variation along Path 1 using a heating sequence of 2 seconds (see text)

The variation in temperature in Figure 7 follows Path 1 (Figure 4) and shows a maximum temperature difference of only 6°C. This is roughly the same as that found for the moving air jet.

This is an important outcome for the CHARM process since it indicates that direct electrical heating is a viable option to the traditional process providing the heaters are controlled in this sort of fashion. Of course this can be implemented in practice by means of a programmable microcontroller such as a PIC or a PLC.

5 Experimental Verification

For completeness, the simulations were verified by experiment with the temperature profiles measured using a thermal imaging camera (FLIR Thermovision A20). Some of these measurements are shown in Figure 8. The results were consistent with the FE Analysis

6 Conclusions

It is shown by simulation and experiments that uniform temperature control in rotational moulding which uses direct electrical heating is achievable. This represents a significant advance in the development of the CHARM process which has been shown to offers the prospect of significant energy reduction - by a factor of at least 2 - over the traditional oven-based process.

The next step in the refinement of the existing CHARM machine is to embody the work described here into a program for a microcontroller (PIC or PLC) which can be used to control the moulding cycle.

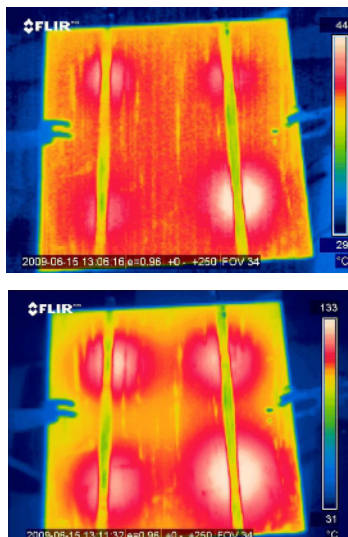


Fig. 8. Thermal images of Aluminium Plate after 1 minute of heating (top) and 5 minutes of heating (bottom). Note that the vertical strips are the strangle bands used to attach the heaters to the mould. See also, Figure 2.

7 References

- 1 Al-Dawery, I.A.H., J.G.P. Binner, G. Tari, P.R. Jackson, W.R. Murphy, and M. Kearns, Rotary moulding of ceramic hollow wares. *Journal of the European Ceramic Society*, 2009. 29(5): p. 887-891.
- 2 M. Anandha Rao, J.L.T., Principles of Rotational Molding. *Polymer Engineering and Science*, 1972. 12(4): p. 237-264.
- 3 Roy J. Crawford, J.L.T., *Rotational Moulding Technology*. 2002, New York: Williams Andrew Publishing.
- 4 C. T. Bellehumeur, J.S.T., Simulation of Non-Isothermal Melt Densification of Polyethylene in Rotational Molding. *Polymer Engineering and Science*, 2002. 42(1): p. 215-229.
- 5 P. J. Nugent, R.J.C., Liang Xu, Computer Prediction of Cycle Times During Rotational Molding of Plastics. *Advances in Polymer Technology*, 1992. 11(33): p. 181-191.
- 6 G. Gogos, X.L., L. G. Olson, Cycle Time Predictions for the Rotational Molding Process With and Without Mold/Part Separation *Polymer Engineering and Science*, 1999. 39(4): p. 617-629.
- 7 Reduced Energy Consumption in Plastics Engineering (RECIPE) is a European Community funded project, supported by the Intelligent Energy Europe programme (contract number EIE/04/153/S07.38646). Information is published at www.eurecipe.com/
- 8 Final Report to DTI on Project Number TPJ3530B, Novel Energy Reduction and Capital Optimisation in Rotational Moulding, submitted January 8, 2010
- 9 A Comparison between forced Air Convection heating and Direct Electrical heating of moulds in rotational moulding, M J Wright and R J Crawford, *SPE ANTEC*, 45 (1), 1452-1456 (1999)
- 10 Ewa Radziemsk, W.M.L., The Effect of late Size on the Natural Convective Heat Transfer Intensity of Horizontal Surfaces. *Heat Transfer Engineering*, 2005. 26(2): p. 50-53.
- 11 Gael Maranzana, S.D., Benjamin Raemy, Denis Maillet, Experimental estimation of the transient free convection heat transfer coefficient on a vertical flat plate in air. *International Journal of Heat and Mass Transfer*, 2002. 45: p. 3413-3427.
- 12 Xiang-Tuan Xiong, X.-H.L., Yao-Mei Yan, Hong-Bo Guo, A numerical method for identifying heat transfer coefficient, in *Applied Mathematical Modelling*. 2009.

High Efficiency Deep Grinding, an Application with conventional wheels

Andre DL Batako,

AMTReL, The General Engineering Research Institute, Liverpool John Moores University (LJMU), Byrom Street, Liverpool L3 3AF, tel. +44 (0) 151 231 2020, fax. +44 (0) 151 231 22158 Email a.d.batako@ljmu.ac.uk

Abstract. The recently emerged High Efficiency Deep Grinding (HEDG) allows the grinding process to be undertaken at high wheel speed, relatively large depth of cut and moderately high work speed. HEDG, whilst combining the mechanics of high-speed and creep-feed grinding, offers the possibility of achieving very efficient grinding with values of specific energy approaching those of conventional cutting processes. HEDG requires a high power input and consequently needs a well-designed process to secure the workpiece surface integrity, low temperature, and a reduced wear of the grinding wheel. The HEDG process necessitates an optimisation of the grinding parameters to achieve desirable results with minimum wheel wear. A poorly designed HEDG process causes abusive wear of the grinding wheel and leads to a damaged workpiece surface. This paper presents a thermal model that has been used to predict temperature in the HEDG process as a function of process parameters. The work explores an enhanced single-pole thermocouple technique that allows measuring contact temperature in deep cutting. A developed software that operates on the thermal model is used to implement a control strategy and to monitor the grinding process in real time. The results of the tests are presented in terms of measured and predicted temperatures and the specific energy. The paper also puts side by side the performance of metal bond CBN wheel and the high aspect ratio wheel.

Keywords: HEDG, Grinding temperature, Thermocouple, Grinding energy, control strategy, wheel wear.

1. Background

High efficiency deep grinding (HEDG) is a relatively new grinding technology. HEDG, whilst combining the mechanics of high-speed and creep-feed grinding, offers the possibility of achieving very efficient grinding with values of specific energy approaching those of conventional cutting processes. Whilst grain contact temperatures may approach the workpiece material melting temperature, workpiece surface temperatures can be low enough to prevent thermal damage from occurring. The HEDG process reduces the transmission of heat to the finished surface due to the combined effects of large angles of inclination and high work speeds. This allows achieving very high removal rates, without causing thermal damage to the finished component.

Tawakoli [1], has published a study on the concept of HEDG, which left a series of opened questions. Several works in the fundamental understanding of the mechanical and thermal performance of HEDG, Rowe, [2], Rowe *et al* [3] Stephenson *et al* [4] have been undertaken in order to determine the boundaries for HEDG Jin *et al* [5] and Morgan *et al* [6]. Robust and reliable grinding process models have been developed allowing for the exploration of the principles of HEDG. However, the investigation of the extreme limits of HEDG and beyond is still needed. The exploitation of the significant advantages of HEDG is possible through a complete understanding of the physical principles, Stephenson *et al* [4].

Numerous studies have been carried out to identify the relationship between the work-piece thermal damage (burn, residual stress and cracking), Chen *et al* [7] with grinding process parameters. This was achieved through the development of theoretical models of heat transfer within the grinding process to predict the temperature rise at wheel-workpiece interface, [1-8]. For repeatability across a range of grinding process configuration, the theoretical models are validated against actual temperatures measured during grinding, [9-12].

2. Thermal Modelling

Models of heat transfer are used to predict the temperature rise and to control the grinding process in order to avoid thermal damage of the workpiece. In this study a circular arc contact model was used to model the heat transfer at the grinding interface.

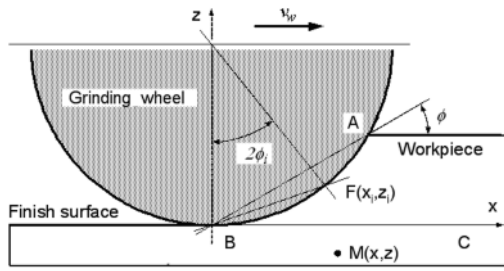


Fig. 1. Circular arc of contact for temperature modelling, adapted from [10].

Figure 1 illustrates schematically a circular arc of contact between the wheel and workpiece for modelling purposes. The contact surface is assumed to lie around a circular arc. The heat source is derived as the summation of infinite moving line sources located around the contact arc. The contact length l_c , is arc AFB . A line heat source at $F(x_i, z_i)$ moves at speed v_w (work speed) parallel to the x -axis at an angle ϕ_i to the finished surface BC . The varying angle ϕ_i is the angle FBC , the maximum value of which along the arc AFB is the contact angle ϕ . The length of the arc, BF is $l_i = d_e \cdot \phi_i$ where d_e is the effective diameter of the grinding wheel. The temperature rise at any point $M(x, z)$, due to the entire heat source AB , is derived as

$$T = \frac{1}{\pi \cdot k} \int_0^{l_c} q \cdot e^{-\frac{v_w}{2 \cdot \alpha} (x - l_i \cos \phi_i)} K_0 \left[\frac{v_w \cdot r_i}{2 \cdot \alpha} \right] dl_i \quad (1)$$

where

$$r_i = \sqrt{(x - l_i \cos \phi_i)^2 + (z - l_i \sin \phi_i)^2} \quad (2)$$

K_0 is the order zero Bessel function of the second kind. α is thermal diffusivity; k is thermal conductivity and q is heat flux (power per unit contact area). For a rigid wheel and workpiece, the contact length for deep cuts is approximated as $l_c \approx \sqrt{a_e \cdot d_e}$. The contact angle is estimated from the contact length and the effective wheel diameter: $\phi = l_c / d_e$

3. Single Pole Thermocouple Technique for Temperature measurement in HEDG

In HEDG, it is essential to measure the actual temperature at the interface between the grinding wheel and the workpiece. This allows understanding of the level of heat generated at the contact arc. The measurement of grinding temperature using the thermocouple is a technique that has been greatly improved over a number of years leading up to an optimised single pole thermocouple with a geometry that is highly reliable [11-12]. There are various methods of setting up a thermocouple within a workpiece to measure temperature

within the grinding contact zone and a number of these methods are reviewed in reference [12]. The improved single-pole thermocouple system was first developed for shallow grinding, where it was observed that the process of temperature measurement was stable, reliable and repeatable. This allowed the technique to be transferred to HEDG), a process that requires long and grindable thermocouples. This investigation uses a single-pole thermocouple configuration that involves inserting a strip of insulated conducting dissimilar metal into the workpiece. A junction is formed with the conducting material of the workpiece at the contact line during grinding by smearing the thermocouple material over the workpiece. The single-pole thermocouples used here are grindable, and provide an advantage over sub-surface double pole thermocouples since the surface temperature reading is direct because the temperature is measured at the contact surface. In this study a constantan strip with optimised configuration was used to form a J-type single-pole thermocouple with ferrous workpiece material.

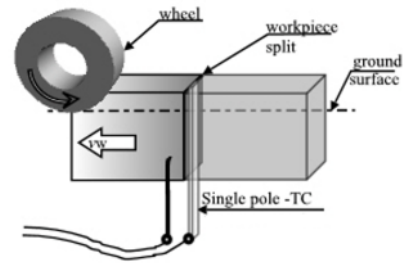


Fig. 2. Single-pole thermocouple configuration in split workpiece

Figure 2 shows a schematic of the set up of a single-pole thermocouple for surface grinding. The thermocouples were calibrated over a range of temperatures using ice and a hot oil bath and their response was linear over the calibration range; no hysteresis was observed between the heating and cooling phases [12].

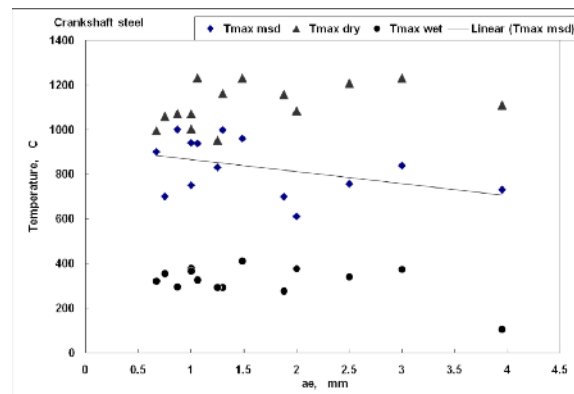


Fig. 3. Actual measured and predicted

Figure 3 illustrates the maximum predicted temperature ($T_{max\ dry}$) and ($T_{max\ Wet}$) as well as the actually measured temperatures ($T_{max\ msd}$). The predicted temperatures $T_{max\ Dry}$ are for the conditions where there would not be any cooling or lubrication when the cooling

fluid would have been burnt out completely. Temperatures T_{max} Wet are predicted for the conditions of good cooling and lubrication where the coolant would have taken away a considerable amount of the heat generated in the grinding contact zone. It is observed from the graph (linear T_{max} msd) that the contact temperatures decrease with the increase of the depth of cut. It is important to note that this would not be the case in conventional shallow cut (see [11-12]) because in HEDG the high work speeds play a critical role in the process.

4. Grinding Control Strategy

After a series of successful grinding tests (a few hundreds of repeatable tests) the single-pole thermocouple configuration was transferred to a specially designed HEDG machine (the 3rd generation of HEDG machine will be released as a commercial test bed by the end of 2010). Several sensors were incorporated in the machine in order to monitor most of process parameters i.e. grinding force, temperature in the grinding zone, work speed, grinding power and the differential pressure in the hydrostatic bearing as shown in Figure 4. It is to notice that due to electrical and other noise that biases the recorded signal from the sensors, hardware and software filtering techniques are used.

The grinding control strategy was developed in two stages: off line and on line. In stage 1, as illustrated in Figure 4 six cutting parameters were logged into a PC using a Labview data logging interface. The data were stored and then manipulated off line using Matlab software package. This allows improving the extraction of required information from the signal and tuning the software.

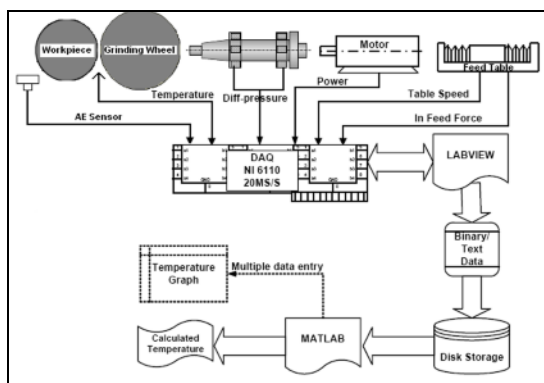


Fig. 4. Schematic of data acquisition for the HEDG system

Figure 5 shows the result of the development in stage 2. Here, the code tested in stage 1 off line was fused to provide an online process monitoring system. The human-machine-interface has two sections: the left panel allows the user to input the process parameters and the critical grinding temperature. The grinding process power and actual temperature is displayed on the right panel.

The raw signals of power and temperature are processed and displayed at the far right at the end of cycle. If the critical temperature has been exceeded a red alarm warns the operator. This is an open system where the operator can modify the grinding parameters based on the previous cycle results. In this system the predicted temperatures are not displayed, only real time measurements are given. This system is for experimental studies as the thermocouple is embedded into the workpiece. However it allows for validation of the thermal model in order to develop an industrial monitoring system (at commercial stage now) that operates autonomously in prediction mode.

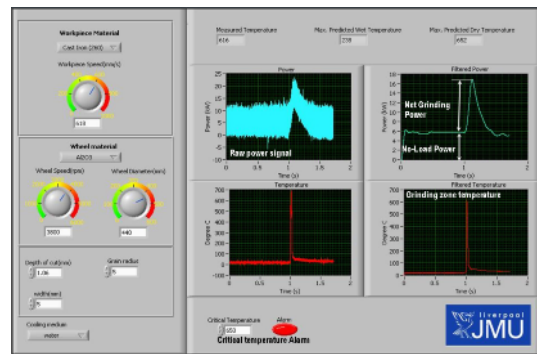


Fig. 5. Stage 2 grinding process monitoring system

5. Grinding Wheel performance in HEDG

HEDG has specific requirements to the machine tool in terms of stiffness and power and to the grinding wheel in terms of its ability to withstand the load and the bond to hold the grits together. The high feed rates increase the load on individual cutting grit leading to an aggressive wheel wear. Figure 6a) shows a conventional aluminium oxide wheel that was in this study.

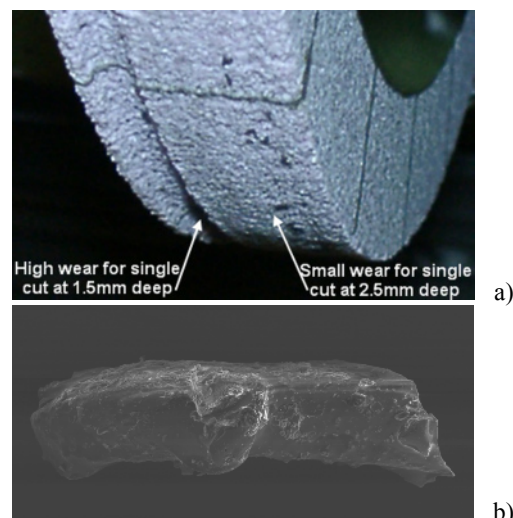


Fig. 6. High aspect ratio alitos (a) and normal grit (b)

The peculiarity of this wheel is that it has high aspect ratio grits (Figure 6b) with more than 50 percent porosity. Figure 6a) illustrates, at the left edge, a hostile wheel wear caused by a single pass with an actual depth of cut of 1.5 mm at a work speed of 517 mm/s (31 m/min) and 45 m/s wheel speed. Conversely, the right edge shows little wear after a single cut at 2.5 mm deep at 279 mm/s (16.7 m/min) feed rate with 80 m/s wheel speed. These two extreme cases illustrate how critical is the selection of HEDG process parameters. It is observed that the selection on the tool is the key to successful HEDG applications. Figure 7 puts, side by side, the effectiveness of two types of wheels tested during this study. The electroplated CBN wheels had the advantage as metal bonded to perform with no wear whereas the aluminium oxide wheels required a strategic approach to the selection of cutting parameters. However it is seen in Figure 7 that the conventional wheel outperformed the CBN wheel in term of energy efficiency.

Low values of specific energy are due partly to high removal rates that generate larger chip thicknesses. It is also possible that the very low specific energy is associated with thermal softening of the workpiece material at the grain contact, due to the very high strain rate and quasi-adiabatic shearing process. Also, low specific grinding energy could be explained by the fact that at high feed rates and deep cuts, the metal structural behaviour changes in nature. Instead of plastic deformation, a brittle fracture may take place. Brittle fracture requires less energy because of minimum internal friction in the material as opposite to plastic deformation. Therefore, for very high material removal, the power consumption versus material removal rates actually lowers dramatically.

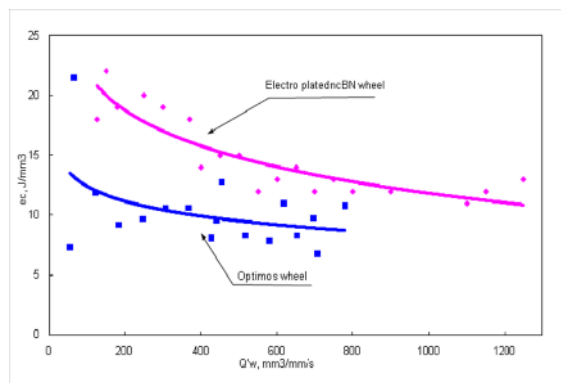


Fig. 7. Specific grinding energy

6. Conclusion

A thermal model for temperature prediction in HEDG has been presented together with a single pole thermocouple technique used to validate the model. Measured

temperatures were given alongside a system for control strategies in HEDG. Characteristics of HEDG process has been given in terms of wheel wear and specific grinding energies. The performance of two grinding wheels was illustrated. It was observed that a proper selection of wheel and cutting parameters are key to successful HEDG application.

Acknowledgement

The author would like to thank the EPSRC for funding this project (Grant GR/R68795) and the project partners: Cranfield University, Castrol Industrial, Element Six, Landis Lund, Renold, St Gobain Abrasives, Stresstech-AST. Gratitude is extended to Prof. B. W. Rowe for his invaluable support.

References

- [1] Tawakoli T, High Efficiency Deep Grinding, 1993, Mechanical Engineering, Publications limited, London.
- [2] Rowe W B, 2001, Thermal analysis of high efficiency deep grinding, International journal of machine tool and manufacture, 41, 1, 1-19, 2001
- [3] Rowe W B, Jin T, 2001, Temperatures in High Efficiency Deep Grinding, Annals of the CIRP, Vol 50, 1, 205-208.
- [4] Stephenson D J, Jin T, Corbett, 2002, High Efficiency Deep Grinding of low alloy steel with plated cBN wheels, Annals of CIRP vol. 51/1/2002 241-244
- [5] Jin T, Stephenson D J, Corbett, 2002, Burn threshold of high-carbon steel in high efficiency deep grinding, Proc Instn Mech Eng, vol. 216 Part B: J Engineering Manufacture, 357-364.
- [6] Morgan M N, Rowe W B, Batako A, 2003, 'Energy Limitations in HEDG and Conventional Grinding', 2003, Key Engineering Materials, v 257-258, 2004, pp 63-68.
- [7] X Chen, W B Rowe, 2000, "Predicting the Transitional Boundary of Tensile Residual Stress in Grinding" Abrasives Magazine, Feb/March, 28-37, 2000.
- [8] Jin T and Stephenson D J, 2003, Investigation of the heat partitioning in high efficiency deep grinding, International journal of machine tool and manufacture, 43, 11, 1129-1134.
- [9] W. B. Rowe, B. Mills and S. C. E. Black, 1996, "Temperature Control in CBN Grinding", *The International Journal of Advanced Manufacturing Technology*, 387-392 (1996).
- [10] Rowe W B, Morgan M N, Batako A, Jin T, 2003, "Energy and Temperature Analysis in Grinding" Keynote Paper, *Sixth Int. Conf. and Exhibition on Laser Metrology, Machine Tool CMM and Robot Performance - LAMDAMAP, 1-4th July 2003, Huddersfield University; Laser Metrology and Machine Performance VI*, 3-23, 2003
- [11] Batako A D L, Morgan M N, Rowe, W B, Walton I M, 2005; Temperature measurement in high efficiency deep grinding (HEDG) using an enhanced single pole thermocouple and PVD techniques, *Laser Metrology, Machine Tool CMM and Robot Performance - LAMDAMAP conference, Cranfield, 27-30 June 2005*, VII, 332-343, 2005.
- [12] Batako A D, Rowe W B, Morgan M N, 2005, Temperature measurement in High Efficiency Deep Grinding, International journal of machine tools and manufacture, 45, 11, 1231-1245, 2005.

Detection of High and Low Temperature in the Grinding Zone using Laser Irradiation Technique

Arif Mohammed¹, Dr. Janet Folkes¹, Dr. Xun Chen²

¹ Department of Mechanical, Materials and manufacturing, University of Nottingham

² School of Computing & Engineering, University of Huddersfield, e-mail: x.chen@hud.ac.uk

Abstract: Grinding burn is a physical phenomenon related to the temperature in grinding zone. This paper presented the detection of high and low temperature in the grinding zone using laser irradiation technique. Two experiments on temperature rise were carried out using laser irradiation and grinding separately. By controlling the laser energy flux and irradiation time the temperature rise can be manipulated. The acoustic emission signals generated during laser irradiation provide signature for monitoring grinding temperature. An ANN model developed based on thermal AE data extracted from laser irradiation was used to detect the thermal AE signatures in grinding experiments, so that the high and low temperatures in the grinding zone can be monitored. Such technique can be used for grinding burn detection. The grinding experiment arranged to identify burn or no burn signature of AE data due to high and low temperatures under given depth of cuts (1.0 mm and 0.1 mm).

Keywords: Laser irradiation, grinding, acoustic emission (AE), temperature, neural network.

1. Introduction

A grinding burn, which is one of the problem that occur to a ground surface, related to the thickness of the thin oxide layer, which in turn is affected by the maximum temperature at the grinding zone [1, 2]. There are many technique based on different sensors have applied to identify grinding burn [3-5]. Acoustic emission (AE) sensor has a higher sensitivity and responsive speed than power and force sensors. For this reason, AE sensors are becoming very popular in process monitoring. Acoustic emission (AE) sensor is very popular in recent years for identifying grinding burn and temperature in process monitoring. However, most researches use AE signals without distinguishing thermally or mechanically induced AE.

Liu and Chen et al. [6] investigated grinding burn and temperature on CMSX-4 materials using AE signal and a thermocouple. In this research, they separated thermal induced AE signals from other AE signals in grinding for the first time by using a laser irradiation simulation method. The laser irradiation was arranged to produce

high and low temperatures on the materials (Inconel718 and MarM002) with different energy flux and irradiation time. They obtained a critical grinding burn temperature at 770°C for CMSX-4 materials by comparing the AE features from the laser irradiation and AE features from the grinding experiment. Liu and Chen [6] also noticed the AE signals under different temperature are of different features. This provides a new way for grinding burn monitoring.

This paper presents an investigation of grinding behaviour using Thermal AE signal signatures. A model based on neural network designed to detect the high and low temperatures in the grinding zone. The training data set consisted of thermal AE data extracted from laser irradiation applied as input to the network. The testing data set consisted of thermal AE data extracted from grinding experiment for verification.

2. Laser Irradiation Tests

The laser irradiation experimental set-up consists of an AE sensor, thermocouple, USB card, preamplifier, PCI-2 based signal processor and specimen of aerospace material of nickel based alloys. All experiment set up carried out in the Lumonics JK704 Nd: YAG laser machine. An E-type thermocouple, which was located on the centre of the laser beam spot, was tightly fixed on the front surface of the workpiece and an acoustic emission (AE) sensor was placed at the opposite side of the workpiece. This thermocouple of E-type covers a temperature range from -40°C to +900 °C. A schematic diagram of laser irradiation and sensor arrangements illustrated in the Fig 1. Other conditions of laser irradiation experiment are presented in Table 1. Laser pulses focused on a point on the surface can be considered as a point source to generate thermal expansion. The results of temperature measured from thermocouple are presented in Table 2. When acoustic

emission caused by the thermal stress occurs on the workpiece, The AE sensor transferred the AE wave into a voltage signal for further analyses.

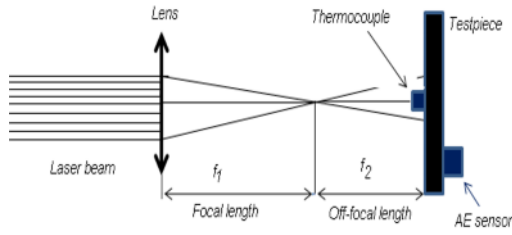


Fig 1. Schematic diagram of laser irradiation optical arrangement

Table 1. Laser specification

Laser	Lumonics:JK704 Nd:YAG
Wave length	1.06 μm
Pulse energy	1.5J
Maximum peak power	2.5kW
Pulse duration	0.06ms
Repetition time	44 Hz
Focal length	120 mm
Beam diameter	12 mm
off-focal length	34~46 mm

Table 2. The calibration temperatures

Laser offset (mm)	Inconel-718 (°C)	MarM-002 (°C)
34	698	492.67
40	324.19	317.79
46	174.33	234.65

A model of surface temperature has been calculated based on the interaction of laser irradiation and workpiece surface thermal energy. If the constant laser energy flux I_0 is absorbed at the workpiece surface and there is no phase change in the material, the heat flow in one dimension then the equation could be written as follows [6, 7],

$$T(0,t) = \frac{2I_0}{K} \eta \left(\frac{kt}{\pi} \right)^{\frac{1}{2}} \quad (1)$$

where, $T(0,t)$ = surface temperature after time t

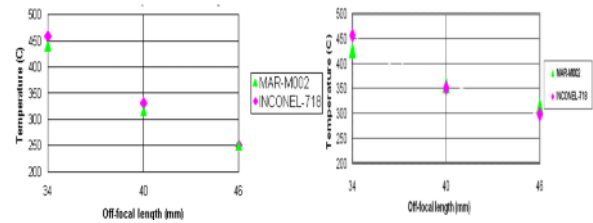
K = thermal conductivity

k = thermal diffusivity

η = absorption coefficient

The absorption coefficient η can be calculated approximately as 19.16 % for Nd: YAG laser for nickel based alloy (MarmM002 and Inconel718). The laser power flux I_0 can be adjusted by the off-focal distance f_2 .

The surface temperatures of calculated and measured values are shown in the Fig 2. The laser energy was on these materials 1.5 J with a pulse width of 0.6 ms. The reasons for slight differences between theory and experiment are the laser focal spot size, thermocouple position and laser penetration into these materials. Thermal conductivity and off-focal distances to these materials (Inconel718 and MarM002) also play an important role to make these differences. The thermal conductivity is the property of a material that does indicate its ability to conduct heat. If the temperature of the materials rises there will be an increase of electron energy exchanges by laser irradiation. The electrons are more likely to interact with the structure of these materials rather than oscillate and re-radiate[7]. These materials (Inconel718 and MarM002) also have different absorption capacity of the radiation because it requires more energy to raise its temperature.



(a) temperature calculated (b) temperature measured

Fig 2. The surface temperature obtained from the experiment.

The STFT (Short Time Fourier Transform) signal processing technique is applied to extract thermal features. The signal features related to high and low temperatures at 34 mm or 46 mm off-focal distances are shown in Fig 3. The signals are sampled at 5 MHz with Kaiser Filter. The result shows in the Fig 3 that AE data extracted from 34 mm offset distances has a higher intensity in the 200-250 kHz frequency range than AE data extracted from 46 mm offset distances in the 150-250 kHz frequency range.

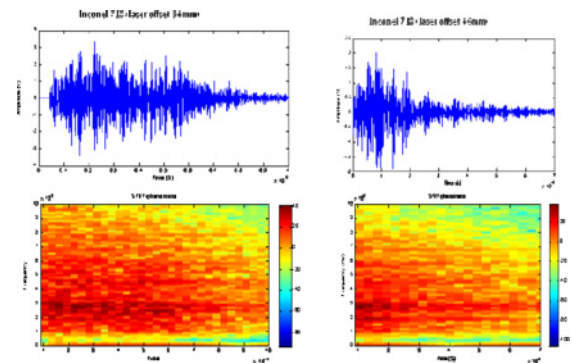


Fig 3. AE signal from laser irradiation, Top: time series data, and down: STFT.

3. Grinding experiments

The grinding experiments were undertaken on a Makino A55 machine centre [8, 9]. The acoustic emission (AE) sensor WD-AL04 placed with the workpiece to detect the AE responses. The main specification of the AE sensor is presented in the Table 3. The grinding was undertaken with a wheel speed of 35 m/s and the depth of cuts at 0.1 mm and 1 mm. The feed rate for the workpiece was 1000 mm/s. No coolant applied. The extracted AE data were used to identify different temperature signatures in relation to grinding burn.

Table 3. AE sensor specification

PAC WD Sensor	
Sensor number/date	AI04(17/11/04)
Construction	Differential
Sensor drive	Up to 100m with
Capability	w/RG-58 AU cable
Dimensions(dia.*ht.)	17*16 mm
Peak sensitivity (dB)	-63.21
Operating frequency range	100-1000 kHz

From each of the experiments, three sets of 1024 AE data points are extracted from start, mid and end sections and applied to FFT for feature recognition. The features acquired from AE data under 1 mm depth of cut represent severe burn on the material due to high temperature while the AE features from data under 0.1 mm depth of cut represent no burn or slight burn due to low temperature. The burn or no burn phenomena shows on the Inconel-718 workpieces relation to AE amplitudes. These results as shown in Fig 4 that AE data extracted from burn sample of 1.0 mm depth of cut has a higher intensity in 200-300 kHz compare to no burn sample of 0.1 mm depth of cut in 150-250 kHz. The energy of AE intensities concentrated at the end of each depth of cut. In the burn sample the burn colours are obviously visible compare to no burn sample shows in the top of the samples.

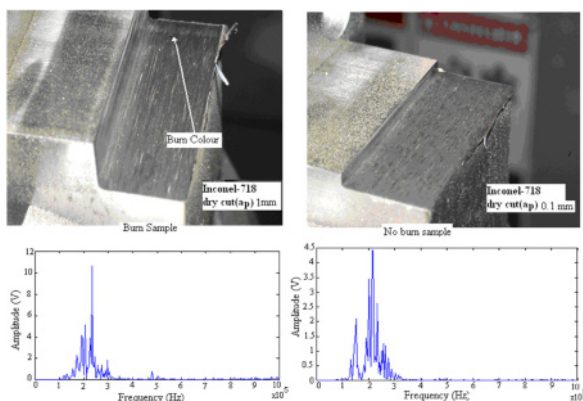


Fig 4. Grinding burn and no burn phenomena which relates to 1.0 mm and 0.1 mm depth of cuts.

Fig 5 shows the grinding with 1 mm depth of cut produces severe burn (20% burn at the end of each grinding pass) while that with 0.1 mm depth of cut produces no burn or slight burn (0-2% burn at the end of each grinding pass). These clear features of burn and no burn phenomena due to high and low temperatures would be a concrete foundation for pattern recognition.

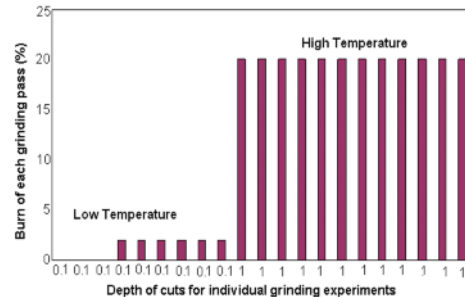


Fig 5. Grinding burn (%) from each grinding pass in relation to 0.1 mm and 1 mm depth of cuts.

4. Pattern recognition: Artificial neural network (ANN) approach

The Neural Network (NN) has been applied since 1960s to identify the state of the machining process and cutting tool. The advantages of neural networks over pattern recognition are that it can easily constitute optimum nonlinear multi-input functions for pattern recognition and that the accuracy of pattern recognition is easily improved by learning[10].

A back propagation neural network has been applied to identify high and low temperatures in relation to grinding burn. During the ANN training process, the STFT AE data were used as inputs and outputs were high and low temperatures. The structural parameters of the ANN are presented in Table 4. Once the network has been defined, network architecture can be created and the network can be trained by optimizing the error function.

Table 4. Construction of the ANN for temperature indication

ANN Parameter	Value
Hidden Layer	2
Input size	STFT:256 Neuron
Transfer function for hidden layer	Tansigmoid
Transfer function for out put layer	Pure Linear
Learning rate	1.00E-11
Momentum	0.95
Algorithm	Backpropagation
Traning	Temperature(high &Low)

The result as shown in Fig 6, the straight line relates by passing through the points of circles where the straight

line defined as the predicted output and points of circles defined as the actual output. The training data set consisted of thermal AE data which extracted from the laser irradiation. The target vector to the network was defined in such a way that the high temperature related to severe burn was assigned a value of 1 and low temperature related to normal condition or no burn condition was assigned a value of -1. After training, the result in the Fig 6 shows the outputs of the network represented each case correctly, where the values concentrated at the values in 1 or -1 respectively.

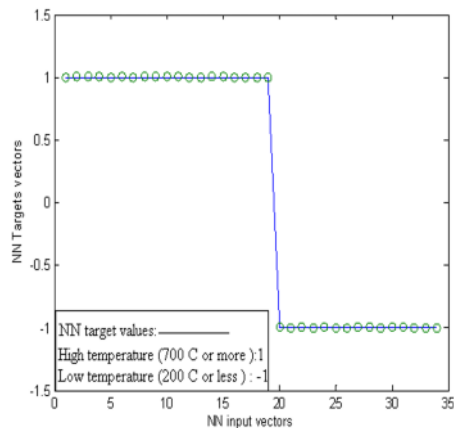


Fig 6. The learnt training set for a NN classification system.

Once the network has been designed and trained by AE data from Laser irradiation tests, it can be tested with AE data extracted from grinding experiment. The testing result should predict the high and low temperatures in the grinding zone. The result shows in the following diagram in the Fig 7, where high temperatures related to severe burn concentrated at the value 1 and low temperature related to no burn concentrated at the value -1. There are a few errors shown in fig 7 and the accuracy using the ANN to judge grinding temperature was about 81% (17/21).

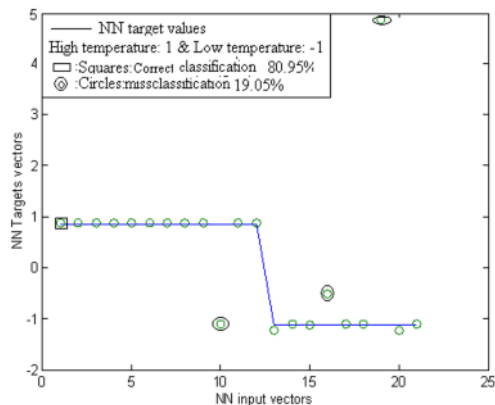


Fig 7. Neural Network verification result of grinding AE data.

5. Conclusion

This paper presented an investigation using AE signal to detect the high and low temperatures in grinding zone in relation to burn and no burn. The materials subjected to grinding are nickel based super alloys which are very sensitive to grinding burn. The laser irradiation induced temperature elevation can be adjusted by off-focal distance to the samples. The surface temperature obtained from laser experiment made a reasonable agreement obtained from theoretical calculation.

An ANN model developed based on thermal AE data extracted from laser irradiation was used to detect grinding temperature using the AE data extracted from grinding experiments. The result of ANN shows a good agreement was achieved with the accuracy around 81%. This affirms that thermal AE signal signature features in laser irradiation can be found in grinding AE signals and can be used for grinding burn monitoring.

References

- [1] Kwak, J.S. and J.B. Song, *Trouble diagnosis of the grinding process by using acoustic emission signals*. International Journal of Machine Tools & Manufacture, 2001. 41(6): p. 899-913.
- [2] Kwak, J.S. and M.K. Ha, *Neural network approach for diagnosis of grinding operation by acoustic emission and power signals*. Journal of Materials Processing Technology, 2004. 147(1): p. 65-71.
- [3] Tonshoff, H.K., T. Friemuth, and J.C. Becker, *Process monitoring in grinding*. Cirp Annals-Manufacturing Technology, 2002. 51(2): p. 551-571.
- [4] Wang, Z., et al., *Neural network detection of grinding burn from acoustic emission*. International Journal of Machine Tools & Manufacture, 2001. 41(2): p. 283-309.
- [5] Malkin, S., *Grinding Technology Theory and Application of Machining with Abrasives* 1989, Dearborn, Michigan: Society of Manufacturing Engineers.
- [6] Liu, Q., X. Chen, and N. Gindy, *Investigation of acoustic emission signals under a simulative environment of grinding burn*. International Journal of Machine Tools & Manufacture, 2006. 46(3-4): p. 284-292.
- [7] Steen, W.M., *Laser Material processing*, ed. T. edition. 2003: Springer.
- [8] Griffin, J., *Pattern recognition of micro and macro grinding phenomenon with a generic strategy to machine process monitoring*, in *Department of mechanical, materials and manufacturing*. 2008, The University of Nottingham: Nottingham.
- [9] Liu, Q., *Pattern Recognition of Grinding Defects and Assessment Strategies of Grinding*, in *Department of Mechanical, Materials, and Manufacturing Engineering*. 2005, The University of Nottingham: Nottingham.
- [10] H.K. Tonshoff, I.I., *Sensors in Manufacturing*. 1.

Investigation of Influences of Wheel Speed on Root Geometrical Dimension of Gas Turbine Blade

A. R. Fazeli Nahrekhalaji¹, M. Sohrabi², S. M. Izadi³

¹ Manufacture Engineer, Mapna Group (Mavadkaran Engineering Co.), Tehran, Iran. (fazeli@Mavadkaran.com)

² Machining Manager, Mapna Group (Mavadkaran Engineering Co.), Tehran, Iran (sohrabi@Mavadkaran.com).

³ Shop Manager, Mapna Group (Mavadkaran Engineering Co.), Tehran, Iran. (moin_izadi@Mavadkaran.com)

Abstract. Creep feed grinding is a recently invented process of material processing. It combines high quality of the workpiece surface, good productivity, and the possibility of automatic control. In this paper, an investigation of the influences of Wheel Speed on the root geometrical dimension for fabricating gas turbine blades using the design of experiments (DOE) are reported. Experimental data is analyzed by analysis of variance and an empirical model. It is found that, increasing the wheel speed causes suitable dimensional changes for the root geometrical dimension with good tolerances.

Keywords: Creep feed grinding, Geometrical dimension, Analysis of variance, Regression, Interactive effect.

1. Introduction

Creep feed grinding is widely used in manufacturing super alloy materials. These materials are usually used in gas turbines, petrochemical equipment and other high temperature applications. Using this approach, higher material removal rates can be achieved by selection of higher depths of cut and lower workpiece speeds. The correct selection of the cutting conditions and the wheel specifications can provide a greater material removal rate and a finer surface quality. One of the most important applications of creep-feed grinding is the production of the aerospace parts used in jet engines such as turbine vanes, and blades where parts should have high strength to the fatigue loads and creep strains (Fig.1). Using creep-feed grinding, higher material removal rates can be achieved by selection of higher depths of cut and lower workpiece speed. The correct selection of the cutting conditions and the wheel specifications can provide a greater material removal rate and a finer surface quality.

The aerospace parts used in jet engines, such as turbine vanes, are typically made from nickel-based super-alloys such as Inconel, Udimet, Rene, Waspaloy, and Hastelloy. They provide higher strength to weight ratio, and maintain high resistance to corrosion,

mechanical thermal fatigue, and mechanical and thermal shocks [1].

S.-B. Wange et al. [2] provided a thermal model that focused on the heat transfer to the cutting fluid, the workpiece and wheel grain for creep feed grinding. In their model, the conduction effect in the moving direction of the workpiece was considered and found to be very significant. Moreover, the thermal partition ratios to the workpiece, fluid and grain were well defined and discussed. The results revealed that the cooling effect of the fluid is crucial especially at larger grinding depths.

Lavine et al. [3] presented a conical grain model, with grain slope set to one. Lavine and Jen [4] derived a separate thermal model including the fluid, wheel and workpiece to predict the occurrence of boiling.

Wange et al. [5] showed that the grinding energy when the fluid begins to cause boiling is defined as the critical grinding energy for the workpiece burning. The results showed that workpiece burning can be predicted or evaluated and so cutting conditions can be selected to avoid those conditions where burning could occur.

Shafto et al. [6] proposed that workpiece burning could be explained by the phenomenon of fluid film boiling.

Ohishi and Furukawa [7] derived a relationship between the grinding heat flux and grinding zone temperature at burning using the fraction of the grinding energy entering into the workpiece at 10%.

Wange et al. [8] modelled the grinding force of creep feed grinding using the improved back propagation neural (BPN) network with a view to avoiding the workpiece burning. The results showed that the grinding energy can be accurately predicted by the application of a grinding force model and that larger sizes of wheel, when available, give a better working efficiency.

1.1 Gas turbine blades

Fig. 2 shows a gas turbine blade. Fig .3 illustrates the important dimension in root of gas turbine blade. Pin gauge (P), valley (V), lobe (L) and traverse (T) are important geometrical dimension in root of gas turbine blade that have high effect in correct assembly of blade onto disk of turbine. If this important dimension is not controlled correctly and if higher than its tolerance, the blade can't assembled onto the disk of turbine.

In this research, the influences of major process parameters of the creep feed grinding process and their interactions such as wheel speed, workpiece speed, grinding depth and dresser speed on the traverse of gas turbine blade have been investigated using the design of experiments (DOE) approach. It is desirable to know the effects of the major parameters and interactive influences among the process parameters on traverse and the relationships between traverse and process parameters to obtain the best conditions for optimum production.

The DOE is a statistical method which is used to find the significance of interactive effects among variables and relations among process parameters using variance analysis. Finally, using this model and suitable geometrical dimension dimension, suitable input parameters has been determined for optimum production.

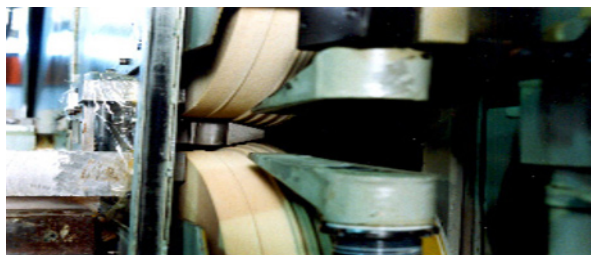


Fig. 1. Creep-feed grinding of gas turbine blade

2. Description of Material

Inconel 738 LC super alloy was chosen as the experimental material. Its chemical composition in terms of all its alloy elements is presented in Table 1; the remainder of its content is nickel.



Fig. 2. Gas turbine blade

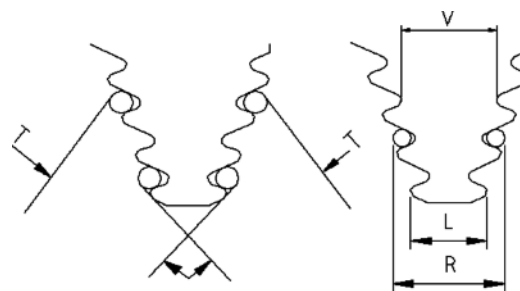


Fig. 3. Geometrical dimensions

Table 1. The chemical compositions of Inconel 738 LC super-alloy

Element	Min	Max	Element	Min	Max
	Percentage			Percentage	
C	0.09	0.13	Nb	0.6	1.1
Cr	15.7	16.3	Ta	1.5	2
Co	8	9	W	2.4	2.8
Al	3.2	3.7	Fe	-	0.3
Ti	3.2	3.7	Si	-	0.05
(Al+Ti)	6.5	7.2	Mn	-	0.05
B	0.007	0.009	S	-	0.003
Zr	0.03	0.06			
Mo	1.5	2			

3. Experimental Modeling

3.1 The measurement of output parameters

Output parameters and traverse dimensions were measured in terms of mm with an inside micrometer 0-25, 0.01 mm precision.

3.2 The input parameters and experiment conditions

Values were specified for the following input parameters: the creep feed grinding wheel speed, workpiece speed, grinding depth, and dresser speed.

The grinding wheel type was Strato / Tyrolit (F13A70FF1) and the coolant fluid type was Cutzol zt 130 (oil Canada).

3.3 The experimental design

It is difficult and expensive to perform many experiments. The DOE method can be employed as an efficient technique to enable the suitable and necessary experiments to be selected with high accuracy. To investigate the main and multiple interactions between parameters, a fractional-factorial design was employed with two levels for each parameter (+,-), and a quadrant fraction with resolution (IV) [9]. Since there are several steps of grinding to accomplish the grinding of root, the grinding steps were divided to three sections (P1, P2, and P3) and in each section, a constant grinding depth was used.

Table 2 shows the input parameter values of the experiments. The procedure included 16 experiments. The absolute value of the difference between the measured dimensions and nominal dimension of traverse was used in the statistical analysis. Therefore using design of experiments and ANOVA analysis, according to the input parameters, this absolute value is minimized.

Table 2. The parameter levels

Parameters	Low Level	High Level
wheel speed (m/s) V	17	25
workpiece speed (mm/min) f	100	180
dresser speed (μm/rev) E	0.05	0.15
grinding depth (mm) P1	0.6	0.9
grinding depth (mm) P2	0.3	0.6
grinding depth (mm) P3	0.04	0.08

4. Analysis of the Experimental Results

Once the experimental results were obtained, the coefficients and analysis of variance (ANOVA) were calculated with MINI TAB software to determine the significance of the parameters, and the P-Values were used to determine which parameter was most significant.

The risk level of less than 0.1 (P-Value) for the parameters in Table 3 shows that the related parameter is significant.

Table 3. The variance analysis (ANOVA) for the traverse

Parameters	Dof	Adj SS	Adj MS	Fo	P
Main Effects	6	0.001	0.0	2.90	0.20
2-Way Interactions	4	0.0016	0.0	5.64	0.09
3-Way Interactions	2	0.0018	0.01	12.5	
Residual Error	3	0.0	0.0		
Total	15				
		R-Sq = %95.59		R-Sq(adj) = %77.95	

Finally, a hierarchical model was developed for the traverse dimension by a multiple linear regression technique. The insignificant terms were removed from the model and the final models were developed with significant terms which were determined by ANOVA equations (1) to (4) for geometrical dimension.

$$T = -0.650 + 0.931 (P1) + 1.270 (P2) + 0.237 (P3) + 0.003 (f) + 0.095 (E) + 0.008 (V) - 0.015 (P1 \times V) - 0.008 (P2 \times f) + 0.01 (P1 \times P2 \times f) + 0.008 (P1 \times P2 \times V) - 0.004 (P1 \times f) \quad (1)$$

$$P = -0.3 + 0.683 (P1) - 0.067 (P2) + P3 - 0.001 (f) + 0.74 (E) + 0.012 (V) - 0.222 (P1 \times P2) - 1.166 (P1 \times P3) + 0.001 (P1 \times f) - 1.366 (P1 \times E) - 0.028 (P1 \times V) \quad (2)$$

$$V = -1.18 + 2.064 (P1) + 0.208 (P2) + 0.093 (P3) - 0.006 (f) + 3.875 (E) + 0.065 (V) - 0.507 (P1 \times P2) + 0.009 (P1 \times f) + 0.009 (P1 \times P2 \times V) - 0.109 (P1 \times V) - 6.75 (P1 \times E) \quad (3)$$

$$\ln(L1) = 29.313 - 37.745 (P1) - 38 (P2) - 12.013 (P3) - 0.149 (f) - 28.379 (E) - 0.654 (V) + 39.809 (P1 \times P2) + 0.15 (P1 \times f) - 0.365 (P1 \times P2 \times f) + 0.890 (P1 \times V) + 28.808 (P1 \times E) + 0.349 (P2 \times f) \quad (4)$$

5. Discussion

Fig. 4 summarizes the workpiece speed on the geometrical dimensions at grinding depth (first section). The results show that increase of wheel speed combined with the increase of grinding depth (first section), produces geometrical dimensions with good tolerances.

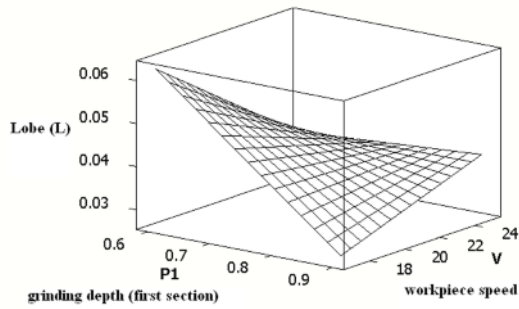


Fig. 4-a. Effect of the workpiece speed on the lobe dimension at grinding depth (first section)

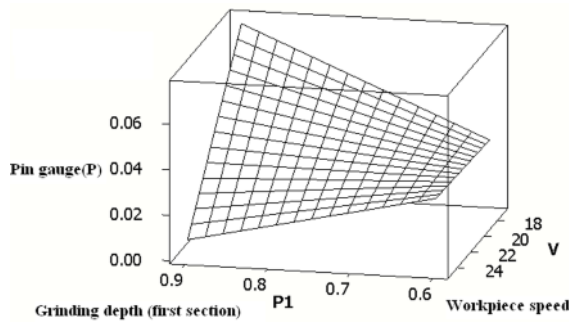


Fig. 4-b. Effect of the workpiece speed on the pin gauge dimension at grinding depth (first section)

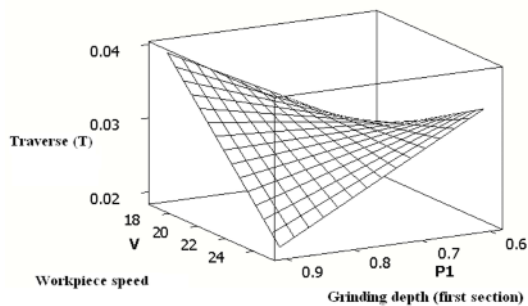


Fig. 4-c. Effect of the workpiece speed on the traverse dimension at grinding depth (first section)

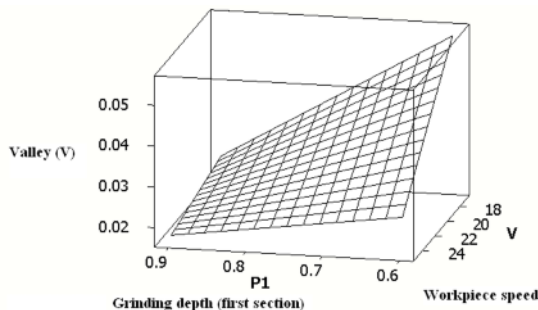


Fig. 4-d. Effect of the workpiece speed on the valley dimension at grinding depth (first section)

6. Conclusion

In this paper, the influences of Wheel Speed on the root geometrical dimensions for fabricating gas turbine blades using the design of experiments (DOE) have been reported. Experimental data is analyzed by analysis of variance and an empirical model. It is found that, increasing the wheel speed causes suitable dimensional changes for the root geometrical dimensions and achieves good tolerance.

Finally, with regards to the large number of effective parameters in the creep feed grinding process, consideration of the creep feed grinding process through the design of experiments is shown to be the efficient method for achieving acceptable results.

References

- [1] Abbas Vafaeseefat (2009) Optimum Creep Feed Grinding Process Conditions for Rene 80 Supper Alloy Using Neural Network. *Int J Precision Engineering and Manufacturing*, Vol. 10, No. 3, pp. 5-11.
- [2] Shih-Bin Wang · Hong-Sen Kou (2004) Selections of working conditions for creep feed grinding. Part (I)—thermal partition ratios. *Int J Adv Manuf Technol.* 23: 700–706.
- [3] Lavine S, Malkin S, Jen TC (1989) Thermal aspects of grinding with CBN wheels. *Annals CIRP* 38(1):557–560
- [4] Lavine S, Jen TC (1991) Coupled heat transfer to workpiece, wheel, and fluid in grinding, and the occurrence of workpiece burn. *Int J Heat Mass Transfer* 34(45):983–992.
- [5] Shih-Bin Wang · Hong-Sen Kou (2006) Selections of working conditions for creep feed grinding. Part (II): workpiece temperature and critical grinding energy for burning. *Int J Adv Manuf Technol.* 28: 38–44
- [6] Shafto GR, Howes TD, Andrew C (1975) Thermal aspects of creep feed grinding. 16th Machine Tool Design Research Conference, Manchester, England, pp 31–37.
- [7] Ohishi S, Furukawa Y (1985) Analysis of workpiece temperature and grinding burn in creep feed grinding. *Bull JSME* 28(242):1775–1781
- [8] Shih-Bin Wang · Hong-Sen Kou (2006) Selections of working conditions for creep feed grinding. Part (III): avoidance of the workpiece burning by using improved BP neural Network. *Int J Adv Manuf Technol.* 28: 31–37
- [9] C. Montgomery, design of experimental & statistical modeling, McGraw Hill, Inc, 22NewYORK, 2005.

Ultra-fine Finishing of Metallic surfaces with Ice Bonded Abrasive Polishing Process

R. Mohan¹ and N. Ramesh Babu²

^{1,2} Department of Mechanical Engineering, Indian Institute of Technology Madras, Chennai, India – 600036.

Abstract. In this paper, a novel ice bonded abrasive polishing process proposed for producing ultrafine surfaces on metallic surfaces is presented. Ice bonded abrasive polishing setup was developed for conducting the experiments under cryogenic conditions. The novelty of the process lies in the method of preparing a cryogenic polishing tool by freezing a mixture of distilled water and ultrafine abrasive particles with suitable cryogenic fluids. Characterization of the tool, by mass balance method, ensured uniform distribution of abrasives throughout the ice matrix. Experiments were conducted on 304L stainless steel in order to examine the improvements in surface finish on work surfaces. Experimental studies have revealed the generation of ultrafine surfaces, yielding roughness values in nanometric range, with the adhesive action of ice and the abrasive action of material by fine abrasive particles.

Keywords: Polishing, Ice Bond, Surface Finish

1. Introduction

Ultrafine surface generation processes have recently been the focus of attention due to requirements for mirror-like surfaces on components used in semiconductor, optical and micro-electro-mechanical systems. Realization of mirror-like finishes on surfaces is possible by using conventional polishing as well as unconventional polishing processes. Unconventional polishing processes make use of chemical dissolution, fluid, optical energies and a combination thereof for surface generation. These processes are capable of producing ultra-fine surfaces with close tolerances and minimal damage to polished surfaces. Hence they are preferred for high precision polishing application even though they exhibit poor material removal rate. On the other hand, conventional mechanical based, fixed abrasive polishing processes are energy efficient in producing fine surfaces but often necessitate dressing to maintain performance of the tool or polishing wheel.

In order to meet ultrafine finishing requirements, efforts have been directed to developing energy efficient fixed abrasive polishing processes that could eliminate the need for dressing the tool. This led to the

development of polishing tools capable of self dressing / replenishing during polishing with the fluids undergoing phase changes. Initially, an approach was proposed to use a frozen mixture of water and abrasives as self dressing polishing tool for polishing of glass and crystals [1]. Experiments conducted on silicon wafers with this kind of polishing tool i.e., frozen colloidal silica, proved the possibility of generating smooth surfaces with the finish of about 7 nm [2]. An attempt was made to use a colloidal Silica tool to conduct experiments on silicon wafers and zerodur glass. The finish on the surface was less than nanometer dimension after cryogenic polishing. The temperature in the polishing was maintained at minus 40 degree Celsius by means of dry ice to ensure the rigidity of the tool [3]. Alternatively, the experiments were conducted on metallic materials (LY12 and YG6 alloys) using frozen water i.e., ice alone as a polishing tool. Though the polishing process took place for longer duration, the experimental observation showed considerable decrease in surface roughness values [4]. Recently, an ice bonded abrasive polishing (IBAP) setup was developed to conduct experiments on a few metallic samples such as copper, aluminium and mild steel. The results showed an improvement in surface finish with the possibility of nano level finish on metallic surfaces [5]. From the above discussion, it is clear that the studies on frozen fluid polishing process of metallic as well as non-metallic materials are limited and deserve some attention to understand the process much better. Thus the present work is designed to understand the ice bonded abrasive polishing process.

In this paper, a novel ice bonded abrasive polishing process proposed for producing ultrafine surfaces on metallic materials is presented. It describes the polishing setup developed for conducting the experiments under cryogenic conditions and the method of characterizing the polishing tool. Experiments were conducted on 304L stainless steel samples to understand the effect of polishing load and rotational speed of the tool on the finish achievable with this process.

2. Development of Experimental Setup

An ice bonded abrasive polishing setup was designed and developed with an aim of in-situ tool preparation and to provide suitable kinematics between the tool and work surface. The schematic diagram of IBAP setup is shown in the Figure 1.

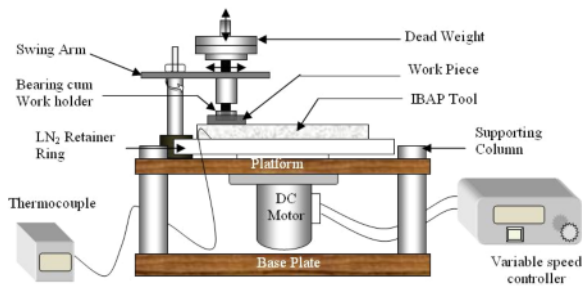


Fig. 1. Schematic illustration of IBAP setup

The setup consists of base plate, supporting columns, platform, permanent magnet DC motor with step-less variable speed controller and dead weight mechanism to apply the load onto the work during polishing of specimens. The base plate and platform are firmly attached to the supporting columns. A permanent magnet DC motor is fastened to the bottom of the platform and its speed is controlled by means of a variable speed controller. The rotational speed of tool can be varied from 60 to 600 rpm. An ice mould of 200 mm diameter with the liquid nitrogen retainer ring is directly coupled with motor shaft and is supported by an axial and thrust bearing in order to ensure enough rigidity and smooth running of the tool.



Fig. 2. Experimental setup

The dead weight loading mechanism meant for applying the normal pressure on the work surface consists of a pivot joint, swing arm, sliding bearing, vertical rod and dead weights. The pivot joint is used to rotate the swing arm in order to position the workpiece eccentrically from the centre of the ice mould. The sliding bearing is fitted at the end of the swing arm. A polished cylindrical rod assembled with a 14 mm ball bearing supports the workpiece against the tool. The polishing pressure is applied over workpiece by adding dead weights with a suitable fixture. Relative motion between the tool and the

workpiece is maintained by means of dynamic friction at the contact zone. The operating temperature of the tool is maintained by pouring liquid nitrogen into the retainer ring and monitoring the temperature by thermocouple. The complete experimental setup along with the controller is shown in Figure 1.2.

3. Preparation and Characterization of Ice Bonded Abrasive Polishing Tool

The first step in IBAP process is the preparation of cryogenic polishing tool by freezing the mixture of distilled water and ultrafine abrasive particles with suitable cryogenic fluids.

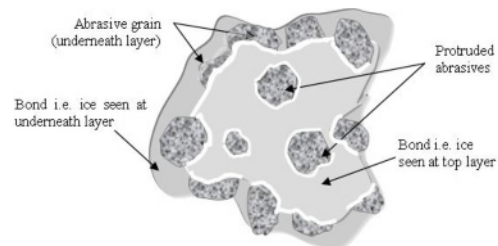


Fig. 3. Schematic representation of structure of the IBAP tool

Figure 3 shows a typical structure of an IBAP tool wherein the spatial arrangement of abrasives within the ice matrix is in a random state. There are certain issues, like uneven distribution, accumulation and partial separation of abrasives in the matrix material, which may arise while forming the tool. Therefore it is essential to know the distribution of abrasives in the ice matrix for the purpose of assessing the tool for ultrafine finishing applications.

3.1 Preparation of Ice Bonded Abrasive Polishing Tool

The fumed silica particles of 4 nm diameter dispersed in distilled water were thoroughly mixed by a magnetic stirrer to form the polishing slurry. The slurry is poured into the ice mould which is surrounded by liquid nitrogen whose temperature is around -196°C. After 1-2 minutes, the frozen mixture of abrasives and water is formed within the setup and is as shown in Figure 4.

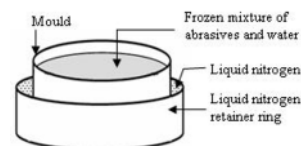


Fig. 4. Frozen mixture of abrasives and water

3.2 Tool Characterization

This section describes the evaluation of the abrasive particle distribution in the ice matrix and the method adopted for preparing the tool surface for performing actual polishing.

3.2.1 Evaluation of abrasive distribution

A cylindrical mould of 75 mm diameter and 125 mm height is filled with a mixture of 2% SiO₂ by weight in distilled water. It is then immersed into a liquid nitrogen bath for 2-3 minutes. After taking the mould out of the liquid nitrogen bath, the mould is heated slowly to separate the tool from the mould.

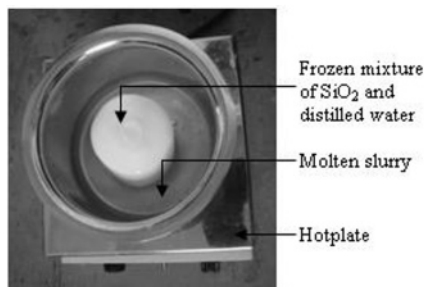


Fig. 5. Frozen mixture of water and SiO₂ melting on a hotplate

Figure 5 shows the frozen mixture of silica with distilled water melted on a hotplate and collected in a container. The molten mixture is poured into a 50 ml burette and the mass measurements are made with a high precision electronic balance having a least count of 0.01gm. The theoretical weight of 50 ml slurry is calculated by assuming the density of fumed silica as 2200 kg/m³. The theoretical and actual mass of slurry obtained at 2% abrasive concentration are listed in Table 1.

Table 1. Comparison of mass of slurry before freezing and after melting of frozen tool

Weight of 50 ml slurry (gram)			Error in %	
Theoretical	Before Freezing	After Melting	Before Freezing	After Melting
50.55	49.57	49.71	1.94	1.66
50.55	49.49	49.73	2.10	1.62
50.55	49.90	49.66	1.29	1.76
50.55	49.64	49.68	1.88	1.72

From the Table 1, it can be noticed that the deviations in the mass of slurry before freezing and after melting are nearly identical and are comparable with theoretically estimated values. The observed deviations are about 1-2 percent thus indicating the uniform distribution of abrasive particles in the ice matrix. Since large temperature gradient exists between the liquid nitrogen and the polishing slurry, the abrasive particles in the

slurry will freeze without any change in their spatial location. The observed deviations are mainly attributed to the loss of mass caused by abrasive particles sticking to walls of the mixing chamber and burette and the errors associated with measurement of 50 ml slurry in the burette. As the deviations are very small compared with the mass of abrasives present in the tool, they might not have a significant effect on polished surfaces. Therefore the IBAP tool can effectively be used for high precision polishing applications.

3.2.2 Dressing

The top surface of the tool will have certain irregularities due to inconsistent solidification of the water-abrasive mixture in the mould. As it could not provide a flat surface for polishing of work surface, the top layer of the tool was dressed to make it smooth and flat. This is done by melting the upper layers of tool with a warm flat plate pressed against the tool surface. In this manner, the frozen mixture of water and abrasives was made ready for scratch free polishing of materials.

4. Methodology

This section describes the method of preparation of the surface before polishing and the choice of process parameters chosen for this study.

4.1 Workpiece preparation

A thick disc shaped, 304L stainless steel (SS) workpiece with 25 mm diameter and 15 mm thick, was chosen for the ice bonded abrasive polishing studies. The work surface was machined on a high precision CNC lathe and ground with a surface grinding machine. Then it was rough ground with SiC 220 mesh size emery sheet in a Struers polishing machine until grinding marks had disappeared from the surface. Fine grinding was carried out with 9 micrometer diamond abrasives on a composite pad. Eventually, the initial surface for ice bonded abrasive polishing was prepared with 3 micrometer diamond abrasives using a polishing pad.

4.2 Selection of process parameters

The polishing tool, prepared by freezing the mixture of distilled water mixed with 4 nm Silica having concentration of 2% by weight, was used for polishing 304L SS samples. The specimens were polished for a period of 15 minutes with the rotational speed of the tool varied in the range of 100, 200 & 300 rpm and a polishing load of 1, 2.5 & 5 psi. The tool was dressed before the start of each experiment. The specimen was positioned over the polishing wheel before commencing the polishing of samples.

In this work, the finish on the work surface before and after polishing was measured by an optical surface

profiler. It is a non-contact, high resolution 3D surface measuring instrument that can measure the roughness in the range of submicron to a few micrometers.

5. Results and Discussion

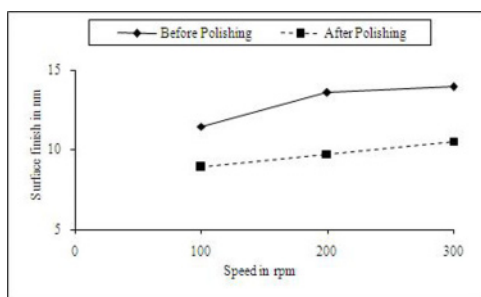


Fig. 6. Effect of rotational speed of the tool on surface finish

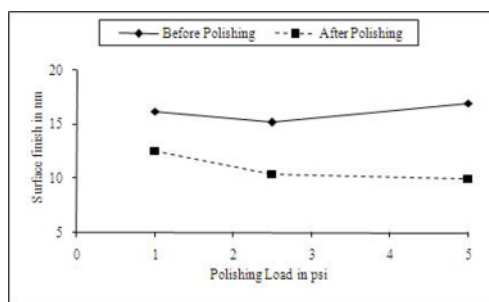


Fig. 7. Effect of rotational speed of the tool on surface finish

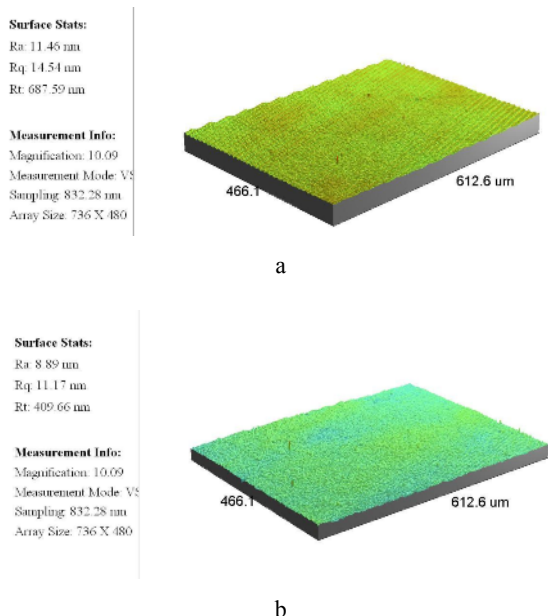


Fig. 8. Surface topography of 304L stainless steel samples a. before polishing; b. after ice bonded abrasive polishing

Figure 6 and 7 show the effect on the surface finish of the rotational speed of the tool and polishing load. The surface roughness of all the samples decreases substantially after 15 minutes polishing. The percentage of improvement in surface finish improves steadily with increase in polishing load whereas it decreases with increase in rotational speed of the tool.

Figure 8 shows a typical surface topography observed on a 304L SS sample before and after IBAP. The final surface finish has reached value of 8 nm from 11 nm due to removal of certain micro peaks on it. Further it can be observed that this process did not induce any scratches on the base material due to soft action of silica particles along with bonding materials i.e., ice.

6. Conclusion

An ice bonded abrasive polishing setup has been developed to perform polishing experiments especially under cryogenic conditions, on stainless steel specimens. The method of preparing the ice bonded abrasive polishing tool has been discussed. The suitability of this kind of tool for ultrafine surface generation applications is ensured by tool characterization. Results of nano level experiments on stainless steel have indicated that this fixed abrasive polishing process has the ability to generate ultrafine surfaces by bringing out new abrasive grits into action from time to time by way of the ice in the tool melting.

Acknowledgement

The authors acknowledge the financial support for this research work provided by the Aeronautical Research and Development Board, Government of India.

References

- [1] Belyshkin D V, (1966) Using ice for polishing glass and crystals, glass and ceramics, 23(10):523-525
- [2] Ohmori H, Moriyasu S, Jeong H, (2000) Ice bonded wheel and its mirror surface grinding, Journal of Japan Society for Abrasive Technology, 44(12):534-537
- [3] Zhang F, Han R, Liu Y, Pei S, (2001) Cryogenic polishing method of optical materials, Proceedings of ICoPE:396-400
- [4] Ding Yuan, Zhang Ming, (2005) Nano machining experiment of metal materials polishing with ice desk, Proceeding of High density microsystem design and packaging and component failure analysis:1-6.
- [5] Mohan R, Ramesh Babu N, (2009) A feasibility study on ice bonded abrasive polishing of metallic materials, Proceedings of copen-6:B18-B23.

Plane surface grinding with application of Minimum Quantity Lubrication (MQL)

L.M. Barczak and A.D.L. Batako

General Engineering Research Institute, Liverpool John Moores University, Byrom Street, Liverpool, L3 3AF

Abstract. Industry is continuously seeking to improve technologies in order to produce items of the highest standards of durability and quality whilst at the lowest possible cost. Moreover, climate change issues have led to a greater focus on greener manufacturing methods. This has posed a challenge to researchers as they try to invent new technologies or further develop existing ones. The Minimum Quantity Lubrication delivery method is one such technology. As the abrasive material removal process is extremely demanding in terms of thermal stability it consumes large amounts of coolants. There have been many attempts to reduce the amounts of fluids used. The MQL fluid delivery technique reduces fluid usage significantly from litres per minute to millilitres per hour. Whilst some researchers have tried to implement the MQL technique in the grinding process, there is still research to be done to fully understand MQL in the grinding process. This study has aimed to improve this understanding through comparative study and the collecting of data for grinding forces (and as a result their ratio), surface roughness and grinding arc temperatures. Three delivery methods were employed - conventional flood cooling, dry grinding and MQL delivery system. Taguchi method was used in respect to the comparison of the effects of the three delivery methods. MQL was found to perform in a very similar manner to conventional delivery, in terms of specific material removal rate and forces. In some specific conditions MQL achieved better results. Furthermore, good results for surface roughness and grinding temperature were obtained in an attempt to create an applicable regime table for MQL in grinding.

Keywords: minimum quantity lubrication, MQL, near dry machining, grinding, forces, forces ratio, temperature.

1. Introduction

In grinding, a key objective is to maximise material removal whilst minimising wear of the abrasive. Heat generated during material removal may influence workpiece durability and fatigue strength, leading to deterioration in the workpiece quality. Therefore, a lubricant or coolant is often used to achieve reduced friction, lowered local temperatures and improved quality of the surface [1-4].

However fluids usage represents a significant part of manufacturing costs. It has been found [5-6] that coolant

costs may be responsible for as much as 17 per cent of a total part manufacturing cost, whereas depreciation and waste disposal contributes for around 54 per cent of cooling costs. Furthermore, those fluids may have a detrimental effect on worker health as well as on the natural environment.

Therefore large potential savings can be made for both – the economy and the environment if the amount of fluids used in grinding could be reduced. This has posed a challenge to researchers as they try to invent new technologies or further develop existing ones. Such a technology, almost nonexistent in grinding but well known in machining, is represented by Minimum Quantity Lubrication (MQL).

In MQL a mixture of pressurised air and lubricant is delivered directly to a machining zone. This fluid delivery technique reduces fluid usage significantly from litres per minute to millilitres per hour [7-9]. Although relatively extensive research [7-11] has been undertaken concerning MQL applied to milling, turning and drilling, MQL in grinding remains little understood. The small number of research publications [7, 11-15] on the subject suggest that there is an applicable regime for MQL in grinding and some tentative explanations are presented.

Results for MQL in grinding look promising. For instance Wojcik and Kruszynski [14] reported very low compressive stresses (high negative values) compared to conventional fluid delivery. Similar conclusions are coming from Silva et al studies [12, 13]. Moreover Silva et al stated wheel wear was reduced under MQL. Tawakoli et al [15] conclusions were that surface finish and quality of hardened steel are better when MQL technique is applied. Also, in MQL grinding the tangential forces are greatly reduced in comparison to fluid cooling. Therefore, further research is highly desirable and the aim of this study was to investigate new areas, previously never explored.

2. Experiment

The purpose of this research was to study grinding performance under MQL and improve the understanding of Minimum Quantity Lubrication phenomena. The objectives of the project were: a comparison of MQL delivery conditions with conventional delivery and dry; measuring temperatures and evaluating them with existing thermal model; recognition of an applicable regime for MQL; identification of potential restrictions for MQL; analysis results in terms of the real depth of cut (RDOC).

Using the data acquisition system and other available measuring tools, a measurement of the following parameters was undertaken: forces – normal and tangential, instantaneous power usage, temperature and surface roughness under following conditions:

1. v_s – wheel speed – 25 and 45 m/s,
2. v_w – worktable speed – 6.5 and 15 m/min,
3. a – applied depth of cut – 5 and 15 μm ,
4. Material type – workpieces made of three materials: EN8 32 \pm 2HRC, EN31 62 \pm 2HRC and M252 \pm 2HRC,
5. Wheel type – universal aluminium oxide WA 100 JV grinding wheel,
6. Dressing – with multi-cluster diamond,
7. Cut type – down grinding,
8. Fluid delivery – conventional fluid delivery, dry machining and MQL.

The real depth of cut was obtained during a separate procedure, using workpieces ground under the same experimental conditions.

An Omega CO2-T thermocouple was adapted to a single pole arrangement to measure contact temperature.

The study was performed on a Dominator 624 Easy, a CNC surface grinding machine. For the purpose of MQL delivery (at 33ml/h rate), Lubrimat L50 by Steidle was used with a purpose designed nozzle.

Taguchi method was used for the experimental design resulting in creation L_8 (2^7) orthogonal array.

The experimental work was performed in three stages: 1) conventional flood delivery grinding (WET), 2) dry grinding (DRY) and 3) minimum quantity lubrication grinding (MQL). Each stage consisted of grinding three materials (EN8, EN31, M2) with all possible combinations of parameters according to the Taguchi's array.

The trials were repeated three times. The results presented here are a mean value of the three measurements.

3. Results

During the study the actual depth of cut was mainly dependent on the material but also on speeds and more importantly cooling type, i.e. WET, DRY or MQL. In the

case of the 15 μm programmed depth of cut, the achieved depth varied between 3 μm to 13 μm .

The actual depth of cut is represented by specific material removal rate Q'_w .

Only two out of twelve (two of three materials, two of eight process conditions) results are presented and discussed as representative for the study.

3.1. Specific tangential force

Due to the high speed of the wheel the tangential force in grinding is mainly responsible for power dissipation. Tangential force obtained during the study was recalculated to a specific tangential force (where F_t - tangential force, b - workpiece/contact width):

$$F_t' = \frac{F_t}{b} \quad (1)$$

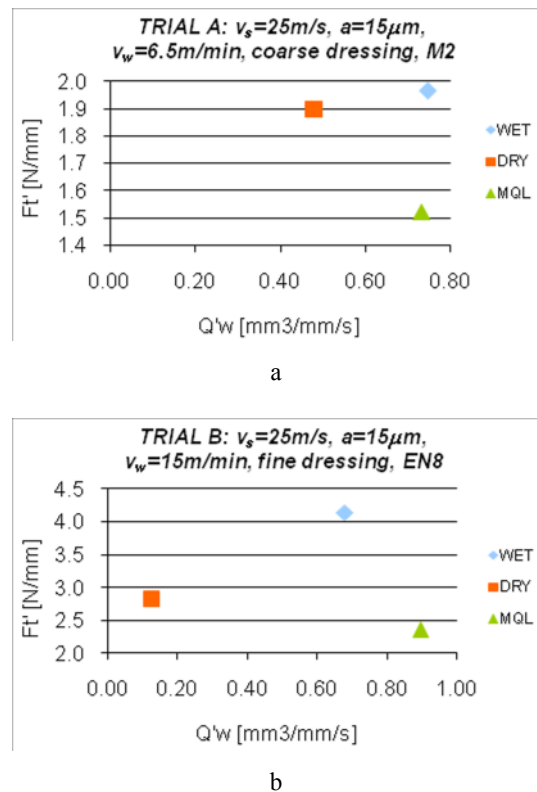


Fig. 1. Specific tangential force as a function of specific material removal rate.

In Trial A (Fig. 1a) a hardened tool steel workpiece (M2) was ground. WET and MQL returned similar RDOC and therefore Q'_w . However MQL produced lower F_t' compared to WET. This indicates the potential for MQL to compete with WET under this combination of material, wheel and workpiece speed. The high F_t' in case of DRY is attributed to the lack of lubrication.

In Trial B (Fig. 1b) mild steel was ground and rather low RDOC values were obtained in all cases. However, MQL Q'_w results were kept on a reasonably high level when compared with WET. Also, in the MQL case a low F_t' can be observed. Such a good MQL performance in terms of cutting and energy efficiency may be a result of the combined effects of workpiece material hardness, which was relatively low in this trial, and good lubrication properties of the MQL oil.

A low F_t' in the case of DRY is due to a very low RDOC obtained during the tests and leads to the conclusion that the DRY process was rather ineffective.

3.2. Force Ratio - Tangential/Normal

In Trial A, Fig. 2a the lowest value of force ratio is observed for MQL. This is indicative of a situation of good lubrication, relatively high specific material removal and reasonable penetration depth.

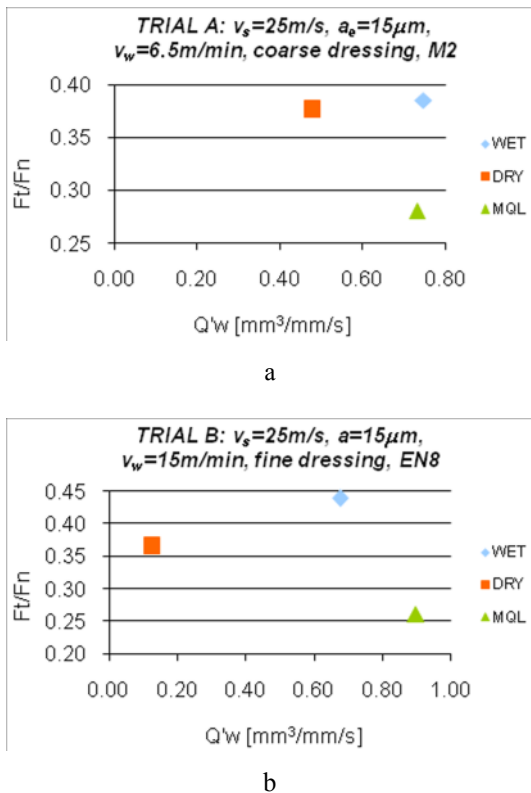


Fig. 2. Force ratio as a function of specific material removal rate.

In Trial B, see Fig. 2b, MQL is seen to yield an increased specific material removal rate and lower force ratio value. This would suggest that MQL is more suited to grinding of soft material in shallow cut with fine dressing than WET. Another outcome of these results is highly significant for MQL and it points strongly toward an applicable regime for MQL i.e. relatively shallow cut operations, for a range of material hardness.

3.3. Surface Roughness

Results for surface roughness (see Fig. 3a) again show the best MQL performance.

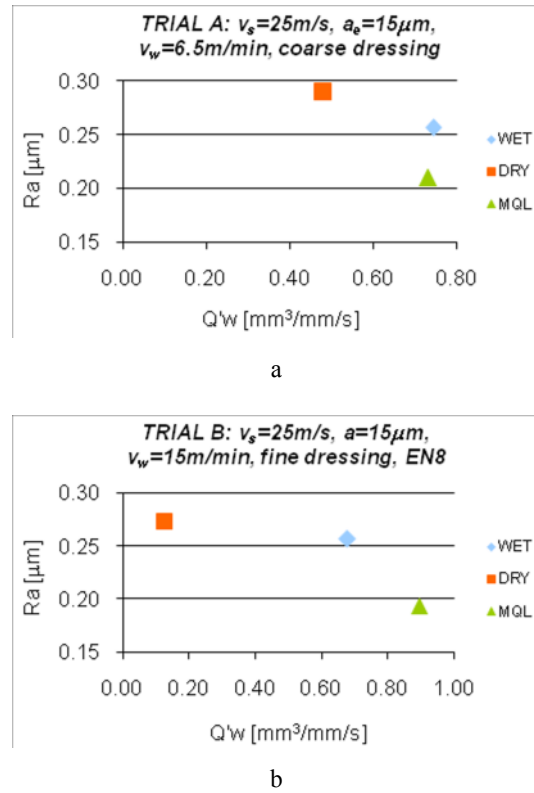


Fig. 3. Surface roughness as a function of specific material removal rate.

The combination of soft material, fine dressing and low wheel speed in Trial B (Fig. 3b) produced poor results for WET. This condition was favourable for MQL and again indicates a large potential for MQL, particularly when grinding softer materials (30-55HRC). It is anticipated, the surface roughness for MQL could have improved had efficient wheel cleaning been present.

3.4. Temperature

Measured temperatures are shown in Fig. 4.

In Trail A (Fig. 4a) the temperature and Q'_w achieved under WET and MQL were very similar, indicating comparable, and almost equal, performance of MQL to WET for the stated conditions.

In Trial B (Fig. 4b) improved cutting efficiency in MQL is noticeable, whilst providing relatively low grinding temperature. This is due largely to the combined effects of lubrication (the lowest friction coefficient was recorded under MQL) and soft material. It is important to indicate, low DRY temperature is due to the process inefficiency, and therefore the grinding temperature was relatively high for the low Q'_w value achieved.

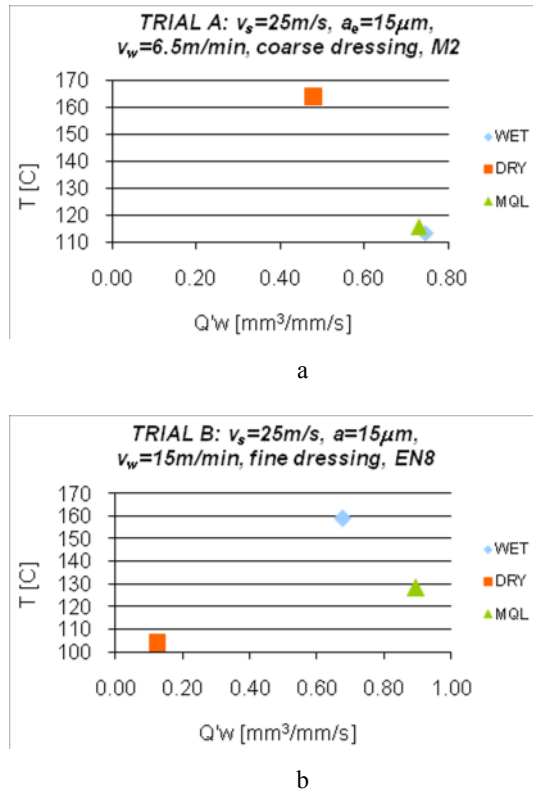


Fig. 4. Temperature as a function of specific material removal rate.

The reason for low cutting efficiency was reasoned to be the fine dressing parameters and soft workpiece material, which is also visible in Trial A (almost 60 per cent Q'_w of WET/MQL with much higher temperature).

4. Conclusions

As a result of this study, the applicable regime for MQL in grinding was determined. Comparable or lower forces were produced by MQL with similar Q'_w levels. MQL generated the lowest force ratio compared to WET and at similar level through all tests. Low grinding temperatures with MQL were observed indicating the capability for low process temperature thus avoiding thermal damage. Low roughness values were recorded with MQL. In general an improved or comparable performance to WET was obtained. Grinding temperatures at contact arc were measured for the first time in MQL. The study results were presented in terms of real depth of cut.

5. Acknowledgment

I would like to thank my Director of studies, Dr Michael Morgan, for his support and efforts put in this study. Gratitude is also due to Prof. Brian W. Rowe and Prof.

Bogdan Kruszynski for their invaluable assistance and vital support.

6. References

- [1] Rowe, W.B., Black, S.C.E., Mills, B., Qi, H.S., Morgan, M.N. (1995) Experimental investigation of heat transfer in grinding. *Annals of the CIRP*, 44/1, 329-332
- [2] Morgan, M.N., Jackson, A.R., Baines-Jones, V., Batako, A., Wu, H., Rowe, W.B. (2008) Fluid Delivery In Grinding. *Annals of the CIRP*, 57/1, 363-366, DOI: 10.1016/j.cirp.2008.03.090
- [3] Batako, A.D., Rowe, W.B., Morgan, M.N. (2005) Temperature measurement in high efficiency deep grinding. *Machine Tools & Manufacture*, 45, 1231-1245
- [4] Marinescu ID, Rowe WB, Dimitrow B, Inasaki I 2004 *Tribology of abrasive machining process* (William Andrew publishing)
- [5] Brinksmeier E, Heinzel C, Wittmann M 1999 *Friction, Cooling and Lubrication in Grinding* *Annals of the CIRP*. 48/2/1999, pp 581-598
- [6] Brinksmeier E, Walter A, Jansen R and Diersen P 1999 *Aspects of cooling lubrication reduction in machining advanced materials*, Proc Inst Mech Engrs Vol 213 Part B, pp 769-778.
- [7] Weiner K, Inasaki I, Sutherland JW, Wakabayashi T 2004 *Dry Machining and Minimum Quantity Lubrication* *CIRP Annals – Manufacturing Technology*, Volume 53, Issue 2, pp 511-537
- [8] Klocke, F., Beck, T., Eisenblatter, G., Lung, D. (2000) Minimal Quantity of Lubrication (MQL) – Motivation, Fundamentals, Vistas. 12th International Colloquium, 929-942
- [9] Barczak, L.M. (2010) Application of Minimum Quantity Lubrication (MQL) in plane surface grinding. PhD Thesis, LJMU
- [10] Rahman, M., Senthil, K.A., Salam, M.U. (2002) Experimental evaluation on the effect of minimal quantities of lubricant in milling. *International Journal of Machine Tools & Manufacture*, 42, 539-547
- [11] Sreejith, P.S. (2008) Machining of 6061 aluminium alloy with MQL, dry and flooded lubricant conditions. *Materials Letters*, 62/2, 276-278
- [12] Silva, L.R., Bianchi, E.C., Catai, R.E., Fusse, R.Y., França, T.V., Aguiar, P.R. (2001) Study on the behaviour of the Minimum Quantity Lubrication - MQL technique under different lubricating and cooling conditions when grinding ABNT 4340 steel. *Journal of the Brazilian Society of Mechanical Science & Engineering*, 2, 192-199
- [13] Silvaa, L.R., Bianchi, E.C., Fusse, R.Y., Catai, R.E., Franc, T.V., Aguiar, P.R. (2007) Analysis of surface integrity for minimum quantity lubricant - MQL in grinding. *International Journal of Machine Tools & Manufacture*, 47, 412-418
- [14] Wójcik, R., Kruszyński, B. (2003) Szlifowanie powierzchni płaskich z zastosowaniem minimalnego wydatku cieczy obróbkowej. *XXVI Naukowa Szkoła Obróbki Ściernej*, 221-225
- [15] Tawakoli, T., Hadad, M.J., Sadeghi, M.H., Daneshi, A., Stockert, S., Rasifard, A. (2009) An experimental investigation of the effects of workpiece and grinding parameters on minimum quantity lubrication - MQL grinding. *International Journal of Machine Tools & Manufacture*, 49, 924-932

Study of the Behavior of Air Flow around a Grinding Wheel under the Application of Pneumatic Barrier

Bijoy Mandal¹, Rajender Singh², Santanu Das³, Simul Banerjee⁴

^{1,4} Department of Mechanical Engineering, Jadavpur University, Kolkata, India

^{2,3} Department of Mechanical Engineering, Kalyani Government Engineering College, Kalyani, India

¹bijoymandal@gmail.com, ²rsingh.iaf@gmail.com, ³sdas_me@rediffmail.com, ⁴simul_b@hotmail.com

Abstract. In grinding process, a stiff air layer is generated around the wheel due to rotation of the porous grinding wheel at a high speed. This stiff air layer restricts fluid to reach deep inside the grinding zone. Conventional method of fluid delivery system is not capable of penetrating this stiff air layer, and generally, results in wastage of large amount of grinding fluid that leads to environmental pollution. Several attempts have been made to adopt certain means to improve better penetration of grinding fluid inside the grinding zone. In this work, formation of stiff air layer has been studied experimentally by measuring the variation of air pressure around grinding wheel periphery at different conditions. A pneumatic barrier set-up has been developed first time for restricting the stiff air layer around grinding wheel. The reduction of air pressure around grinding wheel has been observed at various pneumatic pressures. Using the pneumatic barrier, maximum reduction of air pressure up to 53% has been observed experimentally. This pneumatic barrier system reduces deflection of grinding fluid away from wheel, and hence, the reduction in wastage of grinding fluid, leading to less problem related to environment.

Keywords: Surface grinding, Stiff air layer, Grinding fluid application, Pneumatic Barrier.

1. Introduction

Grinding is a machining process, where a high-speed rotating abrasive wheel is employed. It is associated with high specific energy requirement, and generation of high temperature [1]. Usually, in grinding, large amount of grinding fluid is applied for restricting thermal damages. Main difficulty of application of grinding fluid is formation of a stiff air layer around wheel periphery [1-10] that restricts fluid to reach deep inside the grinding zone.

Shibata and others [2] have stated that the layer of air close to the rotating grinding wheel is carried on the surface of the wheel due to friction of wheel surface with air, and is simultaneously driven outwards by the centrifugal force. Variation of air flow pattern around grinding wheel is reported [3-5] to be dependent on wheel roughness or wheel dressing conditions. The velocity

profile of air layer is also observed to change along wheel width. While some researchers [2, 8-10] have noted that velocity of air layer is nonuniform over the wheel width, and peaks of air velocity or pressure is near to both sides of the wheel, other observations show [3-6] the pressure to be maximum at the centre of wheel width. The distribution of air velocity or pressure in the radial direction changes exponentially decreasing with the distance from the wheel periphery [7-10]. The effect of rexin pasted grinding wheel on air pressure distribution has also been studied [9-10], and it is reported that less amount of air pressure around the rexin pasted wheel is built up compared to that of a normal wheel.

Conventionally applied grinding fluid, in general, is not able to penetrate this stiff air layer, resulting in wastage of larger amount of the grinding fluid. Howes [11] has suggested that lubrication is more important than cooling in grinding, as it reduces the friction, and in turn, total specific energy input. To reduce grinding zone temperature effectively, cutting fluid is needed to enter the grinding zone. Akiyama et al. [12] have investigated to find out an 'effective flow rate' towards achieving this. 20 – 50% of the supply flow rate has been estimated to be the effective flow rate. On the other hand, Engineer et al. [13] have reported that in flood cooling, only 4 to 30% of applied fluid can pass through grinding zone.

Several other attempts [14-18] have been made to adopt some means such that grinding fluid can enter deep inside the grinding zone, and hence, the need of less quantity of fluid. Use of Z-Z method [1], scraper board [2], rexin pasted wheel face [14-16], specially designed nozzle [18], applying fluid in form of high velocity jet [1, 15], etc. can give some favourable results. Ebbrell et al. [17] have suggested to place the fluid delivery nozzle between work surface and wheel centre line for obtaining better fluid penetration through grinding zone.

2. Objective

In this work, formation of stiff air layer is studied experimentally by measuring the variation of air pressure around grinding wheel periphery at different conditions. A pneumatic barrier set-up is developed first time for restricting the stiff air layer around grinding wheel. The reduction of stiff air pressure around grinding wheel is observed at various pneumatic pressures. The effect of pneumatic barrier in fluid flow through grinding zone is also observed

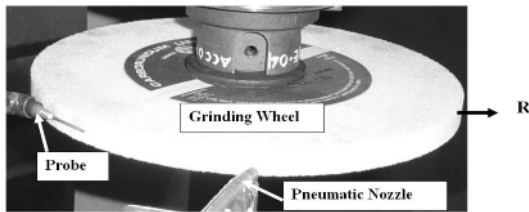


Fig. 1. Experimental set-up

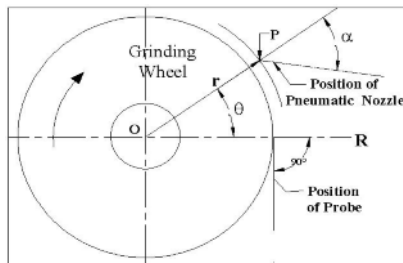


Fig. 2. Schematic diagram of the experimental set-up

3. Experimental Details

In the present work, the grinding wheel is fitted on a three axis CNC milling machine (Make- BFW, India, Model- Akshara VF 30 CNC). The wheel velocity of 20.9m/s has been chosen with a wheel diameter of 200mm. Specification of the wheel used is AA46/55K5V8. A special type calibrated probe, made indigenously, is used to measure air pressure at various points radially outwards from the wheel peripheral surface (R-axis) as shown in Fig. 1. The probe of 1mm outer diameter is set at 0.1mm distance from the middle position of wheel periphery. U-tube inclined manometer with water as manometric fluid and inclination angle of 15° is used to measure the air pressure.

A pneumatic nozzle of 4mm internal diameter is placed on wheel face at different polar co-ordinates (r, θ) (Fig. 2). The polar angles (θ) considered are 30°, 45° and 60°. The pneumatic nozzle is placed 10mm away from the middle position of the wheel periphery, so that curve radius, r becomes 110mm. The pneumatic nozzle is pivoted at P, and swivelled at an angle α . The axis of pivot is parallel to the grinding wheel spindle. The swivel angle (α) is taken as 0°, 30°, 50°, 70° and 90°. Through

this nozzle, compressed air is supplied to block the stiff air layer before the probe. Compressed air is applied with pressure varying from 100 mm to 1600 mm of water. All the experiment sets are repeated twice and average values are shown in the plots.

Another experiment is carried out using a Surface Grinding machine (Make- Maneklal & Sons, India, Model- Parrot) for observing the effect of pneumatic barrier on coolant flow at a wheel velocity of 30m/s. In this experiment, grinding wheel is tangentially placed on workpiece, and fluid is flown through the grinding zone at different flow rates. Grinding fluid is passed through nozzle having 6mm of outer diameter, and placed 10mm above the work surface. Pneumatic nozzle is positioned at 35mm above work surface, and 10mm from wheel periphery at swivel angle (α) of 30°. The pneumatic pressure of 400mm of water is maintained through out these experiments considering substantial gain achieved at this moderate pressure that may be well suited commercially. A special attachment is used to collect and measure the quantity of grinding fluid passing through the grinding zone. Each experiment is repeated two times.

4. Results and Discussion

First set of experiments is carried out at a constant grinding wheel velocity of 20.9m/s maintaining the position of the pneumatic nozzle (r, θ) at (110mm, 30°). The pneumatic pressure is varied from 100mm of water to 1600mm of water, and the swivel angle (α) of pneumatic nozzle is varied from 0° to 90°. Effects of the pneumatic pressure and swivel angle are shown in Fig. 3 and Fig. 4. Substantial amount of reduction in air pressure at the middle position of the periphery of grinding wheel is achieved by using pneumatic barrier. From Fig. 3, the maximum reduction of air pressure at peripheral middle position of grinding wheel is observed at a swivel angle (α) of 50° with a pneumatic pressure of 800mm of water. From Fig. 4, it is seen that the maximum effect of pneumatic barrier is near about 53% at a pneumatic pressure of 800mm of water and at a α of 50°. Face of the pneumatic nozzle is pivoted at point P. Hence, line of action of pneumatic pressure is at a swivel angle (α) with the normal OP (Fig. 2). Line of action of pneumatic pressure is tangential at $\alpha = 65^\circ$. At an $\alpha = 0^\circ$, pneumatic air strikes the wheel perpendicularly. Therefore, the effect of blocking the tangentially flowing air, which is generated around grinding wheel, becomes less. At $\alpha = 30^\circ$ and 50° , compressed air strikes the wheel at polar angles ($\theta + 3^\circ$) and ($\theta + 7^\circ$) respectively. At these swivel angles, effective penetration of stiff air layer by the pneumatic barrier is expectedly observed. However, increasing the swivel angle (α) beyond 50° causes large increase in the distance of striking of pneumatic air with wheel from the probe, and hence, the effect of blocking air layer around grinding wheel becomes less.

Similar experiment is carried out changing the pneumatic nozzle position at $r=110\text{mm}$ and $\theta=45^\circ$, and results are shown in Fig. 5 and Fig. 6. From these figures, it is observed that the effect of pneumatic barrier is maximum corresponding to the pneumatic pressure (barrier) of 400mm of water onwards with swivel angle (α) of 50° . Comparable result is also seen at a swivel angle, α of 30° up to 1200mm of water pressure.

Reduction in air pressure is also observed in Fig. 7 and Fig. 8, where the pneumatic nozzle is placed at $r=110\text{mm}$, $\theta=60^\circ$. It is observed that the maximum effect of pneumatic barrier is at an α of 30° , with the pneumatic pressure of 1600mm of water. Following the observations of the first set of experiments, it can be stated that maximum benefit of applying pneumatic barrier is at a θ of 30° and α of 50° . At higher value of θ , percentage effect of pneumatic barrier decreases, which may be due to large distance of nozzle from probe. At $\alpha=30^\circ$, comparable results have been obtained at higher θ values.

The second set of experiments is performed on a surface grinding machine to measure the fluid flow through the grinding zone. The effect of pneumatic barrier on flooded type fluid flow is shown in Fig. 9 and Fig. 10. It is found out that with the increase in fluid flow through nozzle, more fluid is passed through the grinding zone in both the conditions (Fig. 9). After applying the pneumatic barrier, the fluid passing through the grinding zone is increased substantially. Fig. 10 shows that at lower fluid delivery condition, percentage wastage of fluid is high. Wastage of fluid is reduced by applying pneumatic barrier in all the cases. Due to the application of pneumatic barrier, air layer generated around grinding wheel is suppressed above the fluid delivery nozzle, and, therefore, more fluid enters into the grinding zone. This finding may be effectively utilized in grinding for control of grinding temperature through providing less quantity of fluid. As a result, less pollution may be achieved.

Some of the methods known for suppressing or penetrating the air layer, such as using a scraper board, applying specially designed nozzle, fluid jet, or z-z method, etc. face some practical problems of applicability. Few of these methods need applying large amount of fluid causing large wastage. The pneumatic barrier, on the contrary, can be easily applied and consumes minimum quantity of fluid.

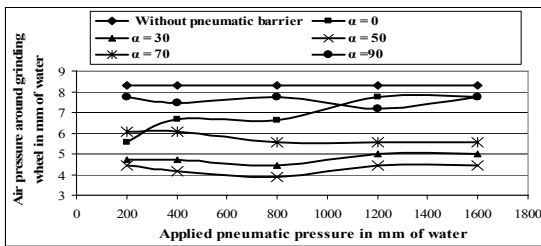


Fig. 3. Plot of air pressure at the middle portion of wheel periphery with the applied pneumatic pressure at a pneumatic nozzle position $r=110\text{mm}$, $\theta=30^\circ$ with different swivel angles (α)

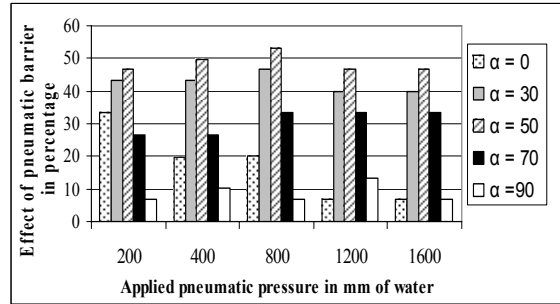


Fig. 4. Effect of pneumatic barrier in percentage at a pneumatic nozzle position $r=110\text{mm}$, $\theta=30^\circ$ with different swivel angles (α)

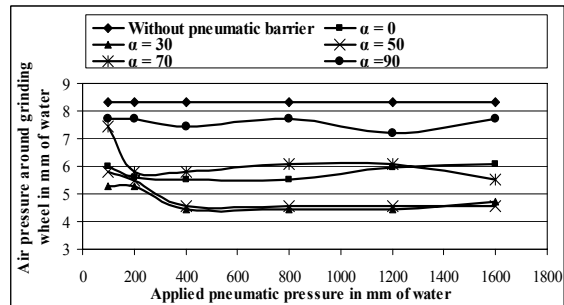


Fig. 5. Plot of air pressure at the middle portion of wheel periphery with the applied pneumatic pressure at a pneumatic nozzle position $r=110\text{mm}$, $\theta=45^\circ$ with different swivel angles (α)

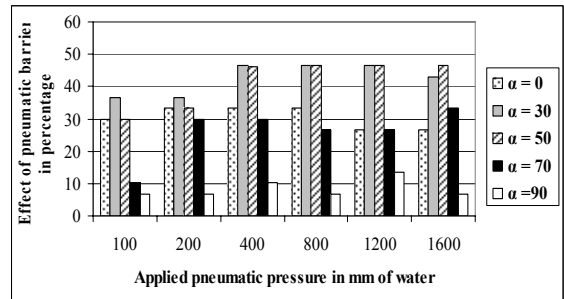


Fig. 6. Effect of pneumatic barrier in percentage at a pneumatic nozzle position $r=110\text{mm}$, $\theta=45^\circ$ with different swivel angles (α)

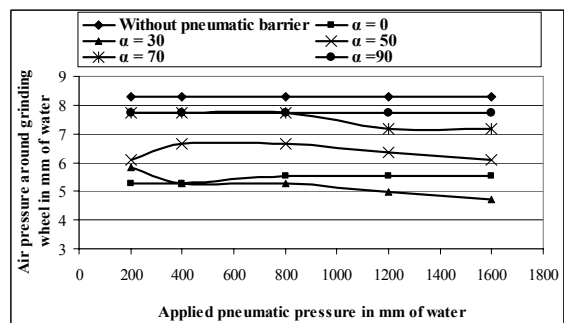


Fig. 7. Plot of air pressure at the middle portion of wheel periphery with the applied pneumatic pressure at a pneumatic nozzle position $r=110\text{mm}$, $\theta=60^\circ$ with different swivel angles (α)

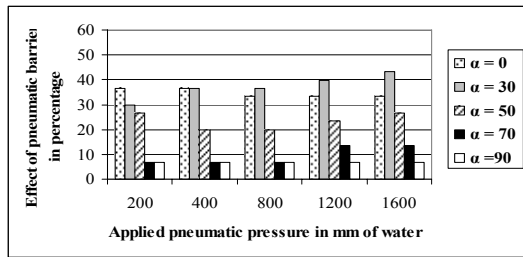


Fig. 8. Effect of pneumatic barrier in percentage at a pneumatic nozzle position $r=110\text{mm}$, $\theta=60^\circ$ with different swivel angles (α)

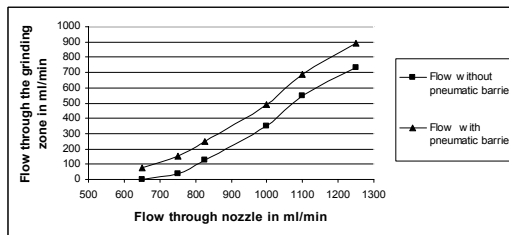


Fig. 9. Plot of fluid flow through grinding zone using flooded type coolant delivery system with a pneumatic barrier having pneumatic pressure of 400mm of water

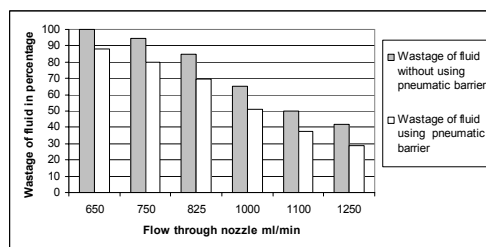


Fig. 10. Wastage of grinding fluid in percentage using flooded type coolant delivery system, using a pneumatic barrier with 400mm of water pressure

5. Conclusion

Following conclusions may be drawn from the experimental investigation carried out.

- The stiff air layer, formed around the grinding wheel, can be effectively suppressed with the use of pneumatic barrier.
- The effect of pneumatic barrier depends on the location of pneumatic nozzle, swivel angle, and pneumatic pressure applied. The maximum effect of pneumatic barrier is found out at 800mm of water pressure with $\theta=30^\circ$ and $\alpha=50^\circ$.
- Fluid flow through grinding zone is observed to increase substantially with the application of pneumatic barrier that can effectively control grinding temperature, and thereby, may be applied effectively, when other known techniques such as use of scraper board, high velocity jet, etc. faces some practical difficulties to apply.

References

- [1] Malkin S, (1990) Grinding Technology: Theory and Application of Machining with Abrasives. Ellis Harwood Publication, U.K.
- [2] Shibata J, Goto T, Yamamoto M, (1982) Characteristics of air flow around a grinding wheel and their availability for assessing the wheel wear. Annals of the CIRP 31/1:233-238
- [3] Radhakrishnan V, Rahman JF, (1977) A preliminary investigation on the condition of the grinding wheel surface by air flow measurements. Annals of the CIRP 25/1: 47-150
- [4] Rahman JF, Radhakrishnan V, (1980) Measurement of grinding wheel surface topography using electro-pneumatic turbulence amplifier system. International Journal of Machine Tool Design and Research 20:189-196
- [5] Radhakrishnan V, Rahman JF, (1981) Functional assessment of the grinding wheel surface characteristics by turbulence amplifier. Trans. of the ASME, Journal of Engineering for Industry 103/2:99-102
- [6] Alenius S, Johansson J, (1996) Air flow and particle distribution around a rotating grinding wheel. Aerosol Science and Technology 25/2:121-133
- [7] Davies TP, Jackson RG, (1981) Air flow around grinding wheels. Precision Engineering 3/2: 225-228
- [8] Wu H, Lin B, Cai R, Morgan MN, (2007) Measurement of the air boundary layer on the periphery of a rotating grinding wheel using LDA. Journal of Physics: Conference Series 76(1), (paper No. 012059)
- [9] Mandal B, Majumder S, Das S, Banerjee S, (2008) Investigation on the formation and control of stiff air-layer around grinding wheel. Proceedings of the 2nd International and 23rd AIMTDR Conference, Chennai, India 375-379
- [10] Mandal B, Majumder S, Das S, Banerjee S, (2010) Predictive modeling and Investigation on the formation of stiff air-layer around the grinding wheel. Advanced Materials Research 83-86:654-659
- [11] Howes T, (1990) Assessment of the cooling and lubrication properties of grinding fluids. Annals of the CIRP 39 (1):313-316
- [12] Akiyama T, Shibata J, Yonetsu S, (1984) Behaviour of grinding fluid in the gap of the contact area between a grinding wheel and a workpiece. Proceedings of the Fifth International Conference on Production Engineering, Tokyo 55-57
- [13] Engineer F, Guo C, Malkin S, (1992) Experimental measurement of fluid flow through the grinding zone. Trans. of the ASME, Journal of Engineering for Industry 114:61-66
- [14] Sarmacharya RS, George MN, Das S, (1998) On the grinding wheel performance through minor wheel modification. Proceedings of the 18th AIMTDR Conference, Kharagpur, India 156-161
- [15] Das S, Sharma AO, Singh SS, Nahate SV, (2000) Grinding performance through effective application of grinding fluid. Proceedings of the International Conference on Manufacturing, Dhaka, Bangladesh 231-239
- [16] Putatunda S, Bandyopadhyay AK, Bose T, Sarkar S, Das S, (2002) On the effectiveness of applying grinding fluid in surface grinding. Proceedings of the National Seminar on Emerging Trends in Manufacturing, Banaras, India 182-187
- [17] Ebbrell S, Woolley NH, Tridimas YD, Allanson DR, Rowe WB, (2000) The effect of cutting fluid application methods on the grinding process. International Journal of Machine Tools and Manufacture 40:209-223
- [18] Banerjee S, Ghosal S, Dutta T, (2008) Development of simple technique for improving the efficacy of fluid flow through the grinding zone. Journal of Materials Processing Technology 197(1-3):306-313

Manufacturing Systems and Management

A cutting plane algorithm for solving single machine scheduling problems with uncertain sequence-dependent setup times

S.H. Zegordi¹, E. Nikbakhsh¹ and M. Modarres²

¹ Department of Industrial Engineering, Faculty of Engineering, Tarbiat Modares University, Tehran, Iran

² Department of Industrial Engineering, Sharif University of Technology, Tehran, Iran

Abstract. In this paper, a variant of the single machine scheduling problem is considered in which the sequence-dependent setup times are assumed to be uncertain and they can take any real value from a closed interval. For tackling the problem, a mathematical model based on the robust traveling salesman problem is proposed for minimizing the makespan. Then, the proposed model is solved via a cutting plane algorithm. Finally, the computational experiments show the effectiveness of the proposed algorithm in comparison with a commercial optimization software generic branch & bound.

Keywords: Scheduling, Single Machine, Sequence-Dependent Setup Times, Traveling Salesman Problem, Interval Uncertainty

1. Introduction

Among various types of scheduling problems, the single machine scheduling problem (SMS) is one of the most widely-studied scheduling problems. One of the main assumptions in SMS literature is the sequence-dependent setup times. The most widely considered performance criterion in the literature for single machine scheduling problem with the sequence-dependent setup times (SMSSDS) is the makespan. This problem is equivalent to the famous traveling salesman problem (TSP). Therefore, SMSSDS can be considered as a strongly NP-Hard problem [1]. Some applications of this problem include chemical compound production, heating and cooling processes, and steel strips rolling.

Various forms of SMSSDS have been studied recently. These studies include optimization of total weighted tardiness [2], considering the deteriorating effect [3], scheduling a single machine with maintenance and jobs due dates [4], proposing MIP model for capacitated lot-sizing in SMSSDS [5], considering past-sequence-dependent setup times [6, 7], and finally considering the effects of learning and deterioration on SMS with past-sequence-dependent setup times [8]. In addition, the concept of uncertainty in SMS has recently received a lot of attention from researchers. Among these studies, processing time is one of the parameters mostly

modeled uncertain via interval [9], stochastic [10], and scenario-based [11] modeling.

The main purpose of this study is to model and solve the single machine scheduling problem with uncertain sequence-dependent setup times and makespan performance criterion. The uncertainty of each setup time parameter is assumed to be in an interval. For this problem, a robust counterpart mathematical model based on the robust TSP and a cutting plane algorithm is presented. To the best of authors' knowledge, the interval uncertainty of sequence-dependent setup times has not been considered in the single machine scheduling problem literature. The main application of this problem is in industries having a heating process where each batch of products requires processing at a different temperature and the required time to prepare the furnace for the next batch of jobs (cooling or heating the furnace) is uncertain. The main reasons for setup time uncertainty can be attributed to errors in parameter forecasting/measurement and errors in implementation of plans [12].

The rest of this paper is organized as follows: In section 2, the research problem and the main idea for tackling the problem is discussed. In sections 3 and 4, the deterministic and robust mathematical models of the research problem are presented. In section 5, a cutting plane algorithm is proposed. Finally, a computational experiment is conducted in section 6, and the conclusions are drawn in section 7.

2. Problem Definition

Consider a manufacturer with a single furnace used for processing various numbers of jobs. Each job has a processing time and a setup time. The required setup time for each job depends on the temperature of furnace used for the previous job. Hence the setup times are sequence-dependent. Since the job orders are periodic, it can be assumed that the last job of the sequence will be again succeeded by the first job of the initial sequence. The real

value of each sequence-dependent setup time parameter can be described via a nominal value and a shift value representing the central value of the uncertain parameter and the maximum possible deviation of the parameter's real value from the nominal value, respectively. Considering the above explanations, the purpose of the research problem is to find a sequence of jobs which minimizes the makespan considering the uncertainties of sequence-dependent setup times.

As discussed in section 1, the deterministic version of SMSSDS is equivalent to TSP. Therefore, the robust counterpart of uncertain SMSSDS can be modeled via constructing a robust TSP model. Limited research has been done on robust TSP. These studies have focused on robust deviation criteria [13,14]. In this study, the budget of uncertainty concept [15] is used for modeling robust TSP. The budget of uncertainty can be defined as the maximum number of uncertain parameters which can deviate from their nominal values [15]. Increasing the uncertainty budget makes the corresponding robust model become more conservative and tends to minimize the worst-case scenario. On the other hand, with the uncertainty budget equal to zero, the corresponding robust model behaves the same as the nominal model.

3. Deterministic Mathematical Model

The single machine scheduling problem with sequence-dependent setup times can be easily modeled as TSP. Consider the symmetric complete graph $G = (N, E)$. In this graph, $N = \{0, 1, \dots, n\}$ is the set of all nodes (jobs), and E is the set of all of arcs connecting the nodes of G . The length of each arc represents the duration of setup for a job (destination of arc) considering the previous job (origin of arc). It is notable that since the sum of processing times in SMSSDS is a constant, the sum of processing times can be neglected. The objective of TSP is to find tour with the least total time (least total setup times) in which the traveling salesman enters to each node exactly once and finally return to its starting node (completing all job). Considering t_{ij} as the setup time for job j considering job i is processed exactly before job j and x_{ij} as the binary variable representing the precedence of job j by job i , the mathematical model for the SMSSDS would be as follows:

$$\text{Minimize} \quad \sum_{\substack{i, j \in N \\ i \neq j}} t_{ij} x_{ij} \quad (1)$$

Subject to:

$$\sum_{i \in N} x_{ij} = 1 \quad \forall j \in N \quad (2)$$

$$\sum_{j \in N} x_{ij} = 1 \quad \forall i \in N \quad (3)$$

$$\sum_{\substack{i, j \in S \\ i \neq j}} x_{ij} \leq |S| - 1 \quad \forall S \subset N, |S| \geq 2 \quad (4)$$

$$x_{ij} \in \{0, 1\} \quad \forall i, j \in N \quad (5)$$

In the above formulation, (1) minimizes the total setup time, and (2) and (3) requires the traveling salesman to enter and leave each node exactly once. Constraint (4), known as the subtour elimination constraint proposed originally by Dantzig, Fulkerson and Johnson [16], eliminates any tour having less than $|N|$ nodes. Finally, (5) defines the decision variable type. It is noteworthy that the assumption of symmetric sequence-dependent setup time matrix does not limit the application of the proposed model and solution algorithm; also implementation of the necessary changes for the asymmetric version are trivial.

4. Robust-Counterpart Mathematical Model

Assume that the nominal value and shift value of each uncertain sequence-dependent setup time is represented via t_{ij} and \hat{t}_{ij} . Therefore, the real value of the uncertain parameter can be described via $\tilde{t}_{ij} \in [t_{ij} - \hat{t}_{ij}, t_{ij} + \hat{t}_{ij}]$. Considering J as the set of uncertain parameters, the budget of uncertainty, Γ , can be selected from the interval $[0, |J|]$. Using a similar notation to [15] for defining supplementary variables, the robust TSP model with budget of uncertainty for traveling times is as follows:

$$\text{Minimize} \quad \sum_{\substack{i, j \in N \\ i \neq j}} t_{ij} x_{ij} + Z\Gamma + \sum_{\substack{i, j \in J \\ i \neq j}} p_{ij} \quad (6)$$

Subject to:

$$\sum_{i \in N} x_{ij} = 1 \quad \forall j \in N \quad (7)$$

$$\sum_{j \in N} x_{ij} = 1 \quad \forall i \in N \quad (8)$$

$$\sum_{\substack{i, j \in S \\ i \neq j}} x_{ij} \leq |S| - 1 \quad \forall S \subset N, |S| \geq 2 \quad (9)$$

$$Z + p_{ij} \geq \hat{t}_{ij} x_{ij} \quad \forall i, j \in J, i \neq j \quad (10)$$

$$x_{ij} \in \{0, 1\} \quad \forall i, j \in N \quad (11)$$

$$p_{ij} \geq 0 \quad \forall i, j \in J, i \neq j \quad (12)$$

$$Z \geq 0 \quad \forall i, j \in J, i \neq j \quad (13)$$

5. Cutting Plane Algorithm

In this section, a method for implementing the Dantzig-Fulkerson-Johnson subtour elimination constraints is proposed in order to solve the uncertain SMSSDS via the cutting plane method originally proposed by Dantzig et al. [16]. Consider the mathematical model proposed for the TSP with budget of uncertainty for traveling times (6-13). After relaxing constraint (9), the aforementioned model is reduced to the assignment problem with budget of uncertainty for assignment costs. If the solution of this problem has no subtour, then it would be a feasible and of course optimal solution for the original TSP with budget of uncertainty of traveling times. If the solution has one or more subtours, then one can add the required subtour elimination constraints to guarantee that the solution of the new model would not have the subtours of the initial solution. This process will be repeated until no subtour is present in the solution of the revised model (figure 1). This approach was initially proposed by Dantzig et al. [16] to solve the deterministic version of the traveling salesman problem with up to 49 nodes. Recently, Applegate et al. [17] have extended the application of this algorithm for solving the traveling salesman problem with one million nodes and more.

Step 0. Build the model (6-8 and 10-13) based on the necessary data and name it P .

Step 1. Solve P .

Step 2. Identify the present subtours in solution of P and name the set containing nodes belonging to k^{th} subtour as U_k . Name the set containing all of U_k sets as U .

Step 3. If U is null, then stop. The solution of P is optimal for the problem (10-19). Else, goto step 4.

Step 4. Add the necessary Dantzig-Fulkerson-Johnson subtour elimination constraints to P as follows and goto step 1.

$$\sum_{\substack{i, j \in U_k \\ i \neq j}} x_{ij} \leq |U_k| - 1 \quad \forall U_k \in U$$

Fig. 1. The proposed cutting plane algorithm.

6. Computational Experiments

In this section, the effect of uncertainty on the objective function value and the solution of the research problem and also the computational power of the proposed algorithm are shown. Since there is no standard set of benchmarks for SMSSDS [19], 5 problem instances from the TSPLIB [18] are selected (table 1). The shift values of setup times are chosen randomly to be between 0.05 and 0.15 of the nominal values. Also, the problem (6-8 and

10-13) along with Miller-Tucker-Zemlin formulation of subtour elimination constraints [20] is solved for the purpose of comparing the proposed method CPU time with commercial optimization software CPU time. Hence, the CPU time of each method is limited to 3600 seconds. The proposed algorithm and model are implemented via GAMS V22.9 and run by a CPLEX optimization engine on a personal computer with a 2.2 GH CPU and 2 GB RAM.

Table 1. Selected Problem Instances

Problem Instance	# of Nodes	Det. Obj. Fun.	Γ
burma14	14	3323	5
bayg29	29	1610	11
berlin52	52	7542	18
eil76	76	538	32
rd100	100	7910	49

First, the amount of uncertainty budget effect on the objective function value is analyzed via a computational study on the first 8 nodes of berlin52 problem instance (Figure 2). It can be observed that along the increase in the budget of uncertainty, the objective function value increases. But after budget of uncertainty reaches 8 and more, the objective function value does not increase. This can be attributed to the fact any feasible TSP solution has $|N|$ binary variables equal to one. This means that variation of at most $|N|$ uncertain parameters would affect the objective function value. It is noteworthy that for Γ equal to zero and 8, the objective function value is equal to the nominal and worst-case objective function values.

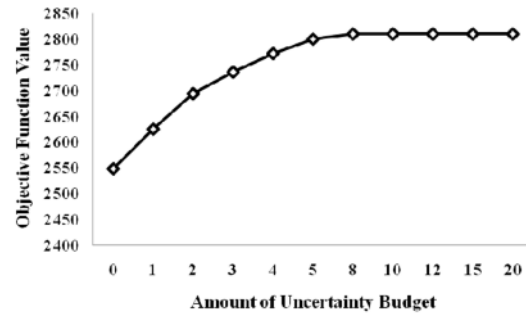


Fig. 2. Berlin52 problem instance.

Next, the effect of the amount of uncertainty budget on the solution is discussed. For this reason, the berlin52 problem instance was solved for all possible integer values of Γ ranging from 0 to 52. The results shows that the solution of the problem remains the same for Γ 's belonging to 4 sets including [0-2], [3-8], [9-35, 38, 43-46, 48, 50, 52], and [36, 37, 39-42, 47, 49, 51]. Therefore, interval uncertainty has a direct effect on the solution of the research problem.

Finally, a computational experiment was run to test the computational power of the proposed algorithm (table 2). The proposed algorithm has been able to solve all of the problem instances optimally in a reasonable amount of time. However, the generic branch & bound implemented via CPLEX was not able to obtain a feasible solution for large problem instances (eil76 and rd100) during the allowed CPU time and just solved small and medium sized instances in a reasonable amount of time. Hence, the proposed algorithm outperforms CPLEX for practical problem instance sizes from both solution quality and computational efforts perspectives.

Table 2. Table with legends of one line

Problem Instance	Robust Obj. Fun.	Prop. Alg. CPU Time (Sec.)	Prop. Model CPU Time (Sec.)
burma14	3551	0.56	1.32
bayg29	1701	1.04	156.45
berlin52	7977	1.98	212.18
eil76	572	4.67	-
rd100	8466	862.68	-

7. Conclusion

In this paper, the single machine scheduling problem with uncertain sequence-dependent setup times was studied. The main application of this problem is in industries with a heating process where each batch of products requires processing at a different temperature and the required time to prepare the furnace for next batch of jobs is uncertain. For this problem, a mathematical model based on robust TSP was proposed based on the uncertainty budget concept. Then, a cutting plane algorithm was developed to solve the problem for practical instances. A computational experiment showed that the proposed method can solve problems with up to 100 jobs in less than 15 minutes which is acceptable for real-world applications of the research problem. Developing algorithms based on branch & cut and metaheuristics for solving the research problem and also considering other types of uncertainty and robustness criteria are the main future research opportunities for this study.

References

- [1] Pinedo M, (2008) Scheduling - Theory, Algorithms, and Systems, Springer, New York, NY
- [2] Tasgetiren MF, Pan QK, Liang YC, (2009) A discrete differential evolution algorithm for the single machine total weighted tardiness problem with sequence dependent setup times. Computers and Operations Research, 36:1900-1915
- [3] Bahalke U, Yolmeh AM, Shahanaghi K, Meta-heuristics to solve single-machine scheduling problem with sequence-dependent setup time and deteriorating jobs. International Journal of Advanced Manufacturing Technology, In Press, DOI:10.1007/s00170-010-2526-5
- [4] Chen WJ, (2008) Sequencing heuristic for scheduling jobs with dependent setups in a manufacturing system. International Journal of Advanced Manufacturing Technology, 38:176-184
- [5] Kovács A, Brown KN, Tarim SA, (2009) An efficient MIP model for the capacitated lot-sizing and scheduling problem with sequence-dependent setups. International Journal of Production Economics, 118:282-291
- [6] Biskup D, Herrmann J, (2008) Single-machine scheduling against due dates with past-sequence-dependent setup times. European Journal of Operational Research, 191:586-591
- [7] Koulamas C, and Kyparisis GJ, (2008) Single-machine scheduling problems with past-sequence-dependent setup times. European Journal of Operational Research, 187: 1045-1049
- [8] Wang JB, Jiang Y, Wang G, (2009) Single-machine scheduling with past-sequence-dependent setup times and effects of deterioration and learning. International Journal of Advanced Manufacturing Technology, 41:1221-1226
- [9] Yin N, Wang JB, Wang D, Wang LY, Wang XY, (2010) Deteriorating jobs and learning effects on a single-machine scheduling with past-sequence-dependent setup times. International Journal of Advanced Manufacturing Technology, 46:707-714
- [10] Wu CW, Brown KN, Beck JC, (2009) Scheduling with uncertain durations: Modeling β -robust scheduling with constraints. Computers & Operations Research, 36:2348-2356
- [11] Leus R, Herroelen W, (2007) Scheduling for stability in single-machine production systems. Journal of Scheduling, 10:223-235
- [12] Ben-Tal A, El Ghaoui L, Nemirovski A, (2009) Robust Optimization. Princeton University Press, Princeton, NJ
- [13] Montemanni R, Barta J., Mastrolilli M., Gambardella L.M., (2007) Heuristic algorithms for the robust traveling salesman problem with interval data. in Proceedings of TRISTAN VI - The Sixth Triennial Symposium on Transportation Analysis, Phuket, Thailand
- [14] Montemanni R, Barta J, Mastrolilli M, Gambardella LM, (2007) The robust traveling salesman problem with interval data. Transportation Science, 41:366-381
- [15] Bertsimas D, Sim M, (2004) The price of robustness. Operations Research, 52:35-53
- [16] Dantzig GB, Fulkerson DR, Johnson SM, (1954) Solution of a large scale traveling salesman problem. Operations Research, 2:393-410
- [17] Applegate D, Bixby R, Chvatal V, Cook W, (2003) Implementing the Dantzig-Fulkerson-Johnson algorithm for large traveling salesman problems. Mathematical Programming, 97:91-153
- [18] Reinelt G, (2010) TSPLIB. Available from www.iwr.uni-heidelberg.de/groups/comopt/software/TSPLIB95/
- [19] Luo X, Chu F, (2006) A branch and bound algorithm of the single machine schedule with sequence dependent setup times for minimizing total tardiness. Applied Mathematics and Computation, 183:575-588
- [20] Miller CE, Tucker AW, Zemlin RA, (1960) Integer programming formulations and traveling salesman problems. Journal of the ACM, 7:326-329

A Knowledge-Based Engineering System for Assembly Sequence Planning

Y. Y. Hsu¹, W. C. Chen², P. H. Tai³ and Y. T. Tsai⁴

¹ 707 Wu Fu Rd., Sec. 2, Hsinchu 30012, Chung Hua University, Taiwan, 300, yyhsu@chu.edu.tw

² 707 Wu Fu Rd., Sec. 2, Hsinchu 30012, Chung Hua University, Taiwan, 300, wenchin@chu.edu.tw

³ 252 Shangying Road, Taoyuan County 33341, Delta Electronics, Inc, Taiwan, 300, d09403015@chu.edu.tw

⁴ 1 Lane 380, Qingyun Road, Tucheng, Delin Institute of Technology, Taiwan, 236, yttsai@dlit.edu.tw

Abstract. In this study, we developed a knowledge-based engineering (KBE) system to assist engineers in promptly predicting a near-optimal assembly sequence. Still further, a three-stage assembly optimization approach with some heuristic working rules was employed to establish the proposed system. In the first stage, Above Graph and a transforming rule were used to create a correct explosion graph of the assembly models. In the second stage, a three-level relational model graph, with geometric constraints and assembly precedence diagrams (APDs), was generated to create a completely relational model graph and a feasible assembly sequence. In the third stage, a robust back-propagation neural network (BPNN) engine was developed and embedded in the Siemens NX system. System users can easily access the volume, weight, and feature number through the Siemens NX system interface, input the related parameters such as contact relationship number and total penalty value, and predict a feasible assembly sequence via a robust engine. As such, three real-world examples were used to evaluate the feasibility of the KBE system. The results show that the proposed system can facilitate feasible assembly sequences and allow designers to recognize contact relationships, assembly difficulties, and assembly constraints of three-dimensional components in a virtual environment type.

Keywords: knowledge-based engineering, assembly optimization, assembly sequence, BPNN.

1. Introduction

Assembly sequence planning (ASP) is a critical technology which achieves product design and facilitates realization. Product design is no more than an important determinant of a business' competitiveness per concept generation, tests evaluation and customers' communication. It was determined that 80% of the costs of a product's lifecycle occur during the initial design stage [1]. Design for assembly (DFA) focuses on product-related factors such as size, weight, symmetry, orientation, and form features, as well as other assembly processes such as handling, gripping, and insertion [2]. Achieving the most effective assembly plan requires a significant amount of time to analyze the combinations of relationships of each component or part with the

assembly process, which may include welding, soldering, adhesive bonding, wiring, press fitting, shrink fitting, brazing, riveting, and other mechanical or electrical fastening; the accomplishment of which numerous standard sequences can be employed without regard to the product configuration, material, or production quantity [3].

In generating assembly sequences, De Fazio and Whitney [4] adopted the exhaustive concept of Bourjault to obtain a complete set of assembly sequences. They generated sequences in two stages: creating precedence relations between liaisons (i.e., physical contacts) or logical combinations of liaisons in a product and then verifying the liaison sequence in terms of graph search theory. However, some components cannot be successfully assembled due to potential geometric constraints. Homen de Mello and Sanderson [5] made a representation of directed AND/OR graphs and disassembly concerns to create feasible assembly sequences. In addition, Kroll [6] used directed graph-based procedures with conventional representations to reduce the number of sorting operations required. However, these direct approaches only apply to orthogonal assembly structures involving six orthogonal directions.

The current essential technology, knowledge-based engineering (KBE), allows engineers to secure product knowledge and incorporate engineering domain skills based on design rules and powerful CAD/CAM applications which are utilized to design, configure, and assemble products. Examples of this include the so-called expert systems, web-based knowledge driven databases and Knowledge Fusion (KF) involving engineering know-how with a knowledge-based language, which captures both geometric and non-geometric attributes of a given part or assembly, writes rules and essentially gives us the ability to capture intelligence and engineering know-how, and becomes a critical part of the business strategy. Numerous researchers have employed an artificial intelligence (AI) tree search or graph-based

search methodology to generate diverse assembly sequences.

Unfortunately, feasible assembly sequences for which the search space explosively increases as the number of design-in components grows are hard to find. To relieve this computational and combinatorial complexity, heuristic rules, ant colony optimization, the algorithm of Self-Guided Ants (ASGA), and genetic algorithms (GAs) are used in the search process [7]. Other studies used the Hopfield and BPNN to generate optimal or near-optimal assembly sequences [8]. However, they merely focus on mathematical model creation rather than constructing an engineering-oriented knowledge-based engineering (KBE) system. To meet this challenge, a KBE system was developed to assist engineers in promptly predicting a near-optimal assembly sequence through a three-stage assembly optimization technique with some heuristic working rules, which can facilitate feasible assembly sequences and allow designers to recognize contact relationships, assembly difficulties, and assembly constraints of three-dimensional (3D) components under the Siemens NX package.

2. Working scheme and processes

Generally, assembly sequence planning consists of feature-based assembly modeling, knowledge-based assembly sequence generation, and interactive assembly planning system demonstration. This study developed a three-stage integrated approach with some heuristic working rules to assist planners in generating the best, most-effective assembly sequence. In the first stage, Above Graph (i.e., the graph illustrates that a part located absolutely or relatively above the other parts) and transforming rules were used to create a correct explosion graph of the assembly models [9]. In the second stage, a three-level relational model graph, with geometric constraints and assembly precedence diagrams (APDs), was generated to create a complete relational model graph and a feasible assembly sequence. In the third stage, the BPNN engine via parameter optimization using the Taguchi method and design of experiment (DOE) was employed to predict the available assembly sequences. The aforementioned BPNN engine, created by a toy car model, as a learning (training) sample, and a toy motorbike model and a brushless DC fan as testing samples, was used to evaluate the feasibility of the proposed model in terms of differences in assembly sequences.

The working concepts and procedures fall into two parts: the first is to construct a graph-based assembly sequence planning and the second is to develop a KBE system with an embedded robust BPNN engine. The proposed flow chart is shown in Fig. 1. A KBE system that renders an NX/KF-based operational interface to access the potential graphs and BPNN-related details via different types of databases is given in Fig. 2.

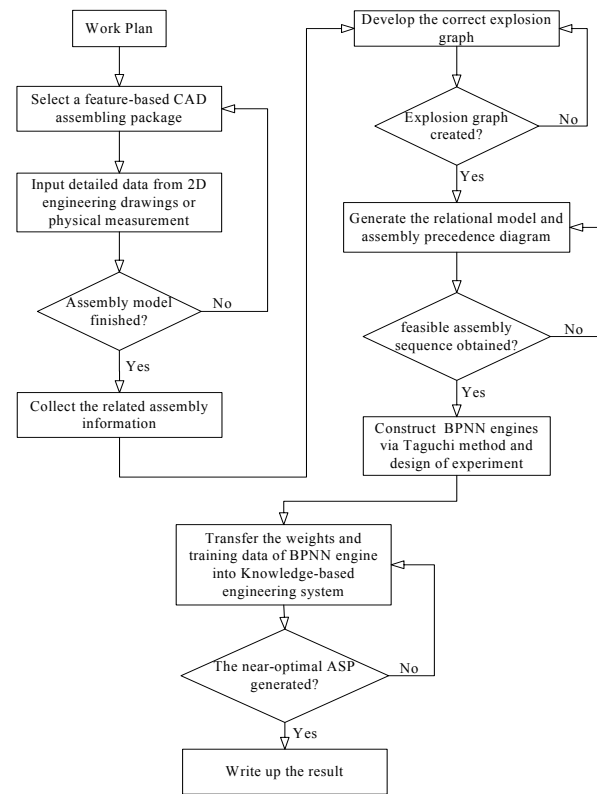


Fig. 1. Flow chart of the proposed study

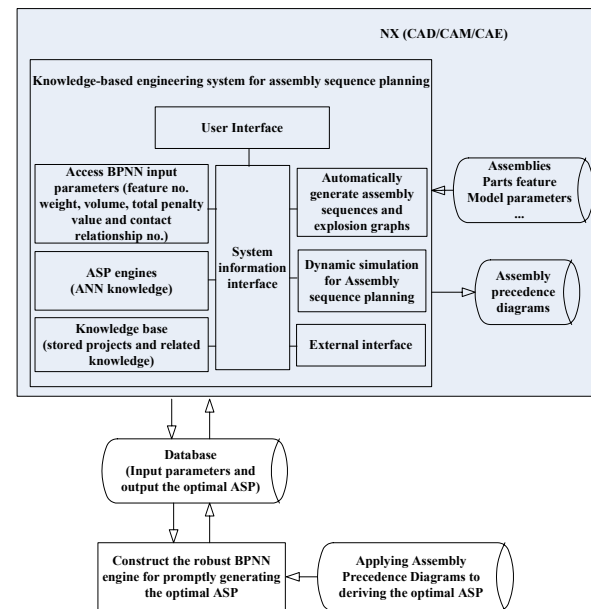


Fig. 2. KBE model for assembly sequence planning

3. Illustrative manually-assembled examples for developing a KBE system

An exploded view can be directly created from the Above Graph, which possesses the contact relationships of a spatial structure. Figure 3 shows the parts list, assembly codes, and exploded view. The validity of each exploded view can be confirmed by the contact relationships of the spatial structure and Above Graphs. Exact assembly plans can be derived by applying a correct exploded view. Figure 4 shows the complete relational model graph (RMG) and assembly precedence diagram (APD) for the proposed training sample of the case study; the entirely developed procedure can be in reference with [9] .

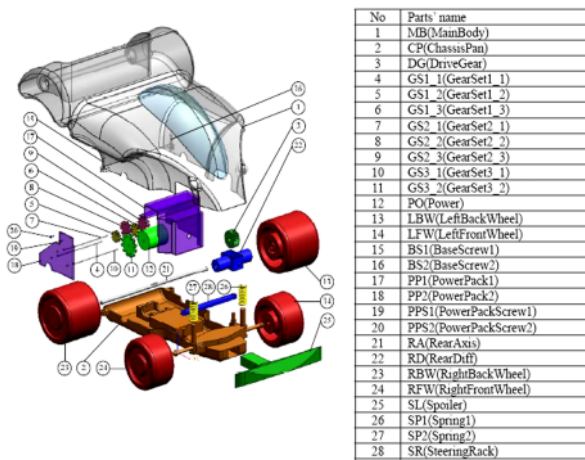


Fig. 3. Parts list and exploded view of a toy car

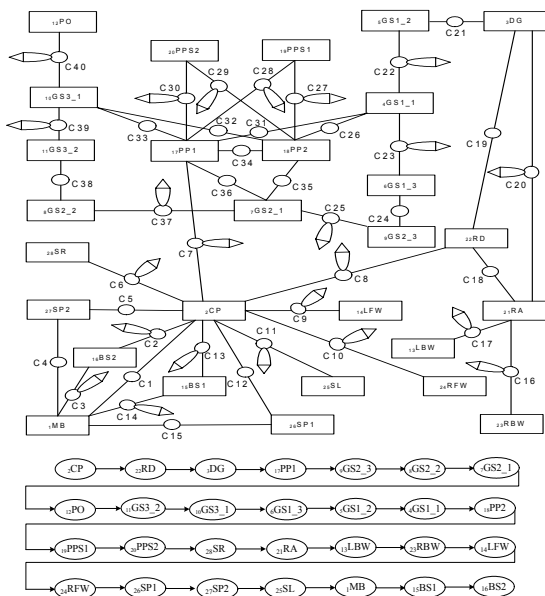


Fig. 4. The RMG and APD of a toy car

A toy car was used as a training sample, while a DC brushless fan and a toy motorbike were employed to test and verify the samples. The characteristics of each assembly part include the number of the assembly incidence (AI), total penalty value (TPV), feature number (FN), weight, and volume. These characteristics are commonly regarded as the larger the better for the assembly sequence priority. The optimal assembly sequences resulting in information on five characteristics of the toy car, motorbike, and DC brushless fan are given in Tables 1, 2, and 3, respectively.

Table 1. The optimal assembly sequence of a toy car

Optimal Assembly Sequence	Parts	AI	TPV	FN	Weight	Volume
1	CP	19	47	9	981.88	125415.99
2	RD	4	8	10	31.42	11246.39
3	DG	5	8	27	4.83	3452.57
4	PP	10	29	11	83.64	29935.98
5	GS2_3	3	5	22	1.96	1397.92
6	GS2_2	3	5	22	1.12	802.85
7	GS2_1	6	16	1	3.07	392.7
8	PO	2	3	2	56.34	20165.61
9	GS3_2	3	5	26	2.28	1628.77
10	GS3_1	6	16	1	3.07	392.7
11	GS1_3	3	5	22	1.08	771.23
12	GS1_2	3	5	22	0.87	623.61
13	GS1_1	6	16	1	3.07	392.7
14	PP2	8	22	11	17.66	6321.76
15	PPS1	4	6	3	0.13	14.99
16	PPS2	4	5	3	0.11	14.86
17	SR	7	4	4	27.58	3522.26
18	RA	7	13	3	29.79	3804.98
19	LBW	2	5	7	308.9	219936.4
20	RBW	2	3	7	307.67	219928.32
21	LFW	2	3	9	176.9	119227.68
22	RFW	2	3	9	164.33	119214.45
23	SP1	2	6	3	9.99	1288.59
24	SP2	2	6	3	9.85	1276.48
25	SL	2	3	2	234.01	83756.14
26	MB	7	17	28	932.5	333750.12
27	BS1	4	10	3	2.38	303.99
28	BS2	4	10	3	2.36	302.45

Table 2. The optimal assembly sequence of a toy motorbike

Optimal Assembly Sequence	Parts	AI	TPV	FN	Weight	Volume
1	MMB1	5	13	20	7.35	7697.04
2	MPE	9	19	4	5.19	5176.46
3	MMB2	5	17	20	6.78	7696.73
4	MS	3	8	2	1.53	2297.29
5	MN	3	10	3	0.78	856.50
6	MW3	1	9	4	8.13	7296.14
7	MB2_1	4	23	3	1.2	1931.29
8	MB2_2	3	16	5	1.41	1892.18
9	MA	8	52	2	3.32	2907.56
10	MW2	2	9	4	8	7295.23
11	MB2_2	4	18	3	1.18	1930.96
12	MB3_1	3	5	5	1.4	1891.72
13	MB1	4	11	4	2.49	3841.38
14	MW1	2	4	4	7.99	7294.86
15	MPN	3	12	5	1.28	1619.55
16	MH1	2	4	3	0.17	231.61
17	MH2	2	3	3	0.15	230.56

Table 3. The optimal assembly sequence of a DC brushless fan

Optimal Assembly Sequence	Parts	AI	TPV	FN	Weight	Volume
1	MMB1	5	13	20	7.35	7697.04
2	MPE	9	19	4	5.19	5176.46
3	MMB2	5	17	20	6.78	7696.73
4	MS	3	8	2	1.53	2297.29
5	MN	3	10	3	0.78	856.50
6	MW3	1	9	4	8.13	7296.14
7	MB2_1	4	23	3	1.2	1931.29
8	MB2_2	3	16	5	1.41	1892.18
9	MA	8	52	2	3.32	2907.56
10	MW2	2	9	4	8	7295.23
11	MB2_2	4	18	3	1.18	1930.96
12	MB3_1	3	5	5	1.4	1891.72
13	MB1	4	11	4	2.49	3841.38
14	MW1	2	4	4	7.99	7294.86
15	MPN	3	12	5	1.28	1619.55
16	MH1	2	4	3	0.17	231.61
17	MH2	2	3	3	0.15	230.56

4. Operational procedures of the KBE system

In this section, two real-world products, a brushless DC fan and toy motorbike, are presented to demonstrate ASP by the KBE system. The operational procedures are

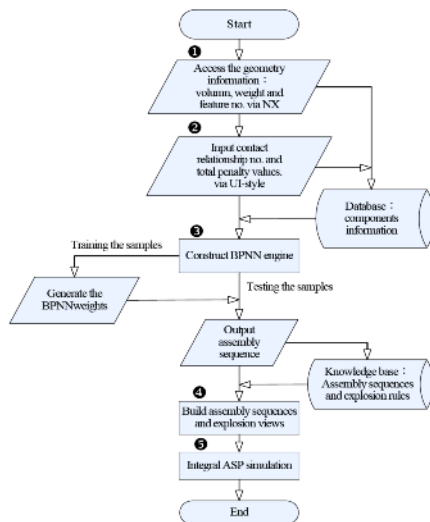


Fig. 5. Operational procedures of the KBE system

shown in Figure 5, and are composed of five steps.

Step 1. Access geometric information in the KBE database on feature numbers, weight, and volume created by the NX CAD modeling system.

Step 2. Input the contact relationship number and TPVs to formulate the training and testing data using the UI-style NX tool.

Step 3. Construct BPNN engines by implementing BPNN training and test processes using the NX KF language.

Step 4. Automatically build the explosion views and generate assembly sequences in terms of “Above” rules of the explosion graph and APD precedence relationships.

Step 5. Conduct an entire ASP simulation through steps 1~5 as instances of interest for an 11-piece DC brushless fan and a 17-piece toy motorbike respectively represented in Figs. 6 and 7.

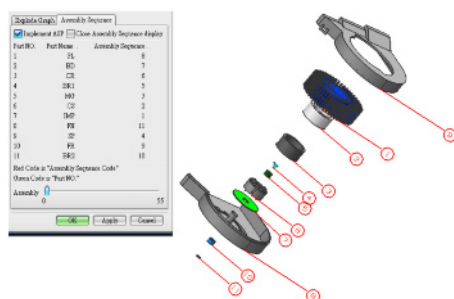


Fig. 6. ASP generation of a DC brushless fan

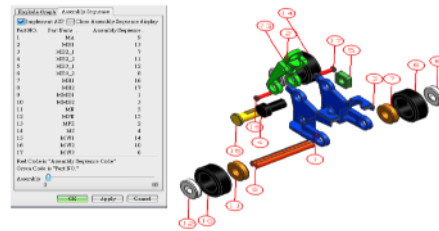


Fig. 7. ASP generation of a toy motorbike

5. Conclusions

Theoretically, an assembly plan can be optimized based on factors of the shortest assembly time and assembly sequence optimization. However, there are uncertain factors prior to the determination of the optimized assembly scheme and the completion of the jig and fixture. The system proposed in this paper adopts a three-stage integrated assembly planning approach to express the complexity of the assembly relations and evaluate the feasibility of the respective assembly sequences in the design phase. The experimental results for the case study verified the feasibility of the KBE system, which facilitates the DFA in potential applications of 3D component models to facilitate the manual or automatic assembly in a virtual environment.

Acknowledgements

Financial support from the National Science Council, Taiwan, ROC, under contract NSC 97-2221-E-216 -026 and Chung Hua University, under contract CHU-98-M-03.

References

- Mascle C, Zhao HP (2008). Integrating environmental consciousness in product/process development based on life-cycle thinking. *Int J Prod Econ* 12: 5-17
- Kai Y, Basem EH (2003). *Design for Six Sigma: a roadmap for product development*, McGraw-Hill, New York
- Crowson RD (2006). *Assembly Processes: finishing, packaging, and automation*. Taylor & Francis, New York
- De Fazio TL, Whitney DE (1987). Simplified generation of all mechanical assembly sequences. *IEEE Trans Robot Automat* 3(6): 640-658
- Homen de Mello LS, Sanderson AC (1991). Representations of mechanical assembly sequences. *IEEE Trans Robot Automat* 7(2):211-227
- Kroll E (1994). Intelligent assembly planning on triaxial products. *Conc Eng: Res Appl* 1(2):311-319
- Tripathi M, Agrawal S, Pandey MK, Shankar R, Tiwari MK (2009). Real world disassembly modeling and sequencing problem: Optimization by Algorithm of Self-Guided Ants (ASGA). *Robot Com-Int Manuf* 25(2009):483-496
- Hong DS, Cho HS (1995). A neural network based computational scheme for generating optimized robotic assembly sequences. *Eng Appl Artif Intell* 8(2):129-145
- Chen WC, Tai PH, Deng WJ, Hsieh LF (2008). A three-stage integrated approach for assembly sequence planning using neural networks. *Exp Syst Appl* 34:1777-1786

Product Family Modeling and Optimization Driven by Customer Requirements

Y. Su

College of Civil Aviation, Nanjing University of Aeronautics and Astronautics Yudao Street, Nanjing, Jiangsu, China

Abstract. One key aspect to improve networked product customization efficiency is to establish optimized and integrated product family models. Based on analysis of the composition of product family, a function and structure skeleton model (FS-SKM) is presented to reduce modeling workload. To quickly model FS-SKM on product resources in distributive enterprises, an intelligent modeling algorithm is presented. Due to dynamic varieties of customer requirements, a dynamic clustering algorithm is presented for persistent implementation of rapid product customization. Finally, Paving Machinery Product is used as a study case to illustrate the effectiveness of the proposed approaches.

Keywords: mass customization, product customization system, supply chain, SMEs, product family, modeling, optimizing

1. Introduction

With the increasing complexity of Product structure in 21th century, distributed production is a principal mode in manufacturing. Small to medial sized enterprises(SMEs), which account for 90 percent in Chinese manufacturing, are the key members of supply chain of complex products. Product resource from SMEs can be integrated into a sharing product platform to efficiently implement rapid customization. Networked product customization system is a bridge connecting customers with enterprises, and also integrates the internal/external information of enterprises. Product family modeling is one key technology of implementing networked product customization. Any customized product is designed based on customer's requirements. At present, market pattern in manufacturing has been changing from relatively stable to dynamic. The dynamic customer requirements lead to the dynamic product family. Extensive literature in product family modeling is based on single enterprise's internal product resource without considering the distributed production and dynamic product family as time goes on. Existing product family modeling methods do not work well on the sharing product platform.

In order to efficiently implement rapid customization of complex products, an integrated sharing product

customization service platform was deeply studied in [1][2]. In this paper, according to the dynamic customer requirements and the distributed production of complex products, an innovative method for product family modeling and optimization is investigated.

2. Product Family Expression

With the increasing complexity of products, the main goal of mass customization design is to establish modularization for product family orienting to customer segmentation[3]. Product family is a cluster of relative products with the same or similar function, structure and performance. Product family model is composed of function model, theory model and structure model[4]. Product family structure is the kernel of design for mass customization. Product family structure model is a cluster of structure of similar products. It represents the composition of the relationship between components. Product family structure is usually organized using a tree structure, and modelled upon function and theory.

Establishing a full product family model for products with diverse types and complex structure not only brings heavy workload, but also leads to inefficient configuration. In product design theory, the skeleton generally represents the backbone structure of the product[5]. In order to reduce the workload of modeling product family and directly provide customers functional customization on sharing product platform, a function and structure skeleton model(FS-SKM) is proposed. Object-oriented modeling is adopted and FS-SKM is expressed using six elements as follows.

$$FS-SKM := \{SKM_ID, SKM_NIDS, SKM_FS, SKM_CIS, SKM_FAS, SKM_DIS\} \quad (1)$$

Where SKM_ID is FS-SKM identifier which is different from other FS-SKM, SKM_NIDS is node identifier set which contains all node identifiers of the FS-SKM,

SKM_FS is function set, SKM_CIS is configuration interface set of FS-SKM nodes, SKM_FAS is functional attribute description set of FS-SKM nodes, and SKM_DIS is the set of internal/external data exchange interfaces.

Considering that the total function of any product is combined by lower subfunctions, FS-SKM can be expressed using tree-like hierarchical structure shown in Fig 1.

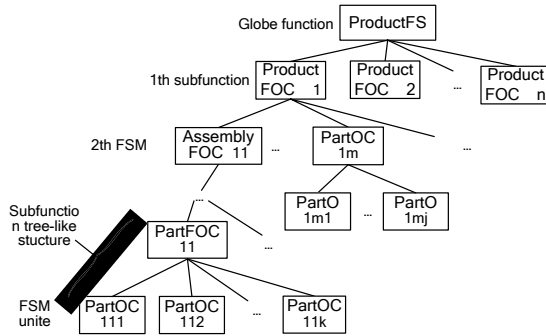


Fig. 1. FS-SKM tree-like hierarchical structure

Each node in the hierarchical structure tree of FS-SKM (Fig. 1) corresponds to a function and structure model (FSM). As the basic component of a product of FS-SKM, FSM is a genuine link interface between customers and enterprises. FSM is denoted using six elements as below.

$$FSM ::= (FSM_ID, FSM_N, FSM_FID, SM_FAS, FSM_CI, FSM_DIS) \quad (2)$$

Where FSM_ID is FS-SKM Identifier which is different from other FS-SKM, FSM_N is the name of FSM, FSM_FID is the parent-node identifier, FSM_FAS is functional attribute description set of SKM nodes, FSM_CI is configuration interfaces, and SKM_DIS is internal/external data exchange interface for FSM.

3. FS-SKM modeling and Optimizing

3.1 FS-SKM Integrated Modeling

There are two major approaches for product family modeling. One approach is to design product family at the development time for new products. The other approach is to reconstruct product family by reorganizing some already designed products. Product family design on sharing product platform is to reconstruct FS-SKM from existing products which are integrated from distributive SMEs. In order to intelligently create FS-SKM, ID3 algorithm[6] is applied and FS-SKM instance study method is presented.

At the beginning of study, FS-SKM is an empty decision tree. It needs to train an instance to predict how to divide the products according to functional attributes of the entire instance space. The set of product instances can be denoted as

$$X = \{x_1, x_2, \dots, x_n\} (n \geq 1),$$

Where x_i is the i^{th} instance, n is the total number of product instances. Let W denote window size and X_1 window. FS-SKM intelligent modeling steps are given as follows.

Step 1. Select a random subset X_1 with W -scale from product instance X .

Step 2. Calculate classified information entropy by utilizing ID3 algorithm.

Step 3. Choose the maximum value of classified information entropy as the standard to select test attributes for each FSM, and form the decision tree of current X_1 window.

Step 4. Sequentially scan all the training instances and identify the exception of current decision tree. If no exceptions, instance training ends.

Step 5. Combine some training examples of current window and some exception found in step 3 and form a window. And then go to step 2.

3.2 FS-SKM Dynamic Optimization

Since customer's requirements are dynamic as time goes on, the initially established FS-SKM will become inaccurate after a period. Therefore, in order to persistently implement rapid deployment design, it needs to carry out dynamic analysis of customer requirements and to provide optimization strategies of current FS-SKM for SMEs.

Considering the dynamic characteristics of customer's requirements and the tree structural characteristic of FS-SKM, ant clustering principle of self-aggregation[7] is applied to dynamic clustering of customization customer requirements.

First, build an ant tree for FS-SKM by applying the basic idea that ants construct tree according to classification model. Each FSM on FS-SKM place an ant. Functional attributes are taken as the pheromone produced by ants.

Second, build a customer product platform P through the root a_0 of FS-SKM ant tree. All discrete customization customers spread randomly on the platform P . There will be a number of customization customers randomly distributed on the platform P as time goes by.

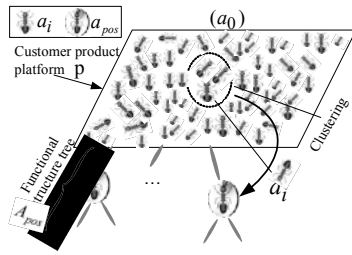


Fig. 2 Customer's product requirements dynamic clustering

Clustering process is given as follows. The first ant is directly connected to the root node a_0 (see Fig. 2). Then moving ants gradually determine their own position on the root node a_0 or other node of FS-SKM ant tree according to the value of functional attribute similarity. At proper time, create new nodes and sub-functional structure tree until all moving ants are connected to FS-SKM ant tree.

4. A Case Study

Following this paper, product family modeling of paving constructuary machinery is taken as a case to verify the effectiveness of proposed approaches. The properties of power type, operation type of paving, paving way, and the paving size are the main impact factors of function modular design of paver product families. Those properties are taken as classification properties to extract functional attributes of FS-SKM. Utilizing the FS-SKM instance study method based on ID3 algorithm, the functional attributes (Table 1) and paver FS-FSM (Fig. 3) are generated. In Fig. 3, the labels on the two-node connection line are the functional attributes with the largest information entropy.

Take functional attributes as pheromone produced by ants. Let paver FS-FSM (see Fig. 3) to be classification mode. Dynamic clustering analysis of customization customer's requirements is carried out by using ant clustering principle of self-aggregation. The analysis results of customization customer's requirements dynamic clustering see Fig. 4. The results show following optimization strategies which impel SMEs optimizing current FS-SKM of paving construction machinery. Table 2 gives the Meaning of Abscissas in Fig. 4

Table 1.1. FSM Functional attributes of paver product family

FSM_ID	FSM_FID	Functional Attribute
1	0	Paving operations
11	1	Stabilized soil, Paving operations
12	1	A variety of materials, Paving operations
13	1	Cement concrete, Paving operations
14	1	Asphalt, Paving operations
111	11	Hydraulic Transmission, vibratory rolling, Stabilized soil, Paving operations
112	11	Hydraulic Transmission, Tyred rolling, Stabilized soil, Paving operations
121	12	Large-scale, Hydraulic Transmission, Traffic Road, Sliding mode, Paving operations
122	12	Medium-scale, Pairs of vibrator compaction, Bridges, Sliding mode, Paving operations
123	12	Small-scale, self leveling, Highway, Sliding mode, Paving operations
131	13	Movable leveling, Electric Power, Cement concrete, Paving operations
132	13	self leveling, Diesel Power, Cement concrete, Paving operations
133	14	Microcomputer control, Large-scale, Multifunction, Asphalt, Paving operations
141	14	Microcomputer control, Medium-scale, Multifunction, Asphalt, Paving operations
142	14	Full hydraulic drive, Small-scale, Multifunction, Asphalt, Paving operations

Table 1.2. The Meaning of Abscissas in Fig. 1.4

Abscissa	1	2	3	4	5	6	7	8	9	10	11	12	13	14
FSM_ID	11	12	13	14	111	112	121	122	123	131	132	141	142	143

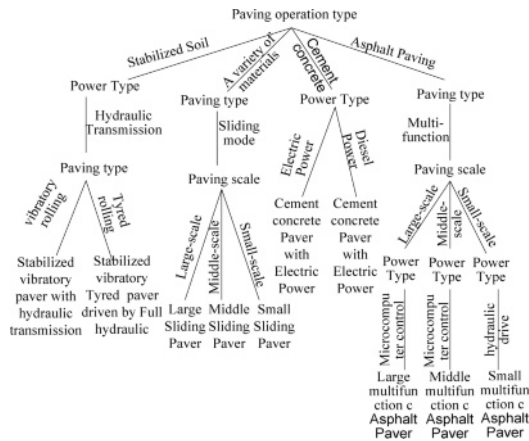


Fig. 3 FS-FSM of paver on sharing product platform

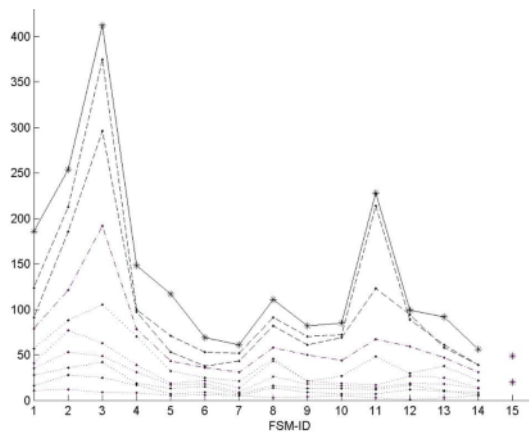


Fig. 4 Dynamic Clustering Analysis of Customized Customer's Requirements

1. Abscissa 1,3,5,9,10,11 show a clear upward trend in customer demand. It indicates these points, corresponding to FSMs with FSM_ID of 12, 13, 111, 123, 131, 132 in Table 1, are the current market leading products. To persistently implement rapid customization design, enterprises should analyze the FSM and suitably optimize product family models with a minimum of product variants to meet the current market customer demand.
2. Abscissa 7,12,13,14 show a slowly growth in customer needs. It indicates that those points, corresponding to FSMs with FSM_ID of 121,141,142,143 in Table 1, are not favoured by customers. Enterprises do not need to spend energy and time to redesign these FSMs to avoid increasing the customization design cost. If there are still only a very small number of customization customers of those FSMs after a considerable period of time, those FSMs can be considered as an individual module and cut off from FS-SKM.

3. In addition, at the moment there is a new customer clustering model FSM above the location of the horizontal axis 15, and it is quickly increasing as time goes by. When the FSM's customers continue to grow to a certain amount, enterprises can consider whether it is necessary to develop and design a new product family.

5. Conclusion and Future Work

This paper has proposed an innovative product family model of FS-SKM for reducing product family modeling workload. Instance study method upon ID3 algorithm is applied to generate FS-SKM at sharing product platform for SMEs. Considering the dynamic customer requirements as time goes on, a dynamic clustering algorithm of customer requirements is presented to provide optimization strategy of product family for SMEs. The proposed approaches have been successfully applied in construction machinery to help SMEs persistent implementation of rapid product customization.

In the future, product family configuration model, configuration method, and optimization algorithm will be investigated.

References

- [1] Yan Su, Wenhe Liao, YuGuo, (2009) Key Technologies for ASP-based Product Customization Service System for SMEs: a Case Study". the International Journal of Advanced Manufacturing Technology, 42(3-4):381-397,.
- [2] Yan Su, Wenhe Liao, Yu Guo, Shiwen Gao, Huibin Shi, (2008) An ASP-based Product Customization Service System for SMEs: a Case Study in Construction Machinery. International Journal of Enterprise Information Systems, 4(1):1-17
- [3] Mitchell M.Tseng, Jianxin Jiao, (1996) Design for mass customization[J]. Annals of the CIRP, 45(1): 153-156
- [4] Bei Yu, Jorgen Skovgaard, (1998) A cofiguration tool to increase product competitiveness[J]. IEEE Intelligent systems, 7/8: 34-39
- [5] Weiss S M, Ralston P R, (2000) An Efficient Easily Skeleton system for product design [M]. Newyork: Addison Wesley Pubishing Company
- [6] Zhongzhi Shi, (2006) Advanced Artificial Intelligence [M].Beijing: science press, 218-222
- [7] H Azzag, C Guinot, G Venturini, (2004) How to use ants for hierarchical clustering[C]. In Fourth International Workshop on Ant Colony Optimization and Swarm Intelligence, Brussels, Belgium, LNCS 3172: 350-357

Transparency in Production by Monitoring the Condition of Molds, Dies and Machines

R. Schmitt¹, M. Harding¹, A. Pavim^{1*}, Y. Cai¹

¹ Chair of Metrology and Quality Management, Laboratory for Machine Tools and Production Engineering, RWTH Aachen University, 52074 Aachen, Steinbachstr. 19, Germany, email: M.Harding@wzl.rwth-aachen.de

* Scholarship holder of the Brazilian CNPq

Abstract: Deep drawing and injection molding play an important role in industrial production processes for many products. For competitive processes, the availability is a major leverage. The approach described in this paper uses the application of sensors on molds, dies and machines to monitor the condition and thereby provide a basis for internal and external services such as condition based maintenance and an accelerated try-out period. Sensors that offer the metrological basis for condition based surveillance are available, but are not sufficiently deployed in production, yet. Research has to be done to investigate effective and efficient combinations of different sensors applied to the production systems. Within this approach the signals of sensors are combined to gather relevant information of the tools' and machines condition to increase the availability of the complete manufacturing system. For deep drawing and injection molding, relevant condition data can be gathered and transformed in continuative steps to valuable information and knowledge about the condition to improve the availability of the analysed manufacturing processes.

Keywords: Condition Monitoring; Product-Service-Systems; Sensors; Tool- and Die Making; Availability

1. Introduction

The tooling industry plays a key role within production industry as surveys show [1], [2], [3]. This is a result of the tooling industries position in the industrial value chain between product development and production and its responsibility in terms of time, costs and quality (Fig 1).

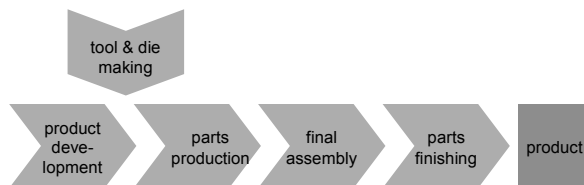


Fig 1. Position of tool and die making within the industrial value chain.

Increasing supply from Eastern Europe and Asia keeps the branch under pressure with an above-average decline in prices [4]. Plain differentiation in prices has not worked out in recent years. One solution to improve the competitive position is to increase the availability of the manufacturing system. Molds and dies severely influence the availability but the influence of the machinery like presses and injection molding machines should not be forgotten, as surveys show, the avoidance of downtime is one important goal which has to be achieved to improve the competitiveness [5].

2. Avoiding Downtime is Crucial

The main reasons for downtimes of presses for metal sheet forming are technical failures (Fig 2) [6]. The following example out of car body production illustrates the importance of avoidance of downtime. In May 2005 at a major automotive company several shifts with over 12.000 employees were affected and 2.000 cars could not be manufactured because of an unexpected downtime in one stamping plant [7].

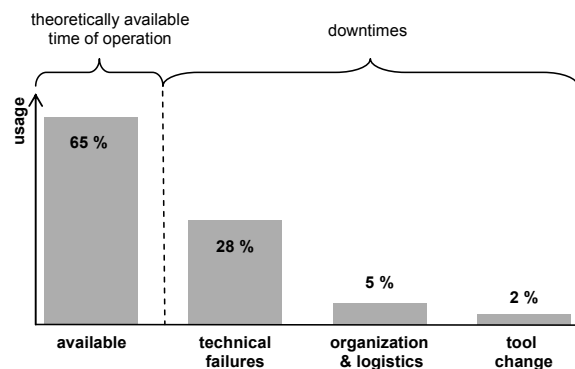


Fig 2. Reasons for down times of presses [6].

The metrological approach to increase the availability of the manufacturing system is to monitor the condition of key components. Damages can thus be detected before breakdown or the breakdown can even be avoided.

The impact of this approach increases even more if the condition monitoring serves as technological base for maintenance related services. These services extend the existing physical products with services, to a product-service-system with a higher value for the clients by targeting the following potentials [8], [9]:

- Reduction of downtimes caused by component wear out or failure.
- Scheduling maintenance measures to non-production times.
- Optimized spare parts management.

A main restraint for the services based on sensor information is the existing shortage of life cycle and process data, which is in general neither gathered nor communicated [2]. Only this feedback enables a learning production which is capable to persist in competitive markets.

3. Knowledge Feedback in Production

In production, knowledge can be acquired in various ways through production metrology. Production metrology's task is the acquisition of quality features of a measurement object. The typical measurement object is the work piece [10]. During and/or after manufacturing the specified inspection characteristics have to be checked. This inspection reduces the likeliness to deliver scrap parts to following process steps. Other objects can also be measurement devices or tools and machines in order to provide effective and efficient production processes; it is relevant to expand the focus of knowledge acquisition on the entire manufacturing chain [10]. Fig 3 shows the cycle of knowledge feedback in manufacturing.

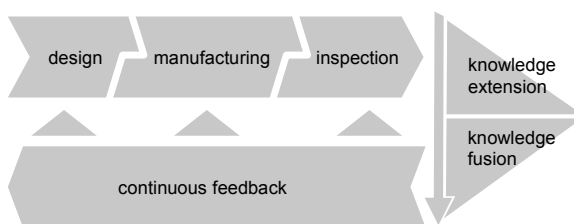


Fig 3. Knowledge feedback in production.

Therefore one relevant focus of knowledge acquisition in manufacturing is to ensure the availability of the production machines. Because the sources and also the forms of appearance of knowledge are various, it needs to be processed and evaluated to obtain a maximum benefit. Knowledge is context-sensitive and in particular dependent on the receiver. Therefore it needs to be processed and forwarded in a comprehensible manner.

Knowledge can be processed by extension and fusion, e.g. to key indicators, which make rapid access to the concentrated knowledge possible. The backward chain enables communication by a continuous knowledge feedback to the various steps of production and can therefore generate benefit by diverse measures. The acquired and processed knowledge can be applied to improve the production chain. This feedback of knowledge enables continuous learning processes in production [11].

4. Structured Procedure to Find the Influencing Factors for Availability

The metrological bases, e.g. robust and reliable sensors for an adequate monitoring of mechanical stresses and strains on the molds and dies or the acceleration and acoustic emissions of the moving components are available, but until now have been applied infrequently. There is a lack of studies on how to combine and fuse the knowledge gained by various sensors. But only a holistic approach, which combines the monitoring of all important influencing factors, allows conclusions about the condition of the manufacturing systems condition.

A structured approach to enable a reliable sensor selection is to identify the main influencing factors on the molds and dies availability systematically. Quality management provides various tools that can be used and adapted here. The used analyzing process consists of the sequential execution of tools already known in quality management (Fig 4). This process can be performed for example in one or several workshops with groups of experts. It is useful to run this process with all stakeholders separately and consolidate the results afterwards to obtain a transparent result.



Fig 4. Process of finding the main influencing variables.

In a first creative gathering, a group of experts discusses influencing factors. To achieve a more reliable result, all available information of the machinery and process has to be gathered and analyzed in advance. The result of this step is a list of influencing factors based on expert knowledge and the available information like maintenance reports. In the second step the influencing factors have to be prioritized. One appropriate tool is the pair wise comparison. This is a structured method to obtain a ranked list of the influencing factors. This is done by the pair wise weighting of the importance of each factor with the other factors [12]. In the third step a modified Quality Function Deployment (QFD) with its tool House of Quality is used to extract the disturbance variables which affect the availability. In general, QFD is

used to realize the customer’s wishes and quality specifications adequately [12], [13]. The central matrix in the House of Quality is used to find out the strengths of the relationship between disturbance variables and the influencing factors for the availability. The results of the QFD can be visualized clearly with the Pareto- or ABC-analysis which show the ranking of the disturbing variables and their cumulative percentage [13]. At this point, for each group of stakeholders a structured set of influencing factors on the availability and the corresponding disturbance variables exist. In the next step these have to be consolidated for each group of stakeholders. A good method is the Affinity Diagram. This is a tool to structure a confusing quantity of facts and ideas under topics to reach a clear structure and wording [13]. Based on the results of the steps before, an Ishikawa Diagram is drawn to visualize the relation between the causes and the availability of the analysed system.

5. Exemplary Discussion of Condition Monitoring Signals

Based on the described analysis the sensors for the condition monitoring can be selected and applied. Below the main objective, to increase the availability, two sub-objectives can be defined as follows:

- The reduction of time needed to optimize the mold or die try-out period.
- The reduction of downtime in production.

For both objectives, the procedures to deal with the sensor data in order to learn more about machinery and tools condition are equal. After the sensor selection and application on the dies and molds, process data has to be accumulated to define reference signals, a “digital finger print” of process, machine and tool. This is needed to reach reliable measurement data and to detect changes in process or condition with the sensors. The next step is the monitoring of the behavior in production to identify signal patterns of incidents. The exclusive use of test stands is not effective because the combination of real production influences heavily affect the measurement conditions. Therefore the analyzed acquisition of measurement data runs always parallel with the part production and real optimization processes.

The following sections deal with three examples for the impact of sensor application to determine the condition of the manufacturing systems for deep drawing and plastic injection molding in order improve the availability. For example at hydraulic presses the condition of the hydraulic oil is an important indicator of the machine state. The hydraulic process constantly induces ageing of the oil for example caused by shearing actions and liquid and solid contamination. The knowledge of the contamination allows initiating maintenance actions on time based on the real condition of the oil. The same applies on the long run to the temperature of components like

pumps and valves. Wear-out of valves and pumps results in friction which causes increasing temperature levels. Preliminary analysis of the sensor data indicates that the failure of some of the components is perceivable several days before. On the short run during undisturbed operation the temperature profile of these components varies little. But in case of some malfunction the temperature profile gets unstable and the level raises (Fig. 5). In this case one of the two parallel operating pumps which pump the hydraulic oil through the heat exchanger had a malfunction. Caused by the relatively low and constant charge of the press this malfunction didn’t influence the operation. Without the temperature sensors the malfunction would have been undetected for a longer time.

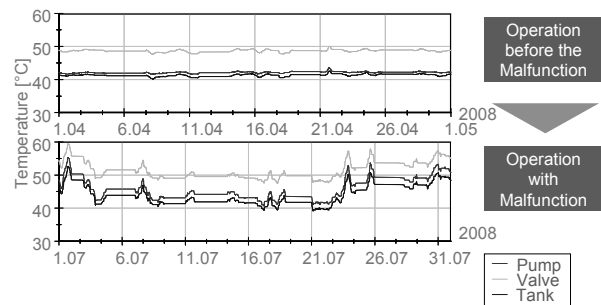


Fig 5. Temperature profile of the components of a hydraulic press during operation and operation with under malfunction

The current state of the art on optimization processes of deep drawing dies needs a lot of time, presses and highly skilled experts to reach production ready dies. This optimization process is not just part of the tool making process; often it is part of maintenance processes after severe technical failures, too. For deep drawing dies, the results show that sensors are capable to shorten the optimization period. With piezoelectric sensors applied on the die, it is possible to detect the stresses and strains on it caused by the metal forming process. Fig 6 shows the normalized signal of a piezoelectric force sensor applied on a blank holder.

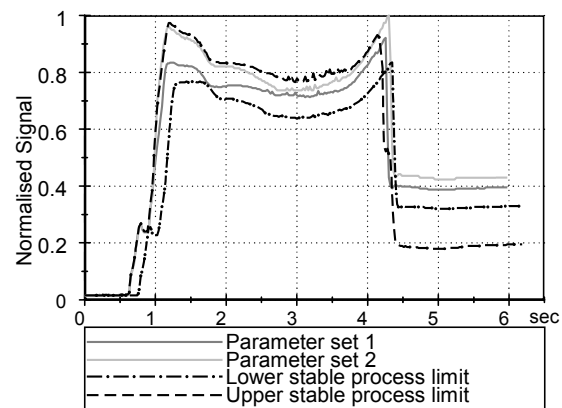


Fig 6. Fact based optimization of forming parameters during try-out.

Due to the size of the tools, it is possible to detect the differences between different locations on the dies component, e.g. the blank holder. The sensors enable a fact-based and therefore shortened optimization period. In the shown example the forming force is reduced between the parameter sets 1 and 2 to centre the forming process between the determined limits of a stable process.

For injection molding tools the results focus on sensors for the monitoring of components which have a strong influence on the availability. An early detection of uprising damages reduces the problem of unplanned downtime. This supports the producing company to reschedule production, plan maintenance actions and order spare parts. Even if a downtime cannot be avoided, a significant reduction is realistic with an early detection of incidents like cracks in heavy loaded components. Fig 7 shows the trend of the maximum and minimum peaks of a sensor which detects the deformation of a locking component of an injection mold. The constant trend of the peaks, which represents a constant deformation of the component during production changes at that time the crack appears. The crack allows a significant higher deformation of the locking component. In this case the initial crack doesn't affect the production process. It is possible to run the process at least some days with the damaged component. But due to the monitoring the producing company is able to reschedule the production and initiate maintenance operations well before the breakdown occurs.

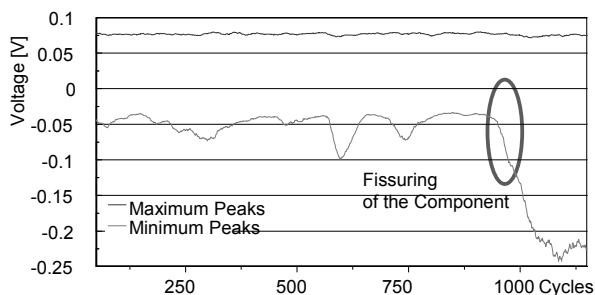


Fig 7. Detection of a crack in a locking component.

6. Summary

The availability of manufacturing is a key factor in competition for producing companies and the supplying tool and die makers. Condition monitoring of important components in combination with sensor based process monitoring enables effective and efficient maintenance measures reducing the unplanned downtime caused by technical failures. The base for a fitting sensor concept has to be a detailed analysis of the weak spots of the mold and dies concept. One feasible way to analyze the influencing factors uses the knowledge of experts to identify the relevant factors. The potential of condition monitoring on the availability of the determined systems has been exemplarily demonstrated.

Acknowledgements

The content is based on the research and development projects "Smart Stamping" and "TecPro" which are funded by the German Federal Ministry of Education and Research (BMBF) and managed by the Project Management Agency Karlsruhe (PTKA). Special thanks to the project partners from industry for their support during the project, especially during the series of measurements.

References

- [1] Cleveland, M., 2002, A Competitive Assessment of the Die and Mould Building Sector, Grand Rapids, Mi.: www.mbs-2003.org, 2005-08-01.
- [2] Holmes, J., Rutherford, T., Fitzgibbon, S., Innovation in the Automotive Tool, Die and Mould Industry, Wolfe, D., Lucas, M. (eds.), 2005, Network Structure of an Industrial Cluster, Queens University, Toronto: p. 119-154. 2005.
- [3] Menezes, J., European Mould Making: Towards a New Competitive Positioning, In: Proceedings of the 4th International Colloquium Tool and Die Making for the Future, September 28-29, Aachen, 2004.
- [4] Schuh, G. et al., Werkzeugbau in China - Chance oder Bedrohung, WZL study, RWTH Aachen University, 2005.
- [5] Schuh, G.; Kampker, A.; Franzkoch, B.; Wemhöner, N., Intelligent Maintenance – Potentiale zustandsorientierter Instandhaltung. ifm electronic GmbH, Essen, p. 6, 2005.
- [6] Bräunlich, H., Blecheinzugsregelung beim Tiefziehen mit Niederhalter – ein Beitrag zur Erhöhung der Prozessstabilität, Verl. Wiss. Scripten Zwickau, p. 19-20, 2002.
- [7] N.N., Historischer Defekt legt VW-Werk lahm, <http://www.manager-magazin.de/unternehmen/artikel/0,2828,357309,00.html>, 2005-05-24, 2005.
- [8] Roy, R., Evaluating PSS Business Models for Machine Tool Industry, in: Proceedings of the Transregio 29 International Seminar on PSS, January 21-22, Bochum, 2008.
- [9] Schuh, G.; Klotzbach, C.; Gaus, F., Designing services based on 'intelligent' press-die-systems, Advances in Life Cycle Engineering for Sustainable Manufacturing Businesses - Proceedings of the 14th CIRP Conference on Life Cycle Engineering June 11-13, Tokyo, 2007.
- [10] Pfeifer, T., Production Metrology, p. 1-2, 2002.
- [11] Aamodt, A., Nygård, M., Data & Knowledge Engineering, Vol. 16, p. 191-222, 1995.
- [12] Blank, H., et al., Qualitätsmanagement für Ingenieure, Springer, Berlin, p. 195, 2003.
- [13] Pfeifer, T., Qualitätsmanagement – Strategien – Methoden – Techniken, Hanser, München, p. 42, p. 313-320, 2002.
- [14] Schulte-Zurhausen, M., Organisation, Vahlen Verlag, München, p. 513-532, 2002.

Simulation Modelling of Product-Service Systems: the Missing Link

Sarocha Phumbua¹ and Benny Tjahjono²

¹ Manufacturing Department, School of Applied Sciences, Cranfield University, Cranfield MK43 0AL, UK
sarocha.phumbua@cranfield.ac.uk

² Manufacturing Department, School of Applied Sciences, Cranfield University, Cranfield MK43 0AL, UK
b.tjahjono@cranfield.ac.uk

Abstract. The Product-Service Systems (PSS) concept requires effective management of resources and supply networks in the long term which involve greater uncertainties than that in the production-based system commonly found in manufacturing companies. This calls for a tool capable of evaluating the impacts of the shift of the business strategy to tactical and operational levels to help firms make decisions. The demand signals between production-based systems and PSS are typically different due to the customer involvements in service activities after product selling. For this reason, existing decision making tools in the production-based context may not be capable to suitably model PSS businesses. Simulation techniques can be used prior to the physical design of complex systems that incorporate internal interactions between entities in supply networks. This paper explores the application of simulation modelling within the PSS context. The current state of simulation modelling of PSS is summarised and the simulation parameters typically used in PSS modelling are described. The analysis shows various shortcomings of work in the literature. Existing simulation modelling approaches should, in fact, be enhanced to address different levels and types of performance measures required in PSS.

Keywords: Product-Service System, Simulation, Modelling technique.

1. Introduction

A Product-Service System (PSS) is an integrated product and service offering that delivers value in use (Baines et al, 2007). The system typically consists of physical products and associated services to support the use of the products. Figure 1 illustrates the difference between traditional purchasing of product and the product-service buying. Traditionally, a customer buys a photocopier hence owns it. During operations of the photocopier the customer needs to maintain and supply the spare parts. In PSS business model, the customer buys the photocopy capability from that photocopier and pays only when using it. The ownership of the photocopier remains with the manufacturer. The manufacturer supplies the appropriate types of photocopier depending on the needs and requirements of the consumers. It is also the

manufacturer's responsibility to service the machine, supply the spare parts, repair and even dispose the photocopier at the end of its life.

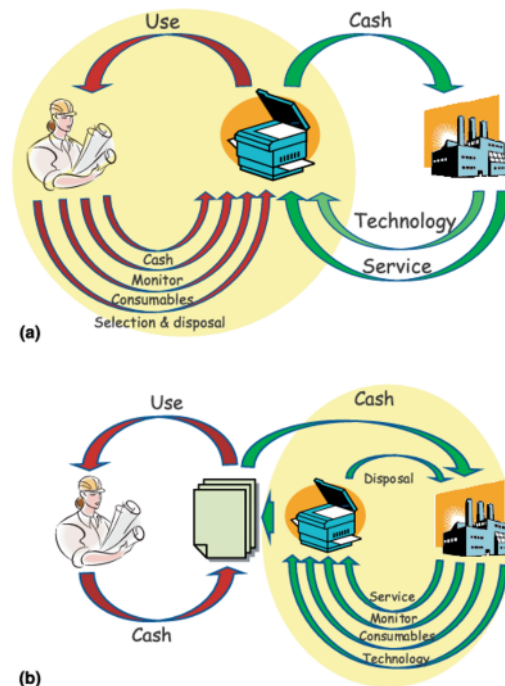


Fig. 1. (a) Traditional purchase of photocopier; (b) purchase of product-service bundle (Baines et al, 2007).

The complexity of modelling PSS can be higher than the traditional production-based system due to several issues. First of all, the demand signal in the PSS business depends on data from the asset (Baines et al, 2009) and customer involvement during the use phase (De Coster, 2008). These factors complicate the forecasting process. Prior to the design process, designers are faced with challenges to design for the whole product lifecycle and

infrastructure (Azarenko et al, 2007) instead of only a single production system. Designers need to take in account interactions between other stakeholders in the supply network. For this reason, traditional production-based design methodology is not appropriate for application in the PSS context (Weber et al, 2004). A dynamic simulation modelling tool is often required to handle these complexities which are greater and different in nature from that of the production-based system. From the PSS viewpoint, simulation modelling is a powerful tool to exploit when investigating the transformation from product-selling organisation to PSS organisation. This paper therefore explores the current state of simulation modelling of PSS.

A number of modelling techniques of PSS already exist in PSS literature. This paper sets out to investigate these techniques and each model's objectives, (in Sections 2 and 3). Parameters of the simulation models found in the PSS literature are summarised in Section 4. Gaps in the current simulation modelling of PSS and opportunities for future research are described in Section 5.

2. Modelling in PSS and its purpose

In this paper, a model is defined as a representation of the system under study, and simulation is concerned with a technique of studying the system's dynamic behaviours. Thus, simulation and modelling can be used to gain insights into the impacts of variables on the entire system and so to predict the likely performance of the system. This section examines existing literature in order to understand the extent to which the models can be used in the PSS context.

Since the PSS concept is relatively young, a modelling method is essential to design it. Several attempts have been made to establish guidelines and open platforms, such as the MEPSS project to provide structures for PSS implementation (Tukker and Tischner, 2004). By considering a system as a combination of product, service, and actor elements, the modelling approach can be initiated from three perspectives. First, a system is modelled based on product or system lifecycle, in which the associated activities, services and actors are added to. The second approach considers flows of service processes and activities, and often assumes that the system can be designed by separating the service component from the product component. The last group views entities as objects in the whole network, which can include products, services, actors, or combinations of them, and defines the interaction between these objects.

Fujimoto et al (2003) and Aurich et al (2006) followed the first approach. Fujimoto et al (2003) divided a model into lifecycle process, product and user sub-models. A network of process such as manufacturing, operation, recycling, and remanufacturing was first represented. The product model consisted of modules

modelled by sets of attributes whilst the user model allocated customers according to types of packages and their behaviours. The paper evaluated the economics and environmental impacts of the proposed offering against other business models. Aurich et al (2006) separated product design activities from service design activities. The inputs and outputs of the processes were first captured then the tasks in each process module that depend on similar resources or could be performed simultaneously were joined to form the product-service integration.

The second approach was adopted by Morelli (2002) and Alonso-Rasgado et al (2004). Both applied the service blueprinting technique developed by Shostack (1982) in an attempt to model service operations. The flow of activities in a system was modelled and separated by the line of visibility to customers. Morelli (2002) designed a specific solution for PSS whereas Alonso-Rasgado et al (2004) developed general methodologies to design their solutions.

The majority of publications applied a third approach, and most of the workers in this group developed techniques to design PSS. The exception is Evans et al (2007) who applied solution maps to design a supply network resulting in a higher level of sustainability benefit. The rest of this group applied service modelling techniques (e.g. Morelli, 2006; Hara et al, 2009; Sakao and Shimomura, 2007; Komoto and Tomiyama, 2008), and ontological representation (e.g. Kim et al, 2009). The models obtained from the PSS literature mostly require further development. In addition, existing tools, such as the Service Explorer, include implicit evaluation the dynamic system

3. Simulation in PSS

This section discusses the simulation of PSS focussing on the usability and applicability of the techniques.

Simulation has been used to improve efficiency, reduce costs, and increase profitability in both manufacturing and service sectors (Robinson, 1994). The technique has benefits over other analytical methods due to its dynamic evaluation feature, which allows 'what-if' analyses to be made prior to the changes of requirements.

Publications on the simulation of PSS typically cover techniques such as discrete-event simulation (DES), agent-based simulation (ABS), and system dynamics (SD). Within the DES, Alonso-Rasgado et al (2004) programmed a list of events in a service support system, whereas Fujimoto et al (2003) and Komoto et al (2005, 2008) simulated PSS using a Life Cycle Simulator (LCS). The LCS simulated stochastic behaviours of component lifetime distribution and dynamic changes of behaviours of actors. Actions performed by actors were described as events and triggered in the product lifecycle and allowed economical and environmental impacts to be calculated based on the occurrence of these event.

The model of Komoto et al (2005) was developed from a set of PSS objects: service, service provider, service receiver, PSS events and product, linked together to form transitions. The events consisted of generation and elimination, deterioration and recovery, whilst the product element comprised operation-critical modules and lifetime-critical modules. Descriptions on state change were programmed. Later, Komoto and Tomiyama (2008) proposed a service CAD tool to integrate and generate scenarios.

Unlike DES, ABS models interactions between agents rather than flows of processes. Buxton et al (2006) used the AnyLogic package to examine dynamic behaviour of a market and assessed the agent's performance in the context of an aero-engine value chain business environment. These agents included the marketplace, the OEM and the engines themselves. The model incorporated all activities during the whole lifecycle of the engines. The run time of fifty years provided long term implications of strategic decisions taken earlier.

Bianchi et al (2009) investigated the transition from a product-oriented manufacturer to a PSS provider. Success and failure factors were captured using qualitative SD but then modelled them quantitatively using Repast. Product-oriented manufacturers and PSS providers were represented as stocks, whilst transition to PSS rate and fail rate were denoted as flows. The rate of the transition was investigated.

4. Factor analysis

The input and output parameters corresponding to the simulation models obtained from the literature are described below. By considering a system consisting of product and service elements, the input parameters can be recognised as properties attached to those elements. Some factors, that cannot be segmented as a product (P) or service (S) related, are categorised as system (SYS). The combination of these parameters results in the model's outputs (O).

Fujimoto et al (2003) **P**: price, product development cycle, failure change rate, weight, material, lifetime, recyclability, process energy, process costs. **S**: monthly fee, collection rate, product change fee. **O**: waste amount, energy assumption, revenue, profit.

Alonso-Rasgado (2004) **S**: time taken to perform the service. **SYS**: the quality and flow of information. **O**: performance level (functional reliability), resource level.

Komoto et al (2005) **P**: module and process costs, lifetime, wear out time, capacity, failure rate, price, reparability, reusability. **S**: activity costs, service fee. **SYS**: number of operations, usage rate **O**: total cost, occurrence of PSS event.

Buxton et al, (2006) **P**: engine flight hours, engine flight cycles. **S**: customer characteristics. **SYS**: sales frequency, volumes, usage characteristics **O**: break even point, net present value, cash flow.

Komoto and Tomiyama (2008) **P**: lifetime, rate of failure occurrence, market size, interval of function release, newness, functionality. **S**: preference of user to service type. **SYS**: duration **O**: life cycle cost.

Bianchi et al, (2009) **SYS**: initial members, aptitude to PSS transition, disappointed with PSS, barriers to PSS, intensity and duration of incentives, first time of activation. **O**: number of product-oriented manufacturers, number of PSS providers.

It can be seen that a high variety exists in input parameters. Product's lifetime, process cost, failure rate and price can be found repetitively in the product element. Only a few of the service inputs have been found in relation to product inputs. However, Bianchi et al (2009) shifted their focus towards top business level, rather than operational level. In all, the measures can be classified as being economical, environmental, financial, and operational. Still, the majority are at the operational level, except those from Bianchi et al (2009) and Buxton et al (2006). In other words, the DES models are interested in the detail level of abstraction whilst those of SD and ABS look at high level abstraction.

5. Discussion and conclusions

This paper investigates the current state of simulation modelling of PSS. Relevant PSS literature has been identified and thoroughly analysed. Input and output parameters have been captured to enable factor analysis. The results reveal several shortcomings in this area.

First of all, the use of visual and interactive simulation tools in PSS modelling is still limited. This function can enhance understanding of the model and the results, improve communication between parties, and simplify model validation and experimentation. Service Explorer, Repast, and AnyLogic could support this but Service Explorer shows no explicit means to handle the dynamic nature of PSS quantitatively. Although LCS can evaluate dynamic performance, it is based on a pre-defined set of rules. Consequently, it may not be efficient to cope with emergent behaviours of multiple the actors typically found in the PSS environment.

Another shortcoming concerns the performance measures. No single model allows different level of measures (operational, tactical and strategic) to be assessed and furthermore no service measure has been addressed. In addition, the main focus of input parameters still relies on the product in comparison with the service element. Simulation models for the availability/capability contracts are also lacking.

Despite the presence of hybrid simulation in manufacturing and service organisations, very few that can be found in the PSS domain include different hierarchies in decision making. Also, there is no clear source that compares different simulation techniques (SD, DES and ABS) in terms of suitability to PSS.

The shortcomings in simulation modelling of PSS literature open up opportunities for future research. To this end, a multilevel evaluation simulation model in which a focus is shifted from product-based systems will be developed. This should significantly contribute to the development in this area.

References

- Alonso-Rasgado T, Thompson G, Elfström B-O, (2004) The design of functional (total care) products: *Journal of Engineering Design*. 15: 515-540
- Aurich JC, Fuchs C, Wagenknecht C, (2006) Life cycle oriented design of technical Product-Service Systems: *Journal of Cleaner Production*. 14: 1480-1494
- Azarenko A, Roy R, Shore P, Shehab E, Tiwari A, (2007) Technical Product-Service Systems: Business Models for High Precision Machine Tool Manufacturers: *Proceedings of the 5th International Conference on Manufacturing Research (ICMR2007)*. Leicester
- Baines TS, Lightfoot HW, Evans S, Neely A, Greenough R, Peppard J, Roy R, Shehab E, Braganza A, Tiwari A, Alcock JR, Angus JP, Bastil M, Cousens A, Irving P, Johnson M, Kingston J, Lockett H, Martinez V, Michele P, Tranfield D, Walton IM, Wilson H, (2007) State-of-the-art in the product-service systems: *Journal of Engineering Manufacture*. 221: 1543-1552
- Baines TS, Lightfoot HW, Kay JM, (2009) Servitized manufacture: practical challenges of delivering integrated products and services: *Journal of Engineering Manufacture*. 223: 1207-1215
- Bianchi NP, Evans S, Revetria R, Tonelli F, (2009) Influencing Factors of Successful Transitions towards Product-Service Systems: a Simulation Approach: *International Journal of Mathematics and Computers in Simulation*. 3:30-43
- Buxton D, Farr R, McCarthy B, (2006) The aero engine value chain under future business environment: using agent-based simulation to understand dynamic behaviour: *MITIP2006*. Budapest
- De Coster R, (2008) Differences in forecasting approaches between product firms and product-service systems (PSS): *The 6th International Conference on Manufacturing Research (ICMR08)*. Brunel university. 539-547
- Evans S, Partidario PJ, Lambert L, (2007) Industrialization as a key element of sustainable product-service solutions: *International Journal of Production Research*. 45: 4225-4246
- Fujimoto J, Umeda Y, Tamura T, Tomiyama T, Kimura F, (2003) Development of Service-Oriented Products Based on the Inverse Manufacturing Concept: *Environmental Sciences & Technology*. 37: 5398-5406
- Hara T, Arai T, Shimomura T, (2009) A Method to Analyse PSS from the Viewpoints of Function, Service Activity, and Product Behaviour: *CIRP IPS2 Conference 2009*. Cranfield
- Kim YS, Wang E, Lee SW, Cho YC, (2009) A Product-Service System Representation and its Application in a Concept Design Scenario: *CIRP IPS2 Conference 2009*. Cranfield
- Komoto H, Tomiyama T, Nagel M, Silvester S, Brezet H, (2005) Life Cycle Simulation for Analyzing Product Service Systems: The Fourth International Symposium on Environmentally Conscious Design and Inverse Manufacturing. 386-393
- Komoto H, Tomiyama T, (2008) Integration of a service CAD and a life cycle simulator: *CIRP Annals - Manufacturing Technology*. 57: 9-12
- Morelli N, (2002) Product-service systems, a perspective shift for designers: A case study: the design of a telecentre: *Design Studies*. 24: 73-99
- Morelli N, (2006) Developing new product service systems (PSS); methodologies and operational tools: *Journal of Cleaner Production*. 14: 1495-1501
- Robinson S, (1994) *Successful simulation: a practical approach to simulation projects*: McGraw-Hill. Maidenhead
- Sakao T, Shimomura Y, (2007) Service Engineering: a novel engineering discipline for producers to increase value combining service and product: *Journal of Cleaner Production*. 15: 390-604
- Shostack GL, (1982) How to design a service: *European Journal of Marketing*. 12: 49-63
- Tukker A, Tischner U, (2004) *New Business for Old Europe: Final report of SUSPRONET*.
- Weber C, Steinbach M, Botta C, Deubel T, (2004) Modelling of Product-Service Systems (PSS) Based on the PDD Approach: *International Design Conference- Design, Dubrovnik*

RFID Deployment at an Airport: A Simulation Study

Can Saygin¹ and Balaji Natarajan

The University of Texas at San Antonio (UTSA), Mechanical Engineering Department, San Antonio, Texas 78249, USA

¹ Corresponding author (can.saygin@utsa.edu)

Abstract. In this paper, the impact of radio frequency identification (RFID) deployment at an airport baggage handling system is investigated. The impact of number of RFID readers at different power levels with varying conveyor (i.e., baggage handling conveyors) speeds on timely delivery of baggage is studied via a simulation. Unlike typical simulation studies related to RFID deployment where any read-rate issues are often ignored, this study captures read rate in a realistic manner in the simulation model by incorporating the effect of 1) number of RFID tags in the interrogation zone, and 2) time that RFID tags spend in the interrogation zone. The layout of the baggage handling system (BHS) at the Hong Kong International Airport and data pertinent to its RFID deployment in 2005 are used to build the simulation model. The study shows that operational visibility to manage timely arrival of bags at their gates can only be obtained by finding the right combination of number of readers, reader power levels, and conveyor speed, not by operating with the highest possible number of readers for maximum read rate at the fastest conveyor speed for maximum throughput.

Keywords: radio frequency identification (RFID), baggage handling systems, tracking and tracing using RFID.

1. Introduction

Radio frequency identification (RFID) technology enables electronic labeling and wireless identification of entities, which facilitates visibility by providing real-time data on location and time. A typical RFID system consists of three components: (1) An electronic data carrying device, called a transponder or tag, (2) Antennas and readers that facilitate tag interrogation, and (3) Software, called middleware, that controls the RFID equipment, manages the RFID data, and distributes information to other remote data processing systems by interfacing with enterprise applications. An RFID system can be considered a wireless communication system since the reader communicates with the tags by using electromagnetic waves at radio frequencies. RFID systems can be categorized as active and passive systems. In an active system, the tag (i.e., active RFID tag) has its own power source, which is a battery, enclosed in the transponder housing. In a passive system, the tag does not

have its own power source; instead it draws power from the reader's radio signals. Passive tags are inexpensive compared with active tags.

2. Literature Review

From tracking-only applications to complex tracing implementations, there are numerous areas, such as manufacturing, logistics, healthcare, or baggage handling as in the case of this paper, which can benefit from RFID (Brewer, Sloan, and Landers, 1999; Lee, Cheng, and Leung, 2004; Michael and McCathie, 2005; Mills-Harris, Soylemezoglu, and Saygin, 2007; Saygin, Sarangapani, and Grasman, 2007; Buyurgan et al. 2009). For an extensive review of RFID-related literature, please refer to Chao, Yang, and Jen (2007) and Ngai et al. (2008).

The commercial aviation industry is another area of application for RFID deployment. Specific applications include baggage handling systems (BHS), airport security, passenger check-in and tracking, and airport equipment maintenance. Ouyang et al. (2008) present an RFID reader design and its application for BHS. As a part of a larger European project (EU FP-6 program), McCoy, Bullock, and Brennan (2005) investigate an automatic tracking system for luggage and passengers, along with its system protocols, to improve airport efficiency and security using RFID technologies. A similar study was presented by Wyld, Jones, and Totten (2005), which examines the use of RFID in airport BHS and security. In their paper, Wong et al. (2006) discuss the impact of radiated emission from RFID systems used at the Hong Kong International Airport.

Read-rate is the ratio of the number of tags that are read over the total number of tags in the interrogation zone of an RFID reader antenna. Read-rates are affected by frequency interference and tag interference, under a common definition of reader collision, which occurs when multiple readers are deployed in a working environment; signals from one reader may reach others

and cause interference (Yu, 2003; Han, Li, and Min, 2004; Cha et al., 2006). Frequency interference occurs when readers operating in the same frequency channel introduce high noise levels at each other and jam the on-going communication with tags. Tag interference occurs when tags are being read by multiple readers simultaneously regardless of the differences in frequency. When tags are located too close to each other and/or interfering with the content of the entity that they are located on, such as water or metal surfaces, tag collision occurs. Another factor is tag congestion, which occurs with too many tags in the interrogation zone not staying there long enough for the reader to identify all of them.

In this study, reader collision (frequency and tag interference) is avoided by not allowing the interrogation zones of readers to physically overlap. Tag collision is assumed to be resolved during the “tag / baggage compatibility” phase of the design process, therefore no tag collision occurs. Tag congestion, however, is a function of conveyor speed, number of bags in the interrogation zone, and range of the interrogation zone, which is the scope of this paper.

3. Airport Baggage Handling Systems

When baggage on a belt conveyor is sorted using bar code labels, the bar code reader must be able to precisely locate and read the baggage tag. The “line of sight” requirement of barcode systems makes RFID a feasible alternative to baggage tracking since RFID does not require line of sight. However, as it is discussed in Section 2, RFID systems are potentially prone to lower read rates due to many factors that affect the operating range including tag orientation, overlap with other tags, environmental noise, absorption, reflection, shadowing, interference, and the effects caused by the presence of metallic material, etc.

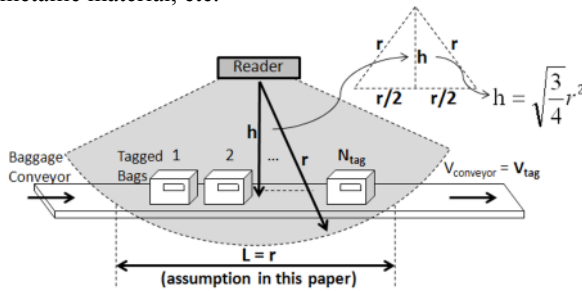


Fig 1. Read range of a reader

In an airport BHS, the main operational objective is to ensure that checked bags are transported without much human intervention to the gates in a timely manner for loading on the airplane. Therefore, reliable and timely identification of baggage is the key to achieving the main operational objective.

In a BHS that uses passive RFID tags, RFID readers need to access and identify tagged bags moving on

conveyors. The formulas used in this study (described in this section) are adopted from the ISO/IEC Technical Report #18001 (2004). The parameters are shown in Figure 1.

The communication time, T_C , between a reader and a tag can be estimated, not considering the internal processing time of both the reader and tag, as follows:

$$T_C = \frac{D_C}{D_r} \times A_{CN} \quad (1)$$

D_r is data transmission rate (bps) and D_C is data capacity of communications (bit). A_{CN} is the number (count) of reads between the reader and the tag. For instance, if a tag is required to be identified twice while in the interrogation zone, then the value of A_{CN} is two.

While in the interrogation zone of a reader, a tagged bag moves a distance of L on the conveyor at a speed of V_{tag} , which is the speed of the conveyor. Therefore, the time a tag remains in the interrogation zone of a reader, T_R , can be calculated as follows:

$$T_R = \frac{L}{V_{tag}} \quad (2)$$

An RFID reader also requires a certain amount of time to detect a tag, T_{det} , in its interrogation zone before identifying the tag. Therefore, the total time needed by a reader to detect the existence of a tag and identifying the tag is simply $T_C + T_{det}$. Hence, this requirement can be combined with Eqn 2:

$$T_R = \frac{L}{V_{tag}} \geq T_C + T_{det} \quad (3)$$

When there are multiple tagged bags, N_{tag} , on the conveyor line in the interrogation zone of a reader, then the total time required to access all the tags can be calculated as follows:

$$T_R \geq (T_C + T_{det}) \times N_{tag} \quad (4)$$

Read range is dependent on the transmitter power output of the reader and in the case of passive tags, on the energizing requirements of the tags. Tag size plays a major role in determining read range. The smaller the tag, the smaller the energy-capture area, therefore the shorter the read range. For a given power setting of a reader and a tag, the read range, r , can be defined as follows according to the Friis free-space equation (Friis, 1946):

$$r = \frac{\lambda}{4\pi} \sqrt{\frac{P_t G_t G_r \tau}{P_{th}}} \quad (5)$$

where λ is the wavelength, P_t is the power transmitted by the reader (Watts), G_t is the gain of the transmitting (reader) antenna (dBi), G_r is the gain of the receiving (tag) antenna (dBi), P_{th} is the threshold power (Watts) to activate the tag, and τ is the power transmission coefficient that ranges between 0 and 1. The Friis free-

space model basically represents the communication range as a circle around the reader. If a tag is within the circle, it is detected by the reader. Otherwise, the tag is not detected.

4. Simulation Model

With an annual passenger throughput of over 40 million in 2008, Hong Kong International Airport (HKIA) is one of the world's busiest airports. The total length of the conveyor system used in HKIA's baggage handling system is 24 kilometers, which includes a combination of 109 straight and 12 circulating conveyors.

Rockwell's ARENA simulation package was used to develop a simulation model of HKIA's baggage handling system. Similar to the actual operation at HKIA, circulating conveyors are used for bags that have not been identified on straight conveyors. If a bag is still not identified after making three loops at a circulating conveyor, then it is sent to the manual recovery conveyor to be identified manually.

Three factors and three levels for each factor (i.e., 27 combinations) are selected in this study:

No. of RFID reader antennas: 121, 145, and 254

Power setting on each reader: 2, 3, and 4 Watts

Conveyor speed: 2, 3, and 5 m/sec (equal to V_{tag})

These factors and their levels yield a combination of 27 scenarios. The minimum number of RFID reader antennas is 121 since each one of the 109 straight and 12 circulating conveyors requires at least 1 reader. The second level of number of readers is 145, which includes a reader for each straight conveyor and 3 readers on circulating conveyors ($3 \times 12 = 36$). Finally, 254 readers include 2 readers on each straight ($2 \times 109 = 218$) and 3 readers on circulating conveyors.

Three performance measures are used to benchmark the performance on 27 scenarios in order to investigate the impact of the levels of each factor:

Effectiveness Ratio (ER): Effectiveness ratio is the main operational performance measure in the airport baggage handling system. It is the ratio of the total number of bags reaching their gates to the total number of checked bags.

Average Travel Time (ATT): It is the average time a bag spends in the baggage handling system and successfully makes it to its gate.

Utilization Rate (UR) of Manual Recovery Station: Utilization of the manual recovery station is the ratio of the busy hours identifying bags to the total number of available hours, which is 18 hours per day. Utilization rate shows the level of human intervention in the identification process.

Table 1. Simulation Results (Average of 8 replications)

Scenario*	ER (%)	ATT (min)	UR (%)
2P 2S 121R	88.0	36.4	40.8
2P 2S 145R	89.4	49.5	39.1
2P 2S 254R	91.4	54.4	38.0
2P 3S 121R	82.5	61.8	49.2
2P 3S 145R	94.8	67.2	45.4
2P 3S 254R	97.1	64.1	44.4
2P 5S 121R	86.3	56.2	50.7
2P 5S 145R	93.2	68.2	46.2
2P 5S 254R	96.1	65.9	49.3
3P 2S 121R	90.1	29.3	38.1
3P 2S 145R	93.0	38.2	35.7
3P 2S 254R	97.8	42.3	34.1
3P 3S 121R	88.3	51.7	43.9
3P 3S 145R	99.1	54.7	39.4
3P 3S 254R	98.8	51.6	38.0
3P 5S 121R	89.7	50.7	47.9
3P 5S 145R	97.5	51.3	39.3
3P 5S 254R	98.7	50.1	38.1
4P 2S 121R	92.6	24.5	33.8
4P 2S 145R	93.7	31.7	34.2
4P 2S 254R	97.9	38.5	33.9
4P 3S 121R	90.4	37.3	34.5
4P 3S 145R	99.3	40.9	35.6
4P 3S 254R	99.8	44.0	34.8
4P 5S 121R	91.4	43.0	37.7
4P 5S 145R	97.5	34.8	37.3
4P 5S 254R	99.8	42.5	36.6

*P: Power, S: Conveyor Speed, R: Number of Reader Antennas

5. Simulation Results

The simulation results, in terms of the three performance measures, are shown in Table 1. The scenario with the lowest setting is 2P-2S-121R (P: Power, S: Conveyor Speed, R: Number of Reader Antennas), which yields ER = 88% (i.e., 4,800 bags out of 40,000 bags/day do not make it to the gates on time), ATT = 36.4 minutes, and UR = 40.8%. 2P-2S-121R is not a viable option. The performance of 2P-3S-121R is worse than 2P-2S-121R: ER = 82.5%, ATT = 61.8 minutes, and UR = 49.2%. Running the conveyor at 3 m/sec, as opposed to 2 m/sec, has an adverse effect on identification of bags via RFID. Both ATT and UR are higher, which means more bags spend time in the circulation conveyor, as well as on the manual recovery station. Increasing the power level from 2 to 3, which is the scenario 3P-2S-121, slightly improves the performance: ER = 90.1%, ATT = 29.3 minutes, and UR = 38.1%.

The scenario with the highest setting is 4P-5S-254R, which yields ER = 99.8% (i.e., only 80 bags out of 40,000 bags/day do not make it to the gates on time), ATT = 42.5 minutes, and UR = 36.6%. Although 4P-5S-254R seems to be the obvious solution, it is critical to investigate other options with slower conveyor speeds and fewer number of reader antennas. The statistical analysis of the scenarios 4P_5S_254R, 4P_3S_254R,

4P_3S_145R, 3P_3S_145R, 3P_3S_254R, and 3P_5S_254R shows that in terms of the difference in ER values, these scenarios are statistically not different. Therefore, the scenarios with $98.7 < ER < 99.8$ are possible alternatives to 4P-5S-254. For instance, 4P-3S-254R shows that bags spend slightly more time (ATT = 44 min) on the conveyor (since the conveyor speed is slower) and the manual recovery station is utilized slightly less (UR = 34.8%) since more bags are identified on the conveyors; probably due to the slower conveyor speed, the reader antennas were able to identify these bags while they were on the straight conveyors.

Due to maintenance and possible interference reasons and to keep the system as reliable as possible, it is advantageous to reduce the number of antennas without losing much performance. 3P-3S-145R shows similar performance characteristics as 4P-5S-254R, at a lower power setting, slower conveyor speed, and with 109 fewer reader antennas. The difference in ER of both scenarios is only 0.7%.

In general, different combinations of levels of each factor can yield similar ER values. The scenarios 2P-5S-145R and 4P-2S-145R have ER of 93.2% and 93.7%, respectively. In 2P-5S-145R, low power level (P=2) and high conveyor speed (S=5) make it difficult to identify bags on straight conveyors. This deficiency is compensated by utilizing the circulating conveyors and the manual recovery station. Therefore, high ER level is maintained through identifying bags on circulating conveyors (ATT = 68.2 min) and at manual recovery station (UR = 46.2%); in other words, bags spend more time in the BHS. When the conveyor speed is reduced to 2S (i.e., tags move slower in interrogation zones) and the power level is increased to 4P (i.e., larger interrogation zones), the scenario 4P-2S-145R has an improved capability to identify bags on straight conveyors, which is shown by reduced ATT of 31.7 minutes and reduced UR of 34.2%. In other words, although both scenarios yield almost the same ER value, 4P-2S-145R has additional benefits.

6. Conclusions

The identification capability of the BHS studied in this paper is a result of its ability to identify tags via RFID technology on straight and circulating conveyors, as well as at the manual recovery station for the bags missed on conveyors. Overall, the effectiveness ratio increases as the identification capability increases. However, identification on circulating conveyors adds to the travel time and identification at manual recovery station adds to its utilization rate. Therefore, ideally, the objective is to achieve the highest effectiveness ratio (ER) with the shortest average travel time (ATT) and the lowest utilization rate (UR) at the manual recovery station. The controllable factors that affect the identification capability are (1) the conveyor speed, which determines the time a

tag stays in the interrogation zone, (2) the reader antenna power level, which determines the size of the interrogation zone, and (3) the number of reader antennas in the system that increases the likelihood of not missing tags. Hence, the simulation data must be analyzed from this perspective.

References

- Buyurgan N, Hardgrave BC, Baylor JL, Walker RT, (2009) RFID in healthcare: a framework for uses and opportunities. *International Journal of Advanced Pervasive and Ubiquitous Computing* 1(1):1-25.
- Cha K, Zawonniok M, Ramachandran A, Sarangapani J, Saygin C, (2006) Interference mitigation and read-rate improvement in RFID-based network-centric environments. *Journal of Sensor Review* 26(4):318-325.
- Chao, C-C, Yang J-M, and Jen W-Y, (2007) Determining technology trends and forecast of RFID by historical review and bibliometric analysis from 1991 to 2005. *Technovation* 27(5):268-279.
- Friis HT, (1946) A note on a simple transmission formula. *Proceedings of the Institute of Radio Engineers (IRE) and Wave and Electrons* 34:254-256.
- ISO/IEC TR 18001 Technical Report (2004) Information technology, automatic identification and data capture techniques - radio frequency identification (RFID) for item management: application requirements profiles. The International Organization for Standardization and the International Electrotechnical Commission.
- Lee YM, Cheng F, Leung YT, (2004) Exploring the impact of RFID on supply chain dynamics. *Proceedings of the 2004 Winter Simulation Conference* 2:1145-1152.
- McCoy T, Bullock RJ, and Brennan PV, (2005) RFID for airport security and efficiency. IEE Seminar on (Ref. No. 2005/11108) *Signal Processing Solutions for Homeland Security*.
- Michael K, McCathie L, (11-13 July 2005) The pros and cons of RFID in supply chain management. *Proceedings of the International Conference on Mobile Business* 623 – 629.
- Mills-Harris MD, Soylemezoglu A, and Saygin C, (2007) Adaptive inventory management using RFID data. *International Journal of Advanced Manufacturing Technology* 32:1045-1051.
- Ngai EWT, Moon KKL, Riggins FJ, and Yi CY, (2008) RFID research: an academic literature review (1995-2005) and future research directions. *International Journal of Production Economics* 112(2):510-520.
- Y, Hou Y, Pang L, Wang D, and Xiong Z, (2008) An intelligent RFID reader and its application in airport baggage handling system. *4th International Conference on Wireless Communications, Networking and Mobile Computing*.
- Saygin C, Sarangapani J, and Grasman SE, (2007) A systems approach to viable RFID implementation in the supply chain. *Trends in Supply Chain Design and Management: Technologies and Methodologies* (Editors: Hosang Jung, F. Frank Chen, and Bongju Jeong) Springer 3-27.
- Wong YF, Wu PWK, Wong DMH, Chan DYK, Fung, LC, and Leung SW, (2006) "RFI assessment on human safety of RFID system at Hong Kong International Airport. *Proceedings of the 17th International Zurich Symposium on Electromagnetic Compatibility*.
- Wyld DC, Jones MA, Totten JW, (2005) Where is my suitcase? RFID and airline customer service. *Marketing Intelligence and Planning* 23(4):382-394.

Failure knowledge based decision-making in product quality

W. Dai^{1,2}, P.G. Maropoulos² and X.Q. Tang¹

¹ School of Mechanical Engineering and Automation, Beihang University, Beijing, 100191, P.R. China

² Department of Mechanical Engineering, University of Bath, Bath, BA2 7AY, United Kingdom

Abstract. Decision-making in product quality is indispensable in order to keep product development at the lowest risk. Based on discussion of the deficiencies of Quality Function Deployment (QFD) and Failure Modes and Effects Analysis (FMEA), a novel decision-making method is presented concentrated on the knowledge network of failure scenarios. An ontological expression of failure scenario is presented together with a framework of failure knowledge network (FKN). A case study is provided according to the proposed decision-making procedure based on FKN. This methodology is applied in the Measurement Assisted Assembly (MAA) process to solve the problem of prioritizing measurement characteristics. A mathematical model and algorithms of Analytic Network Process (ANP) are introduced into calculating the priority of manufacturing characteristics. Therefore, this study provides a practical approach for decision-making in product quality.

Keywords: Decision-making in product quality, Failure knowledge network, Decision-making model, Analytic network process

1. Introduction

The inner and outer environments where the products are being designed and developed are complex and variable. Within such creative and uncertain surroundings, potential risks can never be fully avoided or mitigated [1]. Risk assessments are required at critical decision-making points to keep product development at the lowest risk. Traditionally, this decision-making process is implemented qualitatively by subject matter experts. Among the numerous research papers available in manufacturing system and process planning, most of them focused on the operations which are directly related to the processing phases [2] and only a few discussed the decision-making and optimization in terms of global quality.

Failure knowledge can be employed as a quantitative methodology for decision-making in product quality. Different types of failures, which lead to breakdowns of certain functions, emerge in product processes and enterprise departments with respective possibility during the life cycle of past analogous products. The correlation degrees for each failure with different manufacturing characteristics, such as product functions, product

components, product processes and organizations structure, are essential parts of failure knowledge.

By observing the knowledge network of failure scenarios, it is important to examine the perceived weight of manufacturing characteristics obtained from the market and customers and compare them with the overall consideration at the time of task launch. The decision-making in product quality based on failure knowledge is composed of the following six tasks: (i) predicting and identifying risks and faults, (ii) analyzing the cause and mechanism of the past similar failures, (iii) presenting optional proposals, (iv) selecting the optimal scheme, (v) conducting the designated plan, and (vi) verifying the execution results.

In this paper, a quantitative approach for decision-making in product quality is proposed. An ontological expression of failure scenario is presented together with a framework of failure knowledge network (FKN). The decision-making process in product quality based on FKN is discussed in detail and a case study is provided.

2. Failure knowledge

The main reason why similar failure cases are repeated in practice is that the knowledge of past failures is not well expressed to related people [3]. In order to utilize the knowledge of past failure cases, an efficient and unified method has to be provided for communicating failure experience.

2.1 Expressions of failure cases

Many organizations have constructed databases that store failure information in addition to manuals, documents and procedures [4]. However, because of poor transferring of failure information to other part of the organization, the failure knowledge is not effectively communicated and same failures repeat.

Failure Modes and Effects Analysis (FMEA) is a method to identify and prioritize potential failures in

products or processes, and has been widely applied to acquire and update failure knowledge within the organization [5]. The advantages and disadvantages of FMEA are also extensively examined in both industry and academia. The traditional FMEA uses three factors, Occurrence, Severity, and Detection, to determine the Risk Priority Number (RPN), which can address and prioritize the potential failures rapidly. However, it has remarkable drawbacks: there are deficiencies in the relationship expressions between different failure components. As a result it can not be used as a technique for knowledge formulation. In order to make up this deficiency, failure scenario is introduced [6] and the ontological view of failure scenario is shown in Fig. 1.

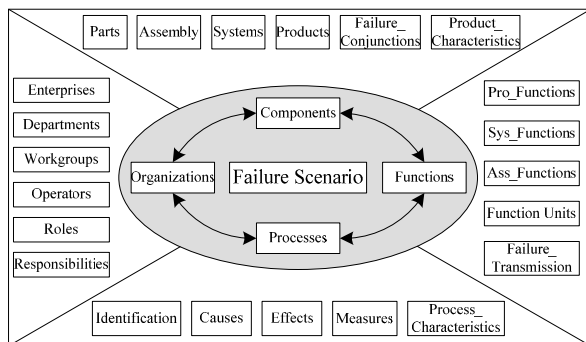


Fig. 1. Ontological view of a failure scenario

Failure scenarios of mechanical products refer to any customer-perceived deviations from the ideal function of the product, including overload, impact, corrosion, fatigue, creep, rupture, deformation, cracking, and so on. There are four entities engaged in a failure scenario: functions, components, processes and organizations. The “component” entity is the carrier of the failure. The amount of failure types regarding one component is finite [7], and different types of failures have conjunctions if they are related to the same component. The conjunctive failures are subject to certain variations of product characteristics, which play a important role in the

occurrence of conjunctive failures. The “function” entity is to record connections between the failure and functions. When the failure takes place, it is usually followed by a breakdown of the corresponding function, and other failures will be stimulated if no measure is adopted. On many occasions a function is interfered by different failures with respective probability, and the breakdown of this function can also arise many other failures. The “processes” entity is to trace the chronological progression of the failure. A failure can be regarded as a unified process, through which input leads to output. As a developing failure becomes evident, the effects will be exposed firstly, and the actions will be taken after analyzing the causes to deal with the event. The “organizations” entity should be regarded as a monitor to take care of the failure scenario. Each individual in the organization has different roles with different responsibilities during the failure process. Their respective actions and behaviors, as well as the failure status, were supervised and classified to construct and improve the quality system.

2.2 Failure knowledge network

In order to structure the failure knowledge, we conduct researches on the connection between characteristics system and triggers, as well as the connection between characteristics system and results. Once the relationship has been identified, it is possible to view the failures, effects, causes, and actions in terms of characteristics, with a trigger leading to a result.

Generally, failure scenarios are induced by unexpected variations of certain manufacturing characteristics during the product development, including design, processing, assembly and validation. For that reason, the relationship between failures and characteristics of both processes and products, as well as experiences dealing with the analogous failures processes, are invaluable knowledge for new product development. This failure knowledge network (FKN) comprises: (i) the connection between failures and product functions, (ii) the relationship between failures

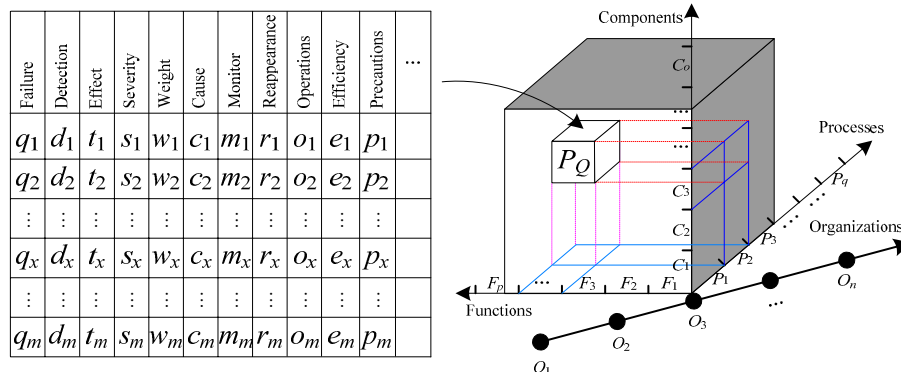


Fig. 2. A schematic of FKN

and product components, (iii) the correlation between failures and organizations, (iv) the association between failures and product processes, and (v) the conjunction among different failures.

As shown in Fig.2, FKN can be described as a four-dimensional matrix, including components, functions, processes and organization. Each element in the matrix is a failure scenario and represents the related failures within the corresponding dimensions. The conventional factors of failures are embodied in the representation, including event, detection, effect, severity, solution weight, cause, monitor, reappearance, operation, efficiency and precaution. The indexes of the factor are provided by subject matter experts and engineers according to the degree of correlation between corresponding characteristics and failures.

3. Decision-making based on failure knowledge network

Traditionally, quality function development (QFD) is employed in decision-making process to map customer requirements to characteristics of design, processing, assembly and validation, known as a top-down approach, in which the qualitative requirements of customers are allocated into the quantitative weights of manufacturing characteristics during product development [8, 9]. A novel approach based on failure knowledge is proposed in this paper, which enables to select the optimal scheme by analyzing the correlation among similar product failures, as well as the relationship between the failures and the manufacturing characteristics.

Here, we propose the use of the analytic network process (ANP) [10] to incorporate the dependence issues between the failures and manufacturing characteristics in Decision-making model. ANP differs from analytic hierarchy process (AHP) in that it allows the inner dependence within cluster and outer dependence among clusters. Based on the hierarchy structure, one can thus calculate the weights of manufacturing characteristics by ANP method. It provides a complete structure to find the interactions between elements and clusters from problems, and then deduce the priority and proportion of each scheme. The ANP method includes two parts: (i) the first part is control hierarchy, which refers to the network relationship of guideline and sub guideline, influencing the internal relationship of systems, (ii) the second part is network hierarchy, which refers to the network relationship between elements and clusters.

As shown in Fig. 3, the representation of decision-making model is based on two parts: decision-making targets and failure knowledge network. The decision-making targets include precaution targets, monitor targets, control targets, and improvement targets. The structure of failure knowledge network includes a cluster of failure scenarios and four other manufacturing

characteristics clusters, namely, functions, components, processes and organizations.

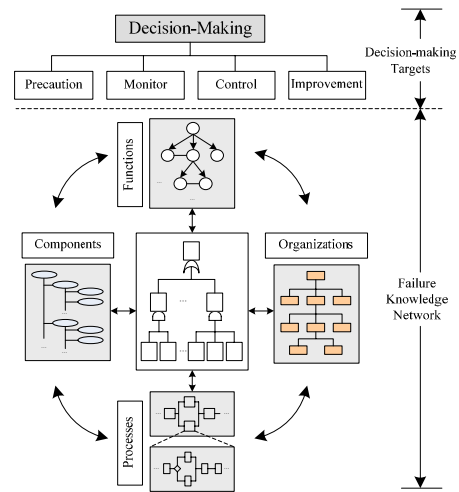


Fig. 3. Decision-making model

The first step of the decision-making methodology is identification of the related failures and characteristics. The second step is determination of the characteristics importance of the clusters. Next, the body of the house will be filled by comparing the characteristics with respect to each target or characteristic. Finally, the interdependent priorities of the characteristics by analyzing dependencies among the targets and characteristics will be obtained. The supermatrix representation of the decision-making model can be obtained as follows:

	<i>G</i>	<i>FS</i>	<i>F</i>	<i>C</i>	<i>P</i>	<i>S</i>
Goals (<i>G</i>)	W_{11}	W_{12}	W_{13}	W_{14}	W_{15}	W_{16}
Failure Scenarios (<i>FS</i>)	W_{21}	W_{22}	W_{23}	W_{24}	W_{25}	W_{26}
Functions (<i>F</i>)	W_{31}	W_{32}	W_{33}	W_{34}	W_{35}	W_{36}
Components (<i>C</i>)	W_{41}	W_{42}	W_{43}	W_{44}	W_{45}	W_{46}
Processes (<i>P</i>)	W_{51}	W_{52}	W_{53}	W_{54}	W_{55}	W_{56}
Organizations (<i>S</i>)	W_{61}	W_{62}	W_{63}	W_{64}	W_{65}	W_{66}

Fig. 4. Decision-making supermatrix

As shown in Fig. 4, $W_{11}, W_{22}, \dots, W_{66}$ are the inner dependency matrices of the targets and characteristics respectively. The other matrices are outer dependency matrices including the column eigenvectors with respect to each target or characteristic.

4. Experimentation and case study

The weight of each characteristic has to be decided before measurement resource planning [11], so the decision-making model is employed to express the relationship between the measurement characteristics and failure scenarios. In the case study, the decision-making target is

to prioritize the measurement characteristics of the large aerospace parts and sub-assemblies in the Measurement Assisted Assembly (MAA) process. Four measurement characteristics, seal gap, aperture gap, aperture step, and location are set to cluster *MC*, and two related failure scenarios are selected as cluster *FS*. From the hierarchy structure, cluster *FS* is the control level, cluster *MC* is regarded as the network level. By extracting information from the failure knowledge network, one can obtain the pairwise comparison matrix, and then evaluate its eigenvectors to group into the supermatrix in Fig. 5.

	<i>FS</i>		<i>MC</i>			
Failure Scenarios (<i>FS</i>)	0.53	0.31				
	0.47	0.69	0			
Measurement Characteristics (<i>MC</i>)	0.13	0.22	0.24	0.27	0.43	0.17
	0.41	0.36	0.30	0.32	0.36	0.38
	0.29	0.11	0.31	0.15	0.08	0.28
	0.17	0.31	0.15	0.26	0.13	0.17

Fig. 5. Decision-making supermatrix in MAA

To group the supermatrix, first transform them into a weighted supermatrix. The constrigent supermatrix in Fig.6 is obtained after multiplying the weighted supermatrix until its constringency, and it can show the weight of each measurement characteristic. The following procedures of measurement planning can be conducted thereafter.

0	0	0	0	0	0
0	0	0	0	0	0
0.28	0.28	0.28	0.28	0.28	0.28
0.33	0.33	0.33	0.33	0.33	0.33
0.20	0.20	0.20	0.20	0.20	0.20
0.19	0.19	0.19	0.19	0.19	0.19

Fig. 6. Decision-making supermatrix in MAA

5. Conclusion

Our study shows that the knowledge from past failures of analogous products is very useful for decision-making in product quality. This research has set up a failure knowledge based framework for decision-making in product quality, and embodies its materialization to calculate the priority and lower the risk of manufacturing characteristics during new product developments. Methodologies developed include (i) identifying relationship between the failure scenario and manufacturing characteristics, (ii) defining failure knowledge network according to the quantitative factor obtained above, and (iii) employing ANP method to deduce the priority and proportion of each scheme. Future work for our research is the construction of an IT-

assistant system that helps to conduct decision-making by making use of the failure knowledge.

Acknowledgments

The authors wish to acknowledge the financial support of the State Scholarship Fund of China as well as the Engineering and Physical Sciences Research Council's Innovative Design & Manufacturing Research Centre at the University of Bath, United Kingdom.

References

- [1] Jerrard, R.N., Barnes, N. and Reid, A., 2008, Design, Risk and New Product Development in Five Small Creative Companies. *International Journal of Design*, Vol. 2/1: 21-30.
- [2] Chen, L.H. and Ko, W.C., 2009, Fuzzy linear programming models for new product design using QFD with FMEA. *Applied Mathematical Modelling*, Vol. 33/2: 633-647.
- [3] Hatamura, Y., Iino, K., Tsuchiya, K. and Hamaguchi, T., 2003, Structure of Failure Knowledge Database and Case Expression. *CIRP Annals - Manufacturing Technology*, Vol. 52/1: 97-100.
- [4] Colding, B.N., 2000, Prediction, Optimization and Functional Requirements of Knowledge Based Systems. *CIRP Annals - Manufacturing Technology*, Vol. 49/1: 351-354.
- [5] Dai, W., Maropoulos, P., Tang, X., Huo, D. and Cai, B., 2009, Quality Planning Based on Risk Assessment. *Proceedings of the 6th CIRP-Sponsored International Conference on Digital Enterprise Technology*, pp. 223-237.
- [6] Kmenta, S. and Ishii, K. Scenario-Based FMEA: A Life Cycle Cost Perspective. *Proceedings of ASME Design Engineering Technical Conferences* Baltimore, Maryland, 2000.
- [7] Arunajadai, S.G., Uder, S.J., Stone, R.B. and Tumer, I.Y., 2004, Failure mode identification through clustering analysis. *Quality and Reliability Engineering International*, Vol. 20/5: 511-526.
- [8] Labodova, A., 2004, Implementing integrated management systems using a risk analysis based approach. *Journal of Cleaner Production*, Vol. 12/6: 571-580.
- [9] Thornton, A.C., 1999, A Mathematical Framework for the Key Characteristic Process. *Research in Engineering Design*, Vol. 11/3: 145-157.
- [10] Saaty, T.L., 1996, *Decision Making with Dependence and Feedback: The Analytic Network Process*. (RWS Publications, Pittsburgh).
- [11] Dai, W., Maropoulos, P., Tang, X., Jamshidi, J. and Cai, B., 2009, Measurement Resource Planning: A Methodology That Uses Quality Characteristics Mapping. *Proceedings of the 6th CIRP-Sponsored International Conference on Digital Enterprise Technology*, pp. 999-1012.

Predicting the End-Of-Life of Defence Electronic Systems at the Conceptual Design Stage

W.M. Cheung¹, P.W. Griffin², L.B. Newnes³, A.R. Mileham⁴, R. Marsh⁵, J.D. Lanham⁶

¹ Northumbria University, Newcastle Upon Tyne, United Kingdom, NE1 8ST, wai.m.cheung@northumbria.ac.uk

^{2,3,4} University of Bath, Bath, United Kingdom, BA2 7AY, {p.w.griffin; l.b.newnes; a.r.mileham}@bath.ac.uk

⁵ University of Southampton, Southampton, United Kingdom, SO17 1BJ, robert.marsh@soton.ac.uk

⁶ The University of West of England, Bristol, United Kingdom, BS16 1QY, john.lanham@uwe.ac.uk

Abstract. The primary objective of the research is to investigate how to estimate disposal costs being undertaken in defence electronic systems by the Original Equipment Manufacturer (OEM) and subsequently to ascertain a novel approach to predicting their end-of-life (EOL) cost. It is intended that the OEMs can utilise this method as part of a full life cycle cost analysis at the conceptual design stage. The cost model should also serve as a useful guide to aid decision making at the conceptual design stage. The novelty of this research is that it identifies the significance of disposal costs from the viewpoint of the OEM and provides a generic basis for evaluation of all the major EOL defence electronic systems.

Keywords: end-of-life, concept design, disposal cost

1. Introduction

Until recently traditional options for EoL processing of waste electrical and electronic equipment (WEEE) like landfill and incineration have prevailed [1]. These options are a concern due to depleting raw materials, pollution, and overflowing waste site. It is well known that Japan has a proactive attitude to electronics recycling [2]. With the Home Appliance Recycling Law in 2001, Japan was one of the first countries to put producer responsibility of electrical and electronic equipment (EEE) into law. The EU followed up by publishing several directives to restrict the quantity and nature of waste arriving at landfills. The WEEE directive [3], for example, requires member states to recycle and recover 50 to 80 per cent of household WEEE and holds the producers of EEE financially responsible. In addition to legislative reasons, OEMs have a higher incentive to design with EoL in mind due to the opportunity costs attached to changing consumer perspectives. This has led to an increasing adoption of “design for environment” to add value by marketing environmentally friendly products. Complementing this is the electronic product environmental assessment tool, which provides a way to

compare electronic products based on environmental performance through eco-labelling [4]. In competitive markets this puts pressure on OEMs to proactively take-back and recover their products at EoL.

Confronted with these issues, OEMs are reacting to the need to implement ‘life cycle thinking’ [5]. According to British Standard BS 8887 [6] and Cheung et al [7], the lifecycle is defined as the “whole life of the product from concept to end-of-life”. It follows that, addressing the entire product lifecycle requires the need for adopting an approach to life cycle cost analysis. The proposed method discussed in this paper will be used to predict the end-of-its-life in terms of costs so that it can be used to assist the designers to make design decisions at the conceptual design stage. In particular, the method can be used to predict how viable for remanufacturing, recycle and refurbishing or simply send it to a landfill.

2. Methodology of the New Approach

The method presented in this section is generic in that it can be applied to all major EoL process options. Thus it is applicable to all EEE in general and not a specific category or type of product.

2.1 Cost categories

Cost categories are linked to the activities that make up the EoL process being modelled. In general, preparation for repair, refurbish and remanufacture include the following process activities [6]:

- Disassembly / Inspection / Testing / Cleaning
- Component exchange, retrieval, or reprocessing
- Assembly, including recombination of parts from different cores

At the next level down, cost categories are measurable resources required to complete the above sub-processes

and can be divided into fixed and variable costs. The main resources have been identified as:

- Labour: to carry out all manual tasks e.g. disassembly, cleaning, etc (variable)
- Replacement components: required where used components are not economically viable to make reusable given the required specification (variable)
- Consumables: lubrication and cleaning solutions (variable)
- Overheads: Equipment, energy, etc (fixed)

2.2 Cost elements

Using a cost element concept, cost categories can be linked to the physical make-up of the product. As shown in the example in Figure 1, [8].

- Product broken down into lower indenture levels
- Life cycle phase when modelled activity occurs

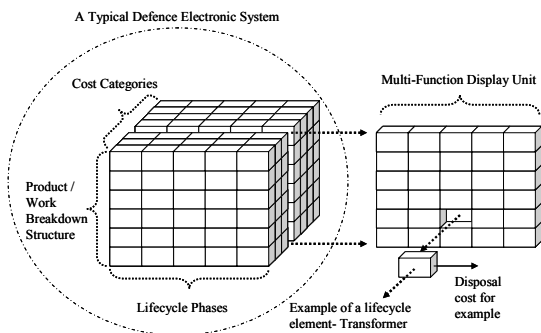


Fig. 1. Cost element concept (Adapted from [7])

The steps that make up preparation for reuse apply to the product at different indenture levels. This is depicted by cost elements in Figure 2.

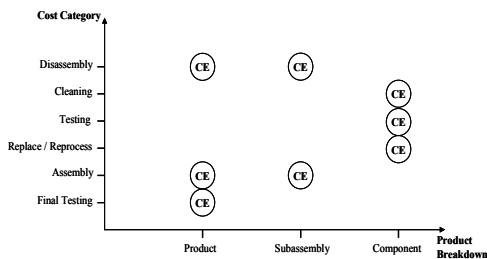


Fig. 2. Cost elements in preparation for reuse

3. Product-Assembly Level Cost Elements

The cost elements at these levels are dominated by disassembly and assembly. Disassembly is a common precondition for recycling or reuse of any component or subassembly within a product [9]. Disassembly is currently manual and incurs high costs [10]. The extent to which a product requires disassembly, and subsequent

reassembly, so that components of interest are separated is the disassembly depth.

3.1 Disassembly depth factor

Disassembly cost is commonly considered proportional to disassembly time, where the constant of proportionality is the labour rate [11], [12]. Disassembly time depends on disassembly depth which can vary depending on the EoL option. To account for this a simple disassembly depth factor is presented that models disassembly depth at an assembly level. The factor represents the disassembly depth necessary to reach targeted components or parts. In the case of remanufacture the product is completely disassembled, [6], [13] thus the factor is 1. The disassembly factor (f) is calculated as follows:

$$f = \frac{\text{Number of assemblies to disassemble}}{\text{Total number of assemblies}} \quad (1.1)$$

An assembly will require disassembling if it satisfies either or both of the following conditions:

- Contains one or more target components
- Contains lower level assemblies that contain target components

The assemblies to disassemble can be determined manually by filtering the initial BOM for the target components, identifying the assembly information for each target component, and visually analysing the assembly structure by counting the assemblies satisfying the above conditions. Figure 8 illustrates the assembly structure of a hypothetical product containing target components.

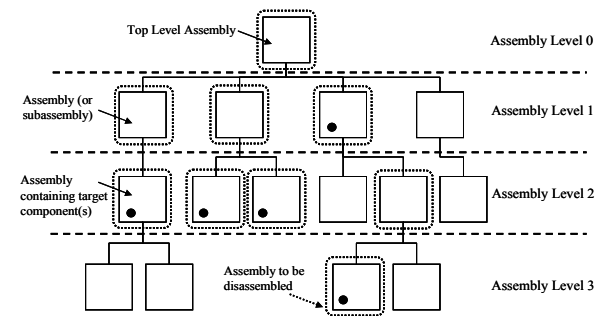


Fig. 3. Assembly layout of hypothetical electronic product

The disassembly depth factor for the example in Figure 3 is $f=9/15 = 0.6$, assuming that:

- Each assembly takes the same time to disassemble.
- Disassembly separates an assembly into its constituent components and lower level assemblies.
- The time to separate one or more target components from an assembly is equal to the time to disassemble the assembly.
- If an entire assembly is targeted, the model treats it as a component.

3.2 Component level cost elements

As shown in Figure 2, the costs incurred here are typically inspection, cleaning, and component replacement, retrieval and reprocessing/rework. These costs vary greatly with the component of interest. Depending on the nature of the component, these costs should be estimated accordingly by the OEM. However, as emphasized by Zhou et al. [14], a common relationship between these costs and the component of interest is component condition. Therefore, this can be modelled to aid cost estimation per component.

4. EoL Process Options

EoL options are identified from the viewpoint of the OEM as shown in Figure 4. An OEM can either implement the take-back and processing of its own EoL products or allow for a non-own-branded Third party organisation (TPO) to arrange this. With the former, it is assumed that the OEM will have in mind key components of interest. In the case of repair, refurbish and remanufacture these components are addressed to ensure that the reused product meets a given specification. In the case of recycling, the components of interest are those that have significant inherent value in their material or reuse respectively. When left to a Non-own-branded TPO, the OEM has no interest in the EoL product and simply pays the necessary fee for obligatory treatment, recovery and safe disposal. Non-reusable or -recyclable materials and components will eventually end up in the collective waste management sphere and be disposed of.

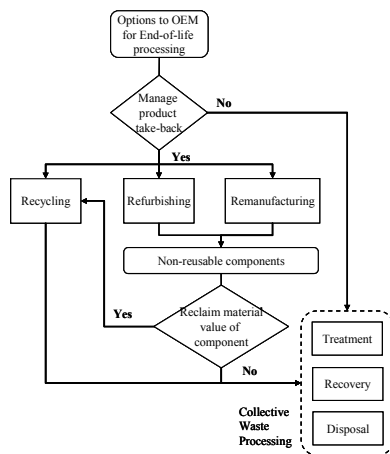


Fig. 4. Options for EoL

5. Cost Equations

A cost equation for each of the three options is presented in this section. The majority are distinguished based on current global definitions.

5.1 Refurbish

According to Zhou et al. [14], electronic product failure rate follows an exponential distribution. This is commonly applied to electronic components too. It can be inferred from BS 8887-2:2009 [6] that refurbishment addresses major components that are not expected to meet a certain specification at product EoL. Regardless of whether some components have failed, they will be targeted for refurbishment. The likely condition of a target component at the time of expected product EoL can be concluded from failure rate data. If the target component is in good condition at product EoL then a relatively minor refurbishing cost would be incurred e.g. cleaning. In contrast, a failed target component will incur higher refurbishing costs e.g. repair, replacement, etc. The likely cost to refurbish, according to component failure/degradation rate data, is estimated to be somewhere between these two extremes.

The profit and cost to refurbish the product can therefore be estimated using the following equations [15]:

$$C_{Re\ refurbish} = \sum_{i=1}^k \{C_{good} e^{-\lambda t} + C_{failure} (1 - e^{-\lambda t})\} + f \times L \times (T_d + T_a) \quad (1.2)$$

- i (target component) k (number of target components)
- C_{good} =expected number of ‘good products’ among ‘ n ’
- $C_{failure}$ = number of parts to be inspected for failure
- t = expected life time of a product (usually per million depends on λ)
- λ = degradation rate (failure per million hours)
- L = labour rate / f = disassembly factor

5.2 Remanufacture

Like refurbishment, remanufacture primarily addresses components within a product that are not up to specification [15]. A remanufactured part or component will generally conform to a higher specification. According to Zussman et al [16] if component life expectancy is less than twice that of the product life expectancy then it may be the cause of renewed product failure after repair and diminish the value of the product for reuse. Therefore, to ensure that a remanufactured product is of at least the same reliability as a newly manufactured product, any target components with a component/product life ratio of two or less must be attended to for either remanufacture or replacement.

The profit and cost of remanufacture is estimated using the following equations [11]:

$$C_{rm} = ((T_d + T_a) * L * f) + (P_f * C_f) + (P_{pd} + P_f * P_{pe} - P_{pd} * P_f * P_{pe}) * C_p \quad (1.3)$$

- C_{rm} = remanufacturing cost / L = labour rate
- T_d = disassembly time / T_a = assembly time
- P_f = probability of fastener failure in disassembly and assembly / C_f = cost of fastener failure

- Ppd = probability of part failure in disassembly and assembly
- Ppe = probability of part failure in fastener-method extraction
- Cp = cost of part failure / f = disassembly factor

The end result is to use the 'cost values' obtained from landfills to compare with the least value obtained from recycling, remanufacturing and reconditioning.

5.3 Recycle

To reclaim material value within the EoL product it is assumed that components made from or containing valuable material are of interest. These components are therefore targeted and removed from the product via disassembly. The condition of the removed components is not important as the recycler is only interested in the material content. The value of the component is the price that the recycler is willing to pay for it per mass of the desired material [5, 10]. For target components that only partially contain valuable material, the material weight is obtained from supplier data. The profit and cost of recycling the product is estimated using the following equations [11]:

$$\text{Recycling cost} = RV_i - RC_i \quad (1.4)$$

$$RV_i = \text{Parts}_i * W_i * MV_m - O_{ci} \quad (1.5)$$

$$RC_i = RT_i * w * f \quad (1.6)$$

- Parts_i = the number of parts of type i
- W_i (kg) = the weight of type i parts
- MV_m (£/kg) = the mass material value of the parts
- RT_i (hr) = the time necessary to remove one type i part, and / w (\$/hr) = the hourly wage
- O_{ci} = Opportunity cost / f = disassembly factor

5.4 Collective waste processing (landfill)

Under the WEEE directive OEMs are obliged to take on the finance of treatment, recovery, recycling and safe disposal of their EEE at end of life. In all member states a collective approach has been adopted. For either Business-to-Business or Business-to-Consumer EEE, cost of treatment and recovery is determined by mass. The cost of treatment per product can therefore be estimated using the following cost equation:

$$C_{\text{treatment}} = M * R_c \quad (1.7)$$

- C_{treatment} = cost of treatment per product
- M = mass of product
- R_c = treatment rate per product category

6. Conclusion

A method of predicting the EoL of EEE based on disposal cost modelling has been defined. The method is being developed using excel spreadsheets and its

associated macro to calculate the disposal costs. This will be used to determine a satisfactory solution of whether the EOL parts of a defence electronic system are viable to be remanufactured, reconditioned or recycled from an early stage of a design concept. A selected subsystem of a defence system will be used as a case study.

References

- [1] Bohr, P, (2008), The Economics of Electronics Recycling: New Approaches to Extended Producer Responsibility, Publisher: VDM Verlag, May 26, Pages: 168. ISBN-13: 978-3639027990.
- [2] Goosey, M, (2009), Introduction and overview: In Hester and Harrison, ed. Electronic Waste Management. Royal Society of Chemistry, Cambridge University Press, Cambridge, UK.
- [3] COM, (2008), Commission of the European Communities, Directive 2008/98/EC on waste and repealing certain Directives. Official Journal of the European Union, Brussels, Belgium.
- [4] Katz, J, et al (2005), Electronic product environmental assessment tool - Development of an environmental rating system of electronic products for governmental. Proceedings of the IEEE International Symposium on Electronics and the Environment, 16-19 May, 1-6.
- [5] González, B and Adenso-díaz, B, (2005), A bill of materials approach for end-of-life decision making in design for the environment. International Journal of Production Research, 43(10), 2071-2099.
- [6] BS 8887-2:2009, British standard: Design for manufacture, assembly, disassembly and end-of-life processing (MADE) - Part 2: Terms and definitions. BSI 2009, ISBN: 0580632853.
- [7] Cheung, W.M., et al (2009) "Standards and inference of design information in through-life costing of defence electronic products", in Part B: Journal of Engineering Manufacture, Publisher: Professional Engineering Publishing, 223(2) 169 - 181, ISSN 0954-4054,
- [8] BS EN 60300-3-6:2004, British standard: Dependability management - Part 3-3: Application guide - Life cycle costing. BSI, ISBN: 0580447065.
- [9] Zussman, E, Kriwet, A and Segiler, G, (1994), Disassembly-orientated assessment methodology to support design for recycling. Annals of the CIRP, 43(1), 9-15.
- [10] Kellner, R, (2009), Integrated Approach to e-Waste Recycling. Electronic Waste Management. In Hester and Harrison, ed. Royal Society of Chemistry, Cambridge University Press, UK.
- [11] Dantec, D, (2005), Analysis of the Cost of Recycling Compliance for the Automobile Industry. Thesis for a Master of Science in Technology and Policy, Massachusetts Institute of Technology, USA.
- [12] Shu, LH and Flowers, WC, (1995) Considering remanufacture and other end-of-life options in selection of fastening and joining methods. Proceedings of the 1995 IEEE International Symposium on Electronics and the Environment, 1-3 May, Orlando, FL, 75-80.
- [13] Ijomah, WL and Childe, SJ, (2007), A model of the operations concerned in remanufacture. International Journal of Production Research, 45(24), 5857-5880.
- [14] Zhou et al. (1996), A cost model for multi-lifecycle engineering design. Proceedings of the 1996 IEEE Conference on Emerging Technologies and Factory Automation, 18-29 Nov, Kauai, HI, USA, 1, 385-391.
- [15] StEP, (2009), Solving the E-Waste Problem (StEP) White Paper: One global understanding of re-use - common definitions. 05 March 2009.
- [16] Zussman, E, Kriwet, A and Segiler, G, (1994), Disassembly-orientated assessment methodology to support design for recycling. Annals of the CIRP, 43(1), 9-15.

Design of Multi-Span Microfixturing Cell for Parallel Assembly of Microparts Using Electrothermally Actuated Microclamps

M. Vismeh¹, M. Hamedi² and P. Salimi³

¹ M.Sc Student of Manufacturing Engineering (University College of Engineering, University of Tehran, Iran)

² Associate Professor of Manufacturing Engineering (University College of Engineering, University of Tehran, Iran)

³ M.Sc Student of Manufacturing Engineering (University College of Engineering, University of Tehran, Iran)

Abstract. Many microparts including the parts used as MEMS components require assembly using parallel assembly techniques. MEMS packaging, including the Wafer Level method, is a prominent process that has been considerably investigated in recent years. In wafer level packaging, either an alignment template (AT) must have special receptor sites according to the micropart geometry and its material or the microcomponents should have additional features like circular and cross pegs for shape recognition stage. In this article, a modular AT which comprises of a microfixturing cell with electrothermal microclamps is presented for positioning and holding microcomponents for later processes like flip chip bonding. The microparts are distributed on the microfixture buffer on a rotary table. After that piezoelectric vibration is induced, stimulated microparts are trapped between the microclamp arms. Then electrical current is applied to create in-plane thermal expansion of the arms. Using this procedure, a micropart is positioned properly and trapped. The rotation of the table continues to lead other microparts to their own positions but the trapped microparts stay standstill. This method enjoys the advantage of omitting the receptor sites. Moreover, in conventional methods, these receptor sites should be designed according to the parts' shapes and their materials. In this novel approach, not only identical clamps are used for diverse assembly configurations, but also the technique is capable of being used for different types of microcomponent materials. Just true positioning of the clamps provides required theme of assembly. Finite element analysis is used to simulate the whole procedure.

Keywords: Microfixturing, Microclamp, MEMS, Microfixturing

1. Introduction

Volume production of microproducts is proliferating these days. Microassembly is a fundamental issue in this context and is required in both packaging of micro-device chips and integration of complex hybrid microsystems.

Current micro-assembly technologies can be categorized as micromanipulator based assembly, wafer-to-wafer devices transfer, fluidic shape-directed self-assembly, and capillary-driven self-assembly. Each of these assembly techniques has its limitations which are investigated in [1] with details. A wafer-level packaging strategy for micro device chips based on uniquely

orienting self-assembly is presented with the following steps: 1) bulk parts are uniquely face-oriented and spread in a single layer; 2) parts are palletized onto an alignment template having an array of receptor sites; 3) parts are anchored one-to-one to receptor sites; 4) each anchored part is fixed to a unique in-plane orientation [2].

Due to limited research in microparts workholding, parallel assembly techniques merits further investigation. Discussed in this paper, is a novel method for designing of microfixturing cell for aligning of microparts to provide primary level positioning in wafer-level packaging strategy. In this construction, microclamps functions are used to locate the parts in the cell. In the next section the principal of microclamp performance is investigated.

2. Electrothermal Microclamps

The microclamp is a device which can be used for locating and holding micro-electro-mechanical-systems. Electrothermally actuated microclamps provide large driving force and sufficient driving distance for some applications. While these microclamps are easy to control, they can also work in high temperatures.

In the method used in this paper, six pairs of microclamps with electrothermal actuation in a microfixturing cell are used to parallel assembling of six microparts with $380 \times 380 \times 20 \mu\text{m}$ size. The configuration of clamps in the cell, secures the accuracy of precisely positioning the microparts.

Resistive joule heating is typically used to power these clamps. The clamp structure is comprised of a thin arm connected to a wide arm, flexure, and two anchors as shown in Fig. 1. In addition to providing mechanical support, the anchors also serve as electrical and thermal connections. When voltage difference is applied to them, current flows through the arms. Due to width difference, the thin arm heats up specifically more than the wide arm

because of having higher resistance and it leads to non-uniform resistive joule heating in the structure. Superior elongation of the thin arm is the consequence of this non-uniformity and is responsible for in-plane bending mode of the microclamp.

2.1 Principal of Microassembly

The assembly process exploits four steps (Fig. 1): Bulk parts are fed on the substrate buffer. In this level, if microparts themselves are featured with special connector pads, there is a need to use a fit part feeder; 2) ultrasonic vibration is induced via piezoelectric pad to reduce the troublesome forces in microscale. Then microparts are distributed to their prearranged positions between two clamps; 3) Voltage difference of 15 volt is applied to the anchors and symmetric in-plane bending of angular exposed microclamps, trap the microparts (Fig. 2), 4) In the last stage, the aligned microparts are transferred to the main assembly board which is loaded by solder bumps or other bonding elements via flip-chip technique.

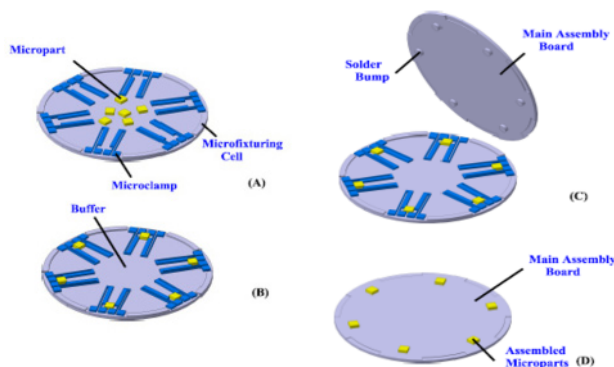


Fig. 1. Four stages of assembly process, A. Parts are feeded on the buffer, B. Parts are positioned by inducing ultrasonic vibration on rotary table, C. Actuated microclamps trap the parts, D. Flip-chip technique transfer parts to main assembly board.

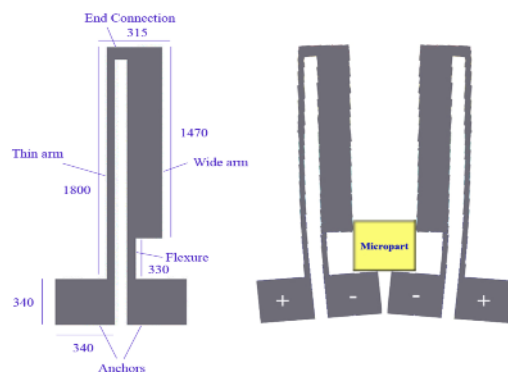


Fig. 2. The microclamp dimensions (μm). After applying voltage difference, The microclamps locate the parts by In-Plane deflection.

2.2 Piezoelectric Actuation System

In micro scale, adhesion could be due to van der Waals, electrostatic forces or surface tension. To overcome these deterrent issues which inevitably exist between microparts, substrate and microclamps, ultrasonic piezoelectric vibrations are induced to silicon substrate. The periodic separation of microparts in small increments of time, is substantiated via ultrasonic sinusoidal vibrations and this helps the microparts better float on buffer surface. Two d.o.f rotary table with angular movement is used to guide and align the parts to their positioning regions. This table, makes it convenient to have access to away positions on substrate (Fig. 3).

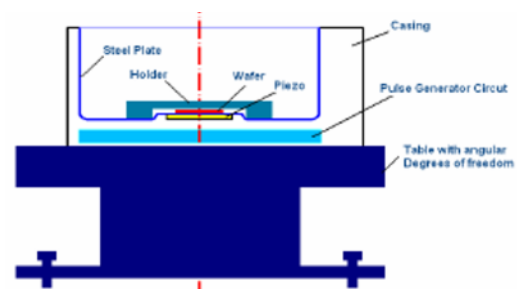


Fig. 3. The piezoelectric actuation set up

3. Design Strategies and Advantages

The integrated design developed in this article, eliminates Alignment Template (AT) in the last stage of DUO-SPASS or semi-DUO-SPASS processes and the main board of assembly directly finishes wafer level packaging.

In DUO-SPASS and Semi-DUO-SPASS processes as described in [2] in detail, an agitated air/water interface is used to uniquely face-orient bulk parts having a single hydrophobic face; after that a hydrophobic carrier wafer palletizes the parts in an air environment, orbital shaking drives the parts until they are anchored to receptor sites; finally, gravitational force uniquely align the parts. The need of having a hydrophobic or hydrophilic layer used in DUO-SPASS is omitted via this method so it is able to be used to assemble different materials without patterning such layers. In addition to this, the disadvantage of using Semi DUO-SPASS for microparts which are subject to ruin in contact with water, is not of concern. The first level of assembly in other methods, is shape recognition that necessitates precisely producing of special features like cross or circular pegs. These additional features require microfabrication processes with high accuracy. [2]. There are situations in which it is not possible to add these features to microparts or it's a costly procedure.

According to [1], most types of microchips have rectangular shapes due to mechanical dicing along

straight lines, but neither fluidic shape-directed self assembly nor capillary-driven self-assembly can align them to unique in-plane orientations. In this novel method, true positioning and orientation of microparts with distinct shapes on different locations on substrate is guaranteed just via choosing appropriate contact points between parts and clamps for parts trapping in line with selecting proper parameters to provide suitable thermal expansion of clamps according to the assembly theme. Contact points are of great importance to prevent sticking between the part and clamp. Decreasing the contact between the micropart and the clamp body, the clamps have angular exposure to each other and the full contact of the micropart side is subsided by corners contact. This strategy is highly efficient in the flip-chip step of the assembly process.

With respect to the size of clamps and microparts in this paper, when the clamps are not actuated, they do not let the microparts move between clamps in different locations. This advantage is paramount to reduce assembly time. There comes a situation in which the material of the micropart is as the same as the microclamp. In such cases, applying negative voltage to thick arm anchor prevents occurring short circuit.

3.1 Fabrication Considerations and Analysis

The material considered for fabrication of microclamp and substrate is silicon. Reaching to a suitable bonding between anchors and substrate, it is necessary to use two different types of silicon known as p-type and n-type. In this case, the pair of clean, mirror-polished silicon surfaces are brought to contact at room temperature after hydrophilic surface formation. Bonding strength reaches the fracture strength of silicon bulk after heating the surfaces in 1000 °C [10].

In order to evaluate the feasibility of the conceptual design, a transient electrothermal actuation analysis is carried out considering the actuation sequence and duration of complete cycle. A commercially available finite element software is used to simulate the clamp behavior [11]. The output of interest throughout the analysis is the relationship between input current and clamp displacement.

In this article, identical to [3], constant value of electrical resistivity is used to cross out the dependence of this characteristic to fabrication material doping level. The constant material properties are summarized in Table 1.

On the other hand, In comparison with conduction along the arm, Surface heat transfer by convection takes a substantial amount of heat. Different values of thermal conductivity (K) over temperature, as noted in Table 2 have been considered. As indicated in Table.2, thermal expansion coefficient (α) increases with temperature; Young's modulus decreases with temperature rise, consequently, the product of Young's modulus and thermal expansion coefficient which is responsible for the

thermal stresses remains almost constant [5]. In other words:

$$E(t) \times \alpha(t) \cong cte \quad (3.1)$$

Table 1. Thermophysical properties of silicon [3].

Property	Value
Young's modulus	169 GPa
Poisson ratio	0.3
Electrical Resistivity	4.2e-4 ohm m
Emissivity	0.7
Air conductivity	0.265 Wm ⁻¹ K ⁻¹ [4]
Specific Heat	730 Jkg ⁻¹ K ⁻¹

Table.2. Thermal conductivity [8] and thermal expansion coefficients of silicon [9].

T(K)	K (Wm ⁻¹ K ⁻¹)	$\alpha(\mu\text{mm}^{-1}\text{K}^{-1})$
300	146.4	2.568
400	98.3	3.212
500	73.2	3.594
600	57.5	3.831
700	49.2	3.987
800	41.8	4.099
900	37.6	4.185
1000	34.5	4.258
1100	31.4	4.323
1200	28.2	4.384
1300	27.2	4.442
1400	26.1	4.500
1500	25.1	4.556

Discretizing the geometry of the model, in line with assuming constant convective heat transfer coefficient (h) under specific temperature for each segment, lengthwise coefficients of fluid film are obtained through empirical correlations of horizontal plate outlined in [4]. The corresponding values of film coefficients used in simulation are described in Table.3.

4. Analysis Results

Results showed that time constant of operation is 0.5s for a complete cycle of holding and releasing the micropart and corresponding tip deflection of 17 μm for each clamp obtained. According to the results, microclamp anchors conveniently trap the microparts by 2.5 degree rotation in the cell. Maximum temperature with the magnitude of 892.6K appeared amidst of the thin arm. Displacement and temperature plots of the microclamp are illustrated in Fig. 4 and Fig. 5 respectively.

Table 3. Convection (fluid film) coefficients ($Wm^{-2}K^{-1}$) in terms of temperature (K). U, upper surface of horizontal hot plate, L, lower surface of horizontal hot plate [4]. Refer to Fig. 1.2 for description of the design parameters.

T(K)	Wide arm		Thin arm and flexure		End connection		Vertical wall	Anchor
	U	L	U	L	U	L		U
300	12.1	13.9	18.2	22.9	15.8	25.3	937	10.5
500	38.2	40.1	60.8	70.5	51.4	74.5	1198	35.2
700	41.9	44.2	66.3	77.3	56.5	81.9	1400	38.4
900	44.1	46.8	69.5	81.5	58.9	86.6	1603	40.5
1100	45.3	48.3	72.5	84.2	61.3	90.1	1801	41.6
1300	46.5	50.2	73.4	87.5	63.0	92.8	1994	42.3
1500	46.8	51.3	74.0	88.6	64.1	94.6	2185	42.7

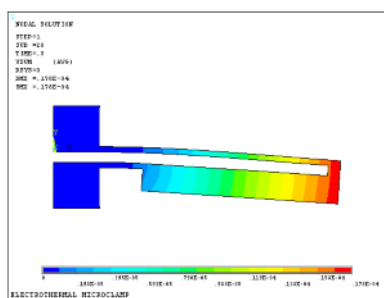


Fig. 4. Displacement contour under applied voltage of 15 V, Mamimum displacement is $17\mu m$.

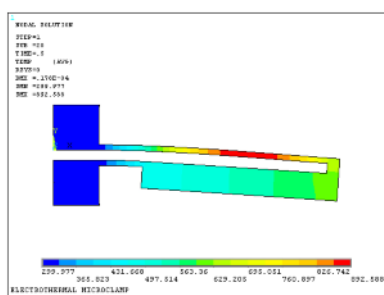


Fig. 5. Temperature contour under applied voltage of 15 V, Mamimum Temperature is 892.558 K in the middle of the thin arm.

5. Conclusion

The novel design and finite element investigation of a microfixturing cell equipped with electrothermal microclamps was discussed in this report. Easy-controllable designed microclamps emerged as appropriate devices to ensure accurate locating and holding of microparts. The analysis helps to find four proper contact points for positioning the micropart. The temperature and scale-dependent boundary conditions that yields the desired displacement according to an applied voltage, are investigated.

The function of the device, operating temperature and its performance ratio, depends on thermal boundary conditions at microclamp anchors. Heat loss to substrate via these anchors showed to be the dominant mode of heat transfer. The design can be used for parallel microassembly purposes in manufacturing of MEMS devices.

References

- [1] Jiandong F, (2006) Self-assembly techniques for massively parallel packaging of MEMS devices. PhD thesis, University of Wshington.
- [2] Jiandong F, F. Bohringer K, (2006) Wafer-level packaging based on uniquely orienting self assembly (the DUO-SPASS processes). Journal of Microelectromechanical systems. 15:531–540
- [3] D Mankame N, Ananthasuresh G K, (2001) Comprehensive thermal modeling and characterization of an electro-thermal-compliant microactuator. J. Micromech. Microeng., 11:452-462
- [4] Incropera, DeWitt, Bergman, Lavine, (2007) Fundamentals of heat and mass transfer, 6th Ed, John Wiley & Sons
- [5] Hill D, Szyszowski W, Bordatchev E, (2006) On modeling and computer simulation of an electro-thermally driven cascaded nickel micro-actuator. Sensors and Actuators. A126:253-263
- [6] Wang W, Svetlana Tatic L, Brown W, Iceman J, Hyun S, Vinci R, (2008) Precision in-package positioning with a thermal inchworm. Sensors and Actuators. A142:316-321
- [7] Kolesar E S, Htun T, Least B, Tippey J, Michalik J, (2008) Optimization of the geometry of MEMS electrothermal actuator to maximize in-plane tip deflection. Mater. Res. Soc. Sympo. Proc. 1052:105-110
- [8] Lide D R, Kehiaian H V, (1994) CRC Handbook of thermophysical and thermomechanical data. Ann Arbor, MI
- [9] Okada Y, Tokumaru Y, (1984) Precise determination of lattice parameter and thermal expansion coefficient of silicon between 300 and 1500 K. J/Appl. Phys. 56:314-320
- [10] Shimbo M, Furukawa K, Fukuda K, Tanzawa K, (1986) Silicon-to-silicon direct bonding method. J.Appl. Phys. 60:2987-2989
- [11] ANSYS coupled field analysis guide, (2007) Commercial ANSYS Software Revision 11, ANSYS Inc.

An Evaluation Method Based on Multiple Quality Characteristics for CNC Machining Center using Fuzzy Matter Element

G.B. Zhang¹, J.H. Pang^{1,2}, G.H. Chen¹, X.L. Ren¹, Y. Ran¹

¹College of Mechanical Engineering, Chongqing University, Chongqing 400044, P. R. China

²Department of Management, Guangxi University of Technology, Liuzhou 545006, P.R. China

Abstract: Most mechanical and electrical products have multiple quality characteristics (QCs) in practice. Since the traditional Taguchi method only focused on one characteristic to control quality of products, the methods of multiple QCs evaluation have become very important for complex manufacturing products. This paper presents an effective evaluation method for quality of computer numerical control (CNC) machining centers by using fuzzy matter element (FME), analytic hierarchy process (AHP) and information entropy. In this study, the multiple-attribute evaluation-making (MAEM) model was built by FME and AHP. Then, information entropy and AHP were adopted to compute the weights of the evaluation indexes of multiple QCs. Finally, these weights were applied to indicate the accurate quality level of CNC machining centers by compound FME. An example of quality evaluation for CNC machining centers was given to illustrate the effectiveness and feasibility of the proposed method.

Keywords: Machining centers; Quality characteristics; Fuzzy matter element; Analytic hierarchy process

1. Introduction

Nowadays, the excellent product quality is becoming the key in competing with others in the market because of global economic integration. The superior product quality means lower manufacturing cost and shorter manufacturing time in manufactures. Thus, the high-quality products with a lower price and appropriate time contribute immensely to the progress of manufacturing organisation in the world market. On the other hand, a product should have the quality of which characteristics are required to satisfy the customers' needs and expectations. These QCs are shown in product specifications as customers perceive, each of which has to satisfy specification request. As a result, some strategies are needed for the quality of manufacturing products satisfying the needs of customers at large.

Rapid development of computers and advanced manufacturing technologies (AMTs) has resulted in a high range of CNC machining centers using. There are multiple QCs of CNC machining centers defined by the manufacturers and their customers. Considering multiple

QCs, the quality evaluation of CNC machining centers is a very complex decision-making process. Many methods are applied to evaluate quality based on arbitrary importance weights to QCs. However, the task of calculating weights becomes more difficult for the increasing number of QCs.

The present paper reports that there are four main evaluation methods for quality of CNC machining centers: AHP and fuzzy comprehensive evaluation technique [1], AHP and grey theory [2], fuzzy AHP [3], rough set theory and genetic algorithms [4], and so on. The quality of CNC machining centers can be evaluated as the degree to which a particular program complies with consumer demand regarding QCs [5].

In this paper, a synthetic method is presented to solve fuzzy evaluation problems of quality of CNC machining centers based on FME, AHP and information entropy. Firstly the MAEM model of both quantitative and qualitative QCs was established for quality evaluation by using FME and AHP. Then, the weight coefficient of evaluation indicators was calculated based on information entropy and AHP. Finally we applied the comprehensive method to evaluate the quality of nine CNC machining centers in the case study.

2. Quality evaluation model based on FME

In this paper, the multiple QCs evaluation model was built based on FME theory. The matter element analysis integration with fuzzy mathematics were introduced to evaluate the quality of CNC machining centers.

Step 1. The definition of FME

If the name of the matter is regarded as M , one of its characteristics is c , the value of characteristic of matter c is x , the value of characteristic n of matter m is $v(x)$, then the matter element can be written as follows [6]:

$$R = \begin{bmatrix} M & c_1 & v_1(x) \\ & c_2 & v_2(x) \\ & \vdots & \vdots \\ & c_n & v_n(x) \end{bmatrix} \quad (1)$$

The ordered group triples R is named as the matter element. When the value of $v(x)$ is fuzzy, it is called the fuzzy matter element [7].

Step 2. Building the compound FME

If matter M is described by n characteristics and given as the characteristics of corresponding fuzzy values, R is called n dimension FME. Ordinarily, supposed n-dimension matter elements of m matters are combined together, then a multidimensional matter element \tilde{R}_{mn} is written as:

$$\tilde{R}_{mn} = \begin{bmatrix} & M_1 & M_2 & \dots & M_m \\ C_1 & v_{11}(x) & v_{21}(x) & \dots & v_{m1}(x) \\ C_2 & v_{12}(x) & v_{22}(x) & \dots & v_{m2}(x) \\ \dots & \dots & \dots & \dots & \dots \\ C_n & v_{1n}(x) & v_{2n}(x) & \dots & v_{mn}(x) \end{bmatrix} \quad (2)$$

Where M_m is the m th matter, C_n is the n th characteristic, $v_{mn}(x)$ is the fuzzy value of characteristic n of matter m.

Step 3. Calculating the preferred membership grade

The preferred membership grade is subject to the corresponding fuzzy value of each assessment indicator in standard samples. Generally, if $v_{mn}(x)$ is an ordinary mathematical function expression, the excellent dependent degree function is calculated as follows by using linear dependence relation Eq.(3) and (4).

The bigger, the more preferred assessment indicator can be calculated as follows :

$$\mu_{ij} = X_{ij} / \max X_{ij} \quad (3)$$

The smaller, the more preferred assessment indicator can be calculated as follows:

$$\mu_{ij} = \min X_{ij} / X_{ij} \quad (4)$$

Where μ_{ij} is the fuzzy value of characteristic j of matter i; X_{ij} is the value of characteristic j of matter i; $\max X_{ij}$ and $\min X_{ij}$ represent the maximal and minimal value of the i th object; $i=1,2,\dots,n, j=1,2,\dots,m$.

Step 4. Standard FME and difference square FME

The fuzzy matter element composed of \tilde{R}_{mn} is named as a standard form. Then, the difference square compound fuzzy matter element R_Δ can be calculated as follows:

$$R_\Delta = \begin{bmatrix} & M_1 & M_2 & \dots & M_m \\ c_1 & \Delta_{11} & \Delta_{21} & \dots & \Delta_{m1} \\ c_2 & \Delta_{12} & \Delta_{22} & \dots & \Delta_{m2} \\ \dots & \dots & \dots & \dots & \dots \\ c_n & \Delta_{1n} & \Delta_{2n} & \dots & \Delta_{mn} \end{bmatrix} \quad (5)$$

Where $\Delta_{ji} = (v_{0i} - v_{ji})^2, i=1, 2, \dots, n; j=1, 2, \dots, m$.

Step 5. Calculating euclid approach degree

Considering the weight coefficient of assessment indicator, information entropy and AHP methods were applied in this paper to determine the relative importance. Supposing $W = (w_1, w_2, \dots, w_n)$ indicates the weights of evaluating indicators. After the weights have been normalized, the compound FME is calculated by Eq.(6) as following:

$$R_{\rho H} = W \times \tilde{R}_{mn} = \begin{bmatrix} M_1 & M_2 & \dots & M_m \\ \rho H_j & \rho H_1 & \rho H_2 & \dots & \rho H_m \end{bmatrix} \quad (6)$$

The Euclid approach degree formula is used to calculate the approach degree of two matter elements in this paper. The ρH_j is adopted to describe the Euclid approach degree, which can be calculated by Eq.(7) as following:

$$\rho H_i = 1 - \sqrt{\sum_{j=1}^n W_j \times \Delta_{ji}} \quad (7)$$

Where $i=1, 2, \dots, n; j=1, 2, \dots, m$; the " \times " is algorithm $M(\cdot, +)$; ρH_i reflects the mutual closeness between number n matter element and the standard matter element, bigger the value is, more closely the two will be, on the contrary, farther the two will be. Lastly, the quality of CNC machining centers can be indicated by ρH_j .

3. Calculating synthesized weight by using information entropy and AHP

3.1 Determining weight by information entropy

Entropy is regarded as a precise measure of the amount of disorder [8]. The entropy can be used to show the information disorder degree in the information theory, and can determine the attribute importance of evaluation index [9].

After the judgment matrix normalized by using Eq.(3) and (4), the entropy value of evaluation index is calculated as:

$$E_j = -\sum_{i=1}^m (h_{ij} \ln h_{ij}) / \ln m \quad (5)$$

Where $h_{ij} = v_{ij} / \sum_{i=1}^m v_{ij}; i=1, 2, \dots, n; j=1, 2, \dots, m$.

The weight of entropy value is calculated as:

$$W_j^e = (1 - E_j) / \sum_{j=1}^n (1 - E_j) \quad (6)$$

Where $j=1,2,\dots,n; 0 \leq w_j^e \leq 1; \sum_{j=1}^n w_j^e = 1$.

3.2 Confirming weight by AHP

Analytic Hierarchy Process (AHP) is an effective method by which a rough result can be obtained. It can solve qualitative decision problems which can be represented

by a hierarchy [10]. Then, decision makers evaluate the elements by making multiple comparisons. Furthermore, AHP provides a useful mechanism capturing both subjective and objective evaluations for checking the consistency of the decision makers' estimate. AHP method is widely used in evaluation problems where information and priority weights of elements can be gotten from decision makers [11].

Firstly, a hierarchical structure of evaluation problems was built by using the AHP methodology. Secondly, a matrix of pair-wise comparisons of elements was constructed to respect to element in the level above. The values in each comparison matrix were defined 1, 3, 5, 7, 9, respectively, with 2, 4, 6 and 8 as intermediate values for comparisons between two successive qualitative judgments. Lastly, the derived priorities were synthesized by decision-makers' judgments, and the weight was obtained by synthesizing results.

3.3 Synthesizing the weights

Supposing that the information entropy weight is $w^e = (w_1, w_2, \dots, w_m)$ and the AHP weight is $w^a = (w_1, w_2, \dots, w_m)$, the synthesized weight matched with the i th assessment indicator is calculated as follows:

$$w_i = (w_i^e \times w_i^a) / (\sum_1^j w_i^e \times w_i^a) \quad (7)$$

Then, the synthesized weight is calculated by $W = (w_1, w_2, \dots, w_m)$.

4. Quality evaluation for CNC machining centers

The quality evaluation model for CNC horizontal milling machining centers was based on multiple QCs in this paper. The indicators for evaluating quality of CNC horizontal milling machining centers are Mean Time Between Failures (MTBF) (C_1), Mean Time to Repair (MTTR) (C_2), Availability (C_3), Positioning Accuracy (C_4), Positioning Repeatability (C_5), Average Warranty Cost Rate (C_6), Price (C_7), Rapid Traverse Speed (X,Y,Z) (C_8) and Main Motor Power (C_9). The statistical information of nine indications of quality evaluation is summarized in Table 4.1.

Table 4.1. Quality evaluation elements of CNC machining centers

C_1	C_2	C_3	C_4	C_5	C_6	C_7	C_8	C_9
900	6.6	95.3	0.02	0.05	9.5	33.6	30	7.0
850	7.3	94.5	0.04	0.06	8.4	30.5	24	7.5
750	8.8	90.6	0.03	0.07	7.8	33.8	28	8.5

800	9.2	92.8	0.02	0.05	9.0	31.2	26	6.5
950	7.8	95.8	0.04	0.06	9.2	28.8	24	7.0
850	7.2	93.5	0.03	0.05	8.8	34.2	28	8.0
750	7.0	96.8	0.05	0.08	8.2	29.5	30	7.5
850	8.0	91.5	0.04	0.07	9.0	30.8	26	6.0
900	8.5	92.6	0.02	0.05	8.6	31.2	28	8.5

Then, \bar{R}_{mn} is calculated according to Eq (2.2) and (2.3),

0.947	1.000	0.995	0.667	0.800	0.821	0.857	1.000	0.857
0.895	0.904	0.986	1.000	0.667	0.929	0.944	0.800	0.800
0.789	0.750	0.946	0.667	0.571	1.000	0.852	0.933	0.706
0.842	0.717	0.969	1.000	1.000	0.867	0.923	0.867	0.923
1.000	0.846	1.000	0.500	0.667	0.848	1.000	0.800	0.857
0.895	0.917	0.976	0.667	0.800	0.886	0.842	0.933	0.750
0.789	0.943	0.894	0.500	0.500	0.951	0.976	0.800	0.800
0.895	0.825	0.955	0.500	0.571	0.867	0.935	0.867	1.000
0.842	0.776	0.916	0.667	0.800	0.907	0.923	0.933	0.706

The R_{λ} is figured up by Eq(2.5), $R_{\lambda} =$

0.003	0.000	0.000	0.111	0.040	0.032	0.020	0.000	0.020
0.011	0.009	0.000	0.000	0.111	0.005	0.003	0.040	0.040
0.044	0.063	0.003	0.111	0.184	0.000	0.022	0.004	0.087
0.025	0.080	0.001	0.000	0.000	0.018	0.006	0.018	0.006
0.000	0.024	0.000	0.250	0.111	0.023	0.000	0.040	0.020
0.011	0.007	0.001	0.111	0.040	0.013	0.025	0.004	0.063
0.044	0.003	0.011	0.250	0.250	0.002	0.001	0.040	0.040
0.011	0.031	0.002	0.250	0.184	0.018	0.004	0.018	0.000
0.025	0.050	0.007	0.111	0.040	0.009	0.006	0.004	0.087

The weight of entropy value is calculated as : $W^e =$

(0.036, 0.072, 0.008, 0.444, 0.276, 0.022, 0.021, 0.039, 0.082)

The mutual comparisons of the nine indexes with respect to the overall goal are shown in Table 4.2. Thus, $\lambda_{max} = 9.7285$, $CI = 0.0911$, $RI = 1.45$, $CR = 0.0628 < 0.10$.

Table 4.2. Comparison matrices of nine indexes

	C ₁	C ₂	C ₃	C ₄	C ₅	C ₆	C ₇	C ₈	C ₉
C ₁	1	3	5	2	6	5	9	3	8
C ₂	1/3	1	3	1/4	4	3	7	2	6
C ₃	1/5	1/3	1	1/6	1	2	3	1	7
C ₄	1/2	4	6	1	1	4	8	2	5
C ₅	1/6	1/4	1	1	1	3	3	1/2	4
C ₆	1/5	1/3	1/2	1/4	1/3	1	2	1/3	2
C ₇	1/9	1/7	1/3	1/8	1/3	1/2	1	1/5	1
C ₈	1/3	1/2	1	1/2	2	3	5	1	3
C ₉	1/8	1/6	1/7	1/5	1/4	1/2	1	1/3	1

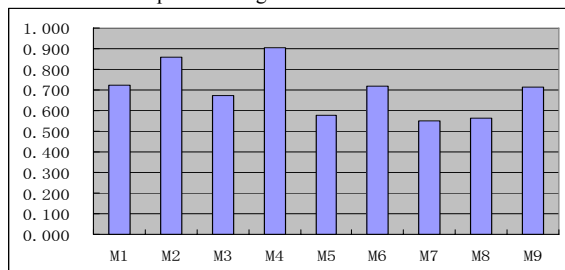
The weight of AHP value is calculated as $W^a = (0.309, 0.148, 0.074, 0.200, 0.077, 0.043, 0.024, 0.100, 0.025)$

Then, the synthesized weight is calculated by $W^e = (0.080, 0.076, 0.004, 0.634, 0.153, 0.007, 0.004, 0.028, 0.014)$

So, the ρ_{H_j} is determined by the FME method with Eq. (2.6) and (2.7), $w = (0.722, 0.860, 0.673, 0.907, 0.577, 0.720, 0.551, 0.564, 0.713)$

The importance degree of nine CNC machine centers is shown in Table 4.3, and the quality of them are sorted as $M_4 > M_2 > M_1 > M_6 > M_9 > M_3 > M_5 > M_8 > M_7$.

Table 4.3. Importance degree of nine CNC machine centers



5. Conclusions

The quality evaluation of CNC machining centers is becoming more and more important due to the sharp market competition. This study presents a fuzzy synthetic valuation method by using FME, AHP and information entropy, of which the calculation is easy to realize through the computer programming. This proposed method can also be used to evaluate the quality of other mechanical and electrical products. Furthermore, this method has been certified much more objective and reasonable because the evaluation results are more consistent with the physical fact. As a result, this method is effective and feasible in solving evaluation problems and can be widely used.

Acknowledgment

This research is sponsored by the National High-Tech. R&D Program of China (No. 2009AA04Z119), National Natural Science Foundation of China (No. 50835008), National Major Scientific and Technological Special Project for “High-grade CNC and Basic Manufacturing Equipment” of China (No. 2009ZX04014-016) and Open Research Foundation of State Key Lab. of Digital Manufacturing Equipment & Technology in Huazhong University of Science & Technology.

References

- [1] HUANG, H. Z., LI, Y. H., XUE, L. H., (2005) A comprehensive evaluation model for assessments of grinding machining quality. *Advances in Abrasive Technology* VIII, 291-292, 157-162.
- [2] LIU, J., LI, C.-F., SUN, W., WEN, B.-C., (2007) Generalized evaluation based on AHP/grey theory for product quality. *Dongbei Daxue Xuebao/Journal of Northeastern University*, 28, 1608-1611.
- [3] YANG, C.-C., CHEN, B.-S., (2004) Key quality performance evaluation using fuzzy AHP. *Journal of the Chinese Institute of Industrial Engineers*, 21, 543-550.
- [4] ZHAI, L.-Y., KHOO, L.-P., FOK, S.-C., (2002) Feature extraction using rough set theory and genetic algorithms - An application for the simplification of product quality evaluation. *Computers and Industrial Engineering*, 43, 661-676.
- [5] WANG, F. K., (2006) Quality evaluation of a manufactured product with multiple characteristics. *Quality and Reliability Engineering International*, 22, 225-236.
- [6] YAN-CHAO, Y., LIN-FU, S., CHENG, G., (2008) A policy of conflict negotiation based on fuzzy matter element particle swarm optimization in distributed collaborative creative design. *Computer Aided Design*, 1009-1014.
- [7] ZHAO, Y. W., ZHANG, G. X., (2002) A new integrated design method based on fuzzy matter-element optimization. *Journal of Materials Processing Technology*, 129, 612-618.
- [8] JIANG, R., LIAO, H., YU, J., FENG, T., ZHAO, C., LI, J., (2009) A model based on information entropy to measure developer turnover risk on software project. *2009 2nd IEEE International Conference on Computer Science and Information Technology (ICCSIT 2009)*, 419-422.
- [9] JIN, F., DING, S., WANG, J., (2008) Principal components projection decision-making based on information entropy weight. *2008 Chinese Control Conference (CCC)*, 413-416.
- [10] AL-AHMARI, A. M. A., (2007) Evaluation of CIM technologies in saudi industries using AHP. *International Journal of Advanced Manufacturing Technology*, 34, 736-747.
- [11] MAHDI, I. M., ALRESHAID, K., (2005) Decision support system for selecting the proper project delivery method using analytical hierarchy process (AHP). *International Journal of Project Management*, 23, 564-572.

Design of a Meso-scale 3-axis Milling with Nanometer Accuracy

Kuang-Chao Fan¹, Fang-Jung Shiou², Kai-Ming Pan², Zhi-Yuan Ke¹, Yjng-Jhih Lin², and Kun-Jin Wu²

¹ Department of Mechanical Engineering, National Taiwan University

² Department of Mechanical Engineering, National Taiwan University of Science and Technology

Abstract. The objective of this research was to develop a meso-scale 3-axis milling machine with a nanometer resolution. The main elements of the Z-axis design of the meso-scale 3-axis milling machine are a pagoda structure, a high speed air bearing spindle, two HR8 ultrasonic motors, a laser diffraction grating interferometer system (LDGI) and a coaxial counter-balance system for the spindle. The optimal geometrical dimensions of the pagoda structure have been determined by ANSYS software. According to the simulation results, the maximum static deformation along the z-axis of the pagoda was about 5.05 nm. Vibration amplitude tests of the Z-axis of a micro-milling machine driven by either an ultrasonic motor or two ultrasonic motors have also been carried out to provide better design information for the Z-axis. The meso-scale 3-axis milling machine is equipped with an X-Y coplanar positioning stage with nanometer resolution, including the low-cost components and two ultrasonic motors, in order to reduce both the complexity and errors resulting from the combination of a long-stroke stage and short-travel stage. The coplanar stage developed by Nation Taiwan University was integrated with two laser diffraction grating interferometer systems as displacement feedback sensors, so that a two-axis closed-loop control was possible. The positioning accuracy of the coplanar stage was about 200 nm after error compensation, base on the test results. A circular positioning test with the radius of 100 μm using the stage developed was tested, and the overall roundness error was about 4.01 μm based on the preliminary test results.

Keywords: Meso-scale 3-axis milling machine, pagoda structure, coaxial counter-balance system, laser diffraction grating interferometer system (LDGI), X-Y coplanar positioning stage

1. Introduction

Over the past decade, the demands for micro-mechanical devices have been increased in digital cameras, mobile phones, sensors, actuators and so on [1]. Thus precision manufacturing processes and machines are needed capable of manufacturing microstructures with 3D complex shapes or free-form surfaces [2]. Therefore, there are more and more research projects focused on high precision machine tool design and manufacturing such as precision turning machines [3], precision grinding machines [4] and micro-milling machines [5].

When designing a precision machine, there are four major subsystems have to be taken into account. These are the

mechanical structure, drive, spindle and control system. The mechanical structure design and analysis of a precision machine have been discussed in [6].

The price of an ultra-precision manufacturing machine is generally more than NTD10 million. For that reason, the objective of this research is to develop an economically priced meso-scale 3-axis milling machine with a nanometer resolution.

2. Meso-scale 3-axis Milling machine tool design and analysis

2.1 The Meso-scale 3-axis milling machine tool

Fig 1. illustrates the conceptual design of a high-precision micro-milling machine tool, including a pagoda structure, the high speed air bearing spindle, two HR8 ultrasonic motors, three laser diffraction grating interferometer systems (LDGI), a micro dynamometer, a coaxial counter-balance system, XY coplanar positioning stage, CNC controller and an industrial PC. Table 1. shows the specification of the high-precision micro-milling machine tool designed.

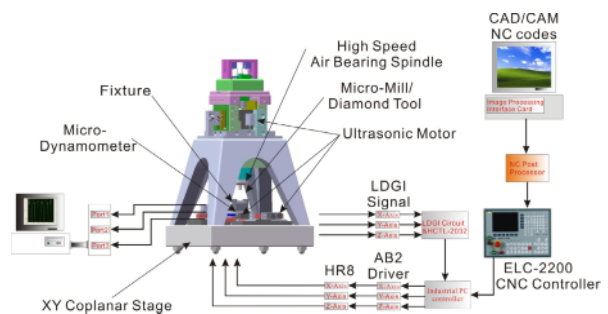


Fig 1. Schematic of the meso-scale 3-axis milling machine tool and control system

Table 1. Machine specification

Machine size (LWH)	500 mm × 500 mm × 600 mm
Working Range (XYZ)	25 mm × 25 mm × 10 mm
Driven system	Ultrasonic motor
Spindle Speed range	80,000 rpm (Max)
Resolution	±1 nm

2.2 Z-axis design and analysis

2.2.1 Optimal geometrical dimensions of the pagoda structure

The design of the pagoda structure of the meso-scale machine tool must take into account the rigidity needed together with the strength needed to withstand the weight of the spindle system. Advantage was taken of previous designs involving several different shapes of the structure, and ANSYS finite element analysis software was used to analyze these. The best pagoda structure was determined on the basis of the one that was the most stable [7]. The design includes some improvements to the features to clamp and integrate the new Z-axis high speed air bearing spindle. The optimal geometrical dimensions of the pagoda structure were determined by the ANSYS software. Fig 2. shows the new design of the granite pagoda to locate and support the Z-axis spindle. The optimal geometrical values of the pagoda structure parameters are listed in Table1.2.

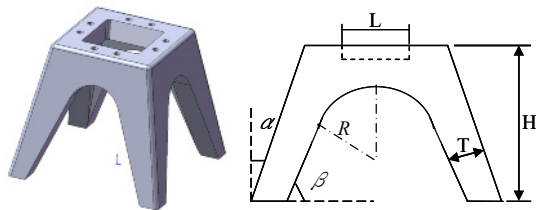


Fig 2. Pagoda and its main parameters

Table 2. Optimal geometrical dimensions of the pagoda structure

Each Part	Size
R	90 mm
Beta	78 deg
T	50 mm
H	430 mm
L	130 mm

According to the simulation results, the maximum static deformation along the z-axis of the pagoda, under the a weight of 17.5 kg, was about 5.05 nm, as shown in Fig 3.

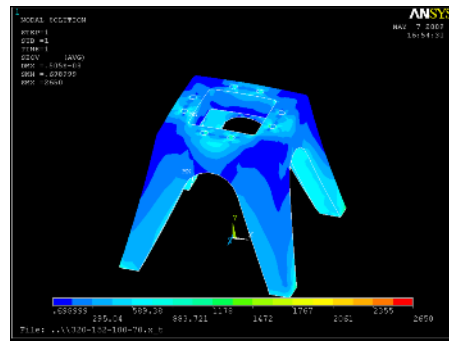


Fig 3. The maximum displacement of the pagoda structure

2.2.2 The high speed air bearing spindle clamp and driving mechanism in Z-axis

There are four main parts in the design of the high speed air bearing spindle clamp and driving mechanism. These are the counterbalance system, LDGI, ultrasonic motor, and high speed air bearing spindle system, as shown in Fig 4. The high speed air bearing spindle clamp and driver consists of two ultrasonic motors to drive the spindle clamp with a seesaw motion. A set of LDGI is used as a displacement feedback sensor with nanometer resolution to measure the displacement of the Z-axis and provide for close loop control.

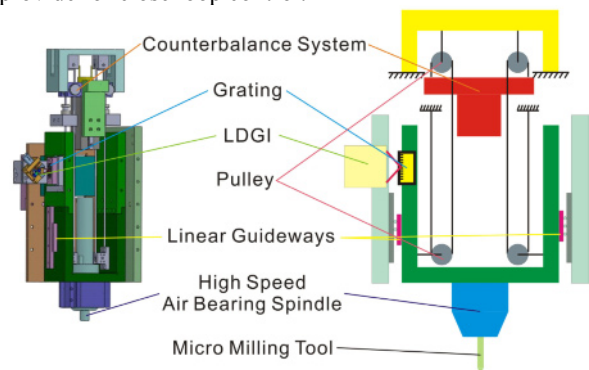


Fig 4. The high speed air bearing spindle clamp and driving mechanism in Z-axis

2.2.3 The main Z-axis parts and preliminary assembly

The studies described in the two previous sub-sections completed the Z-axis design. The parts were then manufactured aand assembled. The assembled three-axis micro-milling machine tool is shown in Fig 5 in two forms, as a solid model, to the left, and as the actual built assembly. The pagoda, the high speed spindle, the two HR8 ultrasonic motors, the LDGI [8] and the counterbalance system can be seen.

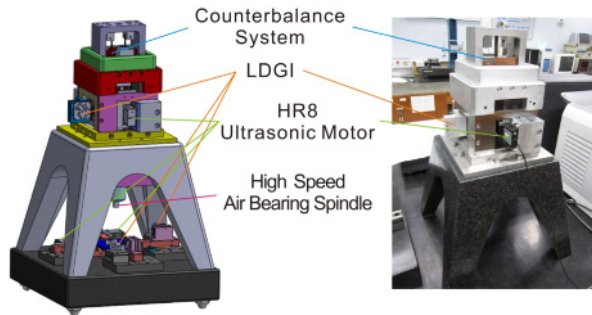


Fig 5. Assembled meso-scale 3-axis milling machine tool

2.3 XY coplanar positioning stage design and analysis

2.3.1 XY coplanar positioning stage design

The coplanar stage developed by Nation Taiwan University was integrated with the two laser diffraction grating interferometer systems as the displacement feedback sensors. Two HR8 ultrasonic motors are used as driving motors, and 8 linear guides are used to perform the coplanar movement without Abbe error[9]. The design of the XY-coplanar stage is shown in Fig 6. and the assembled coplanar stage is shown in Fig 7.

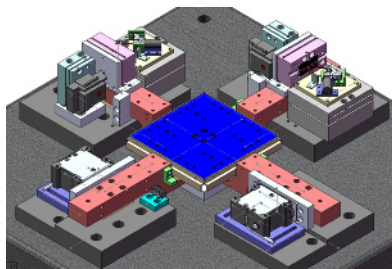


Fig 6. The schematic of XY-coplanar stage

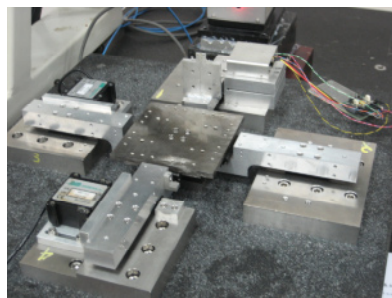


Fig 7. XY-coplanar stage

2.3.2 XY coplanar positioning stage tilting angle of stage at different positions

After assembly, a laser interferometer (SIOS MI-5000) was used to measure the X- and Y-axis tilting angles. Fig 8. shows the measured results of pitch angles. The maximum tilting angles for X- and Y-axis within the travel of 22 mm, were about 5 and 4 arc-seconds respectively. The open loop positioning error for X- and

Y-axis within the travel of 20 mm was about 0.205 μm , shown in Fig. 9.

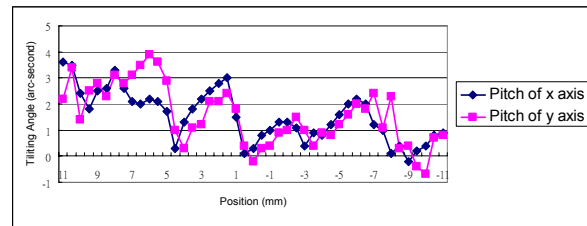


Fig 8. X and Y pitch angle of stage at different positions

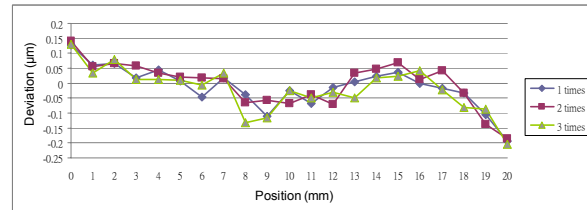


Fig 9. The XY-coplanar stage positioning error of open-loop tests

2.4 System integration and test results

2.4.1 Vibration amplitude test of the Z-axis

This study investigated the vibration amplitude of the z-axis clamp driven either by one ultrasonic motor or by two ultrasonic motors as the design reference. The result showed that the vibration amplitude using two ultrasonic motors is less than that using one ultrasonic motor, as shown in Fig 10.

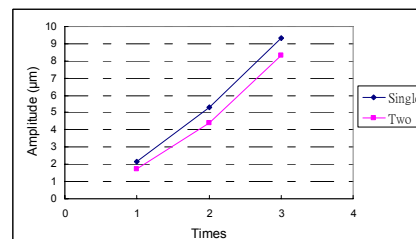


Fig 10. The result of the Vibration amplitude test

2.4.2 Positioning error test and circular positioning test of the XY coplanar stage

To implement the closed loop control of the XY-coplanar stage, a NI DAQ 6259 was adopted in this project. The XY stage control flow chart for the coplanar stage is shown in Fig 11 [10]. The X-, and Y-axis of the coplanar stage were driven by ultrasonic motors, and through a DAQ device to capture the signal of the FPGA connected to the feedback signals of the LDGI and transform its data to the displacement of the stage.

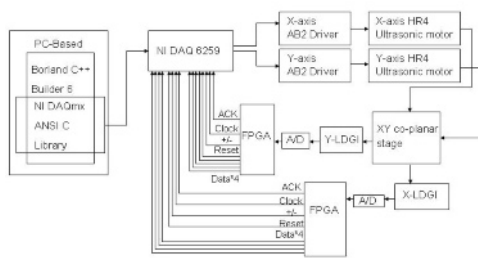


Fig 11. The XY stage control flow chart

The closed loop positioning errors of the X- and Y-axis, were about $\pm 0.1 \mu\text{m}$ within the travel of 11 mm, as shown in Fig 12 and Fig. 13, respectively, according to the test results.

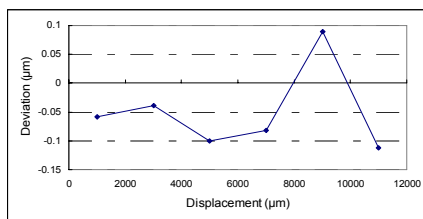


Fig 12. X-axis positioning accuracy

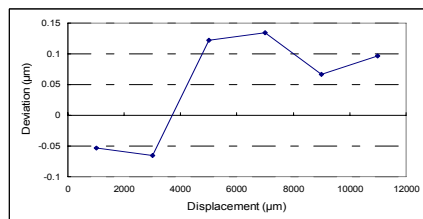


Fig 13. Y-axis positioning accuracy

A preliminary circular test has also been carried out in this study. The roundness error of the circular positioning test is about $4.01 \mu\text{m}$, as shown in Fig 14.

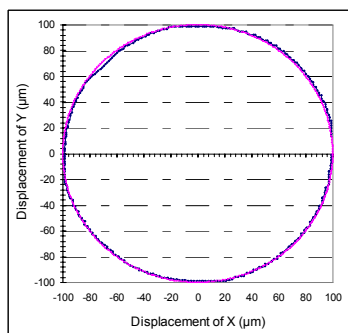


Fig 14. Circular positioning test with the radius $100 \mu\text{m}$

3. Conclusion

A meso-scale 3-axis milling machine tool with a nanometer resolution has been newly developed. Some preliminary test results of the coplanar stage have been carried out. The maximum tilting angles of the new coplanar stage for X- and Y-axis within the travel of 22 mm, were about 5 and 4 arc-seconds, respectively. The open loop positioning error for the X- and Y-axis within the travel of 20 mm was about $0.205 \mu\text{m}$. The vibration amplitude of the Z-axis using two ultrasonic motors is less than that using one ultrasonic motor. The closed loop positioning errors of the X- and Y-axis, were about $0.1 \mu\text{m}$ within the travel of 11 mm. The roundness error of the preliminary circular positioning test was about $4.01 \mu\text{m}$. The accuracy of the machine tool will be further improved in the future using an appropriate control strategy.

References

- [1] Dornfeld, D., Min, S., Takeuchi, Y. (2006) Recent advances in mechanical micromachining. CIRP Annals - Manufacturing Technology, 55 (2), pp. 745-768
- [2] <http://www.cpzl.com/news/articleview/2006-7-14/ar>
- [3] <http://www.nanotechsys.com/index.html>
- [4] <http://www.loadpoint.co.uk/products/machinery/picoace.html>
- [5] <http://www.fanuc.co.jp/eindex.htm>
- [6] Luo, X., Cheng, K., Webb, D., Wardle, F. (2005) Design of ultra-precision machine tools with applications to manufacture of miniature and micro components. Journal of Materials Processing Technology, 167 (2-3), pp. 515-528.
- [7] Fan, K.-C., Fei, Y., Yu, X., Wang, W., Chen, Y. (2007) Study of a noncontact type micro-CMM with arch-bridge and nanopositioning stages. Robotics and Computer-Integrated Manufacturing, 23 (3), pp. 276-284.
- [8] Fan, K.-C., Li, B.-K., Liu, C.-H. (2009) A diffraction grating scale for long range and nanometer resolution. Proceedings of SPIE - The International Society for Optical Engineering, 7133, art. no. 71334J.
- [9] Abbe, C. (1887) Popular errors in metrology. Journal of the Franklin Institute, 123 (2), pp. 115-128.
- [10] Cheng, F., Fan, K.-C., Fei, Y.-T. (2008) A robust control scheme of nanopositioning driven by ultrasonic motor. Proceedings of SPIE - The International Society for Optical Engineering, 7130, art. no. 71301O.

Acknowledgement

The authors are grateful to the Nation Science Council of the Republic of China for supporting this research under grant NSC 97-2221-E-011-050.

A Novel Concept to Design Machine Tool Structures using Multifunctional Materials

F. Aggogeri¹, A. Merlo² and N. Pellegrini¹

¹ University of Brescia, Department of Mechanical and Industrial Engineering, Via Branze, 38, 25123, Brescia, Italy

² Ce.S.I. Centro Studi Industriali, via Tintoretto 10, 20093 Cologno Monzese, Italy

Abstract. This paper reports on a novel concept to design and realise machine tool structures focussing on improvements related to the thermal and dynamic stability of the machine. These involve a large reduction in the mass of moving machine parts and an increase of their stiffness and damping to obtain excellent static, dynamic and thermal stability of the structures, features becoming a “must” to ensure excellent results in terms of technological and cost-saving design effectiveness. The authors have carried out a thorough study of, and testing validation on, multifunctional material prototypes for the moving parts of Ultra High Precision (UHP) machine tools. Two types of multifunctional materials are considered: aluminium foams (AFS), based on sandwiches with cores made of metal foam (open cells), and corrugate-core sandwich panels. Both solutions have incorporated phase change materials (PCMs) in order to maintain the thermal stability when the environmental temperature changes. Additionally, the hybrid materials reduce the weight of the structures, increasing damping performance and guaranteeing an excellent stiffness. The study presents the experimental results and a comparison of the two implementation materials suggested.

Keywords: Multifunctional Materials, Machine Tools, Ultra High Precision Machining

1. Introduction

The introduction of multifunctional materials in machine tool (MT) design and building can offer important advantages in terms of specific stiffness, structural damping, dimensional and thermal stability [1], especially in micro/meso scale level ($10\div 10000\ \mu\text{m}$ range) domain or Ultra High Precision (UHP) machining. This paper focuses on a well-known problem that affects machining accuracy. This problem is the thermally-induced errors arising from thermal deformation of the machine elements caused by internal/external heat sources. There are several methods to solve this problem including temperature control, thermally stable structural designs and error compensation. In this context, a novel approach for thermal error reduction, based on an “a “passive” (self-adaptive) strategy, is proposed. This self-adaptive method consists of a new class of multifunctional materials based on metallic (Aluminium) foam and

corrugate-core sandwiches (Figure 1) impregnated with PCM (Phase Change Material) materials. These materials, used either as a filler or the core of sandwich structures, provide high stiffness-to-weight ratios together with good vibration damping properties and high thermal-stability. The structures described represent a great challenge to MT sector and could open interesting perspectives for applications of advanced materials technologies within this sector.

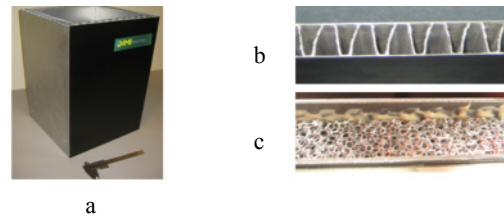


Fig. 1. Multifunctional materials: Al Foam and Al corrugated core sandwiches infiltrated by PCMs.

2. MT multifunctional structures

To study the proprieties and advantages of these classes of materials, authors have designed, realised and tested two prototypes of a moving MT structure (the Z-axis, $300\times 300\times 500\ \text{mm}$, of a precision milling machine) and compared the results with those of conventional materials. The first prototype consists of a structure of sandwiches with the core made of metal foam (open cells, density 20 ppi) material impregnated by a PCM wax Figure 1(a-b).

Metal foams represent a class of materials with low density and novel physical, mechanical, thermal, electrical and acoustic proprieties[2]. They offer potential for lightweight structures, for energy absorption and thermal stability with low costs. These performances can be achieved thanks to their exceptionally high properties in term of stiffness-to-weight ratio and low density with good shear and fracture strength [3]. Metal foams have a cellular structure consisting of solid metal (aluminium)

containing a large volume fraction of gas-filled pores. Their particular structure permits them to be impregnated by other materials (as liquids or foam) such as a PCM wax. The main features of these types of materials are the pore size and the relative density. The pores are polygonal openings and their size defines the number of pores per inch (ppi). The relative density is a fundamental property in order to determine the density of a foam. Using this information, it is possible to choose the most suitable type of foam and calculate the quantity of the PCM material that can be impregnated into the metal foam pores/cells. The main mechanical proprieties of metal foams are excellent stiffness, good shear and fracture strength, and high mechanical damping capacity, parameters that are required to ensure machining accuracy, especially in the submicron range.

The second 3D beam considered is a structure based on sandwich panels with an Aluminium corrugated core. This material guarantees light-weight proprieties without impacting on the MT element stiffness. Corrugated core structures provide less efficient and highly anisotropic load support, and enable opportunities of incorporating a number of different functions in the same structure. In particular their shape features permit to be easily realised and impregnated by a PCM material (as liquid state), Figure 1(a-c). These features includes also acoustic and thermal insulation. Prismatic topology structures can be manufactured by sheet bending or progressive rolling operations, or by extrusion techniques. The corrugation approach is often preferred for low relative density structures made of alloys with high formability. Triangular, flat topped, square or sinusoidal corrugations represent different effective solutions to adopt in sandwich realisation. For both prototypes, the application of Phase Change Materials has been a good solution to solve the thermal issue in MT structure design and building [4]. PCMs take advantage of latent heat that can be stored or released from a material over a narrow temperature range (the so called "plateau"). These materials absorb energy during the heating process as phase change takes place and release energy to the environment in the phase change range during a reverse cooling process. The insulation effect achieved by the PCM depends on temperature and time. In particular, a PCM's temperature remains constant during the phase change. This is useful for keeping the object (i.e. MT components or structure) at a uniform temperature [5-6]. In this study, the authors have used a paraffin wax with a melting point about 31°C, a heat capacity (latent heat) of 130 KJ/kg and a density close to 0.89 Kg/l (solid state at 25°C) to impregnate both hybrid prototypes [7]. The wax is an ecological heat storage material that uses the processes of phase change between solid and liquid (melting and congealing) to store and release large quantities of thermal energy at nearly constant temperature. Other important proprieties are long life product, with stable performance through the phase

change cycles, ecologically harmless and non-toxic and chemically inert.

3. Multifunctional structures and their mechanical proprieties

The main mechanical proprieties of these multifunctional structures are excellent stiffness, good shear and fracture strength, and a high mechanical damping, all proprieties required to ensure machining accuracy, especially in the submicron range [8]. In order to evaluate these features and develop a comparison with other materials used for structural MT components, a theoretical study is undertaken. The study strategy was based on the evaluation of two parameters that can be considered merit indexes: the structural index and the damping coefficient. The structural index is given by the ratio between the cube root of the Young's module E and the density of the material ρ [9-10]. This index involves the material mass and stiffness. For a prescribed stiffness, materials with the same structural index have the same weight. The weight is minimised (and the stiffness is increased) by selecting materials with large structural index values. The static, dynamic and mechatronic behavior of a structure can be translated into values for the structural index and damping. A comparison between steel, aluminium alloys, Mg alloys and metal foams has been developed. The values assumed by the structural index $E^{1/3}/\rho$ and by the damping coefficient η for these materials are given in Table 1.

Table 1. Comparison of material indicators

Material	$E^{1/3}/\rho$ [GPa ^{1/3} /Mg/m ³]	η
Steel	0.77	$6 \cdot 10^{-4} \div 10^{-3}$
Al alloys	1.5	$2 \cdot 10^{-4} \div 4 \cdot 10^{-4}$
Mg alloys	1.9	$10^{-3} \div 10^{-2}$
Al Corrug. Sandw	2.52	$4 \cdot 10^{-3} \div 10^{-2}$
AFS	2.67	$10^{-4} \div 10^{-3}$

The materials characterized by the highest values of the structural index and damping coefficient are the Aluminium Metal Foam and Aluminium Corrugated panels. In the same way, Mg alloys have a high value of damping but they are extremely expensive, especially due to their high manufacturing costs. In the light of these considerations, the authors consider metal foam and aluminium corrugate materials as excellent candidates to enhance the static, dynamic and mechatronic behaviour of MT structural building [11-12]. Nevertheless the thermal issue has not been considered, but it is analyzed in a second phase by introducing PCM materials.

4. Thermal performance of multifunctional structures: experimental trials

The main goal of this research is to develop a thorough thermal analysis of the prototypes infiltrated by the PCM when the environmental temperature is perturbed. In fact, main issue in UHP machining is errors in positioning on account of thermal deformation [13]. It has been demonstrated that errors due to thermal effects account for 30-70% of the total dimensional and shape errors of a workpiece in precision engineering [14-15]. In order to improve thermal accuracy, the authors have infiltrated the lightweight material with a PCMs wax with a typical melting point about 31°C. The experimental tests covered the prototypes previously described. The prototypes were tested in controlled environmental conditions, reducing the variabilities as a consequence. Thermal conditions were obtained and maintained by one thermal source (2 kW), and measured using an infrared thermo-camera and a series of a thermocouples strategically positioned on the prototypes. In first test, the environment was held constant and the investigation was based on temperature trends rather than on static responses; the low variability obtained can be attributed to the repeatability of the experiments. Two observations seemed enough to assess thermal performances.

The trends and responses in the first test were compared with the behaviours of the beams without PCM infiltration. The environmental conditions at the beginning of the experiment were close to 17°C. The tests ended after 18000 seconds and, in any case, after the melting completion of the PCM. The experiment was monitored since the external temperature of the beams impregnated with PCM reaches 40°C. Data collection was by an accurate data acquisition system (sampling frequency of 9Hz). Figure 2 gives the results of Test 1 related to Aluminium Corrugate beams. The environment achieved 55°C after 25 minutes and maintains constant the temperature for 6 hours. The Aluminium corrugated core structure (without PCM infiltration) shows a similar trend. In contrast, the multifunctional structure, impregnated by the PCM materials, shows an important plateau trend.

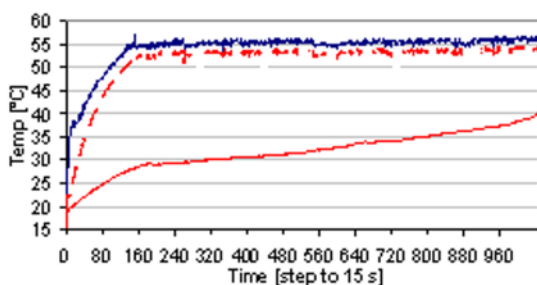


Fig. 2. Thermal data comparison: the Aluminium Corrugate beam with PCM (plateau line) and without PCM (dotted line) infiltration

The plateau ends after completion of the PCM phase transition at approximately 67 minutes, then a linear increase (VarT equal to 0.039 °C/min) of the temperature is observed.

The results of Test 1 are listed in Table 2. The considerable thermal gain due to the multifunctional material should be noted. The thermal gain is proportional to the temperature accumulated by the wax, quantifiable by the area included between the dotted and plateau curves.

The multifunctional material controls the temperature during the plateau. In this case, at the end of the plateau the temperature does not exceed 35°C, instead the structure without the PCM infiltration reaches 53 °C causing potentially relevant consequences on material distortion. From a MT point of view, this effect would lead to undesired shape errors on the workpiece [16-17]. In the same way, the authors carried out thermal trials on the Aluminium Metal Foam structures (Test 2), measuring the thermal gains between the prototypes with PCM and without PCM infiltration. The results are summarised in Table 2. The main indicators considered are:

- TM [minutes]: Time to PCM melting
- TP [minutes]: Duration of the plateau
- T40 [minutes]: Time to 40 °C
- VarT [°C/ minutes]: Trend of the speed increase after completion of the plateau
- AvgTs [°C]: Average difference between thermo-points on the same surface
- ΔT [°C]: Temperature gain at the end of the experiment related to structures without PCM infiltration

Table 2. Test 1 and Test 2 , Performance indicators

Performance Indicator	AFS	Al Corrug. Sandw
TM [minutes]	37	62
TP [minutes]	87	115
T40 [minutes]	300	260
VarT [°C/ minutes]	0.039	0.048
AvgTs [°C]	0.48	0.42
ΔT [°C]	20.14	22.43

It was noted that multifunctional structure has a plateau duration of 87 minutes limiting the thermal noises. In the light of the results, the last step of the study was a direct comparison between the proposed multifunctional structures: aluminium foams (AFS), based on sandwiches with core made of metal foam (open cells), and corrugate-core sandwich panels. Figure 3 highlights the multifunctional prototype behaviours when the environment temperature changes. For both configurations, the thermal gain is noted to provide a significant advantage in terms of thermal error reduction. Then, after the plateau, the temperature of the prototypes

increases with the same speed (close to $0.045^{\circ}\text{C}/\text{min}$). Figure 4 shows the amount of heat absorbed by the multifunctional prototypes during the experiments (it is calculated as the difference between the environment temperature and average temperature on the beams). This diagram is useful to understand the heat storage behaviour of the multifunctional materials when the environment temperature is perturbed.

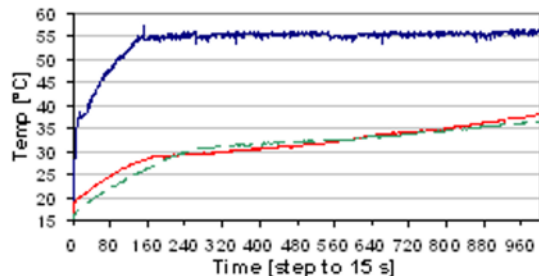


Fig. 3. Comparison between AFS structure (dotted line), Al corrugated structure (plateau line) and environment temperature (sketched line).

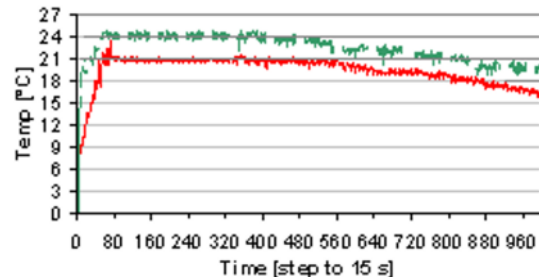


Fig. 4. Heat storage of the multifunctional structures: AFS (dotted line) and Al corrugated (sketched line) structures.

5. Conclusions

This paper has presented an application of novel multifunctional materials to MT design and building. The case studies show the potentialities offered by the utilisation of these advanced materials in the MT sector. In fact, the combination of hybrid materials (Al metal foam and Al corrugated cores) allow increases in the damping of MT moving part structures reducing their masses and guaranteeing the stiffness. In the same way, the paper describes a study of the thermal stability of the MT structures using Phase Change Materials to impregnate the core of the sandwiches. Thermal properties and behaviours of the multifunctional material prototypes have been investigated experimentally. The thermal tests performed on the beams highlight a considerable thermal gain due to the multifunctional materials. Considering these thermal tests, developed in an appropriate room where the temperature was maintained in a specified range, the temperatures measured on the external surfaces of the innovative prototypes do not exceed 40°C , during the plateau phase

and for long duration time. Instead the beams without the PCM infiltration rapidly reach 50°C , causing potentially serious consequences in terms of distortions and shape errors during manufacturing. Using the materials investigated, it is possible to design innovative structures for moving MT parts or components that are able to maintain their temperature constant for long periods, even if there are many heat sources. It is clearly necessary to improve the design and production processes of these structures; nevertheless the structural properties presented are a milestone leading to further studies investigating the static, dynamic and thermal stability.

References

- [1] J.C. Liang, H.F. Li, J.X. Yuan, J. Ni, 1997, A comprehensive error compensation system for correcting geometric, thermal and cutting force induced errors, *International Journal of Advanced Manufacturing Technology* 13 (10) 708-712
- [2] R. Ramesh, M.A. Mannan, A.N. Poo, 2000, Error compensation in machine tools - a review, *International Journal of Machine Tools & Manufacture* 40 1257-1284
- [3] M.F. Ashby, A.G. Evans, N.A. Fleck, L.J. Gibson, J.W. Hutchinson, H.N.G. Wadley, 2000, *Metal Foams: A Design Guide*, Butterworth-Heinemann, Oxford
- [4] M. Week, 1984, *Handbook of Machine Tools: Metrological Analysis and Performance Tests*, Vol. 4, John Wiley and Sons, New York
- [5] A. Merlo, D. Ricciardi, F. Aggogeri, R. Codini, F. Meo, L. Le Lay, 2008, Application of composite materials for light weight and smart structures design of high performance milling machines, in: *Proceedings of the 13th European Conference on Composite Materials*, Stockholm, Sweden
- [6] M. Week, P. McKeown, R. Bonse, U. Herbst, Reduction and compensation of thermal errors in machine tools, *Annals of the CIRP* 44 (2) (1995) 589-598.
- [7] Zalba, J.M.S.T. Man, 2003, Review on thermal energy storage with phase change: materials, heat transfer analysis and applications, *Applied Thermal Engineering*, 23 251-283
- [8] Vinson JR. The behavior of sandwich structures of isotropic and composite materials. Technomic Publishing; 1999.
- [9] Mou J. A systematic approach to enhance machine tool accuracy for precision manufacturing. *Int J Mach Tool Manuf* 1997;37:669-85.
- [10] L.J. Gibson, M.F. Ashby, 1997, *Cellular solid, structure and properties*, second ed., Cambridge University Press, Cambridge DeGarmo EP, Black JT, *Materials and processes in manufacturing*. 9thed. New Jersey: John Wiley&Sons; 2003.
- [11] J. Bryan, 1990, International status of thermal error research, *Annals of the CIRP* 39 (2) 645-657
- [12] T.L. Schmitz, J.C. Ziegert, J.S. Canning, R. Zapata, 2008, Case study: A comparison of error sources in high-speed milling, *Precision Engineering* 32 126-133
- [13] R.H. Harding, 1967, *Morphologies of Cellular Materials. Resinography of Cellular Plastics*, ASTM-STP 414
- [14] J.J. Bikermann. 1973, *Foams*, Springer-Verlang. New York
- [15] E.A. Blair, 1967, *Structures of foamed plastics. Resinography of cellular plastics*, ASTM-STP 414, 84.
- [16] V.S. Deshpande, M.F. Ashby, N.A. Fleck, 2001, Foam topology bending versus stretching dominated architectures, *Acta mater.* 29 1035-1040.
- [17] M.F. Ashby, 1999, *Materials Selection in Mechanical Design*, Butterworth-Heinemann, Oxford.

Design Synthesis of a three legged SPS Parallel Manipulator

A. Khalid¹ and S. Mekid²

¹ School of Mechanical and Manufacturing Engineering, National University of Science & Technology, H-12, Islamabad, Pakistan.

² Mechanical Engineering Department, King Fahd University of Petroleum & Minerals, Dhahran, 31261, KSA.

Abstract. This paper shows the design analysis of a non-conventional parallel manipulator of 3-SPS (Spherical-Prismatic-Spherical) configuration. This configuration is selected with the aim to enhance the manipulator workspace and dexterity in a table-top scale pod. The minimum number of limbs can be three in a parallel kinematic machine (PKM). The limb interference is reduced in a three limb structure unlike the six limbs configuration in the Stewart platform. In contrast, the stiffness is compromised in this structure as the platform cannot take load while standing on three ball joints. In order to deal with this issue, self-lockable spherical joints are designed to be incorporated into the 3-SPS system. The table-top size PKM manipulator is prototyped with the self-lockable spherical joints and its working performance is checked.

Keywords: self-lockable joints, SPS, PKM manipulator.

1. Introduction

PKMs are conventionally used for high load capacity and are known for accuracy using low cost components [1]. In the micro domain or for small size applications like MEMS, the conventional Stewart-Gough platform concept is being exploited. The miniature hexapods are being designed for many applications like optics alignment, hand-held force-torque sensor [2] and for medical applications like spine assist robot [3].

Most of the PKM applications are based on the conventional Stewart-Gough platform design. In the conventional six leg hexapod, the manipulator orientation capability is mainly restricted due to the limb interference. In order to improve the rotational capability, less number of limbs can be used. The minimum number of limbs in the PKM can be three. In a small size pod, large orientation capability is limited. The only way is to increase the size of the manipulator and the actuator travel range. This means that large orientations are not possible with a desktop size pod. This fact highlights the importance of the pod made up with a smaller number of actuators.

The design concept is expected to be a six DOF (Degrees of freedom) system with reduced number of actuators which will present inherent issues that will need

to be solved. It is desirable to use a complete ball joint on both sides of the limb irrespective of the challenges in regards to stiffness and workspace singularities. Ball joints on both sides and three number of limbs can be seen as the least constraint configuration in the PKM design. Also, this configuration may not be able to completely avoid uncontrollable motion. The ultimate objective is to make a physical prototype of such a manipulator having six DOF and is using three number of limbs and six spherical joints in the structure. The physical prototype will then be tested for its performance.

Accurate DOF calculation is a conventional problem in PKM. Gogu [4] reviewed 35 different contributions for the quick calculation of DOF in PKM as there is no universally accepted method so far. Conventional approaches [5-7] generally constitute a quick calculation using a formula for mobility of a manipulator. Out of all the contributions, the Grubler-Kutzbach (GK) equation is currently in wide use for DOF calculation. Hunt [7] and Tsai [5] presented the mobility equation with some modifications of Grubler's formula.

$$M = b(n_c - g - 1) + \sum_{i=1}^p f_{dof} - f_p \quad (1)$$

where

n_c = number of connectors

g = number of joints

f_{dof} = DOF of i^{th} joint

b = mobility number; $b = 3$ for planar mechanisms and 6 for spatial ones.

f_p = Passive DOF about an axis, usually referred as an internal DOF that cannot be used to transmit motion or torque.

Various configurations in PKM can be studied by altering the number of limbs and the type of joints. An overview of the PKM characteristics can be given using different types of joints and varying the number of limbs as shown in Fig. 1 Three properties are discussed. In the first row, all the kinematic limbs are SPS. In the lower rows, a mix of spherical and universal joints is used. The DOF of the manipulators are calculated using GK. DOF

is reducing considerably from top to bottom. From left to right, the number of legs is varied from 3 to 5 and the corresponding stiffness of the system will increase with the addition of each leg. In contrast, the workspace will shrink by adding more legs as each limb will put a constraint on the mobility of the mechanism. A trade-off is required between high stiffness and large dexterous workspace requirement. The best solution will be to use a three-legged system with all spherical joints to get full freedom with no mobility constraint. But the stiffness will be compromised in this scenario. To add stiffness to a system based on all spherical joints is a challenging design task that is addressed in the current research.

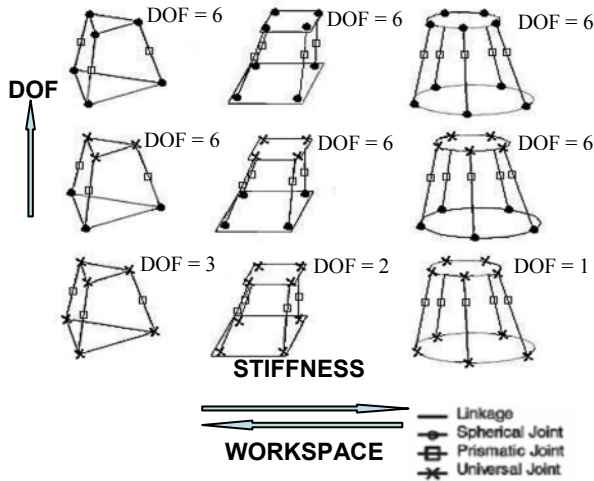


Fig. 1. PKM characteristics

2. Modelling issues

In the conventional Stewart-Gough platform, six DOF are achieved using six actuators and the resulting Jacobian matrix become square. However, the 3-SPS mechanism will lead to the rectangular Jacobian matrix that will require further transformation. The novelty of 3-SPS lies in the three limbs and six spherical joints which make it capable of having six DOF. However, uncontrollable motion may be generated and needs further consideration of special ball joints to make it workable.

2.1 Position Analysis

The three limbs are oriented at 120° apart as shown in Fig 2. The upper platform radius is r_p . For the lower platform, a bigger radius ' r_b ' is assumed. For this platform, the size ratio of r_b/r_p can be varied to check the influence of this variable on output characteristics such as workspace. Let us assume r_b equal to $2 \times r_p$. Hence, the joint coordinates with respect to global reference 'O' for the upper and lower platform can be written as follows.

$$\begin{bmatrix} a_{1x} \\ a_{1y} \\ a_{1z} \end{bmatrix} = \begin{bmatrix} r_p \\ 0 \\ 0 \end{bmatrix}, \begin{bmatrix} a_{2x} \\ a_{2y} \\ a_{2z} \end{bmatrix} = \begin{bmatrix} r_p c_\alpha \\ r_p s_\alpha \\ 0 \end{bmatrix} \text{ and } \begin{bmatrix} a_{3x} \\ a_{3y} \\ a_{3z} \end{bmatrix} = \begin{bmatrix} r_p c_\beta \\ r_p s_\beta \\ 0 \end{bmatrix} \quad (2)$$

$$\begin{bmatrix} b_{1x} \\ b_{1y} \\ b_{1z} \end{bmatrix} = \begin{bmatrix} r_b c_\gamma \\ 0 \\ r_b s_\gamma \end{bmatrix}, \begin{bmatrix} b_{2x} \\ b_{2y} \\ b_{2z} \end{bmatrix} = \begin{bmatrix} r_b c_\gamma c_\alpha \\ r_b c_\gamma s_\alpha \\ r_b s_\gamma \end{bmatrix} \text{ and } \begin{bmatrix} b_{3x} \\ b_{3y} \\ b_{3z} \end{bmatrix} = \begin{bmatrix} r_b c_\gamma c_\beta \\ r_b c_\gamma s_\beta \\ r_b s_\gamma \end{bmatrix} \quad (3)$$

here 'c' and 's' denote 'cos' and 'sin', respectively and γ_i is the inclination angle of the lower platform from the ground. The transformation rotation sequence is the same as given in [8]. The closed loop vector diagram gives the equation in vector term as depicted in Fig. 2.

$$\overline{A_i B_i} = p + {}^B R_A^A a_i - b_i \quad (4)$$

The length of the i th limb is obtained by taking the dot product of the vector $\overline{A_i B_i}$ with itself and taking the square root after expanding.

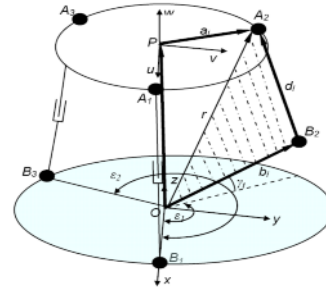


Fig. 2. Three legged SPS mechanism

$$d_i = \pm \sqrt{p^T p + [{}^A a_i]^T [{}^A a_i] + b_i^T b_i + 2p^T [{}^B R_A^A a_i] - 2p^T b_i - 2[{}^B R_A^A a_i]^T b_i} \quad \text{for } i = 1, 2, 3. \quad (5)$$

where d_i denotes the length of the i th limb. Eq. 5) gives the inverse kinematic solution. There are two possible solutions for limb lengths at each given location of the upper platform. One of these solutions has a positive value whilst the other is negative. However, a negative limb length is physically not feasible. The vectors, a_i , b_i are given in eq. (2) and (3), whereas ${}^B R_A^A$ being the transformation rotation matrix.

The mechanism consists of an SS (Spherical-Spherical) pair in each kinematic limb which is actually responsible for the manipulator six DOF and a difficult forward solution problem. Tsai [5] has formulated the direct solution for 6-SPS system. 12 equations are formed including six inverse kinematic equations. Large number of solutions is identified in solving 12 non-linear equations for 12 unknown variables (nine for rotation matrix and three translations). For the 3-SPS system, there will be only nine equations available, i.e., six orthogonal condition equations and three equations from inverse kinematics for the three limbs. Thus, only nine equations are available for the 12 unknown variables making the system unsolvable. Using Raghavan's method [9], in which nine variables are required, only six

equations are available, i.e., three equations from inverse kinematics and three from the trigonometric relations of the rotation matrix elements. This again makes the system unsolvable. The other practical way to do the forward motion in the robot is to use the hook-up table approach. A hook-up table is like a pre-knowledge database using the inverse solution. The controller then read the stored data for forward motion generation.

2.2 Jacobian Analysis

The manipulator is a six DOF system and has a motion in Cartesian space in all six axes. The SPS manipulator has three prismatic actuators. For the conventional Jacobian formulation, differentiating eq. (4) with respect to time yields the Jacobian with three actuators.

$$J_x = \begin{bmatrix} s_1^T & (a_1 \times s_1)^T \\ s_2^T & (a_2 \times s_2)^T \\ s_3^T & (a_3 \times s_3)^T \end{bmatrix}_{3 \times 6} \quad (6)$$

where a_i and s_i denote the vector $\overline{PA_i}$ and $\overline{A_iB_i}$, respectively. However, the conventional Jacobian is composed of non-homogeneous units and lacks physical significance. To avoid the unit inconsistency problem in the conventional Jacobian matrix, Kim and Ryu [10] formulated a dimensionally homogeneous Jacobian matrix. The method defines the vector of kinematic parameters of three points anywhere in the same plane which carries the upper platform spherical joints. Using this technique, a homogeneous Jacobian is formulated for 3-SPS system [11]. Dimensionally homogeneous Jacobian can be used for further analysis like condition number [12], Jacobian inversion and stiffness. But even the dimensionally homogeneous Jacobians are rectangular in size and matrix inversion of these matrices is not possible. Tucker and Perrira [13] showed that the generalized inverses can be taken in robotics for the rectangular matrices using the pseudo inversion technique. The Moore-Penrose generalized matrix inverse [14] is a unique $n \times m$ pseudo-inverse of a given $m \times n$ matrix. Singularities can also be found using Jacobian inversion. Singular configurations are particular poses of the end-effector, for which robots lose their inherent rigidity. The singularity surfaces have also been formed by deriving singularity equations for parallel mechanisms [15]. However, singularity equations for six DOF mechanisms present a complex problem because the determinant of the Jacobian matrix becomes very complicated.

3. Self-lockable spherical joints

As expected that the stiffness is compromised in this system, because the system stands physically on three ball joints. The ball joints are chosen for their inherent characteristics of providing three DOF within a compact volume. However, the six balls can provide

uncontrollable motion, e.g., while translating in any axis, error can be generated because of the unconstrained motion of balls. To overcome this, some sort of constraint or pre-load is required to minimize the error. In this scenario, it is required to design a spherical joint that allows free rotational movement around three axes while the manipulator is running and may stop it-self at any orientation when commanded to stop. Hence, the pre-load provide extra stiffness to the manipulator when the manipulator is running or stopped within the workspace. This special braking system is required in the 3-SPS system for the manipulator to work effectively. Also, some initial holding force will be required so that the manipulator can firmly stand at its starting position when the system is switched off and brakes are not applied. The ball joints are required to be made self-lockable. The self-lockable spherical joint design can have many options in terms of concept and type of actuator selection. It is difficult mechanically to stop the ball completely from rotation. Fig. 3 shows two design concepts which fulfill the design requirement.

Fig. 3(a) shows a sliced ball concept of the spherical joint. The concept shows that the two side flaps of the sliced ball are pushed by the inside actuator. The inner surface of the housing is the obstacle for the pushed flaps. The side flaps are pushed to the housing and the friction between the surfaces is responsible to stop the ball. The end result is a sudden brake or lock in the spherical joint. In Fig. 3(b), the design concept shows the ball supported by the holder strips. An electromagnetic actuator is positioned to stop the rotating ball. But rotational movement of the ball may not be stopped even if a high force is applied. To avoid the single point contact between the ball and the magnetic actuator, the magnet pole is machined to increase the effectiveness of electromagnetic actuator.

The concept selection criteria is that the joint must be easy to make, assemble and function in a miniaturized size. The joint design must provide the table-top size manipulator with high speed within the workspace. A stiff spherical joint is required to operate in synchronization with the linear actuators. Fig. 3(a) shows a design option to be used with a solenoid or piezo type actuators. However, its manufacturing require a hollow ball to be sliced and a miniaturized actuator to be inserted inside the ball. In this case, the actuator push force is limited as the ball joint is required in a small size for a table-top manipulator. For these reasons, the concept presented in Fig 3(b) is found a better choice to prototype.

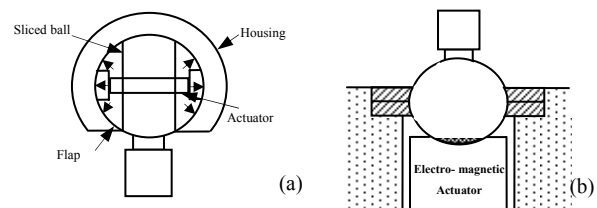


Fig. 3. Self-lockable joint concepts

A commercially available electromagnet actuator is used having a diameter of 25 mm, maximum holding force of 130 N and operates on 12 V, normally used in door locks. The maximum holding force of the magnet is available only to mate with a flat face component. When the ball is placed on the pole of the magnet, the original electromagnet allows only single point contact with the ball which is not enough to stop the ball from rotating. A spherical cavity is cut in the pole of the magnet to increase the surface area of the contact between the ball and the magnetic actuator. The ball is held with the actual holding force but all of this does not actually utilized to stop rotation of the ball. Only the tangential component of the holding force (F_{Bt}) is involved in stopping rotation of the ball as shown in Fig 4(a). The total tangential component of the magnetic holding force for the whole contact surface of the pole is found as 12 N which is only 11% of the total holding force. The rest of the force is normal in direction and does not contribute to stop the rotation of the ball.

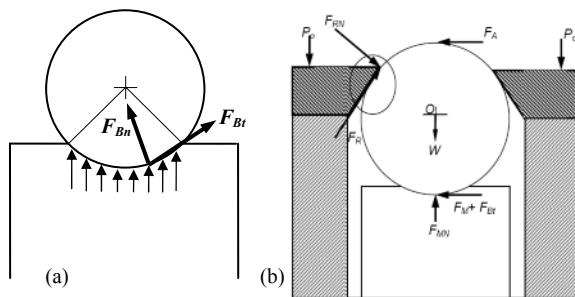


Fig. 3. (a) Tangential and normal components of magnetic holding force (b) Different forces acting on the ball.

Moreover, in the initial pose or for most of the machine's life-time, the electromagnets will remain switched off. The manipulator needs an additional force that remains present all the time (both in on/off situations). But its magnitude should be such that the balls are allowed to move when the PKM is moving and also provide the manipulator with an initial stiffness so that the moving platform can stand on its own. For this purpose, friction is created between the ball and the housing.

Fig 4(b) shows the components of the frictional and magnetic forces in the complete spherical joint design. The joint stiffness is comprised of its constituent components. Friction is provided from the upper ring as well as the magnetic cavity. The other contributing factor is the tangential component of the magnetic force. When the external force F_A is applied on the ball joint from the PKM leg actuator, the ball will attempt to rotate. The rotation of the ball is challenged first at the upper ring where the frictional force F_R will resist rotation of the ball. The second mating surface is between ball and the magnet. The friction force F_M between the ball and magnet also provides resistance to the ball rotation. The third resistance is from the tangential component of the magnetic holding force F_{Bt} that is already calculated. F_{MN}

and F_{RN} are the normal reactions. The total frictional force is found by adding F_R and F_M . Another externally applied load is P_o which is the tightening force of the upper ring. At this place, nuts fasten the whole joint. Force and moment balance equations reveal that the applied force F_A must be known to calculate nut tightening force P_o . As an example, with F_A equal to 40 N, P_o is found as 15 N and the torsional stiffness value is found as 30k Nmm/rad.

Based on the design analysis for a complete spherical joint using the magnetic actuator, a prototype is built for which experimental testing was conducted. As mentioned before that the magnetic pole is machined for the spherical cavity, therefore, a perfect spherical cavity that can exactly match the ball profile cannot be expected.

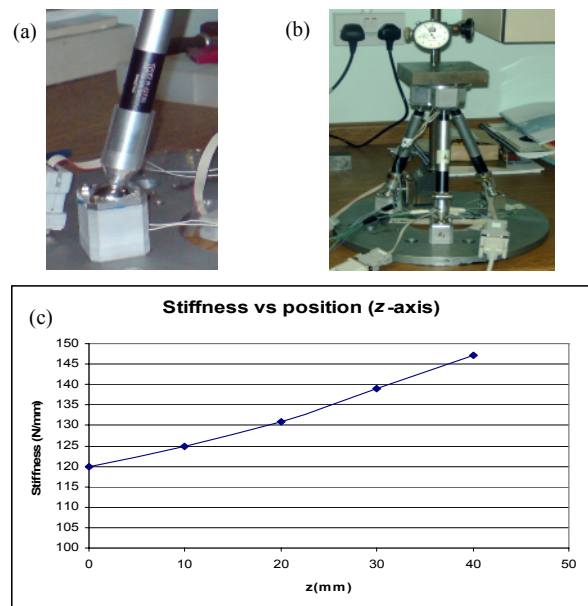


Fig. 4. (a) Physical prototype of self-lockable ball joint (b) 3-SPS manipulator (c) Stiffness vs. position.

Fig 5(a) shows a physical prototype of self-lockable ball joint. Whereas Fig 5(b) is showing the 3-SPS manipulator under load testing. The average stiffness of the manipulator in the z direction is found to be 132.5 N/mm. The trend in Fig 5(c) shows that the stiffness increases with height. Moreover, workspace limit check shows maximum x and y travel of ± 75 mm and the maximum tilt of 22° around x and y axis, respectively. The accuracy tests of the machine are conducted using a CMM machine. The average positioning accuracy is found as $57 \mu\text{m}$ whereas the best positioning accuracy is found as $4 \mu\text{m}$.

The desktop size manipulator can be used for many light weight commercial and industrial applications. With an attached gripper, it is best suited for pick and place machines for small size product production line. The manipulator may also be used for machining and inspection usage by improving its accuracy and stiffness

further. It can also be used in medical surgeries for accurate cutting and placement.

4. Conclusion

3-SPS system is realized, designed and prototyped. The desired type of joint is not found commercially and is found to be a unique requirement because a non-conventional PKM design is followed. The magnetic actuator based joint is found better on the basis of cost, stiffness and ease of manufacture as compared to other options. The designed spherical joint allows free rotational movement around three axes and is able to stop itself in any orientation. The joint size is appropriate to the size of micro machines and can even be used for other robotic applications. A workable three legged SPS manipulator is tested for workspace limit check, stiffness and accuracy and found useful for many applications.

Acknowledgements

The authors would like to acknowledge the support of the University of Manchester (UK), EU project I*PROMS and King Fahd University of Petroleum & Minerals (KFUPM - KSA).

References

- [1] Neugebauer R., Rehsteiner F., Spiewak S. and Wieland F., (1999), "Putting Parallel Kinematics Machines (PKM) to Productive Work," *Annals of the CIRP*, 48(1), 345-350.
- [2] Dwarakanath T. A. and Venkatesh D., (2006), "Simply supported, 'Joint less' parallel mechanism based force-torque sensor," *Journal of Mechatronics*, 16(9), 565-575.
- [3] Merlet J. P., (2006), *Parallel Robots*, Springer, 2nd Ed.
- [4] Gogu G., (2005), "Mobility of mechanisms: a critical review," *Mechanism and Machine Theory*, 40(9), 1068-1097.
- [5] Tsai L. W., (1999), *Robot Analysis: The Mechanics of Serial and Parallel Manipulators*, John Wiley & Sons, New York.
- [6] Bagci C., (1971), "Degrees of freedom of motion in mechanisms," *ASME J. Eng. Industry*, 93(B), 140-148.
- [7] Hunt K. H., (1978), *Kinematic Geometry of Mechanisms*, Oxford Science Publications, Oxford, UK.
- [8] Khalid A. and Mekid S., (2008), "Computation and analysis of dexterous workspace in PKMs," *International Journal of Digital Manufacturing*, 1(1), 10-13.
- [9] Raghavan M., (1993), "The Stewart Platform of General Geometry has 40 configurations," *ASME Journal of Mechanical Design*, 115(2), 277-282.
- [10] Kim S. G. and Ryu J., (2003), "New dimensionally homogeneous Jacobian matrix formulation by three end-effector points for optimal design of parallel manipulators," *IEEE Transactions on Robotics and Automation*, 19(4), 731-737.
- [11] Khalid A., (2009), *Design analysis and synthesis of a non-conventional parallel manipulator with innovative joints*, PhD Thesis, University of Manchester, UK.
- [12] Merlet J. P., (2006), "Jacobian, Manipulability, Condition Number and Accuracy of Parallel Robots," *ASME Journal of Mechanical Design*, 128(1), 199-206.
- [13] Perreira N. D. and Tucker M., (1987), "Generalized Inverses for Robotic manipulators," *Mechanism and Machine Theory*, 22(6), 507-514.
- [14] Campbell S. L. and Meyer C. D. Jr., (1991), *Generalized Inverses of Linear Transformations*, Dover, New York.
- [15] Gosselin C. and Angeles J., (1990), "Singularity Analysis of Closed-Loop Kinematic Chains," *IEEE Transactions on Robotics and Automation*, 6(3), 281-290.

Piezo-Metal-Composites as Smart Structures

R. Neugebauer, L. Lachmann, W.-G. Drossel, S. Hensel, B. Kranz, M. Nestler
Fraunhofer-Institute for Machine Tools and Forming Technology IWU, Chemnitz, Germany

Abstract. In many applications, vibration and noise are unwanted, but often inevitable. For instance, for passengers in an automobile, a reduction of comfort for the passenger is a result. For products like high precision machine tooling, the appearance of unwanted vibrations can cause negative influences on the quality of produced parts. Adaptronic devices can help to improve the vibration and noise behaviour of structures. Today the production of adaptronic structures consists of two process chains: Firstly, the fabrication of structural parts which occurs in a very efficient process with a low production time. Secondly, there is the functional integration step which normally takes place under laboratory conditions and needs a lot of production time. For creating a smart structure, the assembly of the structural part includes the use of a piezo-composite-module. The authors propose a new process chain for this with the material fabrication and functional integration taking place in one process. This can occur through a laminar piezo-module being inserted between two metal sheets and fixed by using a slow curing adhesive. After assembling the sandwich, the semi-cured adhesive allows forming of the sandwich with a reduced generation of tensile loads due to friction between the metal sheets and the piezo-module. As a last step in the process chain, the adhesive fully cures and giving a high stiffness coupling. Experimental tests have been performed to characterize the functionality and to examine the process limits. Numerical studies have evaluated the stresses and strains in the piezo-module during the forming.

Keywords: piezoceramic fibre, macro fibre composite, MFC, adhesive bonded sheets, piezo-metal-compound, deep-drawing, representative volume element, RVE, capacitance, measurement methods

1. Design and manufacturing of Piezo-Metal-Compounds

In order to create shaped intelligent structures, the authors propose the integration of piezo-modules, especially macro-fibre-composites (MFC), between two metal sheets. The joining of the three elements takes place by the use of a 2K-adhesive, which surrounds the MFC and connects it the sheets. To obtain the desired shape, forming takes place when the adhesive has still a low viscosity. Using this approach, the strains resulting from the friction between the layers during forming can be reduced significantly. Hardening of the adhesive finishes after the forming operation has been performed. The approach also enables forming to occur without

destruction of the brittle piezoceramic fibres. The method described allows the production of intelligent, shaped multilayer-compounds in one process chain. More details of the manufacturing are presented in [1] and [2].

2. Forming operations with different MFC positions

To get information about tolerable MFC loads during forming, studies with different geometries and a variation of MFC position were applied. Furthermore different punch and die geometries allow an increasing number of possible forming loads. The production of rectangular cups offers the possibility to place the MFC in regions with higher or lower forming loads. Two rectangular punches, with a width of 120 mm x 80 mm and a double curvature of 100 mm respectively 250 mm on the top of the punch are used. Fig. 1 shows the tool system and the geometries of formed parts with both types of punch. The MFC are integrated in the cup bottom as well as in the upper and the lower radii on the long vertical side of the cup. The aim is to detect possible defects caused by the forming process. Furthermore the functionality of the specimen is to be characterized.

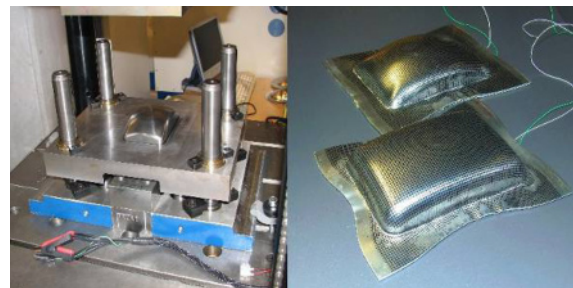


Fig. 1. Tool system and formed parts

3. Test of functionality

The usability of the manufactured specimen as a sensor device depends on the functionality of the compound after forming. For its characterization, different tests can be performed. One method uses the measurement of capacitance. MFC consist of a network of small capacitor cells connected in parallel (fig. 2) [3]. The summation of all capacitances leads to the total capacitance of the MFC.

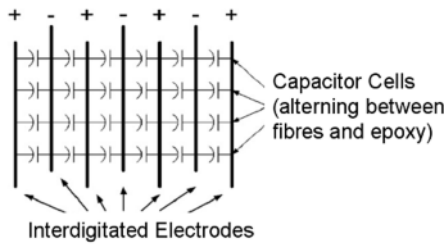


Fig. 2. Schematic buildup of MFC capacitance [3]

Every capacitor cell, which means exactly one part of one piezofibre, located between a pair of positive and negative electrodes, can be described in simplified terms as a plate capacitor, because the influence of the adhesive can be neglected. If this capacitor has no damage (fig. 3. left), its capacitance is calculated with eq. 1. If a crack is induced by too high forming loads, the capacitance is reduced (fig. 3, right).

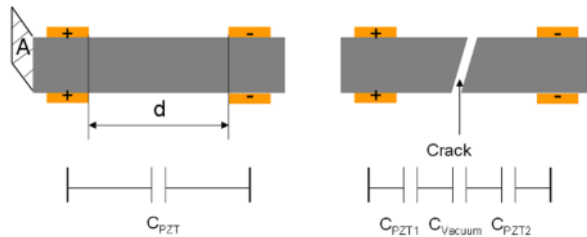


Fig. 3. Influence of cracks on capacitance C_{PZT}

Like a plate conductor with an additional dielectric of lower permittivity ϵ , the capacitance C_{PZT} of the capacitor cell is reduced because of a serial connection of the broken PZT-fibre with a vacuum inside the crack. Its capacitance is computed with eq. 2.

$$C_{PZT} = \epsilon_0 \cdot \epsilon_{rPZT} \cdot \frac{A}{d} \quad (1)$$

$$\frac{1}{C_{PZT-crack}} = \frac{1}{C_{PZT1}} + \frac{1}{C_{vacuum}} + \frac{1}{C_{PZT2}} \quad (2)$$

A crack of 10 μm in the middle of such a capacitor cell, leads to a reduction of capacitance by about factor 38 in this cell. Summation of capacitances of intact and

damaged cells results in a reduced total capacitance in comparison to a non-damaged MFC. The detection of a reduction of the total capacitance during the forming process enables a prediction of induced cracks and a damage of electrodes of the MFC. If no reduction is detectable, no cracks or defects of contacting are expected.

Another possibility for the characterization of functionality is to deflect the compound by a defined displacement. Simultaneously the electrical answer is measured. If the stiffness of the specimen (for example for bended specimen) allows an elastic deformation with little forces, a shaker is used (fig. 4).

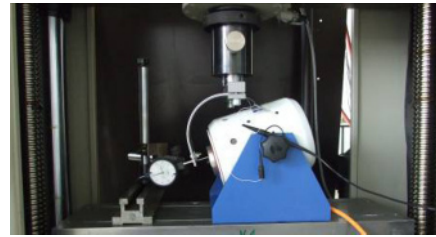


Fig. 4. Test of sensor functionality (bending specimen)

A defined displacement of one end of the specimen causes a strain of the integrated piezoelement. Because of the direct piezoelectric effect, electric charges are induced which are visualized by a voltage metering on an oscilloscope. If the stiffness of the formed specimen is very high, e.g. for rotationally symmetric structures, only a little displacement is possible in the elastic strain range, whereby high forces are necessary. Therefore the generation of a defined displacement can be performed e. g. with a static materials testing machine (fig. 5). To generate a measurable electric signal, a high traverse velocity is necessary. Moving with high velocities and small traverse path in the range of a tenth of a millimetre is not possible because of the position resolution of the machine. Therefore only lower velocity ranges were used.

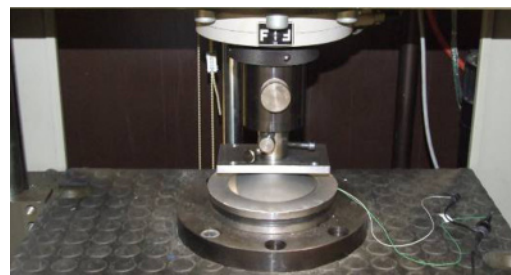


Fig. 5. Test of sensor functionality (with a rotationally symmetric structure)

Result of this is an elastic deformation of the specimen. If the traverse is now moved away quickly, the specimen springs back in its unstressed condition. During this, the MFC is getting stretched and an electric charge is induced. The generated voltage signal is displayed on an

oscilloscope. The amplitude (y) and the time (t) of the voltage signal (fig. 6) depend largely on parameters: displacement of the specimen/traverse path, traverse velocity, functionality of MFC and the geometry of the part.

A closer examination of the area below the voltage peak gives information on the electric charge, generated by the piezo element. The higher the degradation of MFC, the lower is the generated electric charge. Different velocities from 10 mm/min to 100 mm/min were used. The area below the peak is constant, whereby the duration of the signal peak increases and the maximum peak decreases in case of lower velocities.

In order to vary the loading on the inserted MFC, different geometries and positions were determined. The functionality of the specimens is characterized by the measurement of MFC capacitance during the forming process and the evaluation of the electric charge generated by a defined elastic deformation of geometry after the forming process. Table 1 shows the averaged values for capacitance after forming, the remaining functionality (capacitance after forming divided by capacitance before forming) and an equivalent for the generated electric charge by a defined elastic deformation.

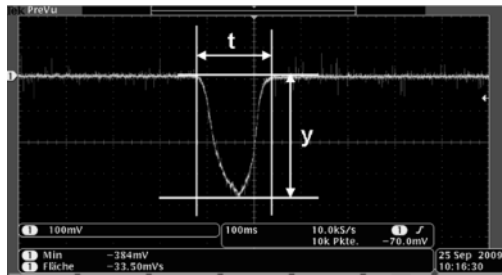


Fig. 6. Signal output of sensor functionality test

It is shown that forming is possible without a damage of MFC (M8528-P1) in the case of positioning the patch on the top of the punch. Even a position in the upper and the lower radii on the long vertical side of the cup allows forming with a reduction of capacitance of 25 %. All of these specimens can be used as a sensor device.

4. Numerical investigation

Deep drawing with punch radii of 100 mm and 250 mm were numerically simulated. The comparison of experimentally and numerically determined punch-force-displacement curves shows good agreement. In the rear region, the simulation force curve for the radius of 100 mm is located below the experimental one. The possible reason is a development of micro-wrinkles, which can only be modeled by a massive increase of mesh density in the forming simulation. With the method [4], detailed described in [5], a back-transformation of forming loads is possible to evaluate the stresses acting on the piezoceramic fibre. In accordance with the experimental results, bending over double-curved punches with bigger bending radii of about 250 mm produces low load levels (max. 90 MPa) which result in zero function degradation. The load level for the 100mm radius punch leads to a maximum fibre stress in the fibre direction of 580 MPa (basic stress level: 450 MPa).

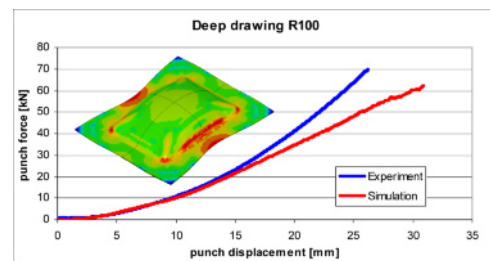


Fig. 7. Deep drawing - punch radius 100 mm

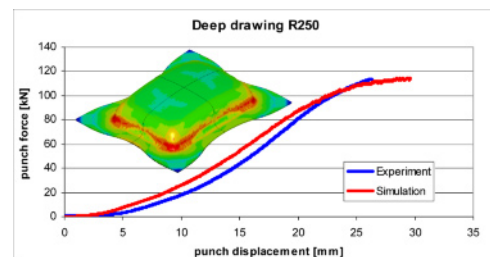


Fig. 8. Deep drawing - punch radius 250 mm

Table 1. Different specimen and function analysis

Specimen	Averaged Capacitance after forming [pF]	Averaged remaining functionality [%]	Averaged electric charge equivalent [mVs]
R100, M8528P1, top of punch	3815	100	477
R250, M8528P1, top of punch	3700	100	633
R100, M2814P1, upper radius	582	90	268
R100, M2814P1, lower radius	620	73	135

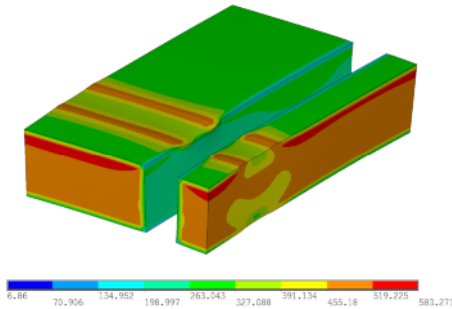


Fig. 9. Fibre stress in fibre direction - punch radius 100 mm

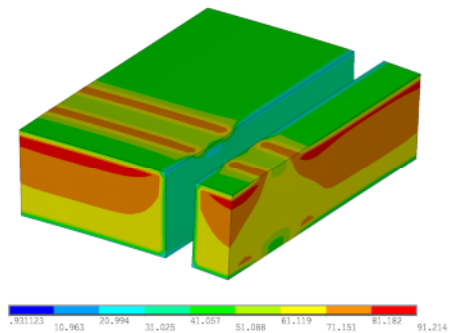


Fig. 10. Fibre stress in fibre direction - punch radius 250 mm

Within the method described, the fibre loads are over-estimated in the simulation due to the linear-elastic nature of the approach. For higher load levels, further numerical investigation for the prediction of the exact material behaviour is planned.

5. Summary

It has been shown that the new process chain with material and functional integration in one process allows the production of piezo-metal-compounds by deep drawing. Different geometries were analysed experimentally and numerically. The specimen can be used as sensor devices. Research for their use as actor devices are planned. For the characterization of the remaining functionality of formed piezo-metal-compounds, measurement of capacitance and a sensor test were performed. Both methods allow the estimation of MFC-functionality after forming. The integration of MFC is possible even in areas of high forming loads. A partially damaged MFC also works as a sensor, whereat the generated electric charge is reduced in comparison with a non-damaged MFC.

Acknowledgement

This Paper is based on the work of the subprojects B1, B2 and C1 of the Transregional Collaborative Research Centre 39 PT-PIESA "High-Volume Production-Compatible Production Technologies for Lightmetal and Fiber Composite-Based Components with Integrated Piezo Sensors and Actuators". The authors gratefully acknowledge the support of the German Research Foundation DFG (Deutsche Forschungsgemeinschaft), which funds this research.

References

- [1] W.-G. Drossel, S. Hensel, B. Kranz, M. Nestler, A. Göschel: Sheet metal forming of piezoceramic-metal-laminar structures - Simulation and experimental analysis, In: CIRP Annals 2009, Manufacturing Technology, August 2009; pp 279-282
- [2] R. Neugebauer, R. Kreißig, L. Lachmann, M. Nestler, S. Hensel, M. Floessel: Piezo Module-Compounds in Metal Forming - Experimental and Numerical Studies, 8th International Conference, In: Mechatronics 2009, Luhačovice, Czech Republic; August 2009
- [3] Sodano H, Lloyd J, Inman D: An experimental comparison between several active composite actuators for power generation, In: Smart Materials and Structures, vol. 15, pp 1211-1216, 2006
- [4] Kranz, B.; Drossel, W.-G.: Rechnerische Beanspruchungsermittlung bei adaptiven Kompositen mit piezokeramischen Fasern, Darmstadt 15./16.03.2006, DVM-Bericht 901, pp 43-52
- [5] Neugebauer, R., Nestler, M., Hensel, S., Drossel, W.-G., and Lachmann, L., "Sheet metal forming of piezo-ceramic-metal-laminar structures – simulation and experimental analysis," ZWF Zeitschrift für wirtschaft-lichen Fabrikbetrieb 105(1/2), – in press– (2010)

A Methodology for Engineering Design Change Management Using Modelling and Problem Solving Techniques

G. Fei¹, J. Gao¹, O.O. Owodunni¹, X.Q. Tang²

¹ Centre for Innovative Product Development, School of Engineering, the University of Greenwich, ME4 4TB, UK

² School of Mechanical Engineering and Automation, Beihang University, Beijing, 100083, China

Abstract: The importance of design change management in engineering product development has been widely reported. However, most research focuses on the engineering change in the manufacturing phase, the later phase of product development. In this paper, a reference model for design change management has been proposed. A modelling method is employed to enhance the traceability of changes occurring between the functional model and the structural model. A matrix based method has been developed to capture change propagations at the structural level and the parametric level of product design. A structural method of change propagation analysis and change impact evaluation has been developed. Finally, conclusions are drawn and scope for further work of this research is indicated.

Keywords: engineering design, change management, product modelling, problem solving, Triz, SysML

1. Introduction

It is recognised that the design stage of product development can determine the largest part of the costs occurring in a product's life cycle. It is critical to keep the early product design consistent and keep all the changes at this stage under control. The importance of design change management (DCM) in engineering product development has been generally reviewed and most research focuses on the engineering change occurring in the manufacturing phase, the later stage of product development [1].

From literature reviewed so far, changes of physical structures have been considered by many researchers. However, most of them focused on propagation changes in the manufacturing phase caused by changes of physical structure, by changes in methods of organisational configurations and working processes [2], and implement change management in computer aided management [3,4]. In this paper, a method for design change management is proposed by putting the emphasis on an analysis of changes between the functional requirement domain and the physical requirement domain. A modelling method is employed to enhance the traceability

of changes occurring between the functional model and the structural model. A matrix based method has been developed to capture change propagations at structural level and the parametric level of product design. A structural method of change propagation analysis and change impact evaluation has been developed.

The research scope of design change management (DCM) is restricted in dealing with changes occurring between functional requirements and physical structures. They are mainly three aspects: (1) capture changes and their propagations between functional requirements and physical structures; (2) identify change modes and solve conflicts arising from design changes; (3) analyse impacts of changes in terms of manufacturing process, developing cost, developing risk. In this paper, we mainly focus on the first aspect

Change of functional requirement may have many reasons, for example, customer demand change, government policy change, or project aim change for competing better with rivals, and so on. Changes occurring in functional requirements may directly affect three aspects of product design. (1) Functional requirement change needs to be verified according to customer requirements to make sure all the changes meet the customer's original demands. (2) Any change of a functional requirement may have potential changes of other functional requirements depending on the interrelationships between them. These changes will be captured in the functional requirement model so that causal impacts can be analysed and controlled. (3) Obviously, any changes in the functional requirement domain will affect physical structures which are correspondingly constructed according to functional requirements.

Change of physical structure is another important part in this research. A lot of situations may give rise to change in the physical structure design, for example, change of functional requirement (discussed above), physical conflict within the solution, solution change on the supplier's side, technical innovation, manufacturing restriction, and so on. Changes of physical structure may

also directly affect three domains, namely the functional requirement domain, the physical structure domain itself and the manufacturing domain. In the functional requirement domain, any changes in the physical structure may change target outputs of related functions. Since one component is possibly involved in realisations of more than one function, the relationships between components and related functions need to be clarified. In the physical structure domain itself, components are linked together by some physical connections, which make it possible to realise some desired functions. Change of a component may potentially change operations of other components, which in turn may change the realisation of related functions. In the manufacturing domain, change of physical structure may change downstream developing activities, such as manufacturing process planning, risk and cost evaluation. Impacts on these product developing activities need to be analysed or re-evaluated.

Conflict solving is one of the issues of most concern in design change management. In many situations, changes of a component or a function may just cause other parts of the design to change correspondingly. However, in some cases, changes may cause functional or physical conflicts. That means they may harm or obstruct operations of other components or realisations of other functions. Some conflicts may not have been recognised in the design phase and have been carried over to the manufacturing phase which may cause a huge amount of cost in later phases. Therefore, an effectively analytical method is needed to identify conflicts in the design phase and solve them as early as possible.

2. The process of design change management

A structural working process would be helpful for designers to achieve their objectives. A diagram of the proposed design change management process is shown in Fig 1. It has four main sections (not shown explicitly). In the first section (top rectangles), dependent relationships among functional requirements and interacting relationships among physical components are clarified. In the second section, the functional model and the physical structure model of engineering products are constructed. Mapping connections between the functional requirement domain and the physical structure domain are also identified. Therefore, designers can be always aware of which interaction in the physical structure is contributing to a realisation of which part of a function. In the third section, changes either in functional requirements or in the physical structures are analysed. Propagations of each design change are identified by following functional dependency relationships and physical interacting relationships. After that, a change propagation matrix is constructed. Weighed values are assigned in the matrix to differentiate the relative importance of each change in terms of changing impacts in functional

requirement domain and physical structure domain. Change impacts are then calculated. In the last section, knowledge based methods are used to solve design conflicts by integrating TRIZ. TRIZ is able to guide designers to find proper solutions for design conflicts via its design principles. By integrating TRIZ with domain knowledge, conflict solving for design change will be more effective and efficient. Due to the page limit, the last section will not be discussed in detail. However, solving conflicts from design changes will be the emphasis of the research work at the next stage.

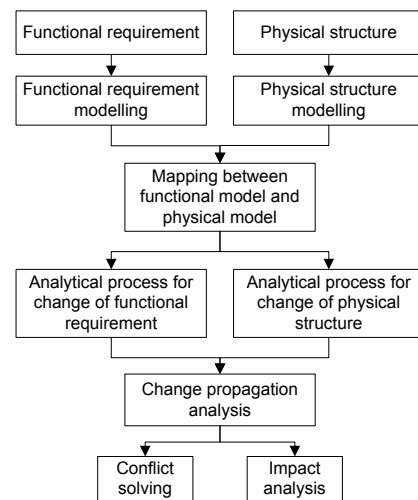


Fig. 1. The process of design change management

3. Analytical method for design change management – an illustrative example

In this section, analytical methods for design change management are introduced and demonstrated with industrial examples from our collaborator. Techniques for analysing design changes include modelling methods for functional requirements and physical structures, a method for constructing matrices for tracing change propagation, and parametric analysis of impact factors of design changes. The industrial example demonstrates a cooling system of a wind turbine which is under development in the collaborative wind turbine design company.

Modelling methods for functional requirements and physical structures are adopted from SysML™ which is a comprehensive system engineering modelling language [5]. The activity diagram of SysML is designed to capture interactions (behaviours referring to SysML) among functions. Each function can be treated as an action which is fed with functional parameters from some actions (functions) and also outputs functional parameters to other actions (functions) as well (an example is shown in Fig. 2). Thus in this paper, when we mention action in terms of functional requirements, we mean functions. The internal block diagram (IBD) captures material, energy and information flows coming in and going out of a

physical structure (example depicted in Fig. 3). Every block in the IDB represents a component (subassembly) of a product at a certain level of detail. Flows attached to a block mean its physical interactions with other components. Functional interactions and physical interactions captured in modelling methods can reflect possible propagation paths of changes.

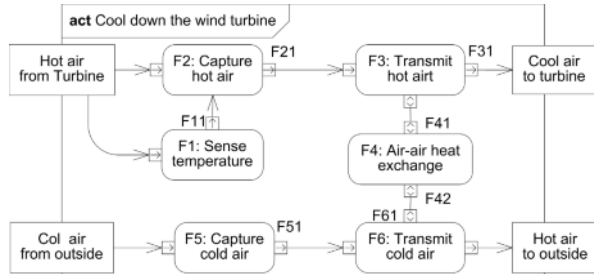


Fig. 2. Activity diagram of a cooling system

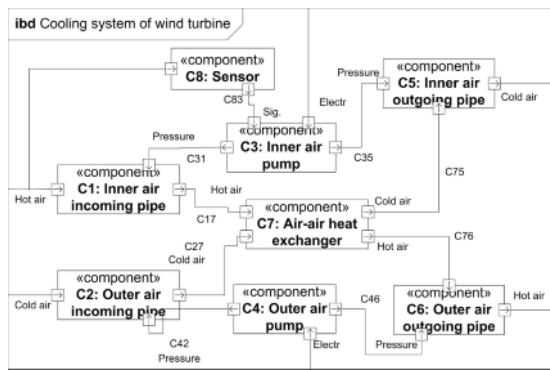


Fig. 3. Internal block diagram of a cooling system

In order to be computer processable, matrix analysis is employed to represent change propagations within and between a functional requirements domain and a physical structure domain. Construction of matrices is based on the results of modelling analyses of activity diagrams and internal block diagrams (depicted in Fig. 4 (a) (b) (c)). In the Fig. 4, propagation matrix (a) represents interactions between functional requirements; propagation matrix (c) represents interactions between physical structures; and propagation matrix (b) represents relationships between functional requirements and physical structures. Basically, activity diagrams and internal block diagrams are directed graphs. Therefore, if there is a flow from function F1 to function F2, the cell (F1, F2) in matrix (a) will be marked to represent this interaction, which is the same in matrix (c). In matrix (b), if a component (e.g. C1) is involved in realising a function (e.g. F2), then the corresponding cell will be marked (e.g. (C1, F2)). The matrix (b) represents relationships between the functional requirement domain and the physical structure domain. It clarifies which physical interactions would influence which functional flows.

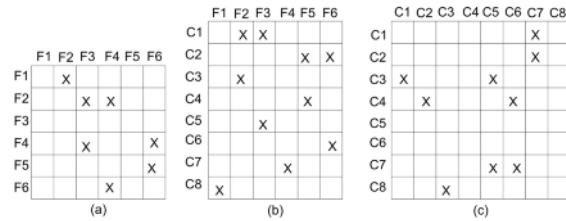


Fig. 4. Matrices of interaction analysis

Depending on different levels of detail at different design stages, a change analysis can be carried out at two levels, i.e. the structural level and the parametric level.

Change analysis at the structural level

Change analysis at the structural level is intended to uncover changes and their propagations by following connections within functional requirements and physical components and relationships between them, where parametric connections are not considered or disclosed. Changes at this level mean changes of an entity, for example a function or a component, but not a part of the entity, for example a functional parameter or a physical parameter. The idea of identifying change propagations and their impacts arising from a change of an entity is described in Fig. 5 (ignore broken line boxes for now).

The relative importance of an entity can be found by comparing entities within a same domain at the same level of detail. The relative importance of a function f in the functional requirement domain can expressed as $FM(f)$. It is calculated by comparing other functions at the same level of detail, in terms of their contributions to the product functionality (1: indifferent; 3: fairly important; 5: very important). The relative importance of a component c in the physical structure domain can be expressed as $CM(c)$. Differing from functional importance, relative importance of a component is obtained by its contributions to related functions and importance of related functions. For example, if $C1$ in Fig. 4 (b) is related with $F2$ and $F3$, then

$$CM(c_1) = CFM(c_1, f_2) \times FM(f_2) + CFM(c_1, f_3) \times FM(f_3) \quad (1)$$

where $CFM(c, f)$ represents the contribution of component C to the realisation of function F .

Interactive relationships can be found from change propagation matrices. Matrices (a), (b), (c) in Fig.4 respectively show the interactive relationships between functions (expressed as $FFM(f, f')$), the interactive relationships between functions and components (expressed as $CFM(c, f)$), and interactive relationships between components (expressed as $CCM(c, c')$). Importance of interactive relationships at this level are qualified by number 0 (no influence), 1(indifferent), 3 (fairly strong), 5 (very strong), which represent how strongly an entity influences another. Therefore, change impact between two functions (f, f') can be calculated as:

$$CI(f, f') = FM(f) \times FFM(f, f') \times FM(f') \quad (2)$$

Change impact between two components (c and c') can be calculated as:

$$CI(c, c') = CM(c) \times CCM(c, c') \times CM(c') \quad (3)$$

Change impact between a function (f) and a component (c) can be calculated as:

$$CI(f, c) = FM(f) \times CFM(f, c) \times CM(c) \quad (4)$$

Fig. 5 describes the change analysis process at the structural change level (not including broken lined blocks).

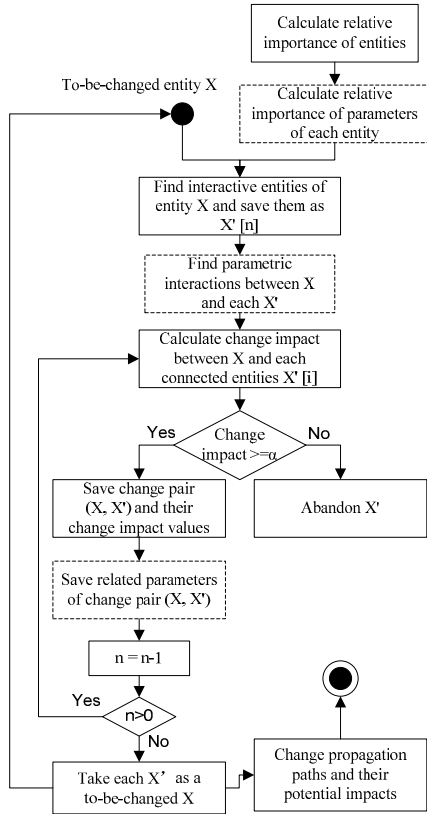


Fig. 5. Change propagations and impacts identification

Change analysis at the parametric level

Change analysis at the parametric level is to find change propagations and evaluate their impacts in the perspective of parametric changes. It has a similar analytical process as the change analysis at the structural level. The differences are that interactive relationships are between parametric flows instead of entities. Interactions of parametric flows are considered in the impacts evaluation of changes.

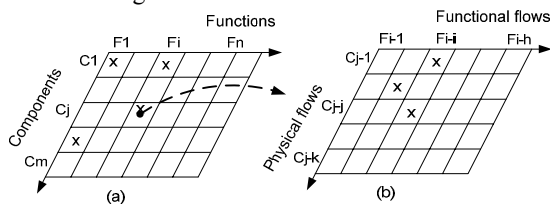


Fig. 6. Interaction analysis of parametric flows

As depicted in Fig. 6, the connections between function F_i and component C_i in Fig. 6(a) are composed of parametric connections shown in Fig. 6(b). Therefore, say if a designer wants to change the parameter C_{jj} of component C_j , the change impact between C_j and function F_i can be expressed as

$$PCIC_{jj, f_{ii}} = FM(f_i) \times (PCM(c_{jj}) \times PCFM(c_{jj}, f_{ii}) \times PFM(f_{ii})) \times CM(c_j) \quad (5)$$

where $PCM(c_{jj})$ represents the relative importance of parameter c_{jj} in component C_j , $PFM(f_{ii})$ means the relative importance of parameter f_{ii} in function F_i , and $PCFM(c_{jj}, f_{ii})$ means importance of contribution from parameter c_{jj} to functional parameter f_{ii} . The analytical process is depicted in Fig. 5 including broken line boxes.

4. Conclusions and Further Work

Any design changes either in functional requirement domain or the physical structure domain will potentially affect operations of other parts. Change propagations and their impacts are difficult to be captured, which makes from uncertainty in product design. A method for design change management has been proposed to tackle this problem by using a modelling method and a specific analytical method. The modelling method captures all the interactions between functions and components. The analytical method helps to trace change propagations and evaluate their potential impacts.

Further work includes synthesising change modes in product design, analysing their change impacts, developing a knowledge based conflict identifying and solving method by integrating method, and a knowledge based technique for non-functional impact evaluation by considering developing process change, developing risk change, and developing cost change. Domain knowledge will be investigated and integrated with TRIZ principles to help designers find solutions for changes and conflicts.

References

- [1] Wright IC. 1997. A review of research into engineering change management: implications for product design. *Des Stud* 18:33–42
- [2] Rouibah, K. & Caskey, K. R. 2003. Change management in concurrent engineering from a parameter perspective. *Computers in Industry*, 50, 15–34.
- [3] Pikosz, P. & Malmqvist, J. 1998. A comparative study of engineering change management in three Swedish engineering companies. *Proceedings of DETC'98*. Atlanta, Georgia.
- [4] Huang, G. Q., Yee, W. Y. & Mak, K. L. 2001. Development of a web-based system for engineering change management. *Robotics and Computer-Integrated Manufacturing*, 17, 255–267.
- [5] OBJECT MANAGEMENT GROUP. 2008. *OMG Systems Modeling Language (OMG SysML) V1.1* [Online]. Object Management Group. Available: <http://www.omg.org/spec/SysML/1.1/PDF> [Accessed 16 May 2009].

Modeling and Analysis of the strength of Adhesively Bond CFRP-Aluminium T-joints

H Cheng¹, K F Zhang¹ and Y Li¹

¹ The Ministry of Education Key Lab of Contemporary Design and Integrated Manufacturing Technical, Northwestern Polytechnical University, Xi'an, China, 710072.

Abstract. The uses of adhesively bond carbon fiber reinforced polymer (CFRP)-aluminium T-joints in aircraft, marine and automotive are rapidly increased but the majority of these applications are based on a lot of special experiments which are purposed to check the joint strength. The strength of adhesively bond which goes along with the technological parameters will influences final product fatigue durability as well as service life. At the same time, as the production environment changes, technological parameters are difficulty to decide. This paper focused on the analysis of the strength of adhesively boned CFRP-aluminum T-joints, developed a new unified model and analysis method. Firstly, the adherends (CFRP and aluminum) are modeled as beams or wide plates, and are considered as generally orthotropic laminates using classical laminate theory. Secondly, by assuming the adhesive layer to be a linear elastic material, and the adhesive thickness and the adhesive Young's modulus are small with respect to the characteristic length of the joint and to the Young's modulus of the adherends, the adhesive layer is modeled. Thirdly, the multiple-point boundary value problem constituted by the governing equations set with the imposed boundary conditions is built, on base of which, the joint strength is solved numerically by using the finite element simulation. Lastly, a case of CFRP aircraft panel adhesively bond is studied, and the result which is compared with the experiments proves that the purposed modeling and analysis method can solve the strength analysis problem of the Adhesively Bond CFRP-Aluminum T-joints efficiently.

Keywords: strength modeling; CFRP-aluminum T-joint; finite element simulation; adhesively

1. Introduction

By virtue of their high specific strength, composite materials are widely used in the aircraft, marine as well as automotive industries. Taking the aerospace industry as an example, applications of carbon fiber reinforced polymer (CFRP) include wing skins, spars, ribs, beams, fuselage bulkheads and so on. Most of the applications are focused on increasing performance, saving weight and reducing manufacturing cost. On one hand the use of CFRP is increasing, and on the other hand, aluminium or aluminium alloy are still the main material in aircraft structure, so CFRP-aluminium jointing become more and

more popular in modern aerospace industry. At the same time, the most common jointing methods of CFRP are bonded and fastened joints. Comparing with fastened joints (bolting, riveting and so on), no fasteners or jointing holes are needed in the process of bonding, and the adhesive jointing is much lighter, the loads are distributed more widely. So the method of an adhesive bond is widely used in the jointing of composite materials, and can provide a much more efficient load transfer than mechanically fastened joint types.

As shown in Fig 1, T-joints are all over the aircraft, including stringer-to-skin joint, spar-to-skin joint, bulkhead-to-skin joint as well as the longeron-to-skin joint. The service life of aircraft is bound up with strength of jointing directly^[1], so the strength of joints is one of the most important problem in the adhesive bond of CFRP-Aluminium T-jointing. Since Volkersen carried out the first attempt of analyzing adhesive bonded joints in 1938^[2], a lot of effort has been devoted to determining the bond strength. The Goland-Reissner solution method for a single-lap joint involves a two-step analysis procedure. Duong used a unified approach for approximating the adhesive stresses in a bond line of a tapered bonded joint or doubler^[3]. Among different numerical approaches, the finite element method (FEM) is the most commonly used technique for stress analysis because it can model extremely complex configurations and easily determine the response at any desired point of a structure. A lot of effort based on 2D or 3D finite elements has been done to analyse the strength of an adhesive bond^[4]^[5]. According to the T-jointing, Theotokogolou and Moan performed a numerical/experimental study of composite T-joints. Their study investigated the behavior of T-joints subjected to tension force up to the ultimate failure^[6]. Stickler and Ramulu performed parametric finite element analyses using commercial software ANSYS to discern the effects of key joint parameters (fibre insertion modulus, fibre insertion filament count, fibre insertion depth, and resin-rich interface zone thickness) on T-joint

displacement and damage initiation load^[7]. In the field of CFRP-Aluminium bonded jointing, ultrasonic, acoustic emission (AE), acousto-ultrasonics (AU), radiography were used for the detection of defects at bonded areas^[8]. Most of the references reviewed can solve the given problem quit well, however, according to the strength of adhesively bond CFRP-Aluminum T-joints, most methods are based on plentiful experiments, a process which costs a lot of time and can not be universal.

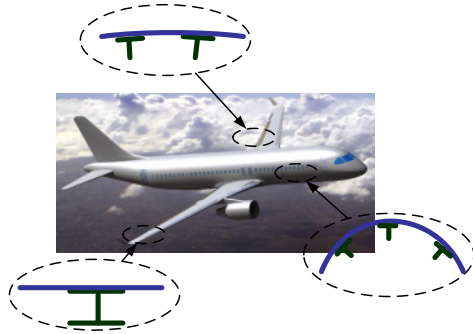


Fig. 1. Te use of T-Joints in aircraft.

In order to analyze the strength of adhesively bond CFRP-Aluminium T-joints, this paper presents a new model for both adherends and adhesive. At the same time, in order to solve the problem numerically, the finite element simulation, equilibrium equations as well as boundary conditions are studied.

2. Modling of adherends and adhesive layer

A typical CFRP-Aluminium T-joint with an adhesive bond is shown in Fig 2. The total model is made up of two parts: adherends (CFRP and aluminium) and the adhesive layer.

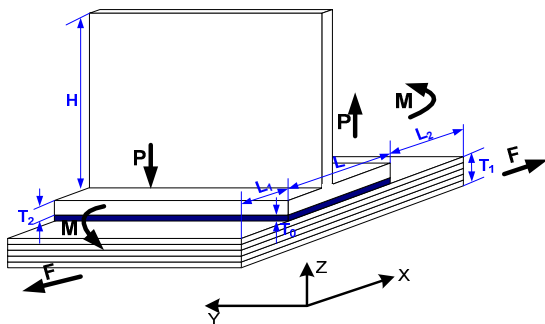


Fig. 2. Typical CFRP-Aluminium T-joints with adhesively bond.

In Fig 2 T_1 stands for the thickness of CFRP, T_2 stands for the thickness of Aluminium, T_0 is the thickness of the adhesive layer. L is the width of adhesive layer H is the height of stiffener. F is the force supplied on X-axis, P is the bonding force, M is the Y-moment.

The adherends of our model have two parts: CFRP and aluminium laminate, and the basic restrictive assumptions adopted for the modelling are as follows.

Assumption 1: The adherends, CFRP or aluminium laminates obey linear elastic constitutive laws.

Assumption 2: The strains are small, and the rotations are very small.

Assumption 3: The midplane of the aluminium laminate is the aluminium laminate itself.

The stress and moment resultants of a differential element in the overlap of adherends is as shown in Fig 3, where τ and σ are the stresses supplied by the adhesive layer.

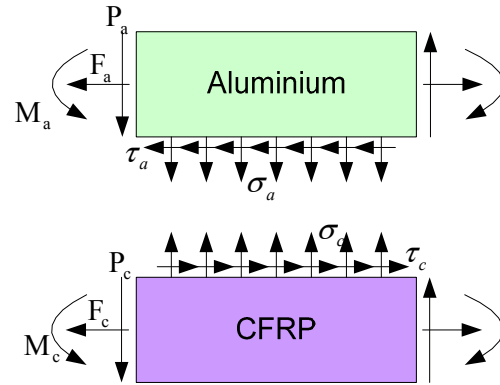


Fig. 3. stress and moment resultants of adherends

According to Fig 3, bending is around the Y-axis, so the displacement can be given by eq. (1), where u_i^0 , v_i^0 and w_i^0 are the displacement in X-axis, Y-axis and around Z-axis respectively of laminate i on the midplane.

$$\begin{cases} u_i^0 = u_i^0(x) \\ v_i^0 = v_i^0(y) \\ w_i^0 = w_i^0(z) \end{cases} \quad (1)$$

According to the classical laminate theory, the constitutive relations for a laminate in bending can be given by eq. (2), where A , B , D are the extensional coupling defined by classical lamination theory.

$$\begin{cases} F = A \bullet u + A \bullet v - B \bullet w \\ M = B \bullet u + B \bullet v - D \bullet w \end{cases} \quad (2)$$

To simplify the model, the displacement of Y-axis is ignored, so for the midplane eq. (2) can be represent as eq. (3).

$$\begin{cases} F = F_{xx} = A_{11}u_{0,x} - B_{11}w_{,xx} \\ M = M_{xx} = B_{11} \bullet u_{0,x} - D_{11} \bullet w_{,xx} \end{cases} \quad (3)$$

According to the Love–Kirchhoff assumptions the displacement of laminate i can be given by eq. (4)

$$u_i = u_i^0 - cw_{,x} \quad (4)$$

The coupling between the adherends of CFRP and aluminium laminate is established through the

constitutive relations for the adhesive layer. The basic restrictive assumptions adopted for the modeling of adhesive layer are as follows.

Assumption 4: The adhesive layer is continuously distributed and the tension and shear springs can be regarded as linear.

According to Fig 3, the stress and moment resultants of a differential element of adhesive layer are as shown in Fig 4. The stresses τ and σ are given by eqs. (5) and (6), where T_1 , T_2 and T_n is the thickness of adherends or adhesive layer as it is shown in Fig 2.

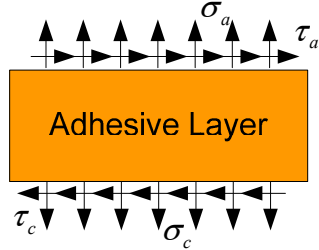


Fig. 4. Stress and moment resultants of adhesive

$$\begin{cases} F_a' = \tau_a \\ P_a' = \sigma_a \\ M_a' = P_a - \tau_a(T_2 + T_0)/2 \end{cases} \quad (5)$$

$$\begin{cases} F_c' = \tau_c \\ P_c' = \sigma_c \\ M_c' = P_c - \tau_c(T_1 + T_0)/2 \end{cases} \quad (6)$$

At the same time, τ and σ are given by eqs. (7) and (8), according to the displacement of adherends, where G_0 is the shear modulus and E_0 is the Young's modulus, u_1 is the displacement on X-axis of CFRP, u_2 is the displacement on X-axis of aluminium laminate, u_0 is the displacement on X-axis of adhesive layer. w_1 is the displacement around Z-axis of CFRP, w_2 is the displacement around Z-axis of aluminium laminate, and w_0 is the displacement around Z-axis of adhesive layer.

$$\begin{cases} \tau_a = G_0 / T_2 \cdot (u_2 - u_0) \\ \sigma_a = E_0 / T_2 \cdot (w_2 - w_0) \end{cases} \quad (7)$$

$$\begin{cases} \tau_c = G_0 / T_1 \cdot (u_1 - u_0) \\ \sigma_c = E_0 / T_1 \cdot (w_1 - w_0) \end{cases} \quad (8)$$

Therefore, the relationship between adherends and adhesive layer can be built as in eqs. (9) and (10).

$$\begin{cases} F_a' = G_0 / T_2 \cdot (u_2 - u_0) \\ P_a' = E_0 / T_2 \cdot (w_2 - w_0) \\ M_a' = P_a - G_0 / T_2 \cdot (u_2 - u_0)(T_2 + T_0)/2 \end{cases} \quad (9)$$

$$\begin{cases} F_c' = G_0 / T_1 \cdot (u_1 - u_0) \\ P_c' = E_0 / T_1 \cdot (w_1 - w_0) \\ M_c' = P_c - G_0 / T_1 \cdot (u_1 - u_0)(T_1 + T_0)/2 \end{cases} \quad (10)$$

3. Boundary conditions

Equations. (9) and (10) not only present the attribute of adhesive layer but also the equilibrium equations. To resolve the strength of adhesive bond, the boundary conditions must be built. In the following the boundary conditions are stated for the T-joint of CFRP and aluminium laminate.

- (1) As shown in Fig 5 (a), in the beginning of the bond area, the moment of CFRP is free, which means for the CFRP $F_x(0) = P_c(0) = M_c(0) = 0$. Turn to aluminium laminate the condition is continuity.
- (2) As shown in Fig 5 (b), at the end of the bond area, the moment of aluminium laminate is free, which means for the aluminium laminate of the T-joint $F_x(T_0) = P_a(T_0) = M_a(T_0) = 0$. Turn to CFRP the condition is continuity.
- (3) Since the condition of CFRP and aluminium laminate is selected to be relatively throughout the bond area, the extensional and transverse deflections, shear and moment resultants in CFRP and aluminium laminate must be continuous.
- (4) Symmetry conditions at the middle of the bond area are used.

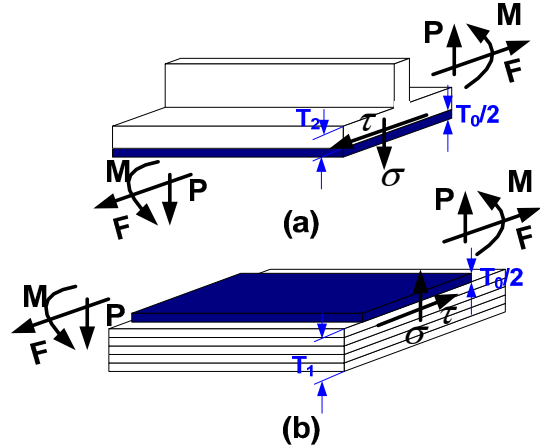


Fig. 5. Boundary conditions of the T-joint

4. Case Studies

The present model is demonstrated by a case study of an aircraft CFRP panel adhesively bonded in a T-type joint; part of the panel, which is made up of CFRP and aluminium laminate, was selected as an example to analyze the strength, and is shown in Fig 6. At the same time, the geometry and material properties of the adherends (CFRP and aluminium laminate) and of the adhesive layer as well as the applied load are given as Table 1, where E is the young's modulus, G is the shear modulus, ν stands for the Poisson's ratio, T is the thickness of the material, and S is the area of adhesive layer.

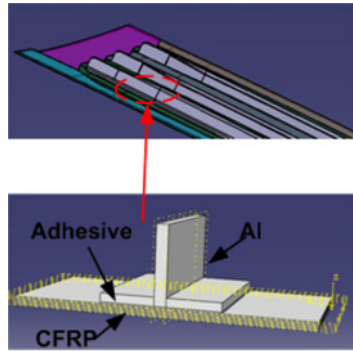


Fig. 6. The case of T-joint

Table 1. Adherends and adhesive properties,

	Adherends		Adhesive
	CFRP	Aluminium	
E	E_x : 131GPa E_y : 8.2GPa E_z : 8.2GPa	72GPa	2.9GPa
G	G_{xy} : 4.5GPa G_{xz} : 4.5GPa G_{yz} : 3.5GPa	\	\
ν	ν_{xy} : 0.281 ν_{yz} : 0.281 ν_{xz} : 0.47	0.31	0.33
T	3mm	3mm	1mm
S	\	\	40mm×50mm

A comparison of the analytical results obtained using our method and the experimental values for this example is shown in Fig 7. The stress component of σ_{xx} is analyzed, from which we can observe that the strength analyzed by our model is basically the same as the result of the experiment and proves the effectiveness of our method.

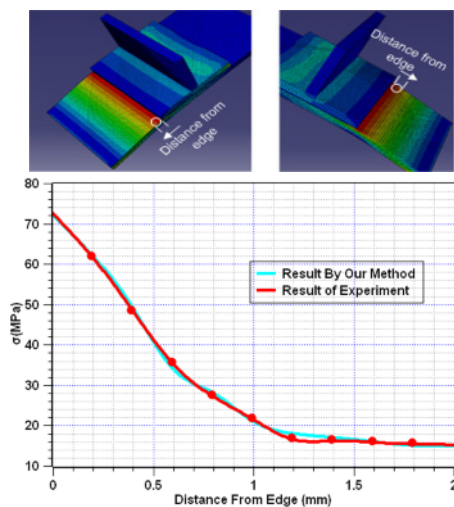


Fig. 7. The result of the case

5. Conclusions

In order to analyze the strength of adhesively boned CFRP-aluminum T-joints, in this paper, a new unified model and analysis method have been developed, and four contributions have been made.

- 1) The adherends of CFRP- Aluminium T-joint are modelled according to the classical laminate theory.
- 2) By assuming the adhesive layer to be a linear elastic material, the adhesive layer of T-joint is modelled.
- 3) Multiple-point boundary conditions are applied, on the basis of which, the joint strength can be solved numerically using a finite element simulation.
- 4) A case study of an aircraft CFRP panel adhesively bond in a type of T-joint is presented to demonstrate the validity of this method.

From a comparison between the results obtained using the proposed method and experiments, it is clear that the proposed strength analysis method gives accurate results for T-joints of CFRP-Aluminium adhesive bond.

Acknowledgements

We gratefully acknowledge the support of National Natural Science Foundation of China (50805119), the Doctorate Foundation of Northwestern Polytechnical University, China (CX200809) and Aoxiang Star Program in Northwestern Polytechnical University, China. We would also like to thank the editors and the anonymous referees for their insightful comments.

References

- [1] Kumari S, Sinha PK, (2002) Hygrothermal analysis of composite wing T-joints Aircraft Engineering and Aerospace Technology 74: 23–37.
- [2] Volkersen O, (1938) Die Nietkraftverteilung in Zugbeanspruchten Nietverbindungen mit Konstanten Laschenquerschnitten. Luftfahrtforschung 15: 41–47.
- [3] Duong CN, (2006) A unified approach to geometrically nonlinear analysis of tapered bonded joints & doublers, Int. J of Solids & Structures 43: 3498–3526.
- [4] Tavakkolizadeh M, Saadatmanesh H, (2003) Strengthening of Steel-Concrete Composite Girders Using Carbon Fiber Reinforced Polymers Sheets. J Struct Eng 129: 30–40.
- [5] Deng J, Lee MMK, Moy SSJ, (2004) Stress analysis of steel beams reinforced with a bonded CFRP plate. Composite Structure 65: 205–215.
- [6] Theotokogolou E, Moan T, (1996) Experimental and numerical study of composite T-joints, Journal of Composite Materials 30: 190–209.
- [7] Stickler PB, Ramulu M, (2001) Investigation of mechanical behaviour of transverse stitched T-joints with PR520 resin in flexure and tension, Composite Structures 52: 307-314.
- [8] Kwon OY, Lee SH, (1999) Acousto-ultrasonic evaluation of adhesively bonded CFRP-aluminum joints, NDT&E International 32: 153–160.

Metal Cutting

This section is in memory of Dr George Barrow who sadly passed away in September 2009. Since the 1960s, Dr Barrow worked at the University of Manchester Institute of Science and Technology, initially as a Lecturer and then as a Senior Lecturer in the Mechanical Engineering Department. His internationally-recognised research was primarily concerned with metal cutting and its application to industrial problems. Although he retired in 1999, he continued to work at the University on a part-time basis until the very last day.

Modelling of Machine Tapping with Straight Flute Taps

N.M. Chen¹ and A.J.R. Smith²

¹ Formerly, graduate student, Department of Mechanical Engineering, The University of Melbourne

² Department of Mechanical Engineering, The University of Melbourne, Australia

Abstract. Taps and tapping operations are amongst the most complex and least understood cutting tools and processes. In this paper, the geometry and specification of straight flute taps are studied and discussed. This is followed by an outline of the development of computer-aided predictive models for side force, thrust force and torque in machine tapping operations, based on Armarego's 'Unified-Generalised Mechanics of Cutting Approach'. The models are verified through simulation studies and comprehensive experimental testing. Good qualitative and quantitative correlations are found for the average thrust and torque. These models allow tool designers and process planners to optimise the generation and use of taps. The results confirm the validity and generic nature of the unified-mechanics of cutting approach.

Keywords: Tapping, taps, geometry, forces, predictive models

1. Introduction

Tapping is a common operation used to produce internal screw threads. Tapping is frequently among the final operations performed on a component so that the added value of a component is often near its peak. Consequently conservative cutting conditions are often used to avoid tap failure that could ruin the part being produced. [1]

Improving the technological performance of machining operations as assessed by the forces, power, tool-life, chip control and component surface finish and accuracy enhances the economic performance of these operations. Early last century, Taylor experimentally established equations relating tool-life to an influencing variable in order to identify optimal cutting speeds. [2]

Since Taylor's time, the 'fundamental' or 'mechanics of cutting' approach [3-5] and the 'semi-empirical' approach (eg [6,7]) to machining modelling have been developed. Nevertheless, a CIRP survey has emphasised the continuing need for reliable quantitative technological machining performance equations and data. [8] Meeting this need is a formidable task due to the numerous variables and the wide spectrum of processes. [4]

Compared with other practical machining operations, the tapping operation does not seem to have received as much attention from researchers. More recently, there appears to have been some research interest in tapping

with a few papers utilising the semi-empirical approach, with some models allowing for eccentricity and contact stress. [9,10] However, no previous attempts are known to have used the more predictive fundamental approach.

This paper considers the geometry of straight-flute taps, followed by an outline of a predictive model for the torque and forces in machine tapping. The model adopts the predictive "Unified-Generalised Mechanics of Cutting Approach" developed at Melbourne University. [3-5] It includes transient and steady cutting, and allows for the many tap and cut geometrical variables, the cutting speed and the tool-workpiece material combination. The model is verified through comprehensive simulations and experiments. Finally, practical empirical-type equations are presented from curve-fitting the simulation data.

2. Geometry and Specification of Taps

The general description and nomenclature for taps and tapping appears in many handbooks.[1,11,12] However, only the most obvious practical dimensions are included in national and international standards such as the tap thread nominal and shank diameters, pitch and various tap axial lengths such as the overall and thread length. [13] Handbooks and tool catalogues provide more geometrical information. [11,12,14] From the literature, the general geometrical features have been identified as shown in Fig. 1 for straight-flute taps. For standard ISO metric taps, the thread angle, α , is 60° , diameter, d , has values between 1 and 56 mm, pitch, P , varies from 0.25 to 5.5 mm; all taps have between 2 and 8 flutes (Z_f), back rake, γ_p , from 5° to 25° , and clearance angle, Cl_p at a specified point on the first full thread between 4° and 6° . The chamfer angle, κ_r , can be quite different depending on whether the tap is a 'taper' tap, intermediate or bottoming tap: ranging from 1.5° to 23° . Examination of Fig. 1 shows that the cutting part of the chamfer is not fully and uniquely described. [15] Further, the flutes and clearance surfaces are ambiguously specified.

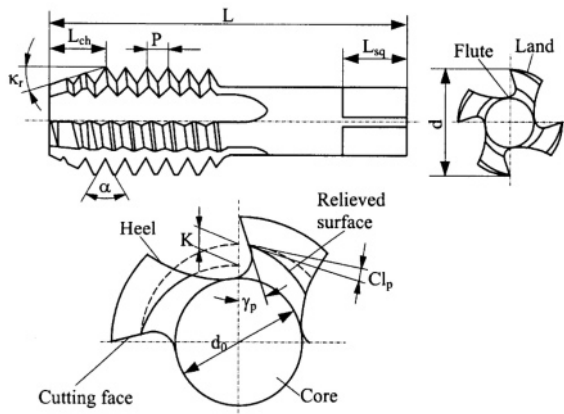


Fig. 1. The principal geometrical features of the straight flute tap

The major cutting edges lie on the conical chamfer surface and the crest of the first full thread. The minor edges lie on the flanks of the threads. Since the minor cutting edges are much smaller than the major cutting edges only the cutting action of the major cutting edges for a tap will be considered. It has been found that a common design at the chamfered section of machine taps involves plane rake faces often with positive rake angles.

Fig. 2 shows the relevant geometry of a four straight flute machine tap of nominal diameter d with back rake angle, γ_{pA} , specified at a selected point A on the

‘truncated’ cutting edge in the chamfered section of the tap. The radius of point A is denoted by r_A .

The elevation in Fig. 2 shows an axial view of the major cutting edge BB’ formed by the intersection of the plane rake face with the chamfered conical surface.

The cutting edge is approximately a straight line due to the small length of cut and rake angle. The cutting edge, is inclined at approximately the chamfer angle, κ_r , to the tap axis as shown in the elevation. In the plan view, the tangential cutting speed V_A , which is the primary motion at point A due to rotating the tap, and the feed speed V_{fA} in the direction of the feed motion appear as their true views. The plan view also shows the resultant cutting velocity V_{wA} at point A and the resultant cutting speed angle δ_A .

Fixed coordinates O-XYZ have their origin O at the centre of the workpiece surface of the hole, and the Z-axis is coincident with the tap axis.

The working normal rake angle, γ_{neA} and angle of inclination, λ_{seA} for any point A on the cutting edge can be determined from [15]

$$\tan \gamma_{neA} = \tan \kappa'_{rA} \sin \eta_A + \frac{\cos \kappa'_{rA} \tan \gamma_{pA}}{\cos \eta_A} + \omega_A \quad (1)$$

$$\tan \lambda_{seA} = \frac{\tan(\delta_A - \eta_A) \cos \kappa'_{rA}}{\sqrt{1 + \tan^2(\delta_A - \eta_A) \sin^2 \kappa'_{rA}}} \quad (2)$$

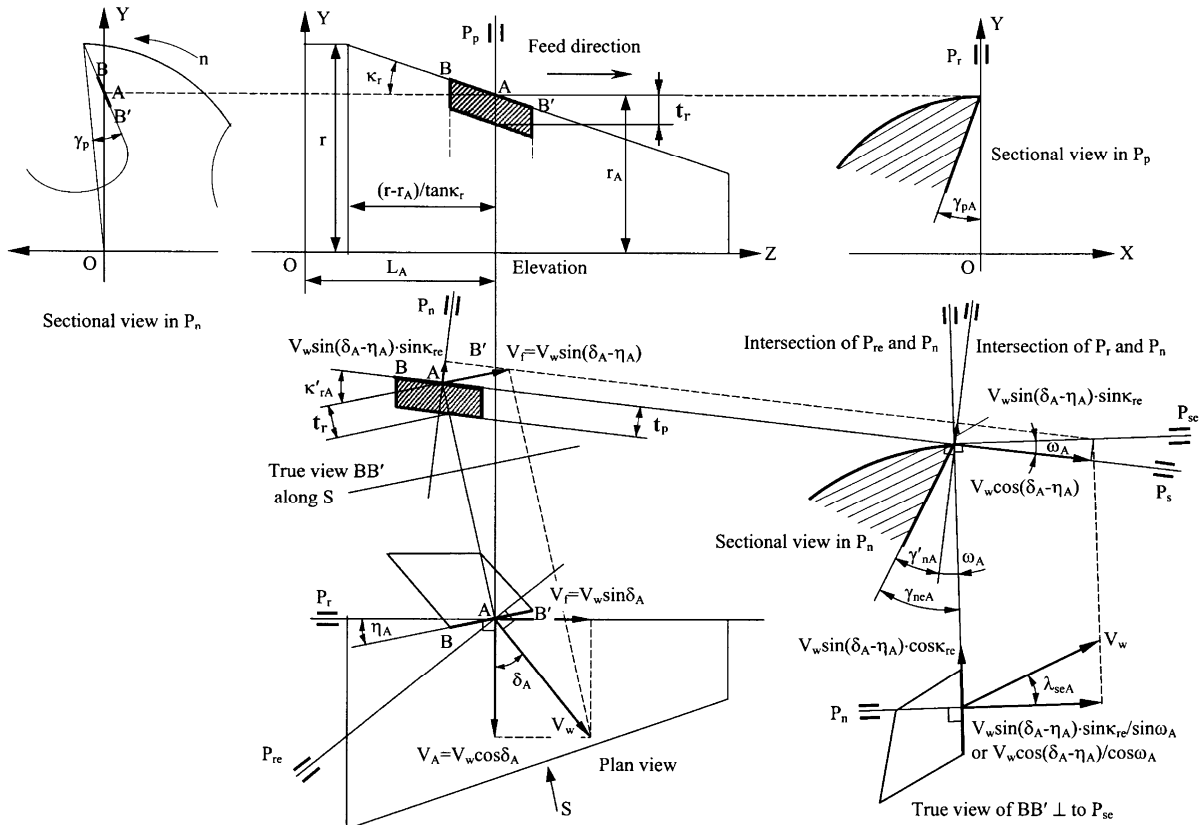


Fig. 2. Relevant cutting edge geometry of plane-face taps with straight flutes

Where κ'_{rA} is the acute angle between the cutting edge BB' and the tap axis in view S: $\tan \kappa'_{rA} = \tan \kappa_r \cos \eta_{A}$. $\cos \eta_{A}$ is the angle between the cutting edge and plane P_r in plan view, γ_{pA} is the back rake in the side view and ω_A is the angle formed between the cutting edge plane P_s and the effective cutting edge plane P_{se} through point A in the sectional view in P_n : $\tan \omega_A = \tan(\delta_A - \eta_A) \sin \kappa'_{rA}$. It can be shown that the effective normal rake angle, γ_{neA} , and angle of inclination, λ_{seA} , vary along the cutting edge.

3. A Predictive Force and Torque Model

The method adopted to model machine tapping divides each major cutting edge j into m elemental classical oblique single edge cutters. The forces on each element i , $\delta F_{p_{ij}}$, $\delta F_{q_{ij}}$ and $\delta F_{r_{ij}}$, are found from the Ernst-Merchant analysis modified to include 'edge' forces. [3] $\delta F_{p_{ij}}$, is in the direction of the resultant cutting velocity (fig. 2); $\delta F_{q_{ij}}$ is normal to $\delta F_{p_{ij}}$, in the P_n plane and $\delta F_{r_{ij}}$ is perpendicular to P_n . Each of these elemental forces is assumed to be concentrated at the middle of the elemental cutting edge.

To predict the elemental forces, it is necessary to know the elemental rake angle (eq. 1), the elemental inclination angle (eq. 2), the width of the element δb_{ij} and cut thickness δt_{ij} obtained from the tap geometry (figure 3), the chip flow angle η_{cij} , found (iteratively) from collinearity between the chip direction and the friction force on the elemental rake face, and the work material shear strength τ , chip length ratio r_1 , friction angle β and edge force coefficients K_{ep} , K_{eq} , K_{er} that can be found from a database. The database contains information for several different tool materials, tool coatings and work materials. To extend the tapping model to material combinations not in the database requires only simple orthogonal experiments with only rake angle, cut thickness and speed varied.

The equation for the elemental force in the P direction is given by eq (1), similar expressions are found for the Q and R components [15].

$$\delta F_{p_{ij}} = \frac{\tau \delta b_{ij} t_{ij} \cos(\beta_{nij} - \gamma_{nej}) + \tan \lambda_{seij} \tan \eta_{cij} \sin \beta_{nij}}{\sin \phi_{nij} \sqrt{\cos^2(\phi_{nij} + \beta_{nij} - \gamma_{nej}) + \tan^2 \eta_{cij} \sin^2 \beta_{nij}}} + K_{epij} \delta b_{ij} \quad (1)$$

$$\text{where} \quad \delta b_{ij} = \frac{\delta L_{ij} \cos \lambda_{seij}}{\cos \eta_{ij} \cdot \cos \kappa'_{rij}} \quad (2)$$

$$t_{ij} = t_r \cos \kappa'_{rij} \cdot \cos \omega_{ij} = \frac{P \sin \kappa'_{rij} \cdot \cos \omega_{ij}}{Z_f \cos \eta_{ij}} \quad (3)$$

$$\tan \phi_{nij} = \frac{r_1 (\cos \eta_{cij} / \cos \lambda_{seij}) \cos \gamma_{nej}}{1 - r_1 (\cos \eta_{cij} / \cos \lambda_{seij}) \sin \gamma_{nej}} \quad (4)$$

$$\beta_{nij} = \tan \beta \cdot \cos \eta_{cij} \quad (5)$$

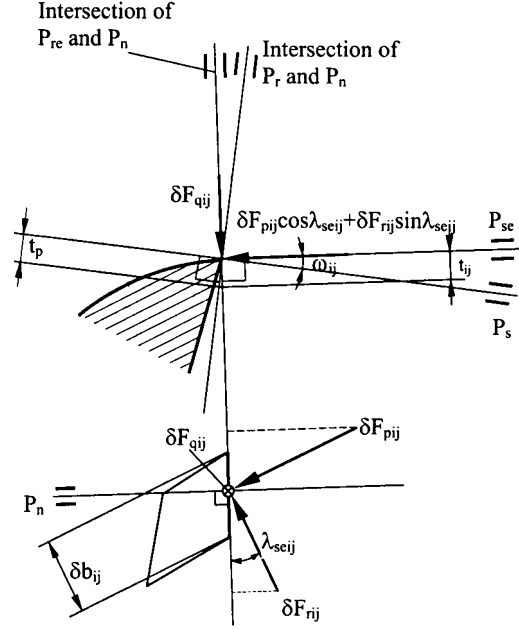


Fig. 3. The force components for element ij on cutting tooth i

$$\tan(\phi_{nij} + \beta_{nij}) = \frac{\tan \lambda_{seij} \cdot \cos \gamma_{nej}}{\tan \eta_{cij} - \sin \gamma_{nej} \tan \lambda_{seij}} \quad (6)$$

In terms of this model, the number of cutting teeth on a metric tap, N_t , is established by

$$N_t = \text{Int} \left[\frac{(d - d_n)(1 - \tan \kappa_r \tan 30^\circ)}{2t_r} \right] + Z_f + 1 \quad (7)$$

Where d_n is the initial hole size. The number of active cutting teeth at a given tap orientation during cutting also needs to be established.

Then the practical elemental forces in tapping, $\delta F_{tang_{ij}}$, $\delta F_{rad_{ij}}$ and $\delta F_{th_{ij}}$, can be obtained from:

$$\begin{aligned} \delta F_{tang_{ij}} = & \sin \eta_{ij} \{ (\delta F_{p_{ij}} \sin \lambda_{seij} - \delta F_{r_{ij}} \cos \lambda_{seij}) \cos \kappa'_{rij} + \\ & [\delta F_{q_{ij}} \cos \omega_{ij} + (\delta F_{p_{ij}} \cos \lambda_{seij} + \delta F_{r_{ij}} \sin \lambda_{seij}) \sin \omega_{ij}] \sin \kappa'_{rij} \} \\ & + \cos \eta_{ij} [(\delta F_{p_{ij}} \cos \lambda_{seij} + \delta F_{r_{ij}} \sin \lambda_{seij}) \cos \omega_{ij} - \delta F_{q_{ij}} \sin \omega_{ij}] \end{aligned} \quad (8)$$

$$\begin{aligned} \delta F_{rad_{ij}} = & (\delta F_{r_{ij}} \cdot \cos \lambda_{seij} - \delta F_{p_{ij}} \cdot \sin \lambda_{seij}) \cdot \sin \kappa'_{rij} + \\ & [\delta F_{q_{ij}} \cos \omega_{ij} + (\delta F_{p_{ij}} \cos \lambda_{seij} + \delta F_{r_{ij}} \sin \lambda_{seij}) \sin \omega_{ij}] \cos \kappa'_{rij} \end{aligned} \quad (9)$$

$$\begin{aligned} \delta F_{th_{ij}} = & \cos \eta_{ij} \{ (\delta F_{p_{ij}} \sin \lambda_{seij} - \delta F_{r_{ij}} \cos \lambda_{seij}) \cos \kappa'_{rij} + \\ & [\delta F_{q_{ij}} \cos \omega_{ij} + (\delta F_{p_{ij}} \cos \lambda_{seij} + \delta F_{r_{ij}} \sin \lambda_{seij}) \sin \omega_{ij}] \sin \kappa'_{rij} \} \\ & + \sin \eta_{ij} [(\delta F_{p_{ij}} \cos \lambda_{seij} + \delta F_{r_{ij}} \sin \lambda_{seij}) \cos \omega_{ij} - \delta F_{q_{ij}} \sin \omega_{ij}] \end{aligned} \quad (10)$$

The elemental torque can be evaluated from $\delta T_{q_{ij}} = \delta F_{tang_{ij}} \times r_{ij}$ given $r_{ij} = r_A$ in fig. 2.2.

The instantaneous torque and thrust for the whole tap are found from summing the elemental torques and

thrusts for each active element. The ‘unbalanced’ side force requires transforming the radial and tangential elemental forces into X and Y components, before summing and performing a vector summation.

By varying the tap and reference tooth angular position by small intervals, the instantaneous forces, torque and power fluctuations during cutting are established. Hence, forces, torque and power in the transient and steady stages of tapping are evaluated.

4. Results

Numerical simulation studies involving three levels of d , P , Z_f , γ_p , κ_r , L_{crest} , d_h and V have been carried out for both uncoated and TiN coated HSS straight flute taps. Experimentally, in excess of 250 holes were tapped; varying d , P , κ_r , and V for TiN coated and uncoated HSS straight flute taps threading S1214 steel.

Overall, the predicted torque, thrust and side force trends are sensible.

Fig. 4 shows the torque over a complete tapping cycle. Good correlation is found between the measured and predicted torque trends and average values. Reasonable correlation is found for the thrust.

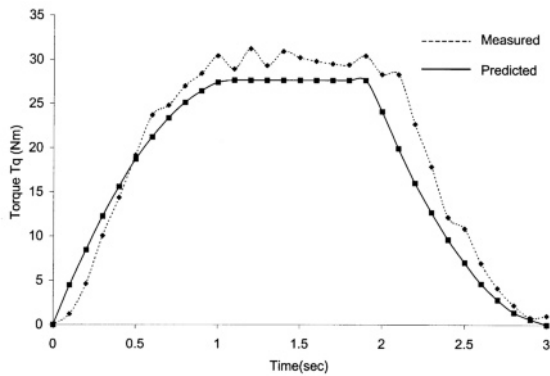


Fig. 4. Experimental and predicted torque ($d=20.45$ mm, $P=2.5$ mm, $\kappa_r=8^\circ$, $Z_f=4$, 250rpm, $d_h=17.55$ mm, TiN-HSS/S1214)

On average, the model over-predicts the torque for tapping with uncoated HSS straight flute taps by about 8% and under-predicts the thrust force by about 13%. The worse correlation between the measured and predicted thrust force is considered to be the result of small feed rate errors greatly affecting the thrust. Similar results were found for tapping with a coating.

The predictions from the simulation study were curve-fitted to establish, ‘empirical-type’ equations for both TiN coated and uncoated HSS taps machining S1214 free machining steel. Eq. (11) and (12) are for the torque (Nm) and thrust (N) for uncoated taps.

$$Tq = 0.436 Z_f^{0.306} d^{1.075} P^{1.607} (\%h)^{1.601} \kappa_r^{-0.29} \gamma_p^{-0.163} V^{0.026} \quad (11)$$

$$Th = 38.01 Z_f^{0.376} d^{-0.177} P^{1.791} (\%h)^{1.671} \kappa_r^{0.459} \gamma_p^{-0.251} V^{0.023} \quad (12)$$

5. Concluding remarks

The design geometry and specification of machine taps have been found ambiguous and generally left to the tool manufacturers’ discretion. The geometry of plane-faced taps has been studied and uniquely specified, from which it has been possible to develop reliable predictive models based on the Unified-Generalised Mechanics of Cutting Approach. The model depends on γ_p , d , P , κ_r , Z_f , L_{crest} , V , d_h , θ_{ri} , δL_{ij} , τ , r_i , β , K_{ep} , K_{eq} .

The above predictive model considers an ‘ideal case’. Detailed studies of eccentricity in tapping need to be carried out, as well as of the flute helix angle. Development of predictive models for tapping forces and torque incorporating eccentricity should follow.

References

- [1] Drozda, TJ and Wick, C (editors), (1983) Tool and Manufacturing Engineers Handbook, Machining, 4th Ed., Soc. Manuf. Engrs, Michigan
- [2] Taylor, FW, (1907) On the art of metal cutting, Trans. Amer. Soc. Mech. Engrs 28:31-248
- [3] Armarego, EJA, (1982) Practical implications of classical thin shear zone analyses, UNESCO-CIRP Seminar on Manuf. Techn., Singapore 167-182
- [4] Armarego, EJA, (1996) Predictive modelling of machining operations – a means of bridging the gap between theory and practice, Proc. CSME, Canada 18-27
- [5] Armarego, EJA, (1998) A generic mechanics of cutting approach to predictive technological performance modelling of the wide spectrum of machining operations, Mach. Sci. & Techn. 2:191-211
- [6] Altintas, Y and Spence, A, (1991) End milling force algorithms for CAD systems, Annals CIRP 40:31-34
- [7] Kapoor, SG, DeVor, RE, Zhu, R, Gajjala, R, Parakkal, G and Smithey, D, (1998) Development of mechanistic models for the prediction of machining performance: model-building methodology, Proc. 2nd CIRP Int. Workshop on Modelling of Machining Operations, USA 109-120
- [8] Kahles, JF, (1987) Machinability data requirements for advanced machining systems, Annals CIRP 36:523-529
- [9] Dogra, APS, DeVor, RE and Kapoor, SG, (2002) Analysis of feed errors in tapping by contact stress model, J. Manuf. Sci. & Engg, Trans. Amer. Soc. Mech. Engr 124:248-257
- [10] Mezentssev, OA, Zhu, R, Devor, RE, Kapoor, SG and Kline, WA, (2002) Use of radial forces for fault detection in tapping, Int. J. Mach. Tools & Manuf. 42:479-488
- [11] Metal Cutting Tool Institute, (1969), Metal Cutting Tool Handbook, 6th Ed.
- [12] Meng, SN *et al* (editors), (1996) Machining Technique Handbook, Vol. 2, Mechanical Industry Publish House, Beijing
- [13] International Organization for Quality, (1975) Short Machine Taps and Hand Taps, ISO 529
- [14] Arshinov, V and Alekseev, G, (1976) Metal Cutting Theory and Cutting Tool Design, English transl., MIR Publications
- [15] Chen, NM, (2005) Computer-aided predictive cutting models for the forces, torque and power in machine tapping operations, PhD thesis, Melbourne University

High Speed MQL Drilling of Titanium Alloy using Synthetic Ester and Palm Oil

E. A. Rahim^{1,2}, H. Sasahara¹

¹ Tokyo University of Agriculture & Technology, Japan, sasahara@cc.tuat.ac.jp

² University Tun Hussein Onn Malaysia, Malaysia, erween@uthm.edu.my

Abstract. Minimum Quantity Lubrication (MQL) machining involves the application of a small quantity of lubricant being dispensed to the tool-workpiece interface. This paper describes the results of applying different MQL lubricant (synthetic ester and palm oil) to the high speed drilling of Ti-6Al-4V. Dry cutting conditions were also used for comparison. It was found that cutting under dry conditions resulted in the shortest tool life due to severe chipping. MQL was found beneficial to the measured factors such as tool life, thrust force, torque and temperature. In addition, the outstanding performance of palm oil in reducing the value of these factors could be attributed to its ability to form a thin film which promotes boundary lubrication during the machining process. This work shows that the palm oil can be selected as a viable alternative to synthetic ester for MQL lubricant.

Keywords: Minimum Quantity Lubrication, High Speed Drilling, Synthetic Ester, Palm Oil

1. Introduction

Cutting fluids, especially fluids containing oil, have become a huge liability because of the health and environmental hazards they pose. Due to an increased awareness of environmental and health issues, industry has made efforts to eliminate or reduce the consumption oil-based cutting fluids. By implementing near-dry machining or a minimal quantity of lubrication (MQL), cutting fluid consumption can be reduced. In dry machining, more friction and adhesion occurring at the tool-workpiece interface consequently results in a higher tool wear rate [1]. The MQL technique involves the application of a small quantity of lubricant dispensed to the tool-workpiece interface by compressed air flow. It has been found that MQL reduces the friction coefficient and cutting temperature compared with dry and flood conditions.

Several experimental studies have investigated the potential of dry [2,3] and MQL [4,5] in the drilling process. It can be summarized that, dry drilling is a success when using coated cutting tools. Moreover, MQL drilling demonstrated a promising performance in terms

of tool life and hole quality. For all lubricants which may be selected, being biodegradable is the most essential criterion for environmental compatibility. Since mineral oil does not have high biodegradability, synthetic ester has been chosen for MQL applications. However, vegetable oil can become an option to synthetic ester. This oil exhibits excellent properties such as high viscosity index, high lubricity, high flash point, low evaporation loss, high biodegradable and low toxicity with regard to its use as a base oil for lubricants [6]. However, investigation of MQL drilling using vegetable oil is still in its preliminary stages and related research remains to be conducted. The work reported here was undertaken to investigate the effect of palm oil as a lubricant in MQL applications on cutting force, workpiece temperature, tool failure modes and wear mechanism when high speed drilling of Ti-6Al-4V.

2. Experimental Setup

The drilling experiments were carried out on a vertical machining center (Mazak Nexus 410-A.) An indexable carbide drill (Mitsubishi TAWNH1400T) which had a diameter of 14 mm and coated with AlTiN was used. It had a point angle of 130° and helix angle of 30°.

2.1 Drilling tests to determine tool life

Drilling tests were carried out on a rectangle plate of Ti-6Al-4V with dimensions of 200 mm x 200 mm x 20 mm. Blind holes were drilled to a depth of 10 mm at a constant cutting speed and feed rate of 60 m/min and 0.1 mm/rev respectively. The MQL and compressed air parameters were the same as in the section of 2.2. The wear of the drill was measured by a vision measuring machine (Mitutoyo). The following tool life criteria were adopted during the trials: (i) Average flank wear, $V_{b(ave)} = 0.2$ mm, (ii) Maximum flank wear, $V_{b(max)} = 0.3$ mm, (iii) Corner

wear = 0.3 mm, (iv) Chipping = 0.2 mm and (v) Catastrophic failure and (vi) Cutting distance = 440 mm.

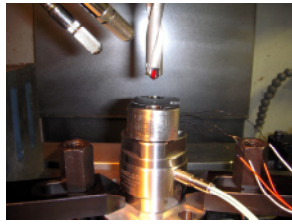


Fig. 1. Experimental setup.

Table 1. MQL parameters

Outlet air pressure (MPa)	0.2
Lubricant flow rate (ml/hour)	Approx. 10.3
Outlet air flow (l/min)	Approx. 165

Table 2. Characteristic of lubricant

Lubricant	Synthetic ester	Palm oil
Density (g/cm ³)	0.95	0.91
Viscosity at 40°C (mm ² /s)	19	40
Viscosity index	137	190

2.2 Drilling tests to measure thrust force, torque and workpiece

The workpiece material used was a round bar of Ti-6Al-4V with a diameter and thickness of 50 mm and 20 mm, respectively. The workpiece material was mounted on a piezoelectric dynamometer (Kistler 9365) as shown in Figure 1. The dynamometer was connected to the charge amplifier and data acquisition system to measure and congregate the thrust force and torque data. The workpiece temperature was measured by a K type thermocouple at two locations, namely TC1 and TC2 positioned at 9 mm and 17 mm respectively from the top surface. The distance between the end wire and hole wall was approximately 1.25 mm. A 14mm diameter through hole was drilled under the action of external MQL. Table 1 details the variable operating parameters for the MQL unit. Synthetic ester oil (MQL SE) and palm oil (MQL PO) were used as the lubricant and their physical characteristics are shown in Table 2. In addition, for dry cutting condition, a compressed air was supplied to the cutting zone. In this test, the cutting speed and feed rate were fixed at 60 m/min and 0.1 mm/rev respectively. An additional test was performed to evaluate the performance of MQLSE and MQLPO. A cutting speed of 60, 80 and 100 m/min were used together with two feed rates of 0.1 and 0.2 mm/rev. The thrust force, torque and workpiece temperature were measured and compared.

3. Results and Discussion

3.1 Tool Life and Failure Mode

The effect of various coolant strategies on the tool life is shown in Figure 2 and Table 3. The result of the dry cutting conditions shows that the flank wear grew rapidly. As a result, an increase in cutting temperature and stress condition accelerates the growth of tool wear. At this condition, the tool suffered from excessive chipping mainly on the flank face after drilling within 48 seconds of the start of drilling. The longest tool life of 195 seconds was obtained using MQL SE and MQL PO conditions after drilling to a length of 440 mm. This was probably due to the effective cooling and lubricating by delivering oil mist to the tool-workpiece interfaces.

Table 3. Tool life and failure modes

Condition	Cutting length (mm)	Failure mode
MQL SE	440	Stopped at 440 mm
MQL PO	440	Stopped at 440 mm
Dry	110	Chipping

Figure 3 shows the growth of tool wear for MQL SE, MQL PO and dry cutting conditions. It can be seen that the tool wear rate (flank and corner wear) for dry cutting was dramatically increased in comparison to the MQL SE and MQL PO conditions. The cutting tool under the dry cutting conditions suffered from severe chipping and excessive corner wear, thus fewer holes were produced. In contrast, MQL SE and MQL PO conditions exhibited the lowest tool wear rate. In addition, the improved performance has been shown by MQL SE and MQL PO with regards to for both flank and corner wear. It is suggested that vegetable based oil such as palm oil provides effective boundary lubrication as the high polarity of the entire base oil allows strong interactions with the lubricated surface.

Figure 4 shows the typical tool failure modes of the cutting tool under various coolant-lubricant conditions. Excessive chipping and uniform flank wear were found to dominate under the dry cutting condition. However, only uniform flank wear was observed under MQL SE and MQL PO conditions. Adhered workpiece material on the cutting tool was observed at all tested coolant-lubricant conditions. This phenomenon had been expected to occur due to the tendency of titanium alloys to weld to the cutting tool during drilling processes. Furthermore, the amount of workpiece material that adhered to the cutting tool was higher under dry conditions than with MQL SE and MQL PO. Therefore, under the dry conditions, the cutting tool is more susceptible to greater fracture (ie. chipping) than under the MQL SE and MQL PO.

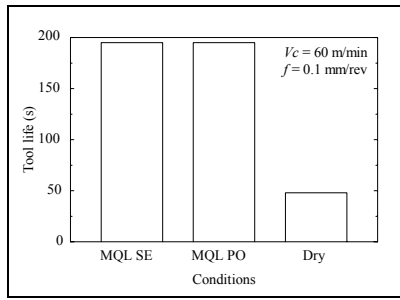


Fig. 2. Tool life at various conditions.

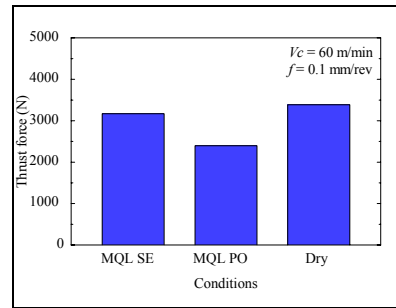


Fig. 5. Comparison of thrust force.

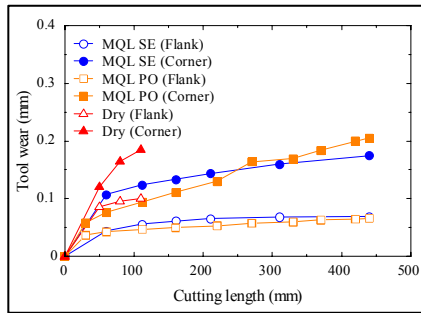


Fig. 3. Tool wear rate at Vc=60 m/min and f=0.1 mm/rev.

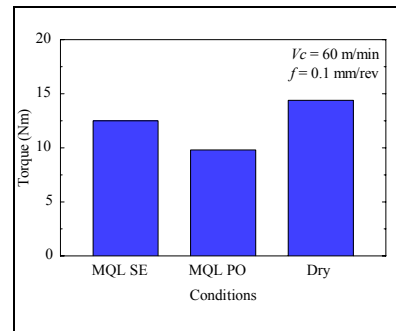


Fig. 6. Comparison of torque.

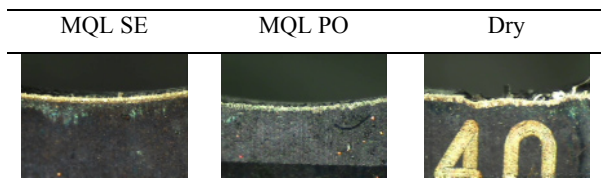


Fig. 4. Tool failure modes.

3.2 Thrust Force and Torque

Figure 5 shows the result on thrust force of high speed drilling of Ti-6Al-4V at the cutting speed of 60 m/min and feed rate of 0.1 mm/rev under various coolant-lubricant conditions. It was observed that dry cutting conditions produced the highest thrust force in comparison with the other coolant-lubricant conditions. This figure also shows that the application of MQL SE and MQL PO are most effective in the drilling process. Figure 6 presents the effect of coolant-lubricant conditions on torque component at the cutting speed of 60 m/min and feed rate of 0.1 mm/rev. The highest torque value was recorded under dry cutting conditions. The torque value for MQL SE was slightly lower than dry cutting followed by MQL PO. Indeed the results presented here show that MQL PO is more effective for lubrication than MQL SE. It provides high strength lubricant films that interact strongly with the contact surfaces resulting in reduced wear and friction.

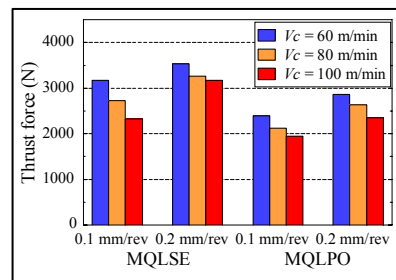


Fig. 7. Comparison of thrust force between MQL SE and MQL PO.

A further experiment was carried out to investigate the effect of various cutting speeds and feed rates on MQL conditions. The thrust force and torque obtained for MQL SE and MQL PO when high speed drilling Ti-6Al-4V is presented in Figures 7 and 8, respectively. It is noted that the thrust force and torque decreased with an increase in the cutting speed. In contrast, these values were increased when the feed rate increased. The torque value for MQL SE associated with the cutting speed of 100 m/min had reduced significantly to 9.6 Nm and 13.7 Nm at feed rate of 0.1 mm/rev and 0.2 mm/rev respectively. MQL PO achieved the lowest torque at a cutting speed of 100 m/min and feed rate of 0.1 mm/rev. Generally, MQL SE produces higher thrust force and torque than MQL PO. It is found that palm oil (MQL PO) exhibits a better lubricating effect under all tested conditions. Palm oil contains more than 50% of palmitic acid and triglyceride structures that provide desirable lubrication [7] thus promoting the boundary lubrication. It was observed that the thrust force and torque were less under MQL PO,

which was mainly due to the reduction of coefficient of friction. Furthermore, the value of the friction coefficient for MQL PO is found to be less than that of MQL SE due to the generation of low cutting temperature. On the contrary, Wakabayashi et al. [8] reported that synthetic ester outperformed vegetable oil in terms of the coefficient of friction.

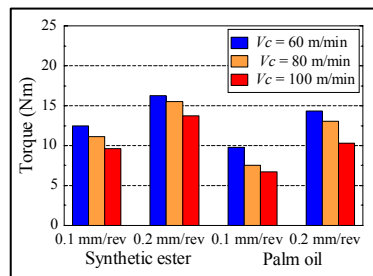


Fig. 8. Comparison of torque between MQL SE and MQL PO.

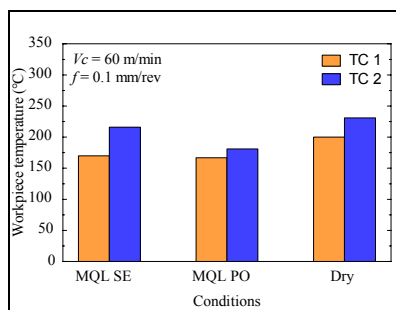


Fig. 9. Comparison of maximum workpiece temperature.

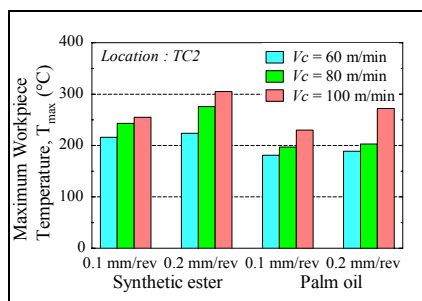


Fig. 10. Comparison of maximum workpiece temperature between MQL SE and MQL PO.

3.3 Workpiece Temperature

Figure 9 shows the influence of the coolant-lubricant conditions on the maximum workpiece temperature. This figure reveals that dry cutting recorded the highest workpiece temperature at locations TC1 and TC2. MQL SE and MQL PO yielded slightly lower temperatures than the dry cutting. MQL conditions give sufficient cooling effect on the machining process thus prolonging the tool life. The rise of temperature in the dry cutting could cause severe wear on the cutting edges and hole enlargement

due to the thermal growth of the drill and the workpiece. Figure 10 shows the values of maximum workpiece temperature obtained at the location TC2. It can be seen that the temperature increased with the cutting speed and feed rate as well as with the lubricants. An increase of the maximum workpiece temperature by the higher feed rate of 0.2 mm/rev was more significant than that when the feed rate of 0.1 mm/rev was used. An increase in the cutting speed is always accompanied by a reduction of the chip thickness. This corresponds with high cutting energy and deformation strain rate. In addition, machining at high feed rate has increased the friction and produced more stress thus increasing the workpiece temperature. All the cases examined in this investigation indicate that the workpiece temperature exhibited by the MQL PO was lower than that by the MQL SE. Vegetable based oil, especially palm oil, provides low evaporation loss when used as a base oil for lubricant [6].

4. Conclusions

Based on the experimental results obtained with the use of MQL during high speed drilling of Ti-6Al-4V, the following conclusions can be drawn:

MQL SE and MQL PO offer 306% improvement in tool life compared with dry cutting conditions. It was found that the application of MQL effectively improves the thrust force and torque resulting in reduced the power consumption. MQL PO has superior lubricating effects thus reduces the high friction during the machining process. In addition, MQL PO has sufficient cooling capability, hence it reduces the machining temperature.

References

- [1] Byrne G, Dornfeld D, Denkena B, (2003) Advancing cutting technology. *Annals of CIRP* 52 (2): 483-695
- [2] Schulz H, Dorr J, Rass J, Schulze M, Leyendecker T, Erkens G, (2001) Performance of oxide PVD-coatings in dry cutting operations. *Surf. & Coat. Technol.* 146-147: 480-485
- [3] Harris SG, Vlasveld AC, Doyle ED, Dolder PJ, (2000) Dry machining-commercial viability through filtered arc vapour deposited coatings. *Surf. & Coat. Technol.* 133-134: 383-388
- [4] Braga DU, Diniz AE, Miranda WA, Coppini NL, (2002) Using a minimal quantity of lubricant (MQL) and a diamond coated tool in the drilling of aluminum-silicon alloys. *J. Mater. Process. Technol.* 122: 127-138
- [5] Kelly JF, Cotterell MG, (2002) Minimal lubrication machining of aluminium alloys. *J. Mater. Process. Technol.* 120: 327-334
- [6] Erhan SZ, Asadaukas S, (2000). Lubricant basestocks from vegetable oils. *Industrial Crops & Products* 11: 277-282
- [7] Masjuki HH, Maleque MA, Kubo A, Nonala T, (1999) Palm Oil and Mineral Oil Based Lubricants – Their Tribological an Emission Performance. *Tribol. Int.* 32: 305-314
- [8] Wakabayashi T, Inasaki I, Suda S, Yoota H, (2003) Tribological Characteristics and Cutting Performance of Lubricant Esters for Semi-Dry Machining. *Annals of CIRP* 52(1): 61-64

Estimation of minimum chip thickness for multi-phase steel using acoustic emission signals

A.J. Mian, N. Driver and P.T. Mativenga

School of Mechanical, Aerospace and Civil Engineering, The University of Manchester, M1 3BB, UK

Abstract. The determination of minimum chip thickness is important for establishing the lower limit of the feasible process window in micro mechanical machining for a given tool and workpiece material. The minimum chip thickness is encountered in micro milling operations owing to the variation in chip load as predicted by the chip density function. This study proposes a methodology to determine the value of minimum chip thickness by analysing acoustic emission (AE) signals generated in orthogonal machining experiments conducted in micro milling. Cutting trials were performed on a near balanced ferrite/pearlite microstructure (AISI 1045 steel) with a range of undeformed chip thicknesses spanning across the tool edge radius. The characteristics of AE r.m.s signals were studied for conditions when the tool was rubbing the workpiece. This base signal signature was used to study and contrast AE signals to other machining parameters. This study enabled the identification of threshold conditions for occurrence of minimum chip thickness. The value of minimum chip thickness predicted by this new approach compares reasonably well with that existing in published literature.

Keywords: Minimum chip thickness, Acoustic emission, Micro cutting

1. Introduction

One of the fundamental issues in micro mechanical machining is the knowledge of minimum chip thickness for a given workpiece material. Unlike the turning process, in slot milling the undeformed chip thickness varies from zero up to a maximum (equal to the feed per tooth) then back to zero during each engagement of a cutting edge. The micromilling process is affected by two mechanisms i.e. ploughing/rubbing and chip removal. In micro-scale cutting, when undeformed chip thickness is less than the minimum chip thickness, only elastic recovery of workpiece material will take place (no material is removed in a form of chip) [1]. In a situation where undeformed chip thickness starts to exceed the minimum chip thickness the chip begins to form through shearing coupled with an elastic deformation of the workpiece. Material is removed completely in the form of a chip when the undeformed chip thickness is considerably greater than the minimum chip thickness.

The minimum chip thickness has been estimated previously using experimental [2], analytical modelling [3-5] and simulation techniques [6, 7] and suggested to lie between 5% and 40% of the tool edge radius. From the study of polished cross sectional view of 0.45% carbon steel chip root, the existence of a stagnation point on the material flow on the rounded edge of the tool has been reported [8]. In turning of mild steel, Komanduri [9] concluded that at cutting depth less than 10 μm a tool with negative rake angle greater than 76° would retard the chip formation process. Abdelmoneim and Scrutton [10] reported similar results in milling of free-cutting brass and fine-grained zinc with 100 μm nominal depth of cut. L'vov evaluated by considering the theory of metal rolling, the minimum chip thickness to be 29.3% of the tool edge radius [11].

Ikawa et al related magnitude of material removal (undeformed chip thickness) to the relative sharpness of the tool edge radius [12]. Kim et al reported that intermittent chip formation was difficult to avoid when the feed per tooth was less minimum chip thickness [13]. Weule et al emphasized strong contribution of material properties on the minimum chip thickness [14]. The coefficient of friction between the tool-workpiece material and material's behaviour in plastic deformation zone were possible factors influencing change in the minimum chip thickness for different work materials [6]. Liu et al highlighted the influence of cutting velocity, thermal softening and strain hardening as well as tool edge radius on the minimum chip thickness of a material [3]. The value of minimum chip thickness also proves useful in identifying optimal cutting conditions since it influences cutting forces [15], tool wear, surface roughness [7, 14], burr formation [16, 17], process stability.

The objective of this paper was to utilise acoustic emission (AE) signal for the prediction of minimum chip thickness. The AE monitoring has an ability to detect micro scale deformation mechanisms within a relatively "noisy" micro cutting background [18]. Previous studies on AE generation in machining [19, 20] have shown the sensitivity of the AE signal to the various contact areas

and deformation regions involved in chip formation. Plastic deformation in metal cutting usually produces continuous AE signal whereas fracture events are the common sources for the burst type AE signals. At the instant of tool engagement, an incremental change of AE r.m.s due to the burst component can be related to the chip formation. The magnitude of AE r.m.s was found to decrease with positive rake angle tool, when compared to negative rake angle tools [21]. The yield strength of workpiece material, strain rates of shear deformations and the volume of the deformation zone were also significant parameters affecting the energy level of the AE signal [22]. The purpose of the study reported here was to exploit AE signal in characterising micro machining mechanisms and hence minimum chip thickness.

2. Micro milling experiments

For the detection of the cutting mode transition along the tool rotation, preliminary orthogonal micro cutting tests were carried out on a Mikron 400 HSM centre. The workpiece of dimensions 100 mm long, 70 mm wide and 10 mm thick was made of AISI 1045 steel. The ferrite phase had an average grain intercept length of 7 μm while the pearlite 52 μm . Single straight flute uncoated end mills (Dixi-7060) were used in micro milling tests (2 mm and 6 mm diameter) to avoid discrepancies associated with radial runout. Prior to each cutting trial, the tools were examined under a SEM. Fig. 1 shows the image of the edge of a fresh tool along with a magnified base view of the tool which was used to estimate the cutting edge radius. The average tool edge radius was found to be 0.84 μm with a standard deviation of 0.52 μm .

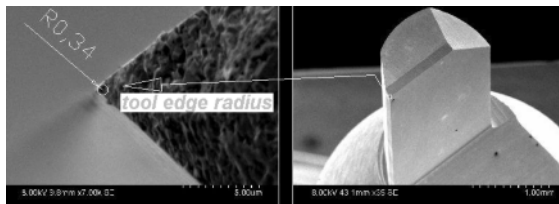


Fig. 1. Single tooth tool

All the experiments were conducted dry, without application of coolant. The AE signal was monitored when the feed per tooth was below the tool edge radius (0.02 and 0.5 $\mu\text{m}/\text{tooth}$) and above the tool edge radius (2 and 10 $\mu\text{m}/\text{tooth}$). For the up milling mode, the maximum chip thickness occurred at the exit of the cut and would theoretically be equal to the feed per tooth since the swept angle was kept constant at 90°. The depth of cut was set at 1 mm. This depth of cut was reported to provide plane strain conditions and reduce the possibility of side spread of material [9]. Spindle speeds of 5000 and 15000 rpm were employed to maintain similar cutting velocity for both tools used. Fresh cutting edges were used, tests were repeated four times.

2.1 AE signal acquisition

AE signals were sampled using an Kistler 8152B1 AE sensor, passed through a Kistler 5125B coupler and then recorded to a Nicolet technologies Sigma 30 digital memory oscilloscope at a sampling rate of 2 MHz per channel. The raw AE signal was bandpass filtered, 50 kHz to 1 MHz and then sent through a preamplifier at a gain of 20 dB to a data acquisition system. The AE r.m.s data were also acquired, from the band pass-filtered analogue signal, with an R.M.S. time constant of 0.12 ms. This is akin to a moving average, continuously updating the R.M.S. value based on the most recent 0.12ms of raw AE output. To retain sufficient amount of information sampling data length of 128, 000 and 64,000 points were chosen for 6 mm and 2 mm diameter tool respectively. The sampled data length contained over five and eight spindle revolution periods with time spans of 0.064 s and 0.032 s respectively.

3. Results and Discussions

3.1 Uncut chip thickness below tool edge radius

Fig. 2 shows the AE signal generated when machining at 0.02 $\mu\text{m}/\text{tooth}$ undeformed chip thickness for a fresh tool and a worn tool. The selected 0.02 $\mu\text{m}/\text{tooth}$ feed per tooth is equivalent to 5% of the tool edge radius and hence much lower than the reported value of minimum chip thickness for the AISI 1045 workpiece material. Fig. 2(a) shows that a fresh cutting tool generates large magnitude AE signatures and the sensor gets saturated in the initial 30° to 40° of the tool rotation. In Fig. 2(b), considerably lower magnitude of AE signal was observed with worn tool (0.09 mm maximum flank wear).

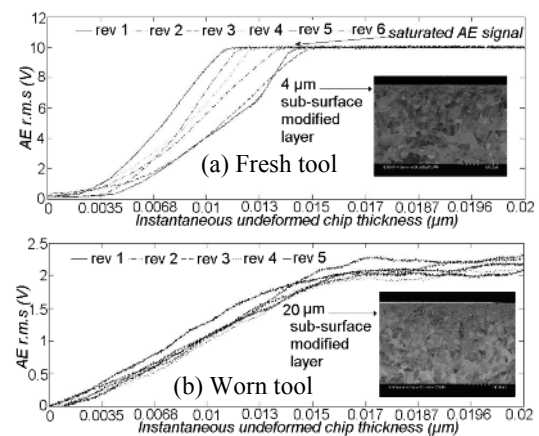


Fig. 2. AE r.m.s signal generated at $f_z = 0.02 \mu\text{m}$; $a_c = 1\text{mm}$; $n = 15000\text{ rpm}$; (a). Fresh tool, (b). Worn tool

Additionally in Fig 2 the insert machined cross-sectional images demonstrate an obvious correlation of machined

subsurface microstructure modification with the corresponding tool wear. AE signature variation as a function of microstructure modification was attributed to the damping rate of the tool/ workpiece system [23]. The increase in damping rate which, in turn, results in low AE amplitude for worn tools is reasonable since machined surface are tempered due to multiple thermal cycles from previous tool rotations. This shows that raw AE signal can be used to determine the influence of the micro cutting on the subsurface microstructure of the workpiece.

Fig. 3 shows the AE r.m.s trends as a function of instantaneous undeformed chip thickness generated at 0.5 $\mu\text{m}/\text{tooth}$ undeformed chip thickness. While AE r.m.s value of the AE signals represents the enveloped curve of both continuous (lower amplitude high frequency signal generally associated with plastic deformation) and burst (high amplitude low frequency signal generally associated with fracture) events occurred during cutting process. Evidence of ductile tearing leading to material separation has been reported recently in micro cutting of Al 2024-T3 at 0.67, 1 and 1.33 undeformed chip thicknesses to tool edge ratios [24].

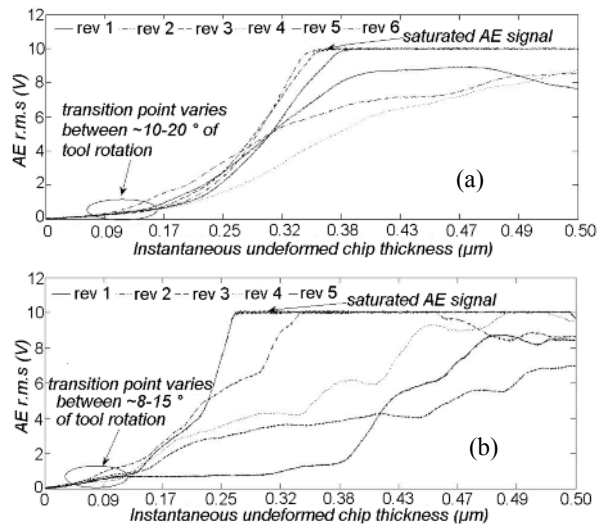


Fig. 3. AE r.m.s signal generated at 0.5 μm chip load; (a) $a_p = 1 \mu\text{m}$; $a_c = 1\text{mm}$; $n = 15000 \text{rpm}$, (b). $a_p = 1 \mu\text{m}$; $a_c = 3\text{mm}$; $n = 5000 \text{rpm}$

One apparent question that can be raised is if the interface zone has a built-up edge (BUE) or not. Based on literature of machining of steel [25], BUE is observed only at lower cutting velocities ($< 40 \text{m/min}$). Moreover, BUE usually occurs over a region on the rake face much higher than the undeformed chip thickness. Therefore, for initial tool rotation a sudden increase in AE r.m.s value due to burst type signal can be linked to the chip initiation. It can be seen that the AE r.m.s follows similar trends in the initial 8° to 20° of subsequent tool rotations and this can be identified as a rubbing signature. The slight variation in the rubbing signature can be attributable to difference in the tool edge radius for

different diameter tools used. Additionally, from the understanding of minimum chip thickness concept, material accumulation from previous passes can also cause variation in the chip initiation. The trends showed that the estimated value of minimum chip thickness lies between 24.7 to 35.5 percent of the tool edge radius. These results are in agreement with the value of minimum chip thickness available in the literature for steel workpiece material [3, 4].

The small waviness due to the burst component of the signal can be observed in AE r.m.s per tool revolution which reflects the workpiece material microstructure effects at micro scale. Since, axial depth of cut (a_p) and radial depth of cut (a_c) are set larger than the grain sizes of the both phases present in the AISI 1045 microstructure, there is more than one grain being cut in each cutting pass. Ferrite which is more a ductile phase than pearlite is more affected by ploughing. Thus, cutting discontinuities between different phases and grain sizes that a micro tool is likely to encounter at an instant of tool rotation can account for variations in the AE r.m.s signature. Nevertheless, above minimum chip thickness trend of AE r.m.s for subsequent tool rotation is closer in the beginning but deviates as the tool approaches the exit angle (swept angle). This suggests that AE produced in ploughing dominated zone is significantly influenced by the damping rate associated with the each tool rotation.

3.2 Uncut chip thickness above tool edge radius

Figures 4 and 5 show the AE signals trends observed at 2 and 10 μm feed/tooth. Both trends depict less AE amplitude and deviation with respect to each other as compared to AE signal produced at 0.02 and 0.5 μm undeformed chip thickness. This shows that extruding and ploughing mechanisms are gradually lessened at undeformed chip thickness higher than the tool edge radius and presenting positive rake angle in the chip formation process. Therefore, a decrease in the AE amplitude can be seen in the both Fig 3.4 and 3.5.

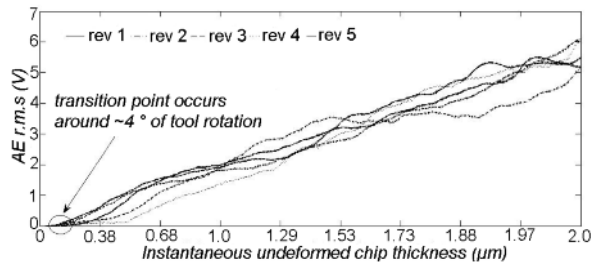


Fig. 4. AE r.m.s signal generated at 2 μm chip load; $a_p = 1$; $a_c = 3\text{mm}$; $n = 5000 \text{rpm}$

Fig. 6 shows the variations in surface residual stress measured by means of a PROTO x-ray diffraction. In both directions of the machined surface, large residual stresses were measured when material removal length

scale is in the order of tool edge radius or below. This provides evidence that material in the vicinity of the tool edge radius will be subjected to a large plastic deformation.

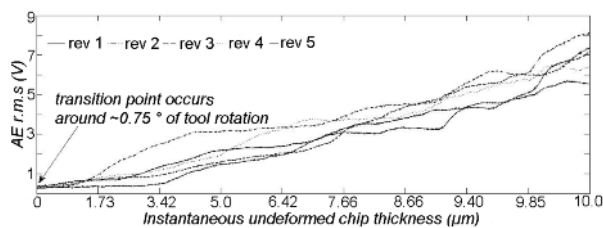


Fig. 5. AE r.m.s signal generated at 10 μm chip load; $a_p = 1 \mu\text{m}$; $a_c = 3\text{mm}$; $n = 5000 \text{rpm}$

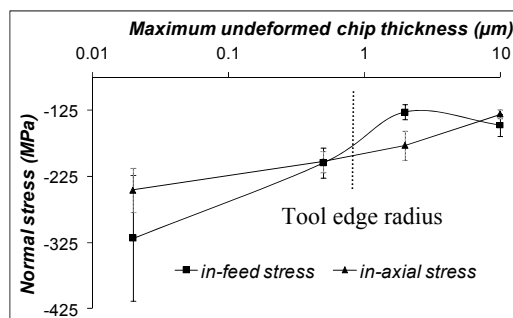


Fig. 6. Machined surface residual stress as a function of chip load

4. Conclusions

The close examination of AE r.m.s trends of a given tool-workpiece interactions reveal that the value of minimum chip thickness can be estimated successfully through the identification of rubbing signature during micro milling process. The value of minimum chip thickness for AISI 1045 steel lies between 24.7 to 35.5 percent of the tool edge radius. The residual stresses increases with decrease in the undeformed chip thickness. AE has potential to provide real-time process monitoring that can through light on machined subsurface microstructural change.

References

- [1] Aramcharoen A, Mativenga PT (2009), Size effect and tool geometry in micromilling of tool steel, *Precision Engineering* 33 (4) 402–407.
- [2] Basuray PK, Misra BK, Lal GK (1977), Transition from Ploughing to Cutting during Machining with Blunt Tools, *Wear* 43:341–349.
- [3] Liu X, DeVor RE, Kapoor SG (2006), An analytical model for the prediction of minimum chip thickness in micromachining, *J Manuf Sci Eng, Trans ASME* 128 (2) 474–481.
- [4] Yuan ZJ, Zhou M, Dong S (1996), Effect of diamond tool sharpness on minimum cutting thickness and cutting surface integrity in ultra precision machining, *J Materials Processing Technol* 62:327–330.
- [5] Son SM, Lim HS, Ahn JH (2005), Effects of the Friction Coefficient on the Minimum Cutting Thickness in Micro Cutting, *Inter J Mach Tools and Manuf* 45 (4-5) 529–535.
- [6] Shimada S, Ikawa N, Tanaka H, Ohmori G, Uchikoshi J, Yoshinaga H (1993), Feasibility Study on Ultimate Accuracy in Microcutting Using Molecular Dynamics Simulation, *Annals CIRP* 42 (1) 91–94.
- [7] Vogler MP, DeVor RE, Kapoor SG (2004), On the Modeling and Analysis of Machining Performance in Micro-Endmilling, Part I: Surface Generation, *J Manuf Sci Eng, Trans ASME* 126 (4) 685–694.
- [8] Ohbuchi Y, Obikawa T (2003), Finite Element Modeling of Chip Formation in the Domain of Negative Rake Angle Cutting *Journal of Manufacturing Science and Engineering, Transactions of the ASME* 125:324–332.
- [9] Komanduri R (1971), Some Aspects of Machining with Negative Rake Tools Simulating Grinding, *International J Machine Tool Design and Res* 11:223–233.
- [10] Abdelmoneim ME, Scrutton RF (1973), Post-machining Plastic Recovery and Law of Abrasive Wear, *Wear* 24:1–13.
- [11] L'vov NP (1969), Determining the Minimum Possible Chip Thickness, *Machine Tool (USSR)* 40 45.
- [12] Ikawa N, Shimada S, Tanaka H (1992), Minimum thickness of cut in micromachining, *Nanotechnology* 3:6–9.
- [13] Kim CJ, Bono M, Ni J (2002), Experimental analysis of chip formation in micro-milling, *Trans NAMRI/SME* 30:1–8.
- [14] Weule H, Huntrup V, Tritschler H (2001), Micro-Cutting of Steel to Meet New Requirements in Miniaturization, *Annals of CIRP* 50 (1) 61–64.
- [15] Vogler MP, DeVor RE, Kapoor SG (2004), On the Modeling and Analysis of Machining Performance in Micro-Endmilling, Part II: Cutting Force Prediction, *J Manuf Sci Eng, Trans ASME* 126 (4) 695–705.
- [16] Lee K, Dornfeld DA (2002), An experimental study on burr formation in micro milling aluminium and copper, *Transactions of the NAMRI/SME* 30:255–262.
- [17] Mian AJ, Driver N, Mativenga PT (2009), Micromachining of coarse-grained multi-phase material, *P I Mech Eng B-J Eng Manuf* 223 (4) 377–385.
- [18] Lee DE, Hwang I, Valente CMO, Oliveira JFG, Dornfeld DA (2006), Precision manufacturing process monitoring with acoustic emission, *Int. J Mach Tools and Manuf* 46 (2) 176–188.
- [19] Kannatey-Asibu Jr. E, Dornfeld DA (1981), Quantitative relationships for acoustic emission from orthogonal metal cutting, *J Eng Industry, Trans ASME* 3 (103) 30–340.
- [20] Uehara K, Kanda Y (1984), Identification of Chip Formation Mechanism through Acoustic Emission Measurements, *Annals CIRP* 33 (1) 71–74.
- [21] Saini DP, Park YJ (1996), A quantitative model of acoustic emissions in orthogonal cutting operations, *J Materials Processing Technol* 58 (4) 343–350.
- [22] Lee M, Thomas CE, Wildes DG (1987), Prospects for in-process diagnosis of metal cutting by monitoring vibration signals, *J Materials Science* 22 (11) 3821–3830.
- [23] Tönshoff HK, Jung M, Männel S, Rietz W (2000), Using acoustic emission signals for monitoring of production processes, *Ultrasonics* 37 (10) 681–686.
- [24] Subbiah S, Melkote SN (2008), Effect of finite edge radius on ductile fracture ahead of the cutting tool edge in micro-cutting of Al2024-T3, *Materials Science and Eng: A* 474 (1-2) 283–300.
- [25] Ramaswami R (1971), Investigation of the secondary shear zone in metal cutting, *Inter J Machine Tool Design and Res* 11 (1) 75–83.

Extension of a Simple Predictive Model for Orthogonal Cutting to Include Flow below the Cutting Edge

G. P. Zou¹, I. Yellowley¹ and R.J. Seethaler²

¹ Department of Mechanical Engineering, University of British Columbia, Vancouver, CANADA

² Department of Mechanical Engineering, University of British Columbia at Okanagan, Kelowna, CANADA

Abstract. The authors describe the extension of a simple predictive model for orthogonal cutting to accommodate flow under the cutting edge. The model utilizes an upper bound approach combined with primary and secondary boundaries that guarantee both force and moment equilibrium of the chip. The calculated results are in general agreement with the experimental observations.

Keywords: Metal Cutting Mechanics, Upper Bound, Edge Forces

1. Introduction

The investigation of forces acting at the tool nose and on the flank of cutting tools has generated considerable interest; usually this has been motivated by an interest in the influence of detailed edge geometry or tool wear on the process. No matter how one visualizes the process it has to be admitted that a new surface is created and the stress system present at the edge must allow this to occur; the energy required in the fracture process at the tool edge has been investigated in detail by Atkins (2003 and 2006).

Previous work addressing the analysis of worn, radiused or chamfered tools utilizing upper bounds and slip line fields has been demonstrated by Zhang et al., (1991), Wardolf et al. (1997), and Manjunathaiah and Endres (2000). Numerical approaches to the problem have been examined by Movahhedy et al. (2002), and Long and Huang, (2005). In this paper the authors seek an approach which will have the capacity to predict the influence of the major variables without recourse to extensive numerical computation or the need for detailed constitutive equations. An upper-bound method coupled with a simple predictive model developed by Yellowley (1987) is developed to analyze flow around and under the tool edge. The approach guarantees chip force and moment equilibrium and incorporates a realistic elastic/plastic rake face contact situation.

2. Upper Bound Solution

Several authors have examined upper-bound models for orthogonal cutting De Chiffre (1977), and Rowe and Spick (1967). Perhaps the best-known approach which (essentially) results in an upper-bound is that due to Merchant (1945). In this paper, a new upper bound solution is proposed, the basic geometry of the model is shown in Figure 1 below.

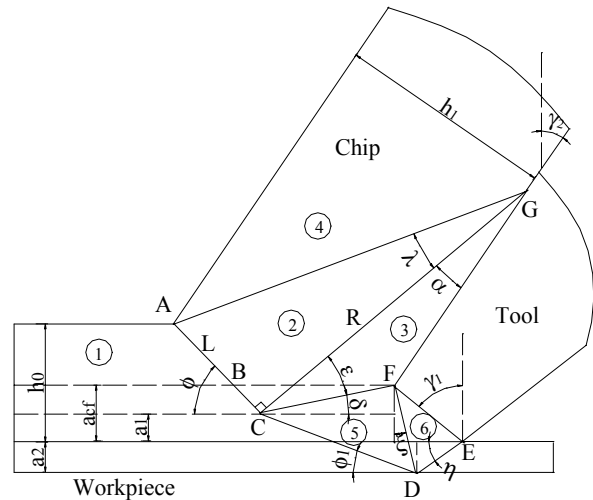


Fig. 1. Proposed Upper Bound Solution for orthogonal cutting with chamfered tools

In the model described above, the upper part of the field corresponds to that proposed by Yellowley (1987). Based on the force equilibrium and moment equilibrium, the relationship of R , L and ϕ is as follows, (see Figure 2).

$$\tan(\phi + \beta_s - \gamma_2) = \frac{(1 + \pi/2 - 2\phi) - (R/L)}{1 - (1 + \pi/2 - 2\phi)(R/L)} \quad (1)$$

and based upon the moment equilibrium of the chip

$$\frac{F_N \cdot z}{L^2} + k \cdot (R/L) - (k/2) \cdot (1 + \pi/2 - 2\phi) \cdot [1 + (R/L)^2] = 0 \quad (2)$$

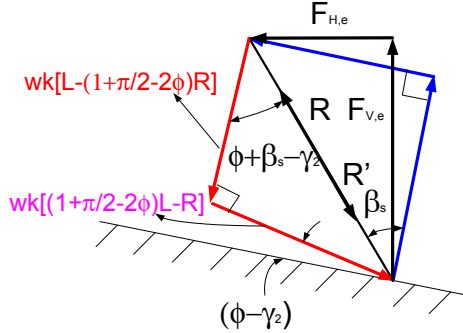


Fig. 2. Force Equilibrium

Where k is the shear yield stress of work material, β_s is the angle of friction in elastic contact zone on the rake face, F_N and z are the normal component of force acting upon elastic region of the rake face contact and distance between the plastic point B and F_N respectively, as shown in Figure 3.

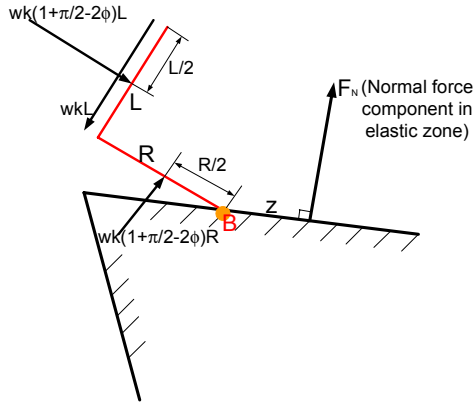


Fig. 3. Moment equilibrium of chip

Assuming a normal stress distribution in the elastic zone of the form

$$\sigma = const \cdot x^n \quad (3)$$

where x is the distance from the end of the chip-tool contact. Then Eqn. (2) can be rewritten as

$$\frac{F_N}{L^2 \sigma_B} \cdot \frac{n+1}{n+2} + k \cdot (R/L) - (k/2) \cdot (1 + \pi/2 - 2\phi) \cdot [1 + (R/L)^2] = 0 \quad (4)$$

Where σ_B is the normal stress at point B.

Based on the proposed Upper Bound solution, the geometry can be defined as follows:

$$a_{cf} = L_{chmf} \cos(\gamma_1) \quad (5)$$

$$L = \frac{h_0}{\sin \phi + (R/L) \cdot (\cos \gamma_2 - \cos \phi)} \quad (6)$$

$$R = L \cdot (R/L), \lambda = \tan^{-1}(L/R)$$

$$a_1 = h_0 - L \cdot \sin \phi \quad (7)$$

$$L_{AC} = L, L_{CG} = R, L_{AG} = \frac{L}{\sin \lambda} \quad (8)$$

$$L_{FG} = \frac{R \cdot \cos \phi - a_{cf} + h_0 - L \cdot \sin \phi}{\cos \gamma_2} \quad (9)$$

$$\varepsilon = \tan^{-1} \left[\frac{L_{FG} \cdot \sin(\phi - \gamma_2)}{R - L_{FG} \cdot \cos(\phi - \gamma_2)} \right], \delta = \pi/2 - (\phi + \varepsilon) \quad (10)$$

$$L_{CF} = \frac{L_{FG} \cdot \sin(\phi - \gamma_2)}{\sin \varepsilon}, L_{CD} = \frac{a_1 + a_2}{\sin \phi_1} \quad (11)$$

In previous slip-line analyses, the angle η is usually assumed equal to the friction angle. Here the final value of η is determined directly within the upper-bound optimization. The angle η is given as

$$\eta = \tan^{-1} \left[\frac{a_2}{L_{CF} \cdot \cos \delta + L_{chmf} \cdot \sin \gamma_1 - (a_1 + a_2) \cdot \cot(\phi_1)} \right] \quad (12)$$

and the angle ξ is given as

$$\xi = \tan^{-1} \left[\frac{(a_1 + a_2) \cdot \cot(\phi_1) - L_{CF} \cdot \cos \delta}{a_{cf} + a_2} \right] \quad (13)$$

Finally the lengths of FD, BG and EF are given by

$$L_{EF} = L_{chmf}, L_{FD} = \frac{a_{cf} + a_2}{\cos \xi}, L_{BG} = R \quad (14)$$

3. Optimization

Having obtained the geometry of slip-line field and the magnitudes of velocity discontinuities from the associated hodograph, power consumption P_T can be calculated.

$$P_T = F_c U_0 = wk(L_{AC} \cdot V_3 + L_{AG} \cdot V_{4,2} + L_{CG} \cdot V_{2,3} + L_{cd} \cdot V_{5,1} + L_{DE} \cdot V_{1,6} + L_{EF} \cdot V_{6,0} + L_{FG} \cdot V_{3,0} + L_{ED} \cdot V_{6,5} + L_{CF} \cdot V_{3,5}) + F_f \cdot V_c \quad (15)$$

Where w is the width of cut and F_f is the “elastic friction force” acting on the tool-chip interface.

The solution to the upper bound is purposely constrained by force and moment equilibrium of the chip; this also speeds the optimization process. For each elastic coefficient of friction the shear angle is incremented and the values of R and L determined from the model, this continues until moment equilibrium is satisfied. There is then a unique solution to the upper part of the field for each elastic coefficient of friction, the energy minimization in essence determines only the position of point D in Figure 1.

4. Force Prediction

The calculation of edge forces or the estimation of stress distributions in the region of the cutting edge is made extremely difficult by the high stress, strain and temperature gradients in the region. The authors here attempt to circumvent some of these problems by using the upper bound method to look at average values over the elements adjacent to the cutting edge and using overall force equilibrium as the means to move from the chip side of the field, (where we have some idea of stress state) to the work side where we have little. This is achieved by equating the forces in the direction of relative velocity with that resulting from the upper bound. It is assumed that the rake face components will not be changed as chamfer geometry changes, (it is demonstrated that this influence is small). It should be realized that this technique only produces interesting results for chamfers that have large negative rake but do not approach 90 degree. The shear stresses acting upon the chamfer and the plastic rake face contact regions are considered equal. The forces acting upon the rake face are assumed equal to those from Yellowley’s model.

4.1 Optimized Slip-Line Fields

Having assumed that the chamfer length does not influence stresses on the rake face, it is instructive to examine the shape of the flow zones as chamfer width is increased. The typical influence of chamfer length is indicated in Figure 4 where large chamfers exhibit a lower boundary that is almost parallel to the incoming velocity, (indicating an almost stagnant zone) and an apparent increase in the curvature of the leading boundary of the shear plane. The latter suggests an increasing hydrostatic stress at the tool edge. The methodology used by the authors to calculate forces on the chamfer is relatively robust in terms of the potential influence of varying slip line curvature. To demonstrate this, the authors show the expected normal stress levels on the chamfer calculated assuming that the leading slip line intersects the rake face either at right angles or in the extreme case at the angle of intersection of CF and the

rake face. Figure 5 shows that there is remarkably little influence between these extremes.

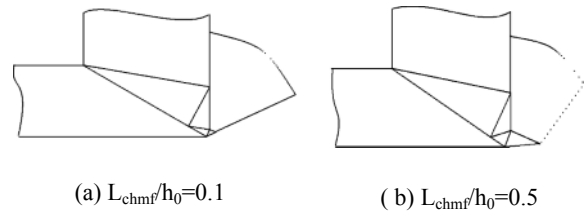


Fig. 4. Upper Bound Solutions for the case of $\gamma_1=70^\circ$, $\gamma_2=0^\circ$, $\beta_s=40^\circ$

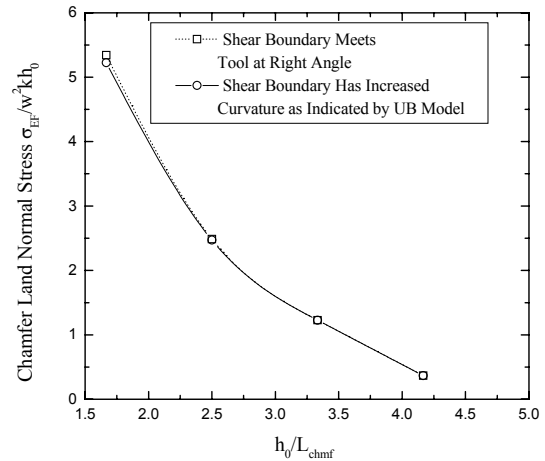


Fig. 5. Calculation of Normal Stress on Chamfer

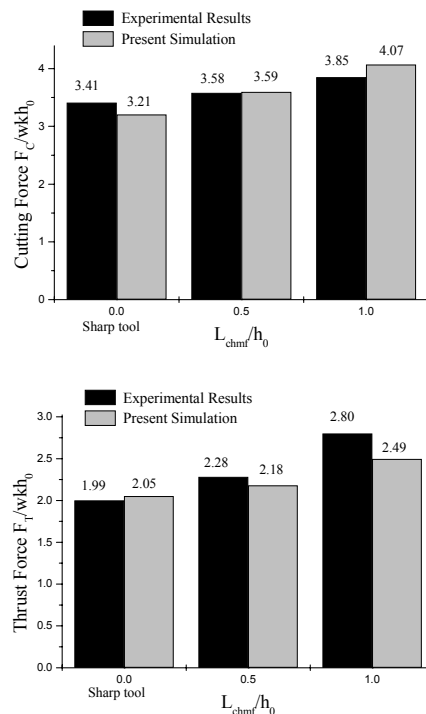


Fig. 6. Cutting and Thrust Force Comparison

4.2 Comparison with Data from Recent Experiments

Here the authors briefly compare the force predictions from the model with recent experimental data. The first series of experiments was conducted by Smithy et al. (2001). The test material is 4130 steel with cutting width $w=3$ mm and uncut chip thickness of 0.2 mm. The yield shear stress at these cutting conditions is $k=585.1$ MPa, and the rake angle is 5° . The model parameters are $\gamma_1=85^\circ$, $\gamma_2=5^\circ$, and $\beta_s=42^\circ$. Figure 6 shows the comparison of the predicted cutting forces with the experimental results.

The second set of experiments concern the cutting of a 0.2% carbon steel using a tool with a 0.1 mm radius tool edge and were reported by Kim et al., (1999). In order to characterize the edge radius the authors have followed the approach suggested by Manjunathaiah and Endres, (2000), as shown in Figure 7, the actual critical angle chosen at point (F) is 30° . The comparison between experiment and FEM results from the previous work and the predictions from this simplified model are shown in Figure 8.

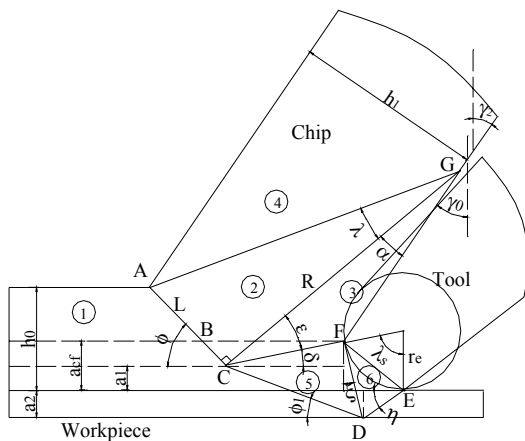


Fig. 7. Radiused Cutting Edge Model

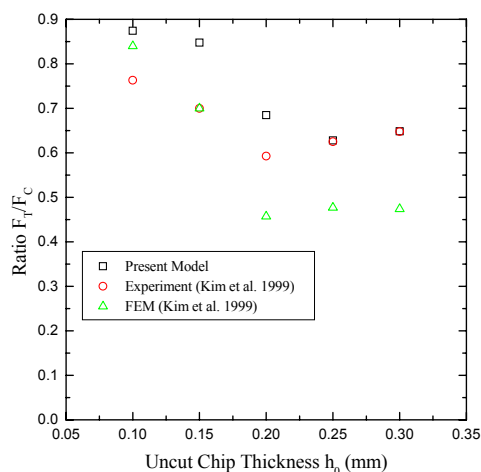


Fig. 8. Change in Force Ratio as Chip Thickness Increases

5. Conclusions

A simple predictive model has been developed for the prediction of forces acting on worn and radiused edge tools. The model does not need extensive calibration, the only unknown parameter in the basic model being the elastic coefficient of friction in the sliding region of the rake face. (The calculation of forces requires the mean shear yield stress to be estimated). The predicted results are in good agreement with experimental results and FEM simulations. The results show that the stress on the wear land increases as the wear land increase in length. It is also confirmed that the ratio of F_T/F_C can be used as a sensitive indicator of tool wear..

Acknowledgements

I Yellowley and R.J. Seethaler gratefully acknowledge research support from the Natural Sciences and Engineering Research Council of Canada under the Discovery Grants Program

References

- Atkins, A.G. (2003). Modelling metal cutting using modern ductile fracture mechanics: quantitative explanations for some longstanding problems, *International Journal of Mechanical Science*, 45, 373-396.
- Atkins, A.G., (2006). Toughness and oblique metalcutting, *Journal of Manufacturing Science and Engineering*, 128, 775-786.
- Kim, K.W., Lee, W.Y. and Sin, H., (1999) A finite element analysis for the characteristics of temperature and stress in micro machining considering the size effect, *International Journal of Machine Tools and Manufacture*, Vol 39, 9, 1507-1524
- Long, Y. and Huang, Y., (2005). Force modeling under dead metal zone effect in orthogonal cutting with chamfered tools, *Transactions of NAMRI/SME*, vol. 33, 573-580
- Manjunathaiah, J. and Endres W. J., (2000). A new model and analysis of orthogonal machining with an edge-radiused tool, *Journal of Manufacturing Science and Engineering*, vol. 122, 384-390.
- Merchant, M. E., (1945). Mechanics of the cutting process, *J. Appl. Phys.*, vol. 16, 318-324.
- Movahhedy, M. R., Altintas, Y. and Gadala, M. S., (2002). Numerical analysis of metal cutting with chamfered and blunt tools, *Journal of Manufacturing Science and Engineering*, vol. 124, 178-188.
- Rowe, G. W. and Spick, P. T., (1967). A new approach to determination of shear-plane angle in macining, *Journal of Engineering for Industry*, 89(3), 530-53
- Smithy, D. W., Kapoor, S. G., and DeVor, R. E., (2001). A new mechanistic model for predicting worn tool cutting forces, *Machining Science and Technology*, vol. 5, 23-42.
- Waldorf, D. J., DeVor, R. E. and Kapoor, S. G., (1998). A slip-line field for ploughing during orthogonal cutting, *Journal of Manufacturing Science and Engineering*, vol. 120, 693-699.
- Yellowley, I., (1987). A simple predictive model of orthogonal metal cutting, *International Journal of Machining Tools and Manufacturing*, vol. 27, no. 3, 357-365.
- Zhang, H. T., Liu, P. D. and Hu, R. S., (1991). A three-zone model and solution of shear angle in orthogonal machining, *Wear*, vol. 143, 29-43.

Drilling Carbon Fiber Reinforced Plastics with Diamond Coated Carbide Cutting Tools

Y. Karpat¹, N. Camuşcu², A. Kılıç³, F. Sonat³, B. Değer³, O. Bahtiyar³

¹ Bilkent University, Department of Industrial Engineering, Ankara, Turkey 06800

² TOBB University of Economics and Technology, Department of Mechanical Engineering, Ankara, Turkey 06560

³ Turkish Aerospace Industries Inc., Ankara, Turkey 06980

Abstract. Carbon fiber reinforced plastics (CFRP) have desirable properties such as high strength-to-weight ratio, high stiffness-to-weight ratio, high corrosion resistance, and low thermal expansion. Due to these properties, they are suitable for use as structural components in aerospace applications. Although components made from CFRP are produced near net shape, additional machining operations such as drilling, milling, and trimming are required to satisfy final design requirements. Machining CFRP laminates is quite difficult due to the extremely abrasive nature of the carbon fibers and low thermal conductivity of CFRP. For this reason advanced cutting tools such as diamond coated carbides and polycrystalline diamond cutting tools are usually employed during machining of CFRP laminates. It is a challenge for manufacturers to machine CFRP materials without causing any damage to the work part (e.g. delamination) while considering the economics of the process. The objective of this study is to investigate through an experimental approach the wear behavior of diamond coated carbide cutting tools during drilling of woven fabric type CFRP laminates as a function of operational parameters.

Keywords: Machining, Drilling, Carbon Fiber Reinforced Polymers

1. Introduction

Lightweight, durable, and corrosion resistant, carbon fiber reinforced plastics (CFRP) have been increasingly used in the aerospace industry to build more reliable and fuel efficient air vehicles. Although composite parts are manufactured near net shape, some additional machining operations such as drilling and milling may be required to meet final design specifications. Drilling is the most common machining process applied to composite laminates and is the subject of this study. While drilling CFRP laminates, cutting tools rapidly wear out due to the highly abrasive nature of the carbon fibers and the low thermal conductivity of CFRP. The heat generated during drilling is localized at the cutting tool edge, thereby causing rapid tool wear. Delamination is a crucial problem when drilling CFRP laminates, since it decreases the load carrying capability of the composites by separating the plies. Delamination is the most important

measure of quality of the drilled hole and is closely controlled during machining.

In the literature, studies on machining CFRP are limited compared with metals; however, the number of studies on machining CFRP laminates has significantly increased in recent years due to the increasing usage of this material in the aerospace industry. Koplev [1] conducted experimental studies on the orthogonal machining of unidirectional CFRP composites and reported the significance of fiber orientation on the chip formation mechanism. It was observed that the brittle fracture is the main cause of chip formation. Caprino et al. [2] also investigated the orthogonal machining of unidirectional CFRP and showed that tool forces are mainly due to the contact between work material and the flank face of the tool. Venu Gopala Rao et al. [3] developed two dimensional finite element models to simulate chip formation during machining of CFRP. They were able to show chip formation via finite element simulation, and their findings support the influence of brittle fracture during chip formation. Lasri et al. [4] also developed a finite element model and identified different modes of failure during chip formation. They calculated sub surface damage as a function of cutting conditions. Santiuste et al. [5] showed through a finite element model that CFRP composites experience less sub surface damage than glass fiber reinforced plastics under the same cutting conditions. Hocheng and Dharan [6] presented an analytical model to predict critical thrust force beyond which delamination occurs. Zhang et al. [7] also developed an analytical cutting model for the orthogonal machining of CFRP laminates to predict cutting forces. On the other hand, experimental studies have been pursued for better understanding of the relationships between process inputs such as machining parameters, tool geometry and process outputs such as cutting forces, torque, tool wear and drilled hole quality. In an extensive experimental study, Chen [8] conducted tests to reveal the relationship between machining parameters and

delamination. A linear relationship between thrust force and delamination when drilling uni-directional CFRP composite laminates was observed. In addition, multi directional CFRP laminates are found to be more favorable than unidirectional laminates in terms of delamination. It was observed that delamination increases with increasing flank wear. Tsao and Hocheng [9] reported the positive influence of using backup plates on delamination, allowing higher feed rates during drilling. Piquet et al. [10] analyzed the effects of drilling tool geometry on the hole quality without using a backup plate. They reported that it is necessary to pre-drill in order to neutralize the chisel edge effect, and the hole quality can be further improved by applying a variable feed rate while machining. Dharan and Won [11] proposed an intelligent control scheme based on an experimental model of the thrust force and torque as a function of cutting parameters. Delamination was detected through force calculations and sensor feedback and machining parameters were adjusted to obtain delamination-free holes. Tsao [12] used the Taguchi method to study the relationship between machining parameters and delamination. A small feed rate was shown to produce low thrust force, thereby decreasing delamination. Shyha et al. [13] investigated the effect of drill geometry and operating parameters when drilling small diameter holes. They found that drill geometry and feed rate are the two main factors affecting tool life. They found that an uncoated carbide stepped drill with 140° point angle yielded the best tool life performance. Rawat and Attia [14] utilized the “machinability maps” approach to select cutting conditions when drilling woven fabric composites. In their approach, delamination level, hole diameter error, hole circularity error, and surface roughness inside the hole were all considered as process outputs dependent on spindle speed and feed rate. They concluded that high cutting speeds lower the thrust force due to thermal softening. Faraz et al. [15] studied the wear behavior of uncoated and coated carbide cutting tools while machining fabric woven CFRP composite laminates under dry cutting conditions. They showed that when worn out, the cutting edge assumes a rounded shape that hinders its ability to cut the material effectively. They also observed a linear relationship between edge rounding and cutting forces. Recently, Iliescu et al. [16] proposed a tool wear model based on the thrust force and machining parameters for CFRP. They concluded that while carbide cutting tools represent tool wear behaviour according to power law, diamond coated cutting tools exhibit a linear relationship at the beginning but power law function at the end. They recommend using cutting tools having 125-130° point angle and diamond coating. They calculated optimum cutting speed for diamond coated cutting tools as 170 m/min and feed as 0.05 mm/rev. Literature reviews on machining composites given by Teti [17] and Abrao [18] emphasize the importance of developing better tool geometries and machining strategies.

In this study, diamond coated carbide tools are tested on fabric woven CFRP laminates through experimental analysis. The diamond coating is grown on the surface of the cutting tool through chemical vapor deposition methods where hydrogen and a gas containing carbon are mixed inside a chamber at very high temperatures. The thickness of the coating and size of diamond particles are shown to be important in terms of tool performance. Diamond coating can be applied to wide range of drill geometries; however, the coating thickness increases the cutting tool edge radius, which is not desirable when machining CFRP laminates.

2. Experimentation

Experimental studies were conducted on a Dörries Scharmann Technologies 5-axis precision machining center with maximum 24,000 rpm rotational speed. The CFRP material used in the study was epoxy impregnated graphite fabric that had 50% carbon fiber content and cured ply thickness of 0.33 mm. Its tensile strength is 520 MPa, elasticity modulus in tension is 52 GPa and density is 1.485 gr/cm³. The CFRP plate had a square shape with edge dimensions of 920 mm and thickness of 10 mm. The test setup is shown in Fig 1. A plate made out of aluminum was used as a backing plate. The thrust force and torque during drilling were measured by a Kistler 9123 rotating dynamometer and its charge amplifier. The cutting force data were collected through a data acquisition system and processed on a personal computer. Diamond coated carbide (Seco Tools) tools having 6.35 mm diameter were used in the experiments.

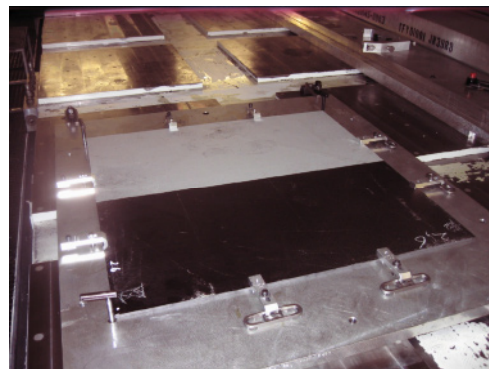


Fig. 1. Test setup

Diamond coated carbide (DCC) cutting tools employed in this study have diamond coating thickness of 10 µm and twist drill geometry with double point angle of 128 and 152°. The tool profile of DCC cutting tools is shown in Fig. 2.

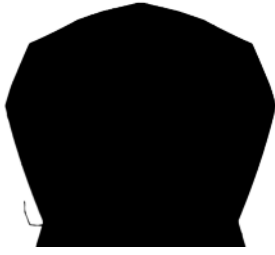


Fig. 2. Tool profile of diamond coated carbide cutting tool

The experimental cutting conditions used in this study are listed in Table 1. The cutting speed and feed levels were selected so that a wide range of cutting conditions were covered during the experiments. All experiments were conducted under wet machining conditions.

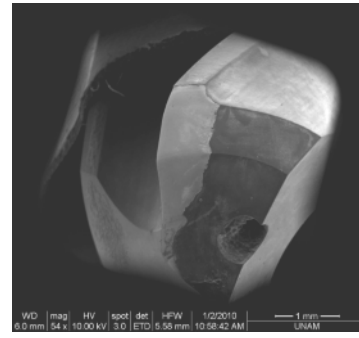
Table 1. Experimental test conditions

Exp.	N (rpm)	f ($\mu\text{m}/\text{rev}$)	f_r (mm/min)
1	15,000	75	1125
2	15,000	225	3375
3	5,000	225	1125
4	5,000	75	375

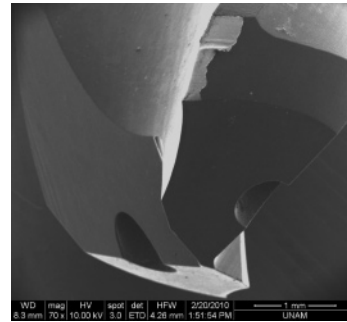
3. Results

The experiments were conducted based on the number of drilled holes. The experiments were stopped after drilling a certain number of holes and the resulting tool wear and hole quality were observed.

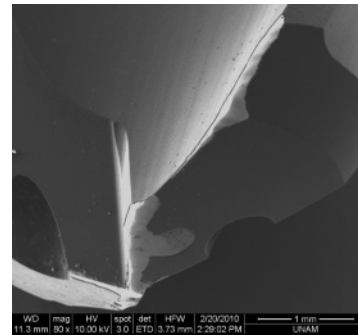
Diamond coatings on carbide tools are known to have difficulty in adhering to the carbide substrate. Fig 3 reveals the wear zone at the flank face of the tool after drilling 1728 holes for each experimental case, and the same problem was observed in all of them. Fracture of the diamond coating is more severe on the flank face than the rake face of the tool. The smallest fracture area on the diamond coating was observed at experimental case #2 where a large feed rate was taken (Fig 3b) at high cutting speed. This experimental case also corresponds to the shortest duration of cut. Experimental case #4 with the lowest feed rate yielded the worst experimental performance in terms of diamond coating fracture zone area and resulted in delamination problems at the exit of the hole due to excessive edge rounding and ineffective cutting performance. Even though diamond coatings were significantly fractured, for experimental cases # 1 and 2 there was no significant delamination at the exit of the holes. This is probably due to the edge radius of the carbide substrate, which is still intact. Fig 4 shows pictures of the drilled holes and Fig 5 reveals the detailed SEM picture of the fracture zone on the cutting tool used in Exp #4. The length of the fracture is about 1 mm.



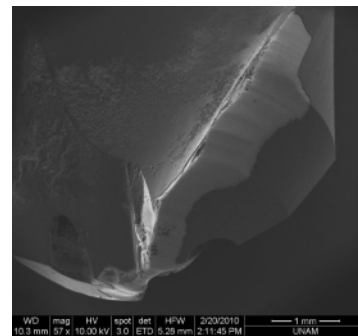
a



b



c



d

Fig. 3. SEM images of the flank face of DCC cutting tools
 a) N=15000 rpm, $f=75 \mu\text{m}/\text{rev}$, b) N=15000 rpm, $f=225 \mu\text{m}/\text{rev}$,
 c) N=5000 rpm, $f=225 \mu\text{m}/\text{rev}$, d) N=5000 rpm, $f=75 \mu\text{m}/\text{rev}$

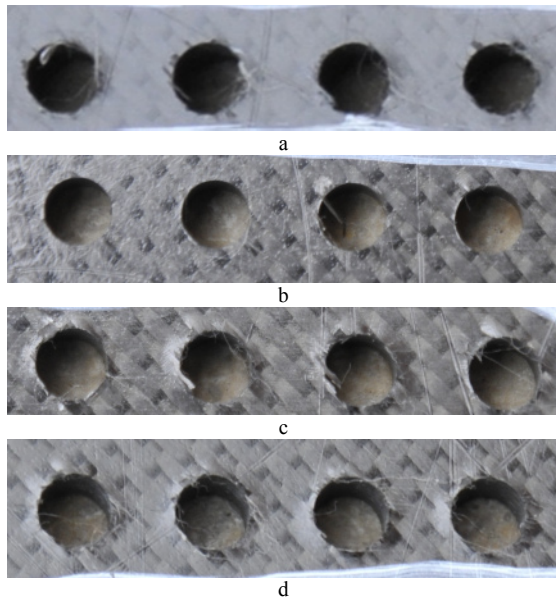


Fig. 4. Photos of the exit of the drilled holes, a) Experimental case #1, b) Experimental case #2, c) Experimental case #3, d) Experimental case #4

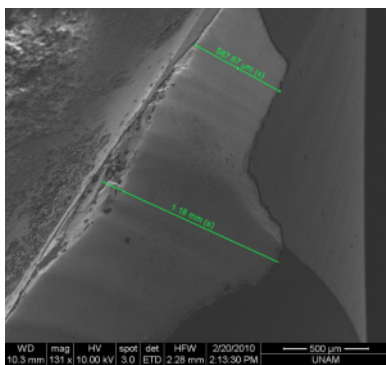


Fig. 5. Detailed view of the fracture zone of the cutting tool used in Experiment #4

4. Conclusions

In this study, drilling of CFRP laminates was studied and the wear and fracture behaviour of diamond coated cutting tools was observed. It is found that a high feed rate results in less damage on the diamond coating after drilling equal number of holes due to short cutting time. The fracture on the diamond coating initiates from two locations: the edge of the clearance face of the tool at the end of the cutting edge at high feeds and from the tip of the tool at low feeds. The fracture then expands away from these points. As a result, the edge of the carbide substrate is exposed and rounded which hinders its performance.

Acknowledgement

The authors would like to thank Scientific and Technical Research Council of Turkey (TUBITAK) for their financial support of this study.

References

- [1] Koplev A, Lystrup A, Vorm T, (1983) The cutting process, chips and cutting forces in machining CFRP, *Composites* (14):371-376
- [2] Caprino G, Santo L, Nele L, (1998) Interpretation of size effect in orthogonal machining of composite materials. Part I: Unidirectional glass fibre reinforced plastics, *Composites Part A*, 29A: 887-892
- [3] Venu Gopala Rao G, Mahajan P, Bhatnagar (2007) Machining of UD-GFRP composites chip formation mechanism, *Composite Science and Tech.* (67):2271-2281
- [4] Lasri L, Nouari M, El Mansori M, (2009) Modeling of chip separation in machining unidirectional FRP composites by stiffness degradation concept, *Composite Science and Tech.* (69):684-692
- [5] Santiuste C, Soldani X, Miguelez MH, (2010) Machining FEM model of long fiber composites for aeronautical components. *Composite Structures.* (92):691-698
- [6] Hocheng H, Dharan CHK, (1990) Delamination during drilling in composite laminates, *J. Eng. Ind.* (112):236-239
- [7] Zhang LB, Wang LJ, Liu XY, (2001) A mechanical model for predicting critical thrust forces in drilling composite laminates, *Proc. Inst. Mech. Eng.* (215):398-405
- [8] Chen WC, (1997) Some experimental investigations in the drilling of carbon fiber reinforced plastic (CFRP) composite laminates. *Int. J. Mach. Tools Manufact.* 37:1097-1108
- [9] Tsao CC, Hocheng H, (2007), Parametric study on thrust force of core drill, *Journal of Mater. Processing* 192:37-40.
- [10] Piquet R, Ferret B, Lachaud F, Swider P, (2000) Experimental analysis of drilling damage in thin carbon/epoxy plate using special drills. *Composites Part A* 31:1107-1115
- [11] Dharan CKH, Won MS, (2000) Machining parameters for an intelligent machining system for composite laminates. *Int. J. Mach. Tools Manufact.* 40:415-426
- [12] Tsao CC, (2008) Thrust force and delamination of core saw drill during drilling of carbon fiber reinforced plastics (CFRP), *Int J Adv Manuf Technol*, 37:23-2
- [13] Shyha IS, Aspinwall DK, Soo SL, Bradley S, (2009) Drill geometry and operating effects when cutting small diameter holes in CFRP, *Int. J. Mach. Tools Manufact.* (49):1008-1014
- [14] Rawat S, Attia H, (2009) Characterization of the dry high speed drilling process of woven composites using Machinability Maps approach. *CIRP Annals- Manufacturing Tech.* (58):105-108
- [15] Faraz A, Biermann D, Weinert K, (2009) Cutting edge rounding: An innovative tool wear criterion in drilling CFRP composite laminates. *Int. J. Mach. Tools Manufact.* (49):1185-1196
- [16] Iliescu D, Gehin D, Gutierrez ME, Girot F, (2010) Modeling and tool wear in drilling of CFRP. *Int. J. Mach. Tools Manufact.* 50:204-213
- [17] Teti R, (2002) Machining of composite materials, *CIRP Annals, Manufacturing Technology* 51:611-634.
- [18] Abrao AM, Faria PE, Campos Rubio JC, Reis P, Davim P, (2007) Drilling of fiber reinforced plastics: A review. *Jour. Materials Processing Tech.* (186):1-7

Research on 3D Groove for Cutting Heat Distribution of Coated Carbide Milling Inserts

Y. He¹, C. J. Li², J. H. Zhou³

¹ East China University of Science and Technology, Shanghai, China, 200237, hy121@ecust.edu.cn

² East China University of Science and Technology, Shanghai, China, 200237, baker-li@hotmail.com

³ East China University of Science and Technology, Shanghai, China, 200237, zhoujhjane@126.com

Abstract. Coated carbide milling inserts are very widely used in modern metal cutting. Affected by interaction such as thermo-mechanical coupling, the cutting process of coated carbide milling inserts with 3D groove is rather complicated. In this paper, a measurement system of transient cutting temperature is developed by both non-contacting and contacting methods. Based on the comparative cutting experiment of three coated carbide inserts with different shapes of 3D grooves, the influence of the shape of the 3D grooves on cutting temperature is analyzed. The distribution of cutting heat ratio among chips, workpiece and insert is quantitatively determined through the method that combines conduction model and the experimental data. The results show that the distribution of cutting temperature and heat can be improved by proper design of the 3D groove and the cutting deterioration can be lowered.

Key words: Coated carbide milling inserts, 3D groove, Cutting heat distribution

1. Introduction

Coated carbide milling inserts are very widely used in modern metal cutting. Affected by interactions such as thermo-mechanical coupling, the cutting process of coated carbide milling inserts with 3D grooves are rather complicated. Cutting temperature is the major subject of interest in the metal cutting process as the heat generated has a great influence on the life time and surface integrity of the tool [1]. Schmidt and Roubik [2] showed quantitatively for the first time that much of the heat generated in cutting was carried out by the chips (~70%-80%) with 10% entering the workpiece, and the remainder going into the tool. Malkin [3] conducted a similar calorimetric study of the grinding process and showed that the major part of the heat generated in grinding is conducted into the workpiece (~80%) and only a small fraction is carried away by the chips and the abrasive grains of the grinding wheel. Research results by Stephenson and Ali [4] on intermittent cutting has shown that temperature depends primarily on the cutting

time and non-cutting time for each cut. In the past few years, several methods have been developed for the measurement of temperature in manufacturing processes, such as thermocouples, infrared radiation (IR), metallographic methods, FEM etc. Kusters determined the entire temperature field with more than 400 thermocouples [5]. Wang et al. [6] used the IR method to study the temperature effects in curled chip formation when cutting a low carbon steel. Recent research concerning heat partition was conducted by Akbar et al. [7].

The temperature distribution can provide critical data and reference for research of insert damage and groove optimization. Previous research focused mostly on the temperature of rake face and tool-chip interface. However, to the best of our knowledge, the influence of the groove on the temperature and heat distribution of the tool, workpiece and chips has not yet been studied. In this paper, milling experiments were carried out to study quantitatively the cutting forces and temperature distribution among the chips, workpiece and tool for the three types of inserts with different groove shape.

2. Experiments

2.1 Milling inserts and workpiece

Three different types of coated carbide milling inserts are chosen for the experiments (see Fig. 1). Inserts B and C have 3D grooves while A has not. Inserts A and C are TiN coated with PVD. Insert B is also coated with PVD. Table 1 shows the geometric parameters of the three types of milling inserts shown in Fig. 1.

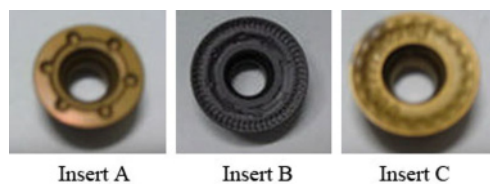


Fig. 1. Three types of milling inserts

Table 1. Geometric parameters of the three types of milling inserts shown in Fig. 1

Insert	Rake angle	Insert diameter(mm)
A	0°	12.00
B	11°	15.87
C	9°	12.00

The workpiece is an AISI 1045 steel block with a length of 150 mm, height of 50 mm and width of 50 mm (see Fig. 3). The workpiece material has a hardness value of 30 HRC.

2.2 Experimental equipments

A transient temperature measurement system was set up (see Fig. 2). The surface temperature of tools and chips are measured using a Thermo Tracer TH7102WX infrared thermal imager. Workpiece temperature is measured using copper–constantan thermocouples. The experimental voltage data is collected using an AgilentTM34970A dynamic data acquisition system.

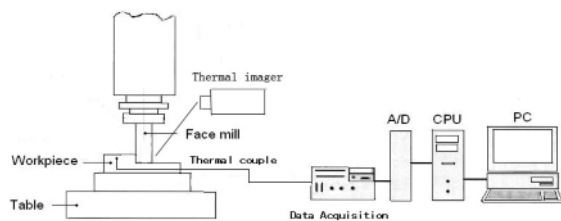


Fig. 2. Schematic drawing of milling temperature measurement system

Fig. 3 shows the arrangement of nine thermocouples embedded in the workpiece. The cutting forces were measured using a KistlerTM9227 dynamometer. Fig. 4 shows the experimental process.

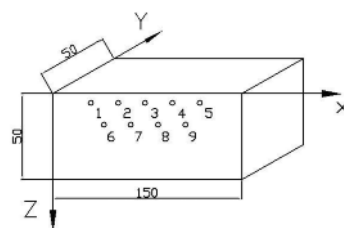


Fig. 3. Arrangement of thermocouples embedded in the workpiece

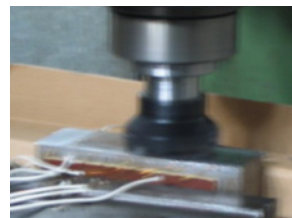


Fig. 4. Experimental process

2.3 Experimental method

The cutting tests are carried out on a XK6325B/6 NC milling machine. To better understand the differences between the three types of inserts, only one insert is mounted on the cutting body during each test. The cutting parameters are as follows: cutting speed V_c is 80m/min, feed rate f_z is 0.12 mm/rev, cutting depth a_p is 1mm, cutting width a_e is 50 mm.

3. Results and analyses

3.1 Calculation of total cutting heat

For each type of the insert, five groups of steady cutting force data are collected. We calculate the total work W according to the work per cut.

Total work is expressed as:

$$W = \frac{l}{f_z} \sum_{i=1}^n F_{ci} \cdot V_c \cdot t = \sum_{i=1}^n (F_x \cdot \cos\psi_i + F_y \cdot \sin\psi_i) V_c \cdot t \quad (1)$$

where F_x and F_y are cutting forces measured by dynamometer, ψ_i is the contact angle (between F_c and F_x), V_c is cutting speed, l is cutting length, n is sampling number per cut and t is sampling period.

Total work W is equal to the total cutting heat generated in the cutting process, that is to say, the total heat Q conducted to workpiece, tool, chips and air.

3.2 Calculation of cutting heat conducted to chips

The temperature of a chip surface is measured using an infrared thermal imager and then the average rise of temperature Δt obtained. It is assumed that the initial

temperature of the chips is equals to the room temperature and the workpiece material density, specific heat capacity and emissivity are constant, no heavy oxide layer is formed during the cutting [8]. Workpiece emissivity is 0.12 [9]. The cutting heat conducted to chips Q_c can be calculated using the following equation:

$$Q_c = m \times c \times \Delta t \quad (2)$$

where m is the weight of the chips, c is specific heat capacity (J/kgK), Δt is the difference between the maximum temperature of the chips in the cutting area and the initial temperature of the chips.

3.3 Calculation of cutting heat conducted to the workpiece

Heat source method is an effective way to determine the heat conduction and distribution. We regard the insert as a line heat source [10] which conveys the temperature into the workpiece. In this experiment, cutting time is only 0.035 s per cut. We use the moving heat source model equation (1.3) which is usually used in vertical milling to calculate the heat conducted to the workpiece:

$$\theta = \frac{q_2}{2\pi\lambda} \exp\left(-\frac{xv}{2a}\right) \int_0^\infty \frac{dw}{w} \exp\left(-w - \frac{u^2}{4w}\right) \quad (3)$$

where θ is workpiece temperature, v is the speed of moving heat source, q_2 is the density of heat source (J/ms), λ is the thermal conductivity (W/mK), a is the thermal diffusivity(m²/s), $w = \frac{v^2}{4a}$ and $u = \frac{v}{2a} \sqrt{x^2 + z^2}$. x and z are the coordinates of thermocouples embedded in the workpiece.

The rise of the steady temperature is collected to calculate the heat source density q_2 . The cutting heat conducted to workpiece Q_w is calculated with the following equation:

$$Q_w = q_2 t l \quad (4)$$

where t is the total cutting time and l is the length of heat source.

3.4 Calculation of cutting heat distribution

In dry cutting, the cutting heat conducted to other medium can be omitted as it is less than 1% [11]. We get the cutting heat distribution among the workpiece(Q_w), tool(Q_t), chips(Q_c) and air(Q_a). (see Table 2).

Table 2. The calculated cutting heat distribution

Insert	Q (J)	Q_c (J)	Q_w (J)	Q_t (J)
A	27329.9	18852.9	4606.7	3870.3
B	19932.6	15734.7	3021.6	1176.3
C	18247.1	13121.8	3747.6	1377.7

Fig. 5 shows the heat distribution ratio among chips, workpiece and tool.

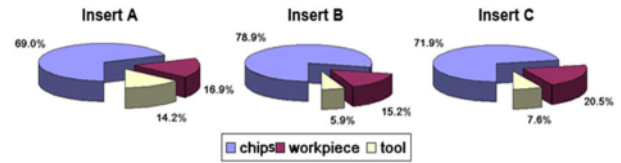


Fig. 5. Heat distribution ratio among chips, workpiece and tool

For the three types of the inserts, the majority of the cutting heat is conducted to the chips and the heat conducted to the workpiece is usually more than it conducted to the tool. Insert B and C with 3D grooves generate less heat than the insert A and chips produced by insert B and C usually take more heat away. The reason can be expressed as follows: first of all, insert B and C both have a positive rake angle, which generates less elastic and plastic deformation; second, 3D grooves can reduce the contact area between chips and rake face, thereby reducing adhesion friction; third, Plastic deformation happens continuously when chips slide on the 3D groove, which enlarges the shear zone. The insert B has the most complex 3D grooves and has the largest shear zone.

3.5 Workpiece temperature measured with thermocouples

Fig. 6 shows the workpiece temperature measured by thermocouples. At the beginning of the milling process (30~55 s), temperature rises quickly for all the three types of inserts. When in the steady state of the milling process (75~95 s), temperature of the insert A keeps rising, while temperature of the insert C falls quickly temperature of the insert B keeps constant at about 35 °C. As we can see, 3D groove of insert B is more complex than that of insert C. For insert B, more heat is conducted to chips than workpiece.

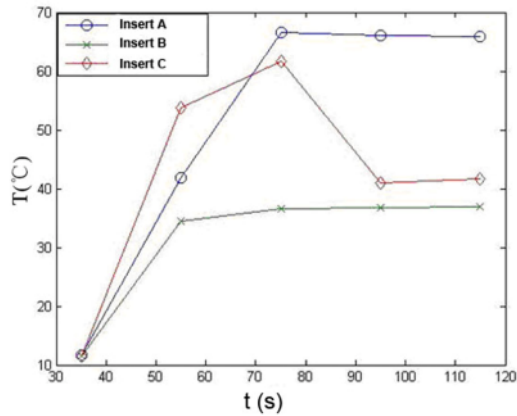


Fig. 6. Workpiece temperature measured by thermocouples (Thermocouples No.1~5, 1.5 mm below the milling surface)

4. Conclusion

In conclusion, we can see that the most significant part of the cutting heat is conducted into the chips and 3D grooves can be used to increase the percentage of the heat carried away by the chips and reduce the cutting temperature as they can reduce the contact area between chips and rake face of milling insert, thus reducing the adhesion friction. The more complex the grooves are, the more cutting heat the chips take away. Meanwhile, the cutting deterioration can be lowered.

References

- [1] M.B. Silva, J. Wallbank, Cutting temperature: prediction and measurement methods— a review, *J.Mater. Process. Technol.* 88 (1–3) (1999) 195–202
- [2] A.O. Schmidt and J.R. Roubik, *Distribution of Heat Generated in Drilling*, Transaction of the ASME 71 (1949)
- [3] S. Malkin, and C. Guo, *Grinding technology: theory and applications of machining with abrasives*, Industrial Press, NY, USA, 2008
- [4] D.A. Stephenson, A. Ali, Tool temperatures in interrupted metal cutting, *J. Eng. Ind. Trans. ASME* 114 (2) (1992) 127–136
- [5] R. Komanduri, Z.B Hou, A review of the experimental techniques for the measurement of heat and temperatures generated in some manufacturing processes and tribology. *Tribology International* 34 (2001) 653–682
- [6] L. Wang, K. Saito, I.S. Jawahir, Infrared temperature measurement of curled chip formation in metal machining, in: *Proceedings of the Transactions of the North American Manufacturing Research Institution of SME, North American Manufacturing Research Conference (NAMRC XXIV)*, Ann Arbor, MI, USA, 1996. 87-92
- [7] F. Akbar, P.T. Mativenga, and M.A. Sheikh, On the heat partition properties of (Ti, Al)N compared with TiN coating in high-speed machining, *Proceedings of the Institution of Mechanical Engineers, Part B: Journal of Engineering Manufacture*, 223, 363-375, 2009
- [8] P.J. Arrazola, I. Arriola a,b, M.A. Davies c, A.L. Cooke c, B.S. Duttererc. The effect of machinability on thermal fields in orthogonal cutting of AISI 4140 steel. *CIRP Annals*.55 (2008)65~68
- [9] M. Kutz, *Heat Transfer Calculations*, McGraw-Hill Professional, NY, USA, 2005
- [10] Z.B. Hou, S.J He, S.X Li et al., *Thermal conduction of solid*, Shanghai: Shanghai Science and Technology Press, 1984. 66-89(in Chinese)
- [11] Z.D Cai, *Metal cutting principle*, Tongji University Press, 1993 (in Chinese)

In-Process Monitoring and Prediction of Surface Roughness on CNC Turning by using Response Surface Analysis

Somkiat, T.,¹ Somchart, A.,² and Sirichan, T.³

Department of Industrial Engineering, Faculty of Engineering, Chulalongkorn University, Phayathai Road, Pathumwan Bangkok 10330, THAILAND (Email:Somkiat.ta@chula.ac.th¹,Somchart_a@hotmail.com²,Sirichan.t@chula.ac.th³)

Abstract. This paper presents a model developed for the prediction of surface roughness based on in-process monitoring of turning of plain carbon steel (S45C) with the coated carbide tool under various cutting conditions. It uses a response surface analysis with the Box-Behnken design based on the experimental results. The in-process cutting force and cutting temperature are measured to analyze their relationship with the surface roughness and the cutting conditions. A tool dynamometer and an infrared pyrometer were employed and installed on the turret of CNC turning machine to measure the in-process cutting forces and cutting temperatures. Models of cutting force ratio and cutting temperature were developed based on the experimental data. The optimum cutting condition is determined referring to the minimum surface roughness of the response surface plot, which is obtained from the surface roughness model. The experimental results show that the cutting temperature increases with an increase in cutting speed. The higher cutting speed gives the better surface roughness. The feed rate is the most significant factor which affects the surface roughness, while a small depth of cut helps to improve the surface roughness. The effectiveness of the surface roughness prediction model has been proved by utilizing an analysis of variance (ANOVA) at 95% confidence level. The minimum surface roughness can be obtained with the optimum cutting conditions from the surface roughness model developed.

Keywords: CNC Turning, Box-Behnken design, Surface roughness, Infrared pyrometer, Cutting force

1. Introduction

Steels such as S45C are most popularly used for mechanical parts. Turning is one of the important cutting processes, which is used to cut these materials in order to obtain the required geometrical shapes.

However, surface roughness cannot be measured while cutting, and, the same time, there are many factors which affect the surface roughness of the machined parts.

It is known that the cutting conditions such as the feed rate, the cutting speed and the depth of cut affect the surface roughness [1]. It is desirable to know the relations of them and the surface roughness. Hence, these cutting

parameters are included in the model to predict the surface roughness.

It is already known that a force sensor is able to generate a signal corresponding to the surface roughness [2]. The feed force is most sensitive to the surface roughness while the main force is affected by the cutting conditions. The main force and the feed force are adopted to examine the surface roughness during the cutting. This involves normalizing and making the cutting forces dimensionless by taking the ratio of the corresponding time records of the feed force F_y to the main force F_z . The cutting force ratio (F_y/F_z) is the important factor to analyze the in-process surface roughness even though the cutting conditions are changed.

The aim of this research is to develop a model for the prediction of surface roughness based on experimental data by using the response surface analysis with the Box-Behnken design in order to determine the optimum cutting conditions to obtain the minimum surface roughness [3-5]. A model using the cutting force ratio and cutting temperature has been developed based on the experimental data in order to check the relations of the cutting conditions and the surface roughness.

2. In-process monitoring of cutting forces and cutting temperatures

The in-process monitoring of cutting forces is used to examine the effects of the cutting conditions on the surface roughness. The in-process cutting forces are monitored during the cutting by employing a dynamometer.

An infrared pyrometer is used to measure the in-process cutting temperature during the cutting. The in-process cutting temperature and cutting forces are then utilized to build a model relating the in-process cutting force, cutting temperature and surface roughness together with the cutting conditions.

3. Models of surface roughness, cutting force ratio and cutting temperature

The second-order response model is normally used when the response function is not known or nonlinear [3-5]. Hence, the functional relations between the responses, which are the surface roughness (R_a), the cutting force ratio (F_y/F_z), and the cutting temperature (T), in the turning process and the investigated independent variables, which are the cutting speed (v), the feed rate (f), and the depth of cut (d) can be represented by the following equations :

$$R_a = \beta_0 + \beta_1(v) + \beta_2(f) + \beta_3(d) + \beta_4(v^2) + \beta_5(f^2) + \beta_6(d^2) + \beta_7(vf) + \beta_8(vd) + \beta_9(fd) \quad (1.1)$$

$$T = \beta_{10} + \beta_{11}(v) + \beta_{12}(f) + \beta_{13}(d) + \beta_{14}(v^2) + \beta_{15}(f^2) + \beta_{16}(d^2) + \beta_{17}(vf) + \beta_{18}(vd) + \beta_{19}(fd) \quad (1.2)$$

$$F_y/F_z = \beta_{20} + \beta_{21}(v) + \beta_{22}(f) + \beta_{23}(d) + \beta_{24}(v^2) + \beta_{25}(f^2) + \beta_{26}(d^2) + \beta_{27}(vf) + \beta_{28}(vd) + \beta_{29}(fd) \quad (1.3)$$

The values of β coefficients used in these equations can be obtained by using the Box-Behnken technique. The analysis of variance (ANOVA) is utilized to prove the effect of the cutting parameters at 95% confident level.

4. Experimental cutting conditions and procedures

A series of cutting experiments were carried out in order to obtain the values of β coefficients in the equations (1.1) to (1.3). The cutting tests were conducted on a commercially available small CNC turning machine as shown in Figure 1. The tool dynamometer and the infrared pyrometer are shown installed on the turret of CNC turning machine in order to measure the in-process cutting force and the in-process cutting temperature, respectively.

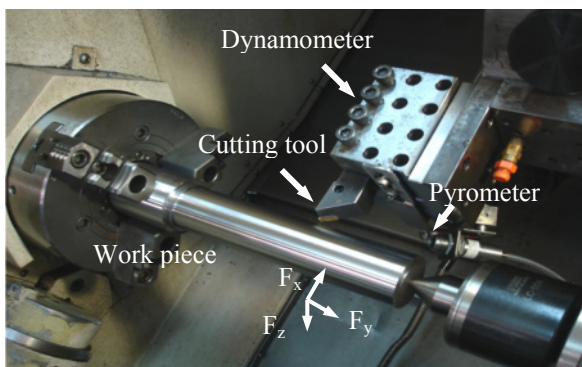


Fig. 1. Illustration of experimental setup

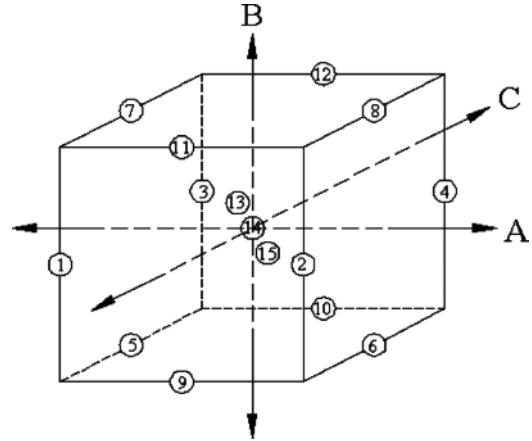


Fig. 2. Box-Behnken design for three variables

Plain carbon steel (S45C) was adopted in the cutting experiments and the cutting tool was coated carbide KC9110 [6].

The design of experiments (DOE) has an effect on the number of experiments required. Hence, the Box-Behnken design consisting of 15 experiments was used in the experiments for the three variables as shown in Figure 2. The Box-Behnken design provides three levels which are low, center, and high for each independent variable as shown in Table 1

Table 1 Levels of independent variables of the cutting condition parameters

Levels	Coding	Cutting speed, v (m/min)	Feed rate, f (mm/rev)	Depth of cut, d (mm)
Low	-1	150	0.15	0.50
Center	0	250	0.175	0.75
High	+1	350	0.20	1.00

5. Experimental results and discussion

5.1 Response Surface Analysis

According to the experimentally obtained results, the second-order response model representing the surface roughness (R_a) can be expressed by the following equation:

$$R_a = 10.304 - 0.013v - 147.417f + 8.036d - 0.000016v^2 + 525.4f^2 - 1.697d^2 + 0.1253vf + 0.0022vd - 33.056fd \quad (1.4)$$

By following in the same manner, the second-order response functions of the cutting temperature and the cutting force ratio can be expressed by the following equations:

$$T = -3.21875 + 0.2075v + 3640f + 278d - 0.000113v^2 - 7400f^2 - 174d^2 - 0.90vf + 0.18vd - 480fd \quad (1.5)$$

$$(F_y/F_z) = 3.371 - 0.00383v - 22.652f + 0.6935d + 0.000031v^2 + 47.27f^2 + 0.2498d^2 + 0.01199vf + 0.000166vd + 2.2616fd \quad (1.6)$$

Table 2 ANOVA table for the second-order response function of the surface roughness

Source	DF	Seq SS	Adj MS	F	P
Regression	9	11.0021	11.0021	26.13	0.001
Residual Error	5	0.2340	0.2340		
Lack of fit	3	0.2053	0.2053	4.77	0.178

The results of ANOVA for the second-order response function of the surface roughness is shown in Table 2. The P-value is less than 0.05, and hence the surface roughness model developed is quite adequate. It is understood that the cutting speed, the feed rate, and the depth of cut have the most significant effect on the surface roughness. Moreover, the lack of fit test is 0.178 which means that there is no lack of fit according to the significant level of 95%.

Figure 3 shows the response surface plot of the predicted surface roughness (R_a) as a function of the cutting speed and the feed rate at the depth of cut of 0.5 mm from equation (1.4). The figure clearly shows that the surface roughness increases mainly with an increase in the feed rate.

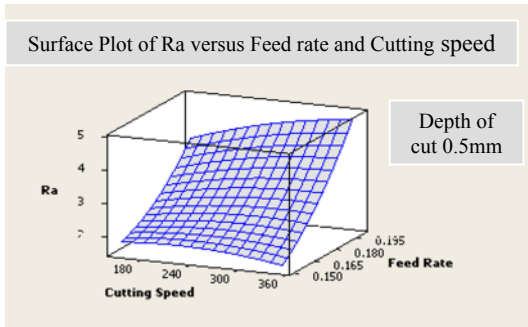


Fig. 3. Surface plot of predicted surface roughness versus cutting speed and feed rate at the depth of cut of 0.5 mm

A response optimization was performed to check the optimum cutting condition for the minimum surface roughness as shown in Figure 4. The surface roughness decreases while the cutting speed increases. The minimum surface roughness can be obtained at the high level of the cutting speed, and at the low levels of the feed rate and the depth of cut respectively. Referring to the minimum surface roughness, the experimentally obtained optimum cutting

condition is the cutting speed of 350 m/min at the feed rate of 0.15 mm/rev, and the depth of cut of 0.5 mm.

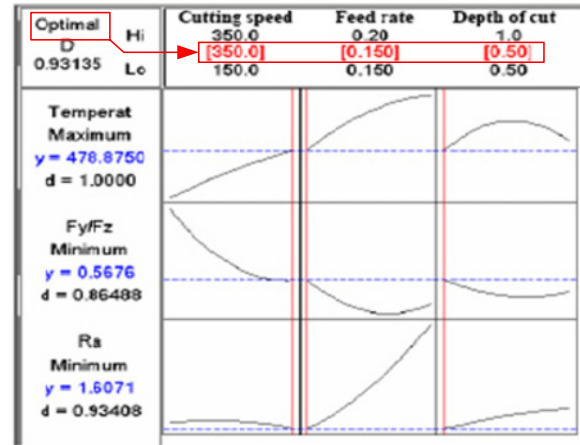


Fig. 4. The optimization chart for minimum surface roughness for cutting plain carbon steel by using a coated carbide tool

A better surface roughness is obtained when the cutting speed is high enough to avoid the built-up edge [2]. The other reason is the work material becomes softer and easy to cut due to the higher cutting temperature which leads to a low cutting force ratio at the greater cutting speed as shown in Figure 4.

An increase in the feed rate results in an increment of the surface roughness which corresponds to the theoretical surface roughness as shown in Figure 4.

The better surface finish is obtained at the small depth of cut of 0.5 mm as shown in Figure 4. The larger depth of cut causes the higher cutting force which results in the higher surface roughness. It is concluded that the surface roughness can be improved by cutting with the small depth of cut.

5.2 Verification of the models

Additional cutting tests were conducted in order to verify the optimum cutting condition and the models of the surface roughness prediction, the cutting force ratio and the cutting temperature.

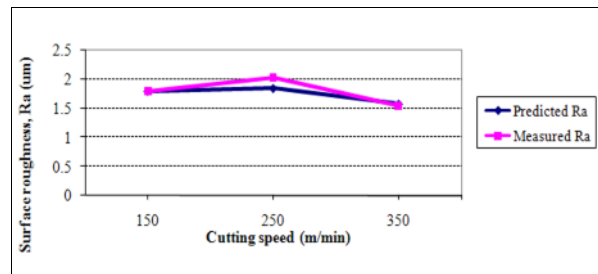


Fig. 5. Illustration of the measured R_a and the predicted R_a

Figure 5 shows that the experimentally measured surface roughness is close to the surface roughness predicted obtained from equation (1.4). It is concluded that the surface roughness model developed can be effectively used to predict the surface roughness under various cutting conditions.

Figure 6 shows the experimentally measured cutting temperature and the predicted temperature obtained from equation (1.5). It is implied that the experimentally obtained model of the cutting temperature can be used to estimate the in-process cutting temperature, cutting force and surface roughness even though the cutting conditions are changed.

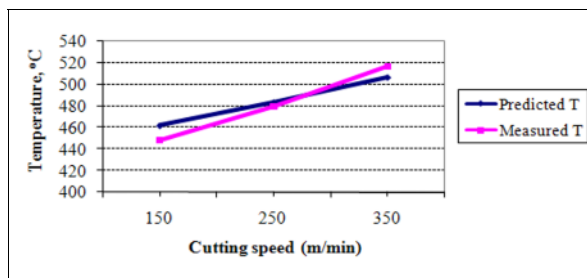


Fig. 6. Illustration of the measured T and the predicted T

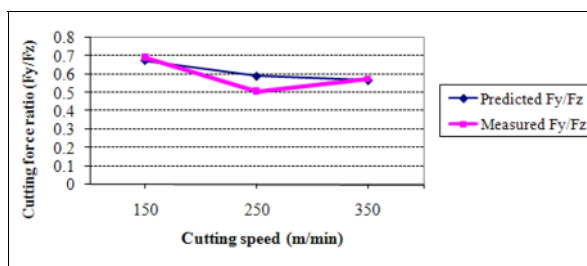


Fig. 7. Illustration of the measured F_y/F_z and the predicted F_y/F_z

The experimentally measured cutting force ratio is fitted to the predicted cutting force ratio as shown in Figure 7. It is seen that the cutting force ratio decreases while the cutting speed increases as the cutting speed directly affects the cutting temperature as shown in Figure 6.

According to Figures 5 to 7, the relations of surface roughness, the cutting temperature, and cutting force ratio show the same trend while the cutting speed increases. It can be stated that the cutting force ratio can be used to estimate the surface roughness during the cutting. The phenomena of the cutting force ratio and the surface roughness correspond with the cutting temperature.

6. Conclusions

In-process monitoring has been used to measure the cutting temperature and the cutting force by employing the infrared pyrometer and the tool dynamometer

respectively in order to examine and analyze their effect on the surface roughness under various cutting conditions during the cutting.

The resulting surface analysis with the Box-behnken design was utilized to develop a model to predict the surface roughness represented by the second-order response function. The experimentally obtained results clearly show that the feed rate is the most significant factor affecting the surface roughness, followed by the cutting speed. It has been proved that the surface roughness prediction model developed can be effectively used to predict the surface roughness with the 95% confidence level.

The relations of the surface roughness, the cutting temperature, and the cutting force ratio show the same trend. The effects of cutting conditions on the surface roughness can be well explained by the in-process cutting force and cutting temperature. It is concluded that the cutting force ratio can be used to predict the in-process surface roughness during the cutting. The in-process monitoring of cutting temperature is useful to analyze the in-process cutting force ratio and surface roughness.

The experimentally determined optimum cutting condition is a cutting speed of 350 m/min, at a feed rate of 0.15 mm/rev, and a depth of cut of 0.5 mm.

Acknowledgement

This work was supported by The Thailand Research Fund (TRF) from March 2009 to March 2011.

References

- [1] Somkiat T, (2009) In-process investigation of turning process applied with and without cutting fluid: *Journal of mechanical engineering*. 6: 85-102
- [2] Moriwaki T, Shibasaki T, Somkiat T (2004) Development of in-process tool wear monitoring system for CNC turning: *International Journal of Japan Society of Mechanical Engineers. Series C* 47(3): 933-938
- [3] Box GEP, Behnken DW, (1960) Some new three level designs for the study of quantitative variables: *Technometrics*. 2(4): 455-475
- [4] Raviraj S, Raghuvir P, Srikanth SR, Vasanth K, (2008) Machinability study on discontinuously reinforced aluminium composites (DRACs) using response surface methodology and Taguchi's design of experiments under dry cutting condition: *Mj.Int.J.Sci.Tech*. 2(01): 227-239
- [5] Elmagrabi NH, Che Haron CH, Jaharah A, Ghani Gusri AI, Yasir MS, Yanur B, (2008) Dry machining of titanium alloys and its impact on the environment and tool life: *International Conference on Environmental Research and Technology*. 773-777
- [6] Kennametal Inc. (2004) *Lathe tooling Catalog*. A54-A55

Influence of Edge Beveling on Burr Formation in Face Milling of an Aluminium Alloy

Partha Pratim Saha¹ and Santanu Das^{2*}

¹ Eastern Railway Workshop, Kanchrapara- 743 145, India, partha_kpa@rediffmail.com.

² Department of Mechanical Engineering, Kalyani Government Engineering College, Kalyani- 741 235, India.

* Email: sdas_me@rediffmail.com.

Abstract. A burr is a plastically deformed and projected material usually adhering to the exit end of a machined surface. The exit burr generated in face milling operations at the edge of a workpiece requires a deburring process to overcome potential difficulties in assembly, problems in surface texture and injury to the operator. If a suitable strategy is used to minimize the burr formation, then the time and cost involved in a deburring operation would be saved to a large extent. In railways and other industries, deburring of milled surfaces is a problem. This paper reports an investigation to solve the problem by beveling exit edges of the workpiece. Experiments have been performed on aluminium alloy blocks (alloy 4600-A,M) to find out the effect on exit burr formation of cutting conditions and different exit edge bevel angles. Results of the experimental investigation in vertical milling of workpieces with 120° in-plane exit angle under dry condition are presented in this paper. It is found that an exit edge bevel angle of 15° provided leads to negligible burrs at all machining conditions.

Keywords: Face milling, Burr formation, Edge beveling, In-plane exit angle

1. Introduction

In machining processes, undesirable projections of material beyond the edge of a workpiece, known as burrs, are created due to plastic deformation. The presence of burrs in a precision component causes difficulties in assembly of machined components. To obtain a component free from burrs, deburring processes are traditionally employed involving additional cost. Gillespie [1] found that cost of deburring and edge finishing may constitute as much as 30% of the total cost of precision components, and the additional processes can be a source of significant dimensional errors. Hence, if formation of burrs during machining can be minimized or prevented by some means, there would be great benefit to industry. In the past, several attempts have been made to understand the mechanism of burr formation and to find measures to minimize it.

Pekelharing [2] did experiments on burr formation and analyzed the formation process using an elastic finite element method. Kishimoto et al. [3] experimented on normalized carbon steel to investigate primary and secondary burrs. They determined the cutting conditions and tool geometries facilitating the formation of burrs. On the other hand, Iwata et al. [4] analyzed the burr formation mechanism through direct observation of orthogonal machining using SEM and finite element analysis. Nakayama and Arai [5] made a detailed observation on burr formation and classified machining burrs. Ko and Dornfeld [6] experimentally investigated a quantitative model of burr formation for ductile materials in orthogonal machining. Sikdar [7] reported the possibility of a reduction in burr formation through the optimization of exit edge bevel angles of workpieces under different machining conditions. Park [8] did experiments on burr formation and tried to analyze the formation process using FEM with some success. Lin [9] observed the results of face milling stainless steel blocks to conclude that the height of burrs strongly depends on the type of milling process. Avila [10] studied the effect of cutting parameters and tool geometry on burr height and thickness, using aluminium silicon alloys, and reported significant improvements in edge quality by optimizing the parameters selected. Avila and Dornfeld [11] observed that the largest burrs were formed on ductile materials at high radial engagement during face milling operations. Olvera and Barrow [12] investigated the influence of machining parameters on burr formation in face milling and end milling. Saha and Das [13, 14] experimented on burr formation in face milling to find how to minimize burr formation by optimizing the edge bevel angle using medium carbon steel and nickel-chrome alloy steel workpieces. Aurich et al. [15] recently made a detailed analysis and review of the formation of burrs and its control strategies.

The work presented studied the influence of different machining conditions and different edge bevel angles on

burr formation in high production face milling of 4600-A,M aluminium alloys using uncoated P30 carbide inserts. Experiments were carried out to find the optimum machining condition to eliminate or significantly reduce burr formation.

2. Experimental Investigation

The face milling of 4600-A,M aluminium alloy was used to study the effect of cutting velocity (V_c), feed per tooth (S_z) and exit edge bevel angle (θ) on the amount of burr formed at the exit edge of the workpiece under dry condition. Details of experimental set up and machining conditions are shown in Table 1.1. In experiment set-I, milling is performed with eight different exit edge bevel angles (θ) and a constant in-plane exit angle (Ψ) of 120° (Fig 1) at 452 m/min cutting velocity and 0.036 mm/tooth feed, to observe the corresponding variation of burr formation. Following the observation that large burrs are formed within a 15 to 30 degree range of θ , experiment set II was carried out within these exit edge bevel angles (Table 1). Machining parameters were chosen following a full factorial design of experiments. The machining parameters chosen are with combinations of cutting velocity (V_c) and feedrate (S_z) with their high and low values, and also with medium V_c and S_z values repeated twice. Burrs have been observed using a tool makers microscope (Mitutoyo, Japan make). They are classified using a 10 point specified in Table 2.

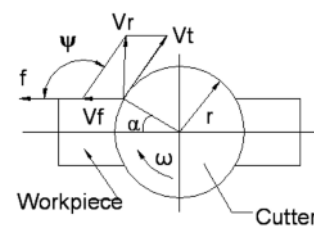
3. Results and discussion

Experimental findings of experiment set-I is shown in Figure 2 (a). It is clear from the figure that the amount / height of the burrs formed decreases uniformly from 0° to 15° exit edge bevel angle (θ), and then shows an increasing trend up to 45° θ . Increasing burr height with large values of θ may be caused by the availability of less back up material at the exit portion of the workpiece. With a smaller edge bevel angle as shown in Figure 1.1 (b), a gradual reduction in depth of cut occurs at a lower rate when the tool approaches the exit edge. This results in a reduced requirement for back up material to resist burr formation. A higher exit edge bevel angle (θ) causes a steeper bevel and hampers the slow gradual reduction of depth of cut, thereby needing more back up material to restrict formation of burrs.

On the other hand, a very low exit edge bevel angle is very close to having no bevel edge, and both lack substantial backup material thereby resulting in intense burr formation. For eight experiments in set-I, negligible burrs are observed at 15° exit edge bevel angle.

Observing the trend of burr formation in experiment set-I, exit edge bevel angles of the test pieces in

experiment set-II are chosen between 15° and 30° (Table 1), at 5° intervals wherein minimum burr is expected to form. The extent of burrs formed is also tested without an exit edge bevel. Results observed in experiment set-II are shown in Figure 3 (a-f). Negligible burr formation is seen at $\theta=15^\circ$ in most of the cases. Only in Figure 3 (b) for high cutting velocity and low feed condition, a minimum tiny burr is formed at 15° bevel angle. Under medium speed-feed conditions with both the two repeated experiments, similar trend in burr formation has been found; at 15° exit edge bevel angle minimum burr is seen as shown in Figure 2 (c-d). Without any exit edge bevel, a large burr has been found in all machining conditions. This may be due to the absence of back up support material. When edge bevel angle is less, there is more back up material resulting in lower burr formation, in general. This is also seen in these experimental results. Figure 4 (a) shows the amount of burr formed after milling a job with no edge bevel angle at a cutting velocity of 452 m/min and feed of 0.036 mm/tooth, while Figure 4 (b) shows no burr formation burr with 15° edge bevel angle made on the test piece. These two photographs clearly indicate the effect of appropriate edge bevel on the job in controlling the burr formation.



ω = speed of the cutter, V_t = cutting velocity at exit edge, ψ = in-plane exit angle
 V_f = feed velocity, V_r = resultant velocity,
 α = radial engagement angle

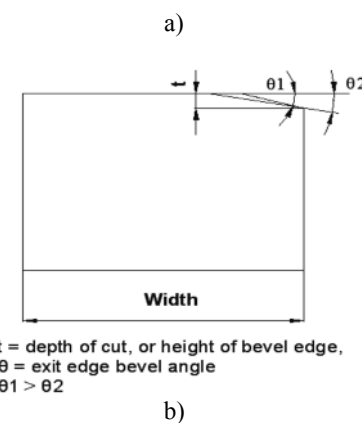


Fig 1. a) Definition of in-plane exit angle, Ψ , in milling operation, b) Sketch of the job with the exit edge beveled

Table 1. Experimental set up

Machine Tool	Vertical knee type milling machine, Model: FN 2V Group, Make: HMT Ltd. (India) Main motor Power: 5.5 kW			
Cutting Tool	Cutter diameter: 128.6 mm, Cutter type (Positive rake): R/L 265.2-125 ME- 20 AL (Sandvik) Insert: SPKN 1203 ED R, SM30 (HW)- P30 (Sandvik)			
Job Material	Aluminum Alloy (Alloy 4600 - A, M), Hardness: 170 BHN, Tensile strength: 165 MPa, Size: 80x60x40 mm ³			
Machining Conditions		Cutting velocity, V _c (m/min)	Feed, Sz (mm/tooth)	Exit edge bevel angle, θ (degree)
	Experiment Set I	452	0.036	0, 10, 15, 20, 25, 30, 35, 40 and 45
	Experiment Set II	452	0.036	0, 15, 20, 25 and 30
		452	0.022	
		363	0.027	
		363	0.027	
		286	0.036	
		286	0.022	

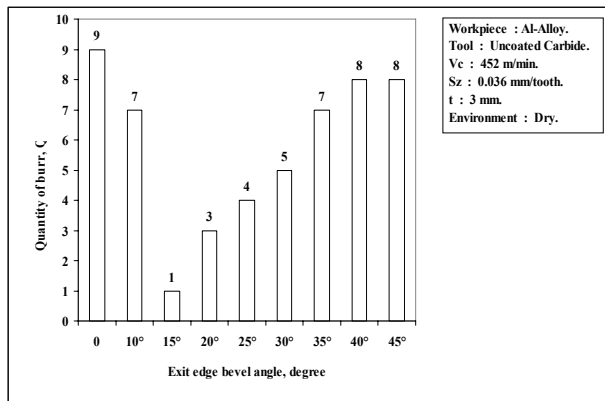
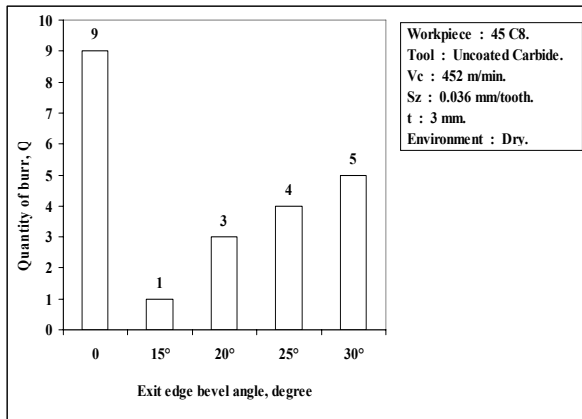


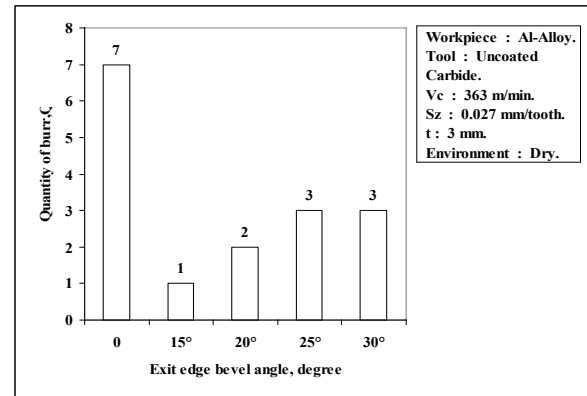
Fig. 2. Plot of variation of qualitative amount of burr formed with different exit edge bevel angles with high cutting velocity and feed for experiment set –I

Table 2. Assessment of amount (height) of burrs in 10-point scale

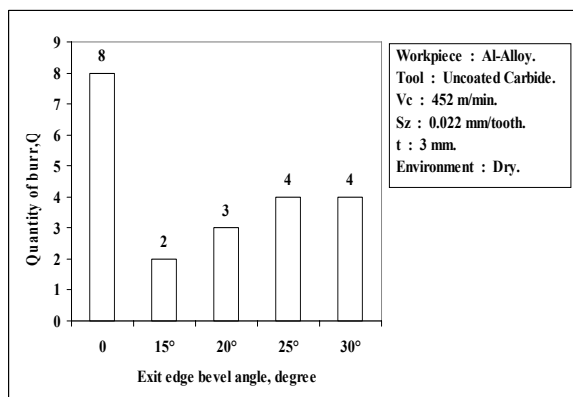
Scale value	Qualitative amount of burr observed
1	Negligible burr up to 0.025mm height
2	Tiny burr having height from 0.025 mm to less than 0.05 mm
3	Very small visible burr having height from 0.05 mm to less than 0.1 mm
4	Small burr having height from 0.1 mm to less than 0.15 mm
5	Significant burr having height from 0.15 mm to less than 0.2 mm
6	Medium size burr having height from 0.2 mm to less than 0.225 mm
7	Large burr having height from 0.225 mm to less than 0.25 mm
8	Large burr having height from 0.25 mm to less than 0.5 mm
9	Large burr having height from 0.5 mm to less than 1 mm
10	Very large burr having height greater than 1 mm



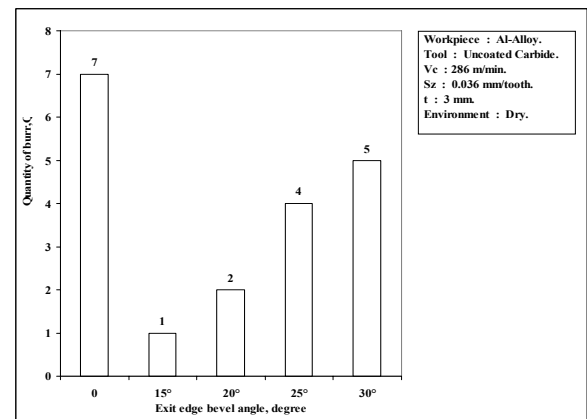
(a)



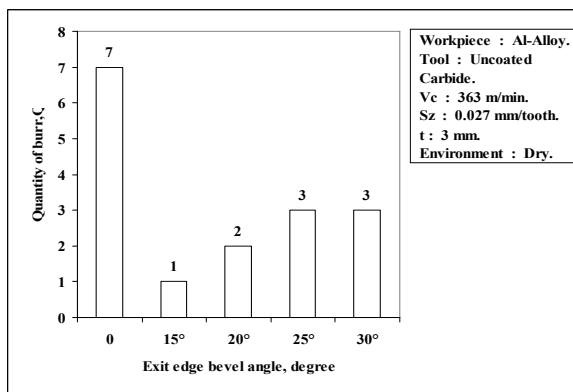
(d)



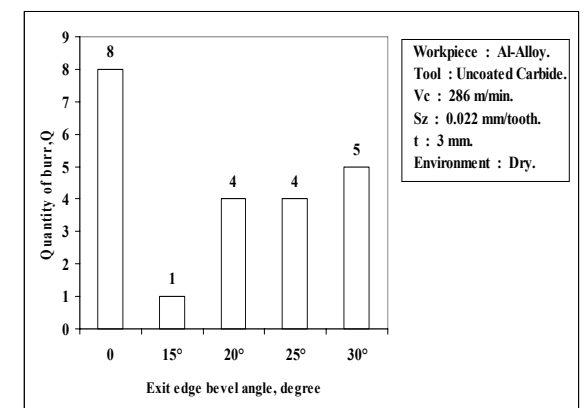
(b)



(e)



(c)



(f)

Fig. 3. (a-f) Plot of variation of qualitative amount of burr formed with different exit edge bevel angles with different combination of cutting velocity and feed for experiment set –II

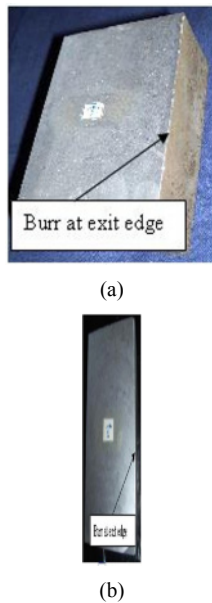


Fig. 4. Photographic view of typical specimens (a) for no bevel angle, (b) for 15 degree edge bevel of the job

4. Conclusion

Based on the observation of milling burr formation at the exit edge of aluminum alloys during vertical axis milling under dry conditions, the following conclusions may be drawn:

- Exit edge beveling of the job has a distinct effect on reducing the burr formation compared with that of the machining parameters.
- At all machining conditions, a minimum burr has been observed at 15° exit edge bevel angle that may be due to presence of high back up support material at the exit edge of the test piece.

References

- [1] Gillespie LK, (1973) The formation of machining burrs. M. S. Thesis, Utah State University, Logan: UT.
- [2] Pekelharing AJ, (1978) The Exit angle failure in interrupted cutting. *Annals of the CIRP*, 27 (1): 5-10.
- [3] Kishimoto W, Miyake T, Yamamoto A, Yamanaka K, Takano K, (1981) Study of burr formation in face milling. *Bulletin of the Japan Society of Precision Engineering*, 15: 51-52.
- [4] Iwata K, Ueda K, Okuda L, (1982) Study of mechanism of burr formation in cutting based on direct SEM observation. *Journal of Japan Society for Precision Engineering*, 48 (4): 510-515.
- [5] Nakayama K, Arai M, (1987) Burr formation in metal cutting. *Annals of the CIRP*, 36 (1): 33-36.
- [6] Ko SL, Dornfeld DA, (1991) A Study on burr formation mechanism. *Transaction of the ASME, Journal of Engineering Materials and Technology*, 113 (1): 75-87.
- [7] Sikdar C, (1993) Effect of cutting edge modification on machining characteristics and performance of coated carbide face milling inserts. Ph. D. Dissertation, IIT, Kharagpur, India.
- [8] Hashimura M, Chang YP, Dornfeld DA, (1999) Analysis of burr formation Mechanism in orthogonal cutting, *Transaction of the ASME, Journal of Manufacturing Science and Engineering*, 121 (1):1-7, University of California: California.
- [9] Lin TR, (2000) Experimental study of burr formation and tool chipping in the face milling of stainless steel. *Journal of Materials Processing Technology*, 108: 12-20.
- [10] Avila MC, (2003) The effect of kinematical parameters and tool geometry on burr height in face milling of Al-Si alloys. LMA Annual Research Reports, University of California. Berkeley: California.
- [11] Avila MC, Dornfeld DA, (2004) On the face milling burr formation mechanism and minimization strategies at high tool engagement. LMA Research Reports Submitted to University of California, Berkeley: California.
- [12] Olvera O, Barrow G, (1996) An experimental study of burr formation in square shoulder face milling. *International Journal on Machine Tools and Manufacture*. 36(9): 1005-1020.
- [13] Saha PP, Das D, Das S, (2007) Effect of edge beveling on burr formation in face milling. *Proceedings of 35th International MATADOR Conference*, Taipei, Taiwan; 199-202.
- [14] Saha PP, Das S, (2009) A simple approach for minimization of burr formation using edge beveling of alloy steel workpieces. *Proceedings of the International Conference on Advances in Mechanical Engineering*, Surat, India; 943-948.
- [15] Aurich JC, Dornfeld D, (2009) Burrs- analysis, control and removal. *Annals of the CIRP*, 58(2): 519-542.

Experimental Investigations on Drilling of Woven CFRP Epoxy Laminates: The Effect of Pilot-hole or Drill Chisel Edge on Delamination

A. Faraz¹ and D. Biermann¹

¹ Institute of Machining Technology (ISF), Baroper Strasse 301, Technische Universität Dortmund, 44227 Dortmund, Germany.

Abstract. The demand for carbon fibre reinforced plastics (CFRPs) in lightweight-engineering applications is rapidly growing. Drilling of CFRP composites is a challenging task due to their inhomogeneous, anisotropic and abrasive material characteristics. Delamination in drilling CFRPs is encountered as one of their major material-quality related defects. Drilling is usually performed as a post-manufacturing operation for components and subassemblies; consequently, its better control becomes essential. Many researchers have, hitherto, stressed the need for a pilot-hole prior to performing final drilling. And this is in order to minimise the hole exit delamination by negating the chisel edge effect of a drill bit. This article compares the results of experimental investigations on two different drilling operation-modes: Normal drilling and subsequent drilling conducted on some predrilled pilot-holes in woven CFRP epoxy laminates. Two uncoated cemented carbide drills were used. The thrust force during the drilling operation and the quantitative results (via a non-dimensional delamination factor) of the induced hole entry and exit delamination, respectively, for both operation-modes are compared and discussed. The main objective of this work is to analyse the practical impact of a pilot-hole or conversely that of the chisel edge on the observed hole exit delamination. The obtained results are interestingly different to what is found generally in literature. This research highlights the need to concentrate more on the quality and the design of the cutting edges of a drill bit, rather than to concentrate mainly on the role of its chisel edge.

Keywords: Drilling, CFRP, laminate, delamination, pilot-hole, chisel edge.

1. Research Motivation and Objectives

A lot of research has been carried out, hitherto, to model analytically and empirically the critical thrust force – required for the onset of the hole exit delamination damage – in drilling CFRPs (or FRPs in general) for various drills. The work of Hocheng and Dharan [1] was the initiative; and later on, it has mostly been exploited by various other researchers. Jain and Yang [2] claimed that the contribution of a drill chisel-edge to drilling thrust force could be up to 40-60%. Similarly, via another analytical approach, Won and Dharan [3] concluded that the chisel-edge is the main contributor to drilling thrust

force. Tsao and Hocheng [4] explained its main reason by clarifying that the chisel-edge of a twist drill actually pushes the material ahead it during its action, rather than cutting it, thus giving rise to the thrust force. Through their analytical approach, they showed that the risk of the hole exit delamination slightly increases due to a theoretical reduction (by a maximum of 11%) in the so called critical thrust force during a subsequent drilling mode. However, the delamination could still well be avoided due to an enormous reduction (of about 25-50%) in the drilling thrust force which proves beneficial for that subsequent-mode. Interestingly, Langella et al [5] have also quoted that the contribution of the chisel-edge to thrust force could be as high as 80% at higher feedrates.

On the other hand, Bhatnagar et al [6] proposed that the theoretical models for predicting critical thrust force needed more emphasis. In their work, for some types of drill bits, the observed drilling thrust force did not correlate well with the observed exit delamination. Similarly, Abrao et al [7] also discovered in their investigations that one of the selected drills, which produced the highest drilling thrust magnitude, created less delamination. In a very recent study, Faraz et al [8] also encountered almost similar results while investigating the drilling thrust force and exit delamination observed for a few specialised drill bits in conducting subsequent drilling operation-mode. They suggested to concentrate more on the drill cutting edge in order to counter the hole exit delamination, instead of holding its chisel-edge as the major responsible factor for the said damage.

The aim of this research was to study experimentally the effect of a drill chisel-edge or a pilot-hole mainly on the observed quantitative hole exit delamination results. This idea was derived on behalf of the results of the experimental study carried out as given in reference [8]. Various researchers consider the geometry of a drill bit and its cutting edge design as very important aspects for determining the delamination damage.

2. Experimental Details

In this study, CFRP laminates with a thickness of 10 mm were used as workpiece material. Some of the important details of the selected composite material are listed in Table 1. Two different types of cemented carbide (uncoated) twist drill bits having the same diameter of $D = 8$ mm, and the geometries as detailed in Table 2, were utilised. Drill T1 is a conventional twist drill, recommended suitable for applications with abrasive work-materials like CFRPs. However, T2 is not suitable for the same work-material.


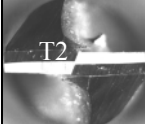
Table 1. Properties of CFRP laminates used in this study

Resin type	Epoxy E201 (hot-cured)
Weave type	Twill 2/2
Laminate density, ρ (g/cm ³)	1.55
Fibre volume content/fraction (%)	55-60
Tensile strength (MPa)	760
Young's modulus, E (GPa)	70
Flexural strength (MPa)	780
Shear modulus, G (GPa)	55
Resin glass transition temperature, T_g (°C)	140
Carbon fibre type	HT (high tenacity) fibre
Roving	12K (DIN 65184)

The drilling tests were carried out on a 3-axis, vertical CNC machining centre 'Chiron Magnum High Speed II (FZ 12S)'. A constant cutting speed of $v_c = 80$ m/min, and two different feedrate conditions were applied: $f = 0.05$ mm/rev, and $f = 0.35$ mm/rev. Also, two different drilling-modes were chosen: Normal drilling, and a subsequent one with two different predrilled pilot-holes (diameters: $\varnothing = 4$ mm and $\varnothing = 5.5$ mm). No coolant was used during the tests.

The in-process drilling thrust F_t was acquired using a 'Kistler 9125A' rotary dynamometer. Signals were transmitted through an A/D card further to store in a desktop PC (software 'LabView').

Table 2. Drill bits utilised in this study

Drill Name	No. of Lips	Point Angle (°)	Rake Angle (°)	Clearance Angle (°)
 T1	2	118	29	8
 T2	2	85	0	18

For the quantification of delamination around a drilled hole, various researchers have implemented more or less a similar concept. It is usually based on the maximum-width or -diameter of the observed delamination, and which is marked by a dashed-line circle in black colour as shown in Fig. 1. However, according to Romoli and Dini [10], such criterion may generally have an inherent incoherence. Therefore, in this study, an equivalent delamination criterion to that used by them has been implemented, which is denoted by DF and is given by relation (1) as below [9]:

$$DF = \left(\frac{A_{del} - A_{nom}}{A_{nom}} \right) \% \quad (1)$$

where, A_{del} is the cumulative peripheral damage area (the area covered by the black curve showing the true or actual delamination as in Fig. 1); while, A_{nom} is the nominal area of the hole (marked by the white circle).

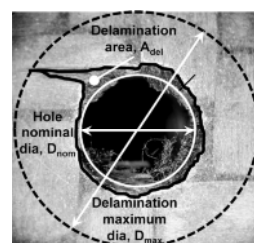


Fig. 1. Delamination quantification [9]

Delamination was measured using digital image processing based on the pixel-count technique in conjunction with stereomicroscopy. The full details can be perused in reference [9] of this article.

3. Results and Discussions

Fig. 2a clearly reveals the considerable reduction in the thrust force magnitudes observed in the subsequent drilling-modes with both pilot-hole diameters. The observed reduction of thrust force in case of a pilot-hole with diameter $\varnothing = 4$ mm is about 50%. Only half of the material or volume removal is required in conducting subsequent drilling on this pilot-hole diameter. There is no contribution of the drill chisel-edge to the observed thrust force. Also, a reduction of about 70% in thrust magnitude can be seen in case of the pilot-hole with larger diameter $\varnothing = 5.5$ mm.

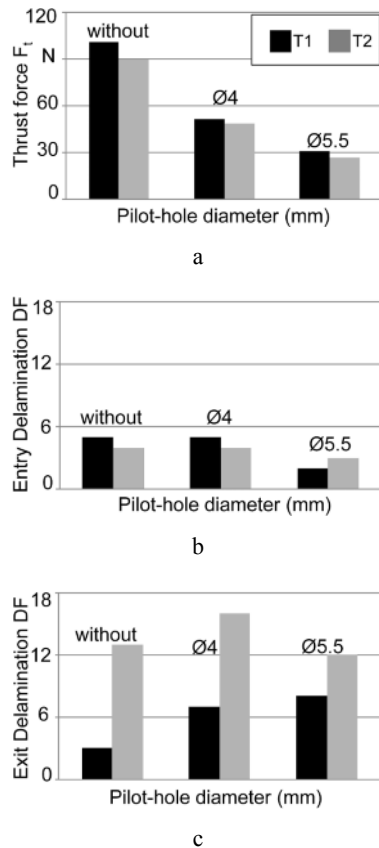


Fig 2. The observed a. thrust force; and the delamination at b. hole entry; and at c. hole exit; at $f = 0.05$ mm/rev and $v_c = 80$ m/min

The corresponding quantitative delamination results (hole entry and exit periphery, respectively) do not have the same trend. Referring to Fig. 2b, the trend of the entry delamination, when compared across the various drilling-modes, is not much appealing with regard to the application of pilot-holes. Pilot-holes have almost never been recommended or tested for hole entry delamination in archival literature. Meanwhile, the trends for the corresponding quantitative hole exit delamination results are mostly contradictive, as depicted in Fig. 2c. In contrast to the substantial reduction observed for the thrust magnitudes for both types of the selected tools (as in Fig. 2a), the corresponding exit delamination magnitudes generally increased in the subsequent drilling-modes. Moreover, the delamination was also comparatively higher in conducting subsequent drilling on the pilot-hole with the larger diameter ($\text{Ø} = 5.5$ mm). The said trend is quite clearly observable for T1. However, for T2 no specific tendency is discernible.

The tests were repeated at a higher feedrate value of $f = 0.35$ mm/rev to compare the results with the previous ones. Its results are given in Fig. 3. It can be seen from Fig. 3a that the thrust force for T1 in normal drilling-mode increased up to a magnitude almost four times greater than the corresponding one observed in Fig. 2a. While for T2, it is about two-and-a-half times higher. It is also noteworthy here that the reduction in the thrust magnitudes for T1 is approximately 6 and 12.5 times while performing subsequent drilling on the pilot-holes with diameters $\text{Ø} = 4$ mm and $\text{Ø} = 5.5$ mm, respectively. This difference is not that much significant when compared to that for T2. Where, it is about 2.5 and 5 times in case of the two selected pilot-hole diameters. This might be a proof of a much higher contribution of a drill chisel-edge to drilling thrust force [3-5], especially for T1 at higher feedrates in normal drilling-mode.

Now referring to Fig. 3b, no definite trend for the hole entry delamination is recognisable for both tools while comparing results across the various drilling-modes. For T1, the entry delamination decreases slightly, as previously (Fig. 2b). But, it increases in case of T2. Interestingly, the quantitative magnitudes of the hole exit delamination for both tools in various drilling-modes, as in Fig. 3c, have almost the same level as that for the corresponding ones as observed above in Fig. 2c. Moreover, the increased magnitudes of the hole exit delamination are evident here as well, for both types of tools and the selected subsequent drilling-modes (Fig. 3c). This may be attributed to a much significant reduction of the critical thrust force, required for the onset of exit delamination, in subsequent drilling operation-mode. The cutting mechanism for free fibres (previously cut) across the entire pilot-hole periphery might be changed, because they (fibres) are no more in a continuous form. It simply means that they are no longer held tightly or strongly together, being unsuitable to cut in contrast to their condition as in case of a normal drilling-mode. Across the entire pilot-hole exit periphery, the fibres prone to more easily bend (not cut) under the action of the progressing cutting edges of a twist drill bit [8].

The above results show very explicitly that the exit delamination must not mainly be attributed to the role of the chisel-edge of a drill bit. Rather, the design and geometry of its cutting edges, its corners, their sharpness or roundness [9], etc, may also play a decisive role in causing or developing the hole exit delamination.

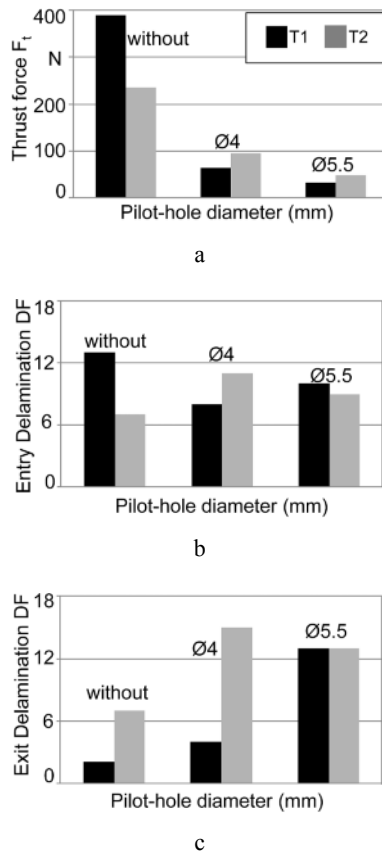


Fig 3. a. Drilling thrust force; b. entry DF; c. exit DF; at $f = 0.35$ mm/rev and $v_c = 80$ m/min

4. Conclusions

Following key conclusions may be drawn on behalf of the main findings of this research:

- In subsequent drilling-mode, the relative variation in the observed thrust magnitudes is quite little at different feedrates applied, depending apparently on the drill point-angle.
- The hole exit delamination for T1 considerably increased in both subsequent drilling operation-modes for both of the selected feedrate values.
- The variation in the hole exit delamination observed for T2 in subsequent drilling operation-modes was arbitrary.

- The larger the diameter of a predrilled pilot-hole, the much lesser may be the critical thrust force required for hole exit delamination.
- The mathematical models for correlating thrust force with hole exit damage are not that straight. Much more limitations have got to be applied.
- The geometry and the design of a drill bit seem to play major role in causing the hole exit damage, rather than mainly its chisel-edge.

References

- [1] Hocheng H, Dharan CKH, (1990) Delamination during drilling in composite laminates. *Journal of Engineering for Industry (Transactions of the ASME)* 112:236-239
- [2] Jain S, Yang DCH, (1993) Effects of feedrate and chisel edge on delamination in composites drilling. *Journal of Engineering for Industry (Transactions of the ASME)* 115(4):398-405
- [3] Won MS, Dharan CKH, (2002) Chisel edge and pilot hole effects in drilling composite laminates. *Journal of Manufacturing Science and Engineering (Transactions of the ASME)* 124:242-247
- [4] Tsao CC, Hocheng H, (2003) The effect of chisel length and associated pilot hole on delamination when drilling composite materials. *International Journal of Machine Tools and Manufacture* 43:1087-1092
- [5] Langella A, Nele L, Maio A, (2005) A torque and thrust prediction model for drilling of composite materials. *Composites: Part A* 36:83-93
- [6] Bhatnagar N, Singh I, Nayak D, (2004) Damage investigations in drilling of glass fiber reinforced plastic composite laminates. *Materials and Manufacturing Processes* 19(6):995-1007
- [7] Abrao AM, Rubio JCC, P.E, Davim JP, (2008) The effect of cutting tool geometry on thrust force and delamination when drilling glass fibre reinforced plastic composites. *Materials and Design* 29:508-513
- [8] Faraz A, Heymann T, Biermann D, Experimental investigations on drilling GFRP epoxy composite laminates using specialised and conventional uncoated cemented carbide drills. *Materials and Manufacturing Processes (Article in press)*
- [9] Faraz A, Biermann D, Weinert K, (2009) Cutting edge rounding: an innovative tool wear criterion in drilling CFRP composite laminates. *International Journal of Machine Tools and Manufacture* 49(15):1185-1196
- [10] Romoli L, Dini G, (2008) Experimental study on the influence of drill wear in CFRP drilling process. *Proceedings of the 6th CIRP International Conference on Intelligent Computation in Manufacturing Engineering, Naples, Italy*

Modeling of hard turning: effect of tool geometry on cutting force

Z.Y. Shi^{1,a}, Z.Q. Liu^{1,a}, C.M. Cao^{1,a}

¹ School of Mechanical Engineering, Shandong University, Jinan250061, China

^a Key Laboratory of High Efficiency and Clean Mechanical Manufacture (Shandong University), Ministry of Education

Abstract. Hard machining for manufacturing dies and molds offers various advantages, but the productivity is often limited, mainly by tool life. This study investigates the influence of cutting tool geometry on the cutting forces by utilizing finite element simulations (FEM). A set of cutting conditions in numerical FEM were conducted by using four different shaped cutting tools and axial force, radial force and tangential force were found. The results of this research help to explain the conclusion that for cylindrical control, the equation of the actual geometry of the S-shaped inserts involved in cutting is a sphere; that of C-shaped, D-shaped and T-shaped inserts involved in cutting is an ellipsoid with different lengths of short-half axis.

Keywords: tool geometry, material flow stress, short-half-axial, cutting force

1. Introduction

The most common manufacturing process in industry is cutting [1], and FEM has become a major tool in calculating the cutting process variables such as forces, temperatures and stresses [2]. The hard turning of ferrous metal parts that are hardened usually between 45-70 HRC, can be performed dry using ceramic coating tools. In macro machining, the primary cutting edge mainly participates in the cutting process. However, the whole nose of the cutting tool participates in a micro-cutting process due to the metal removed is very little [3]. The cutting force in cutting processes is very important for analyzing the effect of the tool geometry, and there are three different approaches for calculating the forces including: analytical, mechanistic, and numerical [4]. The advantages of using numerical simulation is the cutting forces can be predicted without spending time and money with experimental procedures, therefore improving productivity and reducing costs [1, 5].

In this work, DEFOERM-3D was used to simulate the turning process and the effects of tool geometry parameters on cutting forces in micro-cutting were predicted. Results of the research help to explain the conclusion that for cylindrical control. The equation of the actual geometry of the S-shaped inserts involved in

cutting is a sphere, while that of C-, D-, and T-shaped inserts involved in cutting is an ellipsoid with different lengths of short-half axis.

2. Geometry modeling

In traditional machining, the actual geometry of the cutting tool involved is determined by the major cutting edge. In micromachining, in contrast, the actual geometry involved in machining is determined by the major cutting edge, the minor cutting edge and the third edge called the back-side cutting edge. So the cutting tool's nose radius, cutting edge radius etc. have to be considered.

According to ISO code, the tool geometry can be divided into S-, C-, T- shapes etc according to the tool nose angle α . In this paper, four different cutting tools C-, D-, T- and S-shapes tools are selected, meaning the tool angle α is 80°, 55°, 60°, 90° respectively, to investigate the effects of tool geometry on cutting forces.

The cutting tools were also classified into cylindrical control and conical control according to the shape of the flank.

By comprehensively considering the tool shape and the control model of the flank, the cutting tools were classified into four different types including S- and non-S-shaped tools with cylindrical control and conical control. In this paper, because of the limitation of experiments, only S- and non-S-shaped tools with cylindrical control tools are discussed.

In this paper, the model of the actual geometry of the cutting tools involved in machining are developed by using mathematical analysis methods. First, three-dimensional models of the tool nose and major and minor cutting edges are established. Then the transformation matrixes from local coordinate system to global coordinate system are described. Finally the solving processes are carried out and the actual geometry involved in machining is obtained [6]. For S shape tools, the actual geometry involved in machining is a sphere, which is now given in Eq. 1:

$$\left(x-\frac{P}{2}\right)^2+\left(y-\frac{Q}{2}\right)^2+z^2=\frac{R^2+r_1^2+r_2^2}{2}-\frac{Q^2+P^2}{4} \quad (1)$$

where P is the distance between the coordinate system centre of the side cutting edge to the tool nose centre in X direction, Q is the distance between the coordinate system centre of the main cutting edge to the tool nose centre in Y direction, R is the nose radius, r₁ is the major cutting edge radius, and r₂ is the minor cutting edge radius.

For non-S-shaped tools, such as C-, D-, T-shape tools, the actual geometry involved in cutting can be expressed as shown in Eq. 2. According to Yao [7], the projection of the actual geometry of cylindrical control inserts with non-S shape involved in machining in x-y plane is an ellipse, so the 3-D geometry involved in machining is ellipsoid.

$$\begin{cases} \left(2-\cos^2\frac{\alpha}{2}\right)x^2+\left(2-\sin^2\frac{\alpha}{2}\right)y^2+2\sin\frac{\alpha}{2}\cos\frac{\alpha}{2}xy=R^2+r_2^2-r_1^2 \\ z=t \end{cases} \quad (2)$$

where α is the tool nose angle.

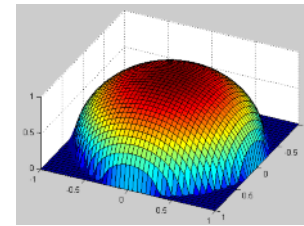
Fig. 1 shows the actual geometry depicted by Matlab 7.0 according to Eqs. 1 and 2; where Fig. 1a shows the S-shaped tools, 1b shows the C-shaped tools, 1c shows the D-shaped tools, and 1d shows the T-shaped tools, both the major and the minor cutting edge radii are set to be 0.04 mm, and the tool nose radius is set to be 0.2 mm. It can be seen that the three-dimensional graphics of 1a shows a sphere, and the second half of 1b, 1c and 1d are all ellipsoids which gives good consistency Eq. 1 and Eq. 2. By analyzing the three graphics of Fig. 2b, 2c and 2d, it can be seen that length of the short-half-axis of the ellipsoids are different according to the shape of the cutting tools. The longest short-half-axis corresponds with D-shaped tool, whose tool nose angle is 55°, then comes the T-shaped tool, with a tool nose angle of 60°, and finally comes the C-shaped tool, with a tool nose angle of 80°. So, the conclusion can be drawn that with an increase in the tool nose angle, the short-half-axis of the ellipsoid determined by the tool cutting edge and tool nose decrease.

3. Computer Simulation

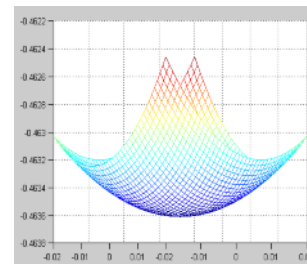
3.1 Modeling of Workpiece

Bars of stainless steel AeroMet100, 55 mm in diameter and 60° arc-types were used, as shown in Fig. 2. During the FEM simulation process, the main problem is considering the flow stress of the workpiece. According to Yang [8], when the material’s strain rate is 10s⁻¹, the strain-stress curves in 950°, 1000°, 1050°, 1100° can be derived and by using the material property manager, enabling Fig. 3 to be finally derived. Thus, the property

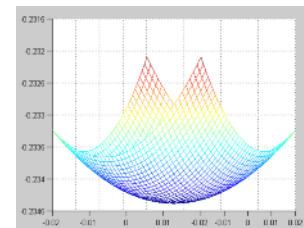
of the new material AeroMet100 can be added into the software, and this makes the simulation results more exact.



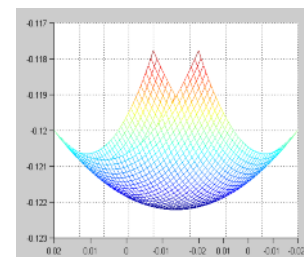
a



b



c



d

Fig. 1. Three-dimensional graphics of actual geometry a. Sketch map of S-shaped tool; b. Sketch map of C-shaped tool; c. Sketch map of D-shaped tool; d. Sketch map of T-shaped tool

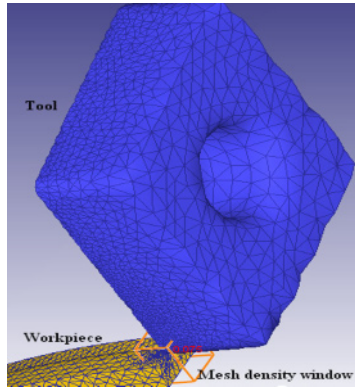


Fig. 2. Cutting process model

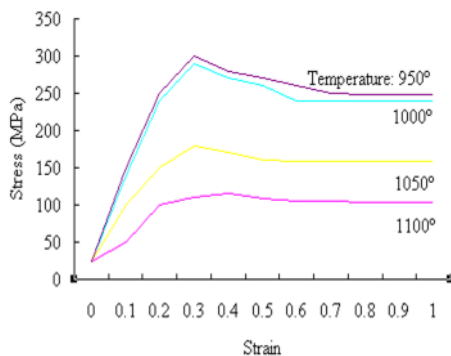


Fig. 3. Flow stress data of AeroMet100

3.2 Contact Friction Model & Heat Transformation

The relationship between the cutting tool and the workpiece was set to be a Master-slave relationship, making sure that the workpiece material will not soak into the cutting tool.

Fig. 4 shows the main view of the cutting process. It can be seen that the chip area varies along the tool nose from the feed rate to zero, and there must exist an intermediate value which is equal to the nose radius. When the chip area is smaller than the nose radius, no chip comes into being, and only a rubbing action occurs during the cutting process. Meanwhile, when the chip area is larger than the nose radius, a chip will be produced and shearing action occurs during the cutting process. So the chip area can be divided into a rubbing area and a shearing area, and the friction model has to be considered seriously. In this paper, for simplicity, the friction model between the cutting tool and the chip is characterized as a shear friction model with the friction coefficient set to be 0.2 [9].

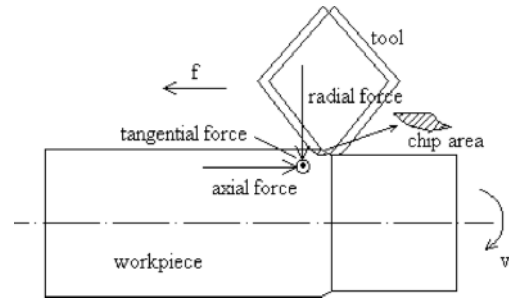


Fig. 4. Main view of the cutting process

The room temperature of the cutting tool and workpiece was set to be 20°, and the coefficient of heat transformation was set to be 11 N/sec/mm/C [10].

The simulation process is shown diagrammatically in Fig. 5.

4. Results and Discussion

Table 1 shows the resulting forces as predicted by the FEM simulation. By analyzing the four shaped tools' resultant forces, it can be concluded that the cutting force generated by the D-shaped tool was substantially higher than the equivalent forces of the other tools. The next highest one was the T-shaped tool, then the C-shaped tool and finally the S-shaped tool. An earlier conclusion was that the longest short-half-axis of the ellipsoid corresponds with D-shaped tool, whose tool nose angle is 55°, the next longest is the T-shaped tool, with tool nose angle is 60°, the next the C-shaped tool, with tool nose angle is 80°, and finally is the S-shaped tool with tool nose angle 90°. These relationships between the cutting forces and the inserts shape have been obtained: the longest of the short-half-axis corresponding to the smallest tool nose angle and the greatest of the cutting forces. This may be due to the ellipsoid with longest short-half-axis having most contact area, which in turn makes heat dissipation better and the cutting temperature lower. When the cutting temperature is reduced, the workpiece material begins to harden, which finally causes the cutting force to increase. By the same token, the magnitude of other cutting tools' cutting forces can be explained and the relationships between the cutting forces and the cutting tools' shape can also be explained.

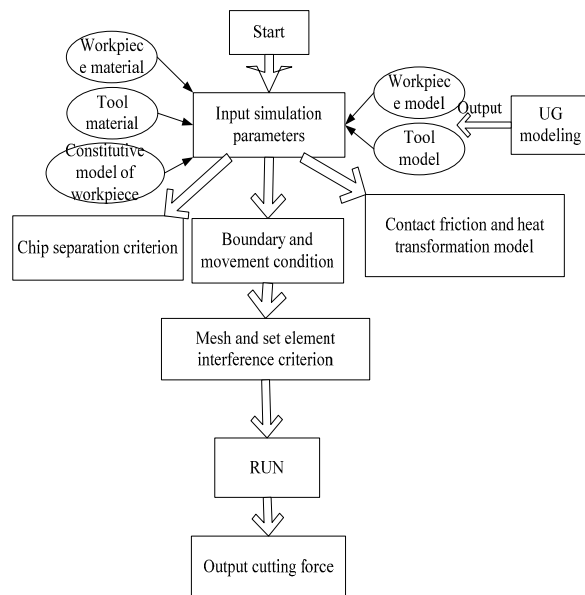


Fig. 5. Flow chart of simulation process

Table 1. Table with legends of one line

Insert type	Simulations		
	Axial force (N)	Radial force (N)	Tangential force (N)
C	39.4	94.2	78.4
D	40.3	101.5	86.2
T	38.1	98.4	84.1
S	32.1	72.6	62.7

5. Conclusions

The following conclusions can be drawn:

- 1) The simulated model combined with the 3D model built in UG can predict the cutting forces preferable.
- 2) Different from conventional cutting, in this model the cutting forces in X, Z directions are far higher than the cutting force in the Y(axial) direction.
- 3) The cutting force of the D-shaped tool was substantially higher than the other shaped tools, the second highest was the T-shaped tool, and then the C-shaped tool and finally the S-shaped tool.
- 4) The longest of the short-half-axis corresponded with the smallest tool nose angle and gave the greatest of the cutting forces.

Acknowledgement

This project is supported by National Natural Science Foundation of China (through grant no. 50675122 and 50828501), Foundation of Shandong Province of China for Distinguished Young Scholars (2009 JQB01027) and National Basic Research Program of China (973 Program 2009CB724401).

References

- [1] Davim JP, Maranhao C, Jackson MJ, Cabral G, Gracio J, (2008) FEM analysis in high speed machining of aluminium alloy (Al7075-0) using polycrystalline diamond (PCD) and cemented carbide (K10) cutting tools. *Int. J. Adv. Manuf. Technol.* 39: 1093-1100.
- [2] Ceretti E, Lazzaroni C, Menegardo L, Altan T, (2000) Turning simulations using a three-dimensional FEM code. *J. Mater. Process. Technol.* 98: 99-103.
- [3] Liu ZQ, (1999) Repetitive measurement and compensation to improve workpiece machining accuracy. *Int. J. Adv. Manuf. Technol.* 15: 85-89.
- [4] Lai XM, Li HT, Li CF, Lin ZQ, Ni J, (2008) Modeling and analysis of micro scale milling considering size effect, micro cutter edge radius and minimum chip thickness. *Int. J. Mach. Tools. Manuf.* 48: 1-14.
- [5] Altintas Y, (2000) *Manufacturing automation: Metal cutting mechanics machine tool vibrations and CNC design.* Cambridge University Press, Cambridge.
- [6] Shi ZY, Liu ZQ, (2009) The actual geometry of the cutting tool involved in machining. *Int. J. Adv. Manuf. Technol.* (in press, Doi 10.2007/s00170-009-2081-0)
- [7] Yao NX, Wang ZH, Chen ZJ, (1988) *Application of Math in Tool Design.* Mechanical Industry, Beijing.
- [8] Yang XH, Zhang SH, (2007) Hot deformation behavior of ultrahigh strength steel AerMer100. *Journal of Plasticity Engineering* 14: 121-126.
- [9] Tang ZT, (2008) *Residual stresses and deformations of aerospace aluminum alloy in machining.* (Dissertation Shandong University).
- [10] Dong HY, (2004) *The FEM simulation of overall structure of the aviation in machining.* (Dissertation Zhejiang University)

Selection of optimal process parameters for gear hobbing under cold air minimum quantity lubrication cutting environment

Genbao Zhang¹, Hongjun Wei¹

¹ College of Mechanical Engineering, Chongqing University, Chongqing, China

Abstract. Cold air minimum quantity of lubrication (CAMQL) in machining is a preferable alternative to conventional flood lubricating systems from the viewpoint of cost, ecology and human health issues. Therefore, it is necessary to select proper process parameters in order to enhance machinability for a given work material. The present study aims at determining the optimum amount of MQL and the most appropriate cold air temperature and feed rate during hobbing of medium carbon steel (C45, DIN) using YG6X hard alloy tool. The Taguchi technique with the utility concept, a multi-response optimization method, has been proposed for simultaneous minimization of tooth-face roughness and tool wear. The experiments were planned as per Taguchi's L9 orthogonal array with each experiment performed under different conditions of MQL, cold air temperature and feed rate. The analysis of mean (ANOM) and analysis of variance (ANOVA) on multi-response signal-to-noise (S/N) ratio were employed for determining the optimal parameter levels and identifying the level of importance of the process parameters. The optimization results indicated that MQL of 40 ml/h, cold air temperature -45°C and a feed rate of 0.2 mm/r is essential to simultaneously minimize tool wear and tooth-face roughness.

Keywords: cold air, gear hobbing, minimum quantity lubrication, Taguchi method, tool wear, tooth-face roughness

1. Introduction

In the gear hobbing process, high cutting zone temperature causes dimensional deviation and premature failure of cutting tools, and also impairs the surface integrity of the product by inducing tensile residual stresses and surface and subsurface microcracks in addition to rapid oxidation and corrosion [1]. Especially, in high speed-feed machining, application of conventional cutting fluid fails to penetrate the chip-tool interface and thus cannot remove the cutting heat effectively [2].

Cold air minimum quantity of lubrication has been considered as one of the solutions for reducing the amount of lubricant to address the environmental, economical and mechanical process performance concerns [3]. It was suggested by many researchers that

the cold air and MQL techniques in machining processes [4-7] applied this technique in reaming process of grey cast iron and aluminum alloy with coated carbide tools. With this technique, significant reduction in tool wear and improvement in surface quality of the holes have been observed compared with dry cutting. The MQL technique was used in turning of AISI 1040 steel, clearly indicating that a mixture of air and soluble oil machining was better than conventional flood coolant system [8]. The investigations on aluminum alloy indicated that the MQL technique is preferable for higher cutting speeds and feed rates [9].

As seen from the literature, the cold air and MQL technique suggests several advantages in machining processes. Most of the experimental investigations on machinability aspects are limited to the role and effectiveness of cold air and MQL over dry and wet machining. However, in order to achieve the best surface quality on a machined surface with minimum tool wear, every cutting condition, cold air temperature and amount of MQL should be carefully selected. Nowadays, no systematic research work has been reported in the literature to determine the optimum quantity of lubricant with appropriate cutting conditions and cold air temperature for achieving better machinability. Hence, an attempt has been made in this paper to enhance the machinability characteristics in hobbing of medium carbon steel using hard alloy tool, taking quantity of lubricant, cold air temperature and feed rate as the process parameters. In this paper, Taguchi method has been employed to determine the best combination of the process parameters by simultaneously minimizing tooth-face roughness and tool wear.

2. Experimental procedure

The cold air device was set as Fig.1. In the present study, three parameters, namely, quantity of lubricant (Q), cold air temperature (T) and feed rate (f) were identified and

the ranges of the cutting conditions were determined through preliminary experiments. Each parameter was investigated at three levels to study the non-linearity effect of the parameters. The identified parameters and their associated levels are given in Table 1. According to Taguchi quality design concept, for three levels and three factors, nine experiments are to be performed and hence L9 orthogonal array was selected as shown in Table 2.

The machining tests were performed on Direct-drive small module gear hobbing machine YK3610 with a maximum spindle speed of 4500 rpm; cold air generator was employed with MQL Device; the milling mode was up milling; 1000r/min cutting speed, 0.4 Nm³/min cold air flow and 0.6MPa cold air pressure were used throughout the experiment. The work-pieces (C45) according to DIN specification (12164:1998) with the following mechanical properties were used for turning: $\sigma_b=600\text{N/m}$, $\sigma_s=355\text{N/m}^2$, $\delta_s>16\%$, $\varphi>40\%$. The YG6X hard alloy tool was used with following geometric parameters: pressure angle 20°, spiral angle 17°, gear module 1.25, precision grade AA. The surface roughness (Ra) on turned components was measured using a Hommelwerke T1000 profilometer, and tool wear VB was measured by Nikon SMZ1500 Stereo Microscope System.



Fig. 1. Cold air device and In-situ processing

3. Experimental results and discussion

At present, the multiple performance, namely, Ra and VB , are to be minimized and hence “smaller the better type” quality characteristic has been selected for each response. The S/N ratio associated with the responses, Ra and VB are given by

$$\eta_1 = -10 \log_{10} (Ra^2) \quad (1)$$

$$\eta_2 = -10 \log_{10} (VB^2) \quad (2)$$

In the utility concept, the multi-response S/N ratio for each trial in an orthogonal array is:

$$\eta = \omega_1 \eta_1 + \omega_2 \eta_2 \quad (3)$$

Where ω_1 and ω_2 are the weighting factors related with S/N ratio of each of the responses Ra and VB , respectively. In the present work, weighting factor of 0.5 for each of the responses is considered, which gives equal priorities to both Ra and VB for simultaneous minimization. The computed values of S/N ratio (η) for each response and the multi-response S/N ratio for each trial in the orthogonal array are illustrated in Table 2.

The two-factor interaction effects of process parameters on multi-response S/N ratio are analyzed in Fig. 2. In Fig. 2 “a” shows the interaction effects due to feed rate and air temperature. It can be observed from Fig. 2a that there exist considerable mutual interaction effects between feed rate and air temperature. However, when the feed rate is high (0.4mm/r), the effect of change in temperature from -25°C to -45°C is minimum. The maximum interaction effect exists when the feed rate is 0.2mm/r, with decrease in temperature from -25°C to -45°C. Further, it can be seen that the machinability is highly sensitive to air temperature variations for the two values of feed rate, 0.2mm/r and 0.3mm/r studied. And “b” illustrates the interaction effect due to quantity of lubricant and air temperature and it can be seen that the effect of change in air temperature on machinability at any quantity of lubricant is negligible. Similarly, the machinability is highly sensitive to air temperature variations irrespective of quantity of lubricant. A similar pattern is also observed in the interaction effects due to quantity of lubricant and feed rate as depicted in “c”.

The result of ANOM is represented in the response plot as exhibited in Fig. 3. The level of a parameter with the highest S/N ratio is the optimal level. Thus, the optimal process parameter setting for the present study is A3, B1 and C3. Hence, the best combination values for simultaneously minimizing surface roughness and tool wear are: Quantity of lubricant 40 ml/h; Feed rate 0.2mm/r; Air temperature -45°C.

Table 3 presents the result of ANOVA on multi-performance characteristics. As seen from ANOVA table, the Quantity of lubricant has major contribution (53.63%) in optimizing the multiple performance characteristics followed by cold air temperature

Table 1. Process parameters and their levels

Factor	Code	Unit	Levels		
			1	2	3
Temperature T	A	°C	-25	-35	-45
Feed rate f	B	mm/r	0.2	0.3	0.4
Quantity of lubricant Q	C	ml/h	0	20	40

Table 2. Orthogonal array, response and the computed values of S/N ratio

Trial no.	Levels of process parameters				Response			S/N ratio		
	A	B	C	Error	Ra/ μm	VB/mm	η_1 (dB)	η_2 (dB)	η (dB)	
1	1	1	1	1	1.20	0.450	-1.58	6.93	2.68	
2	1	2	2	2	1.19	0.360	-1.51	8.87	3.68	
3	1	3	3	3	1.16	0.231	-1.29	12.79	5.75	
4	2	1	2	3	1.07	0.313	-0.59	10.09	4.75	
5	2	2	3	1	0.76	0.330	2.38	9.64	6.01	
6	2	3	1	2	0.87	0.385	1.21	8.29	4.75	
7	3	1	3	2	0.74	0.251	2.61	12.01	7.31	
8	3	2	1	3	0.78	0.481	2.38	6.34	4.36	
9	3	3	2	1	0.81	0.286	1.89	10.87	6.38	

Table 3. result of ANOVA on multi-performance characteristics

Factor	Degrees of freedom	Sum of squares	Mean square	Value of F	significance	Percentage
A	2	5.9217	2.9608	42.0568	**	35.01
B	2	1.4516	0.7258	10.3096	*	7.94
C	2	8.9957	4.4979	63.8906	**	53.63
Error	2	0.1408	0.0704			3.42
Total	8	16.5098	2.0637			

$$F_{0.01}(2,2)=99.00 \quad F_{0.05}(2,2)=19.00 \quad F_{0.1}(2,2)=9.00$$

(35.01%). However, the feed rate has the least effect (7.94%) in controlling the multi-response. Further, it is also observed that ANOVA has resulted in 3.42% of error contribution, clearly indicating that the interaction effects of process parameters are negligible for simultaneously minimizing tooth-face roughness and tool wear

After selecting the optimal level of process parameters, the final step is to predict and verify the multiple performance characteristics. The predicted optimum value of S/N ratio (η_{pred}) is:

$$\eta_{pred} = m + \sum_j^p \left[(m_{i,j})_{\max} - m \right] \quad (4)$$

Where $(m_{i,j})_{\max}$ is the S/N ratio of optimum level i of parameter j , m is the overall mean of S/N ratio and p is the number of parameters that affect the machinability characteristics. The predicted S/N ratio of multiple characteristics using Eq. (4) for A3, B1 and C3 parameter level combination is 7.14 dB.

In order to judge the closeness of the experimental value of S/N ratio (η_{expt}) with that of the predicted value

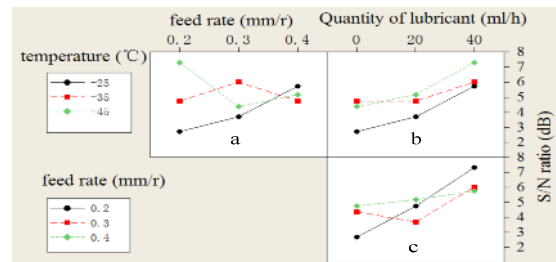
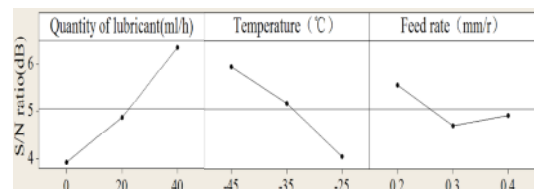
(η_{pred}), the confidence interval (CI) of η_{pred} for the optimum process parameter level combination at 95% level is determined. The CI is given by [12]:

$$CI = \sqrt{F_{(1,ve)} V_e \left(\frac{1}{n_{eff}} + \frac{1}{n_{ver}} \right)} \quad (5)$$

where $F_{(1,ve)}$ is the F value for 95% confidence interval; ve is the degrees of freedom for error; V_e is the mean

square of error; $n_{eff} = (N/(1+v))$, N = total trial number in orthogonal array and v = degrees of freedom of p factors; n_{ver} is the confirmatory test trial number.

If the prediction error $|\eta_{pred} - \eta_{expt}|$ is within the CI value, then the optimum factor level combination and additive model for the factor effects in this experiment are valid. In the present study, for the optimal process parameter settings, η_{expt} is 7.31 dB. Hence, the prediction error is 0.17 dB, which is within the CI value of ± 1.522 dB, thus justifying the adequacy of the additivity of the model.


Fig. 2. Interaction effect plot between process parameters

Fig. 3. Factor response plot for multiple performance characteristics

From the Taguchi optimization results, it is found that high MQL is required for minimizing both tooth-face roughness and Tool wear. This can be explained by the fact that the surface roughness increases under minimum MQL due to more intensive temperature and stresses at tool chips. The high MQL improves surface finish depending upon work-tool material through controlling the deterioration of auxiliary cutting edge of abrasion, chipping and built-up edge formation. Further under high MQL, specific cutting force decreases due to reduction in cutting temperature especially at main cutting edge where built-up edge formation is more predominant.

It is also observed from the factor response plot of Fig.3 that high MQL with low to medium cold air temperature is necessary to minimize both surface roughness and tool wear. This is due to the fact that cold air with lower temperature could remove heat more effectively and hence tooth-face roughness and tool wear decreases. On the other hand, at high cold air temperature, coolant may not have enough cooling capacity to remove heat accumulated at cutting zone resulting in less reduction of temperature under high MQL, and hence results in poor surface finish and tool wear increasing. Further, at low cold air temperature, heat generated is successfully disposed to higher MQL as compared to lower MQL, thus decreasing the tool wear and hence better machining takes place without ploughing on work material. From the micrographs of tool wear of Fig.4, we can find completely different tool wear pictures under different cutting parameters. The flank face wear shown in picture "a" was much wider than picture "b", and the nose of tool existed obvious depressions. And it showed again that low temperature and high MQL could decrease tool wear and tooth-face roughness effectively.

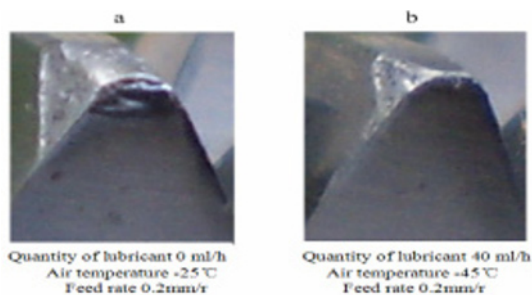


Fig. 4. Micrographs of tool wear

As seen from the response plot, the requirement of feed rate is not significant to both tooth-face finish and tool wear. The reason might be, at lower cold air temperature and high MQL, most of the heat is transferred quickly enough and the friction is decreased effectively. And under high MQL with low cold air temperature, there is a reduction in adhesion of work material and consequently friction force, which in turn reduce the tool wear. Hence, although more heat is generated because of high material removal rate, good surface roughness and tool wear still can be gained.

4. Conclusions

From the present investigation, the following conclusions are obtained:

1. The ANOM on multi-response S/N ratio shows an optimum MQL of 40ml/h, cold air temperature of -45°C and feed rate of 0.2mm/r is necessary to simultaneously minimize tooth-face roughness and tool wear.
2. ANOVA illustrates that quantity of lubrication is the dominant parameter followed by cold air temperature and feed rate in optimizing the machinability.
3. ANOVA also shows that the error contribution is 3.42%, clearly indicating the absence of the interaction effects of process parameters on optimization of multiple performance characteristics.

Acknowledgment

This project is supported by the National High-Tech. R&D Program, China (No. 2009AA04Z119), the National Natural Science Foundation, China (No. 50835008), the National Major Scientific and Technological Special Project for "High-grade CNC and Basic Manufacturing Equipment", China (No. 2009ZX04014-016), and Open Research Foundation of State Key Lab. of Digital Manufacturing Equipment & Technology in Huazhong University of Science & Technology.

References

- [1] P. Leskover and J. Grum: The metallurgical aspect of machining, *Ann.CIRP* 35 (1) (1986) P. 537–550.
- [2] H.K. Tonshoff and E. Brinkomeier, Determination of the mechanical and thermal influences on machined surface by microhardness and residual stress analysis, *Ann. CIRP* 29 (2) (1986) P. 519-532.
- [3] Heinemann, R., Hinduja, S., Barrow, G., Petuelli, G., 2006. Effect of MQL on the tool life of small twist drills in deep-hole drilling. *Int. J. Mach. Tool Manuf.* 46, 1–6.
- [4] Chen Decheng, Suzuki Yasuo and Sakai. *Chinese Journal of Mechanical Engineering* Vol. 36(11) (2000) P.70-74.
- [5] Machado, A.R., Wallbank, J., 1997. The effect of extremely low lubricant volumes in machining. *Wear* 210, 76–82.
- [6] Davim, J.P., Sreejith, P.S., Gomes, R., Peixoto, C., 2006. Experimental studies on drilling of aluminium (AA1050) under dry, minimum quantity of lubricant, and flood-lubricated conditions. *Proc. ImechE Part B: J. Eng. Manuf.* 220, 1605–1611.
- [7] Lugscheider, E., Knotek, O., Barimani, C., Leyendecker, T., Lemmer, O., Wenke, R., 1997. Investigations on hard coated reamers in different lubricant free cutting operations. *Surf.Coat.Technol.* 90, 172–177.
- [8] Dhar, N.R., Islam, M.W., Islam, S., Mithu, M.A.H., 2006. The influence of minimum quantity of lubrication (MQL) on cutting temperature, chip and dimensional accuracy in turning AISI-1040 steel. *J. Mater. Process. Technol.* 171, 93–99.
- [9] Kelly, J.F., Cotterell, M.G., 2002. Minimal lubrication machining of aluminum alloys. *J. Mater. Process. Technol.* 120, 327–334.

The Formation of Adiabatic Shear Bands as a result of Cryogenic CNC Machining of Elastomers

V.G. Dhokia¹, S.T. Newman¹, P. Crabtree¹ and M.P. Ansell¹

¹ Department of Mechanical Engineering, University of Bath, Bath, UK, BA2 7AY

Abstract. Traditional polymer forming methods have concentrated on moulding technology. CNC Machining of a low-density material, such as an elastomer even at significantly reduced temperatures presents a number of challenges, with one being the generation of a machining phenomenon termed adiabatic shear band formation. As a result of this, tool degradation and increased part surface roughness can occur. The adiabatic shear band formation is a region on a chip where the ductile properties of the material being machined have been exceeded and the heat generated does not have sufficient time to dissipate. This leads in some cases to permanent material damage resulting in reduced fatigue resistance. With the machining of elastomers, the adiabatic shear formation has the potential to be even more evident, leading to rapid material degradation and poor surface finish characteristics. In this paper, cryogenic manufacturing is reviewed, ethylene vinyl acetate (EVA) and Neoprene materials are machined illustrating and the resulting adiabatic shear band formations are illustrated.

Keywords: Adiabatic, Cryogenic, CNC

1. Introduction

Machining is a major aspect of the creation of consumer products and has many industrial applications. Two major areas of machining technology are turning and milling and both have contributed to the continuing evolution of manufacturing and design.

With the evolution of manufacturing paradigms from craft production to personalised product manufacture, there is becoming a need to explore new methods of manufacturing. One such method, which is currently being developed at The University of Bath, is that of cryogenic machining of soft low-density materials for the production of personalised orthotic insoles and sports shoe soles. One of the novel aspects of this research involves the CNC machining of different elastomers and it is at this point that further research is required.

Machining an elastomeric material, even at significantly reduced temperatures presents a number of challenges, which most notably involves the generation of a machining phenomenon termed adiabatic shear band formation. This is only evident in materials that exhibit low thermal conductivity and this includes the common

metals, titanium and stainless steel. As a result, these two materials often present challenges when being machined, which include rapid tool degradation and increased surface roughness. This paper demonstrates the state of the art in cryogenic manufacturing and the novel concept of cryogenic CNC machining of elastomers. Using this process, a number of sample chips produced during the cryogenic machining of EVA and solid neoprene are shown to depict the formation of adiabatic shear bands.

2. Adiabatic shear band formation

The adiabatic shear formation is a region on a chip where the ductile properties of the material being machined have been exceeded, leading in some cases to permanent material damage and increased surface roughness. When machining elastomeric materials, this has the potential to be even more evident, leading to potentially inferior products.

Serrated chips and adiabatic shear band formation is often observed in machining materials that exhibit poor thermal properties such as low thermal conductivity or low specific heat and as a result the inability to dissipate heat rapidly [1]. An adiabatic shear band can be defined as a narrow, nearly planar region of very large shearing that occurs in some metals and alloys as they experience intense dynamic loading at the point of cut [2] and in the case of cryogenic CNC machining, rapid and intense changes in material temperature. Materials that exhibit poor thermal properties, such as plastics, rubbers and to some extent titanium, generate heat within the shear zone, which does not have sufficient time to escape. This raises the temperature of the cutting zone leading to an adiabatic shear band formation, which is more evident in machining an elastomeric material such as a rubber [3]. Adiabatic shear bands are the results of thermo-chemical instabilities at the point of cut [4].

It has also been recognised that shear bands form as a result of the balance between hardening and softening of the material [4]. During a machining cycle, plastic strain

incompatibilities are initiated near defects at the cutting interface thus achieving localised stress concentrations, leading to chip breakage. If the strain rate is high enough, the process is classified as adiabatic [5]. The adiabatic shear instability modifies the chip formation, thus the chip become segmented and chip breaking becomes difficult [6]. A considerable amount of research in adiabatic shear band formation has been conducted on turning applications [4, 7, 8].

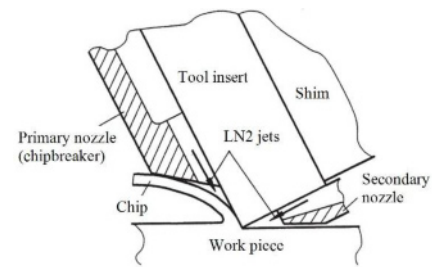


Fig 1: Cryogenic spray jetting – Two nozzles [16].

3. State of the art in cryogenic manufacturing

The application of cryogenic science is not new technology and was first used to liquefy oxygen and nitrogen [9]. It was subsequently used to improve the structural properties of steel parts by placing them in cold environments, such as the Swiss did during the Second World War [10]. In the middle part of the last century, liquid oxygen and liquid hydrogen were used as propellants for rockets, with the first being the infamous Nazi V2 rocket [11]. Recently cryogenic science has been used in two major areas, namely, cryogenic processing and hard metal machining.

3.1 Cryogenic processing

Cryogenic processing involves placing metal parts into a nitrogen environment to permanently convert the retained austenite into the harder constituent martensite, providing a structurally stronger component. This increases the part hardness, reduces stresses within the part and increases fatigue resistance [12]. Schiradelly *et al.* [13] discuss the use of cryogenics in various different branches of motor sport engineering, showing that parts have increased life span as a result of the cryogenic process, without suffering any detrimental affect. Wurzbach *et al.* [10] examined a silicate bronze alloy impeller, which was degrading rapidly in use. A cryogenic process was used to treat the impeller and was shown to improve its hardness and wear resistance, thus extending its life indefinitely.

3.2 Cryogenic hard metal machining

Cryogenic hard metal machining is where the majority of academic literature is focused and is concerned with using liquid nitrogen (LN₂) in place of conventional oil based coolants, primarily in CNC turning applications. A number of authors have identified systems for cryogenic hard metal machining involving spray-jetting systems [14-17]. Hong *et al.* [16] developed the system as illustrated in figure 1 for turning of titanium alloy using carbide tooling. The principal aim of this configuration was to apply the LN₂ to the primary and secondary cutting zones to reduce heat build up and to rapidly remove any swarf build up.

Wang *et al.* [18] describe a spray jetting system used for machining hard-to-cut materials, where a single LN₂ nozzle setup was designed to penetrate the cutting zone. Unlike other systems there is a reservoir, which allows for constant LN₂ flow. These are two examples of systems developed for cryogenic hard metal CNC turning. There is minimal research on using cryogenic methods for vertical CNC machining.

The notable exception is a study conducted by Rahman *et al.* [19] on chilled air machining in end milling. The experiment consisted of using two nozzles, which directed chilled air (-30°C) towards the tip of the milling cutter. The results obtained illustrate that chilled air can offer comparable results to flood cooling, and in some cases proves to be better.

There is limited research concerned with cryogenic elastomer machining. The exception being Shih *et al.* [3] who investigated the machining of solid carbon dioxide cooled elastomers and elastomer chip morphology analysis [1]. The conclusion of the study showed that end milling of elastomers performed better when the elastomer was cryogenically cooled.

3.3 Cryogenic CNC machining of elastomers

The use of soft elastomeric material machining is based on the need to remove the moulding process, which can be expensive and does not allow for constant design change. Direct CNC machining of elastomers provides the ability to change designs instantaneously, providing a realistic opportunity to produce personalised products and support a method in which the concept of on demand manufacture for consumer products is achievable.

The cryogenic machining facility at the University of Bath has been designed to machine a range of soft materials, which include neoprene and EVA. The major aim of the cryogenic process is to freeze a soft material below its glass transition temperature (T_g) value and then to directly machine it. T_g is the temperature at which a material shows similarities to that of a glass type structure. Figure 2 provides a representation of the cryogenic soft material machining process for producing personalised shoe soles.

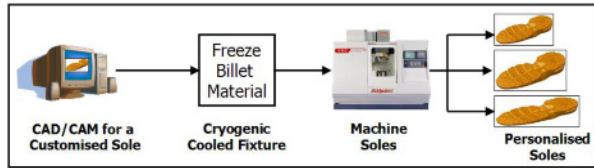


Fig 2: The cryogenic machining concept for soft materials

The cryogenic CNC machining facility consists of a cryogenic fixture designed to securely clamp a test part sample and 18mm diameter vacuum jacketed piping that feeds directly from a 120-litre high pressure Dewar into a custom designed fixture. The temperature of the fixture is monitored using a thermal probe. Material is placed directly into the fixture and is cooled using LN₂. It is at this point that the material can be effectively machined.

4. Methodology

Using the cryogenic CNC machining process a number of materials were machined. The following section provides examples of the Scanning Electron Microscope (SEM) chip morphology images for chips produced by the cryogenic machining experiments, which clearly indicate adiabatic shear band formations in three of the images.

5. Experimental Results

A number of sample chips were taken from the machining experiments and analysed using an SEM. Figure 3 illustrates a sample of chips taken from a design of experiments machining strategy. Some of the chips can be seen to have smooth, clean cut surfaces, others have many lines, creases and curled edges and are not always separated from their neighbour.

Figure 4 shows a machined chip sample of solid neoprene rubber, showing a series of lines, which are considered to be examples of adiabatic shear band formations. The wavy line patterns that can be seen on the chip surface is indicative of the adiabatic phenomenon that is observed in materials that have low thermal conductivity. This is due to the inability of the material to dissipate the heat generated fast enough, which is a function of two things. Unlike with first sample, the depth of cut is smaller therefore this suggests that the freezing process was not keeping the cutting interface temperature at or below its T_g value, thus resulting in the adiabatic shear band forming. The chip is considered to be adequate, however there are significant deformation indications. The adiabatic shear band formation is a key indicator for the cryogenic CNC machining process as this demonstrates insufficient freezing of the elastomer being machined. This would ultimately result in a poorly machined part, with weakened areas.



Fig 3: A sample of solid Neoprene chips produced using the cryogenic CNC machining process

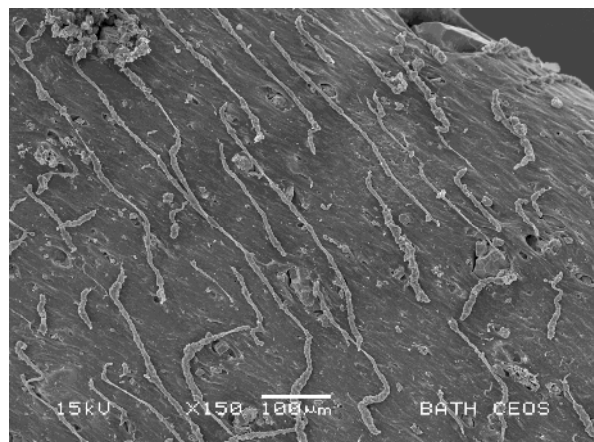


Fig 4: A machined Neoprene sample chip with adiabatic shear band across the chips surface

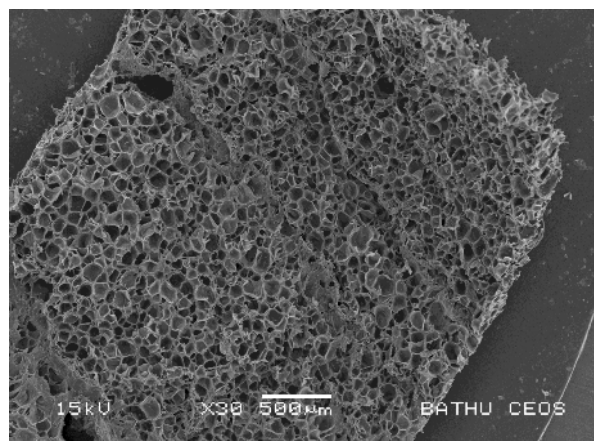


Fig 5: A machined EVA sample chip with adiabatic shear bands across the surface

Figure 6 depicts a chip surface with little adiabatic shear band formations, which suggests that the material T_g has been maintained throughout the machining cycle. This is an

ideal machining scenario as this is likely to reduce material damage and reduce surface roughness.

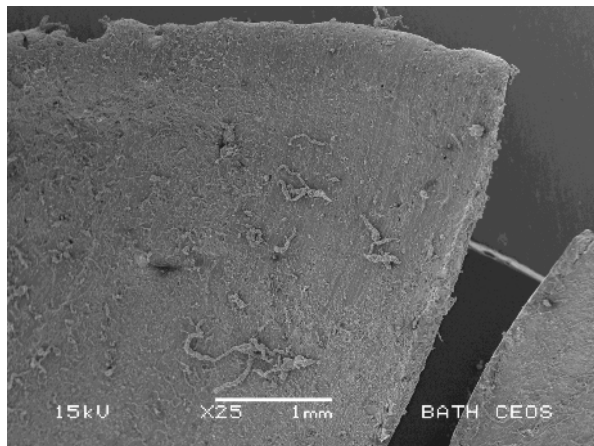


Fig 6: A machined EVA sample chip, with no indicated shear bands

6. Conclusions

This paper has illustrated and demonstrated a new process for rapidly machining elastomeric material on conventional CNC machine tools using liquid nitrogen freezing techniques. The phenomenon of adiabatic shear band formation has also been demonstrated as a result of the cryogenic machining process. The results from the SEM micrograph imaging show clear indications of shear band formations across the chip surface as a result of not maintaining material T_g throughout the process and this is considered to be undesirable as it is likely to affect the materials surface quality. Ideally, providing the materials T_g is maintained, the adiabatic shear band formation will remain relatively small and provide adequately machined elastomer products.

References

- [1] Shih, A.J., Luo, J., Lewis, A.M. and Strenkowski, J.S., Chip morphology and forces in end milling of elastomers. *Transactions of the ASME*, **126**, (2004), pp.
- [2] Wright, T.W., *The physics and mathematics of adiabatic shear bands*. 2002, Cambridge: Cambridge University Press.
- [3] Shih, A.J., Lewis, M.A. and Strenkowski, J.S., End milling of elastomers fixture design and tool effectiveness for material removal. *Journal of Manufacturing Science and Engineering*, **126**, (2004), pp. 115 - 123.
- [4] Molinari, A., Musquar, C. and Sutter, G., Adiabatic shear banding in high speed machining of Ti-6Al-4V: Experiments and modeling. *International Journal of Plasticity*, **18** (4), (2002), pp. 443-459.
- [5] Bassim, M.N., Study of the formation of adiabatic shear bands in steels. *Journal of Materials Processing Technology*, **119** (1-3), (2002), pp. 234-236.
- [6] Ning, Y., Rahman, M. and Wong, Y.S., Investigation of chip formation in high-speed end milling. *Journal of Materials Processing Technology*, **113**, (2001), pp. 360 - 367.
- [7] Belhadi, S., Mabrouki, T., Rigal, J-F. and Boulanour, L., Experimental and numerical study of chip formation during straight turning of hardened AISI 4340 steel. *Proceedings for the Institute of Mechanical Engineers Part B: Journal of Engineering Manufacture*, **219**, (2005), pp. 515-524.
- [8] Burns, T.J. and Davies, M.A., On repeated adiabatic shear band formation during high-speed machining. *International Journal of Plasticity*, **18** (4), (2002), pp. 487 - 506.
- [9] Hands, B.A., *Cryogenic engineering*, ed. B.A. Hands. 1986, London: Academic press.
- [10] Wurzbach, R.N. and Defelice, W., Improving component wear performance through cryogenic treatment. *Lubrication Excellence*, Noria Corporation, (2004), pp.
- [11] Timmerhaus, K.D. and Flynn, T.M., *Cryogenic process engineering*. 2nd edition ed. International Cryogenics Monograph Series, ed. Klaus D. Timmerhaus and T.M. Flynn. 1989, New York: Plenum press.
- [12] Reitz, W. and Pendray, J., Cryoprocessing of materials: A review of current status. *Materials and Manufacturing Processes*, **16** (6), (2001), pp. 829 - 840.
- [13] Schiradellay, R. and Diekman, F.J., Cryogenics, the racer's edge. *Heat Treating Progress*, (2001), pp. 43 - 49.
- [14] Wang, Z.Y., Rajurkar, K.P., Fan, J., Lei, S., Shin, Y.C. and Petrescu, G., Hybrid machining of inconel 718. *International Journal of Maching Tools and Manufacture*, **43**, (2003), pp. 1391 - 1396.
- [15] Hong, S.Y., Markus, I. and Jeong, W.C., New cooling approach and tool life improvement in cryogenic machining of titanium alloy Ti-6Al-4V. *International Journal of Machine Tools and Manufacturing*, **41**, (2001), pp. 2245 - 2260.
- [16] Hong, S.Y., Ding, Y. and W-C., J., Friction and cutting forces in cryogenic machining of Ti - 6AL-4V. *International Journal of Machine Tools and Manufacture*, **41**, (2001), pp. 2271 - 2285.
- [17] Venugopal, K.A., Tawade, R., Prashanth, P.G., Paul, S. and Chattopadhyay, A.B., Turning of titanium alloy with TiB2 - coated carbides under cryogenic cooling. *Proceedings of International Mechanical Engineers*, **217**, (2003), pp. 1697 - 1707.
- [18] Wang, Z.Y. and Rajurkar, K.P., Cryogenic machining of hard to cut materials. *Wear*, **239**, (2000), pp. 168 - 175.
- [19] Rahman, M., Kumar, A.S., Salam, U.-M. and Ling, M.S., Effect of chilled air on machining performance in end milling. *The International Journal of Advanced Manufacturing Technology*, **21**, (2003), pp. 787 - 795.

Analysis of process parameters in the micromachining of Ti-6Al-4V alloy

S.I. Jaffery, N. Driver and P.T. Mativenga

School of Mechanical, Aerospace and Civil Engineering, The University of Manchester, M1 3BB, UK

Abstract. The demand for manufacturing technologies for micro components and features has been increasing in aerospace, biomedical, electronics, environmental, communications and automotive industries. Since titanium alloys are widely used in aerospace and biomedical applications, the development of micromachining technologies for these materials is of particular interest. This study employs statistical analysis techniques to evaluate the contributions of the different process parameters towards tool life and product quality in micro-milling in comparison with macro-milling. The establishment of key process variables would ultimately help in reducing production costs by reducing the cost of tool replacement and minimizing product rejection.

Keywords: micromachining, titanium alloy, analysis of variance

1. Introduction

Most traditional manufacturing processes are unable to create micro-features with required dimensional accuracy [1]. In such applications, mechanical micro machining is a candidate process. Micromachining can be defined as mechanical machining of features with tool engagement less than 1 mm, exploiting geometrically defined cutting edges [2]. An alternative description of micro machining defines the process in terms of the workpiece grain size, when the uncut chip thickness is less than the average size of the smallest grain type [3]. Specific to the milling process, there is a suggestion in literature that micro-milling should be defined as the process that utilizes endmills varying in diameter from 100-500 μm , with edge radii in the range from 1-10 μm [4]. The view of the authors is that micro milling is machining with tools of diameter 1 to 999 μm and this process can take place when the tool edge radius is comparable to the material grain size or undeformed chip thickness.

Mechanical micromachining demands research due to variations brought by work materials, component interfaces and functional shapes [5]. In most cases, an edge radius comparable or larger than the undeformed chip thickness leads to a high effective negative rake angle, promoting material elasto-plastic effects. Thus a major difference between macro and micromachining is

the increase in the workpiece material's shear flow stress with decrease in the size of the uncut chip thickness.

Typically in micro machining, the undeformed chip thickness is of the order of microns or less [6] and as a result, the workpiece material can not be assumed homogenous due to the presence of different phases and grain sizes that the tool is likely to encounter. Added to these issues are the effects of material strain hardening, subsurface plastic deformation and material separation effects. With regards to the material microstructure effects, it has been reported that when the tool dimensions or a feature to be generated is of the same order as the grain size, the material cannot be treated as isotropic [2]. In this case, the cutting mechanism differs substantially from macromachining.

1.1 Titanium alloys in micromachining applications

The typical applications of titanium based alloys are in the aerospace and medical applications due to their high strength to weight ratio, corrosion resistance and biocompatibility. Both these fields rely heavily on the use of micro microfeatures and components. Biotechnology in particular has been cited as having vast potential for micro-parts as medical tools are increasingly operating at cellular level [7]. Furthermore, since both aforementioned fields also require stringent quality checks, research into the micromachining of titanium alloys is of particular interest. While considerable research is being carried out in the micromachining of ferrous alloys, as a science, micromachining of titanium alloys is still considered to be in its rudimentary stage [8]. The challenge in machining titanium alloys is chiefly the high tool wear associated with the reactivity of titanium with tool materials, and its low thermal conductivity [9]. Moreover, the development of suitable tool coatings is still in progress for these alloys. For any industrial process, determination of the effects of input parameters on productivity is of paramount importance. This study therefore aims to quantify the effects of machining parameters, namely feedrate (f), cutting speed (V_c) and depth of cut (a_p) on tool life and surface finish. It also aims to investigate the feasibility of generating process

maps of flank wear and surface roughness for micromachining titanium based alloys by analysing the key process variables (KPV's) for micromilling.

2. Experimental details

Slot milling experiments were designed using L4 arrays to carry out statistical process analysis. Since L4 arrays accommodate linear effects, the levels of parameters were selected such that the arrays do not cover points of inflection that have been reported by previous literature [6, 10, 11]. These points are expected to lie at feedrates equal to minimum chip thickness and tool edge radius. Accordingly, two sets of micro milling conditions were selected. In the first set, the feedrates values were varied from the minimum chip thickness to the average tool edge radius. In the second set, the feedrate values ranged from the average tool edge radius to the upper limit recommended by the tool suppliers.

The tools used in the micromachining experiments were 500 μm diameter DIXI-7240 uncoated carbide tools. The average grain size of the tools as reported by the manufacturers was 0.2 to 0.5 μm . The macro-milling tests used TPMN160308-H13A inserts manufactured by Sandvik. These inserts were mounted on a 32 mm diameter end-mill tool holder. These tools are representative of those actually used in industrial operations. It may also be noted that while single flute tools are recommended for research purposes to minimize runout effects, such tools are rarely produced and used for industrial micro-milling. All unused micro-milling tools were first examined under a Hitachi S3400N scanning electron microscope (SEM) for their edge radii. Care was taken and only tools having minimum variation in their edge radii were selected from the set. Figure 1 shows a typical micrograph obtained for this purpose. The mean edge radius for the tools used was found to be on average 1 μm (varying between 0.8-1.2 μm).

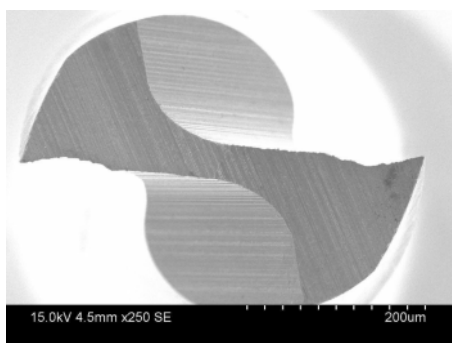


Fig. 1. A typical microtool as seen under an SEM

For comparison with macromilling operations, a set of macromilling experiments was similarly conducted based on the L4 array. The parameters were selected based on

ranges of values recommended by the tool manufacturers. All micromilling experiments were conducted on a Mikron® HSM 400 vertical milling machine while macromilling experiments were conducted on a Takisawa vertical milling center. The two machines used are typical of milling platforms used in micro and macroscale cutting domains. The accuracy of each of the machines is appropriate for micro and conventional machining respectively. The results obtained in conventional machining agree with known trends and hence supporting the use of the Takisawa machine in the investigation. All experiments, macro as well as micro-milling tests were conducted in dry conditions so as not to mask the effects of process variables.

2.1 Determination of minimum chip thickness

The minimum chip thickness (t_c) can be defined as the minimum undeformed thickness of chip that can be removed stably from a work surface for a given cutting edge radius [12]. Since minimum chip thickness is directly related to the tool edge radius [13], advances in tool manufacturing that lead towards sharper tool edges and less fragility can reduce t_c . Typically, the values for minimum chip thickness range from 5-43% of the tool edge radius [6]. The variation in these values can be attributed to the elastic/plastic deformation of the different workpiece materials considered as well as tool rigidity. Tool sharpness has been reported to have a strong influence on the machined surface integrity in terms of its surface roughness, microhardness, residual stress and the dislocation density [14].

The first step towards defining the experimental plan was to define the machining parameters for the L4 arrays based on the objectives mentioned in section 3. For this purpose, the minimum chip thickness for the workpiece material was determined using the procedure proposed by Liu et al [15]. In this method, the sudden surface height change, that is generated with transition from rubbing / ploughing to chip formation phase, is measured. Milling tests were conducted for different feedrates over the range recommended by the tool suppliers. The side wall surface was then examined using a WYKO® NT-1100 white light interferometer (Vertical Measurement: 0.1 nm to 1 mm, Vertical Resolution: 0.1 nm, RMS Repeatability: 0.01 nm [16]). Figure 2 shows the value for minimum chip thickness obtained using this method. The average value for this parameter comes out to be around 0.4 μm . The levels of feedrate for the L4 array was set from this knowledge of the minimum chip thickness. All experiments were repeated twice to confirm repeatability of results.

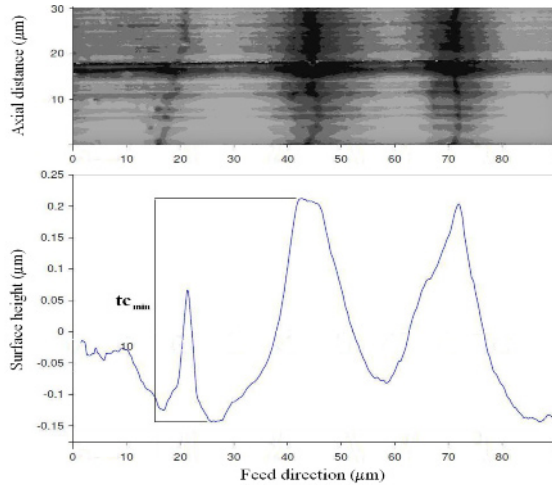


Fig. 2. Minimum chip thickness obtained from the surface profile

3. Results and Discussions

The experimental results were obtained in the form of the surface roughness of the milled slots (R_a) and tool flank wear (VB). These results are presented in the form of L4 arrays in tables 1 and 2 respectively. The tool flank wear was determined by examining the used tools under the scanning electron microscope. The surface of the micro-slots was examined using WYKO® NT-1100 white light interferometer while the surface roughness for macro-milling tests was measured using Talysurf surface profiler along the feed direction. For accuracy, the surface roughness was measured at 5 equidistant locations on the slot floor and the average of these values were used in the analysis. The values obtained are of the order reported by previous researchers [6, 10, 17].

3.1 Analysis of variance

After having designed the experiments, the results obtained were statistically analyzed using the statistical tool known as *analysis of variance* (ANOVA). The basic

idea behind ANOVA is to break down the total variability of the experimental results into components of variance and then assess their significance in terms of contribution ratio (CR) [18]. The variation components are those associated with factor effects or random variation (residual). The contribution ratios of machining parameters towards surface roughness and tool flank wear were calculated using the standard statistical formulae [18]. Table 3 presents ANOVA for surface roughness.

Analysis of main effects for surface roughness (R_a) indicates that below edge radius, low feed, low cutting speed and high depth of cut give better surface finish. When operating above the edge radius, low R_a occurs at low feed, high cutting speed and low depth of cut; a trend consistent with that shown in the case of macro milling. In macroscale milling, the feedrate is the most dominant parameter to control surface finish at 90% significance, compared with 83% in micro milling above the edge radius. When cutting below the edge radius, all three variables have a significant effect on surface finish. In this case, feedrate is most dominant at 53%. The optimal process variables amongst those tested were found at $f = 0.45 \mu\text{m/tooth}$, $V_c = 25 \text{ m/min}$ and $a_p = 60 \mu\text{m}$ when machining with undeformed chip thickness below edge radius. Above the edge radius these parameters occur at $f = 3 \mu\text{m/tooth}$, $V_c = 50 \text{ m/min}$ and $a_p = 30 \mu\text{m}$ while during macro-milling these are found to be $f = 0.1 \text{ mm/tooth}$, $V_c = 75 \text{ m/min}$ and $a_p = 1 \text{ mm}$.

Table 4 presents ANOVA for flank wear, where residual effects were found to be more dominant. Unlike the case for macro-milling, the contribution of random variables (Res) on tool wear for micro-milling is significantly higher. Micro-milling below edge radius appears more prone to residual effects than micro-milling above edge radius. This can be attributed to the fact that the fragile microtools are more prone to small changes in environmental variables. In the case of macro-machining, these variations are essentially negligible. When micro-machining below edge radius, tools are more prone to residual effects for flank wear. This trend can be linked to the reduced tool stability in the latter case as minimum chip thickness and elastic recovery effects become more

Table 1 Levels of the cutting parameters in the L4 arrays for surface roughness (R_a)

Micro milling below edge radius				Micro milling above edge radius				Macro-milling			
f ($\mu\text{m}/\text{tooth}$)	V_c (m/min)	a_p (μm)	R_a (μm)	f ($\mu\text{m}/\text{tooth}$)	V_c (m/min)	a_p (μm)	R_a (μm)	f (mm/tooth)	V_c (m/min)	a_p (mm)	R_a (μm)
0.45	25	30	0.058 0.062	3	25	30	0.219 0.216	0.10	50	1.0	0.29 0.30
0.45	50	60	0.073 0.083	3	50	60	0.201 0.198	0.10	75	1.5	0.28 0.26
0.90	25	60	0.100 0.109	6	25	60	0.342 0.340	0.15	50	1.5	0.53 0.55
0.90	50	30	0.238 0.241	6	50	30	0.280 0.277	0.15	75	1.0	0.48 0.46

Table 2 Levels of the cutting parameters in the L4 arrays for flank wear (VB)

Micro milling below edge radius				Micro milling above edge radius				Macro-milling			
f ($\mu\text{m}/\text{tooth}$)	V_c (m/min)	a_p (μm)	VB (μm)	f ($\mu\text{m}/\text{tooth}$)	V_c (m/min)	a_p (μm)	VB (μm)	f (mm/tooth)	V_c (m/min)	a_p (mm)	VB (μm)
0.45	25	30	12.1 9.0	3	25	30	7.1 11.0	0.10	50	1.0	39 37
0.45	50	60	14.1 15.0	3	50	60	15.1 13.9	0.10	75	1.5	47 50
0.90	25	60	12.2 8.1	6	25	60	14.1 17.0	0.15	50	1.5	58 56
0.90	50	30	11.6 8.1	6	50	30	15.9 16.8	0.15	75	1.0	62 59

Table 3 ANOVA for surface roughness (Ra) vs cutting parameters

Source	df	Micro milling below edge radius				Micro milling above edge radius				Macro-milling			
		SS	MSS	F-ratio	CR	SS	MSS	F-ratio	CR	SS	MSS	F-ratio	CR
f	1	21189	21189	829	53	20564	20564	5251	83	0.09	0.09	271	92
V_c	1	11705	11705	458	29	3265	3265	834	13	0.01	0.01	19	6
a_p	1	6920	6920	271	17	970	970	248	4	0.00	0.00	1	0
Res	4	102	26		1	16	4		0	0.00	0.00		1
Total	7	39917			100	24815			100	0.10			100

Table 4 ANOVA for flank wear (VB) vs cutting parameters

Source	df	Micro milling below edge radius				Micro milling above edge radius				Macro-milling			
		SS	MSS	F-ratio	CR	SS	MSS	F-ratio	CR	SS	MSS	F-ratio	CR
f	1	13.29	13.29	2.67	17	34.86	34.86	10.93	41	338	338	71	69
V_c	1	6.90	6.90	1.39	4	19.41	19.41	6.09	21	85	85	18	17
a_p	1	9.42	9.42	1.89	9	10.63	10.63	3.33	10	41	41	9	7
Res	4	19.92	4.98		70	12.76	3.19		28	19	5		7
Total	7	49.52			100	77.65			100	482			100

dominant. Overall, the results show that micro-machining above edge radius tends to be closer to macro-machining rather than micro-machining below edge radius. This is despite the fact that both types of micro-machining experiments were performed on the same machine, while macro-machining experiments were carried out on a different machining centre.

4. Conclusions

- The dominance of cutting parameters differs in micro-machining as compared with macro-machining.
- While feedrate is the dominant factor in macro-milling for control of surface roughness, the contribution ratio of cutting velocity and depth of cut increases in the micro domain.
- Micro-milling operations carried out above tool edge radius are easier to predict and control as compared with those done below edge radius due to less contribution of residual effects on tool life and surface finish.
- In micromachining, the contribution of process variables is more deterministic on surface roughness while tool wear is driven by stochastic factors.

Acknowledgements

The authors would like to thank the support offered by the Engineering and Physical Sciences Research Council (EPSRC) UK under the ELMACT grant DT/E010512/1.

References

- [1] Kim C-J, Bono M, Ni J (2002), Experimental analysis of chip formation in micromilling. *Trans. of NAMRI*; XXX:247-54.
- [2] Dornfeld D, Mina S, Takeuchi Y (2006), Recent Advances in Mechanical Micromachining. *CIRP Annals - Manuf. Tech.* 55(2):745-68
- [3] Simoneau A, Ng E, Elbestawi MA (2006), Chip formation during microscale cutting of a medium carbon steel. *Int'l J. Machine Tools and Manuf.* 46(5):467-81.
- [4] Vogler MP, DeVor RE, Kapoor SG (2004), On the Modeling and Analysis of Machining Performance in Micro-Endmilling, Part I: Surface Generation. *J. of Manuf. Sci and Eng.* 126(4):685-94
- [5] Chae J, Park SS, Freight T (2006), Investigation of Micro-cutting Operations. *Int'l J. of Mach. Tools & Manuf.* 46:313-32.
- [6] Mian AJ, Driver N, Mativenga PT (2009), Micromachining of coarse-grained multi-phase material. *Proc. Inst. of Mech. Eng. B: J. of Engg Manuf.* 223(4):377-85.
- [7] Masuzawa T (2000), State of the Art of Micromachining. *CIRP Annals - Manuf. Tech.* 49(2):473-88.
- [8] Schueler GM, Engmann J, Marx T, Haberland R, Aurich JC. Burr Formation and Surface Characteristics in Micro-End Milling of Titanium Alloys. *Proc. CIRP Int'l Conf. on Burrs.* Univ. of Kaiserslautern, Germany: 2009.
- [9] Jaffery SI, Mativenga PT (2009), Assessment of the Machinability of Ti-6Al-4V Alloy using the Wear Map Approach. *Int'l J. of Adv. Manuf. Tech.* 40:687-96.
- [10] Mian AJ, Driver N, Mativenga PT (2010), A comparative study of material phase effects on micro-machinability of multiphase materials. *Int'l J. of Adv. Manuf. Tech.* DOI: 10.1007/s00170-009-2506-9
- [11] Son SM, Lim HS, Ahn JH (2005), Effects of the friction coefficient on the minimum cutting thickness in micro cutting. *Int'l J. of Mach. Tools & Manuf.* 45:529-35.
- [12] Taniguchi N (1983), Current Status in, and Future Trends of, Ultraprecision Machining and Ultrafine Materials Processing. *CIRP Annals - Manuf. Tech.* 32(2):573-82
- [13] Ikawa N, Shimada S, Tanaka H (1992), Minimum thickness of cut in micromachining. *Nanotechnology.* 3:6-9.
- [14] Yuan ZJ, Zhou M, Dong S (1996), Effect of diamond tool sharpness on minimum cutting thickness and cutting surface integrity in ultraprecision machining. *J. of Mat. Proc. Tech.* 62(4):327-30.
- [15] Liu X, DeVor RE, Kapoor SG (2006), An analytical model for the prediction of minimum chip thickness in micromachining. *J. of Manuf. Sci. and Eng.* 128:474-81.
- [16] Wyko NT 1100 Optical Profilers Brochure (2003)
- [17] Mantle AL, Aspinwall DK (2001), Surface integrity of a high speed milled gamma titanium aluminide. *J. of Mat. Proc. Tech.* 118(1-3):143-50.
- [18] Logothetis N. Managing for total quality-from Deming to Taguchi and SPC. Hertfordshire: Prentice Hall Int'l (UK) Ltd.; 1992.

Tool Orientation Effects on the Geometry of 5-axis Ball-end Milling

Erdem Ozturk and Erhan Budak¹

¹ Manufacturing Research Laboratory, Sabanci University, Istanbul, Turkey
Tel: +90 216 483 95 19, Fax: +90 216 483 95 50

Abstract. 5-axis ball-end milling has found application in various industries especially for machining of parts with complex surfaces. Additional two degree of freedoms, namely, lead and tilt angles make it possible to machine complex parts by providing extra flexibility in cutting tool orientation. However, they also complicate the geometry of the process. Knowledge of the process geometry is important for understanding of 5-axis ball-end milling operations. Although there are considerable amount of work done in 3-axis milling, the literature on 5-axis ball-end milling is limited. Some of the terminology used in 3-axis milling is not directly applicable to 5-axis ball end-milling. Hence some new process parameters and coordinate systems are defined to represent a 5-axis ball end-milling process completely. The engagement zone between the cutting tool and the workpiece is more involved due to the effects of lead and tilt angles. In this paper, effects of these angles on the process geometry are explained by presenting CAD models and analytical calculations.

Keywords: 5-axis, ball-end milling, lead and tilt angles, process geometry

1. Introduction

5-axis milling is a geometrically complex process since there are two additional rotational degrees of freedom, namely lead and tilt angles, compared to 3-axis milling. They define the cutting tool orientation with respect to surface normal direction. Visualization of their effect on the process geometry is not straightforward; however, the understanding of the process geometry is a very important step in process modeling. Hence, in this paper, the effects of lead and tilt angles on the process geometry are presented.

There has been considerable amount of work done on modelling of sculptured surface geometry in 3-axis ball-end milling. Although rotational degrees of freedoms are not available in 3-axis ball-end milling, there may be inclination in both feed and cross-feed directions due to CNC interpolations on the sculptured surface. Geometry of these processes is similar to the 5-axis ball-end milling geometry. Imani et al. [1] presented machining cases with up-hill angle in 3-axis ball-end milling which corresponds to application of positive lead angle in 5-axis ball-end milling. For different up-hill angles they showed the

calculated engagement boundaries which are determined using the ACIS geometric engine [2]. Later, Kim et al. [3] included the effect of tilt angle on the engagement region. In their notation, ramping corresponds to application of lead angle while contouring matches with the application of tilt angle. Combined effect of lead and tilt angle on the engagement region on the ball-part of the tool was shown by Lamikiz et al. [4] by cutting an inclined plane with a sloped feed direction in a 3-axis milling machine tool. Later, Fontaine et al. [5] applied the same notation with Kim et al. [3] for different machining strategies but added the effect of cross-feed direction where they refer to it as up/down milling. In this paper, the terminology in 5-axis ball end milling is introduced firstly. The process parameters and coordinate systems are defined. Then, combined and independent effects of lead and tilt angles on engagement regions between the tool and workpiece are explained by CAD models and analytical calculations. For the engagement calculations, engagement model presented by Ozturk and Budak [6] is used. In this model, the engagement regions in both ball and cylindrical zones can be calculated. Effect of lead and tilt angles on maximum uncut chip thickness is also illustrated on a representative case.

2. Terminology in 5-axis ball-end milling

In order to represent position and orientation of a cutting tool at an instantaneous point along a tool path, three coordinate systems need to be defined (Fig. 1(a)). The first one is a fixed coordinate system called the machine coordinate system (MCS). It consists of X, Y, Z axes of the machine tool, its origin is the home position. The second one is the process coordinate system (FCN). In the FCN coordinate system, F is the feed direction, C is the cross-feed direction and N is the surface normal direction. The origin of the FCN is at the ball-centre of the cutting tool, and thus it is a moving coordinate system. Moreover, F, C and N directions change along a tool path depending on the workpiece geometry and machining

strategy selected. Tool coordinate system (TCS) is the third coordinate system and its origin is also the ball centre of the tool. x and y axes are transversal axes of the tool and z is along the tool axis direction. TCS defines the orientation of the cutting tool with respect to FCN. Lead angle defines the rotation of the cutting tool around C axis whereas the tilt angle is the rotation of the tool around F axis (Fig.2). Therefore, TCS is the rotated form of FCN with lead and tilt angles.

Some of the terminology in 3-axis milling is not directly applicable to 5-axis milling for definition of the process parameters. Due to the effects of lead and tilt angles, the tool axis is not parallel to the surface normal (Fig.2). Hence, the cutting depth term (a) is used to define the depth removed from the workpiece in the surface normal direction instead of the axial depth term (Fig. 3(a)).

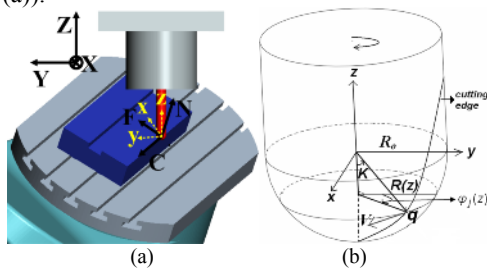


Fig. 1. (a)Coordinate systems (b) Ball-end mill geometry.

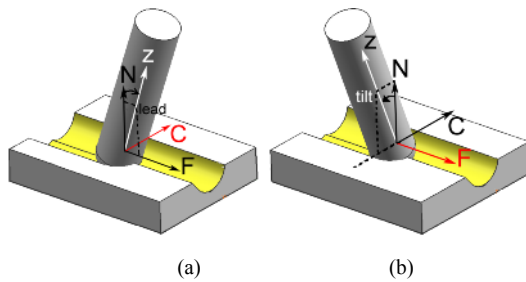


Fig. 2. (a)Lead angle (b) Tilt angle.

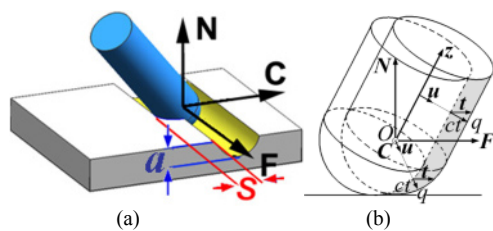


Fig. 3. (a)Cutting depth a , step over s (b)Uncut chip thickness ct

Radial depth term is replaced with step over term as radial depth expression may result in confusion due to the effects of ball-end mill geometry, lead and tilt angles on radial directions. The step over s is the distance between the adjacent tool paths in C axis as shown in Fig. 3(a). Milling mode, i.e. up and down milling, definitions can be ambiguous for 5-axis ball-end milling due to the complex engagement regions. Because of the effects of tool geometry, lead and tilt angles, there may be two

different immersions zones which cannot be represented with a start and exit angle pair. For that reason, another parameter, cross-feed direction is used in order to define the direction of the uncut material. If uncut material is in the positive C axis with respect to the milling tool, the cross-feed direction is positive, and vice-versa. For example, in the cases presented in Fig.2 and Fig. 3(a), the cross-feed direction is negative. Cases with positive and negative cross-feed direction are analogous to up and down milling in 3-axis end milling, respectively, in the sense of the uncut material direction. After lead, tilt angles, cutting depth, step over and cross-feed direction parameters are defined at an instant, the instantaneous relative position and orientation of cutting tool with respect to workpiece are completely defined. Uncut chip thickness ct (Fig. 3(b)) is variable along the cutting edge locally in both tangential and axial directions. Local uncut chip thickness depends also on lead and tilt angles as formulated in [6].

3. Engagement regions and uncut chip thickness under the effects of lead and tilt angles

The visualization of effects of lead and tilt angles on the engagement regions between the tool and workpiece is not very easy in 5-axis ball-end milling. In this section, their effects are shown by CAD models and simulations. For calculation of engagement regions, a previously developed engagement model [6] is applied on representative cases. In the example case, cutting depth, step over and radius of the ball-end mill are 6 mm. Helix angle on the clockwise-rotating tool is 30° and cross-feed direction is negative.

In the absence of lead and tilt angles, CAD model of the process is shown in Fig.4. In this case, TCS and FCN coincide. The projection views of the 3D engagement region in two orthogonal planes namely, CN and CF planes, are also presented in Fig.4. It's seen that the engaged region is variable along the tool axis. The variation of engagement boundaries along the tool axis is plotted in Fig.4 where ϕ_{st} and ϕ_{ex} represent start and exit angles, respectively. There is 180° immersion close to the tool tip ($z=-6\text{mm}$) while the immersion width decreases for the higher z positions. As the name implies, immersion width is defined as the amount of angular immersion at a z -level.

When lead and tilt angles are applied on the cutting tool, the shape of the engagement region changes. This is illustrated for application of 30° lead and tilt angles in Fig. 5 where the calculated engagement boundaries are also presented. In this case, it's seen that both ball and cylinder zones of the cutting tool are in contact with the workpiece.

Positive lead angle shifts the engagement region to the higher positions along the tool axis while negative lead angle moves the engagement to the lower sides of the tool. Moreover, lower immersion widths takes place

with positive lead angles with respect to negative lead angle cases. In order to justify these comments, effect of lead angle on the immersion width on different z-coordinates is presented in Fig. 6 for the example case. Since it is a 3D surface, the 2D projections of the surface in two orthogonal planes are also plotted in the figure to show the variation with more detail. Norm_z is the ratio of z-coordinate with respect to ball-end mill radius. It is seen that the comments about the effect of lead angle and observations from the Fig.6 match well. Although not presented here, similar effects are also seen for lower and higher cutting depth and step over cases.

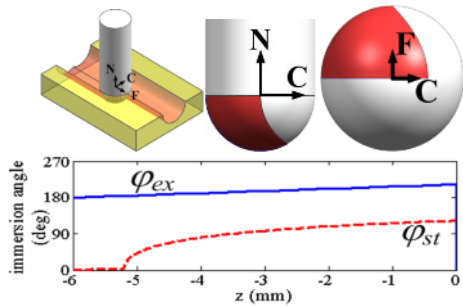


Fig. 4. Engagement region (lead,tilt=0°)

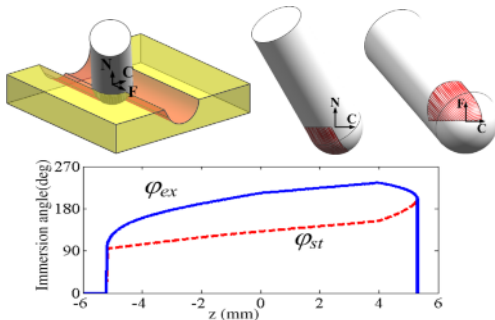


Fig. 5. Engagement region for the example case (lead,tilt=30°)

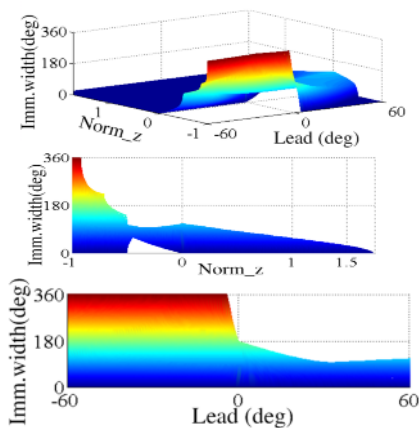


Fig. 6. Effect of lead angle on immersion width (tilt=0°)

Local radius $R(z)$ increases as the z-coordinates of the engagement region increases (Fig.1 (b)). This results in

higher cutting speed values in the engagement region. Since cutting speed increases tool wear, the engagement regions with higher z coordinates cause higher tool wear. Moreover, resulting cutting torque and power due to each cutting flute increases because of higher local radii and higher cutting speed. On the other hand, immersion widths decrease with higher z coordinates. In this case, the probability of having more than one flute in cut decreases since pitch angle between the flutes might be higher than immersion widths at these locations. As a result, it is difficult to derive a general conclusion about the required cutting torque and power since there are two contradicting effects.

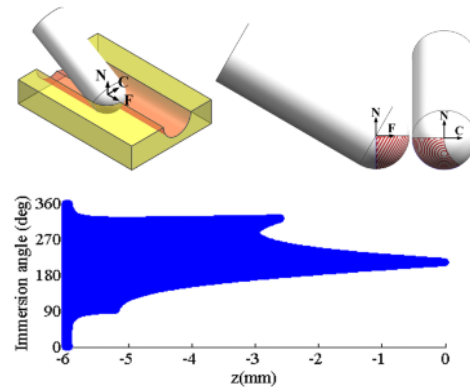


Fig. 7. Engagement region (lead=-60°,tilt=0°)

In order to show the effect of lead angle on the engagement in more detail, for a large negative lead of -60°, 3D and 2D views of the engagement regions are presented in Fig. 7. In this case tilt angle is 0°. Calculated engagement region is also demonstrated. In this case, it is seen that in regions close to the tool tip, the immersion width is 360° which means that there is full immersion in this zone. Tool-tip contact with the workpiece is generally not preferred due to additional ploughing/indentation forces and resulting tip marks on the finished surface. It is seen from Fig. 7 that for higher values of z coordinates, the immersion width decreases. It is interesting to note that between $z=-3$ mm and $z=-2.6$ mm positions, there are two start and exit angles, i.e. the tool engages and disengages with the workpiece two times at these z positions. In this case, this zone on the tool stays behind the finished surface for a short duration but then the tool engages with the workpiece again. This occurs depending on the step over and cutting depth for negative lead angles.

Effect of tilt angle is very much dependent on the cross-feed direction. If tilt angle and cross-feed direction have the same sign, the tool axis is oriented away from the uncut part of the workpiece. In this case, tilt angle decreases the z-coordinates of the engagement region. On the other hand, if tilt angle and cross-feed direction have opposite signs, tool axis is oriented through the uncut part of the workpiece and z-coordinates of the engagement region increase (Fig.2 (b), Fig.3 (a)). As can be seen from

these figures, positive tilt angle results in engagement regions with higher z coordinates. Effect of tilt angle on immersion width on different z coordinates is presented in Fig.8 for the example case. As expected, z-coordinates of the engagement region are lower when tilt angle is negative since cross-feed direction is negative in the example case. At the same time, immersion width is higher in these cases. Similar effects are seen in calculations performed for cases with lower and higher step over and cutting depth values.

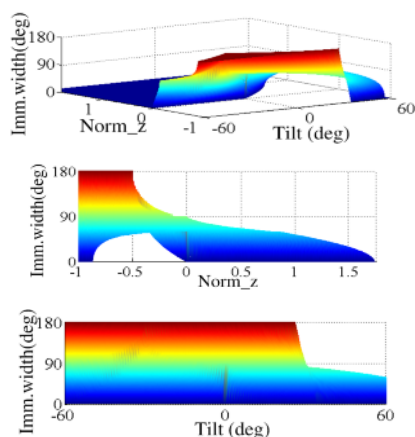


Fig. 8. Effect of tilt angle on immersion width (lead=0°)

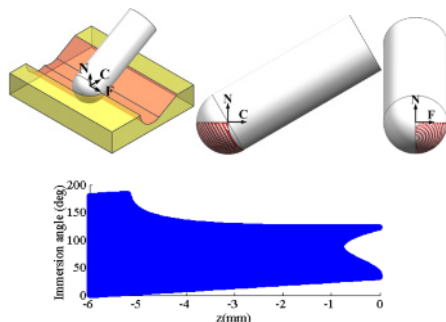


Fig. 9. Engagement region (lead=0°, tilt=-60°)

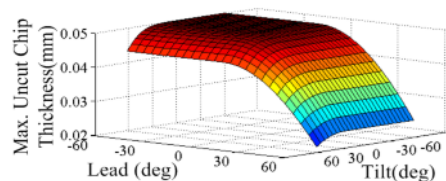


Fig. 10. Lead and tilt angle effect on maximum uncut chip thickness. ($s=6\text{mm}$, $a=6\text{mm}$, $R_c=6\text{mm}$, feed per tooth=0.05mm)

Tilt angle effect on the engagement region is presented on the example case with application of 0° lead and -60° tilt angle in Fig. 9. In this case, there is 180° immersion in the regions close to the tool tip and it decreases for higher z coordinates. Two different immersion zones on the same z-position presented in the previous negative lead case, are also seen in this example between $z=-0.8\text{mm}$ and

$z=0\text{mm}$. In this case, the tool loses contact with the workpiece due to the material removed by the previous pass and gets into contact again which is shown better in the CN plane view of the engagement region in Fig. 9. Negative tilt angle has an effect similar to the up-milling effect in 3-axis flat-end milling for a clock-wise rotating tool. In other words, the tool starts cutting from the final surface which may result in poor surface finish quality. On the other hand, positive tilt angle has a similar effect for counter-clockwise tools.

Lead and tilt angles also affect the local uncut chip thickness values on the cutting edge. The effect of lead and tilt angles on maximum uncut chip thickness is presented in Fig. 10 on a representative case. Especially when the cylindrical part of the ball-end mill is in cut, positive lead angle results in a considerable decrease in maximum uncut chip thickness since lead angle defines the inclination of the tool in feed direction. However, in cases where ball region of the tool is in cut only, lead and tilt angles do not change the maximum chip thickness. They only change the location where maximum chip thickness is reached.

4. Conclusion

In the paper, the effects of lead and tilt angles on the process geometry are shown. Their effects on the engagement regions between the cutting tool and workpiece and maximum uncut chip thickness values are shown to be very significant. An interesting phenomena where there are more than one immersion zone on the same z position was presented on two example cases. The authors believe that the presented results help visualization of 5-axis ball-end milling process geometry which is very important for modeling the mechanics and dynamics of these processes.

References

- [1] Imani, B.M., Sadeghi, M.H., Elbestawi, M.A. (1998) An improved process simulation system for ball end milling of sculptured surfaces. *International Journal of Machine Tools & Manufacture* 38:1089–1107
- [2] ACIS geometric engine, <http://www.spatial.com>
- [3] Kim, G.M., Cho, P.J., Chu, C.N. (2000) Cutting force prediction of sculptured surface ball-end milling using Z-map. *International Journal of Machine Tools & Manufacture* 40: 277–291.
- [4] Lamikiz, A., Lopez de Lacalle, L.N., Sanchez, J.A. Salgado, M.A. (2004) Cutting force estimation in sculptured surface milling. *International Journal of Machine Tools & Manufacture* 44:1511–1526.
- [5] Fontaine, M., Moufki, A., Devillez, A., Dudzinski D. (2007) Modelling of cutting forces in ball-end milling with tool–surface inclination Part I: Predictive force model and experimental validation *Journal of Materials Processing Technology* 189: 73–84
- [6] Ozturk, E., Budak, E., (2007) Modeling of 5 axis Milling Processes. *Machining Science and Technology* 11(3): 287-311

On deposition and characterisation of MoS_x-Ti multilayer coating and performance evaluation in dry turning of aluminium alloy and steel

S. Gangopadhyay¹, R. Acharya², A. K. Chattopadhyay² and S. Paul²

¹ Department of Mechanical Engineering, National Institute of Technology Rourkela, Orissa-769008, India

² Department of Mechanical Engineering, Indian Institute of Technology Kharagpur, West Bengal-721302, India

Abstract. In recent times, MoS_x or MoS_x-based composite solid lubricant coatings have demonstrated some potential in environment-friendly dry machining. However, most of the previous studies were restricted to drilling and milling operations. In the current research work, MoS_x-Ti coating with TiN underlayer was deposited using pulsed DC closed-field unbalanced magnetron sputtering (CFUBMS) technique. The deposited film was characterised using field emission scanning electron microscopy (FESEM), grazing incidence X-ray diffraction (GIXRD), scratch adhesion test and Vickers microhardness test. The performance test of the coating was carried out in dry turning of ISO AlSiMg aluminium alloy and IS 80C6 high carbon steel with uncoated and MoS_x-Ti (with TiN underlayer) coated cemented carbide inserts. Results indicated that coated tool arrested the tendency of formation of built-up material during machining of aluminium alloy resulting in superior workpiece surface finish compared to that for uncoated tool. During dry turning of high carbon steel, the same coated tool resulted in reduction in axial cutting force in the entire range of cutting velocities (32 to 230 m/min). During machining at higher cutting velocity the same coating provided effective diffusion barrier by restricting crater wear.

Keywords: solid lubricant coating, sputtering, characterisation, turning, aluminium alloy, high carbon steel.

1. Introduction

Recently, dry machining and minimal quantity lubrication (MQL) have assumed immense significance primarily due to modified environmental regulation combined with health and safety concerns related to cutting fluids. Advances in the types of coatings applied to cutting tools have been the major driving force to study the feasibility of dry machining [1]. However, desirable performance can be expected if the coating is wear and abrasion resistant having sufficiently high anti friction or anti sticking properties.

MoS₂ is a well known solid lubricant coating material. However, its low hardness combined with poor resistance to oxidation and humidity has prevented its wide application in machining. Although, co-deposition of MoS_x with various metal dopants like Au, Ti, Cr, W, Zr etc improved structural and mechanical properties of

pure MoS_x coating [2-4], the application of such MoS_x-based composite coatings was mainly restricted to drilling and milling operations [3, 5-6]. Significant improvement in performance could not be obtained in turning with MoS_x-Ti coated tools due to higher machining temperature encountered [7]. Similarly, during turning of steel cemented carbide tool coated with MoS_x-Zr composite coating exhibited better tool life compared to uncoated insert when working only in the lower range of cutting speed (< 120 m/min) [8]. Therefore, the potential of MoS_x-based composite coatings in turning of ferrous and non-ferrous alloy has not been fully explored. In the current investigation, a double layer coating consisting of MoS_x-Ti multilayer with TiN underlayer (TiN/MoS_x-Ti) has been deposited using pulsed DC closed-field unbalanced magnetron sputtering. The characteristics of the coating were evaluated using scanning electron microscopy (SEM), grazing incidence X-ray diffraction (GIXRD), scratch adhesion test and Vickers microhardness test. Finally, the performance of the coating was studied in the dry turning of aluminium alloy and high carbon steel.

2. Experimental Details

Deposition was carried out on cemented carbide inserts (ISO K10 grade, make: Widia) of two different geometries as shown in Table 1. The cutting tool substrates were thoroughly cleaned ultrasonically by alkaline solution, trichloroethylene and isopropyl alcohol prior to deposition. After ion cleaning of the substrates, a thin (~100 nm) Ti interlayer was deposited to promote improved film-substrate adhesion. This was followed by deposition of an underlayer of TiN, with a thickness of 2-2.5 μm, to improve load bearing capacity of the coating. Functional top layer of MoS_x-Ti coating (over TiN) of around 1.5 μm thick was deposited by simultaneous sputtering from vertically mounted MoS₂ and Ti targets using Ar as sputtering gas. The sputtering was conducted

in an in-house dual cathode system operated in pulsed DC closed-field unbalanced magnetron mode. The power supplies for both the targets as well as substrates were operated with a pulse frequency of 35 kHz and duty cycle of 90%. The coating was deposited at a working pressure of 0.3 Pa, substrate temperature of 200°C and pulsed substrate bias voltage of -50 V.

Table 1. Details of workpiece, cutting tools and machining condition

Workpiece material	AlSiMg alloy	IS 80C6 steel
Chemical composition (wt%)	Si-0.658, Fe-0.140, Cu-0.005, Mg-0.549, Mn-0.032, Ti-0.018 with rest Al.	C-0.786, Si-0.043, Mn-0.563, P-0.025, S-0.053, Cr-0.056 with rest Fe.
Insert designation	SPUN 12 03 08	SNMA 12 04 08
Tool geometry (ORS)	0°, 6°, 6°, 6°, 15°, 75°, 0.8 (mm)	-6°, -6°, 6°, 6°, 15°, 75°, 0.8 (mm)
Cutting velocity (m/min)	150, 200, 250, 300	32, 77, 130, 230
Feed (mm/rev)	0.14	0.20
Depth of cut (mm)	1	2
Machining duration (s)	10	10

After deposition, the microstructure and phases of the coating were studied using scanning electron microscopy (SEM) and X-ray diffraction (XRD). Coating-substrate adhesion was evaluated using scratch test and composite microhardness of the coating was determined by Vickers microhardness test with a load of 0.5 N.

The performance of the coating was then evaluated in dry machining of AlSiMg aluminium alloy and IS 80C6 (AISI 1080) high carbon steel. The purpose of this study was to investigate the response of MoS_x-Ti coating (with TiN underlayer) against both ferrous and non-ferrous alloys in dry turning operation. The composition of workpiece materials, details of cutting tools and machining conditions are provided in Table 1. Uncoated carbide inserts were also used for comparison of performance. It is evident from Table 1 that cutting velocity was varied from 150 to 300 m/min during machining of aluminium alloy and that from 32 to 230 m/min during machining steel. After each cut, the inserts were examined using both optical microscopy,

SEM and energy dispersive spectroscopy (EDS) by X-ray. Roughness of the machined surface was studied using a surface profilometer after machining of aluminium alloy. Axial cutting force (P_x) was measured using a piezoelectric type dynamometer during machining of steel with both uncoated and coated inserts. However, in the current investigation, the tests could not be repeated due to non-availability of sufficient number of coated inserts.

3. Results and Discussion

3.1 Characterisation of the coating

Figure 1 shows SEM micrographs depicting surface morphology and fractograph of MoS_x-Ti coating with or without TiN underlayer. The surface morphology was found to be smooth. SEM image of fractograph revealed formation of multilayer of MoS_x and Ti as evident from Fig. 1(b). Formation of multilayer structure might be attributed to the configuration of the system and slow rotation (3 rpm) of the substrates during deposition. Previous studies have indicated formation of MoS_x-metal multilayer structure arrests columnar growth of MoS_x leading to good mechanical properties of coating [2]. Figure 1(c) reveals microstructure of MoS_x-Ti coating with TiN underlayer.

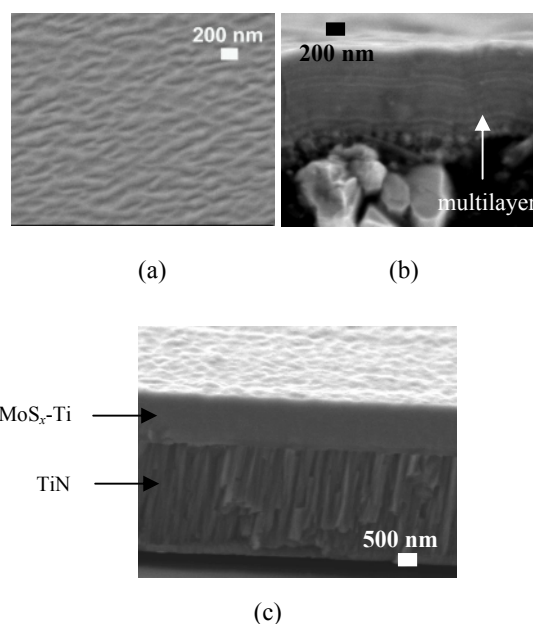


Fig. 1. SEM micrographs of showing (a) surface morphology, (b) fractograph of MoS_x-Ti coating and (c) fractographs of MoS_x-Ti with TiN underlayer

Figure 2 shows low angle XRD spectrum for MoS_x-Ti coating. Presence of multiple peaks at very low angles

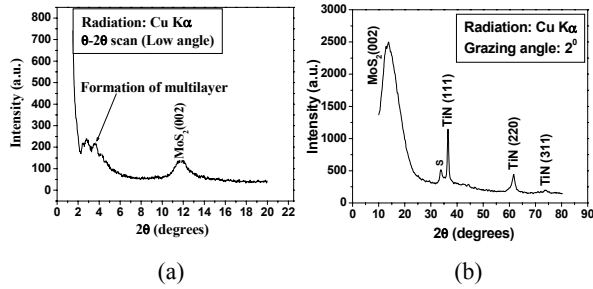


Fig. 2. (a) Low angle XRD and (b) GIXRD spectra of MoS_x-Ti coating with TiN underlayer

also indicates the formation of multilayer structure. However, GIXRD spectrum for MoS_x-Ti coating with TiN underlayer shown in Fig. 2 (b), highlights basally oriented MoS_x (111) phase. Different phases of TiN have also been detected because of TiN underlayer. Scratch test indicated critical load in excess of 80 N and composite Vickers microhardness of the coating was found to be around 20 GPa.

3.2 Performance evaluation in machining

Figure 3 demonstrates optical micrographs of uncoated and coated inserts after dry machining of aluminium alloy with different cutting velocities. The figure clearly indicates severe formation of built-up layer (BUL) on tool rake surface which is a common problem encountered during machining of aluminium or its alloys. However, MoS_x-Ti multilayer coating with TiN underlayer significantly arrested material adhesion on tool surface as evident from Fig. 3. This was further confirmed from SEM and EDS analyses. The superior anti-sticking property of MoS_x might have played a major role in arresting build-up of work material on rake surface of the insert. Figure 4 shows the variation of surface roughness (R_a) with cutting velocity for both uncoated and coated inserts. Though the variation of surface roughness with cutting velocity was not significant, the surface roughness has been significantly reduced with MoS_x-Ti coated insert (with TiN underlayer).

Figure 5 reveals variation of axial cutting force (P_x) with cutting velocity during dry machining of high carbon steel with uncoated and coated carbide inserts. It is evident that coated tool provided a reduction of cutting force (9 to 17%) in the operational range of cutting velocity. Excellent anti-friction properties of solid lubricant MoS_x phase could be primarily responsible for this. The conditions of tool rake surface have been depicted in Fig. 6. It may be observed that uncoated insert suffered from major crater wear as cutting velocity was increased up to 230 m/min. This might be attributed to the poor resistance to diffusion of uncoated carbide insert. However, resistance to crater could be significantly improved with MoS_x-Ti coating with TiN underlayer, which can be clearly seen from Fig. 6. It may be observed that though removal of coating took place

particularly at low cutting velocity, most of the coating was intact while machining at higher cutting velocity. This was further confirmed using EDS analysis. The superior characteristics of this double layer coating system compared to its uncoated counter part might be ascribed to good solid lubricant properties of MoS_x, while Ti maintained structural integrity and good adhesion characteristics of MoS_x. TiN provided improved load bearing capability of the coating.

Cutting velocity (m/min)	Cutting tool	
	Uncoated	Coated
150		
200		
250		
300		

Fig. 3. Optical micrographs of uncoated and coated turning inserts after machining of aluminium alloy with different cutting velocities

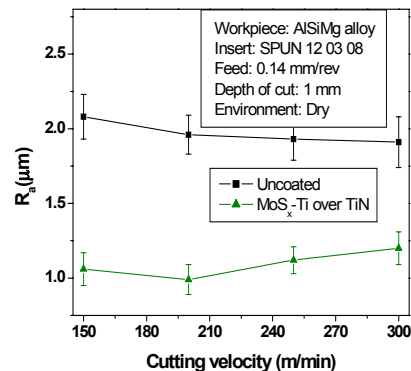


Fig. 4. Variation of workpiece surface roughness (R_a) with cutting velocity during dry turning of aluminium alloy with uncoated and coated inserts

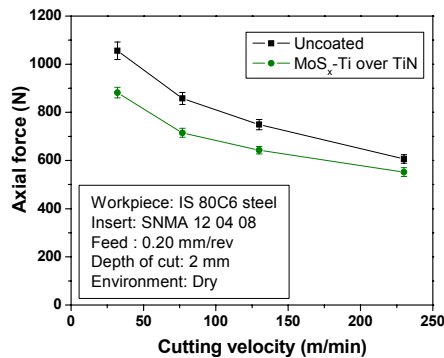


Fig. 5. Variation of axial cutting force (P_x) with cutting velocity during dry turning of steel with uncoated and coated inserts

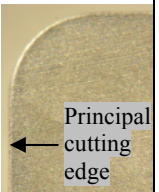

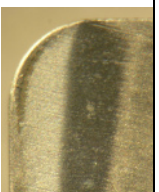
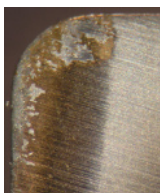
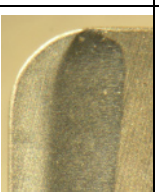
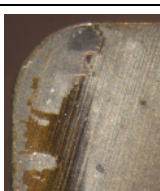
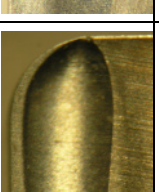
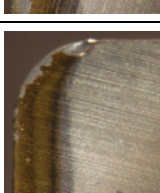
Cutting velocity (m/min)	Cutting tool	
	Uncoated	Coated
32		
77		
130		
230		

Fig. 6. Optical microscopic images showing rake surfaces of uncoated and coated turning inserts after machining of steel with different cutting velocities

4. Conclusion

In the current study, MoS_x-Ti coating with TiN underlayer was deposited using dual cathode pulsed DC

CFUBMS technique followed by characterisation and performance evaluation of the coating in dry turning of aluminium alloy and high carbon steel. The following conclusions may be drawn from the current investigation:

- The structure of MoS_x-Ti coating has been found to be multilayer.
- The coating exhibited reasonably good adhesion with the cutting tool substrate and composite microhardness.
- During dry turning of aluminium alloy the coating helped to restrict the formation of BUL resulting in superior workpiece surface finish compared to that with uncoated insert.
- During dry turning of high carbon steel, the same tool resulted in reduction in axial cutting force in the range of 9 to 17% and provided much better resistance to crater wear compared to that with its uncoated counterpart particularly at higher cutting velocity (230 m/min).

Therefore, the double layer coating system has exhibited some promise in dry turning of steel and aluminium alloy. However, further investigation should be undertaken to study its performance in comparison with various conventional hard coatings during machining of ferrous and non-ferrous alloys.

5 References

- [1] Klocke F, Eisenblätter G, (1997) Dry cutting. CIRP Annals - Manufacturing Technology 46 (2): 519-526.
- [2] Hilton, M. R., Bauer, R., Didziulis, S. V., Dugger, M. T., Keem, J. M., Scholhamer, J. (1992), Structural and tribological studies of MoS₂ solid lubricant films having tailored metal-multilayer nanostructures, Surface and Coatings Technology, Vol. 53, Issue 1, pp. 13-23.
- [3] Teer DG, Hampshire J, Fox V, González V B, (1997) The tribological properties of MoS₂/metal composite coatings deposited by closed field magnetron sputtering. Surface and Coatings Technology 94-95: 572-577.
- [4] Renevier NM, Fox VC, Teer DG, Hampshire J, (2000) Coating characteristics and tribological properties of sputter-deposited MoS₂/metal composite coatings deposited by closed field unbalanced magnetron sputter ion plating. Surface and Coatings Technology 127: 24-37.
- [5] Renevier NM, Lobiondo N, Fox VC, Teer DG, Hampshire J, (2000) Performance of MoS₂/metal composite coatings used for dry machining and other industrial applications. Surface and Coatings Technology 123: 84-91.
- [6] Wain N, Thomas NR, Hickman S, Wallbank J, Teer DG, (2005) Performance of low-friction coatings in the dry drilling of automotive Al-Si alloys. Surface and Coatings Technology 200: 1885-1892.
- [7] Renevier NM, Oosterling H, König U, Dautzenberg H, Kim BJ, Geppert L, Koopmans FGM, Leopold J, (2003) Performance and limitations of MoS₂/Ti composite coated inserts. Surface and Coatings Technology 172: 13-23.
- [8] Jianxin D, Wenlong S, Hui Z, Jinlong Z, (2008) Performance of PVD MoS₂/Zr-coated carbide in cutting processes. International Journal of Machine Tools and Manufacture 48: 1546-1552.

Novel Developments in Cutting and Grinding of Preheated Billets

O. Mgaloblishvili¹, K. Inasharidze² and M. Shvangiradze³

¹ AMTReL, The General Engineering Research Institute, Liverpool John Moores University (LJMU), Byrom Street, Liverpool L3 3AF, UK, tel. +44(0) 151 2312020 Fax: +44(0) 151 231 2158, E-mail: o.mgaloblishvili@ljmu.ac.uk

² Shota Rustaveli State University, Faculty of Engineering and Technology, 53, Ninoshvili str., Batumi, Republic of Georgia, tel: +995 994 39411 (mob), E-mail: keti1@inbox.ru

³ Georgian Technical University, 68 Kostava str., Tbilisi, Republic of Georgia, tel: +995 937 39255 (mob), E-mail: shvango@gmail.com

Abstract. The rate of material removing by cutting or grinding and the tool life may significantly increase when machining the workpiece preheated up to the optimal temperature. It equally relates to structural steels, cast irons and to difficult to cut alloys. Specific mechanical energy needed to remove material decreases with increase the workpiece temperature but giving the rise to thermal energy input into the cutting tool. Tool-work interface temperature is a limiting factor restricting the process productivity.

Novel schemes of cutting with variable cutting edge and the moving cutting area allow controlling the interface temperature and tool life at an optimal level equally with the high rate of material removing. Original schemes of cutting with variable cutting edge and corresponding machine tools have been designed, manufactured and put into the practice. Two additional new versions have been proved on laboratory test beds. The results are promising and at present, machine tools are on a designing stage. These processes that carried out within the cycle of metallurgical conversion by using the technological heat of workpiece result in substantial energy savings and shortening the manufacturing cycle. Practical examples of such technologies are demonstrated.

Keywords: cutting, grinding, preheated workpiece, variable cutting edge, energy saving technology.

1 Introduction

A large variety of new structural and tool materials with specific physical and mechanical properties have been developed for the growing needs of space, aircraft, automotive, machine tool, instrument engineering and other branches of industry. To attain the necessary physical, mechanical and other properties for these materials it requires their machining at different stages of manufacturing processes – starting from removing the surface defect layer from ingots and forgings, accomplishing with finishing operations.

Current trends in the development of both the cutting tool and the structural engineering materials directed on the increase of hardness, bending strength, fracture toughness, and on the raise the resistance to wear at

elevated temperatures. Therefore, it is becoming more and more problematic to choose an appropriate tool material for efficient machining of hard structural materials with specific properties.

Owing to elevated strength, hardness and the low machinability it is becoming necessary to develop new methods and technologies for efficient machining the components from these materials by cutting and grinding together with ensuring contemporary requirements to the energy saving manufacturing.

Since early fifties of last century the fundamental studies of hot machining by cutting had been carried out in the Production Engineering Research Laboratory at Georgian Technical University (Tbilisi, Republic of Georgia). Only the results obtained there are presented in this paper.

2 Some features of hot machining

The essence of hot machining lies in the fact that with increase the workpiece temperature the hardness and shear strength both in the primary and the secondary shear zones decreases in proportion with thermal softening of work material and if it becomes possible to retain the required cutting ability of tool material at elevated cutting temperatures then considerable increase in the rate of material removal and the process efficiency are expected.

It is difficult to determine the response of work material to hot machining from the results of standard tension, compression or other mechanical tests. T. Loladze [1] proposed the method of determination the shear stresses directly by cutting the materials preheated over the wide range of temperatures.

Fig.1 illustrates the values of the shear strength as a function of temperature for the typical representative work materials. In contrast with nickel based high-

temperature alloys the hot machining is most efficient for work hardening high manganese steel.

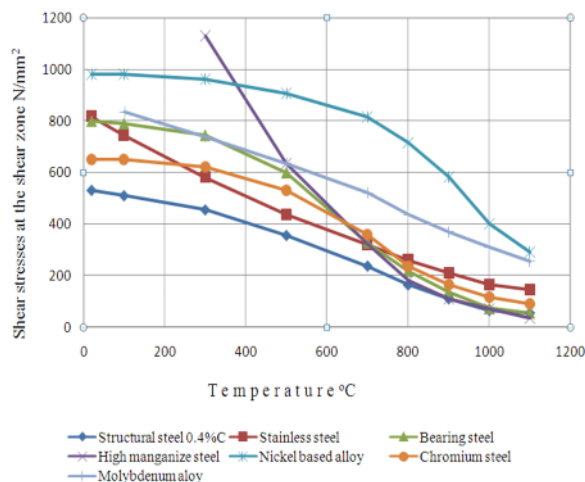


Fig. 1. Temperature dependence of the shear strength at the shear zone for different classes of work materials [1]

At high values of strain and strain rates the shear stresses at chip-tool or at tool-work interfaces can be assumed equal to the shear stresses in chip formation zone for the same values of temperatures and may be found from the curves in Fig. 1.

3 The ways of control the cutting temperature

Tool-work interface temperature is a limiting factor restricting the process productivity and the cutting tool life. The earlier studies [2-4, 8] showed that shear stresses at the shear zone, preheated workpiece temperature and the cutting speed exert the most influence on cutting temperature. When work material is preheated at such degree that the shear stresses lessen 3-4 times compared to that at room temperature, the increase of uncut chip thickness has minor influence on the cutting temperature rise. This fact allows more than 8-10 times increase uncut chip thickness for the same level of cutting temperature without any restriction in the width of cut other than the power of machine tool.

The thermal energy input into the cutting tool significantly increases with the rise of temperature gradient between cold tool and hot workpiece. The heat flux is especially high at initial stage [2, 3 and 4].

It had been theoretically ground and experimentally proved [2-4, 6] that an interface temperature can be controlled by varying the heat exchange conditions together with taking into consideration the features of continuous, periodical and interrupted cutting.

Continuous cutting (turning) characterizes by steady state heat exchange. An interface temperature can be reduced by intensive internal cooling of cutting tool insert

alongside with using the tool material of high thermal conductivity [2-4].

The contact temperature drop for periodical (planing, broaching) and for interrupted cutting (milling) is based on the features of tool heating at an initial stage of cutting when the temperature in interface exponentially rises and approaches the value under the steady-state conditions. Cutting temperature may be controlled by varying both the cutting speed and the cutting length [2, 6]. At certain cutting conditions an interface temperature is lower than temperature of preheated workpiece [2, 5, 6, 8].

4 New schemes and methods of machining with variable cutting edge

Foregoing results were the bases for developing the new methods of removing the surface defect layers from ingots, blooms and billets of cylindrical or conical shape. Ideally, these processes have to be carried out within a cycle of metallurgical conversion or heat treatment when billets are in hot state in conformity with the basic technological process. Such opportunity is economically the most advantageous to other cases when workpiece has to be purposely heated.

Fig. 2 illustrates the new method of removing a defect layer from the long bloom by planing with wide cutting tool [6]. Preheated long workpiece is preliminarily turned at certain angle against the vector of cutting speed. This allows reducing the length of cut and thereby to control cutting temperature at optimal level. The width of cutting edge and its orientation provide orthogonal cutting. Defect layer from each side of bloom may be removing in one pass.

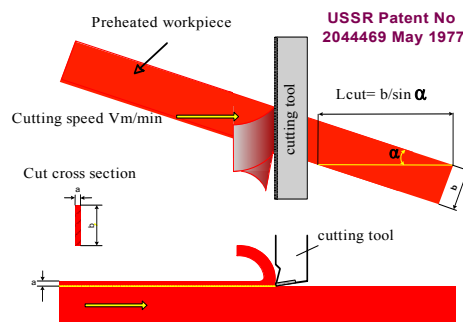


Fig. 2. The scheme of planing with variable cutting edge for removing the whole allowance in one pass from long (up to 3m) rolled steel of square cross section.

The highly efficient method of machining the outer surface of cylindrical and conical ingots and billets called roto-planing [5, 7] is presented in Fig. 3. The process is carried out at simultaneous rotation of a disk type cutter block with radially located straight blades and the workpiece.

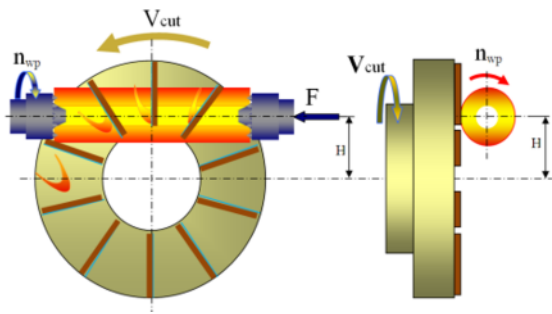


Fig. 3. Kinematics of the process of roto-planing the outer surface of cylindrical billet

Kinematics of process provides variable cutting edge, large width of cut, orthogonal cutting, chip fragmentation and favourable conditions for cutting tool allowing practically uniform wear along the cutting edge at optimal combinations of cutting parameters. The only lack of the method is that width of chip and as a result the cutting force varies along the cutting edge and what is more it is sign-variable too. By varying the process parameter H it possible to control force or temperature distribution along the cutting edge, but its value obtained from minor alteration of cutting force as criteria of optimization contradicts to similar criteria for temperature distribution along the cutting edge. The prototype is illustrated in Fig. 4.

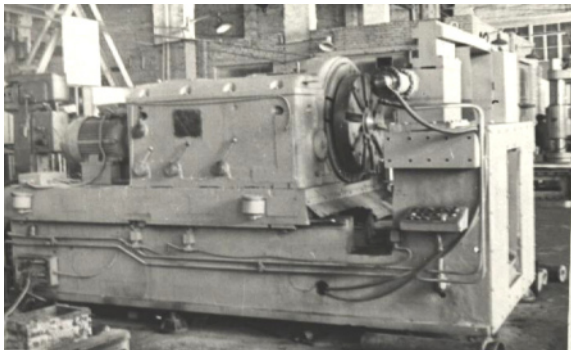


Fig. 4. The roto-planing machine tool propotipe

New improved methods are schematically presented below in Figs. 5, 6 and 7.

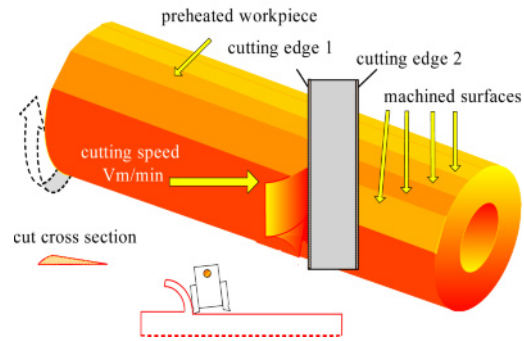


Fig. 5. The scheme of planing with variable cutting edge for removing the defect layer with occluded sand from the outer surface of as-cast cylindrical billet in hot state

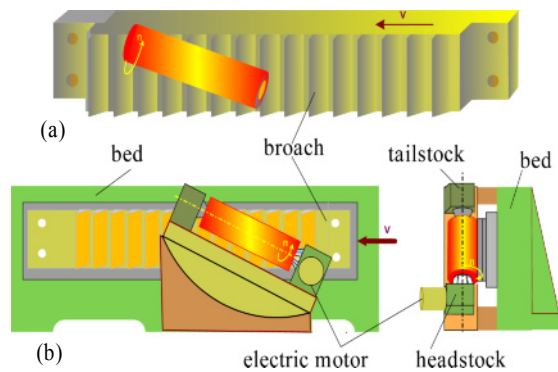


Fig. 6. Schematic illustration of (a) -broaching a preheated cylindrical billet; (b) – a version of roto-broaching machine tool

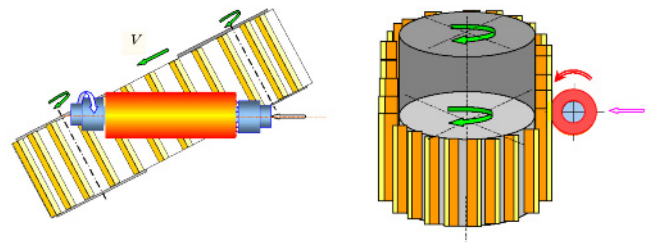


Fig. 7. Schematic illustration of continuous broaching when removing defect layer with occluded sand from the outer surface of as-cast cylindrical billet in hot state

The common for all these improved methods of cutting are uniform distribution of both the cutting forces and the temperatures along the variable cutting edge. Orthogonal cutting, the possibility of easy control the length of cut and the wear rate for each working area of cutting edge are significant advantages of all proposed methods of cutting. Moving heat source along the cutting edge lessens the temperature gradient and as a result the thermal stresses in the cutting wedge decrease.

The method of machining presented in Figures 3 and 5 have been used when removing the defect layer with occluded sand from the outer surface of as-cast cylindrical billet in hot state. Bimetallic cylindrical billets were made by centrifugal casting and machined in hot state (850-900C). Machining time did not exceed 1.5 minutes. From such bimetallic half finished article have been made bimetallic bars.

One of the final product namely the bimetallic high speed steel end cutter is presented in Fig. 8.



Fig. 8 General view of bimetallic end milling cutter and cross section of the initial bimetallic bar

A unique technology of production of bimetallic bars for manufacturing the cutting tools has been developed jointly in Georgian Technical University (Tbilisi) and Ukrainian State Tube Institute (Dnepropetrovsk) [9].

Up-to-date highly efficient processes of metal conversion – centrifugal casting of cylindrical bimetallic ingot, machining of ingot by cutting in the hot state and extrusion of machined billet into the bimetallic bar are the basis for this technology.

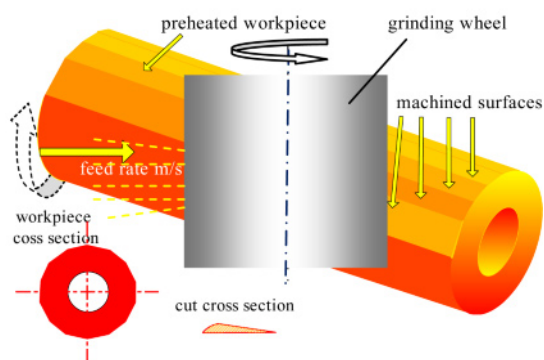


Fig. 9 Schematic illustration of hot grinding with variable working area on the wheel

Promising is the method of gridding with a variable working area on the wheel when removing defect layer with occluded sand from the outer surface of as-cast cylindrical billet in hot state (see Fig.9).

5 Conclusion

Hot machining is most efficient when carried out within the cycle of metallurgical conversion or heat treatment as the billets are in hot state and no extra heating sources required. This is economically the most advantageous to other cases when workpiece has to be purposely heated.

Preheating of work material allows significantly increase the uncut chip thickness and if the product of threshold values of cutting speed and feed rate increases then the hot machining is efficient and may be attained by proper cooling of cutting tool and by selection of optimal cutting scheme.

For wide utilization of hot machining it is necessary to design and manufacture new type of dedicated machines and cutting tools adapted to specific conditions of hot machining.

References

- [1] Loladze T.N., Betaneli A.I. Strength of cutting tool. Chapter V, in "Development of the Science of Metal Cutting". «Mashinostrojenie», Moscow 1967 (in Russian).
- [2] Loladze T.N., Razmadze G.I., Mgaloblishvili O.B., Khomasuridze V.S. Cutting Temperature when Hot Milling. Thermophysics of technological processes, Tolyatti, 1972 (in Russian).
- [3] Tsotshadze V.V. Cutting Temperature when turning Preheated Materials. "Vestnik Mashinostrojenija" №11, 1963 pp. 51-53 (in Russian).
- [4] Loladze T.N. Strength and Resistance to Wear of Cutting Tool. Mashinostrojenije, Moscow, 1982, 320p (in Russian).
- [5] Loladze T.N., Razmadze G.I., Mgaloblishvili O.B., Shvangiradze M.G. "Machine -tool for Machining the Outer Surfaces of Bodies of Revolution". Patent of USSR № 766749, 6.06.80, Moscow, 1980, (in Russian).
- [6] Loladze T.N., Razmadze G.I., Mgaloblishvili O.B., Shvangiradze M.G. "The Method of Machining Flat Surfaces" Patent of USSR №570460, Moscow, 1973.
- [7] Loladze T., Mgaloblishvili O., Shvangiradze M., Razmadze G., Khomasuridze V., Rukhadze O. The Method of Machining the Outer Surfaces of the Bodies of Revolution. Patent of USA №4.205.933 dated 03.06.1980. Patent of Germany №2.28.581 dated 07.06.1984. Patent of France 2.395.804 dated 25.02.1983 Patent of Japan №1213045, 1983
- [8] Loladze T., Mgaloblishvili O., Tsereteli R. "The Method of Machining of Cast-Iron Components" Patent of USSR № 395447, Moscow, 1973
- [9] Loladze T.N., Gerasimov V.G., Shvangiradze M.G. et al. "The Method of Manufacturing the bimetallic bars for the cutting tool" Patent of USSR № 1813606 " , 1982.

Investigation of the Cutting Forces and Tool Wear in Laser Assisted Milling of Ti6Al4V Alloy

S. Sun^{1,5}, M. Brandt^{2,5}, J. E. Barnes³ and M. S. Dargusch^{4,5,6}

¹ IRIS, Faculty of Engineering and Industrial Sciences, Swinburne University of Technology, Victoria, Australia

² School of Aerospace, Mechanical and Manufacturing Engineering, RMIT University, Victoria, Australia

³ Lockheed Martin Aeronautics, Advanced Development Programs, 86 S. Cobb Dr., Marietta, GA, 30063-0660 USA

⁴ School of Mining and Mechanical Engineering, University of Queensland, St Lucia, Brisbane, Qld 4072, Australia

⁵ CAST Cooperative Research Centre, Australia

⁶ Defence Materials Technology Centre, Australia

Abstract. The current investigation evaluates laser assisted machining, which uses an external laser beam to heat and soften the material to be machined locally in front of the cutting tool and offers an alternative approach to improving the machinability of titanium alloys. By reducing the cutting resistance, the cutting tool sees less pressure and life is enhanced. This paper reports on the cutting forces and tool life during laser assisted milling of Ti6Al4V alloy. Cutting forces, especially the force in the feed direction, reduce dramatically with laser beam assistance. The reduction of feed force depends on the laser power, depth of cut and cutting speed. This paper also discusses the major tool failure mode observed during both conventional and laser assisted milling operations.

Keywords: Laser assisted machining, reduction of cutting force, cutting speed, depth of cut, tool wear.

1. Introduction

Titanium and its alloys are in increasing demand in the aerospace industry due to their attractive properties, such as high strength-to-weight ratio, low thermal conductivity and ability to retain their strength at high temperatures [1]. However, these properties also make the titanium alloys hard to machine [2].

The poor machinability of titanium and its alloys is due to the high temperature at the cutting zone and high pressure at the cutting tool edge. The former is due to the low thermal conductivity of titanium and dramatically increases with increasing cutting speed. The chemical reactivity between titanium and cutting tool materials is severe at high temperatures.

Continuous efforts are being undertaken to improve the machinability of titanium so as to increase the material removal rate and extend tool life. Enhanced cooling techniques such as cryogenic machining [3,4] and high pressure coolant [5-7] have been reported to effectively increase tool life.

Laser assisted machining (LAM) uses a laser beam to locally heat and soften the workpiece in front of the cutting tool. The temperature rise at the shear zone dramatically reduces the yield strength of the workpiece, which leads to a reduction in the cutting pressure on the cutting tool edge. Improvements in machinability using laser beam assistance has been reported when machining titanium alloys [8-10] in terms of lower cutting forces, longer tool life and better surface finish with lower deformation in the machined subsurface. The optimum material removal temperature for turning Ti6Al4V alloy is found to be 250 °C [8,11].

The most investigations reported to date on laser assisted machining of titanium alloys have been carried out in the turning operations. Improvement in tool life during laser assisted milling is important for this technology to be adopted by industry because the milling operation represents the largest proportion of machining when manufacturing aerospace components.

This paper reports on a systematic investigation of cutting forces and tool wear during laser assisted milling of Ti6Al4V alloy. The results show improvements in machinability of Ti6Al4V alloy with laser assistance.

2. Materials and Experimental Procedures

The workpiece used in this study is Ti6Al4V alloy. The microstructure of this alloy is shown in Figure 1. It contains primary α with grain size of 17 μm and lamellar colonies α'/β with spacing of 2 μm . The hardness of the workpiece is 285~342 Hv.

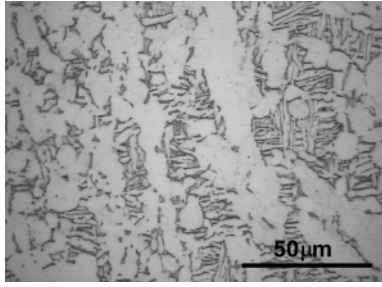


Fig. 1. Optical micrograph of the workpiece material.

Conventional up cut end milling, where the workpiece moves in a direction against the rotation of the cutter, was conducted under dry condition. The workpiece was clamped onto a Kistler 9256A dynamometer, which was bolted onto the mill to measure the cutting forces in the X, Y and Z directions as shown in Figure 2. A cutter with a diameter of 40 mm and 4 carbide inserts (490R-08T3-154861) supplied by Sandvik were used. Its primary rake angle and clearance angle are 30° and 6° respectively.

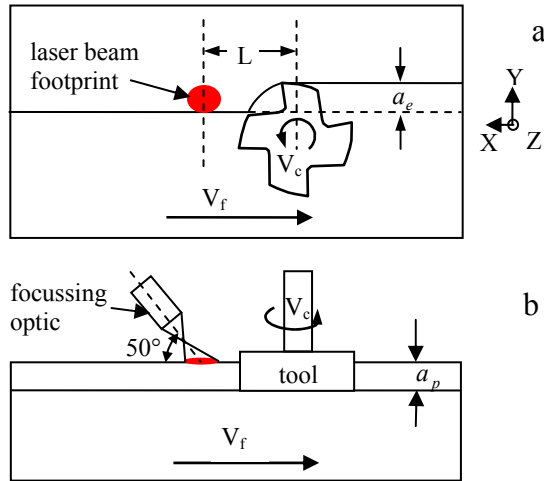


Fig. 2. (a) top and (b) front views of laser assisted milling set-up.

A 2.5 kW Nd:YAG laser was used in the experiments. The laser beam was delivered by a 15 m long optical fiber and defocused by an optical lens with a focal length of 200 mm. The laser beam was incident onto the workpiece surface at an angle of 50° to avoid the reflection of laser beam to the cutting tool holder. The distance between the focal lens and workpiece surface was 240 mm, which produced a laser footprint of 5x7 mm² on the workpiece surface. The minor axis of the elliptical laser beam covered the radial depth of cut ($a_e = 5$ mm). The processing parameters, including the cutting speed (V_c), axial depth of cut (a_p) and laser power (P) were investigated and are listed in Table 1. The feed rate was set at $f_z = 0.1$ mm/tooth for all the tests.

The cutting conditions for the tool life are listed in Table 2. The tool-beam distance L was set at 43.5 mm

because of the significant reduction in cutting force and small through thickness temperature gradient found by previous investigation.

Table 1. Summary of processing parameters.

Fixed parameters		Varied parameters
$V_c = 130$ m/min	$a_p = 0.5$ mm	P=350, 510, 750, 1000, 1250 W
$V_f = 400$ mm/min $L = 28.5$ mm	$a_p = 1.0$ mm	P=350, 510, 750, 1000, 1250 W
	$a_p = 1.5$ mm	P=350, 510, 750, 1000, 1250 W
	$a_p = 2.0$ mm	P=350, 510, 750, 1000, 1250 W
$f_z = 0.1$ mm/tooth $L = 28.5$ mm	P=750 W	$V_c = 90, 130, 160, 190$ 220, 250 m/min
$a_p = 0.5$ mm	P=1000 W	$V_c = 90, 130, 160, 190$ 220, 250 m/min

Table 2. Parameters for the tool life assessment.

V_c m/min	a_e mm	a_p mm	f_z mm/tooth	L mm	P (W)
200	5	1	0.1	43.5	0, 750, 1000

3. Results and discussion

3.1 Reduction in cutting forces during laser assisted milling

Since the rotation of the cutter is against the workpiece feed direction, the impact of the force on the primary cutting edge of the tool is significant in the X direction. Therefore, the resultant force examined in this study is the feed force in the X direction, i.e., F_x .

The variation of feed force over time is shown in Figure 3. The force reduced dramatically in a period (Δt) after the laser was turned on, the time delay ($\Delta t = L/V_f$,

where V_f is the workpiece travel velocity, i.e. the feed speed) is due to the tool-beam distance.

The comparison between conventional milling and laser assisted milling in this study is based on the reduction of force in the feed direction, i.e.:

$$\text{Reduction of force} = \frac{\Delta F}{F_{\text{conventional}}} \times 100\% \quad (1)$$

The effect of laser power on the reduction in feed force at different axial depths of cut is shown in Figure 4. The magnitude of the reduction of the feed force increases with increasing laser power, the maximum force reduction is 55%. Higher laser power is required to achieve the maximum force reduction for the larger depth

of cut. A further increase in laser power does not result in further reduction in feed force after the maximum force reduction is 55% is achieved.

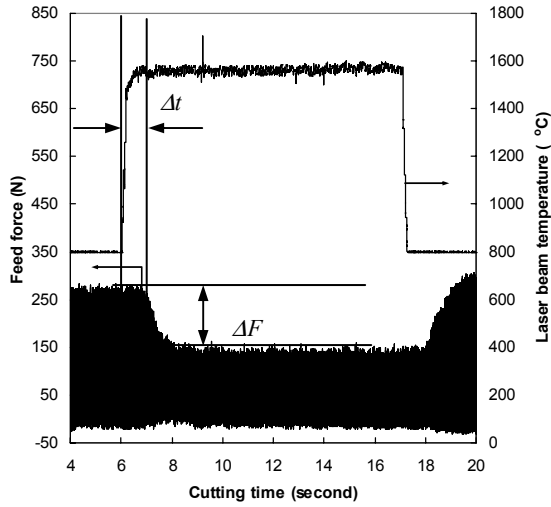


Fig. 3. Feed force and laser beam temperature during milling at a cutting speed of 220 m/min and depth of cut of 0.5 mm.

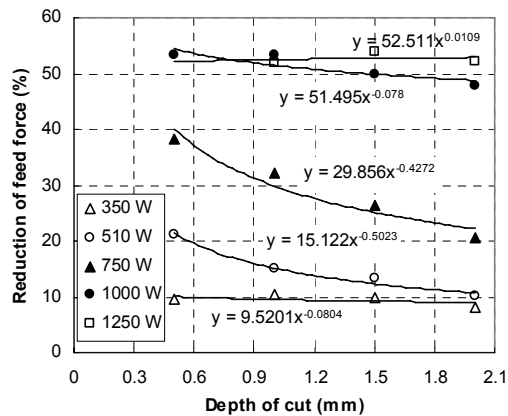


Fig. 4. Effect of laser power and axial depth of cut on the reduction in feed force.

The difference in force reduction with different depths of cut under both low (350 W) and high (>1000 W) laser power is small. The effect of depth of cut is significant at the laser power range between 350 W and 1000 W. Higher laser power for a deeper cut is required to achieve the same force reduction as that at a shallow cut within this range.

The exponents of the power type relationship between force reduction and depth of cut at the laser powers of 510 W and 750 W are close to -0.5, indicating that thermal diffusion is dominant in this laser power range.

The reduction in feed force with increasing cutting speed at constant feed per tooth of 0.1 mm is shown in Figure 5. The force reduction initially increases with cutting speed from 90 m/min and reaches a maximum at

cutting speeds of 130 m/min and then drops to a minimum at cutting speeds of 160 and 220 m/min at an incident laser power of 750 and 1000 W respectively.

In order to keep the feed per tooth constant, the feed speed increases with increasing cutting speed. The laser beam interaction time reduces with increasing feed speed.

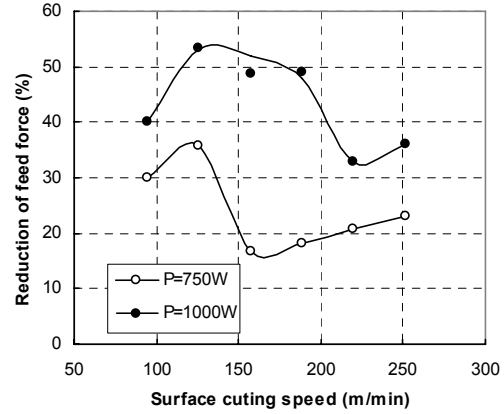


Fig. 5. Effect of surface cutting speed on the reduction in feed force at incident laser power of 750 and 1000 W.

Therefore, the change in the magnitude of force reduction with increasing cutting speed is the result of the combined effects of the reduced beam interaction time, reduced beam-tool delay time and increased heat generation by the cutting tool. The effects of the beam interaction time and beam-tool delay time on the temperature at the cutting edge need further investigating in order to interpret the effect of cutting speed on the feed force reduction.

The abrupt drop in force reduction at cutting speeds of 160 and 220 m/min at the laser power of 750 and 1000 W can be attributed to the phase transformation that occurs at the laser heated layer before it enters into the cutting zone. The phase transformation produces harder martensite which results in a higher cutting force.

It also shows in Figure 5 that the maximum reduction of cutting force can be achieved at higher cutting speeds with higher laser power.

3.2 Effect of laser beam on tool failure

The cutter is periodically engaged with the workpiece because the radial depth of cut ($a_e = 5$ mm) is much smaller than the cutter diameter (40 mm) and the cutting tool edge undergoes severe cyclical impact and thermal fluctuations when it engages and disengages with the workpiece so chips are easily welded onto the cutting tool edge due to high cutting temperature. All these effects lead to tool edge chipping, which is the main tool failure mode in conventional milling [2], especially when milling at high speed and feed [12]. Significant chipping is observed after removing 3.6 cm^3 of material in dry milling.

Similar to LAM of Si_3N_4 ceramic and Inconel 718 alloy, tool edge chipping is significantly improved in laser assisted milling of Ti6Al4V alloy. Chipping was observed after removing 8.4 cm^3 of material at an incident laser power of 750 W. The reduction of chipping is attributed to the reduced dynamic impact on the cutting edge due to the local softening of the workpiece.

A comparison of tool chipping obtained when dry conventional and laser assisted milling is shown in Figure 6. The breakage of the cutting edge in conventional milling occurred along the full depth of cut (1 mm), while the chipping in laser assisted milling only occurred at the surface of the cut where the temperature is the highest in the workpiece. The rest of the cutting edge is still sharp without any damage.

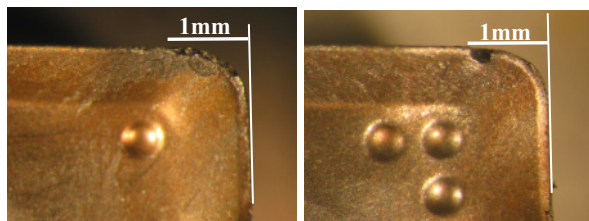


Fig. 6. The rake faces of the cutting tools after (a) 3.6 cm^3 of material removed by conventional milling and (b) 8.4 cm^3 of material removed by LAM.

A further increase in the laser power results in overheating of the workpiece surface and a tendency for chip adhesion to the cutting tool edge, leading to a reduction in strength of the carbide tool. It was observed that significant tool chipping occurred after only removing 1.2 cm^3 of material at the incident laser power of 1000 W. Therefore, laser power should be controlled to ensure that the tool is not overheated.

4. Conclusions

Laser heating the workpiece surface in front of the milling cutter dramatically reduces the cutting forces. The reduction of feed force increases with laser power until it reaches a maximum value of about 55%.

The effect of depth of cut on the force reduction at low and high tested laser power is insignificant. The force reduction for intermediate laser power decreases with increasing depth of cut.

The magnitude of the reduction in cutting force shows a complex dependence on cutting speed exhibiting a minimum at a certain cutting speed. This speed increases with laser power. The dramatic drop of force reduction is believed to be due to the martensite transformation in the heated layer, which makes this layer harder to machine.

Tool edge chipping is the dominant tool failure mode in dry milling of Ti6Al4V alloy because of the dynamic impact on the tool edge when it engages the workpiece and thermal fatigue of the tool. Thermal softening of the

workpiece by the laser beam effectively reduces the dynamic impact on the tool edge leading to a significant reduction in tool chipping. However, laser power should be controlled to avoid overheating and degradation of the cutting tool.

Acknowledgments

The authors would like to thank Mr. G. Thipperudrappa for his assistance in operating the mill. The authors also gratefully acknowledge the CAST Cooperative Research Centre and Lockheed Martin Advanced Development Programs for the financial support and permission to publish this work. The CAST Cooperative Research Centre was established and is supported under the Australian Government's Cooperative Research Centres Programme.

References

- [1] Boyer, RR, (1996) An overview on the use of titanium in the aerospace industry, *Materials Science & Engineering A213*, 103-114.
- [2] Ezugwu, EO, Wang, ZM, (1997) Titanium alloys and their machinability—a review, *Journal of Materials Processing Technology* 68, 262-274.
- [3] Hong, Y, Markus, I, Jeong, W-C, (2001) New cooling approach and tool life improvement in cryogenic machining of titanium alloy Ti-6Al-4V, *International Journal of Machine Tools & Manufacture* 41, 2245-2260.
- [4] Wang, ZY, Rajurkar, KP, (2000) Cryogenic machining of hard-to-cut materials, *Wear* 238, 168-175.
- [5] Machado, AR, Wallbank, J, Ezugwu, EO, Pashby, IR, (1998) Tool performance and chip control when machining Ti-6Al-4V and Inconel 901 using high pressure coolant supply, *Machining Science and Technology* 2, 1-12.
- [6] Nandy, AK, Gowrishankar, MC, Paul, S, (2009) Some studies on high-pressure cooling in turning of Ti-6Al-4V, *International Journal of Machine Tools & Manufacture* 49, 182-198.
- [7] Palanisamy, S, Townsend, D, Scherrer, M, Andrews, R, Dargusch, MS, (2009) High pressure coolant application in milling titanium, *Materials Science Forum* 618-619, 89-92.
- [8] Dandekar, CR, Shin, YC, Barnes, J, (2010) Machinability improvement of titanium alloy (Ti-6Al-4V) via LAM and hybrid machining, *International Journal of Machine Tools & Manufacture* 50, 174-182.
- [9] Germain, G, Morel, F, Lebrun, J-L, Morel, A, (2007) Machinability and surface integrity for a bearing steel and a titanium alloy in laser assisted machining (optimisation on LAM on two materials), *Lasers in Engineering* 17, 329-344.
- [10] Sun, S, Harris, J, Brandt, M, (2008) Parametric investigation of laser-assisted machining of commercially pure titanium, *Advanced Engineering Materials* 10, 565-572.
- [11] Barnes, JE, Shin, YC, Brandt, M, Sun, S, (2009) High speed machining of titanium alloys, *Materials Science Forum* 618-619, 159-163.
- [12] Lacalle, LNLd, Pérez, J, Llorente, JI, Sánchez, JA, (2000) Advanced cutting conditions for the milling of aeronautical alloys, *Journal of Materials Processing Technology* 100, 1-11.

Numerical Techniques for CAM Strategies for Machining of Mould and Die

R. Ur-Rehman¹, C. Richterich², K. Arntz¹, and F. Klocke¹

¹Fraunhofer IPT, Steinbachstrasse 17, 52074 Aachen Germany

²ModuleWorks GmbH, Rietterstrasse 12a, 52072 Aachen Germany

Abstract. The complex design of moulds and dies based upon complicated features and usage of harder materials is a continuous challenge for the development of manufacturing technology for these parts. In this paper we present an algorithm for handling this challenge as well as its implementation by using numerical techniques for the calculation of CNC tool-path. The algorithm consists of multiple stages and each stage achieves a partial objective of tool-path planning and optimization. An individual step in these stages implements trochoidal milling process under uniform machining load conditions and in multiple layers to machine a mould with complex deep cavity. The resulted CNC tool-path achieves bulk material removal of the work piece to a contour near shape with uniform rest material which ensures stable finish milling process subsequently. The method is applicable to dies as well with the same performance.

Keywords: moulds and dies, numerical techniques, rough machining, trochoidal milling, CNC tool-path, triangulated mesh, rough machining, uniform rest material

1. Introduction

Moulds and dies are the most persistently used tooling throughout in all the sectors of the manufacturing. The complexity of the machining of moulds and dies is increasing due to simultaneous combination of features such as steps, sharp corners on the walls, narrow pockets on floor and multiple islands. Figure 1 shows a typical design of a mould with such features.

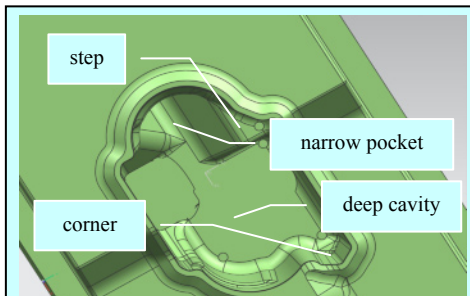


Fig. 1. CAD model of a mould with typical features

At the same time the requirement to build moulds and dies with harder materials, to increase their usage life (hardness reaching in the range of 50HRC), have increased the requirement to develop new processes as well as new methods for planning the machining of such parts. These processes should maximize material removal, minimize tool wear and reduce overall cost of manufacturing a mould or a die. The work at [1-4] present a comprehensive survey of requirements for the milling processes for moulds and dies.

The generation of NC tool path for moulds and dies have been handled traditionally through the utilization of developed algorithms for pocket machining [5]. These approaches were based upon the contour offset method. Over the time, algorithms for the sculptured surface machining and space-filling curves have also been in usage for the NC tool-path planning for dies and moulds [6, 7]. A survey of various methods for solving the NC tool-path generation problem is also present at [7-9].

Trochoidal milling process has been established for its stability, constant loading on the milling tool and accordingly on machine spindle as well [10, 11]. Author has established this process at the Institute of Production Technology (IPT) for machining under high-speed conditions as well under multi axis milling of free formed surfaces. Therefore, trochoidal machining is selected for investigation and implementation scope of this work as well. In the following sections, we present a combination of various individual methods and their integration for the calculation of the trochoidal tool-path.

2. Numerical techniques in NC tool-path planning

The focus of the numerical techniques is to find the approximate tool-path positions with in given tolerance. These tool-path positions are collision free and satisfy the criterion of position continuity. In the following sections, the discussion focuses on the determination of a configuration space in the first step and then this

configuration space has to be filled with trochoidal tool-paths.

2.1 Configuration space determination

The configuration space creation method is based on the model of mutual intersection of a polygon mesh of the part geometry and the CSG model of the milling tool [6], [14] at individual static positions or by moving along a curve.

The configuration space data model is based on an axis aligned quad tree. The data model is established in two stages. The first stage creates the base net with quads of same size while the second stage does the actual refinement. To be able to represent topology conditions such as neighbouring information the configuration space is stored in a multi-resolution half-edge model [13]. The data stored in the net - such as tool tip position and contact point on the bounding positions - is obtained by a sequential application of tool dropping functionality in the ModuleWorks components library by dropping the milling tool along various orientation and at the end the z-axis values are compared [15]. This results into an accurate linear approximation of the configuration space.

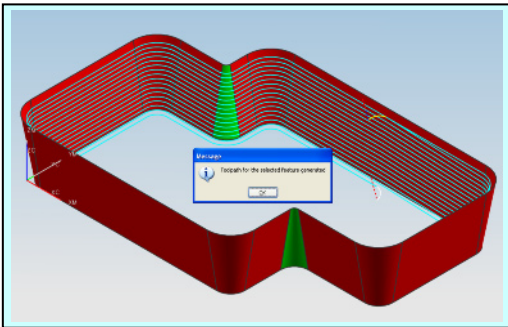


Fig. 2. Configuration space generated for a simplified model – the blue curves are used as bounding curves for trochoidal too-paths

The configuration space achieved in this way represents the position and orientation at boundaries for the trochoidal tool-path. In the next calculation steps the configuration space is used as the boundary conditions.

2.2 Trochoidal tool-path in parametric space

Depending upon the dimensional parameters of the individual bounding contours achieved from the step at 2.1 above a two dimensional parametric space is established. The two axes of the parametric space represent individually the two linear dimensions of a bounding area (length and width) formulated in this parametric space.

Within the parameters of the bounding area, a series of discrete trochoid curve is generated and individual segments are linked with position continuity. The

position of any individual point k in parametric space is determined by:

$$p_k(i, j) = f(l, w, a) \quad (1.1)$$

where l and w are two dimensional parameters of the parametric slot at a selected position and a is the distance between two neighbouring trochoid curves. The function utilizes the parametric equation of trochoid enhanced with the introduction of new factors explained below

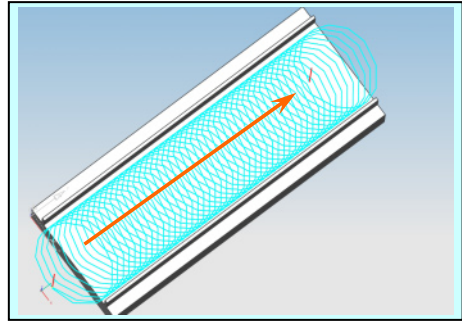


Fig. 3. Trochoidal tool path in parametric space – represented on a test part

As shown in the Figure 3 (above) the trochoidal tool-path in the parametric space are connected curves advancing in a straight direction.

2.3 Space frame conversion

The parametric space builds up an analogy to the real geometry. In order for the data in parametric space to be usable on the real part a space frame transformation has to be carried out.

The transformation has two steps first scaling transform of the parametric dimensions and then a rotational transformation is applied. The transform is applied to each individual points of the trochoidal paths segments from the parametric space. The resulting tool-path in real space is still within the bounds of the configuration space in real space determined earlier.

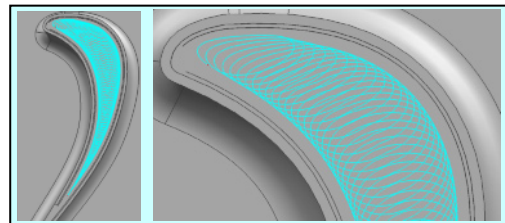


Fig. 4. The trochoid too-path transformed into real work space for an example part

The resulting tool-path satisfies the position continuity criterion. However, the tool-path is examined separately for

tangential continuity and additional smoothing functionality is developed for handling these tangential discontinuities.

The smoothing method principally trims the parts with such discontinuities and puts new segments that satisfy the smoothing criterion.

2.4 Process parameters verification

The advantage of establishing the trochoidal curves in the parametric space are first it is a good method to represent the real system in analogy and secondly various criterion can be combined into the position calculation function (1.1) to improve the function against give criterion.

Two main criterion are combined into this function:

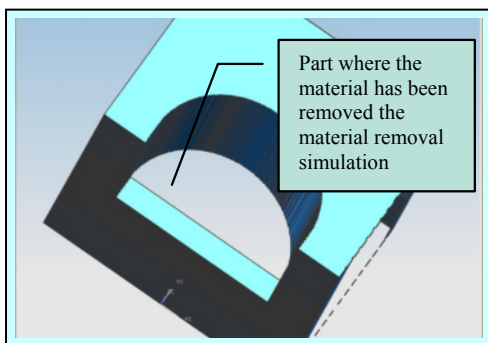
1. Uniform tool and material engagement
2. Consideration for movements in material and in air over the parts of trochoid curve segment

For the first criterion individual factors have been introduced which modify the position of individual point by shifting it along the parametric dimensions in this way the equation (1.1) is modified as that;

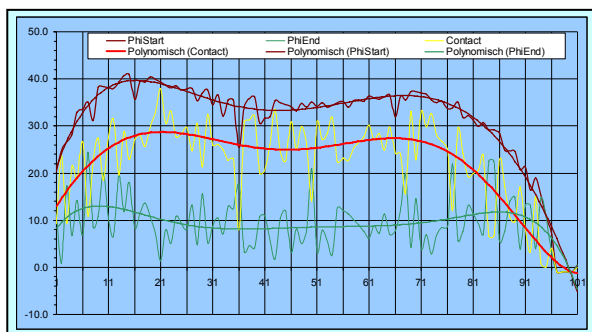
$$p_k(i, j) = f(l, w, a) \pm f(b_1, b_2, w) \quad (1.2)$$

$$b_1, \& b_2 < 1.0$$

b_1 , and b_2 are the individual factors and by their values have been fixed by experiment



(a)



(b)

Fig. 5. Verification of the process conditions. (a). the resulted material model after the material removal simulation (b) the results of the contact angle (red line) analysis for a single trochoid cut

For the second criteria, each individual segment is broken into individual parts and the parts that are out side the material i.e. on the return part of the trochoid are kept shorter as compared to the parts that are inside the material. Accordingly, different feed values are assigned to each individual part as well.

The verification of the process parameters is performed by the evaluation of relevant engagement of the milling tool and the material. This is achieved through a numerical model of the material/tool engagement for the removal of the material [15, 16]. The results are demonstrated in Figure 5. The red line in Figure 5-b shows the mean values of the contact angle over one selected trochoidal segment.

3. Implementation and verification

The implementation of the methods briefly explained above in a standalone system is not a feasible task for a single individual in a limited time. Therefore, an established system at ModuleWorks GmbH, for calculation of multi-axis machining tool-paths, has been selected [15]. In this systems called “MSurf” the above defined algorithm has been integrated as add on component.

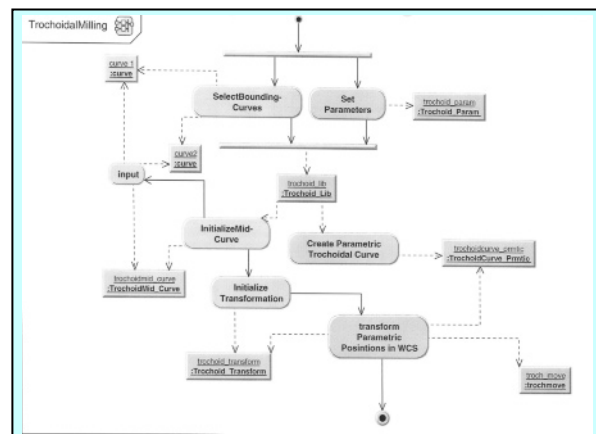


Fig. 6. The activity flow diagram of implemented algorithm

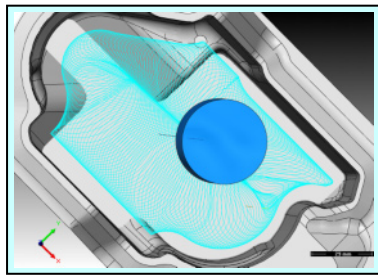
The integration of the algorithm uses service-client architecture and the complete algorithm is accessible by the main system through a single and simple interface.

The verification of the algorithm is done pre-selected tests cases which includes simple models such as shown in Figures 2, 3 and 4. The verification uses the simulations of the calculated out put including material removal simulation.

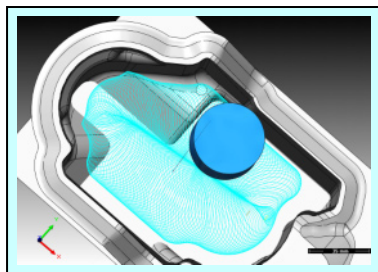
4. NC path planning for moulds

For the real geometry the tool path planning has been done under various objectives, namely to produce by rough machining a shape that is close to the final contour, rough machining under uniform cutting load conditions for milling tool (to reduce tool wear and machine chatter etc.) or machining under “High speed cutting” conditions. For moulds and dies, this requires machining strategies that can handle corners, edges, steps etc. and at the same time deliver a higher material removal rate.

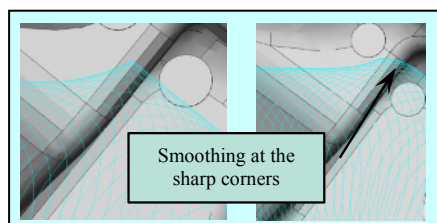
The trochoidal tool-path planning can be carried out in a variety of conditions. Depending upon the criterion trochoidal path planning can handle corners, edges, steps as well as the tool-path that is optimized for high speed machining conditions. A trochoidal machining operation is defined with a specific sets of parameters and simultaneously handle multiple features.



(a) – Tool-path planning for slow and finer tool-paths



(b) – Tool-path planning for fast (HSM) tool-paths



(c) – smoothing of sharp corners at the boundary of trochoidal tool-path

Fig. 7. Results of tool-path planning under various conditions

5. Conclusion

In this paper the use of two numerical techniques for defining and implementing the algorithm for trochoidal milling method for moulds and dies have been stated. With the help of configuration space and calculation in parametric space, methods it is possible to calculate tool-paths for models of complex moulds as well as dies. Utilizing, the concept of parametric space the method allows building into the tool-path different optimization criteria in analogy and immediately reflects its effects for the real geometry. The technique of building the tool-path first in a an analogy work space and then transfer it to real model space can also be extended for other processes because of its ease to inherently build into the tool-path planning various optimization criteria.

Acknowledge

The authors appreciate the contributions and support of AWF (Aachener Werkzeug und Formenbau) Colloquium. The cooperation of colloquium partners is highly regarded.

References

- [1] T. Altan, B.W. Lilly, J.P. Kruth, W. König, H.K. Tönshoff, C.A. van Luttervelt, and A.B. Khairy, (1993) *Advanced Techniques for Die and Mold Manufacturing*. CIRP Annals - Manufacturing Technology, 42 (2), pp 707-716
- [2] F. Klocke, S. Knodt, S. Altmüller, and A. Bilsing, (1999) *Fraesverfahren stellen hohe Ansprüche an Werkzeug und Maschine*. Werkstattstechnik wt, 1999, no. 89/10, pp.451-455.
- [3] T. Altan, B. Lilly, and Y.C. Yen, (2001) *Manufacturing of dies and molds*. Annals of the CIRP 50(2), pp. 405–423
- [4] E. Gasparraj, (2006) *Practical Tips for High Speed Machining of Dies and Molds*. MMS online (www.mmsonline.com/articles/) February.
- [5] M. Held, (1991) *On the computational geometry of pocket machining*. Lecture notes in computer science, no. 500.
- [6] B. K. Choi, R. B. Jerard, (1998) *Sculptured surface machining - Theory and applications*. Dordrecht: Kluwer.
- [7] S. S. Makhanov, W. Anotaipaiboon, (2007) *Advanced Numerical Methods to Optimize Cutting Operations of Five Axis milling machines*. Springer
- [8] D. Dragomatz and S.A. Mann, (1997) *Classified bibliography of literature on NC tool path generation*, Comput Aided Design 29 (3), pp. 239–247
- [9] D. Dragomatz, (1995) *Numerical control tool path generation using space-filling curves and pixel models*. Master's Thesis, University of Waterloo, Canada.
- [10] M. Otkura and I. Lazoglu, (2007) *Trochoidal milling*, Journal of Machine Tool and Manufacture 47 pp. 1324-1332
- [11] M. Rauch, E. Duc and J.Y. Hascoet, (2009) *Improving trochoidal tool paths generation and implementation using process constraints modelling*, Int. Journal of Machine Tool and manufacture 49 pp. 375-383
- [12] M. Meinecke, (2009) *Prozessauslegung zum fünfachsigem zirkularen Schrappfräsen von Titanlegierungen*. PhD Thesis RWTH Aachen

- [13] P. Kraemer, D. Cazier, D. Bechmann, (2007) Multi-resolution Half-Edges. Proceedings of SCCG'07 (Spring Conference on Computer Graphics), pp. 242-249.
- [14] Introduction to 5-axis technology, www.moduleworks.com ModuleWorks GmbH.
- [15] F. Klocke, K. Arntz, T. Bergs, L. Glasmacher, C. Richterich, (2009) Technology based tool path conversion for simultaneous 5-axis milling in tool and die making. 5th International Conference and Exhibition on Design and Production of MACHINES and DIES/MOLDS
- [16] M. Kaymakci, I. Lazoglu, Y. Murtezaoglu (2006), Machining of complex sculptured surfaces with feed rate scheduling. Int. J. of Manufacturing Research 1 (2) pp. 157 - 175
- [17] M. Stautner, A. Zabel, (2005) Optimizing the multi-axis milling process via evolutionary algorithms. CIRP international workshop on modeling of machining operations

Net Shape Laser Butt Welding of Mild Steel Sheets

R. M. Eghlio, A. J. Pinkerton and L. Li

Laser Processing Research Centre (LPRC), School of Mechanical, Aerospace and Civil Engineering, The University of Manchester, Sackville Street, Manchester M60 1QD, United Kingdom.

Abstract. In laser welding, the weld bead is normally extended above or below the parent material surfaces due to melt flow and rapid solidification. This paper presents a study of achieving net shape (i.e. weld bead is flat to the parent material surfaces) butt welding of 1.5 mm mild steel sheets using a continuous wave single mode fibre laser (maximum 1 kW) at a range of laser powers, welding speeds and laser focal point positions. A series of experiments were performed using statistical design of experiment (DoE) techniques and analysis of variance (ANOVA) to identify significant variables and their interactions affecting the weld characteristics. The work shows that it is possible to obtain net shape welds on either the upper and lower surfaces of the material studied. There is an approximately linear relationship between upper surface weld bead offset from the surface and the welding speed. A welding speed of above 100 mm/sec is required for achieving net-shape butt welding at 500-550 W laser power.

Keywords: f laser, butt welding, net shape.

1 Introduction

Over the last few decades, the application of laser welding and joining techniques has increased steadily with the advent of high powered industrial laser systems. Attributes such as high energy density and accurate focusing allow high speed processing for precision assemblies [1]. Compared with some of other traditional welding processes (e.g. arc welding and plasma welding) laser welding can generate higher aspect ratio welds (a ratio of depth over width) with lower heated affected zone (HAZ) sizes and little thermal deformation [2]. Because of laser's ability to weld reproducibly at very high speeds using Computer Numerical Control (CNC) at a competitive price, laser welding is competitive in a variety of industrial applications [3].

Laser welding falls within the group of high-energy-density beam processing technology with the potential to produce welds of high characteristic ratios and it has the benefit of not needing a vacuum system [4,5]. Over the last few years the availability of high power fibre lasers has also enabled high energy efficiency welding to take

place [6, 7]. Lasers are useful for welding thin materials, where strict requirement for workpiece fit-up and thermal distortion control are recognized challenges [8] and for welding thicker plates where thermal distortion is the main problem [9]. This is particularly useful for devices in, for example, the medical industry and aerospace components where formation of discontinuities (pore, void and hot crack) and distortion after laser welding could lead to the part failing quality criteria or failing in service [10].

In the melt pool a high temperature gradient is generated and rapid melt flow takes place. As a result, rapid solidification of the weld can cause the weld bead to form above or below the parent material surfaces. The main driving mechanisms of the fluid flow are the friction force of metal vapour from the capillary, the movement of the capillary relative to the work piece, the temperature-dependent surface tension gradient (Marangoni forces) and thermal expansion of the weld pool and capillary relative to the joined workpiece [11-13]. An important factor that affects the weld geometry is the Peclet number. By increasing the Peclet number, the cross section of weld bead can vary from a rectangular to a triangular geometry in cross section [14]. Beam absorption coefficient, thermal diffusivity, melting and boiling points, among the range of physical properties have been found to be the major factors affecting the weld pool geometry [15].

Earlier work by the authors has shown that a net shape weld for laser bead-on-plate welds for the upper surface and lower surface of a plate can be obtained and that welding speed is the most critical parameter for weld bead geometry control [16, 17].

This paper investigates the feasibility of achieving Net Shape Butt Welding (NSBW) of mild steel materials using a fibre laser. Laser net-shape butt welding has so far not been shown before. Therefore this study would open up a new area of research. A design of

experiments and statistical modelling technique was used in this investigation.

2 Experimental Design and Procedures

2.1 Design of Experiments and Methodology

The experiments are divided in two parts; the first part (A) was carried out through design of experiment using Design Expert 7.0, and the second part (B) experiments were run under a constant laser power, focal point position and gas flow rate with variable speeds.

2.1.1 Part (A)

In this part of the investigation, an L 35 orthogonal array, which consisted of three columns and 35 rows, was applied. The experimental design was based on three groups of welding parameters with five levels of each. The selected welding parameters for this research are: laser power, welding speed and laser beam focal point position (Fpp, positive means above the surface and negative means below the surface). Table 1 shows the design factors and parameter levels.

Table 1. Design factors and variables

Variables	Levels				
laser power (W)	500	525	550	575	600
welding speed (mm/s)	90	95	100	105	110
Fpp (mm)	-3	-2.5	-2	-1.5	-1

2.1.2 Part (B)

In this part of the investigation, experiments were carried out under a constant laser power, focal point position and gas flow rate with variable speeds from 65 mm/s to 125 mm/s. Table 2 shows the laser welding variables.

Table 2. Process parameters for Part (B) experiments

Parameters	Units	Rate
Laser power	W	600
Welding speed	mm/s	65-125
Focal point position	mm	2.5
Ar gas pressure	kPa	100

2.2 Laser welding preparation and methodology

Laser welding was performed on mild steel plates (0.16% – 0.29% carbon), of 50 mm × 50 mm × 1.5 mm thickness, and 50 mm × 25 mm × 1.5 mm thickness. They were butt welded using a 1 kW single mode fibre laser. The samples were mounted on a CNC motion

system and clamped during the welding process as shown in Figure 1. The coaxial assist gas was Argon with a gas pressure of 100 kPa. The focal distance of the lens was set according to Tables 1 and 2, and the gap between the welding nozzle and the sample was 5 mm. The nozzle which used for experimentation has an exit aperture of 2 mm. The investigation in this study included 35 experiments in part A and 12 experiments in part B.

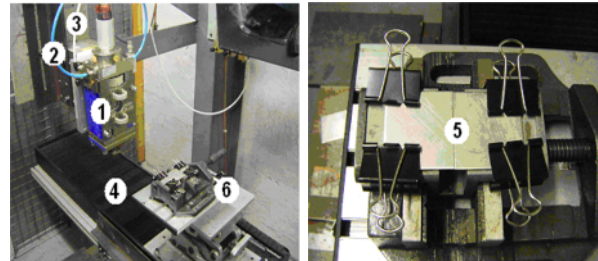


Fig. 1. Experimental setup: 1) laser head, 2) cooling jacket, 3) shielding gas, 4) high speed linear motor traverse table, 5) Experimental samples clamped on the table and 6) adjustable vertical manual table.

2.3 Sample preparation

Following the welding experiments, the samples were cross-sectioned perpendicular to the weld direction, and mounted in a resin, polished with diamond slurry to 6 μm and 3 μm surface finishes and finally etched with Kroll's reagent (1 ml nitric acid and 9 ml methanol) for approximately 60 seconds for further examination. The microstructures were imaged using Polyvar microscopy. For each sample, the welding bead offset from the parent material surfaces was measured in terms of the top height (TH), top width (TW), bottom length (BL), and bottom width (BW), as shown in Figure 2.

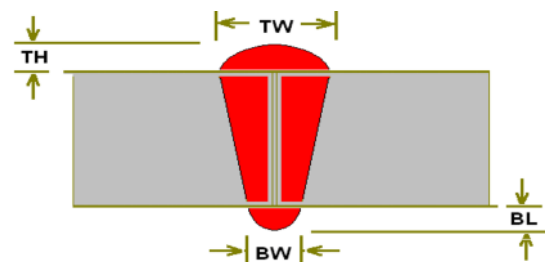


Fig. 2. Schematic diagram of the cross section of sample

2.4 Response surface methodology

A response surface method (RSM) was used to classify the significant processing factors and quantify interactions between the parameters. The analysis of variance (ANOVA) was used to identify the importance of the input parameters and their correlation with the

weld characteristics. In this paper only two output parameters were examined: Top Height (TH) and Bottom Length (BL).

3 Results and Discussion

3.1 Weld Profiles

Figure 3 shows some examples of welds achieved. Near net shape on the top surface has been demonstrated. In addition, the weld bead profiles were positively tapered. On the other hand, in Figure 4, bottom weld bead near net shape welds are demonstrated. Depending on the parameter combinations used, diverse combinations of convex surface beads, undercutting and dropout were also seen.

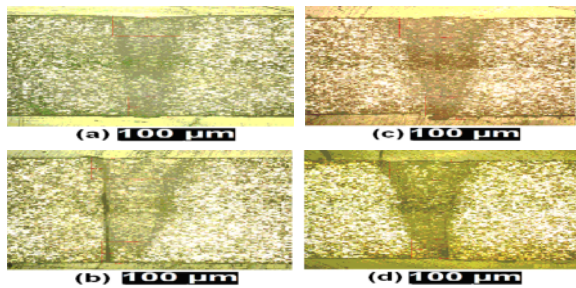


Fig. 3. Examples of near net shape from the top side with welding parameters: (a) laser power (P): 550 W, welding speed (S) 100 mm/s, and Fpp: -3.00 mm, (b) P: 525 W, S: 105 mm/s, (c) P: 550 W, S: 90 mm/s, and Fpp: -2 mm, and Fpp: -1.50 mm, (d) P: 550 W, S: 100 mm/s, and Fpp: -1.0 mm.

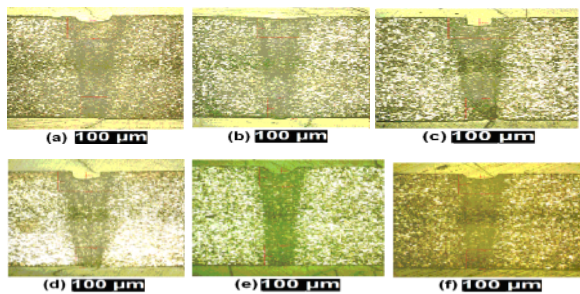


Fig. 4. Examples of near net shape from bottom side with welding parameters: (a) P: 575 W, S: 95 mm/s, and Fpp: -1.5 mm, (b) P: 550 W, S: 100, and Fpp: -3.00 mm, (c) P: 550 W, S: 100 mm/s, (d) P: 600, S: 100, and Fpp: -2.00 mm, (e) P: 550, S: 100, and Fpp: -3 mm, (f) P: 500 W, S: 100 mm/s, Fpp: -2mm.

3.2 Weld Bead Offset from the Top Surface

Figure 5 shows the parameter interaction effect of welding speed and power on the weld bead offset from the top surface, at a focal plane position of -2.5 mm (below the surface). The values in the graph show the weld bead offset values in μm . It is clear that positive values of top height are formed at higher speeds at laser powers below 550 W. At the speed increases the top height will increase. This trend will reverse if the laser power is above 550 W. This means that control of the welding parameters, commonly given in terms of either specific energy or line energy, is important to achieve net shape welding. The top height values vary from $-300 \mu\text{m}$ to $175 \mu\text{m}$. An important point here to be mentioned is that zero top weld bead offset (net shape) occurs at welding speeds above 100 mm/s and a laser power between 500 W and 550 W.

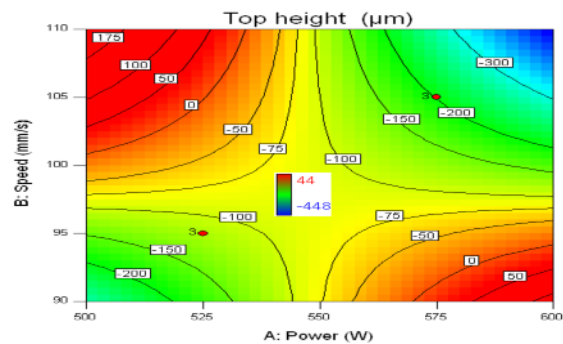


Fig. 5. Effect of power and speed on Top Height

3.3 Relationship between welding speed and top height

Based on the results in part (A) it was recognized that focal point position -2.0 mm was more effective to achieve net-shape welding, experiments were run under a constant laser power 600 W, focal point position -2.0 mm and a gas flow rate 100 kPa, and the speed was variable from 65 mm/s to 125 mm/s. From Figure 6 it can be seen that the weld bead offset over the top surface, i.e. top height, changes from negative to positive as the speed increases, passing through zero at the speed of approximately 100 mm/s.

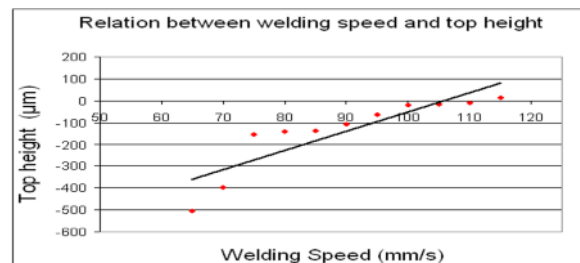


Fig. 6. Relation between welding speed and Top Height

3.4 Weld Bead Bottom Offset

Figures 7 show the effect of welding speed and laser power on the weld bead bottom surface characteristic. It's clear that bottom lengths, i.e. weld bead bottom offset from the surface, approaches to a zero (net shape) at a speed over 95 mm/s and power less than 575 W. Net shape on the bottom surface would be useful for pipe welding, where the machining will be complicated, and non-zero bottom weld bead offset might affect the fluid flow. The values of the bottom length vary from negative 76 μm to positive 74 μm . Furthermore, it can be noticed that as the welding speed decreases the bottom length will increase.

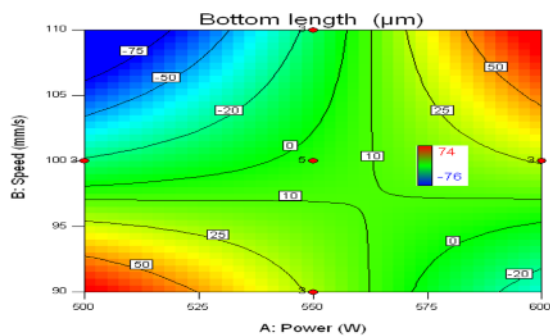


Fig. 7. Effect of power and speed on Bottom Length

4 Conclusion

Net shape butt welding of mild steel sheets has been demonstrated using a single mode fibre laser. A specific set of welding parameters were found to achieve the net shape welding (for either the top and the bottom welds) at different parameters of laser power, welding speed and focal point position. There is a linear correlation between the welding speed and top height; as the speed increases the top height changes from negative to positive. A negative fpp is found to improve surface quality in most circumstances.

Using a fibre laser for the welding process creates a very efficient use of the material components, and has the potential to minimize the total cost of the production. Further investigations are in-progress to understand the mechanical and physical properties of the welds and model the behaviour of weld bead.

Acknowledgement

The Libyan Government is gratefully acknowledged for its financial support of a PhD studentship for one of the authors through the Cultural Affairs Libyan People's Bureau – London.

References

1. J. O. Milewski and E. Sklar, (1997) Modeling and design of energy concentrating laser welding joints. First asm international conference on welding and joining science and technology, Madrid, Spain, March 10-13.
2. S. A. Tsirkas, P. Papanikos, and T. Keramanidis, (2003) Numerical simulation of the laser welding process in butt-joint specimens. *Journal of Materials processing Technology* 134, (59-69).
3. W. W. Duley, 1999. *Laser welding: Wiley-Interscience*
4. W. M. Steen, (2003) *Laser material Processing: 3rd Edition Springer-Verlag London Limited.*
5. K. Chen, Z. Wany, R. Xiao, and T. Zuo, May 10 (2006) Mechanism of laser welding on dissimilar metals between stainless steel and W- Cu alloy. *Chinese Optics letters*, , vol. 4, No. 5, (294-296).
6. Y. Kawahito, M. Mizutani & S. Katayama (2007) Elucidation of high-power fibre laser welding phenomena of stainless steel and effect of factors on weld geometry. *Journal of Applied Physics* 40, (5854-5859).
7. K. Kinoshita, M. Mizutani, Y. Kawahito, and S. Katayama, (2006) Phenomena of welding with high-power Fiber Laser. paper 902 *ICALEO Congress Proceedings*, (535-542).
8. J. Xie and A. Kar, (1999) Laser Welding of Thin Sheet Steel with Surface Oxidation. *Weld. J. Res.* 78, (343s-348s).
9. I. Miyamoto, (LPM 2002) Challenge to advanced laser materials processing in Japanese Industry. Focused on laser precision Microfabrication, *RIKEN Review No. 50* (January, 2003).
10. R. Steiner, (2006) New Laser technology and future applications. *Journal of Medical Laser Application* 21 (131-140).
11. W. Sudnik, D. Radaj, S. Breitschwerdt and W. Erofeew (2000) Numerical simulation of weld pool geometry in laser beam welding. *Journal Phys. D: Appl. Phys.* 33 (200) 662-671
12. H. Lijun, L. Frank & M. Srinivas Venkata (2005) Thermal behavior and geometry model of melt pool in laser material process. *Journal of Heat Transfer Vol. 127, No 9*, pp. (1005-1014).
13. H. Ki, P. S. Mohanty, and J. Mazumder, (June 2002) Modeling of Laser keyhole welding: part 1. Mathematical modeling, numerical methodology, role of recoil pressure, multiple reflections, and free surface evaluation. *Metallurgical and materials transactions a Volum 3 33A* (1817-1830).
14. K. Kazemi, and J. A. Goldak (2009) Numerical simulation of laser full penetration welding. *Computational Materials Science* 44, (841-849).
15. R. Rai, J. W. Elmer, T. A. Palmer and T. DebRoy, (2007) Heat transfer and fluid flow during keyhole mode laser welding of tantalum, Ti-6Al-4V, 304L stainless steel and vanadium. *Journal of Heat Physics D: Applied Physics.* 40 (5753-5766).
16. R. M. Eghlio, A. J. Pinkerton and L. Li, (2009) Investigation of Net-Shape Welding of Mild Steel Sheets with a 1 kW Single Mode Fibre Laser. *ICMR 09*, University of Warwick, UK, P 84 (303-307).
17. R. M. Eghlio, A. J. Pinkerton and L. Li, (2009) Fibre Laser Net - Shape Welding of Steels. *ICALEO Congress Proceedings*, P 101 (1402-1408).

Humping Modeling in Deep Penetration Laser Welding

E.H. Amara

CDTA, Laser Material Processing Team, Po Box 17Baba-Hassen, 16303 Algiers, Algeria, Email: amara@cdda.dz

Abstract. Deep penetration laser welding is studied at processing speeds leading to the humping phenomenon. Matter melting, vaporization and re-solidification are considered through the implementation of User Defined Functions (UDFs) used with CFD Fluent code. The dynamic mesh method implementation allows the occurrence of regular humps apparition to be simulated.

Keywords: Laser welding, deep penetration, keyhole, free surface deformation, CFD, humps formation.

1. Introduction

Nowadays, there is growing interest in fast deep penetration laser welding for economical and environmental reasons. For processing speeds above 20 m/min, the humping regime is reached. It is characterized by weld seams with large swellings of quite ellipsoidal shape, separated by smaller valleys [1-2]. The resulting humps constitute a major obstacle for fast laser welding making a worthwhile topic to study. The associated physical processes are very complex phenomenon to understand from basic principles, due to the simultaneous occurrence of solid, liquid, gas and plasma states in a small volume. Experimental approaches have been proposed to understand humps formation, and data were compiled to verify the related models [2,3], and theoretical studies based on analytical models were also developed [4, 5]. Few simulations of the humping phenomenon have been proposed. Cho [6] developed a very interesting simulation in arc welding, by using the CFD-Flow3D code, where the Volume Of Fluid (VOF) method has been implemented to track the solid-liquid interface. In this paper, a 3-D transient modeling of deep penetration laser welding at high processing speeds is proposed. A finite volume numerical resolution of the fluid flow and the heat transfer governing equations is performed by Fluent CFD code [7]. We consider through free surface deformation, the vaporization and keyhole formation, the induced melt pool movements, and the re-solidification. In order to involve these complex mechanisms, the specific boundary conditions and the temperature dependent physical properties, procedures

called user defined functions (UDFs), have been developed to be used interactively with the Fluent solver. The recoil pressure mechanism has been included in the UDFs which is among the main causes of the free surface deformation. Tribel'skii [8] determined theoretically the shape of the free surface of the melt, undergoing deformations due to the recoil pressure. The various aspects on the interaction of high-power optical radiation with a liquid have been reviewed in [9], and Samokhin [10] investigated the influence of evaporation on the melt behaviour during laser interaction with metal. In a previous work [11], the free surface deformation has been studied using the VOF method, while in this paper, the resulting keyhole and humps are studied by implementing dynamic mesh and enthalpic approaches.

2. Modeling

We consider initially, a flat free surface, and a temperature of 300K on the whole volume of the sample. During the welding process, the regions representing the melt bath, the keyhole and the weld joint are represented on Figure 1. The involved physical mechanisms in the model are the local laser energy absorption, the induced melting and vaporization, and then the re-solidification.

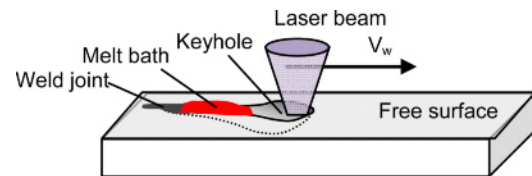


Fig. 1. The sample during the welding process

When the deposited laser energy is beyond the material vaporization threshold, the free surface undergoes deformation while it is irradiated by the laser beam. The amount of the deformation is calculated through the

displacement Δd , by considering the local drilling velocity described by Semak *et al.* [12], such as:

$$\Delta d = v_d \Delta t \tag{2.1}$$

where Δt is the simulation time step. The drilling velocity, v_d , is proportional to the absorbed laser intensity following the relation:

$$v_d = K I_{abs} \cos(\alpha) \tag{2.2}$$

where K is a proportionality factor, I_{abs} the absorbed laser intensity, and α the beam incidence angle over the sample surface. Fabbro *et al.* [13] calculated 2-D keyhole profiles by considering segments evolution under the effect of the drilling, closing and processing velocities. In the 3-D calculation, the normal vectors on surface elements irradiated by the laser beam are considered. I_{abs} is thus needed in order to calculate the free surface deformation, and knowledge of the local incident angle α is also required. Next, the free surface is considered as an envelope where each surface element is identified by the normal vector \vec{A}_N while A_x , A_y and A_z are the vector components, Figure 2. The modulus of \vec{A}_N and the vector components are data reachable from Fluent which updates the mesh geometry after each time step. Thus one can obtain the incidence angle α through the relation:

$$\cos(\alpha) = A_z / |\vec{A}_N| \tag{2.3}$$

and then the absorbed intensity as (for a gaussian beam) :

$$I_{abs} = A (2P/\pi r_1^2) \cos^{1.2}(\alpha) \exp(-2r^2/r_1^2) \tag{2.4}$$

where A is the absorption coefficient of the material, related to the used laser wavelength, P the laser power, and r_1 the beam focal spot radius.

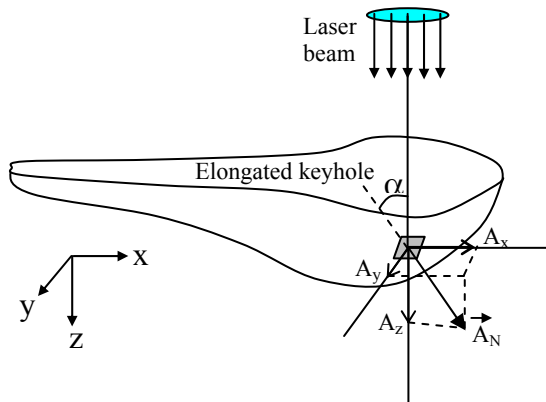


Fig. 2. 3-D schematic representation of the keyhole, and a surface element, with its normal vector

In the approach, the laser beam is considered to move over the free surface of the sample at a welding speed v_w . As shown on Figure 3, the position r is calculated such

as $r = [((l-x)^2 + y^2)]^{1/2}$, where $l = x_0 + v_w t$, with x_0 the initial position of the laser beam on the sample surface, and v_w the welding velocity. If $r \leq r_1$, I_{abs} is calculated following equation (2.4), else if $r > r_1$, then I_{abs} is equal to zero. Thus knowing the local absorbed laser intensity, at each surface element, the drilling velocity v_d is deduced which is then used to calculate surface elements displacements, and then the whole envelope deformation is obtained for the 3-D geometry.

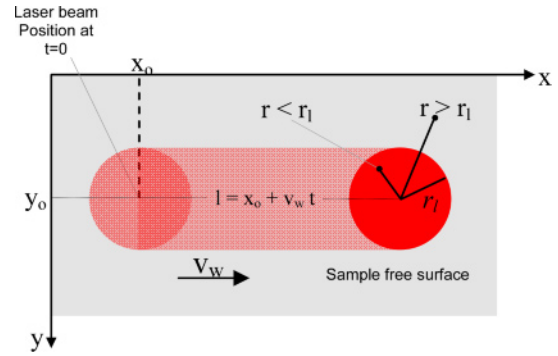


Fig. 3. Representation of the laser beam on the free surface

The material melting and re-solidification are calculated by an enthalpic method, while the surface tension variation due to the temperature difference produces a stress on the wall which is taken into account in this modeling. This stress, called Marangoni stress is given by $\tau = (d\sigma/dT)\nabla_s T$, where $d\sigma/dT$ is the surface tension gradient and $\nabla_s T$ is the surface gradient. In the case of iron, we have taken $d\sigma/dT = -10^4$ N/m/K [14]. It has been noticed that the inclusion of the surface tension effect through this gradient is of high importance for the observation of humps.

3. Results and discussions

In the simulation the experimental beam parameters given in reference [2] have been used. The laser power is taken equal to 4kW, the beam diameter is 600 μ m and the laser wavelength is 1.06 μ m (Nd_YAG laser). An Iron sample is considered, its absorption coefficient A is 0.3, for the used wavelength and the proportionality coefficient K is taken equal to $3 \cdot 10^{-11}$ (m/s)/(W/m²).

The physical properties are considered to vary with the temperature. From Duley [15], the following expressions for the density and heat conductivity were deduced:

$$\rho(T) = -0.4522T + 7755.7 \text{ in [kg/m}^3] \tag{3.1}$$

$$k(T) = -0.0218 T + 76.307 \text{ in [W/m/K]} \tag{3.2}$$

Whereas, the latent heat effects with the temperature distribution, results in increasing of the heat capacity given by Toyerskani *et al.* [16] is applied such as:

$$C_p^*(T) = \frac{1}{T_m - T_a} \left[L_f + \int_{T_a}^{T_m} C_p dT \right] \quad (3.3)$$

C_p^* is the modified heat capacity. By developing (3.3), for a latent heat of fusion $L_f = 2.76 \cdot 10^5$ J/kg, an approximation of the heat capacity C_p^* [J/kg/K] is obtained as a function of the temperature such as:

$$C_p^*(T) = 2.6137 \cdot 10^{-4} T^2 + 0.12034621 T + 124 \quad (3.4)$$

The laser beam displacement velocity used in the simulation is 0.8 m/s (~50 m/min). On the parallelepipedal sample with dimensions of 15 mm x 2 mm x 1 mm, a 3-D structured mesh made up of triangular cells on walls and tetrahedral cells inside the volume is generated. The sample geometry, the domain meshing and the boundary reservation are performed by the pre-processor Gambit of Fluent softwares. Fluent solver is used to solve the corresponding Navier-Stokes equations by finite volume discretizing. The boundary conditions and temperature dependant material properties are introduced by the mean of user-defined functions, or UDF, written in C programming language. These UDFs are used to customize Fluent and adapt it to a particular need required by the modeling. They can be used in various applications such as customizing boundary conditions or the definition of work-pieces' physical properties depending on the temperature. They can be loaded interactively during the calculation procedure, allowing the enhancement of the standard features of the calculation code. In this modeling, UDFs have been developed to introduce the operating conditions, the different involved physical mechanisms such as laser energy deposition and recoil pressure, and the specific boundary conditions related to the problem. The study performed was relatively complex since to make evident the humping phenomenon, a 3-D approach had to be used, and also to take into account the keyhole formation from the initial instant $t=0$, when the laser beam drops onto the material surface. The deformation process due to matter vaporization, while the laser beam moves on the free surface, is calculated by a dynamic mesh technique. The dynamic mesh was difficult to stabilize, and many configurations have been tested before finding the suitable mesh. When the boundary displacement is large compared with the local cell sizes, the cell quality can deteriorate or the cells can become degenerate. This invalidates the mesh (e.g., results in negative cell volumes) and consequently, will lead to convergence problems when the solution is updated to the next time step. To circumvent this problem, the cells or faces that violate the skewness or size criteria, are agglomerated and are locally remeshed. If the new cells or faces satisfy the skewness criterion, the mesh is locally updated with the new cells (with the solution interpolated from the old cells). Otherwise, the new cells are discarded.

In Figure 4 the results of the laser absorbed energy distribution are given. The recoil pressure induced by vaporization acts by pushing the metallic liquid layer generated on the keyhole front, to move around the keyhole towards the bulk of the molten pool in the rear region. The distribution of the dynamic pressure representing the recoil effect on the metallic liquid is represented on Figure 5.

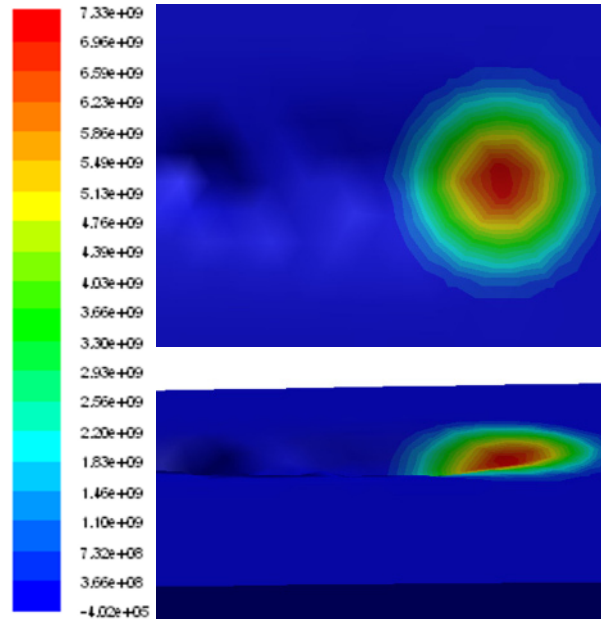


Fig. 4. Contours of total surface heat flux (W/m^2)

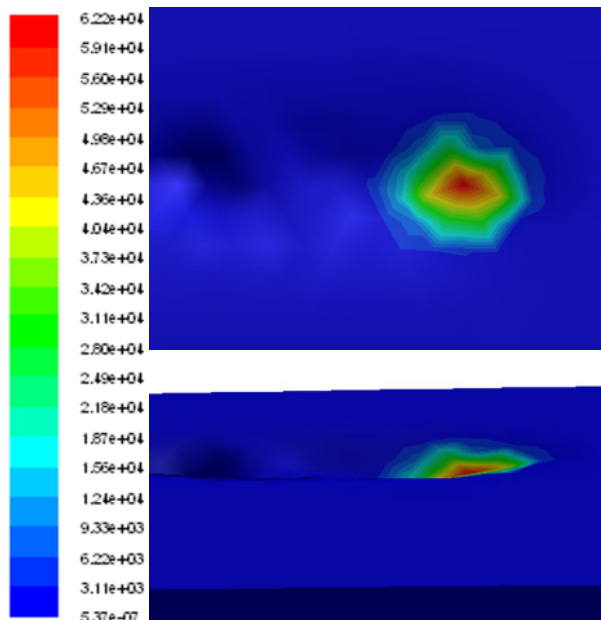


Fig. 5. Dynamic pressure (Pascals) on the keyhole front

Figure 6 represents the temperature distribution from different views. The bird's eye view shows clearly the elongated keyhole and its dimension. Figure (3.4) represents an experimental result [2] showing clearly an elongated keyhole and a hump formation.

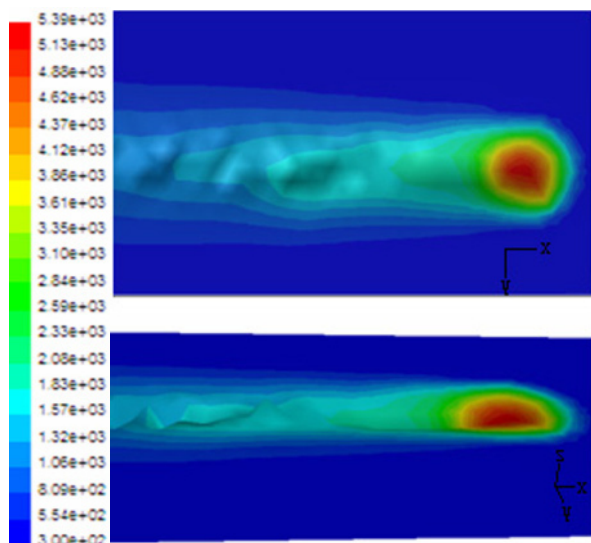


Fig. 6. Temperature field distribution

From Figures 6 and 7, it can be concluded that there is some similitude between the experimental observation and the numerical simulation.



Fig. 7. Experimental observation of humps formation (courtesy of R. Fabbro, LALP)

The last result concerns observation of the humping phenomenon. Occurrence of humps is clear on Figure 8 which shows the sample with the molten bath and the re-solidified region. We can see the growth appearing behind the molten bath which suggests humps formation.

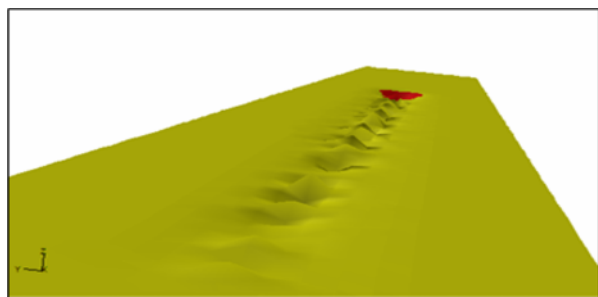


Fig. 8. Sample surface viewed from the rear side.

4. Conclusion

We made evident humps formation at high welding speeds, by developing procedures in order to insert the main physical mechanisms, implementing the dynamic mesh technique and the specific boundary conditions in the calculation process using the CFD Fluent code. The results obtained still have to be enhanced especially the humps shape, and for that purpose, future work will include the Bernoulli equation in the model.

References

- [1] Fabbro R, Slimani S, Doudet I, Coste F, Briand F, (2006) Experimental study of the dynamical coupling between the induced vapour plume and the melt pool for Nd-Yag CW laser welding. *J. Phys. D: App. Phys.*, 39: 394-400.
- [2] Fabbro R, Slimani S, Coste F, Briand F, (2008) Characteristic melt pool hydrodynamic behaviours for CW Nd-Yag deep penetration laser welding. 3rd Pacific International Conference on Applications of Lasers and Optics PICALO 2008, Conf. Proc. LIA Pub#402, 3:173-178.
- [3] Soderstrom E, Mendez P, (2006) Humping mechanism present in high speed welding. *Science and Technology of Welding and Joining*, 11: 572- 579.
- [4] Kumar A, Debroy T, (2006) Toward a Unified Model to Prevent Humping Defects in Gas Tungsten Arc Welding. *Welding Research*, 292s-304s
- [5] Gratzke U, Kapadia PD, Dowden JM, Kroos J, Simon G, (1992) Theoretical approach to the humping phenomenon in welding processes. *J. Phys. D: Appl. Phys.*, 25:1640-1647,
- [6] Cho MH, Lim YC, Farson DF, (2006) Simulation of Weld Pool Dynamics in the Stationary Pulsed Gas Metal Arc Welding Process and Final Weld Shape. *Welding Research*, 271s-283s
- [7] www.fluent.com (2009) Ansys, Inc.,
- [8] Tribel'skii MI, (1978) Shape of the liquid-phase surface in melting of highly absorbing media by laser radiation. *Sov. J. Quantum Electron.*, 8: 462-466.
- [9] Bunkin FV, Tribel'skii MI, (1980) Nonresonant interaction of high-power optical radiation with a liquid. *Sov. Phys. Usp.* 32: 105-133.
- [10] Samokhin AA, (1983) Influence of evaporation on the melt behavior during laser interaction with metals. *Sov. J. Quantum Electron.*, 13:1347- 1350.
- [11] Amara EH, Fabbro R, (2008) Modeling of gas jet effect on the melt pool movements during deep penetration laser welding. *J. Phys. D: Appl. Phys.*, 41:055503.
- [12] Semak V, Matsunawa A, (1997) The role of recoil pressure in energy balance during laser materials processing. *J. Phys.D: Appl. Phys.*, 30: 2541-2552.
- [13] Fabbro R, Chouf K, (2000) Keyhole modeling during laser welding. *J. Appl. Phys.*, 87 : 4075-4083.
- [14] Cipriani FD, (1991) Etude numérique de la convection thermocapillaire dans un bain fondu créé par laser. Doctorate Thesis de, p. 162, N° 207.91.93, Aix-Marseille II Univ..
- [15] Duley WW, (1976) CO₂ Lasers: Effects and Applications. Acad. Press, New York .
- [16] Toyerskani E, Khajepour A, Corbin S, (2003) Three-dimensional finite element modeling of laser cladding by powder injection: Effects of powder federate and travel speed on the process. *J. Laser Appl.* 15:153-160.

Keyholing or Conduction – Prediction of Laser Penetration Depth

D.B. Hann¹, J. Iammi³, J. Folkes²

¹ Division of Energy and Sustainability, Faculty of Engineering, University of Nottingham, NG7 2RD, UK

² Division of Manufacturing, Faculty of Engineering, University of Nottingham, NG7 2RD, UK

³ National Metal and Materials Technology Center (MTEC), Thailand Science Park, Pathumthani, 12120, Thailand

Abstract. In laser material processing understanding the laser interaction and the effect of processing parameters on this interaction is fundamental to any process if the system is to be optimised. Expanding this to different materials or other laser systems with different beam characteristics makes this interaction more complex and difficult to resolve. This work presents an innovative way to understand these interactions in terms of mean surface enthalpy values derived from both material parameters and laser parameters. From these fundamental properties the melt depth for any material can be predicted using a simple theory. By considering the mean enthalpy of the surface, the transition from conduction limited melting to keyholing can also be accurately predicted. The theory is compared to experimental results and the predicted and observed data are shown to correspond well for these experimental results as well as for published results for stainless steel and for a range of metals.

Keywords: Keyholing, Conduction, Laser welding, penetration depth, enthalpy

1. Introduction

Lasers have played a significant role in material processing for many years and have found their niche in many industrially related laser applications [1,2]. Material processing data, optimum cutting or welding parameters and process windows for various materials and specific laser systems have been reported and numerical modelling has been used to validate experimental and theoretical results for such processes [1,2,3]. Correlations of the melt or weld pool geometry with specific process and or physical parameters including interaction time, power or energy density, velocity, energy per unit length and material properties are common [4,5]. Research to correlate the different laser types and to actively predict the resultant material interaction based on these parameters has been undertaken and generalised tables produced [5,6]. Research, however, that attempts to fundamentally understand and present this data is often presented in a format that is complex and difficult to use. This research explores the limitations of presenting processing data in terms of the laser material interaction

parameters of intensity and interaction time and presents an innovative way to understand these interactions in terms of mean surface enthalpy values derived from both material and laser parameters. This approach is then validated by expanding the concept to data obtained from other lasers and materials so that the melt depth for any material can be predicted using a simple theory.

2. Experimental Set-up

Bead on plate welds were performed in 6 mm thick AISI 304. A set of experiments was designed with six levels of laser power (from 300 W to 2000 W) and three levels of welding speed (from 1000 mm/min to 3000 mm/min). The bead on plate welds were made at the focus position by using the different process fibres (200, 400 and 600 μm) with the same setup. After making the bead on plates, the samples were cut in the middle of the welds, transverse to the direction of the welds. Then the samples were polished and etched to expose the weld profile which can then be measured with a microscope. After measurement, the penetration depth was plotted against the process parameters to show the relationship.

3. Results and discussions

The experimental data from laser welding process is typically presented in terms of laser power and welding speed. It has been suggested that presentation of the data in terms of energy or power density and interaction time would be better format. Fig.1 shows the penetration depth against power density for different welding speeds using a 200 μm fibre. Similar graphs can be plotted for penetration depth against interaction time (see Fig. 2).

Table 1 Some of the equation relating laser welding and materials properties

Property	Symbol and units
Speed of weld	U (m/s)
Half-width of Gaussian beam	σ (m)
Radius to e^{-2} of Gaussian beam	$r = \sqrt{2}\sigma$ (m)
Characteristic thermodynamic time	$t_c = \frac{r^2}{\alpha}$ (s)
Dimensionless depth	$\delta^* = \frac{\delta}{r} = \frac{\delta}{\sqrt{2}\sigma}$
Peclet number of Weld	$Pe = \frac{U\sigma}{\alpha}$
Interaction time	$t = \frac{r^2}{\alpha}$ (s)
Power density	$P_A = \frac{P}{\pi r^2}$ (W/m ²)

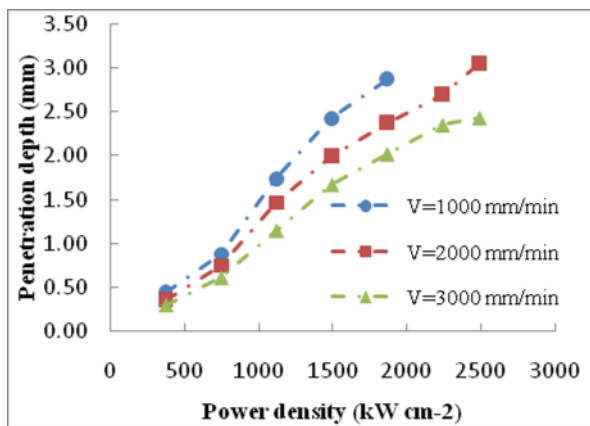


Fig. 1. Shows the penetration depth against power density for different welding speeds using 200 μm fibre

However, a closer look of these Figures (Fig. 1 and Fig. 2) suggests that there are a number of possible penetration depth for the same interaction time at the given power density as seen Fig.3 which shows the penetration depth with interaction time (spot diameter divided by the welding speed) for a constant laser power density. A number of the possible parameters and derived quantities are shown in Table 1. It clearly shows that the interaction time cannot be used unless another term which related to the change in diameter of the beam/fibre is accounted for.

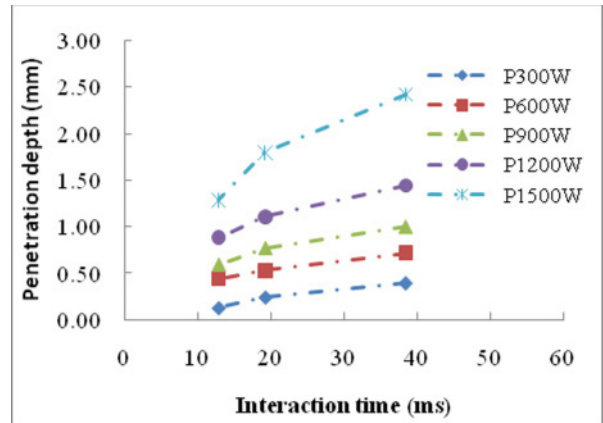


Fig. 2. Shows the penetration depth against interaction time for different laser power using 400 μm fibre

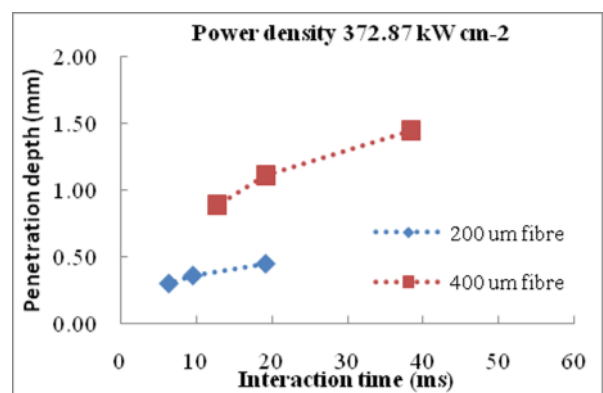


Fig. 3. Penetration depth as a function of interaction time using various process fibre diameters at constant power density

Fig.4 shows another common way of presenting the data: the penetration depth with power density for a constant interaction time. Again, there are a number of potential depths for any particular power density, for the same interaction time and a similar logic applies, in that another factor that needs to be account for if these results are to be understood.

Courtney and Steen [2] suggested that penetration depth was related to the square root of velocity. Fig.5 shows results for the three fibre sizes in this manner demonstrating that all the data converge for each fibre however the lines are of different gradients for the different fibre diameters.

These results indicated that a term relating to the different fibre diameters and therefore beam diameters is required if these values are to be compared.

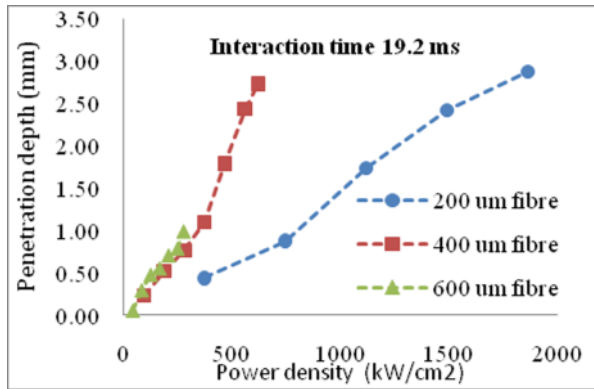


Fig. 4. shows the penetration depth with Power Density. Again, there are a number of possible depths for the same heat input which indicates the usefulness of the data in this format is limited.

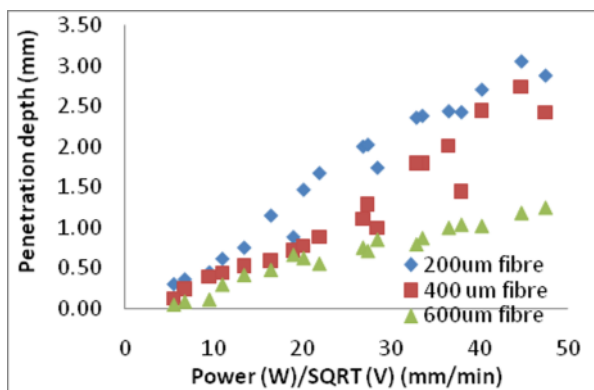


Fig. 5. Power / $\sqrt{\text{velocity}}$ plotted against experimentally measured penetration depth for the 200, 400 and 600 μm fibres

From these results, it can be stated that the interaction time, power density and heat input are limited in their usefulness when defining the penetration depth in laser welding process.

The laser process involves a large number of parameters including power, traverse rate, beam size, material properties (surface absorption, thermal conductivity and thermal diffusivity) and also the dimension of the workpiece. For laser material processing a simple relationship between the laser processing and material parameters to enable a quick and easy determination of the process and parameters is required. Ion et al. [6] have suggested that the laser material processing problem can be simplified by identifying dimensionless groups of the process parameters. They have defined a number of process diagrams for laser processing based on the normalized beam power and a dimensionless variable (the Peclet number) for laser-material interaction. The process diagram in [6] shows a complex relationship, but does define a single weld depth for a particular beam power and a particular Peclet number.

However the relationship is difficult to deduce from their diagrams as they are essentially data the best fit line occurs when 3D visualizations of the experiment space. It would be much better to provide a simple relationship between the laser processing and material parameters so that simplified determination of transitions can be determined.

The data shown in this paper can be analysed using standard data reduction techniques by optimizing the data to fit to a function $\delta = f_n(B \cdot \frac{P}{\sigma^3 U^{1/2}})$. When this function is optimized to the experimental

$$\delta = f_n\left(B \cdot \frac{P}{\sigma^3 U^{1/2}}\right) \quad (1)$$

Here B is a normalization constant such that the parameters are dimensionless. In this case B has units of $J^{-1} m^2 s^{-1}$. Fig. 6 shows the data presented in this manner and it can easily be seen that there are two main regimes of depth, possibly corresponding to conduction and keyholing modes of welding.

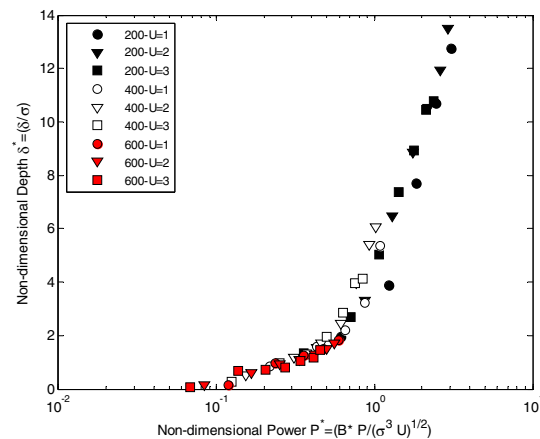


Fig. 6. shows the normalised depth as a function of the laser parameters only. All the data has now collapsed onto a single line.

This expression only considers the laser parameters. It should be obvious that the material parameters should be included in this discussion to account for different materials. Dimensionally the units of B can be constructed from the relevant thermodynamic quantities of thermal diffusivity (α), the absorption coefficient (η), a non-dimensional constant (C) and enthalpy needed to reach melting point (H) by the relationship

$$B = \frac{H C}{\eta \alpha} \quad (2)$$

This suggests that the non-dimensional power can be written as

$$\delta^* = f_n \left(\frac{\Delta H}{\Delta h} \right) \quad (3)$$

It should be noted that dimensionally this can be written as

$$\delta^* = f_n \left(C \frac{\Delta H}{h} \right), \text{ where } \Delta H \propto \frac{P}{\sqrt{2} \pi r^2} \quad (4)$$

This suggests that the depth of the weld is a function of the relative enthalpy increase of the weld compared to an initial enthalpy value. Since this contains both laser and material thermodynamics properties, this should be true for many metals.

Fig.7 shows that the dimensionless depth calculated from the experimental data varies with this parameter and the data from Rai et al. [3] which covers four different metals and making an estimate of the value of C. This shows a sharp transition between the conduction welding and the keyhole welding that occurs when the maximum enthalpy of the material reaches the boiling point.

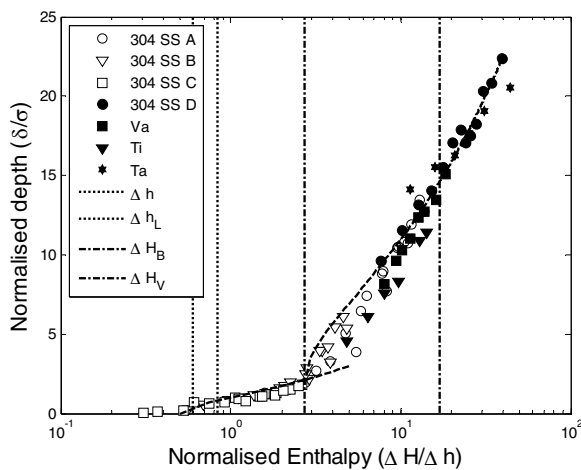


Fig. 7. Graph showing the normalized depth against the normalized Enthalpy of welding spot including experimental data from this work and also shows Rai et al [3].

The data from the different metals shows a close correlation for this showing that the derived expression can be used to estimate the weld depth for many different welding cases. The vertical lines in figure 7 represent the enthalpy ratios for liquidus and solidus temperature (Δh and Δh_L) and for onset of boiling and vaporisation (ΔH_B and ΔH_V). The advantage for this presentation of the data is that due to Richard's and Trouton's rule these ratios are fairly constant for most materials, so the ratio of the enthalpy will be true for a wide variety of metals and plastics [7].

4. Conclusions

The work carried out under this study can be summarized as follows:

There are a number of possible penetration depths for the same interaction time at given power densities and vice versa. Therefore, a term relating to the fibre diameter and beam diameter is required if these values are to be compared.

Dimension analysis technique has been used to propose a different way to presenting the data where the penetration depth is linked to mean-enthalpy of the material surface. As a result, a laser welding process diagram is established which cover not only data from this study but also other different materials and laser types.

Using the laser process diagram established in this research, it relates the transition of conduction welding and keyhole welding to the mean enthalpy ratio. This relationship has the potential to predict the onset of melting and transition to keyhole mode welding for any laser system and material, since the mean enthalpy ratio at vaporisation is similar in all materials.

5. References

- [1] Steen WM, (2003) Laser Material Processing. Springer, 3rd ed. London.
- [2] Steen WM, Courtney GHC, (1979) Surface heat treatment of En8 steel using 2 kW continuous-wave CO₂ laser. Metals Technology 6(12).
- [3] Rai R, Elmer JW, Palmer TA, DeBroy T, (2007) Heat Transfer and Fluid flow during keyhole mode laser welding of tantalum, Ti-6Al-4V, 304L Stainless steel and Vanadium. Journal of Physics D: Applied Physics 40:5753-5766
- [4] Quintino L, Costa A, Miranda R, Yapp D, Kumar V, Kong CJ, (2007) Welding with high power fibre lasers – A preliminary study. Materials and Design 28:1231- 1237
- [5] Suder W, Williams S, Colegrove P, (2009) Absolute spot size effect on penetration depth in laser welding. 5th Int. WLT- Conf Lasers in Manufacturing, Munich 53-58
- [6] Ion JC, Shercliff HR, Ashby MF, (1992) Diagrams for laser materials processing. Acta Metallurgica et Materialia. 40 (7):1539-51.
- [7] Bejan A, (1993) Heat Transfer. John & Sons, Inc

Dual Focus Nd:YAG Laser Welding of Titanium Alloys

J. E. Blackburn¹, C. M. Allen², P. A. Hilton² and L. Li¹

¹ Laser Processing Research Centre, The University of Manchester, United Kingdom, M60 1QD

² Laser and Sheet Processes Group, TWI Ltd, Cambridge, United Kingdom, CB21 6AL

Abstract. Dual focus Nd:YAG laser welding has been considered as a method to reduce the formation of porosity in titanium alloy laser welds. The effects of the foci orientation, foci separation, welding speed and power distribution ratio on the resulting porosity have been examined using response surface methodology. Both transverse and in-line foci orientations, with controlled foci separations and welding speeds, can be used to establish a stable keyhole and vapour plume regime, promoting low porosity welds. The weld metal porosity levels can be reduced to within levels stipulated in stringent aerospace weld quality criteria.

Keywords: laser, welding, titanium, Nd:YAG, dual focus, porosity.

1. Introduction

As a result of their excellent mechanical properties and corrosion resistance, α , α/β and β titanium alloys have been incorporated into aerospace designs for several decades [1]. Environmental and economic pressures are increasing the demand for weight savings in commercial airframes, which is driving further demand for titanium components in the sector [2]. Despite being of high quality, machined titanium components have uneconomical buy-to-fly ratios compared with structural steels and aluminium alloys. The production of near-net-shape components by keyhole laser welding could reduce material wastage significantly and increase production rates. However, weld metal porosity can be formed when keyhole laser welding [3]. This is of particular concern for high-performance, fatigue-sensitive applications, such as primary airframe structures and aeroengine components, whose weld seams are typically dressed, allowing pores to break the surface, act as stress concentrators and reduce the fatigue resistance of the weld [4]. Consequently, stringent weld quality criteria are applied to welded components in the aerospace industry [5].

Several researchers have reported that welding with a dual focus laser beam is an effective method of reducing weld metal porosity in other materials [6,7,8]. Weld metal porosity can be reduced when welding AA5083 and A356

aluminium alloys with a Nd:YAG laser beam if a dual focus configuration is utilised [6]. Observation of the plasma behaviour when welding AA5052 aluminium alloy with a CO₂ laser beam suggested that there was less variation in its behaviour if a dual focus technique was used [7]. For CO₂ laser welding of C-Mn steels, the variation of electron density in the plasma above the keyhole was found to defocus the incident laser radiation and affect the power density delivered to the workpiece, therefore influencing keyhole behaviour [9]. A dual focused CO₂ laser has also been reported to reduce weld metal porosity when welding SUS 304 austenitic stainless steel [8]. The keyhole behaviour was observed using an in-situ X-ray transmission method, which revealed the two keyholes coalesced to form one larger keyhole and it was suggested that this prevented the generation of gas bubbles in the weld pool.

Dual focus Nd:YAG laser welding has been considered here as a method to control the behaviour of the keyhole and weldpool, and reduce the formation of porosity when welding titanium alloys.

2. Methodology

2.1 Materials and Material Preparation

Experimental bead-on-plate (BOP) tests were performed on 3.25mm thickness Ti-2.5Cu plates. The TiO₂ layer on the workpiece surface, which is hygroscopic and will adsorb moisture from the atmosphere, was removed with an abrasive paper. The workpiece surface was then cleaned and degreased with acetone immediately prior to welding.

2.2 Equipment and Experimental Procedure

All bead-on-plate (BOP) tests were produced using a Trumpf HL4006D Nd:YAG rod laser (beam parameter product of 23mm.mrad). An optical fibre, of 600 μ m core diameter, delivered the laser radiation to a HIGHYAG

process head, which contained a dual focus forming module. This allowed control of the foci orientation (see Figure 1), the foci separation and the power ratio between the focused beams. The foci had beam waists of $450\mu\text{m}$, and the beam waists were always set coincident with the top surface of the workpiece. A laser power of 4.1kW at the workpiece was used for all experiments. Test pieces were clamped in the same welding jig, which was traversed with respect to a stationary processing head in the downhand position. A trailing shield and a 10mm^2 cross-section copper efflux channel were both supplied with argon gas to prevent oxidation of the top and bottom of the weld metal respectively.

Observation of selected welding conditions was performed using two high speed cameras; a MotionPro X4, and a Photron SA-3. The Photron SA-3 was synchronised with a copper vapour laser (CVL) and utilised to observe changes in the keyhole and weldpool behaviour, whilst the dynamic behaviour of the vapour plume was recorded with the MotionPro X4. An imaging frequency of 10kHz was used.

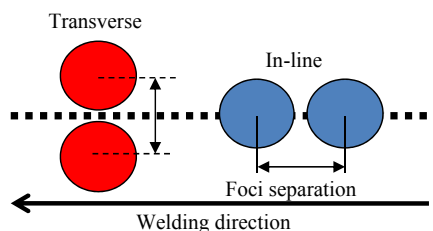


Fig. 1. Foci orientations investigated.

2.3 Process Variables

The effects of four process variables on the resultant weld quality were examined. Table 1 details the range of values considered for each variable.

Table 1. Process variables investigated.

Variables	Range
Foci orientation	transverse or in-line
A: Welding speed (mm/s)	33.33 – 100mm/s
B: Foci separation (mm)	0 [†] - 1.45mm
C: Power ratio [‡] (leading:trailing)	50:50, 60:40, 78:22

[†]i.e. a single $450\mu\text{m}$ diameter spot

[‡] varied in the in-line spot configuration only

2.4 Porosity Assessment

Radiographic examination was performed (according to BS EN 1435:1997) to determine the weld metal porosity content. Indications $\geq 0.05\text{mm}$ in diameter could be detected using this technique. Pore counts were performed over a 76mm weld length, and the diameters of all the pores in this length were summed to determine the accumulated length of porosity. Internal weld qualities were compared against a stringent quality standard that is

representative of those developed for high-performance, fatigue-sensitive aerospace applications. For 3.25mm thickness material, the limits stipulated for the maximum pore diameter and maximum accumulated length of porosity (per 76mm weld length), are 1.0 and 1.7mm respectively.

3. Results and Discussions

3.1 Welding Performance

The maximum welding speeds that resulted in consistent full penetration for both foci orientations, with spot separations of 0 to 1.45mm , are shown in Figure 2. Three data sets are included for the in-line foci orientation, relating to the BOP tests produced with power ratios of 50:50, 60:40 and 78:22. It can be seen from Figure 2 that, full penetration was possible at higher welding speeds when operating with the in-line foci orientation compared with the transverse orientation. This is as expected, given the increased volume of material processed when welding in the transverse foci orientation.

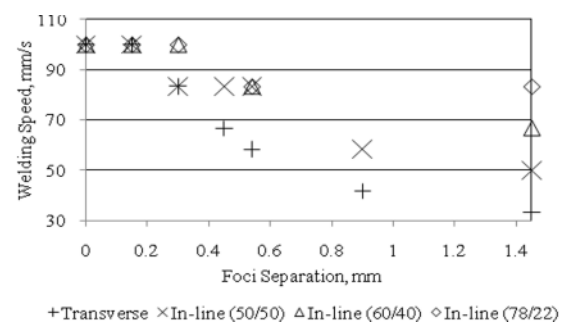


Fig. 2. Limits of full penetration.

3.2 Statistical Analysis

The weld metal porosity data, generated from the examination of the radiographs, was analysed with response surface methodology (RSM) to establish the relationship between the weld metal porosity and the process variables. Although statistical methods were not used to design the dual focus experiments performed in this work, the range of experiments performed is similar to a fractional high-order factorial experiment. Design-Expert 8.0.1 was used to analyse the historical data. The data sets generated from the different foci orientations were analysed separately, and included a large number of repeated welding conditions so that the prediction variances could be minimised. The limits where design points could be created were constrained, using the data from Figure 2, so that only those conditions giving full penetration were analysed. In order to minimise the residuals, a square root transformation was applied to the

transverse data (52 BOP tests), and a \log_{10} transformation was applied to the in-line data (91 BOP tests). In both data sets, a cubic model gave the most complete description of the response. In the case of the transverse foci orientation, those BOP tests produced with foci separations $>0.54\text{mm}$ were not included in the statistical analysis. Analysis of variance (ANOVA) was used to determine p-values (i.e. statistical significance) of the individual terms. The models were reduced by removing those terms with p-values >0.10 (unless they were required to support hierarchical terms) using a backward elimination technique.

Various diagnostic checks of the residuals were performed to ensure that the model satisfies the assumptions of the ANOVA (i.e. ensuring the factors are fixed not random). The studentised form of the residuals was used in all the plots. No abnormalities were found in any of the residual plots. Additional graphical tests were carried out to provide a measure of the influence, potential or actual, that individual runs may have. No runs were found to have a high degree of influence or leverage over the model. Table 2 details the β coefficient values, in terms of actual factors, for both models.

Table 2. β coefficient values, in terms of actual factors, for the transverse (sqrt porosity) and in-line models (\log_{10} porosity).

Coefficient	Transverse	In-line
β_0	9.76E+0	7.58E+0
β_A	-1.74E-1	-1.78E-1
β_B	4.11E+1	-8.84E+0
β_C	n/a	not significant
β_{AB}	-1.29E+0	not significant
β_{AC}	n/a	8.31E-5
β_{BC}	n/a	-1.91E-2
β_{ABC}	n/a	5.15E-4
β_A^2	9.15E-4	not significant
β_B^2	4.76E+1	not significant
β_A^2B	8.07E-3	-1.62E-3
β_{AB}^2	1.03E+0	not significant
β_B^2C	n/a	-2.22E-2

3.3 Transverse Foci Orientation Porosity

Lower welding speeds produced larger pores, up to a maximum diameter of 0.4mm. At higher welding speeds the majority of the pores were 0.1-0.2mm in diameter. Figure 3 shows a significant increase in weld metal porosity at welding speeds below 65mm/s. According to Figure 3, BOP tests meeting the stringent subsurface weld metal porosity criteria ($\leq 1.7\text{mm}$ accumulated length per 76mm weld length) can be produced at a range of welding speeds (~ 70 to 100mm/s), if a suitable foci separation was chosen. Within this speed range, decreases in speed, and hence proportionate increases in heat input, necessitated an increase in the foci separation if porosity formation was to be minimised. Particularly low levels of weld metal porosity ($\leq 1.0\text{mm}$ accumulated length per

76mm weld length) are predicted to form when a welding speed of $\sim 80\text{mm/s}$ is used with a foci separation of $\sim 0.15\text{mm}$. Two BOP tests produced with a welding speed of 83.33mm/s and a foci separation of 0.15mm, had accumulated lengths of porosity of 0.8 and 1.4mm.

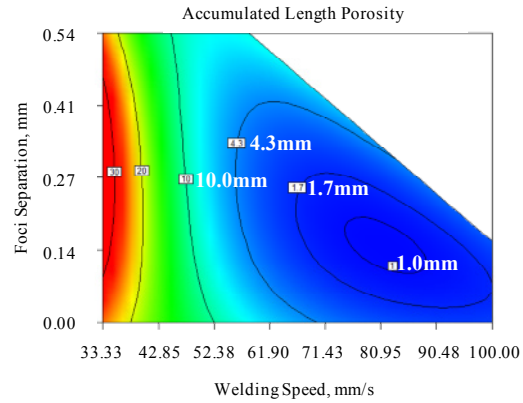


Fig. 3. Contour graph detailing the effects of the welding speed and the foci separation on the formation of porosity in the weld metal.

3.4 In-line Foci Orientation Porosity

The β coefficient values of the statistically significant terms are shown in Table 2. As with the transverse foci configuration, BOP tests produced at welding speeds above $\sim 75\text{mm/s}$ generally had pore diameters of 0.2mm or less. Those BOP tests produced at slower welding speeds and with an even power ratio contained pores with diameters up to 0.5mm. At higher power ratios between the leading and trailing spots, the occurrence of larger diameter pores decreased. Comparing the response surfaces for the different power ratios shows that having a higher power density in the leading spot than the trailing spot significantly reduces the formation of porosity when welding with foci separations greater than $\sim 0.45\text{mm}$. As observed from high speed video, this is a result of moving from a dual keyhole regime (50:50 power ratio) to a regime where the leading keyhole is dominant (78:22 power ratio) and the welding process is very similar to that produced with a single laser beam. At spot separations $<0.45\text{mm}$ the change in power ratio had little influence on the weld metal porosity.

However, even though a significant decrease in the porosity levels occurred when utilising spot separations $>0.45\text{mm}$ and high power ratios, the lowest levels of porosity are predicted to occur when utilising a 50:50 power ratio with a relatively high welding speed and a foci separation between 0.15 and 0.30mm. A BOP test produced with a welding speed of 83.33mm/s and a foci separation of 0.30mm is predicted to have an accumulated length of porosity of 1.4mm. Three experimental results produced with the same parameters, had accumulated lengths of porosity values of 0.8, 1.0 and 1.1mm. Both the statistical model and the experimental results were in agreement, and indicated

that the weld metal porosity criteria could not be met by utilising a single focused spot.

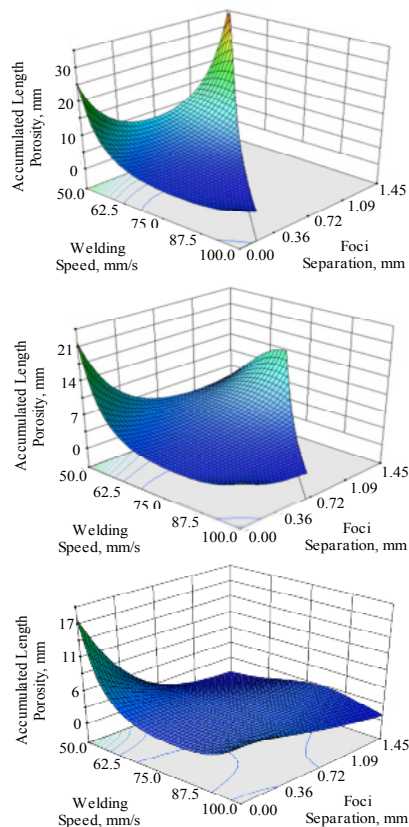


Fig. 4. Response surfaces for the effect of welding speed and foci separation on porosity formation, for spot intensity ratios of 50:50 (top), 60:40 (middle), and 78:22 (bottom).

3.5 High Speed Observations

The dual focus technique can reduce the weld metal porosity content to within stringent aerospace standards, at spot separations of 0.15-0.30mm, in both the in-line and transverse foci orientations. Analysis of the high speed observations of the weld pool has shown that with these spot separations, one, elongated or widened, keyhole is present. This is in agreement with previously reported work [8]. This elongated or widened keyhole does not collapse as frequently as a keyhole produced with a single focused beam. This agrees with the analysis of the vapour plume observations. The vapour plume emitted from an elongated keyhole is more constant and does not fluctuate as frequently compared with a single focused beam (Figure 5) [7]. This suggests a more constant power density is delivered to the workpiece when welding in an optimised dual focus mode, which will reduce the occurrences of keyhole collapse and, subsequently, the formation of porosity in the weld metal.

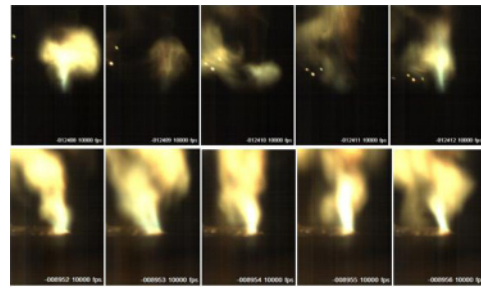


Fig. 5. Images of the vapour plume when welding with a single focus (top) and an optimised dual focus (below). 100 μ s intervals.

4. Conclusions

This work has investigated the feasibility of reducing the formation of porosity in the weld metal when Nd:YAG laser welding titanium by using a dual focus technique. The results have been analysed by RSM and the models indicate that the weld metal porosity can be reduced to within levels stipulated by stringent aerospace criteria, if a relatively small foci separation and a suitable welding speed are utilised. Observation of the welding process using two high speed cameras has shown that a small foci separation increases the keyhole stability and hence reduces the occurrences of keyhole collapse and the formation of weld metal porosity.

Acknowledgements

This work was funded by the Industrial Members of TWI, and also by EPSRC grant no. C537750. Materials were kindly provided by Aeromet and Boeing. The Photron high speed camera and the CVL were loaned from the EPSRC Engineering Instrument Pool.

References

- [1] R.R. Boyer, (1996) An overview on the use of titanium in the aerospace industry. *Materials Science and Engineering* 213:103-114.
- [2] Hall, D, (2009) Titanium demand in an uncertain world. *European Titanium Conference*, Birmingham, UK.
- [3] A. Matsunawa, (2001) Problems and solutions in deep penetration laser welding. *Science and Technology of welding and Joining* 6:351-354.
- [4] D.V. Lindh, G.M. Peshak, (1969) The influence of weld defects on performance. *Welding Journal* 48:45s-56s.
- [5] P. Hilton, J. Blackburn, P. Chong, (2007) Welding of Ti-6Al-4V with fibre delivered laser beams. *Proceedings of ICALEO 2007*, 887-895.
- [6] A. Haboudou, P. Peyre, A.B. Vannes, G. Peix, (2003) Reduction of porosity content generated during Nd:YAG laser welding of A356 and AA5083 aluminium alloys. *Materials Science and Engineering* 363:40-52.
- [7] J. Xie, (2002) Dual Beam Laser Welding, *Welding Journal* 10:283s-290s.
- [8] T. Hayashi, K. Matsubayashi, S. Katayama, S. Abe, A. Matsunawa, A. Ohmori, (2003) Reduction mechanism of porosity in tandem twin-spot laser welding of stainless steel. *Welding International* 17:12-19.
- [9] J. Greses, (2003) PhD thesis. University of Cambridge.

Product design for welding

Antti Salminen^{1,2}, Jouko Kara¹, Marko Vattulainen², Aki Piironen²

¹ Laboratory of Welding Technology and Laser Processing, Lappeenranta University of Technology, Lappeenranta, Finland

² Machine Technology Centre Turku Ltd, Finland

Abstract. The utilization of laser is growing for various applications. These applications have been mostly among those of car manufacturing and car components. Only lately, partly due to lower sales among car manufacture, the applications among machine building has been getting growing interest and quite a few applications has been coming public. The laser cutting and welding can usually provide low production costs and trough put time if efficiently utilized. One real obstacle to overcome prior further utilization is the adapting the real potential of laser into the structure of the product. The advantages of laser welding in product design are only seldom realized. Still this would be an important factor to be taken into account and would justify the laser investment in several cases. This paper deals with development of procedures for product design for welding. Systematic procedure gives potential to modulation and cost effectiveness gained with that. The procedure starts from common rules of design for automated and robotized welding since the basic criteria of those should also be fulfilled for welding. Some typical examples are shown and a collection of ways to utilize laser in product design.

Keywords: Product design, laser cutting, DFMA, Design For Welding -model, manufacturing-friendly design

1. Introduction

Manufacturing companies know their own technical problems, but the initiation of development is often difficult or not even started. Smaller companies often lack the possibilities and knowledge of new production methods and product development.

This article give some tips for the welding product development, design implementation and development of welding used in the workshop. Product design is a demanding task because the usability and the cost of the product are decided at the design phase. Designers need to know the different manufacturing methods and the idea of manufacturing-friendly design, so that they can take into account manufacturability and assembly considerations. A good welding construction has a minimal amount of welding. Both modulation and standardization, as well as substitutive methods to welding have been used. This article presents manufacturing-friendly "Design For Welding" -model,

that goes through the specific features of welded structure from the point of view of design.

The design knowledge is reduced because the design is outsourced to outside of the company and manufacturing is diversified suppliers. These design subcontractors often do not have access or the skills to improve the product manufacturing-friendly. The designers are also often too little information about the manufacturing processes and manufacturing-friendly production. The old experience of the designers can also be a burden, because it is accustomed to doing things a certain way, and new manufacturing methods are not enough time or the know considered. Many times the company needs outsider person to tell that something should be subject to change and develop. The threshold for starting development work is often high.

Laser welding is a excellent example about a production method providing new opportunities for product design. These advantages can be of much higher advantage than those obvious ones achieved directly like high speed and small heat input [1, 2].

2. Model for design for welding

Traditionally, industrial and engineers want to improve manufacturability by increasing and improving production automation. Production automation investments are huge and at some point in the automation is no longer a cure for the manufacture of the product. For this reason, companies have begun to use the manufacturing-friendly design, for example DFMA known method (Design for manufacturability and assembly).

Manufacturing-friendly design starting point is to avoid the design and manufacture of the product in the known disadvantages, so that the already known manufacturing defects do not attempt to solve, but a product designed to avoid known problems. The method

is designed to prevent costly re-design and to ensure in advance that the product needs to make changes afterwards. The method has advantages that it can increase your productivity without investment. Most of the problems of the manufacturability are caused by too difficult a construction, where automation is not taken into account [3].

Manufacturing-friendly design planning does not exist on the source material, which should be applied directly to the welding or welding design. Various planning model is also suitable for welded product design, but they do not take into account the details of a welded structure. This new “design for Welding” -model (DFW) combines the advantages of DFMA and concurrent engineering design (CE) and is linked to the information of requirements and opportunities of welding processes [4].

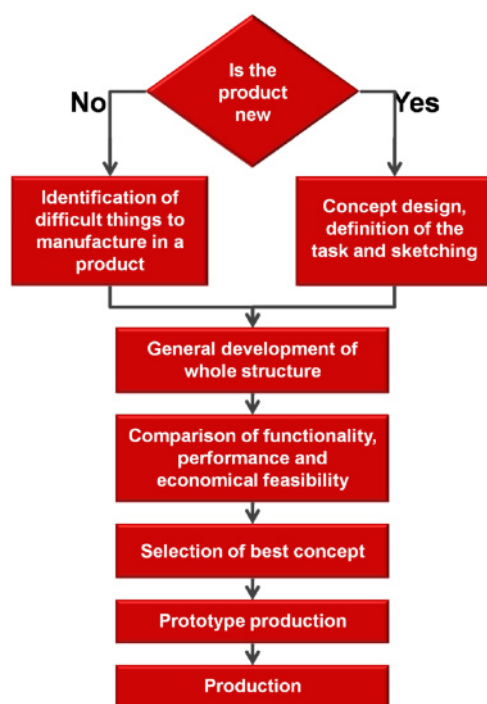


Fig. 1. Design for welding procedure [4]

Manufacturing-friendly product design is a challenge, because the design should take into account manufacturability and assembly considerations. The designer is also able to evaluate and compare the manufacturability and assembly of different construction options such that they can offer the best option to the market. Designer decides product functionality, performance and economical feasibilities, so strongest affect on the product price can be gained by investing in the design. Product design project should spend more time to optimize the product concept, manufacturing-friendly design and modularity, than selection and design

of individual components or thinking about the specific details [4].

This DFW model goes through a welded structure design implementation. Welding manufacturing-friendly model can also be used for other manufacturing processes, since many of the manufacturability aspects are common to different manufacturing methods. Manufacturing-friendly design aims to reduce the order-specific design, welding, post-processing and tooling.

3. Design procedure

The design project starts by check of the product status in production. Is the product new or should one improve the old product. The old product in the case focuses on the well-known product lines to solve the problem and to simplify the product. The design of a new product starts from the design of a concept of an ideal product. During this phase we consider the function of the initial product by various aspects, requirements and outline a draft of the product. Concept sketching often begins from a model of the product which is already in the production of the company itself or competitors of it [4].

Next chart box is “General development of the whole structure”. There checking basics design rules whole products. At this stage, the product should be subdivided into modules, which are developed separately and try to get a product as simple as possible. In this stage of development is the product geometry, dimensions, details, list of necessary parts and equipment, and we consider all of what consists of the product.

Good designer identify at an early stage the most likely method of manufacture to the product. Product components have to grouped material, geometry, and the action of the various groups whose production can be considered separately. Although the designer has in mind the likely method of manufacturing, does not agree with the comparison of alternative methods to be omitted. Many of the parts can be done for example by casting, machining or welding, although often, however, the conclusion is the method of the preparation methods are known and can be done manually [4].

Inside the “General development of the whole structure”-box is “design of manufacturability” and “finalizing of manufacturability/weldability” boxes. Figures 2 and 3. Finalizing of manufacturability / weldability-box goes through a welded structure and check different manufacturing and assembly stages and detailed DFM rules e.g. for welding. Welded structure has to think welding process and materials requirements, and compares the various methods from parts of the series of operations to the number and total time. Also have to know welding method, strength of the welds, government articles, welding quality class, tolerances, weld position, heat input, welding sequence and many other things that comes up for welding [4].

When the entire structure of the general development of the box has been completed and one or more of the product concept alternatives are chosen which differ from the material, production, design, or other basis structure, the comparison of these different versions of the criteria for choosing the best product concept. Comparison of product variations has to do by functionality, performance and economical feasibility. The comparison can be used for scoring, or some other method which can be shown to the best concept. To calculate the cost of the product to the product must include all costs and expenses to be throughout its life cycle. Manufacturability of the cheapest product is not necessarily the cheapest overall, but you should consider how easy the product is maintained, for example. The next can begin prototyping and testing. Production is the next step when everything is in order [4].

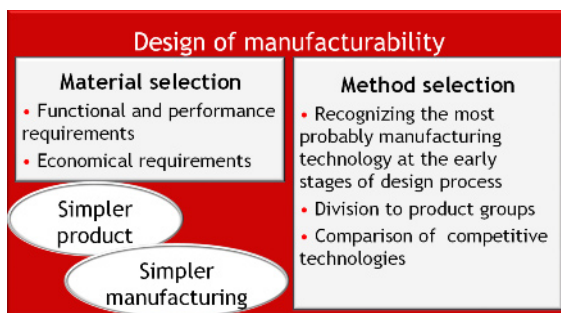


Fig. 2. Design of manufacturability box is inside the general development of the whole structure –box

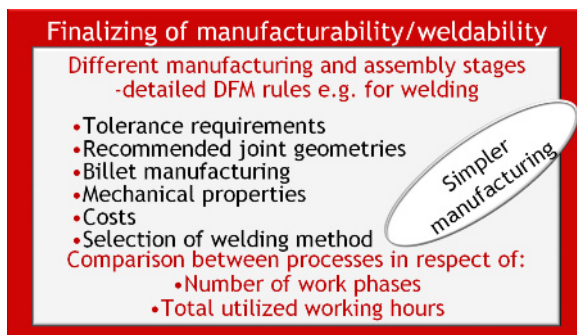


Fig. 3. Finalizing of manufacturability/weldability box is inside the general development of the whole structure –box

4. Application examples

There is some typical laser collection of ways to utilize laser in product design. As we know the use of laser enables different ways to save material and fulfill the functions of product case by case.

One method reduce welding and simplify assembly is slot and tab method, see Figures 6 and 7. This is exact and quick method to simplify product construction and production.

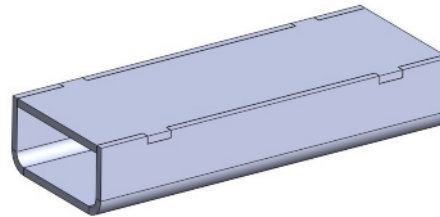


Fig. 4. Slot and tab method to do personalized beam. Design makes the fixture manufacturing easier and the accuracy of final product better than the conventional structures.

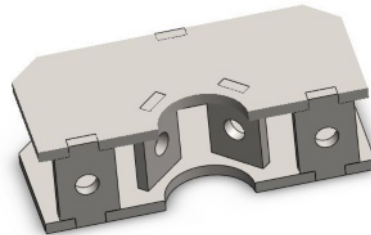


Fig. 5. Slot and tab method to reduce welding work and simplify assembly. In practise the desing can also resist the distortions and strengthen the structure by proper dimensions and shapes agains the load in use.

Other method to simplify the fixturing, lower the material cost and still to retain the accuracy is to use jigsaw joint where you can laser cut sheet metal various shapes and at one time reduce loss of sheet.

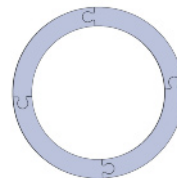


Fig. 6. Jigsaw joint

A whole family of products utilizing desing for welding is laser welded all steel sandwich panels. The do comprice of thin sheet and due to structure and high quality together with low distortion provide strengh of a structure typically achieved of considerably higher weight [5, 6]. These structures are typically weight – strenght optimized solutions and have been utilized in some applications. There are several different structures of sandwich panel types available such that for various cases it is possible to select the basic structure. Typically all of them are desigen based on the automatisasion of welding process even to the highes level of automatisasion. Figure 7 shows the different types of sandwich panels. In practice the firs generation sandwich panel having continuous core is off highest weight and most difficult to manufacture. The optimum solution naturally by weight is the I-core structure that really minimizes the

weight still ensuring high mechanical properties. Unfortunately welding through the face sheet hitting to middle of I-core that in optimum case has thickness of about 1 mm, is really difficult in case of any larger panel.

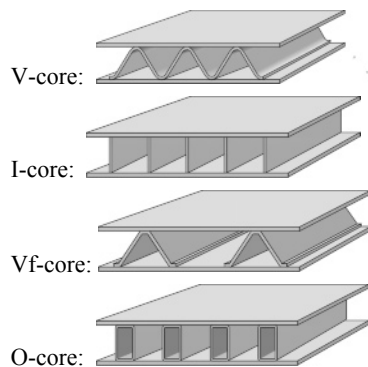


Fig. 7. Sandwich panel designs [6, 7]

The original V-core was considered logn to be off best stiffness, but quite soon the problems of part manufacture forced the design to so called free core desings from which the Vf is the most common. So actually in this case breaking the desing rule of lowering number of components makes the manufacturing more difficult than using the property vise optimiced cores.

A simple application with still a remarkable savings gained with design is a webtrain of a aluminum ship, see Figure 8. These structures change in shape, but typically can be parametrised. The typical idea to manufacture these structures is to stack weld components and then weld them on site manually [8].

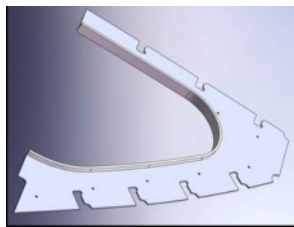


Fig. 8. Aluminum webtrain [8]

As unlogical as possible is that the welding procedures used causes distortion that can be avoided by cutting the welding work into small sections thus making the manufacture more difficult and through put slower. Analysis of the structures showed that fillet joint between a web and a flange of a webtrain is a crucial component for boat building. By taking these webtrains into boat premanufactured stiff components the whole boat building is easened and some part of the work can be done automatized. The stiffer components can resist distortions and keep the whole stucture stiffer. The procedure also removes difficult position welding and enables automated part manufacture in normal production environment [8].

5. Conclusions

A careful analysis about the function of the product and ease of automatization of the welding task for existing design can show potential for improvement of product and production. The developed model is the first step in road to production of better products with lower cost. In some constructions it will require real a lot of work but realising the objectives it is typically worth working out. This utilisation requires different way of thinking from the whole company personnel and continuous support of the management.

Acknowledgements

The project was done as part of Finnish national research projects ForMeri funded by European Regional Development program and Finnish industry.

References

- [1] Salminen, A. and Ion, J., Design for laser-based production. - Production research 1993. Proc. of the 12th (ICPR) International Conference on Production Research, Lappeenranta Finland, 16-20 August, 1993. Advances in Industrial Engineering. Vol. 17. Elsevier. Amsterdam 1993. s. 199-200
- [2] Salminen, A., Moisio, T. and Martikainen J., Design for Laser Welded Products. Proceedings of 8:th Int. Conf. on Applications of Laser & Electro-Optics, ICALEO'89, 15.-20.10.1989, Orlando, Florida USA. 9 pp.
- [3] Lohtander, M., DFM/DMFA -erään selluteollisuuden komponentin muuttaminen valmistusystävällisemmäksi. Tutkimusraportti 34: LTKK digipaino. Lappeenranta 2002, 33 s. ISBN 951-764-676-3. In Finnish.
- [4] Vattulainen M., Welding Production development and manufacturing-friendly design, Master's thesis, 2009, Lappeenranta, Finland.71 p.
- [5] Kujala, P. and Salminen, A., Laser Production and Fatigue Strength of All-Steel Sandwich Panels, Proceedings of 17th Int. Conf. ICALEO'98, November 16-19, 1998. Orlando, USA, Laser Institute of America, p. F66-F75.
- [6] Kujala, P. and Salminen, A., Optimum Solutions for Laser Welded All Steel Sandwich Panels, Proceedings of 18th Int. Conf. ICALEO'1999, November 15-18, 1999. San Diego, USA, Laser Institute of America, p. D110 – D119.
- [7] Vilpas, M., Kujala, P., Salminen, A., Alenius, M. and Kyröläinen A., Development of laser welded stainless steel sandwich panels for lightweight vehicles – design, manufacturing and properties. Proc. of 19th Int. Conf. ICALEO'2000, September 2-5, 2000. Detroit, USA, Laser Institute of America, p. C156-C165.
- [8] Salminen, A., Purtonen, T., Tolvanen, J., Huttunen, M. and Isotalus, J., A Study about Suitability of Different Welding Processes for the Production of Aluminum Stiffeners for Ship Structure. Proc. 28th Int. Conf. on Lasers and Electro Optics ICALEO 09, Orlando, Florida, November 2-5, Laser Institute of America. P. 697-704.

Studies on the Effect of Process Parameters on the Shear Performance of Joints of Aluminium Alloy Produced by Adhesive Joining, Spot Welding and Weld-Bonding

M. D. Faseeulla Khan¹, D. K. Dwivedi^{1*}, P. K. Ghosh¹

¹ Department of Mechanical & Industrial Engineering, Indian Institute of Technology, Roorkee, Uttarakhand, India-247667

* Corresponding author: E-mail: dkd04fme@iitr.ernet.in; Phone: +91-1332-285826; Fax: +91-1332-285665

Abstract. In the present study, significant parameters of weld bonding namely surface roughness, curing temperature, curing time, welding current, weld cycles and electrode load and their ranges were identified by conducting pilot experiments for the adhesive bonding and resistance spot welding. The tensile shear resistance of the adhesive joint, resistance spot welds and weld-bonding was evaluated by applying uni-axial tensile shear load on the lap joints and applying tensile shear load and the results were obtained in the terms of ultimate shear load (USL). The maximum shear load carrying capacity was found in case of adhesive joints produced using surface roughness with 220 emery grade cured at temperature 120°C for 60 min. A maximum USL was obtained in case of spot weld joints produced using welding current 13kA, weld load 0.5 kN and weld time 8 cycles. The strength of adhesive joint was found to be more than the resistance spot weld joint. The optimized parameters of spot welding and adhesive joining were used to develop the weld-bond.

Keywords: Weld-bonding, Adhesive bonding, Resistance spot welding, Ultimate shear load (USL), Aluminium sheet.

1. Introduction

Joining of metals by employing spot welding in combination with adhesive bonding called weld-bonding has drawn considerable attention of numerous scientists and industrialists. Applications of weld-bonding have extended up to the sophisticated areas like the air craft industry, missile technology and others. Thus the weld bonding is defined as a resistance spot weld process variation in which the spot weld strength is augmented by adhesive at faying surface [1].

2. Weld bonding

The weld bonding process is essentially resistance spot welding of parts that subsequently have their overlapping areas adhesive bonded. The Soviet Union initially

developed this technology, which was called as ‘Glue Welding’, which was ‘Flow-in’ method Fig.2.1(a), where by the parts were welded together and then an adhesive was flowed in to the joint. A low viscosity adhesive was used which penetrate the overlap joint by capillary action and was subsequently cured. The technique used in the united states and in various places of Europe is the ‘Weld-Through’ method Fig.1(b), where by the adhesive is applied to the parts to be joined, spot welded and subsequently cured [2].

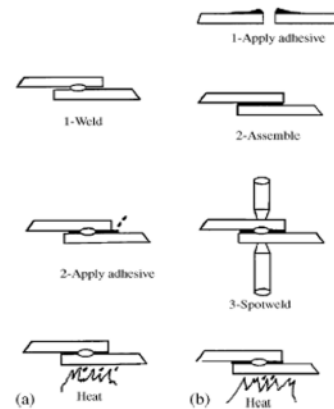


Fig. 1. (a) Flow-in technique, (b) Weld-through technique [10]

Compared to the resistance spot welding, the weld-bonding has the following advantages regarding the joint strength (in order of importance) [3, 4]:

1. Superior fatigue strength (up to two thirds of the ultimate shear force).
2. Higher static strength.
3. Higher corrosion resistance (no crevice or friction corrosion).
4. Higher capacity of energy absorption when subjected to impact loading.

5. Higher capability of damping when subjected to vibration.

Compared to adhesive bonding, weld-bonding has the advantage of suppressing continuous creep in the adhesive layer so that the creep strength of the joint is strongly increased [3].

The properties of weld bond largely depend up on surface characteristics of the substrate and the type of adhesive used. For an optimum joint strength the welding parameters for the preparation of weld bond differ from those used in case of conventional spot welding [5]. In the view of the above promising future of using weld bond in automobile industries, an effort has been made in this investigation to study the effect of relevant parameters on weld bond characteristics of aluminium sheet.

3. Experimental Procedure

3.1 Adhesive Joining

The commercial aluminium sheets (A1050) of thickness 0.85 mm were adhesive bonded by application of epoxy adhesive (consists of equal amount of resin and hardener by weight). Epoxy resin adhesive refers to the adhesive which cures chemicals containing epoxy group with amines and acid anhydride. Epoxy is a copolymer and it is formed from two different chemicals. These are referred to as the "resin" and the "hardener". The resin consists of monomers or short chain polymers with an epoxide group at either end. Most common epoxy resins are produced from a reaction between epichlorohydrin and bisphenol-A, though the latter may be replaced by similar chemicals. The hardener consists of polyamine monomers, for example Triethylenetetramine (TETA). When these compounds are mixed together, the amine groups react with the epoxide groups to form a covalent bond. Each NH group can react with an epoxide group, so that the resulting polymer is heavily cross linked, and is thus rigid and strong.

The process of polymerization is called "curing", which can be controlled through temperature and choice of resin and hardener compounds where the process can take from few minutes to hours. Some formulations benefit from heating during the cure period, whereas others simply require time, and ambient temperatures.

Before application of adhesive the surface of the specimen was cleaned mechanically using emery paper of different grades (120 to 600 grade) followed by wiping with acetone in order to obtain oxide free different surface roughness and required surface degreasing respectively. After getting sufficient strength to the adhesive joint, curing at 120°C was employed for different curing times.

Scheme of adhesive joining:

Sample material: Commercial aluminium sheet (1050) of 0.85 mm thickness.

Sample size: 100×25×0.85 mm

Overlap length: 7 mm

Emery grades: 120, 220, 400 and 600

Curing times: 20, 40, 60, 80 and 100 min

Type of adhesive: 2-C Plain Epoxy Resin (Resinova manufacturers, ISO 9001 : 2000)

3.2 Resistance Spot Welding

The aluminium sheets of thickness 0.85 mm were resistance spot welded using the PECO-Bench spot welding machine of capacity 64 kVA. Before welding the faying surfaces of the specimen were cleaned mechanically by rubbing with 400 emery grade paper followed by wiping with acetone in order to remove the excess oxides and grease from the surface. Resistance spot welding was carried out by using water cooled conical Cu electrode. Welding was carried out using varying the welding current and weld time at given voltage and electrode force respectively.

Scheme of resistance spot welding:

Sample material: Commercial aluminium sheet (A1050) of 0.85 mm thickness.

Sample size: 100×25×0.85 mm

Overlap length: 25 mm

Welding current: 7, 9, 11 and 13 kA

Welding time: 6, 8, 10 and 15 Cycles

Welding load: 0.5 and 0.6 kN

Electrode: Copper electrode

3.3 Weld Bonding

The aluminium sheets of thickness 0.85 mm were weld bonded by application of adhesive followed by resistance spot welding. Before application of adhesive, the surface of the specimen was cleaned mechanically with 220 emery grade followed by wiping with acetone in order to obtain oxide free different surface roughness and required surface degreasing. Then the adhesive (consisting equal amount of resin and hardener) was applied on the faying surfaces. By holding the faying surfaces in right position (lap joint of shear test specimen) the resistance spot welding was carried out by using the water cooled Cu alloy electrodes as described earlier. The welding was carried out using the above mentioned resistance spot welding machine of capacity 64 kVA. Welding was carried out by varying the welding current, weld time and welding load. The weld joints were prepared as per specifications to produce tensile shear test specimens. After welding curing was also employed to the joints at optimum conditions of temperature of 120°C for 60 minutes to facilitate adhesive bonding and cross linking. Scheme of weld bonding (adhesive plus resistance spot welding):

Sample material: Commercial aluminium sheet (1050) of 0.85 mm thickness.
 Sample size: 100×25×0.85 mm
 Type of adhesive: 2-C Plain Epoxy Resin (Resinova manufacturers, ISO 9001 : 2000)
 Overlap length: 7 mm (width equal to overlap)
 Emery grade: 220
 Curing time at 120°C for 60 min
 Welding currents: 7, 9, 11 and 13 kA
 Welding times: 1, 2, 3, 4, 6 and 8 cycles
 Welding load: 0.5 kN
 Electrode: Copper electrode

3.4 Shear Test

The shear test of the joints produced by adhesive joining, spot welding and weld-bonding was carried out by uniaxial tensile shear loading on two ends of the lap joints. The sub size area of overlap used in case of the preparation of adhesive joint is primarily to ensure the failure from the joint, so that the effect of various parameters on the joint strength can be studied. The test was carried out at a cross head speed of 1mm/min on a hydraulically operated dynamic universal testing machine (Mohr & Federhaffag Mannheim-Germany). The ultimate shear load (kN) and failure mode characteristics were studied.

4. Results and Discussion

4.1 Effect of Curing Time on Strength of the Adhesive Joint

The effect of curing time (at curing temperature of 120°C) on adhesive joint strength (having equal joint area) of aluminum of varying surface roughness is shown in Figure 2. It can be observed that at a given surface roughness of aluminum the ultimate shear load (USL) carrying capacity of the adhesive joint increases with increase of curing time up to about 60 min followed by a decrease in it with further increase in curing time up to 100 min. The decrease in joint strength with the increase of curing time beyond 60 min possibly happened due to degradation (bond breaking) of the adhesive under long thermal treatment which adversely affects the adhesive strength.

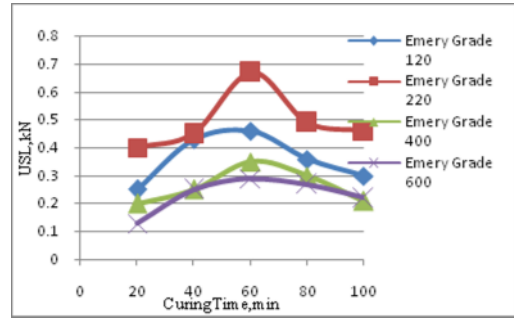


Fig. 2. Effect of curing time on strength of the adhesive bonded joint at different emery grades.

4.2 Role of Surface Roughness on Adhesive Joining of Aluminum

The effect of surface roughness of different emery grades on ultimate shear load (USL) carrying capacity of the joint (produced using 60 min curing time at 120°C temperature) has been shown in Figure 3. It can be observed that the decrease in surface roughness increases the joint strength up to emery grade of 220 and further decrease in surface roughness (with increase in emery grade number) lowers the joint strength. Higher the grade number of emery paper lower is surface roughness. An increase in joint strength with the decrease in surface roughness may be primarily caused by the enhancement in mechanical locking where as the decrease in joint strength with a further decrease in surface roughness may be primarily caused by the reduction in surface area of adhesive bonding.

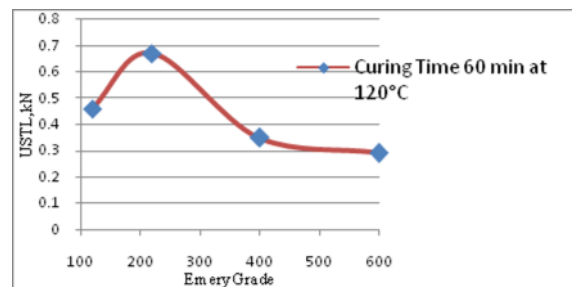


Fig. 3. Role of surface roughness on strength of the adhesive bonded joint.

This is possible because the surface roughness affects the joint strength in two ways: a) surface area of adhesive bonding increases with lower surface roughness resulting from using higher grade of emery paper and b) by providing mechanical locking primarily depends upon geometry of surface roughness which varies with the change in grade of emery paper. It is known that the 120 grade emery paper offers higher surface roughness compare to 220 emery grade paper. Joints produced on aluminium sheets having greater roughness facing surface (obtained from 120 grade emery paper) resulted lower shear load carrying capacity of joints produced compare

to that produced on smoother surface (obtained from 220 grade emery paper) due to presence of high peak and valleys on the surface which in turn results in insufficient adhesive filling in the valleys and creates porosity and so lower shear strength capability.

4.3 Shear Strength of Resistance Spot Weld

Figure 4. It is observed that for welding current of 7 and 9 kA, an increase in weld time up to 8 cycles enhances the ultimate shear load (USL) bearing capacity of spot weld followed by a decrease in it with a further increase in weld time up to 10, 15 cycles. The increase in ultimate shear load (USL) bearing capacity of the weld with the increase of weld time up to 8 cycles is primarily caused by the increase in diameter of weld nugget while the decrease in ultimate shear load (USL) bearing capacity of weld prepared at the weld time of 10, 15 cycles was caused by a significant expulsion occurred during welding. At a higher welding current (11 and 13 kA) the increase in weld time from 6 to 8 cycles has also been found to increase the ultimate shear load (USL) bearing capacity of the weld significantly. However, at both these welding currents, the weld joint using higher weld time beyond 10, 15 cycles could not be produced due to excessive expulsion and melting of the region.

It is also observed that at a given weld time of 6, 8 and 10 cycles the increase in welding current enhances the ultimate shear load (USL) bearing capacity of weld significantly primarily due to providing sufficient heat to form proper nugget size, when no expulsion was found to occur (Figure 5).

Figure 6 shows the effect of welding load (for applying pressure during spot welding) on strength on spot welding of aluminium sheet at different welding times. It is observed that increase in welding load at 13 kA has reduced the strength of the spot welding joint. This is due to fact that as load is increased the contact resistance and the heat generated at the interface decreases. Therefore, to maintain the level of heat needed for sound spot weld, either amperage or weld time must be increased to compensate heat reduction owing reduction in contact resistance.

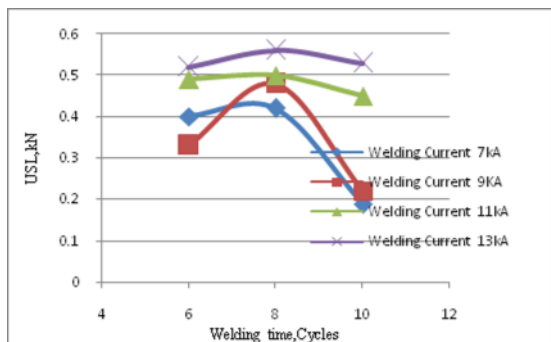


Fig. 4. Effect of welding time on strength of the spot welding of aluminium at different welding currents and welding load of 0.5 kN.

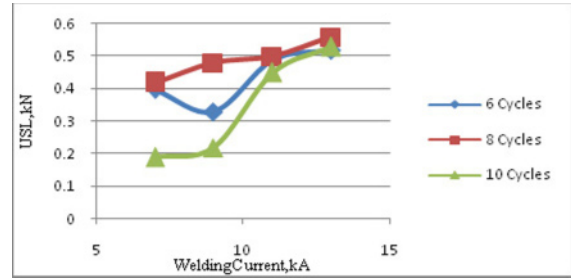


Fig. 5. Effect of welding current on strength of the spot welding of aluminium sheet at different welding cycles.

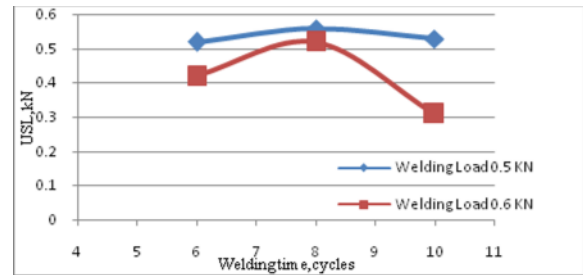


Fig. 6. Effect of welding time on strength on spot welding of aluminium sheet at different welding load.

4.4 Shear Strength of Weld-Bonding

In weld-bonding joint could be made only in four cases. Weld-bond was developed 9 kA welding current for 1 cycle welding time. But in the case of welding current 7 kA weld-bonding was not observed due to insufficient current.

Figure 7 shows the effect of welding current on strength of the weld-bond of aluminium sheet at welding time 1 cycle. It is observed that increase in the welding current from 9 kA to 11 kA increases the strength of the weld-bond joint and further increase in welding current up to 13 kA there is drop in strength of the weld-bond joint. This is due to moderate expulsion was observed in the case of welding current 13 kA.

Figure 8 shows the effect of welding time on strength of the weld-bond of aluminium sheet at different welding current levels. At 2 cycles welding time and 11 kA and 13 kA welding current, weld-bonds cannot be produced due to severe expulsion [27]. Increase in weld time at high current levels leads to severe expulsion and electrodes are indented completely in sheets. It is believed that the presence of adhesive between the faying surfaces acting as an insulator and produces more heat on the surfaces and leads to melting of the sheet.

At weld-bond produced using 11 kA welding current and 1 cycle welding time showed the maximum strength because of sufficient weld nugget diameter was observed compared to in the case 9 kA welding current at 1 and 2 cycles welding time. Similarly in the case of 13 kA welding current a moderate expulsion was observed which in turned lowered the strength of the weld-bond joint. Combinations of 9 kA welding current, 2 cycles

weld time and 13 kA welding current, 1 cycle weld time showed the same tensile shear strength (0.98 kN). It indicates that low welding current at high welding time and high welding current at low welding time gives the approximate equal results in shear strength of the aluminium weld-bonded joint.

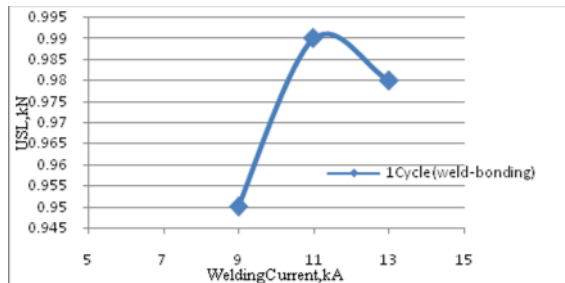


Fig. 7. Effect of welding current on strength of the weld-bond of aluminium sheet at welding time 1 cycle.

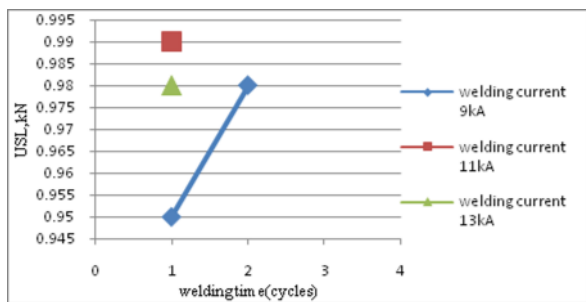


Fig. 8. Effect of welding time on strength of the weld-bond of aluminium sheet at different welding current levels.

Figure 9 shows the comparative study of spot welding and weld-bonding with respect to welding time. In case of spot welding effect of welding time was observed from 6 cycles onwards while in the case of weld-bonding welding time was 1 and 2 cycles [27]. Because in weld-bonding presence of adhesive acts an insulator and produces more heat on the metal surface which in turn lowers the weld time for same heat requirement for joining.

Figure 10 shows the comparative studies of spot welding and weld-bonding with respect to welding current. With same welding current the weld-bonding joint has the maximum shear load compare to spot welding joint. Because due to combination of spot welding and adhesive bonding in weld-bonding increases the area of the weld-bonding joint and thus the strength of the weld-bonded joint increased. In spot welding nugget is acting as a notch on the metal surface and thus result in lowering the strength of the spot welding joint. Spot welding combined with adhesive bonding results in increasing the area of the joint and increases the shear strength of the aluminium weld-bonded joint nearly 1.75 times of the spot welded aluminium joint.

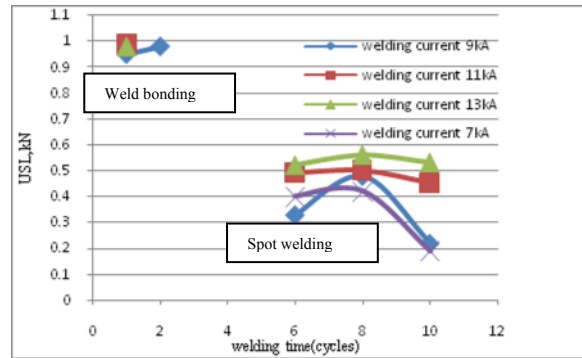


Fig. 9. Comparison of spot welding and weld-bonding with respect to welding time.

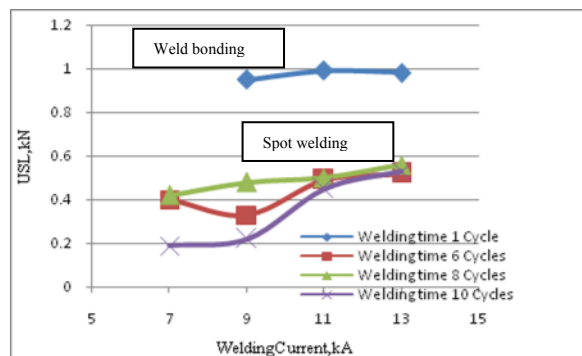


Fig. 10. Comparison of spot welding and weld-bonding with respect to welding current.

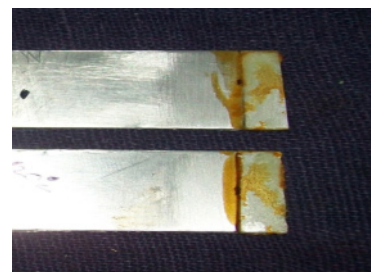


Fig. 11. Shows the fracture surface of the adhesive joint (cured at 120°C for 60 min, surface prepared with 220 emery grade paper)



Fig. 12. Typical pictorial shows failure mode from nugget in spot welding during shear testing.



Fig. 13. Failure mode of weld-bonding specimen.

5. Conclusions

The observations of the present investigation can be concluded as follows.

1. The roughness of the faying surface affects the tensile shear strength of adhesive joint. A surface roughness of 220 emery grade gives maximum tensile shear strength to adhesive joints between aluminium sheets.
2. The preparation of adhesive joint by using commercial adhesive (2-C Epoxy Resin) cured for 60 min at 120°C has been found to give maximum strength joint.
3. The spot weld of aluminium sheets produced using 13 kA welding current, 0.5kN welding load and 8 cycles weld time resulted maximum ultimate tensile shear load carrying capacity.
4. A maximum ultimate shear load bearing capacity of the weld-bond was obtained in weld-bonds produced using 11 kA welding current and 1 cycle welding time.
5. Weld-bonds produced about 1.75 times stronger joint of aluminium sheets (in terms of tensile shear strength) than spot welds. Moreover, weld-bonds were produced using much lower welding current and shorter welding time than spot weld joints.
6. The ultimate tensile shear load of adhesive joint was more than the resistance spot weld. While tensile shear load carrying capacity of weld-bond is more than the spot welding and adhesive bonding individually.

References

- [1] Metal Hand Book, Vol. 6, Tenth Edition. 125-150.
- [2] Schwartz .Metal Joining Manual, MC Graw Hill Edition. 46-62.
- [3] Welding Hand Book AWS: Vol. 3. Seventh Edition. 2-23 & 338-358.
- [4] Prof. Dr-Ing. Friedrich Exchorn and Dipl-Ing. Bernd H. Schmitz, Aachen, (1989) Comparative testing of standardized spot-welded sheet-steel hollow sections with and without bonding at the joints: Schewissen Schneider. E38-E39.
- [5] Narra Sambasivarao, (1997) Studies on Weld Bonding of Aluminium”, M.E. Dissertation: Department of Mechanical and Industrial Engineering: University of Roorkee ,Roorkee.
- [6] Recommended Practices for Resistance Welding, AWS. 1-12.
- [7] Nicholas J. Delollis. Adhesives for Metals: 11-15.
- [8] S. Semerdjiev. Metal to Metal Adhesive Bonding: 28-30.
- [9] Delvecchio. E.J. Resistances Welding Manual. Vol. 1: 187-225.
- [10] Adhesive Applications and Bonding Process: Adhesives Technology Hand Book. 183-208.
- [11] S.M. Darwish, (2004) Thermal stresses developed in weld-bonded joints: Journal of materials processing technology. Number 153-154: 971-977.
- [12] P.C. Wang, S.K. Chisholm, G. Banas and F.V. Lawrence, Jr., (1995) The roll of failure mode, resistance spot weld and adhesive on the fatigue behaviour of weld bonded aluminium: Welding Journal. Vol. 74: Number 2: 41S-47S.
- [13] K.C. WU, (1977) The mechanism of expulsion in weld bonding of anodized aluminium: Welding Journal. Vol. 56: Number 8: 238S-244S.
- [14] Baohua Chang et al, (1999) Studies on the stress distribution and fatigue behaviour of weld bonded lap shear joints: Journal of Materials Processing Technology. Number 108: 307-313
- [15] S.M. Darwish, (2002) Characteristics of weld-bonded commercial aluminium sheets (BS.1050): Journal of Materials Processing Technology. Number 23: 169-176.
- [16] Baohua Chang et al, (1997) Comparative studies on stresses in weld-bonded. Spot welded and adhesive-bonded joints: Journal of Materials Processing Technology. Number 87: 230-236.
- [17] K.C. WU, (1975) Resistance spot welding of high contact-resistance surfaces for weld-bonding: Welding Journal. 436S-439S.
- [18] A. Al-Samhan et al, (2003) Strength prediction of weld-bonded joints: International Journal of Adhesion & Adhesives. Number 23: 23-28.
- [19] B.H. Chang et al, (1999) A Study on the role of adhesives in Weld-Bonded joints: Welding Research Supplement: 275S-279S.
- [20] S.M. Darwish et al, (2004) Peel and shear strength of spot welded and weld bonded dissimilar thickness joints: Journal of Material Processing Technology. Number 147: 51-59.
- [21] Edward M. Petrie, (2007) Adhesive Bonding of Aluminium Alloys: Metal Finishing : 49 -56.
- [22] S.M.H. Darwish et al, (2000) Critical assessment of weld-bonded technologies: Journal of Material Processing Technology. Number 105: 221-229.
- [23] Janneke Vervloed et al, (2005) The influences of overlap length, bond line thickness and pretreatment on the mechanical properties of adhesives: Focussing on bonding glass: The Adhesion Institute.
- [24] Jun Hee Song and Jae Kyoo Lim, (2001) Bonding strength in structural adhesive bonded joint: Metals and Materials International, Vol. 7. Number 5: 467-470.
- [25] Yong Yin et al, (2005) Creep stress redistribution of single-lap Weldbonded joint: Mechanics of Time-Dependent Materials. Number 9: 91-101.
- [26] V.F. Stroganov et al, (2007) Epoxy polymer in adhesive technologies of pipeline joint: Polymer Science. Vol 49: Number 3: 269-271.
- [27] Jones T.B, (1995) The Mechanism and Properties of Weld-bonded Joints: Sheet Metal Industries. Number 72: 27-31.
- [28] Biswajit Tripathy et al, (2008) Vibration and buckling characteristics of weld-bonded rectangular plates using the flexibility function approach: International Journal of Mechanical Sciences. Number 50: 1486-1498.
- [29] A.M. Pereira et al, (2010) Analysis of manufacturing parameters on the shear strength of aluminium adhesive single-lap joints: Journal of Materials Processing Technology. Number 210: 610-617.

Influence of Electron Beam Local Annealing on the Residual Stresses for the joints with Electron Beam Welding of near α titanium alloy

FU Peng-fei^{1,2}, FU Gang¹, Gong Shui-li¹, WANG Ya-jun²

¹ National Key Laboratory of Science and Technology on Power Beam Processes, Beijing Aeronautical Manufacturing Technology Research Institute, Beijing, China, 100024

² School of Materials Science and Engineering, Huazhong University of science and technology, Wuhan, China 430074

Abstract. To reduce the negative influence of residual welding stresses in aeronautical products, electron beam(EB) local annealing after electron beam welding(EBW) was studied for near α titanium alloy of Ti-Al-Sn-Zr. The appearance of the welded joints was observed, and the residual welding stresses for EBW and EB local annealing were measured by the drilling-hole method. The results showed that the gradient of the longitudinal residual stresses lowered along the central line of vertical welds after EB local annealing, and the peak stresses lowered 40% more than those of as-welded; , transverse residual stresses changed a little. Along the welds, the longitudinal stresses were also decreased after EB local annealing, and the equilibrium region of the residual stresses was located in the centre of the plate.

Keywords: electron beam, local annealing, welding, residual stresses

1. Introduction

With the increasing demands arising from aero engine developments, materials with high strength, long fatigue life and excellent reliability are required for engine components. Titanium alloys are regularly used for such components due to their advantages, such as low density, high specific strength, and corrosion resistance.

Instead of conventional welding, the technology of EBW has been applied to the compressor, combustor and casings of aero engines because of its advantages which include high power density, high efficiency, low deformation and great depth-to-width ratios. The compressor disks of the AJI-31 Φ turbofan engine, the EJ200 engine and industrial gas turbines have been welded by EBW in Russia, America and Europe[1-5]. In China, EBW is particularly suitable for application in new aero engines [4].

During welding, temperature gradients and asymmetric heat expansion induces thermal stresses and distortions, and ultimately welding residual stresses formed. High residual tensile stresses decrease the joints' fatigue strength and corrosion resistance, whereas the

components' stability under high compressive stresses is improved [6-8]. Although the residual stresses of EBW joints are lower than the yield stress, vacuum annealing must be applied after EBW to improve the properties and the qualities of the aero components [9].

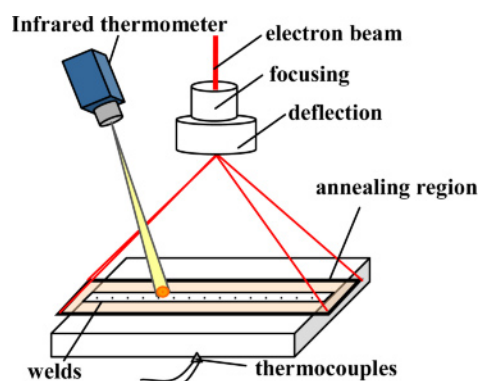
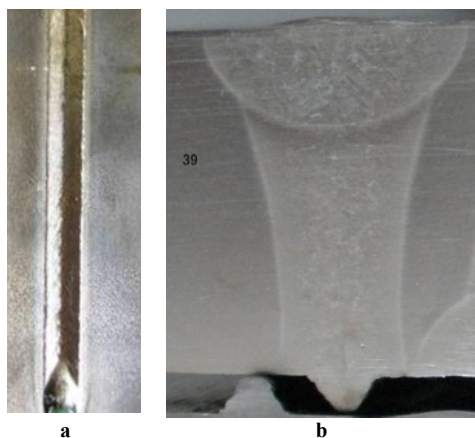
In Beijing Aeronautical Manufacturing Technology Research Institute (Bamtri), electron beam local annealing was investigated to find its effectiveness for reducing welding residual stresses and distortions for titanium alloy after EBW. Residual welding stresses were measured by the drilling-hole method, and the influence of EB local annealing was investigated.

2. Experimental procedures

The material investigated was Ti-Al-Sn-Zr alloy, which is one of the near α high temperature titanium alloys. Test plates had dimensions of 280 \times 180 \times 12 mm. Before EBW, platinum-rhodium thermocouples were fixed to the materials, and connected to a DX1012 temperature recorder to measure the heat treatment temperatures. The temperature on the upper surface was measured by Reytech infrared thermometer outside the chamber. EBW and post-welded heat treatment were accomplished by a ЭЛН(electron beam welding machine). Adjusting focusing currents and deflection parameters, EB local annealing was carried out by continuous rectangular scanning (shown as Fig. 1). In Bamtri, the temperature of EB annealing finished was 850~870 $^{\circ}$ C, maintained for 30min. The parameters of EBW and EB local annealing are shown in Table 1. The test plates assembly is shown in Fig. 2, the width of the front and back weld were 7 mm and 2 mm respectively. The joints' shapes were defined as Bell pattern according to the references [1, 11].

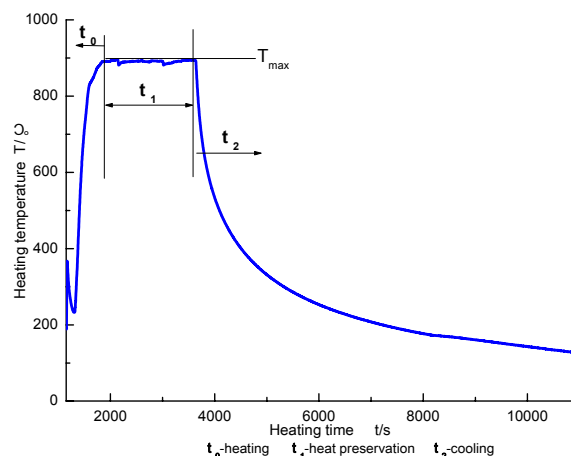
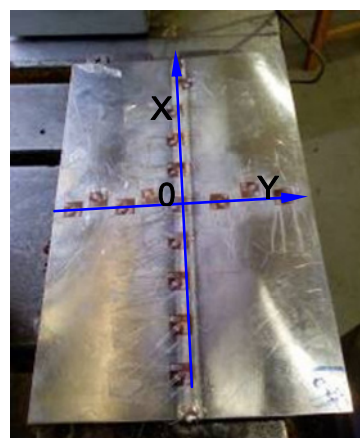
Table 1. Parameters for welding and heat treatment

Process	Voltage /kV	Beam current /mA	Speed /mm.m in-1	Scanning Spot mode
welding	60	130	800	—
Heat treatment	60	50~60	—	100×50

**Fig. 1.** Diagram of EB local annealing**Fig. 2.** Photograph of the welds :a,appearance; b,cross section

The annealing temperature curve was measured in a position 6mm from welds center by thermocouples. The curve is shown in Fig.3.

According to the design of measurement positions, strain gauges of BX120-3CA were fixed to the surface of the welding plates (as in Fig. 4). The resistance values of strain gauges were $120 \pm 0.1 \Omega$, and the sensitivity of the resistance strain measurement of YJD-1 was $2.18 \pm 1\%$. Residual welding stresses of as-welded and post-weld heat treatment conditions were measured by the drilling-hole method. With regard to the release of residual strain after drilling holes, the strain values were measured every 15 min, until measurement errors were twice less than $5 \mu\epsilon$ [12].

**Fig. 3.** Temperature curve of EB local annealing**Fig. 4.** welding plates and measurement position

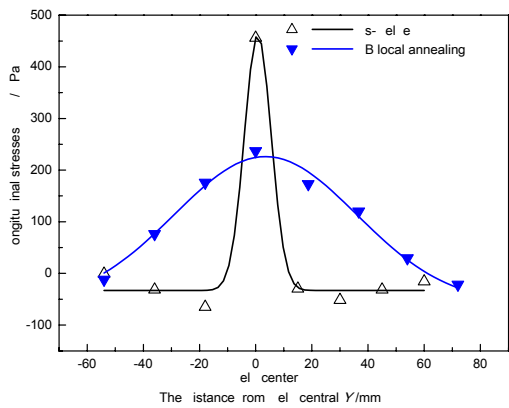
3. Results and discussion

3.1 Residual stresses along the vertical and centre lines of the welds (Y)

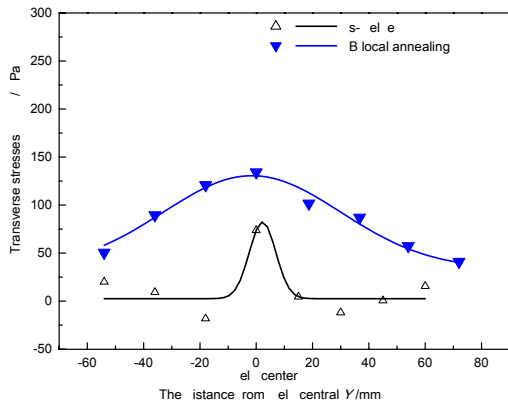
After EBW and EB local annealing, the distribution of residual stresses along the vertical and centre line (Y) of the welds is shown in Fig. 5, for readings located on the front welds. The as-welded joints were not heat treated. The results showed that the longitudinal stresses of the welds were higher than the transversal stresses, which had greater gradients and higher peak stress than the welds for as-welded joints. Longitudinal residual stresses in the welds were tensile stresses and the values of the tensile stresses gradually decreased with increase of the distance from weld center, even the compressive stress in base metal. After EB local annealing, the distribution of residual stresses had changed, and the stresses' transition from the welds to base metal became gentle. Compared

with as-welded, the peak of longitudinal tensile stresses in weld center obviously decreased by over 40%, which reached 236 MPa from the as-welded of 456 MPa. The transversal stresses after EB local annealing slightly increased with as-welded joints.

Due to the penetration of the welding process (Fig. 1), residual stresses were also induced on the back welds (shown in Fig. 6). The distribution of the back welds was the same as the front welds. Compared with as-welded, the longitudinal tensile stresses in weld center decreased by over 40% after EB local annealing, and the transversal stresses also lowered by over 50%. From reference [13], it was deduced that EB local annealing would induce a micro-change of microstructure and the recovery of residual strain, and inner stresses would be redistributed. With the increase of the heat treatment time, the stress gradient would become gentle and peak stress also lower.



(a)



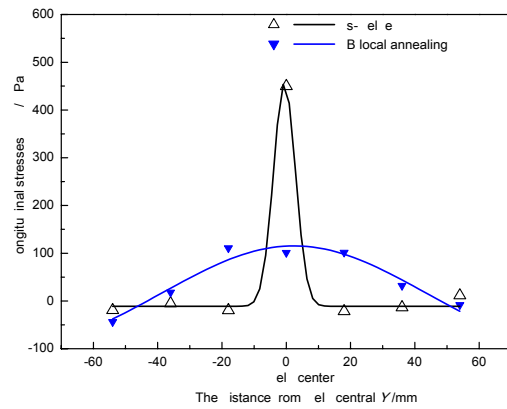
(b)

Fig. 5. Residual stresses along Y on the front welds: a, longitudinal stresses; b, transversal stresses

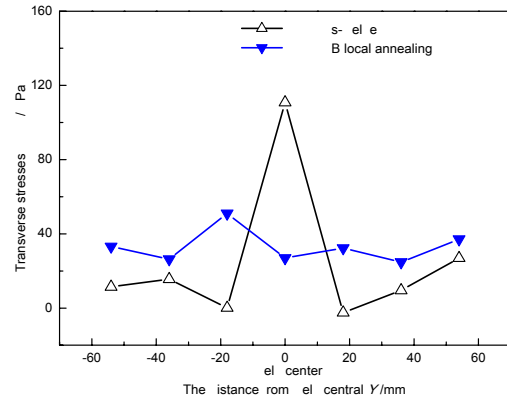
3.2 Residual stresses along the welds (X) on the front welds

Residual stresses of EBW and EB local annealing along the welds are shown in as Fig. 7. The results show that all the longitudinal residual stresses were high tensile

stresses, and the transverse stresses were low tensile stresses. Compared with EBW, the longitudinal stresses after EB local annealing were decreased by 40–65% in the region of (-50, 50) mm, which reached 150–220 MPa. And the transverse stresses were 60–130MPa, as near as makes no difference with as-welded. In the region of (-50, 50) mm, the longitudinal stresses were uniformly distributed for EBW or EB local annealing, and the same with the transverse stresses. It was concluded that the stresses' equilibrium area existed in the middle of the plates (-50, 50) mm, which was a similar result to reference [14].



(a)



(b)

Fig. 6. Residual stresses along Y on the back welds: a) longitudinal stresses; b) transversal stresses

4. Conclusions

The welds of the Bell shape and fine configuration were produced by the appropriate welding process for Ti-Al-Sn-Zr alloy with 12 mm thickness. Compared with as-welded (EBW), the residual stresses were redistributed in the vertical direction after EB local annealing, and the gradient of the longitudinal stresses obviously decreased, which the peaks lowered by over 40%. The transverse

stresses only changed a little. Along the welds, a stresses' equilibrium area existed in the centre of the welding plates, and the longitudinal stresses in this section also obviously decreased.

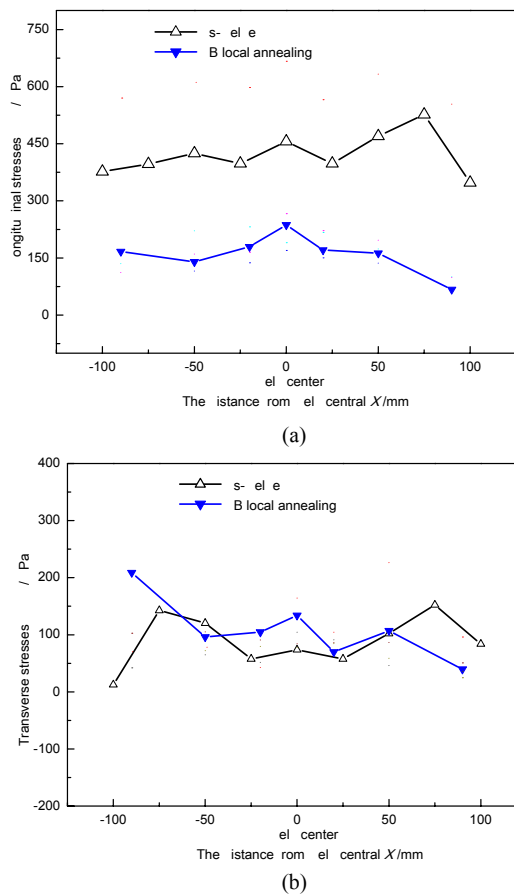


Fig. 7. Residual stresses along the welds(X):a, longitudinal stresses, b, transversal stresses

References

- [1] Zhiyong Mao. Analysis of EBW technology in large commercial jet manufacturing application, *Aeronautical Manufacturing Technology* 2009: (2) :92-94.
- [2] Shuili Gong, Huaixue Li, Xin Li, et al. Application and development of high power beam process technology, *Aeronautical Manufacturing Technology* 2009: (14): 34 -39
- [3] O.E. Kosing, R. Scharl, H.J. Schmuhl. Design improvements of the EJ200 hp compressor. from design verification engine to a future all blisk version *Proceedings of ASME TURBO EXPO 2001: Land, Sea, and Air, USA, 2001: 1-6 (2001GT0283)*
- [4] Wenjun Kang, Yangmin Liang, ChengYong Ruan. Shaft neck of compressor with electron beam welding, *Proceedings of the Fourteen National Welding Conference of China 2009: Har Bin: 6-17.*
- [5] M.B. Henderson, D. Arrell, M. Heobel, et al. Nickel-Based Superalloy Welding Practices for Industrial Gas Turbine Applications[J]. *Science and Technology of welding and joining*. 2004,9(1)
- [6] Radaj Dieter. *Welding thermal effects-Temperature fields, residual stresses and distortion*, Translated by Xiong Dijing and Shi YaoWu. Beijing: Mechanical Industry Pres, 1997:10-50
- [7] Aiping WU, Haiyan Zhao, Qingyu Shi, et al. Prediction and Control of Stress and Distortion in Welded Structure used in Aviation and Aerospace Fields, *Aeronautical Manufacturing Technology* 2009: (24): 26-30
- [8] Jianguo Yang, Xueqiu Zhang, Xuesong Liu, et al. Analysis and discussion on welding residual stress and strain, *Welding & Joining* 2008:(4):7-10
- [9] GUO Shao-qing, GU Wei-hua, YU Huai, et al. Effect of Postweld Heat Treatment on Microstructure and Properties of Electron Beam Welded TC18 Joint. *Journal of Aeronautical Materials* 2006:2(3):116-121
- [10] Wang Yajun, Guan Yongjun, Fu Pengfei, et al. Study on shape factor of the fusion-solidification zone of electron weld beam [J]. *China Welding*, 2008, 17(4):62-68
- [11] WANG Ya-jun, FU Peng-fei, GUAN Yong-jun. Methods of Studying Welds Shape of TC4 Alloy with EBW, *Journal of Aeronautical Materials* 2009:29(2): 53-56
- [12] FU Pengfei, HUANG Rui, LIU Fangjun, et al. Microstructure and residual stress of TA12 titanium alloy with electron beam welding, *Transactions of the China Welding Institution* 2007:28 (2): 82-84
- [13] Zhili Feng. *Processes and mechanisms of welding residual stress and distortion [M]*. Cambridge England: Woodhead Publishing Limited, 2005
- [14] FU Pengfei, LIU Fangjun, FU Gang, et al. Study of electron beam post-weld local heat treatment for TC4 titanium alloy and residual stress measurement of weld, *Nuclear Techniques* 2006:29 (2): 136-139.

Similar and Dissimilar Welding of Ductile Cast Iron

M. El-Shennawy¹ and A. A. Omar²

¹ Industrial Engineering Department, Faculty of Engineering, Fayoum University, El-Fayoum 63111, Egypt

² Mechanical Engineering Department, Benha High Institute of Technology, Benha University, Benha, Egypt-Now on leave to Taif University, KSA.

Abstract. In this research an experimental study has been carried out to investigate various procedures for welding ductile cast iron (DCI) by similar and dissimilar welding. Preliminary experiments were conducted which showed failed welded specimens in many cases where shielded-metal arc welding (SMAW) process using AWS 6013 welding electrodes was employed. In the light of these results, new and modified welding procedures were applied using both SMAW and tungsten inert-gas (TIG) welding processes for both similar and dissimilar joints. Dissimilar joints included joints with a combination between DCI and ST37 and DCI with stainless steel 304 (ST. ST. 304). There was dissimilarity not only in the welded steel type but also in the welded thickness. A variety of different thicknesses was joined together; namely 6, 7 and 8 mm plate thicknesses. Welded specimens were tested visually at the beginning. Then, examination of both microstructure and microhardness of welded joints were carried out. Tensile strength, macrohardness and impact value for selected welded specimens were determined and compared with microstructure and microhardness results. Successful similar and dissimilar welded joints proved the applicability of using the new welding techniques for DCI.

Keywords: Welding, ductile cast iron, welding ductile cast iron, MMAW, TIG, similar welding, dissimilar welding.

1. Introduction

The automotive, agriculture and pipe industries are the major users of ductile cast iron. It is used for critical automotive parts, such as crank shafts, front wheel spindle supports, disk brake calipers, complex shapes of steering knuckles, engine connecting rods, truck axles and many other parts in automotives [1]. In such applications welding is carried out to connect parts from, for example, carbon steel to cast iron; carbon steel steering tubes to malleable iron flanges, or small tube and heat exchangers shells of carbon steel welded to end caps or heads of ductile iron, are two practical examples [2]. Ductile iron castings are also used for a variety of machinery applications, marine components, and equipment used in the paper and glass industries.

The weldability of ductile cast iron depends on its original matrix [3-4]. Similar welding of ductile cast iron has received considerable investigations among researchers [5-9]. Dissimilar welding of ductile iron with other materials has received limited interest, especially with fusion welding processes [10] - dissimilar joining using diffusion bonding received better attention when dealing with other grade of cast iron like gray cast iron [11] or martensitic stainless steel [12]. Friction welding for joining with aluminum has also been investigated [13]. There is still lack of information about the usage of various welding processes and different welding techniques and about the weldability of similar and dissimilar welded joints made from cast iron and steels in general.

It is well known that any heat treatment, with the exception of austempering, reduces fatigue properties and above-room-temperature fracture resistance. [14]. This promoted the authors to perform welding without external/extrinsic preheating. Interpass heating was implemented in the welding as internal/intrinsic preheating. This could reduce the previously mentioned effect of preheating and reduce the cost of welding.

In this research similar and dissimilar welded joints of pearlitic ductile cast iron have been made using different welding processes and various techniques. A new technique has been developed for welding cast iron by mixing two different filler wires of steel and stainless steel filler wire. Dissimilar joints included ductile cast iron with mild steel ST. 37 and with stainless steel ST. ST. 304. There was also dissimilarity in the welded thicknesses, where the stainless steel plate thickness was 6 mm, the mild steel plate thickness was 7 mm and the ductile iron plate thickness was 8 mm.

2. Experimental Work

Pearlitic ductile cast iron ASTM A536 (100-70-03) with chemical composition shown in Table 1 was used for

similar and dissimilar welded joints. Mild steel ST. 37 and stainless steel ST. 304 - with chemical compositions shown in Table 1- were the two other material selected to get dissimilar welded joints with ductile cast iron. The experiments were divided into two main parts. First, preliminary experiments, in which both bead on plate and welded specimens were produced were carried out using different welding procedures. These can be summarized in Table 2. Preheating was applied for some specimens while others were welded without preheating. Some were welded with SMAW using E6013 electrode and others with ENiFe-CI (Esab ok 92.58) electrodes and some were TIG welded using E309 filler wire. Regardless the welding condition, all specimens welded with SMAW using E6013 electrode failed and fractured at WZ either during or after depositing the second pass. Figure 1 shows examples of failed specimens. All other specimens which were welded with SMAW using Esab ok 92.58 electrodes and those which were welded with TIG using E309 filler wire succeeded, but specimens had the defect of lack of root penetration. The chemical composition of electrode and filler wire adopted in the study is shown in Table 3.

In the light of such results of the preliminary experiments, new experiments with some modified procedures were adopted. Extrinsic preheating (using oven, flame, etc.) was prevented and more concentration on intrinsic preheating was made. Intrinsic means preheating resulting from multipass welds. Joint types and combinations are summarized in Table 4, coupled with welding condition in each case. Schematic representations for joint design used for both similar and dissimilar welding and the procedure of using the new technique of mixing the filler wire E309 with E6013 SMAW electrode are illustrated in Figs. 2-3. Examples of successful welded specimens from similar and dissimilar welding are shown in Figs. 4-5.

3. Results and Discussion

Visual examination of the similar and dissimilar welded specimens showed successful joints as depicted in Figs. 4-5. Samples for metallurgical examination and microhardness tests were extracted from welded specimens. Results for the microstructural examination and microhardness for selected specimen are shown in Figs. 6-8. Fig. 9 shows the maximum hardness values.

Figure 6 shows the microstructure of the as cast ductile iron, it is pearlitic matrix with ferrite halos around graphite nodules. Figure 7 shows the optical micrographs of the weld, fusion and heat affected zones of the specimens welded with different welding processes and procedures and with various filler wires described above.

Using steel electrode E6013 gave the rise to the hard zones with martensite and ledeburite structure as shown in Fig. 7(a). Its highest microhardness value reached 798 HV at the fusion boundary which is more than 4 times the

original hardness of the ductile iron raw material (184 HV) as shown in Fig. 8(a). This is also beneficial when using this type of filler wire when hardfacing of ductile iron is required. Such a hard structure was also found in some other welded specimens, such as similar SMA welded joints using buttering technique (664 HV at fusion boundary) and TIG welded joints using 309 stainless steel filler wire (591 HV at fusion boundary) as depicted in Figs. 7(b) and (c) and Fig. 8(b). Using austenitic filler wire E309 promoted the formation of carbides at fusion and HAZ regions.

Using the ENiFe-CI electrode (so called Esab in the text and graphs) with the SMAW process showed lower hardness values (353 HV at fusion boundary) which is nearly twice the original raw material hardness as shown in Fig. 8(c). The lowest microhardness value among similar welded joints; namely 311 HV, was recorded for the joint welded using the new technique of mixing the filler wires of 6013 and 309 during welding. This microhardness value is about 1.5 times the value for the raw material. It is worth mentioning that the highest value of this joint is located at the weld region and not the fusion or HAZ regions. The Microhardness in other regions of this joint is lower and therefore the fusion and HAZ regions are less hard and have less possibility for cracking. The microstructure of this joint is shown in Fig. 7(d). Less martensitic and ledeburitic structure is revealed and some austenitic structures are formed.

Dissimilar welded joints showed high hardness values in all specimens regardless of the welding procedure adopted. The lowest microhardness value was recorded for dissimilar joint of ductile iron with stainless steel 304 welded using ENiFe-CI electrode. The hardness was 404 HV at both fusion boundaries of stainless steel and ductile iron. Figs. 7(e)-(i) show the martensitic and ledeburitic structure which raised the microhardness values to reach 650-700 HV. Fig. 7(j) shows the austenitic dendritic microstructure of the weld zone for dissimilar welded joint ductile-stainless with ENiFe-CI.

Tensile and impact tests for some selected specimens were done. An impact value of 18 J was recorded for similar welded and dissimilar welded joints used ENiFe-CI electrode. Microhardness values at the weld zone for joints welded using ENiFe-CI electrode were 200 HV for similar and dissimilar joints as shown in Figs. 8(c), (f) and (h). A much lower value of 1.9 J for dissimilar joint ductile-stainless steel 304 using E309 was found and the lowest value was 0.68 J for dissimilar joint of ductile-mild steel with buttering. Dissimilar joint ductile-stainless steel 304 using E309 had 400-500 HV microhardness at weld zone as shown in Fig. 8(g). In case of buttering the E6013 electrode is used as filler wire to build the weld zone in which the notch of the impact test specimen was inserted. This joint showed a high hardness value of about 500-600 HV at the weld zone as shown in Fig. 8(e). A very low toughness was recorded, as expected.

The tensile strengths of some welded specimens were measured. A similar welded joint using TIG welding with

Table 1 Chemical composition for the raw materials used in the study

	C	Si	Mn	P	S	Cr	Ni	Al	Co	Cu	Ti	Mg	Fe
DCI	3.83	2.68	0.232	0.050	0.005	0.022	0.015	0.017	0.009	0.011	0.013	0.020	Rest
M. St.	0.157	0.211	0.489	0.009	0.012	0.063	0.037	0.042	0.009	0.039	0.001	-----	Rest
SS304	0.08	1	2	0.045	0.030	18	8	-----	-----	-----	-----	-----	Rest

Table 2 Chemical composition for the electrode/filler wire used in the study

Joint Type	Process	SMAW									TIG
		AWS 6013						ESAB, ok 92.58, 3 sp.			309
B.O.P		W.P.H* 700°C	WT.P. H**	X	X	X	X	X	X	X	X
		-----	-----	X	X	X	X	X	X	X	X
Similar Welds		W.P.H, 400 °C	WT.P. H	W.P.H, 400 °C	WT.P.H, 6 sp.						
		Fractured at WZ after 1 min.	Fractured at WZ during 2 nd pass	Fractured at WZ during peening by hammer after 1 st pass	Fractured at WZ after 2 nd pass completed and specimen fallen down to the ground-1 st pass was left to cool	Fractured at WZ after finishing 2 nd pass	Succeeded with lack of root penetration				

Table 3 Chemical composition for the electrode/filler wire used in the study

	C	Si	Mn	P	S	Cr	Ni	Cu	Fe
E6013	0.08	0.24	0.4	0.02	0.015	-----	-----	-----	Rest
E309	0.06	0.5	1.8	-----	-----	24	13.5	0.1	Rest
ENiFe-CI	1	0.8	0.8	-----	-----	-----	Rest	-----	43

Table 4 Combinations and welding procedure for similar and dissimilar welds

Joint Type	Process	SMAW		TIG	BUTTERING	MIX
		AWS 6013	ESAB ok 92.58 → ENiFe-CI	E309	309TIG → 6013SMAW	6013 SMAW + 309
	B.O.P	√	√	√	X	√
	Similar Welds (DCI/DCI)	√	√	√	√	√
	Dissimilar Welds (DCI/M.St)	X	√	√	√	X
	Dissimilar Welds (DCI/St.St)	X	√	√	X	X

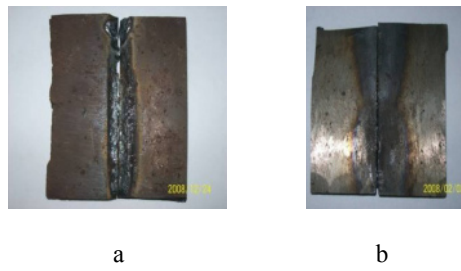


Fig. 1. Examples of failed similar welded joints of DCI/DCI either (a) with preheat or (b) without preheat.

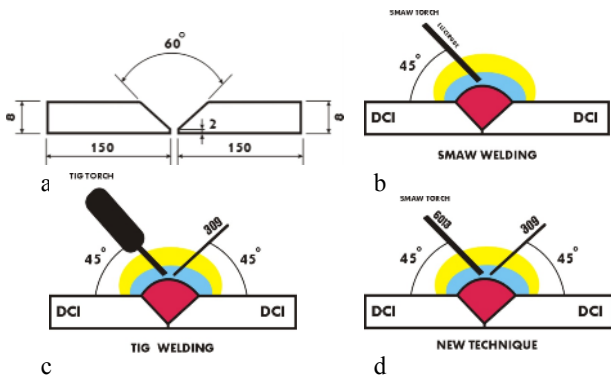


Fig. 2. Schematic representation for (a) joint design, (b) SMAW, (c) TIG and (d) new technique (SMAW6013+filler309).

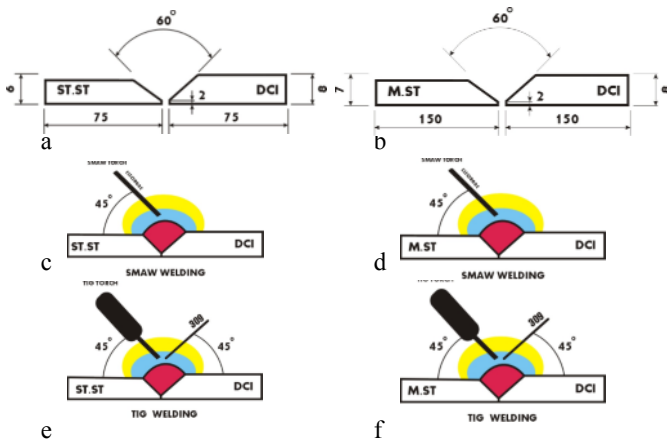


Fig. 3. Schematic representation for dissimilar joint design of (a) DCI/St.St, (b) DCI/M.St, (c) and (d) SMAW used for both joints and (e) and (f) TIG used for both joints.



Fig. 4. Examples for similar welded specimens of ductile cast iron made by various welding procedures.

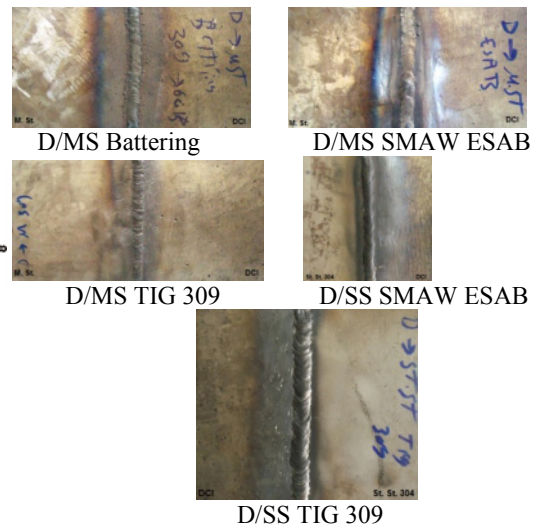


Fig. 5. Examples for dissimilar welded specimens of ductile cast iron with stainless steel 304 and mild steel 37 made by various welding procedures.

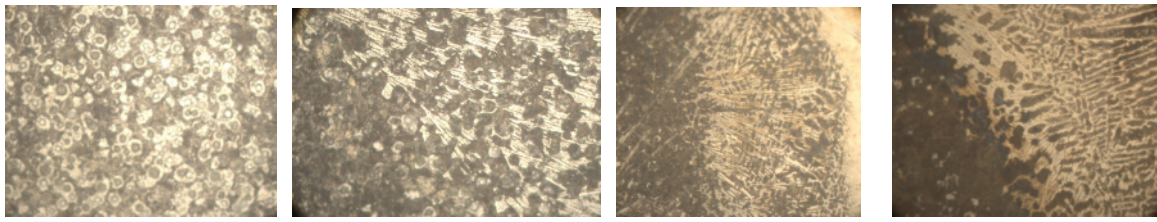


Fig. 6. BM, DCI, x500

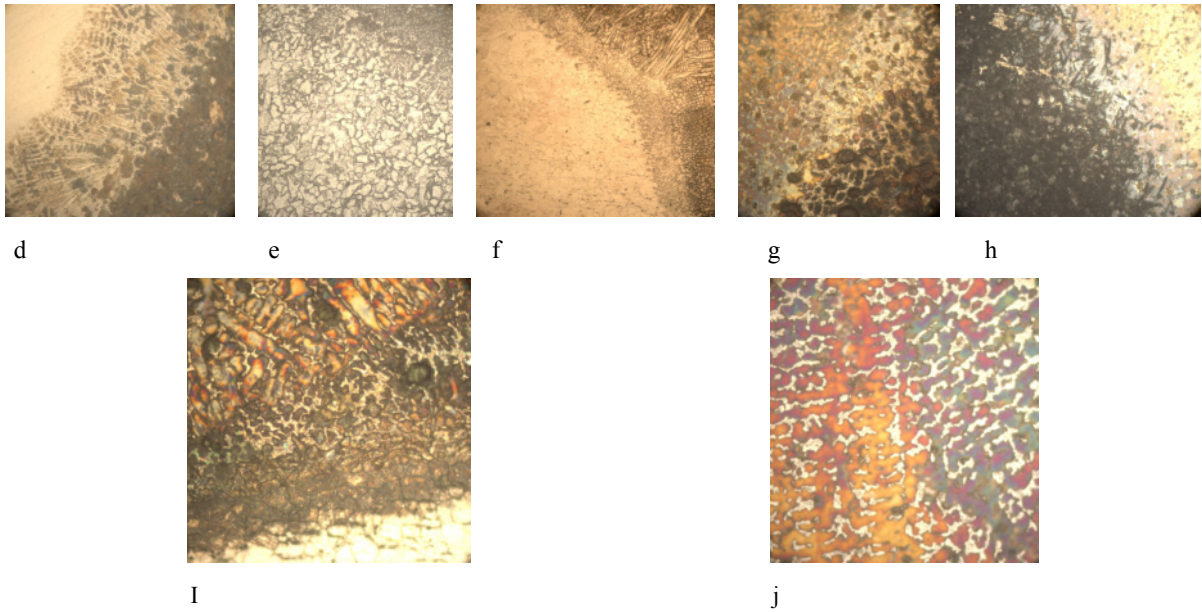


Fig. 7. Microstructure of similar and dissimilar welded joints, (a) WFB, DCI/DCI, x500, 6013, (b) WFB, DCI/DCI, x500, 309, (c) WFB, DCI/DCI, x500, 309 buttering, (d) WFB, DCI/DCI, x500, mix, (e) WFB, DCI/M.St, x500, 309-Buttering, (f) WFB, DCI/St.St., x200, 309-St.St. Side, (g) WFB, DCI/St.St., x500, 309-DCI Side, (h) WFB, DCI/St.St., x500, Esab - DCI Side, (i) WFB, DCI/St.St., x500, Esab - St. St. Side, (j) WZ, DCI/St.St., x500, Esab welded BM, DCI, x500.



Fig. 8. Microhardness distribution along BM, FB, HAZ and WZ for similar and dissimilar welded joints.

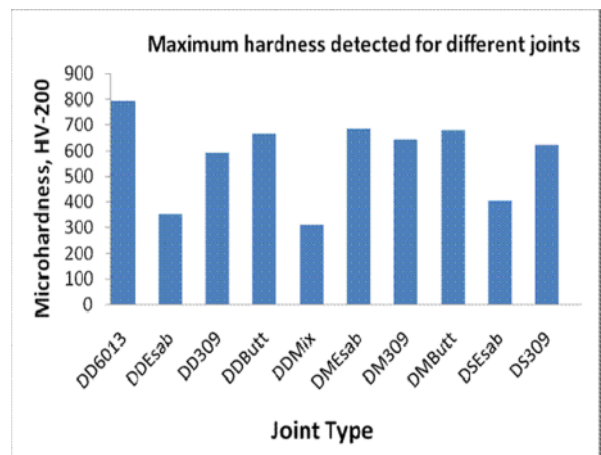


Fig. 9. Maximum microhardness values for similar and dissimilar welded joints.

E309 showed a tensile strength of 296 MPa; fracture occurred at the HAZ. The joint made using SMAW with ENiFe-CI electrode showed 286 MPa and fracture occurred at the WM. In a dissimilar welded joint with mild steel ST. 37 made by SMAW using ENiFe-CI electrode, the tensile strength was 357 MPa and fracture occurred at the HAZ.

4. Conclusions

From the current results, the following concluding remarks can be drawn:

1. Ductile cast iron can be welded without preheating.
2. Dissimilar joints of ductile cast iron with mild steel and stainless steel 304 revealed successful combinations.
3. Using steel electrode when welding ductile cast iron by SMAW process raises the microhardness to very high values (800 HV). This can be beneficial when hardfacing ductile cast iron for special applications.
4. Stainless steel electrode with high nickel (E309) promoted the formation of carbides, which raises the microhardness values for either similar or dissimilar joints welded by TIG welding.
5. The Buttering technique did not show better results than those obtained with steel electrode E6013 or stainless steel filler wire E309.
6. Using an ENiFe-CI electrode is recommended for similar welding of ductile iron and dissimilar welding of ductile with stainless steel 304.
7. A new technique has been developed in this study and applied to similar welding of ductile iron where a mixing of both steel electrode E6013 and stainless steel electrode E309 gave the best results where a lower microhardness were recorded. The toughness is expected to be better than other joints welded by various techniques.

References

- [1] Metals Handbook, 9th ed. Vol. 1, "Properties and Selection: Irons Steels and High Performance Alloys", ASM, Metals park, Ohio, 1993, p 99.
- [2] S. D. Kiser and Bob Irving, "Unraveling the mysteries of welding cast iron", *Welding J.* 72 (1993), pp. 39-44.
- [3] Metals Handbook, 9th ed. Vol. 6, "Welding, brazing and soldering", ASM, Metals park, Ohio, 1993, pp. 1748-1781.
- [4] ANSI/AWS D11.2-89, "GUIDE FOR WELDING IRON CASTINGS", American Welding Society, 1989.
- [5] E. M. El-Banna, "Effect of preheat on welding ductile cast iron", *Materials Letters* 41 (1999) 20-26.
- [6] E. M. El-Banna, m. S. Nageda and M. M. Abo El-Saadat, "Study of restoration by welding of pearlitic ductile cast iron", *Materials Letters* 42 (2000) 311-320.
- [7] Jefferson's Welding Encyclopedia, Eighteenth Edition, Edited by Robert L. O'Brien, American Welding Society, pp. 78-82.
- [8] M. Pascual, J. Cembrero, F. Salas and M. Pascual Martines, "Analysis of the weldability of ductile iron", *Materials Letters* 62 (2008), pp. 1359-1362.
- [9] M. Homma, T. Wada and K. Yamaya, "Welding of cast iron and nodular graphite cast steel, II: Arc-welding of nodular graphite cast steel", *Science reports of the Research Institutes, Tohoku University, Ser. A, Physics, chemistry and metallurgy*, Vol. 12 (1960), pp. 448-455.
- [10] N. Fuji, H. Suzuki, T. Sengoku, T. Onuma and K. Yasuda, "Bending strength of nodular graphite cast iron/mild steel welding joints by various welding process and residual stress measurement", *Bulletin of the Polytechnic University A. Science, Technology and Art*, Vol. 35 (2006), pp. 7-12.
- [11] N. Özdemir, M. Aksoy and N. Orhan, "Effect of graphite shape in vacuum-free diffusion bonding of nodular cast iron with gray cast iron", *J. Mat. Proc. Tech.* 141 (2003), pp. 228-233.
- [12] K. Sedat, "The effect of the welding temperature on the weldability in diffusion welding of martensitic (AISI 420) stainless steel with ductile (spheroidal graphite-nodular) cast iron", *J. Mat. Proc. Tech.* 186 (2007), pp. 33-36.
- [13] Y. Song, Y. Liu, X. Zhu, S. Yu and Y. Zhang, "Strength distribution at interface of rotary-friction-welded aluminum to nodular cast iron", *Trans. Nonferrous Met. Soc. China* 18 (2008), pp. 14-18.
- [14] Metals Handbook, 9th ed. Vol. 1, "Properties and Selection: Irons Steels and High Performance Alloys", ASM, Metals park, Ohio, 1993, p 91.

Recognition of Contact States in Robotized Assembly Using Qualitative Wavelet Based Features and Support Vector Machines

Z. Jakovljevic¹ and P. B. Petrovic¹

¹ Department for Production Engineering, Faculty of Mechanical Engineering, University of Belgrade, Serbia, zjakovljevic@mas.bg.ac.rs

Abstract. This paper presents a method for recognition of contact states in robotized assembly using an example of cylindrical peg into hole part mating. Starting from force quasi-static model, offline features extraction using Discrete Wavelet Transform and teaching (classification) using Support Vector Machines is carried out. Thus obtained class boundaries together with features extracted from signals of generated contact force vector are used for recognition of contact states on-line. Proposed method is tested using intensive real world experiments.

Keywords: Part Mating, Contact State Recognition, Discrete Wavelet Transform, Support Vector Machines

1. Introduction

During robotized part mating process considerable geometrical and dynamical uncertainties which lead to errors in fine motions are inherently present. The most cost effective solution for part mating with uncertainties is active compliant robot motion which assumes the correction of robots nominal trajectory according to force feedback, i.e., according to compliance which correlates measured force and motion correction. Active compliance robot control assumes that each contact situation between moving object (MO) and environmental object (EO) generates certain form of generalized force (force/torque).

Topologically, objects in contact are convex and concave 3D polyhedra which are contacting through three topological elements (surface, edge and vertex). Based on work presented in [1] and [2] principal contacts (PC) and contact states (CS) can be introduced. PC represents unique contact between a pair of surface elements which are not the boundary elements of other contacting surface elements [1]. CS between two polyhedra is a set of PC's. Unlike for the convex polyhedra, for concave polyhedra, CS can consist of more than one PC. This makes the recognition of CS in the latter case more complex.

Active system for compliant robot motion demands following active components: 1) interactive active motion commands planner; 2) system for recognition of contact, and 3) controller for execution of planned compliant motion commands. Based on detail review of the active compliant motion in [3] the authors conclude that although there has been significant research in different components of active compliant motion system, there is a lack of research in interfaces between these components, especially in the recognition system functions which transform low level measurement signals into high level contact primitives suitable for intelligent planners.

In this paper we propose the method for recognition of CS's in cylindrical peg-into-hole part mating whose training is based on the model of forces generated in each CS.

2. Contact State Recognition Machine

Fig. 1 gives architecture of the machine for on-line recognition of contact states during cylindrical part mating process. Basic features which are taken directly from process are represented by six-components vector of contact force \mathbf{F} between MO and EO. Using certain transformations τ components of the force \mathbf{F} are transduced into patterns - features vectors \mathbf{X} . Transformations τ are the result of off-line features extraction and selection. After transduction, classification is carried out using class boundaries, also defined in off-line training process. At the classification output the class to which the pattern belongs is obtained - this class corresponds to the CS in which the part mating process is currently. The information about CS is handed over to the planner which, based on the motion plan, gives commands to robot control system for further action.

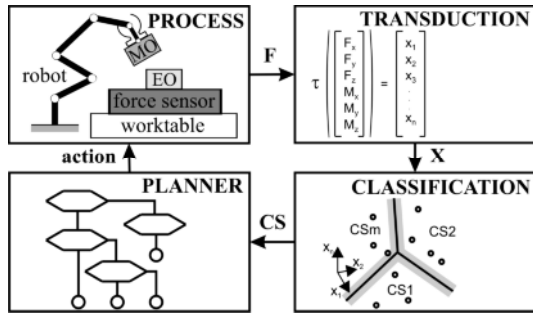


Fig. 1. Architecture of on-line recognition machine

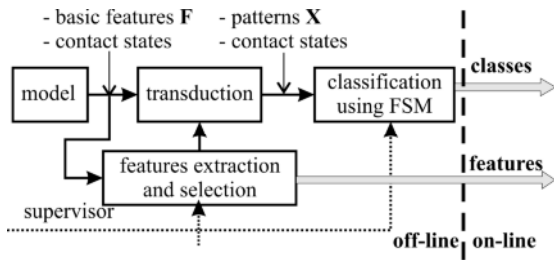


Fig. 2. Architecture of off-line training machine

Off-line training of recognition machine (Fig. 2.) is based on the quasi-static model of generated forces. From modeled force vector representative and discriminative features are extracted and selected. Thus obtained patterns are then classified and class boundaries for on-line classification are generated.

2.1 Quasi-static Model of Forces

The quasi-static model of forces in cylindrical part mating is based on the work presented in [4] and it is summarized in Fig. 3 and Table 1. Since parts are centrally symmetric, the whole model is given in one cross section in which the contact was made. The components X_{CC} , Z_{CC} and M_{CC} of contact force F in compliance center (CC) are presented.

Given model assumes [4] that the parts in contact are absolutely rigid, that the friction is Coulomb and given by friction coefficient μ , gravitational and inertial forces are neglected, etc. The truly dynamical nature of the part mating process is neglected here. Dynamical model which would introduce impact at CS transition, elasticity of parts, and dynamical nature of friction [5] would be too complex for implementation. Experiments (section 3) have shown that the trends of signals obtained in real world correspond to quasi-static force models and that the effects of dynamic phenomena (with no stick-slip) can be introduced by adding the white noise of 30dB – noise intensity is considerable. The changes of force components in time for one case of part mating using adopted model are shown in Fig. 4. Intensity of force is

highly dependent on initial position and orientation error (e_0, θ_0).

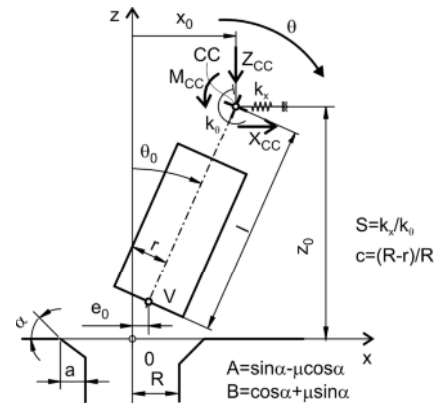
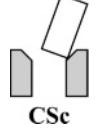


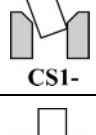
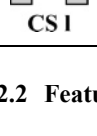


Fig. 3. Quasi-static contact force model

Table 1. Quasi-static contact force model

CS	Quasi-static model of generated forces
 CSc	$X_{CC} = k_x ((z'-z)/\text{tg}\alpha)/(1-SI(1-B/Ar))$ $Z_{CC} = k_x B/A((z'-z)/\text{tg}\alpha)/(1-SI(1-B/Ar))$ $M_{CC} = \left(\frac{B}{A}r-1\right)k_\theta \frac{(z'-z)/\text{tg}\alpha}{1-SI(1-B/Ar)}$
 CS1+	$X_{CC} = k_x \frac{e_0 - cR - (z+b-1)\theta_0}{1+S(z+b)(z+b-\mu r)}$ $Z_{CC} = \mu k_x \frac{e_0 - cR - (z+b-1)\theta_0}{1+S(z+b)(z+b-\mu r)}$ $M_{CC} = k_\theta S(z+b-\mu r)X_{CC}/k_x$
 CS2	$X_{CC} = k_x [cR(1-2l/(1-z-b))-x_0]$ $Z_{CC} = 2\mu \frac{X_{CC}(1-\mu r) - M_{CC}}{1-(z+b)} - \mu X_{CC}$ $M_{CC} = k_\theta (2cR/(1-z-b) - \theta_0)$
 CS1-	$X_{CC} = k_x (e_0 - cR)/(1+SI(1-\mu r))$ $Z_{CC} = \mu k_x (e_0 - cR)/(1+SI(1-\mu r))$ $M_{CC} = k_\theta S(1-\mu r)X_{CC}/k_x$
 CS1	$X_{CC} = k_x (x_0 - cR)$ $Z_{CC} = \mu k_x (x_0 - cR)$ $M_{CC} = k_\theta \theta_0$

2.2 Feature Extraction and Selection

Analysis of Fig. 4 leads to conclusion that the selected features should be qualitative and independent on force level. Relations given in Table 1 show that the character of dependence (linear, nonlinear constant) of force component from insertion depth, that is, time (since insertion velocity is constant) is different for some CS's.

Nevertheless this character is for given CS the same for all three components of force. This leads to selection of one component – Z_{CC} as the first feature X_1 , and two more features X_2 and X_3 can be extracted as follows:

$$X_1 = Z_{CC}; X_2 = X_{CC}/Z_{CC}; X_3 = M_{CC}/Z_{CC} \quad (1)$$

Character of time dependence of selected features X_1 , X_2 and X_3 for possible CS's is listed in Table 2. This character is different for different CS's. The only exceptions are states CS1- and CSI. Nevertheless these states are not necessary to differ because the same sequence of motion given by planner can be used. The most important is correct recognition of CS2 since this CS is made of two PC's and it can lead to jamming or wedging and failure of part mating process.

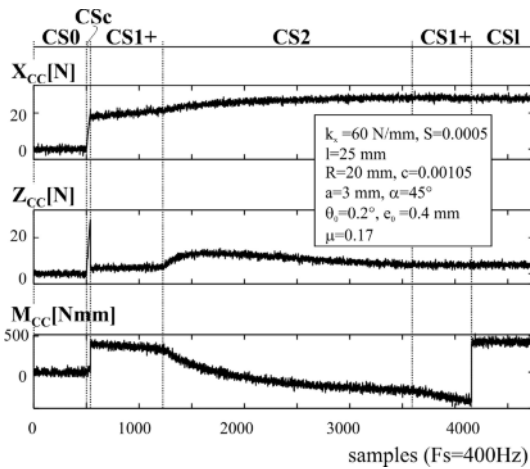


Fig. 4. Quasi-static contact force model with 30dB of noise

As long as features that describe the character of signal change in time can be extracted, they would be discriminative and representative and would lead to robust classification. Technique for features extraction and primary signal processing (de-noising) must have properties of good time localization and real-time applicability. These are the main reasons for selection of Discrete Wavelet Transform (DWT) [6]. The crucial characteristic of wavelets for the problem at hand is that wavelets from Daubechies family (db) have first N (N is the order of wavelet) vanishing moments. This means that db wavelets are orthogonal to polynomials $1, x, x^2, \dots, x^{N-1}$. Consequently, in all regions in which signal is well approximated by polynomial of order $N-1$ wavelet (detail [6]) coefficients will be zero. We have chosen the 4th level detail coefficients obtained by DWT of X_1 , X_2 and X_3 using the first order db wavelet (db1) as features denoted by X_{1db1} , X_{2db1} and X_{3db1} . These features should be equal zero in regions where the corresponding X_1 , X_2 or X_3 is constant.

Before features are generated signal is de-noised in order to eliminate the noise and highly dynamical and stochastic phenomena disregarded in the quasi-static

model. For signal de-noising DWT is employed again because, unlike conventionally used IIR or FIR low-pass filters, it is characterized by phase correctness and good time localization. Since further analysis of signal employs db1, the wavelet for de-noising should be db of the order higher than 1 or wavelet from another family [6]. In order to keep the time for de-noising as low as possible, we have chosen the wavelet db2.

Table 2. Character of force components change in time

	CSc	CS1+	CS2	CS1-	CSI
X_1	linear	non-lin	non-lin	const	const
X_2	const	const	non-lin	const	const
X_3	const	linear	non-lin	const	const

2.3 Classification

The representation of features vectors $[X_{1db1} X_{2db1} X_{3db1}]$ in 3D feature space is given in Fig. 5. Total of 465,504 patterns is generated for different part mating cycles with initial errors in the range of $e_0 \in [0, 3\text{mm}]$ and $\theta_0 \in [0, 1^\circ]$. Since working with noised data components of features vectors are rarely equal, but they are close to zero. Real-time operation demands simple classification and working with real world data in the presence of huge uncertainties and noise asks good generalization properties of classification machine. These are the main reasons for choice of Support Vector Machines (SVM) [7] for classification.

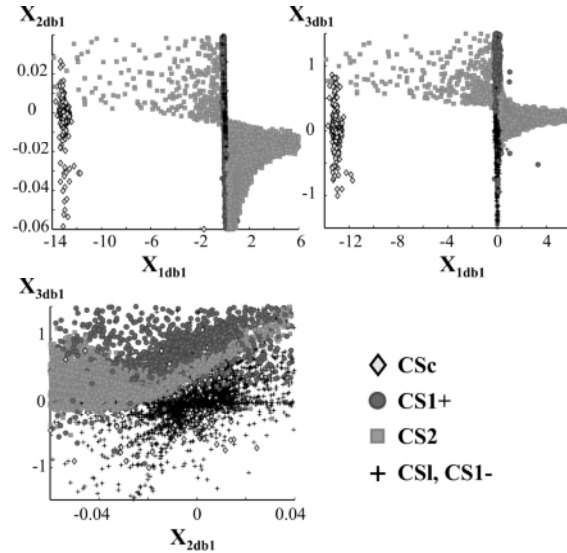


Fig. 5. Representation of generated patterns in feature space

In each classification step one class is separated. Fig. 6 shows the class boundaries obtained using SVM with linear kernel functions for recognition of CSc, CS2, CS1 and CSI/ CS1-. CS0 is recognized as CS in which the Z_{CC} force level is below 5N.

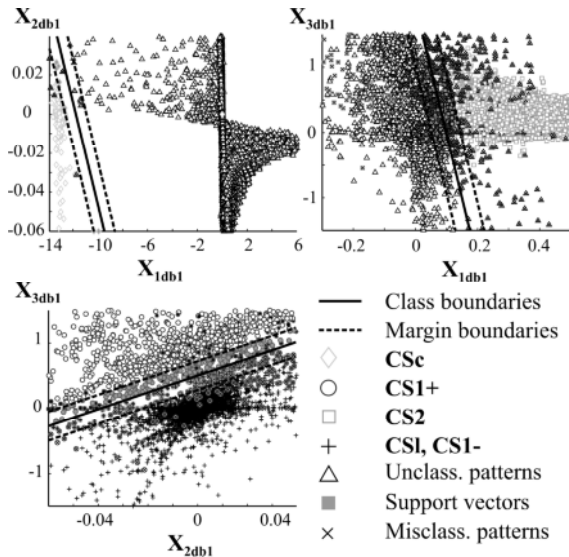


Fig. 6. Generated class boundaries

3. Experimental verification

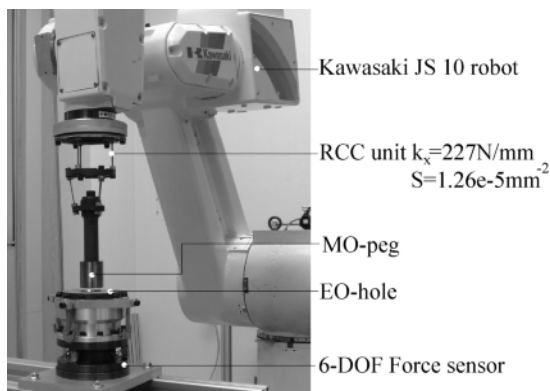
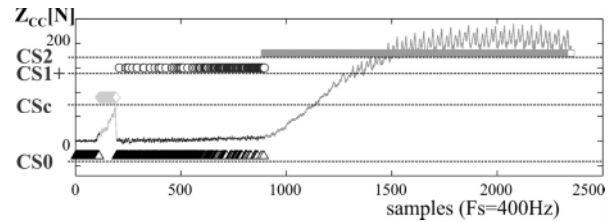


Fig. 7. Experimental installation

Proposed CS recognition machine is evaluated using real world experiments. Experimental installation (Fig. 7) consists of Kawasaki JS10 robot arm equipped with custom made RCC unit for compliance compensation. The six-component custom made strain-gauge force sensor is put on the worktable, and EO with hole is mounted on it. The mating parts have diameter $D=40\text{mm}$, clearance ratio $c=5e-4$, chamfer $3/45$, and are made of cemented steel. Force signal is sampled by 400Hz. Z_{CC} component obtained during one part mating cycle together with the results of recognition of CS's using proposed machine is shown in Fig. 8.

Fig. 8. Recognition of CS's parallel with acquired Z_{CC} force

4. Conclusion

Model based teaching of CS recognition machine proposed in this paper has advantages over the teaching based on experimental data. Available priori information is exploited and numerous experiments with questionable outcomes due to great uncertainties and small clearances in assembly process are avoided. The selected features are independent on parts geometry, the change in friction coefficient and on the system rigidity as long as it is not highly dependent on insertion depth. Thus, proposed machine is generally applicable for considered class of part mating tasks.

Experimental verification has shown the satisfactory results in real world application.

References

- [1] Xiao J, Liu L, (1998) Contact states, Representation and Recognizability in the Presence of Uncertainties. Proceedings of International Conference on Intelligent Robots and Systems 1151-1156, Victoria, Canada
- [2] Lau HYK., (2003) A hidden Markov model-based assembly contact recognition system, *Mechatronics*. 13: 1001-1023
- [3] Lefebvre T, Xiao J, Bruyninckx H, De Gersem G, (2005) Active compliant motion: a survey, *Advanced Robotics*. 19/5: 479-499
- [4] Whitney DE, (1982) Quasi-Static Assembly of Compliantly Supported Rigid Parts, *Transactions of ASME, Journal of Dynamic Systems Measurement and Control*. 104: 65-77,
- [5] Vukobratovic M, Potkonjak V, Matijevic V, (2001) Contribution to the study of dynamics and dynamic control of robots interacting with dynamic environment, *Robotica*. 19: 149-161
- [6] Daubechies I, (1992) Ten Lectures on Wavelets, CBMS-NSF regional conference series in applied mathematics. 61, SIAM, Philadelphia
- [7] Vapnik VN, (2000) The Nature of Statistical Learning Theory, Springer-Verlag, New York

Linear Axes Performance Check on a Five-Axis Machine Tool by Probing an Uncalibrated Artefact

T. Erkan and J.R.R. Mayer

Département de génie mécanique, École Polytechnique de Montréal, C.P. 6079, Station Downtown, H3C 3A7 Montréal (QC), Canada

Abstract. In this paper, a method is proposed for a rapid performance check of the three linear axes of a five-axis machine by probing a reconfigurable uncalibrated 3D master ball based artefact. The artefact composed of independent master balls is assembled directly to the machine table thus providing flexibility in the number and positions of the balls according to the machine topology and geometry. However, this reconfigurability attribute hinders precise knowledge of artefact's geometry, so it is uncalibrated. During a test, both rotary axes move to obtain the desired location (relocalisation) of the artefact. Then, for each relocalisation the linear axes are used to perform the probing. A distance based analysis is conducted for the performance check of the linear axes. The analysis is limited to the artefact geometry distortion and not its location thus excluding the potentially erroneous artefact relocalisation accomplished by the rotary axes. Tests are conducted in a laboratory on a five-axis horizontal machine. The results show that the artefact and the proposed method provide a practical tool for assessing the volumetric distortion of linear axes of a five-axis machine.

Keywords: five-axis machine tool, linear axes errors, on-machine probing, ball artefact

1. Introduction

Five-axis machine tools allow high productivity for the machining of large and complex monolithic parts such as those found in the aerospace field. They offer a significant reduction in the number of required setups by orienting the tool relative to the workpiece with two rotary axes. There are different methods for the performance evaluation of a five-axis machine. One of them is the parametric method where the error parameters are measured individually. It requires special instrument and experienced personnel. The other is the volumetric method where the effects of all error parameters are measured in combination. One method involves the measurement of an artefact using on-machine probing to obtain the machine volumetric status.

Artefacts are widely used for coordinate measuring machine (CMM) performance evaluation [1-3]. De Aquino Silva et al. [3] designed an uncalibrated ball

artefact for volumetric error evaluation and uncertainty analysis of a four-axis CMM. The measured ball centre coordinates at the first location of the artefact were accepted as the nominal values. From that initial data, the nominal coordinates for other measurement locations were calculated. The difference between the measured and the calculated coordinates were used to explain the volumetric errors of the CMM.

Most machine tools also have on-machine probing capability, usually used for part setup compensation. However, the idea of using a three-dimensional probe for machine tool inspection reaches back into the early 1980s. A calibrated cube array artefact composed of eight cubes was proposed by Choi *et al.* [4] to quickly assess the positioning errors of a 3-axis machine tool. Bringmann and Kung [5] created a pseudo 3D artefact by mounting a 2D ball plate in different locations for fast testing and calibration of machine tools, robots and CMMs with three linear axes. The precise translational and rotary shifts between locations were assured using kinematic couplings which have high repeatability. Woody *et al.* [6] developed a technique to transfer the accuracy of a CMM to a machine tool by measuring a part with fiducials both on the CMM and on the machine tool.

In previous studies on machine tools, the artefacts were used as standard parts which were calibrated on CMMs and then measured on machine tools to evaluate their performance. In this paper a volumetric error analysis for linear axes of five-axis machine tools is presented. Section 2 presents the uncalibrated 3D ball artefact on which the probing is performed. Section 3 addresses the distance based analysis. The experimental results are given in section 4 followed by a conclusion.

2. Artefact design

The artefact is designed to exploit the on-machine probing capability to perform a rapid volumetric assessment of the machine [7]. It is composed of independent (unconnected) master balls mounted at the tips of rods of different lengths forming a 3D artefact. One of the most important characteristics of the artefact is its reconfigurability. The machine table becomes an integral part of the artefact with the rods screwed directly to its standard threaded fixturing holes. Therefore, it provides flexibility in the number and positions of the balls within the machine working and probing envelop. Fig. 1 shows an artefact component and components mounted on a machine table forming a four-ball artefact.

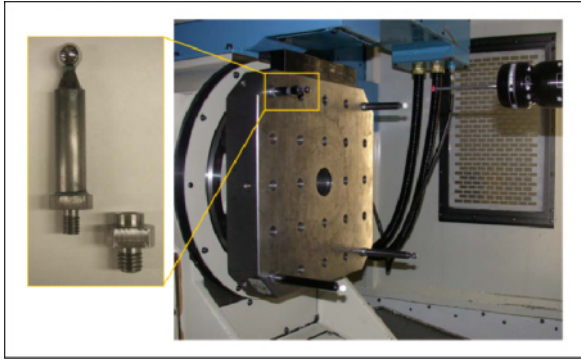


Fig. 1. Artefact component and a four-ball artefact.

This reconfigurability attribute hinders precise knowledge of the artefact's geometry, so it is uncalibrated.

3. Distance based analysis

The artefact is aimed at a five-axis machine with three linear and two rotary axes. During a test, both rotary axes move to obtain the desired position (relocalisation) of the artefact. Then, for each relocalisation the linear axes are used to perform the probing. A distance based analysis which takes into consideration the variation of the distances between the master balls is performed. The distance d_{ij} between the ball i b_i and the ball j b_j is calculated as

$$d_{ij} = \sqrt{(x_i - x_j)^2 + (y_i - y_j)^2 + (z_i - z_j)^2} \quad (1.1)$$

where x_i , y_i and z_i are the measured centre coordinates of b_i . Since the artefact is uncalibrated there is no reference length, so as an alternative the deviation of the distance between b_i and b_j for the k^{th} location of the artefact from the mean is calculated as

$$\varepsilon_{ij,k} = d_{ij,k} - \bar{d}_{ij} \quad (1.2)$$

where $d_{ij,k}$ is the measured distance for location k and

$$\bar{d}_{ij} = \frac{\sum_{k=1}^n d_{ij,k}}{n} \quad (1.3)$$

where n is the number of locations. Fig. 2 illustrates the six distances of a four-ball.

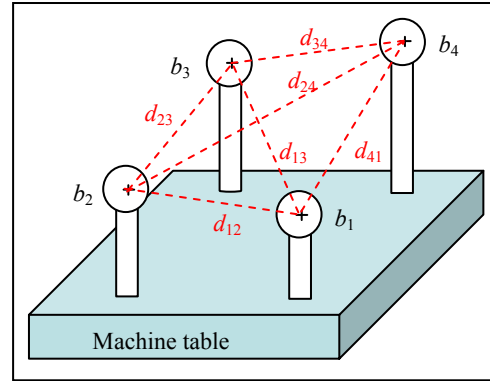


Fig. 2. Distance analysis on a four-ball artefact.

The distance method analyses the artefact geometric distortion from one location to another and not its location and so excludes the potentially erroneous artefact relocalisation accomplished by the rotary axes. In other terms, it only considers the effect of linear axes (which are active during artefact probing) and of course any artefact deformation.

The method does not require a calibrated artefact as long as the artefact stability is ensured. In order to evaluate the artefact stability at different orientations during a measurement session the artefact in Fig. 1 including the balls and the machine table was brought to a CMM and measured for three orientations with the objective of generating gravity induced ball rod deflections: one horizontal where the machine table is mounted parallel to the CMM table, and two vertical where the machine pallet is mounted perpendicular to the CMM table with two orientations (0° and 180°). The deformation range of the artefact geometry was $\pm 1.5 \mu\text{m}$ [7].

4. Experimental results

The experiments are conducted on a five-axis horizontal machine with WCBXFZYT topology. The four-ball artefact is probed in fourteen locations ($b=45^\circ, c=0^\circ$); ($b=45^\circ, c=30^\circ$); ($b=30^\circ, c=60^\circ$); ($b=30^\circ, c=90^\circ$); ($b=15^\circ, c=120^\circ$); ($b=15^\circ, c=150^\circ$); ($b=0^\circ, c=0^\circ$); ($b=0^\circ, c=180^\circ$);

($b=-15^\circ, c=210^\circ$); ($b=-15^\circ, c=240^\circ$); ($b=-30^\circ, c=270^\circ$); ($b=-30^\circ, c=300^\circ$); ($b=-45^\circ, c=330^\circ$) and ($b=-45^\circ, c=360^\circ$) and the measured centre coordinates of each ball at each location are used to calculate the six distances. In order to determine the repeatability, the relocalisation sequence was repeated five times and measurements were taken each time. Fig. 3 to Fig. 6 show the variation of selected distances given in Fig. 2 (d_{12}, d_{23}, d_{34} and d_{41} , respectively) as a function of the rotary axes' locations and for successive measurement runs.

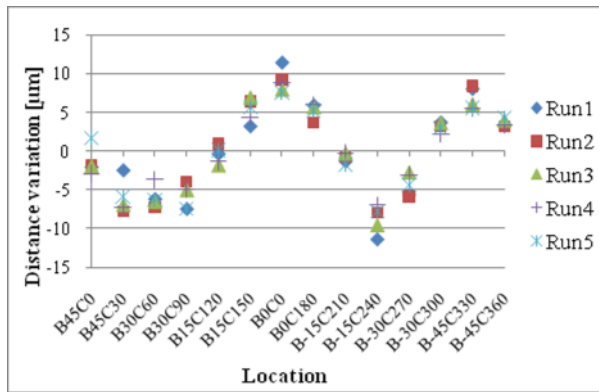


Fig. 3. Variation of d_{12} .

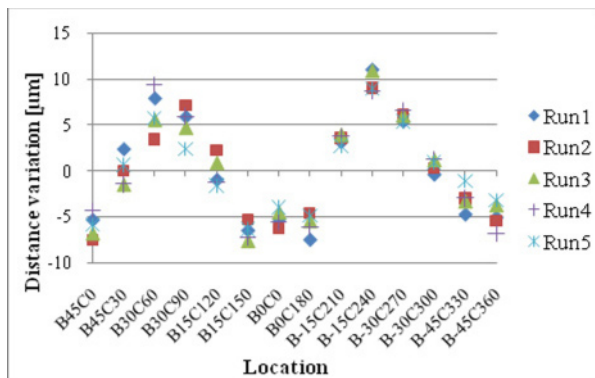


Fig. 4. Variation of d_{23} .

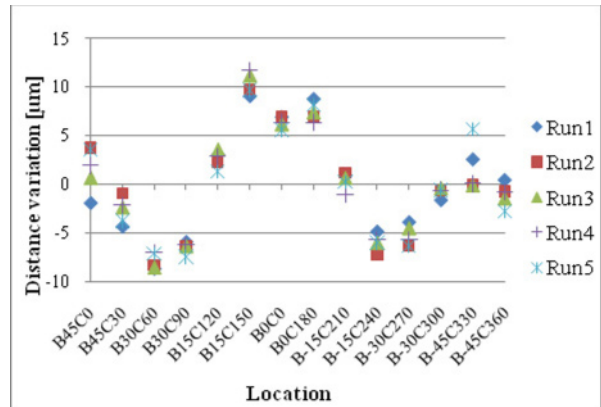


Fig. 5. Variation of d_{34} .

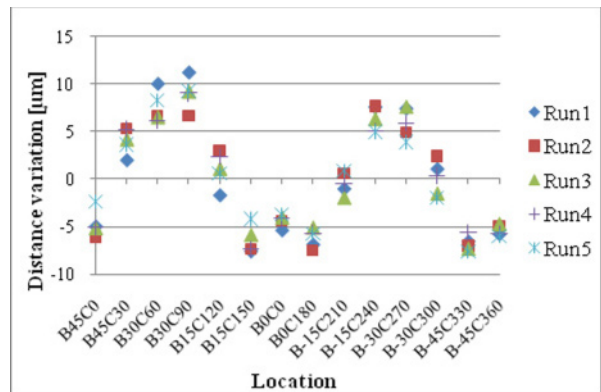


Fig. 6. Variation of d_{41} .

The figures above indicate a symmetric variation tendency with respect to the $b=0^\circ$ location. In fact, left and right hand side locations of $b=0^\circ$ generate the same vector components' magnitudes Δx , Δy , and Δz between the balls. Fig. 7 illustrates how $c=0^\circ$ and $c=180^\circ$ as well as $c=120^\circ$ and $c=240^\circ$ correspond to the same Δx , Δy , and Δz for d_{12} , d_{23} , d_{34} and d_{41} . In addition, d_{12} and d_{34} (also d_{23} and d_{41}) have similar variations as their vector components' magnitudes are alike.

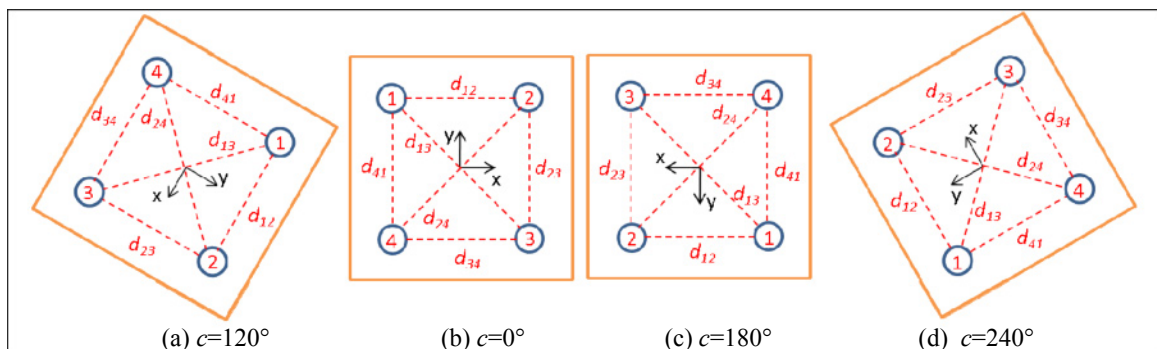


Fig. 7. Artefact locations during the tests

As seen in Figs. 8 and 9 for d_{13} and d_{24} the variation is rather cyclic because these distances pass through the centre of rotation. They generate the same Δx , Δy , and Δz between $c=0^\circ-180^\circ$ and $c=180^\circ-360^\circ$. For example, in Fig. 8 d_{24} 's components' magnitudes at $c=120^\circ$ are identical to the ones at $c=300^\circ$ instead of $c=240^\circ$.

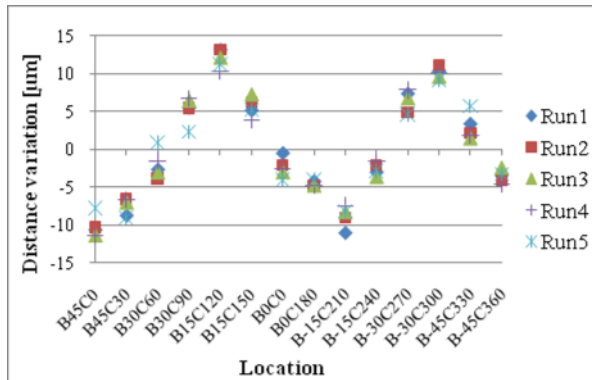


Fig. 8. Variation of d_{13} .

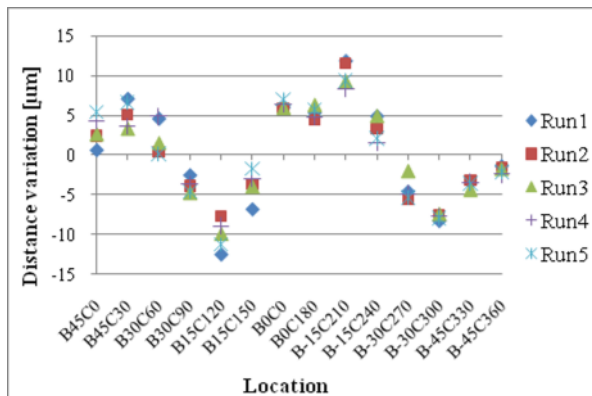


Fig. 9. Variation of d_{24} .

The behaviour presented above may indicate dominance of scaling errors of the linear axes, because the scaling errors produce the same effect provided that Δx , Δy , and Δz covered by the linear axes from one ball to another at one location remain the same at another location even though the orientation changes. However, this behaviour should be analysed in detail by simulating the scale and squareness errors of the linear axes. It could also suggest optimal locations to reveal key error sources.

The results show that the maximum distance variation range is $24.4 \mu\text{m}$ for d_{24} and the maximum range between each run is $6 \mu\text{m}$ for d_{23} at $b=30^\circ$, $c=60^\circ$.

5. Conclusion

In this study a distance based analysis is applied to an uncalibrated artefact that is probed on a five-axis machine. The method excludes any erroneous location caused by the rotary axes and provides the artefact geometry distortion affected only by the linear axes and the artefact stability. The results show that the artefact and the proposed method provide a rapid and practical tool for assessing the volumetric distortion of linear axes of a five-axis machine. Further work is required to assess how typical machine error sources affect the distance measured. It could also suggest optimal locations to maximize the observable effects.

Acknowledgement

This work was funded by Pratt and Whitney Canada. The authors thankfully acknowledge the support of Guy Gironne with the experimental work.

References

- [1] Zhang GX, Zang YF, (1991) Method for machine geometry calibration using 1-D ball array. *CIRP Annals-Manufacturing Technology* 40/1:519-522
- [2] De Aquino Silva JB, Burdekin M, (2002) A modular space frame for assessing the performance of co-ordinate measuring machines (CMMs). *Precision Engineering* 26/1:37-48
- [3] De Aquino Silva JB, Hocken RJ, Miller JA, Caskey GW, Ramu P, (2009) Approach for uncertainty analysis and error evaluation of four-axis co-ordinate measuring machines. *International Journal of Advanced Manufacturing Technology* 41/11-12:1130-1139
- [4] Choi JP, Min BK, Lee SJ, (2004) Reduction of machining errors of a three-axis machine tool by on-machine measurement and error compensation system. *Journal of Materials Processing Technology* 155-6/1-3:2056-2064
- [5] Bringmann B, Kung A, (2005) A measuring artefact for true 3D machine testing and calibration. *CIRP Annals-Manufacturing Technology*. 54/1:471-474
- [6] Woody BA, Smith KS, Hocken RJ, Miller JA, (2007) A technique for enhancing machine tool accuracy by transferring the metrology reference from the machine tool to the workpiece. *Journal of Manufacturing Science and Engineering, Transactions of the ASME*. 129/3:636-643
- [7] Erkan T, Mayer JRR, Dupont Y, (2009) Reconfigurable uncalibrated 3D ball artefact for five-axis machine volumetric check. *Proceedings of the 9th International Conference and Exhibition on laser metrology, machine tool, CMM and robotic performance LAMDAMAP 2009*, London, UK. Bedford: Euspen 19-27

A Holistic Approach to Quantifying and Controlling the Accuracy, Performance and Availability of Machine Tools

Peter Willoughby^{1,*}, Mayank Verma¹, Andrew Peter Longstaff², Simon Fletcher²

¹ Machine Tool Technologies Ltd., 307 Ecroyd Suite, Turner Rd, Lomeshaye Business Village, Nelson, BB9 7DR, UK

² Centre for Precision Technologies, University of Huddersfield, West Yorkshire, UK

Abstract With today's ever increasing demand for improved accuracy and faster material removal rates, CNC machine tool manufacturers and users are under pressure to supply and maintain machinery with a high degree of accuracy and performance. Although some machine tool users have their machines "checked", there is no formal method of establishing the capability of a machine tool as an overall measure of its performance, accuracy and availability. This paper identifies the key performance indicators for modern CNC machines and highlights the technical difficulties in understanding machine tool capability. To solve the problem, a novel method of measuring, analysing and controlling the overall capability is presented. The philosophy and process of machine performance evaluation, optimisation and monitoring (MPEOM) is explained. The paper also illustrates how conventional "Lean" techniques can be utilised to simplify the complex area of machine tool metrology allowing for the integration of the process into modern manufacturing systems.

Keywords: Lean manufacturing, Metrology and measurement, Sustainable manufacturing, Precision machining, Condition monitoring.

1. Introduction

Many high precision manufacturers are aware of the problematic areas within their processes and the impact they have on the cost and ability to remain competitive. Although quality, performance and availability levels might be measured in some form, the data only represents the symptoms of underlying problems within the manufacturing process. As a result, manufacturers usually engage in process improvement where 'Lean' strategies such as Kanban, Kaizen, TPM and Six Sigma are implemented to improve organisational efficiency and overall equipment effectiveness (OEE), Gibbons [1]. Unfortunately this process improvement will often stop at the machine tool level due to the complexity of machine tool systems and a skills shortage throughout the industry. ISO DIS 263003-1(E) Machine Tools – Reliability, availability and capability provides an indirect

measurement of capability by evaluating the machining process. This methodology was developed in the automotive industry and is particularly suited to large batch manufacturing due to its use of statistical process control (SPC). The short term capability of a specific process can be evaluated, however should the process be changed or a different area of the machine be required then capability of the asset is no longer known.

1.1 Machine tool complexity

CNC machine tools are continuously increasing in flexibility and functionality, but the added complexity leaves many end-users struggling to keep up with the technology. When the capability of the machine tool is in question, not only is it often unknown, but methods of establishing it are also unclear. This leads to a situation where assumptions, based on non-factual or untraceable information, are made and proliferate among all relevant departments. As a result, the equipment is isolated from organisational quality systems. Figure 1 illustrates a typical manufacturing system where all other processes are managed by some kind of auditable or "Lean" system. The interface of the machine tool into this system is often disregarded.

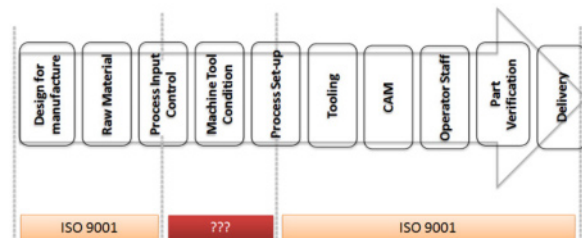


Fig. 1. Managing the manufacturing process

In many cases the machine tool will be ‘maintained’ by performing scheduled service and calibration activities, as recommended by the original equipment manufacturer (OEM) or a quality system. However, the value added by these actions is often unknown and potentially minimal. An OEM might not wish to highlight failings in their machine that indicate non-reliability and any end-user generated system requires a high level of knowledge to provide a comprehensive study.

Take for example, a company who has the linear accuracy of their machine regularly recalibrated to ISO 230-1. This gives a piece of information, but what is its worth in isolation from the required component output? If linear compensations mean it passes the calibration, does this mean the machine has been corrected for its inherent angular or straightness errors? If these are not mechanically maintained then the machine will eventually fail to produce the correct parts, even with a certificate proving its “capability”.

As a result, the machine tool is often not optimised and its problems only addressed once a failure event occurs which requires urgent attention, such as a breakdown or loss of product quality. In these cases it is common that the cause cannot be confidently identified and that “patches” are applied to ‘fire fight’ the machine back into production. Examples or such practice are commonly seen through the re-working of parts via offsets being applied into part programs or unnecessary replacement of entire machine tool components such as ballscrew systems. In both cases the root cause is never identified and so remains unresolved, making recurrence inevitable.

The following section illustrates how a machine tool can be categorised and its capability can be holistically analysed.

1.2 Machine tool characteristics

A machine tool can be broken down into three general characteristics which will govern its overall capability:

- Mechanical Characteristics
- Electrical / Electronic Characteristics
- Metrology Characteristics

The characteristics above are typically treated in isolation from one another. Historically, these three functions have been dealt with by different machine design departments and different end-user maintenance departments. The effect of these characteristics has a direct impact on the performance characteristics of a machine tool:

- Power
- Speed
- Accuracy & Reliability

When investigating the relationship between these characteristics (Figure. 2) it becomes apparent that to improve OEE these performance characteristics cannot be treated in isolation.

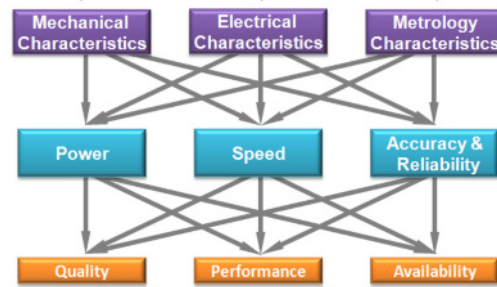


Fig. 2. Machine Tool – OEE Matrix

This matrix can be used to help identify key areas of non-conformance, through utilising techniques such as fish bone root-cause analysis as specified by Ishikawa [2]. Once all critical sources of non-conformance are identified we then need a method of addressing and controlling them.

1.3 Total productive maintenance (TPM) and Six Sigma

The concept of total preventative maintenance was presented over twenty years ago by Nakajima [3]. It was recognised that the effective application of modern technology can only be achieved through people, starting with the operators and maintainers of that technology and not through systems alone. TPM is now considered as a ‘Lean’ improvement method established as an enabling tool to capitalize on true operational effectiveness.

Six sigma is a business management strategy originally developed by Motorola (USA) in the 1980s [4]. It has the aim of improving the quality of manufacturing processes, product and services through a set of methods including statistical process control, business improvement methodologies and management systems.

Both TPM and Six Sigma have similar aims and frameworks for improving OEE on a shop floor and organisational perspective, however the way in which these techniques can be implemented to today’s machine tools is still unclear. An attempt to address this problem has been made by Saunders [5]. Here a typical manufacturing process has been broken down into gated processes using a hierarchical pyramid system. At the centre of Six Sigma methodology is the DMAIC (Define, Measure, Analyse, Improve, Control) model, where project teams are created to tackle specific problems to reach Six Sigma levels of performance. On the other hand TPM can be seen to be implemented in a multitude of ways but with no formally defined approach that can be considered as an industry standard for implementation on high precision machine tools. It is argued [4] that although TPM and Six Sigma have very close links in terms of strategy the former focuses primarily upon quality issues and the latter on reliability.

Through employing techniques used in both TPM and Six Sigma we can propose a methodology for establishing and continuously improving machine tool capability. The following section introduces this in the

implementation of such a system via a machine tool service and calibration based organisation.

It has been seen from industrial experience of others that the separate implementation of 'classic' lean approaches regularly fail due to large financial, human and technical requirements which end-users are unlikely to be able to justify or provide. A strategy has consequently been developed that requires a simple yet effective system to facilitate an approach to any manufacturing cell irrespective of size, location and complexity. This system, called MPEOM, has been applied to a full spectrum of machine tools ranging from small manual lathes to very large multi-axis gantry machines and is presented in the following section.

2. The MPEOM™ Framework

MPEOM™ (Machine Performance Evaluation Optimise Monitor) is a six stage continuous improvement process which can be used to evaluate, optimise and monitor the condition of machine tool systems. It is a 'lean' tool that can be used to pull the machine into a quality system and creates the structure of TPM. The cycle can be seen as shown in Figure 3.

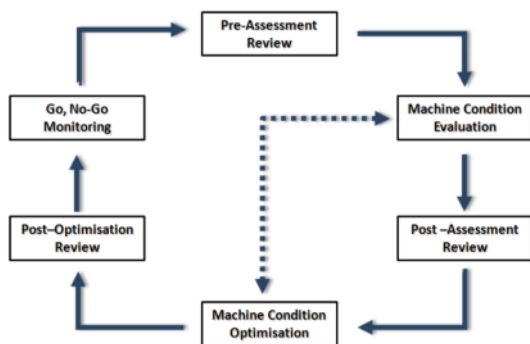


Fig. 3. The MPEOM cycle

The system picks up on a lean strategy often used in TPM and Six Sigma. It is an evolution of a Plan, Do, Check, Act cycle and can also be compared to the five stage DMAIC process. Each stage of the MPEOM™ process will be explained in the following section of this paper.

2.1 Pre-assessment review

The pre-assessment review brings together manufacturing engineers, production, maintenance and machine tool specialists. During this review the part or range of parts produced on a selected machine and the machining process key performance variables (KPVs) are analysed and formalised. The results of the meeting include:

- classification of the machine as reliability or accuracy biased
- a clarification of machine performance requirements
- identification where part/process specific auditing/measurement actions are required

- a metrology index based on machine configuration
- measurement equipment requirements

2.2 Machine condition evaluation

Once objectives have been set for the machine, it is then audited. During this audit critical mechanical, electrical/electronic and metrological characteristics of the machine are investigated. This includes assessment of:

- all main mechanical components
- all main electrical and electronic components
- the machine's axial geometry to ISO 230 – 1 and OEM specifications
- the machine's structural geometry to ISO 230-1 and OEM specifications
- the machine's measuring systems in accordance to ISO 230 - 2
- the machine's dynamic capability in accordance to ISO – 4
- artefact accuracy

During this evaluation non-intrusive tasks can be carried out also, which can include cleaning of the machine, adjustments and optimisations to any minor machine faults and its geometry and measuring systems.

2.3 Post-assessment review

The data collected on the machine is presented to the representatives from the maintenance and production departments through comprehensive reporting and charting. All machine issues or out of tolerance metrology items that could not be rectified during the evaluation stage are flagged. Concessions are negotiated, based on budget and time available for optimisation and the level of performance that is required from the machine. Once an agreement has been reached by the team, plans are formulated for any rectification and optimisation work on the machine.

2.4 Machine condition optimisation

The optimisation of the machine is a sub-cycle within the MPEOM process, consisting of four levels. Level 1 involves optimisation which can be carried out non-intrusively such as adjusting machine geometry using conventional mechanical alignment techniques, adjustment of CNC controller setting and general servicing actions. Should it be agreed that this would be insufficient a Level 2 optimisation is subsequently used. This would consist of a partial rebuild of the machine using the machine and process requirements as the specification guideline. Such corrective action could include removal of critical machine components for repair and/or re-engineering. A Level 3 optimisation option is also offered normally for high accuracy applications or for situations where time and cost

restraints are prohibitive. This would involve the use of hardware and software utilising a volumetric compensation system (VCS) to compensate the geometric and positioning errors of the machine to remove up to 70% of errors left after the other levels of correction were ineffective Postlethwaite [6].

Level 4 is only used when it can be shown that all previous levels of correction would not meet requirements for the machine tool accuracy and reliability specification. In this case, a decision would be made to rebuild, redesign or replace the machine. Here the information from previous stages in the MPEOM process would be used as part of the specification and acceptance of new machinery or validation of correct redesign, retrofit and rebuild of the machine.

2.5 Post optimisation review

During optimisation new data will have been collected on the mechanical, electrical and metrological condition of the machine. This data along with any collected from the initial audit will represent the machine capability 'benchmark' condition. The data is reviewed and a preventative maintenance schedule is agreed between all concerned, again based on part and performance requirements. This will involve the implementation of a Go, No-Go / sustainment program.

2.6 Go, No-Go system

A "Go, No-go" system is set up for the machine operators and maintenance staff to use to ensure that non-conforming parts on the machine are not produced and that regular failure points are monitored to predict breakdown. The system is based on the benchmark data collected and relevant KPVs identified earlier on in the process. Data is collected from the machine and can include but not limited to circularity Ballbar, vibration analysis, oil condition monitoring, artefact probing. These tests are carried out non-intrusively and on a defined schedule, where tolerance bands are set to flag and predict when intervention is next required.

3. Conclusion

Although machine tools are complex systems, problems of accuracy and reliability can be addressed by breaking them down into their key characteristics. By adopting "lean" manufacturing philosophies it is possible to involve all departments across a manufacturing plant to make targeted decisions on the key performance variables for machine tool performance, accuracy and availability.

This paper presents such a strategy, which has already been successfully applied to a wide range of manual and CNC machine tools.

The MPEOM system presented in the paper provides a conduit for defining, establishing and maintaining a machine's required characteristics according to the rigours of the production requirement. It acts as best practice, but with the constant review process enabling efficient adoption of new technology as it becomes available.

At this stage only the static rigid body errors are addressed. There is scope in the future to analyse the non-rigid body errors associated to thermal displacement, load, deflection etc.

At present there is no clear ISO guideline for Machine Tool Capability across the full industrial spectrum. This continuing research exercise will contribute to redressing this shortfall.

References

- [1] Gibbons, P. M. (2006), "Improving overall equipment efficiency using a lean six sigma approach". *International Journal of Six Sigma & Competitive Advantage*, Vol. 2 No. 2
- [2] Ishikawa, K. (1990); (Translator: J. H. Loftus); "Introduction to Quality Control"
- [3] Nakajima, S. (1988), *Introduction to Total Productive Maintenance (TPM)*, Productivity Press, Portland, OR
Nakajima, S. (1989), *TPM Development Program: Implementing Total Productive Maintenance*, Productivity Press Inc., Cambridge, MA
- [4] Stamatis, D. H. (2004), *Six Sigma fundamentals: A complete guide to the system, methods, and tools*, New York Productivity Press
- [5] Saunders, M. (2007), "White Paper – Manufacturing process improvement", Renishaw Plc, United Kingdom.
- [6] Postlethwaite, S.R. & Ford, D.G., "A practical system for 5 axis volumetric compensation" *Laser Metrology and Machine Performance IV*, pp 379-388, 1999
- [7] ISO 230-1:1996, Test code for machine tools – Part 1: Geometric accuracy of machines operating under no-load or finishing conditions
- [8] ISO 230-2:2006, Test code for machine tools – Part 2: Determination of accuracy and repeatability of positioning numerically controlled axes
- [9] ISO 230-4:2005, Test code for machine tools – Part 4: Circular tests for numerically controlled machine tools
- [10] ISO 230-7:2006, Test code for machine tools – Part 7: Geometric accuracy of axes of rotation
- [11] ISO 9001:2008, Quality management systems – Requirements
- [12] ISO/DIS 26303-1, Machine tools – Reliability, availability and capability – Part 1: Capability evaluation of machining processes on metal-cutting machine tools

Development of a Small 3-axis Angular Sensor for Real-time Abbé Error Compensation on Numerically Controlled Machine Tools

K.C. Fan, S.M. Chen and S.Y. Lin

Department of Mechanical Engineering, National Taiwan University, Taiwan, ROC

Abstract. Abbé error is the inherent systematic error in all numerically controlled (NC) machine tools. Any angular error of the moving stage will result in the position offset of the ideal cutting point. The existing method using error budget obtained from prior calibration can only compensate for the mean positioning errors, which are not temperature dependent. In this paper, the development of a small three-axis angular sensor is developed. It uses DVD pickup head technology. The pitch and yaw angles are detected based on the autocollimation principle while the roll angle is detected using the pendulum principle. Three angular sensors are integrated into one single module unit so that it can be installed in the proper location of the moving stage. Using kinematic analysis, the Abbé error can be significantly compensated for in real time.

Keywords: machine tools, Abbé error, angular sensors, error compensation

1. Introduction

Abbé error is the inherent systematic error in all numerically controlled (NC) machine tools. Since it was proposed by Professor Abbé in 1890, the Abbé principle is regarded as the first principle in the design of precision positioning stages, machine tools and measuring instruments. It defines that, in displacement measurement, the reference should be in line with the displacement to be measured or on its extension. Bryan made a further generalized interpretation that if the Abbé principle cannot be applied in the system design, either the slideway that transfers the displacement must be free of angular motion or the angular motion data must be obtained to compensate the Abbé error by software [1, 2]. Following the Abbé principle, Bryan extended the concept to straightness measurement [1] and Zhang extended it to other geometrical measurements [3].

In the past, some special approaches were taken which focused on designing machines that attempted to have no Abbé offset or minimize it. One approach was to use a laser interferometer as a measuring reference resulting in an expensive machine, such as the "Ultimat" Coordinate Measuring Machine (CMM) [4], the

Nanomeasuring machine (NMM) [5], the AFM system [6] and the diamond turning machine [7]. The other way is to increase the machine size in order to mount a measuring scale on the extension of the functional axis, such as the high-precision 3D-CMM [8] and the Micro-CMM [9].

Nowadays, most existing machine tools and CMMs still cannot comply with Abbé principle because the scale axis is always parallel to the moving axis. A very popular way to improve the accuracy is to store the positioning or volumetric errors through a prior calibration process and then compensate these error budget with software, which is called the feed-forward compensation. Although this strategy complies with the generalized Abbé principle, it can only compensate for the mean systematic positional errors. The angular errors are subject to temperature changes. It is known that if the Abbé principle is not possible in the system design, one effective method is to obtain the real time angular data and compensate for the Abbé error in software or hardware.

This paper reports on the development of a small three-axis angular sensor using DVD pickup head technology. The pitch and yaw angles are detected based on the autocollimation principle while the roll angle is detected using the pendulum principle. Three angular sensors are integrated into one single module unit so that it can be installed in the proper location of the moving stage. Using kinematic analysis, the Abbé error can be significantly compensated in real time.

2. Abbé Error in Machine Tools

A general type 3-axis machine tool was designed with three serial linear axes. Each axis is equipped with a linear scale or a rotary encoder as a position feedback sensor, which is offset from the cutting axis by a distance L . During the motion, the angular error (θ) of the stage will cause actual positioning error (δ) of the cutting point, as shown in Figure 1. The corresponding Abbé error is

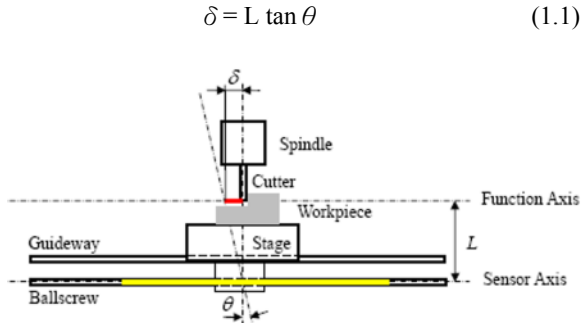


Fig. 1. Abbé error in one axis

Eq. (1.1) applies only to the case when a rotary encoder is mounted on the servomotor that is in line with the ballscrew, which is right underneath the moving stage. In a case when a linear scale is mounted as the measuring sensor, it has an additional horizontal offset from the cutting axis, as shown in Figure 2. The corresponding Abbé error is expressed by

$$\begin{bmatrix} \delta_X \\ \delta_Y \\ \delta_Z \end{bmatrix} = \begin{bmatrix} -\theta_Z \cdot L_Y + \theta_Y \cdot L_Z \\ \theta_Z \cdot L_X - \theta_X \cdot L_Z \\ -\theta_Y \cdot L_X + \theta_X \cdot L_Y \end{bmatrix} \quad (1.2)$$

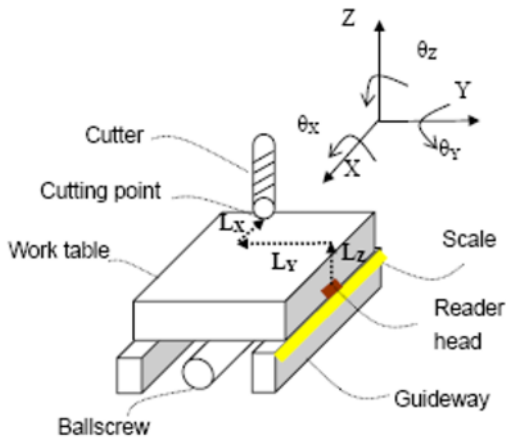


Fig. 2. Abbé error of linear scale

From Eq. (1.2), it is understood that if the angles can be detected, the realtime Abbé errors can be calculated. This implies the importance of sensing angular errors on the machine tool.

3. Development of Angular Sensors

In each axis motion there are three angular errors, namely pitch, yaw and roll. For a commercial machine tool, these angular errors should be as small as possible in order to maintain the geometrical accuracy. An acceptable machine tool normally can tolerate angular errors of a

few arc-seconds. Because the machine tool market is very competitive, for any value added functionality would require low cost sensors. Commercially available angle measuring instruments, such as autocollimators or laser interferometers, have a high price and a bulky size and cannot be used as the sensor. Some researches adopt laser diode and optical components in association with a 2D photodetector to build up miniature angle sensors for pitch and yaw [10, 11]. Some other researches directly make use of the optical components of the pickup head of a CD [12] or DVD [13, 14] and modify it to become a miniature 2D angle sensor. Since the DVD pickup head is cheap in price and stable in performance, the design reported also makes use of the optoelectronic effects of a DVD pickup head to develop a small 3-axis angular sensor. It is composed of an autocollimator, for pitch and yaw angles, and an optoelectronic level for roll angle. Details are described below.

3.1 The DVD Autocollimator

A typical DVD or CD pickup head is an autofocus sensor that employs the astigmatism principle. The authors' group has studied the devices for many years and has modified the head into geometrical measurement sensors such as the autofocus sensor [15], straightness sensor [16] and accelerometer [14]. The necessary associated techniques matured in our laboratory, such as the auto power control (APC) circuit, quadrant detector's signal processing circuit, and calibration instruments.

Figure 3 shows the schematic diagram of a 2D collimation modified from the original autofocus principle [15]. The laser beam is projected onto the plane mirror, and the reflected laser beam is then focused at the centre of the four-quadrant photodiode. If the plane mirror tilts a small angle in the Y direction (yaw angle), the position of the focused light spot will shift across the surface of the photodiode in X direction. Similarly, when the mirror rotates in the X direction (pitch angle), the spot moves in Y direction. As shown in figure 4, the photodetector transforms the incident energy of the focused light spot into electrical current signals. Deviations of the focused light spot from the centre of the photodiode produce corresponding changes in the magnitudes of the electrical signals output by the four quadrants. By applying an appropriate circuit, the X- and Y-coordinates of the focused light spot are related to the voltage signals of the individual quadrants by the following expressions:

$$\begin{aligned} X &= K \frac{(V_1 + V_4) - (V_2 + V_3)}{V_s} \\ Y &= K \frac{(V_1 + V_2) - (V_3 + V_4)}{V_s}, \end{aligned} \quad (1.3)$$

where V_i is the voltage of quadrant i , V_s is the sum of four-quadrant voltages, and K is a constant.

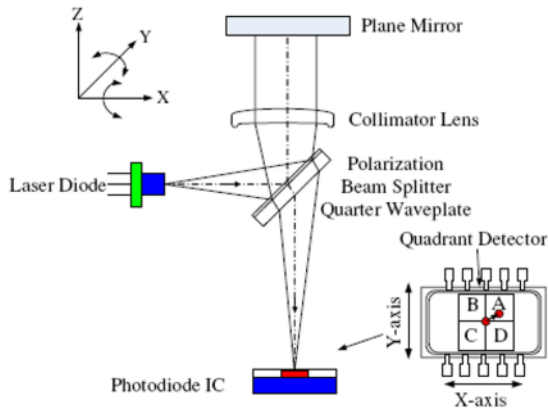


Fig. 3. Optical system of 2D collimation

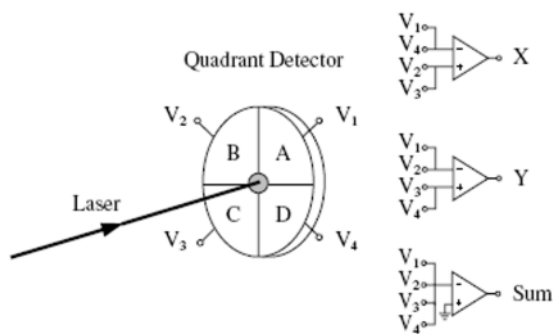


Fig. 4. Four-quadrant detector outputs

The pickup head used is made by Hitachi Co., model HOP-1000. This small 2D angle sensor was calibrated by a triple beam laser interferometer, made by SIOS Co. The pitch and yaw angles have an accuracy of ± 0.8 arcseconds within the range of ± 20 arcseconds. These specifications are good enough to measure the angular motion of the machine tool table.

3.2 DVD Optoelectronic Level

Similar to the autocollimation principle, the scheme to measure the roll angle is to mount the plane mirror onto a pendulum block, as shown in Figure 5. With the proper selection of the wire, mass and damper, the level can be stabilized in one second. It is also calibrated by a triple beam laser interferometer. The accuracy was found to be at the same level as the autocollimator.

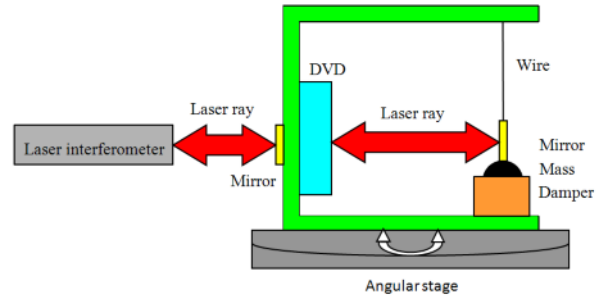


Fig. 5. DVD level and its calibration setup

4. On-Machine Experiments

4.1 Testing on Machine Tool

In the on-machine experiment, these two angle modules are integrated into one unit. The level sensor is placed on the moving table. The plane mirror of the autocollimator is placed on the side wall of the level. The pickup head for the autocollimator is mounted on the bearing housing of the ballscrew. The experimental setup is shown in figure 6. The machine tool used is a 3-axis CNC machining centre of encoder feedback type. A laser interferometer (HP5529) is used to calibrate the positioning error in the X-direction. In order to eliminate the angle induced from the foundation deformation, a special setup of the laser interferometer is used, shown in Figure 7. In practice, the laser axis of Figure 7 is higher than the collimated beam axis of Figure 6. The only Abbé offset is in the Z direction, so that equation (1.1) applies in this case. Figure 8 shows the results that the original positioning errors (the difference between the laser interferometer reading and the encoder reading) are in the range of $\pm 4 \mu\text{m}$. After the Abbé error compensation, it reduces to less than $\pm 1 \mu\text{m}$.

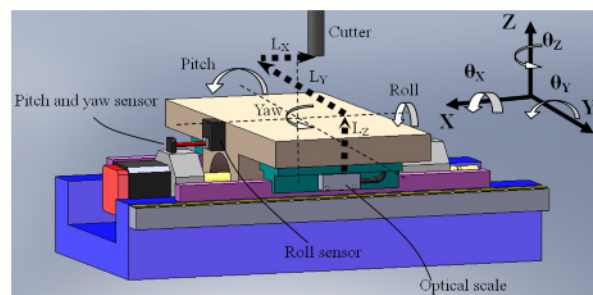


Fig. 6. On machine tool mounting of the 3-axis angle sensor

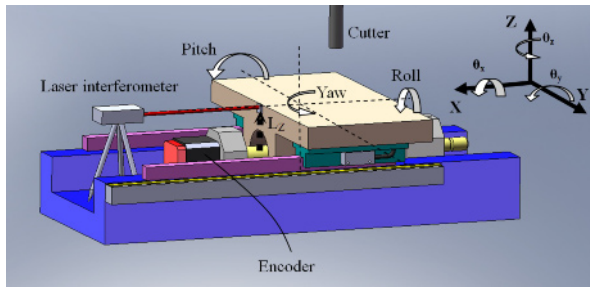


Fig. 7. Mounting the laser head on the machine base

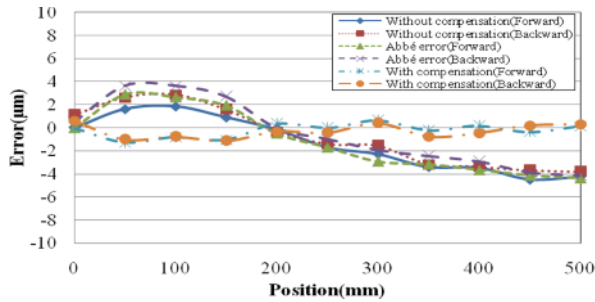


Fig. 8. Positioning errors, with and without compensation

4.2 Testing on a Stage with a Linear Scale

It is not easy to find a machine tool that is equipped with a linear scale as feedback sensor. Therefore, an optical measuring machine with scale feedback was selected for test. Figure 9 shows the experimental setup with the 3-axis angular sensor placed on the table top and two laser lines are selected for positioning error tests (Case A and Case B). The effective Abbé offsets are Lz and Lx . In this case, equation (1.2) is applied. Figure 10 shows the results of case A and Figure 11 shows the results of case B. Since the offset of Lx is larger in case A, the positioning error is accordingly larger. After implementing the Abbé error compensation the errors are reduced to a very small amount.

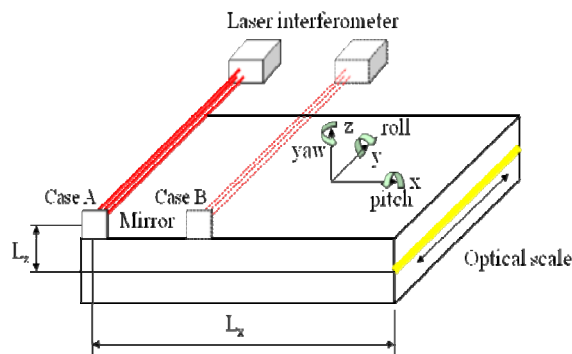


Fig. 9. Setup of the test on a linear stage

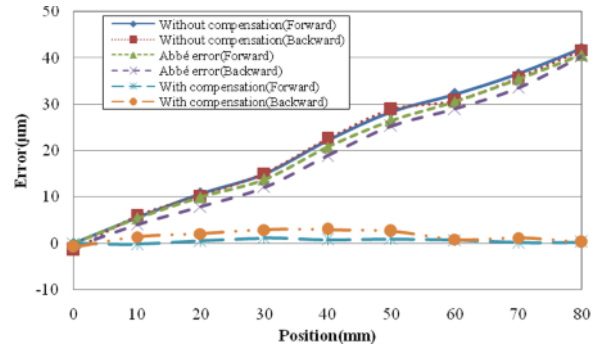


Fig. 10. Positioning errors of Case A

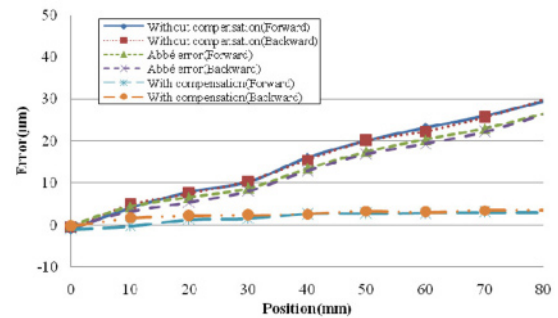


Fig. 11. Positioning errors of Case B

5. Conclusions

This paper proposes the concept that the Abbé error can be compensated in realtime if the angular motions are known. A 3-axis angular sensor for pitch, yaw and roll measurements have been developed based on the DVD pickup head technology. Embedding this sensor in the machine tool slide, all positioning errors can be significantly compensated in real time. This methodology can be expanded to all three axes of a machine tool for the compensation of volumetric errors in real time.

References

- [1] Bryan JB, (1979) The Abbé Principle Revisit: An Updated Interpretation, Precision Engineering, Vol. 1, No. 3, 129-132.
- [2] Wright DA and Bryan JB, (1980) Letters, Precision Engineering, Volume 2, Issue 1, Page 2.
- [3] Zhang GX, (1989) A Study of the Abbé Principle and Abbé Errors, Annals of CIRP, Vol.38, No.1, 525-529.
- [4] Bryan JB and Carter DL, (1979) Design of a new Error-corrected Co-ordinate Measuring Machine, Precision Engineering, Vol. 1, 125-128.
- [5] Jäger J, Manske E., et al, (2002) Nanopositioning and - Measuring Technique, 7th International Symposium on Laser Metrology, Novosibirsk, Russia, Vol. 4900, 755-762.

- [6] Kim DM, Lee DY and Gweon DG, (2007) A new nano-accuracy AFM system for minimizing Abbe errors and the evaluation of its measuring uncertainty, *Ultramicroscopy*, Volume 107, Issues 4-5, 322-32.
- [7] Bryan JB, (1979) Design and construction of an ultraprecision 84 inch diamond turning machine, *Precision Engineering*, Vol. 1, 13-17.
- [8] Vermeulen MMPA, Rosielle PCJN and Schellekens PHJ, (1998) Design of a High-Precision 3D-Coordinate Measuring Machine, *CIRP Annals*, Volume 47, Issue 1, 447-450.
- [9] Fan KC, Fei YT, et al, (2006), Development of a low cost Micro-CMM for 3D Micro/nano Measurements, *Measurement Science & Technology*, Vol. 17, 524-532.
- [10] Jabczynski JK, (1995) Optoelectronic sensor of two-dimensional angular displacements: idea and preliminary test results, *Proceedings of SPIE*, Vol.2634:112-116.
- [11] Gao W., (2002) A compact and sensitive two-dimensional angle probe for flatness measurement of large silicon wafers, *Precision Engineering*, Vol.26, No.4: 396-404.
- [12] Armstrong TR, (1992) Autocollimator based on the laser head of a compact disc player, *Measurement Science & Technology*, Vol.3, No.11:1072-1076.
- [13] Shimizu H, (2004) An electrical pen for signature verification using a two-dimensional optical angle sensor, *Sensors and Actuators (A)*, Vol.111, No.2: 216-221.
- [14] Chu CL, Lin CH and Fan KC, (2007) Two-dimensional optical accelerometer based on commercial DVD pick-up head, *Measurement Science and Technology*, Vol.18: 265-274.
- [15] Fan KC, Chu CL and Mou JI, (2001) Development of a Low-Cost Autofocusing Probe for Profile Measurement, *Measurement Science and Technology*, Vol. 12: 2137-2146.
- [16] Fan KC, Chu CL, Liao JL and Mou JI, (2003) Development of a High Precision Straightness Measuring System with DVD Pick-up Head, *Measurement Science & Technology*, Vol. 14: 47-54.

Micro-scale co-ordinate metrology at the National Physical Laboratory

J. D. Claverley^{1,2} and R. K. Leach¹

¹ National Physical Laboratory, Hampton Road, Teddington, TW11 0LW, UK

² james.claverley@npl.co.uk

Abstract. The development of the co-ordinate measuring machine (CMM) dramatically improved metrology in manufacturing environments. As modern manufacturing techniques have developed to supply products with ever decreasing dimensions, which depend on more accurate geometric specifications of micro-scale parts, developers of CMMs have responded accordingly. Initially, micro-scale probes for CMMs were developed and then, following further demand for micro-scale measurements, dedicated CMM platforms (micro-CMMs) were designed. The effectiveness of these micro-CMMs depends entirely on their ease of use and the access afforded by the probes to high aspect ratio features on micro-scale parts. The National Physical Laboratory (NPL) has purchased a commercial micro-CMM and is using it to perform traceable measurements with the aim to better understand the limits of this technology. Initial work, both at NPL and around the world, has suggested that current micro-CMM platforms are capable of higher measurement accuracy than is achieved with existing probes. To address this imbalance, NPL has developed a micro-scale probe that promises to realise the full potential of micro-CMMs. This paper presents the current research being undertaken on the commercial micro-CMM at NPL along with the recent advances in probe development.

Keywords: micro-co-ordinate metrology, micro-CMM, micro-CMM probe, micro-manufacturing.

1. Introduction

Co-ordinate measuring machines (CMMs) are a common sight in many precision manufacturing facilities. They have been invaluable in increasing the accuracy and speed of measurements taken in a manufacturing environment and have been keenly investigated in research environments. The use of CMMs in research environments has helped develop a better understanding of measurement uncertainties as well as helping to identify areas for improvement in manufacturing processes and precision engineering [Leach 2009]. The prevalence of CMMs and their extensive use in industry has meant that developments in the area of co-ordinate metrology have been led almost exclusively by the requirements of precision manufacturing engineers.

Early CMMs were large and bulky, relying on granite metrology blocks to mount measurement samples and on probing systems that were triggered with physical contact switches. Similar principles still hold today, although high accuracy CMMs are now often instrumented with precision glass or ceramic scales, and in some cases, for traceability, interferometers [Bosch, 1995]. This enables the most modern CMMs to achieve 10 nm precision on their measurement scales. However, probe development has lagged behind for some years, with most CMM manufacturers content with simply miniaturising their current probe technology to fit the ever more accurate machines. High accuracy probes tend to rely on piezo-resistive strain gauges or optical trigger mechanisms to increase the repeatability and accuracy of triggering for surface detection.

Significant research time has been spent designing ever more versatile probe heads that still maintain the measurement accuracy demanded by modern manufacturing standards. An early breakthrough in CMM research was the development of the scanning head, which is able to maintain contact with the measurement surface while scanning a path taking a high density of data points. Further developments have included the development of reflex heads [Weckenmann 2004] that incorporate precision angle measurement into the probe system, enabling it to index to certain angles during measurement. This and other developments enable CMMs to become more versatile, measuring truly three-dimensional objects without the need for moving the artefact for access.

2. Current micro-CMM research at NPL

A more recent requirement of CMMs is that they should stay in step with developments in micro-manufacturing, which is already very well versed in machining, assembly and design at the micro-scale. An early solution to the lag in metrological capability was to custom build CMMs capable of micro-scale measurements. Indeed, many

National Measurement Institutes (NMIs) and other research laboratories built their own CMMs to meet this demand. NPL designed and built a “mini-CMM” that was capable of measuring to an uncertainty of 100 nm within a measurement volume (50 x 50 x 50) mm [Lewis 2003]. The NPL mini-CMM was fully traceable, by virtue of three orthogonal linear and three angular interferometers. The probing head of the mini-CMM set a new precedent for probe design parameters. The mini-CMM probe, which formed the basis of the new NPL micro-CMM probe, is discussed later.

To further the understanding of micro-CMMs in a manufacturing environment, NPL has purchased a commercial Zeiss F25 machine capable of taking micro-scale measurements to sub-micrometre accuracy in 2.5D within a measurement volume (100 x 100 x 100) mm. This micro-CMM is being used as both a research tool and a calibration tool for customers and is shown in Figure 1.

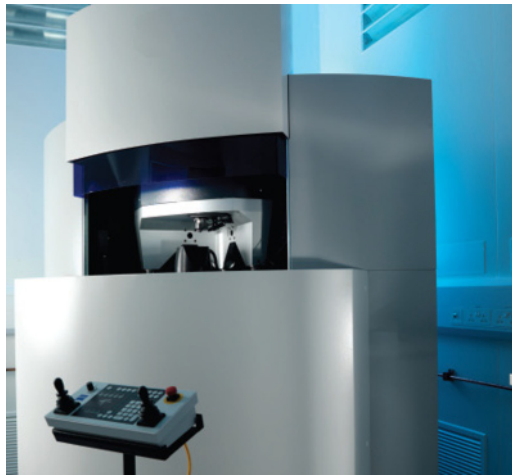


Fig. 1. The NPL micro-CMM

Research being conducted on the machine is of interest on an international scale. Current work includes a pan-European project with three other NMIs to investigate the compatibility of measurements taken on three different measuring instruments. The project will compare measurements of five identical artefacts on two identical commercially available micro-CMMs (Zeiss F25s), a purpose built micro-CMM [Küng 2007] and a micro-x-ray tomography instrument. Results from the comparison will help design transfer artefacts that will be used to cross reference micro-metrology tools.

NPL is also a major partner in the EC-funded EUMINAFab consortium, a pan-European infrastructure aimed at solving major challenges in the field of micro- and nano-scale manufacturing and offering open-access to manufacturing and metrology facilities [Kautt et al. 2009]. One of NPL's inputs to the project is the investigation into handling and mounting techniques for micro-scale products during manufacture and verification.

NPL is assessing the metrology capabilities of all the partners and comparing all handling procedures, including product mounting and cleaning before measurement.

Recent work completed on the micro-CMM has included: extensive verification of micro-fluidic devices produced by micro-injection molding; collaborating with the Agency for Science, Technology and Research (A*STAR) in Singapore to further our understanding of CMM axis alignment and verification of precision manufactured microwave wave-guides.

3. Micro-probe research at NPL

When work began on the NPL mini-CMM in the late 1990s it became apparent that a new paradigm in probe design was required to reach the accuracy demanded by industry [Lewis 2003]. The resulting probe, a three flexured, isotropic probe instrumented with capacitance sensors, constituted a breakthrough in probe design and has since been licensed to a commercial partner (IBS Precision Engineering). This was not developed further, however, and is now competing in a market with many micro-CMM probes capable of similar and higher accuracy. A wide array of micro-CMM probes are available for commercial micro-CMMs, that have tip diameters ranging from 50 μm to 300 μm with probing forces as low as 10 μN (see [Weckenmann 2004] for a review).

There are issues that need to be addressed to ensure maximum accuracy from any micro-CMM prob. These include; isotropy - the probe's ability to exert equal forces in all directions while probing; and exerting low probing forces in general - to reduce damage and to enable high accuracy sensing of surface contact coupled with high repeatability. It is also essential to understand the effect of surface forces on micro-scale probing. The probe's ability to counteract these surface forces will be essential in ensuring that accuracy is not hindered by false triggering and adhesion to measurement surfaces. The design that is being developed at NPL to address these issues is shown in Figure 2.

The requirement for probe isotropy and low probing forces dictated the specifics of the probe design. The three flexure elements, arranged in a triskelion, are required to exert equal forces in all three probing axes that the probe will operate. The need for the probe to vibrate is in direct response to the need for the probe to counteract the interaction forces that are prevalent at such small scales [Stoyanov et al. 2008].

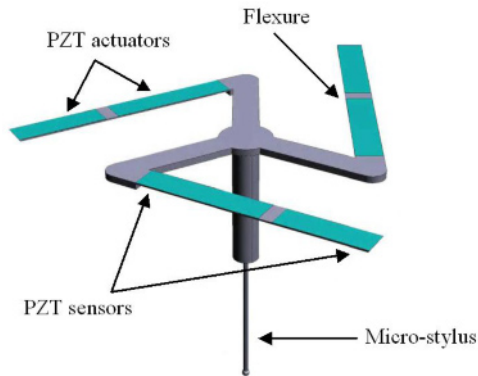


Fig. 2. A schematic diagram of the vibrating micro-CMM probe

The probe should also be able to access the many high aspect ratio structures that are common in micro-scale devices. The ability of the probe to accurately measure high aspect ratio features will be dependant on the dimensions and aspect ratio of the stylus. Investigations were carried out to determine the optimum dimensions of the stylus using a finite element model [Claverley and Leach 2009]. The optimisation of the stylus design had to include the limitations of micro-manufacturing. The resulting micro-styli have suitable aspect ratios for a range of micro-scale metrological applications whilst still being within the limits of manufacture at the micro-scale. A micro-stylus design that is currently being investigated is a 100 μm diameter shaft that tapers to 50 μm , is 2 mm long and is tipped with a 70 μm diameter spherical tip.

A finite element model has been used to determine the isotropy of the device, and investigate the effect of dimensional changes of the flexures on the overall spring constant of the micro-CMM probe.

Work has been carried out to model the surface interaction forces present in close-to-surface probing [Claverley et al. 2010] [Seugling et al. 2008]. These surface forces, insignificant in macro-scale CMM probing, become increasingly disruptive when using a micro-stylus with tip radius reduced below around 100 μm [Bos 2009]. A graph of the effect of each adhesive surface force with respect to stylus tip radius is shown in Figure 3.

It can be seen that as the size of the contacting elements is reduced, the adhesion forces not only reduce, but also change priority. At tip radii of less than 100 μm , the gravitational force is no longer dominant.

A similar effect also occurs when the distance between the stylus tip and the measurement surface is reduced below 10 μm . As this distance is reduced, the interaction forces tend to increase, resulting in a 'snap in' of the probe to the measurement surface; an effect which can cause false triggering and damage to both the probe and the measurement surface [Meli and Küng 2007]. These adhesion forces will also act to stick the probe to the measurement surface while retracting, resulting in a 'snap back' when the adhesions forces fail, which could again cause damage to the probe.

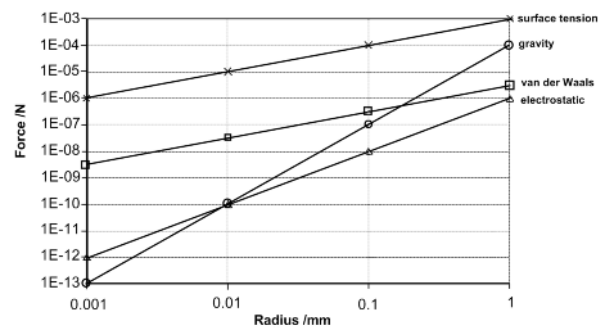


Fig. 3. Adhesion forces (Van der Waals, surface tension and electrostatic) between spherical objects and a flat surface compared with the gravitational force [Van Brussel et al. 2000]

Counteraction of these surface forces is essential if a micro-CMM probe is to be accurate whilst probing with micro- to nano-scale accuracy. Therefore, the NPL micro-CMM probe was designed such that it can vibrate. These vibrations are forced on to the probe tip through six piezo-electric actuators (two on each leg) and can be controlled such that 3D probing is possible. The vibrations are also constantly controlled such that the probing vector is always normal to the surface.

To best understand the surface forces and the effect that they will have on measurements taken at the micro-scale, a mathematical model to describe a driven oscillator subject to a damping force was developed. The individual surface forces were investigated and modelled and were input into the vibration model as a damping force on the micro-probe.

An expression for the minimum required amplitude of vibration to counteract the surface forces was developed. This theoretical minimum was compared to experimental data on a real device, collected using a laser Doppler vibrometer. Initial experiments have confirmed that the vibration of the probe is suitable to counteract the surface interaction forces.

The interaction of the micro-CMM probe with the surface forces will also result in a change in the vibration characteristics of the probe. Rather than measuring direct contact with the measurement surface, the probe will work in a non-contact mode. Changes in the amplitude and frequency of the probe are measured using six piezo-electric sensors deposited on the legs of the probe (two on each leg, either side of the piezo-electric actuators).

The micro-CMM probe flexures are made in nickel using typical MEMS production methods such as deposition and chemical etching. A sol-gel spinning technique enabled the piezo-electric elements to be deposited onto the flexures to a well-controlled thickness. It is essential that the thickness of the piezoelectric films be controlled during production because the thickness of the sensors is responsible for 83 % of the sensitivity of the device output [Sun et al. 2009]. The flexures are produced as a single element, packaged onto a silicon chip for easy handling. This chip is shown in Figure 4.

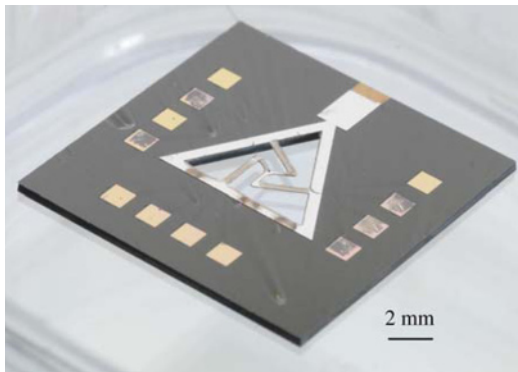


Fig. 4. The micro-CMM probe chip. The flexures can be seen in the centre. The micro-stylus will be assembled onto the central island to form the vibrating micro-CMM probe.

The stylus is produced separately and must be assembled onto the flexures to produce a fully working device. This micro-assembly challenge relies on the ability to accurately align the stylus and the alignment feature on the flexures and make a permanent join between them [Smale et al. 2009].

4. Future work

Development of the micro-CMM probe is ongoing. Theoretical values from analytical models of interactions between the vibrating probe and the surface and finite element models of the mechanical dynamics of the micro-CMM probe are being tested and verified [Sun et al. 2009].

Real devices, produced by the methods described previously, are being tested to confirm isotropy.

Acknowledgements

This work was funded by the UK National Measurement Office Engineering and Flow Metrology Programme 2008 to 2011. The authors would also like to thank Christopher Jones (NPL), Cliff Fowkes (Six Sigma Ltd.), Florine Hiersemenzel (King's College, London) and our colleagues at the Institute for Manufacturing (University of Cambridge), the Centre of Excellence in Customised Assembly (University of Nottingham) and the Microsystems and Nanotechnology Centre (Cranfield University).

References

- Leach, R. K. (2009) *Fundamental principles of engineering nanometrology*. Elsevier.
- Bosch J. A., ed. (1995) *Coordinate measuring machines and systems*. Marcell Dekker, New York.
- Weckenmann, A., Estler, T., Peggs, G., McMurtry, D.: Probing systems in dimensional metrology, *Ann. CIRP* 54, pp 657–684 (2004)
- Lewis, A. J. (2003) A fully traceable miniature CMM with sub-micrometre uncertainty. *Proc. SPIE* 5190, pp 265–276
- Küng A., Meli F., Thalmann R. (2007) Ultraprecision micro-CMM using a low force 3D touch probe. *Meas. Sci. Technol.* 18:319–327
- Kautt M., Anson S. M., Saile V., Scholz S., Fugier P., Lambertini V., Abad E., Dirne F., Loeschner H., Leach R. K. (2009) Facilitating open innovation in micro and nano technology by providing open access to a pan-European toolbox called EUMINAfab. *Proc. 5th Annual International Conference on Multi-Material Micro Manufacture (4M) and International Conference on Micro Manufacturing (ICOMM)*. Karlsruhe, Germany. September 2009, pp 11–24.
- Stoyanov, S., Bailey, C., Leach, R. K., Hughes, B., Wilson, A., O'Neill, W., Dorey, R. A., Shaw, C., Underhill, D., Almond, H.J.: Modelling and prototyping the conceptual design of 3D CMM micro-probe, *Proc. 2nd ESITC, Greenwich, 1st-4th Sept*, pp 193–198 (2008)
- Claverley, J. D., Leach, R. K. (2009) A vibrating micro-scale CMM probe for measuring high aspect ratio structures. *Microsyst. Technol.* DOI 10.1007/s00542-009-0967-2. Published online 24th December 2009.
- Claverley, J. D., Georgi, A., Leach, R. K. (2010) Modelling the interaction forces between an ideal measurement surface and the stylus tip of a novel vibrating micro-scale CMM probe. *International Precision Assembly Seminar (IPAS)*, Chamonix. Feb 14th-17th 2010.
- Seugling R. M., Darnell I. M., Florando J. N., Woody S. C., Bauza M., Smith S. T. (2008) Investigation scaling limits of a fibre based resonant probe for metrology applications. *Proc. 23rd ASPE Annual Meeting and 12th ICPE*. Portland, OR, USA. 19th-24th Oct 2008.
- Bos, E. (2007) *Tactile 3D probing system for measuring MEMS with nanometer uncertainty: Aspects of probing, design, manufacturing and uncertainty*. Thesis (PhD). Eindhoven University of Technology.
- Van Brussel H., Peirs J., Reynaerts D., Delchambre A., Reinhart G., Roth N., Weck M., Zussman E. (2000) Assembly of Microsystems. *Ann CIRP* 49(2):451–472
- Meli F., Kung A. (2007) AFM investigation on surface damage caused by mechanical probing with small ruby spheres. *Meas Sci Technol* 18:496–502
- Sun Y., Fowkes C. R., Gindy N., Leach R. K. (2009) Variation risk analysis: MEMS fabrication tolerance for a micro CMM probe. *Int J Adv Manuf Technol*. doi:11.1007/s00170-009-2251-0
- Smale D., Ratchev S., Segal J., Leach R. K., Claverley J.D. (2009) Assembly of the stem and tip of an innovative micro-CMM probe. *Proc. Lamdamap 2009*, Brunel University, UK, 30th June–2nd July 2009, pp 442–451

Coating Thickness Measurement

P. May¹ and E. Zhou^{2*}

¹ Elcometer Ltd. Edge Lane, Manchester, M43 6BU, UK E-mail: philip.may@elcometer.com

² School of the Built Environment and Engineering, University of Bolton, Deane Road, BL3 5AB UK

* E-mail: E.Zhou@bolton.ac.uk

Abstract. Eddy current techniques are favoured for measuring the properties of conductive coatings on magnetic substrates because the skin effect ensures that only the coating or region at or just below the surface of a magnetic substrate is inspected. The data acquired from eddy current sensors, however, is affected by a large number of variables, which include sample conductivity, permeability, geometry, and temperature, as well as sensor lift-off. The multivariable properties of sample coatings add an even greater level of complexity. This research project is therefore motivated by the need for a measuring instrument, which can intelligently adapt to the large number of variables that affect eddy current measurements on steel. Sensor model optimisation against experimentally generated data is undertaken, leading to the development of accurate and fast inversion models based on artificial neural networks. Neural network architecture, operation and training are discussed, which includes an algorithm for neural network normalisation and calibration. System tests are finally undertaken on a wide range of plated samples. This research demonstrates that an intelligent measuring system incorporating a ferrite-cored sensor can provide high accuracy while operating over a wide frequency range.

Keywords: Eddy current technique, Coating thickness, Intelligent measurement, Neural network

1 Introduction

The multi-variable properties of steel and its coatings have been successfully measured using the eddy current technique, which is often favoured over other methods because of cost, portability and the skin effect ensuring that only the coating or region at or just below the surface of the coating is inspected. Most commercial eddy current instruments require a simple calibration on a certified standard. When an instrument calibration fails to provide accurate results, because substrate-coating variation exceeds the acceptable limits of the calibration process, model-based multi-frequency testing is often employed. This form of testing normally requires the use of a PC for model inversion and highly accurate air-cored detection coils, which are difficult to manufacture. As a result, model-based eddy current inversion is restricted to the laboratory.

Ferrite-cored coils are known to overcome many of the problems associated with air-cored coils, the benefits of which include high sensitivity and dynamic range, and low thermal drift. Ferrite is also readily available in a wide range of grades and can be manufactured to close mechanical tolerances. If artificial neural networks can be trained to reproduce the input-output mapping of ferrite-cored sensor models, then ferrite-cored sensors used in conjunction with multi-frequency model-based inversion is possible for portable test equipment.

The decision-making flexibility of model-based systems is of particular benefit where heat-treated steel or alloying is involved e.g., anticorrosive duplex systems on steel, protective coatings on duplex stainless steel, plating, thermal spray or hot dip galvanising.

2 Sensor Development

Almost all published research on the multi-frequency eddy current inspection of conductive half-spaces makes use of air-cored absolute coils; other coil arrangements are considered an unnecessary complication (Harrison DJ, Jones LD, Burke SK, 1996). The air-cored coil remains the preferred sensor for model-based inversion because closed-form solutions for air-cored sensors are the only accurate solutions known to exist. A theoretical model however, is only effective when used with precision wound coils, which are difficult to manufacture.

Ferrite-cored sensors exhibit much stronger signals than air-cored. Stronger signals provide enhanced signal-to-noise ratios and increased sensitivity and dynamic range, which are essential for accurate measurement (Moulder JC, Uzal E, Rose JH, 1992, Blitz J, 1991, Ida N, 1986). A typical equation for the inductance L of a ferrite-cored sensor is given below:

$$L = \mu_0 \mu_{rod} N^2 \pi \frac{r_0^2}{l} \quad (1)$$

l is rod length, r_0 is core radius, N coil turns and $\mu_{rod} = L_k/L_o$ (where L_k is the self-inductance of a cored coil and L_o is the inductance without a core).

Equation (1) clearly shows that when $\mu_{rod} > 2.0$ the sensor core contributes more magnetic flux than the sensor coil. This means that a ferrite-cored coil can have M^2 turns removed to have the same inductance as an equivalent air-cored coil (i.e., a coil where $\mu_{rod} = 1$). Reducing the number of turns effectively makes the length and cross sectional area of the coil smaller in relation to the core, which removes the need for precision-wound coils.

A novel ferrite-cored sensor is shown in Figure 1 (May P, Zhou E, Morton D, 2007a). The sensor is comprised of three coaxial coils, a central source coil, which carries a current I amps, and two sense or pick-up coils in a differential configuration.

The sensor of Figure 1 was designed to meet a requirement of maximum flux-linkage of the sensor core with the test medium, for the given coil arrangement. Most eddy current coil designs keep the effective coil radius close to the thickness of the layers being measured for optimum sensitivity and dynamic range (Moulder JC, Uzal E, Rose JH, 1992). The effective coil radius of this sensor was 2.3 mm, however the actual effective radius of the sensor was much less due to the flux-focussing influence of the ferrite core. Core length-diameter ratio was kept as small as possible at 3.0.

Sensor tests demonstrated source coil inductance was independent of core loss and core initial permeability. Sensor tests also demonstrated coil inductance, sensitivity, and dynamic range was significantly better than that of an equivalent air-cored coil. Low levels of measurement uncertainty made this sensor highly suitable for numerical modelling.

3 Sensor Optimisation

Along with a novel sensor design, a numerical model $f(\mathbf{x})$ of the sensor was developed for accurate depth profiling of layered materials, where independent variable \mathbf{x} are the parameters that characterise the sensor (i.e., coil dimensions and turns, core dimensions and permeability etc). This model solved the generalised operator equation $L\phi = h$ using the Green's function $G(\mathbf{r}; \mathbf{r}')$ to reproduce

the magnetic vector potential of filamentary currents impressed on the sensor ferrite core-air interface (May P, Zhou E, Morton D, 2007b). Given this, optimisation of the sensor model proceeded by defining the cost function $c(\mathbf{x}) = f(\mathbf{x}) - g(\mathbf{x}^*)$, where $g(\mathbf{x}^*)$ is the target function based upon experimental data. An optimal solution is given by minimising the square of the cost function.

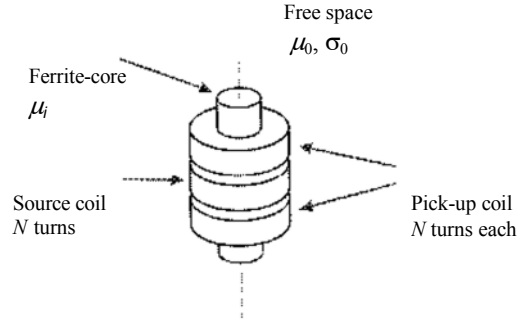


Fig. 1. Ferrite-Cored Eddy Current Sensor

Given that \mathbf{x}^* is the true value of \mathbf{x} , which is unknown, and given that the speed of convergence of \mathbf{x} on \mathbf{x}^* has no bearing on overall outcome, a first order Taylor polynomial was used to represent the effect of making a small change to \mathbf{x} . If $\mathbf{x}^{(0)}$ represents an initial guess at \mathbf{x}^* and $\mathbf{x}^{(1)}$ a revised estimate, then

$$f(\mathbf{x}^{(1)}) = f(\mathbf{x}^{(0)}) + (Df(\mathbf{x}^{(0)})^T)(\mathbf{x}^{(1)} - \mathbf{x}^{(0)}) \quad (2)$$

where $Df(\mathbf{x}^{(0)})$ is the calculated gradient at $\mathbf{x}^{(0)}$.

Substitution of equation 2 gives the cost function $c(\mathbf{x}^{(1)})$:

$$c(\mathbf{x}^{(1)}) = f(\mathbf{x}^{(0)}) + (Df(\mathbf{x}^{(0)})^T)(\mathbf{x}^{(1)} - \mathbf{x}^{(0)}) - g(\mathbf{x}^*) \quad (3)$$

Each new value for $c(\mathbf{x}^{(1)})$ requires the recalculation of $f(\mathbf{x}^{(0)})$ and $Df(\mathbf{x}^{(0)})$, which proceeds iteratively (i.e., $\mathbf{x}^{(0)}$, $\mathbf{x}^{(1)}$, ..., $\mathbf{x}^{(n)}$) until convergence on \mathbf{x}^* is achieved. The method is a form of gradient descent.

Source coil inductance readings of measured plastic shims placed on copper, aluminium, brass, steel ($\mu_i = 80$, $\sigma = 7.0 \text{ MSm}^{-1}$) and ferrite ($\mu_i = 250$) plates were made to

Table 1. Optimised Model Statistical Comparison

	Pearson Correl r	Std Error (μH) S_{xy}	Accuracy (mean) %
Coated Plate Response	0.999951	0.684	0.029
Frequency Response	0.999926	1.048	0.138
Core Position	0.999975	1.179	0.058

optimise the sensor model. Model optimisation was also performed by moving the sensor core relative to the source coil (no test plates present) and by taking zero lift-off swept frequency readings on all plates. Training examples for $f_i(\mathbf{x}^{(k)})$, $Df_i(\mathbf{x}^{(k)})$ and $g_i(\mathbf{x}^*)$ were generated from model simulations and experimental data (taken using a G^W INSTEK LCR-821 meter) at two different frequencies (1kHz and 10 kHz). Optimised model results, subject to constraints that were chosen to ensure that \mathbf{x} remains within realistic limits, are given in Table 1. Model constraints are given below:

- Core length $c_l = 6.00$ mm.
- Core radius $0.988 \text{ mm} < c_r < 1.00$ mm.
- Core permeability $900 < \mu < 1100$.
- Sensor zero lift-off $0.5 \text{ mm} < z_l < 0.45$ mm.
- Coil inner radius $r_1 = 1.455$ mm.

The average difference between measured values of \mathbf{x}^* and their numerical estimates \mathbf{x} , after model optimisation, was 4.2 microns; optimised core permeability was within the specified manufacturers tolerance.

4 Neural Network Model Inversion

A neural network was selected as the inversion element for this work due to its speed, where some level of real time processing was considered essential for online process control. The use of the sensor numerical model to perform this task, because of complexity and run-time, was not considered practical.

The selection of sampling frequencies was dictated by the need for maximum profile information within the frequency bandwidth and minimum data processing. Regression analysis revealed the frequency spacing: 0.3, 0.6, 1.25, 2.5, 5.0, 10.0 and 20.0 kHz to be optimal for a wide range of conductive coatings on steel.

The most relevant study of eddy current neural network inversion reconstructs non-magnetic conductivity profiles using a simple multilayer perceptron (Glorieux C, Moulder J, Basart J, and Thoen J, 1999). A similar MLP was planned for this work, where the inputs to the neural network were source-coil inductance measurements I_i taken at sample frequencies f_i . The neural network output T was the calculated coating

thickness or conductivity. In order that network input-output vectors were mapped correctly, some form of network training was essential. Since vector I_i is frequency dependent, data conditioning was required in order to make network training more efficient. This was accomplished by normalising the standard deviation $I^{(std)}$ and mean $I^{(mean)}$ of all vectors from the input training set, giving:

$$I_i^{(norm)} = \frac{(I_i - I_i^{(zero)} - I^{(mean)})}{I^{(std)}}, \quad (4)$$

where $I_i^{(zero)}$ is zero lift-off inductance at frequency f_i .

3500 example pairs were generated from the sensor numerical model and the data divided into two equal parts (i.e., estimation and validation subsets) for cross validation. Although good generalisation was the primary goal of training, an overall mean squared error of 10^{-10} was set as the target performance of the estimation subset. Network training was conducted using MATLAB[®] and the Levenberg-Marquardt algorithm, which was implemented in a batch format. Two MLPs were trained, one for the measurement of coating thickness and the other for coating conductivity. Both neural networks were fully connected.

The MSE target for the thickness MLP was achieved with one layer of 8 sigmoid neurons and a single linear output neuron. The MSE target for the conductivity MLP required a single layer of 10 sigmoid neurons and a single linear output neuron. A regression analysis of network performance (i.e., network response to corresponding target) gave the square of the Pearson correlation coefficient $r^2 = 0.99998$ for both networks.

5 Results

Copper and brass foils of varying thickness were selected to cover the range metallic non-magnetic coatings on steel; plastic foils were chosen as non-conductive coatings. Cold rolled low carbon steel plate (BS1449 1991, grade CS4 H5) was purchased as a substrate due to its widespread use in construction. Seventeen plates of this grade were tested in total, of which three were selected as representative of the batch. Before any coated

Table 2. Mean Coating Thickness and Conductivity

	Cu_1	Cu_2	Cu_3	Cu_4	Cu_5	Br_1	Br_2	Br_3	Br_4	PI_1	PI_2	PI_3
Actual Thickness μm	10.7	48.7	104.6	179.9	215.8	13.8	37.6	52.0	104.3	51.4	97.2	176.6
Actual Cond MS/m	57.8	57.8	57.8	57.8	57.8	15.8	15.8	15.8	15.8	0.0	0.0	0.0
Rdg Thickness μm	9.5	51.1	104.0	179.5	224.1	14.2	38.0	52.1	104.8	51.5	96.6	174.7
Rdg Cond MS/m	51.9	53.6	53.8	51.8	50.5	12.3	14.1	13.5	13.3	0.0	0.6	0.1

plate tests were conducted, the copper, brass and plastic foils were measured using a Solartron LE/25/P linear encoder. All foils were measured to an uncertainty of $\pm 0.8 \mu\text{m}$. Foils were then placed on each plate and a flat non-conductive weight (i.e., a plastic block) applied to ensure an airless contact between all media. The sensor was finally positioned (through a small hole located in centre of the weight) onto each coated sample and source coil inductance taken. A system calibration was performed on each sample before testing commenced.

Normalised sensor inductance is shown in Figure 2, including the appropriate numerical model estimate (marked (NN)), for a selection of foils.

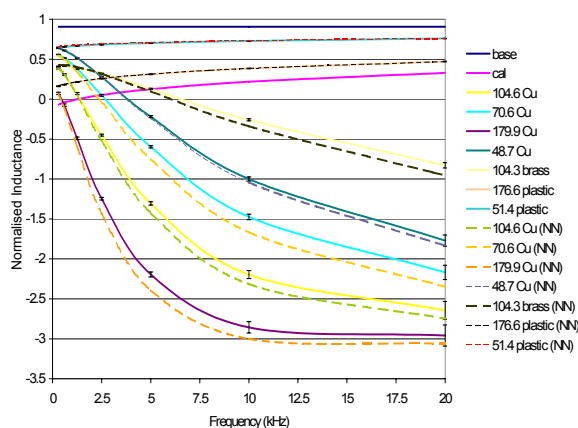


Fig. 2. Sensor Normalised Inductance

The level of correlation between theoretical and experimental curves was determined by taking the square of the Pearson correlation coefficient r^2 , which was 0.9996 for all coated plate tests.

Coating thickness and conductivity was determined for each sample by taking inductive measurements and running the thickness and conductivity neural networks. Table 2 gives the mean values of some of the copper (Cu), brass (Br) and plastic (Pl) coated plate tests.

The average thickness error of all foils tested on all plates was $0.3 \mu\text{m}$; see Table 2. The true value of the conductivity of metallic coatings was consistently underestimated, where the mean conductivity error was found to be -3.6 MS/m .

Based on the above results and further extended tests, the following specification is proposed for this measuring system:

- $2 \mu\text{m} + 3\%$ of actual coating thickness.
- $2 \text{ MS/m} + 10\%$ of actual coating conductivity.

6 Conclusion

An accurate ferrite-cored eddy current sensor was developed, which had a reduced dependency on coil

winding, core losses and variations of core permeability. A numerical model of the sensor was developed and optimised for multi-frequency profiling of two layer materials.

Artificial neural networks were selected as inversion elements, which is entirely unique for ferrite-cored sensors used on steel. Two multi-layer perceptrons, having a single layer of sigmoid neurons and a single linear output neuron, were all that was required for accurate coating thickness and conductivity classification. Neural network input and output vectors were normalised by referencing all network inputs to zero lift-off and by using a mean and standard deviation scaling algorithm.

Three steel plates (grade CS4 H5) were selected for tests, of which one was chosen as a reference and used for sensor model optimisation. Swept frequency curves of normalized inductance and their associated numerical estimates were generated on these plates, which were in good agreement with a correlation coefficient $r^2 = 0.9996$. Increasing levels of error however were observed on all normalized inductance curves for increasing frequency, coating thickness and coating conductivity. Measured coating thickness and conductivity, for all coated plate tests, was found to be accurate to within $2 \mu\text{m} + 3\%$ and $2.0 \text{ MS/m} + 10\%$ of actual values.

Three causes of measurement error were identified. The first was foil stacking, which was worse for thick multiple foils. The second was a method of calibration that was optimised for thin foils and became increasingly erroneous with increasing foil thickness, frequency and conductivity. The final source of error was due to the sensor numerical model, which was developed for a two-layer substrate-coating combination and tailored for use with coatings deposited on the reference plate only.

References

- Blitz, J. (1991) Electrical and Magnetic Methods of Non-destructive Testing. 1st edition, Adam Hilger. ISBN: 0-7503-0148-1.
- Glorieux C, Moulder J, Basart J, Thoen J, (1999) The Determination of Electrical Conductivity Using Neural Network Inversion of Multi-frequency Eddy Current Probe Data. Journal of Physics D. Vol. 32, pp. 616-622.
- Harrison DJ, Jones LD, Burke SK, (1996) Benchmark problems for defect size and shape determination in eddy-current non-destructive evaluation. Journal of Non-destructive Evaluation, Vol. 15, No. 1.
- Ida N, (1986) Non-destructive Testing Handbook, Vol. 4, 2nd edition, section 19.
- May P, Zhou E, Morton D, (2007a) The Design of a Ferrite Cored Probe. Sensors and Actuators A, Vol. 136, pp. 221-228.
- May P, Zhou E, Morton D, (2007b) Numerical modelling and implementation of ferrite cored eddy current probes. NDT&E international, Vol. 40, pp. 566-576.
- Moulder J, Uzal E, Rose JH, (1992) Thickness and Conductivity of Metallic Layers from Eddy Current Measurements. Review of Scientific Instruments, Vol. 63, No. 6, pp 3455-3465.

Digital Alignment of a reconstructed Hologram for Measurement of Deterioration of Tools

S. Huferath-von Luepke¹, T. Baumbach², E. Kolenovic³, C. Falldorf¹ and C. von Kopylow¹

¹ Bremer Institut für angewandte Strahltechnik, Klagenfurter Str. 2, 28359 Bremen, Germany

² a&a technologies GmbH, Kohlenstr. 1, 28217 Bremen, Germany

³ Syperion GmbH & Co. KG, Hermann-Köhl-Str. 7, 28199 Bremen, Germany

Abstract. We present a novel method to overcome the limitations of comparative digital holography (CDH) due to misalignment of test objects. The method is based on the modification of the master hologram written in the spatial light modulator (SLM). Using the full three dimensional information of the master object, the reconstructed wave front of the master object can be modified regarding its position and angles. Therefore, the applied algorithm can be understood as a complementary approach in the Fourier domain to the matching algorithm in object space. In this paper we describe the algorithm and present related experiments.

Keywords: comparative digital holography, spatial light modulator, adaptive wave front modification

1. Introduction

Comparative digital holography (CDH) [1] is a suitable method to compare the shape or the deformation of two nominally identical, but physically different objects. It is based on the two wavelengths contouring technique where two holograms with a slightly different wavelength are generated. The result may be considered to be a hologram with a synthetic wavelength. This is necessary for the shape measurement.

The comparative measurement is carried out in two steps: in the first step, the so called master hologram is recorded with a conventional setup for digital holography shown in Fig. 1.1a. The second step is the recording of the comparative hologram [1]. This is done by illuminating the test object with the objects wave front which stored the information of the master hologram. Therefore the master hologram is written into a spatial light modulator (SLM) which is introduced into the object beam, see Fig. 1.1b. Since both steps are independent, they can be carried out in different places. For the two steps two mostly identical setups have to be considered [1,2,3].

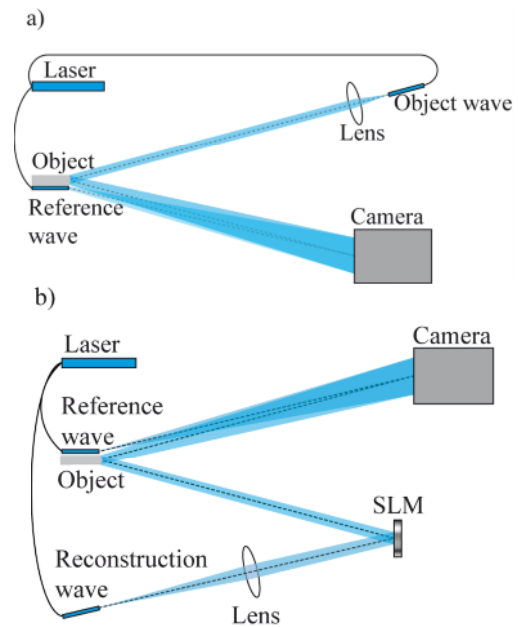


Fig. 1 a) Setup for recording of the master hologram; b) Setup for illuminating the test object with the master hologram via spatial light modulator (SLM)

For a successful comparison of two objects the reconstructed wave field of the master object has to be projected very precisely onto the test object. An imprecise adjustment will lead to additional interference patterns, which are not associated to the desired difference measurement of the objects. Since the access of the full 3D information of the master object is given, the wave front of the master object can be numerically modified by means of signal processing, enabling the solely measurement of the objects difference. In this

paper we describe how these modifications can be done numerically and present related results.

2. Reconstruction algorithm

The applied reconstruction algorithm uses the stepwise propagation of wave fields through different imaging planes. The algorithm is based on Rayleigh's first integral formula [4]:

$$b'(x) = \frac{1}{i\lambda} \int_{-\infty}^{\infty} \int_{-\infty}^{\infty} h(\mathbf{u}) r'(\mathbf{u}) \frac{e^{ik\rho}}{\rho} \cos(\theta) d(\mathbf{u}), \quad (1)$$

with

$$\rho = \sqrt{(x-\xi)^2 + (y-\eta)^2 + d^2}. \quad (2)$$

Where $b'(\mathbf{x})$ is the reconstructed wave field of the object $b(\mathbf{x})$, $h(\mathbf{u})$ is the hologram, $r'(\mathbf{u})$ represents the reference wave and d the distance between object and hologram plane. Due to the square root the numerical reconstruction of Eq.(1) is time intensive. In order to reduce the calculation effort, approximations of the diffraction integral have been developed [4,5]. For our algorithm we use the Fresnel approximation. Hence, for small lateral distances the distance ρ can be approximated by

$$\rho \approx d \left[1 + \frac{(x-\xi)^2}{2d^2} + \frac{(y-\eta)^2}{2d^2} \right] \quad (3)$$

for the phase and $\rho \rightarrow d$ for the denominator, and for the approximation of small angles $\cos(\theta)$ will be 1. Inserting Eq.(3) and the other approximations into Eq.(1) the reconstruction reduce to:

$$b'(\mathbf{x}) = S_1(\mathbf{x}) \cdot F^{-1} \left\{ h(\mathbf{u}) r'(\mathbf{u}) S_2(\mathbf{u}) \right\} \left(\frac{\mathbf{x}}{\lambda d} \right), \quad (4)$$

with

$$S_1(\mathbf{x}) = \frac{1}{i\lambda d} e^{-i\frac{2\pi d}{\lambda}} e^{-i\frac{\pi}{\lambda d} |\mathbf{x}|^2}, \quad (5)$$

and

$$S_2(\mathbf{u}) = e^{-i\frac{\pi}{\lambda d} |\mathbf{u}|^2}. \quad (6)$$

Here, $F^{-1}\{\dots\}$ is the operator of the two-dimensional inverse Fourier transformation, and λ is the wavelength.

The CDH setup we use is based on the lensless Fourier holography. That means that object and origin of

the (spherical) reference wave are located in the same plane which is parallel to the hologram plane (Fig. 1). Consequently, the spherical reference wave can be written as [6]:

$$r'(\mathbf{u}) \propto e^{i\frac{\pi}{\lambda d} |\mathbf{u}|^2}. \quad (7)$$

By applying Eq.(7) into Eq.(4) the reconstructed wave field $b'(\mathbf{x})$ is described by:

$$\begin{aligned} b'(\mathbf{x}) &= S_1(\mathbf{x}) \cdot F^{-1} \left\{ h(\mathbf{u}) \right\} \left(\frac{\mathbf{x}}{\lambda d} \right) \\ &= P_d \left\{ h(\mathbf{u}) \right\} \left(\frac{\mathbf{x}}{\lambda d} \right), \end{aligned} \quad (8)$$

where P_d is the propagation operator.

As mentioned in section 1.1 the test object must be covered very precisely by the reconstructed wave field originated by the master hologram which is generated by the SLM. This means the reconstructed wave field of the master hologram has to be aligned laterally and with the proper tilt. This can be realised numerically by using the Fourier shift theorem [7]. From the Fourier shift theorem we know, that a ramp within the frequency domain leads to a shift within the spatial domain. By means of the operator P_d introduced above, we can constitute this as follows:

$$b''(\mathbf{x}) = P_d \left\{ h(\mathbf{u}) \cdot e^{i\Delta\phi_B(\mathbf{u})} \right\} \left(\frac{\mathbf{x}}{\lambda d} \right) \quad (9)$$

$$= P_d \left\{ h(\mathbf{u}) \right\} \left(\frac{\mathbf{x} + \Delta\mathbf{x}}{\lambda d} \right) e^{i(\Delta\phi_B(\mathbf{u}) + \phi_0)},$$

with

$$\Delta\phi_B(\mathbf{u}) = 2\pi \frac{\Delta\mathbf{x} \cdot \mathbf{u}}{\lambda d}, \quad (10)$$

$$\phi_0 = \pi\lambda d \Delta\mathbf{x}^2, \quad (11)$$

where $b''(\mathbf{x})$ is the shifted reconstructed hologram, $\Delta\phi_B(\mathbf{u})$ the phase ramp, and ϕ_0 a constant phase term. Regarding Eq.(9), it can be seen, that, if a ramp is written into the hologram plane the reconstructed object is shifted by $\Delta\mathbf{x}$ in the object plane. However, the ramp remains. From Eq.(10) and (11) it can be seen that the wavelength is the only variable which is changed when the two master holograms, which are needed for the generation of the

synthetic wavelength, were recorded. In our case the difference between the two wavelengths is small (about 0.4nm) so that the subtracting of the two holograms allows the neglecting of the ramp.

Applying Eq.(9) on the phase calculation leads to:

$$\begin{aligned} \arg[b_i'(\mathbf{x})] &= \phi_i \\ &= \arg[S_{1i}(\mathbf{x})] + \Delta\phi_{B_i}(\mathbf{u}) + \phi_{0i} \\ &\quad + \arg[F^{-1}\{h_i(\mathbf{u})\}]\left(\frac{\mathbf{x}}{\lambda d}\right). \end{aligned} \quad (12)$$

With this equation the reconstructed master hologram can be shifted in the reconstruction plane in order to perform position corrections.

The modification can also be used for compensating tilts of an object. That means the object will be rotated with a small angle along the x or y axis or both together within the object plane $b'(\mathbf{x})$. Hence, the shift theorem of the Fourier transformation can be used again by adapting Eq.(12) accordingly:

$$\begin{aligned} \arg[b_i'(\mathbf{x})] &= \phi_i \\ &= \arg[S_{1i}] + \Delta\phi_{B_i}(\mathbf{x}) + \phi_{0i} \\ &\quad + \arg[F^{-1}\{h_i(\mathbf{u} + \Delta\mathbf{u})\}]\left(\frac{\mathbf{x}}{\lambda d}\right), \end{aligned} \quad (13)$$

with

$$\Delta\phi_B(\mathbf{x}) = 2\pi \frac{\mathbf{x} \cdot \Delta\mathbf{u}}{\lambda d}. \quad (14)$$

Hence, we can apply digitally a tilt and displacement to the holographic representation of the master object and therefore compensate the misalignment of the test object.

3. Active modification of the reconstructed wave front

The numerical solution for reposition of holograms described in section 1.2 will be evaluated in this section experimentally. To demonstrate the capability of the active modification we show the influence of two alignment errors. One will be the lateral displacement and the other a twist between the reconstructed master object

and the test object. The object we use to demonstrate the modification of the wave field is a deep drawing tool with a diameter of 5mm (Fig. 2). Our request is to measure the abrasion of micro deep drawing tools using shape comparison. Therefore we use the comparative digital holography.

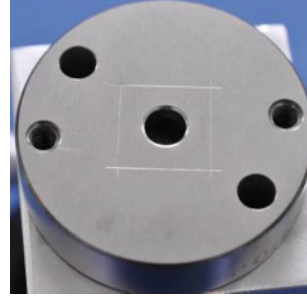


Fig. 2 Picture of the deep drawing tool

3.1 Lateral adjustment of the wave front

As shown above, a lateral adjustment of the wave front in the object plane is equivalent to an additional phase ramp in the wave field of the hologram. Id est, to get the reconstructed master hologram at the same position as the test object we have to add a phase ramp into the master hologram. To demonstrate this effect we show in Fig. 3 a phase hologram (Fig. 3a) and the associated numerically reconstructed intensity image of the deep drawing tool (Fig. 3b).

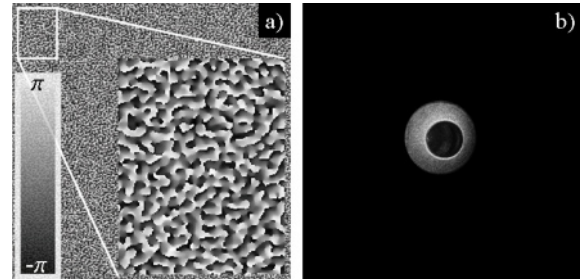


Fig. 3 Central object position with no phase ramp within the hologram: a) phase hologram of the deep drawing tool; b) numerically reconstructed intensity image of the deep drawing tool

Fig. 4a illustrates a phase hologram of the same deep drawing tool but with a lateral adjustment and Fig. 4b shows the associated numerically reconstructed intensity image. Compared to Fig. 3a a higher frequency in Fig. 4a is clearly observable. In order to shift the object by $\Delta\mathbf{x}$ we add a phase ramp $\Delta\phi_B(\mathbf{x})$ by using Eq.(12) to the hologram. This has to be done with both holograms of the master object whereas the phase of the phase ramp has to be modulated to the used wavelength.

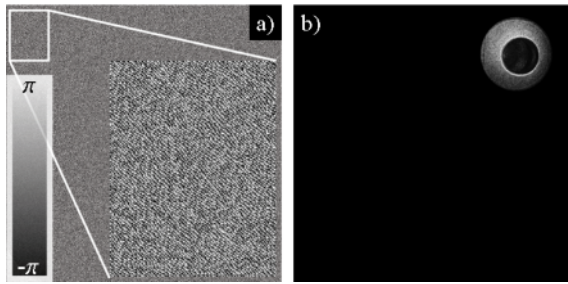


Fig. 4 Non axial object position with a phase ramp within the hologram: a) phase hologram of the deep drawing tool; b) numerically reconstructed intensity image of the deep drawing tool

The gradient of the phase ramp depends on the lateral shift of the two objects and the distance between hologram and object plane. The phase ramp can be defined in two ways. The first method is comparing the outcome of the comparative measurement with a simulation of the object shifting which is based on the master hologram. Here, both objects have to be nearly identically. The second method is an iterative method. Thereby a small phase ramp will be added upon the master hologram and the result of the shape measurement will be analysed. Decreasing of the interference pattern leads to a further adding of a ramp and increasing to a subtraction of a ramp. This is done until adding as well as subtracting increases the interference pattern. This can be automated easily.

3.2 Rotation of the wave front

A rotation of the object along the z axis leads also to misalignment errors. To compensate this error the reconstructed wave front of the object has to be rotated.

Rotating of a hologram is quite easy. But having an off axis setup (like we have), rotating of a hologram means to rotate the reconstructed wave front of the object around the zero order (image centre). As seen in Fig. 5a this kind of rotation rotates the object but also change the position of the object. With that the master object would not cover the test object.

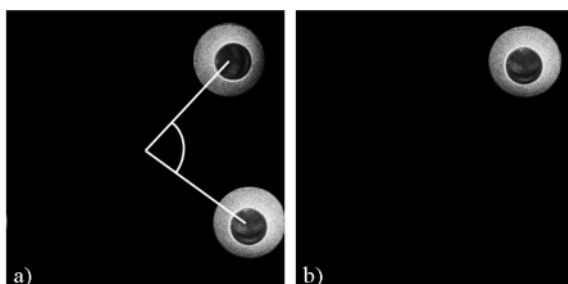


Fig. 5 a) Rotation of the object around the zero order and b) Rotated object considering the phase ramp

To avoid this, a phase ramp can be written into the hologram, so that the zero order and the object will overlap each other axially. Now the hologram will be rotated. After rotation the afore applied phase ramp is erased, replacing the object to its origin. Fig 5b shows the reconstructed image of the deep drawing tool which is rotated by 80 degree.

If the surface normal of the object is not in direction of the optical axis an additional tilt is generated, which can be compensated after rotating the object.

4. Conclusion

The presented theoretical approach was used to develop an iterative algorithm to compensate the misalignment errors which are critical for the comparative measurement. This algorithm allows a complete adjustment of the wave front of the master object relative to the alignment of the test object.

Thus we have a good approach for the robust application of the comparative digital holography. In future work the wave front modification algorithm will be automated in order to enable quality control of several objects.

Acknowledgements

The authors thank the Deutsche Forschungsgemeinschaft (DFG) for supporting the subprojects B3 (Werkzeuglebensdauer) and B5 (sichere Prozesse), in the Collaborative Research Centre SFB 747, Micro Cold Forming (Mikrokaltumformen) and R.B. Bergmann and P. Huke for exciting discussions and support.

References

- [1] Osten, W., Baumbach, T., Jueptner, W., "Comparative digital holography", *Opt. Lett.* 27(20), 1764 (2002)
- [2] v. Kopylow, C., Baumbach, T., Osten, W., Jueptner, W., "Comparative Digital Holography for Application in Quality Assurance during Production", *Prod. Eng. WPG XII*(1), 137 (2005)
- [3] Baumbach, T., v. Kopylow, C., Jueptner, W., "Formvergleich zweier Objekte an unterschiedlichen Standorten mit digitaler Holografie", *tm* 73(3), 120 (2006)
- [4] Goodman, J., "Introduction to Fourier Optics", Roberts & Company (2005)
- [5] Kreis, T., "Handbook of Holographic Interferometry", Weinheim: Wiley-VCH, (2005)
- [6] Wagner, C., Seebacher, S., Osten, W., Jueptner, W., "Digital Recording and Numerical Reconstruction of Lensless Fourier Holograms in Optical Metrology", *Appl. Opt.* 38(22), 4812 (1999)
- [7] Hackbusch, W., Schwarz, H., Zeidler, E., "Teubner-Taschenbuch der Mathematik", B. G. Teubner Stuttgart, (1996)

Implementation of decision rules for CMM sampling in a KBE system

Álvarez, B.J.¹, Cuesta, E.¹, Martínez, S.², Barreiro, J.² and Fernández, P.¹

¹ University of Oviedo, Dpt. of Manufacturing Engineering, Campus of Gijón, 33203 Gijón, SPAIN

² University of León, Dpt. of Manufacturing Engineering, Campus de Vegazana, 24071 León, SPAIN

Abstract: This work presents a methodology for setting the number and spatial distribution of inspection points in the automatic inspection of parts using Coordinate Measuring Machines. This methodology collects the existing knowledge about sampling rules in automatic inspection. The final purpose is to store this knowledge in a KBE platform oriented to the inspection planning process and based on the MOKA methodology.

Keywords: Sampling, CMM, Inspection Planning, Knowledge Based Engineering (KBE)

1. Introduction

Inspection planning is a good candidate for implementing a Knowledge Based Engineering (KBE) system because the repetitive and well-known decisions that it involves. However, most of this knowledge is today implicit in the expert mind and disseminated on a huge variety of researches. This work deals with the identification of knowledge in the scope of CMM inspection sampling, which will serve as a basis for a detailed representation and implementation in a KBE platform.

There are several activities involved in the inspection planning process, such as identification of features to be inspected, analysis of accessibility, determination of part orientation, determination of resources and others. In a more detailed level, selection of points and path generation for the inspection of each feature must be carried out.

This paper shows the work of elicitation and structuring of knowledge related to the number and distribution of contact points. This allows the translation of the knowledge to rules of direct application in the process.

Factors that affect the decision about CMM sampling are related to three main constraints: part specifications, process capability and inspection equipment accuracy. Although recommendations about point sampling can be found in standards, inspection software and previous researches, it has not been established a solution about sampling that takes into account all the factors aforementioned.

2. Decision rules for an optimal CMM sampling

An optimal sampling strategy in CMM inspection should be defined taking into account not only the number of inspection points but also the distribution of those points over the surfaces of the feature to be inspected.

Different levels of decision must be established when considering an automatic decision chart oriented to KBE. At the top level, most of researchers start considering the type of the feature to inspect (cylinder, plane, sphere, freeform surfaces, etc.) and the type and value of the specified tolerance. In the methodology developed in this work, a new and crucial contribution is considered besides the aforementioned idea: more important than the type of feature to inspect is the type of tolerance, that is, whether the tolerance is related to the workpiece form error or not. Form error inspection requires a number of points about one order of magnitude larger than inspection of dimensional or position tolerances [1].

Form error inspection demands a dense and vast point distribution, in order to cover the largest portion of the feature surface. This distribution should be capable of capturing the maximum form deviation. The values of these form errors are often close to the CMM reliability. In this case, a practical and economical limit given by ISO14253 standard [2] would be: $T/2U = 3$, which, in the case of CMM measurement, could be translated as $MPE < T/6$, where T is tolerance, U is CMM uncertainty and MPE denotes the Maximum Permissible Error [3].

In the inspection of non-form errors (such as distance between planes, location of centres and axes, distance between axes or whatever combination between them) the second level of decision is governed by the inspection time and the relative error, that is, the relation between feature size and its specification accuracy.

On the other hand, when inspection of form errors is considered, inspection time is at second place. In addition, the level of decision is now related to the amount of parts to be inspected. When the lot size is high, it is essential a detailed inspection of an initial part. In fact, if a particular feature is measured routinely as part of industrial production, it will be appropriate to learn about

that feature by making initially (and periodically thereafter) detailed measurements of the part. From such measurement, it is easy to deduce a sampling strategy that is economical for the target uncertainty and the effect of using it [4]. This procedure of measurement is the only way to optimize the sampling strategy and reduce inspection time without compromising the planning reliability. This level of decision is based directly on prior knowledge and it is corroborated by several publications [4-7] where the suitability of measuring an initial part, with closely related real features, is recommended.

Of course, if the part has a combination of form errors and dimensional tolerances that affect the same feature, the denser sampling (*form error sampling*) is preferred.

The next level of decision is related to the available resources. Nowadays, two types of sensors can be mounted on a CMM: contact sensors (touch-trigger and scanning probes) or non-contact sensors, (i.e. Laser Triangulation Sensors -LTS-, which can capture massive pointclouds). In the first type, measurement can be carried out with touch-trigger probes (discrete contacts) or by scanning probes (continuous contact). Scanning probes can acquire several hundred surface points each second as well as to acquire discrete points in a similar way to touch-trigger probes.

2.1 Inspection of *non-form* tolerances

In the case of dimensional tolerances and non-form tolerances, that is, orientation and location type, i.e. parallelism, symmetry, concentricity, etc., three options can be considered in terms of size-accuracy relationship: low, moderate and maximum accuracy.

2.1.1 Low accuracy (*Minimum inspection time*)

The sampling size is equal to the minimum number of points necessary to define the feature plus one point. Thus, 3 points for a line, 4 for a plane, 4 or 5 for a circle, 5 for a sphere, 6 for a cylinder or a cone, etc. This strategy applies to the measurement of initial datum features for manual alignments prior to automatic alignments.

2.1.2 Moderate accuracy / *Fair*

In this case, it is not necessary to know the entire surface thoroughly, therefore only a sufficient number of points is needed for assuring the measurement accuracy. It is advisable a stratified random or a uniform distribution with a minimum number of points given by BS7172 standard [8]. For example, it would take 5 points for a line, 7 for a circle, 9 (grid of 3x3) for a plane or sphere, 12 (4x3) for cylinders, 12 for ellipses, etc.

2.1.3 Maximum accuracy

There are two possible reasons for choosing this option. The first one, when tolerance is near the limit of the CMM uncertainty, even as a *non-form* tolerance. The second one when knowledge of the entire surface (in

terms of dimensional extension) is required. In both cases, the number of points must be greater than the ones in the option 2.1.2 and the distribution does not need to be uniform (or quasi-uniform). Before deciding the optimal sampling strategy, another level of decision should be carried out taking into account the available resources.

- In the most common case, when only a touch trigger sensor is available, a stratified random distribution can be used (BS7172) taking at least one point in a series of random intervals uniformly distributed [4]. Moreover, as a maximum accuracy is required, several measurement repetitions (in practice, between 3 to 10) are considered appropriate, postprocessing the results statistically.
- However, if a scanning probe is available, probing is faster and denser, which enables a better surface covering of the feature. The KBE system provides the option of using all points (no filter), or to consider other filters to optimize the subsequent computations and eliminate redundant information: uniform filter, filter per curvature, and Polar Gaussian filter. The latter is used in rotational parts using the concept of UPR (Undulations Per Revolution). The inclusion of this option in the KBE methodology is now justified in the current features of recent sensor models (Renishaw's SP25M, ZEISS's VAST XT, Mitutoyo's MPP-100 Scanning Probe, etc.). All of them already have a similar cost to the touch-trigger probes, are more compact than before, and have similar protection devices for crash damage. Other automated inspections devices (not CMM), which generates 2D scanning profiles, could also be placed within this item, such as electronic probes, axial probes, LVDT, etc.
- In the last case, a laser sensor is available. Whenever the accuracy of the sensor is several times higher (at least six) than the specified tolerance, a laser sensor could be used for metrological purpose [9]. In this case, the use of this type of sensors allows a huge reduction in inspection time with an optimal surface covering. However, this sensor always captures extended pointclouds and therefore gives too much information than that required to detect one or more single dimensional tolerances, and consequently it will require further pointcloud filtering. Most of the CMM software applications include at least three filters: filter by curvature, by spheres or by cubes (cubical grid). The curvature filter can be very useful to eliminate chamfers, fillet radii and boundaries which always distort the measurement of dimensional tolerances.

2.2 Inspection of geometrical tolerances (form errors)

As discussed above, the requirement to know the whole surface of the features is more important than the requirement to minimize the inspection time. To know if a prototype is available or not constitutes the first level of decision when planning an optimal feature inspection affected by form errors. An initial part should be inspected in detail to obtain an initial accurate value for the form error and then improve the sampling strategy.

Although the information provided by the prototype part may seem a simple fitting to the real part (in future on-line inspection), the level of fitting is actually high when the manufacturing process can be known. For instance, knowledge about the machine-tool, the cutting tool, the clamping system, etc. would let to predict values of UPR (ISO/TS 12181-2 [10]), the value of maximum form deviations (MFD) or, in other cases, the range of roughness for all the parts of the series.

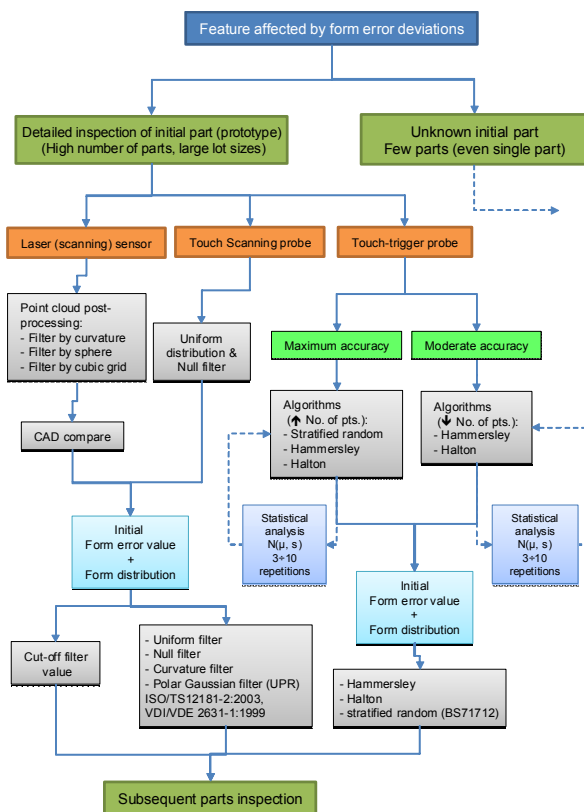


Fig. 1. Decision rules layout corresponding to form tolerances inspection

Therefore, the first bifurcation in the chart (fig. 1) is given by two opposite terms: medium-large series (with an initial part) or single part (without known part). The first option corresponds to a detailed inspection and quality control for medium or large series whereas the second option is best suited to a calibration laboratory, single set-up parts inspection or in the subcontracted metrology field.

In both cases, the next level of decision is similar to the one for dimensional (non-form) tolerances with the maximum accuracy constraint (section 2.1.3). Again, three types of resources could be considered: touch-trigger, scanning or laser sensor. The use of laser sensor corresponds to reverse engineering techniques applied to CAD-part comparisons in free-form inspection, large sheet-metal parts, automotive assembly lines, etc.

2.2.1 Medium or Large Series (high lot size), with initial part.

Here, the inspection of an initial part (or parts) is always performed as a pattern sampling (fig. 1).

- When scanning sensor is available, a uniform distribution with null filter could be applied to the feature, which allows a characterization of its form-deviation function. This information will be used as a basis for obtaining a detailed sampling planning for subsequent measurements. An adequate type of filter and filter (cut-off) value will define the detailed planning: Uniform, Curvature or Gaussian Polar [10, 11].
- When there is only a touch-trigger probe sensor, a new classification has to be carried out (fig. 1):

- Maximum accuracy. In this case, iterative sampling with a high number of points should be chosen. Several types of distributions could be selected for this sampling: stratified random, Hammersley sequence or Halton sequence. The last two distributions provide a better discrepancy, using the same number of points, than the uniform one [12]. Thus, both of them must be preferred instead of uniform distribution. In the event that the form deviation were so tight that it compromises the CMM maximum permissible error (MPE), this measurement must be repeated (3~10 times) to assure the CMM reliability. Finally, the best of the previous distributions would be applied for all the subsequent parts.
- Moderate accuracy. Similarly to the previous case, an iterative sampling would be done, but with fewer points than before and only choosing between two algorithms: Hammersley or Halton. The ulterior statistical treatment (3~10 repetitions) is now optional. From this stage the same analysis than before could be done.

2.2.2 Unknown part, unique part or low lot size.

Now, the decision charts are very similar. In fact, if a scanning probe is available then the case is the same than the one in section 2.2.1, that is, null filter and without any iterative process. If there is only a touch-trigger sensor, the case is the same than the *maximum accuracy case*

mentioned, testing which is the best distribution among the stratified random, Hammersley or Halton.

3. Implementation in a KBE system

The knowledge identified in the previous sections makes sense within an automated inspection process. Actually a KBE platform is being developed for representing and storing the knowledge related to the CMM inspection planning. The knowledge required in this process is vast, being the point number and its distribution one of the key aspects. To achieve this, the rules identified have been introduced in such platform. The methodology followed for the knowledge representation is MOKA [13]. However, there is some knowledge related to resources and functions which are not included in MOKA. The insufficiency of the ontology is due to the fact that in our context the final product is the inspection process planning which is a process. The ontology used in this work is a MOKA modification for the inspection domain. MOKA methodology was developed for structuring the knowledge to engineering design and non to engineering processes (manufacturing or inspection activities). The types of object do not become reusable as proposed [14]. For example, considering the entities in MOKA, they describe components of the product design. But within the context of this survey, the entities are also linked to processes, such as lot size. The same idea can be applied to activities. These activities consist in geometry recognition, manufacturing identification, inspection operations definition, etc. They represent domain activities. This implies that activities can be classified in two types, those related to the domain and those related to the reasoning that allows definition of the process planning. For it, the ontology proposed is composed of six knowledge objects: Illustration, Constraint, Activity, Rule, Entity and a new one, Resource (ICARER), which are later decomposed into sub-objects. In particular, the identified knowledge for the point number and distribution is represented mainly using the Rule object, which is mainly linked to Activity and Resource, and secondary to Entity objects. The Knowledge Engineering tool PCPACK [15] has been utilized for the purpose of capturing and formalizing the domain knowledge involved in the CMM inspection planning process.

4. Conclusions

The KBE decision rules identified in this work are divided in two groups depending on their application to dimensional (and non-form geometrical tolerance) or form geometrical tolerance verification. In first case, different rules are applied considering the tightness of the tolerance band. Inspection time-cost and available technologies (sensor type) were considered. In the case of

form tolerances, an additional analysis is needed depending on the lot size to be inspected. If the lot size is large, a detailed inspection of an initial part should be performed, so that a sampling strategy can be defined that provides an acceptable balance between measurement economy and accuracy of the result. At the lowest level of decision, the best distribution and a suitable form value are achieved.

Acknowledgements

We gratefully acknowledge the financial support provided by the Spanish Minister of Science and Innovation through project DPI2008-01974.

References

- [1] Hocken RJ, Raja J, Babu U, (1993) Sampling issues in coordinate metrology. ASME Transactions, Journal of Manufacturing Review 6: 282–294
- [2] ISO 14253-1:1998 Geometrical Product Specifications (GPS) - Inspection by measurement of workpieces and measuring equipment - Part 1: Decision rules for proving conformance or non-conformance with specification
- [3] ISO 10360-2:2009 Geometrical product specifications (GPS) - Acceptance and reverification tests for coordinate measuring machines (CMM) - Part 2: CMMs used for measuring linear dimensions
- [4] Flack D (2001) Measurement good practice guide: CMM measurement strategies. National Physical Laboratory (NPL) No.41
- [5] Badar MA, Raman S, Pulat PS, (2005) Experimental verification of manufacturing error pattern and its utilization in form tolerance sampling. Int. J. Mach. Tools Manufact. 45: 63–73
- [6] Edgeworth R, Wilhelm RG, (1999) Adaptive sampling for coordinate metrology. Precision Engineering 23: 144–154
- [7] Zhao F, Xu X, Xie SQ (2009) Computer-aided inspection planning-The state of the art. Computers in Industry 60: 453–466
- [8] BS 7172:1989: Guide to assessment of position, size and departure from nominal form of geometric features
- [9] Martínez S, Cuesta E, Barreiro J, Álvarez B, (2010) Analysis of laser scanning and strategies for dimensional and geometrical control. Int J. Adv. Manuf. Technol. 46:612–629
- [10] ISO/TS 12181-2:2003 Geometrical Product Specifications (GPS) - Roundness - Part 2: Specification operators
- [11] VDI/VDE 2631 Part 1, 1999-06, Form measurement – Principles for the measurement of geometrical deviations
- [12] Lee G, Mou J, Shen Y, (1997) Sampling strategy design for dimensional measurement of geometric features using coordinate measuring machine. Int. J. Mach. Tools Manufact. 37: 917–934
- [13] Stokes, M. (2001). Managing Engineering Knowledge. MOKA: Methodology for Knowledge Based Engineering Applications. Professional Engineering Publishing Limited.
- [14] Ammar-Khodja S, Perry N, Bernard A. (2008) Processing knowledge to support knowledge-based engineering systems specification, Concurrent Engineering: Research and Applications, 16:89–101
- [15] PCPACK5, Software Package, Version 1.4.6R, Epistemics, Nottingham, United Kingdom, 2008.

Machine Vision System for Inline Inspection in Carbide Insert Production

Robert Schmitt¹, Ingrid Scholl², Yu Cai¹, Ji Xia¹, Paul Dziwoki², Martin Harding¹ and Alberto Pavim³

¹ Laboratory for Machine Tools and Production Engineering (WZL) RWTH Aachen University, Steinbachstraße 19, Aachen, 52074, Germany

² Department of Electrical Engineering and Information Technology, Aachen University of Applied Sciences, Eupener Str. 70, Aachen, 52066, Germany

³ Scholarship holder of the Brazilian CNPq

Abstract. In steps of the production chain of carbide inserts, such as unloading or packaging, the conformity test of the insert type is done manually, which causes a statistic increase of errors due to monotony and fatigue of the worker and the wide variety of the insert types. A machine vision system is introduced that captures digital frames of the inserts in the production line, analyses inspects automatically and measures four quality features: coating colour, edge radius, plate shape and chip-former geometry. This new method has been tested on several inserts of different types and has shown that the prevalent insert types can be inspected and robustly classified in real production environment and therefore improves the manufacturing automation.

Keywords: metrology, optical measurement, industrial image processing, part recognition, automation

1. Introduction

The product spectrum of cutting material manufacturers consists of a large variety of insert geometries, which only differ by small details such as coating colour, edge radius, plate shape and chip-former geometry. An example carbide insert and its four remarkable features are shown in Figure 1.

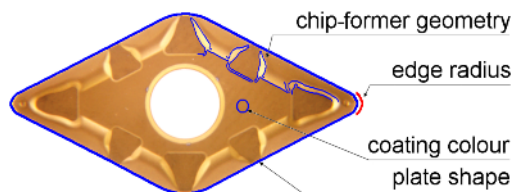


Fig. 1. A carbide insert and its four features.

To satisfy the quality requirements of the customers, there are several measurement and testing tasks in the life cycle of carbide inserts. However, in some production steps, the conformity test regarding the plate type is done manually. It causes a statistic increase of errors, which

depending on the sorting or inspection tasks could be 5 to 35 percent [1, 2].

For example, due to the extensive preparations and the long processing times, different production lots of inserts are combined for an economic and reliable coating. Currently manual insert tests are used for the unloading of the coating machine. It is cost-intensive and involves a risk of interchanging for the subsequent packaging.

Generally a carbide insert type with a false edge radius causes dimension fault by machining, an inappropriate chip shape is formed by using a false chip-former geometry and an incorrect or erroneous coating leads to increased tool wear. Thus, this series process is negatively affected and it causes unnecessary costs.

Therefore, the main objective of this research project is to develop a machine vision system for inspection of coating colour, measurement of the insert edge radius as well as classification of the plate shape and chip-former geometry. This prototype should realise a fast, robust and automated measurement and inspection of carbide insert in the production line.

2. Machine vision system

The following section presents the development of the hardware system as well as the implementation of the image processing for the carbide insert inspection.

2.1 Hardware system

The developed prototype consists of the following hardware modules: illumination unit, camera/optic-system and mechanical system.

The illumination has a decisive influence on the image quality of the test inserts and is important for the performance of a machine vision inspection. To record all

the necessary information for the different measurement and classification tasks, the illumination concept of the insert inspection system employs a combination of three different lighting types (Figure 2). The diffuse LED ring light as bright-field illumination provides a homogeneous illumination of the entire insert without disturbing reflections on the surface, which is a prerequisite for a classification of the coating colour. By means of an LED ring light as dark-field illumination, a significant highlighting of chip-former geometry is enabled. The use of an LED-based transmitted light illumination ensures a clear outer contour of the insert.

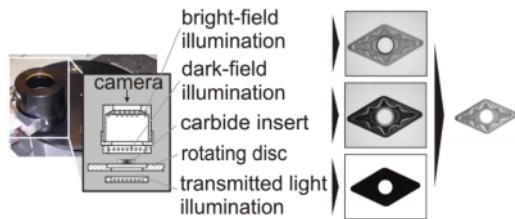


Fig. 2. Illumination unit developed at WZL.

For this project, a colour camera with a $1/2''$ CCD chip and a resolution of 1280 x 960 pixels is selected, which provides an enough area of the field of view (31 mm x 24 mm) and a fine pixel resolution ($22.7 \mu\text{m}$).

To get more space for components of further possible automation and to reach a sufficient depth of field, a working distance up to 400 mm is selected for this machine vision system of insert inspection.

Corresponding to this working distance, a zoom lens with an adjustable focal length of 17.5 mm to 105 mm and an aperture setting of 1.8 to 16 is used in this prototype, which allows a flexible image acquisition for the insert inspection.

The necessary depth of field is set to 2 mm for the insert inspection, with which from the thinnest to the thickest insert of the representative sets can be pictured sharply.

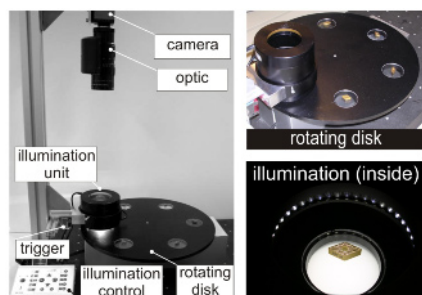


Fig. 3. Machine vision prototype for insert inspection.

To simulate an inline inspection of carbide inserts in the production line, a practically relevant mechanical system is designed and implemented (Figure 3). The inserts are fed to the view field of the fixed mounted camera/optic-system by a motorized rotating disc, in which six

plexiglass windows are embedded. In this way the supplied insert can be grabbed with both reflected and transmitted light. A reflexion light sensor, which is associated with the rotating disc, is also integrated in the prototype as an external trigger for the camera.

2.2 Image processing

The basic image processing tasks are the following: image acquisition, segmentation, inspection of coating colour, measurement of the edge radius and classification of plate shape and chip-former geometry. In the following, the goal of each task and the necessary image processing steps are described in detail.

2.2.1 Image acquisition

The image of a carbide insert is acquired with all the three illuminations: bright-field, dark-field and transmitted light (Figure 2). The camera and the insert handling system are synchronised by the trigger. As the insert comes into the camera view field, the trigger sends an impulse to the camera and releases image acquisition. As a result, a well focused insert image is provided. The background of the image is illuminated homogeneously, which is helpful for the subsequent insert segmentation.

2.2.2 Segmentation

After the digital frame capture, the insert is separated from the image background. Since the closed outer boundary of carbide insert represents sharp discontinuities in the image, an edge based segmentation method is used. After the edge detection, the outer contour of the insert, corresponding to the boundary of the largest connected region, can be robustly identified and extracted.

2.2.3 Inspection of coating colour

For extraction of features that represent the colour information a circular region of interest (ROI) is defined, which is automatically placed on a plateau that covers only the coating colour and contains no chip-former geometry.

Preliminary studies show that the HSV colour model (hue, saturation and value) is suitable for a clear separation of the four prevalent coating colours (gold, silver, copper and black). For extraction of the colour feature vector, the RGB image delivered by the colour camera is converted in the HSV colour space. The averages of these three HSV colour values within the above defined ROI are calculated as a feature vector.

Due to its quick and easy expandability for further colour classes, the nearest neighbour classifier is selected for the classification of the insert coating colour [3].

2.2.4 Measurement of edge radius

For measuring the radius an auxiliary arc is drawn which is concentric to the edge radius of the insert. From the auxiliary arc a line search method arranges radially

extending search lines equidistantly to find the insert edge points (Figure 4, left).

The edge points, namely the intersection points of search lines with the insert edge, are located by analysing the gray-value profile of the edge. The gray-value profile of an insert edge is represented by six pixels (Figure 4, right). The gray-value profile between these sampling points is approximated by an interpolation using a polynomial of 5th degree, whose median inflexion point describes the location of the edge point effectively. Since the inflexion point lies usually between two pixels, the edge points are determined in subpixel accuracy.

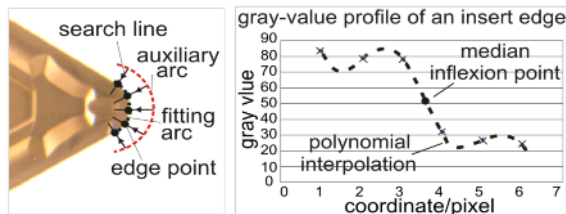


Fig. 4. Algorithmic of edge radius measurement.

All the edge points found by the line search method are fitted with a circular arc by applying the least squares method [4]. The radius of the fitted arc corresponds to the desired edge radius of the insert.

The calculated edge in pixel is converted by the calibration factor of the used camera/optic-system to the standard metric unit. By performing the camera calibration and compensation of optical distortion with the method of Zhang [5], the calibration factor of the machine vision prototype is determined with a master insert, whose edge radius is measured by a contour graph as reference.

2.2.5 Classification of insert geometry

For the classification of present plate shape and chip-former geometry of the carbide insert, an approach is developed on the basis of the SIFT (scale-invariant feature transform) method [6].

The SIFT method is computation-efficient, invariant to scale and rotation variety and relatively robust to illumination and viewpoint changes [7]. Because of these characteristics the SIFT method can be employed in the insert inspection system for a real-world application, by which insert images captured from production line appear enlarged, contracted and rotated.

There are three main considerations to use SIFT method in this application. After some key points in position and scale of the image are localized, a feature vector is formed from a particular local image region around each key point, which builds a distinctive and concise description of this key point. Based on these detected key points and extracted feature descriptors, the test insert is identified with an object matching method.

In order to reduce the computation complexity, based on the fact that the chip-former geometry of inserts is

ordered axially symmetrical, its feature is measured only with a quarter of the insert image (Figure 5, left).

Key point detection

In order to create feature vectors, which describe the input insert scale invariant, the key point detection is completed in the scale space, which represents simultaneously all the possible scales of the image structure according to the scale space theory [6].

The scale space of the input image of the carbide insert is defined as a function produced from the convolution of a Gaussian with various scales.

Key locations are defined as local maxima and minima of the result of difference of Gaussians function applied in scale space (Figure 5). Each confirmed key point is used to generate a feature vector that describes the local image region.

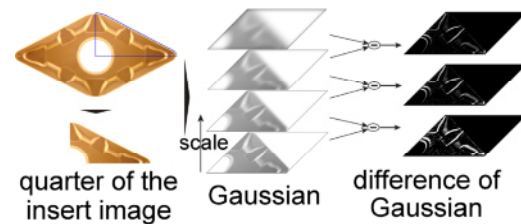


Fig. 5. Key point detection of the SIFT method.

Feature descriptor

The feature descriptor of a key point is created in a neighbourhood region around the key point location. The gradient magnitude and orientation at each image sample point in this region is computed (Figure 6, left).

Before descriptor conformation, to each key point a consistent orientation based on local image properties is assigned. The gradient orientation at each pixel is rotated relative to this key point orientation and therefore the SIFT method achieves invariance to image rotation [6].

An orientation histogram, which has eight directions, is created by summarizing the samples over each 4x4 subregion (Figure 6, middle). These added samples are weighted by a Gaussian window, indicated by the overlaid circle.

The descriptor is formed from a vector containing the values of all the orientation histogram entries, corresponding to the lengths of the arrows in the middle of Figure 6. In this way a SIFT feature vector is generated and assigned to each key point.

An insert quarter with all detected key points and the corresponding feature descriptors is visualised on the right side of Figure 6.

Matching

The classification of plate shape and chip-former geometry is performed by matching each key point independently to the database extracted from training images. For this matching the Euclidean distance between corresponding feature vectors is calculated. By

thresholding or applying the nearest neighbour distance ratio method (NNDR) to this distance the best candidate match for each key point is identified [6].

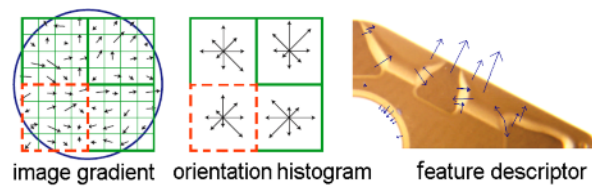


Fig. 6. Feature descriptor of the SIFT method.

3. Experimental results

3.1 Test results

We evaluate the inspection method on real carbide inserts, which have different geometries from different manufacturers. An example test set is given in Figure 7.



Fig. 7. A test set of carbide inserts.

The result for the inspection of the coating colour is that all the inserts are assigned to the correct colours. So that there is a classification rate of 100% for the used samples. A detection performance for the classification of the plate form and the chip-former geometry can be estimated from a sample of 336 real tests at a height of above 92%.

3.2 Measurement uncertainty

The uncertainty of the edge radius measurement on the calibrated machine vision system is also evaluated.

Based on the German guideline VDA 5 [8], the inspection equipment applicability of this machine vision system is validated, by which the smallest testable tolerance of the edge radius is calculated to be 0.18 mm. According to the standard ISO 6987 the nominal size of the edge radius has a tolerance of 0.2 mm. Thus, the developed machine vision system can be classified after the VDA 5 as suitable for edge radius measurement.

3.3 Performance evaluation

In this project, we also develop a software tool, similar to the method proposed in [7], which quantitatively analyses the performance of the methods that compute the local feature descriptors for inserts observed under different viewing conditions.

Our experiments show, as concluded similarly in [7], that the SIFT descriptor is more distinctive than other local feature descriptors and therefore appropriate to characterize the carbide inserts for classification of the plate shape and chip-former geometry.

For example, in Figure 8 it is to observe that the SIFT descriptor performs better than a moment-based local feature descriptor [7], because the SIFT descriptor gives a higher recall for any precision. It means that more detected key points are correctly matched and furthermore the local image regions of the test insert are described more distinctively. As shown in Figure 8, using of different matching strategies, thresholding or NNDR, has also an important influence on the classification result.

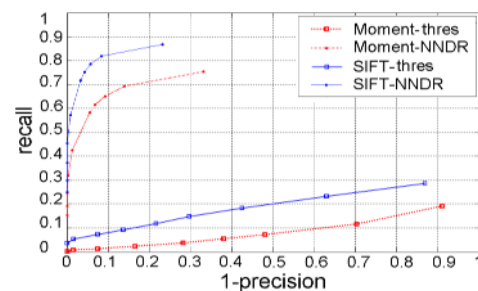


Fig. 8. Performance evaluation of local descriptors.

4. Summary

This paper describes the development of a machine vision system for an automated inline inspection in carbide insert production. The requirements and solutions of the hardware and software components are represented. Test results on real inserts show that the proposed system can achieve robust performance for inline insert inspection.

References

- [1] Pfeifer T., (2002) Production metrology, Oldenbourg.
- [2] Hermes R., (2007) Entwicklung flexibler Bildverarbeitungsketten zur Klassifikation und Verschleißmessung an Wendeschneidplatten, dissertation, RWTH University.
- [3] Waszkewitz P., (2006) Machine vision in manufacturing: handbook of machine vision, pp. 693-774, Wiley-VCH.
- [4] Jähne B., (2002) Digital image processing, Springer.
- [5] Zhang Z., (1999) Flexible camera calibration by viewing a plane from unknown orientations: Proceedings of International conference on computer vision.
- [6] Lowe D., (2004) Distinctive image features from scale-invariant keypoints: Intern. journal of computer vision, 60, 2.
- [7] Mikołajczyk K., Schmidt C., (2005) A performance evaluation of local descriptors: IEEE transactions on pattern analysis and machine intelligence, 10, 27, pp. 1615-1630.
- [8] VDA 5, (2003) Qualitätsmanagement in der Automobilindustrie. Prüfprozesseignung. Verband der Automobilindustrie e.V. (VDA), Germany.

Assembly Tolerance Analysis including Flatness: Using Virtual Mating Plane

Tang Shuilong¹, Yu Jianfeng¹, Li Yuan¹ and Yang Haicheng^{1,2}

¹ Ministry of Education Key Lab of Contemporary Design& Integrated Manufacturing Technology, Northwestern Polytechnical University, Xian 710072, China

² China Aerospace Science and Technology Corporation, Beijing, 100048, China

Abstract. Fits of flat surfaces is one of the most popular ways for parts assembly. In order to take the flatness into account during the assembly tolerance analysis process, a virtual mating plane (VMP) is established. With micro-motion plane, a mathematical definition of the VMP using three various parameters to describe its characteristics is presented. Based on the VMP, the flatness could be decomposed into translation and rotation of the part to assemble in the following step under the reference coordinate system (RCS). The translation is defined by the flatness tolerance and the rotation by the flatness tolerance and the mating plane size. Then the global coordinate system (GCS) of the assembly is established, the rotation matrix (RM) is used to represent the parts' position. And a vectorial dimension chain is constructed to finish the assembly tolerance analysis. Finally, an aircraft wing sub-assembly is chosen to validate the methodology.

Keywords: Virtual Mating Plane(VMP); Micro-motion Plane (MIMP); Flatness; Tolerance Model

1. Introduction

Assembly tolerance analysis is a quite important and efficient way to validate the rationality of the tolerance design, prevent product quality problems and improve the product assembly accuracy. It has become a hit among researchers worldwide and it has given birth to large fruits too.

Skowronski^[1] presented Monte Carlo simulation for tolerance analysis. Bjorke^[2] and Shui_Shun Lin^[3] established a tolerance analysis model based on beta distribution. Jeffrey G. Dabling^[8] carried out research on three dimensional assembly kinematics tolerance analysis incorporating geometrical variation. Elisha Sack and Min-Ho Kyung^{[4]-[6]} proposed a kinematics tolerance analysis algorithm with parameters for mechanical systems of high kinematics pairs. These researchers solve the problems in their particular situation. But they merely deal with dimension tolerance. B. K. A. Ngoi^[9] presented a “catena” method for assembly tolerance stack analysis including geometrical tolerance, but he did not take the rotation effect of the flatness into consideration.

The location and form tolerance can not be ignored because of its effects on product accuracy, especially for the complex product such as aircraft which has higher quality requirement. So the virtual mating plane (VMP) is established to decompose the flatness of the fitting plane. The translation and deflection of the flatness can be mapped to the dimension chain to finish the tolerance analysis of the plane-fit assembly.

2. The Virtual Mating Plane

It is obviously that the two mating planes would totally contact if they are flattening enough. However, if one of them is not flattening enough or both are not, the real fitting of the two planes would be point-to-plane or point-to-point. A fitting plane that pass through these contact points can be established to finish the assembly. And the plane is defined as the virtual mating plane (VMP). Figure 1 shows the two fitting planes with virtual mating plane.

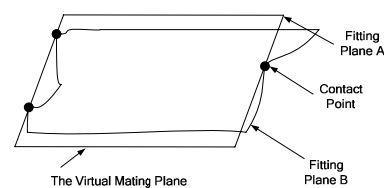


Fig. 1. Plane fits including flatness

According to the ASME tolerance standard specification, the tolerance zone is the intermediate zone defined by two parallel planes with special distance. Its position and direction can both vary. Figure 2 shows us the flatness tolerance zone. Absolutely, the deformation of the real surface would not exceed the tolerance zone. And the upper plane of the tolerance zone is the extreme position of the virtual mating plane. Therefore, the position and direction of the virtual mating plane can be obtained via the flatness tolerance zone.

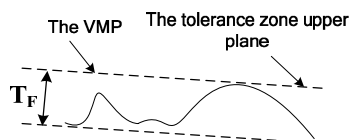


Fig. 2. The flatness tolerance zone and the VMP

The variation between the virtual mating plane and the idea plane is always quite minor in the real assmbly process. So the micro-motion plane with three parameters is introduced to difine the virtual mating plane in a mathematical way. The VMP’s position and direction can be obtained by calculating these parameters.

2.1 The Micro-motion Plane

In order to define the micro-motion plane (MIMP), the reference coordinate system (RCS) is established firstly. The Z axis is always along the normal direction of the micro-motion plane but not parallel to it. Generally, a plane has two degrees of freedom (DOF) in rotation and one in translation. By restricting the three DOFs, the position of the MIMP in the RCS is confirmed. So the MIMP can be defined by three independent parameters. The three parameters which defines the MIMP in Fig. 3 are:

- d_z , the intercept of the MIMP in the RCS;
- θ_x , the included angle of the MIMP to the X axis of the RCS;
- θ_y , the included angle of the MIMP to the Y axis of the RCS.

The tilt angle and intercept of the plane in Fig. 3 all have positive value. The MIMP can be expressed by Eq. (1). (X, Y, Z) stands for any point in the reference coordinate system.

$$Z = X \tan \theta_x + Y \tan \theta_y + d_z \tag{1}$$

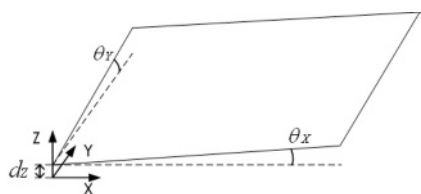


Fig. 3. The parameters of MIMP

2.2 The Reference Coordinate System(RCS)

It is the basis to establish a proper reference coordinate system for mathematical representation of the virtual mating plane. In the coordinate system, the variation of the virtual mating plane can be totally described. The flatness is the variation of the substrate’s profile height to the idea plane. It describes the smoothness of the part’s real surface.

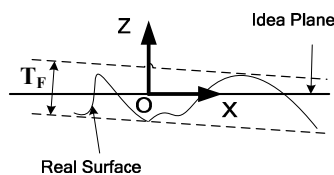


Fig. 4. The reference coordinate system

So, the reference coordinate system should lay on the idea plane of the part’s real surface. The XY plane is generally coincident to the idea plane, the Z axis is parallel to the normal direction and the original point can be any point on the idea plane. Figure 4 shows the reference coordinate system.

2.3 Parameters of The VMP

Figure 5a shows a solid part and its dimensional tolerance is T_s . The dimensional tolerance represents the location variation range of the part’s upper surface. Figure 5c shows the front view of the part’s flatness tolerance zone and its extreme position. According to the front view, the idea plane of the upper plane is the diagonal plane of the flatness tolerance zone.

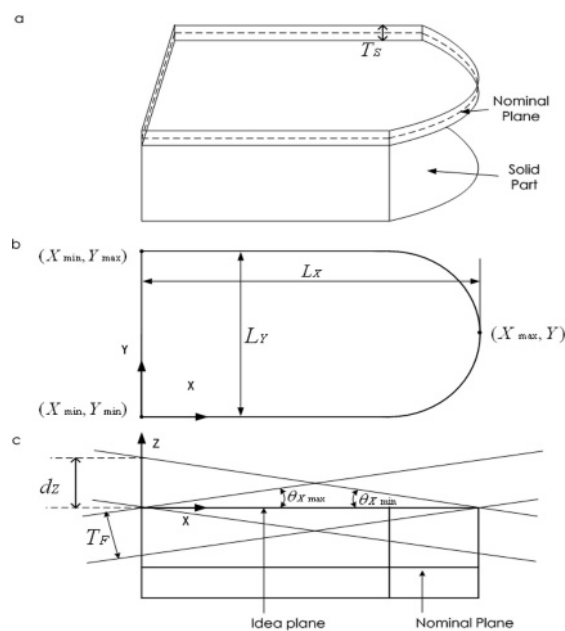


Fig. 5. a) Solid part with dimensional tolerance; b) Top view of dimensional tolerance zone; c) Front view of dimensional tolerance zone.

2.2.1 The Rotation Parameter

According to Fig. 5, in order to calculate the maximum rotation angle $\theta_{x\max}$ and the minimum rotation angle $\theta_{x\min}$, we need L_x which is the distance along the X axis between the two extreme points in the reference coordinate system. Similarly, for calculating $\theta_{y\max}$ and $\theta_{y\min}$, L_y is the distance along the Y axis between the

two extreme points. As shown in Fig. 5b, L_x can be obtained by formula:

$$L_x = X_{\max} - X_{\min} \quad (2)$$

According to geometric computation, the minimum deflection angle can be obtained.

$$\theta_{x \min} = \sin^{-1} \frac{T_F}{X_{\min} - X_{\max}} \quad (3)$$

In the same way, we can get the maximum deflection angle.

$$\theta_{x \max} = \sin^{-1} \frac{T_F}{X_{\max} - X_{\min}} \quad (4)$$

Therefore, the deflection angle of the virtual mating plane around axis Y can be determined.

$$\sin^{-1} \frac{T_F}{X_{\min} - X_{\max}} \leq \theta_x \leq \sin^{-1} \frac{T_F}{X_{\max} - X_{\min}} \quad (5)$$

Similarly, the deflection angle of the virtual mating plane around axis X can be determined.

$$\sin^{-1} \frac{T_F}{Y_{\min} - Y_{\max}} \leq \theta_y \leq \sin^{-1} \frac{T_F}{Y_{\max} - Y_{\min}} \quad (6)$$

2.2.2 The Translation Parameter

It is approximately true that $\cos \theta_x = 1$ because the deflection angle θ_x of the virtual mating plane is quite small. So the intercept of the virtual mating plane on the Z axis can be obtained by the following formula.

$$d_z = \frac{T_F}{\cos \theta_x} \approx T_F \quad (7)$$

3. Assembly Tolerance Analysis Based On VMP

Dimension chain is the most typical methodology for tolerance analysis. In this section, a vectorial dimension chain is established. The translation and rotation of the virtual mating plane in the reference coordinate system is mapped to the dimension chain.

3.1 The Global Coordinate System

The global coordinate system is a three-dimension coordinate system with a special point on the part as its origin. In the paper, it serves as a basis for the analysis and computation of assembly tolerance.

As mentioned in the above sections, the virtual mating plane translates and rotates from the idea plane. This makes the position of the parts which are to assemble in the next steps changing. That is to say, the tolerance accumulation direction would deflect. In order to describe the parts' spatial position and the tolerance accumulation direction variation, the global coordinate system (GCS) is necessary. In the GCS, the composing loops of the vectorial dimension chain can be located.

3.2 The Rotation Matrix

The rotation matrix describes the space pose of the parts and the dimension chain loops in the assembly global coordinate system. The reference coordinate system is introduced because of the considering of the deflection of the parts caused by the flatness of fitting planes. The rotation matrix is made up of two portions: the rotation matrix RM_{PL} describing the deflection of the part in the reference coordinate system and the rotation matrix RM_{LG} describing the deflection of the reference coordinate system relative to the global coordinate system. The product matrix of RM_{PL} and RM_{LG} represents the part's space pose in the global coordinate system.

$$RM_{PG} = RM_{PL}RM_{LG} \quad (8)$$

Actually, the rotation of the plane fitting parts would affect the space position of parts assemble in the following steps. It is called the rotation accumulation which is shown in Fig. 6. And the reference coordinate system of each part can be determined and calculated before the tolerance analysis procedure. So the space pose of the parts can be determined by the following formula in the actual analysis process.

$$RM_{PG} = RM_{LG} \prod_{j=1}^i RM_{PL}^j \quad (9)$$

3.2 Mapping of The Flatness to The Dimension Chain

As mentioned above, the flatness can be divided into translation movement and deflection movement. The translation movement can be treated as the composing loop of the dimension chain directly. It involves in the tolerance accumulation analysis. The deflection movement makes the following assembly parts deflecting, and the deflection angle is determined by the rotation matrix RM_{PG} . A typical vectorial dimension chain is shown as Fig. 6.

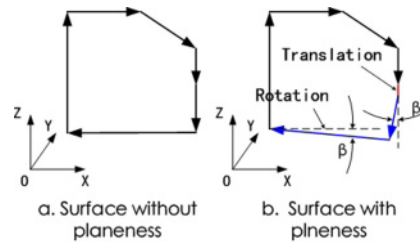


Fig. 6. The vectorial dimension chain

The assembly tolerance analysis is carried out according to the following formula after the establishment of the vectorial dimension chain.

$$\vec{A}_\Sigma = \sum_{i=0}^n \vec{A}_i \quad (10)$$

4. Case Study

Figure 7a shows an assembly drawing of a special aircraft wing. In the assembly, part A and part B fit by two planes (plane A and plane B) which belong to separate part. And the relative position from point C to the base plane of part A must be guaranteed after the assembly. The tolerance of the distance is about ± 0.13 as designed in the engineering job. Because of the length along the axis Y is far larger than that along the axis X, the deflection angle θ_x is far larger than θ_y according to the deflection angle calculating formula. Therefore, only the deflection angle around the Y axis is taken into consideration in this case. Thus, the space vectorial dimension chain is converted to the vectorial dimension chain in the coordinate plane XOZ. Figure 7b shows the vectorial dimension chain based on the part dimensions.

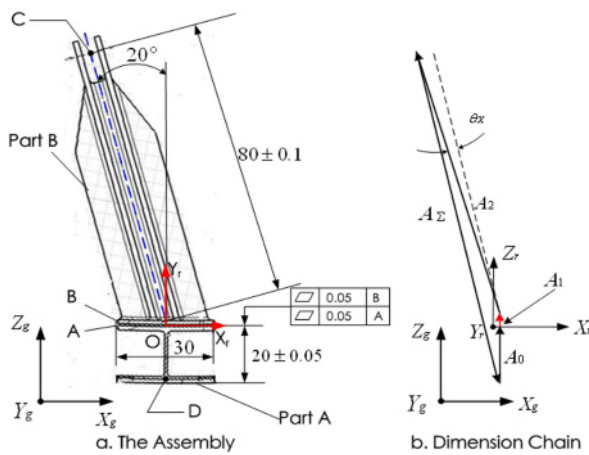


Fig. 7. Assembly case

For tolerance analysis, it is necessary to establish the assembly's global coordinate system $O_g X_g Y_g Z_g$ and the reference coordinate system $O_r X_r Y_r Z_r$ at the fitting plane of part A and part B. Obviously, the rotation angle of the reference coordinate system relative to the global coordinate system equals zero. The dimension loop A_1 represents the translation motion when the flatness tolerance of plane A and plane B is decomposed. It serves as the composing dimension chain loop directly. The basic dimension of the loop is zero, and the tolerance equals the flatness. θ_x represents the deflection caused by the flatness. The deflection makes the A_2 loop deflecting.

Thus, the rotation matrix of part B under the reference coordinate system is:

$$RM_{Pl} = [\theta_x, \theta_y, \theta_z]^T$$

$$\text{And, } -\sin^{-1} \frac{1}{300} \leq \theta_x \leq \sin^{-1} \frac{1}{300}, \theta_y = 0, \theta_z = 0.$$

The assembly tolerance analysis of this case is carried out using Monte Carlo simulation according to the vectorial

dimension calculation method. The probability of the close loop (desired dimension) meets the design requirement is about 82.001% when taking the flatness of the fitting plane into consideration. It is much smaller than the probability (97.482%) that not taking the flatness into account. The analysis result approximately agrees with the actual conditions. The assembly accuracy can not be ensured preferably and force assembly is frequently needed because the flatness of the fit planes was not taken into consideration during the design procedure. As a result, the tolerance should be reassigned to reduce the tolerance of some special part.

5. Conclusion

In order to meet the increasing accuracy requirement, we have to take the location and geometrical form tolerance into account. The flatness is divided into translation movement and deflection movement of the fitting part using the virtual mating plane (VMP). The translation and deflection are mapped to the vectorial dimension chain. It makes the coupling analysis between flatness and dimension tolerance becoming reality. The analysis result demonstrates the feasibility of the methodology. Meanwhile, determining the position of the assembly parts in the three dimensional space and establishing the vectorial dimension chain for tolerance analysis provides some experience to the disposal of other types of location and geometrical form tolerance.

References

- [1] Skowronski V Jt, Turner J U. Using monte-carlo variante reduction in statistical tolerance synthesis [J]. Computer-Aided Design, 1997, 29(1): 63-69.
- [2] BJORKE O. Computer-Aided Tolerancing [M]. New York: ASME Press, 1985.
- [3] Lin Shuishun, Wang Hsu-pin, Zhang Chun. Statistical Tolerance Analysis Based on Beta Distribution [J]. Journal of Manufacturing Systems, 1997, 16(2): 150-158.
- [4] Elisha Sacks, Leo Joskowicz. Parametric Kinematic Tolerance Analysis of Planar Mechanisms [J]. Computer-Aided Design, 1997, 29(5): 333-342.
- [5] Elisha Sacks, Leo Joskowicz. Parametric Kinematic Tolerance Analysis of General Planar System [J]. Computer-Aided Design. 1998, 30(9): 707-714.
- [6] Min-Ho Kyung, Elisha Sacks, Nonlinear Kinematic Tolerance analysis of planar mechanical systems[J]. Computer-Aided Design, 2003, 35: 901-911.
- [7] wu Y Y, SHAH J J, DAVIDSON J K. Computer modeling of geometric variations in mechanical parts and assemblies [J]. Journal of Computing and Information Science in Engineering. 2003, 3(3): 54-63.
- [8] Jeffrey G. Dabling. Incorporating geometric feature variation with kinematic tolerance analysis of 3D assemblies. Brigham Young University: Master Dissertation, 2001.
- [9] B. K. A. Ngoi, L. E. N. Lim, P. S. Ang and A. S. Ong. Assembly Tolerance Stack Analysis for Geometric Characteristics in Form Control – the “Catena” Method [J]. Advanced Manufacturing Technology, 1999, 15:292-298.

Inspection of defects in CFRP-Foam Layered structure composite plates of aerospace materials using lock-in thermography

Liu Junyan¹, Wu Song², Wang Yang¹ and Wang Zhilan³

¹ School of Mechatronics Engineering, Harbin Institute of Technology, Harbin, P.R.China

² Aerospace Research Institute of Material & Processing Technology, Beijing, P.R.China

³ Beijing Earth Station, Beijing,

Abstract: Inspection of aerospace components has always been a challenge. Lock-in thermography is an active technique which is popularly being used for the nondestructive evaluation of subsurface defects in composite materials such as carbon-fiber-reinforced-polymer (CFRP) in aircraft structures. CFRP-foam layered structure composite is often used for anti-heat and adiabatic material in aerospace components. In this paper, a finite element analysis (FEA) of 3D heat conduction is developed in order to investigate the behavior of thermal waves in the CFRP-foam layered structure plates with finite thickness under convective and radiate conditions. The FEA simulation is then utilized to predict the magnitude and phase differences produced by CFRP face-sheet subsurface defects to obtain the optimum inspection parameters. The simulation results are compared with the experimental data. The use of optimum inspection parameters of lock-in thermography to detect PVC modeling defects of CFRP-foam layered structure is also presented in this paper.

Keywords: thermal analysis, FEA, Layered structures, non-destructive testing. Introduction

1. Introduction

Infrared thermography has been successfully used as an NDT&E technique in many applications. Contrary to passive thermography, in which the objects or features of interest present naturally a thermal contrast with respect to the rest of the scene; the active thermography requires an external source of energy to induce a temperature difference between defective and non-defective areas in the specimen under examination [1]. In recent years, composite materials became the quickest developed materials for special uses in aerospace and military constructions. The increasingly wider use of these materials is caused by their properties and technologies used for their manufacture. The CFRP-Foam Layered structure, composed of a foam layer between two multi-layer CFRP face-sheets, is very common on aerospace parts, and it is used for anti-heat and adiabatic

components of structures in the extreme working conditions. The typical defects of CFRP-foam layered composites are delimitations and lack of adhesives. These defects can come into play both in manufacturing processing of materials as well as during in-service use of components. The distinct characteristic of the aerospace industry is the importance of inspection during the various stages of fabrication. There is a parallel increasing need for a fast, reliable and economical nondestructive testing and evaluation technique which is where Infrared thermography becomes of greater interest as a diagnostic method for detection of defects in composite materials [2]. The thermographic techniques has been researched to apply to the inspection of subsurface defects in some composites materials, such as GLARE, CFRP, honeycomb and some hybrid composites. The pulse thermography or transient thermography methods are always applied for NDT of composite materials [3-7]. Numerical modeling of composite subsurface defect by pulse thermography has been used to investigate the defect information with specific material configuration [8]. The methodology of pulse phase thermography (PPT) and the associated signal analysis are often used to find subsurface defects [9]. Many defect detection methods have been studied for defect classification, such as neural network, fuzzy analysis, and so on [10].

Lock-in thermography utilizes an infrared camera to detect the surface temperature of a thermal wave propagating into the material and then produces a thermal image, which displays the local variation of thermal wave in phase or magnitude [11-13]. In the Lock-in thermography image, there are differences in amplitude and phase between defective areas and non-defective ones. Hence, lock-in thermography is used to inspect subsurface defects. The thermal wave is very sensitive to the interface between two materials so it is a suitable for the detecting the subsurface defects, determining materials properties and measuring the thickness of

coatings [14]. Some experiments has been carried on the inspection of the subsurface defects of composite materials by lock-in thermography, and the experimental results showed that lock-in thermography is easy and fast operation method for CFRP subsurface defect under 4mm depths [15,16]. The modulated frequency and analysis time are important factors for inspection subsurface defects of composites materials, (CFRP or hybrid composites) by using lock-in thermography. In order to obtain the best inspection result, it is important that the optimum inspection parameters, which can lead to maximum differences between defective area and non-defective ones for given kinds of subsurface defect are used.

This paper presents a theoretical and simulation analysis and experimental investigation of lock-in thermographic inspection of CFRP-Foam Layered structure composites. The finite element model for lock-in thermographic evaluation of plates with finite thickness under convective and radiate conditions is used to analyze the behavior of thermal waves in CFRP-foam layered composites in which defects have been implanted and to obtain the optional inspection parameters. Experiments to verify the simulation results of phase differences between defective areas and non-defective ones and determine the detectivity of lock-in thermographic inspection of CFRP-foam layered composite were performed. From the FEM simulation analysis and experimental investigation, the factors affecting the detectivity are discussed.

2. FEM models

An opaque and three-dimensional plate is considered, the plate is surrounded by air. The front surface of plate is subjected to plane harmonic heat which is sinusoidal law time-variation. The distributed heat flux of heat source is given as following:

$$q_0(t) = \frac{q_{max}}{2}(1 - \cos(2\pi f_e t)) \tag{1}$$

where $q_0(t)$ is the heat flux density, q_{max} is the maximum of heat flux density, f_e is the modulated frequency of external excitation heat flux and t is the time.

The object tested is treated as the solid, and it is analyzed in the system of Cartesian co-ordinates. In the theoretical model, a sample consists of three layers and two different characteristic defects. Defect1 is air and the defect2 is the PVC implanted in the interface between CFRP and foam, whereas all these elements have shapes of parallelepipeds (Fig. 1).

The transient process of the thermal conduction in the object defines areas in the three-dimensional system of Cartesian co-ordinates which can be described with following system of equations:

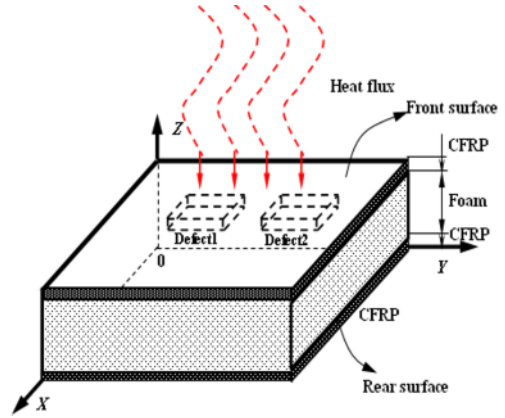


Fig. 1. The 3D scheme of sample with defects

$$\frac{k_{ix}}{\rho_{ix}c_{ix}} \frac{\partial^2 T(X,Y,Z,t)}{\partial X^2} + \frac{k_{iy}}{\rho_{iy}c_{iy}} \frac{\partial^2 T(X,Y,Z,t)}{\partial Y^2} + \frac{k_{iz}}{\rho_{iz}c_{iz}} \frac{\partial^2 T(X,Y,Z,t)}{\partial Z^2} = \frac{\partial T(X,Y,Z,t)}{\partial t} \tag{2}$$

where k_{ix} , k_{iy} , and k_{iz} are the thermal conductivity of the i^{th} layer material on the direction of X , Y , and Z (w/Kg·m); ρ_{ix} , ρ_{iy} , and ρ_{iz} are the density of the i^{th} layer material on the direction of X , Y , and Z (Kg/m³) and c_{ix} , c_{iy} , and c_{iz} are the special heat of the i^{th} layer material density on the direction of X , Y , and Z (J/Kg·°C).

In order to solve this model, the initial conditions, boundary conditions and coherence conditions are required, and these conditions are described by following equations.

Initial condition:

$$T(X, Y, Z, t = 0) = T_{am} \tag{3}$$

where T_{am} is the ambient temperature.

In order to simplify the model solution, the CFRP materials and foam materials are assumed to homogeneous, and the heat flux diffusions in the direction of X and Y are neglected due to the area per layer being greater than the thickness on the boundary surface. Hence, the boundary conditions are divided into the front surface, the rear surface and adiabatic surface.

Boundary condition for the front surface:

$$-k_{1z} \frac{\partial T_{top}(X, Y, Z = L_z, t)}{\partial z} = q_0(t) - h_{top}(T_{top}(X, Y, Z = L_z, t) - T_{am}) \tag{4}$$

Boundary condition for the rear surface:

$$\begin{aligned}
 & -k_{3z} \frac{\partial T(X, Y, Z=0, t)}{\partial z} \\
 & = h_{bottom} (T(X, Y, Z=0, t) - T_{am})
 \end{aligned} \quad (5)$$

Adiabatic condition for other surface:

$$\begin{aligned}
 \frac{\partial T_i(X, Y, Z, t)}{\partial X} & = 0 \\
 X=0, Y=0, L_y; X=L_x, Y=0, L_y
 \end{aligned} \quad (6)$$

$$\begin{aligned}
 \frac{\partial T_i(X, Y, Z, t)}{\partial Y} & = 0 \\
 Y=0, X=0, L_x; Y=L_y; X=0, L_x
 \end{aligned} \quad (7)$$

where h_{top} is the heat exchange coefficient of the front surface ($J/m^2 \cdot ^\circ C$), h_{bottom} is the heat exchange coefficient of the rear surface ($J/m^2 \cdot ^\circ C$), L_x , L_y and L_z are the specimen dimensions.

To the interface per layer of material, the coherence conditions of temperature and heat flux are given as following equations.

$$T_i(X, Y, Z, t) = T_{i+1}(X, Y, Z, t) \quad (8)$$

$$k_{ix} \frac{\partial T_i(X, Y, Z, t)}{\partial X} = k_{(i+1)x} \frac{\partial T_{i+1}(X, Y, Z, t)}{\partial X} \quad (9)$$

$$k_{iy} \frac{\partial T_i(X, Y, Z, t)}{\partial Y} = k_{(i+1)y} \frac{\partial T_{i+1}(X, Y, Z, t)}{\partial Y} \quad (10)$$

$$k_{iz} \frac{\partial T_i(X, Y, Z, t)}{\partial Z} = k_{(i+1)z} \frac{\partial T_{i+1}(X, Y, Z, t)}{\partial Z} \quad (11)$$

Equations (2) to (11) describe the temperature distribution of CFRP-foam layered with harmonic sinusoidal law heat flux stimulated, and the model describes what the thermal stimulus should be to heat a sample as well as an estimate of what inspection parameters can be used to detect the defects in given materials, and how factors affect the defect detectivity as well as what material thickness may be successfully tested.

Lock in thermography detectivity is evaluated by calculating amplitude and phase difference (the difference between defective area and phase of non-defective area) using:

$$\Delta A = A_{defect} - A_{nondefect} \quad (12)$$

$$\Delta Ph = Ph_{defect} - Ph_{nondefect} \quad (13)$$

where ΔA is the amplitude difference of temporal variation, A_{defect} is the amplitude value of the defective area, $A_{nondefect}$ is the amplitude value of the non-defective area, ΔPh is the phase difference between the defective area and the non-defective area, Ph_{defect} is the phase value of the defective area and $Ph_{nondefect}$ is the phase value of the non-defective area.

The 3D heat conduction model is solved by applying commercial FEM software MSC-Marc, and the solution method is implicit integration. The CFRP-foam layered structure composite specimen is a plate which is $200mm \times 200mm \times 54mm$ (CFRP thickness is $2mm$) with two defects that are $40mm \times 40mm \times 0.1mm$. The FEM meshing includes 14784 elements and the MSC-Marc Hex8 hexahedron heat transfer 3D solid element was used to model the specimen as a 3D object (in Fig. 2). The resolution chart program of MSC-Marc is shown in Fig. 3.

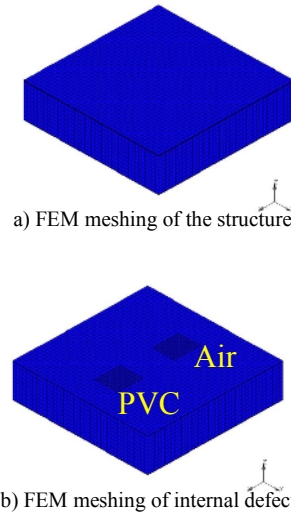


Fig. 2. FEM grid meshing of simulation

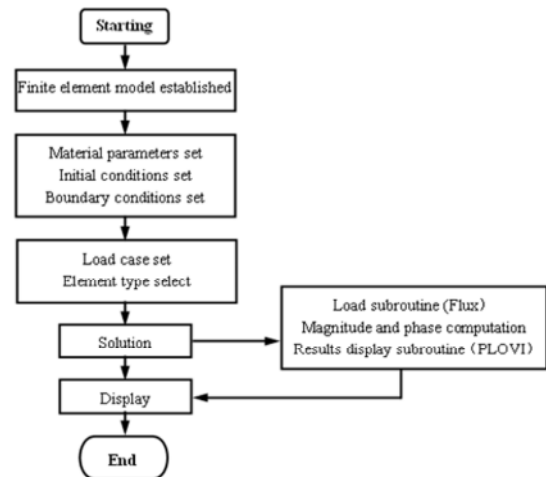


Fig. 3. The resolution chart program of MSC-Marc

3. Experimental procedure

3.1 Specimen

The specimens used in the work are CFRP-foam layered structure composites with PVC implanted in the interface between CFRP sheets face and the foam which is used to model the lack of adhesives defects. The CFRP sheets face thickness of each specimen is 2 mm, and specimens are shown in Fig. 4.

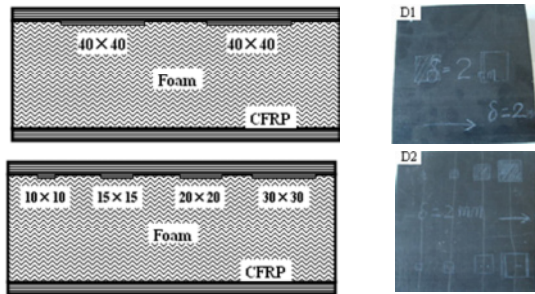


Fig. 4. Test specimens

3.2 Experimental set up

The schematic diagram and experimental set up is shown in Fig. 5. Two lamps are used to apply an external excitation heating source. A signal source generates the sine-wave type signal which is used to control the power amplifier to make the light heat flux change according to harmonic sine-wave signals.

The analysis material properties used in the model are given in Table 1. The boundary heat exchanged coefficient and the initial temperature used in model are listed in Table 2, and the simulation and experimental parameters are listed in Table 3 and Table 4.

Table 1. Thermal properties of materials [17]

Material	Heat conductivity (W/m ² °C)	Special heat (J/Kg.°C)	Density (Kg/m ³)
CFRP	0.8	1200	1580
Air	0.07	1007	1.1774
PVC	0.14	1300	1000
Foam	0.033	1200	140

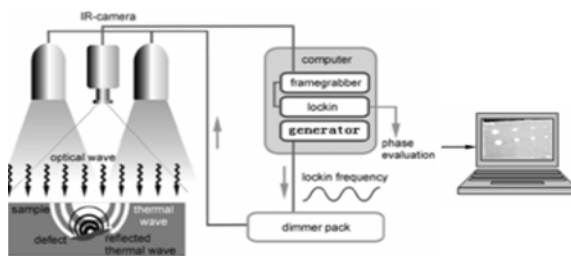


Fig. 5. The schematic diagram and experimental set up

Table 2. Boundary and initial conditions parameters

$h_{top}(W/m^2K)$	$h_{bottom}(W/m^2K)$	$T_{am}(K)$
12.2	11.8	300

Table 3. Simulation and experimental parameters

Modulated frequency f_e (Hz)	0.030	0.042	0.085
Sample analysis periodic numbers Pe	1	2	3
Heated source power P(W)	2000		

Table 4. Simulation Parameters

Modulated frequency f_e (Hz)	0.030	0.042	0.085
Sample analysis periodic numbers Pe	3		
Heated source power P(W)	1000	2000	

4. Results and discussion

4.1 Simulation results

The amplitude image and phase image of the simulation can illustrate the modeling defects shape for given analysis periodic numbers and different modulated frequencies from Fig. 6.

For given heated source power, Fig. 7 shows the amplitude difference and phase difference between the central point of a defective area and a non-defective area according to the modulated frequencies and analysis periodic numbers by FEM simulation. From this figure, it can be observed that amplitude and phase differences are not similar for different kinds of defect. For the air defect of CFRP-foam layered composite, maximum amplitude and phase difference can be obtained by using little modulated frequency f_e and more analysis periodic numbers Pe . And for the PVC modeling defect of CFRP-foam layered composite, the inspection parameter of modulated frequency and analysis periodic numbers Pe should be selected as optimum to obtain the maximum phase difference. In the simulation, the modulated frequency $f_e=0.042\text{Hz}$ and analysis periodic numbers $Pe=2$ should be selected as the optimum inspection

parameters for the PVC model defect of CFRP-foam layered composite.

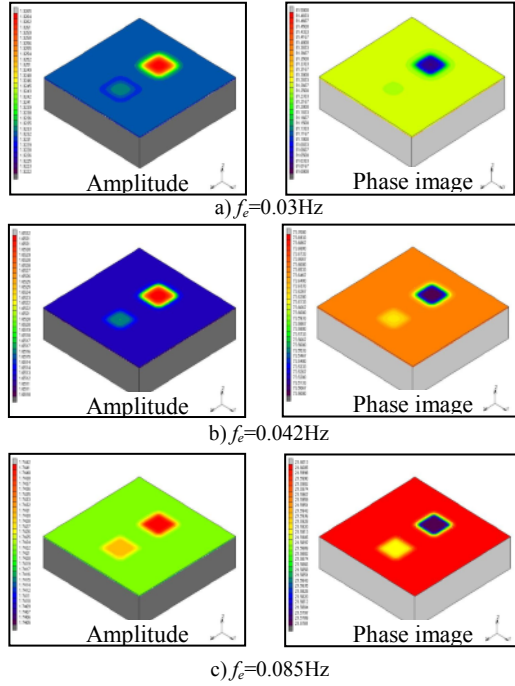


Fig. 6. Amplitude and phase distribution of

For given analysis periodic numbers, the amplitude and phase difference between central point of defective area and non-defective area according to heated source power and modulated frequencies are plotted in Fig. 8. It can be found, the amplitude and phase difference are increased when the heated source power was increased at given modulated frequency.

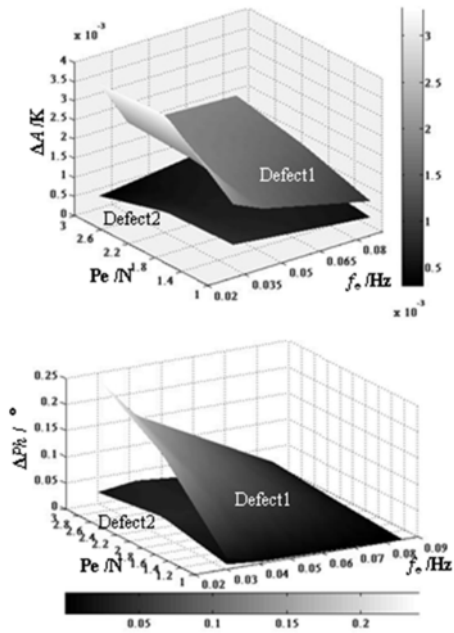


Fig. 7. Simulation results of amplitude and phase difference

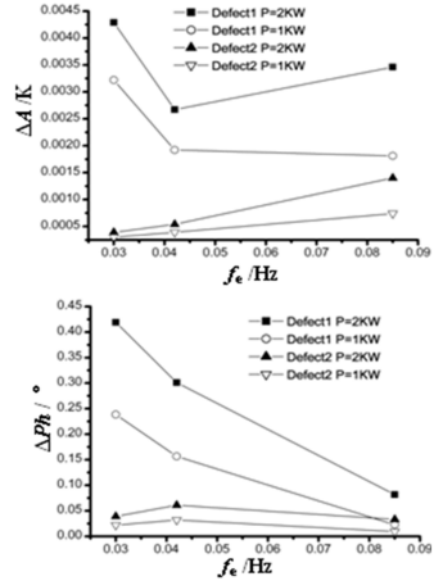


Fig. 8. The effect on amplitude and phase difference by heated source power

4.2 Experimental results

Fig. 9 shows the D1 CFRP-foam layered composite experimental results of amplitude and phase image according to modulated frequencies and analysis periodic numbers for a given heated source power $P=2\text{KW}$. From the figure, the PVC modeling defect shape and location can be easily distinguished from phase image at modulated frequency $f_e=0.03\text{Hz}$ and $f_e=0.042\text{Hz}$, especially, the image contrast is higher in the phase image compared with amplitude image. The PVC modeling defect is almost not identified by amplitude and phase image at modulated frequency $f_e=0.087\text{Hz}$ for all given analysis periodic numbers.

The materials properties, stimulation heat flux, boundary condition and surface emissivity are reference values in FEM simulations, so the phase difference of simulation should be revised by given following equation.

$$\Delta Ph_t = K_M \cdot K_S \cdot K_E \cdot K_B \cdot \Delta Ph \quad (14)$$

where ΔPh_t is the revision phase difference, K_M is the material property coefficient, K_S is the stimulation heat flux coefficient, K_B is the boundary condition coefficient and K_E is the surface emissivity coefficient.

The revision phase difference of FEM simulation for PVC modeling defect is shown in Fig. 10, and the phase difference for D1 specimen experimental results is shown in Fig. 11. From Fig. 10 and Fig. 11, the revision phase difference surface shape is similar to the phase difference surface of the experimental results, and the optimum inspection parameters are obtained such that the modulated frequency f_e is selected as $f_e=0.042\text{Hz}$, and analysis periodic numbers Pe is selected as $Pe=2$, which is used to detect the PVC kind of defect for CFRP-foam

layered composite in lock-in thermography. The FEM simulation provides an effective method to obtain the optimum inspection parameters by using lock-in thermography and avoids the much more experiments to find the optimum inspection parameters in lock-in thermography.

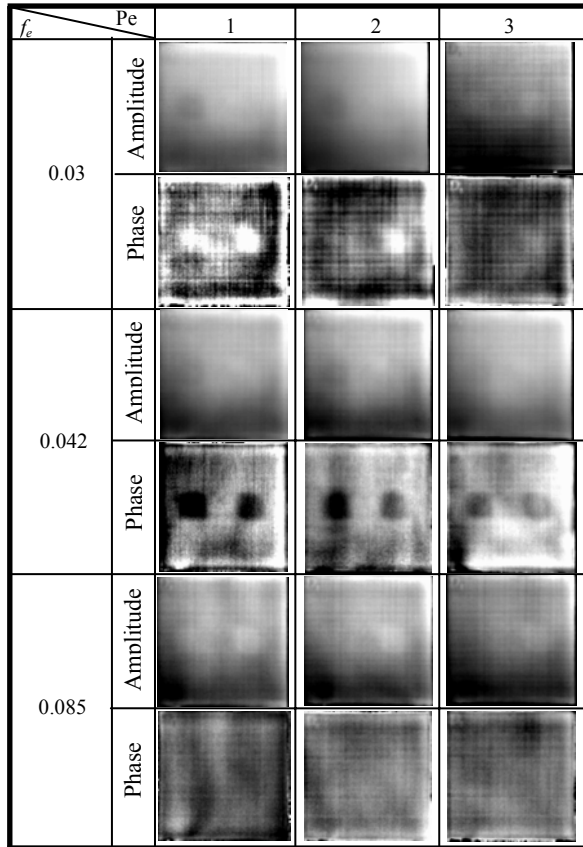


Fig. 9. Experimental results of D1 CFRP-foam

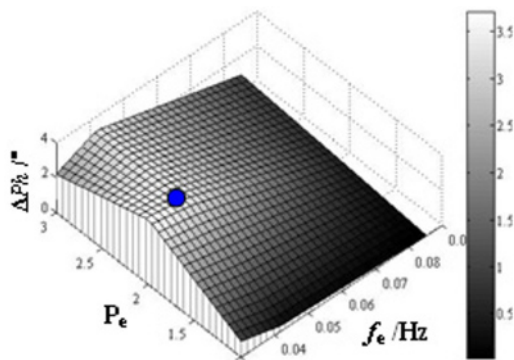


Fig. 10. Revision phase difference of simulation results

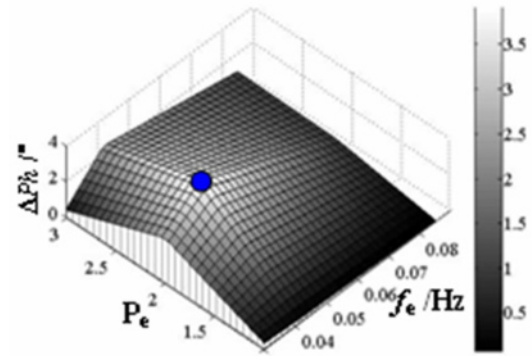
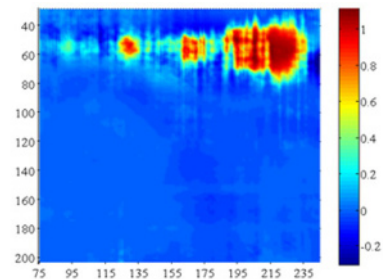
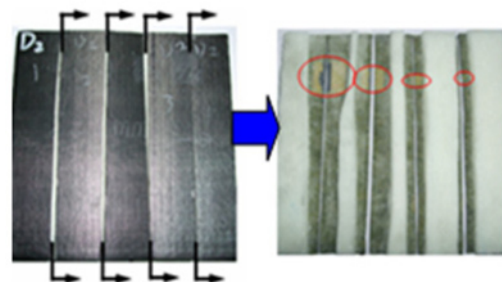


Fig. 11. Phase difference of experimental results



(a) Defect detection result



(b) PVC modeling defect distribution

Fig. 12. Experimental results of D2 specimen

Fig.12 (a) shows the defects detection result of CFRP-foam layered composite D2 specimen under conditions of the optimal detection parameters (modulated frequency $f_e=0.042\text{Hz}$, analysis periodic numbers $P_e=2$, and heated source power $P=2\text{KW}$) by using lock-in thermography, Fig.12 (b) shows the optical image of D2 specimen and the PVC modeling defects distribution. It can be found from the figure 12 that the smallest size PVC defect is active to identify the shape and location in the image under given inspection parameters. Lock-in thermography is an active technique which is used for CFRP-foam layered composite nondestructive evaluation.

5. Conclusion

In this paper, a finite element model (FEM) of 3D heat conduction is developed to investigate the behavior of thermal waves in CFRP-foam layered structure plates with finite thickness under convective and radiated conditions. The FEM simulation is utilized to predict the amplitude and phase differences produced by CFRP sheet-face subsurface defects, which is air and PVC modeling defect. For given CFRP thickness which is 2mm, the optimum inspection parameter is obtained by amplitude and phase difference of the simulation results. The modulated frequency selected should be a small value, and the analysis periodic numbers should be selected of greater value for air kinds of defect by using lock-in thermography. For PVC kinds of defect, the simulation results are similar to the experimental results, the optimum inspection parameters are selected such that the modulated frequency should be selected from 0.04Hz to 0.05Hz, and the analysis periodic numbers is 2 periods for the CFRP sheets face thickness 2mm by using lock-in thermography. The optimum inspection parameters of lock-in thermography are used to detect PVC modeling defects of CFRP-foam layered structure, the small size defects shape and location are satisfied to be identified under conditions of given optimum inspection parameters by using lock-in thermography. IR Lock in thermography is an effective technique for CFRP-foam layered composite nondestructive testing and evaluation.

Acknowledgement

The authors are grateful for the financial support of National Nature and Science Found of China for this research project (60776802/F01) and Supported by the 111 Project (B07018).

References

- [1] Clemete Ibarra-Castanedo, Marc Genest *et.al* Inspection of aerospace materials by pulsed thermography, lock-in thermography and virbothermography: A comparative study. *Thermosense XXIX*, edited by Kathryn M. Knettel, Vladimir P. Vavilov, Jonathan J.Miles. Proc. Of SPIE Vol.6541, 654116 (2007).
- [2] Waldemar Swiderski. Lock-in thermography to rapid evaluation of destruction area in composite materials used in military applications. Sixth International Conference on Quality Control by Artificial Vision, SPIE Vol.5132 (2003)
- [3] R. J. Ball, and D. P. Almond. The detection and measurement of impact damage in thick carbon fibre reinforced laminates by transient thermography. *NDT&E International*, Vol. 31, No. 3, p 165-173, 1998
- [4] V. Dattoma, R. Marcuccio, C.Pappalettere, and G. M. Smith. Thermographic Investigation of sandwich structure made of composite material. *NDT&E International* 34 (2001) 515-520
- [5] N.P. Avdelidis, B.C. Hawtin and D.P. Almond. Transient thermography in the assessment of defects. *NDT&E International* 36 (2003) 433-439
- [6] Nicolas P. Avdelidis, Clemente Ibarra-Castanedo, Zaira P. Marioli-Riga, Abdelhakim Bendada and Xavier P. V. Maldague. A study of active thermography approaches for the non-destructive testing and evaluation of aerospace structures. *Thermosense XXX*, edited by Vladimir P. Vavilov, Douglas D. Burleigh, Proc. of SPIE Vol. 6939, 693918, (2008)
- [7] T.J. Ahmed, G.F. Nino, H.E.N. Bersee, A. Beukers. Heat emitting layers for enhancing NDE of composite structures. *Composites: Part A* 39 (2008) 1025-1036
- [8] M. Krishnapillai, R. Jones, I.H. Marshall, M. Bannister and N. Rajic. NDTE using pulse thermography: Numerical modeling of composite subsurface defects. *Composite Structures* 75 (2006) 241-249
- [9] G. Zauner, G. Mayr and G. Hendorfer. Application of wavelet analysis in active thermography for nondestructive testing of CFRP composites. *Wavelet Applications in Industrial Processing IV*, edited by Frédéric Truchetet, Olivier Laligant. Proc of SPIE Vol. 6383, 63830E, (2006)
- [10] T. D'Orazio, C. Guaragnella and M. Leo, P. Spagnolo. Defect detection in aircraft composites by using a neural approach in the analysis of thermographic images. *NDT&E International* 38 (2005) 665-673
- [11] G.Busse, D Wu and W.Karpen. Thermal wave imaging with phase sensitive modulated thermography. *Journal of Applied Physics*. 1992.01:3962-3965.
- [12] O.Brcitenstein, M. Langenkmp. Lock-in Thermography Basics and Use for Functional Diagnostics of Electronic Components. [M], Springer series in Advanced Microelectronics. Springer-Verlag Berlin, Heidelberg; 2003. P13.
- [13] Liu Junyan, Wang Yang *et.al*. Research on CFRP Materials Nondestructive testing by IR Lock-in Thermography. International Symposium on Photoelectronic Detection and Imaging 2009: Advances in Infrared Imaging and Applications, edited by Jeffery Puschell, Hai-mei Gong, Yi Cai, Jin Lu, Jin-dong Fei, Proc. of SPIE Vol. 7383, 73833U.
- [14] Datong Wu, Gerd Busse. Lock-in thermography for nondestructive evaluation of materials. *Cen. Therm.* (1998): 693-703
- [15] F. Escourbiac, S. Constans, X. Courtois and A. Durocher. Application of lock-in thermography non destructive technique to CFC armoured plasma facing components. *Journal of Nuclear Materials* 367-370 (2007) 1492-1496
- [16] Carosena Meola, Giovanni Maria Carlomagno, Antonino Squillace and Antonio Vitiello. Non-destructive evaluation of aerospace materials with lock-in thermography. *Engineering Failure Analysis* 13 (2006) 380-388
- [17] Xavier P.V. Maldague. *Nondestructive Evaluation of Materials by Infrared Thermography* [M]. Springer-Verlag, London Berlin Heidelberg New York. p23.

Image Processing Methods For Online Measurement In Radial-Axial Ring Rolling

H. Meier^{1,a}, J. Briselat^{1,b}, R. Hammelmann^{1,c}, H. Flick^{1,d}

¹ Chair of Production Systems, Dept. of Mechanical Engineering, Ruhr-University Bochum

² ^a meier@lps.rub.de, ^b briselat@lps.rub.de, ^c hammelmann@lps.rub.de, ^d flick@lps.rub.de

Abstract. The process of radial-axial-ring rolling is a hot forming process that produces rings with high mechanical load capacity. Rings produced using this mechanism are especially deployed as wheel rims for trains, reactor vessels of nuclear power plants, flanges and highly stressed bearing rings, which are used in wind turbines, and have a diameter ranging from 0.1 up to 9 meters. Nowadays, the control uses input data from mechanical- or laser-sensors. For example, the thickness of the rings is measured by the distance between the main roll and the mandrel. The common property of sensors used in conventional controls is the ability to deliver one value per time unit. Therefore, the conventional control cannot detect most of process errors or unintended deformations of the ring. With the research project *Image processing in radial-axial ring rolling* the Chair of Production Systems develops a solution to expand the conventional control with an image processing system, as it is utilized in other manufacturing processes, in order to obtain additional information about the geometry of the rings and about process behaviour to detect processing irregularities immediately they occur.

Keywords: Radial-Axial Rolling of Rings, Image Processing, Manufacturing Control, Metrology and Measurement

1. Introduction

1.1 Radial-Axial Ring Rolling

The process of radial-axial-ring rolling is a hot forming process, used for producing seamless rolled rings.

Rings produced by rolling have a high mechanical load capacity and are typically used as bearing rings, wheel rims for trains, rocket flanges, gearing components for wind turbines and reactor vessels in nuclear power plants. The dimension of these rings reaches diameters up to 9 m, heights up to 2.80 m and weightings up to 60 t (1). The profile of such rings varies from standard squared profiles to complex internal and/or external profiles, which are required for example for turbine components.

Typically workpieces have a temperature of around 1200°C at the beginning of the process. Depending on the process strategy, the properties of the ring-rolling

machine, the material of the ring, and some other factors, the temperature varies during the process (1). Figure 1 shows the typical layout of modern radial-axial ring rolling machines. It contains a stationary main roll and a mandrel, which is moved towards the main roll to reduce the ring's thickness. On the opposite side of the ring two axial rolls reduce the rings height. Because of the constancy of the volume of the material, the ring's diameter grows into the direction of the axial rolls. Thus, the axial pass has to move backwards during the rolling process. Two centering rolls ensure rings remain correctly positioned in the radial-axis ring rolling machine.

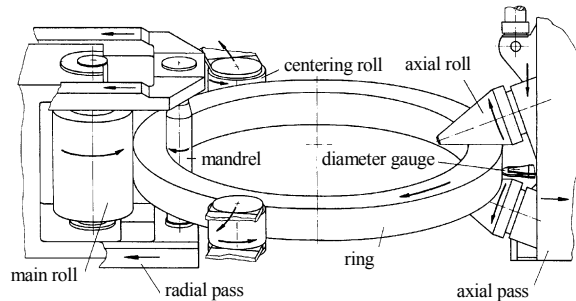


Fig. 1. Principle of radial-axial ring rolling (2)

1.2 Process Errors And Errors Of The Rings Shape

Although ring rolling is a very old and established process, which evolved over 150 years, it is still in the focus of research over the last 40 years (3). The sustained research in this field is caused by the complexity of this process and the consequential difficulty to explain the reasons for process errors and unwanted workpiece deformations, which are often explained by antedated process errors. An example of a typical process error is the fact that sometimes the ring begins to climb upwards in the radial pass during the process for often unknown reasons. Typical defects of form are non-circularity, dishing or conicity.

Process errors are often avoided by using well-known process strategies or are eliminated symptomatically. For example, the mandrel is pitched towards the main roll frequently to avoid the ring climbing, but in consequence the risk for other deformations (such as conicity and non-circularity of the ring) grows (4).

To enhance the economy of manufacture, the industry needs to produce near net-shaped rings (5). Therefore, research in the field of radial-axial ring rolling is, on the one hand, focused on upgrading the properties of the product, mostly by enhancing the repeat accuracy and steadiness of the process, and on the other hand, focussed on enhancing the properties of the radial-axial ring rolling machines (6).

1.3 Process Control

A proper rolling schedule is, in combination with a proper geometry of the blank, essential to achieve the intended geometry of the ring (7). The control of the process uses different inputs. Several data are used by the control of the machine. The information about the desired ring's geometry after finishing the process and information about the geometry of the blank is uploaded to the control. The relation between those two geometries is described in a so called rolling-curve (fig. 2), which describes the relation between the radial and the axial roll closure rate over the whole process. Combined with several other data, for example a time plot of the roll-force (6), this rolling schedule controls the process from its starting to the intended ring geometry. In summary, the process strategy for the rolling of rings is defined before the process actually starts.

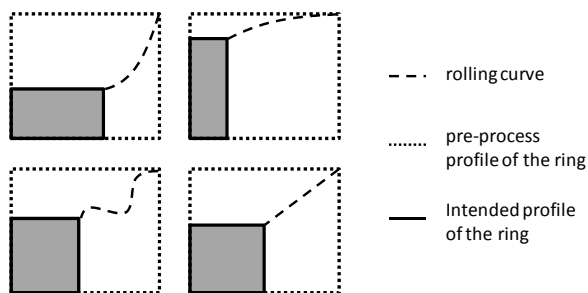


Fig. 2. Different rolling curves for different cross sections and different strategies

Information about the rings' geometry is nowadays measured during the process via mechanical or laser sensors. This data specifies the thickness of the ring, measured as the distance between mandrel and main roll, the height of the ring, measured as the distance between the two axial rolls, and the ring's diameter, measured as the distance between the main roll and a diameter gauge on the opposite side of the ring. Several other sensors, such as pressure gauges and revolution counters complete the sensor system of modern ring rolling machines.

1.4 The task at hand

The common property of sensors used in conventional controls is the ability to deliver one value per time unit. Therefore, with the setup used and adjustment of the sensors, the conventional control cannot detect most process errors or unintended deformations of the ring.

In figure 3, two of the typical problems are represented. Neither the rings non-circularity (a) nor the climbing of the ring (b) can be detected by actual sensor systems reliably.

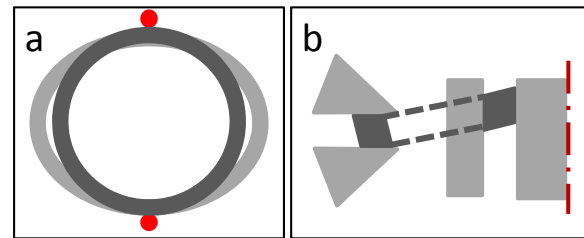


Fig. 3. Typical non-detected problems during the process: non-circularity (a) and climbing of the ring (b)

Today, as mentioned before, most of the existing process errors are avoided by using well known process strategies, using constructional solutions that consider greater tolerances in the dimensioning of the final ring geometry or post-process correction of the ring's form.

Indeed it would be preferable to detect process errors and unwanted deformations of the ring during the process in order to be able to react with an adequate strategy. Therefore it is necessary to attach sensors which deliver additional information about the rings' geometry, the rings' location in the machine, etc.

2. Method Of Resolution

2.1 Image Processing Systems – A Possible Solution

An alternative is given by the application of an image processing system. The advantage of such a system is the fact that one camera can detect a huge amount of information per time unit. Because of the progress in the field of image processing technology, it is expected, that such a system should attain the required accuracy for delivering information usable for ring rolling processes now or in the near future. Furthermore, a great advantage of image processing systems is their flexibility which is achieved by using intelligent software algorithms.

Anyway, image processing systems could enhance the conventional process control in the field of radial-axial ring rolling.

2.2 The Research Project “Image Processing In Radial-Axial Ring Rolling”

Within the research project *Image Processing In Radial-Axial Ring Rolling*, funded by the *Deutsche Forschungsgemeinschaft DFG*, the Chair of Production Systems is at the stage of developing a solution to adapt such a system to a radial-axial ring rolling machine.

The project is divided into two phases. The focus of the first phase is the testing of the measuring capability of image processing systems in the environment of radial-axial ring rolling with its changing lighting conditions and its steam which is for example generated by the descaling of the ring's surface, and the limited space. The second phase will have its focus on the control of the process employing information obtained from the image processing system.

In addition, the first phase deals with different subjects. At the beginning of the research it is necessary to choose adequate image processing components, to develop a concept for the integration of the hardware components into the radial-axial ring rolling machine as well as integration of the software aspects into the existing control software of the ring rolling machine. Finally, the measuring operations will be realized under real industry conditions.

3. State of the Development

The focus of the research project is to test the measuring capability of image processing systems in the field of radial-axial ring rolling and to find out basic questions and answers about the implementation of an image processing system, such as what kind of edge detection delivers the best results or how can different types of cameras or lenses etc. be compared. Also, the image processing system has to be flexible. Thus, different components were chosen for integration into the radial-axial ring rolling machine. The system has an intelligent camera, which contains an image processing processor and is able to deliver evaluated data. Furthermore, the system has other cameras without an integrated processor, so an image processing computer is necessary to evaluate the data from these cameras. Also different lenses are applied to compare the measuring capability of telecentric and non-telecentric lenses.

While the rolling process is running, the position of the ring changes constantly relative to the ring-rolling machine. The ring's midpoint moves with half of the diameter growth in the direction of the axial pass. The ring's outer shell is moving with the full diameter growth in the direction of the radial pass. Therefore, depending on the favoured measuring point, it is not possible to fix the image processing system directly to the radial-axial ring rolling machine. Because of this, a system for moving the cameras, containing linear guides and a stand-alone control unit, had to be developed. The camera-

control system contains linear guides, on which the cameras can be mounted. The motion control is realised via a software NC system and can be connected with the control of the ring rolling machine via EtherCAT, an Ethernet based bus system.

First image processing algorithms for basic measurement functions were developed and tested off-line. The first results of online measurement experiences are now presented: In the first experiences the ring's height was measured to show the basic measuring ability of image processing systems on hot steel rings. In fig.4, the experimental set up is shown.



Fig. 4. Experimental setup: camera focussed on ring

For measuring the ring's height the intelligent camera was kept stationary. Therefore, the area of interest has to be big enough to capture the whole area of the rings destination during the rolling process. Hence, the precision of the measurement results is, without using subpixel-edge detection method, (which uses mathematical interpolation between pixels), limited to 0.66 mm.

In figure 5, the results of two series of measurements are shown. These graphs compare the value of the ring's height measured by the image processing system with the value measured by the conventional sensor system which is integrated into the ring rolling machine. The first graph (measurement 1) contains the results of a process in which the rings thickness and diameter were changed but without reducing its height. The second graph (measurement 2) contains the result of a constant height of the ring at the beginning, and a growing height at the end of the process. Both process strategies are designed for testing the image processing system.

Up to now, the results indicate that the precision of the image processing system with the setup used in the first experiments does not yet reach the precision of the conventional sensor systems. However, it will be improved in the near future as not all parameters have currently been taken under consideration. But the basic capability of these systems for measuring rings during the process has been established.

The absolute value from the image processing system differs around a maximum of eight percent from the value measured by the conventional measuring system, and the trend of the value is the same. The divergence is possibly based on different reasons, which will be the focus of upcoming analyses.

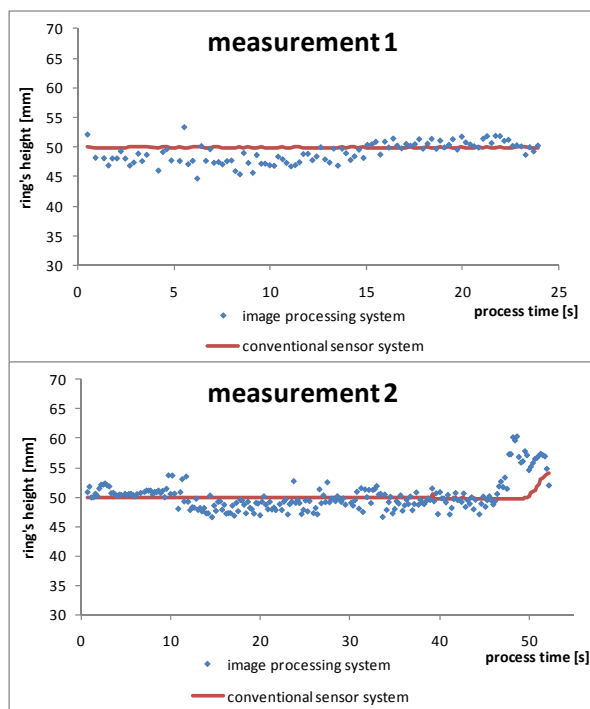


Fig. 5. First results of online measurement

Due to the fact that the rings' temperature, as mentioned before, varies during the process, the brightness of the image varies as well. Therefore, a topic of upcoming research is a dynamic adjustment of binary mapping- and edge-detection parameters. As non-telecentric lenses were used in the experimental setup, there are optical distortions in the images used for measuring the values. Upcoming research will analyse the effectiveness of calculative correction and its difference towards the adaption of telecentric lenses.

4. Summary And Outlook

First experiences prove, that it is actually possible to measure the geometry of the ring during the process of radial-axial ring rolling. In upcoming work, the focus will be on enhancing the precision of the measurement results. It is expected that the image processing system can deliver the missing data for detecting process errors or unwanted ring deformations in real time.

Remaining working points of the first project phase will have their focus on the reproducibility of the measurement results and the improvement of the measurements' accuracy, for example by using the subpixel method for the edge-detection, a closer distance between objective and object, and the application of telecentric lenses. Furthermore, the protection of the image processing hardware against heat, steam and scales and the implementation of dynamic parameter adjustment of image processing algorithms to compensate changing lighting conditions will be part of the focus of the work. The experiences will be repeated with different screens and different types of algorithms to work out the optimal combination of software and hardware components. Finally there will be a focus on the measuring fault and on the improvement of the calibration of the camera system.

The second period of the project will have its focus on the connection between measuring system and process control. A concept for a communication of the process control with the image processing system has to be developed. To assign the information delivered by the image processing system about possible irregularities, boundary conditions have to be defined, e.g. for the rings non-circularity or the height of the ring in the radial pass during the process. Therefore, a theoretic consideration of the process, among others based on existing process simulations, will be within the scope of the research.

References

- [1] Golz J. Prozesssychrone Simulation der Temperaturverteilung in radial-axial gewalzten Ringen mit Rechteckquerschnitt. Bochum (Germany): Shaker; 2008. p. 20,29.
- [2] NN Technologie des Ringwalzens auf Radial-Axial-Ringwalzmaschinen. Thyssen Maschinenbau GmbH Schulungsseminar. P. 13.
- [3] Allwood JM. The development of ring rolling technology. Steel Research 22006; int. 76, No.2/3: 112.
- [4] Lieb A, Wiegels H, Kopp R. Rundheitsmessung an warmgewalzten Ringen. Stahl u. Eisen 1990; 110 Nr. 9: 83-87.
- [5] Lindemann M. Nahtlose Ringe im 20-Sekundentakt. Umformtechnik 2006-2: 27.
- [6] Kneissler A. Multisensorstrategie zur Optimierung des Anwalzverhaltens beim Radial-Axial-Ringwalzen. Bochum (Germany): Shaker; 2008.
- [7] Koppers U. Flexibles Walzen von Ringen mit Profilquerschnitt – Grundlagen. Umformtechnik 1992; 26: 334.

Cognitive Production Metrology: A new concept for flexibly attending the inspection requirements of small series production

T. Pfeifer¹, R. Schmitt, A. Pavim*, M. Stemmer², M. Roloff and C. Schneider³, M. Doro.

¹ Laboratory for Machine Tools and Production Engineering WZL at RWTH Aachen University, Chair of Metrology and Quality Management, Steinbachstraße 19, 52074 Aachen, Germany

² Intelligent Industrial Systems S2i, Federal University of Santa Catarina UFSC, Department of Automation and Systems DAS, Campus Universitário, P.O. Box 476, 88040-900 Florianópolis, Brazil

³ Fundação Centros de Referência em Tecnologias Inovadoras CERTI, LABelectron, Campus Universitário, P.O. Box 5053, 88040-970 Florianópolis, Brazil

* Scholarship holder of the Brazilian CNPq

Abstract. The current trend for product individualisation and customer satisfaction results in a demand for smaller and flexible production series with a considerable diversity of components. This paper discusses the inspection requirements of small series production and presents the new concept of Cognitive Production Metrology (CPM) as an innovative solution to increase the manufacturing efficiency within flexible production lines. This is intended to contribute directly to reducing the complexity of pilot production series, for speeding up the production start time and assuring a maximum quality level for the process and product in dynamic environments. Fundamental tools for the conception of cognitive and autonomous quality assurance systems, such as agent-based and knowledge-based systems, as well as the use of different and combined measurement and inspection systems are introduced in an example scenario at the end.

Keywords: Small series production, cognitive production metrology, sensor data fusion, agent-based and knowledge-based systems, self-optimisation

1. Introduction

Small series production is characterised by different authors in distinct ways [1,2] in what concerns its nomenclature and definition. A common idea can be understood from the different researches in this area [3]: small series production focuses on the manufacturing of a big product variety in a limited period of time, while having a low production volume (possibly unitary). The time for processing a complete production batch is random and the different products have distinct complexity levels, which causes constant changes in the production flow. The big diversity and the continuous introduction of new products in a small series production environment bring a series of problems related to quality assurance, such as [3]:

- lack of predictability about process behaviour and product quality;
- constant change of quality documentation, such as inspection plans;
- increased setup cycles and few disposable products to be used for rigging processes;
- short time to observe and correct the process during production;
- difficulties for re-using information and performing corrective actions;
- lack of data for decision taking.

The major challenge faced by a quality assurance system applied to small series production facilities is to be ready to guarantee the quality level for the first run (“first time right on time”). The goal is to manufacture products with the same adequate quality level from the beginning of the production.

Small series production requires a change of paradigms, because its technical, organisational and economical strategies are totally different from mass production [4]. Therefore, it is becoming increasingly important to develop quality assurance architectures that are modifiable, extensible, reconfigurable, adaptable, and fault tolerant [5].

This work discusses the concept of Cognitive Production Metrology as well as some key technologies that are of high relevance to support its principles.

2. Self-optimisation and the concept of Cognitive Production Metrology

In order to cope with the challenges of small series production, manufacturing, assembly and metrological systems must constantly adapt themselves to dynamic production circumstances. Intelligent systems that offer the capability to react autonomously and flexibly to their surrounding environmental conditions or to the interference of external users/systems, by modifying their goals and adapting their parameters/structure in response to these dynamic factors, are called self-optimised systems [6].

These systems are usually able to learn from their own experiences, which may help in predicting new events and optimising behaviour in future situations. By definition, self-optimisation is characterised by the sequential accomplishment of three steps [6]: 1) analysis of the current system situation, 2) determination of the (new) system objectives, and 3) adaptation of the system behaviour to the new surrounding conditions.

Three main aspects are relevant for conceiving self-optimised technical systems (Fig. 1) [7]:

- **Flexibility and mutability:** to perceive the different relevant external stimuli from the environment and be able to adapt itself to pre-defined or new working situations. Sensor data fusion and agent-based systems are relevant technologies to fulfil these requirements;
- **Autonomy:** to react proactively against the environment changes and guide the system to desired and safe states of operation in an independent way, without the intervention of external operators. Agent-based and knowledge-based systems allow introducing the desired autonomy factor for such technical systems;
- **Cognition:** to be able to learn from its own experiences, take intelligent decisions and respond to the environment in a safe and robust manner. Knowledge-based systems provide adequate tools to represent knowledge and allow reasoning and learning capabilities.

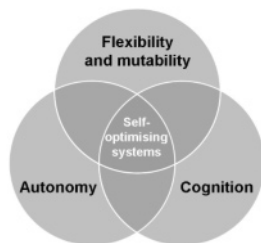


Fig. 1. Flexibility/mutability, autonomy and cognition as basic aspects for the conception of self-optimised systems

Based on the definition of self-optimised systems, the Cognitive Production Metrology (CPM) introduces a

new quality management concept for the small series production. It relies on metrological systems that are able to automatically and independently define inspection tasks (holistic planning) as well as autonomously apply them to a large number of product variants, making use of different measurement and inspection systems. Cognitive software modules undertake the responsibility for the dynamic correction or adaption of process parameters and inspection configurations as well as over fault-tolerance capabilities.

3. Vision of the CPM project

To achieve such goals, the focus of CPM concentrates on two main research directions (Fig. 2):

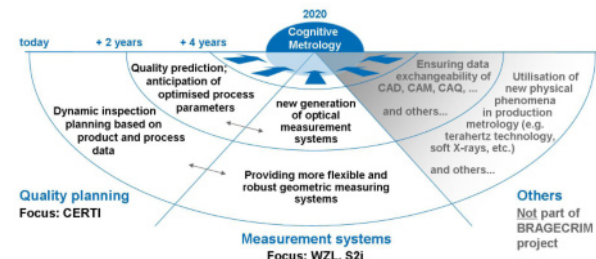


Fig. 2. Vision of the CPM project and contributions from each project partner to achieve the project goals

- **Quality planning:** focuses on the one side on the automatic and dynamic generation of inspection plans (choice of adequate sensors) based on the product and process data. On the other side, the quality prediction of processes and products is concerned, anticipating possible process parameter changes for dynamic production improvement.
- **Measurement systems:** focuses on the flexible integration and data fusion of different optical measurement systems into prototypes and test production lines, aiming at a more robust and reliable perception about process and product features. This integration allows combining 2D and 3D information acquired from different sources, as well as the intelligent analysis of the acquired data, correlating possible product quality failures with the corresponding process deviations.

Figure 3 illustrates the general architecture of the project, where the main research directions and technologies needed for the CPM solution are highlighted in a logical processing chain sequence.

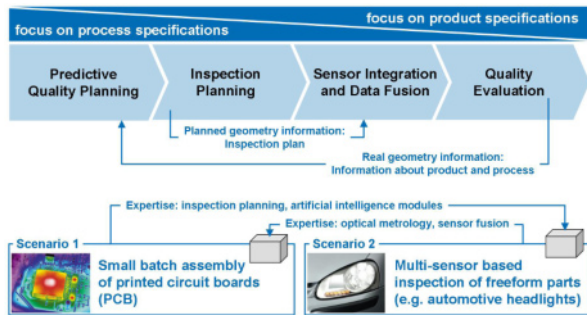


Fig. 3. CPM processing chain, detailing exchange of information and expertise among project validation scenarios

As frequently occurs in small series production facilities, there is hardly time to react to production failure and quickly reconfigure the process parameters, or even to setup the inspection equipment again. The production batch size is simply not big enough for generating representative statistical data. Therefore, a predictive quality planning module, based on information (product and process quality statistics) from previous production experiences and from current production environment conditions, can contribute significantly to reducing the ramp-up time of the production batch.

Next in the sequence, according to the current production state and product characteristics, an inspection plan must be provided for the product. The inspection plan can be generated by analysing the product planned geometry information contained in its model and also its critical past inspection results. It defines which main features of the product must be tested and inspected and how these features can be best measured according to the sensor infrastructure available. In small series production, the automatic definition of inspection planning is a big challenge, due to the need for a dynamic redefinition of the sensors application, according to the product variant under inspection.

The next step consists of the metrological solution, which is needed for monitoring and measuring process parameters as well as product qualitative features. The great number of product variants and process parameters demands the use of different sensing strategies for acquiring different kinds of information. The integration of multiple sensors within the production line must be performed allowing inline (or even in-process) inspection, avoiding interference in the constant flow of material or creating longer setup times. The optimised combination of the sensor data is a real challenge and must be performed in concurrent (focusing on redundancy and measurement uncertainty), complementary or cooperative (focusing on completeness and robustness of the measurement) ways, according to the goals of the current inspection plan. The results provided from the fused data are analysed and evaluated, in order to identify the product and process quality indices, correlate failures with process parameters, generate production statistics and present relevant quality visual data (2D+3D) regarding the product inspected.

This information is fed back to be used for process control and quality prediction.

This solution is meant to be applied and validated inside two different scenarios. The first scenario consists of the assembly of printed circuit boards (PCB) and concentrates its efforts especially on the cognitive monitoring of the process parameters for predicting and optimising the ramp-up of the production.

The second scenario consists of the multi-sensor based inspection of freeform parts and concentrates its efforts especially on the flexible inspection of the product features, integration of sensors and fusion of the acquired data for a robust quality evaluation. The cooperation and interdependence between both validation scenarios is clearly defined by the needed exchange of expertise from both sides, in order to handle the complete CPM chain for both scenarios.

4. An example scenario

The second scenario mentioned is based on an industrial automatic test machine for the inspection of automotive headlights, available on the shop floor of the WZL at the RWTH Aachen University. (Fig. 4).



Fig. 4. Automatic test machine on the shop floor of WZL

In order to intelligently inspect a bigger product variant featuring free forms and to attend to the challenging requirements of a flexible production line, the test machine is being re-engineered regarding:

- **Sensor integration and data fusion:** new optical measurement systems – flexible machine vision systems, stereo and time-of-flight cameras – are being integrated to the test machine, in order to expand its current sensing capabilities for inspecting a bigger spectrum of product variants. The combination of data from multiple sensors focuses on the completeness of the measuring task, on the improvement of the signal-to-noise ratio, measurement uncertainty, robustness and time [8].

- **Flexible machine control:** the old (inflexible) PLC-based machine control has been changed to a PC-based agent-based system interacting with a soft-PLC logic control. Different planning, routing, inspection and manipulation agents assume individual (smaller) tasks inside the system and cooperate or compete among themselves in order to split the system control complexity [9]. This new control strategy focuses on the flexible and optimal use of production and metrological resources, allowing new measurement systems to be inserted, reallocated or even removed from the test machine without affecting its functionality.
- **Intelligent planning behaviour:** the test machine must react properly according to the current product variant to be inspected. Cognitive planning modules are under development in order to create automatic inspection plans considering the product variant features, some important production parameters (cost, time, quality) and also past inspection experiences. These cognitive modules are strongly based on methods from the research area of artificial intelligence, which provide technical systems as a basis for knowledge representation and inference skills, in order to accomplish tasks during a cognitive cycle: perceiving, reasoning, learning, planning and acting [10].

The agent-based machine control system has already proven to be adequate for the improvement of the product inspection efficiency/flexibility. Further developments focus on the data fusion of the different measurement principles and the application of cognitive agents assuming inspection planning tasks.

5. Conclusions and Perspectives

CPM defines a new paradigm for metrological and quality assurance systems within the field of small series production, in order to make it economically viable while flexibly guaranteeing the quality of processes and products.

The first (and current) phase of the project concentrates on the implementation of flexible multi-sensor based inspection platforms as well as on the generation of automatic inspection plans for the two validation scenarios (PCB assembly, inspection of freeform parts). In this first phase, special sensor data fusion and agent-based systems will provide the common basis for prototype implementation.

The second (future) phase of the project will concentrate on developing cognitive software modules to be applied on top of the previous prototype platforms, in order to predict and evaluate process and product quality, allowing intelligent and autonomous decision making and the adaptation of processes.

Acknowledgments

The authors would like to thank the DFG (German Research Foundation) and CAPES (Coordination for the Improvement of Post-graduated Personnel) for the support of this research within the Brazilian-German Collaborative Research Initiative on Manufacturing Technology and the DFG for the support within the Cluster of Excellence "Integrative Production Technology for High-Wage Countries".

References

- [1] Pyzdek T, (1993) Process Control for Short and Small Runs. *Quality Progress* 51–60
- [2] Lin S, Lai Y, Chang S, (1997) Short-run statistical process control: Multi-criteria part family formation. *Quality and reliability engineering international* 13(1):9–24
- [3] Doro MM (2009) Solução integrada para auxiliar na garantia da qualidade na produção em pequenos lotes. Doctor thesis, Faculty of Mechanical Engineering at the Federal University of Santa Catarina, Florianópolis, Brazil
- [4] Mahoney RM, (1997) High-Mix Low-Volume Manufacturing. Prentice Hall, p. 222
- [5] Setchi RM, Lagos N, (2004) Reconfigurability and reconfigurable manufacturing systems: state-of-the-art review. 2nd IEEE International Conference on Industrial Informatics INDIN 529–535
- [6] Gausemeier J, Frank U, Giese H, Klein F, Oberschelp O, Schmidt A, Schulz B, Vöcking H, Witting K, (2004) Selbstoptimierende Systeme des Maschinenbaus: Definition und Konzepte. HNI-Verlagsschriftenreihe
- [7] Schmitt R, Pavim A, (2009) Flexible Optical Metrology Strategies for the Control and Quality Assurance of Small Series Production. SPIE EOM, Optical Measurement Systems for Industrial Inspection VI (7389), p. 738902-1 - 738902-12
- [8] Russer H, León FP, (2007) Informationsfusion – Eine Übersicht. *Technisches Messen* 74(3):93-102
- [9] Russel SJ, Norvig P, (2003) Artificial Intelligence: A Modern Approach. Prentice Hall series in artificial intelligence, Prentice Hall/Prentice Education
- [10] Beetz M, Buss M, Wollherr D, (2007) Cognitive Technical Systems — What Is the Role of Artificial Intelligence? *KI 2007: Advances in Artificial Intelligence* 4667, 19-42

The Metrology Enhanced Tooling for Aerospace (META) Framework

O.C. Martin¹, J.E. Muelaner¹, D. Tomlinson², A. Kayani² and P.G. Maropoulos¹

¹ Department of Mechanical Engineering, University of Bath, Bath, UK.

² Composite Structures Development Centre, Airbus UK Limited, Bristol, UK

Abstract. Aerospace manufacturers typically use monolithic steel fixtures to control the form of assemblies. This tooling is very expensive, has long lead times and has little ability to accommodate product variation and design changes. Since the tool setting and recertification process is manual and time consuming, monolithic structures are required in order to maintain the tooling tolerances for multiple years without recertification. This paper introduces the Metrology Enhanced Tooling for Aerospace (META) Framework which interfaces multiple metrology technologies with the tooling, components, workers and automation. This will allow rapid or even real-time fixture re-certification with improved product verification leading to a reduced risk of product non-conformance and increased fixture utilization while facilitating flexible fixtures.

Keywords: dimensional metrology, measurement, tooling, fixture, assembly, META.

1. Introduction

Traditional aerospace assembly fixtures are monumental steel and concrete structures configured for one aircraft type only. The traditional build philosophy maintains and verifies assembly tolerances by locating components in the fixture using pins and build slips. The combined tolerance of the fixture and location pins / slips must therefore be less than the assembly tolerances (ideally <10% although this is rarely possible). Verification involves manually rotating pins and moving slips to ensure that the assembly is not straining against the fixture. Fig 1 shows the traceability route for the assembly verification process.

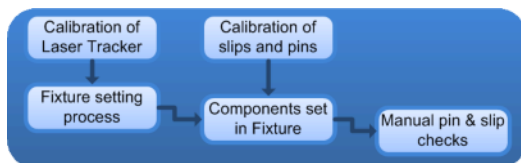


Fig 1. Traceability Route for Assembly Dimensional Uncertainty

Currently fixtures are set with a laser tracker during both commissioning and recertification. This manual

recertification process is a significant improvement on previous processes but still takes a number of days for a large fixture. Therefore tooling is typically only re-certified a number of years after its commissioning with an increased risk of non conforming products moving to the next process step undetected. Ensuring that the tooling remains stable during the periods between recertification is critical and this is one of the key drivers for employing such monolithic fixtures.

The size and complexity of fixtures means that they typically have construction lead times in excess of 6 months making late design changes or the employment of concurrent engineering a challenge. It is estimated that assembly tooling accounts for approximately 5% of the total build cost for an aircraft [1] or 10% of the cost for the air frame [2]. Fig 2 shows how these issues are a consequence of the traditional build philosophy.

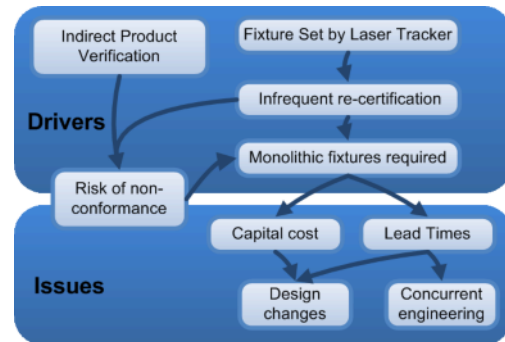


Fig 2. Issues caused by Traditional Build Philosophy

Quality issues, lead times and initial non-recurring costs (NRCs) could be reduced through the increased use of metrology in aerospace tooling. Improved metrology could allow rapid fixture recertification and direct product verification. These changes would reduce the risk of product non-conformance and increase tooling utilization while facilitating a move away from hard tooling and towards soft tooling, that is: away from large, static structures and towards reconfigurable and flexible

tooling [3]. However, in order to achieve this paradigm shift, a strong metrological infrastructure is required to maintain accuracies within the tooling and the assembly process, Maropoulos et al [4] endorse this: *the key requirement for large-scale assembly is to overcome the constraints associated with the physical size of products and assemblies and the corresponding dimensional and form tolerances.*

2. Metrology Enhanced Tooling for Aerospace

The key to moving beyond the traditional build philosophy, with its dependence on monolithic fixture structures, is the increased integration of multiple metrology instruments. This integration allows the use of large scale instruments to monitor the fixture structure and to locate localized instruments which measure product features and tooling pick-ups. Furthermore, environmental monitoring can be used to increase accuracy by applying corrections for errors due to effects such as thermal expansion.

Using the current metrology hardware and software, it is possible to create such a network but it requires considerable time from highly skilled experts and there are many issues involved in data capture, storage and reuse in multiple formats. These difficulties are preventing the benefits of the metrology from being realized.

The Metrology Enhanced Tooling for Aerospace (META) framework is a metrological software environment providing a common platform for the design of metrology enhanced tooling, the acquisition of measurement data and for the subsequent storage and processing of that data. The advanced nature of this framework will facilitate the use of sophisticated multi-instrument networks integrated within tooling to remove the current barriers to low cost and rapid and high quality manufacture of aerospace structures.

A large scale measurement network would effectively surround and monitor key characteristics of the tooling using photogrammetry, interferometer networks or an indoor GPS system. Located within the large scale measurement network would be localized scanning or single targeting measurement devices such as: laser radars, 6 DOF portable coordinate measuring machines (PCMMs), actuators, sensors, CMM arms, scanners, etc. These instruments would provide fine measurement of difficult features, freeform surfaces and tooling pick-ups, consequently enhancing part location and verification.

Utilising local metrology systems seated within a larger metrological environment can widen the scope of data collection and control. For example linear scales could be placed on slideways, actuators could measure

blind bores (with additional encoders), and force feedback could ensure forces are correct, thus removing human influences – especially in relation to easily deformed wing skin panels.

Potentially this [META environment] could provide a platform for automation, determining the sources and magnitude of any dimensional variations that the components are presently experiencing during the manual assembly stage [5]. Personnel working within the META environment could also benefit from the metrology; augmented reality could enable accurate positioning and manufacture of assemblies. Additionally, health and safety legislation considerations could be integrated into the system – ensuring workers are safe before automated processes commence.

3. The META Framework Architecture

The META framework relies on the effective synergy of complimentary instruments and interfaces accommodated by a strong software platform (Fig 3). The software is split into three levels: the top-level is a graphical user interface (GUI), which runs off of a low-level analytical core which in turn feeds to / from a database where measurement results are stored. In order to fully integrate with the Product Lifecycle Management (PLM) system, the GUI should be within *Catia* software for design, within *Delmia* for process planning and be a stand-alone application for shop floor use, giving essential information for a non-metrology specialist that could be tailored to the different working environments. The GUI utilises information generated from the core software. The core is where a majority of the instruments interface and associated algorithms are executed; this could be based on a commercially available software package, such as *SA*. Webb *et al* suggest the integration of multiple metrology systems for metrology assisted assembly by employing a decentralized service oriented software architecture [6].

3.1 Functions of the measurement network

The measurement network is separated into three sets of functions; primary functions checking the position of the tooling, components and assemblies. A set of secondary functions aiming to enhance the assembly process directly; and lastly the tertiary functions that collect data for future learning and documentation – these [functions] are detailed in Fig 4.

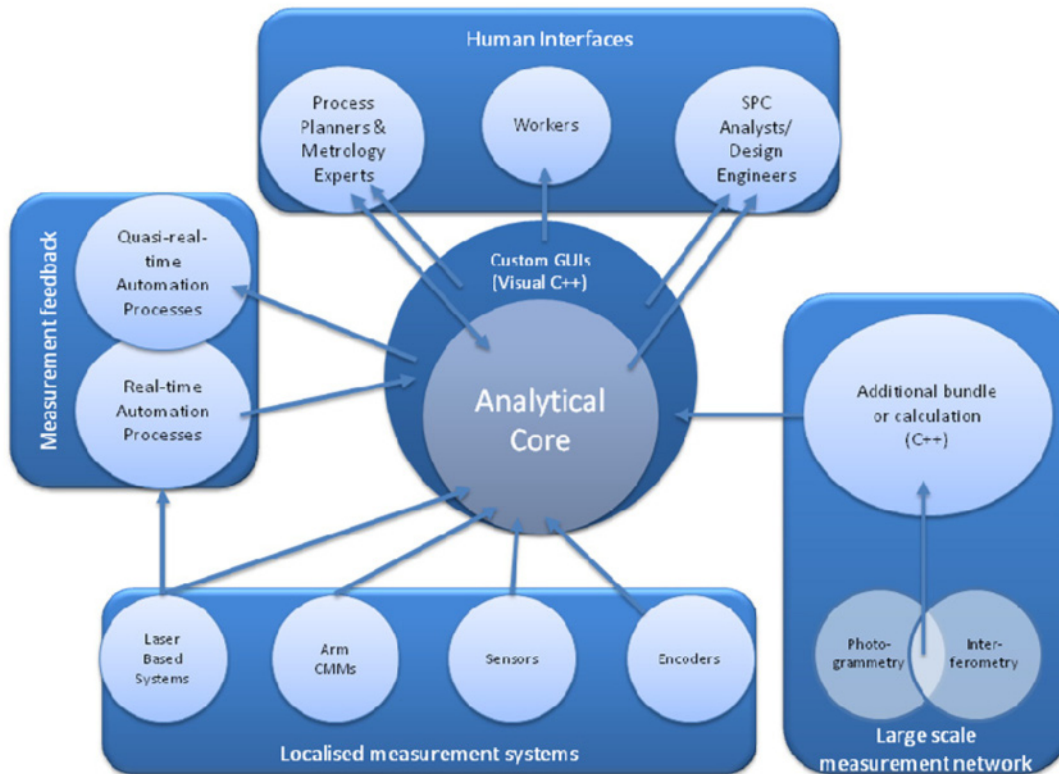


Fig 3. The META Framework Architecture

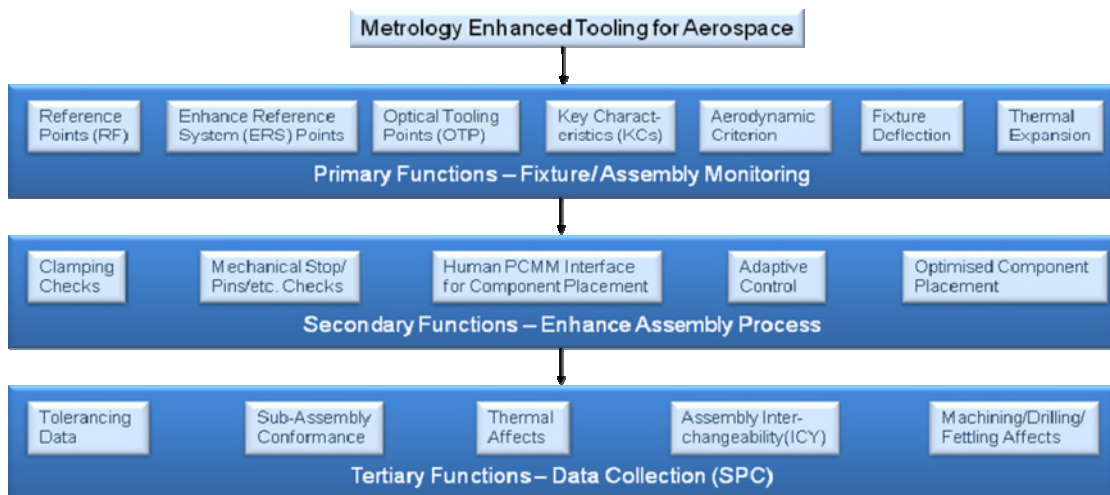


Fig 4. Measurement network functions

META’s primary functions require a quasi-real-time metrology system to monitor the key characteristics of the tooling and assembly which are in a quasi-static configuration. This monitoring eliminates the need to recertify fixtures periodically, removing the need to take

the fixture out of production – current practice can take weeks to recertify and rework a fixture, causing down time that has increasing impact as production rates increase. Control of tooling does not require real-time feedback as the movements can be iterative, unlike a

machining operation. Machining operations and automation, where an iterative loop is not appropriate, must run directly from information fed from an instrument – for example a laser tracker – and not through the core software.

The tertiary function is the collection of information. This [information] could not only enhance the tooling and assembly during operation, but begin a large scale data collection for the use of SPC, providing learning for future optimization of the assembly processes.

4. Future Considerations

Metrology Enhanced Tooling for Aerospace (META) encompasses: hardware development, integration of existing technologies, automation, human interfaces and industrial deployment within a framework where the metrology creates an environment surrounding the tooling; measuring the tooling itself, assembly features, automation and the employees working within the tooling environment. Enabling technological advances in large volume metrology are paramount in order to achieve this.

Currently, the main disadvantage associated with laser based systems (such as a laser tracker) is their ability to take only a single measurement at one given time; even though 6 DOF tracking is achievable with laser trackers, this can only be applied at one point of interest at a time, and without the reduced uncertainty of multilateration. On the other hand, photogrammetry can make many measurements within the field of vision; however, a single roving camera typical in industry cannot track a point of interest – essential for re-setting / re-work or automation. Commercially available stereo pairs of cameras allow the tracking of points but with a loss of accuracy and a considerable rise in NRCs. Additionally, placement of metrology systems within the control loop of a manufacturing cell must satisfy prerequisites such as: autonomous operation, high reliability, high speed measurement, and flexibility [7]. Specific metrology hardware solutions that enable the META framework are not currently available.

It follows that, a key prerequisite for the META framework is the availability of instruments that are capable of making multiple measurements simultaneously in real time. Currently, cost is prohibitive due to the large number of instruments required. Solutions to this might include calibrated versions of consumer grade digital cameras or the construction of the laser based systems inexpensively so that a multitude of stations can work together in a mass instrument network. Without such advances, line-of-sight issues and real-time monitoring will not be resolved.

A successful geodetic network of frequency scanning interferometers fed from a single laser source [8] has been achieved at CERN when monitoring the ATLAS particle detector – this makes multiple stations very inexpensive, line-of-sight issues can be resolved, and low measurement uncertainty obtained using multilateration. In addition, these metrology systems must be robust to ensure that every-day factory floor occurrences do not affect the stability of the system. It is also important that cultural factors are addressed, such as changing the industrial perception that metrology should be employed at the verification stage - following production and assembly - rather than being an active element of the manufacturing sequence itself [4].

The core of the META framework relies on developments in creating an accurate, robust, and flexible metrological environment, from which many tooling, assembly and manufacturing processes and applications can reside.

5. References

- [1] Rooks B. Assembly in aerospace features at IEE seminar. *Assembly Automation*. 2005;25(2):108-11.
- [2] Burley G, Odi R, Naing S, Williamson A, Corbett J. Jigless aerospace manufacture - The enabling technologies: SAE International 1999.
- [3] Muelaner JE, Maropoulos PG, editors. Large Scale Metrology in Aerospace Assembly. 5th International Conference on Digital Enterprise Technology; 2008; Nantes, France.
- [4] Maropoulos PG, Guo Y, Jamshidi J, Cai B. Large volume metrology process models: A framework for integrating measurement with assembly planning. *CIRP Annals - Manufacturing Technology*. 2008;57(1):477-80.
- [5] Saadat M, Cretin C. Dimensional variations during Airbus wing assembly. *Assembly Automation*. [Technical Paper]. 2002;22(3):270-9.
- [6] Webb P, Ye C, To M, Al-Thraa S, Kayani A. A Framework for the Fusion of Multiple Metrology Sources for Measurement-Assisted Assembly. SAE AeroTech Congress and Exhibition; Seattle, Washington, USA: SAE International, Warrendale, Pennsylvania, USA; 2009.
- [7] Gooch R. Optical Metrology in Manufacturing Automation. *Sensor Review*. 1998;18(2):81-7.
- [8] Gibson SM, Coe PA, Mitra A, Howell DF, Nickerson RB. Coordinate measurement in 2-D and 3-D geometries using frequency scanning interferometry. *Optics and Lasers in Engineering*. 2005;44(1):79-95.

Application of 3D Printing for the Rapid Tooling of Thermoforming Moulds

S. Junk¹ J. Sämann-Sun² M. Niederhofer³

^{1,2} University of Applied Sciences Offenburg, Campus Gengenbach, Faculty of Business Administration and Engineering, Klosterstr. 14, 77723 Gengenbach, Germany

³ University of Applied Sciences Offenburg, Faculty of Mechanical Engineering and Process Engineering, Badstr. 24, 77652 Offenburg, Germany

Abstract. Today, thermoforming moulds are mostly produced using conventional mould-building technologies (e.g. milling and drilling) and are made of metal (e.g. aluminium or steel) or hardwood. The tools thus produced are very robust, but are only cost-effective in mass production. For the production of small batches of thermoformed parts, there is a need for moulds which can be produced quickly and economically. A new approach which significantly reduces the production time and cost is the 3D printing process (3DP). The use of this technology to produce thermoforming moulds offers many new options in the geometries which can be manufactured, and in manufacturing time and costs. In a case study of a thermoformed part (a scaled automotive model), the pre-processing of the CAD model of a mould is demonstrated. The mould can be printed within a few hours, and is sufficiently heat-resistant for moulding processes. The important advantages of moulds printed in 3D, in comparison to moulds built using conventional technologies, are the ability to create any shape of channels for the vacuum and the simplification in the production of tool mock-ups. This paper also discusses the economics of the technique, such as a comparison of material costs and manufacturing costs in relation to conventional production technologies and materials.

Keywords: rapid prototyping, rapid tooling, 3D printing, thermoforming, mould manufacture, CAD model

1. Introduction

Since the mid-1980s, a variety of rapid prototyping (RP) processes have been developed. The common aspect of all of these processes is that the prototypes are made directly and additively. This type of manufacture means that component data produced via CAD can be used to manufacture components directly, without the use of any other tools. Additive manufacture means that the parts are built up in layers, by adding material. This is clearly different to conventional manufacturing processes where, generally, (as in the way a sculptor works) a part is produced by removing material from a larger blank [1].

The various RP processes differ above all in the material used. This ranges from plastics, used for example for stereo lithography (STL), for 3D printing

(3DP) or fused deposition modeling (FDM), through to metals and sand such as used for selective laser sintering (SLS). Another important characteristic which varies between the processes is the strength of the models produced. While high strength is achievable with laser sintering, which for instance enables tool inserts to be produced for injection moulding, 3D printing can currently only produce low strength models, which are only sufficient for use in presentations or as functional models [2].

2. Thermoforming of plastic sheets

In thermoforming (Fig. 1), a thin plastic sheet is clamped into a frame and heated to its thermoforming temperature. The heated sheet is then pulled over a mould (male die) and thus takes up its shape. To ensure that the sheet is applied as closely as possible to the shape of the tool, the tool can also include channels in which a vacuum is produced to pull the sheet onto the shape of the tool. The reshaped plastic sheet can then cool on the tool and towards the end of the process can be removed. Typical applications for thermoforming are, for example, the manufacture of packaging, transport containers with recesses for the goods to be transported and inner linings. Thus far, thermoforming tools have been made from a variety of materials, depending on the complexity of the contours and the number of parts to be made [3].

For single items and small quantities, owing to the ease of machining, tools made of hardwood have been used so far. For higher quantities, owing to the higher resistance to wear, tools made of metal (e.g. aluminium) are used.

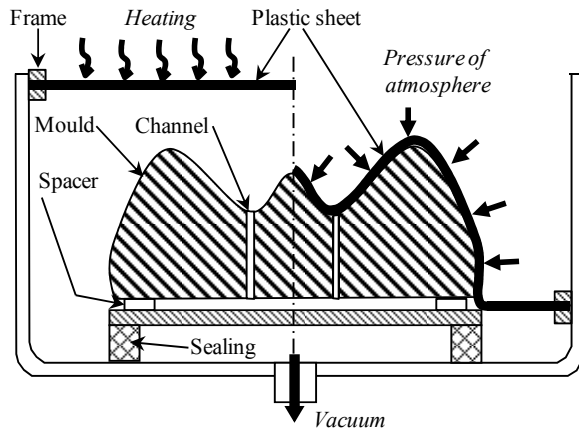


Fig. 1. Start (left) and end (right) of the thermoforming process of plastic sheet

3. Introduction to rapid tooling

The use of certain additive manufacturing processes for rapid tooling (RT) of tools for injection moulding has been investigated for a few years. [4]. This RP process mostly concerns selective laser sintering, as this process uses tool steels, whose characteristics are suitable for the high loads which are generally required in tool making regarding strength and temperature.

The advantage of being able to directly manufacture the tools is exploited here. This means that it is not necessary to programme and operate conventional CNC-machines via a computer aided manufacturing (CAM) system. This significantly reduces the number of steps involved, thus shortening the time to manufacture injection moulding tools. However, almost all RP processes require some sort of subsequent processing, e.g. impregnation or polishing of the tools created (see Fig. 2).

In addition, the additive processes do offer the option of creating new geometries, which cannot be made with conventional machine tools. Within the tool, channels can thus be made which do not have to be straight along a drill axis. On the contrary, any channel shape is possible (e.g. angled or spiral), which cannot be manufactured conventionally. Apart from that, the cross-section of the channels can be varied at will. This means that cross-sections don't have to be just round, they can be oval or polygonal. Also, at the interfaces from one geometry to another, the designer is not limited by the drill geometry.

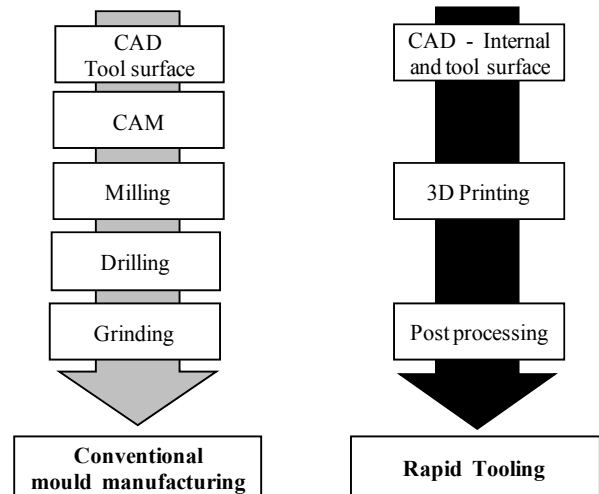


Fig. 2. Comparison of conventional mould manufacturing and the rapid tooling process

4. The 3D printing process

An investigation is now to be carried out as to whether the RP process of 3D printing is suitable for the manufacture of tools for the thermoforming of plastic sheets, as the loads and temperatures that occur are significantly lower than, for example, those arising during plastic injection moulding.

The 3D printing process is shown in Fig. 3. An approx. 0.1 mm thick layer of plaster powder is applied from a supply reservoir to a model. The excess powder lands in a second reservoir. The print head then moves across the newly applied layer of powder and applies the binding agent and the colour. The colour model results from the bound powder. The remaining powder in the construction chamber stays as powder and will be removed later on. The piston in the construction chamber then moves down by the thickness of the layer, the recoater applies a new layer of powder and the process starts again. During the post-processing, the superfluous powder in the construction chamber is sucked away. Then the model is removed and any loose powder is blown off using compressed air. The resulting rough model is still comparatively fragile. The rough model is thus generally impregnated with a resin. This reduces the fragility of the model and increases its strength.

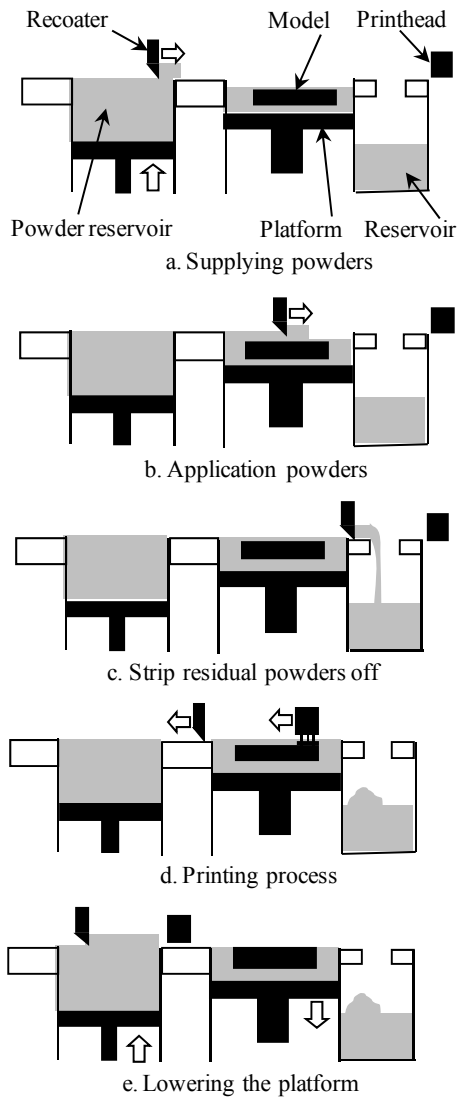


Fig. 3. 3D printing process

5. Example for rapid tooling with 3D printers

To investigate possible uses, a miniature, 1:12 scale model of a car was used (see Fig. 4). Here, the geometry of the die must first be constructed. This geometry consists of an external contour and an internal cavity. This cavity consists of the channels for the vacuum and the holes to fix the die onto the base plate of the thermoforming machine. In addition, spacers must be designed in so that the vacuum can be created beneath the die.

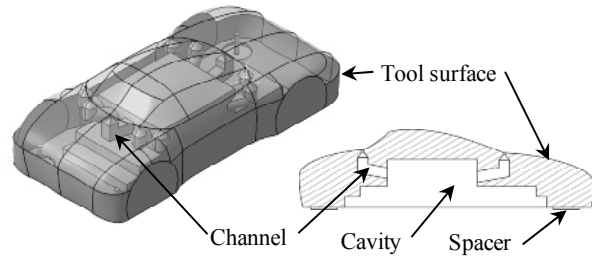
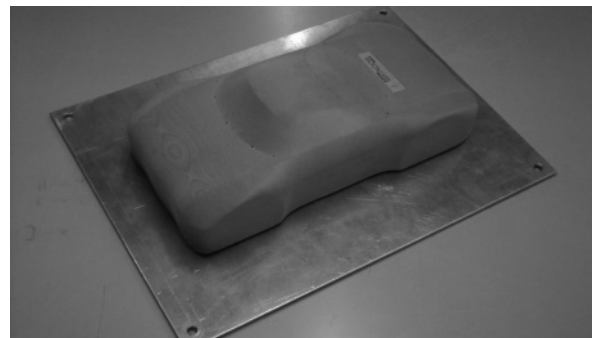
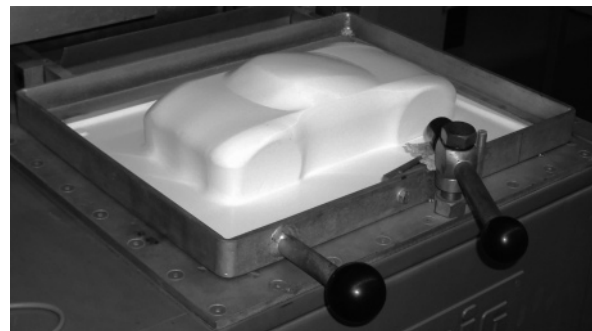


Fig. 4. CAD model of the mould and section of the channels

This example makes the shaping options of the additive process clear (see Fig. 4). Both the location of and the cross-section of the channels for vacuum were optimised. Also, the interior of the die was largely hollowed out so as to reduce the amount of powder used. The spacers and the fixing holes were integrated into the tool at the CAD stage, which means that they do not have to be added later on.



a. Mounted mould



b. Thermoformed plastic sheet

Fig. 5. Thermoforming mould and test result

The 3D printing of the tool then takes about 8 to 10 hours. For the impregnation afterwards, about another 1.5 hours are needed.

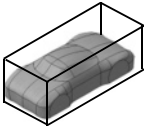
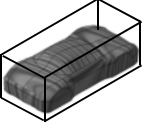

6. Results of the test

As part of the tests, plastic sheets of rigid PVC (according to DIN EN ISO 1163-1:99, initial wall thicknesses from 0.5 mm till 1.0 mm) and sheets of PS (according to DIN EN ISO 14631:99, initial wall thickness 0.5 mm) were moulded. These sheets proved to be suitable for moulding (see Fig. 5). The printed tool is quite capable of withstanding the thermal stress from 120 to 180 °C, at least for low quantities.

7. Economic considerations

When considering the economics of 3D printing in comparison to conventional tool manufacture, both the costs for the tool material are considered as well as the manufacturing costs.

Table 1. Comparison of the economics of conventional mould manufacturing and the rapid tooling process

Material used	Aluminium	Hardwood	Powder
			
Raw material	2.2 dm ³	2.2 dm ³	1.3 dm ³
Costs per kg	100 %	38 %	476 %
Material costs	100 %	19 %	167 %
Manufacturing Process	Metal Milling machine	Wood Milling machine	3D-Printer
Hourly rate	100 %	56 %	19 %
Manufacturing costs	100 %	51 %	14 %

When comparing the material costs (see Table 1.) it can be seen that conventional manufacturing of the mould e.g. using milling and drilling, consumes significantly more raw material. This demonstrates the advantage of the 3D printer in that only the powder material (note the lower density than metal) required for the final shape is consumed and all of the excess material can be re-used. Nevertheless, the powder used for 3D-Printing is significantly more expensive than conventional materials like aluminium or hardwood.

For the manufacturing costs, large differences result from the very different production machinery. The purchase and operating costs of 3D printers thus lay clearly below those of many other RP systems [5] and below those of conventional CNC machines. The hourly rates for rapid tooling machines are thus cheaper in comparison to other processes. With this advantage, they can more than compensate for the relatively high material costs by the cheaper hourly rates.

8. Summary

This investigation has shown that moulding tools for thermoforming can be produced using 3D printing. During the design, channels and holes as well as additional geometry (e.g. spacers) can be integrated into the CAD model. Some conventional operations (e.g. CNC programming, drilling) become unnecessary. It only takes a few hours to make a mould. Despite the relatively high material costs and owing to the cheaper hourly rates, rapid tooling with 3D printers represents an economic alternative to conventional tool-making, especially for low quantities.

Acknowledgments

We would like to thank Prof. Dr.-Ing. Hochberg and Prof. Dr. rer. nat. Vinke from the Faculty of Mechanical Engineering and Process Engineering for their support in the production of the CAD model and the thermoforming tests.

References

- [1] Gibson I., Rosen W.R., Stucker B.: Additive Manufacturing Technologies; Springer, London; 2010
- [2] Junk S.; Sämman-Sun J.: Application of 3D colour printing for the rapid prototyping of functional models; in: Innovative developments in design and manufacturing – Advanced Research in Virtual and Rapid Prototyping, Taylor & Francis, London, 2010
- [3] Schmid D. et. al.: Industrielle Fertigung - Fertigungsverfahren; Verlag Europa Lehrmittel, Haan-Gruiten, 2008
- [4] Gebhardt, A.: Rapid Technology: Rapid Prototyping – Rapid tooling – Rapid Manufacturing; Verlag Hanser, Munich, 2007
- [5] Kim G.D., Oh Y.T.: A benchmark study on rapid prototyping processes and machines; in: Proceedings of the Institution of Mech. Engineers, Part B (Journal of Eng. Manufacture), Professional Eng. Publishing; Birmingham, AL (USA), 2008

Printing Characteristics and Performance of Polymer Thick Film Inks for Direct Write Applications

Liang Hao^{1*}, Sandeep Raja², Mike Sloan¹, Richard Robinson¹, Jennifer McDonald³, Jagjit Sidhu³, Christopher Tuck² and Richard Hague².

¹ School of Engineering, Computer Science and Mathematics, University of Exeter, Exeter, UK

² Wolfson School of Mechanical and Manufacturing Engineering, Loughborough University

³ Advanced Technology Centre, BAE Systems, Filton, Bristol, UK

* Correspondence: Dr. Liang Hao, Department of Engineering, Computer Science and Mathematics, University of Exeter, EX 4 4QF, UK, Tel: +44 (0) 1392 263665, Email: l.hao@ex.ac.uk

Abstract. Polymer thick film (PTF) inks have been adopted for DW applications to be printed and post cured to produce electronic tracks. DW needs to use an optimal combination of unique PTF inks, substrates and curing processing parameters to achieve good printing characteristics, performance and durability. This study has investigated the printing performance of two different conductive PTF inks (silver and hybrid inks) specifically measuring the surface roughness, resistance and track profile of the PTF tracks cured at different temperatures on smooth alumina and rough carbon fibre substrates. The results show the viscosity, substrate surface roughness and ink composition influence the surface profile as well as the resistance of the printed tracks. The curing temperature was found to play a predominant role upon the function of the printed tracks; most notably increased conductivity was seen at higher cure temperatures. By comparing two inks with distinctly different viscosities, one could see the advantages and disadvantages upon performance, with strong effects upon the track profile.

Keywords: Direct Write (DW), Polymer Thick Film (PTF), Viscosity, Curing, & Surface Morphology.

1. Introduction

Direct Write (DW) is an emerging group of technologies that enable the rapid fabrication of mesoscopic electronic devices onto conformal, large area components for aerospace and defence applications. Devices include electrical interconnects and sensors for structural health monitoring, bringing the benefits of weight reduction and functional improvements of structural components^{1,2}. There are many printing methods for DW applications; this study concentrates on the micropen printing approach. This system uses a computer driven x-y stage for printing Polymer Thick Film inks (PTF) in a CAD defined pattern using a micro-scale nozzle deposition system. This technology is capable of printing multilayer material structures on non-planar substrates and high-density circuitry with integrated passive components³.

PTF inks are versatile in the way one can simply change the composition of the inks to tailor the printing performance and functions of electronic devices made by DW. Most PTF inks are composed of a polymer binder which is usually dissolved in a solvent. This acts as a carrier for electrically functional materials, such as dielectrics, silver or copper particles. The DW of PTF inks normally starts with a fluid PTF held at a specific viscosity at room temperature. This enables the micropen nozzle to deposit the inks on the surface of the substrate. The second part of the process is the curing. During the curing process the solvent is evaporated and cross-linking of the polymer matrix occurs, holding and connecting the functional particles within the PTF in place while providing adhesion to the substrate⁴. Normally, a temperature range between 90°C-200°C is required to initiate curing within PTF inks. The degree of cure is then a function of the cure temperature and cure time. The performance and quality of a directly written PTF deposit therefore, requires the optimisation of material rheology and curing processing.

It has been found printing resolution and morphology influence the conductivity of electronic patterns. Previous study showed that electrical parameters such as resistance, are affected by the line geometry and topography of the electronic track⁵ and a high surface roughness could result in high surface resistance⁶. The printing quality of DW elements depends on high-quality starting materials, typically with specially tailored chemistries and/or rheological properties⁷. The printing profile and morphology can be also influenced by the substrate materials and curing process. This study characterises the printing characteristics of two different silver loaded PTF inks cured at different temperatures on different substrates. It analyses the effects of three parameters, substrate surface roughness, curing

temperature and viscosity on the printing and functional performance of the PTF inks.

2. Experimental Method

Two commercial PTF silver inks sourced from Gwent Electronic Materials (GEM) Ltd⁸ were used in this study. The first ink is a silver based heat curable ink containing approximately 55 % solid content. The supplier recommended curing for 10 minutes at 130°C in a conventional oven. The second ink is a hybrid silver/silver organo-metallic (50/50) low resistance ink. At high temperatures, (>160°C) the organo-metallic component decomposes into silver nano-particles which fuse, thereby increasing the electrical conductivity of the composition.

An oscillation test using a rotational rheometer (TA Instruments AR2000) is used to determine the viscosity of the PTF inks as a function of temperature.

Both the silver and hybrid PTF inks were deposited on aluminium 2024 (coated with an aluminium oxide layer), alumina ceramic and carbon fibre substrate by a micro-pen DW process at the Advanced Technology Centre (ATC), BAE Systems. The process is relatively simple in operation; ink is ejected from a syringe by the application of a piston or pressurised air. The ejected ink forms a slurry on the substrate which is dependant on the nozzle diameter, deposition rate (or flow rate), and deposition speed. Following a DW process, silver PTF tracks were cured for thirty minutes, at 100°C, 130°C and 150°C and hybrid PTF tracks at 150°C, 180°C and 200°C in order to investigate the effect of curing above and below the supplier's recommended temperature.

The surface profile and roughness of the printed tracks and substrate were characterised using a talyscan (Taylor Hobson) using the contact stylus. Using the surface topology obtained by the talyscan one could measure the height and width of the printed tracks. A digital multimeter (Calktek CM1200T) is used to measure the resistance of the printed tracks using Ohm's law, by connecting two probes at each end of the track.

3. Results and Discussion

3.1 Viscosities of the Inks

The viscosity of the silver and hybrid ink as a function of temperature is presented in Fig. 1. It is most common for DW printing processes to be carried out at room temperature therefore, it is important to note the initial viscosities of the silver and hybrid at 25.27Pa.s and 81.58Pa.s respectively. This plays a large role in the formation of the tracks, because the increased viscosity can amplify the surface tension of the fluid⁹. Hence, the ink with the higher viscosity and surface tension is more

likely to hold its printed profile with less spreading on substrates. The silver ink holds a consistent low viscosity until 64°C when the initial onset of cure takes place. Then the viscosity rises to around double its initial value and it then goes through a secondary cure onset. After this it increases sharply to around 8×10^4 Pa.s and then rises to a maximum of 9×10^5 Pa.s; the latter slow rise is because the material does not receive excess energy from the raised temperature as the time lapses. The silver inks initial low viscosity leads to reduced forces acting upon the print head which could prevent the chance of clogging of micro-nozzle and thus improve print consistency and reduce maintenance of the DW system. The hybrid is initially at a higher viscosity but by increasing the temperature, a minimum viscosity can be achieved at 68.7°C of 14.24 Pa.s as opposed to the silver inks minimum of 20.01 Pa.s at 48.2°C, suggesting printing at elevated temperatures then cooling/quenching the material on the substrate could be an approach to tailor the printing performance such as holding the shape of the tracks. Post 68.7°C, the hybrid ink shows a steady increase in viscosity until around 90°C when the gradient becomes steeper. Note that the hybrid does not reach a plateau like the silver inks; this is due to its ideal cure temperature being around 180°C.

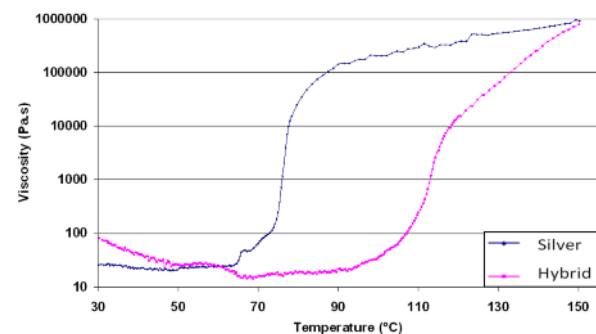


Fig. 1. Viscosities of Silver and Hybrid inks during a temperature ramp

3.2 Printing Performance of the Inks on Different Substrates

The aluminium oxide layer on aluminium and the alumina ceramic are smooth with average surface roughness, R_a , of 0.24 μm and 0.27 μm respectively; while carbon fibre has a very rough microscopic surface with R_a of 13.3 μm , over 31 times rougher than the ceramic. Because the alumina and aluminium substrates have very similar surface roughnesses, only alumina and carbon fibre were considered for the rest of the comparison study. The highest rough peak on the surface of the ceramic alumina is 8.5 μm height and the coordinated weave of the carbon fibre substrate creates the highest surface peaks of 75 μm height.

Fig. 2 shows the track profile of the printed hybrid and silver ink tracks on the alumina and carbon fibre substrates. The track profiles for the hybrid ink are much higher and more defined than the silver ink. The hybrid printed tracks also exhibit a rougher surface than the silver printed tracks on both alumina and carbon fibre. This is because the hybrid inks have a higher viscosity and therefore holds its printed profile, while the lower viscosity silver inks are likely to flow outwards, thus reducing the profile of the track and lead to a smoother surface.

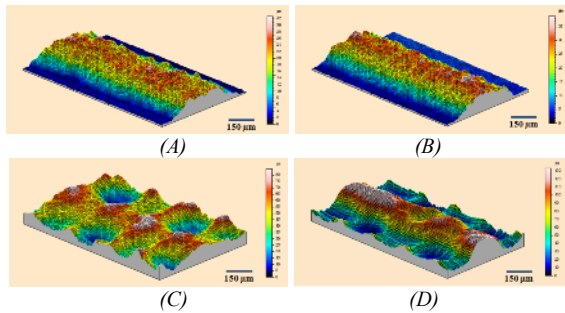


Fig. 2. Surface profiles of (a) the printed silver ink on alumina, (b) the printed hybrid ink on alumina, (c) the printed silver track on carbon fibre, (d) the printed hybrid on carbon fibre

These results show that both the surface roughness of substrates and the ink type have a significant influence on the surface roughness of the printed track for both inks. The R_a of the cured silver tracks on carbon fibre substrate (R_a 4.74) more than doubles that on the alumina substrate (R_a 2.27); while for hybrid inks, the R_a of the cured tracks on the carbon fibre substrate (R_a 6.1) is nearly triple that on the alumina substrate (R_a 2.51). These results also show that the surface roughness of the cured tracks is correlated to, but not directly proportional to that of the substrates as the surface roughness is 31 times the differences between the alumina and carbon fibre substrates.

3.3 Printing Performance at Various Cure Temperatures

Due to its low surface roughness, alumina was used as a substrate to investigate the effects of curing temperature on the printing performance and resistances of the silver and hybrid inks. Fig. 3 shows the surface roughness of the printed hybrid and silver tracks cured at different temperatures. For hybrid tracks, the surface roughness decreased with increasing curing temperature, indicating that a higher degree of curing could result in the better surface quality. The highest surface roughness is presented on the hybrid tracks cured at 150°C. For the silver ink, the surface roughness of the tracks cured at 130°C is higher than that cured at 100°C, this is possibly because the track cured at 100°C was not completely cured and contained some solvents which may help to smooth the surface. The lowest surface roughness however, is observed when the silver inks were cured at

150 °C implying that a higher degree of curing reduces the surface roughness of the printed tracks.

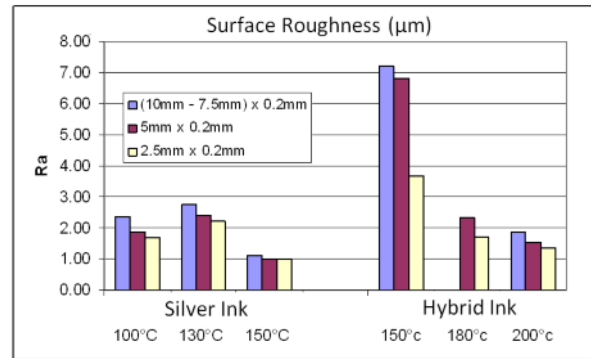


Fig. 3. Surface roughness of the printed tracks on alumina substrate cured at different curing temperatures

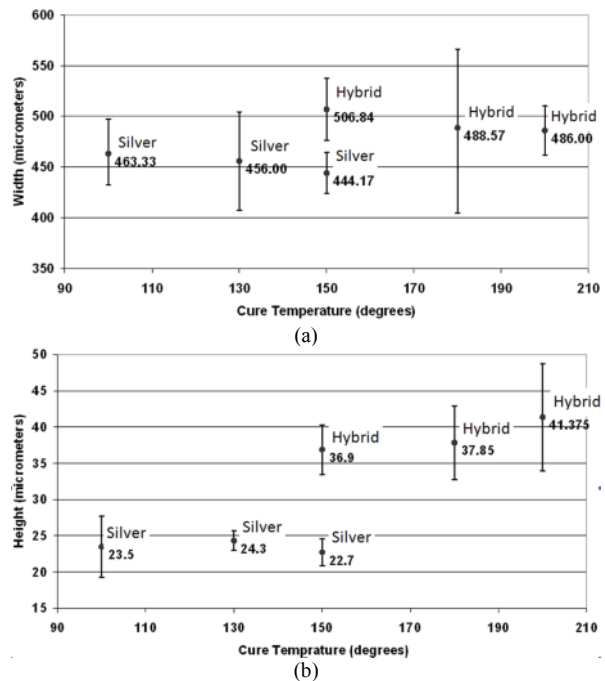


Fig. 4. Comparison of silver & hybrid track a) width, b) height of the printed tracks cured at different curing temperatures

Fig. 4. Comparison of silver & hybrid track a) width, b) height of the printed tracks cured at different curing temperatures

shows the width and height of the silver and hybrid tracks cured at different temperatures. The large variations in the track widths makes it difficult to make any definitive conclusions, but the average width of both inks indicates that tracks decrease as the curing temperature increases. At the same curing temperature, the width of the hybrid ink tracks is wider than that of silver tracks when using the same printing conditions. The standard deviation of the data obtained indicates that there is a correlation between the two inks. The cure

temperature advised by the manufactures is in reality the least repeatable, the silver ink at 130°C having a standard deviation of 10% from the average. The hybrid ink at 180°C is even larger at 16%. In both cases, optimum repeatability is achieved when curing above their recommended curing temperature: silver at 150°C gives 4% deviation less and the hybrid at 200°C gives 5%. Neither of the two inks show a good correlation between the printed height and the curing temperature. The minimum deviation can be seen with silver ink cured at the mid temperature whereas the hybrid sees its most repeatable state at the lowest temperature. This fact alone proves that curing temperature has a large role to play in the profile of a printed track.

Fig. 4 shows clearly the relationship between the resistance of the silver and hybrid tracks with cure temperature. The resistance decreases as the curing temperature is progressively increased (this can be seen using the line of best fit inclusive of both inks). The greatest change in resistance in the silver tracks is between 100°C to 130°C cure temperature. A further increase of curing temperature to 150°C resulted in a very marginal decrease of 0.2Ω in resistance. This additional drop in resistance could be due to the drop in track surface roughness. Another explanation for this is that the increased temperature may give the flakes the energy to deform in its solid state to connect with other flakes, resulting in better conductivity⁷. The resistances of the hybrid ink tracks are lower than those of silver tracks and follow the same characteristics with increasing curing temperature. For example when using a cure temperature of 150°C, the hybrid ink (1.43Ω) has almost half the resistance of the silver track (2.9 Ω) even though the hybrid ink exhibits a higher surface roughness. When curing the hybrid ink at higher temperatures, the nanoparticles within the resin are designed to sinter thereby reducing the resistance of the track further. However, any additional drop in resistance due to sintering only equates to a further 10% reduction between 150°C to 210°C.

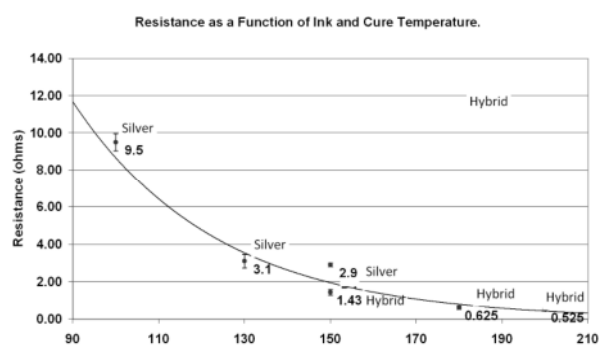


Fig. 4. Resistance at different cure temperatures

4. Conclusions

This research found that the viscosity of the inks, the substrate surface roughness and curing temperature are influential factors governing the printing and electrical performance of conductive PTF inks for DW application.

The silver PTF inks have lower viscosity than the hybrid inks at room temperature for DW printing. The silver inks therefore resulted in the better surface roughness for the printed tracks. If surface roughness is one of main criteria, then the silver ink may be the optimum choice in this respect. In contrast the higher viscosities of the hybrid ink allow it to hold its shape and produce a more defined track profile on rough substrates.

The surface roughnesses of alumina and carbon fibre substrates influence the surface quality of the printed tracks for both inks. The printed tracks on rougher carbon fibre substrate exhibited larger R_a and resistances than the smooth alumina.

Despite the hybrid ink exhibiting higher surface roughnesses, it has lower resistance on both rough and smooth substrates as well as the lower sensitivity to substrate surface roughness. Hence, hybrid inks are a good ink candidate for DW applications if rough substrates are used and low resistance is required.

The resistance of the printed tracks reduces as the curing temperature increases. Optimal curing temperature is 130°C for the silver and 190°C for the hybrid ink, curing above this temperature only brings a marginal reduction in resistance, but requires more heat energy.

References

- [1] Lewis, J.A. and G.M. Gratson, *Direct writing in three dimensions*. Materials Today, 2004. 7(7-8): p. 32-39
- [2] Pique, A. and D. Chrisey, *Direct-Write Technologies for Rapid Prototyping Applications: Sensors, Electronics and Integrated Power Sources*. 2002: Academic Press
- [3] Clem, P.G., et al., *Micropen Printing of Electronic Components*, in *Direct-Write Technologies for Rapid Prototyping Applications: Sensors, Electronics and Integrated Power Sources*, A. Pique and D. Chrisey, Editors. 2002, Academic Press
- [4] Prime, R.B., *Characterization and Cure of Dielectric and Conducting Polymer Thick Films*. Polymer Engineering Science, 1992. 32: p. 1286-1289.
- [5] Sanderson, A.E., *Effect of Surface Roughness on Propagation of the TEM Mode*. Advances in Microwaves, 1971. 7
- [6] Marinov, V. and Y. Atanasov. *Improved Direct Write Technology for High Frequency Interconnects on Flexible Substrates*. in *Proceedings of IMAPS 2006, 39th International Symposium on Microelectronics*. 2006. San Diego, California, USA
- [7] Chrisey, D.B., *MATERIALS PROCESSING: The Power of Direct Writing*. Science, 2000. 289(5481): p. 879-88
- [8] Gwent Electronic Materials Ltd, Available from www.g-em.com
- [9] Schonhorn, H., *Surface tension, viscosity relationship for liquids*. Journal of Chemical and Engineering Data, 1967. 12(4): p. 524-525

Effect of work piece volume on statistically controlled rapid casting solution of aluminum alloys using three dimensional printing

Rupinder Singh¹ and Rajinder Singh²

¹ Faculty of Production Engineering, Guru Nanak Dev Engineering College, Ludhiana (India)

² Research Scholar, Dept. of Production Engineering, Guru Nanak Dev Engineering College, Ludhiana (India)

Abstract. The purpose of the present investigations is to study the effect of work piece volume on shell wall thickness reduction for a statistically controlled rapid casting solution of aluminum alloy using three dimension printing. The results of the study suggest that work piece volume has an unnoticeable effect on shell wall thickness reduction (for the selected range of work piece volume). The research proved that a shell wall thickness with a value less than the recommended one (12mm) is more suitable from dimensional accuracy and economic points of view. Final castings produced at different shell wall thicknesses are acceptable as per IS standard (UNI EN 20286-I (1995). Keeping in mind the cost effectiveness, one (01) mm shell wall thickness has been recommended for production of casting.

Keywords: Statistically controlled, aluminum alloy, three dimensional printing

1. Introduction

Prototypes can constitute a strategic means, not only for functional and assembly tests or to obtain the customer's acceptance, but to outline eventual critical points in the production process [1]. The relevance of rapid casting (RC) techniques consists on increasing parts' availability in a short time [2]. The initial capital cost can thus be repaid through a reduction of costs and time for the following phases of development, engineering and production, as well as through non-monetary advantages [3].

In this field, innovative solution are now available based on the three dimensional printing (3DP) process, which can extend RC possibilities [4]. A key issue regarding the shell casting process is the production of the pattern in the case of a prototype casting, for which the traditional die casting is uneconomical [5]. 3DP can meet this requirement, producing single/few parts in short times and without tooling costs [6].

The present research regards shell patterns obtained by 3DP on which the ceramic shell can be built and then joined (as in the conventional process) to obtain the cavity for pouring metal. Experimental studies regarding

this solution are lacking in the literature, in particular the technological feasibility in the case of thin-walled parts needs to be assessed [5]. Many researchers have worked at reducing the shell wall thickness for a cost effective RC solution [7]. However, hitherto, for statistically controlled aluminum shell casting, no one has reported the effect of work piece volume on reducing shell wall thickness from the recommended one (12mm), in order to reduce the cost and time of production, as well as to evaluate the dimensional accuracy and mechanical properties.

2. Methodology

Aluminum castings were prepared at three different volumes corresponding to three different outer diameter of work piece (that is corresponding to $\text{\O}60$ mm, $\text{\O}50$ mm and $\text{\O}40$ mm). Figure 1 shows the dimensions of the benchmark part of diameter 50 mm.

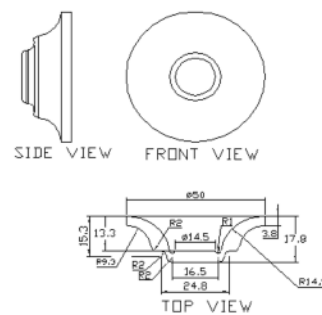


Fig. 1. Benchmark dimensions

All the dimensions of benchmarks corresponding to $\text{\O}60$ mm and $\text{\O}40$ mm have been fixed in same proportion, corresponding to $\text{\O}50$ mm. After the selection of the benchmark, the component to be built was modelled using CAD. The CAD software used for the modelling

was UNIGRAPHICS Ver. NX 5. Shell patterns were prepared at different thickness. The thickness values for shells were 12, 11, 10, 9, 8, 7, 6, 5, 4, 3, 2 and 1 mm. The CAD models of upper and lower shells were converted into STL (standard triangulation language) format also known as stereolithography format. Moulds were manufactured in 3DP (Z Print machine, Model Z 510) with Z Cast 501 powder and parts were heat treated at temperature of 110°C for 1 hour. The aluminium alloy was poured for obtaining the technological prototype. The measurement paths for the internal and the external surfaces of the benchmark have been generated through the measurement software of the ‘GEOPAK v2.4.R10’ co-ordinate measuring machine (CMM). These paths direct the movements of the CMM probe along trajectories normal to the parts surface. About 70 points have been measured on the external surface. For each point the machine software evaluates the deviations between the measured positions and the theoretical ones for the X, Y, Z coordinates. Table 1 shows variation in hardness of castings prepared with respect to shell thickness (mm).

Table 1. Observations of Hardness Testing

Shell Thickness (mm)	Rockwell Hardness No. for different work piece diameter		
	φ60 mm	φ50 mm	φ40 mm
12	57	54	51
11	56	57	53
10	55	59	58
9	56	52	52
8	52	57	54
7	54	58	58
6	56	58	56
5	55	59	53
4	54	59	54
3	56	55	56
2	57	58	52
1	52	51	57

It should be noted that in casting neither higher nor lower hardness is desirable [8]. This is because if casting is of high hardness, usually it is brittle and with lower hardness it will be of ductile nature. In the present experimental study the variation in hardness value is not too much. The only reason to measure and compare hardness value is, to show that for optimum size shell thickness prepared by 3DP, castings produced have little variation in hardness. So there will not be any problem in its functional operations.

The results of the dimensional measurements have been used to evaluate the tolerance unit (n) that derives starting from the standard tolerance factor i, defined in standard UNI EN 20286-1 [9]. The values of standard

tolerances corresponding to IT5-IT18 grades, for nominal sizes up to 500mm, were evaluated considering the standard tolerance factor ‘i’ (μm) indicated by the following formula, where D is the geometric mean of the range of nominal sizes in mm [10].

$$i = 0.45 \times D^{1/3} + 0.001 \times D \tag{1.1}$$

In fact, the standard tolerances are not evaluated separately for each nominal size, but for a range of nominal sizes. For a generic nominal dimension D_{JN} , the number of the tolerance unit’s n is evaluated as follows:

$$n = 1000(D_{JN} - D_{JM})/i \tag{1.2}$$

Where D_{JM} is measured dimension. The tolerance is expressed as a multiple of i: for example, IT14 corresponds to 400i, with n = 400. Table 2 shows classification of different IT grades according to UNIEN 20286-1. After this for each value of outer diameter, corresponding value of ‘n’ were calculated, the latter taken as a reference index for evaluation of tolerance grade. Further (based upon observations of Table 1.2), to understand whether the process is statistically controlled six sample of aluminum alloy pieces were casted for best shell wall thickness value that is 1mm for three different volume corresponding to Ø60, Ø50, Ø40 mm.

Table 2. IT Grades of outer diameter (Ø60, Ø50, Ø40 mm)

Shell Thickness mm	D_{JM} for φ60	$D_{JN} = \phi 60$ mm	D_{JM} for φ50 mm	$D_{JN} = \phi 50$ mm	D_{JM} for φ40 mm	$D_{JN} = \phi 40$ mm
12	59.855	IT10	49.815	IT11	39.900	IT10
11	59.605	IT12	49.825	IT11	39.940	IT8
10	59.820	IT10	49.875	IT10	39.905	IT9
9	59.810	IT11	49.780	IT11	39.790	IT11
8	59.585	IT12	49.825	IT11	39.815	IT11
7	59.865	IT10	49.715	IT12	39.890	IT10
6	59.810	IT10	49.375	IT14	39.720	IT12
5	59.555	IT12	49.700	IT12	39.740	IT12
4	59.445	IT12	49.845	IT10	39.695	IT12
3	59.455	IT12	49.760	IT11	39.445	IT13
2	59.890	IT9	49.415	IT13	39.510	IT13
1	59.540	IT12	49.590	IT13	39.705	IT12

On measurement of outer diameter with CMM, the dimensions obtained at 1 mm shell wall thickness for Ø60 mm are shown in Table 3.

Here: A=above the mean, B=below the mean, U=Up from previous reading, D=Down from previous reading

Table 3. Bench mark dimensional value at 1mm shell wall thickness for Ø60 mm

S. No	Observation	Mean	Above or below Mean	Up or Down
1	59.54	59.588	B	
2	59.588	59.588	B	U
3	59.561	59.588	A	D
4	59.603	59.588	A	U
5	59.616	59.588	A	U
6	59.622	59.588	A	U
			E _{AB} =1	E _{UD} =2

3. Results and Discussion

Now if the mean and standard of the population that has a normal distribution is μ and σ respectively then for variable data X the standard normal deviate Z is defined as [11]:

$$Z = \frac{X_i - \mu}{\sigma} \tag{1.3}$$

Where X_i is the variable data obtained, μ is the mean of data and σ is the standard deviation.

3.1 Calculation for Z (standard normal deviate) above and below at 1mm shell thickness, or 60mm

$$E (run)_{AB} = \left(\frac{N}{2} + 1\right) \tag{1.4}$$

Where N is the number of observations and $E (run)_{AB}$ is the expected number of run above and below

$$E (run)_{AB} = \left(\frac{6}{2} + 1\right) = 4 \tag{1.5}$$

$$\sigma_{AB} = \sqrt{\frac{N+1}{4}} \tag{1.6}$$

Where σ_{AB} is the standard deviation of above and below

$$\sigma_{AB} = \sqrt{\frac{6+1}{4}} = 1.118 \tag{1.7}$$

$$Z_{AB} = \{RUN_{AB} - E(run)_{AB}\} / \sigma_{AB} \tag{1.8}$$

Where RUN_{AB} is the actual number of run obtained above and below

$$Z_{AB} = \frac{9-4}{1.118} = -2.6834 \tag{1.9}$$

P=NORMSDIST(Z), when the value of Z is negative in Microsoft Excel software

$$P_{AB} = 0.003645 \tag{1.10}$$

$$E (run)_{UD} = \frac{2N-1}{2} \tag{1.11}$$

Where $E (run)_{UD}$ is the expected number of run up and down.

$$E (run)_{UD} = \frac{2 \times 6 - 1}{2} = 3.667 \tag{1.12}$$

$$\sigma_{UD} = \sqrt{(16N - 29)/90} \tag{1.13}$$

Where σ_{UD} is the standard deviation for up and down

$$\sigma_{UD} = \sqrt{(16 \times 6 - 29)/90} \tag{1.14}$$

$$\sigma_{UD} = 0.8628 \tag{1.15}$$

$$Z_{UD} = \{RUN_{UD} - E(run)_{UD}\} / \sigma_{UD} \tag{1.16}$$

$$Z_{UD} = (2-3.667)/0.8628 \tag{1.17}$$

$$Z_{UD} = -1.5840 \tag{1.18}$$

P=NORMSDIST(Z), when the value of Z is negative in Microsoft Excel software

$$P_{UD} = 0.56597 \tag{1.19}$$

Normally decision making is done with certain margin of error ‘ α ’ and taken as equal to 0.005 that is there can 5% chances in arriving at wrong conclusion. Now for decision making:

If $P_{AB} < \alpha$ OR /and $P_{UD} < \alpha$, then non-random pattern exist. In the present case P_{AB} are $< \alpha$ indicates existence of non random pattern. Now exercise of predicting various statistical or drawing conclusions should not be undertaken unless the normality of distribution has been verified. Even if one has a large data, superimposing of normal curve on the histogram it is more difficult task than it to be imagined. For histogram one require minimum of 50 observations, however more the better and for assessing whether the underlying distribution is normal or not becomes more difficult when the number of observations is fewer. For cumulative probability plot (Pi):

$$Pi = (S.N-0.5)/N \tag{1.20}$$

Where S.N is serial number of data observation arranged in ascending order, N is total number of observations in the data set. If the standard normal deviate follows normal distribution that has mean $\mu =0$ and standard deviation $\sigma =1$, then:

$$f(Z) = \frac{1}{\sigma} \sqrt{\frac{2}{\pi}} e^{-\frac{Z^2}{2\sigma^2}} \tag{1.21}$$

The equation above follows normal probability curve and any date close to it also follows normal probability

curve. The values of standard normal deviate were calculated using cumulative probability and dimensional values were arranged in ascending order as shown in Table 4.

Table 4. Standard normal deviate and cumulative probability in ascending order at 1mm shell wall thickness for Ø 60 mm

S.No	Pi(Cumulative Probability)	Std. Nor. Deviate Z	Dimensional Value in mm
1	0.08333	-1.38299	59.54
2	0.25	-0.67449	59.561
3	0.416667	-0.21043	59.588
4	0.58333	0.21043	59.603
5	0.75	0.67449	59.616
6	0.91667	1.382994	59.622

Based on Table 4, a normal probability curve was drawn to predict the probability as shown in Figure 2. As observed from Figure 2, the aforesaid data follows non random pattern and is under normal probability curve. So, there are very strong chances that the process is under statistical control, however X-bar chart and R-bar chart cannot be drawn due to less number of observational data. Similarly normal probability curve was drawn to predict the probability of process under statistical control for the shell thickness of 1mm for Ø50 mm and Ø40 mm.

Here shell production cost and time is decreasing as the shell thickness is decreasing from 12 mm to 1 mm. This is due to the fact that material used to produce shell is decreasing as shell thickness is decreased. The shell production cost and time is reduced by 67.38% and 44.87% (for work piece of Ø60 mm), 64.51% and 44.62% (for work piece of Ø50 mm), 69.50% and 59.64% (for work piece of Ø40 mm) respectively at 1mm shell wall thickness.

4. Conclusions

It is feasible to reduce the shell thickness from the recommended value of 12 mm to 1 mm. The tolerance grades of the castings produced from the different thicknesses were consistent with the permissible range of tolerance grades (IT grades) as per standard UNI EN 20286-I (1995). Instead of a 12 mm shell thickness of mould in the Z Cast process of casting of aluminium alloys one can select a 1 mm shell thickness, as observed from similar/better dimensional results and mechanical properties. The results are in line with the observations made otherwise [12]. Further there is an unnoticeable effect of work piece volumes on reduction of shell wall thickness. Strong possibilities are observed for the process under statistical control for the best set shell thickness (1 mm) in the case of aluminium alloy, irrespective of work piece volume.

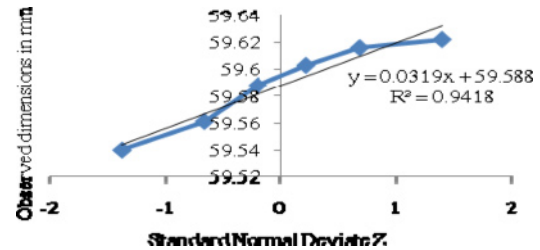


Fig. 2. Normal probability curve of selected bench mark at 1mm shell wall thickness for Ø60 mm

Acknowledgment: The authors are thankful to AICTE, New Delhi for financial support under CAYT grant.

References

- [1] Wang, W., Conley, J. G. and Stoll, H. W., (1999) Rapid tooling for sand casting using laminated object manufacturing process. *Rapid Prototyping Journal* 5(3): 134-140.
- [2] Wang, D. X., Leng, H. W. and Chen, S., (2007) Recent advances in colour rapid prototyping. *Int. J. Precision Technology* 1(1): 133-138.
- [3] Karapatis, N. P., Griethuysen, J. P. S., and Glardon, R., (1998) Direct rapid tooling: a review of current research. *Prototyping Journal* 4: 77-89.
- [4] Singh, J. P. and Singh, R., (2008) Investigations for reducing wall thickness in low brass rapid casting using three dimensional printing. *Proc. of International conference on Advances in mechanical engineering (AME 2008), India*, p. 878-883.
- [5] Singh, R. and Verma, M., (2008) Investigations for reducing wall thickness of aluminum shell casting using three dimensional printing. *Journal of achievements in materials and manufacturing engineering* 31: 565-569.
- [6] Sachs, E. M., Haggerty, J. S., Cima, M. J. and Williams, A. P., (1994). Three dimensional printing techniques, U. S. Patent 005340656.
- [7] Bassoli, E., Gatto, A., Iuliano, L., and Violante, M. G., (2007) 3D printing technique applied to rapid casting. *Rapid Prototyping Journal* 13: 148-155.
- [8] Singh, J. P. and Singh, R., (2009) Comparison of rapid casting solutions for lead and brass alloys using three dimensional printing. *Proc. of IMechE Part C, Journal of Mechanical Engineering Sciences* 223: 2117-2123.
- [9] Kaplas, M. and Singh, R., (2008) Experimental investigations for reducing wall thickness in zinc shell casting using three dimensional printing. *Proc. of IMechE Part C, Journal of Mechanical Engineering Sciences* 222: 2427-2431.
- [10] Singh, J. P. and Singh, R., (2009) Investigations for statistically controlled rapid casting solution of lead alloys using three dimensional printing. *Proc. of IMechE Part C, Journal of Mechanical Engineering Sciences* 223: 2125-2134.
- [11] Devor, R. E., Chang, T., and Sutherland, J. W., (2005) *Statistical quality design and control contemporary concepts and methods*. Pearson Prentice Hall (Second edition), New Jersey 78-91.
- [12] Dimitrov, D., W., Schreve, K., and Beer, N., (2006) Advances in three dimensional printing – state of the art and future perspectives. *Rapid Prototyping Journal* 12(3): 136-147.

Using Additive Manufacturing Effectively: A CAD Tool to Support Decision Making

P.C. Smith and A.E.W. Rennie
Department of Engineering, Lancaster University, Lancaster, UK

Abstract. Additive manufacturing (AM) describes the use of layer manufacturing technologies (LMT) to directly produce end use parts. More commonly, LMT have been used as a method to accurately and quickly produce prototype models sometimes referred to as rapid prototyping or 3D printing. Presently, however, LMT is utilised to produce polymeric and metallic parts directly from computer aided design (CAD) model data. While advancements in machine and material technology are reasons for the ability to directly manufacture components using LMT over producing only models and prototypes, the lack of available and reliable data concerning these advancements limits the effective adoption of the technology as a substitute for other manufacturing methods. To decide when AM can be used effectively, data needs to be at the disposal of designers so that they may make decisions about manufacturing of the parts they design. Current trends in CAD software development bring design support tools into the CAD environment, as a method to increase effectiveness into the design process. A support system to guide effective use of LMT would follow this trend and give instant access to information and support decision making for designers in a CAD environment. This research collates, through information gathering and experimentation, process and material data for layer technologies and aims to develop a CAD tool for the support and guidance in decision making about appropriate and effective use of AM.

Keywords: Additive Manufacturing, CAD

1. Introduction

Historically, in the early developmental days of additive technologies, LMT was utilised to produce prototype models that were used as part of a product development strategy. It was not used to produce actual products themselves. Two decades later and additive technologies are used to manufacture many end use parts in metals and polymers including many mimic materials designed to reproduce the properties that might be found in non additive engineering materials [1, 2, 3, 4, 5, 6, 7]. As additive technology improves, produces more materials and becomes more applicable to more sectors, the number of designers and engineers that wish to consider its use will rise. This creates a need for reliable, detailed material and process information that is accessible and up to date.

Additive technology can free design activity to unrestricted levels and offer a flexible manufacturing system which can be lean and extremely agile. In order to take advantage of these qualities, designers and engineers need to have access to all information that will help make decisions on materials and processes early in new projects. Other researchers who wrote on the subject of the effect of additive technologies on current design strategy eluded to the fact that additive technologies would mean more work is done in a CAD environment up to the stage of manufacturing [8] and this seems to have emerged as the current trend. Presently, designers need to be able to work smoothly in a single environment to fully be effective using contemporary technologies. In this way, if more information were at hand regarding additive technologies, concepts that consider them as candidate processes and materials can be tested and validated.

2. Design Issues

There are special circumstances to be considered when it comes to designing a part for manufacture using LMT [7, 8]. As a pre-cursor to existing research, authors documented the potential advantages of additive technologies in manufacturing over non additive manufacturing technologies. Tool-less manufacturing made possible by AM placed more responsibility on the designer or engineer to consider the functional requirements of a product over any future restrictions they may encounter and to be more creative in their solutions. Geometry could be complex and added to designs for free. Yet, more research has revealed a more pragmatic understanding of additive technologies and the factors that define them from one another as with non-additive technologies. Each technology has its own set of parameters or rules. For example, in terms of metal processing, the density of the fabricated parts by the partial-melting systems varies from 45% to 85% of the

theoretical density [1]. It is possible to control material properties such as pore size within a material [9]. Polymer processes vary in their performance and material property characteristics over time and in varying environmental conditions [7]. All processes and materials used in AM have limits on minimum achievable wall thicknesses and minimum details that can be produced.

As we will see from the next section of this paper, a successful decision support tool for material selection should present both numerical data and case based data in various formats to give the designer as much ammunition as possible to make a justified decision [10]. All information regarding the design issues brought about by additive technologies is important for new product developments.

3. Materials Selection

Concerning selection strategies for matching material to a design, four basic steps can be observed as a theoretical basis for future work (Fig 1). Design requirements must be translated into a specification for materials and also processes. Following this, available materials are screened to eliminate those that do not meet the specification. This leaves a sub-set of the original menu of materials that can be considered suitable candidates. A scheme for ranking the surviving sub-set tabulates the most promising candidates and further information provided about the top ranked candidates assists in making an informed decision on a suitable material [11]. The question of which material will satisfy a design, considering non-additive engineering materials, requires a vast knowledge of currently available materials. It can be problematic when there are around 80,000 engineering materials to choose from and around 1000 different ways to process them [11]. Therefore it is important to discover the amount of available additive materials compared to non-additive engineering materials.

A survey conducted by the authors into commercially available materials revealed that there are around 135 additive materials available used by around 12 different additive technologies spread over around 44 different technology platforms. By comparison, the number of materials and processes is significantly smaller than of non-additive engineering materials and processes and so the task of finding a material to satisfy a design or to discover that a design cannot be satisfied should pose a much simpler task. The actual true number of additive materials is probably much higher than the figure published here. However, the survey conducted via the web, did not account for specialist in-house materials developed and used in isolation and materials under development. The information gathered was true in February 2010, the month the survey was conducted.

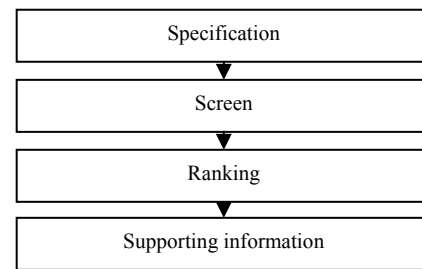


Fig. 1. Four basic steps to selection strategy

In the selection of materials, designers need material information at every stage of the product development cycle. This information is defined using different methods of language [11]. Material properties such as density can be expressed as numerical values and are precise. The ability of a material to be injection moulded is Boolean and returns a 'YES' or a 'NO' answer and is definitive. Other properties such as corrosion resistance are ranked in sets in fuzzy values, 'GOOD' or 'FAIR' or 'POOR', for example [11, 12, 13]. Clear definition of material properties is essential as it is an imperative part of the index of material data sets which is essential to a successful search strategy with suitable returns. The different material properties can themselves be classified to be used as decision criteria. Material mechanical properties include stiffness, hardness etc. Material physical properties concerns cost, density, thermal conductivity, etc. As well as material properties, process properties can also be classified into decision making criteria. Geometric properties like overall dimensions, wall thicknesses. Technological properties such as surface finish and production properties including production volumes are all seen as decision criteria [12, 13]. Most material and process data for non-additive materials and processes is well documented and can be obtained in handbooks and other reference texts. Additive materials, however, are not so advanced. Information is sparse and fragmented. If, for successful material selection support, property data is essential for decision making criteria, then the material properties of AM materials must be known. The authors are engaged in some experiments using fused deposition modelling (FDM) materials which have produced some results on mechanical property and significant other research regarding material properties is ongoing in institutions around the world. However, at present OEMs and vendors seem to be the most easily accessed resource for data. Due to the infancy of the technologies, there are as yet no handbooks or definitive reference texts of data. While the range of materials and processes remains relatively small and navigable, the availability of information to back up data is limited. Where material data is missing, innovative methods are required to make estimations and fill the gaps in the knowledge as full and equal data sets for all materials are required for a true and fair comparison and selection [11].

3.1 Selection methods

According to previous work there are two main components of a material selection strategy. They are a comprehensive database of information with specific data attached at each level and an information system including large amounts of support information in varied formats [11, 13]. In terms of actual strategy for material selection, three main candidates are defined in literature on the subject.

3.1.1 Free searching

Free searching based on qualitative analysis is fast and offers all available material options to a designer or engineer that fit the criteria they set, this strategy needs precisely detailed inputs. The steps of such a strategy are to define the function of the component in question, define the constraints and define free variables. Function could be to support a load case, constraint could be a range of operating temperature and free variable are elements the designer can choose to be variable. Once defined, the problem can be addressed using the three remaining steps used to match material to a design defined by Ashby [11]. Those of screen, rank and support information. [11, 14, 15].

3.1.2 Questionnaire based guide

A questionnaire strategy guides users through structured lines of questioning that leads to decision making. Using this strategy compensates for lack of knowledge on the users part by implementing the knowledge of an expert or experts in the field, however, this strategy does not innovate – it will only return results that are already known to an expert. New materials and processes that do not exist at the time of the questionnaire design will not feature in the returns. Questionnaires do offer resolution but are difficult to create and maintain with up-to-date information [11, 14, 15].

3.1.3 Case based reasoning

Analogy based selection strategy, referred to as inductive reasoning and analogy or case based reasoning, keeps a database of existing case study examples that are indexed so they may be searched for similar cases to a new problem. Typically the database is indexed with keywords. For example, if a design requirement is recyclability, search a case based database for recyclable designs, find similar cases and use the cases to synthesise a new solution and test it. Case based reasoning is a search tool – it creates nothing nor refines anything, this way it is simple to operate if there is sufficient effort applied to the indexing of the database and the quality of indexed material [11, 14, 15].

When we talk about material and process selection and bringing the decision of material and process closer to the design, we talk about concurrent engineering, making all design activities parallel to one another. As such, a good material and process decision support system can

overcome bottlenecks to concurrent engineering which include supported early decision making and feedback facilitating technology. Both would support an efficient concurrent engineering strategy [12].

4. Additive manufacturing materials selection

Considering the theoretical foundation to successful material matching that has been discussed here, the authors are constructing an additive technology specific material and process decision making tool for use within a current CAD environment. Initially the tool has been constructed with very limited functionality. A database has been constructed of available additive material and process data sets that are equal to one another and sufficient enough to allow for static stress analysis under normal conditions (Fig 2).

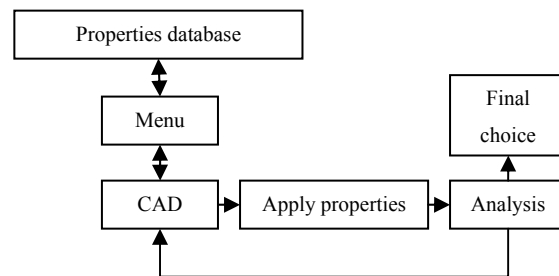


Fig 2. Initial database tool structure

From within a current CAD environment, a menu can be called containing one bottom level set of additive material data listed by names. If a material is selected from this menu, then the properties of that material is applied to the active part in the CAD environment or to the selected parts in an assembly and the part can be analysed using finite element analysis (FEA) to determine its suitability. In this way the tool uses a free search style selection strategy, however screening is a manual operation which requires repeated analysis of available materials until a suitable candidate is found. Information needed to make decisions about material and processes are brought into a CAD environment where the designer will be working. However, in its current state, a tool of this kind is obviously too limited and does not satisfy any of the criteria set out in this paper and confronts neither of the bottlenecks to concurrent engineering. The next stage is to implement a screening function to the tool. Firstly, a search function needs to be added which can handle input of requirements based on numerical material property data. An alternative to data input is to automatically screen a part for fitness to use all available AM materials and processes. The tool, programmed using Visual Basics.Net language, will, by traversing the list of features such as extrusions or sketches used to design the

part, return values that can be checked against rules that are set to evaluate a part's suitability to an additive process and material. Dependant on the rules and the returned values, the part will be screened for suitability to certain additive technologies and materials. Screening is an important element of material selection as it brings about the material subset which can be checked for matching material properties to design requirements and also allows for information to be fed back to a designer (Fig 3). Once a part is selected, the screening process begins to loop eliminating materials and processes that do not fit with the properties of the feature values returned. The final part of the tool to be added is case based information. Case information is recognised as an imperative part of a material selection strategy and is already adopted by some designers when making decisions about AM materials. It is important as numerical and fuzzy data is sparse.

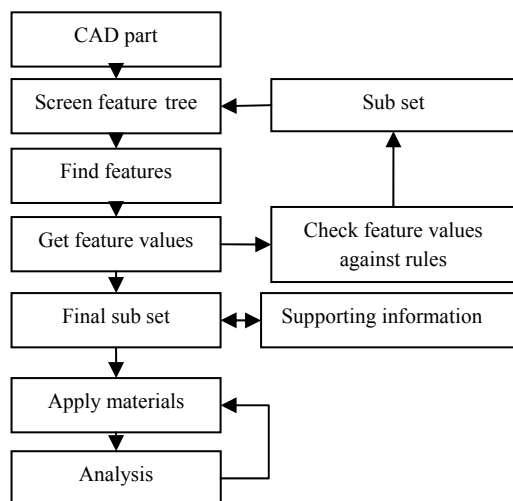


Fig. 3. Basic tool structure for feature traversal, rule checking and sub set creation.

5. Conclusion

Further work is ongoing in the construction of an AM material selection tool. The main area for continued development is in the writing of rules that will control the screening process. To do this well requires detailed, reliable data for additive technologies. The authors will continue to experiment with current metal and polymer processes to ascertain property information that will inform the tool development as well as collate data from other institutions involved in AM data research.

Acknowledgments

The authors acknowledge ESPRC for funding this research through a PhD studentship.

References

- [1] E.C.Santos, M.Shiomi, K.Oskakada & T.Laoui (2006) Rapid manufacturing of metal components by laser forming / *International Journal of Machine Tools & Manufacture* 46 1459–1468
- [2] T.B.Sercombe & G.B.Schaffer (2003) Rapid Manufacturing of Aluminum Components / *Science Magazine* 301 1225–1227
- [3] C.P.Paul, P.Ganesh, S.K.Mishra, P.Bhargava, J.Negi, A.K.Nath (2007) Investigating laser rapid manufacturing for Inconel-625 components / *Optics & Laser Technology* 39 800–805
- [4] P.Rochus, J.Y.Plessier, M.V.Elsen, J.P.Kruth, R.Carrus, T.Dormal (2007) New applications of rapid prototyping and rapid manufacturing (RP/RM) technologies for space instrumentation / *Acta Astronautica* 61 352–359
- [5] J.P.Kruth, L.Froyen, J.V.Vaerenbergh, P.Mercelis, M.Rombouts, B.Lauwers (2004) Selective laser melting of iron-based powder / *Journal of Materials Processing Technology* 149 616–622
- [6] J.P.Kruth, B.Vandenbroucke, J.V.Vaerenbergh, P.Mercelis, (2005) Benchmarking of different sls/slm processes as rapid manufacturing techniques / *Int. Conf. Polymers & Moulds Innovations (PMI), Gent, Belgium*
- [7] R.Hague, S.Mansour, N.Saleh, R.Harris (2004) Materials analysis of stereolithography resins for use in Rapid Manufacturing / *Journal of materials science* 39 2457–2464
- [8] R.Hague, I.Campbell, P.Dickins (2003) Implications on design of rapid manufacturing / *Proc. Instn Mech. Engrs Vol. 217 Part C: J. Mechanical Engineering Science*
- [9] G.V.Salmoria, C.H.Ahrens, P.Klauss, R.A.Paggi, R.G.Oliveira, A.Lago (2007) Rapid Manufacturing of Polyethylene Parts With Controlled Pore Size Gradients Using Selective Laser Sintering / *Materials Research Vol. 10 No. 2* 211–214
- [10] P.C.Smith & A.E.W.Rennie (2008) Development of an Additive Layer Manufacturing Selection Tool for Direct Manufacture of Products / *Procs. Solid Freeform Fabrication Symposium* 507 - 518
- [11] M.F.Ashby, Y.J.M.Brechet, D.Cebon, L.Salvo (2004) Selection strategies for materials and processes / *Materials and Design* 25 51–67
- [12] S.M.Sapuan (2001) A knowledge-based system for materials selection in mechanical engineering design / *Materials and Design* 22 687–695
- [13] R.E.Giachetti (1998) A decision support system for material and manufacturing process selection / *Journal of intelligent manufacturing* 9 265–276
- [14] R.Amen & P.Vomacka (2001) Case-based reasoning as a tool for materials selection / *Materials and Design* 22 353–358
- [15] Y.Braechet, D.Bassetti, D.Landru & L.Salvo (2001) Challenges in materials and process selection / *Progress in materials science* 46 407–428

Dynamic strength and fracture toughness analysis of beam melted parts

J.T. Sehr¹, Prof. G. Witt²

¹ University of Duisburg-Essen, Institute for Product Engineering, Manufacturing Technology, Lotharstr. 1, 47057 Duisburg, Germany

² University of Duisburg-Essen, Institute for Product Engineering, Manufacturing Technology, Lotharstr. 1, 47057 Duisburg, Germany

Abstract. Today's advancement of the market requires innovative thoughts and further development of additive manufacturing processes like beam melting (Direct Metal Laser-Sintering). Among the huge number of additive fabrication methods, the direct manufacturing of metal parts in a powder bed using a laser or electron beam is called *beam melting*. This neutral term is relatively new and was used in the VDI Guideline 3404 for the first time. In general the additive fabrication differs from conventional technologies by its layerwise and additive joining together material to a physical part. For the construction and the use of beam melted parts and in order to reduce the risk of mechanical defects in a part, a comprehensive material understanding is essential. Cracks caused by dynamic loads can be avoided in advance by dynamic analysis, appropriate design and correct manufacturing of the parts. For this reason, dynamic strength analysis (using a rotating bending test) of beam melted parts made of stainless steel has been applied and Woehler curves for different survivabilities determined. To highlight the resistance of beam melted parts to operation and production damage, the fracture toughness (stress intensity factor) of beam melted parts has also been investigated.

Keywords: Additive fabrication, beam melting (Direct Metal Laser-Sintering), Rapid Manufacturing, e-manufacturing, dynamic strength (Woehler), fracture toughness, stress intensity factor, dimensioning of parts, Stainless Steel GP1

1. Dynamic strength analysis of beam melted parts

The calculation and dimensioning of beam melted parts exposed to dynamic loads become more and more important especially with regard to the increasing number of Rapid Manufacturing applications. Damage caused by fractures resulting from fluctuating stress can be avoided by appropriate designs and correct manufacturing of parts [1],[2]. For this reason, dynamic strength analysis by Woehler fatigue tests of beam melted parts made of stainless steel (GP 1) are reported in this paper. Here the fatigue strength under repeated bending stresses is discussed and evaluated by the nominal stress approach. According to DIN 50100 [3], the fatigue strength is de-

scribed as the maximum stress amplitude oscillating around a given mean stress, that a specimen can endure for endless cycles ($N_D = 10^7$) without breaking and without unacceptable deformation.

2. Manufacturing and finishing of rotating bend test specimen

By rotating bending tests of 40 specimens of beam melted stainless steel (GP 1) made on an EOSINT M 270 machine with standard exposure strategies of the laser, Woehler curves are determined. After beam melting the specimens are turned and finished to the desired geometry and dimensions shown in Figure 1.

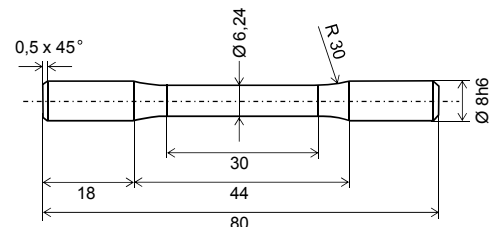
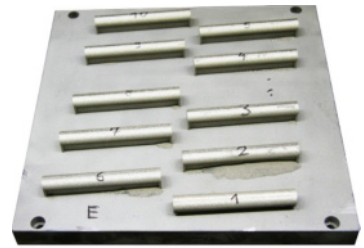


Fig 1. Geometry and dimensions of rotating bending test specimen

The initial and beam melted geometry for the specimen is cylindrical with a diameter of 12 mm and a length of 86 mm (cf. Fig. 2 a). This oversize of the specimen allows for the reduction of warping caused by residual stresses of the horizontal oriented specimen on the build platform. One of the four build platforms with a set of beam melted specimens (10 pcs.) and ready finished specimens are shown in Figure 2. Here the ready turned specimens are also polished in different steps to reduce the surface roughness to a minimum since dynamic loaded parts show high sensitivity to surface imperfection.



a - Build platform with a set of specimens



b - Ready finished specimens

Fig 2. Rotating bending test specimens

3. Rotating bending test

In carrying out the Woehler test, several equivalent test specimens are investigated at defined and graded oscillating stresses and out of this, the resulting number of cycles that lead to fracture of the specimen is determined [3]. The adjusted amplitudes of loadings alternating around the mean stress of $\sigma_m = 0 \text{ N/mm}^2$ are constant for each specimen during the Woehler test. To define and adjust the amplitudes, a load increase test is carried out on one of the beam melted specimens. This procedure is necessary because no reference values for the fatigue strength are given for this specific beam melted material. So the upper bending amplitude of the loads is set to 500 N/mm^2 and lowered, step by step, at 10 N/mm^2 for different specimens until one specimen reaches the fatigue strength limit of $N_D = 10^7$ cycles without breaking. If this result can be repeated three times the corresponding bending stress is the preliminary bending fatigue stress. To back up the results, four specimens are tested for each load.

4. Evaluation and interpretation of the results

For the investigation of the Woehler curves from the data described before, several equations can be found in references. Here the Woehler curves are described in the form of a double logarithmical illustration by Basquin. Thereby the fatigue characteristic is shown as a straight line which is limited at the top by the yield strength and at the bottom by the fatigue strength of the material [1, 2, 4].

The two constants m and K are calculated by the method of least squares with the software Fatigue 1.1 [4]. Afterwards the fatigue strength lines for different surviv-

abilities are calculated with the linear equation (1.6) and are shown in Figure 3. Also the result of each tested specimen can be seen by the blue rhombuses.

$$(\sigma/\sigma_D)^m = (N_D/N) \quad (1.1)$$

after conversion

$$N = N_D \cdot \sigma_D^m / \sigma^m \quad (1.2)$$

with

$$K = N_D \cdot \sigma_D^m \quad (1.3)$$

is

$$N = K \cdot \sigma^{-m} \quad (1.4)$$

taking the logarithm

$$\lg N = \lg K - m \cdot \lg \sigma \quad (1.5)$$

converting to a linear equation

$$\lg \sigma = \lg K/m - \lg N/m \quad (1.6)$$

nomenclature:

σ = stress amplitude [N/mm^2]

σ_D = fatigue strength [N/mm^2]

N = number of cycles

N_D = limit of cycles ($= 10^7$)

m = Woehler curve exponent

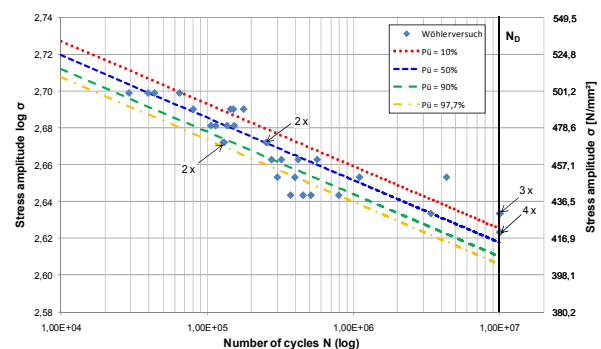


Fig 3. Woehler curves

With these Woehler curves, conclusions on the failure of beam melted parts can be made for different survivabilities between 10 % and 97,5 % at specific loads. Most of the results of the tested specimen are inside or near the range of these survivabilities. The intersections of these lines with the line of the limited cycles ($N_D = 10^7$) represent the stress amplitude for each survivability that a specimen can withstand for ever. In general, the stress amplitude for a survivability of 90 % is given as the fatigue strength [5]. Here it is $\sigma_{bw} = 407,45 \text{ N/mm}^2$. Beam melted parts exposed to this specific stress value can withstand 10.000.000 cycles or more without breaking with a survivability of 90 %. Compared with the range of fatigue strengths of conventional manufactured parts made of the same material and axial loads (364 - 542 N/mm^2 [6]) the value determined here lies in between.

5. Fracture toughness analysis of beam melted parts

Besides static and dynamic strength analysis, knowledge of the fracture toughness of parts is essential for their dimensioning. With it, indications of the amount of stress required to propagate a preexisting flaw can be made. Thus it is one of the most important material properties since the occurrence of flaws are not completely avoidable in the processing or fabrication of parts. In this section, the fracture toughness is investigated according to DIN EN ISO 12737 [7, 8].

6. Manufacturing and finishing of compact tension (CT) test specimen

As a specimen, the disk shaped compact tension geometry according to ASTM E399 [9] is chosen that corresponds to the standard compact tension specimen in DIN EN ISO 12737 with regard to the main dimensions (cf. Figure 4.). Fixed dimensions are not given in these standards because all dimensions have to fulfill the special requirements of the linear-elastic fracture mechanics and with it they depend on material characteristics. For this reason only the interdependent dimensions are given.

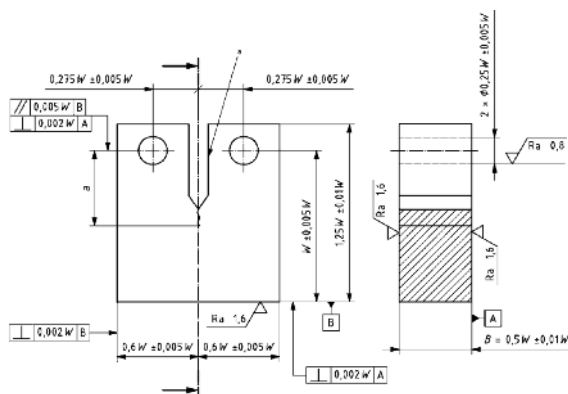


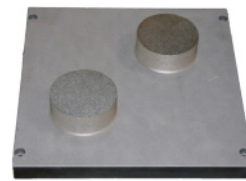
Fig 4. Standard compact tension specimen [8]

Not until all investigations are complete can the validation of the geometry be controlled according to special criteria and with it according to a valid critical stress intensity factor (K_{Ic}). All in all, six specimens of beam melted stainless steel (GP 1) are made with standard exposure strategies of the laser (cf. Figure 5 a).

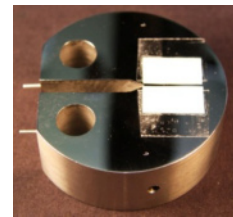
The chosen dimensions of the specimen are thickness $B = 1 \text{ in} \pm 0.02 \text{ in}$ and width to load line $W = 2 \text{ in} \pm 0.01 \text{ in}$. Again the oversized specimens are machined after beam melting to the desired geometry and prepared for testing (cf. Figure 5 b).

7. Fracture toughness test

The fracture toughness test begins with the initiation of the flaw by cyclic loadings (10 Hz) of 20,000 N and 15,000 N with stress ratios of $R = 0.1$. The loading is transferred to the specimen by bolts in the boreholes. The fatigue crack initiates and propagates starting at the top of the Chevron-notch and is stopped after 4-5 mm. The crack propagation is controlled by measuring the voltage potential at the two electrodes on the left side of the specimen in Fig. 5 b. Before carrying out the tensile test, the two electrodes are replaced by a displacement transducer for measuring the crack opening. According to DIN EN ISO 12737, the tensile test is carried out at a rate of rise of the critical stress intensity factor of $0.5\text{--}3.0 \text{ MPa}\sqrt{\text{m/s}}$.



a - Build platform with two specimens



b - Ready prepared specimen

Fig 5. CT test specimen

8. Evaluation and interpretation of the results

After the specimen is broken, several dimensions such as thickness (B), width to load line (W) and the mean crack length (a) are measured from the photographs as illustrated in Figure 6.

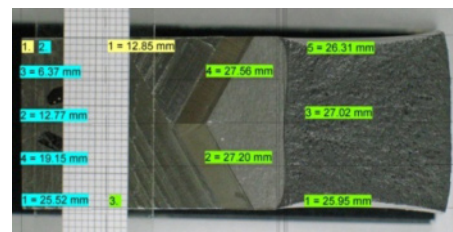


Fig 6. Digital measurement of a CT test specimen (fracture surface)

The crack surface of the fatigue fracture is smooth and light whereas the surface of the final fracture is rough and dark. It turns out that all results of the measurements fulfill the criteria for the linear-elastic fracture mechanics

so far. And with it, the preliminary critical stress intensity factor K_Q can be calculated as follows [8]:

(1.7)

with

K_Q = preliminary critical stress intensity factor

F_Q = specific force F [kN]

B = thickness [cm]

W = width to load line [cm]

$f(a/W)$ = correction function

$$f\left(\frac{a}{W}\right) = \left(2 + \frac{a}{W}\right) \cdot \frac{0,886 + 4,64 \left(\frac{a}{W}\right) - 13,32 \left(\frac{a}{W}\right)^2 + 14,72 \left(\frac{a}{W}\right)^3 - 5,6 \left(\frac{a}{W}\right)^4}{\left(1 - \frac{a}{W}\right)^3}$$

a = mean crack length [cm]

The determination of the force F_Q for each specimen can be described and explained by the force-deflection graph in Figure 7.

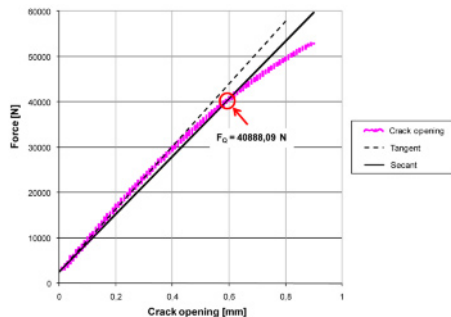


Fig 7. Determination of the force F_Q for sample No. 6

At the beginning of the graph, the force progression shows linear-elastic characteristics up to a crack opening of about 0,4 mm which then flattens at higher forces. To determine the force F_Q a tangent line is drawn at the linear-elastic part of the graph. Then a second line is drawn on the graph with the 0.95-fold slope of the slope of the tangent. Now the force F_Q is defined as the intersection of this secant with the stress-strain curve. For sample No. 6 the force F_Q is 40888.09 N. Table 1 summarises some values of the CT specimen necessary for the validation of a critical stress intensity factor (K_{Ic}).

From the table, it can be seen that the requested relative strength of F_{max}/F_Q is not achieved, being smaller than 1.1 as specified by DIN EN ISO 12737. Also the second criterion for a valid critical stress intensity factor cannot be fulfilled, it says that the thickness (B), the crack length (a) and the ligament length ($W-a$) of each specimen must be bigger than the value calculated by the equation $2.5 \times (K_Q/R_{p0,2})^2$ with $R_{p0,2}$ representing the yield strength. So the requirements of the linear-elastic fracture mechanics are not fulfilled and for that reason the determined values for the preliminary critical stress intensity factor K_Q cannot be equalized with the valid critical stress intensity factor K_{Ic} . This result can be explained by too

small a thickness of the specimen and the relative high ductility of the beam melted material. Related to this, the plastic zone here is too big compared with the elastic deformed material of the specimens.

Table 1. Single values of the forces and of the preliminary critical stress intensity factors

Sample No.	F_{max} [N]	F_Q [N]	F_{max}/F_Q	K_Q [MPa√m]
1	59066,07	37614,21	1,57	87,47
2	63957,78	41515,99	1,54	92,04
3	63734,44	40975,25	1,56	90,52
4	78524,09	42489,63	1,85	80,28
5	65717,28	44712,16	1,47	94,73
6	64851,15	40888,09	1,59	90,24
Mean	65975,14	41365,89	1,60	89,21

It can be assumed that before the specimens break in the tensile test, an obvious plastic deformation occurs at the top of the crack. Nevertheless, the mean value of the preliminary critical stress intensity factor is $K_Q = 89.21 \text{ MPa}\sqrt{\text{m}} \pm 4.98 \text{ MPa}\sqrt{\text{m}}$. Even though this preliminary value does not represent a valid critical stress intensity factor, it can be taken for a first dimensioning of beam melted parts especially because no comparative values for beam melted materials exist in references. Probably the valid K_{Ic} -value is slightly smaller than the K_Q -value. To equalize these two values, the dimensions of the test specimen must be enlarged significantly and this could lead to problems in the beam melting process especially with regard to the effective building volume of the machine and economics. Comparing this determined K_Q -value of beam melted parts to K_{Ic} -values ($K_{Ic} = 29.7 - 158 \text{ MPa}\sqrt{\text{m}}$ [6]) of conventional made parts of the same material number (1.4542), it can be seen that the K_Q -value is in between.

References

- [1] Haibach, E. Betriebsfestigkeit - Verfahren und Daten zur Bauteilberechnung. Berlin Heidelberg : Springer Verlag, 2006. ISBN: 978-3-540-29363-7.
- [2] Radaj, D. und Vormwald, M. Ermüdungsfestigkeit - Grundlagen für Ingenieure. Berlin Heidelberg : Springer Verlag, 2007. ISBN: 978-3-540-71458-3.
- [3] Werkstoffprüfung - Dauerschwingversuch - Begriffe Zeichen Durchführung Auswertung. DIN 50100 Februar 1978.
- [4] Naubereit, H. und Weihert, J. Einführung in die Ermüdungsfestigkeit. München Wien : Carl Hanser Verlag, 1999. ISBN: 3-446-21028-8.
- [5] Matek, W., et al. Roloff/Matek - Maschinenelemente. Braunschweig Wiesbaden : Vieweg Verlag, 1995. ISBN: 3-528-74028-0.
- [6] Granta Design Limited. CES EduPack Software. Cambridge, United Kingdom : s.n., 2009.
- [7] Rösler, J., Harders, H. und Bäker, M. Mechanisches Verhalten der Werkstoffe. Wiesbaden : B.G. Teubner Verlag, 2006. ISBN: 978-3-8351-0008-4.
- [8] Metallische Werkstoffe - Bestimmung der Bruchzähigkeit (ebener Dehnungszustand). DIN EN ISO 12737 Oktober 2005.
- [9] Standard Test Method for Linear-Elastic Plane-Strain Fracture Toughness K_{Ic} of Metallic Materials. ASTM E399 - 90 USA, 1990.

An additive method for photopatterning of metals on flexible substrates

J.H.-G. Ng¹, D.E.G. Watson¹, J. Sigwarth¹, A. McCarthy², H. Suyal², D.P. Hand³, T.Y. Hin⁴ and M.P.Y. Desmulliez¹

¹ Microsystems Engineering Centre (MISEC), Heriot-Watt University, United Kingdom.

² Optical Interconnects Group, Heriot-Watt University, United Kingdom.

³ Applied Optics and Photonics Group (AOP), Heriot-Watt University, United Kingdom.

⁴ Wolfson School of Mechanical and Manufacturing Engineering, Loughborough University, United Kingdom.

Abstract. Here we present an additive and cost effective process for plastic electronic manufacturing. Metal tracks are fabricated on polyimide substrates via simple chemical processes combined with direct laser writing or photomask exposure. Laser write speed up to 0.5 m.s^{-1} and metal track linewidth as low as $5 \mu\text{m}$ were achieved. Further, this process was easily extended to 3D manufacturing; a helical silver track was written onto a cylindrical substrate. Selective electroless plating was also demonstrated on the photopatterned microstructures which showed promising conductivity close to that of bulk silver metal.

Keywords: polyimide, laser, direct writing, 3D manufacturing, ion-exchange, silver, electroless plating, fine linewidth, flexible circuits, plastic electronics.

1. Introduction

Rapid, cost effective prototyping and manufacturing is gaining increasing attention amongst academic researchers and industries. This is driven by the future demands of customisable and low volume production of high technology devices. To meet these demands, some drastically different fabrication methodologies have emerged recently with the aim of replacing traditional techniques which are either time-consuming or lacking adaptability.

In the field of plastic electronic technology at present, various routes on a roadmap to a standard manufacturing process are being developed. One such route, presented in this paper, is an additive method for photopatterning of metals on polyimide flexible substrate that comprises a multitude of benefits. These include eliminating the use of evaporation or any vapour phase chemical precursors and therefore no vacuum chambers are needed. The reliance on photoresist processing or expensive stencil masks for printing and proprietary conductive paste or ink is also unnecessary.

The present method developed by our group utilised a photoreactive coating which upon illumination of light with suitable wavelength, assisted the photochemical

reduction of silver ions on a polyimide substrate [1]. The silver ions were first incorporated into a thin depth of the substrate surface by potassium hydroxide (KOH) modification and then a simple ion-exchange process using a silver nitrate (AgNO_3) solution. After exposure to light, the silver ion source in the exposed area was reduced to metallic silver particles. The exposure can be carried out by laser direct-writing or via a photomask exposure system. Since the metalisation is a photochemical reduction process instead of a thermally driven mechanism, it has an advantage of allowing low energy fluence source to be used. Therefore ultra-fine resolution feature can be realised whilst the effects of excessive laser energy diffusion and thermal degradation to the substrates can be minimised.

After washing out the unreacted silver ions and an annealing step, the patterned silver particles serve as an active seed layer for subsequent electroless plating in order to produce a thicker layer with better conductivity.

The morphology of the laser written tracks and the effects of write speed are presented along with a demonstration of 3-dimensional fabrication. Also discussed are conductivity results of electrolessly plated microstructures, which were patterned with a photomask exposure system.

2. Experimental Setup

2.1 Substrate preparation

Kapton HN ($50 \mu\text{m}$) from DuPont was used as a substrate. After cleaning rinse steps of acetone, isopropyl alcohol and deionised water, this was treated in 1 M KOH at 50°C for 5 minutes to cleave the imide rings within the polymer matrix and allow potassium ions to bond electrostatically with the carboxylic acid ions. It was then immersed in 0.1 M AgNO_3 solution at room temperature

for 15 minutes, exchanging the potassium ions with silver ions. Samples were then spray-coated with 100 g.l⁻¹ methoxypolyethylene-glycol (MPEG) in absolute ethanol. This coating served as a reducing agent during the photopatterning step.

2.2 Direct laser writing exposure

The first photopatterning method was laser direct writing using a HeCd laser of wavelength 325 nm with Gaussian TEM₀₀ beam profile. The maximum available power at the writing plane was ~3 mW. Different focussing lenses were used to provide spot sizes ranging from a few microns up to approximately 35 μm . Various write speeds up to 0.5 m.s⁻¹ were employed.

2.3 Photomask exposure

Samples were also patterned using a Tamarack mask aligner UV-exposure system using a roughly collimated light source, emitting in the range 250 - 450 nm, for various times at an intensity of ~50 mW.cm⁻². A chrome on glass photomask was used, with the exposed areas forming the silver seed-layer regions.

2.4 Post-Exposure Treatment

After exposure the samples were submerged in 1% w/w sulphuric acid solution for 15 minutes to remove the unreduced silver ions from the substrate before annealing in an oven at 300 °C for various times. This step induced both the reimidisation of the previously cleaved imide ring and the agglomeration of silver nanoparticles.

2.5 Electroless Plating

The plating was carried out using two baths. The first was a formaldehyde EDTA based copper bath Circuposit 4750 sourced from Rohm & Haas. This bath was operated at a temperature of 53°C and a pH near 13. The second was a cyanide based silver bath ESM series (ESM 100 and ESM 500) from Polymer Kompositer AB, Sweden. This particular product was chosen as the less alkaline pH was more favourable for polyimide substrates. For plating, the bath was heated to 67°C, and the pH was adjusted to values in the range of approximately 7 to 9.

2.6 Characterisation

Characterisation of the samples was carried out using optical microscopy using a Leica DM LM microscope, a Zygo white light interferometer, field emission gun scanning electron microscope (FEGSEM), scanning electron microscope (SEM) and a four-point probe station.

3. Laser Direct-Writing Results

3.1 Morphology

In the present direct-write approach, silver particles can be formed in situ during laser writing from the metal ion source in the substrate. The beam profile of the laser light can directly change the geometry of the written lines. Fine linewidth from less than 15 μm down (Figure 1) down to about 10 μm (Figure 2) have been demonstrated.

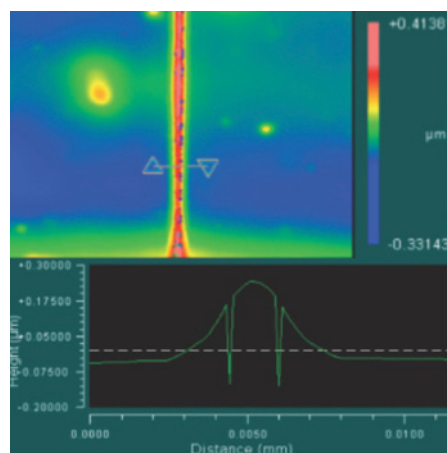


Fig. 1 Zygo white light interferometry profile of a silver track directly metalised by CW UV laser scanning.

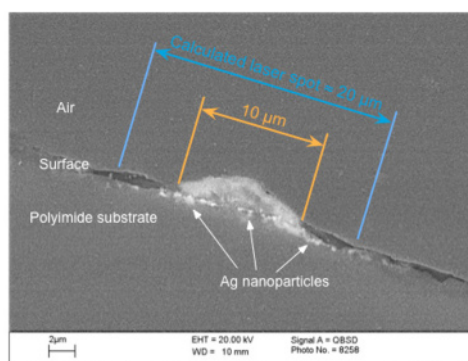
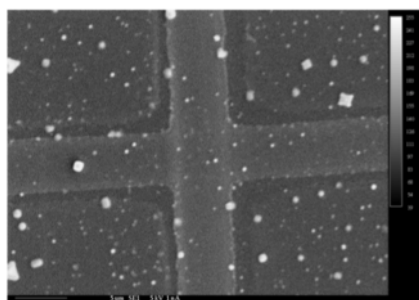


Fig. 2 FEGSEM image of cross-section of laser written track.

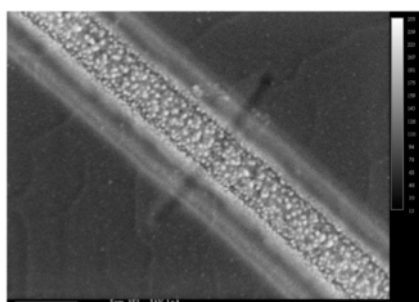
The white light interferometry profile above showed that silver aggregates were grown above the surface of the substrate from the Ag⁺ ion source embedded within the substrate. This is believed to be the result of the extremely rapid nucleation of silver particles from the UV photoreduction of the Ag⁺ ions. The height profile of the silver deposit mirrors the Gaussian shape of the laser intensity profile. A cross-section of a track was imaged by FEGSEM as shown in Figure 2. It can be seen that a thin layer of silver nanoparticles was formed just underneath the surface of the substrate. At the centre of the laser spot where the incident energy was most intense,

a much larger amount of silver aggregates were protruding from the surface of the substrate.

The SEM images (Figure 3) below showed laser direct-written tracks with ultra fine linewidth of $\sim 5 \mu\text{m}$ demonstrated. The high magnification image (Figure 3b) clearly showed that the centre of the track consisted of a rough nanoparticle morphology with a particle size distribution between 100 – 700 nm. The shoulders of the Gaussian beam profile with a much weaker intensity caused a significantly slower rate of photoreduction of silver ions on both edges of the track, and hence a lower density of metallic silver present.



a



b

Fig. 3 SEM images of: (a) laser direct-written tracks with linewidth $\sim 5 \mu\text{m}$; (b) high magnification image.

3.2 Effects of Write Speed

The effects of varying the laser write speed, and therefore the energy fluence, on the profile of the tracks were investigated (Figure 4). It was found that at higher write speeds such as $10,000 \mu\text{m}\cdot\text{s}^{-1}$, a uniform, reflective silver track with straight track edges was formed. At slower write speeds, it can be observed that the silver at the centre of the track became discontinuous islands or disappeared completely. This phenomenon could be attributed to the excessive laser energy at such slow write speeds causing degradation of the polymer substrate underneath the silver. The silver nanoparticle surface morphology at the track centre serves as a catalyst to initiate electroless plating. Figure 5 shows a microcoil plated with the electroless copper bath.

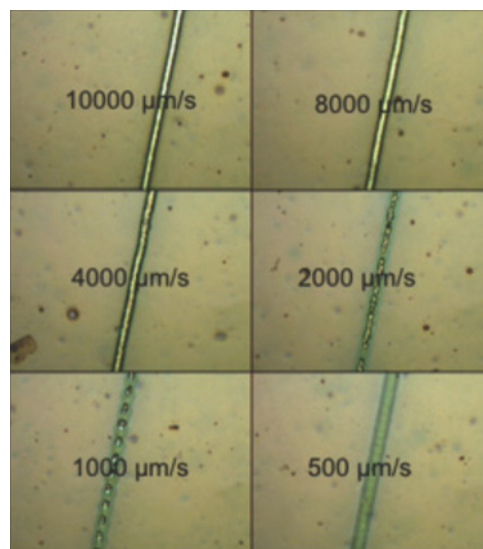


Fig. 4 Microscope images of tracks produced by different laser writing speeds

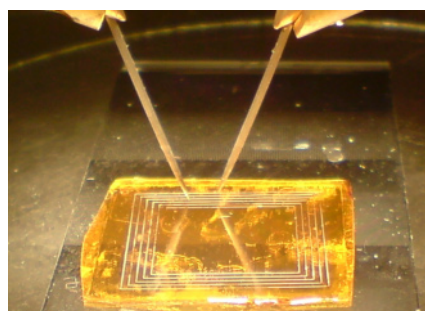


Fig. 5 An electroless Cu plated micro-coil fabricated by laser direct-writing.

3.3 3-Dimensional Direct-Writing

The direct-writing method presented here uses a dry photoreactive coating and was carried out simply in an air atmosphere. Since no evaporation or lamination steps are required in the entire fabrication process, it allows the flexibility for the photopatterning to be carried out on contoured or 3-dimensional (3D) surfaces. A long helical metal track on a cylindrical polyimide substrate was fabricated by laser direct-writing whose setup is shown in Figure 6. A fine linewidth track of $15 \mu\text{m}$ was directly written on a 1 cm diameter polyimide cylinder, with a helix spacing of about 0.1 cm. A continuous coil of 20 turns was demonstrated, shown in Figure 7. This 3D patterning technology is envisaged to enable the manufacturing of advanced 3D interconnection for packaging. The process lends itself to low cost manufacturing of planarised or 2.5D structures such as spiral inductors or interdigital elements used in components such as capacitors or inter-digital electrodes.

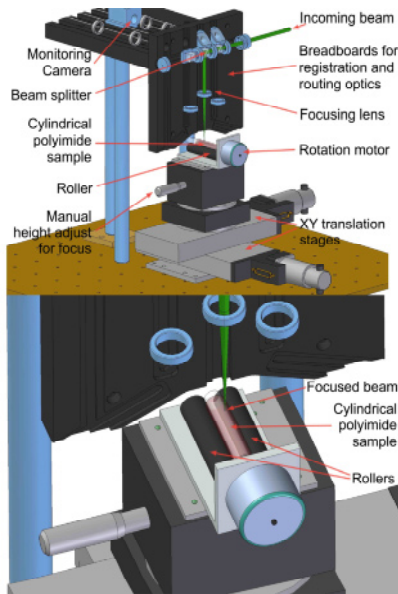


Fig. 6 Schematic diagram of the 3D laser writing set up.

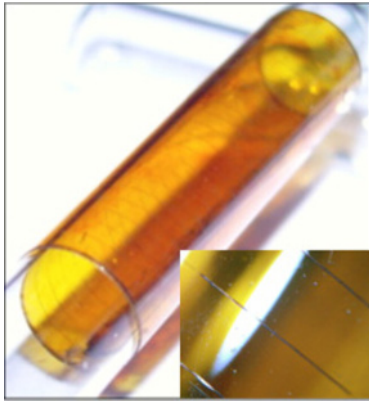


Fig. 7 Long silver helix track fabricated by a laser on glass pipette coated with a polyimide film. Inset showed magnified image of the track with a linewidth $\sim 15 \mu\text{m}$.

3.4 Photomask Exposure and Plating Results

Electroless plating was applied to grow a conductive silver layer on microstructures as shown in Figure 8. Samples were immersed in the bath for approximately 6 minutes, until the plated layer was visibly distinguishable to the naked eye. Plating heights of $\sim 2 \mu\text{m}$ were produced. Using the resistance measured by a probe station the resistivity, ρ , was found by:

$$\rho = R \frac{A}{l} \quad (1)$$

where A and l are the cross-sectional area and length of the measured section respectively and R is the measured resistance. A value of $7.6 \times 10^{-7} \Omega\cdot\text{m}$ was measured

between the points shown in Figure 8. This value is an order of magnitude higher than that of bulk silver ($1.59 \times 10^{-8} \Omega\cdot\text{m}$). However, the parameters of the bath can be optimised to improve the plated silver quality. The ESM bath was found to produce more consistent plating in terms of selectivity and under/over-plating compared to the Circuposit Cu bath in the present process.

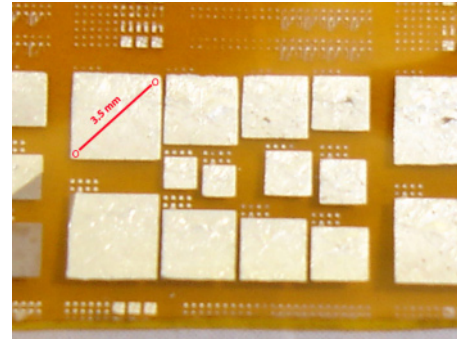


Fig. 8 Image showing the microstructures plated with electroless Ag. Red line indicates points of resistivity measurement.

4. Conclusion

The present process is easy to use, requires low cost raw materials, does not require sophisticated equipments and due to its additive nature is low on waste materials. Feature sizes as small as $\sim 5 \mu\text{m}$ have been demonstrated.

Further advantages are that process can be easily adapted for 3-D manufacturing, reduced processing steps leading to quicker turnover times, and the amount of proprietary products (photoresist material, developer solution, conductive paste or ink) required is minimized.

The less alkaline ESM bath was found to produce more consistent results due to the pH sensitivity of polyimide [2]. The bath was also more configurable, therefore more suitable during process development as well as showing promising conductivity and selectivity during initial tests.

Acknowledgement

This work was supported by the EPSRC-funded project 3D-Mintegration, referenced EP/C 534212/1.

References

- [1] Ng JHG, Desmulliez MPY, Prior KA, Hand DP. Ultra-violet direct patterning of metal on polyimide. *Micro & Nano Letters*. 2008;3:82-89.
- [2] Ng JHG, Desmulliez MPY, Lamponi M *et al*. A direct-writing approach to the micro-patterning of copper onto polyimide. *Circuit World*. 2009;35:3-17.

An investigation of the EREE-based low carbon manufacturing on CNC machine

S. Tridech and K. Cheng

Advanced Manufacturing and Enterprise Engineering Department, School of Engineering and Design, Brunel University, Uxbridge UB8 3PH, United Kingdom. Emails: sakda.tridech@brunel.ac.uk; kai.cheng@brunel.ac.uk

Abstract. In CNC based machining, there are many factors, such as cutting process parameters set-up, material and cutting tool selection and machine utilization planning associated with the manufacturing process, which can lead to ineffective energy consumption, irrational resource utilization and waste generation, and consequently the large impact on carbon footprint resulted from the process. The conception of energy and resource efficiency and effectiveness (EREE) based low carbon manufacturing focuses on efficiency and effectiveness in utilizing energy/material resources and minimizing the waste generation in CNC machining. Therefore, it is essential to investigate and develop the industrial feasible/reliable methodologies and solutions applicable to CNC machines and operations. In this paper, a systematic modelling, simulation and implementation approach is proposed, which cover three parts: energy efficiency, resource utilization and waste minimization in CNC machining and operations. Energy efficiency of machine is determined by studying on the drive/actuation motors using fuzzy inference engine (FIS) while resource utilization planning is carried out by optimizing the process based on cutting parameters, material and cutting tool using the models with MATLAB-based programming. Waste minimization of the machine is evaluated specifically on idle time, machine scrap components and downtime by applying discrete event simulation, etc. This paper also presents a case study on a CNC manufacturing system with application perspectives and optimized results on energy consumption. Finally, the paper concludes with the discussion on the EREE-based low carbon manufacturing approach, its potential and applications, and future research agenda.

Keywords: Energy and resource efficiency and effectiveness (EREE) in CNC machining, resource utilization, waste minimization, carbon footprint, CNC machining and optimization

Nomenclature

- p workpiece type; $p \in \{1, 2, \dots, P\}$
 m machine type; $m \in \{1, 2, \dots, m\}$
 n operation for workpiece p ; $n \in \{1, 2, \dots, N_p\}$
 S_{pn} set of machine that can perform operation n of workpiece p ;
 S_{mp} set of part type that can perform on machine m ;
 S_{np} set of operation of part type that can perform on machine m ;
 x_{nmp} operation n of work-piece p perform on machine m

1. Introduction

Sustainable manufacturing has been proposed as a timely topic since, the awareness of environmental impact especially on carbon footprint and energy consumption associated with manufacturing systems has been more considered as a crucial factor in the past few years [1]. Regarding to this conception, the energy and resource efficiency and effectiveness (EREE) in manufacturing a part is now becoming an important part of the total cost associated with the product and its manufacturing process chain. Therefore, it is essential and much needed to understand EREE-based issues at the manufacturing process/machine, shop-floor, factory/enterprise and even the manufacturing supply chains in order to reduce energy consumption, optimize resource utilization and even minimize waste [2].

In a CNC manufacturing system, most of manufacturers focus on machining parameters (cutting speed, depth of cut, feed rate) as they can reflect on process efficiency and performance characteristics. However, a schism arises when the rising of energy demand and the constraint of energy supply are becoming the most prior manufacturing criteria. On the other hand, it could be implied that it is difficult to optimize CNC process parameters throughout production system in order to achieve both typical requirements and environmental issues [3].

This paper proposes the generic modelling of EREE-based low carbon manufacturing on CNC machines which aims to develop a systematic approach for addressing the issues described above in a scientific manner.

2. EREE-based LCM: Conception

As shown in Fig.1, the conception of EREE-based LCM which consists of three characterisations: energy efficiency, resource utilization and waste minimization as proposed by the authors [4]. This conception is developed to enhance the manufacturing system in term of evaluating amount of energy consumption at each work station, shop-floor and manufacturing with maximum efficiency and effectiveness, optimizing the utilization of the existing resource capacity/constraints and even minimizing waste that can occur from each manufacturing process throughout the production line, including component scrapping, machine down time, idle time and operator errors etc. However, this conception is not being developed for only environmental and energy criteria but also concerned with simultaneously maintaining the optimal manufacturing performance covering the cost, quality, delivery time and sustainability.

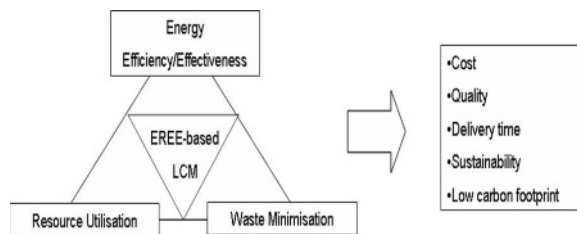


Fig. 1. The conception for EREE-based LCM.

3. Generic modelling of EREE-based LCM for CNC machines

The generic modelling of EREE-based LCM aims to reduce unnecessary energy consumption in the manufacturing process, optimize and maximize existing resource/constraint in the system, minimize waste associated with the specific process and eventually achieve the lowest amount of carbon footprint. The methodology for the design of the generic modelling of EREE-based LCM is illustrated in Fig. 2.

The methodology consists of three important parts: energy modelling, production optimization and process simulation, which can be described as the strategic planning system for EREE-based LCM.

The energy modelling provides the ability to evaluate the amount of energy consumption of a workpiece when cutting parameters (cutting speed, depth of cut, feed rate) were changed on initial conditions set-up. The decision maker is able to select the specific energy modelling associated with the specific machine (different machine has different energy model) in order to specify the desire cutting parameter and observe the changed value of consumed energy. In this research, the principle of fuzzy

inference engine (FIS) [5] is used to establish the energy model for the CNC machine.

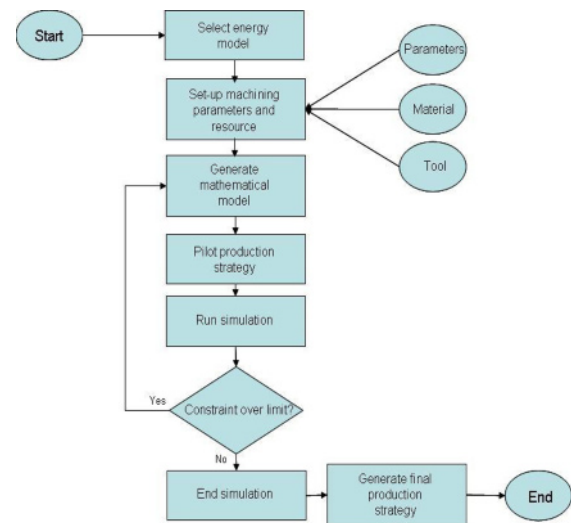


Fig. 2. The design methodology for EREE-based LCM.

The model uses fuzzy rule to evaluate the amount of energy consumption depending on all input parameters. To generate fuzzy rule base, the cutting trial experiments were undertaken on a CNC machine which is connected with data acquisition device. Each workpiece was cut with different cutting parameters. The data obtained from data acquisition will show the value of energy consumption affected by cutting parameters. The set of data, then, is used to analyze with statistic method called 'response surface methodology (RSM)' to generate function for fuzzy rule base. In Fig. 3, the method of fuzzy rule base establishment is illustrated.

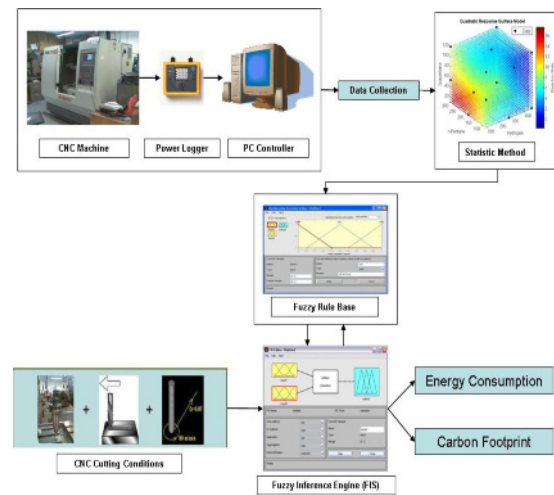


Fig. 3. Energy modelling establishment.

In optimization of the CNC manufacturing system, the theory of operation research is used to formulate the mathematical model of the interested system. The energy

modelling (FIS) which represents the energy performance of the specific machine is used as the objective function together with other objective functions (cost, time, etc.). The resource capacity and manufacturing requirement are transformed into system constraint equations. For example, work-piece '1' can be manufactured by machine A, C and D, the equation is stated in the following mathematical model constraint. In this research, the interested system used as a case study is a flexible manufacturing planning system. The objective of this work is to produce work orders with minimization of energy consumption, cost of production and total production time. The mathematical model, then, is formulated with multi-objective fuzzy integer programming [5-7] to eliminate the conflict between objective functions. The example of mathematical modelling is expressed as follows.

3.1 Objectives

Minimization of energy consumption of CNC machine:

$$x_{ijk} \begin{cases} 1 & \text{if operation } j \text{ of workpiece } i \text{ perform on machine } k \\ 0 & \text{if else} \end{cases}$$

$$V_1(f_1(x)) = \begin{cases} 1 & \text{if } f_1(x) < g_1 \\ 1 - \frac{\sum f_1(x) - g_1}{a_1} & \text{if } g_1 \leq f_1(x) \leq g_1 + a_1 \\ 0 & \text{if } f_1(x) > g_1 + a_1 \end{cases}$$

$f_1(x)$ represents the energy modeling of CNC machine
 g_1 represents goal of system energy consumption
 $g_1 + a_1$ represents exceed limit of energy consumption
 $V_1 f_1(x)$ represents fuzzy value of energy consumption

Minimization of cost of production is:

$$V_2(f_2(x)) = \begin{cases} 1 & \text{if } f_2(x) < g_2 \\ 1 - \frac{f_2(x) - g_2}{a_2} & \text{if } g_2 \leq f_2(x) \leq g_2 + a_2 \\ 0 & \text{if } f_2(x) > g_2 + a_2 \end{cases}$$

$f_2(x)$ represents the cost of production function
 g_2 represents goal of cost of production
 $g_2 + a_2$ represents exceed limit of cost of production
 $V_2 f_2(x)$ represents fuzzy value of cost of production

Minimization of total production time is:

$$V_3(f_3(x)) = \begin{cases} 1 & \text{if } f_3(x) < g_3 \\ 1 - \frac{f_3(x) - g_3}{a_3} & \text{if } g_3 \leq f_3(x) \leq g_3 + a_3 \\ 0 & \text{if } f_3(x) > g_3 + a_3 \end{cases}$$

$f_3(x)$ represents the total production time function
 g_3 represents goal of total production time
 $g_3 + a_3$ represents exceed limit of total production time
 $V_3 f_3(x)$ represents fuzzy value of total production time

3.2 Constraints

Each work-piece can be performed on one machine;

$$\sum_{k \in S_{pn}} x_{ijk} = 1, \forall i, j \tag{1}$$

Each machine can perform more than one work-piece;

$$\sum_{i \in S_{mp}} \sum_{j \in S_{np}} x_{ijk} \geq 1, \forall k \tag{2}$$

After all objective functions and resource constraints are set-up, the mathematical model for optimizing energy consumption, resource utilization and other manufacturing performance is formulated in the form of fuzzy integer programming as follows:

$$\begin{aligned} & \text{Max Min } \lambda \\ & \text{s.t. } \lambda \leq v_n(f_n(x)) \\ & h_i(x) \leq H_i \\ & 0 \leq \lambda \leq 1 \end{aligned} \tag{3}$$

To solve the problem in this research, the mathematical modeling is transformed into adaptive matrix in M-file function of MATLAB based programming. The genetic algorithm (GA) is used as the main method to cope with this situation. However, the completion of EREE-based low carbon manufacturing is not achieved yet although the optimization planning for CNC manufacturing system obtained from GA running can provide both optimal energy efficiency and resource utilization. Because of wastes at many hidden points, the factors such as idle time, operator errors, and maintenance down time, etc, can appear as uncertain situation. Hence, the last section of this generic modelling is established by discrete event system simulation using ProModel. The system layout and process sequence is based on the resource constraints using in mathematical modelling of the second part. For the advantage of using simulation method, each CNC machine can be assigned with the data distribution of maintenance downtime, break-down period and idle time

etc. The optimization of energy efficiency and resource utilization in the CNC manufacturing system can thus be tested on whether it is possible to use in the real situation or not. In Fig. 4, the screen short of the system simulation is illustrated.

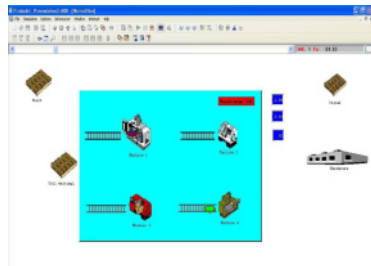


Fig. 4. The caption from simulation part of the system

4. Case study and applications

In this section, the proposed modelling is implemented through a case study of CNC manufacturing system. In this case, there are four types of workpiece waiting to be machined. Each workpiece has different process and each process has a set of alternative machines which can be selected to use. For instance, workpiece1 has three processes and the first process can be performed by machine: A and D according to Tables 1, 2 and 3. The objective of this case study is to manufacture these workpieces with the minimum of energy consumption,

low production cost and less total production time. The details of energy consumption, cost of production and production time are illustrated in Tables 1, 2 and 3 respectively. Table 4 and Figure 5 (x: energy consumption, y: production cost and z: production time) provide the optimal results after the modelling was run in MATLAB. To illustrate the results in Table 5, scenario no.1 can be described that machine: D is used to perform process 3 on workpiece 3 (w3:3). It can be concluded from the results that scenario no.1 can make the trade off among three objectives: energy consumption, production cost and production time while the scenario no.2 can perform with effective energy consumption and total production time but cause high amount of cost of production.

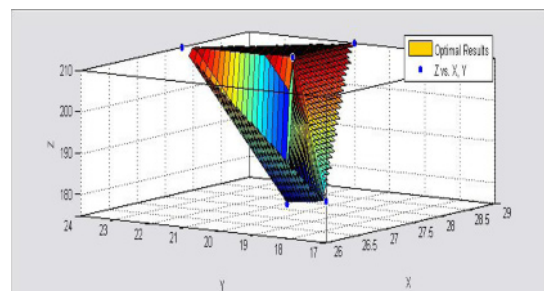


Fig. 5. Surface graph of optimized results.

Table 1. Energy consumption (kWh) for machining the workpiece

	Workpiece									
	1		2		3		4			
	Process			Process			Process			
	1	2	3	1	2	1	2	3	1	2
Machine: A	2.2		2.5		3.2		2.8		2.3	2.5
Machine: B		4	3.8			4		3.9	3	3.3
Machine: C		1.8	2.9	2.8	3.5	3.1			2.7	
Machine: D	3			1.7			2	2.5	1.9	

Table 2. Cost of production (£) for machining the workpiece

	Workpiece									
	1		2		3		4			
	Process			Process			Process			
	1	2	3	1	2	1	2	3	1	2
Machine: A	1		1		3		2		2	2
Machine: B		3	2			1		4	3	3
Machine: C		1	3	4	2	1			4	
Machine: D	2			4			3	1	1	

Table 3. Production time (min) for machining the workpiece

	Workpiece									
	1			2		3			4	
	Process			Process		Process			Process	
	1	2	3	1	2	1	2	3	1	2
Machine: A	10		25		30		15		20	20
Machine: B		20	20			10		20	30	30
Machine: C		10	40	35	20	15			10	
Machine: D	30			25			20	15	15	

Table 4. Scenarios of optimized result

Scenario specification					Optimized results				
Scenario No.	MC:A	MC:B	MC:C	MC:D	Production time (min)	Electricity consumption (kWh)	Output rate (part/min)	Cost of production (pounds)	λ
1	(w1:1) (w1:3) (w3:2) (w4:1) (w4:2)	N/A	(w1:2) (w2:1) (w2:2) (w3:1)	(w3:3)	185	26	0.022	17	0.762
2	(w1:1) (w2:2) (w3:2) (w4:2)	(w1:3) (w3:1) (w3:3)	(w1:2)	(w2:1) (w4:1)	175	27.8	0.021	21	0.5

5. Conclusions

This paper proposes an EREE-based low carbon manufacturing approach for CNC machines and associated CNC machining operations. The integrated modelling intends to integrate different dimensions of LCM, including energy efficiency, resource utilization and waste minimization, to consequently achieve low carbon footprint in the CNC machining process.

Currently, the methodology is being implemented although it needs to be further validated with more industrial CNC machining trials and simulations to improve its robustness. The details of trial data and simulations will be presented in the near future.

References

[1] Ball P.D., Evans S. and Ellison D. Zero carbon manufacturing facility – towards integrating material, energy, and waste process flows: Proceeding of The Institution of Mechanical Engineers, Part B: Journal of Engineering Manufacture, 2009, Vol. 223, pp. 1085-1096.

[2] Tridech, S. and Cheng, K. An investigation on the framework for EREE-based low carbon manufacturing: Proceeding of The 5th International Conference on Responsive Manufacturing ‘Green Manufacturing’, 2010, 11-13 January.

[3] Ahilan, C., Kumana, S. and Sivakumaran, N. Multi-objective optimization of CNC turning process using grey based fuzzy logic: International Journal of Machining and Machinability of Materials, 2009, Vol. 5, No. 4, pp.434-451.

[4] Tridech, S. and Cheng, K. Low carbon manufacturing: characterization, theoretical models and implementation: Proceeding of The 6th International Conference on Manufacturing Research (ICMR08), 2008, 9-11 September, pp.403-412.

[5] Zadeh, L.A. Fuzzy sets: Information and Control, 1965, Vol. 8, pp.338-353.

[6] Mishra, S., Prakash., Tiwari, M.K. and Lashkari, R.S. A fuzzy goal-programming model of machine-tool selection and operation allocation problem in FMS: a quick converging simulated annealing-based approach, International Journal of Production Research, 2006, Vol. 44, No. 1, pp.43-76.

[7] Zimmermann, H.J. Fuzzy programming and linear programming with several objective functions: Fuzzy Sets and Systems1, 1978, pp.45-55.

Reduced Energy Consumption by Adapted Process Chains

E. Brinksmeier, D. Meyer, M. Garbrecht, J.-W. Huntemann and R. Larek
Foundation Institute of Materials Science, ECO-Center, Badgasteiner Str. 3, 28359 Bremen, Germany

Abstract. All thermal and thermochemical methods for the manufacturing of surface hardened components demand the application of high temperatures which are accompanied by significant emission of CO₂. At the ECO-Center of the Foundation Institute of Materials Science in Bremen, alternative manufacturing processes have been developed, which avoid a final heat treatment and allow surface hardening with a significantly reduced energy consumption. Two of these approaches are grind hardening and cold surface hardening. The grind hardening effect uses the heat produced by the machining process. The high temperatures combined with self-quenching of the workpiece generate a short-term austenitization and subsequent martensitic transformation. Cold surface hardening represents a way to profit from special properties of the machined materials. Workpieces with a high amount of metastable austenite can be machined in their soft state and a subsequent induction of high stresses by a mechanical process such as deep rolling results in a martensitic transformation of the surface. Both process chains are applicable for the manufacturing of surface hardened components with high surface quality and compressive residual stresses at the surface. In the future, the alternative process chains presented combined with reliable tools for the prediction of CO₂-emission resulting from machining processes will allow a significant reduction of CO₂ per produced component.

Keywords: Process Chains, Steel, Heat treatment, Grind Hardening, Cold Surface Hardening, Energy Consumption

1. Introduction

Due to increasing loads during operation, more and more steel components nowadays demand a wear resistant surface with high hardness and excellent surface roughness. Surface hardened steel components conventionally are produced by process chains including thermal or thermochemical treatments and therefore include significant energy consumption. Common heat treatments such as induction hardening [Pan99], nitriding [Jun98] or carburizing [Cla09] generate temperatures within the range of 1000°C at the surface to induce a microstructural transformation. The high temperatures are held for hours and cause the formation of austenite, which transforms into martensite due to rapid subsequent quenching. As most heat treatments cause shape deviations (distortion), the components are finished by machining processes such as grinding, honing or lapping.

Taking into account that a medium heat treatment shop such as the one at the Foundation Institute of Materials Science (IWT, Bremen) with a building area of about 700 m² consumes 1,000,000 kWh per year, which is equivalent to a CO₂-emission of about 610 t, the enormous potential of reducing energy consumption by alternative process chains without final heat treatment steps becomes obvious. Consequently, both an investigation of replacing the thermal techniques and the assessment of energy consumption in manufacturing processes are required.

The major influence of the surface integrity of machined or surface hardened surfaces on the functional performance in terms of wear resistance or fatigue life was identified by Field and Kahles in the 1970's [Fie71]. Some of the most important surface and sub-surface properties affecting the surface integrity are roughness [His77, Kal01], hardness [Hir05], hardness penetration depth [Bro99] and residual stresses [Kris01]. Consequently, surface hardening and subsequent finishing are the most crucial steps in the production chain regarding the resulting properties of the component.

2. Alternative Process Chains

Since 1995, the ECO-Center at the IWT Bremen has developed innovative process chains, which avoid a final heat treatment of steel components. In the following sections, two innovative options will be presented: grind hardening and cold surface hardening. In Figure 1, the shortened process chains are presented and compared with the conventional way of producing surface hardened components. In both cases, the energy consuming heat treatment is substituted by a manufacturing process which is performed subsequent to the soft machining of the components.

2.1 Grind Hardening

Grind hardening represents a thermomechanical technique of surface hardening. Due to the high thermal

conductivity of steels and a large contact zone between workpiece and tool, the heat flux in grinding processes mainly occurs in the workpiece. Undesired side effects of the heating such as thermal damage of the workpiece surface are well described in literature as grinding burn, which usually is accompanied by tensile residual stresses.

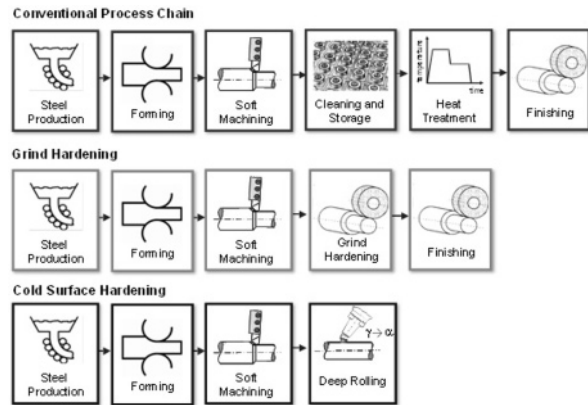


Fig. 1. Comparison of the conventional process chains and heat-treatment-free process chains.

From 1994, a new approach to utilize the heat transferred to the workpiece to induce a microstructural transformation in the outer surface layers was investigated [Bri94]. Brockhoff and others revealed, that by the right choice of grinding parameters, the thermal effects allow for a short time austenitization of the sub-surface material followed by a self-quenching effect as the bulk material stays rather unaffected [Bro99]. According to Zhang et al. [Zha09], the temperature of the surface increases up to 900 °C within the first 0.5 s of the process and decreases to about 300 °C within the following 0.8 s. Figure 2 illustrates the thermal impact during the grind hardening process.

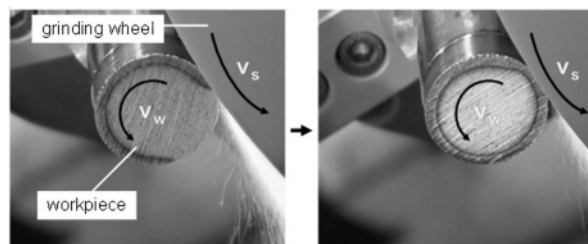


Fig. 2. Surface hardening of a cylindrical workpiece (diameter = 20 mm) by grind hardening.

The grind hardening effect can be used to realize hardness penetration depths of up to 1 mm. The most important factors influencing the hardening result are the specific cutting power P_c'' and the contact time of Δt ($= l_g/v_{ft}$). As shown in Figure 3, an area was identified by Heinzl ensuring that the surface is grind hardened and not thermally damaged [Hei09].

By a subsequent finishing step, which can be performed at the same machine tool, a hardened surface with high surface quality can be generated without any

additional heat treatment. Instead of generating CO₂ for a thermal or thermochemical surface hardening method, the grind hardening method takes advantage of the unavoidable heat generation occurring in grinding.

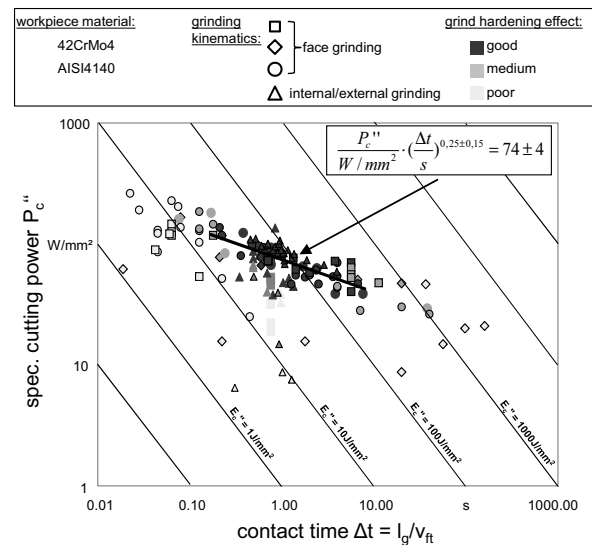


Fig. 3. Working area of the grind hardening effect [Hei09].

Recent investigations aim to transfer the findings to industrial applications [Bri05], the development of predictive models [Zae09a] and the assessment of the heat density distribution during grind hardening [Zae09b].

2.2 Cold Surface Hardening

The second alternative process chain for the production of surface hardened components which avoids a final heat treatment is referred to as cold surface hardening [Bri08a].

In cold surface hardening, highly alloyed steels with a high content of retained austenite at room temperatures are used. The microstructure of these materials (e.g. AISI D2 (X210Cr12) or AISI D3 (X155CrMoV12-1)) is stable enough to avoid martensitic transformation due to the mechanical loads during turning or milling processes. Therefore the workpieces can be machined in a rather soft state. Subsequent to the soft machining, high mechanical loads are applied to the surface, resulting in a comprehensive martensitic transformation within the sub-surface.

As Garbrecht described, the most effective process to apply mechanical loads to cylindrical workpieces is deep rolling [Gar06]. Deep rolling is widely used to generate surfaces with high surface quality showing compressive stresses and an increased surface hardness. In conventional deep rolling processes, the hardness alterations are based on pure strain hardening (dislocations within the crystal lattice) [Roe03], whereas in cold surface hardening, the high stresses result in a strain induced martensitic transformation (SIMT) and

higher hardness values compared with strain hardening. The experimental setup for a deep rolling process using a hydrostatically supported ceramic ball is illustrated in Figure 4.

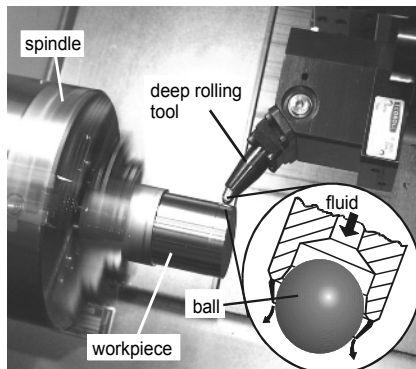


Fig. 4. Surface hardening of a cylindrical workpiece by cold surface hardening [Bri08a].

The process chain of cold surface hardening is shortened considerably compared with the conventional production line (see Figure 1), as turning and deep rolling processes can be performed on the same machine tool without unclamping the workpiece [Bri08b]. Furthermore, the resulting surfaces show hardness penetration depths of up to 1 mm, high compressive stresses and roughness within the range of finished components. Consequently, the deep rolling process is the final step of the process chain.

As Meyer [Mey10] found, the most important parameters influencing the surface properties of cold surface hardened components are the diameter of the applied ceramic ball d_b and the deep rolling force F_r . The dependence of the hardness penetration depth on the deep rolling force is summarized in Figure 5 for varying ball diameters. As the relationship between hardness penetration depth and the deep rolling force shows a linear character, it is possible to predict the hardening results.

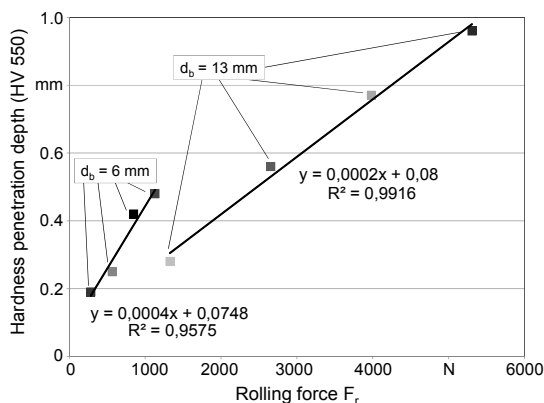


Fig. 5. Relationship between the applied deep rolling force and the resulting hardness penetration depth.

The potential to reduce CO₂ emission by cold surface hardening is remarkable, as after soft machining no additional machine tools are required. At this point it has

to be mentioned, that for the generation of these results, microstructures with a high content of retained austenite were created by a previous heat treatment to have defined stable varied microstructures. In the future, this step could be easily included into the steel production. Due to conflicting demands of the soft machining and the hardening steps, the method is still limited to a narrow field of microstructures which show the required stability properties. Future work will aim on a combination of mechanical and cryogenic effects to allow for the application of more stable microstructures in cold surface hardening.

3. Prediction of Energy Consumption

Predictive methods are necessary to quantify and minimize the amount of energy needed in each manufacturing step efficiently. Typically, the energy consumption of machine tools is measured during machining experiments and the results are being used to evaluate the efficiency of machine components and the overall process. This is not very specific and several authors have requested the development of new, simulation based predictive methods [Mue08, Neu08]. The known and established methods for the simulation of machining processes such as the Multibody-Simulation, FEM-analysis or Computer Aided Control Engineering are, however, complex and time-consuming in their implementation. Furthermore, the accuracy and resolution that can be achieved with these methods is not needed to simulate and optimize the consumption of electric power. Therefore another approach has been developed at the ECO-Center of the Foundation Institute of Materials Science in Bremen.

The discrete-event modeling approach, which is mainly used for logistics simulation, has been adapted to describe the behavior of machine tools. It is assumed that each component has either the status 'off' or 'on' with a given level of power consumption. Oscillations and other continuous behaviour, which typically are also modeled by the above mentioned approaches, are ignored. The machine model includes representations of all components and subsystems. They are set in their respective status by a discrete-event subsystem that reads and evaluates the corresponding NC-code. Loads on spindle and axis are calculated depending on the actual operation. Two-axis turning on a Weiler DZ 32 CNC machining centre and surface grinding on a Blohm Profimat HSG 412 have been simulated so far and show promising results. Figure 6 shows the simulated versus the measured power consumption of a turning operation in C60 steel. The simulated levels of energy consumption as well as the duration of each operation show a good correlation with the measured results.

In the next step, the model will be used to optimize machining operations and machine configuration. Time-consuming experiments with different parameter sets can

be done automatically. The available model also allows a direct linking to an optimization algorithm, e.g. simplex algorithm, which alters the input parameters automatically to minimize the output.

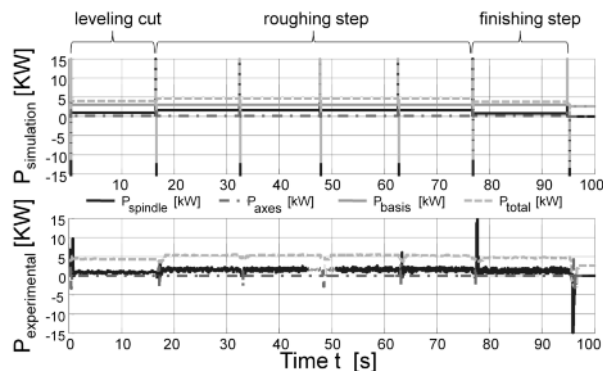


Fig. 6. Comparison of simulated and experimental data of three-step-turning process.

4. Summary and Outlook

By the choice of alternative process chains for the production of surface hardened components, energy consuming heat treatments can be avoided. This can be achieved by either utilizing the heat, which is generated within a grinding process, or by the use of steels showing suitable microstructures to allow a martensitic transformation due to the introduction of mechanical loads. The potential to reduce CO₂ emission is obvious and must be quantified in future research. Predictive models will play a decisive role, as the simulation of varying process steps will be possible with a minimum of experimental effort.

Acknowledgements

The authors thank the German Research Foundation (DFG) and the Federal Ministry of Education and Research (BMBF) for the project's funding and the assistance of the working committees "Materials" and "Manufacturing Technologies" of the Forschungsvereinigung Antriebstechnik e.V. (FVA).

References

- [Fie71] Field, M.; Kahles, J.F.: Review of Surface Integrity of Machined Components. *Annals of the CIRP*, 20/2, 1971, pp. 153-163.
- [His77] Hisakado, T.: The influence of surface roughness on abrasive wear. *Wear*, 41/1, 1977, pp. 179-190.
- [Kal01] Kalin, M.; Jahanmir, S.; Iwes, L.K.: Effect of counterface roughness on abrasive wear of hydroxyapatite. *Wear*, 252/9-10, 2002, pp. 679-685.
- [Hir05] Hiroyuki, S.: The effect on fatigue life of residual stress and surface hardness resulting from different cutting conditions of 0.45%C steel. *International Journal of Machine Tools and Manufacture*, 45/2, 2005, pp. 131-136.
- [Bro99] Brockhoff, T.; Brinksmeier, E.: Grind-Hardening: A Comprehensive View. *Annals of the CIRP*, 48/1, 1999, pp. 255-260.
- [Kris01] Kristoffersen, H.; Vomacka, P.: Influence of process parameters for induction hardening on residual stresses. *Materials & Design*, 22/8, 2001, pp. 637-644.
- [Pan99] Pantleon, K.; Keßler, O.; Hoffmann, F.; Mayr, P.: Induction surface hardening of hard coated steels. *Surface and Coatings Technology*, 120-121, 1999, pp. 495-501.
- [Jun98] Jung, M.; Walter, A.; Hoffmann, F.; Mayr, P.: High Pressure Nitriding of Austenitic Stainless Steels. *Proc. 11th Congress of the IFHT / 4th ASM Heat Treatment and Surface Engineering Conf. in Europe*, 19-21.10.98, Florence, Italy, Vol. 1 (Ed.: D. Fiarro, E.J. Mittemeier), Associazione Italiana di Metallurgia, Milan, 1998, pp. 281-289.
- [Cla09] Clausen, B.; Surm, H.; Hoffmann, F.; Zoch, H.-W.: The influence of carburizing on size and shape changes. *Mat.-wiss. u. Werkstofftech.*, 40, 2009, 5-6, pp. 415-419.
- [Bri94] Brinksmeier, E.; Brockhoff, T.: Randschicht-Warmebehandlung durch Schleifen. *Journal of Heat Treatment and Materials (HTM)*, 49/5, 1994, pp. 327-330.
- [Zha09] Zhang, J.; Ge, P.; Jen, T.-C.; Zhang, L.: Experimental and numerical studies of AISI1020 steel in grind-hardening. *International Journal of Heat and Mass Transfer*, 52/ 3-4, 2009, pp. 787-795.
- [Hei09] Heinzel, C.: Schleifprozesse verstehen - Zum Stand der Modellbildung und Simulation sowie unterstützender experimenteller Methoden. *Habilitation, University of Bremen*, 2009.
- [Bri05] Brinksmeier, E.; Minke, E.; Wilke, T.: Investigations on Surface Layer Impact and Grinding Wheel Performance for Industrial Grind-Hardening Applications. *Annals of the German Academic Society for Production Engineering (WGP)*, 1, 2005, pp. 35-40.
- [Zae09a] Zäh, M. F.; Föckerer, T.; Brinksmeier, E.; Heinzel, C.; Huntemann, J.-W.: Experimentelle und numerische Bestimmung der Einhärtetiefe beim Schleifhärten. *wt-online*, 1/2, 2009, pp. 49-55.
- [Zae09b] Zäh, M. F.; Brinksmeier, E.; Heinzel, C.; Huntemann, J.-W.; Föckerer, T.: Experimental and numerical identification of process parameters of grind-hardening and resulting part distortions. *Annals of the German Academic Society for Production Engineering (WGP)*, 3, 2009, pp. 271-279.
- [Bri08a] Brinksmeier, E.; Garbrecht, M.; Meyer, D.: Cold surface hardening. *Annals of the CIRP*, 57/1, 2008, pp. 541-544.
- [Gar06] Garbrecht, M.: Mechanisches Randschichthärten in der Fertigung. *Dr.-Ing. Dissertation, University of Bremen*, 2006.
- [Roe03] Röttger, K.: Walzen hartgedrehter Oberflächen. *Dissertation Dr.-Ing. RWTH Aachen, Shaker Verlag, Aachen*, 2003.
- [Bri08b] Brinksmeier, E.; Garbrecht, M.; Meyer, D.; Dong, J.: Surface Hardening by Strain Induced Martensitic Transformation. *Annals of the German Academic Society for Production Engineering (WGP)*, 2, 2008, pp. 109-116.
- [Mey10] Meyer, D.; Dong, J.; Garbrecht, M.; Hoffmann, F.; Brinksmeier, E.; Zoch, H.-W.: Mechanisch induziertes Härten. *Journal of Heat Treatment and Materials (HTM)*, 65/1, 2010, pp. 37-45.
- [Mue08] Müller, E.; Engelmann, J.; Strauch, J.: Energieeffizienz als Zielgröße in der Fabrikplanung. *wt Werkstattstechnik online*, 2008, Heft 7/8.
- [Neu08] Neugebauer, R.: Energieeffizienz in der Produktion, Untersuchung zum Handlungs- und Forschungsbedarf, *Fraunhofer Gesellschaft*, 2008.

Model-Based Predictive Consumption of Compressed Air for Electro-Pneumatic Systems

P. Harris¹, G. E. O'Donnell¹, T. Whelan²

¹ Department of Mechanical and Manufacturing Engineering, Trinity College Dublin, Ireland.

² Hewlett-Packard (Manufacturing) limited, Liffey Park Technology Campus, Leixlip, County Kildare, Ireland.

Abstract: In this paper, a deterministic approach to modelling the air consumption of an electro-pneumatic system is proposed. A dynamic event driven model is developed in Matlab Simulink and interfaced with a Programmable Logic Controller. The model is tested against an experimental system in order to assess validity. Finally the effect of throttled flow on air consumption is examined.

Keywords: Compressed air, energy efficiency, modelling, automated assembly

1. Introduction

Electro-pneumatic systems are widely employed in a diverse range of production processes. However, the energy efficiency of such systems can be low due to a number of factors including poor maintenance, energy inefficient production control systems, the open loop nature of pneumatic circuits, and the lack of a total cost of ownership based approach to component acquisition [1, 2]. In addition to technical reasons, behavioural aspects play an important role in the low energy efficiency of compressed air (CA) systems, with a general lack of understanding in industrial facilities as to where compressed air is used, for what purpose, how efficiently and at what cost [3].

The compressed air system for a typical plant consists of supply, distribution and end-use subsystems. In this paper, the end-use aspect of the CA system is examined. Pneumatic systems, embedded in production equipment, consume pressurised air in its transformation to useful work or in some cases for process control applications such as cooling, drying and cleaning [4]. In this paper the air consumers of a system are classified into two categories: passive and active [5].

Passive consumers refer to consumers of a continuous nature such as blowers, air knives & nozzles, open pipes and leakage. Active consumers consume pressurised air on a periodical basis and typically for a short duration. Examples include linear cylinders and rotary actuators

used in conjunction with Programmable Logic Controller's (PLC) to automate machines.

Recent research by Al-Dakkan et al has focused on the energy efficiency of various control strategies, in particular using sliding mode approach for pneumatic servo systems [6, 7]. Yang et al [8] investigated the use of a bypass valve control to utilise exhaust air in order to increase the energy efficiency of pneumatic drives. The analysis is carried out through an examination of actuator air consumption. Cai et al proposed taking an energy based approach whereby the energy available to do mechanical work can be assessed [9].

In this paper a deterministic dynamic model of a single pneumatic drive and a pneumatic system consisting of two linear cylinders is presented. The approach taken is based on the fact that theoretically, the air consumption function transitions from one value to another at moments when individual loads are activated and deactivated [5]. An event based model is therefore a suitable simulation paradigm. The challenge is to efficiently model the system's response to changing actuation profiles. In an industrial system, this profile is determined by a programmable controller and initiated by a products/workpiece presence. This systems type approach allows for the air consumption model to be scaled for use in production processes.

2. Modelling approach

The most commonly utilised active consumer in an industrial system is the linear cylinder. Pressurised air is consumed in extending and retracting the cylinder. The governing air mass consumption equations are given in eq (1) and (2). Additionally the volume of tubing between the valve bank or individual directional control valve and the cylinders is included in the model.

$$m_{\text{ex}} = \left\{ s \cdot \frac{\pi D^2}{4} + l \cdot \frac{\pi d^2}{4} \right\} \left[\frac{P_1}{P_2} \right] \rho \quad (1)$$

$$m_{rt} = \left(s \cdot \left[\frac{\pi D^2}{4} - \frac{\pi d^2}{4} \right] + l \cdot \frac{\pi d_i^2}{4} \right) \left[\frac{P_1}{P_2} \right] \cdot \rho \quad (2)$$

where m = mass of air, s = stroke, D = bore diameter, d = rod diameter, P = pressure, ρ = density, dt = tubing internal diameter, l = length of tubing.

For a given electro-pneumatic system, the pressure ratios, bore sizes, stroke lengths, tubing volume, sonic conductance and critical ratio parameters are assumed constant. The system's air consumption is then a function of the activation of the individual components. Previous research [5] considered the problem as stochastic, however in this paper, the problem is viewed as deterministic due to the fact that component activation is dependant on the controlling program in the PLC. The activations of loads at subintervals (N) can be described by the activation matrix (A_m) [5]. Each row then represents the activation of an individual actuator at subintervals. For a system of multiple components, matrix multiplication can be used to solve the total consumption for sub-periods (eq.3). Applying the superposition theorem means that the overall compressed air usage of the system is the sum of the individual component consumptions.

$$M_{total} = \begin{bmatrix} a_{11} & a_{12} & \dots & a_{1N} \\ a_{21} & \dots & \dots & \vdots \\ \vdots & \dots & \dots & \vdots \\ a_{n1} & \dots & \dots & a_{nN} \end{bmatrix}^T \begin{bmatrix} m_1 \\ m_2 \\ \vdots \\ m_n \end{bmatrix} \quad (3)$$

2.1 Simulation model

Matlab Simulink and the Open Process Control (OPC) toolbox add-on were used for building the model. The top level Simulink diagram is illustrated in Figure 1.

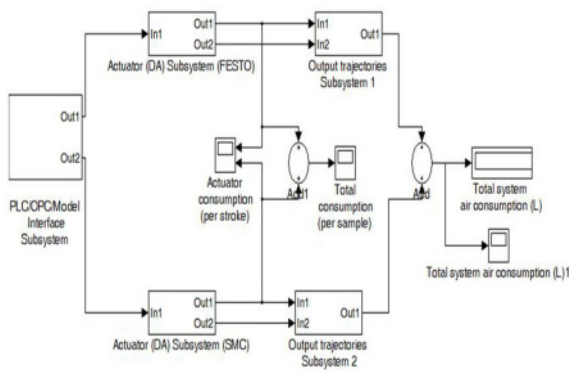


Fig. 1. Top level diagram (Simulink)

The interface subsystem configures and reads data items from the OPC server. A MATRIKON OPC server was utilised to interface the PLC with the model. OPC architecture involves using a server to read data from a device such as a PLC and provide this data to a client, in this case the Simulink model. The benefit of using OPC is that it eliminates the need for custom coding between the model and vendor specific communication protocols. Additionally the model can interface with any OPC server (to Data Access specification 2.05) ensuring modularity. The PLC therefore drives the model.

Figure 2 shows the model flow chart. The actuator subsystem consists of the actuator specific equations described by Equations 1 and 2 and edge evaluation. Active and passive consumers require different edge evaluation strategies due to the fact that active components consume air during transition periods (e.g. 0-1, 1-0), whilst passive types consume air for the duration of a positive bit input signal. Additional differences arise between actuators. Single acting cylinders consume air on an extend stroke only and thus require a rising edge detection capability. Double acting cylinders require both rising and falling edges to be detected. The output trajectories subsystem consists of display scopes for instantaneous and total air consumption. The simulation results are written to a workspace for further analysis and visualisation. The model employs a variable step solver to solve the simulation.

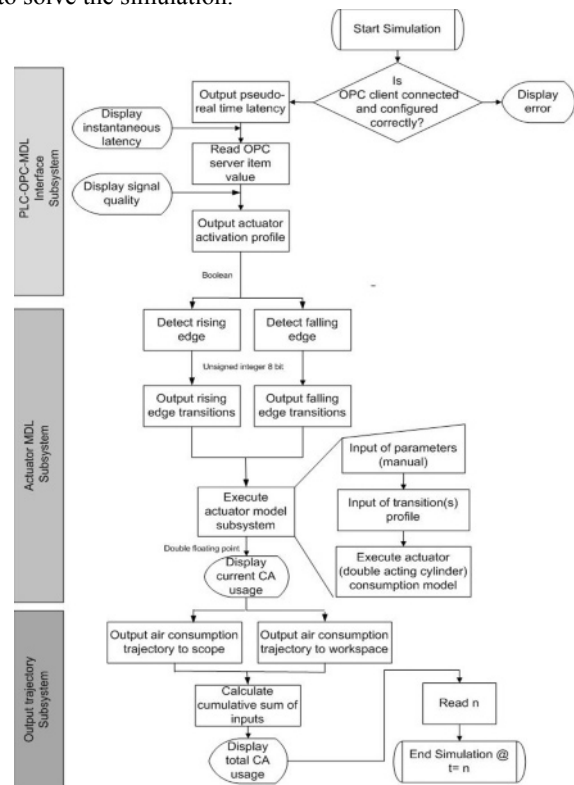


Fig. 2. Model Flowchart (pneumatic drive)

3. Experimental setup

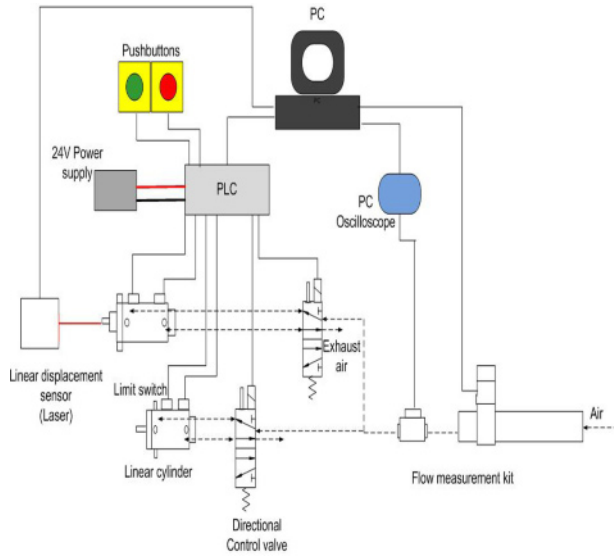


Fig. 3. Schematic illustration of experimental apparatus

Figure 3 shows a schematic illustration of the experimental setup. The power and signal element components of the system are shown in table 1. The upstream air supply was regulated at 3 bar(g) and the air filtered to a quality of 5 micron. The velocity profile of the cylinder was controlled by throttling the airflow with a one way flow control valve. Magnetic-reed limit switches were attached to the cylinder ends and used for proximity sensing.

Table 1. Primary electro-pneumatic equipment details

Component	OEM	Model	Details
Linear cylinder	FESTO	DSNU-25-50	Double acting, standard
Linear Cylinder	SMC	NCDQ2-B63-10D	Double acting, compact
Directional Control Valve (x2)	FESTO	MVH-5-1/8-S-B	5/2 solenoid actuated
PLC	OMRON	CQM1-CPU21	Max I/O points: 128

A range of flow sensors, for ultra low to industrial scale flow rates, were employed as part of the measurement system. Additionally a Micro-Epsilon laser sensor was utilised for linear displacement sensing (Figure 3). A PC oscilloscope was used in order to log analogue voltage signals from required flowmeters and the laser displacement sensor. The model sampled OPC data items at 10 Hz. The OPC server was set to sample the PLC bit addresses at a rate of 10 Hz.

In order to examine the sensitivity of the recorded flowrate to actuator velocity, the flow was adjusted using a one way flow control. The linear position sensor was utilised to calculate the velocity, in order that the total consumption for a range of velocities could be examined. A sampling rate of 1000Hz was used on the PicoScope to record displacement and flowrate.

4. Results

Figure 4 shows the results from the model and the experimental investigations examining the air consumption per stroke. The individual pneumatic drive model predicted the total consumption for the test period with an error of 0.41%.

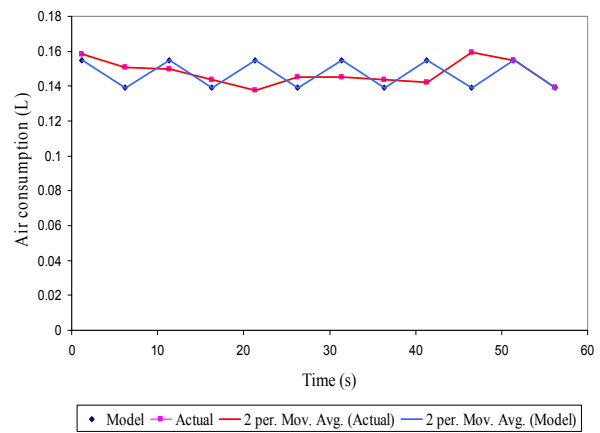


Fig. 4. Pneumatic drive air consumption, measured and modelled

The velocity and flowrate profiles for throttled and unthrottled flow are illustrated in Figure 5(b-c). An unthrottled extend stroke is shown in Figure 5(a). It can be seen that the maximum flowrate occurs after maximum velocity has been reached. According to Fleischer [10], this is caused by the piston moving out ahead of the pressure wave once motion is initiated. This is particularly relevant for this study where only a frictional load is involved. After the cylinder has completed the stroke, it still consumes a residual flowrate as equalisation occurs between the regulated upstream system pressure and drive chamber pressure.

The velocity and flowrate profile for a throttled extend stroke is shown in Figure 5(b). Throttling the flow by adjusting the one way flow control valve on the exhaust line causes a rise in exhaust chamber pressure, and a decrease in differential pressure between cylinder chambers resulting in lower actuator velocity. Additionally, during a reciprocating motion, extend and retract strokes are charged to an equal supply pressure resulting in a mass of air opposing piston motion [10].

However, it can be seen in Figure 5(c) that the velocity of initial extend throttled stroke is higher. Unlike an in-cycle reciprocating stroke, the pressure in the exhaust chamber has had sufficient time to decay to atmospheric pressure. Consumption of throttled flow appears to be less with a longer stroke time, although throttling the initial stroke has little effect on air consumption.

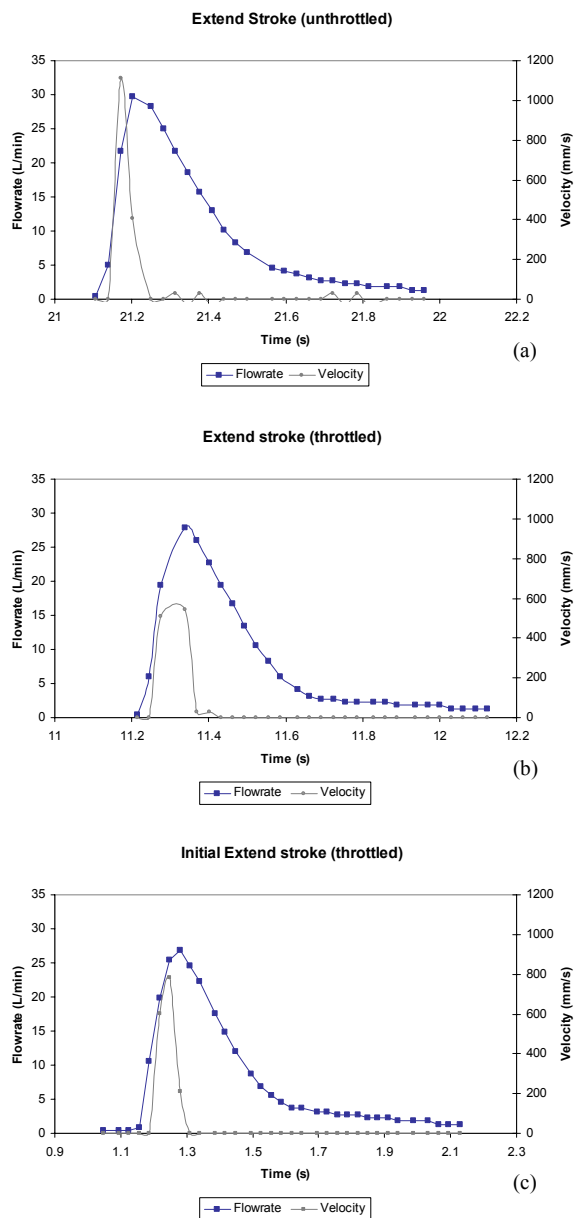


Fig. 5. Velocity & flowrate response for (a) unthrottled and (b,c) throttled flow

5. Conclusions & future work

A PLC driven consumption model of a pneumatic system has been presented in this paper. Results indicate that the consumption of a single drive can be modelled accurately using the developed Simulink model. Additionally, it has been found that actuator velocity and actuator cycle time are factors that must be accounted for in system level modelling of the air consumption of a pneumatic system. Both the developed model and the experimental apparatus provide a platform to examine more complex electro-pneumatic automation systems. A robust statistical analysis of the model against measured consumption for a range of pneumatic components (active and passive) and for a range of control programs is required. The model also requires capacity to take throttled flow and cycle rates into account.

Acknowledgements

The authors gratefully acknowledge funding from the Irish Research Council for Science, Engineering & Technology (IRCSET) and Hewlett Packard Manufacturing (Ireland) Ltd through the enterprise partnership scheme.

References

- [1] Yuan CY, Zhang T, Rangarajan A, Dornfeld D, Ziemba B, Whitbeck RA, A decision-based analysis of compressed air usage patterns in automotive manufacturing. *Journal of Manufacturing Systems*, 2006. 25(4): p. 293-300.
- [2] Harris P, O'Donnell GE, Whelan T, An Evaluation of Compressed Air Consumption Efficiency of an Automated Assembly Production Module, in 26th International Manufacturing Conference 2009: Trinity College Dublin, Ireland.
- [3] Radgen P, Blaustein E, Compressed Air Systems in the European Union: Energy, Emissions, Savings Potential and Policy Actions. 2001: Fraunhofer Institute.
- [4] Improving Compressed Air System Performance: A Sourcebook for Industry. 1998, Compressed Air Challenge, Office of Energy Efficiency and Renewable Energy, U.S.
- [5] Parkkinen R, Lappalainen P, A consumption model of pneumatic systems. in Industry Applications Society Annual Meeting, 1991., Conference Record of the 1991 IEEE. 1991.
- [6] Al-Dakkan KA, Barth E.J, Goldfarb M, A Multi-objective sliding mode approach for the energy saving control of pneumatic servo systems. in ASME International Mechanical Engineering Congress & Exposition. 2003. Washington, D.C.
- [7] Al-Dakkan KA, Goldfarb M, Barth EJ, Energy saving control for pneumatic servo systems. in Advanced Intelligent Mechatronics, 2003. AIM 2003. Proceedings. 2003 IEEE/ASME International Conference on. 2003.
- [8] Yang A, Pu J, Wong CB, Moore P, By-pass valve control to improve energy efficiency of pneumatic drive system. *Control Engineering Practice*, 2009. 17(6): p. 623-628.
- [9] Cai M, Kawashima K, Kagawa T, Power Assessment of Flowing Compressed Air. *Journal of Fluids Engineering*, 2006. 128(March).
- [10] Fleischer H, Manual of Pneumatic Systems Optimisation. 1995, New York, NY: McGraw-Hill.

Schottky Solar Cells Based on Graphene and Silicon

X. M. Li, H. W. Zhu, K. L. Wang, J. Q. Wei, C. Y. Li and D. H. Wu

Key Laboratory for Advanced Manufacturing by Material Processing Technology and Department of Mechanical Engineering, Tsinghua University, Beijing 100084, P. R. China

Abstract. The paper describes the combination of conductive, semi-transparent graphene films with a n-type silicon wafers to make solar cells with power conversion efficiencies up to 1.5% at AM 1.5G. The Schottky junction solar cells reported here can be extended to other semiconducting materials instead of silicon, in which graphene serves multiple functions as an active junction layer, charge transport path and transparent electrode.

Keywords: Schottky junctions, solar cells, graphene

1. Introduction

Graphene [1] is yet another fascinating carbon nanomaterials discovered recently besides carbon nanotubes (CNTs). Thus far, five typical polymorphs of crystalline carbon, including fullerene (e.g. C_{60}), CNTs, graphene, graphite and diamond, have been identified and therefore a comprehensive paradigm for carbon from zero- to three-dimensions are finally established. The unique single atomic layer structure of graphene endows it with a range of promising properties, including high carrier mobility, high electrical and thermal conductivities and high transparency and strength [2].

Schottky junctions are attractive alternatives for photovoltaic devices which convert light energy into electrical energy with a respectable conversion efficiency and faster switching speeds because they are primarily majority carrier devices. Carbon (e.g. graphene, CNTs) is one of the materials being considered as a potential replacement of silicon for energy harvesting and future computing. Graphene has the potential for creating thin film devices and device integration, owing to its two-dimensionality and structural flatness.

The paper reports on the combination of conductive, semi-transparent graphene films with an n-type silicon (n-Si) wafer to make solar cells with power conversion efficiencies up to 1.5% at AM 1.5G.

2. Experimental

2.1 Materials preparation

A simple preparation method was employed for large area monolayer graphene using Ni foils as substrates and ethanol as carbon source. Preparation techniques of graphene can be categorized into two major groups:

1) Exfoliation of graphitic layers. Starting from graphite or CNTs, graphene could be obtained by “peeling off” single- or a few- layers from its parent substance using various solid- [1] or liquid-phase [3-5] exfoliation approaches.

2) in-situ growth. Graphene would be formed under certain condition in which temperature, atmosphere and carbon source meet the criteria of carbon crystallization. Epitaxial growth, an adaptation of traditional graphite preparation method, is an effective technique to secure large area graphene films. Combining with chemical vapour deposition (CVD), large area, high quality, uniform graphene films have been obtained on polycrystalline Ni thin films [6,7] by optimizing the carburization and controlling the cooling rate.

The ethanol CVD process was carried out in a quartz tube (one-inch in diameter) furnace with a Ni foil (purity>99.5%) located in the middle of the furnace. The Ni substrate was gradually heated to 1000 °C in an Ar/H₂ (200/100 mL/min) flow for 1 h before ethanol was introduced. In a typical CVD growth, ethanol was delivered at a feeding speed of 20 μL/min in an Ar/H₂ (800/200 mL/min) flow for 5~10 min. After growth, the Ni foil was withdrawn from the heating zone and cooled down to room temperature at a fast cooling rate of 10 °C/s. In this process, supersaturated carbon in Ni/C solid solution was precipitated at the step edges and graphene is formed.

Freestanding graphene films were obtained by detaching the graphene from the Ni in an acid solution (e.g. HNO₃) or FeCl₃ solution, followed by rinsing with de-ionized water.

2.2 Solar cell assembly

n-Si (100) wafers (doping density: $1.5\sim 3\times 10^{15}\text{ cm}^{-3}$) with a 300 nm SiO_2 layer were patterned by photolithography and wet-etching of oxide (by hydrofluoric acid solution) to make square windows (0.1 cm^2) where the n-Si was exposed. The front and back contacts were made using sputtered Au on the SiO_2 and Ti/Au on the back side of the n-Si. A free-standing graphene film was then transferred to the top of the patterned wafer and dried to make a conformal coating with the Au layer and the underlying n-Si. In this configuration, graphene serves as the semi-transparent upper electrode and the anti-reflection layer.

3. Results and discussion

3.1 Structural characterizations of graphene

Growth features of graphene produced on Ni foils was investigated by using an Hitachi S-4500 field emission scanning electron microscope (SEM). Fig. 1a shows the SEM images of Ni foil after graphene growth. Ni foil is a polycrystalline material with numerous randomly-distributed grain boundaries of about $10\mu\text{m}$. Growth of graphene is confirmed in these figures by the presence of graphene wrinkles. It can be seen that for Ni foils, there is no clear correlation between wrinkle distribution and the layout of grain boundaries. Similar to the interference color difference of graphene on SiO_2/Si substrate, graphene of different layers on Ni displays different color/contrast in optical image (Fig. 1b). Based on Raman measurements, correlation between the color/contrast and graphene layer number is established. As shown in Fig. 1c, the monolayer graphene region is highlighted with green color.

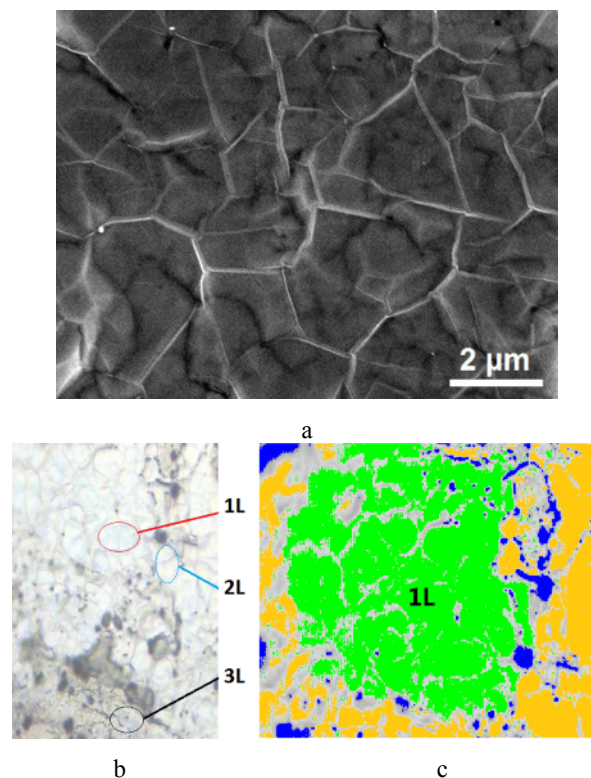


Fig. 1. Structural characterizations of graphene

3.2 Solar cell characterization

The graphene/n-Si solar devices were tested with a solar simulator (Thermo Oriel 91192-1000) under AM 1.5 condition. The current-voltage data were recorded using a Keithley 2601 SourceMeter. Forward bias was defined as positive voltage applied to the graphene film (Fig. 2a).

It was found that n-Si forms a Schottky junction with graphene film as the difference between their work function is large enough, and the carrier density of n-Si is moderate. A space charge region accompanied by the built-in field ($>0.55\text{ V}$) is formed in the n-Si near the graphene/n-Si interface, suggesting that the graphene film simultaneously serves as a transparent electrode and an active layer for electron/hole separation and hole transport [8].

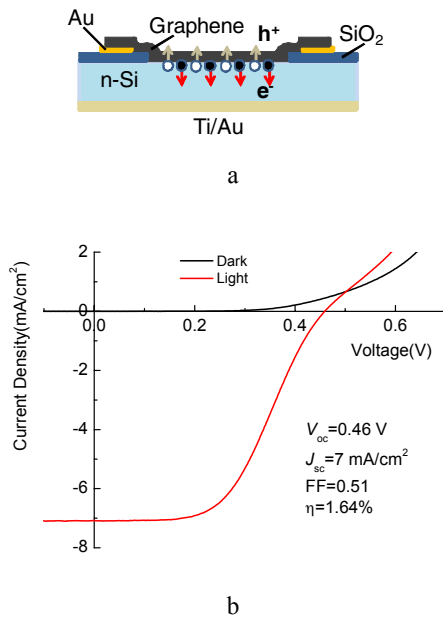


Fig. 2. Solar cell characterization

Light current density-voltage (J - V) data recorded from a typical graphene/n-Si cell yields a down-shift curve with an open-circuit voltage (V_{oc}) of 0.46 V, a short-circuit current density (J_{sc}) of 7.0 mA/cm² and a fill factor (FF) of 51 %, which corresponds to an overall solar energy conversion efficiency (η) of 1.64%. This photovoltaic value has been reproducible and was repeatable for measurements made over approximately a three-month period. The overall efficiency could be further increased with improvements in V_{oc} and J_{sc} by means of, for example, transmittance/conductivity optimization of graphene films, surface passivation of silicon.

4. Conclusions

In summary, the paper introduces a Schottky solar cell composed of graphene film and n-type silicon. Conversion efficiencies of up to 1.5% were achieved under AM1.5 illumination. This photovoltaic concept provides a new trend to develop carbon-based solar cells and elucidates a class of photovoltaic devices which have the merits of low cost, easy fabrication and material universality.

References

- [1] Novoselov KS, Geim AK, Morozov S V, Jiang D, Zhang Y, Dubonos S V, Grigorieva I V, Firsov A A, (2004) Electric field effect in atomically thin carbon films. *Science* 306:666–669
- [2] Geim AK, (2009) Graphene: status and prospects. *Science* 324:1530–1534
- [3] Li XL, Wang XR, Zhang L, Lee S, Dai H, (2008) Chemically derived, ultrasmooth graphene nanoribbon semiconductors. *Science* 319:1229–1232
- [4] Hernandez Y, Nicolosi V, Lotya M, Blighe FM, Sun Z, De S, McGovern IT, Holland B, Byrne M, Gun'Ko YK, Boland JJ, Niraj P, Duesberg G, Krishnamurthy S, Goodhue R, Hutchison J, Scardaci V, Ferrari AC, Coleman JN, (2008) High-yield production of graphene by liquid-phase exfoliation of graphite. *Nature Nanotechnology* 3:563–568
- [5] Tung VC, Allen MJ, Yang Y, Kaner RB, (2009) High-throughput solution processing of large-scale graphene. *Nature Nanotechnology* 4:25–29
- [6] Reina A, Jia X, Ho J, Nezich D, Son H, Bulovic V, Dresselhaus MS, Kong J, (2009) Large area, few-layer graphene films on arbitrary substrates by chemical vapor deposition. *Nano Letters*, 9:30–35
- [7] Kim KS, Zhao Y, Jang H, Lee SY, Kim JM, Kim KS, Ahn JH, Kim P, Choi JY, Hong BH, (2009) Large-scale pattern growth of graphene films for stretchable transparent electrodes. *Nature* 457:706–710
- [8] Li XM, Zhu HW, Wang KL, Cao AY, Wei JQ, Li CY, Jia Y, Li Z, Li X, Wu DH, (2010) Graphene-on-silicon Schottky junction solar cells. *Advanced Materials* DOI: 10.1002/adma.200904383

Variation of Engine Performance and Emissions Using Ethanol Blends

A. A. Abuhabaya¹ and J. D. Fieldhouse²

¹ Huddersfield University, Queensgate, Huddersfield HD1 3DH, United Kingdom

² Huddersfield University, Queensgate, Huddersfield HD1 3DH, United Kingdom

Abstract. The limited fossil fuel resources along with the increased public concerns about pollution levels have increased the need for alternative fuels for use in internal combustion engines. This study is to investigate the variation of the engine performance and exhaust emissions of a spark ignition engine. A spark ignition engine running with gasoline and gasoline blended E5, E10 and E20. Effects of engine speeds between 1000 and 3500 rpm with intervals 500 rpm and throttle valve 25%, 50%, 75% and full throttle, on the engine performance and the emission concentrations are investigated. Improved engine performance and reduced emissions are observed with ethanol addition.

Keywords: Fossil fuel, Alternative fuels, Engine performance, Exhaust emissions

1 Introduction

The Commission Green Paper “Towards a European strategy for the security of energy supply”, sets the objective of 20% substitution of conventional fuels by alternative fuels in the road transport sector by the year 2020 [1]. An extensive worldwide search is underway for alternative fuels to replace the conventional fossil fuels. The main reason is the increased prices, the very limited resources for such fossil fuels and increasing stringent environmental regulations. Growing concerns about greenhouse gas emissions will lead to an increase in biofuels and oxygenated fuels productions [2]. The application of biofuels [3, 4] and oxygenated fuels [5, 6] plays an important role in the alternative fuel for the internal combustion engines. The possible alternative fuels available in the market are diverse. Among the alternatives, ethanol usually comes from biomass that includes crops rich in sugar, starch or cellulosic material. Both spark ignition and diesel engines can use ethanol. It can be used as mixture with gasoline, both as a fuel, or after conversion into ETBE (Ethyl, Tertiary, Butyl, Ether), as an anti-knock additive.

Ethanol yields lower carbon dioxide (CO₂) emissions than gasoline and diesel. It produces low carbon

monoxide (CO) and unburned hydrocarbons (HCs) emissions compared with gasoline but higher ones compared with diesel. The effects of ethanol addition to gasoline on a spark ignition engine performance and exhaust emissions were investigated experimentally and theoretically. It was found that the ethanol addition to gasoline has caused leaner operation and improved the combustion process. Engine performance parameters such as power and efficiency were increased with increasing ethanol amount in the blended fuel as a result of improved combustion. Regarding the exhaust emissions, the use of the gasoline–ethanol blends in spark ignition engine dramatically reduced the CO concentrations. However, NO concentrations were adversely affected due to the increased cylinder temperature with increasing ethanol proportion in the blend. As a result of these, many investigations of ethanol fuels have been carried out and applied to automotive engines, special interest being taken by the agricultural segments of society [7, 8].

However, it is true that ethanol fuel still has limitations in applying ethanol to engines and is widely used for automobile applications because of a cold-start problems resulting from modification of the engine design and fuel supply system in spark ignition engines. Moreover, the relatively low Reid vapour pressure compared with gasoline poses a challenge in spite of many advantages of ethanol. In addition, the high boiling point (78 °C) of ethanol causes vaporization difficulties in cold conditions, which leads to the cold-start problem. For this reason, fuels with lower ethanol content such as gasohol containing 10 vol% ethanol have been used in unmodified engines in previous research [9, 10]. There has been much research into the engine performance and emission characteristics of spark ignition engines fuelled with ethanol-gasoline blends.

The utilisation of the ethanol blends in spark ignition engines was reported by Hsieh et al. [11]. They experimentally investigated the variations of the engine performance and the emission levels using ethanol–gasoline blends with blending ratios of (0, 5, 10, 20, and 30%). Hsieh et al. reported that the use of ethanol–

gasoline blends slightly increased the output brake torque of the engine. They presented the variation of the output torque as a function of the throttle valve opening percentage, and reported increased torque with the engine load, at fixed speed. They claimed that the increase was a result of the increased fuel quantities admitted to the cylinders. Higher engine torque of the blends compared with the gasoline, was also reported. In conclusion, they pointed out that ethanol addition has enhanced the combustion process, compared with gasoline. Hsieh et al. reported that the emission concentrations of the carbon monoxide (CO) and the unburned hydrocarbons (HC) were decrease with blending, as a result of the blending leaning effect of the fuel air mixture. However, increased concentrations of carbon dioxide (CO₂) were reported because of the enhanced combustion process with blending. The authors noted that the nitric oxide emissions (NO_x) were independent on the ethanol content.

Al-Hasan [12] experimentally investigated the effects of utilising unleaded gasoline–ethanol blends on the performance and exhaust gas emissions of spark ignition engine. He tested petrol engine and evaluated the brake specific fuel consumption (BSFC), the engine volumetric efficiency, the brake thermal efficiency, the brake power and the brake torque. He also measured the concentration of the carbon monoxide (CO), carbon dioxide (CO₂) and the unburned hydrocarbons (HCs) for unleaded gasoline–ethanol blends with various blending ratio, at 75% of the engine load and at variable engine speeds of 1000, 2000, 3000 and 4000 rpm. He reported increased fuel consumption i.e. fuel mass flow rate with the increased ethanol amount in the blend. Wu et al. [9] also investigated the effect of the ethanol blends on the performance and emissions. Leaner conditions were reported with the increased ethanol in the blend. The engine torque slightly increased with blends and the emissions CO and HCs decreased, due to the oxygen enrichment. Jia et al. [13] investigated the emission characteristics of motorcycle engine utilising ethanol blend E10 (10% ethanol and 90% gasoline). They reported decreased CO and HC concentrations with the blend and slight decrease of the NO_x. However, they reported increased NO_x with the increased ethanol in the blend. Song et al. [14] investigated the effects of ethanol, as engine additive, on the emissions. They tested various ethanol blends and measured regulated emissions of CO, HC and NO_x. They reported that ethanol addition produced lower regulated emissions compared with the other additive. The main conclusion of this study was the better effects of ethanol on the exhaust emissions. They tested various ethanol blends and measured regulated emissions of CO, HC and NO_x. They reported that ethanol addition produced lower regulated emissions compared with the other additive.

2 Experimental Apparatus

As shown in Figure 1, the apparatus consists of eddy current dynamometer, exhaust gas emissions analyser, control system and data recording system.



Fig. 1. Photograph of the study state engine rig.

The engine used in this study has the specifications listed in table below.

Table 1. Test engine specifications.

Type	Spark ignition engine
Model	Nissan-Nissan Micra
Number of cylinder	4
Bore (mm)	73.0
Stroke (mm)	82.8
Stroke volume	1386 CC
Compression ratio	9.9
Power (KW@rpm)	65@5200
Torque (Nm@rpm)	128@3200
Cooling system	Water cooled
Charging	Naturally aspirated
Fuelling system	Multi point fuel injection system
Ignition system	Electronic ignition

3 Engine Performance Results and Discussion

3.1 Effect of engine speed on brake torque

Figure 2 shows that higher brake torque is obtained with the ethanol blends compared with gasoline, at all speeds. This may be attributed to the increased anti-knock

resistance with ethanol addition, which increased the blends octane number. Generally, it was found that E20 performed the best, specifically at speeds higher than 1000 rpm, compared with the other fuels.

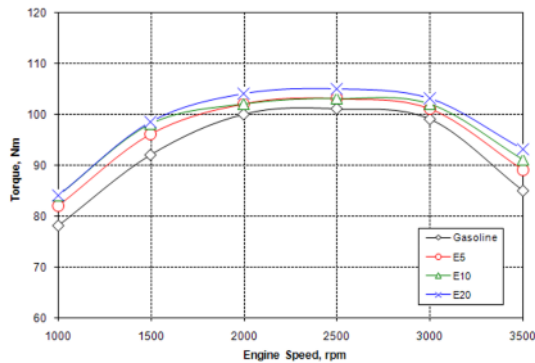


Fig. 2. Brake torque versus engine speed, at 25% full throttle

3.2 Effect of engine speed on (BSFC)

As shown in Figure 3 decrease in the BSFC with speed is found and reached minimum at speed of about 2500 rpm. At higher speeds, further increase of speed increased BSFC. It is depicted from these figures that lower BSFC is found with the blended fuels over the range of test speeds. The more the added ethanol in the blend decreased more the BSFC.

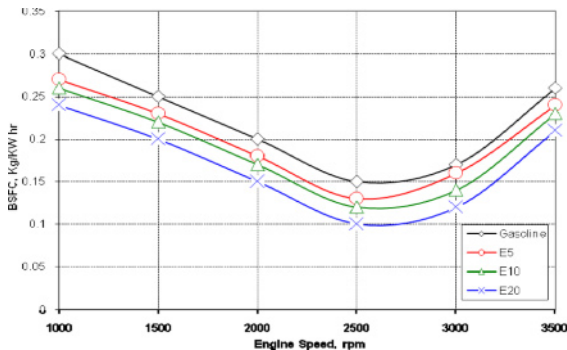


Fig. 3. BSFC versus engine speed, at 25% full throttle

3.3 Effect of engine speed on brake thermal efficiency

Substantial increase of the brake thermal efficiency is found with the engine speed. It reached maximum at speed of about 3000 rpm. For speeds higher than 3000 rpm, recognised decrease in efficiency is found. Also shown in Figure 4 is that the lowest brake thermal efficiencies are found with gasoline. The efficiency increased with the addition ethanol and reached maximum with E20 blend.

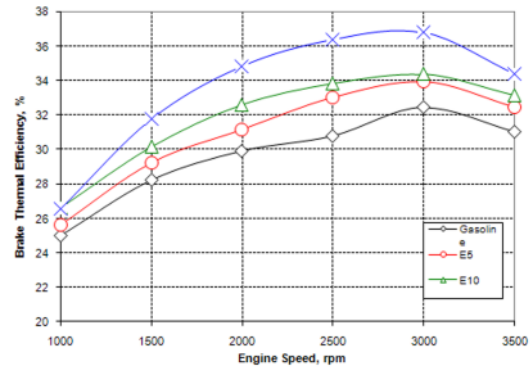


Fig. 4. Thermal efficiency versus engine speed, at 25% full throttle

4 Exhaust Emission Results and Discussion

4.1 Effect of throttle setting on the hydrocarbon

As shown in Figure 5, the throttle valve increase up to 75% has nearly no effect on the HC concentration. Further throttle valve increase, up to 100% considerably increases the HC, at speed of 2000 rpm. This may be attributed to the increased turbulence generated with the throttle valve increase. The blend E5 showed the highest HC concentration compared with the other tested fuels. This behaviour of E5 is clear at the highest throttle valve of 100%. However, at the other throttle setting, the difference is not significant.

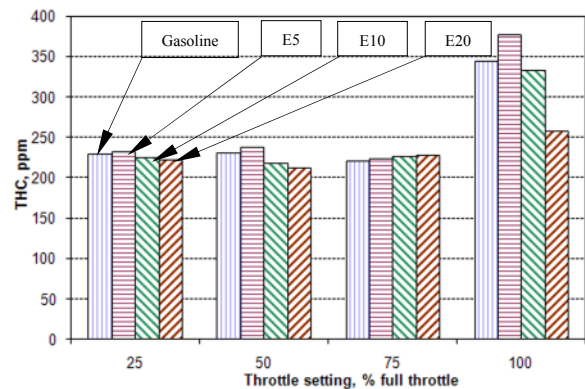


Fig. 5. Effect of throttle on the HC at engine speed of 2000 rpm

4.2 Effect of throttle setting on the carbon monoxide

As shown in Figure 6, the increase of the throttle valve resulted in increased CO (%) emissions. This is may be because the increased throttle requires more charge combustion (fuel and air mixture), which may produce more CO emissions.

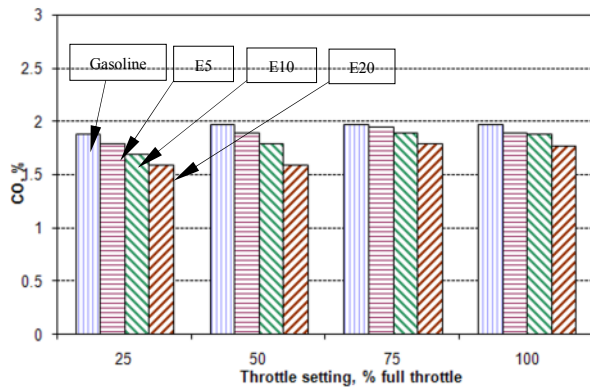


Fig. 6. Effect of throttle on the CO₂ at engine speed of 2000 rpm

5 Conclusions

To analyse the effects of ethanol fuel on the combustion performance the reduction of exhaust emission were investigated in a four-cylinder spark ignition engine fuelled with an ethanol– gasoline blended fuel (E5, E10 and E20) as alternatives to petroleum gasoline fuel under various experimental conditions. The following conclusions were drawn from the results.

1. The brake torque and the brake specific fuel consumption were measured; the brake thermal efficiency was evaluated, as performance parameters, at 25 % of full throttle, for various engine speeds. The engine brake torque increased with engine speed. It reaches maximum at certain speed, then extremely remained decrease at maximum speed.
2. Ethanol blends produced higher torque, compared with gasoline, at all speeds, at speeds higher than 2000 rpm, E20 performed best, compared with the other fuels as it produced 3.8% higher torque than gasoline, at 2500 rpm. At speeds of 3000 and 3500 rpm, it produced 3.9% and 8.6% higher torque than gasoline respectively.
3. Lowest brake thermal efficiencies are found for gasoline, for all test speeds. All blends showed recognised increase in the brake thermal efficiency with the speed. The maximum efficiency is found at speed of 3000 rpm. At speeds higher than 3000 rpm, the efficiency decreased considerably.
4. Blending gasoline with ethanol reduced the CO₂ and HC concentration.
5. Throttle valve increase, up to 100% considerably increases the HC, at speed of 2000 rpm.
6. At higher throttle valve of 100%, E20 blend showed the lowest HC.
7. The addition of ethanol decreased these emissions and the lowest is found with blend E20.

6 References

- [1] Directive 2003/30/EC on the promotion of the use of biofuels or other renewable fuels for transport, (2003) 8 May 2003, on the promotion of the use of biofuels or other renewable fuels for transport”, Official Journal of the European Union, L 123/43.
- [2] Yoon SH, Ha SY, Roh HG, Lee CS, (2009) Effect of bioethanol as an alternative fuel on the emissions reduction characteristics and combustion stability in a spark ignition engine. *Journal of Automobile Engineering* 223:941-951
- [3] Pouloupoulos SG, Philippopoulos CJ, (2003) The effect of adding oxygenated compounds to gasoline on automotive exhaust emissions. *Trans. ASME, J. Engng Gas Turbines Power* 125: 344-350
- [4] Marriott CD, Wiles MA, Gwidt JM, Parrish SE, (2008) Development of a naturally aspirated spark ignition direct-injection flex-fuel engine. *SAE technical paper* 20008-01-0319
- [5] Zhang J, Qiao X, Guan B, Wang Z, Xiao G, Huang Z, (2008) Search for the optimizing control method of compound charge compression ignition (CCCI) combustion in an engine fueled with dimethyl ether. *Energy Fuels* 22:1581-1588
- [6] Cataluna R, Silva R, Menezes EW, Ivanov RB, (2008) Specific consumption of liquid biofuels in gasoline fuelled engines. *Fuel* 87:3362-3368
- [7] Jeuland N, Montagne X, Gautrot X, (2004) Potentiality of ethanol as a fuel for dedicated engine. *Oil Gas Sci. Technol* 59:559-570
- [8] Topgul T, Serdar Y H, Cinar C, Koca, A, (2006) The effect of ethanol–unleaded gasoline blends and ignition timing on engine performance and exhaust emissions. *Renewable Energy* 31:2534-2542
- [9] Wu C W, Chen RH, Pu JY, Lin TH, (2004) The influence of air–fuel ratio on engine performance and pollutant emission of an SI engine using ethanol–gasoline-blended fuels. *Atmospheric Environment* 38:7093-7100
- [10] Yuksel F, Yuksel B, (2004) The use of ethanol– gasoline blend as a fuel in an SI engine. *Renewable Energy* 29:1181–1191
- [11] Hsieh WD, Chen RH, Wu TL, Lin TH, (2002) Engine performance and pollutant emission of an SI engine using ethanol–gasoline blended fuels. *Atmospheric Environment* 36:403–410
- [12] Al-Hasan M, (2003) Effect of ethanol–unleaded gasoline blends on engine performance and exhaust emission. *Energy Conversion and Management* 44:547–1561
- [13] Jia LW, Shen MQ, Wang J, Lin, MQ, (2005) Influence of ethanol–gasoline blended fuel on emission characteristics from a four-stroke motorcycle engine. *Journal of Hazardous Materials* A123:29–34
- [14] Song CL, Zhang WM, Pei YQ, Fan GL, Xu GP, (2006) Comparative effects of MTBE and ethanol additions into gasoline on exhaust emissions. *Atmospheric Environment* 40:1957–1970

EDM performance is affected by the white layer

José Duarte Marafona

Departamento de Engenharia Mecânica, Faculdade de Engenharia da Universidade do Porto
Rua Dr. Roberto Frias, 4200-465 Porto, Portugal

Abstract. The aim of this article is to show that the thickness and thermal conductivity of white layer affect the material removal rate and electrode wear rate in the process of electrical discharge machining. To study this effect a semi-empirical model was used and the assumption was made that the material of both the workpiece and electrode is removed by evaporation. The results of the model show an increase in the material removal rate with the increase of the white layer thickness. There is a value of thermal conductivity of the white layer that minimizes the material removal rate. Moreover, there is always an increase in the material removal rate when comparing with workpiece without white layer. There is a value of thermal conductivity of the white layer that minimizes the electrode wear rate. The white layer thickness does not have a significant effect on the electrode wear rate. This article demonstrates that the process of electrical discharge machining is not only influenced by the thermal properties of the material of the workpiece but also by the metallurgical modifications that occur during the machining.

Keywords: Electrical discharge machining (EDM), White layer, Material removal rate (MRR), Electrode wear rate (EW), thermal conductivity, Finite element model (FEM).

1. Introduction

Electrical discharge machining (EDM) is a non-traditional manufacturing process where the material is removed by a succession of electrical discharges, which occur between the electrode and workpiece that are submersed in a dielectric liquid such as kerosene or deionised water. The process of electrical discharge machining is widely used in the aerospace, automobile and moulds industries to manufacture hard metals and their alloys.

In the process of electrical discharge machining a discharge channel is created where the temperature reaches approximately 12,000°C [1-4], evaporating the dielectric and material from both electrodes. When the discharge ceases there is a fast cooling on the surface of the workpiece creating a heat affected zone that contains the white layer. This layer contains several hollows, spheroids, fissures and micro fissures. Carbon is the main element of its composition and influences both its hardness and thermal conductivity [5]. The white layer

thickness depends on the workpiece material, power used to cut the workpiece and the applied electrical polarity.

Electrical discharge machining is governed by a thermal phenomenon [6, 7], therefore not only removes material from the workpiece but also causes metallurgical changes on its surface. Thus, the properties of the base material are changed as well as its hardness [8-10] and thermal conductivity [5], which affect the performance of the process.

On the one hand, it is known that the material removal rate decreases when there is a decrease in the surface roughness of the workpiece. On the other hand, there is an increase in the material removal rate simultaneously with the reduction of surface roughness of workpiece, according to Abbas et al. [11]. Therefore, the author has decided to investigate the effect of thickness and thermal conductivity of the white layer on material removal rate and electrode wear rate.

2. Experimental methodology

The effect of thickness and thermal conductivity of the white layer on material removal rate and electrode wear rate was studied using a semi-empirical model. The radius of vaporised area was found numerically using the finite element model. The radius of the cylindrical discharge channel (R) is equal to 0.788 μm and its electric conductivity is calculated according to Equation (1).

$$\sigma = (GI) / (\pi R^2 E) \quad (1)$$

where σ is the electric conductivity, G is the gap width, I is the applied current passing through the discharge channel, E is the applied voltage taken equal to 23 V, and R is the discharge channel radius.

The volume of material removed (V) is based on the shape of spherical segment for the eroded cavity. Thus, the radius of vaporised area (r) and the maximum depth of the eroded cavity (h) were used to calculate the volume removed according to Equation (2).

$$V = (\pi h (3r^2 + h^2))/6 \quad (2)$$

The maximum depth (h) of the cavities of erosion in the surface of the electrodes is independent of the vaporised area and is calculated, considering that the initial shape of eroded cavity is cylindrical, according to Equation (3).

$$h = \beta\tau/\rho \quad (3)$$

where β is the evaporation rate of material of the electrode, ρ is the mass density and τ is the time of the pulse used in material removal.

Two values of current intensity together with the optimum pulse duration were taken from the machine's handbook. The current intensity values selected were 2.34A and 37.1A while its optimum pulse duration was 18 μ s and 560 μ s respectively.

According to the author, the white layer should be seen as a parameter that affects directly the material removal rate, which was not done until now. Marafona and Araújo [12] showed that the workpiece hardness affects the material removal rate and the workpiece surface roughness, mainly due to the interactions between initial hardness and electrical parameters. The white layer with a high amount of carbon is formed due to the effect of heat power used in the electrical discharge that causes the decomposition of the dielectric oil and the migration of its elements to the workpiece, which increases the carbon equivalent and reduces its thermal conductivity [5]. Therefore, these interactions can be surely substituted by the white layer in the finite element model, because the decomposition of dielectric oil and the diffusion of its elements into the workpiece material are very difficult to implement.

The workpiece material is wrought iron containing 0.5% carbon. To evaluate the effect of white layer thickness we used thicknesses that range between 5 μ m and 55 μ m in a steel containing 1.5% carbon. Pure copper was the electrode material. The physical and thermal properties of both the electrodes are dependent on temperature. The effect of thermal conductivity of the white layer was evaluated with the properties of three steels, each of them containing 0.5%, 1% and 1.5% of carbon and a thickness of 15 μ m and 55 μ m for the current intensities of 2.34A and 37.1A, respectively. The higher the amount of carbon in steel the lower its thermal conductivity, as was pointed out by Marafona [5].

This methodology was designed to a die-sinking EDM machine, AGIE COMPACT 3. The EDM performance is related to the efficiency which is determined in the EDM process by the material removal rate (MRR) and the electrode wear rate (EW). Quality is determined by the accuracy and surface roughness.

This experimental methodology enables to determine the white layer as a significant contributor to the material removal rate and the electrode wear rate.

3. experimental results

The experimental results were collected from the handbook of a die-sinking EDM machine AGIE COMPACT 3. This handbook provides the pulse duration used with two possibilities for the pause: a standard value and a threshold value. The minimum volume of material removed from the workpiece depends on the material removal rate achieved experimentally, pulse duration and threshold value of pause. It is expected that the volume of material removed from the workpiece and the electrode should vary between the maximum and minimum. It is also possible to estimate the volume removed from the electrode and the workpiece with high accuracy if the value of pause and frequency is known.

3.1 Effect of white layer on material removal rate

Marafona and Araújo [12] stated that the initial workpiece hardness and its interaction with the electrical parameters influence the material removal rate. Thus, white layer as a product of interaction between the electrical parameters and workpiece material has the effect reported by the authors, since the white layer has a hardness greater than that of the base material and depends on the applied current intensity. That interaction is very difficult to simulate in the finite element model, because there is the need to produce the decomposition of dielectric oil and the diffusion of its elements into workpiece material. The hardness of white layer is associated with the amount of carbon, which is in return linked to its thermal conductivity, as pointed out by Marafona [5]. Therefore, the white layer is used as an independent variable and the effect of its thickness and thermal conductivity on material removal rate in the EDM process was studied.

3.1.1 Effect of thermal conductivity of white layer

The thermal conductivity of the workpiece material has a significant influence on material removal rate in the EDM process, according to Salah et al. [7]. However, the change of thermal conductivity in the white layer occurs in a reduced thickness and, hence, the study of its effect on material removal rate.

The volume of material removed from the workpiece increases with the decrease of thermal conductivity using the current intensity of 2.34A and it is always greater than the volume removed from the workpiece without white layer, as can be seen in Figure 1. Thus, an increase in the amount of carbon in the white layer reduces its thermal conductivity and increases the material removal rate. The theoretical volume of material removed from the workpiece is in good agreement with the experimental value obtained with the standard pause (18 μ s).

Figure 2 shows that the volume of material removed from the workpiece for the current intensity of 37.1A is closer to the minimum volume removed experimentally. This behaviour is opposite to current intensity of 2.34A,

where the volume removed is closer to the maximum volume removed experimentally. This indicates that the contribution of long pause, for the volume of material removed from the workpiece, is more significant the higher it is.

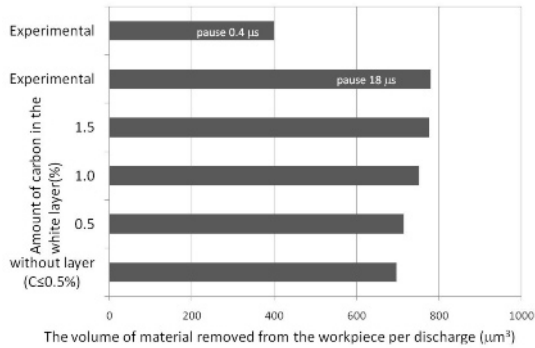


Fig. 1. Effect of thermal conductivity of the white layer on MRR for the current intensity of 2.34A.

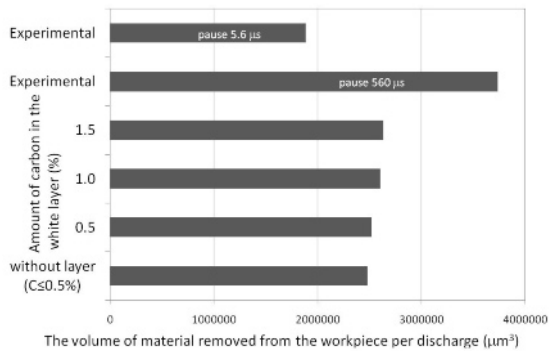


Fig. 2. Effect of thermal conductivity of the white layer on MRR for the current intensity of 37.1A.

3.1.2 Effect of white layer thickness

The effect of white layer thickness on the volume of material removed from the workpiece, for the current intensities of 2.34A and 37.1A, is shown in Figures 3 and 4. These trends show that the volume of material removed increases with the increase of white layer thickness.

The increase in the material removed from the workpiece with the increase in white layer thickness is opposite to the idea that the rate of material removal decreases and assumes a constant value during machining. However, this concept was formulated based on the speed of penetration and not on the rate of material removal. The author's philosophy is that the cavity eroded on the workpiece's surface changes in shape during the machining tending to assume a standard pattern, which has a reduced depth and a large radius (spherical segment) at the end of the machining.

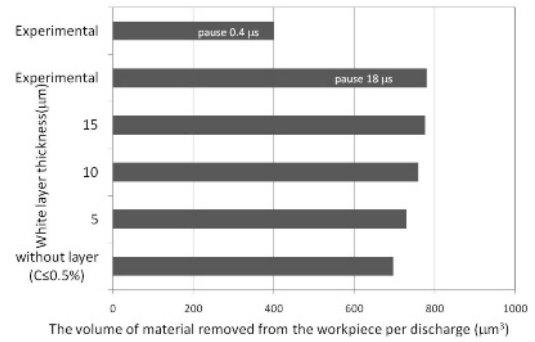


Fig. 3. Effect of white layer thickness on MRR for the current intensity of 2.34A.

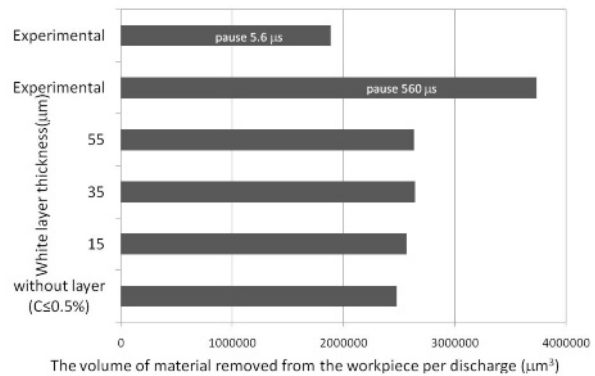


Fig. 4. Effect of white layer thickness on MRR for the current intensity of 37.1A.

3.2 Effect of white layer on electrode wear rate

The assumption that the metallurgic modification of workpiece material does not affect the electrode wear rate was never demonstrated. However, it is clear in this study that the change of thermal conductivity of the workpiece affects the heat distribution between the electrodes since the process of EDM is governed by the thermal phenomenon.

The white layer thickness may influence the electrode wear rate if it affects the receding time in the erosion of the cavity in the surface of the copper electrode. If this time is shorter than the standard pulse time, it means that less material is removed by evaporation.

3.2.1 Effect of thermal conductivity of white layer

The thermal conductivity of the workpiece affects the material removal rate and the tool wear rate. A perceptible change of thermal conductivity of the workpiece surface will affect the distribution of heat between the electrodes. A different distribution of heat by the electrodes changes the receding time in the erosion of cavities.

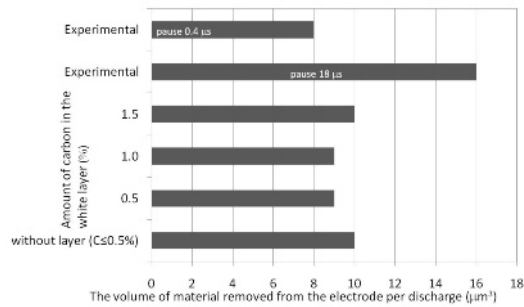


Fig. 5. Effect of thermal conductivity of the white layer on EW for the current intensity of 2.34A

Figure 5 shows that there is a thermal conductivity of the white layer that leads to a lower electrode wear rate. It is also possible to confirm that there is not always a decrease in the electrode wear rate with the reduction of thermal conductivity of the white layer.

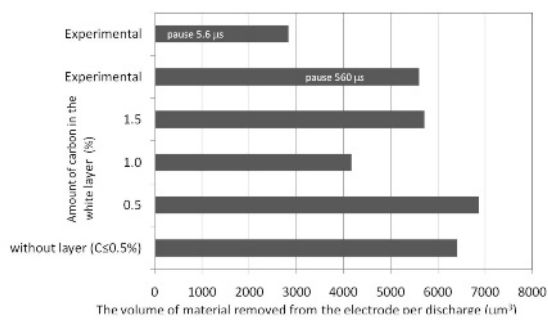


Fig. 6. Effect of thermal conductivity of the white layer on EW for the current intensity of 37.1A

The analysis of the effect of thermal conductivity of the white layer on electrode wear rate for the current intensity of 37.1A is similar to the result obtained for a current intensity of 2.34 A, because the electrode wear rate does not always decrease when there is a reduction in the thermal conductivity of the white layer, as can be seen in Figure 6. Moreover, the results show an experiment with higher electrode wear rate than the workpiece without white layer. However, there is a minimum electrode wear rate when the white layer contains 1% of carbon, as it happened for the current intensity of 2.34A.

3.2.2 Effect of white layer thickness

This study shows that the electrode wear rate is affected by the current intensity value. Figure 7 shows that the electrode wear rate is not affected by the white layer thickness for the current intensity of 2.34A. However, the electrode wear rate is always lower in the presence of white layer for the current intensity of 37.1A, and it reaches a minimum at the white layer thickness of 35μm, as can be seen in Figure 8.

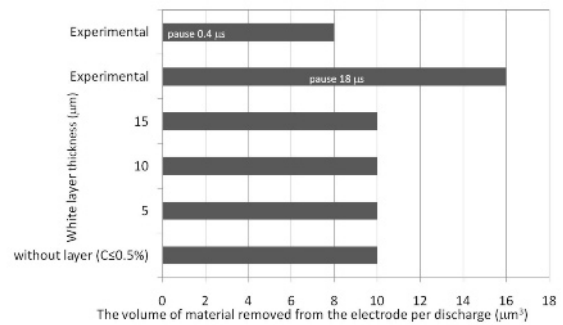


Fig. 7. Effect of white layer thickness on EW for the current intensity of 2.34A

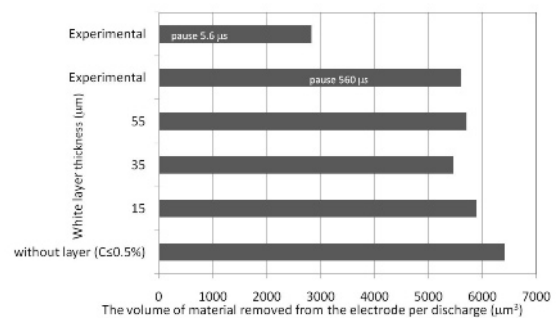


Fig. 8. Effect of white layer thickness on EW for the current intensity of 37.1A

4. Conclusion

The research shows that the material removal rate and the electrode wear rate are directly dependent on the thickness and thermal conductivity of the white layer. This is demonstrated by the results of the semi-empirical model used in the research.

The material removal rate increases with the increase in the white layer thickness. There is an increase in the material removal rate with the thermal conductivity of the white layer. Therefore, there is always an increase in the material removal rate in the presence of white layer. It was also demonstrated that the electrode wear rate is dependent on the white layer thickness, because there is always a decrease in the electrode wear rate comparatively to the workpiece without white layer. There is a random behaviour in the electrode wear rate with the thermal conductivity of the white layer. However, there is a thermal conductivity value of the workpiece that minimizes the electrode wear rate.

In conclusion, this article demonstrates that the electrical discharge machining process is not only influenced by the thermal properties of the workpiece base material but also by its metallurgic modifications during the machining process.

References

- [1] Albinski K., Musiol K., Miernikiewicz A., Labuz S., Malota M., (1995) Plasma temperature in Electro-Discharge Machining, Proceedings 11th International Symposium for ElectroMachining, April 17-21, EPFL Lausanne, Switzerland 143-152.
- [2] Patel M.R., Barrufet M.A., Eubank P.T., DiBitonto D.D., (1989) Theoretical models of the electrical discharge machining process-II: the anode erosion model, *Journal of Applied Physics* 66 (9) 4104-4111.
- [3] DiBitonto D.D., Eubank P.T., Patel M.R., Barrufet M.A., (1989) Theoretical models of the electrical discharge machining process-I: a simple cathode erosion model, *Journal of Applied Physics* 66 (9) 4095-4103.
- [4] Van Dijck F., (1973) Physic-Mathematical analysis of the Electro Discharge Machining Process, PhD thesis, Katholieke University, Heverlee, Netherlands 61-62.
- [5] Marafona J.D., (2009) Black layer affects the thermal conductivity of the surface of copper-tungsten electrode, *Int. J. Adv. Manuf. Technology*, 42 (5) 482-488.
- [6] Zingerman A.S., (1956) The effect of thermal conductivity upon the electrical erosion of metals, *Journal of Technical Physics (USSR)*, 1 (2) 1945-1958.
- [7] Salah N. B., Ghanem F., Atig K.B., (2006) Numerical study of thermal aspects of electric discharge machining process, *Int. J. Mach. Tools and Manufacture*, 46 (7-8) 908-911.
- [8] Lee L.C., Lim L.C., Narayanan V., Venkatesh V.C., (1988) Quantification of surface damage of tool steels after EDM, *Int. J. Mach. Tool Design and Research*, 28 (4) 359-372.
- [9] Lee L.C., Lim L.C., Wong Y.S., Lu H.H., (1990) Towards a better understanding of the Surface Features of Electro-Discharge Machined Tool Steels, *Journal of Materials Processing Technology*, 24 (C) 513-523.
- [10] Lee L.C., Lim L.C., Wong Y.S., Fong H.S., (1992) Crack susceptibility of electro-discharge machined surfaces, *Journal of Materials Processing Technology*, 29 (1-3) 213-221.
- [11] Abbas N.M., Solomon D.G., Bahari Md. F., (2007) A review on current research trends in electrical discharge machining, *International Journal of Machine Tools & Manufacture*, 47 1214-1228.
- [12] Marafona J.D., Araújo A., (2009) Influence of workpiece hardness on EDM performance, *International Journal of Machine Tools & Manufacture*, 49 (9) 744-748.

Development of a hybrid method for electrically dressing metal-bonded diamond grinding wheels

A. Sudiarso¹ and J. Atkinson²

¹ Department of Mechanical and Industrial Engineering, Faculty of Engineering, Gadjah Mada University, Jl. Grafika No. 2 Yogyakarta 55281 INDONESIA. Corresponding author: a.sudiarso@ugm.ac.id

² School of Mechanical, Aerospace and Civil Engineering, The University of Manchester, PO Box 88 Sackville Street Manchester M60 1QD UK

Abstract. In order to restore its cutting ability, a grinding wheel needs a periodic dressing process to remove dulled grains from its cutting face and then to disclose new and sharp grains beneath. An electrical dressing method was developed recently for overcoming the limitations of the conventional dressing methods available in relation to a diamond wheel because of the hardness of its abrasive grains and the durability of its bonding material. Development of a hybrid electrical dressing method for metal-bonded diamond grinding wheels is proposed in this paper. This method consists of a combination of electrochemical and electro-discharge dressing. The dressing method was implemented on a surface grinder with twin copper electrodes and two AC power supplies. Both on-line (in process) dressing and off-line dressing have been performed using static and dynamic electrodes. The results show that a better wheel profile and a better surface roughness are produced using the proposed method compared with the traditional SiC wheel dressing technique. It is concluded that more consistent results can be achieved by applying in-process electrical dressing.

Keywords: electrochemical, electro-discharge, hybrid electrical dressing, metal-bonded diamond grinding wheel

1. Introduction

Dressing is a periodic process needed for restoring grinding wheel cutting ability. The process is performed by removing dulled grains from the wheel cutting face and then disclosing new and sharp grains underneath. A diamond wheel with metal bond material requires an advanced method of dressing. Using a conventional method to dress the wheel has been proved to be ineffective and uneconomical because of the high hardness of the abrasive grains and the bonding material durability [1].

Since electrochemical and electro-discharge machining are capable of dealing with conductive materials such as metals, their application for dressing of metal-bonded diamond wheels has already been tried. For example, Schopf *et al.* [2] combined electrochemical and electro-discharge dressing in centreless grinding. The

application was implemented with a single electrode supplied with a DC power supply via a pair of brushes. Both electrical dressing methods have their own characteristics and advantages. The electro-discharge method is responsible for macro-geometrical removal whereas the electrochemical method is required to produce sufficient grit protrusions.

In this paper, a hybrid electrical dressing method for metal bonded diamond wheels is proposed. Both electrochemical and electro-discharge techniques are combined to dress a metal-bonded diamond wheel using twin copper electrodes and AC power supplies.

2. Design Considerations

Suzuki *et al.* (1991) designed an electrochemical dressing system using an AC power supply [3]. However, the design did not incorporate electro-discharge dressing and the electrodes used were coupled together such that the same gap width was set for both electrodes.

The available combined electrical dressing designed by Schopf *et al.* only used a single electrode. Therefore, the electrochemical and electro-discharge dressing are done alternately during the dressing period and that tends to increase the dressing time required.

The present proposal for a hybrid electrical dressing system attempts to combine electrochemical and electro-discharge dressing using an AC power supply and twin electrodes. Since the gap width requirement for the two processes are different, dynamic twin electrodes are used. These are supported by two servomotors, one for each electrode, allowing a different gap width to be set for each electrical process. This allows electrochemical and electro-discharge dressings to be performed individually as required, rather than conducted in a repeated alternating pattern with single electrode.

As an electro-discharge system is introduced in the design, a variable frequency power supply is used to observe the optimum frequency needed for effective hybrid electrical dressing. Furthermore, the use of an AC supply results in machining both the wheel and the electrode. This develops the shape of the electrodes to follow the change of the wheel curvature and hence keeps the dressing area almost constant. Moreover, using an AC power supply eliminates the need for a carbon brush by connecting the electrode with the phase of the AC supply.

3. Development Stages

3.1 Hardware Implementation

An experimental set-up was arranged for the hybrid electrical dressing system as shown in Figure 1. Twin electrodes were used during the dressing process. One electrode was used for electro-discharge dressing and the other one for electrochemical dressing. An Acoustic Emission (AE) sensor was used for monitoring the wheel condition [4]. The diamond wheel used had 8-inch diameter and 0.75 inch thickness.

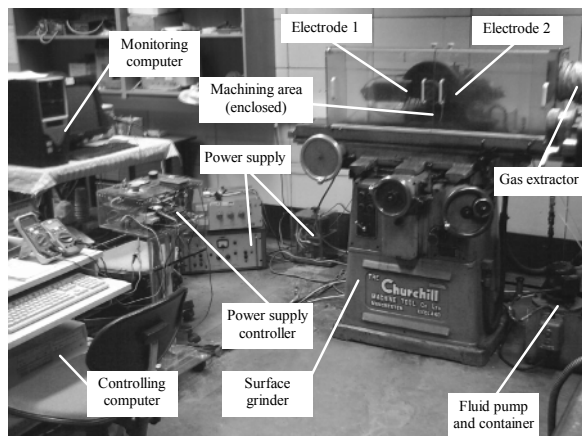


Fig. 1. Experimental setup for the hybrid electrical dressing method

The workpiece samples used are tungsten carbide inserts. Three inserts were clamped by means of insert holders on a flat magnetic chuck and ground at a same time. An energy disperse X-ray (EDX) analysis of the tungsten carbide inserts was done and found that apart from tungsten, carbon and oxygen, there are other elements of carbide inserts. These are titanium, cobalt, niobium and tantalum.

3.2 Software Implementation

The system was designed to provide three types of electrode movement that can be chosen during a dressing process, namely static or manual, pecking and auto-gap mechanisms [5]. A feedback control system was

incorporated in order to regulate the electrode movement or gap width during a dressing process.

In order to accommodate all of the above mechanisms, custom-built software was developed and is called JaSDressIt. The software incorporates real-time monitoring and in-process control functions. Figure 2 shows a screen shot of the software.



Fig. 2. Custom-built software to monitor and control the dressing

4. Reference Results

Diamond grinding wheels are traditionally dressed by the wheel manufacturers using a rotating SiC wheel. During dressing, the diamond wheel remains on the machine spindle and the rotating SiC wheel is placed under the wheel. The diameter of the dressing wheel is usually smaller than the grinding wheel.

In the present work, before a new bronze bonded diamond wheel was used for grinding workpieces, its profile was examined. Using an impression material, the wheel profile was duplicated and then the profile was measured using a laser sensor. The result gave a maximum of 160 μm relative height or protrusion, as shown in Figure 3.

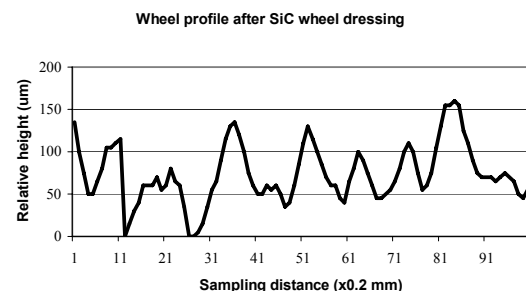


Fig. 3. A wheel profile, dressed by SiC wheel method

The new bronze-bonded diamond grinding-wheel was then used for grinding tungsten carbide workpieces. There were three carbide inserts ground simultaneously for a total of three passes. Each pass had a 0.01 mm set

depth. Two workpiece feedrates were used, i.e. low and high feedrates. The low feedrate was 4.7 cm/s whereas the high feedrate was 15.8 cm/s. Each ground insert was then measured using a calibrated surface roughness meter. The average results are shown graphically in Figure 4.

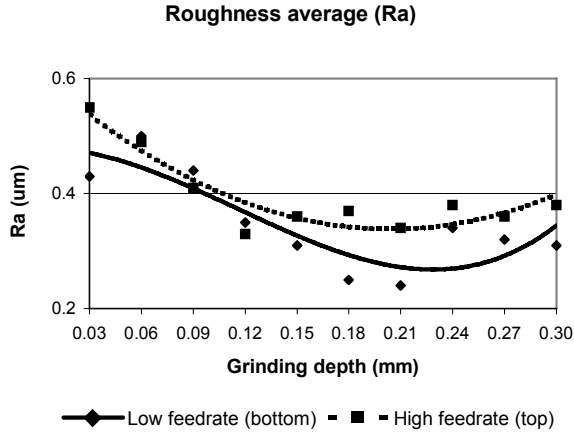


Fig. 4. Average surface roughness of carbide inserts after initial grinding

The lowest surface roughness (Ra) produced for the low feedrate was 0.24 μm whereas for the high feedrate, the lowest surface roughness was 0.33 μm. The average surface roughness for the low feedrate was 0.35 μm whereas the high feedrate produced an average of 0.40 μm. These results were used as references for further analysis and comparison with the results from proposed hybrid electrical dressing method. It is clear from the Figure 4 that the surface roughnesses of the inserts produced were inconsistent. It took several passes to achieve its best roughness before starting to get worse or deteriorated.

5. Electrical Dressing Results

Voltage characteristics during a discharge were observed at two different frequencies, i.e. 50 Hz and 500 Hz, as shown in Figure 5. Obviously, the duration of discharge is shorter at a higher frequency.

A discharge is classified as a spark if it has a discharge duration of approximately 1 μm – 1 ms whilst a duration of about 0.1 s (100 ms) is classified as an arc [6]. Therefore, the discharge shown is considered as a spark rather than an arc.

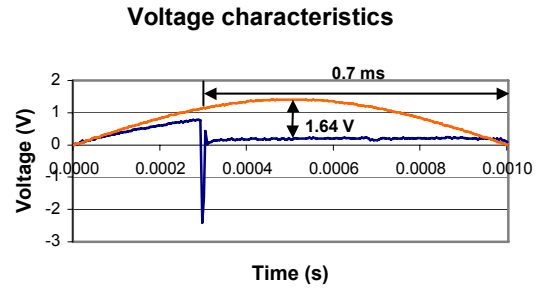
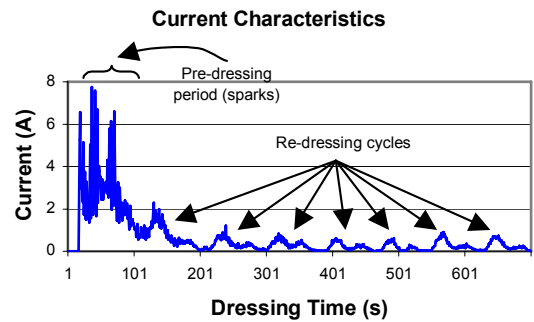


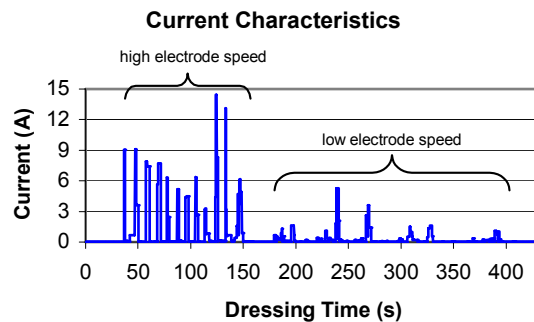
Fig 5. Voltage characteristics during a discharge 500 Hz [7]

Typical current characteristics during an electrical dressing mainly depend on the electrode movement, whether it is static or dynamic, and also the status of the dressing process i.e. whether it is on-line (in-process) or off-line. Two typical current characteristics observed are shown in Figure 6.

More current fluctuation is expected when sparks occur. During online dressing, there is a period called pre-dressing initiated at the beginning of the process whilst during the rest of the process re-dressing cycles occur. Re-dressing cycle is a result of the removal of a copper oxide layer during grinding.



(a)



(b)

Fig. 6. Typical current characteristics during electrical dressing (a). static and online [7]; (b). auto gap

Meanwhile, a dynamic electrode may guarantee more sparks throughout the dressing period than static one. Pecking with increment produces intense sparks during dressing until the minimum distance or gap is reached. Dynamic movement with an auto-gap produces sparks at the closest distance, or gap, between the electrode and the wheel for a short period only because of a rapid electrode retraction.

The wheel profile was examined after electrically dressing with the proposed method. The result is shown in Figure 7. The maximum relative height measured was 440 μm . Comparing the results from Figure 3 (after a SiC wheel dressing) with Figure 7 (after the proposed hybrid electrical dressing) shows that a better wheel profile was produced by the hybrid electrical dressing method than by the traditional SiC wheel dressing method. More protrusion was produced using the proposed method.

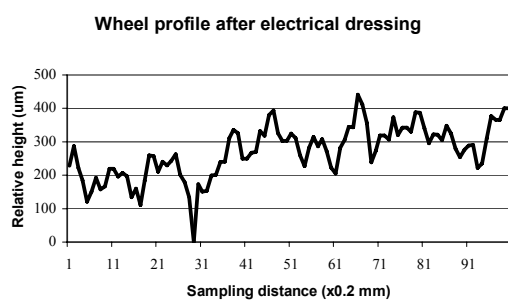


Fig. 7. Diamond wheel profile electrically dressed by the hybrid electrical dressing method

Moreover, roundness of the wheel was measured using a laser sensor. A maximum peak-to-peak deviation of 0.4 mm or 0.4% of the wheel radius was found after the hybrid electrical dressing.

Table 1 shows a comparison of surface roughness as produced by a traditional SiC wheel dressing method, the present hybrid electrical dressing method and the previous electrochemical discharge dressing research [2]. The results show that the present hybrid electrical dressing method using AC power supplies and twin electrodes produce better results compared with both the traditional dressing method and the previous research using a DC power supply and a single electrode.

Table 1. Comparison of surface roughness

Surface Roughness (Ra, μm)	SiC Wheel Dressing	Hybrid Dressing	Previous Research [2]
Minimum	0.24	0.20	-
Average	0.31	0.22	0.26

References

- [1] Golabczak, A, (2001) Selected problems of electrochemical and electrodischarge dressing of grinding wheels with metal bond. Proceedings of the ISEM XIII vol II:851-868.
- [2] Schopf, M, Beltrami, I, Boccadoro, M, Kramer, D, (2001) ECDM (electro chemical discharge machining), a new method for trueing and dressing of metal-bonded diamond grinding tools. Annals of the CIRP 50/1:125-128.
- [3] Suzuki, K, Uematsu, T, Yanase, T, Honma, M, Asano, S, (1991) Development of a simplified electrochemical dressing method with twin electrodes. Annals of the CIRP 40/1:363-366.
- [4] Kwak, JS, Song, JB, (2001) Trouble diagnosis of the grinding process by using acoustic emission signals. International Journal of Machine Tools and Manufacture 41:899-913.
- [5] Sudiarso, A, (2008) In-process electrochemical discharge dressing of metal-bonded diamond grinding wheels. PhD Thesis, The University of Manchester.
- [6] McGeough, JA, (1988) Advanced method of machining. Chapman and Hall Ltd.
- [7] Sudiarso, A, Atkinson, J, (2008) In-process electrical dressing of metal-bonded diamond grinding wheels. Engineering Letters 16/3:308-310.

Robust Parameter Design and Multi-Objective Optimization of Electro-Discharge Diamond Face Grinding of HSS

Gyanendra Kumar Singh¹, Vinod Yadava^{1*} and Raghuvir Kumar¹

¹Mechanical Engineering Department, Motilal Nehru National Institute of Technology Allahabad (INDIA)-2111004

*Corresponding Author: E mail: vinody@mnnit.ac.in

Abstract: In this paper a hybrid methodology comprising of Taguchi methodology and Response surface methodology has been applied for multi-objective optimization of Electro-Discharge Diamond Face Grinding (EDDFG) process. The approach first uses the Taguchi quality loss function to find the optimum level of input machining parameters such as wheel speed, current, pulse on-time and duty factor. The optimum input parameter values are further used as the central values in the response surface method to develop and optimize the second-order response model. The three quality characteristics material removal rate (MRR), wheel wear rate (WWR) and average surface roughness (ASR), which are of different nature, have been selected for optimization. The developed response surface model for each MRR, WWR and ASR has been found by TMRSM and the results of hybrid approach has been compared with the results of a Taguchi Methodology approach.

Keywords: Hybrid machining, Diamond grinding, Electro-discharge machining (EDM), Robust design, Optimization, Taguchi methodology (TM), Response surface methodology (RSM), Hybrid methodology.

1. Introduction

For realistic progress in industries, there is a need for continuous evolution of new machining process with the development of advanced engineering materials. Recently, a new trend has been introduced to combine the features of different machining processes. Such machining processes are called as hybrid machining processes (HMPs). HMPs are developed to exploit the advantages of each of the constituent machining process and diminish the disadvantages of each constituent process. It has been observed that sometimes, hybrid machining process enhances the material removal rate (MRR), increases the capabilities of the constituent processes, and widen the area of application of the constituent processes. HMPs also reduce some of the adverse effects of the constituent processes when they are applied individually.

Some HMPs are developed by combining metal bonded abrasive grinding with either EDM or ECM. Hybrid processes of ECM and grinding is called electro-

chemical abrasive grinding (ECAG) where as combination of EDM and grinding is known as electro-discharge abrasive grinding (EDAG). When metal bonded diamond grinding wheel is used in EDAG then the process is termed as Electro-Discharge Diamond Grinding (EDDG).

The concept of combining EDM and diamond-grinding for machining electrically conducting very hard materials was first originated in the former USSR [1-3]. The hybrid process termed as electrical discharge diamond grinding (EDDG) utilizes a metal bonded diamond-grinding wheel where the work is subjected to the simultaneous influence of diamond grains and electrical sparks which cause abrasion and surface melting, respectively.

EDDG can be operated in three different configurations: (1) Electro-Discharge Diamond Surface Grinding (EDDSG), (2) Electro-Discharge Diamond Cut-off Grinding (EDDCG), and (3) Electro-Discharge Diamond Face Grinding (EDDFG).

EDDFG is performed using flat face of the metal bonded diamond grinding wheel. In this mode, the metal bonded diamond grinding wheel rotates about vertical spindle axis and fed in a direction perpendicular to the machine table. While machining, the rotating wheel is fed downwards under the control of servo system. The metal bonded grinding wheel and the work surface are physically separated by a gap which depends on the local breakdown strength of the dielectric for a particular gap voltage setting. Thus, the workpiece is simultaneously subjected to heating due to electrical sparks occurring between the metal bonded grinding wheel and the workpiece, and abrasion by diamond grains with protrusion height more than the inter-electrode gap width. In this mode, the diameter of the metal bonded diamond grinding wheel is usually kept greater than that of the cylindrical workpiece diameter.

In most of the experimental investigations of the EDDG process, researchers have varied one factor at a time to analyze the effect of input process parameters on

output quality characteristics or responses [4-8]. But this technique requires a large number of experimental runs because only one factor is varied in each run, keeping all other factors constant. Also, in this technique, the interaction effects among various input process parameters are not considered. To overcome these problems, some researchers have incorporated design of experiments methodologies such as the response surface methodology (RSM) and Taguchi methodology (TM). However, no such research work has been observed by the authors, related to EDDFG.

Different hybrid approaches have recently been used for the optimisation of different machining processes. Taguchi method with fuzzy logic [9] or with grey relational analysis [10] has been used to optimise the electrical discharge machining process with multiple machining performances. Chiadamrong [11] has suggested a sequential integration approach of TM and RSM to optimise the multiple process characteristics in manufacturing system. He demonstrated the hybrid methodology by taking a case study of printed circuit board manufacturing plant and found a significant reduction in quality loss.

In the present paper a hybrid methodology comprising of Taguchi method and Response surface method (TMRSM) has been used to develop the response models and to optimise the EDDFG process for multiple quality characteristics such as MRR, WWR and ASR. Firstly, TM is applied to determine the optimum machining parameters for multiple quality characteristics (MRR, WWR and ASR). The output (optimum parameter values) from TM is further used as central value in RSM. The second-order response model for MRR, WWR and ASR has been developed by performing the experiments using the central composite rotatable design (CCRD) matrix [12]. The results of multi-objective optimisation using only Taguchi's quality loss function have also been compared with the results of hybrid approach.

2. Experimental procedure and machining parameters

The Experimental studies were performed on an ELEKTRA PULS EDM machine attached with self designed grinding attachment in face grinding mode (Fig. 1). The setup consists of a metal bonded grinding wheel, motor, shaft, v-belt and bearings, mounted on the ram of the machine to rotate the metal bonded grinding wheel about an axis perpendicular to the machine table. While machining, the rotating wheel is fed downwards with servo control mechanism, for material removal in the face configuration mode. The metal bonded grinding wheel and the work surface are physically separated by a gap, the magnitude of which depends on the local breakdown strength of the dielectric for a particular gap voltage setting. The workpiece is thus simultaneously subjected to heating due to electrical sparks occurring between the metal bonded grinding wheel and the workpiece, and

abrasion by diamond grains with protrusion height larger than the inter-electrode gap.

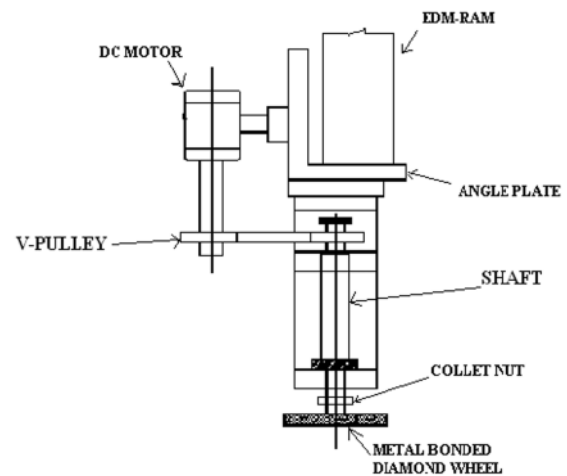


Fig. 1. EDDFG setup

During experimentation the effect of various input parameters such as wheel speed, current, pulse on-time, and duty factor on the output parameters such as MRR, WWR and ASR have been studied. Experiments were performed on 25 mm diameter cylindrical workpiece made of high speed steel (HSS). The spark erosion oil was used as dielectric liquid. Each workpiece was machined for 60 minutes before measuring output parameters. Each set of experiment was repeated three times. Amount of material removal after 60 minutes was obtained by finding weight difference before and after machining using precision electronic digital weight balance with 0.1mg resolution. The MRR is calculated by using the following formula:

$$MRR (mm^3 / min) = \frac{(W_i - W_f) \times 1000}{t \times \rho} \quad (1.1)$$

where W_i is initial weight of workpiece in gram (before machining); W_f is final weight of workpiece in gram (after machining); t is machining time in minutes; ρ is density of workpiece (7.8 g/cm^3).

The WWR is calculated by using the following formula:

$$WWR (g / min) = \frac{W_{wi} - W_{wf}}{t} \quad (1.2)$$

where W_{wi} is initial weight of wheel in gram (before machining); W_{wf} is final weight of wheel in gram (after machining); t is machining time in minutes.

A Mitutoyo SJ-201 at 0.8 mm cut-off value was applied to measure the average surface roughness (ASR) of each machined specimen.

The numerical values of machining parameters at different levels are shown in Table 1. A pilot experimentation is done to decide the range of input parameters.

Table 1 Machining parameters and their levels

Symbol	Machining Parameters	Level 1	Level 2	Level 3
S	Wheel speed (RPM)	700	875	1050
C	Current (A)	4	6	8
P	Pulse on-time (μ s)	50	100	50
DF	Duty factor	0.57	0.63	0.70

In the present case, four parameters each at three levels with no interaction effect has been considered. The total degree of freedom (dof) has been calculated as [14]:

$$\text{dof} = (3 - 1) \times 4 + 1 = 9.$$

Hence, a standard L_9 orthogonal array (OA) is selected for experimental design matrix.

Table 2 Factors and their coded levels in CCRD

Symbol	Factors	Coded levels				
		-2	-1	0	1	2
S	Wheel speed	700	875	1050	1225	1400
C	Current	4	6	8	10	12
P	Pulse on-time	40	70	100	130	160
DF	Duty factor	0.47	0.55	0.63	0.71	0.79

The control factors, their numerical and coded values used in CCRD matrix are shown in Table 2. The CCRD matrix contains total 31 runs with 2^p factorial runs, 2p axial runs, and 7 centre point runs. The number of control factors (p) in present case are four. Therefore, the total number of runs is $2^4 + 2 \times 4 + 7 = 31$.

The central value of machining parameters corresponding to code '0' is the optimum parameter level obtained from multi-objective optimisation using TM. The value of 'a' in CCRD is calculated as: $a = (2^p)^{1/4} = 2$.

Therefore, the coded values for different levels in CCRD are -2, -1, 0, 1, and 2.

3. Response surface modelling

Second-order response surface model each for MRR, WWR and ASR has been developed from the experimental response values. The model developed using MINITAB software is

$$\begin{aligned} \text{MRR}(\text{mm}^3/\text{min}) = & 1.08611 + 0.31932s + 0.18853c - 0.02278pt + \\ & 0.27012df + 0.07037s^2 + 0.01355c^2 - 0.04519pt^2 \\ & - 0.02819df^2 - 0.02735sc + 0.01355spt + 0.02739sdf \\ & - 0.04255cpt - 0.02436cdf + 0.0261ptdf \end{aligned} \quad (1.3)$$

$$\begin{aligned} \text{WWR}(\text{g}/\text{min}) = & 0.006026 + 0.000359s + 0.003493c + 0.002139pt + \\ & 0.004860df + 0.000092s^2 + 0.000106c^2 + 0.000240pt^2 \\ & + 0.000998cdf^2 - 0.000117sc - 0.000013spt - 0.000322sdf \\ & + 0.001486cpt + 0.003052cdf + 0.001788ptdf \end{aligned} \quad (1.4)$$

$$\begin{aligned} \text{ASR}(\mu\text{m}) = & 3.51571 + 0.04667s + 0.15667c + 0.09083pt + \\ & 0.24167df + 0.07690s^2 - 0.15185c^2 - 0.03310pt^2 \\ & - 0.03435df^2 + 0.02125sc + 0.03625spt + 0.01875sdf \\ & + 0.02000cpt - 0.06000cdf + 0.09500ptdf \end{aligned} \quad (1.5)$$

where s is wheel speed (RPM), c is current (A), pt is pulse on-time (μ s) and df is the duty factor.

To test whether the data are well fitted in these model or not, the calculated S value of the regression analysis for MRR, WWR and ASR has been obtained as 0.1995, 0.002194 and 0.2031, respectively, which are smaller and R^2 value for three responses are 89.4%, 94.1% and 83.9%, respectively. The value of R^2 (adj) for MRR, WWR and ASR are 80.2%, 89.0% and 69.8%, respectively. These are moderately high (except R^2 (adj) for ASR which is moderate) therefore model fits the data. Hence, the data for each response are well fitted in the developed models.

Table 3 Result of ANOVA for developed models

Source	MRR model		WWR model		ASR model	
	F-value	p-value	F-value	p-value	F-value	p-value
Regression	9.68	0.000	18.39	0.000	5.94	0.001
Linear	31.80	0.000	50.51	0.000	13.59	0.000
Square	1.60	0.222	1.51	0.247	5.75	0.005
Interaction	0.32	0.917	8.22	0.000	0.98	0.471
Lack-of-fit	6.09	0.019	3.25	0.081	0.82	0.626

Analysis of variance (ANOVA) and subsequently F-ratio test and p-value test have been carried out to test the adequacy of the developed mathematical models for MRR, WWR as well as ASR. Table 3 shows the results of ANOVA, p-value of the source of regression model and linear effects are lower than 0.01 for the responses. Developed regression model and linear effect of parameters for the responses are significant. Calculated F-value of the lack-of-fit for MRR, WWR and ASR are 6.09, 3.25 and 0.82 respectively, which are lower than the critical value of the F-distributed on 7.87 as found from standard table at 99% confidence level. Therefore, the developed second-order regression model for MRR, WWR and ASR are adequate at 99% confidence level.

4. Results and discussion

4.1 Multi-objective optimisation results using Taguchi approach

The experimental values of responses MRR, WWR and ASR have been obtained by using OA design matrix. The quality loss values for different quality characteristics in each experimental run are calculated using [13, 14]. The normalised quality loss for quality characteristics in each

experimental run has been calculated using [15]. The total normalised quality loss (TNQL) and MSNR for multiple quality characteristics MRR, WWR and ASR has been calculated using [15]. These results are shown in Table 4. In calculating total normalised quality loss three unequal weights i.e. $w_1=0.6$ for MRR, $w_2=0.3$ for WWR, and $w_3=0.1$ for ASR has been assumed based on experience. In the present case, MRR is higher-the-better (HB) type and WWR as well as ASR are smaller-the-better (SB) type. The optimum levels of different control factors are wheel speed at level 3 (1050 RPM), current at level 3 (8 A), pulse on-time at level 2 (100 μ s), and duty factor at level 2 (0.63). A better feel for the relative effect of the different factors can be obtained by the decomposition of the variance, which is commonly called ANOVA. It is a computational technique to estimate quantitatively the relative significance (F-ratio), and also the percentage contribution of each factor on quality characteristics. The ANOVA given in Table 5 shows the percentage contribution of different control factors on multiple quality characteristics (MRR, WWR and ASR) in increasing order as: pulse on-time (3.42%), wheel speed (19.84%), duty factor (34.03%) and current (42.70%).

Table 4 Total normalized quality loss (TNQL) and multiple S/N ratio (MSNR)

Exp. No.	TNQL	MSNR (dB)
1	0.6574	1.8216
2	0.2157	6.6602
3	0.1954	7.0880
4	0.2831	5.4796
5	0.4227	3.7392
6	0.1344	8.7140
7	0.2294	6.3939
8	0.1586	7.9961
9	0.1614	7.9190
Mean MSNR (η_m)		6.2013

Table 5 ANOVA Table

Factor	SS	df	V	F	PC (%)
S	7.794	2	3.897	5.796	19.84
C	16.775	2	8.387	12.475	42.70
P	1.344 [#]	2	0.672	-	3.42
DF	13.37	2	6.685	9.943	34.03
EP	1.344	2	0.672		
Total	39.28	8			

[#]pooled factors

Table 6 Results of confirmation experiment using Taguchi method

	Initial Setting	Optimum values	
		Prediction	Experiment
Level	$S_1C_1P_1DF_1$	$S_3C_3P_2DF_2$	$S_3C_3P_2DF_2$
MRR	0.4114	-	1.8254
WWR	0.00060	-	0.005223
ASR	3.4847	-	3.312
MSNR (dB)	1.8216	10.6819	10.3991
Improvement of MSNR = 8.5775 dB			

The confirmation experiment is performed by conducting a test with optimal setting of the factors and levels previously calculated. The predicted value of MSNR and that from confirmation test are shown in Table 6. The improvement in MSNR at the optimum level is found to be 8.5775dB. The value of MRR (mm^3/min), WWR (g/min) and ASR (μm) at this optimum level are 1.8254 mm^3/min , 0.005223 g/min and 3.312 μm against the initial process parameter setting of 0.4114 mm^3/min , 0.00060 g/min and 3.48 μm .

4.2 Multi-objective optimisation results using hybrid approach

The mathematical model developed for MRR, WWR and ASR are shown in Eqs. (1.3), (1.4) and (1.5), respectively. From the developed models, it is clear that the wheel speed, duty factor, square effect of wheel speed, and interaction effect of wheel speed and duty factor are significant factors for MRR because the absolute value of corresponding coefficients for these terms are quite high in comparison of other terms. Likewise, the WWR is significantly affected by current, duty factor and square effect of duty factor and interaction effect of current and duty factor. The ASR is significantly affected by current, duty factor, square effect of wheel speed, and interaction effect of pulse on-time and duty factor.

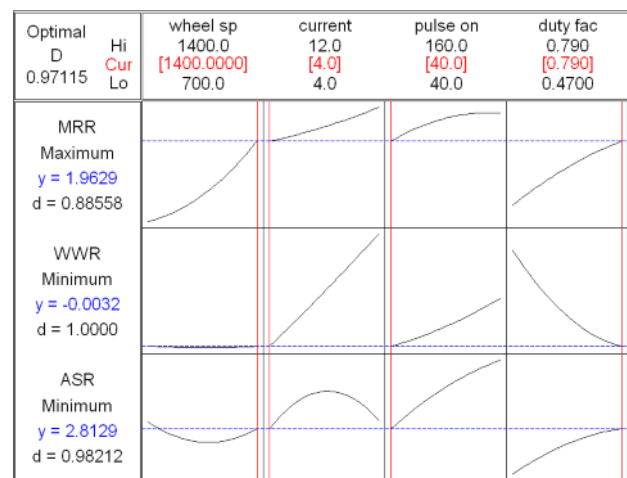


Fig. 2. MINITAB results of multi-objective optimisation using hybrid approach. D, composite desirability; d, individual desirability; Hi, highest parameter values; Lo, lowest parameter values; Cur, current or optimum values; wheel sp, wheel speed; current; Pulse on, pulse on-time; duty fac, duty factor.

The simultaneous optimisation of weighted response for MRR (weighting factor = 0.6), WWR (weighting factor = 0.3) and ASR (weighting factor = 0.1) is obtained by using MINITAB software. The multi-objective optimisation results are shown in Fig. 2. The results show the graphical representation of individual factor effects at different level on MRR, WWR and ASR, and optimum parameter level has been suggested for

maximum MRR and minimum WWR as well as ASR. The composite desirability D and individual desirability d (which depend on weighting factor and nature of quality characteristics) are also shown in result. The predicted optimal values of MRR, WWR and ASR in multi-objective optimisation are $1.9629 \text{ mm}^3/\text{min}$, -0.0032 g/min and $2.8129 \text{ }\mu\text{m}$, respectively, at wheel speed = 1400 RPM , current = 4 A , pulse on-time = $40 \text{ }\mu\text{s}$, and duty factor = 0.79 . The confirmation test at predicted optimum parameter setting gives MRR = $1.9457 \text{ mm}^3/\text{min}$, WWR = 0.001266 g/min and ASR = $2.91 \text{ }\mu\text{m}$. The optimum quality values of MRR, WWR and ASR obtained from Taguchi approach and hybrid approach have been compared in Table 7. The results show that three quality characteristics have improved considerably when hybrid approach has been applied.

Table 7. Comparison of results of Taguchi approach and hybrid approach

Quality characteristics	Optimization technique	
	Taguchi approach	Hybrid approach
MRR (mm^3/min)	1.8254	1.9457
WWR (g/min)	0.005223	0.001266
ASR (μm)	3.312	2.91

5. Conclusions

In EDDFG, the re-solidified layer with micro-cracks and thermal residual stresses in the workpiece due to spark discharges are eliminated by abrasion action of the diamond wheel. Hence, disadvantages of both the diamond grinding and EDG process can be removed by erosion action of spark discharges and vice versa. Therefore, this particular configuration can be applied for the machining of flat surface, fragile and thin plates. Based on the modelling and optimisation results, the following conclusions can be drawn.

1. The optimum value of MRR, WWR and ASR obtained from multi-objective optimisation using Taguchi method only are $1.8254 \text{ mm}^3/\text{min}$, 0.005223 g/min and $3.312 \text{ }\mu\text{m}$, respectively while using the hybrid approach these values are $1.9457 \text{ mm}^3/\text{min}$, 0.001266 g/min and $2.91 \text{ }\mu\text{m}$, respectively. Hence a considerable improvement of quality characteristics has been found with hybrid approach of TMRSM.
2. The developed response surface models for MRR, WWR and ASR have been found adequate. It has also been found that the linear parameters are significant for the models.

References

- [1] Grodzinskii EY, (1979) Grinding with electrical activation of the wheel surface. *Machines and Tooling* 50 (12): 10-13
- [2] Vitlin VB, (1981) Model of the electro-contact-abrasive cutting process. *Soviet Engineering Research* 1(5): 88-91
- [3] Grodzinskii EY, Zubotava LS, (1982) Electro-chemical and electrical discharge abrasive machining. *Soviet Engineering Research* 2(3): 90-92
- [4] Aoyama T, Inasaki I, (1986) Hybrid Machining - Combination of electrical discharge machining and grinding. *Proceeding of the 14th North American Manufacturing Research Conference SME* 654-661
- [5] Rajurkar KP, Wei B, Kozak J, Nooka SR, (1995) Abrasive electro-discharge grinding of advanced materials. *Proceeding of the 11th International Symposium of Electro-machining (ISEM-11)* 863-869
- [6] Koshy P, Jain VK, Lal GK, (1996) Mechanism of material removal in electrical discharge diamond grinding. *International Journal of Machine Tools Manufacture* 36(10): 1173-1185
- [7] Koshy P, Jain VK, Lal GK, (1997) Grinding of cemented carbide with electrical spark assistance. *Journal of Materials Processing Technology* 72: 61-68
- [8] Choudhary SK, Jain VK, Gupta M, (1999) Electrical discharge diamond grinding of high-speed steel. *Machining Science and Technology* 3(1): 91-105
- [9] Lin JL, Wang KS, Yan BH, Tarn YS, (2000) Optimization of the electrical discharge machining process based on the Taguchi method with fuzzy logics. *Journal of Materials Processing Technology* 102: 48-55
- [10] Narendar PS, Raghukandan K, Pai BC, (2004) Optimization by Grey relational analysis of EDM parameters on machining Al-10%SiC_p composites. *Journal of Materials Processing Technology* 155-156: 1658-1661
- [11] Chiadomrong NA, (2003) Sequential procedure for manufacturing system design. *Science Asia* 29: 57-65
- [12] Cochran WG, Cox GM, (1959) *Experimental designs*. Bombay: Asia Publishing House
- [13] Ross PJ, (1988) *Taguchi technique for quality engineering*. New York: McGraw Hill
- [14] Phadke MS, (1989) *Quality engineering using robust design*. Englewood CL: Prentice-Hall
- [15] Antony J, (2001) Simultaneous optimization of multiple quality characteristics in manufacturing processes using Taguchi's quality loss function. *International Journal of Advanced Manufacturing Technology* 17:134-138
- [16] Montgomery DC, (1997) *Design and analysis of experiments*. New York: Wiley

Analysis of Non-limiting Current Resistance and Isopulse Power Supply for WEDM

C.J. Li, Y.F. Guo, J.C. Bai, Z.S. Lu

Department of Manufacturing and Automation Engineering, Harbin Institute of Technology, Harbin 150001, China

Abstract. Wire electrical discharge machine (WEDM) is one of the effective and important methods for machining complex parts and hard cutting materials. The power supply plays an important role in WEDM, which influences the machining precision and cutting speed. The energy efficiency of traditional pulse power for WEDM is less than 25%, because of the use of current-limiting resistance. In the paper, a novel Pulsed width modulated (PWM) half bridge power supply has been developed, eliminating the current-limiting resistance, so the energy efficiency is increased and the energy saving effect is remarkable. Nevertheless, this power supply has adopted a discharge control strategy of breakdown waiting, making the single discharge energy being equal and improving the cutting speed.

Keywords: WEDM, Isopulse Power Supply, Non-limiting Current Resistance, Energy Saving

1. Introduction

Wire Electrical Discharge Machining (WEDM) technology is widely used in industries such as mould and aerospace manufacturing. In China, more than 300,000 High Speed -WEDM (HS-WEDM) machine tools are in use. In HS-WEDM, the wire on the frame moves to-and-fro at a high speed with a pulse power supply connected. The anode of the power supply is joined with the work-piece and the cathode is joined with the wire. Sparks are generated when the distance between the wire and the work-piece is tiny. Thus a very high temperature can be achieved in the gap. The metal is melted and washed out by the discharging pressure and working fluid. The main structure of the HS-WEDM can be seen in the Fig.1. It is the principle of the HS-WEDM that sparks between the wire and the work-piece erode material.

The machine has some advantages: excreting crumbs well, cutting speed high, cutting bigger thickness of work-piece, electrode wire can have repeated use, machine tool structure is simple, running cost is low, etc[1]. However, most of these are traditional pulse power supply of HS-WEDM machine tools, and the main circuit of the power contains current-limiting resistance, which

results in low energy efficiency and large pulse power volume.

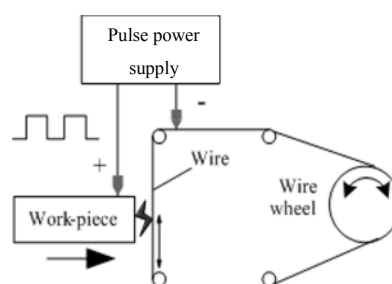


Fig. 1. Sketch of the HS-WEDM

2. Pulse Power Supply of HS-WEDM

In HS-WEDM, the pulse power supply plays an important role to supply the thermal action of electric discharges to achieve material removal. The metal removal rate and the surface finish depend on the magnitude and duration of discharge [2,3].

In most of the HS-WEDM tools, in order to limit the machining current and prevent the occasional short circuit, the main circuit of the commonly used pulse power contains a current-limiting series resistor R behind the power switch VT as shown in the Fig.2 [4]. Evidently, a large amount of heat is generated when the current flows through the resistor resulting in energy losses in the machining process. The energy efficiency can be calculated grossly as follows:

Supposing that the work voltage of the transistor pulse power is 100V and the average voltage between the tool electrode and the work piece is stable at 25V, the remaining 75V drops across the current-limiting resistor and hence the energy efficiency is only 25%.

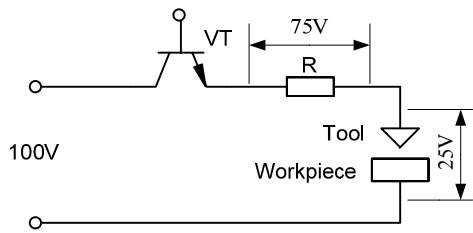


Fig. 2. Schematic Diagram of the traditional pulse power supply

In order to increase the energy efficiency, the new type of resistor-less pulse power proposed in this paper employs the structure of a novel half-bridge network power amplifier and the strategy of PWM. The half-bridge converter main circuit is shown in Fig.3. In the half-bridge converter circuit, two sets of IGBT (TL1, TL2 and TR1, TR2) are used as switches. When the power discharges, two sets of the IGBT are switched on and the power through the power supply, discharge side inductance L , discharge side resistor r_b , discharge wires and discharge gap, TR1 and TR2 to the ground. L consists of the inevitable lead inductance, self-inductance in the discharge gap and any other stray inductances in the discharge path. The resistance of the discharge wires and the spark gap during discharge constitute r_d . D_1 and D_2 are fly-wheel diodes. D_3, D_4, R_3, R_4, C_1 and C_2 constitute two sets of RCD snubbed circuits which are used to protect the switches from voltage surge caused by the sudden turning off [5,6]. Fast recovery diodes DL_1, DL_2 and DR_1, DR_2 are anti-parallel diodes in the switches which are also used to protect the IGBT.

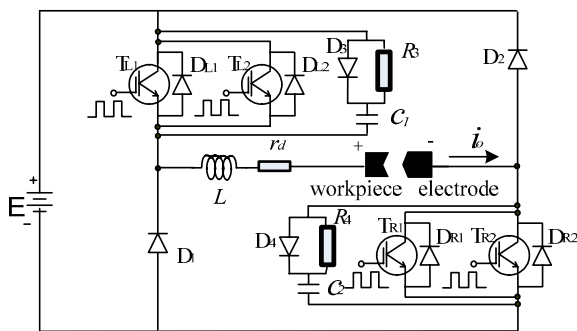


Fig. 3. The schematic diagram of half-bridge converter main circuit

3. Switching Methodology

There is a large rapid increase in the current during rough machining with large pulse width when using resistor-less pulse power. If the current intensity transcends the affordability of the wire electrode, the wire electrode will be burned and excessive current will harm the switch transistor. In this half-bridge network, when the drive

IGBT is off, the fly-wheel diodes are used to smooth out the electrical surges caused by the sudden changes in electrical flow.

For this half-bridge network, the following operational sequences are taken to generate the proper electrical pulse which is safe for switching IGBTs in the gap. The current in the discharge is shown in Fig.4.

1) The left and the right IGBTs are all switched on in time t_0 . The power streams from source through the left IGBT, discharge wire, gap and the right IGBT to ground. The current in the gap rises rapidly to I_1 which is safe for the switches.

2) The left or the right IGBT is switched off in time t_1 . If the left one is off, the energy stored in L streams through the circuit, which consists of D_1 , wire, gap and the right IGBT, to the ground. If the right one is off, the energy streams through another circuit, which consists of the left IGBT, wire, gap and D_2 , and goes back to the source. In that time, the current decreases to I_2 .

3) The step 1 and 2 are repeated several times. The on-time is t_2 and the off-time is still t_1 . The current oscillates between I_1 and I_2 . While the IGBT in the left or right side is switched on and off repeatedly, the IGBT in the other side is always is turned on.

4) The left and the right IGBTs are all switched off. The energy stored in the wire inductance streams through fly-wheel diodes, D_1 and D_2 , and back to source. The current decreases rapidly to zero.

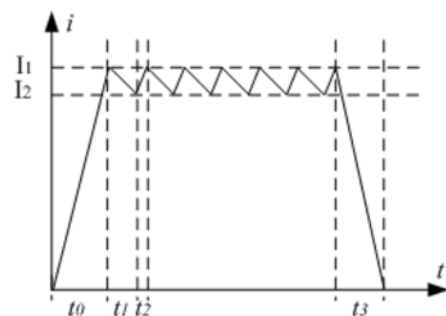


Fig. 4. Theoretical current waveform in the discharge gap

In Figure 6, a trapezoidal current waveform with sawtooth form on the top can be seen. Compared with the normal rectangular current waveform, the current peaks at $(I_1+I_2)/2$. The peak current is dependent on the simultaneous on-time (t_0) of switches in both sides of the bridge in the beginning of the pulse. In this power supply, several IGBTs are combined in parallel connection with collectors and emitters in each side to protect the switches. These IGBTs are switched by turns to decrease the working frequency of every one for reducing the transient thermal impedance of the IGBT.

Fig.5 shows gap voltage and current waveforms of normal discharges. During the on-time the output current is around 25 A and the output maintaining voltage is around 20V.

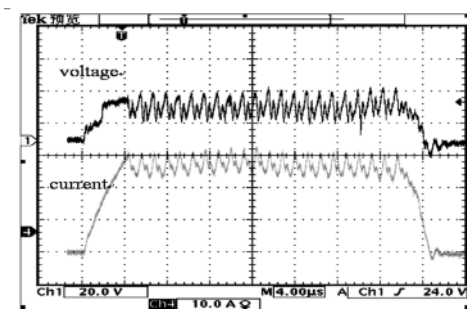


Fig. 5. Voltage and Current Wave of PWM Control

4. Design Principles of Isopulse Machining

Isopulse Principle. In the process of WEDM, single pulse energy depends on gap discharge voltage, gap current and discharge duration. The relationship can be described as followed:

$$W_M = \int_0^{te} u(t)i(t)dt \quad (1)$$

- W_M — single pulse discharge energy (J);
- te — single pulse discharge duration (μ s);
- $u(t)$ — gap discharge voltage (V);
- $i(t)$ — gap discharge current (A).

After the breakdown of the dielectric, the discharge maintaining voltage is invariable with the same machining parameters [6]. Since the gap voltage is fixed, the current peak is constant. So if the single pulse discharge duration is invariable in a discharge period, the single discharge energy W_M is equal too. That realizes isopulse machining.

Discharge Control Strategy: In the WEDM, great changes happen between the discharge gap voltage before discharge breakdown with a value at about 80V and that after discharge breakdown with a value at about 20V [3], Whether the discharge gap breaks down can be distinguished by detecting the discharge gap voltage.

In this paper, isopulse machining is realized by making use of the discharge breakdown signals to control the generation of pulse signals in the pulse control circuit after the voltage appears in the gap. If breakdown signals were not detected, waiting signals would be sent by pulse control circuit so that the pulse signals would maintain their current state unless the discharge breakdown signals were detected. Fig.6 is the schematic of detection Circuit for isopulse processing.

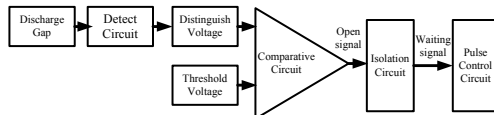


Fig. 6. The schematic of detection Circuit for isopulse processing

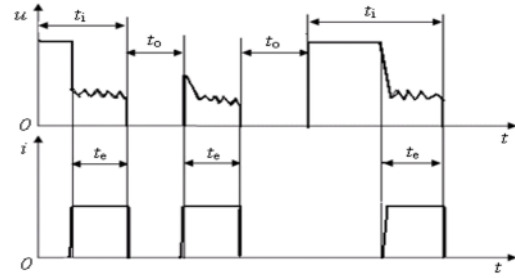


Fig. 7. The waveform of voltage and current for isopulse generator

As shown in Fig. 6, comparisons are drawn between the discharge gap voltage detected through detect circuit and distinguish voltage circuit and the fixed threshold breakdown voltage. If the disposed discharge gap voltage is higher, it is indicated that the gap is open state and hence the voltage is considered to be a no-load signal which will disconnect the isolation circuit to output a delay signal so that the control signal cannot overturn and keep itself in waiting state.

If the detected distinguish voltage is lower than the fixed threshold, it is indicated that the gap has reached breakdown and the waiting signal will not be generated. Signals with normal pulse width and pulse interval are sent out by the pulse control circuit to ensure equivalence between current pulse width and fixed pulse width, and the equal single pulse energy as well.

As shown in Fig. 7, once the breakdown signal is detected, a drive signal te will be sent out by the pulse control circuit control circuit to engender discharge voltage in the gap. The foregoing steps are repeated in the next following discharge cycle. In this way, pulse voltage ti may be not equal, but discharge current pulse te is equal, resulting in the equivalence of discharge energy generated by each pulse. Accordingly, isopulse machining is realized.

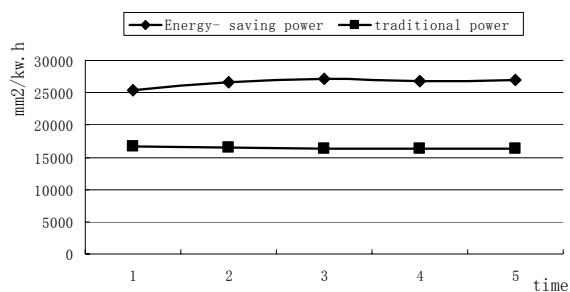
5. Machining Experiment Results and Discussion

Two experiments have been conducted in order to draw a comparison between the energy efficiency of the energy-saving isopulse power supply and that of a traditional pulse power supply (current-limiting resistor). The same type of HS-WEDM machine tools are used in the experiments. The electrode is molybdenum wire ($\Phi 0.18\text{mm}$), and the work-piece is tungsten alloy with a depth of 48mm. With the same machining current, the experimental data is shown in Table 1.

Table 1. Experimental data of energy-saving power and traditional pulse power supply

	Processing area (mm ²)	Power consumption (kw.h)	Time consumption (h)	Area per hour (mm ² /min)	Area per electricity (mm ² /kw.h)
Energy-saving isopulse power supply	28527.92	1.12	7	67.76	25471.4
	53640.04	2.02	13	68.77	26554.5
	77246.48	2.84	18.83	68.36	27199.5
	104503.8	3.91	25.8	67.42	26727.3
	125602.8	4.65	31.2	67.1	27011.4
traditional pulse power supply	52305.2	3.14	14	62.29	16657.7
	59924.6	3.63	16	62.42	16508.2
	71920.92	4.39	19.3	62.0	16382.9
	83608.8	5.11	22.5	61.93	16361.8
	138387.8	8.45	38	60.7	16377.3

Fig.8 shows the experimental data for Comparison of Two Power for Area per Electricity. From the Fig. 8 and Table 1, it can be seen that, despite of unit energy or unit time, the machining area of the resistor-less pulse power is larger than that of traditional current-limiting resistor pulse power. Energy efficiency and cutting speed of energy-saving isopulse power supply are larger than the traditional power supply. The reason for this is that heat generated by the main loop reduces due to the cancellation of the current-limiting resistance, and consequently more energy can be used in spark discharge machining.

**Fig. 8.** Comparison of Two Power for energy efficiency

6. Conclusion

With the structure of a novel half-bridge network power supply and the strategy of pulse width modulation, the energy-saving pulse power proposed in this paper can control the peak values of the current. Furthermore, adopting a discharge control strategy of breakdown waiting, power can satisfy isopulse machining with equal single pulse discharge energy. Moreover, due to the

abandonment of the current-limiting resistance, remarkable energy savings have been achieved. The experimental result shows that the energy efficiency increases and the cutting speed enhances for the energy saving pulse power supply.

Acknowledgment

This work was sponsored by the "863" Program of China (No.2007AA04Z345), NSFC (NO.50875065) & (NO.50875064). The authors would like to thank Jiangsu Dongqing CNC Machine Tool Co., Ltd for giving help to this research.

References

- [1] Hau G. Lee F. C. Soft-switching technique for PWM converter. *IEEE Transactions on Industrial Electronics*. 1995, 42(6): 595-603
- [2] Fuzhu Han, Shinya Wachi, Masanori Kunieda, 2004, Improvement of Machining Characteristics of Micro-EDM using Transistor Type Isopulse Generator and Servo Feed Control, *Precision Engineering* (28)378-385
- [3] Liu Jinchun, Bai Jicheng, Guo Yongfeng, 2008, Non-Traditional Machining, China Machining Press, P10-34.
- [4] Song Boyan, Zhao Wansheng, Shao Geliang, 2001, Current Type of Electrical Discharge Machining Pulse Generator. *China Mechanical Engineering*, 12(4):386-389 (in Chinese)
- [5] Mu Xinhua, Dou Feijin, 2004, Close-Loop Design of Pulse Power Supply for Electrical Discharge Machining, *Transactions of NanJing University of Aeronautics & Astronautics*. vol.21No.3.
- [6] Shang Lei. 2001, Study of New Type Soft-switching Capacitor Charging Techniques. *High Power Laser and Particle Beams*, 13 (2): 241-244

Some Aspects of Surface Integrity Study of Electro Discharge Machined Inconel 718

S. Rajesha^{1*}, A. K. Sharma¹, Pradeep Kumar¹

¹ Mechanical and Industrial Engineering Department, Indian Institute of Technology Roorkee, Roorkee, Uttarakhand-247667, India.

* Corresponding author: rajeshashivanna@gmail.com

Abstract: Inconel 718 superalloy is widely used in many applications requiring higher material strength. Electro Discharge Machining (EDM) is a popular process for machining this superalloy owing to its high thermal resistance and high hardness. In the current work, electro discharge machining was carried out on Inconel 718 using 99.9% pure copper as an electrode with tubular cross section. Thirty two sets of machining trials were conducted as per the design of experiments using the central composite design (CCD) method. The effect of process parameters like pulse current, duty factor, sensitivity, gap control and dielectric flushing pressure on the formation of recast layer, heat affected zone and spattered EDM surface was analysed. Machined samples were characterized for few surface integrity factors through field emission scanning electron microscope (FE-SEM), and surface roughness measurement. The microstructures of the EDM processed Inconel 718 reveal formations of a white layer on the machined surface. It was observed that the process parameters, base material properties and white layer composition have significant influence on crack formation and its propagation. Different modes of crack propagation were identified. Surficial and vertical cracking were predominantly observed in the recast layer; most of the vertical cracks were found to have progressed till the end of the recast layer. The interferential zone acted as a barrier to crack propagation due to the non-homogeneities of metallurgical phases. Crack propagation was observed varying significantly with pulse current and duty factor.

Keywords: EDM, Inconel 718, Recast layer, Microstructure, Surface finish.

1. Introduction

Electro discharge machining is a non conventional machining process, which is extensively used in industry for processing of difficult-to-machine materials and different shapes with reasonable precision. At present, EDM is a widely accepted machining technique used for all types of conductive materials including metals, metallic alloys, graphite, composites and ceramic material. It is based on the principle of removing material from the workpiece by means of repeated electrical discharges created by an electric pulse generator at short intervals between two electrodes (tool and workpiece).

The electric sparking causes the workpiece temperature to rise above melting point leading to material removal in the molten state and evaporation. Molten material between the workpiece and tool gap is flushed using dielectric fluid. Some molten materials experience a resolidification due to critical cooling by the fluid. This layer is a mix of carbon elements of dielectric fluid, melting workpiece and melting electrode. Post machining, this layer forms a recast structure with micro-cracks and craters during resolidification.

The phenomenon of surface modification has been investigated in the EDM process for over five decades. It was first reported by Barash and Kahlon [1965], when mild steel was eroded in liquid medium paraffin using a copper electrode. After the process, it was noticed that the workpiece was coated with a very hard layer which was difficult to remove. This was attributed to the carburization of the layer due to the hydrocarbon medium and its subsequent quenching. High surface hardness, excellent thermal stability and better wear resistance of the white layer and its phase transformation have also been reported by Venkatesh and Parasnis [1972]. The EDM machined surface was characterized by Lee et al. [1988 and 1992]. The authors had investigated the depth of the recast layer and quantified it with respect to the process parameters and surface roughness. It was reported that with constant dielectric fluid flushing the condition, the thickness of recast layer shows a relationship with the pulse energy irrespective of the tool material (steel). Marafona and Wykes [2000] found that while machining with low current intensity and length pulse duration, a layer of carbon was deposited on the tool leading to reversal in tool wear. Further, to improve the material removal rate (MRR) with nominal increase in tool wear rate (TWR), a high current intensity can be used. Analysis also showed that the layer contained carbon content and steel elements such as iron and chromium. It was likely that the carbon came from the dielectric medium.

Klocke et al. [2004] investigated the influence of powder suspended dielectrics on the recast layer of Inconel 718 EDMed surface. They reported that physical properties of the powder additives play an important role in changing the recast layer composition and morphology. Bhattacharyya et al. [2007] investigated some surface integrity aspects of an EDMed surface and reported that peak current and pulse-on duration significantly influence various criteria of surface integrity such as surface roughness. Che-ChungWanga [2009] investigated the formation of recast layer using L18 orthogonal arrays and reported that larger pulse duration and positive polarity of the workpiece could create a thicker recast layer than negative polarity, while machining Inconel 718. Tsai et al. [2003] observed that recast layers are difficult to remove due to high cohesion and hardness compared to the base material and induce poor surface quality. Such recast structures greatly affect fatigue strength and shortens service life [Abu Zeid, 1997]. Thus, relevant literatures indicate there is ample scope for studying the effect of various process parameters on surface integrity of Inconel 718 electro discharge machined surface.

In the present work, Inconel 718 was the workpiece material and 99.9% pure copper as electrode for experiments using an NC-EDM machine. Thirty two sets of machining trials were conducted as per the Response Surface Method (RSM) with central composite design. The effect of process parameters like pulse current, duty factor, sensitivity, gap control and dielectric flushing pressure on formation of recast layer and spattered EDM surface were analysed. Machined samples were characterized for some surface integrity factors through field emission scanning electron microscope (FE-SEM) and 3D surface profilometer.

2. Experimental Procedure

The experiments were conducted using a ZNC-EDM machine (Sparkonix Ltd., India). Inconel 718 material of dimensions, 21 mm diameter and 20 mm length was used as workpiece for the experimental trails. Inconel 718 has an average hardness value of 414 Hv. A cylindrical tube of 12 mm external and 9 mm internal diameter made of 99.9% pure electrolytic copper was used as the electrode. Commercially available kerosene (electrical cond.: $1.6 \times 10^{-14} \text{Sm}^{-1}$, and dynamic Viscosity: 0.92mPas) was used as the dielectric fluid. The experimental set-up is shown in the Fig. 1.

The workpiece was cut by wire EDM (make: Electronica, EL10-VGA, India) prior to trails. A special fixture was designed to hold the cylindrical work pieces to eliminate any possibility of misalignment. The work pieces were connected to positive polarity while the electrode was maintained at negative polarity. A side flushing method was employed for dielectric fluid to flush through nozzle. During the experiments, the hole depth of 20 mm and

diameter of 12 mm was machined throughout. The process parameters and depth of cut was programmed in the NC controlled unit. The servo moves up 5 mm above the initial position after completion of machining.



Fig. 1. Pictorial view of the experimental set-up

Table 1 Levels of process parameters used in the experiments.

S. No.	Process Parameters	Sym bol.	Level				
			-1.57	-1	0	+1	1.57
1.	Pulse Current (A)	A	6	9	12	15	18
2.	Duty Factor	B	0.67	0.72	0.77	0.82	0.87
3.	Sensitivity Control	C	3	4	5	6	7
4.	Gap control	D	0	1	2	3	4
5.	Flushing Pressure (Kg/cm ²)	E	0	0.25	0.5	0.75	1

The process parameters and their levels were decided based on trail experiments and are shown in the Table 1. The experiments were performed according to the plans arrived at using design expert version 6.1 (DE V6.1). The experiment matrix of RSM with coded levels is shown in the Table 2. Fig. 2 shows a photograph of the copper electrode used and the workpiece before and after machining.

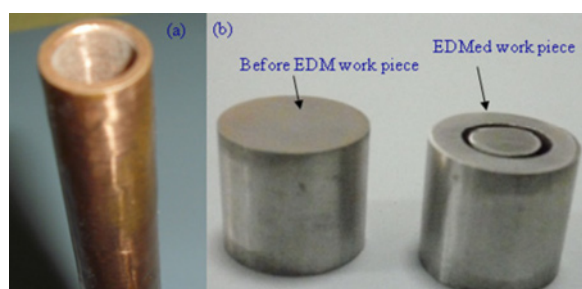


Fig. 2. (a) Cu electrode, (b) Inconel 718 work piece

Table 2 Experimental matrix of the CCD (RSM)

Experiment no.	Process Parameters (coded levels)				
	A	B	C	D	E
1	-1	-1	-1	-1	1
2	1	-1	-1	-1	-1
3	-1	1	-1	-1	-1
4	1	1	-1	-1	1
5	-1	-1	1	-1	-1
6	1	-1	1	-1	1
7	-1	1	1	-1	1
8	1	1	1	-1	-1
9	-1	-1	-1	1	-1
10	1	-1	-1	1	1
11	-1	1	-1	1	1
12	1	1	-1	1	-1
13	-1	-1	1	1	1
14	1	-1	1	1	-1
15	-1	1	1	1	-1
16	1	1	1	1	1
17	-1.57	0	0	0	0
18	1.57	0	0	0	0
19	0	-1.57	0	0	0
20	0	1.57	0	0	0
21	0	0	-1.57	0	0
22	0	0	1.57	0	0
23	0	0	0	-1.57	0
24	0	0	0	1.57	0
25	0	0	0	0	-1.57
26	0	0	0	0	1.57
27	0	0	0	0	0
28	0	0	0	0	0
29	0	0	0	0	0
30	0	0	0	0	0
31	0	0	0	0	0
32	0	0	0	0	0

3. Results and Discussion

32 sets of experiments were performed during the investigation. Machined surfaces were cut perpendicular to the tool (machining) direction and polished well by a rotary polishing machine using 600, 800 and 1200 mesh size silicon carbide abrasive sheets. Further polishing was carried out with velvet and diamond paste at 100 rpm for about 15 min and cleaned with acetone. Both sectional and surface of the EDM machined Inconel 718 workpieces were examined for surface integrity factors through a field emission scanning electron microscope.

3.1 Recast Layer Formation

The effect of the process parameters on the recast layer thickness of EDM processed Inconel 718 workpiece using the copper electrode was examined. The results are illustrated in Figs. 3–5. The SEMs of the cross section of the EDMed surfaces are presented in the Figs. 3(a)–5(a), while the Figs. 3(b)–5(b) show the EDMed surfaces. It

was observed from the microstructure of the machined surfaces that the thickness of the recast layer increases as the pulse current increases. As the current increases, intensity of the spark also increases leading to an increase in size of craters, consequently the quantity of the molten material produced per unit time increases. Meanwhile, the dielectric flushing may not be capable of instantly removing all the molten material produced due to the high pulse current. During the subsequent rapid cooling, molten material re-solidifies to form thick recast layer with deep craters. The thickness of this recast layer formation will depend upon the volume of molten material produced during the machining due to high pulse current and the flushing pressure of dielectric fluid. This is supported by observations made from SEM micrographs (Figs. 3(a), 4(a) and 5(a)).

It is observed from Figs. 5(a) that recast layer thickness increases with increases in the duty factor. When the duty factor increases, the pulse on duration also increases in comparison with pulse off duration. Larger pulse on duration allows the electro discharge energy to penetrate deeper into the material causing increase in the volume of the molten material. The increased volume of molten material does not get removed by the dielectric fluid flushing duration. This eventually results in thicker recast layer. However, from the Fig. 3(a) it is observed that although there is an increase in duty factor, the recast layer thickness is not large. This may be due to an optimum combination of the other process parameters like sensitivity control, gap control and high flushing pressure. Here, the molten material and EDMed debris are effectively flushed away from the machining zone due to the high flushing pressure which, in turn, helps in minimizing the thickness of the recast layer.

3.2 Surface Crack

The surface crack density varies with changes in pulse current for different pulse-on durations due to rapid quenching of the molten material and shrinkage stresses after each electro discharge. It is observed from the Figs. 3(b), 5(b) and 6 that surface crack density increases with pulse current for a constant duty factors. Overall, it was observed that the surface crack increases with increasing pulse current. Fig. 6 shows that at low pulse current, white layer formation is more uniform with reduced micro cracks. More intensive cracking was noticed around craters and locations where there is a presence of peak [Fig. 5(b), and 7]. Fig. 7 also exhibits an increase in the surface crack intensity due to an increase in duty factor and induced stress. From the analysis of the SEM micrographs, it was observed that cracks were consistently progressing perpendicular to the machining direction and barely penetrating beyond the recast layer. However, Fig. 5 shows severe cracking in the parent material parallel to machined direction too, due to high pulse current and other parametric combinations owing to a step rise in the temperature of the workpiece above the

critical point. This causes an increase in energy inside the material and sudden quenching leads to higher thermal stresses in parent the material leading to the observed severe crack formation.

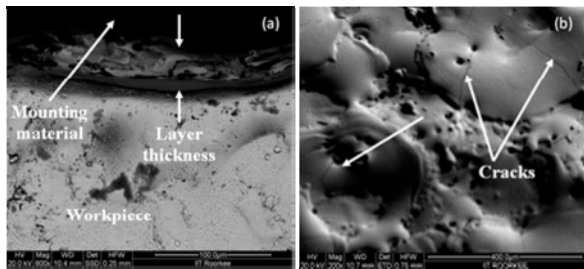


Fig. 3. SEM micrograph of Exp. Run No.27

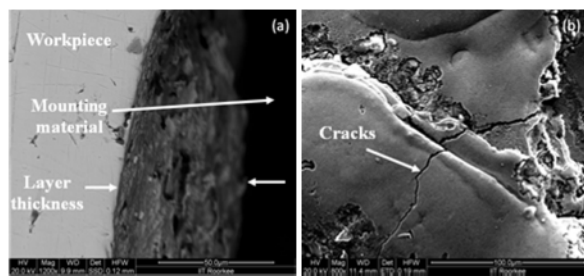


Fig. 4. SEM micrograph of Exp. Run No.2

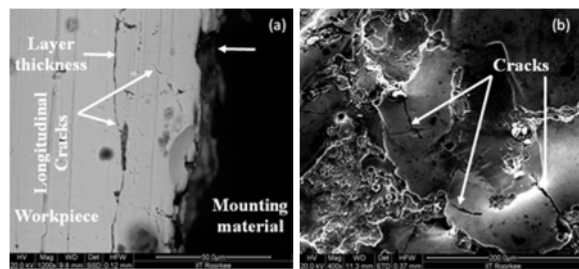


Fig. 5. SEM micrograph of Exp. Run No. 18



Fig. 6. SEM micrograph of Exp. Run 17

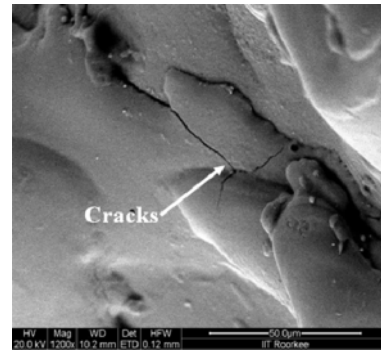


Fig. 7. SEM micrograph of Exp. Run No. 7

3.3 Chemical Composition of the Recast Layer

The principle of electro discharge machining involves developing sparks between the electrode and the workpiece. During electric sparking, the workpiece and tool temperature rises above the melting point leading to material removed in its molten state and evaporation. Molten material between the workpiece and the tool is flushed away using the kerosene dielectric fluid. The dielectric fluid is exposed to high temperature and reacts with oxygen to form carbon and carbon monoxide. Some of the carbon particles mix with the molten material and form a recast layer, allowing further quenching beside that with the tool material and some molten materials experience evaporation along with carbon monoxide. Meanwhile the carbon and alloys of the parent material start solidifying on the surface of the tool electrode. This layer minimises the wear rate of the tool to some extent leading to reduction in material removal rate. Table 3 shows the difference between the chemical composition of the recast layers and the parent material. The presence of copper in the recast layer indicates the tool erosion during the machining. Hardness of the recast layer increases significantly due to higher carbon percentage in the layer. Table3 and SEM micrograph of machined surface indicate presence of carbon in the EDMed surface of the workpiece.

Table 3 Chemical composition of EDM processed Inconel 718 workpiece surface (recast layer).

Elements	Before the EDM Process (workpiece)	After the EDM process (recast layer)
	Av. Weight %	Av. Weight %
Ni	51.05	33.72
Fe	19.95	13.35
Cr	18.83	12.76
Nb	5.52	5.22
Mn	0.03	0.00
C	0.04	13.65
Co	0.04	0.00
Al	0.26	0.22
Si	0.04	0.28
Ti	1.08	0.93
Mo	3.1	4.50
Cu	0	5.67
O	0	2.24
Other	0.06	7.47
	100.00	100.00

3.4 Surface Roughness

The effects of the various process parameters on the surface roughness were evaluated using the optical profile meter (Make: Veeco V2, India). The surface roughness (R_a) value varies with pulse current and duty factor. Average surface roughness while machining with higher pulse current is observed to be less as shown in Fig. 8 while compared with that of Fig. 9. The influence of the duty factor on roughness is, on the other hand, observed to be in the similar trend as that of crack formation. Higher duty factor is attributed to transmission of high pulse energy, which accelerates severe cracking on the recast layer resulting in poorer surface finish. Thus, it indicates that an increase in duty factor greatly affects the surface quality. Figs. 10 and 11 illustrate that an increase in pulse current also increases the R_a value. The higher input power associated with increase in pulse current causes more distortion on the machined surface due to more frequent molten material expulsion. This leads to an increase in R_a value.

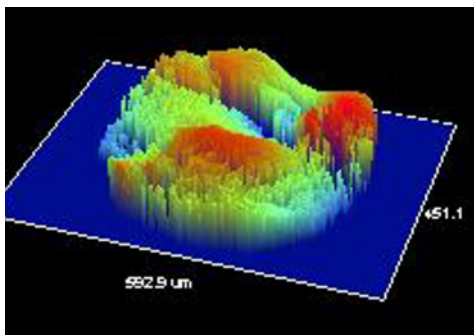


Fig. 8. 3D Profile of surface roughness [Exp. Run No.2; R_a 5.36 μ m]

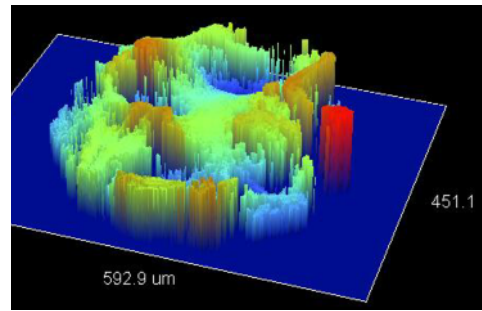


Fig. 9. 3D Profile of surface roughness [Exp. Run No.7; R_a 6.41 μ m]

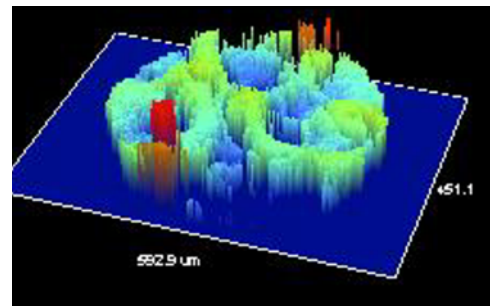


Fig. 10. 3D Profile of surface roughness [Exp. Run No.17; R_a 2.36 μ m]

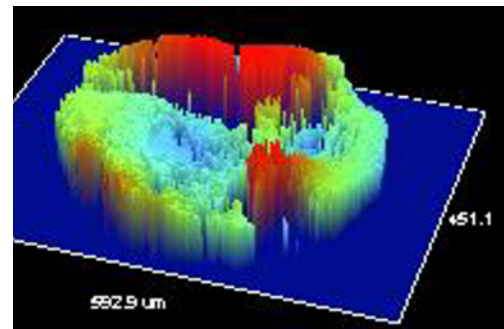


Fig. 11. 3D Profile of surface roughness [Exp. Run No. 18; R_a 9.96 μ m]

4. Conclusions

Experiments were carried out on Inconel 718 material in a ZNC-EDM. From the preliminary results, the following conclusions are drawn:

- Thickness of the recast layer increases with increase in the duty factor and pulse current.
- Crack formation is due to induced stress during sudden quenching of molten material with dielectric fluid.
- Micro cracks are formed even at low pulse current.
- Major crack propagation is perpendicular to the direction of tool electrode.
- Intensive cracking is centered around craters and peaks.

- Complex carbides are formed along with eroded tool material and get deposited in the recast layer.
- Surface roughness is highly influenced by duty factor followed by pulse current.

Acknowledgment

The authors would like to thank Department of Science and Technology, New Delhi, Government of India, for their financial support towards this research project. (Project number: SR/S3/MERC-106/2007).

References

- [1] Abu Zeid, O.A., (1997), On the effect of electrodischarge machined parameters on the fatigue life of AISI D6 tool steel, *Journal of Material Process. Technol*, 68: 27–32.
- [2] Barash, M.M., Kahlon, C.S., (1965), Experiments with electric spark toughening, *International Journal of Machine Tool Design & Research*, 4: 1–8.
- [3] Bhattacharyya. B., Gangopadhyay S., Sarkar B.R., (2007) Modelling and analysis of EDM_{ED} job surface integrity, *Journal of Materials Processing Technology*, 189:169–177.
- [4] Che Chung Wanga, Han Ming Chowb, Lih Dai Yangb, Chun-Te Luc, (2009), Recast layer removal after electrical discharge machining via Taguchi analysis: A feasibility study, *Journal of Materials Processing Technology*, 209:4134–4140.
- [5] Klocke F., Lung D., Antonoglou G., Thomaidis D., (2004), The effects of powder suspended dielectrics on the thermal influenced zone by electrodischarge machining with small discharge energies, *Journal of Materials Processing Technology*, 149 :191–197.
- [6] Lee L.C., Lim L.C, Narayanan V, Venkatesh V.C., (1988), Quantification of surface damage of tool steels after EDM. *International Journal of Machine Tools and Manufacture* 284:359–372.
- [7] Lee L.C., Lim L.C, Wong Y.S., (1992), Crack susceptibility of electro-discharge machined surfaces. *Journal of Materials Processing Technology*, 29: 213–221.
- [8] Marafona, J., Wykes, C., (2000), A new method of optimizing material removal rate using EDM with copper tungsten electrodes, *International Journal of Machine Tools & Manufacture*, 40 (2):153–164.
- [9] Tsai, H.C., Yan, B.H., Huang, F.Y., (2003), EDM Performance of Cr/Cu-based composite electrodes. *International Journal of Machine Tools & Manufacture*, 43 (3):245–252.
- [10] Venkatesh, V.C., Parasnis, S., (1972), Surface transformation in high speed steel after electro discharge machining, *Proceedings of the 5th AIMTDR Conference, IIT, Roorkee, India*, 639–649.

Advances in Direct Metal Deposition

J. Mazumder^{1,2}, and L. Song¹

¹ University of Michigan, 2350 Hayward, 2040 GGB, Ann Arbor, MI , USA 48109-2125

² POM Group Inc., Auburn Hills Michigan, USA 48326-2461

Abstract. Quest for a material to suit the service performance is almost as old as the human civilization. An enabling technology which can build, repair or reconfigure components layer by layer or even pixel by pixel with appropriate materials to match the performance will enhance the productivity and thus reduce energy consumption. With the globalization, “Economic Space” for an organization is now spread all across the globe. Closed loop Direct Metal Deposition (DMD) has the potential to embrace both the challenges and change the manufacturing as we know it. Rapid Fabrication of three-dimensional shapes of engineering materials such as H13 tool steel and Nickel super alloys are now possible using Direct Materials Deposition (DMD) technique as well similar techniques such as Light Engineered Net Shaping (LENS) or directed light fabrication (DLF). However, DMD is has closed loop capability, which enables better dimension and thermal cycle control. This enables one to deposit different material at different pixels with a given height directly from a CAD drawing. The feed back loop also controls the thermal cycle. *New Sensors are either developed or being developed to control geometry, cooling rate, microstructure, temperature and composition.* Flexibility of the process is enormous and essentially it is an enabling technology to materialize many a design. Several cases will be discussed to demonstrate the additional capabilities possible with the new sensors. Conceptually, one can control the machine installed in Rochester (USA) to remotely manufacture a product from Manchester(U.K) through internet or satellite connection. This enable one to design in one country and manufacture near the customer. Such systems will be a natural choice for a Global “Economic Space”.

Keywords: Laser processing, additive manufacturing, Direct Metal Deposition (DMD), process control, process monitoring, remote manufacturing

1. Introduction

The well-known adage that the “Early Bird gets the Worm” is true for any industry, in this era of “Information Technology.” The cycle of consumer taste for a product is shortening, and therefore, the need for the industry to go to the market with shorter lead time is becoming more of a necessity than a desire. Concurrently desire for improved performance at cheaper cost puts conflicting demands on design engineers. For example, more people want cheaper and safer air travel that

requires lighter planes with lower fuel consumption plus higher load-carrying capacity. It is not smart to just scale up a present design to increase capacities. Thinking out of the box is a must to engineer materials with properties to match the performance desired by modern consumers. Synthesis of Topological design, Heterogeneous CAD and Direct Metal Deposition (DMD) offer opportunities to engineer material properties to match desired performance [1].

What is Direct Metal Deposition (DMD)?

It is a Solid Freeform Fabrication (SFF) technique that enables production of realistic components with 0.01 inch accuracy, and properties similar to wrought materials with close to 100% density. Direct Metal Deposition, or DMD, is a layer based additive manufacturing process that uses a high powered laser to melt powdered metals and make deposits, with the objective of making fully dense three dimensional objects. The laser beam is focused just above a metal substrate surface, where the deposition is to occur. A coaxial powder stream is focused into the melt pool formed at the substrate surface. This powder is melted upon entry into the melt pool. The substrate is attached to a CNC multi-axis system, and by moving it around, a two dimensional layer can be deposited. By building successive layers on top of one another, a three-dimensional object is formed. Any designed structure can be fabricated layer by layer from a digital database.

Closed Loop DMD is a synthesis of multiple technologies including lasers, sensors, a Computer Numerical Controlled (CNC) work handling stage, CAD/CAM software and cladding metallurgy. Direct Metal Deposition, developed in the Center for Laser Aided Intelligent Manufacturing (CLAIM) at the University of Michigan [1, 2], is a laser-cladding-based process that makes fully-dense freeform metallic parts layer by layer (Fig.1). *The key characteristic of the DMD process, which distinguishes it from other similar laser-cladding-based SFF processes, is the integrated feedback system.* Closed loop control of the DMD process is

useful not only to achieve near net shape but it also provided additional control over temperature history and thus microstructure. In recent years, joint research effort between University of Michigan and POM Group Inc., have led to significant advances in the monitoring and control of DMD process. This paper describes some of the advances in system control development. They are described in the next section.

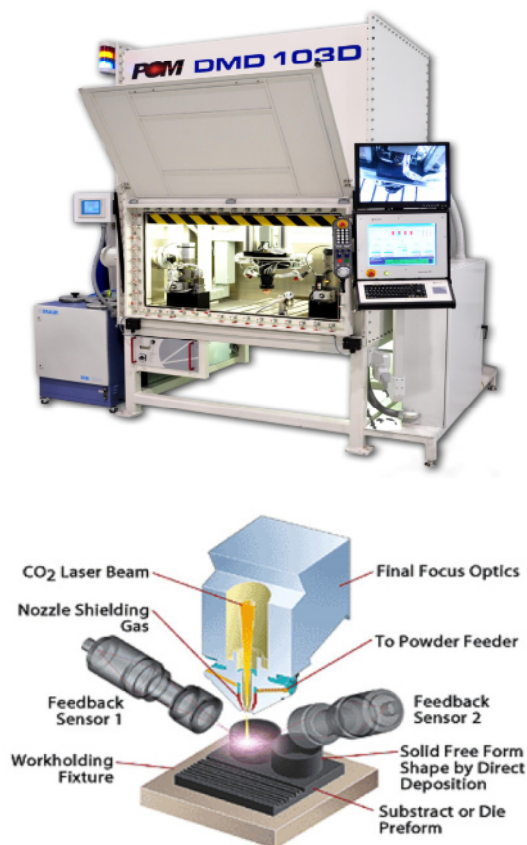


Fig. 1. DMD process with active height controller

2. System control

Recent advances have developed monitoring and control capabilities of: i) Geometry, ii) Temperature, iii) Composition, and iv) microstructure. Microstructure capability was not available to scientific and engineering community until this invention disclosed at the University of Michigan[3].

2.1 Geometry control

The basic function of the height controller is to limit the maximum height of metal deposition. The cladding height is monitored using three lens that are located at 120° spacing in x-y plane and 45° corresponding to the

laser beam [1]. The three collecting lens are fiber-pigtailed to three high speed CCD cameras, where the cladding images are obtained. The image processing unit includes setting a detection threshold of the brightness of the pixels and calculating the centroids of the cladding height from the images obtained from each camera. The building height at each layer is a preset value. The three calculated cladding heights are compared to the reference height. The robustness of the height detection is fulfilled by the logic that overbuilt is determined by the results of the two cameras out of three. A thin wall figure-8 deposition using this controller is shown in Figure 2 with a dramatically improved dimensional accuracy compared with the one without controller.

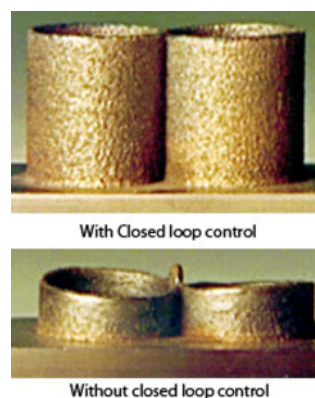


Fig. 2. Example of fabrication with closed loop control and without closed loop control

2.2 Temperature and cooling rate control

A dual color pyrometer with selected wavelength away from the laser radiation has been used to monitor the melt pool temperature. The measured temperature can be used to feed back to a real time controller to track the melt pool temperature to a preset value. During the DMD process, the controller calculates the optimized control value and sends a control signal to adjust the laser power each time step it obtains an updated melt pool temperature. Figure 3(a) shows the controlled temperatures and the laser actions using a generalized predictive control algorithm that was implemented in a real time controller during laser cladding H13 tool steel process. The melt pool temperature was successfully tracked to the preset temperature profile. This controller has been used to control the heat input during laser cladding on an uneven surfaced substrate. The controller has been able to compensate the cladding on the lower side as shown in Figure 3 (b). By monitoring the temperature as a function of time, we can calculate the cooling rate. Microstructure evolution is dependent on cooling rate. In-situ monitoring of cooling rate will enable us to control the microstructure and thus properties

by using cooling rate as the input to a closed loop controller to modify laser power and speed.

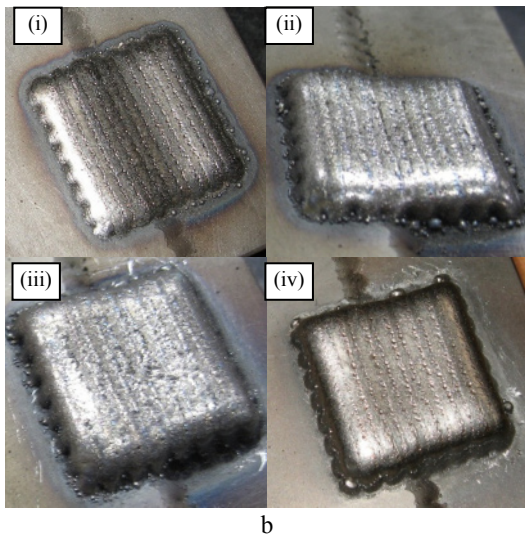
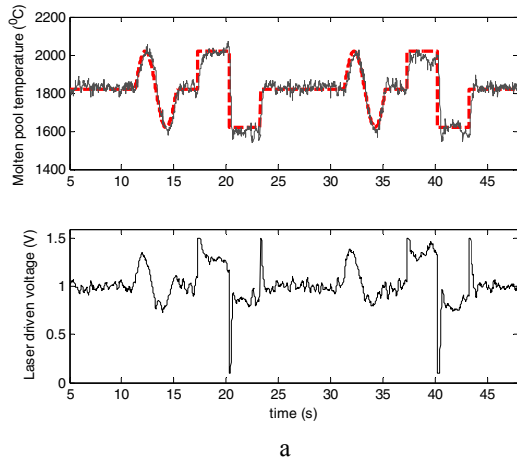


Fig. 3. a) Experimental results of tracking the melt pool temperature to sinusoidal and squared shaped temperature profile. Red curve, preset temperature profile; black curve, experimental results; b) pictures of the deposition at (i) 10th layer, (ii) 20th layer, (iii) 30th layer and (iv) 40th layer

2.3 Composition Sensor

During direct metal deposition (DMD), plasma plume is generally a by-product due to the laser induced plasma. Therefore, real time spectroscopic analysis can be used for composition prediction by optical emission spectroscopy of the generated plasma, and further a full spatial compositional evaluation of the manufactured products can be obtained. Figure 4(a) shows the emission lines of pure chromium powder, pure iron powder and mixed nickel and iron powder with 50/50 weight ratio during a CO₂ laser aided direct metal deposition process.

Figure 4(b) shows the relationship between the measured Cr/Fe spectral line intensity ratios and the Cr/Fe composition weight ratios. A second order polynomial fitting was used to form the calibration curves. By measuring the plasma line intensity ratios and compare them the calibration curve, the composition ratio of different element can be obtained

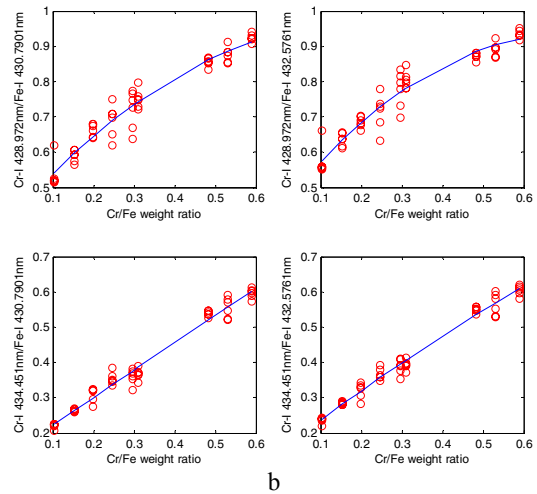
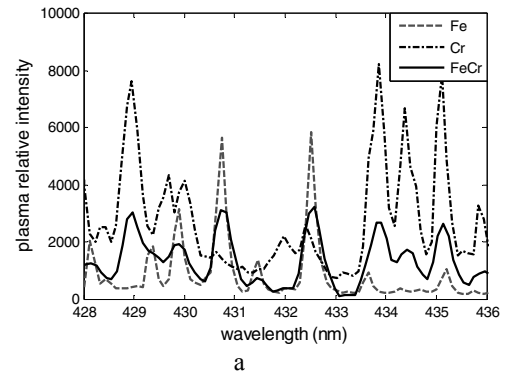


Fig. 4. a) Emission lines of chromium powder, pure iron powder and mixed chromium and iron powder with a 50/50 weight ratio from direct metal deposition process; b) Plasma Cr/Fe line intensity ratio versus Cr/Fe weight ratio. Red circles: measured data; blue lines: second order polynomial fitting

2.4 Microstructure Sensor [3]

During DMD process, powders of different elements melted into the molten pool and solidify onto the substrate. Different elemental combinations will experience different phase changes and form into different microstructures, depending on the composition, cooling rate and heat treatment. We discovered that there exist a strong correlation between the physical parameters of a plasma plume and the final microstructures. Therefore, we believe that the spectral line acquired from the plasma immediate prior to solidification can be a valid indicator for the crystal structure. Electron

population of different energy state or the transition probability of the emission lines, affects the plasma parameters. This relationship can be used to predict the microstructure from the plasma characterization. For example, Figure 5 showed the correlation between Ti/Fe line ratios and the microstructure of the Ti-Fe alloys with different weight ratios. We can see that the line intensity has an odd point when eutectic microstructure was obtained.

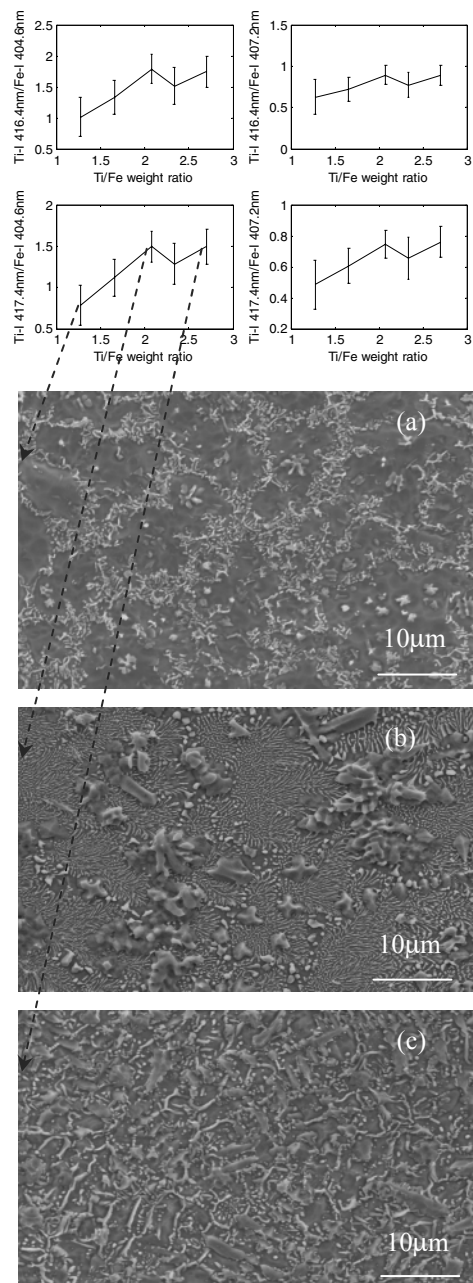


Fig. 5. Relationship between the four Fe-I/Ti-II line ratios and Ti weight percentage and the corresponding microstructure

3. Conclusion

The recent advances in DMD system control offer the capability to monitor or control geometry, temperature, composition and Microstructure from the collected light at the laser material interaction zone. Never in the history of any manufacturing was in-situ monitoring of phase transformation possible. All these monitoring sensors will enable one to produce products with desired properties directly from the solid CAD data. By integration of homogenization method, DMD with closed loop control can also produce meta-materials such as metallic structure with negative co-efficient of thermal expansion [1]. POM recently built a DMD machine capable of remote manufacturing [4]. This capability enable one to design in one country and manufacture near the consumer in another country. Such systems will be a natural choice for a Global "Economic Space". For research community, it will open frontiers for creating designed materials[1]with desired performance Characteristics.

Acknowledgements

Authors would like to thank continued support from Office of Naval Research and Advanced Technology Program from Dept. of Commerce for making this research possible.

References

- [1] Mazumder J., Dutta D., Kikuchi N. and Ghosh A., "Closed loop direct metal deposition: art to part," *Optics and Lasers in Engineering*, 34 (2000) 397-414
- [2] Mazumder J., Choi J, Nagarathnam K, Koch J and Hetzner D. "Direct Metal Deposition (DMD) of H13 tool steel for 3-D components: microstructure and mechanical properties." *J. Metals* 1997, 49(5), 55-60
- [3] Song L., Wang C. and Mazumder J., "Sensor for In-Situ Identification of Phase Transformation during the Direct Metal Deposition and Other Material Synthesis Processes" Invention disclosure #4561, University of Michigan
- [4] U.S. Patent #6,580,959 "System and method for remote direct material deposition process" Inventor: J. Mazumder, June 17, 2003

Effect of processing parameters in manufacturing of 3D parts through laser direct metal deposition

M. J. Tobar J. M. Amado, J. Lamas, A. Yáñez
Universidade da Coruña, D. de Ingeniería Industrial II, Ferrol, E-15403, Spain.

Abstract. Laser cladding is a flexible technique which allows to deposit a wide variety of alloy protective coatings on metal substrates. By means of multilayer processing 3D objects can be created, a technique which is commonly known as 3D cladding or laser direct metal deposition (LDMD). This fabrication approach is a promising technique in the field of design and manufacturing technology, as it permits the direct one-step creation of parts with the desired shape and engineered composition for a particular application. In this work a study is presented on the fabrication of thin metal parts of Inconel 718 by means of laser direct metal deposition. It is shown that the deposition efficiency and the geometrical uniformity of the fabricated element are basically determined by the suitable combination of input laser specific energy (J/mm^2) and the laser step height set on consecutive laser scans. In order to guarantee the industrial reliability of the technique, on-line processing control and monitoring procedures are of major importance. A closed loop control method based on a photodiode IR sensing device has been tested which resulted in a substantial improvement of the finishing quality of the fabricated samples.

Keywords: Laser Rapid Manufacturing, Laser cladding.

1. Introduction

Rapid prototyping/manufacturing with lasers comprehend a wide variety of techniques which allow to directly fabricate solid elements from 3D CAD models in a layer-by-layer manner. Among them stand the selective laser sintering (SLS), and 3D cladding, also referred to as laser direct metal deposition (LDMD)[1][2][3]. The latter is basically an extension of laser cladding whereby 3D shapes are built by overlapping multiple layers according to the predetermined solid model. Compared to SLS, it offers a higher flexibility in application, as it can be employed not only to fabricate new parts or prototypes, but also to repair worn components or built small details in existing components. Moreover, by using 3D cladding, high density parts, close to the theoretical one, are built.

In this work a study on laser direct metal deposition of a Ni-based superalloy, Inconel™ 718[4], is presented. This alloy is of wide use in aeronautic applications in virtue of its good strength, high resistance to oxidation

and corrosion at high temperatures and good weldability. It owes its properties to a modified composition with Niobium content, which promotes a fine dispersion of γ' precipitates (besides the common superalloy γ' precipitates) in the face centered cubic Ni matrix γ . Laser fabrication with Inconel 718 has already been studied in SLS techniques and direct metal deposition of thick parts[5]. Other procedures, as 3D cladding with graded compositions of Inconel 718 and Ti-based alloys[6] or laser annealing of Inconel 718 components to improve its microstructure[7], have also been investigated. The present study is devoted to the fabrication of thin metal parts by means of 3D cladding. The work focuses on the influence of processing parameters on the geometry, deposition efficiency and microstructure of the fabricated element. Finally, the impact of online control methods during laser processing will be presented.

2. Experimental procedure

The experimental setup consisted of a high power 2.2 kW Nd-YAG laser system (ROFIN DY022) equipped with a laser head for coaxial powder feeding (PRECITEC YC50). The laser beam is driven onto the workpiece by means of a 5-axis robotic ABB arm. The laser power, scanning speed, spatial positions and trajectories of each particular process are programmed in a custom PC application and further converted into operating commands to the robotic machine system. The laser head design comprises a modular arrangement for installing sensing devices for coaxial inspection of the interaction area. A germanium photodiode, mainly sensitive to wavelengths ranging from 1400 to 1600 nm, was included in this arrangement. This allowed for online monitoring of the IR signal emitted by the interaction area on a ~ 4 mm diameter spot. The signal read within this spot was tested to be mainly proportional to the melt pool size. A PC application synchronizes this monitoring

element with the process development and displays the detected IR signals. Control routines based on PID algorithms were also developed to optionally control and supervise the laser process.

A series of tests on fabrication of thin (~ 1 mm width) walls of Inconel 718 were done. Fabrication was performed on austenitic stainless steel AISI 304 as substrate using a powder alloy of particle size ranging from 45 to 90 μm . Wall samples were made by superimposing single laser scans along 20 mm length. Eleven successive scans were performed, amounting to ~ 5 mm wall height. The coaxial feeding system delivers a powder jet stream with a focus sitting at 12 mm beneath powder nozzle. In order to obtain the desired wall thickness, the laser beam was vertically adjusted so as to set a beam spot diameter $d = 1$ mm at this distance. The powder mass flow rate (g/s) was varied for each process scan speed so as to deliver 25 mg/mm at the fabrication point. Nitrogen was used as shielding and powder carrier gas. After fabrication all samples were transversally cut, polished and electrolytic etched for optical inspection and metallographic examination

3. Results and discussion

Table 1 lists the processing parameters used for each of the fabricated samples, namely the laser power P , the scanning speed v and the step height increase value set between consecutive cladding scans in the laser head position. Their external aspect is the one shown in Fig. 6(a), where an undulated surface finish due to successive laser scans can be noticed. Examples of optical micrographs of the cross sectional cut of the wall pieces are shown in Fig. 1 and Fig. 2, which also reveal the pattern of layer-by-layer deposition. None of the produced samples presented relevant defects as cracks, pores or lack of bonding with the substrate. It is concluded that Inconel 718 allows for 3D laser fabrication within a sufficiently wide process window.

The wall width, height and transverse area were measured on the corresponding cross-sectional images. These values are to be taken within ~ 0.1 mm error as they depend on the particular point along the wall where the transversal cut was made. The measured area yielded the efficiency for powder catchment, that is, the fraction of delivered powder which is effectively fused into the fabricated sample. Also, relating the area of the last (upper) cladding section to the area between layer patterns, the fraction of the previously deposited material which is remelted on laser scanning could be estimated. This remelting factor is listed in Table 1. Finally, the results will also be discussed in terms of the specific laser energy $P/(d \cdot v)$ applied during the cladding process.

Table 1. Data summary of experimental tests.

Sample Nr.	Scan Speed (mm/s)	Laser Power (W)	Specific energy (J/mm^2)	Step height (mm)	Wall width (mm)	Wall height (mm)	Powder efficiency (%)	Remelting factor (%)
1	5	250	50	0.3	1.1	4.5	17	44
2	5	300	60	0.3	1.3	4.5	18	46
3	5	350	70	0.3	1.2	4.1	18	50
4	5	250	50	0.4	1.1	4.7	18	30
5	5	300	60	0.4	1.4	4.6	20	45
6	5	350	70	0.4	1.4	4.7	22	45
7	5	250	50	0.5	1.1	5.3	21	24
8	5	300	60	0.5	1.3	4.9	23	30
9	5	350	70	0.5	1.4	5.1	25	36
10	5	250	50	0.6	1.1	4.7	19	24
11	5	300	60	0.6	1.4	4.9	24	41
12	5	350	70	0.6	1.5	5.2	27	44
13	8	250	30	0.3	1.0	3.9	13	33
14	10	300	30	0.3	1.0	3.7	12	33
15	15	450	30	0.3	0.9	3.4	10	49

3.1 Dimensional aspects

Though most of the fabricated samples comply with the pretended 1 mm width and 5 mm height wall dimensions, variations were obtained depending on the process parameters. Values listed in Table 1 suggest that once the feeding rate is established, the overall height and width result from a combination of the specific energy and the step height employed in the process. Because of the larger energy available for fusing the alloy material, powder catchment efficiency increases with the applied specific energy. This increased powder deposition has to be reflected in the dimensions of the sample. Therefore wall sections processed at 30 J/mm^2 show reduced height as compared to those processed at 50, 60 or 70 J/mm^2 . However, at a certain value of the specific energy, the wall height is determined by the step height value set between consecutive scans. This effect is illustrated in Fig. 1 which shows the cross sections corresponding to samples 1 and 10, processed at step heights of 0.3 mm and 0.6 mm respectively. This can be explained in terms of a distance mismatch between the surface of the underlying deposited layer and the position of the powder jet focus. At 0.6 mm the powder stream focuses above or nearby the surface layer. As the step height is decreased, the jet stream fails to focus on this surface, consequently the powder is dispersed, the catchment efficiency is reduced, and hence, the wall height decreases.

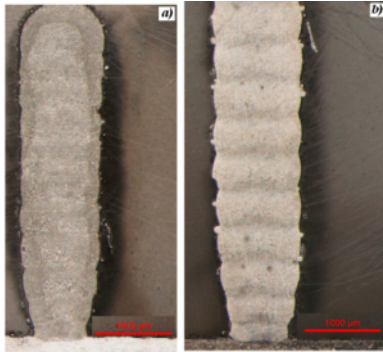


Fig. 1. Cross sectional view of samples 1(a) and 10(b), processed with the same parameters except for different laser step heights among consecutive scans (0.3 mm and 0.6 mm respectively).

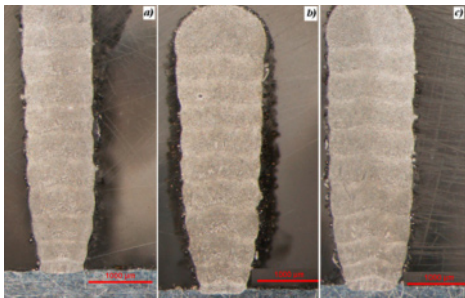


Fig. 2. Cross sectional view of samples 4(a), 5(b) and 6(c), processed with the same parameters at increasing laser input power (250 W, 300 W and 350 W respectively).

The process settings of specific energy and the step height also determine the wall height to width ratio. Fig. 2a) shows the cross section of sample 4. The first two layers show reduced deposition efficiency due to the large heat dissipation of the hot melted material onto the cold substrate. As deposition continues the accumulation of heat reduces the dissipation rate, increasing the clad surface temperatures and thus favouring the efficiency for powder catchment. At a certain point an equilibrium is achieved and the wall height/ width ratio tend to stabilize. As the laser power is raised, corresponding to samples 5 and 6 and shown in Fig. 2 b) and c), the total input energy is increased and so is the overall wall temperature and powder deposition. However, the larger amount of deposited material does not translate in an increased wall height, it rather widens due to the step height setting which reveals shorter than should be for this case. It is also noted that as a consequence the remelting factor raises accordingly. Adapting the process step height for this condition the height/width ratio increases, as demonstrated by samples 9 and 12. Nevertheless it should also be taken into account that the larger height to width ratios are always accompanied by an increased undulated appearance in the wall surfaces. This may be an inconvenient if a near net shape product with minimum post machining needed is being pursued.

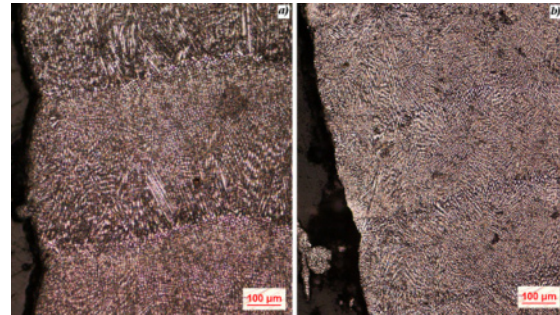


Fig. 3. Different dendritic microstructure observed in samples with low (sample 7) and high (sample 15) remelting factors.

3.2 Microstructure

As shown in Fig. 3, microstructure inspection of the samples reveals a typical fine dendritic pattern associated to the high cooling rates in laser process. The dendrite growth mechanism depends basically on the temperature gradient and the cooling rate, therefore different dendrite size and directions are observed within the cross sections. As explained in [8], during cladding dendrite growth occurs transversally to the solidification front, which moves along with the scanning speed. This gives the structure seen in Fig. 3 a), with dendrites changing direction from transversal at the layer-by-layer interface (bottom of the solidification front) to longitudinal (transversal to the cross section plane). For samples with higher remelting factors a coarsening of the dendritic structure, as seen in Fig. 3 b), was observed. This could be related to a higher heat accumulation and lower cooling rates. Microhardness profiles along wall height in corresponding samples gave slightly higher values for patterns with the coarse dendrite pattern (~300 HV) than for those with finer structure (~250 HV). Although this subject needs further study, it could be addressed to the reduced cooling rates and accumulated heat favouring the precipitation of intermetallic hard phases.

3.3 Online control of the process

The laser cladding process encompasses a multiple and complicated thermal and fluid phenomena associated to the interactions of the laser beam, the fluid circulation on the meltpool and the gas and powder jet streams. In the laser fabrication process, any process instability, as locally changing layer temperatures or deposition rates, result in a non-uniform finish of the fabricated piece. In order to overcome this critical issue, particularly for the processing of thin parts, online control tools are needed. With this aim, a closed loop control method based on the photodiode sensor was tested. As described in the experimental section this sensing device detects the IR radiation emitted by the melting area and yields an intensity signal proportional to the size of the melted area. A PID algorithm was developed so as to maintain a constant value of this signal during the process by acting

on the laser power P . In other words, a certain value of the photodiode signal is preset which should correspond to the desired deposition conditions. Then, during the fabrication process, the photodiode signal is read and the PID algorithm estimates the laser power needed to reduce or increase the melted temperature/area and drive the photodiode signal to the preset value.

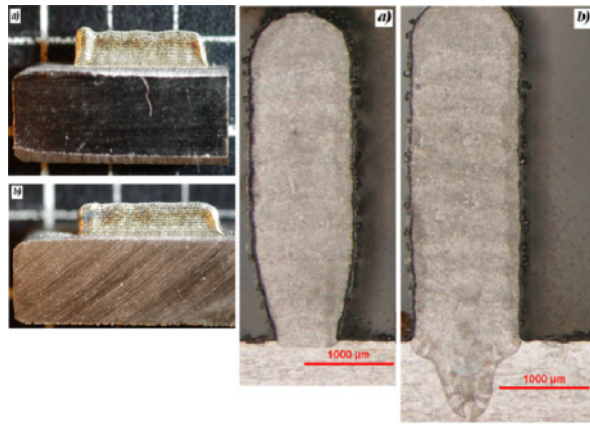


Fig. 4. Wall samples and corresponding cross sectional view processed without control (a) as compared to that obtained with closed-loop control (b)

Fig. 4(a) shows one of the wall samples made without online control where different build heights are clearly visible along the wall length. The cross section of this sample, shows the already described feature of increasing width from substrate interface to upper layers. The photodiode signal (1000 Hz sampling rate) corresponding to this sample is given in Fig. 6, where the eleven deposited layers are distinguished as well as the increasing signal accompanying the increasing deposition rate. The dotted line in the figure denotes the value selected as preset photodiode signal for closed loop control of this process. The result of the same process conditions under online control is the sample shown in Fig. 5 (b). It is seen that the varying building heights have been substantially smoothened, showing a more uniform finish. Besides, a cross sectional view of the sample in Fig. 6 (b), shows that the control loop has succeeded in maintaining a constant width along the deposition process.

4. Conclusions

Fabrication of thin walls (~1 mm width) of Inconel 718 by means of laser direct metal deposition with a high power Nd-YAG laser has been studied. Samples free of pores, cracks or bonding defects have been obtained within a rather wide process window, demonstrating the feasibility of the technique. The height/width ratios and the powder deposition efficiency obtained in the

fabrication are mainly determined by a combination of the specific energy (J/mm²) and the step height set between consecutive laser scans. Though a reasonable finish may be obtained by an adequate selection and optimization of these process parameters, online control methods are advisable in order to guarantee the uniformity of the fabricated part. A close-loop control method based on the IR radiation emitted by the melting area, coaxially read by a photodiode sensing device, has been tested which resulted in a substantial improvement of the finishing quality of the fabricated samples.

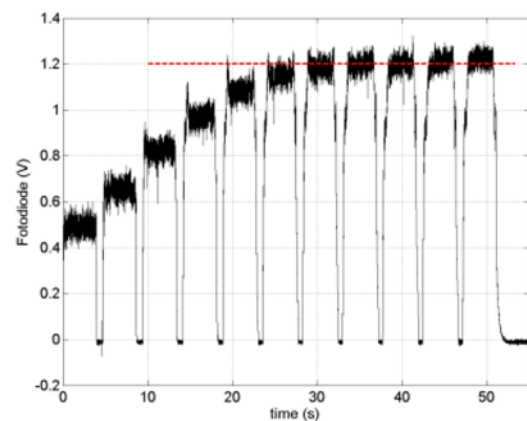


Fig. 5. Photodiode signal lecture corresponding to sample in Fig. 4(a). Dotted line is the preset signal chosen for the PID control algorithm.

Acknowledgements

The authors acknowledge the financial support from Spanish MICINN under project DPI2008-06664.

References

- [1] Griffith, M.L., Keicher, D.M., Atwood, C.L., Romero, J.A., Smugeresky, J.E., Harwell, L.D. and Greene, D.L. (1996), Solid Freeform Fabrication Symposium, University of Texas at Austin, Austin, TX
- [2] J Lewis, G.K. and Schlienger, E. (2000), *Materials and Design*, Vol. 21 No. 4, pp. 417-23.
- [3] Mazumder, J. and Stiles, E. (2000b), ICALCO, Laser Institute of America, Dearborn, MI.
- [4] J.R. Davis (Ed.) "Nickel, Cobalt and their alloys" (2000) ASM International
- [5] X. Zhao, J. Chen, X. Lin, W. Huang. *Mater. Sci. Eng A* 478(2008) 119-124
- [6] M.S. Domack, J. M. Baughman. *Rapid Prototyping Journal* 11 (2005) 41-51
- [7] L. Liu, A. Hirose, K. F. Kobayashi. *Acta Materialia* 50(2002) 1331-1347
- [8] M. Gaunann, S. Henry, F. Cleton, J.D. Wagniere, W. Kurz. *Mater. Sci. Eng. A* 271 (1999) 232-241

A numerical investigation of powder heating in coaxial laser metal deposition

Juansethi Ibarra-Medina¹, Andrew J Pinkerton¹

¹ Manufacturing and Management Group, School of Mechanical Aerospace and Civil Engineering, The University of Manchester, Sackville Street, Manchester M60 1QD, United Kingdom

Abstract. Understanding the interaction phenomena between the powder stream, the laser beam and the substrate is a key aspect for improving use of laser metal deposition. In this work, the powder stream is simulated under realistic deposition conditions. The stream of particles conveyed by inert gas through a coaxial deposition nozzle is first modelled and the interaction of particles with the laser beam investigated using a lumped capacitance approach, considering both particle heating and attenuation of the laser intensity. It is found that particles are initially rapidly heated while irradiated by the laser beam. This heating mainly depends on particle trajectory and incident energy, but attenuation also plays an important role. Experimental verification using stream imaging and deposition with a Laserline 1.5 kW diode laser shows good agreement between measured and simulated results. The model adds to existing models of the powder stream, and is capable of predicting particle trajectories, thermal and phase evolution.

Keywords: Coaxial deposition, numerical modelling, powder stream, powder heating.

1. Introduction

Coaxial laser metal deposition is a process in which a gas-propelled flow of metallic powder is melted and fused to a substrate base through the use of a high energy laser beam. This bonding depends on various processing conditions, such as laser power, flow rate of powder material, heating of the substrate and powder, stream shape and position of substrate. From these, formation of stream shape and heating of particles are not easily controllable but important for good process quality so have been the subject of various studies. A number of works have focused on analysing purely the behaviour of the powder stream [1-2]. Others have investigated the effects of laser interaction during the in-flight time of particles before hitting the substrate material [3-5]. Some simplifications made in previous works, such as the absence of a substrate [6], the assumption that the powder stream does not diverge after merging, that particle velocities are constant [7], or that there is no laser energy

attenuation [8], have left some gaps in our present knowledge about stream heating and its effects on melt pool dynamics and effective bonding.

In this work, the complicated powder stream is first analysed with a numerical model to characterise its behaviour. Then, the particle heating is calculated using a lumped capacitance approach. Experimental verification is made in two phases. First, the dimensions of the stream without the use of a laser beam are measured using imaging techniques. Then, powder heating is recorded using thermal imaging techniques.

2. Numerical modelling

2.1 Modelling of powder flow

The finite-volume method is used to model the motion of particles and gases through and after leaving the deposition nozzle. Fig. 1 shows the three dimensional non-uniform grid used for the simulation. Only half of the problem is modelled, due to symmetry. The behaviour of the carrier and central gas flows are calculated using mass and momentum balance equations. Powder particles are modelled using the Lagrangian expression:

$$m_p \frac{dV_p}{dt} = \frac{A_p \rho_g C_D}{2} (V_g - V_p) |V_g - V_p| + m_p g + f \quad (1.1)$$

Where m_p is the mass of the particle, d_{vp} is the change of particle velocity in the time dt , v_g is the velocity of the surrounding gas flow, ρ_g is the density of the gas, g is the gravity constant, f is an external source force, A_p is the area of the particle, and C_D is the particle drag coefficient. The commercial software package CFD-ACE+ produced by ESI Group was used for gas and particle flow calculations.

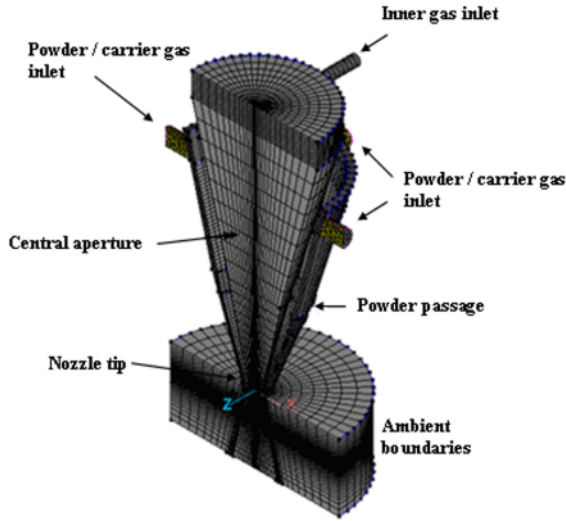


Fig. 1. Three dimensional domain of the coaxial nozzle and underlying substrate. Half domain due to symmetry

2.2 Modelling of powder heating

It is considered that powder particle heating is influenced by various phenomena such as: energy absorption from laser beam, particle melting, heat losses due to convection to the surrounding gases, and radiation to the environment. A lumped capacitance approach is used and the energy balance calculated at each time step using the expression:

$$\frac{4}{3} \pi r_p^3 \rho c_p \Delta T = I \eta_p \pi r_p^2 \Delta t - h(T - T_\infty) 4 \pi r_p^2 \Delta t - \varepsilon \sigma (T^4 - T_\infty^4) 4 \pi r_p^2 \Delta t - X L_f \frac{4}{3} \rho \pi r_p^3 \quad (1.2)$$

where r_p is the particle radius, ρ is the density, c_p is the specific heat, ΔT is the increase of particle temperature, I is the laser energy intensity, η_p is the absorption coefficient of the powder material, Δt is the time a particle is irradiated or in this case the time step, h is the convective heat transfer coefficient, T is the powder temperature, T_∞ is the temperature of the surrounding gas, ε is the emissivity value of the powder, σ is the Stefan-Boltzman constant ($5.67 \times 10^{-8} \text{ W/m}^2 \text{ K}^4$), L_f is the latent heat of fusion, and X is an integer which has the default value of 0 but takes the value 1 if T equals the melting temperature and is increasing or -1 if T equals the melting temperature and is decreasing. Laser beam intensity, I , is assumed to have a Gaussian distribution at any transverse plane, according to the following expression:

$$I = \frac{2I_0}{\pi r_l^2} e^{-\frac{2r^2}{r_l^2}} \quad (1.3)$$

Where r_l is the laser beam radius, and r is the radial distance to the centre of the beam. It is assumed that there is no shadowing of particles by each other. Hence, attenuated laser intensity is computed with the following expression.

$$I_{atten} = I \cdot \frac{dS - (N_p \pi r_p^2)}{dS} \quad (1.4)$$

where I_{atten} is the laser intensity after particle clouding, at a dS surface element, N_p is the number of particles over the surface element dS .

3. Experimental verification

The setup of the experiment used to measure powder stream formation and in-flight temperature distribution of powder particles comprises a custom-built coaxial deposition nozzle, used to deliver a stream of stainless steel 316L powder particles which range in size from 53 μm to 150 μm . A SIMATIC-OP3 disk powder feeder is used to accurately supply the powder at 0.58 g/s and the powder is conveyed using a constant flow of argon gas at a rate of 5 dm^3/min . A central flow of argon gas used to shield the working area from oxygen is set at a 4 dm^3/min .

For the measurement of powder stream geometry, the laser is turned off, and no substrate is positioned below the nozzle. The method of light reflected from particles is used [10]. For measurement of powder heating, a Laserline LDL 160-1500 diode laser is positioned as it would be during deposition; the laser beam focal plane is 7.5 mm below the nozzle's tip and the beam waist is 1.5 mm. A Thermovision A100 thermal camera is positioned at the same level as the emerging powder stream and captures the stream temperature with the laser on, and the measurements are transmitted to a workstation, where the data is processed using proprietary software. Results are gathered for three power levels (1000 W, 660 W and 500 W).

4. Results and discussion

Fig. 3 shows the modelled powder stream inside and after leaving the nozzle. Two interesting aspects of powder stream formation, which have been considered rarely before, can be seen. Firstly, powder particles travelling inside the coaxial nozzle's powder passage experience various collisions against the passage walls. Such collisions greatly influence the overall powder stream focal position and stream diameter. In this model, particles undergo an average of seven collisions before leaving the nozzle. Secondly, the powder stream emerges from the nozzle having an annular shape, but the powder concentration is much higher at four equidistant zones

within the annulus, corresponding to the positions the powder was injected through the powder inlets, as shown in Fig. 1. After converging, powder particles cross each other and continue their trajectory, thus the stream effectively and gradually starts to split into four spreading streams that diverge from the central axis, as shown in Fig. 2 (a)-(c).

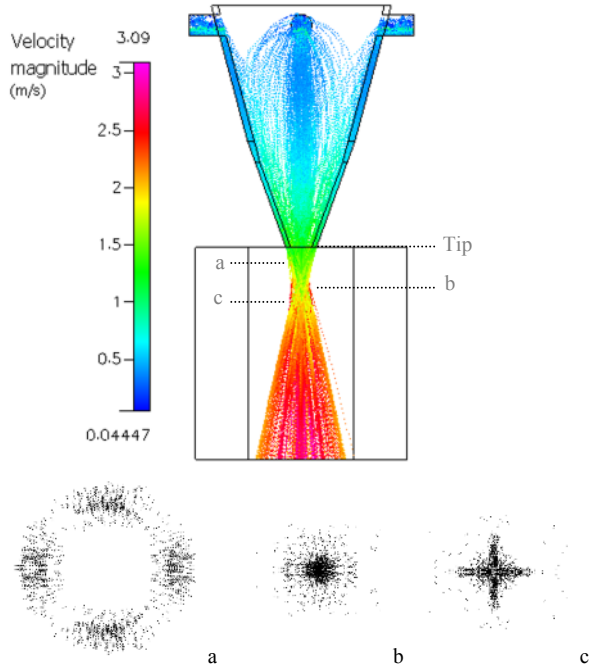


Fig. 2. Modelled powder stream (side view) & transverse particle distribution at different in-flight positions: a) 4 mm above stream focus point, b) at stream focus point: 8 mm, c) 3 mm below stream focus point. Carrier gas flow: 5 dm³/min. Inner gas flow: 4 dm³/min. Powder flow rate: 0.0058 g/s

The model predicts the powder stream to focus at a distance of 8.2 mm below the nozzle. This is in good agreement with experimental observations, which showed that the stream consolidates slightly before a distance of 8 mm. Fig. 3 shows the average particle concentration in any plane, calculated from the powder mass flow rate and the volume defined by the outer circumference of the stream at any distance from the nozzle.

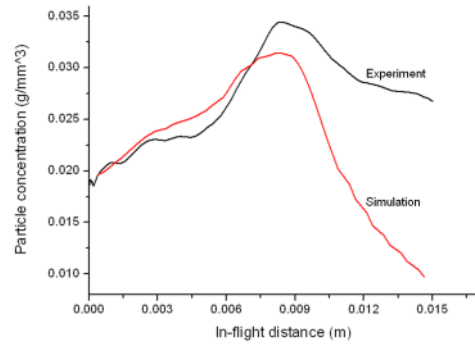


Fig. 3. Particle concentration along axial distance. Carrier gas flow: 5 dm³/min. Inner gas flow: 4 dm³/min. Powder flow rate: 0.0058 g/s.

Experimental and modelled concentration curves agree up to the maximum concentration point. After this the experimental curve falls less sharply than the simulation curve, which is probably due to the fact that experimental values may be higher than reality due to some illumination of particles at the edges of the stream caused by diffuse reflection from illuminated particles.

Fig. 4 shows the modelled temperature distribution along the centre of the stream when the substrate is positioned 20 mm below the nozzle.

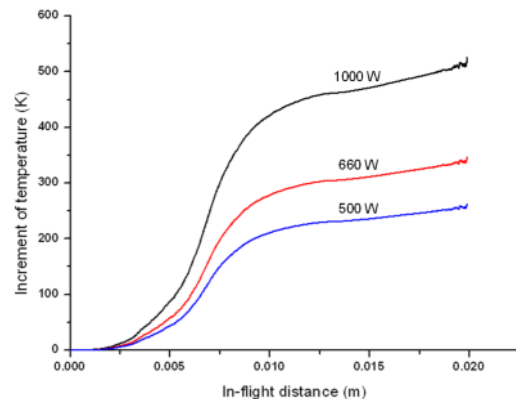


Fig. 4. Modelling results. Powder stream heating along central axis, with respect to laser power. Laser focus: 0.0075 m. Beam diameter: 0.0015 m. Substrate position under nozzle: 0.02 m, powder flow rate: 0.58 g/s

Particle temperature remains unaltered immediately after leaving the nozzle. As the powder stream gradually consolidates and particles approach the central axis, they meet with the laser beam and experience an increasing heating, which shows a steep slope until they reach the focus point of the laser at 0.0075 m. Temperature continues to steadily increase afterwards, although such increments are more gradual. Temperatures along the centre of the stream increase to higher levels when the laser power is augmented but the trend is consistent regardless of the laser intensity.

This behaviour can be compared with that observed experimentally, as shown in Fig. 5. Note that the different scale compensates for the powder stream transparency,

which hinders absolute temperature readings by thermal imaging. The experimental trends for particle heating agree well with modelled heating curves.

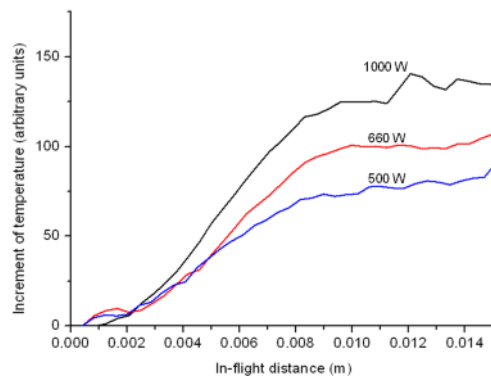


Fig. 5. Experimental influence of laser power on stream heating. Temperature is measured along the central axis. Substrate position under nozzle: 20 mm. Powder flow rate: 0.58 g/s

The verified model can be applied where it is impossible to measure experimentally. For example, Fig. 6 shows the effect of using different powder sizes on overall stream heating. Particles with the largest diameter (150 μm) are heated significantly less than those with the smallest diameter (50 μm).

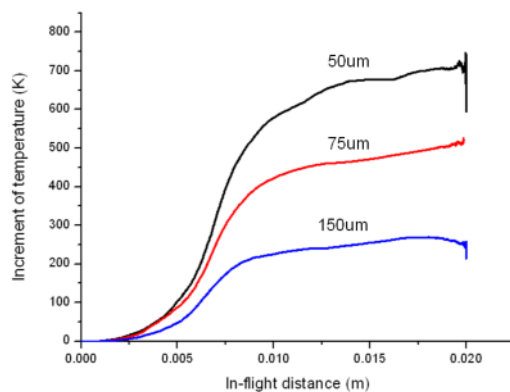


Fig. 6. Modelling results. Powder stream heating along central axis with respect to particle diameter. Laser focus 0.0075 m under nozzle's tip. Beam diameter: 0.0015 m. Substrate position under nozzle: 0.02 m. Powder flow rate: 0.58 g/s

5. Conclusions

A numerical model for analysis of the interaction between the powder stream and the laser beam has been developed. It is able to predict the stream geometry and shape, as well as velocity and trajectory of flying particles, and there is good agreement with experimental observations. The model is also able to calculate particle heating, considering heat gains from laser irradiance, heat losses from convection, radiation and phase change and variations in the intensity of the beam due to attenuation. The trend in particle temperature increase is confirmed with experimental results. The flexibility of the model makes it a useful tool both as a nozzle design aid and as a component of future, more comprehensive models of the process.

References

- [1] Pan, H., et al. (2006). "The investigation of gravity-driven metal powder flow in coaxial nozzle for laser-aided direct metal deposition process". *Journal of Manufacturing Science and Engineering-Transactions of the Asme*, 128(2): 541–553.
- [2] Pinkerton, A.J. and L. Li (2004). "Modelling powder concentration distribution from a coaxial deposition nozzle for laser-based rapid tooling". *Journal of Manufacturing Science and Engineering Transactions of the Asme*, 126(1): 33–41.
- [3] Pinkerton, A.J. (2007). "An analytical model of beam attenuation and powder heating during coaxial laser direct metal deposition". *Journal of Physics D. Applied Physics*, 40(23): 7323–7334.
- [4] He, W., Zhang, L. And Hilton P. (2009) "Modelling and validation of a direct metal deposition nozzle" *International Conference on the Application of Laser and Electro-Optics*, Orlando, FL, USA.
- [5] He, X. and J. Mazumder (2007). "Transport phenomena during direct metal deposition". *Journal of Applied Physics*, 101(5).
- [6] Wen S.Y., Shin Y.C., Murthy J.Y. and Sojka P.E. (2009) "Modelling of coaxial powder flow for the laser direct deposition process". *International Journal of Heat and Mass Transfer* (52): 5867–5877
- [7] Huang, Y.L., et al. (2005). "Interaction between laser beam and powder stream in the process of laser cladding with powder feeding". *Modelling and Simulation in Materials Science and Engineering*(13): 47–56.
- [8] Liu, C.Y. and J. Lin (2003). "Thermal processes of a powder particle in coaxial laser cladding". *Optics and Laser Technology*, 35(2): 81–86.

Laser cladding of NiCr-WC metal matrix composites: dependence on the matrix composition

J. M. Amado, M. J. Tobar, A. Yáñez

Universidade da Coruña, D. de Ingeniería Industrial II, Ferrol, E-15403, Spain.

Abstract. The development of hard-facing coatings has become technologically significant in many industries where wear can cause severe damage on different components. One approach is the production of metal matrix composites (MMC) layers, consisting of a mixture of hard ceramic phases immersed in a ductile metal matrix. In this work, a study of the development of NiCr-WC hard-facing layers by means of laser cladding (LC) is presented. For the reinforcement phase, spheroidal fused tungsten carbides have been used by virtue of its exceptional hardness which may range from 2500 HV up 3300 HV. The properties of the layers are analyzed and discussed in relation to the LC parameters used in the process.

Keywords: laser cladding, hardfacing, MMC, tungsten carbides, NiCr-WC

1. Introduction

Laser cladding (LC) [1] with metal matrix composites (MMC) has shown high potential for enhancing wear resistance. MMC are a mixture of hard, reinforcing phases immersed in a ductile metal matrix. The reinforcement constituent is normally a ceramic or a compound of a refractory metal as titanium, tungsten or chromium carbide. The matrix is usually a Ni or Co based alloy which enhances the layer resistance to corrosion, particularly at high temperatures.

This paper reports studies of the deposition of Ni based MMC layers on low carbon steel components by means of LC. Tungsten carbides have been chosen as the hard phase, given its high melting point, high hardness, low thermal expansion and good wettability by molten metals. LC should further provide with more dense coatings, metallurgical bonding with substrates and minimal thermal distortion as compared with other more standard deposition methods such as thermal spraying.

In the present investigation, two premixed NiCr-WC MMC powders are used, developed by the manufacturer, Technogenia, for coating applications with high power lasers. The company produces spheroidal fused tungsten carbides, under the name of Spherotene®, having extremely high hardness, monophasic composition and a

very smooth finish. These carbide particles are used as reinforcing WC phases in the above referred MMC. Different concentrations of spheroidal fused tungsten particles with other types of Ni-based alloys have already been used by other authors [2,3].

2. Spheroidal fused Tungsten Carbides

According to the W-C binary phase diagram, tungsten carbide can exist as three phases, W_2C , $W_{1-x}C$ and WC. The equiatomic WC form has a simple hexagonal structure and forms at carbon contents above 50 at.%. Below 42 at.% carbon, an eutectic reaction yields a mixture of WC and W_2C , where the W_2C fraction dominates at contents below 37%. The W_2C form, with a hcp structure, is recognized as the hardest phase. However it is also more brittle than the simple hexagonal WC. Finally, in the narrow range between 37 at.% and 39 at.% carbon content, a fcc structure may form corresponding to the non-stoichiometric $W_{1-x}C$ phase. This phase is metastable and can only be stabilized at room temperature by means of very high cooling rates.

WC compound melts incongruently, this is, it decomposes above its melting point (2776 °C) producing free carbon. At this temperature (2776 °C), free carbon sublimes, leading to porosity in the coating. In contrast to WC, both W_2C and $W_{1-x}C$ phases melt congruently. Different tungsten carbide are commercially available.

Angular Fused (or cast) Tungsten Carbide: Obtained by eutectic reaction of liquid carbon and tungsten, followed by conventional casting. The solid is then crushed to the desired size. Phase composition is about 80% W_2C and 20% WC which, together with the eutectic structure, results in a hardness ranging between 2200-2400 HV. It has high brittleness due to the large content in W_2C . Their angular shape may promote stress concentrations.

Pure Tungsten Carbide: Obtained in solid state by carburization of tungsten oxides. The particles produced,

of 100% WC composition, are generally too small to be used as they would be easily dissolved by the metallic matrix. Therefore they are usually mixed, pressed and sintered with a metallic (Co, Ni) binder conforming the so-called cemented carbides. Hardness is between 2000-2200 HV.

Spheroidal Fused Tungsten Carbide: Starting from fused tungsten carbides, particles are re-melted and atomized to produce spherical shapes at high cooling rates. During the process, homogenization procedures are followed so as to obtain a composition in the $W_{1-x}C$ phase range, which is further stabilized by using very high cooling rates. Monophasic spheres of cubic $W_{1-x}C$ phase are finally obtained. Hardness is between 2600-3300 HV.

3. Experiments

Two premixed NiCr-WC powder alloys, Technolase60s and Technolase40s, were employed for the LC experiments. Both include Spherotene® as hard WC particles. The nominal Cr content in the NiCr matrix is 12-14%wt. and 8-11 % wt. for Technolase60s and Technolase40s respectively. Data from the manufacturer assigns a nominal hardness of 60Hrc to Technolase60s and of 40Hrc to Technolase40s, due to the different Cr contents of the NiCr matrices. Tungsten carbide concentration is about +60% by weight in both cases. Accounting for the different densities of the NiCr alloy particles and fused carbides, ~8 and ~16 gr/cm³ respectively, around 40%-45% volume percentage of carbides is to be expected in the deposited coatings. Nominal Spherotene® carbide size is +40-160µm.

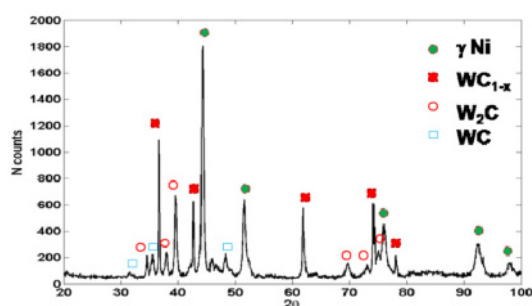


Fig. 1. XRD analysis of NiCr-WC alloy with spheroidal fused tungsten carbides.

A XRD phase composition analysis of the two powders used is seen in Fig. 1. Besides the γ -fcc phase associated to the Ni-based alloy, peaks corresponding to the different tungsten carbide forms are present. The diffraction pattern is dominated by the presence of the monophasic $W_{1-x}C$, evidencing the fundamental microstructure spheroidal fused carbides. The presence of

WC and W_2C could be addressed to homogenization defects in the fabrication procedure. In fact, during metallographic inspection of the coatings produced, pores inside of some of the tungsten spheres are visible, indicating WC decomposition and pore formation during production of the tungsten particles.

The LC system consisted of a 2 kW industrial Nd-YAG laser (Rofin DY022). Powder feeding is performed coaxially by means of a powder feeder (Sulzer-Metco Twin10c). The laser beam was defocused to a beam diameter of $d=3.5$ mm on the working surface. Cladding was performed on 5 mm thick plates of low carbon steel C25. N_2 was used as shielding and powder carrier gas. All samples were cut transversally, ground, polished and etched. Microhardness measurements were performed. A liquid penetrant dye test was used to study the crack susceptibility.

4. Results and Discussion

Studies on the morphology of the deposited Technolase60s in terms of the laser cladding process parameters were performed [4] depending on laser output power $P[W]$, scanning velocity $v[mm/s]$ and powder mass flow rate $f[gr/s]$. The power density applied, $P/d^2[W/mm^2]$, and alloy interaction time under the beam, $d/v[s]$, have a major effect on the quality of the MMC coatings. A pattern of uniformly distributed carbide spheres in the metal matrix is observed, but rather large pores are observed within the deposited material, which were related to decomposition following dissolution of the WC spheres. Dissolution of tungsten carbide yields matrix hardness values of 1000 -1400 HV, significantly higher than the nominal 700 HV (60 HRC) value.

With this in mind, several tests were performed on extend areas coatings of C25 by overlapped laser scans, at 35%-40% overlapping ratios. Substrates were preheated to 400°C prior to deposition. Preheating prevents crack formation reducing the cooling rates and diminishes stresses. It should be noted that in laser cladding, the beam energy is partially absorbed by the powder and the rest of flux melts the substrate surface. If thermal conductivity of the metal substrate is high, as with C25, substantial power densities must be applied in order to effectively melt the metal surface. Besides, the melting point of C25 is higher than that of the NiCr alloy (1530°C and 1038°C respectively). In summary, the projected clad material is subjected to an undesirable high energy irradiation. If substrate temperature is raised, its thermal conductivity is somewhat reduced, the laser absorption increases and the power needed for melt pool formation is significantly reduced. Therefore the cladding process can be performed with less laser energy.

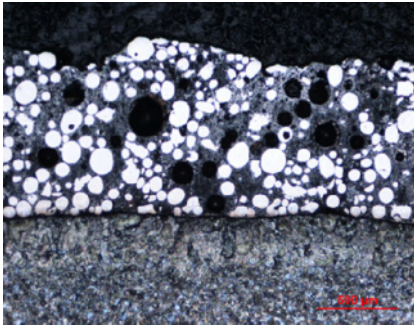


Fig. 2. Cross-section of a sample of NiCr-WC coating deposition by laser cladding. Wrong selection of process parameters may lead to large pores in the coating.

An optical micrograph of one of the coating samples obtained is shown in Fig. 2. The NiCr-WC is metallurgical bonded to substrate with minimal dilution. And the white WC spheres are distributed within the metal matrix. Large black pores are observed mainly in the overlapping areas, due to dissociation following dissolution of carbide spheres.

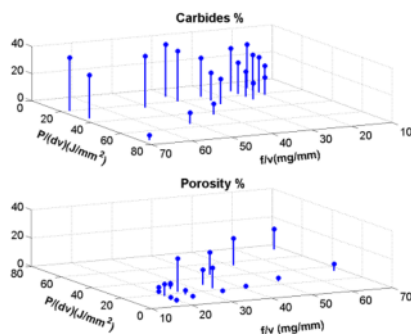


Fig. 3. Porosity and carbide concentration (in volume %) for examined NiCr-WC layers in terms of specific energy $P/(dv)$ and feeding rate f/v .

All samples were inspected by image analysis searching for the number of pores and the dissolved tungsten carbide. As noted earlier, P/d^2 and d/v should be minimized in order to avoid pore formation. The samples were thus classified according to their specific energy $P/(dv)$, encompassing the two referred parameters. Classification was also performed in terms of the powder feeding rate f/v on the substrate. In principle, lower or higher feeding rates imply thinner or thicker coatings, which will need less or high power densities for an effective cladding on the substrate. The analysis results for porosity and carbide content in the clad layers are shown in Fig. 3. The volume fraction of carbides increases towards the lower specific energies up to the nominal value of carbide concentration for each feeding rate. Missing spheres at high energies are assumed to be caused by dissolution in the matrix. This relates to the

higher amount of porosity in increasing values of $P/(dv)$. In points where carbide concentration is nearly 40%, porosity is insignificant.

Based on the above results, a parameter phase space for optimum cladding deposition was envisaged, as given in Table 1. A total of 27 layers of Technolase60s were deposited corresponding to three different laser power values within pointed ranges for each of the feeding rates and scan speed conditions. Pore free layers with good bonding with substrate and minimal dilution were obtained in all cases. Volume concentration of tungsten carbide spheres ranges is close to 40% in all cases.

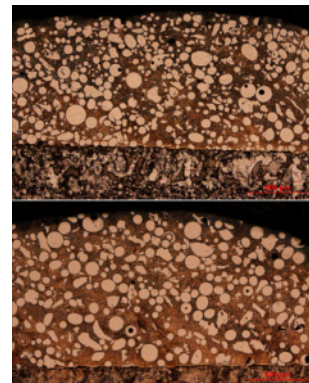


Fig. 4. Technolase60s layers Up(1) 35 mg/mm, 10 mm/s and 800 W. Down(2): 35 mg/mm, 30 mm/s and 1700 W.

Table 1. Parameter phase space for Technolase60s and Technolase40 clad deposition ($d=3.5$ mm).

f/v (mg/mm)	$P/(vd)$ (J/mm ²)	v (mm/s)	P (W)	f (g/s)
25	[10-20]	10	350-700	0.25
		20	700-1400	0.50
		30	1100-2000	0.75
		40	1400-2000	1.00
35	[15-25]	10	550-900	0.35
		20	1100-1750	0.70
		30	1600-2000	1.00
40	[20-30]	10	700-1100	0.40
		20	1400-2000	0.80

Cross section examples of some of the layers processed at 35 mg/mm are shown in Fig. 4, with corresponding microhardness measurements given in Table 2. Values obtained at four different places on the NiCr matrix are given. Carbide values correspond to a single measurement. Matrix hardness close to the nominal 700 HV value of the NiCr matrix of Technolase60s alloy indicates a very low dissolution of the tungsten carbides. Carbide hardness also reproduces the 3000 ± 500 HV value claimed by the manufacturer. The structure of the deposited coating therefore matches the MMC requirements.

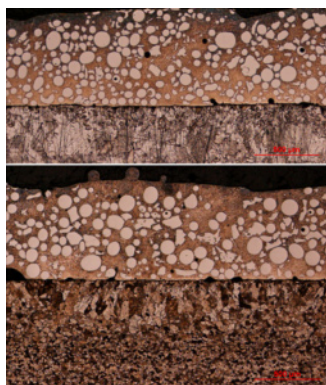


Fig. 5. Technolase40s layers Up(1) 35 mg/mm, 10 mm/s and 800 W. Down(2): 35 mg/mm, 30 mm/s and 1700 W.

Cracking could not be avoided in any of the samples of Technolase60s. On average, 10 cracks were observed along 40 mm lengths perpendicular to the laser scanning path. Dissolution of the smallest carbide spheres could act as source of mixed tungsten carbide formation and crack initiation. However, it has also been noted [5] that chromium in NiCr alloys, as well as boron, results in precipitation of hard and brittle mixed carbides and borides within the matrix. Alloys giving hardness as high as 700HV are assumed to have a rather high content of chromium, thus an already large amount of hard phases must precipitate in the matrix, irrespectively of the tungsten presence. In order to study the effect of Cr on the crack susceptibility, some coatings using Technolase40s, a powder with less Cr and NiCr matrix hardness of 40 Hrc, were made. Cross section examples of some of the layers processed at 35 mg/mm are shown in Fig. 5. Microhardness measurements corresponding to this samples, are given in Table 2. Matrix hardness is close to the nominal 400 HV of Technolase40s alloy indicating a very low dissolution of the tungsten carbides. Carbide hardness also reproduce the 3000 ± 500 HV value claimed by the manufacturer. Fig. 6 shows the difference in the cracks susceptibility of coatings of Technolase60s (A) and Technolase40s (B) applied with the same parameters. The lower Cr content reduces the number of cracks. Crack free coatings can be obtained using a Ni matrix without Cr [2].

5. Conclusions

NiCr-WC MMC layers using a commercial premixed alloy powder have been deposited by LC. Reinforcement tungsten particles consist in spheroidal fused tungsten carbides, characterized by a monophasic $W_{1-x}C$ fcc-phase composition and exceptional hardness yielding values in the range 3000 ± 500 HV. Parameter selection must be performed

in order to obtain pore free layers, searching for the lowest laser energy densities compatible with an effective clad deposition and metallurgical bonding with the substrate. Porosity grows with laser energy; this has been correlated to the dissolution of carbide particles. Optimum parameter ranges have been identified for depositing layers on low carbon C25 steels substrates. Within this range, NiCr-WC layers comply to MMC requirements, retaining their nominal size and hardness.

Table 2. HV measurement samples are shown for Technolase60s (T60s) and Technolase40s (T40s) samples.

Sample	Metal Matrix (HV0.2)		Carbide Spheres (HV0.2)
1 (T60s)	934	884	2842
	884	896	
2 (T60s)	746	849	2987
	921	806	
3 (T40s)	596	570	2706
	535	518	
4 (T40s)	518	552	2360
	421	497	

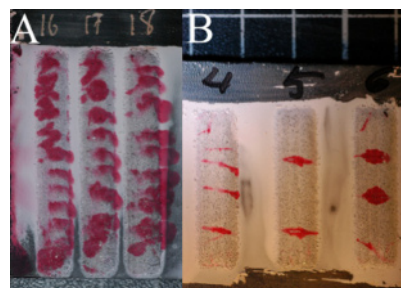


Fig. 6. Cracks in coatings of Technolase60s (A) and Technolase40s (B) produced with the same parameters.

Acknowledgements

This work has been done under the financial support of Xunta de Galicia, project reference 08DPI024CT, Programa de Diseño y Producción Industrial.

References

- [1] W.M. Steen, Laser Material Processing (3rd ed.), Springer-Verlag, London-Berlin Heidelberg (2003).
- [2] Van Acker, K., Vanhoyweghen D., Persoons R., Vangrunderbeek J., Wear 258 (2005) p.194.
- [3] Huang S.W., Samandi M., Brandt M., Wear 256 (2004), p.1095.
- [4] J.M. Amado, M.J. Tobar, J.C. Alvarez, J. Lamas, A. Yáñez. Applied Surface Science 10 (2009), p.5553.
- [5] R.C. Gassmann. Materials Science and Technology. 12 (1996), p.691.

Wettability analysis of CO₂ laser surface patterned nylon 6,6 samples soaked in simulated body fluid (SBF)

D.G. Waugh and J. Lawrence

Wolfson School of Mechanical and Manufacturing Engineering, Loughborough University, Leicestershire, LE11 3TU, UK

Abstract. Simulated body fluid (SBF) has been used previously by others as an aid in predicting the bioactivity and osseointegration potential of materials. This paper details a study carried out using a CO₂ laser to induce a number of surface patterns which inherently modified both the surface chemistry and surface topography of nylon 6,6 and gave rise to a difference in apatite response. These induced patterns caused a reduction in hydrophilicity with contact angles of up to +10° being observed. Furthermore, following immersion in SBF for 14 days, each sample was weighed revealing an increase in weight of up to 0.029 g indicating that an apatite layer had begun to form. In addition, energy dispersive X-ray (EDX) analysis identified the presence of calcium and phosphorous, two elements which support osteoblast cell response. When comparing with an as-received sample, it was found that the laser induced patterned samples gave rise to more layer crystals forming suggesting a more optimized surface for osteoblast cell growth and proliferation.

Keywords: CO₂ laser, nylon 6,6, wettability, biocompatibility, simulated body fluid (SBF).

1. Introduction

It has been demonstrated previously that polymers can be used for biological applications [1, 2]. The polymer surface can be optimised for these various applications through surface modification where either the surface topography or surface chemistry is altered. These modifications can be brought about by using numerous methods such as radiation grafting [3], lithography [4], coating technologies [5] and plasma surface modification [6]. Laser surface treatment and patterning [2, 7] offers a convenient means of modifying the surface of a material on both the micro- and nano-scale without compromising the bulk properties of the material, which can be seen to be of great importance when applied to fields such as biomimetics. This is on account of previous work which has identified a high dependence of the modifications on cell-material interactions [8].

One can deduce from the literature that a change in the surface chemistry or surface topography will greatly

affect the wettability characteristics of a material [9]. As a direct result of this, it would be a great advantage to those throughout the biomedical industry if, by knowing the wettability of a material, one could predict how a material will react in the intended application.

Simulated Body Fluid (SBF) has been used in the past by others to aid in predicting the bioactivity and osseointegration potential of materials [10]. It should also be noted here that employing SBF experiments *in vitro* does not fully reproduce the *in vivo* environment for bone formation, as stated by Roach et al. [8] these *in vitro* techniques involving SBF allow for a sufficient rapid screening of materials in the endeavour of development and optimization.

This paper details the effect of soaking nylon 6,6 samples in SBF after CO₂ laser patterning. In addition to this, the characteristic wettability for each sample studied was determined in the endeavour to link wettability to the resulting response of the samples being immersed in SBF.

2. Experimental Techniques

2.1 CO₂ laser patterning procedure, topography, wettability and surface chemistry

The details of how the CO₂ laser patterning procedure and analysis of topography, wettability and surface chemistry have been detailed before by Waugh *et al* [2]. Five samples were used for this experimentation; As-received (AR), 50 µm trench (T50), 50 µm hatch (H50), 100 µm trench (T100) and 100 µm hatch (H100) patterns.

2.2 *In vitro* simulated body fluid (SBF) experimentation

Simulated body fluid (SBF) is a liquid which has inorganic ion concentrations equivalent to those of human extracellular fluid (human blood plasma). The SBF was

prepared by using a magnetic stirrer hotplate (RCT Basic; IKA, GmbH) keeping the solution at a constant temperature of 36.5°C. 500 ml of distilled water was put into an autoclaved 1000 ml beaker and stirred until the constant temperature of 36.5°C was reached. At this time the chemicals given in Table 1 were added in order until the sodium sulphate (#9) had been added.

Table 1. Amounts and order of reagents to prepare 1000 ml SBF

Order	Reagent	Amount
1	Distilled water	750 ml
2	(NaCl)	7.996 g
3	(NaHCO ₃)	0.350 g
4	(KCl)	0.224 g
5	(K ₂ HPO ₄ ·3H ₂ O)	0.228 g
6	(MgCl ₂ ·6H ₂ O)	0.305 g
7	(~0.1 M in H ₂ O) (HCl)	40 ml
8	(CaCl ₂)	0.278 g
9	(Na ₂ SO ₄)	0.071 g
10	(CH ₂ OH) ₃ CNH ₂	6.057 g
11	(~0.1 M in H ₂ O) (HCl)	Adj. of pH

Once the sodium sulphate (#9 in Table 1) had been added, the Tris(hydroxymethyl) aminomethane (#10 in Table 1) was supplemented into the solution less than a gram at a time in order to avoid local increase of pH. Finally, in order to adjust the pH value to 7.4, hydrogen chloride (#11 in Table 1) was added and the beaker was then filled to 1000 ml using distilled water.

The samples were then placed into sterile 30 ml glass containers, immersed in 30 ml of SBF and placed into an incubator to keep the temperature constant at 37°C for seven days. Prior to being immersed in the SBF, the five nylon 6,6 samples were weighed using a balance (S-403; Denver Instrument, GmbH). Once the 14 days had elapsed, the samples were removed from the SBF, rinsed lightly with distilled water and allowed to air dry in a clean room. Once fully dry, the samples were weighed and the difference in weight before and after being immersed in the SBF was determined. Following this the samples were gold coated and analysed using optical microscopy and scanning electron microscopy (SEM). Furthermore, the samples were analysed using EDX in order to identify elements present after the immersion in SBF.

3. Results and Discussion

3.1 Effects of CO₂ laser patterning on topography

From Figure 1 it can be seen that the CO₂ laser patterning gave rise to significant modification of the nylon 6,6 surfaces in terms of topography. That is, the laser patterned samples (see Figures 1(b) – (e)) appeared to qualitatively have a considerably larger roughness in comparison to the 3-D profile of the as-received sample (see Figure 1(a)).

3.2 Effects of CO₂ laser patterning on wettability characteristics

From previous work [2] and available literature [11], it can be seen that surface properties, which are reported to have major influences on the wettability characteristics [12], have the potential to be modified using numerous techniques. Table 2 shows that the roughness had considerably increased using the laser patterning (samples T50, T100 – H100) in comparison to the as-received sample (AR). This contrast can be identified through the Sa and Ra roughness parameters insofar as the as-received sample (AR) had an Sa and Ra of 0.126 and 0.029 µm, respectively, where the Sa and Ra for the laser patterned samples increased by up to 0.51 and 0.156 µm, respectively.

The polar component, γ^p , and total surface energy, γ^T , two parameters known to potentially affect the wettability [7], decreased significantly for the laser patterned samples (T50, T100 – H100). This reduction in surface energies, along with increased surface roughness brought about an apparent increase in contact angle inherently making the nylon 6,6 less hydrophilic. These observations do not necessarily coincide with current theory [7] which states that for a significant increase in surface roughness, a hydrophilic material ought to produce a more hydrophilic surface with the contact angle effectively decreasing [13]. It is possible to explain this phenomena by the plausible existence of a mixed state wetting regime, in which both Wenzel and Cassie-Baxter regimes are present over the solid-liquid interface [14].

Hao and Lawrence [7] found that a rise in surface oxygen content in turn gave rise to a reduction in the contact angle. But Table 2 suggests the resulting surface oxygen content in this work may not be the main contributing factor in determining the outcome of the contact angle.

Finally, the results obtained as seen in Tables 2 and 3 attests to an evident and significant rise in contact angle which can be attributed to the reduction in apparent surface energies, γ^p and γ^T , which arise as a direct result of the mixed state wetting regime can be ascribed to the liquid-surface interaction owing to variations in the laser-induced surface topography. As in previous work [2], it can then be extrapolated that both the closely linked apparent surface energies and surface topography appear to be the main driving force in the resulting contact angle.

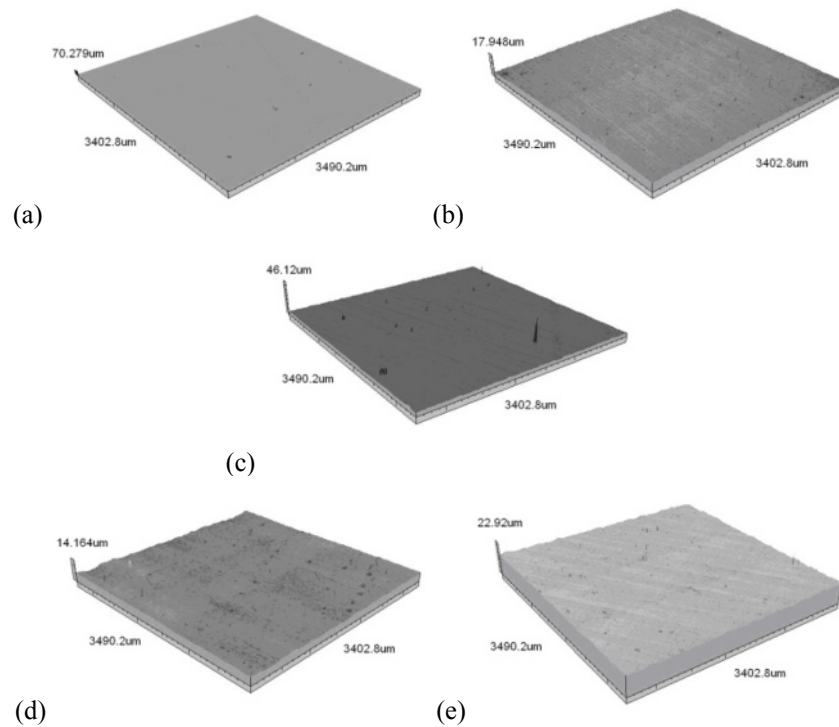


Fig. 1. Continuous axonometric images for each of the nylon 6,6 samples – (a) As-received (AR) (b) 50 μm trench (T50) (c) 100 μm (T100) (d) 50 μm hatch (H50) and (e) 100 μm hatch (H100).

Table 2. Measured values for surface roughness, contact angle and surface energy parameters for each sample.

Sample ID	Sa	Ra	γ^p	γ^D	γ^T	Surface Oxygen Content	Contact Angle
AR	0.126 μm	0.029 μm	17.69 mJm^{-2}	29.66 mJm^{-2}	47.34 mJm^{-2}	13.26 %at.	56.4 ⁰ ±1.2 ⁰
T50	0.636 μm	0.148 μm	12.24 mJm^{-2}	28.63 mJm^{-2}	40.87 mJm^{-2}	14.33 %at.	66.0 ⁰ ±4.0 ⁰
T100	0.297 μm	0.185 μm	16.86 mJm^{-2}	29.83 mJm^{-2}	46.69 mJm^{-2}	14.05 %at.	57.5 ⁰ ±2.4 ⁰
H50	0.423 μm	0.103 μm	10.93 mJm^{-2}	31.64 mJm^{-2}	42.58 mJm^{-2}	14.99 %at.	65.8 ⁰ ±2.9 ⁰
H100	0.326 μm	0.155 μm	13.63 mJm^{-2}	30.37 mJm^{-2}	44.00 mJm^{-2}	14.84 %at.	62.2 ⁰ ±2.3 ⁰

3.3 Effects of CO₂ laser patterning on simulated body fluid (SBF) response

From the SEM images (see Figure 2) it was observed that only a very small amount of sediment was present on the as-received samples (see Figure 2(a)) in comparison to the other samples which had undergone CO₂ laser patterning (see Figures 2(b) – (e)). This was also confirmed by weighing the samples before and after the immersion in SBF as can be seen in Figure 3. That is, the laser patterned samples weighed at least 0.008 g more than compared to the as-received sample. Following on, it can be extrapolated from this that through CO₂ laser patterning of nylon 6,6, the ability to promote the formation of an apatite layer can be sufficiently improved.

From the contact angle results given in Table 2 and the difference in mass shown in Figure 3, it is possible to ascertain that an increase in contact angle has appeared to have a more positive impact on apatite response. What is more, this enhancement in the promotion of apatite layers forming could also be attributed to the significant increase in surface roughness.

Through EDX analysis, it was found that following the formation of the apatite crystals, phosphorous and calcium was present on the surface of the nylon 6,6 samples. This is of importance due to phosphorous and calcium having to be present in order for an apatite to form which would inherently increase the bioactivity of the material. The sediments analysed also incorporated sodium, magnesium and chlorine which had all been present in the SBF and indicates that these elements would also make up some of the apatite layer formed.

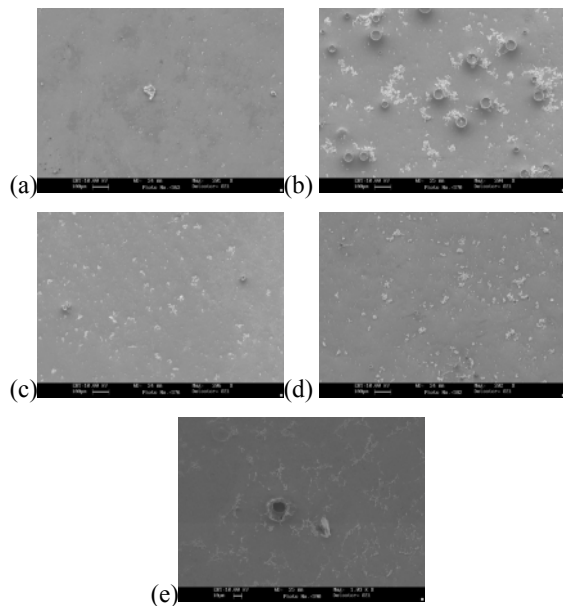


Fig. 2. SEM images of (a) AR, (b) T50, (c) T100, (d) H50 and (e) H100 after immersion in SBF for 14 days.

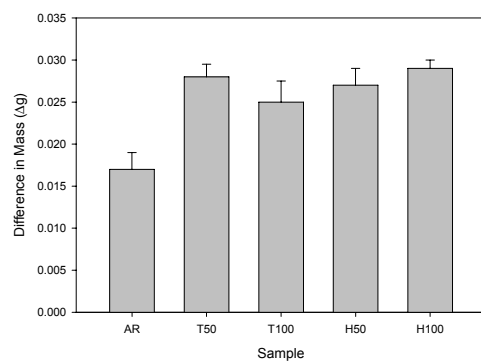


Fig. 3. Difference in mass before and after immersion in SBF for all samples.

4. Conclusions

It has been shown through experimentation that a relatively inexpensive CO₂ laser marker has the ability to significantly modify the surface properties of nylon 6,6. For instance, the characteristic contact angle increased for the laser patterned samples increased by up to +10° in comparison to the as-received sample. This can be explained by the likelihood of a mixed-state wetting regime which arises through the patterning of the material surface. What is more, the surface modifications have also been seen to have a positive impact on the formation of apatite layers under immersion in simulated body fluid (SBF), implying that enhanced osteoblast cell response can be achieved using CO₂ laser surface treatment when compared to the as-received sample.

Acknowledgements

The authors would like to thank their collaborators: Directed Light Inc., East Midlands NHS Innovation Hub, Nobel Biocare and Photomachining Inc. for all of their much appreciated support. The authors greatly acknowledge Chemical Engineering, Loughborough University for use of their biological laboratory. This study is also financially supported by the EPSRC (EP/E046851/1).

References

- [1] Nagano M, Kitsugi T, Nakamura T, Kokubo T, Tanahashi M, (1996) Bone bonding ability of an apatite-coated polymer produced using a biomimetic method: A mechanical and histological study *in vivo*. *Journal of Biomedical Materials Research* 31:487-494.
- [2] Waugh DG, Lawrence J, Morgan DJ, Thomas CL, (2010) Interaction of CO₂ laser-modified nylon with osteoblast cells in relation to wettability. *Materials Science in Engineering C* 29:2514-2524.
- [3] Benson RS, (2002) Use of radiation in biomaterials science. *Nuclear Instruments and Methods in Physics Research B* 191:752-757.
- [4] David C, Wei J, Lippert T, Wokaun A, (2001) Diffractive grey-tone phase masks for laser ablation lithography. *Microelectronic Engineering* 57-58:453-460.
- [5] Zhao Q, Wang C, Liu Y, Wang S, (2007) Bacterial adhesion on the metal-polymer composite coatings. *International Journal of Adhesion & Adhesives* 27:85-91.
- [6] Chu PK, (2007) Enhancement of surface properties of biomaterials using plasma-based technologies. *Surface and Coatings Technology* 201:8076-8082.
- [7] Hao L, Lawrence J, (2005) *Laser Surface Treatment of Bio-Implant Materials*. New Jersey, USA: John Wiley & Sons Inc.
- [8] Roach P, Eglin D, Rohde K, Perry CC, (2007) Modern biomaterials: a review-bulk properties and implications of surface modifications. *Journal of Materials Science: Materials in Medicine* 18:1263-1277.
- [9] Jung YC, Bhushan B, (2007) Wetting transition of water droplets on superhydrophobic patterned surfaces. *Scripta Materialia* 57:1057-1060.
- [10] Song W, Jun YK, Han Y, Hong SH, (2004) Biomimetic apatite coatings on micro-arc oxidized titania. *Biomaterials* 25:3341-3349.
- [11] Daddin S, (2002) Surface modification of LDPE film by CO₂ pulsed laser irradiation. *European Polymer Journal* 38:2489-2495.
- [12] Zhang J, Kang J, Hu P, Meng Q, (2007) Surface modification of poly(propylene carbonate) by oxygen ion implantation. *Applied Surface Science* 253:5436-5441.
- [13] Jung YC, Bhushan B, (2006) Contact angle, adhesion and friction properties of micro- and nanopatterned polymers for superhydrophobicity. *Nanotechnology* 17:4970-4980.
- [14] Lee SM, Kwon TH, (2007) Effects of intrinsic hydrophobicity on wettability of polymer replicas of a superhydrophobic lotus leaf. *Journal of Micromechanics and Microengineering* 17:687-692.

Fast parallel diffractive multi-beam laser surface micro-structuring

Z. Kuang¹, D. Liu¹, W. Perrie¹, J. Cheng¹, S. P. Edwardson¹, G. Dearden¹, K. G. Watkins¹

¹ Laser Group, Department of Engineering, University of Liverpool, L69 3GH, UK.

Abstract. Fast parallel short pulsed laser surface micro-structuring is demonstrated using a spatial light modulator (SLM). Multiple independently controllable femtosecond and picosecond processing beams have been generated and complex parallel surface micro-structuring demonstrated on a number of materials. In addition, high-throughput processing is demonstrated by combining a high repetition rate picosecond laser output, 2.5W at 1064 nm and repetition rate of 20 kHz with $P > 1.2W$ diffracted into 25 parallel beams. This has the effect of creating an “effective” repetition rate of 500 kHz without restrictive scan speeds.

Keywords: SLM, parallel processing, Femtosecond laser, Picosecond laser.

1. Introduction

Laser surface micro-structuring of materials (e.g. metals and semi-conductors) with ultrashort laser pulses can demonstrate high precision with little thermal damage due to the ultrafast timescale in which energy is coupled to the electronic system [1, 2]. In metals, this reduces heat diffusion during the temporal pulse length to the nanometer scale, comparable to the optical skin depth, provided the fluence F is kept in the low regime, where $F < \sim 1 \text{ J cm}^2$ [4, 5]. Consequently, the pulse energies used at low fluence for micro- and nano-structuring are often $< 10 \text{ mJ}$ while high gain regenerative amplifier systems running at $\sim 1 \text{ kHz}$ repetition rate provide mJ level output pulse energies. The need to highly attenuate the output beam can have a severe limit on potential throughput. This restriction may be one of the reasons why industrial uptake of kHz femtosecond systems has been limited.

Spatial light modulators (SLM) are a dynamic diffractive optical element which can modulate the phase of an incoming wavefront. By applying a computer generated hologram (CGH) to the SLM, one can transform the incident beam intensity distribution (e.g. Gaussian) into that desired for micro-manipulation, for example, in multi-trapping of micro-particles in optical tweezers [5, 6], or material micro-processing first demonstrated recently by Hayasaki et al. [7, 8]. The ability to address these devices in real time and

synchronize with the scanning method adds an additional flexibility for surface micro-structuring [9-11]. Here, we demonstrate parallel processing of a surface with arbitrary multiply diffracted spots through the application of CGHs.

2. Experiments

The experiments were conducted using a Clarke-MXR CPA2010, with 160 fs pulsewidth, 775 nm central wavelength, 1 mJ pulse energy, 1 kHz repetition rate and a High Q IC-355-800 Nd:VAN regeneratively amplified picosecond (ps) laser system with a pulse duration of 10 ps, wavelengths of 355, 532 and 1064 nm and repetition rate of 5 ~ 50kHz.

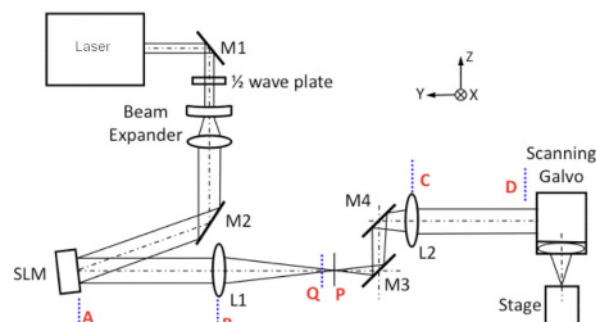


Fig. 1. Experimental setup (M1, M2, M3, M4: mirrors, L1, L2: lenses, D: the plane where the light field at A was reconstructed; Q: target to block zero order; P: the focal plane of L1 and L2)

The experimental setup is schematically shown in Fig. 1. The Gaussian laser beam was reflected by mirrors M1 and M2, and then expanded to 6 mm diameter using $\times 3$ beam expander before reflection from the SLM liquid crystal device. The diffracted beam was imaged from the surface (Plane A) of the SLM to the entrance (Plane D) of the scanning galvanometer with a 4f optical system, where distance $AD = 4f$ and distance $AB = BP = PC = CD = f = 300 \text{ mm}$. The undiffracted zero order

component was separated from the higher order beam and blocked by a small target at Plane Q.

Therefore, only the diffracted beam entered the scanning galvanometer and was focused by a flat field f-theta lens with $f = 100$ mm. An Aerotech computer-controlled 5-axis stage (x , y , z and a goniometer) was used in order to enable accurate positioning. By synchronizing the scanning galvanometer with the stage, a large sample could be processed, providing great flexibility and accuracy. An optical microscope with Nikon Digital Sight camera system and a white light interferometer from Veeco (WYKO NT1100) were used to analyze the ablated samples.

Two SLMs were used in this study, Hamamatsu X10468-04 and Holoeye LC-R2500. These are both pixelated electrically addressed reflective SLMs. It is worth noting that the X10468-04 has a dielectric mirror, for 1064nm, which provides 95% light utilization efficiency, but can only work with a specified wavelength range. By comparison, the LC-R2500 is equipped with a metallic coated mirror that offers lower light utilization efficiency around 75%, but covers a wide wavelength range from visible to near infrared (NIR).

In order to generate high quality fast computer-generated holograms (CGHs), the iterative Fourier transform based on the Gerchberg-Saxton (GS) algorithm [6] and weighted Gerchberg-Saxton (GSW) algorithm [12] were performed within a LabView environment [5].

Different materials such as silicon and Ti6Al4V were employed in the study.

3. Results and Discussion

Fig. 2 demonstrates the control of the SLM device to give multiple processing spots. It can be seen that a CGH can be generated from a simple binary image to produce a diffractive spot pattern around the zero order spot at the centre on Ti64. This zero order can then be removed by inserting a block at point Q in fig. 1.

While static holograms are useful, processing by real time control of the CGHs is demonstrated in Fig. 3. This shows a pattern comprising 121 holes completed by real time playing of 15 stored CGHs at 20 Hz refresh rate, and demonstrates the formation of the pattern which was completed within 0.75 s. The incident pulse energy on the SLM was $E_p \sim 300$ mJ.

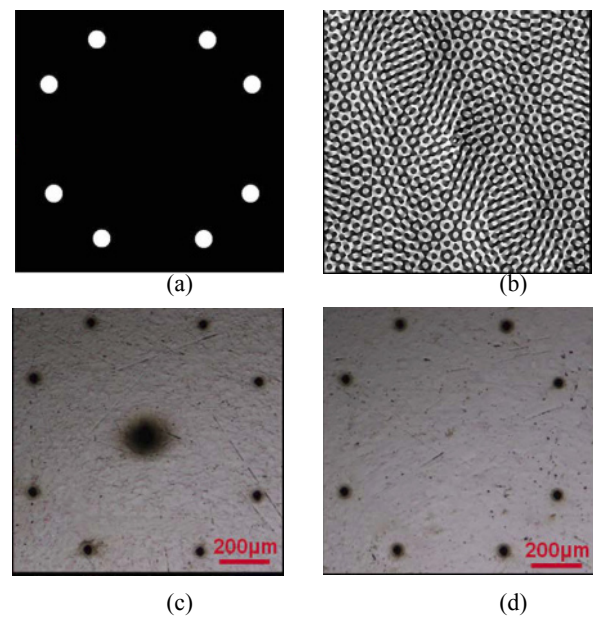


Fig 2. Control of the SLM. a) binary image of geometry, b) GCH, c) Result on Ti64 d) Removal of zero order.

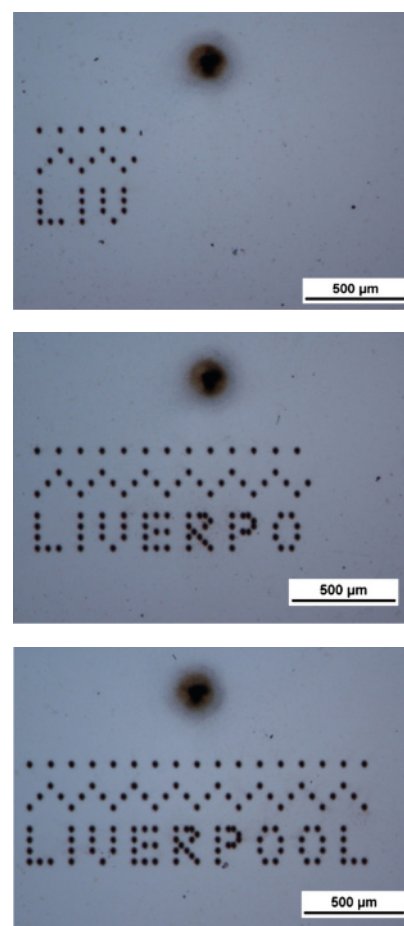


Fig 3. Pattern completed by real time playing 15 series of CGHs at 20 Hz refresh rate (50 ms duration per CGH).

Control of the CGHs can be combined with the galvo system to demonstrate parallel processing with fixed spot geometry. However, the symmetry of the position of multiple beams can greatly affect the intensity distribution across all beams [13]. Fig. 4 (a) shows a common multi-beam pattern with perfect symmetry for parallel processing, however, the symmetric multibeam suffers from low intensity uniformity even using iterative algorithms like GS (~60%). One approach to solve this problem is to introduce a small amount of random displacement to the multi-beam pattern, since for most algorithms such as GS, lenses and gratings and generalized adaptive additive, spatial randomisation can significantly reduce intensity variation [13]. Another method is to use the GSW algorithm, which can obtain >90% uniformity even with a symmetric pattern. However, the calculation speed of GSW is slower than that of GS.

Here, the first method was adopted. The beams were slightly misaligned in the Y direction, but kept the same separation in the Z direction, as shown in Fig. 4 (b), in order to optimize energy distribution across the multibeam.

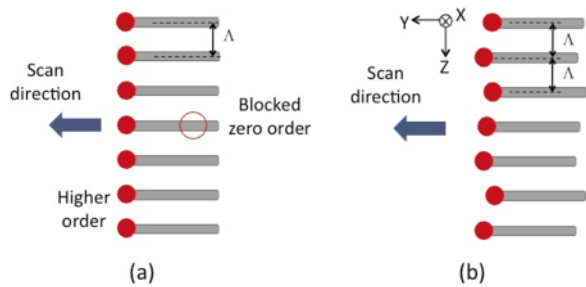


Fig. 4. Schematics of (a) a symmetric multi-beam pattern and (b) an asymmetric multi-beam pattern for parallel processing.

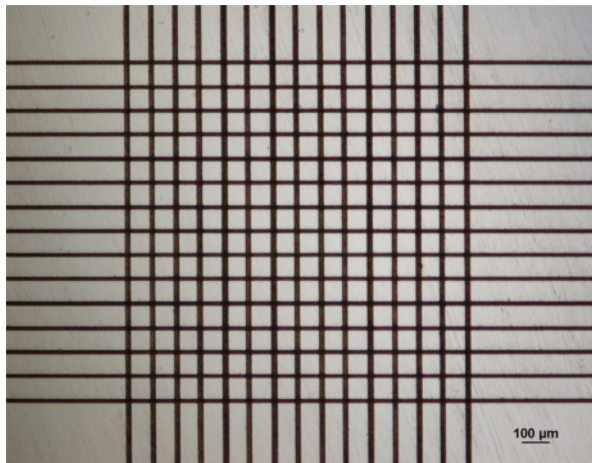


Fig. 5. 15 beams parallel processing of silicon sample.

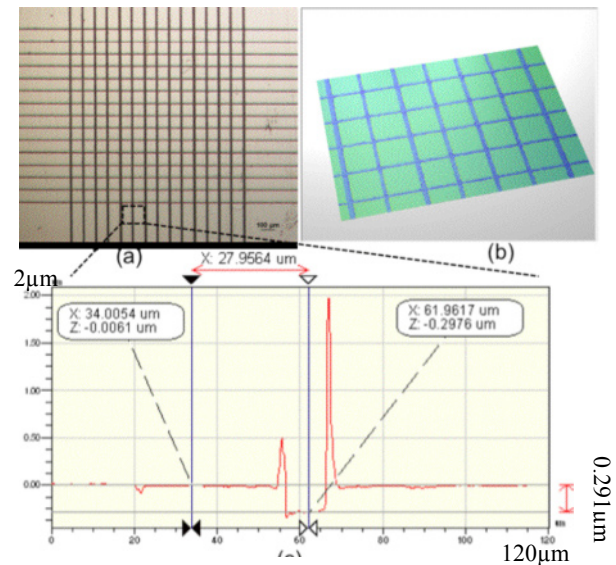


Fig. 6. Parallel processing of Silicon using 15 beams. (a) Optical micrographs; (b) 3D surface profile; (c) Cross-sectional profile of a single line.

Fig. 5 shows the microscopic image of the silicon sample that was scribed using 15 asymmetric beams, as depicted in Fig. 4 (b), produced using the X10468-4 SLM at 532 nm wavelength, 10ps pulse length and 5kHz repetition rate. The 15 beams with total incident pulse energy of 21 μJ , (1.4 $\mu\text{J}/\text{pulse}/\text{beam}$) were scanned orthogonally with two CGHs at 10 mm/s to produce the cross hatched pattern. As can be seen in Fig 6, the scribe lines are ~ 500 nm deep and 14 μm wide, while the pitch was 86 μm . Adjusting the CGH can control the pitch, and applying lower laser pulse energies reduces the scribe width. No thermal damage to the surrounding area was observed.

By combining real time control of the CGHs with scanning, diffractive multi-beam processing has significant potential to produce complex surface micro-machining patterns. Fig. 7(a) and (b) illustrates this on a polished Ti6Al4V substrate where 6 micro-channels, a-f were generated by applying the appropriate CGHs at 50 Hz refresh rate while simultaneously scanning the diffracted spots at a speed of 1 mm/s. The resulting micro-channels a-f are ~40 μm wide and ~10 μm deep. The large channel above, again is due to the zero order (which can be blocked). Ti6Al4V, which is a metallic alloy widely used in aerospace and bioscience, has a relatively low ablation threshold (0.1 J/cm^2) hence the advantages of diffractive multi-beam processing are demonstrated as extensive attenuation was largely avoided.

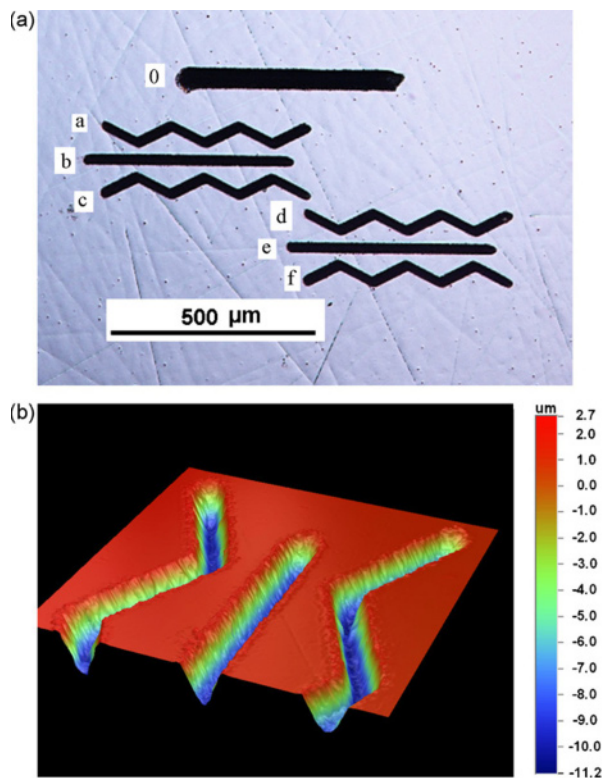


Fig. 7. Micro-channels obtained by combining CGHs real time control with galvo scanning. (a) Whole pattern view (5x objective); 6 channels a–f were generated by the diffractive beams while the wider channel 0 above was formed by zero order beam and (b) 3D larger zoom view by Wyko NT1100 optical surface profiler, where 10 mm deep (10 times over scan).

4. Conclusions

The results obtained demonstrate that precision diffractive multi-beam ultrafast laser micro-structuring using an SLM is a novel method to increase processing throughput.

Synchronizing of hologram application with scanning techniques can produce complex 2 and 3D structures.

High speed parallel and selective patterning has demonstrated production methods with high throughput, great flexibility and excellent precision, a potentially important step in the high speed processing of materials. Future work such as optimization of CGH calculation, true synchronisation and high power processing will be carried out.

Acknowledgments

The authors gratefully acknowledge the support of the North West Development Agency (NWDA) and Technology Strategy Board (TSB), through project PARALASE.

References

- [1] X. Liu, D. Du, G. Mourou, Laser ablation and micromachining with ultrashort laser pulses, *IEEE J. Quant. Electron.* 33 (1997) 1706–1716.
- [2] B.N. Chichkov, C. Momma, S. Nolte, F. von Alvensleben, A. Tunnermann, Femtosecond, picosecond and nanosecond laser ablation of solids, *Appl. Phys. A* 63 (1996) 109–115.
- [3] R. Le Harzic, D. Breitung, M. Weikert, S. Sommer, C. Fohl, S. Valette, C. Donnet, E. Audouard, F. Dausinger, Pulse width and energy influence on laser micromachining of metals in a range of 100 fs to 5 ps, *Appl. Surf. Sci.* 249 (2005) 322–331.
- [4] W. Perrie, M. Gill, G. Robinson, P. Fox, W. O'Neill, Femtosecond laser microstructuring of aluminium under helium, *Appl. Surf. Sci.* 230 (2004) 50–59.
- [5] J. Leach, K. Wulff, G. Sinclair, P. Jordan, J. Courtial, L. Thomson, G. Gibson, K. Karunwi, J. Cooper, Z.J. Laczik, M. Padgett, Interactive approach to optical tweezers control, *Appl. Opt.* 45 (2006) 897–903.
- [6] G. Sinclair, J. Leach, P. Jordan, G. Gibson, E. Yao, Z. Laczik, M. Padgett, J. Courtial, Interactive application in holographic optical tweezers of a multi-plane Gerchberg–Saxton algorithm for three-dimensional light shaping, *Opt. Express* 12
- [7] Y. Hayasaki, T. Sugimoto, A. Takita, N. Nishida, Variable holographic femtosecond laser processing by use of a spatial light modulator, *Appl. Phys. Lett.* 87 (2005) 031101.
- [8] H. Takahashi, S. Hasegawa, Y. Hayasaki, Holographic femtosecond laser processing using optimal-rotation-angle method with compensation of spatial frequency response of liquid crystal spatial light modulator, *Appl. Opt.* 46 (2007) 5917–5923.
- [9] Z. Kuang, W. Perrie, J. Leach, M. Sharp, S. P. Edwardson, M. Padgett, G. Dearden and K. G. Watkins, *Appl. Surf. Sci.* 255, (2008) 2284–2289
- [10] Z. Kuang, D. Liu, W. Perrie, S. P. Edwardson, M. Sharp, E. Fearon, G. Dearden and K. G. Watkins, *Appl. Surf. Sci.* 255, 13–14, (2009) 6582–6588,
- [11] Z. Kuang, W. Perrie, D. Liu, S. P. Edwardson, J. Cheng, G. Dearden, K. G. Watkins, (2009) *Applied Surface Science*, 255, 2009, p. 9040–9044
- [12] R. D. Leonardo, F. Ianni, and G. Ruocco, *Opt. Express* 15, (2007) 1913–1922.
- [13] J.E. Curtis, C.H.J. Schmitz, J.P. Spatz, Symmetry dependence of holograms for optical trapping, *Opt. Lett.* 30 (2005) 2086–2088.

Effect of different processing parameters of Ti: Sapphire femtosecond laser on human dental dentine

Lingfei Ji^{1,2}, Lin Li¹, Hugh Devlin³, Zhu Liu⁴, David Whitehead¹, Zengbo Wang¹, Wei Wang¹, and Jiao Jiao¹

¹ Laser Processing Research Centre, School of Mechanical, Aerospace and Civil Engineering, University of Manchester, Sackville Street, Manchester M60 1QD, United Kingdom

² Institute of Laser Engineering, Beijing University of Technology, Beijing 100022, People's Republic of China

³ School of Dentistry, The University of Manchester, Higher Cambridge Street, Manchester, M15 6FH, UK

⁴ Corrosion and Protection Centre, School of Materials, University of Manchester, The Mill, Manchester M60 1QD, United Kingdom

Abstract. The process of dentine removal by ultra-short pulse laser is a promising technique for pain-free dental restoration. The aim of this work was to analyze the characteristics of human dentine ablated by a fs-laser of 800 nm wavelength and 1 kHz repetition rate. Precise ablation with clear boundary whereas without cracks and debris can be obtained. The transmittance of the dentine tissue was about 2.7% and the absorption coefficient was about 3.19 cm^{-1} at 800 nm. The processed morphology, especial for heat-affected zones, of the dentine was investigated over wide ranges of laser fluences and pulse numbers. The fluence threshold results of dentine were determined as 0.45 J/cm^2 according to the experimental dependence of the ablated depth versus laser fluence. The heat and energy conducting effects of dentine tubules, which is the feature structure, were analyzed by Scanning Electron Microscopy and Wyko Optical Profiling System. The finding of Raman mapping analysis of phosphate indicated that the chemical components and structure of the dentine remained intact before and after ablation. This study confirmed the potential of fs-laser precision micro-fabrication in dentistry.

Keywords: fs-laser ablation; dentin; heat-affected zone

1. Introduction

Basing on plasma-induced ablation which is believed to achieve accurate and painless treatment of tooth, the application of ultra-short pulse (USP) lasers (pulse length $< 100 \text{ ps}$) technology for dentine removal has been demonstrated to be promising during the last few years [1-8]. Due to the limitation of mode-locking technique, previous studies are mainly on the nano-, subpico- and picosecond (ps) laser ablation of human tooth as well as a comparative analysis among them [7, 9, 10]. Processing with femtosecond pulses affords considerable advantages over nanosecond pulses, such as nanoselective removal, where ablated spot dimensions are below that achieved when longer pulses are focused to the minimum spot size dictated by optical physics. It is well-established that fs-

laser treatment reduces thermal and shockwave effects compared with nano- or picosecond laser ablation because of its shorter pulse width. In the research on the effect of laser focusing position on the ablation of enamel and dentine, optical focal position was determined that gave the minimum hole diameter [11, 12]. A more detailed study on the interaction between fs-laser and hard tooth tissue under different processing conditions is necessary for the practical applications of fs-laser treatment in dentistry.

In the present paper, a Ti:Sapphire fs-laser with a 1 kHz repetition rate was used in the ablation of dentine experiments. The ablation characteristics on dentine with different fs-laser processing parameters were analyzed.

2. Experimental

In order to determine the intrinsic effects of fs-laser ablation on dentine without other interference from caries or soft residue, the whole extracted teeth were sterilized and rinsed in a 25% hydrogen peroxide solution, and then subjected to ultrasonic cleaning with pure water and ethanol. Each tooth was sectioned longitudinally by a diamond saw microtome (Struers Accutom-5).

A Coherent Libra fs Ti:Sapphire amplifier with 800 nm (NIR) wavelength, TEM00 beam mode and $< 100 \text{ fs}$ pulse length was focused on the surface of dentine with a focal spot of $\sim 30 \mu\text{m}$ diameter. Single pulse and multiple pulse ablation at various laser fluences from 0.2 J/cm^2 to 3.68 J/cm^2 was carried out. The output frequency of the system was fixed at 1 kHz. The output power can be varied from 1 mW to 1 W via the use of a polarisation attenuator. The interval distance between each laser spot was 0.10 mm in row and 0.35 mm in column to ensure enough space to avoid ablation interference with each

other. The layout of the laser spots and the laser irradiation time (the input pulse number) were realized by the execution of G-code program. Ablation threshold was determined with a single pulse so as to reduce the negatively cumulative effects of heat and shockwave due to multiple pulse inputs. The details of the ablated site morphological characteristics and heat affected zones (HAZ) were examined by Scanning Electron Microscopy (SEM) and Wyko Optical Profiling System (Wyko, Veeco, NT 1100-2). Laser Scanning Con-focal Microscope (LSCM, Olympus, OLS 3000) was used to examine and measure the morphology and the depth of the ablated profile. The element analysis of the un-ablated and the ablated tissue were measured by Raman mapping.

3. Results and Discussion

Results obtained from the optical spectrum measurements, the transmittance of dentine at 800 nm was less than 15%, whereas, the absorbance values of the hard tissue was 0.383. With a thickness of 1.2 mm of the measured section samples, the absorption coefficient of dentine was determined to be 3.19 cm^{-1} at 800 nm, which is the maximum among those of three hard tissues of human teeth: enamel, dentine and cementum.

The ablation rates as function of the laser fluences corresponding to dentine is depicted in Fig. 1 by measuring the ablation depth under different laser power of 4, 8, 11, 15, 26 and 41 mW. The laser fluences were scaled logarithmically, giving a nearly linear dependence of the ablation rate. By extrapolating the experimental dependence of the ablated depth versus laser fluence to the 'zero' depth, the data for ablation thresholds of dentine can be deduced as 0.45 J/cm^2 .

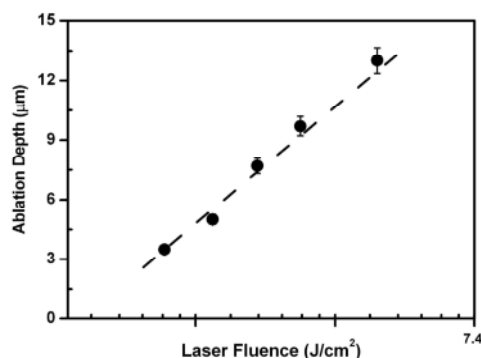


Fig. 1. Ablation rates as a function of laser fluences corresponding to dentine.

For all ablated samples, the material removal remains localized in the area of laser spot, lower fluence of 1.13 J/cm^2 with a single shot was found enough to fabricate a hole with clearer boundary matching to the beam section (Fig. 2a). With the increase of pulse number under the

same laser fluence, the depth increased obviously with (Fig. 2b). No melted material or detritus from the ablation or surface cracks or fissures around or from the holes were evident.

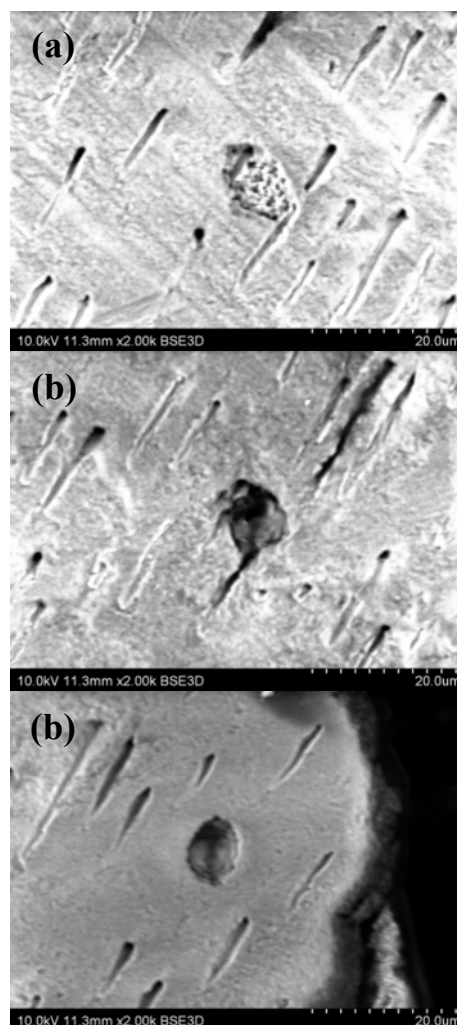


Fig. 2. SEM microscopy of femtosecond laser ablation of human dentine

Dentin has more weight percentage of organic material and has a very porous structure, in comparison with other dental hard tissues. Under equal laser fluences, the ablation should become easier owing to more evaporation of organic matter and water. However, the transmission of the input energy would show a "non-uniform effect" because of the non-uniform resistance coming from the mass distribution of dentine tubules with high mineral content lacking of collagen. The preferential ablation in dentine existed which was observed by comparison of Fig. 2(b) and Fig. 2(c). The ablated site in Fig. 2(b) was on the dentine tubule zone while that ablated with the same laser parameters in Fig. 1(c) was out of the tubule zone. The enlarged ablation effect parallel to the surface in Fig. 1(b) derived from the broken-open dentine tubules

with several-nanometer in diameter and several-micrometer in length can be observed. It indicated that the characteristics of fs-laser ablation on dentine not only depends on the laser parameters but also on the particular composite structure.

In Fig. 3, a crack has developed on surface near the ablated hole, which was probably caused by mechanical shock during drilling. The hole edge near the crack (left) and the crack edge (right) are sharply defined by clear boundary without micro-cracks developing from or along the crack, which shows the inhibition of heating and shockwave affect of fs-laser ablated spot in dentine was notable. Surface data of the holes on the dentine were measured by Wyko, and the surface roughness Ra is below 2 μm .

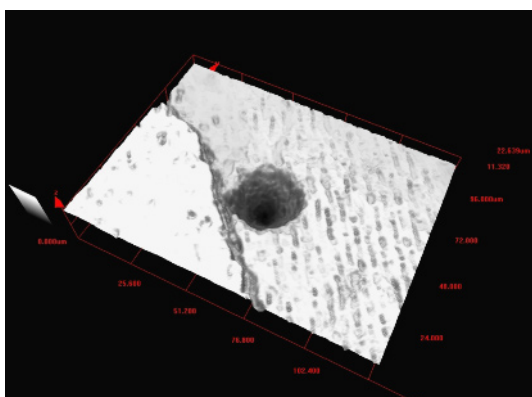


Fig. 3. LSCM micrograph of the fs-laser ablated dentine surface.

Analyses of mineralized tissues and calcified materials using Raman spectroscopy have demonstrated that a phosphate (PO_4^{3-}) vibrational mode was indicated by a strongest peak at 960 cm^{-1} . The Raman mapping image of phosphate from the un-ablated region to the ablated region, which was marked by the red line in Fig. 4, was carried out for the analysis of elements.

From Fig. 4, the most intense peaks at 960 cm^{-1} of the phosphate symmetric stretching vibrational mode (ν_1) in the Raman spectrum of dentine substance were observed. The results of Raman scattering showed that the Raman relative intensity of dentine did not changed significantly by fs-laser ablation. Phosphate did not decompose from the dentine substance in the ablated areas. The results provide direct evidence that fs-laser ablation does not affect the chemical composition of dentine tissues which is beneficial for the biomaterial to remain intact of the chemical components and structure.

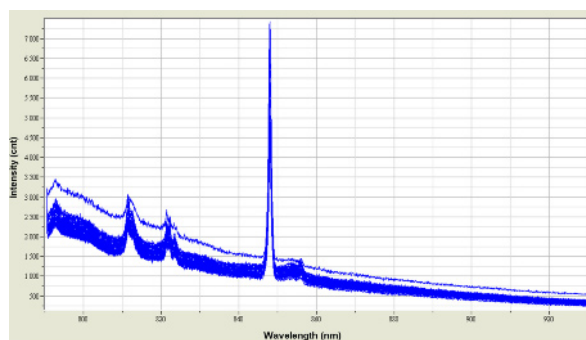


Fig. 4. The Raman mapping spectra of phosphate of the fs laser ablated and ablated region in dentine.

4. Conclusion

For the fs-laser ablation of dental hard tissues, we have investigated the ablation with single pulse under a medium fluence of 2.12 J/cm^2 , multipulses under lower fluence of 1.13 J/cm^2 and several pulses (3 pulses) under higher fluence of 3.68 J/cm^2 . Well-defined holes with minimal heat affected zone (HAZ) ablated in dentine tissues were obtained. The threshold results of fs-laser ablation in dentine tissue were determined to be 0.45 J/cm^2 . Ablation efficiency was illustrated by the curve of ablation depth as a function of laser fluence. Because of the slight discrepancy of the thermal conductivity and diffusivity caused by the heterogeneity of dentine entity, it should be normal that there is some difference on the hole geometry in different region even under the same laser ablation conditions. The potential of fs-laser precise ablation in dental was demonstrated and confirmed.

Nevertheless, according to the present study, it also appears that the characteristics of fs-laser ablation on dental tissues depends not only on the laser parameters, but also on the particular composite structure, the thermal and mechanical properties of the biomaterial. Additional studies are required not only for designing the potential laser systems, but also for optimizing the processing method as well as better understanding of the mechanisms of action. The dental structure influences, even the chemical dependence, must be taken into account in laser interaction with the dental materials. In the current case that ablation conditions (e.g. ablation threshold, ablation efficiency and focus position giving minimum diameter) are demonstrated. There are still many problems demanding prompt solution even in the experimental use of USP lasers in dentistry. For example, how to improve the geometry of the fs-laser ablated tapered hole and how to control the focusing distance real-time on uneven surface of the tooth are both points of them.

References

- [1] Niemz, Markolf H, (1995) Ultrashort laser pulses in dentistry: advantages and limitations. *SPIE Vol. 3255:84-91*
- [2] Reza B, Jamshid P, Norbert G, Friedrich L, Maziar M, (2007) Comparative evaluation of the effects of Nd:YAG and Er:YAG laser in dentin hypersensitivity treatment. *Lasers Med. Sci. 22:21-24*
- [3] Tielemans M, Compere Ph, Geerts SO, Lamy M, Limme M, Moor De RJG, Delmé KIM, Bertrand MF, Rompen E, Nammour S, (2009) Comparison of microleakages of photo-cured composites using three different light sources: halogen lamp, LED and argon laser: an in vitro study. *Lasers Med. Sci. 24:1-5*
- [4] Serbin J, Bauer T, Fallnich C, Kasenbacher A, Arnold WH, (2002) Femtosecond lasers as novel tool in dental surgery. *Appl. Surf. Sci. 197-198:737-740*
- [5] Tetsuo I, Yoshio H, Keiji F, Kan N, Masayo M, Takanori K, JianRong C (2006) Femtosecond pulse laser-oriented recording on dental prostheses: a trial introduction. *Dent. Mater. J. 25(4):733-736*
- [6] Serafetinides AA, Khabbaz MG, Makropoulou MI, Kar AK (1999) Picosecond laser ablation of dentine in endodontics. *Lasers Med. Sci. 14:168-174*
- [7] Lüko W, Andrea H, Mark HN, Thomas P (1996) Preparation of dental hard tissue with picosecond laser pulses. *Lasers Med. Sci. 11:45-51*
- [8] Wolfgang K, Jörg K (1994) Femtosecond pulse laser ablation of metallic, semiconducting, ceramic, and biological materials. *SPIE Vol. 2207:600-611*
- [9] Rode AV, Madsen NR, Kolev VZ, Gamaly EG, Luther-Davies B (2004) Subpicosecond and picosecond laser ablation of dental enamel: comparative analysis. *Commercial and Biomedical Applications of Ultrafast Lasers IV. Proceedings of SPIE Vol. 5340:76-86*
- [10] Krüger J, Kautek W, Newsely H (1999) Femtosecond-pulse laser ablation of dental hydroxyapatite and single-crystalline fluoroapatite. *Appl. Phys. A 69[Suppl.]:S403-S407*
- [11] Lizarelli RFZ, Costa MM, Carvalho-Filho E, Nunes F D, Bagnato VS (2007) Selective ablation of dental enamel and dentin using femtosecond laser pulses. *Laser Phys. Lett. 5:63-69*
- [12] Lizarelli RFZ, Costa MM, Carvalho-Filho E, FD Nunes, Bagnato VS (2007) Selective ablation of dental enamel and dentin using femtosecond laser pulses. *Laser Phys. Lett. 5:63-69*

Forming microchannels on a glass substrate by CO₂ laser

Z. K. Wang¹, H. Y. Zheng^{1*}, V. C. Tan² and C. Y. Lam²

¹ Singapore Institute of Manufacturing Technology (SIMTech), 71 Nanyang Drive, Singapore, 638075

² School of Mechanical & Aerospace Engineering, Nanyang Technological University, 50 Nanyang Avenue, Singapore 639798

* Corresponding author: hyzheng@simtech.a-star.edu.sg, Tel: +65 -67932450 Fax: +65 -67916377

Abstract. A continuous strip of glass layer can be directly peeled off by a single scan of a CO₂ laser beam over a soda lime glass substrate at a high speed. A new process parameter - laser energy line-deposition rate (abbreviated as LELDR hereafter, the amount of energy per unit length per unit time), has been introduced to guide the selection of laser power and scan speed for the glass stripping process. It was found that continuous glass strips were formed when LELDR ranged from 0.002 mJ/mm/s to 0.004 mJ/mm/s. The channels were free of cracks with sizes from 20 μm to 40 μm in depth and from 200 μm to 280 μm in width. When LELDR exceeded 0.005 mJ/mm/s, cracks were observed along the laser beam path on the glass. When LELDR were below 0.0015 mJ/mm/s, a cracking belt was formed.

Keywords: CO₂ laser, glass machining, micromachining, microchannel.

1. Introduction

Microchannels are the key features of microfluidic devices [1]. Transparent glasses remain commonly used substrates for such devices because of their excellent optical property, chemical and thermal stability and ease of electro-osmotic flow [2,3], despite the trend towards the use of polymer substrates [4]. Glass channels are normally formed by wet chemical etching [2]. As wet chemical etching involves multiple steps such as photomask design and photolithography, it is time consuming and may not be the best solution for small scale production and rapid prototyping of microchannels. Laser micromachining of glass is considered as a promising technique due to its significant process flexibility and direct writing by integrating CAD/CAM software.

In earlier work, it was reported that a continuous strip of glass was peeled off along the moving path of a CO₂ laser beam and thus created grooves on borosilicate glass and soda lime glass [5]. The current paper reports investigations of laser processing

conditions to allow for “peeling off” of the glass strip to form designed microchannels on soda lime glass.

2. Experimental

A commercially available 1.1 mm thick soda lime glass substrate, microcope slide Cat No. 7101, was used and its surface was irradiated by a CO₂ laser beam (Synrad J48-2W). The laser beam has a gaussian profile in energy distribution, a power of 25 W in continuous wave (CW) mode, M² of 1.2 and diameter of 7 mm. The laser beam was focused by a F-Theta-Ronar lens of 150 mm in focal length and was scanned on the glass surface through a galvanometer scanner at a scan speed of up to 2000 mm/s.

The laser allows modulating of CW mode into pulse mode through a pulse generator, and thus the various powers were achieved and employed to study the channel forming process by adjusting the duty cycle (DC), i.e., pulse width modulation, at a fixed laser frequency of 5 kHz. A positive defocus, i.e. the focal point was 1.5 mm above the glass sample surface, was employed to reduce the possibility of crack generation due to the reduced laser energy density at the focus.

3. Results and discussion

3.1 Glass strip peeling off induced by laser irradiation

Figure 1 is a plot correlating the laser scan speed, laser pulse duty cycle and laser power density. It was observed that a continuous strip of glass layer was peeled off with a single beam scan over the moderate ranges of laser power densities and scan speeds, i.e., at low speeds and low power densities or at high speeds and high power

densities. The peeling process was characterized with an optical microscope and scanning electron microscope (SEM). Figure 2 shows optical images (Fig.2a and c) and SEM images (Fig.b, d and e) of glass strips and formed grooves. The strip thickness represents the groove depth. The grooves have clean edges and are free of cracks (Fig. 3a).

With a decrease in scan speed outside the moderate range, the glass was in molten state due to the increased beam-glass interaction, which led to cracks along the beam path in the rapid melting-solidification process (Fig.3b). In contrast, with an increase in scan speed outside the moderate range, crash-like cracks and fragments were produced along the laser irradiated belt (Fig.3c). Further increase in scan speed resulted in discontinuous, isolated cracks or fragments or no noticeable changes in the beam path as shown in Fig. 3d. This may imply that the laser power density was insufficient to cause glass stripping.

3.2 Optimal energy deposition rate to induce microchannel formation on glass substrate

To avoid a trial-and-error method in the glass stripping process, it is necessary to understand the laser thermal energy deposition with regards to the key process parameters. A laser as a thermal source deposits its energy into the glass substrate during the beam-glass interaction. The amount of thermal energy deposited into the glass is mainly controlled by the absorbed laser power and the beam-glass interaction time (i.e. the scan speed). The deposited thermal energy heats the glass to different temperatures and may cause the melting and vaporising of the glass. The temperature will be thus determined by the deposited amount of the energy and the deposition time of the energy. The two parameters combined actually expresses the energy deposition rate.

If the energy deposition rate along the beam path is defined as the amount of the energy deposited into the glass per unit length per unit time, it can be expressed as the moving velocity of energy from a single laser pulse. Thus, the plot of LELDR against the laser power (duty cycle) and power density were calculated and are shown in Fig. 4. It clearly indicates that as long as the LELDR were maintained in the range of from near 0.002 mJ/mm/s to 0.004 mJ/mm/s, microchannels free of cracks were formed on the glass substrate. At a given scan speed, high laser power input would lead to a high LELDR; and inversely low power input would lead to a low LELDR. The values of the LELDR in Fig. 4 corresponds well with the laser parameters in Fig. 1.

As the LELDR exceeded 0.005 mJ/mm/s, the glass appeared to be over-heated and was observed in molten state. Cracks were produced during the rapid solidification of the laser scanned region. When the LELDR were set below 0.0015 mJ/mm/s, a cracking belt was seen. Further reduction in the LELDR to below 0.001 mJ/mm/s resulted in non-continuous cracking due to

insufficient and inconsistent heating. Thus, LELDR may be used as a guide for choosing process parameters for glass strip peeling.

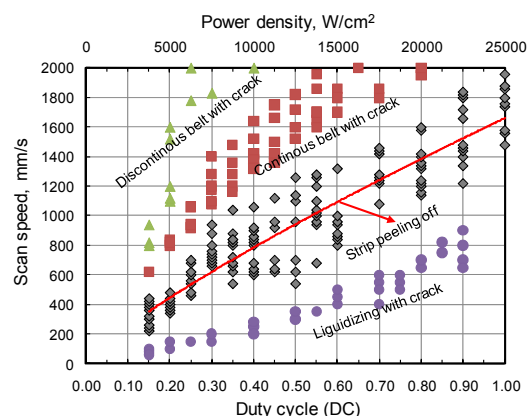


Fig. 1. Moderate ranges of laser parameters for glass strips peeling off.

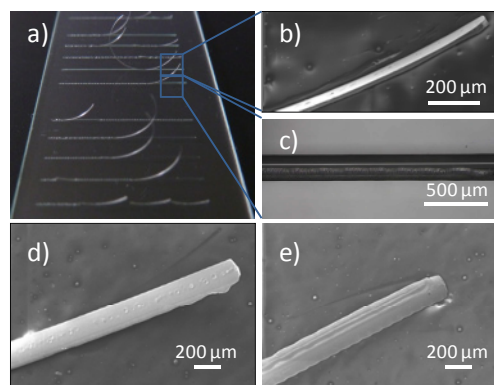


Fig. 2. CO₂ laser-induced peeling of glass strips from a soda lime slide under a laser duty cycle of 0.15 and scan speed of 240 mm/s. a) a plane view of glass strips, b) an enlarged plane view of a continuous glass strip, c) top view of a microgroove formed by glass strip peeling, d) top view of the glass strip and e) backside view of the glass strip.

It is noticed that the glass strip peeling is in a form of soft bending of a solid layer of glass (Figs. 1a and 1b). It implies that the glass layer temperature reached the glass softening point in the laser heating process. The softening of the glass layer makes it possible to deform or bend, and thus to be peeled off as a strip by contraction along the laser beam scan path without cracking. In contrast, when the glass is in the molten state, strip peeling could not occur. When the temperature is below softening point but exceeding the glass strain point, a cracking belt is produced and therefore no strip peeling can be achieved. The investigation on the relationship between LELDR and glass temperature is being studied.

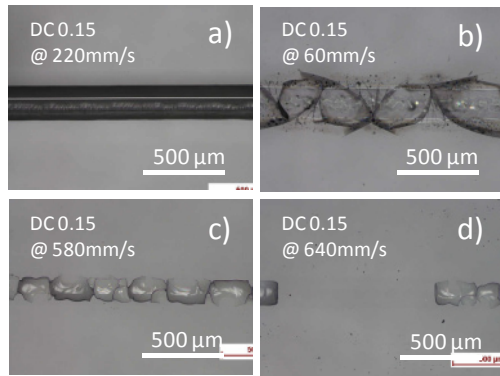


Fig. 3. Morphologies induced by laser irradiation under various scan speed ranges. a) microchannel formed by laser peeling at a moderate scan speed, b) melting with cracks at a slow speed, c) continuous cracking belt at a high speed and d) discontinuous cracking belt at a high speed.

3.3 Characterisation of the microchannel

Under the optimal laser energy deposition rates, microchannels of varying geometries were fabricated on soda lime glass substrates. The geometric dimensions of the microchannels in three-dimensions (3D) and two-dimensions (2D) were characterized using a Stylus Profilometer (Taylor-Hobson Form Talysurf Series 2). The cross-section of the channel was measured to be a U shape as shown in Fig. 5. A smooth sidewall in the channel was achieved. The part appeared to be rough and shallow at the right bottom of the channel, however, this could be caused by an asymmetric distribution of laser energy or a tilted laser beam from poorer alignment of the optics. The geometric size of the channel measured by the stylus profiler was 36 μm in depth and 220 μm in width. Under the optimal range in LELDR from 0.0018 $\text{mJ}/\text{mm}^2/\text{s}$ to 0.004 $\text{mJ}/\text{mm}^2/\text{s}$, varied channel sizes were fabricated from 20 μm to 38 μm in depth (Fig. 6) and from 200 μm to 280 μm in width (Fig. 7).

As the microchannels used in microfluidics are not only in a linear straight structure but also often in a non-linear structure, fabrication of the microchannel in a curved shape at varied radii was attempted. Furthermore, horizontally overlapping the laser beam with a certain pitch between two scans was also carried out such that a wider channel width could be achieved. For example, a 540 μm width channel was obtained by scanning with the laser beam with three overlapped passes at a horizontally shifting pitch of 150 μm . The typical profiles of the microchannels are shown in Fig. 8. Thus, it shows that the laser peeling process is a flexible and efficient method to fabricate various microchannels on glass substrate.

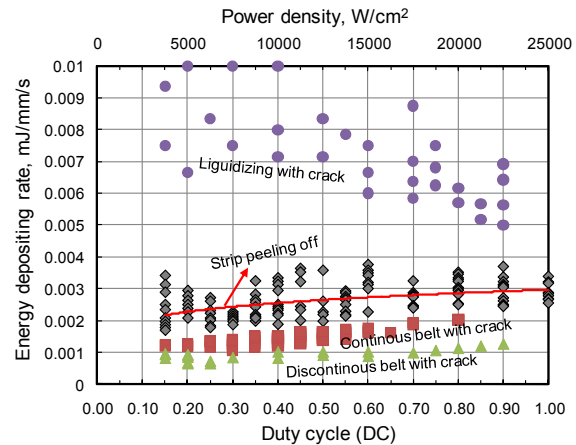


Fig. 4. Optimal LELDR for inducing strips peeling off.

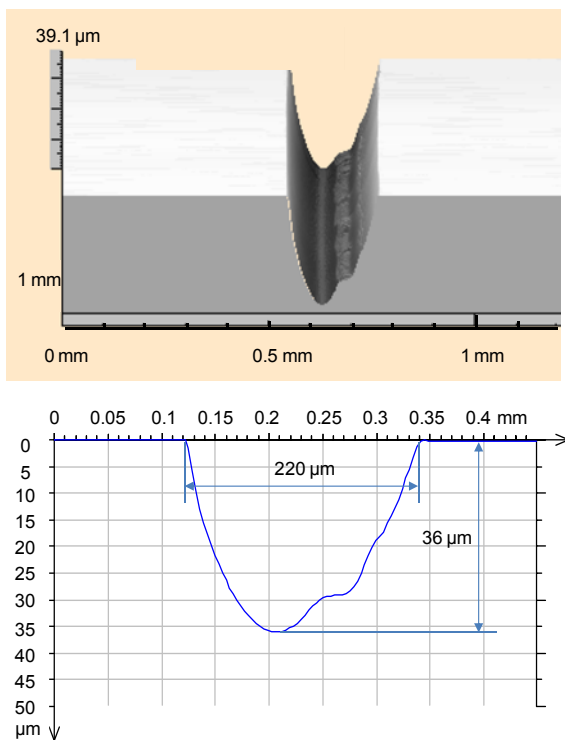


Fig. 5. Profiles (3D and 2D) of the microchannel formed at LELDR of 0.0034 $\text{mJ}/\text{mm}^2/\text{s}$ (duty cycle of 0.15 and scan speed of 220 mm/s).

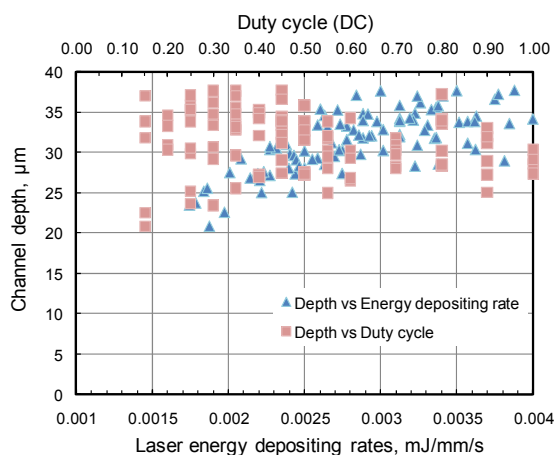


Fig. 6. Microchannel depth as a function of LELDR and energy duty cycle.

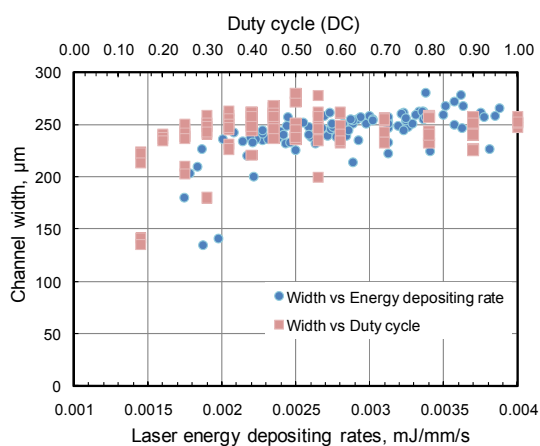


Fig. 7. Microchannel width as a function of LELDR and energy duty cycle.

4. Conclusion

A continuous strip of glass layer can be peeled off along the moving path of the laser beam under a single scan of a CO₂ laser beam at a high speed, thus forming microchannels on soda lime glass substrate. LELDR can be used to provide a guide for choosing laser parameters (laser power and scan speed) for glass strip peeling off. Various microchannels have been successfully fabricated on soda lime glass substrates by the laser-induced peeling process which is free of post process and wet chemicals.

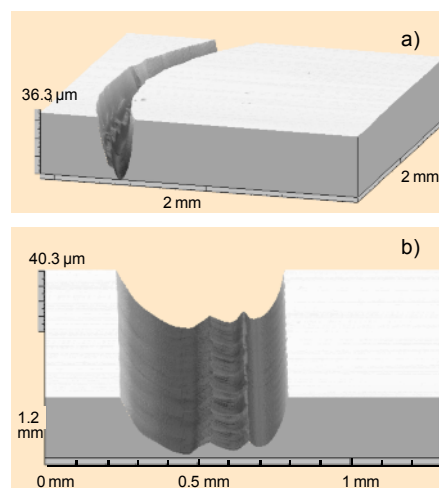


Fig. 8. 3D profiles of varied microchannels. a) a curved shape with a radius of 2 mm obtained at energy duty cycle of 0.2 and scan speed of 380 mm/s, and b) multiscan of laser beam horizontally at an overlapping pitch of 150 μm.

References

- [1] Whitesides GM, (2006) The origins and the future of microfluidics. *Nature* 442:368-373
- [2] Huikko K, Kostianen R, Kotiaho T, (2003) Introduction to micro-analytical systems: bioanalytical and pharmaceutical applications. *Eur. J. Pharm. Sci.* 20:149-171
- [3] Ahn CH, Choi JW, (2007) Microfluidics and Their Applications to Lab-on-a-Chip, in *Springer Handbook of Nanotechnology*, 2nd Edition, Bharat Bhushan, Ed. New York: Springer, pp. 523-548.
- [4] Becker H, Gärtner C, (2008) Polymer microfabrication technologies for microfluidic systems. *Anal. Bioanal. Chem.* 390:89-111
- [5] Zheng HY, Lee T, (2005) Studies of CO₂ laser peeling of glass substrates. *J. Micromech. Microeng.* 15:2093-2097

Influence of pressure on aluminium plasma expansion produced by a nanosecond laser pulse: a numerical study

S. Aggoune¹, F. Vidal² and E. H. Amara¹

¹ Centre de Développement des Technologies Avancées-Laser Material Processing Team, Po. Box 17, Baba-Hassen 16303, Algiers, Algeria

² Institut National de la Recherche Scientifique- Energie, Matériaux et Télécommunications, 1650 Boulevard Lionet-Boulet, Varennes, Québec, J3X IS2 Canada

Abstract. This work deals with a numerical study of the expansion and extinction phase of an aluminium plasma, created by nanosecond laser ablation into air. Two series of pressures are considered: (150 mTorr, 300 mTorr, 600 mTorr) and (1.3 Torr, 3Torr, 10 Torr). The plasma expansion is studied by means of a two-dimensional numerical model over a time interval of 10 μ s. The resolution of the Navier-Stokes equations shows that in general the plasma dynamics in the presence of a gas follows three successive stages, appearing after the laser pulse: (1) a rapid expansion stage of the ablated particles, (2) a deceleration stage due to the interaction with the ambient gas, and (3) a stopping stage dominated by particle diffusion on the long term. In this paper, we study the effect of the pressure of the ambient air on the behaviour, size, and mean temperature of the plasma. The calculation results are in overall agreement with experiments.

Keywords: Ablation, plasma, expansion, nanosecond, laser, pressure.

1. Introduction

The expansion of a plasma produced by pulsed laser ablation into a background gas is a complex process due to the interplay of several physical mechanisms, which include: deceleration, diffusion, recombination, thermalization, formation of shock waves, splitting of the plume into two components, etc. The modelling of plasma expansion has been the subject of several investigations. In particular, J. R. Ho et al. [1] studied plasma expansion produced by pulsed lasers (ns, excimer) for various fluences and targets. They showed that, initially, the flow of the vapour is one-dimensional. Then, after a while, a recirculation of the velocity field takes place to produce a two-dimensional flow. Another study, devoted to nanosecond laser ablation of Cu targets, was made by A. Bogaerts and Z. Chen [2]. The expansion of the plume takes place in an ambient gas of helium at 1 atm. The plasma expansion is simulated by solving the Navier-Stokes equations, taking into account the effect of the ambient gas. These authors find, in agreement with

experiments, that the velocity of ionized particles is greater than that of non-ionized ones. Other authors, such as Basillais et al. [3], investigated the effects of the fluence, the focal spot size, the pressure, and the nature of the surrounding gas, on the plasma expansion. Their study showed that, in vacuum, the ablated species propagates linearly with constant speeds, estimated to 10⁴ m/s. However, in a background gas, the plume behaves differently, as the background gas slows down the plasma expansion and maintains a high temperature longer with regard to that of vacuum.

The effect of nitrogen and oxygen pressure on the expansion of titanium plasma was the object of a study done by C. Dutouquet and J. Hermann [4]. These authors observed the confinement of the plume and the increase of its temperature with the pressure at the end of the laser pulse, for pressures of 1.3, 7, 13 and 70 Pa. Finally, A. K. Sharma and R. K. Thareja [5] investigated the dynamics of laser ablation of aluminium in ambient nitrogen, with a pressure varying from 0.01 to 70 Torr, using ICCD images of the expanding plasma plume. They showed that at pressures of 0.01 to 1 Torr, plasma expansion follows the shock model [6, 7], whereas from 10 to 70 Torr, plasma expansion follows the drag model, which can be used to estimate the stopping distance of the plume [8, 9].

In general, the plasma expansion in an ambient gas follows three successive regimes [10-12]:

- i) Free expansion of the ejected species similar to the one which occurs in vacuum;
- ii) Slow expansion due to confinement by the ambient gas;
- iii) Stop of the expansion (replaced by particle diffusion).

In this article, we discuss the effects of the pressure on the velocity, size, and mean temperature of a laser-produced aluminium plasma, by resolving numerically the Navier-Stokes equations by means of the Fluent software.

2. Modelling

Numerical simulations of the plume expansion and mixing with the ambient gas were performed using a classical hydrodynamic model. The numerical resolution of the Navier-Stokes system of equations is based on the discretization method of Patankar [13].

The simulations were carried out under the following assumptions:

- (a) The plume is composed of a mixture of the metal vapour and of the ambient gas.
- (b) Local thermodynamic equilibrium holds everywhere inside the mixture.
- (c) Mass and energy are conserved (no source terms in the equations).
- (d) Radiative losses are neglected.
- (e) The initial shape of the plume is a sphere tangent to the surface (see Fig. 1), with a radius of 3 mm [8, 9].
- (f) The starting time is the end of pulse.

The equations of conservation are written as follows:

$$\frac{\partial \rho}{\partial t} + \text{div}(\rho \mathbf{V}) = 0 \quad (S = 0)$$

$$\frac{\partial(\rho \mathbf{V})}{\partial t} + \text{div}(\rho \mathbf{V} \mathbf{V}) = -\text{div}(\boldsymbol{\tau})$$

$$\frac{\partial(\rho H)}{\partial t} + \text{div}(\rho \mathbf{V} H) = \text{div} \left[\frac{K}{C_p} \text{grad}(H) \right]$$

$$\frac{\partial(\rho w_{Al})}{\partial t} + \text{div}(\rho \mathbf{V} w_{Al}) = \text{div} \left[\rho D_{Al}^m \text{grad}(w_{Al}) + D_{Al}^i \text{grad}(\ln T) \right]$$

In these expressions, ρ is the total mass density of the medium, V the velocity and S is the mass source term (set to zero here); τ in the second equation denotes the momentum tensor. C_p , K and H are the specific heat at constant pressure, the thermal conductivity and the enthalpy, respectively. In the last equation, which corresponds to the conservation of chemical species, w_{Al} and D_{Al} are the mass fraction and diffusion coefficient of aluminium into air, respectively. The time step used in the simulations is 10^{-8} s, and the number of grid points is 500, spaced uniformly.

Figure 1 illustrates the cylindrical coordinates system (r , z) used to perform the simulations.

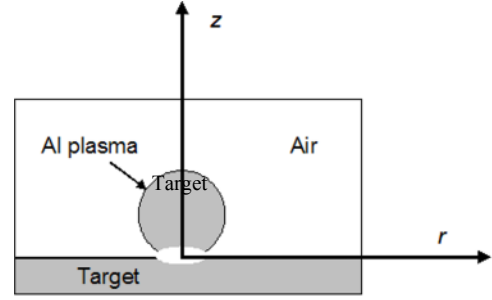


Fig. 1. Computational domain

The initial conditions of the aluminium plasma are: $w_{Al} = 1$ (for a particle density of 10^{19} cm $^{-3}$), $T_i = 30000$ K and $V_i = 11771$ m/s ($V_i = 2V_s / (\gamma - 1)$, V_s being the initial sound speed), where $\gamma = 5/3$ is the ratio of specific heats for monatomic gases, k_B is the Boltzmann constant, and m is the mass of the aluminium plume atoms.

The initial conditions of the background gas are: a variable pressure P_a and room temperature $T_a = 300$ K. The conditions on the remainder aluminium target are: $\partial T / \partial z = 0$, $V = 0$ (slip condition), and $w_{Al} = 0$ (meaning that the target is surrounded by the air). At the fictive walls: $\partial T / \partial z = \partial T / \partial r = 0$, $P = P_a = \text{variable}$, and $w_{Al} = 0$, this last condition meaning that aluminium is completely surrounded by pure air.

3. Results

3.1 Plume Size and Shape

Figures 2 and 3 show the expansion length of the plume in the presence of air as a function of time. Two air pressure series are chosen to study the behaviour of the plume: low (150, 300, 600 mTorr) and moderate pressures (1.3, 3, 10 Torr).

As can be seen in Figs. 2 and 3, at the beginning, the plasma expands as in vacuum. The leading edge of the plume moves away with a practically constant velocity, which is measured from the slope of the displacement-time graphs, and varies between 1.75×10^4 m/s and 0.85×10^4 m/s for the two extreme pressure of 150 mTorr and 10 Torr, respectively.

After some tens or hundreds of nanoseconds, according to the pressure, the ejected particles interact strongly with the ambient gas and transfer their kinetic energy. The plume then decelerates. When the pressures of air and of the aluminium plume become equal, the plume expansion stops.

The drag force model provides a good approximation of this stage until the complete stop of the plume. The

drag force model, states that the plume extension as a function of time is determined by the expression $R(t) = R_0(1 - \exp(-\beta t))$, where R_0 is the stopping distance of the plume and β is the slowing down coefficient, such that $R_0\beta = v_0$, where v_0 is the plume expansion velocity. The drag force model thus predicts that the plume will eventually come to rest due to resistance from collisions with the background gas. The values of the fitting parameters are $\beta = 0.002 \text{ ns}^{-1}$ and $R_0 = 16.5 \text{ mm}$ for $P = 1.3 \text{ Torr}$; $\beta = 0.001 \text{ ns}^{-1}$ and $R_0 = 8.5 \text{ mm}$ for $P = 10 \text{ Torr}$. These values are close to those found in experiments [8, 9].

In the first series of pressures (low pressures) shown in Fig. 2, the complete stop of the plume is not apparent and the expansion continues after 10 μs ; only the slowing is observed. On the other hand, the three stages appear clearly in the second series of curves (moderate pressures), shown in Fig. 3.

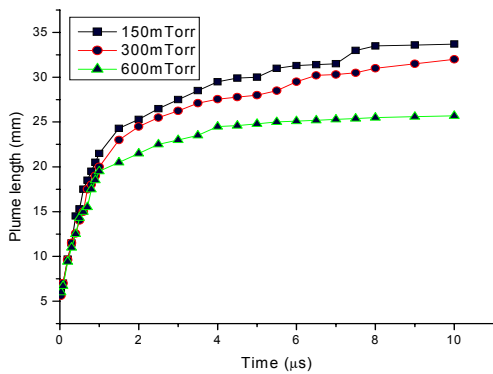


Fig. 2. Position-time plot of the aluminium front plume for low pressures.

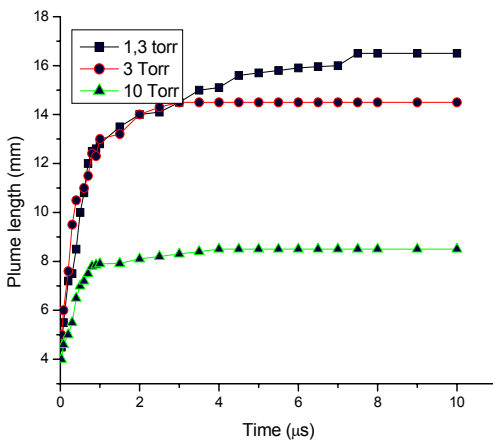


Fig. 3. Position-time plot of the aluminium front plume for moderate pressures.

Figure 4 illustrates the shape of the plume at various times (columns) and pressures (rows). The first time represented corresponds approximately to the initial condition, where the plume is assumed spherical. As time passes, the plume front becomes sharpened, as can be seen in Fig. 4b.

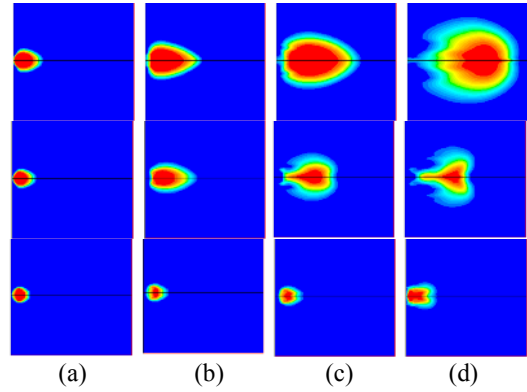


Fig. 4. Contours of mass fractions of aluminum at various times: (a) 0.01 μs , (b) 0.5 μs , (c) 1 μs et (d) 5 μs , taken for each pressure of: 150 mTorr, 1.3 Torr and 10 Torr.

Later, sharpening of the plume disappears, as shown in Figs. 4c and 4d, as a consequence of the confinement by the ambient air. At a fixed time of 1 μs , the length L of the plasma decreases with the pressure ($L \propto P^{0.16}$), as can be seen in Figure 5.

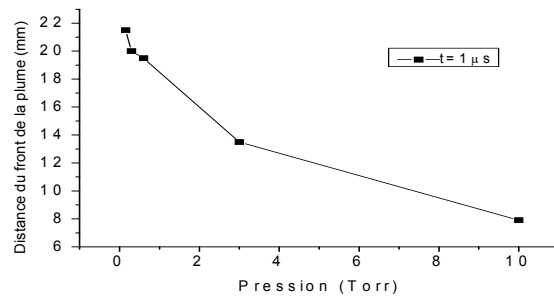


Fig. 5. Plume length versus pressure of air at 1 μs .

3.2 Temperature profiles

Figures 6 and 7 show the evolution of the average plume temperature as a function of time. The abrupt decrease of temperature observed at the first moments of the expansion, in both series of pressures, is essentially due to the fact that, at the end of the laser pulse, the plasma expands without being fed with energy. Since the radiative losses were not taken into account in their model, it follows that the work of the pressure forces is responsible of this cooling. Indeed, initially the pressure of the plume is much higher than that of the ambient gas and thus the plume expands as if air was not present. A.K. Sharma and R.K. Thareja [5] confirmed this result experimentally.

Figure 6 (low pressures of air) shows a slight decrease of the temperature as the pressure increases. Indeed, the plasma expands easily in the ambient gas and even diffuses through it. Thus there is a relatively low interaction between both media. We think that it is a

diffusion that causes a decrease of average temperature when the pressure increases.

In the case of the second series of pressures (moderate pressures, shown in Fig. 7.), it can be seen that the temperature decrease is abruptly interrupted near 1 μ s. For this range of pressures, the plasma generates a strong shock wave in the ambient gas. As the pressure increases, the plasma meets a more and more dense and impenetrable "wall" where it heats up as a result of compression. From Fig. 7. one can deduce the following behaviour:

- For 1.3 Torr: $T \propto t^{-1.06}$ for $2 \mu\text{s} < t < 10 \mu\text{s}$.
- For 3 Torr: $T \propto t^{-0.80}$ for $2.2 \mu\text{s} < t < 10 \mu\text{s}$.
- For 10 Torr: $T \propto t^{-0.38}$ for $2.4 \mu\text{s} < t < 10 \mu\text{s}$.

This clearly indicates that the plasma cools down more slowly as the pressure increases [4].

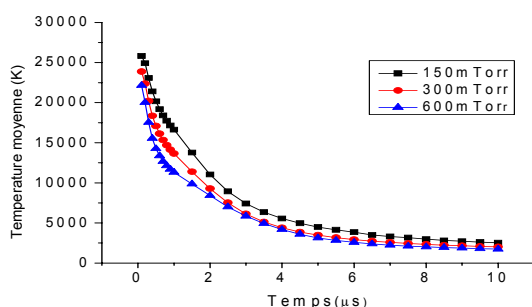


Fig. 6. Mean temperature as a function of time for low pressures.

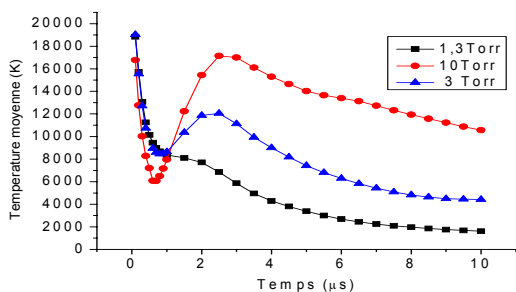


Fig. 7. Mean temperature as a function of time for moderate pressures.

4. Conclusion

The Fluent software was used to simulate the expansion of a laser-produced plasma in ambient air for various pressures. The increasing confinement of the plume with the rise of the pressure was noticed.

In the series of low pressures (150-600 mTorr), the process is mainly governed by the diffusive mixing, so the plasma average temperature falls when the pressure increases. On the other hand, in the series of moderate pressures (1,3-10 Torr), the plume front is strongly compressed, the plasma heats up as a result of compression. The simulation results on the time evolution of the plasma radius are in good qualitative agreement with the measurements of Sharma and Tharaja [5] since we both observe that the maximum plasma radius decreases and saturates faster as the ambient pressure increases. The mean plasma temperature increases with the pressure of air. We also observed a peak of the average temperature entailing a reheating of the plume due to the generation of a shock wave in the ambient gas.

References

- [1] J. R. Ho, C. P. Grigoropoulos et J. A. C. Humphrey, *J. Appl. Phys.* 79, 7205-7215, (1996)
- [2] Annemie Bogaerts, Zhaoyang Chen et Davide Bleiner, 21, 384-395, *Journal of Analytical Atomic Spectrometry*, (2006)
- [3] A. Basillais, C. Boulmer Leborgne, J. Mathias, N. Laidani, A. Laurent, J. Perriere, *Appl. Phys. A*, 71, 619-925, (2000).
- [4] C. Dutouquet, J. Hermann, *Laser induced fluorescence probing during pulsed-laser ablation for three-dimensional number density mapping of plasma species*, *J. Phys.D: Appl. Phys.*, 34, 3356-3363, (2001)
- [5] A. K. Sharma, R. K. Thareja, *Plume dynamics of laser produced aluminium plasma in ambient nitrogen*, *Appl. Surf. Scien.*, 243, 68 (2005)
- [6] D.B. Geohegan, *Thin solid Films* 220,138(1992).
- [7] Thum-Jaeger A, Sinha B K and Rohr K P *Phys. Rev. E* 63 016405 (2001).
- [8] S. S. Harilal , C.V. Bidhu, M.S. Tillack, F. Nadjmabadi and A. C. Gaeris, *J. Appl. Phys.* 93, 2380(2003).
- [9] S. S. Harilal , C.V. Bidhu, M.S. Tillack, F. Nadjmabadi and A. C. Gaeris, *J. Phys. D: Appl. Phys.* 35, 2935(2002).
- [10] A Gomes, A Aubretton, J J Gonzalez and S Vacqui'e, *J. Appl. Phys. D*, 37, 689-696, (2004)
- [11] A. Bogaerts and Z. Chen, *Spectrochimica acta, Part B* 60, pp, 1280-1307, (2005)
- [12] J. Gonzalo, C. N. Afonso, J. M. Ballestros, *Appl. Surf. Sci.* 109/110, 606 (1997).
- [13] Patankar S V, *Numerical Heat Transfert and Fluid Flow* (New York: McGraw-Hill), (1980).

Consolidation behaviour and microstructure characteristics of pure aluminium and alloy powders following Selective Laser Melting processing

P.G.E. Jerrard¹, L. Hao, S. Dadbakhsh and K.E. Evans

¹ Advanced Technology Research Institute, School of Engineering, Mathematics and Physical Sciences, University of Exeter

Abstract. Selective Laser Melting (SLM) is an additive manufacturing process that directly consolidates metal powders to form near net shape or net shape components. A few commercial SLM systems have started to process a select choice of aluminium alloys. These alloys are generally based on conventional casting alloys that do not represent the highest performance aluminium alloys for aerospace application. This paper studies the consolidation behaviour and resulting microstructure of pure aluminium, 6061 alloy powder and a mixture of 6061 alloy powder with copper powder under different SLM processing parameters. It has found that the addition of copper powder to 6061 Al powder considerably changes the consolidation behaviour and the microstructure evolution, resulting in a denser and much finer microstructure. This work therefore demonstrates the premise to develop specific aluminium alloy powders for the SLM process and enabling the fabrication of high performance aluminium based products.

Keywords: Selective Laser Melting, Aluminium, Alloy, Mixture.

1. Introduction

Selective Laser Melting (SLM) is a process belonging to the additive manufacturing family [1]. The SLM process deposits fine metallic powder layer by layer (typically 20-100 μ m thick), using a laser to scan and consolidate a cross section of the desired part in each layer [2]. The heat energy supplied by the laser is sufficient to ensure the bonding of each layer to the previous layer. As such, the SLM process can be thought of as a large scale laser welding/cladding operation [2]. Through the SLM process, parts with complicated geometries can be manufactured, hence much interest is shown in this technology by aerospace and automotive industries (amongst others) who desire the capability to produce parts with advanced internal structures [3].

The consolidation mechanisms behind SLM are still largely misunderstood [4] and so the choice of materials available for SLM processing has grown slowly. The first materials offered for SLM processing consisted of steels [5] that had a high weldability ('weldability' being a comparative measure of how easy a material is to use in welding [6]). Unfortunately, whilst steels are certainly

robust structural materials, they do not typically offer the same specific strengths attainable by titanium and aluminium alloys. Selected titanium alloys are processable by SLM [7] but their high costs make them only viable choices for the most high value components. This leaves aluminium alloys – mainstay materials of the aerospace and automotive industries – a logical choice to pursue.

The dilemma that faces Al alloy use in SLM is the fact that the alloys that are more suited for welding are not the strongest available. There is also the fact that the high temperatures attained in SLM could lead to cracking in produced parts [8]. Due to the nature of SLM, there is not the same extent of heat treatment control as there is in more conventional alloy manufacturing techniques; that is to say, whilst there has been research into the simulation of heat transfer in SLM processing [9], there is no escaping the fact that a laser must form the part by continually raster-scanning a cross-section of the part in question. Hence, rather than try and impose a potentially advanced scanning method that may or may not work depending on geometry, it makes sense to instead use a material that will play to the strength of the thermal nature of the process. This is one reason why materials such as precipitation hardening steels may be successfully processed by SLM. The Al alloys currently available in SLM are based on casting alloys [10] due to the combination of weldability and material molten flow behaviour; there is a growing consensus [11] that SLM may need aluminium alloys that have not been considered viable before in conventional processing.

The research represented in this paper examines the possibility of using customised aluminium alloys in SLM to produce a part that has the mechanical properties of the highest performing aluminium alloys using customised powder mixtures.

2. Method

Since there is very little literature surrounding the use of aluminium and its alloys in SLM, it was decided that a batch of experiments would be run using a select choice of metallic powders. The powders used were produced by gas atomisation, had a maximum particle size of $63\ \mu\text{m}$ and are listed in Table 1.

Table 1. Materials used and suppliers

Powder	Supplier
Pure Al	Alpoco
6061 Alloy	Alpoco
Pure Cu	Sandvik Osprey

Pure Al was used as a reference material. 6061 alloy was used due to its successful use by Wong [12] to produce experimental heat sink parts in SLM and the fact that it responds well to heat treatment/welding; 6061 also has an advantage in that its corrosion resistance is unaffected by quenching rate [8]. Since 6061 has a low percentage of added elements [13], this also makes 6061 a logical choice for a base alloy. Finally, pure copper was used as an additive to produce custom Al-Cu based alloys.

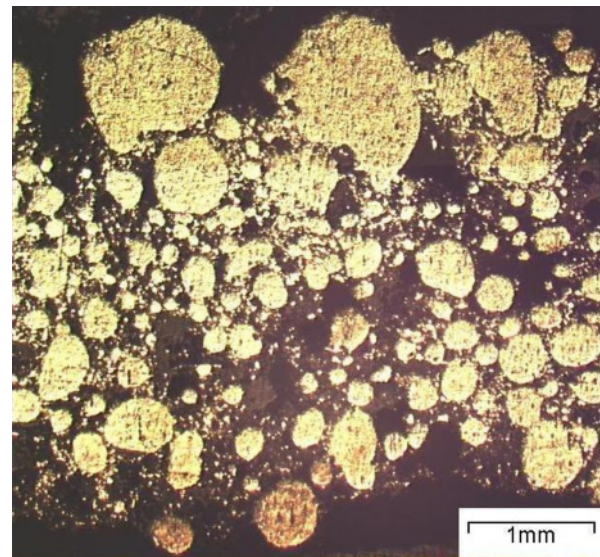
To produce samples, a $140\times 140\times 10\ \text{mm}$ powder bed of material was prepared for each combination of materials in a commercial SLM machine [14]. Powder mixtures were prepared beforehand by using a specially designed mixing tool; successful mixing was confirmed through Energy-Dispersive X-ray spectroscopy (EDX) [15] on consolidated samples. Samples were produced from: unexposed pure Al powder (powder that was kept in an argon atmosphere from manufacture to processing); exposed pure Al powder (powder that had been sieved in air and left to stand for approximately 16 hours); unexposed 6061 powder; exposed 6061 powder; exposed 6061 powder + 6% wt Cu powder; exposed 6061 powder + 30% wt Cu powder.

A single layer 7×7 grid pattern of $10\times 10\ \text{mm}$ squares was then scanned onto the surface of the powder bed using the SLM Realizer's built-in laser: an IR Fibre laser operating at $1064\ \text{nm}$ and a $200\ \mu\text{m}$ spot diameter. All samples were produced with a $25\ \mu\text{m}$ hatching spacing based upon previous work [16]; laser power was varied from 20 to 100 W and scanning speed was varied from 20 to 250 mm/s. Argon was used to inert the build chamber, keeping oxygen levels at $\leq 0.5\%$ during processing.

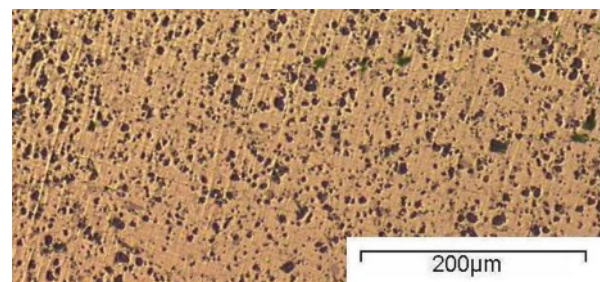
For microstructure analysis, an etchant consisting of 46.2cc HF (40% conc.), 7.6cc HCl (37% conc.) and 46.2cc distilled water was used as recommended in the Metals Reference Book [17].

Macrohardness testing was undertaken on samples containing 6061 powder using a Vickers indenter with 20 kg load and a 30 s dwell time [18].

3. Results



a



b

Fig. 1. Optical micrographs of a cross-section of a typical consolidated pure Al sample: a. shows an overview (the laser has struck the top surface); b. shows microporosity evident in the globules (note sample is unetched)

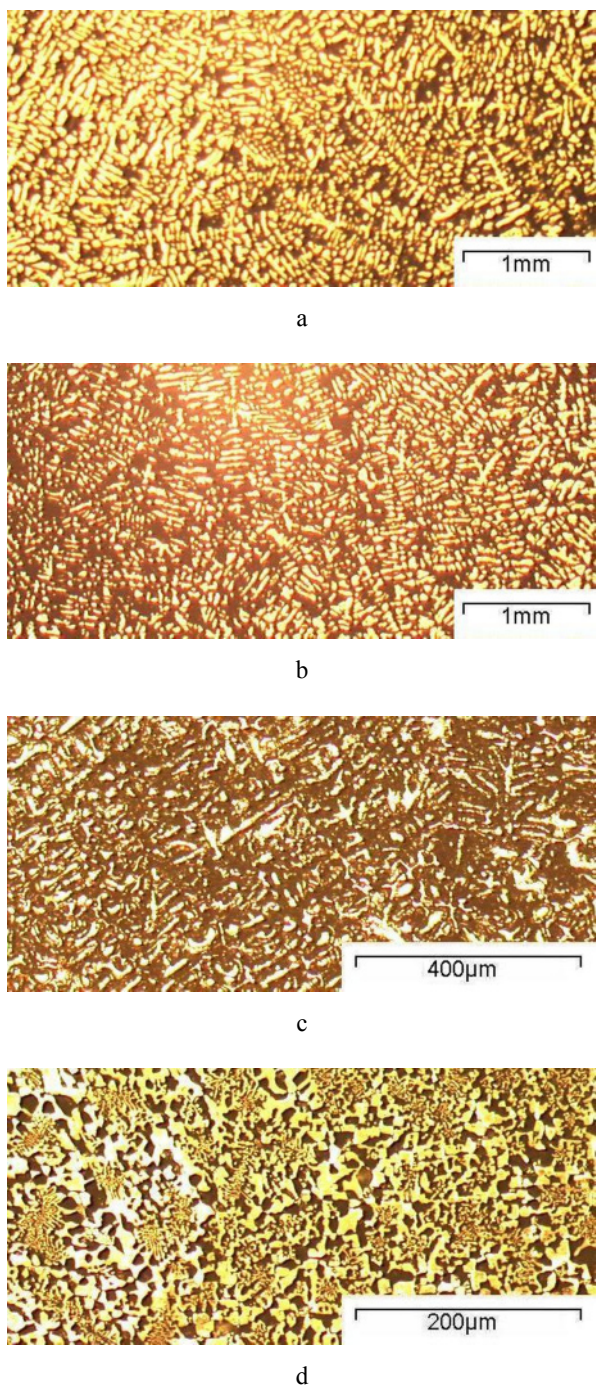


Fig. 2. Optical micrographs of consolidated and etched 6061 samples: a. 6061 kept under inerted conditions; b. 6061 exposed to air prior to processing; c. exposed 6061 + 6%wt Cu; d. exposed 6061 + 30% Cu (please note that all samples were produced at a laser power of 100W and a scan speed of 20mm/s)

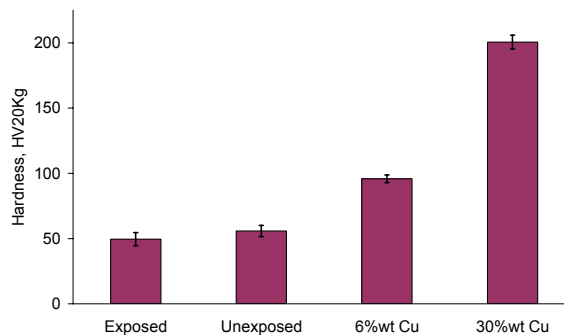


Fig. 3. Comparison of 6061 alloy powder and mixtures. Error bars represent the standard deviation over five samples.

The pure Al produced large globules of material that contained evidence of microporosity (see Fig. 1); this was unaffected by whether the pure Al powder had been exposed to air prior to processing or not. Varying laser power and scan speed only affected globule size and could do nothing to successfully consolidate a large sample; microporosity was completely unaffected, being present in any globule formed. Adding 6% Cu powder was found to have no effect in reducing either the balling phenomenon or microporosity. As a result the pure aluminium samples were deemed unsuitable for further testing.

The 6061 alloy was found to have superior consolidation compared to pure Al. The microstructures of the samples produced from 6061 alloy are shown in Fig. 2. Samples produced using only 6061 alloy show a dendritic structure whilst those produced with Cu additions show a dramatic change.

A sample was taken from each experiment batch using 6061 powder and machined into a cuboid approximately $3 \times 2 \times 2$ mm. This cuboid was used to calculate density: all samples achieved $96.5 \pm 0.5\%$ density.

4. Discussion

Figure 1 shows a typical attempt to consolidate a pure Al sample. Al has a natural tendency to 'ball' [4], that is to form small globules of consolidated material rather than one consolidated globule. This is due to Al's poor wetting angle [13]. The formation of micropores are a typical flaw from welding aluminium; micropores could have also been the result of trapped gas between particles or hydrogen that has been inadvertently atomically stored from production of the powder [19].

The 6061 powder clearly shows a far superior consolidation (Figs. 2 a and b) compared to pure Al, which can be explained by the additional elements present (mainly silicon and magnesium); these materials improve the overall weldability of the alloy [13]. The improvement in consolidation can be attributed to 6061's

better weldability. There is no evidence of microporosity at the same level of magnification as in Fig. 3.1 b. However exposure to air prior to production of samples has resulted in a slight change to microstructure, which can be attributed to the formation of oxide on the surface of the 6061 powder particles. Both microstructures show a rapidly cooled structure that is commonly seen in Al alloy casting [8].

The addition of Cu powder to 6061 dramatically changes the resultant microstructure (Fig. 2 c and d). In the case of adding 6%wt powder, the microstructure has been considerably refined, although still seems to suffer from excess oxide from the exposed 6061 powder. Adding 30%wt Cu to 6061 further changes the microstructure, resulting in a stereotypical eutectic structure [20] perhaps composed of 6061 Al and Cu (and/or some Al-Cu intermetallics): the additional Cu apparently removes most, if not all, of the oxide.

The hardness results in Fig. 3 show that the 6061 powder does benefit from being kept under an inert atmosphere prior to processing. The exposure to air reduces the sample's average hardness by approximately 5HV20kg. As is expected, adding Cu improves the hardness of the resultant material. Adding 6%wt Cu approximately doubled the hardness whereas adding 30% Cu effectively quadrupled the hardness of the base alloy. In the case of the 6% Cu mixture, this can be attributed to solid solution strengthening and grain refinement; for the 30%wt Cu mixture, the combination of a fine eutectic structure and the formation of AlCu₂ intermetallics will cause the increase.

5. Conclusion

The work presented in this paper has set out to show the advantages of customised alloy usage in SLM, demonstrated by the consolidation of powder mixtures of 6061 alloy and Cu. The results show that by picking a base alloy that has a high weldability rating and a sensible additive, customised alloys become a logical choice in the SLM process. In the case of 6061 + 30%wt Cu, the additive also seems to have removed any oxidation. The microstructure analysis of samples shows that samples are subject to very high cooling rates. While this is to be expected due to the nature of the SLM process, this reaffirms that materials chosen for SLM should ideally be able to take advantage of a rapid quenching rate. Eutectic compositions seem to especially benefit from the inherent cooling rate.

The authors intend to continue the research presented in this paper and have recently produced promising results with multilayer samples. These samples will allow further testing of mechanical properties and hence will allow a more in depth evaluation of the use and application of customised aluminium alloys in SLM.

Acknowledgements

The authors would like to thank Dr Neil Sewell for writing the custom software used to drive the SLM Realizer to manufacture the samples.

References

- [1] Levy GN, Schindel R, Kruth JP. Rapid manufacturing and rapid tooling with layer manufacturing (LM) technologies, state of the art and future perspectives. *CIRP Ann. Mfg Technol.*, 2003, 52(2), 589–609.
- [2] Kruth JP, Levy G, Klocke F, Childs THC. Consolidation phenomena in laser and powder-bed based layered manufacturing. *CIRP Ann. Mfg Technol.* 2007, 56(2), 730–759.
- [3] Hopkinson N, Hague RJM, Dickens PM. *Rapid Manufacturing*. Oxford: Wiley; 2005.
- [4] Rombouts M, Kruth, JP, Froyen L, Mercelis P. Fundamentals of selective laser melting of alloyed steel powders. *CIRP Ann. Mfg Technol.*, 2006, 55(1), 187–192.
- [5] T. Wohlers and T. Gornet. Viewpoint: History of additive fabrication (part 1). *TCT Magazine*, March 2008.
- [6] West EG. *The Welding of Non-Ferrous Metals*. London: Chapman & Hall Ltd; 1951.
- [7] Osakada K, Shiomi M. Flexible manufacturing of metallic products by selective laser melting of powder. *International Journal of Machine Tools and Manufacture*. 46(11), 2006, 1188–1193.
- [8] *ASM metals handbook*. Vol 4, 1991 (ASM International, Metals park, Ohio).
- [9] Zaeh MF, Branner G, Krol TA, (2009) A three dimensional FE-model for the investigation of transient physical effect in Selective Laser Melting. *Proceedings of the 4th International Conference on Advanced Research and Rapid Prototyping* 415-424
- [10] <http://www.concept-laser.de/> (accessed 23rd February 2010)
- [11] Todd I, *The Development of Metallic Materials for Additive Layer Manufacturing: Which Materials Suit Which Platforms and What We Can Do to Improve Properties?* *Proceeding of TCT Live 2009*; 2009 Oct 20-21.
- [12] Wong M, Tsopanos S, Sutcliffe CJ, Owen I. Selective laser melting of heat transfer devices. *Rapid Prototyping Journal*, 2007, 13(5), 291-297.
- [13] *ASM metals handbook*. Volume 2, 1992 (ASM International, Metals Park, Ohio).
- [14] SLM Realizer manufactured by MTT, available from <http://www.mttgroup.com> (accessed 23rd February 2010)
- [15] Hitachi S3200N Scanning Electron Microscope. <http://em.hitachi-hitec.co.uk/> (accessed 23rd February 2010)
- [16] Jerrard PGE, Hao L, Evans KE. Selective Laser Melting of Pure Aluminium – A Preliminary Study. *Proceedings of the 10th National Conference on Rapid Design, Prototyping and Manufacturing*; 2009 June 12th, High Wycombe, MJA Print; 2009, p. 45-52.
- [17] Smithells CJ. *Metals Reference Book*, 2nd ed. vol 1. New York: Interscience Publishers Inc; 1955.
- [18] FM-1E Vickers indenter, Future-Tech Corp. <http://www.futuretechcorp.com> (accessed 23rd February 2010)
- [19] Praveen P, Yarlagadda PKDV, Kang MJ. Advancements in pulse gas metal arc welding. *Journal of Material Processing Technology*, 164, 2005, 1113-1119.
- [20] *ASM metals handbook*. Volume 9, 2004 (ASM International, Metals park, Ohio).

Influence of distortion on part accuracy of Indirect Metal Selective Laser Sintering

Zakaria K^{1,2} and Dalgarno KW¹

¹ School of Mechanical and Systems Engineering, Newcastle University, NE1 7RU, United Kingdom
Phone: +44 (0)191 222 8995, Fax: +44 (0)191 222 860, khidzir.zakaria@ncl.ac.uk; kenny.dalgarno@ncl.ac.uk

² Faculty of Mechanical Engineering, Universiti Teknologi Malaysia, 81300 UTM Skudai, Johor, Malaysia
Phone: +60-7-5534857, Fax: +60-7-5566159, khidzir@fkm.utm.my

Abstract. This paper reports on an investigation of dimensional accuracy in Indirect Metal Selective Laser Sintering (IMSLS). An experimental programme with a series of simple parts has been carried out to establish dimensional accuracy of metal parts made using the 3D systems of Indirect SLS process. In parallel basic engineering science and experimental results have been used to analyse the relative loads experienced by different parts. The experimental results show that the level of distortion experienced by parts which undergo infiltration is much less than that of parts which were deliberately not infiltrated, indicating that the early availability of liquid phase is key in avoiding distortion. Analysis has also shown that the propensity for deformation to develop during a sintering or sintering/infiltration step is directly related to the level of stress being experienced by the structure. These two findings show that the application of engineering science to indirect metal SLS could bring parts which are less distorted at the sintering/infiltration stage.

Keywords: Indirect Metal Selective Laser Sintering (IMSLS), dimensional accuracy, distortion

1. Introduction

Indirect Metal Selective Laser Sintering (IMSLS) is an additive layer manufacturing (ALM) technique which allows steel/bronze composite parts to be made through a combination of selective laser sintering of a polymer coated steel powder to create a “green” part, followed by furnace infiltration of the green part with bronze. The resulting parts are fully dense functional components which can be exploited for demanding engineering applications, such as injection moulding tooling [1].

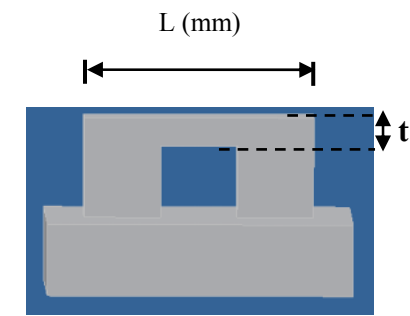
The aim of this study was to investigate the dimensional accuracy of the IMSLS process, and in particular the distortion of overhanging parts, which previous work identified as a major concern [2].

2. Experimental Details

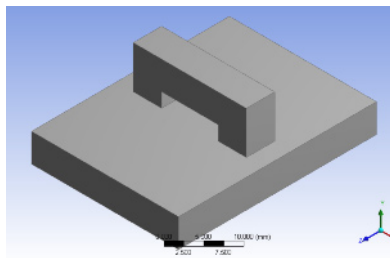
2.1. Part manufacture

This work has examined the 3D Systems indirect SLS process, using polymer coated steel powder (Laser Form ST 200). A full description of this process can be found in [3]. A simple beam shape, shown in Figures 1 (a) and (b) was created as a test piece in order to evaluate the distortion of the overhanging structure. Beams were designed with length (L) = 15 mm and width of the beams (t) = 2, 4, 6, and 8 mm; and with $L = 50$ mm and width $t = 2.67, 4, 5.33$ and 8 mm. Once the parts had been designed *.stl files were generated from the 3D CAD model and sent to a 3D Systems (Vanguard™ SLS machine) for manufacture.

The default processing parameters of laser power, outline power, scan space, building rate, layer thickness and bed temperature (44 W, 20 W, 0.08 mm, 177 mm/min, 0.08 mm and 95°C) were used to create the “green” parts as shown in Figure 2 (a). The bronze infiltrant (Cu 89 Sn 11) was located on top of the support structure as illustrated in Figure 2 (b). The parts and bronze material were then heated together in the furnace to produce the “brown part” as shown in Figures 2 (c) and (d). The furnace temperature cycle was heated gradually at a rate 110°C/hour from ambient temperature to reach a maximum of 1075°C, then hold steady for 3 hours before cooling at the natural rate of the furnace. Parts were sintered both with and without bronze in order to investigate the effect of the weight of the bronze.



(a) Beam dimension



(b) 3D model of beam

Fig. 1. Design case study



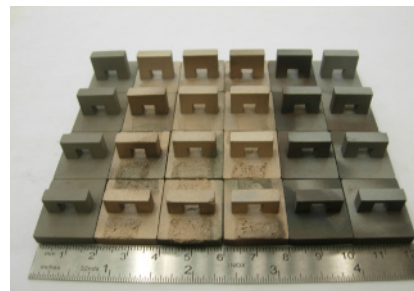
(a) "Green" parts develop by SLS machine



(b) Bronze material arrangements with "green" parts before being placed in furnace



(c) Furnace infiltration and sintering



(d) "Brown" parts completed after furnace infiltration process

Fig. 2. Main steps in building metal parts using IMSLS process

2.2. Part Assessment

The part weight was recorded at the "green" and "brown" stages using a precision balance (Good Scale GSW-30K). The downwards distortion of the beam overhang was assessed by measuring the extent to which the midpoint of the beam had bowed, relative to the position of the ends of the beam, as shown in Figure 3. These were measured using Kemco CMM 400 (upper side) and Nikon profile projector V-16D (lower side).

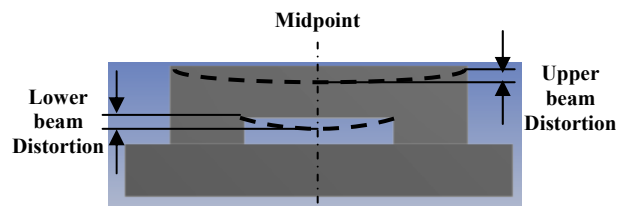


Fig. 3. Measurement of beam

3. Results

The results summarised are shown in Figures 4 to 7.

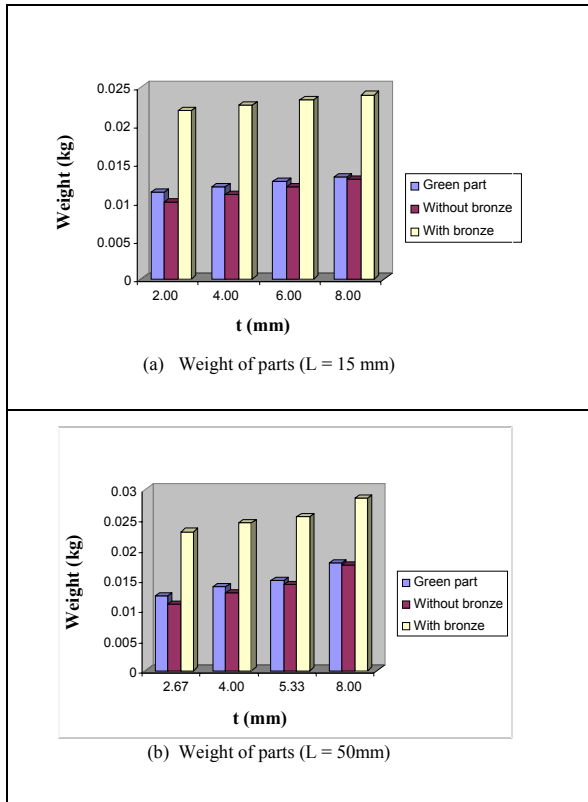


Fig. 4. Weight measurements for beams with (a) L= 15 mm and (b) L= 50 mm.

The results presented in Figure 4 compare the weight of parts for both beams, whereas Figures 5 and 6 (dimensional analysis of distortion) and 7 show the beam analysis (with and without bronze) of L = 50 mm was performed.

Figures 5 and 6 present the average distortion measured at the midpoint of the specimens, and the error bars represent the minimum and maximum values measured at the midpoint of the parts.

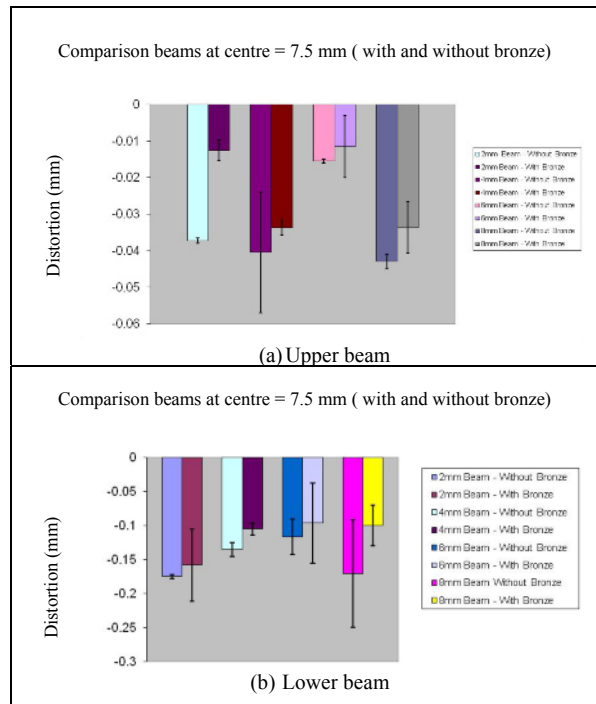


Fig. 5. (a) Upper and (b) lower beam reflection for beams with L = 15 mm

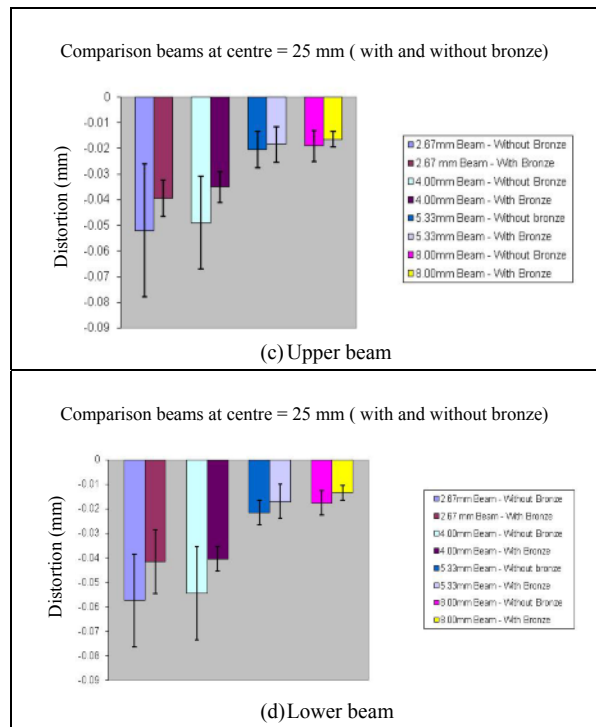


Fig. 6. (c) Upper and (d) lower beam reflection for beams with L = 55 mm

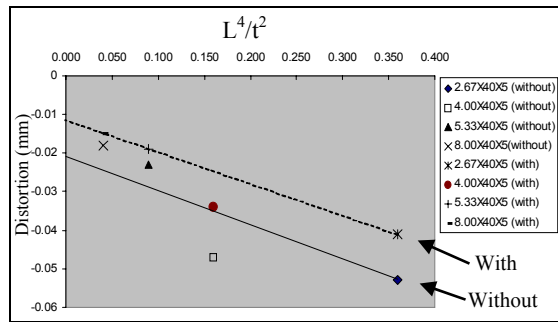


Fig. 7. Plot of upper beams ($L = 50$ mm) distortion against L^4/t^2

4. Discussion and conclusions

The results for both beams show that the effect of the bronze infiltrant on the weight of the structures is significant. However, this additional weight does not cause greater distortion when parts are being sintered, as beams of both $L = 15$ mm and $L = 55$ mm show very similar levels of distortion when processed with and without bronze. This suggests the availability of liquid material during the infiltration acts to enhance sintering and offset any effect that the additional weight has in causing distortion.

To understand the effect of beam size, Figure 7 shows a plot of distortion of the $L = 50$ mm beam, processed (with and without) bronze against L^4/t^2 . For a given material L^4/t^2 indicates the compliance of a beam as it increases.

References

- [1] Ilyas IP, Taylor CM, and Dalgarno KW, (2005) Production of plastic injection mould tools using Selective Laser Sintering and high speed machining, *6th National Conference on Rapid Design, Prototyping and Manufacturing*. pp. 73- 80.
- [2] Zakaria K, and Dalgarno KW, (2008) Assessment the Manufacture of Complex Metal Parts using Indirect Selective Laser Sintering, *9th National Conference on Rapid Design, Prototyping and Manufacturing*. pp. 107-117.
- [3] http://www.3dsystems.co.jp/documents/products/material/duraform/LaserForm_ST_200_LS_mat_E.pdf. Retrieved 12th February 2010, 15:20 GMT.

Surface Roughness Studies in Selective Laser Sintering of Glass filled Polyamide

Vineet Srivastava, S.K. Parida, Pulak M. Pandey

Department of Mechanical Engineering, Indian Institute of Technology Delhi, New Delhi, India

Abstract: Selective Laser Sintering (SLS) is one of the most rapidly growing Rapid Prototyping (RP) processes, mainly due to its ability to process various materials. Prototypes made by SLS are widely used in product development as they can be used for product testing. Prototypes, therefore, should have an appropriate surface finish for functional performance as well as aesthetics. However, prototypes made by the SLS process have comparatively high surface roughness due to the stair stepping effect. From the strength aspect, Glass Filled (GF) Polyamide is also being used. However surface roughness model for GF Polyamide as a material for laser sintering has not yet been reported in the literature. Surface roughness of the prototypes depends on the various process parameters. This paper attempts to study the effect of process parameters, namely build orientation, laser power, layer thickness, beam speed, and hatch spacing, on surface roughness. Laser power, layer thickness and orientation were found to be the three most important parameters affecting surface roughness of the parts. Empirical models have been developed for estimating the surface roughness of the parts.

Keywords: Selective Laser Sintering (SLS), Glass filled (GF) Polyamide, surface roughness, Response Surface Methodology (RSM).

1. Introduction

Selective Laser Sintering (SLS) is one of the most rapidly growing RP processes, mainly due to its ability to process various materials, such as polymers, metals, ceramics, and composites. Any material in powder form which can be sintered by the laser can be used in making the prototypes without geometric complexity. The size of the part that can be made in a SLS system depends on the size of machine bed platform. SLS uses fine powder which is spread by a re-coater on the machine bed and scanned selectively using laser beam such that surface tension of grains is overcome and they are sintered together. Before the laser scans, entire machine bed is preheated to just below the melting point of material. Laser power is adjusted to bring selected powder areas to a temperature just sufficient for powder particles to get sintered. Build platform moves down by one layer thickness to facilitate new powder layer and process is

repeated for all subsequent layers to complete the part. Sintered material forms part while un-sintered powder remains in its place to support the structure and may be cleaned away once the part is complete. [1].

Currently, prototypes built utilizing layer manufacturing technology can be employed as functional prototypes and as patterns or tools for different manufacturing processes, such as vacuum casting, investment casting, injection moulding, die casting, and sand casting. Therefore, the surface finish of the part should be good enough to ensure the functional requirements. However, layer-by-layer deposition in SLS leads to staircase effect on the part's surface and detracts from the part's surface finish, similar to other RP processes [2].

Several attempts have been made to model the surface roughness of RP parts. Pandey et al. [2] proposed a stochastic model to predict surface roughness of FDM parts. They considered layer thickness and build orientation as the two most significant process variables. Parts with different build orientation were fabricated on FDM- 1650 to study the surface roughness characteristics. They measured surface profiles of the different faces using Surf Analyzer 5000. Based on the actual surface profiles, they proposed the surface roughness model. Tumer et al. [3] showed experimentally that layer thickness and part orientation affect the surface quality of the SLS parts. Parameters varied in their experiments were laser power, layer thickness and build orientation. A factorial experimental design was used for the purpose of determining the effect of the process parameters on the surface finish. An empirical model was developed by regression to predict the root mean square surface roughness.

Reeves and Cobb [4] presented a mathematical model to predict the surface roughness of stereolithography parts in terms of layer thickness, surface angle and layer profile. They proposed two different expressions to predict surface roughness of upward and downward-facing surfaces. For downward facing surfaces, an effect known as print through has been found to help in

improving the surface finish. Ahn et al. [5] proposed a methodology to predict the surface roughness of LM processed parts. A roughness distribution expression that could obtain surface roughness values for all surface angles was introduced using measured roughness data and interpolation. A prediction application was presented, and the validity and effectiveness of the proposed approach was demonstrated through several application examples.

Bacchewar et al. [6] made attempts to study the effect of process parameters on surface roughness of laser sintered polyamide parts. Central Composite Rotatable Design (CCRD) of experiments was used to plan the experiments. Analysis of variance (ANOVA) was used to study the significance of process variables on the surface roughness. In the case of upward-facing surfaces, build orientation and layer thickness were found to be significant parameters. In downward facing surfaces, build orientation, layer thickness and laser power were found to be significant. Empirical models were developed for estimating the surface roughness of the parts. A trust-region-based optimization method was employed to obtain a set of process parameters for obtaining the best surface finish.

It is evident from the literature review that most of the previous work is concentrated towards FDM and stereolithography. One attempt [6] seems to be made for SLS process using polyamide powder also. Surface roughness model for SLS with glass filled polyamide as a material has not yet been reported in the literature. When components require better stiffness and thermal properties than polyamide, Glass filled polyamide is preferred over polyamide. In SLS there are many input parameters which can be changed to get desired surface quality of the parts. Some of these input variables are laser power, beam speed, build orientation, hatch spacing, part bed temperature, layer thickness, scan length etc. Laser power determines the severity of the temperature and sintering of the powder, hence the level of power has a significant effect on the surface quality. Beam speed also decides the amounts of energy input during sintering and hence sometimes contribute towards surface quality of the parts. Orientation and layer thickness causes stair stepping in SLS parts which lead to bad surface finish. Hatch spacing was also found to affect the surface roughness of the SLS prototypes.

The present work aims at determining the effect of parameters namely laser power, beam speed, hatch spacing, build orientation and layer thickness on the surface roughness of the parts made from Glass filled Polyamide. Typical parts were built according to the experimental parameters and levels using EOS P 380 workstation. Surface roughness of the parts, both upward and downward facing surface were captured using Talysurf Instrument. Two different second order empirical models are developed for predicting the surface roughness of "upward" and "downward" facing surfaces. A confirmation experiment has been carried out based on

empirical models and predicted results were found to be in good agreement with experimental findings.

2. Planning of Experiments

In this study, the experimental plan has five controllable variables, namely, laser power, beam speed, orientation, layer thickness, and hatch spacing. A total of 32 experiments were carried out with independent variables at five different levels [7]. Energy density (E), which is given by equation (1), below, was considered while setting the levels of laser power, beam speed, and hatch spacing

$$E = \frac{P}{V \times Hs} \quad (1)$$

Here, E is energy density (J/mm^2), P is laser power (W), V is beam speed (mm/s), and Hs is hatch spacing (cm). From the experience it is known that the sintering does not occur if the value of E is below $1 \text{ J}/\text{cm}^2$ and polymer degradation starts above $4.8 \text{ J}/\text{cm}^2$. Therefore, the range of the laser power, beam speed, and hatch spacing were selected as 25 to 37 W, 2500 to 4500 mm/s, and 0.025 to 0.045 cm, respectively. Build orientation was considered in the range of 0° to 90° . The values of layer thickness were fixed by considering the capabilities of the SLS machine.

Glass-filled fine polyamide used in the present work for carrying the experiments was supplied by EOS, Germany. Typical wedge-shaped parts were modelled in Pro/ENGINEER® (Fig. 1) to evaluate the surface roughness characteristics. The positions and build orientation of specimens were fixed in Magics software. The STL files were then checked for errors and repaired.

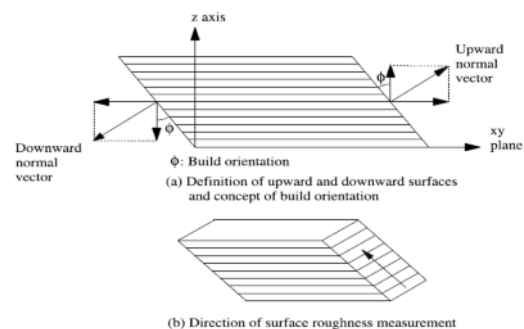


Fig. 1. Typical part modeled to evaluate the surface roughness

Once the orientation and positions were fixed, the specimens were sliced into layers using a slicing module of the Magics software. Sliced files were then repaired using EOS RP tools and transferred to the SLS machine. The specimens were produced on an EOS P 380 SLS workstation. Surface roughness measurement was then carried out using a Form Talysurf system.

3. Analysis of the Experimental Data

3.1 Surface Roughness Modeling for Upward Facing Surfaces

Surface roughness model for upward facing surfaces was developed by analyzing the surface roughness data and has been given below as equation (2).

$$Ra_{up} = 987 - (4.98 \times X_1) - (0.0948 \times X_2) - (1.55 \times X_3) - (7.38 \times X_4) - (4684 \times X_5) + (0.0154 \times X_1^2) + (151 \times X_1 \times X_2) + (0.000533 \times X_2 \times X_4) + (0.0107 \times X_3 \times X_4) \quad (2)$$

Where Ra is the expected centerline average surface roughness value for either the surfaces facing upward or facing downward. X_1, X_2, X_3, X_4 and X_5 are the parameters namely laser power, beam speed, orientation, layer thickness, and hatch spacing respectively. ANOVA was used to check the adequacy of the developed model. The F-ratio of the predictive model was calculated and compared with the standard tabulated value of the F-ratio for a specific confidence interval. According to the F test and ANOVA, it is clear that the model is significant and also adequate due to the tabular F value for 95% confidence limit (2.65) being lesser than the model F value (5.82). The lack of fit is also not significant because the model fits properly according to the data points. Percentage contributions for each term of the model are shown in Fig. 2. The figure shows that build orientation is the most influential parameter affecting surface finish.

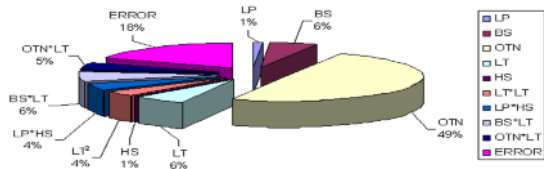


Fig. 2. Percent Contribution of different factors towards the model

3.2 Surface Roughness Modeling for Downward Facing Surfaces

A second-order model was obtained for the surface roughness of the downward-facing surfaces using experimental data and the obtained second-order model is as given below.

$$Ra_{down} = -537 + (1.06 \times X_1) - (0.00366 \times X_2) + (0.008 \times X_3) + (0.248 \times X_4) + (1496 \times X_5) + (0.00002 \times X_2^2) - (0.00043 \times X_3^2) - (1456 \times X_5^2) - (0.00683 \times X_1 \times X_3) - (1.77 \times X_1 \times X_5) - (0.000063 \times X_2 \times X_4) + (0.00172 \times X_3 \times X_4) \quad (3)$$

ANOVA was used to check the adequacy of the developed model. According to the F test it is clear that the model is significant and also adequate due to the

tabular F value for 95% confidence limit (2.65) being lesser than the model F value (22.32). The lack of fit is also not significant. Percentage contributions for each term of the model are shown in Fig. 3. The figure shows that build orientation and layer thickness are the most influential parameters affecting surface finish.

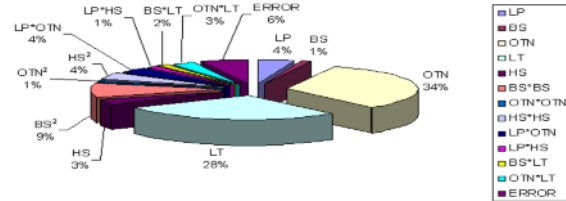


Fig. 3. Percent Contribution of different factors towards the model

4. Effect of Process Parameters on Surface Roughness

4.1 Upward facing Surface

From the main effect plots shown in Fig. 4 for upward facing surface, it is clear that orientation is the most important parameter. Beam speed and layer thickness are the next two important parameters which also contribute towards the surface roughness of the model.

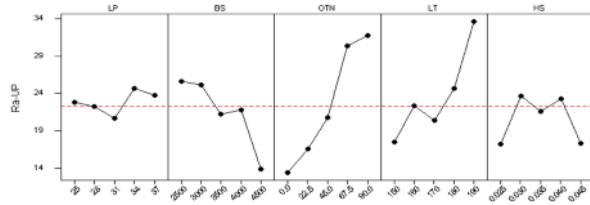


Fig. 4. Main Effect plots for the upward facing surface

The variation of surface roughness with respect to laser power and beam speed has been presented in Fig. 4. The figure shows that surface roughness increases with increase in laser power. An increase in laser power increases energy density of laser spot. The increased energy density causes the increased penetration of laser energy and increases the surface roughness. A similar phenomenon has also been reported in the sterialithography process [4] and when polyamide was used in SLS [6]. The surface roughness has been found decreasing with increase in beam speed. This may be due to the fact that increase in beam speed results in reduced energy density of the laser spot and hence improved surface finish.

It is observed that surface roughness increases with increase in orientation. It is a general characteristic of RP processes that increase in build orientation results into steeper stair steps and caused rougher surface. Again at higher layer thickness values, surface roughness values are higher and at lower layer thickness, they are lower.

But due to the presence of quadratic effect of layer thickness in the model, the roughness values are lower in the range of 160 to 170 microns as shown in Fig. 6. The reason for obtaining minimum roughness value in the range of 160 to 170 microns may be that the intermediate edge profile is neither too sharp in steps nor there is uniform teeth edge profile favoring the corner sintering during contouring of the laser beam.

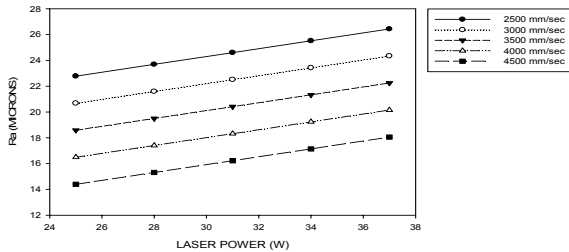


Fig. 5. Effect of laser power and beam speed on surface roughness for the upward facing surface

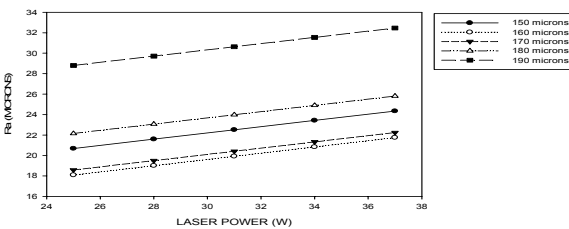


Fig. 6. Effect of laser power and layer thickness on surface roughness for the upward facing surface

4.2 Downward facing Surface

The main effect plots among the different parameters and the surface roughness values shows that the orientation and layer thickness are the major factors affecting the surface roughness of the parts, as given in Fig. 7. Laser power and hatch spacing also showed minor effect on surface roughness.

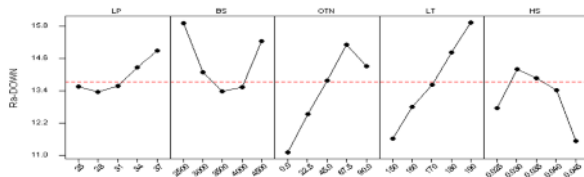


Fig. 7 Main effect plots for the downward facing surface

At different beam speeds, when the laser power is increased, the surface roughness increases which can be observed from Fig. 8. However it has been observed that for beam speed of 3500 mm/sec, the surface roughness is minimum followed by 4000 mm/sec. At beam speed of 2500 mm/sec, the surface roughness was observed to be on the higher side. This trend is observed due to variation in energy density, which is related to beam speed as given in eq 1.

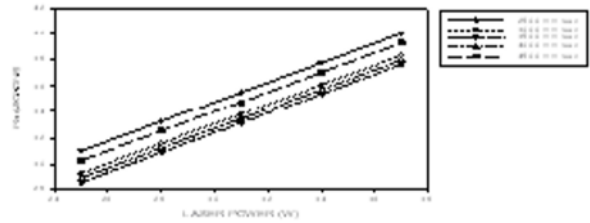


Fig. 8. Effect of laser power and beam speed on surface roughness for the downward facing surface

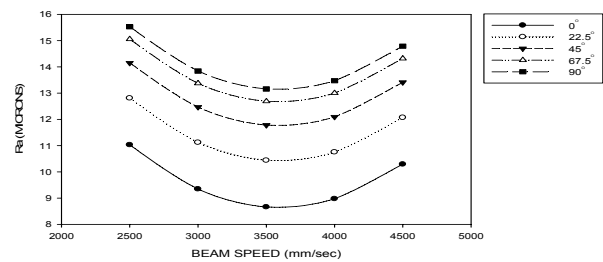


Fig. 9. Effect of beam speed and orientation on surface roughness for the downward facing surface

It can be seen from Fig. 9, that when the beam speed is varied for different orientations, initially surface roughness decreases and then increases. This trend is obtained because beam speed is related to energy density as given in eq 1. When the beam speed is lower, energy density is higher as a result there is over sintering and conversely when beam speed is higher, energy density is lower so there is under sintering. As a result surface roughness increases in both the cases. At 3500 mm/sec beam speed, the sintering is uniform so the surface roughness is lower corresponding to other beam speeds. It was also observed that increase in layer thickness results in increase in surface roughness. This trend is obvious as increasing layer thickness dominates the stair stepping effect and hence enhanced surface roughness.

5. Conclusions

- The effect of process parameters on the surface roughness of glass filled polyamide SLS parts was studied with the help of central composite rotatable design (CCRD) of experiments. Laser power, layer thickness and the orientation are the three most important parameters which contribute towards surface finish of the parts.
- The effects of significant parameters have been discussed for up and down facing surfaces in relation with the physical phenomena that may cause these variations.
- To predict the surface roughness of up and down facing surfaces, second-order response surface models were developed. ANOVA was used to establish adequacy of the developed models.

References

- [1] Chua C.K., Leong K.F., Lim C.S., (2000) *Rapid Prototyping: Principles and Applications*, World Scientific.
- [2] Pandey P.M., Reddy N.V., Dhande S.G., (2003) Improvement of surface finish by staircase machining in fused deposition modeling. *Journal of Material Processing Technology* 132, 323–333.
- [3] Tumer I.Y., Thompson D.C., Wood K.L., Crawford R.H., (1995) Characterization of surface fault patterns with application to a layered manufacturing process, *Journal of Manufacturing System*, 17(1) 23–36.
- [4] Reeves P.E., Cobb R.C., (1997) Reducing the surface deviation of stereolithography using in-process technique. *Rapid Prototyping Journal*, 3, 20–31.
- [5] Ahn Dae keon, Kim Hochan, Lee Seok hee, (2009) Surface roughness prediction using measured data and interpolation in layered manufacturing, *Journal of Materials Processing Technology*, 209, 664–671.
- [6] Bacchewar P.B., Singhal S.K., Pandey P.M., (2007) Statistical modelling and optimization of surface roughness in the selective laser sintering process, *Proceedings of the Institution of Mechanical Engineers, Part B: Journal of Engineering Manufacture*, Volume 221(1), 35–52.
- [7] Montgomery D.C., (1991) *Design and analysis of experiments*, John Wiley, Singapore.

Finite Element Modelling of the Laser Forming of AISI 1010 Steel

J. Griffiths¹, S. P. Edwardson¹, G. Dearden¹ and K. G. Watkins¹

¹ Laser Group, Department of Engineering, University of Liverpool, L69 3GH, UK

Abstract. Laser forming offers the industrial promise of controlled shaping of metallic and non-metallic components for prototyping, correction of design shape or distortion and precision adjustment applications. In order to fulfil this promise in a manufacturing environment the process must have a high degree of controllability, which can be achieved through a better understanding of its underlying mechanisms. One area of limited understanding is that of the variation in bend angle per pass observed during multi-pass laser forming along a single irradiation track, notably the decrease in bend angle per pass after many irradiations. Finite Element (FE) modelling can be used to ascertain which of the various process parameters (such as graphite burn-off, geometrical effects, variation in absorption etc) contribute towards this phenomenon and subsequently the magnitude of their contribution.

Keywords: Laser Forming, TGM, FEM

1 Introduction

Laser forming (LF) is a process for the shaping or correction of distortion in metallic components through the application of laser irradiation without the need for permanent dies or tools. It has potential for widespread application in the manufacturing industry as a means of avoiding wasteful machining operations. However, for this potential to be realised, a greater understanding of the underlying mechanisms of the process is required.

The LF process involves generating thermal stresses within a substrate using a defocused beam. Depending on the desired effect, the process parameters can be altered to either induce elastic-plastic buckling or plastic compressive strains. The mechanism employed in this work is the Temperature Gradient Mechanism (TGM), which bends the sheet metal out of plane towards the beam. A steep thermal gradient is generated locally along the irradiation path, inducing more thermal expansion on the upper surface of the substrate. Upon cooling, providing the temperature was raised enough to cause sufficient thermal strain, plastic contraction occurs in this upper surface, creating a bend angle of 1-2°.

In order to establish the required thermal gradient the depth of heating must be relatively small compared to the

sheet thickness, this being achieved through an acceptable combination of traverse speed, spot size and laser power.

Initially the sheet bends away from the beam slightly as the flow stress on the upper surface is reduced. The magnitude of this counterbend is negligible compared to the resulting bend angle but is nevertheless detrimental to the process as it reduces the compressive stresses acting upon the region of plastic flow. With further heating the yield stress of the material is reached and any further expansion is converted into plastic compressive strain. Upon cooling this plastic compression is residual, and the associated conservation of volume or shortening on the upper surface causes the sheet to bend towards the beam.

Whilst the bend angle per pass is fairly constant initially (typically over the first 15-20 passes) there is a fall off associated with the angle of bending achieved with successive irradiations after this. A number of factors have been identified as contributing to this [1] and how this depends on the complex interrelation of process parameters and substrate thermo-mechanical properties.

In order for laser forming to realise its potential as a fully controlled process in a manufacturing environment an understanding of this variation in bend angle per pass is essential. The research presented in this paper focuses on attaining a higher degree of controllability through computer based simulation and modelling as a means of process development. A full thermo-mechanical simulation of the LF process is presented and utilised both to identify possible process mechanisms and reduce the number of practical experiments required to characterise the process.

2 Experimental

An experimental study was conducted on graphite coated 80x80x1.5mm AISI 1010 steel coupons using a 1.5 kW Electrox CO₂ TEM₀₀ laser with a 3-axis Galil CNC beam delivery system, custom written control software and operating in continuous wave mode. A cantilever

arrangement was used for processing, with the coupons being clamped at one edge (Fig. 1).

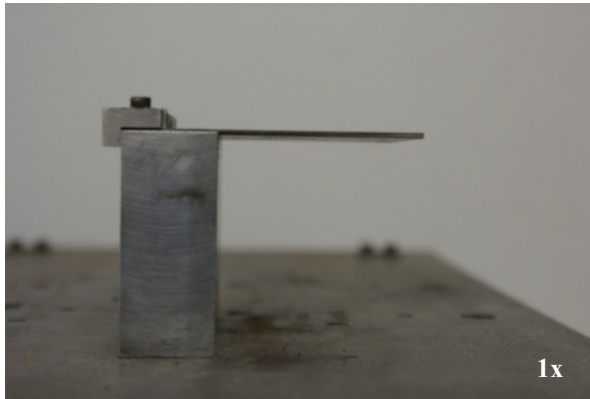


Fig. 1. Edge clamped cantilever arrangement

To fully understand the thermal aspects of the LF process a FE model was developed. A 2005 element thermo-mechanical simulation of the laser forming of 80x80x1.5 mm AISI 1010 steel, using multiple irradiations, was developed using COMSOL MultiPhysics version 3.5a (Fig. 2).

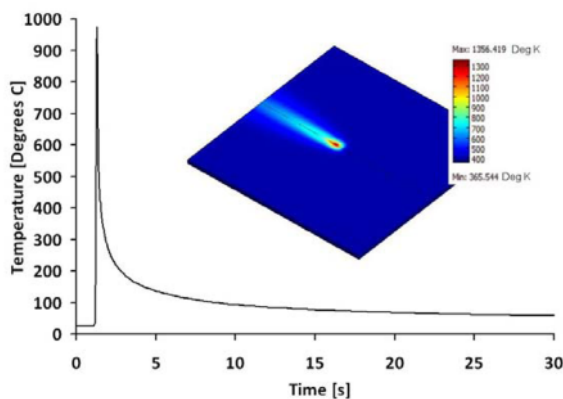


Fig. 2. Comsol MultiPhysics FE model output for the top surface directly on the laser scan line. 80x80x1.5mm mild steel AISI 1010, 760W, 5.5mm beam diameter, 35mm/s, 80% absorption, edge clamped

Material properties were sourced from the ASM Metals Handbook, COMSOL's built in materials library and via experimentation. Thermal expansion coefficient (α), Young's modulus, Poisson's ratio, specific heat capacity (C_p), thermal conductivity (k), density (ρ) and yield stress were all considered temperature dependant and validated against empirical results. The incident laser beam was approximated by a Gaussian distributed heat source and an absorption coefficient of 0.8.

3 Results

Numerical and experimental results and discussion on three factors which influence the bend angle per pass are discussed in the following subsections. These factors are thermal effects, variation in absorption and geometrical effects. In addition a numerical and experimental investigation into the development and of edge effects is also presented.

3.1 Thermal effects

With multiple irradiations an associated build up in temperature within the coupons occurs, which subsequently affects the bend angle per pass. Such elevated temperatures can be both beneficial and detrimental and therefore a dwell time between passes must be used which best suits the process. Increased temperatures can reduce the flow stress of the component, making it easier to plastically deform. Conversely, the temperature gradient achievable between the top and bottom surface of the component along the irradiation line can be diminished, reducing the subsequent bend angle.

The magnitude of influence temperature effects have on the LF process is most apparent during the early stages, in this case within the first six passes. After this point a thermal equilibrium between energy input and free convective cooling during the dwell time between irradiations is reached (Fig. 3). The number of passes prior to reaching this equilibrium is both material and process parameter dependant.

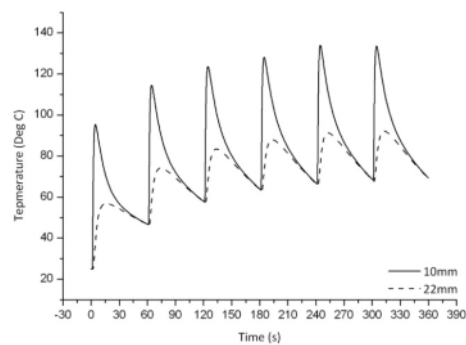


Fig. 3. FE simulation of temperature at 10mm and 22mm from the irradiation path over the first six passes. 80x80x1.5mm mild steel AISI 1010, 760W, 5.5mm beam diameter, 35mm/s, 80% absorption

The bend angle per pass for both the experiment and simulation over the first six passes reveals an initial increase prior to the fall off associated with the LF process (Fig. 4).

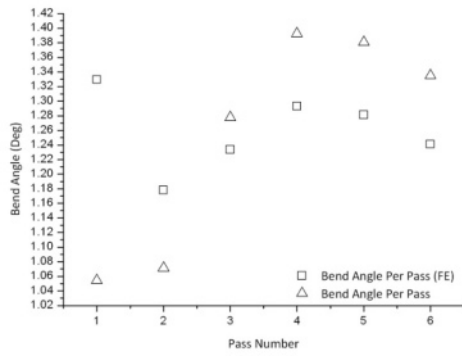


Fig. 4. Experimental and simulated bend angle per pass over the first six passes. 80x80x1.5mm mild steel AISI 1010, 760W, 5.5mm beam diameter, 35mm/s, 80% absorption

The beneficial effects of a build up in temperature appear to last up to the fourth pass before the temperature gradient is adversely affected and the bend angle per pass is reduced.

An FE simulation of the first six passes was conducted in which three material thermal properties were varied within +/-20% of their initial value. These were the thermal conductivity, specific heat capacity and thermal expansion coefficient, with their effect on the cumulative bend angle after six passes studied (Fig. 5).

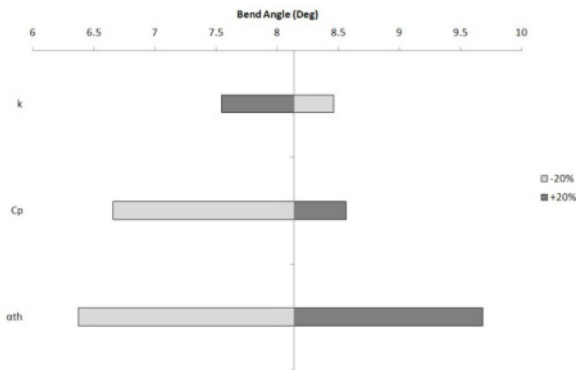


Fig. 5. Effect of varying k, Cp and α_{th} on the cumulative bend angle after six passes. 80x80x1.5mm mild steel AISI 1010, 760W, 5.5mm beam diameter, 35mm/s, 80% absorption

From Fig. 5 it is clear that the thermal expansion coefficient has the largest influence on bend angle. An increase in thermal expansion subsequently increases the amount of plastic contraction that can occur upon cooling, resulting in more plastic deformation.

In assessing the effect of varying the values of k and Cp the thermal diffusivity (α , 1.1) is a useful parameter to consider.

$$\alpha = \frac{k}{\rho C_p} \tag{1.1}$$

The higher the value of α , the more rapidly a substrate can adjust to changes in temperature and return to a thermal equilibrium with its surroundings. Fig. 6 depicts the effect on α when k and Cp are varied within +/-20% of their initial value.

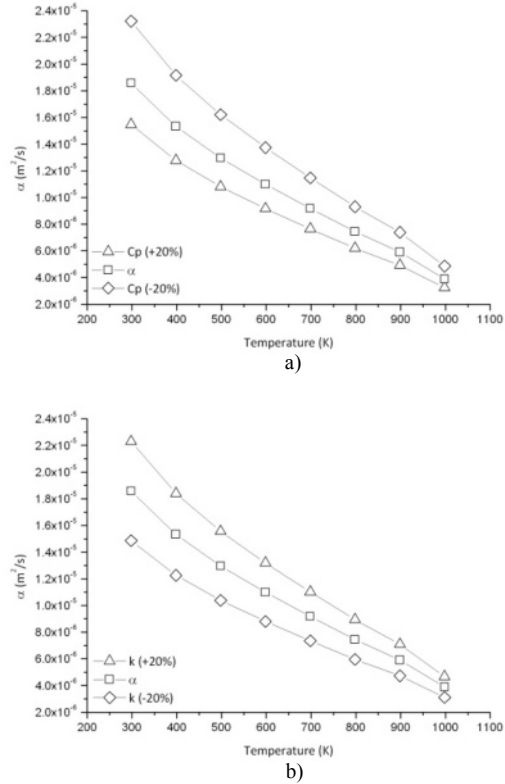


Fig. 6. The effect of varying a) Cp and b) k on α_{th}

It would appear as though in the early stages of the LF process a lower value of α is preferable.

3.2 Variation in absorption

Absorption effects play a key role in the LF process and as such have a large degree of influence on the bend angle per pass. Typically, a defocused beam is employed in order to achieve sub-melting temperatures on the top surface of the component. To aid the coupling of laser radiation into the component a graphite coating is applied. Research at the University of Liverpool [2] has shown that with successive irradiations this coating is degraded or ‘burnt off’, reducing the amount of energy coupled into the component with subsequent passes. This has a direct effect on the bend angle per pass. Fig. 7 shows cumulative bend angle and the bend angle per pass for both the experimental process and the analogous FE simulation.

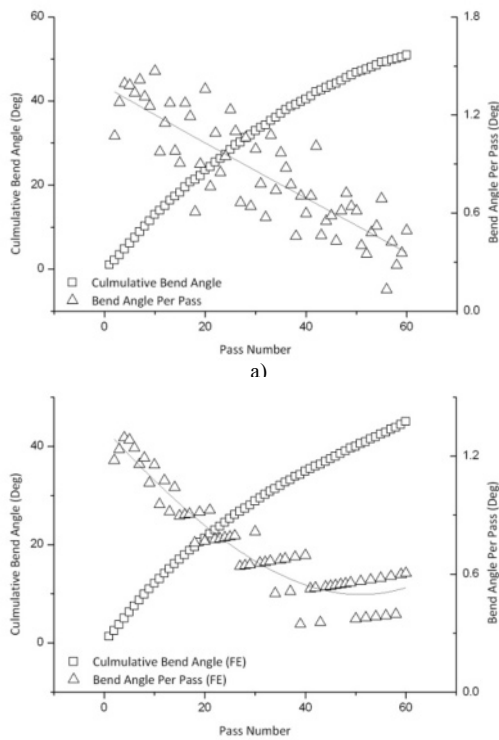


Fig. 7. Cumulative bend angle and b) the bend angle per pass for a) experimental and b) simulation of LF of 80x80x1.5mm mild steel AISI 1010, 760W, 5.5mm beam diameter, 35mm/s, 80% absorption

It is important to note that, in the FE simulation, the absorption coefficient is kept constant at 0.8. The simulated trend is identical to the experimental until around 35 passes where it stabilises as the experimental trend continues to fall. This suggests that graphite burn off becomes detrimental to the process only after a significant number of passes. This could be due to either less energy being coupled into the component as it becomes more reflective or the loss of the secondary heat source that the burning graphite provides.

Table 1. R , $D_{(max-min)}$ and α_B for both experimental and simulated single pass LF of 80x80x1.5mm mild steel AISI 1010, 760W, 5.5mm beam diameter, 35mm/s

		FE			Experimental		
V_1 (mm/s)	V_2 (mm/s)	R	$D_{(max-min)}$ (mm)	α_B (Deg)	R	$D_{(max-min)}$ (mm)	α_B (Deg)
35	35	92.524	0.011	1.205	3.921	0.131	1.162
35	37.5	104.597	0.01	1.165	26.822	0.222	1.260
35	40	116.932	0.008	1.152	95.243	0.144	1.068
35	42.5	98.271	0.067	1.08	44.221	0.0725	0.932
35	45	17857.14	0.037	1.027	274.125	0.198	0.794

3.3 Geometrical effects

With increasing bend angle the initially circular beam incident on the components surface becomes more elliptical in shape [3] (Fig. 8).

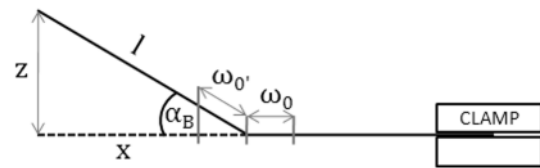


Fig. 8. The geometrical effect in LF for an edge clamped arrangement

This has the effect of reducing the energy density of the beam, with a significant reduction in power density (>20%) occurring at bend angles greater than 35°, this remaining the case regardless of spot size. The relationship between bend angle, initial beam radius and irradiation area A is described by (1.2).

$$I = I_0 \frac{A_0}{A} \quad (1.2)$$

A simulation was conducted in order to see the effect that such a corresponding decrease in energy density had on initial bend angle, as depicted in Fig. 9. A combination of both a Gaussian and modified Gaussian intensity distribution (1.3, 1.4) was applied to two separate boundaries along the irradiation path. The modified Gaussian distribution used separate beam radius values in the x and y axis to give the elliptical shape associated with the geometrical effect.

$$I = I_0 e^{-\left(\frac{x^2}{w_x^2} + \frac{y^2}{w_y^2}\right)} \quad (1.3)$$

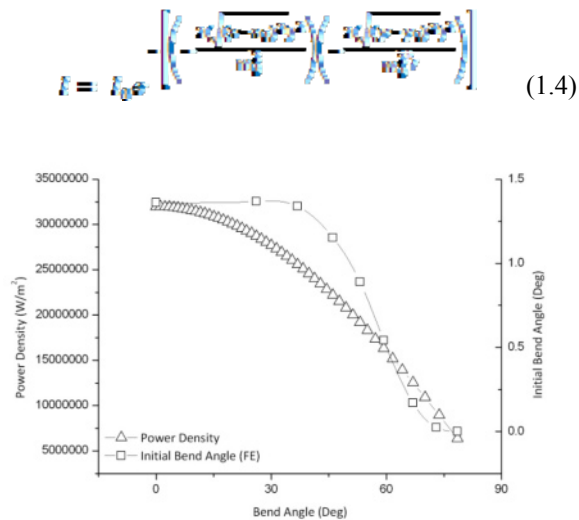


Fig. 9. Effect of reducing energy density on simulated initial bend angle. 80x80x1.5mm mild steel AISI 1010, 760W, 5.5mm beam diameter, 35mm/s, 80% absorption

From Fig. 9 it can be seen that the reduction in energy density associated with the geometrical effect becomes highly detrimental at bend angles of $\sim 35^\circ$.

3.4 Edge effects

A single pass FE simulation of the LF process was conducted and the development of the resultant asymmetrical edge effect [4] was monitored. This effect consists of a large inflection on the leaving edge of the plate which can be attributed to less effective conductive cooling and thus a greater amount of plastic contraction. Such asymmetrical edge effects are undesirable. A subsequent FE simulation was conducted in which the traverse speed was varied to reduce the line energy after the beam reaches the halfway point of the sheet (Fig. 10). This has the effect of reducing the amount of heat which the leaving edge was required to dissipate.

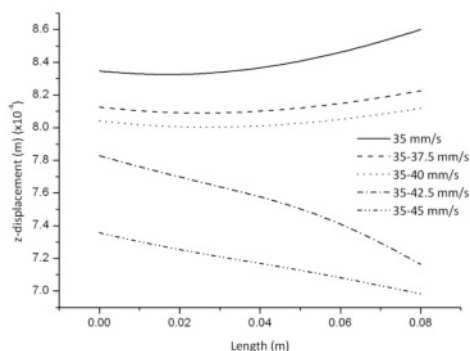


Fig. 10. Single pass FE simulation of edge effects with different scan strategies. 80x80x1.5mm mild steel AISI 1010, 760W, 5.5mm beam diameter, 35mm/s, 80% absorption

From the simulation results the optimum combination of traverse speeds was found to be 35 mm/s and 40 mm/s. This was confirmed by calculating the radius of curvature (R) and the difference in displacement between either edge ($D_{(\max-\min)}$), as in Table 1. Analogous experimentation was conducted which also found this combination of traverse speeds to be optimal.

4 Conclusions

FE modelling of the LF process has been used to ascertain which of the various process parameters presented here (thermal effects, geometrical effects, variation in absorption) contribute towards variation in bend angle per pass with multiple irradiations and subsequently the magnitude of their contribution. Thermal effects were found to be confined to the early stages of the process, becoming less influential as thermal equilibrium is reached. Geometrical and absorption effects become dominant later in the process with increasing deformation and graphite burn-off respectively.

Additionally, FE simulations were used to analyse the development of undesirable asymmetric edge effects in 2D LF and subsequently devise new scan strategies to eradicate them. Analogous experimentation was conducted in order to validate these simulations.

5 References

- [1] S. P. Edwardson, J. Griffiths, K. R. Edwards, G. Dearden, K. G. Watkins, Laser Forming: Overview of the Controlling Factors in the Temperature Gradient Mechanism, IMechE Part C, 2010
- [2] C. Carey, W. J. Cantwell, G. Dearden, K. R. Edwards, S. P. Edwardson, J. D. Mullett, C. J. Williams, K. G. Watkins, Effects of Laser Interaction with Graphite Coatings, Laser Assisted Net Shape Engineering 5, Lane 2007, Pp673-686
- [3] I. Prithwani, A. Otto, M. Schmidt, J. Griffiths, K. Watkins, S. P. Edwardson, G. Dearden, Laser Beam Forming of Aluminium Plates under Application of Moving Mesh and Adapted Heat Source, Proceedings of the Fifth International WLT-Conference on Lasers in Manufacturing 2009, Munich, June 2009
- [4] Jiancheng Bao, Y. Lawrence Yao, Analysis and Prediction of Edge Effects in Laser Bending, Journal of Manufacturing Science and Engineering, 54, Vol. 123, February 2001

The effect of laser beam geometries on laser forming of sheet metal

S. Jamil, M.A. Sheikh, L. Li,
Laser Processing Research Centre (LPRC), School of Mechanical Aerospace and Civil Engineering, University of Manchester, M60 1QD, UK

Abstract. In recent years laser beam forming has emerged as a new and very promising technique to form sheet metal by thermal residual stresses. There are many advantages of laser forming compared to conventional sheet bending. Among these include design flexibility, production of complex shapes, which is unachievable by the conventional methods, forming of thick plates, possibility of rapid prototyping etc. Many numerical and experimental investigations of laser forming processes were carried out to understand the mechanisms and the effects of various parameters on the characteristics of the formed parts. The objective of this work is to investigate the effect of different beam geometries on laser bending process of metal sheets. In this paper, a comprehensive thermal and structural finite element (FE) analysis is conducted to investigate the effect that these laser beam geometries have on the process and the final product characteristics. To achieve this, the temperature distribution, deformation, plastic strains and stresses produced by different beam geometries are compared numerically.

Keywords: Laser forming, bending, beam geometries, finite element method, temperature gradient mechanism, sheet metal.

1. Introduction

One of the advantages of laser beam forming compared to conventional flame bending is its ability to accurately control the size and geometry of the heat source. In the area of optics, many studies [1-2] explain the methods and design approaches to produce a variety of beam shapes such as line, rectangular, star, D-shape, annular, cross etc. Currently, whilst there are many studies on laser parameters such as power, feed rate and beam size etc, there is very limited work on the effects of different beam geometries on laser bending. One possible method of varying the temperature distribution, and hence the strain and stress distribution, without changing the input power or the scanning speed, is by modifying the geometry of laser beams. This paper describe the results of numerical investigations of the effect of rectangular beam geometries, on laser bending process of sheet metal which is dominated by the Temperature Gradient Mechanism (TGM).

To date, many forming mechanisms have been suggested [3-6]. In particular, Temperature Gradient

Mechanism (TGM) has been extensively studied and reported in literature. When the material surface is irradiated with a laser beam, a fraction of the laser energy is absorbed into the material. Hence the laser energy is deposited on a very thin layer of material. The layers of the material close to the irradiated surface are at higher temperature than those away from the surface, thus creating a steep temperature gradient within the thickness of the material. Hence the material layers close to the surface expand more. This differential thermal expansion produces thermal stresses in the material leading to counter-bending of the sheet away from the laser beam. The yield strength and the flow stress of the material decreases with increasing temperature. When the generated thermal stress exceeds the yield stress of the material, further expansion of the heated region results in into compressive plastic deformation. After the laser scan, the surface is rapidly cooled which causes thermal contraction. The thermal contraction results in the local shortening of the surface layers thus causing the sheet to bend towards the laser beam, as illustrated in Figure 1.

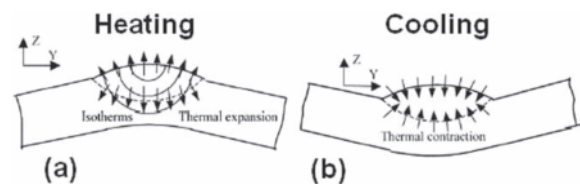


Fig. 1. Thermal gradient mechanism of laser bending (a) the heating process and (b) the cooling process [5]

2. Numerical Modelling

2.1 Finite Element equations

The finite element equation for transient heat transfer analysis can be expressed as follows [7]:

$$[C][\dot{T}] + [K]\{T\} = \{Q(t)\} \quad (1)$$

Where $[C]$ is the specific heat matrix, $[\dot{T}]$ is the time derivative of temperature, $[K]$ is the heat conductivity matrix, $\{T\}$ is the temperature, $\{Q(t)\}$ is the heat flux.

Material used in this model is 1.0584 (D36) which is shipbuilding steel. Temperature dependency of material properties is considered including Poisson's ratio, elastic modulus and yield stress [8].

For the case of transient thermal stresses generated due to laser scanning with no damping or external forces/loadings, the nonlinear transient structural equation based on FEM can be written in the matrix form as follows:

$$[K(T)]\{u(t)\} = \{F^{th}(t)\} \quad (2)$$

Where $[K(T)]$ is the temperature dependent stiffness matrix, $\{F^{th}(t)\}$ is the thermal load vector, $\{u(t)\}$ is the nodal displacement vector. Thermal load vector $\{F^{th}(t)\}$ can be evaluated by using,

$$\{F^{th}\} = \int_{vol} [B]^T \frac{E\alpha(T)\Delta T}{1-2\nu} \delta dV \quad (3)$$

Where $[B]$ is the strain displacement matrix, E is the elastic modulus, ν is the Poisson's ratio, ΔT is the temperature difference, and δ is the matrix $[1 \ 1 \ 1 \ 0 \ 0]^T$.

Total strains can be evaluated from nodal displacements by using,

$$\{\varepsilon\} = [B]\{u\} \quad (4)$$

where $\{u\}$ is the nodal displacement vector. The difference between total strain and thermal strain gives mechanical strain which consists of plastic and elastic strain components as expressed below:

$$\{\varepsilon\} - \{\varepsilon^{th}\} = \{\varepsilon^{pl}\} + \{\varepsilon^{el}\} \quad (5)$$

Where $\{\varepsilon\}$ is the total strain vector, $\{\varepsilon^{th}\}$ is the thermal strain vector, $\{\varepsilon^{pl}\}$ is the plastic strain vector, $\{\varepsilon^{el}\}$ is the elastic strain vector.

2.2 Specimen material, size

In the present numerical study, the commercial non-linear finite element code, ANSYS is used. Model parameters are as follows:

- Dimension of the plate: 300mm x 150mm x 6mm
- Plate material: Shipbuilding 1.0584 (D36) [8]
- Power of laser: 1.5kW
- Laser beam velocity: 0.3m/min

The problem is symmetric and therefore only half of the plate is modelled with symmetric boundary conditions as shown in Fig 2. Laser heating is modelled as moving heat

flux with ANSYS Parametric Design Language (APDL) used to incorporate the laser beam motion. All exposed surfaces are subjected to convection but heat losses due to radiation are not considered as they are very small.

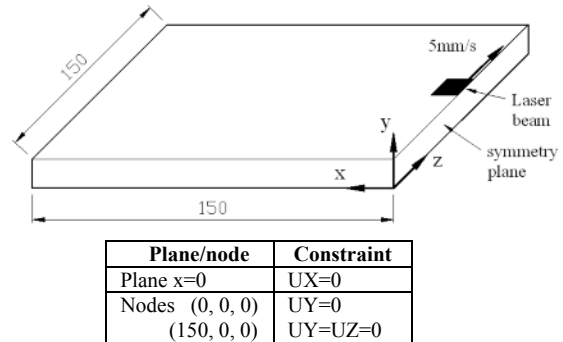


Fig. 2. Boundary condition of the half plate modelled

2.3 Beam geometries

To investigate the effect of various beam geometries on the laser bending process, five beam geometries with different dimensions along the axial and transverse directions of the scan were chosen as shown in Fig 3. The area of each beam was kept constant at 200mm² to maintain the power intensity and hence the same amount of energy transferred into the specimen.

REC-H	SQUARE	REC-V	TRI-F	TRI-R
A = 25mm B = 8mm	A = 14.1mm B = 14.1mm	A = 8mm B = 25mm	A = 21.5mm B = 18.6mm	A = 21.5mm B = 18.6mm

Fig. 3. Laser beam geometries with similar effective area used in FE simulations

The basic assumptions for the model are as follows:-

- (i) Material is isotropic.
- (ii) Laser intensity distribution is assumed to be uniform
- (iii) Bauschinger's effect is neglected
- (vi) Von-Misses criterion is used for plastic yielding.
- (v) Energy dissipation due to plastic deformation is neglected when compared with the energy involved in the thermal process.

3. Results and discussion

3.1 Thermal analysis

Figure 4 shows temperature against time for all the five beam geometries measured at the centre of scanning paths (0, 6, 75). For each beam, the temperature starts rising approximately when the beam enters the reference point.

The temperature increases rapidly until the beam leaves the point and the temperature starts dropping. From the figure it is seen that the beams that have a longer dimension in the scanning direction with respect to its lateral dimension, produce higher temperatures despite of the fact that the power intensity and the beam effective area is similar for all beams. This is mainly due to the longer beam-material interaction for the beams with longer dimensions in the scanning direction.

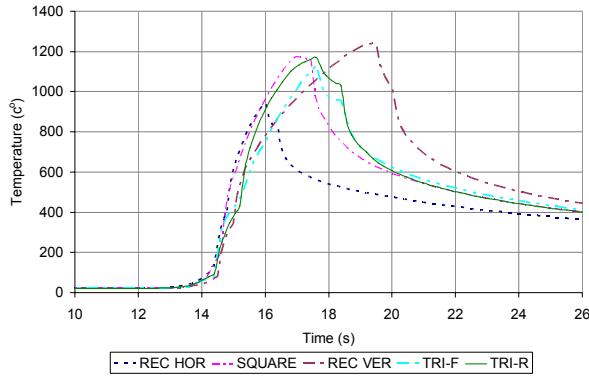


Fig. 4. Temperature vs time at reference point (0, 6, 75)

The duration of the beam-material interaction, given by t_s , is the ratio of the axial length, d_{ax} , to the scanning speed, v , ($t_s = d_{ax}/v$). Beam REC-V which has the longest axial length, gives the highest temperature of 1240°C. However, its lateral temperature spread (along the x-direction) is narrower compared to the other beams

3.2 Structural analysis

Table 1 shows the results of the displacements for each beam. The SQUARE beam has the largest average bending angle followed by the REC-H, TRI-F, REC-V and TRI-R. The displacements of the free edge were measured at both the beam entrance side, UY_i (150, 6, 0), and the beam exit side, UY_f (150, 6, 150) to observe the edge effects. For all cases, higher displacement occurs on the beam exit side rather than the entrance side. This agrees with general findings and has been established to be caused by a higher temperature at the exit path rather than the entrance [9]. From table 1, it is interesting to note that REC-V and TRI-F both produce the lowest percentage angle variation compared to the rest of the beams. This could definitely help in cases where high tolerance accuracy is needed especially when a small angle adjustment is required in a single pass scan. REC-H produces the highest edge effect with 10.7% angle variation between the entrance and the exit angle, followed by TRI-R with 9.3%. From this result it could be concluded that the beams with a narrow leading edge such as REC-V and TRI-F produce less bending angle variation. On the other hand beam with wider leading edge such as REC-H and TRI-R produce higher bending angle variation.

Another type of edge effects is the curvature of the scanning line which is shown in figure 5. All beams produce concave profiles. Again, REC-H produces the highest edge effect with the maximum displacement of 0.14mm. Interestingly, both the triangular beams, TRI-F and TRI-R, produce lower distortion along the scanning line with the maximum displacements around 0.07mm.

Table 1. Results of displacement and bending angle

Items	Unit	REC-H	SQUARE	REC-V	TRI-F	TRI-R
Beam entrance side, UY_i	mm	0.952	1.178	0.8383	0.866	0.797
Beam exit side, UY_f	mm	1.054	1.259	0.8757	0.913	0.871
$\Delta UY = UY_f - UY_i$	mm	0.102	0.081	0.0374	0.047	0.074
% variation (Edge effect)		10.7%	6.9%	4.5%	5.4%	9.3%
UY_{ave}	mm	1.003	1.219	0.857	0.8895	0.834
Average bending angle, α_b	°	0.766	0.931	0.655	0.680	0.637

However TRI-R produces a variation of 9.3% in the bending angle along the scanning line, while TRI-F produces only 5.4% variation (table1). This leads to the conclusion that TRI-F is the better option for lower edge effects.

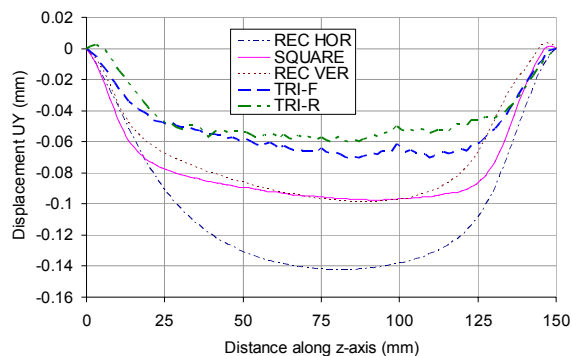


Fig. 5. Vertical displacement along the scanning path ((0, 6, 0) to (0, 6, 150))

At the end of the cooling period, the width of the plastically deformed zone on the irradiated surface is about the width of the laser beam. This is the cause for different deformation behaviour from different beam geometries. The sum of plastic strains is zero at any given time based on the assumption of constant volume during plastic deformation. Generally, the materials under the spot scan shrink in the x-direction (transverse) and expand in the thickness direction. Small shrinkage also occurs in the z-direction (laser beam movement direction) which contributes to the the edge effect.

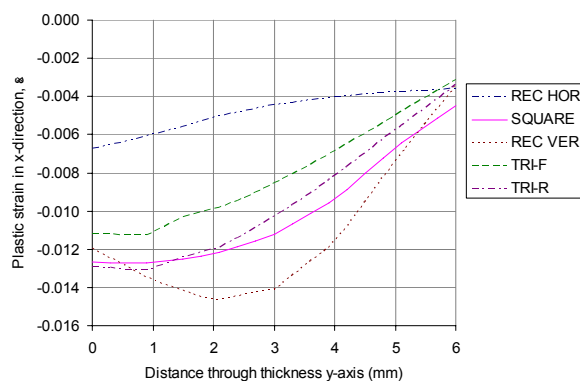


Fig. 6. Plastic strain, ϵ_x , through the thickness direction

Figure 6 shows the plastic strain, ϵ_x , measured in the middle of the plate from the top surface (0, 6, 75) to the bottom (0, 0, 75). Generally, for TGM processes, one would expect the plastic strain, ϵ_x , to be higher at the top surface and gradually decreased through the thickness which is true for all beams in fig. 6 except REC-V. For REC-V the maximum plastic strain occurs at 2mm below the top surface which suggests that an Upsetting

Mechanism (UM) occurs besides TGM. This explains the reason for the low bending angle for this beam, despite having the highest maximum temperature and plastic strain.

4. Summary and conclusions

A numerical study of the effects of five different beam geometries on laser bending of sheet metal, dominated by TGM, has been carried out. From the thermal analysis, it was established that the maximum temperature of the specimen depends strongly on the duration of the beam-material interaction. Higher temperatures influence development of higher plastic strain due to the temperature-dependant yield stress. The width of the plastically deformed zone which is related to the transverse width of the beam, contributes to the different plate deformation behaviours by different beams.

TRI-F is seen as the best beam for applications where high accuracy tolerance is needed especially when a small angle adjustment is required in a single pass scan. It could be concluded that the beams with a narrow leading edge are preferable to produce less bending angle variations compared to the ones with wider leading edge. This study forms the basis for more investigations on the effects of different beam geometries on laser forming.

References

- [1] Bewsher, A, Powell, I & Boland, W (1996) Design of single-element laser-beam shape projectors. *Applied Optics*. 35: 1654-1658.
- [2] Berges, J, Unnebrink, L & Henning, T (1999) Mask adapted beam shaping for material processing with excimer laser radiation. *Proc. of SPIE*. 3573: 108-111.
- [3] Hsieh, H-S & Lin, J (2005) Study of the buckling mechanism in laser tube forming. *Optics & Laser Technology*. 37: 402-409.
- [4] Vollertsen, F, Komel, I & Kals, R (1995) The laser bending of steel foils for microparts by the buckling mechanism-a model. *Modelling and Simulation in Materials Science and Engineering*. 3: 107-119.
- [5] Hu, Z, Kovacevic, R & Labudovic, M (2002) Experimental and numerical modeling of buckling instability of laser sheet forming. *International Journal of Machine Tools and Manufacture*. 42: 1427-1439.
- [6] Geiger, M & Vollertsen, F (1993) The mechanism of laser forming *CIRP*. 42: 301-304.
- [7] Ansys (2003) Structure with material non-linearities and coupled filed analysis guide. *ANSYS Theory Manual*. Canonsburg, PA, ANSYS Inc.
- [8] Kyrsanidi, Ak, Kermanidis, Tb & Pantelakis, Sg (2000) An analytical model for the prediction of distortions caused by the laser forming process. *Journal of Materials Processing Technology*. 104: 94-102.
- [9] Bao, J & Yao, Yl (2001) Analysis and prediction of edge effects in laser bending. *Journal of Manufacturing Science and Engineering*. 123: 53-61.

Towards Controlled 3D Laser Forming

S.P. Edwardson¹, J. Griffiths¹, G. Dearden¹, K. G. Watkins¹

¹ Laser Group, Department of Engineering, University of Liverpool, Liverpool, L69 3GH, UK

Abstract. 2-Dimensional laser forming can currently control bend angle, with reasonably accurate results, in various materials including aerospace alloys. However, this is a different situation for 3-Dimensional laser forming. To advance this process further for realistic forming applications and for straightening and aligning operations in a manufacturing industry it is necessary to consider larger scale controlled 3D laser forming. The work presented in this paper uses a predictive and adaptive approach to control the laser forming of mild steel and aluminium sheet into a desired surface. Key to the control of the process was the development of a predictive model to give scan strategies based on a required geometry and the surface error. The forming rate and distribution of the magnitude of forming across the surface were controlled in the closed loop by the process speed. When the geometry is not formed within one pass, an incremental adaptive approach is used for subsequent passes, utilising the error between the current and desired geometry to give a new scan strategy, thus any unwanted distortion due to material variability can be accounted for and distortion control and removal is possible.

Keywords: Laser Forming, Bending, 3D, closed loop.

1. Introduction

The inspiration behind Laser Forming (LF) originates in the flame bending or “line-heating” process. Flame bending uses an oxy-acetylene torch as a heat source and has been used extensively for the curving and straightening of heavy engineering components. However an oxy-acetylene torch lacks the subtleties of a laser. With minimal heating to surrounding material the use of a laser makes it easier to regulate energy absorption in localised areas. This allows for much greater control in the forming of a work-piece. Combine this with CNC control and the possibilities of an automated forming process become apparent.

LF has become viable for the shaping of metallic components, as a means of rapid prototyping and for adjusting and aligning. LF is of significant value to industries that previously relied on expensive stamping dies and presses for prototype evaluations. Relevant industry sectors include aerospace, automotive, shipbuilding and microelectronics. In contrast with conventional forming techniques, this method requires no mechanical contact and thus promotes the idea of ‘virtual

tooling’. It also offers many of the advantages of process flexibility and automation associated with other laser manufacturing techniques, such as laser cutting and marking [1].

The process employs a defocused laser beam to induce thermal stresses without melting in the surface of a work-piece in order to produce controlled distortion. These internal stresses induce plastic strains, bending or shortening the material, or result in a local elastic plastic buckling of the work piece depending on the mechanism active [2].

LF can be split into two groups, basic single line 2D forming that produces shapes that are folds of varying angles, and more complicated multi-line 3D forming that produces continuous surfaces. 3D forming comprises ‘developable forming’, which is a series of 2D bends producing a surface with a single curvature and ‘non-developable forming’ which makes use of the shortening mechanism to produce a surface containing a double curvature.

To advance the LF process for realistic forming applications and for straightening and aligning operations in a manufacturing environment, it is necessary to consider controlled 3D LF. In order to compete directly with conventional forming techniques, such as die forming, the process must be proven to be reliable, repeatable, cost effective and flexible. It is the potential flexibility of 3D laser forming that offers the greatest benefit. A change to required part geometry could be implemented easily through the CAD driven process, which can be compared to the expensive and in-flexible hard tooling requirements of the die forming process.

The work presented here on 3D laser forming aims to prove the viability of this technique as a direct manufacturing tool and as a means of correcting unwanted distortion. To this aim, progress towards repeatable closed loop controlled 3D LF is presented.

2. Experimental

Initial 3D LF investigations [3] were based around a purely empirical approach to establish rules for the positioning and sequencing of the irradiation lines required for the controlled 3D laser forming of symmetrical/uniform saddle and pillow ('dome') shapes from rectangular 400x200x1.5mm mild steel CR4 sheet. It was concluded from this work that the development of an on-line monitoring system with predictive distortion correction abilities is a requirement if any 3D laser forming operation is to be used in a manufacturing environment. This is due to the unknowns that can be present when forming in an open-loop set-up, such as residual stresses and variability in the absorption of the incident laser radiation.

A foreseeable problem with a system which makes online distortion correction during processing is that the final geometry of the part is not reached until sometime after processing has stopped, when the plate has cooled somewhat and the elastic stresses have been released leaving a plastically formed part [4]. This suggests that a strategy of a one off single pass to produce a required geometry would be extremely difficult to predict and control. A more sensible method of producing a required geometry would be to increment towards it over a number of passes, taking surface measurements after each pass so as to have the ability to take account of any errors due to unwanted distortion. With the forming of saddle, pillow shapes and any non-developable shape the magnitude of forming is limited when using the TGM as it is principally an out of plane forming mechanism, where non-developable shapes need an in plane, or shortening, mechanism [5]. Because of the added complexity in forming non-developable parts, it is easier to consider a largely developable shape, with some slightly non-developable areas. In previous studies [5, 6] lines of constant height were used to calculate the irradiation path. For this investigation lines of constant angle are used. Because the shape is mostly developable and is therefore a series of 2D bends the idea behind lines of constant angle is very simple. In 2D LF, when using the TGM to achieve a bend, a line is scanned at a right angle to the direction of the bend (fig. 1.).

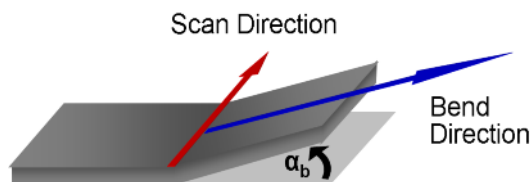


Fig. 1. Schematic of a two dimensional bend.

This method treats each segment as an individual 2D bend and simply connects the angles that are equal. The contours are spread in equal increments of angle. The

angle increment between each contour is then used to calculate the speed of the scan lines.

Speed here is used to control the energy input, which is one of the main influencing parameters of bend angle [2]. The speed is calculated from a 2D investigation where a series of 2D bends were formed at various speeds to generate bend angle calibration data.

This method forms the part evenly and reduces the possibility of over forming at the edges which is a drawback with using contours of constant height [5, 6]. It was concluded from earlier empirical studies [3] that, in order to develop control of the process of 3D laser forming, it was necessary to have the ability to define the surface to be formed. The desired shape (based on a form of aircraft cowling) may be defined by a Bezier surface patch (fig. 2.) in Matlab.

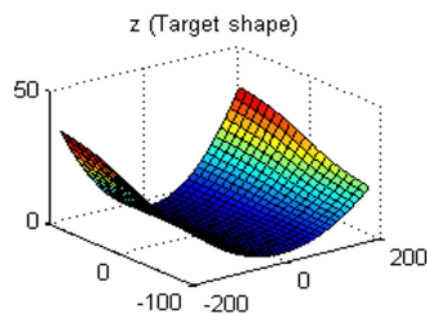


Fig. 2. Interpolated points defining desired shape

This mathematical function allows the definition of a continuous 3D surface from only a limited number of supplied coordinates for the surface (e.g. 16), the rest of the data then being interpolated over a given range.

In addition it was realised that as the scan strategy prediction is geometry based the error between a given shape and a desired shape could form the basis for a further scan strategy. Contours of error between two surfaces are akin to the error between a flat sheet and a desired shape that give the contours of angle. This can allow for the correction of a formed shape if the desired shape is not formed by the initial prediction. Thus an iterative method can be used to increment towards a desired shape. This method also allows for the correction of unwanted distortion in a pre-formed shape, by forming on both sides of a component.

The experimental study was conducted on LF of graphite-coated 1mm thick AA 5251 using a 1.5kW Electro CW CO₂ laser with a 3-axis Galil CNC beam delivery system with custom written control software. The aluminium was cut into 400x200mm and 100x80mm coupons a 3D LF study and 80x80mm coupons for a 2D LF study. The coupons were used to produce calibration data via simple 2D bends for the 3D study. A diode laser range finder, mounted on the z-axis of the LF system, was used to verify/measure the bend angles in 2D LF and also the surface shape in 3D LF, by using control software to create a co-ordinate measuring machine (CMM) set-up.

The samples were held in place on the workstation table using a centre clamp; this required a hole to be drilled in the centre of the plates for a bolt to pass through.

3. Results and Discussion

Using an iterative approach based on the error between the current and desired surfaces it was possible to produce a component to within -5mm and $+3\text{mm}$ maximum error in $200\times 80\text{mm}$ AA 5251 at 200W . This demonstrated both accurate 3D LF and a means of distortion correction as the system can create a new strategy based on the current shape. The final shape is shown in fig 3.

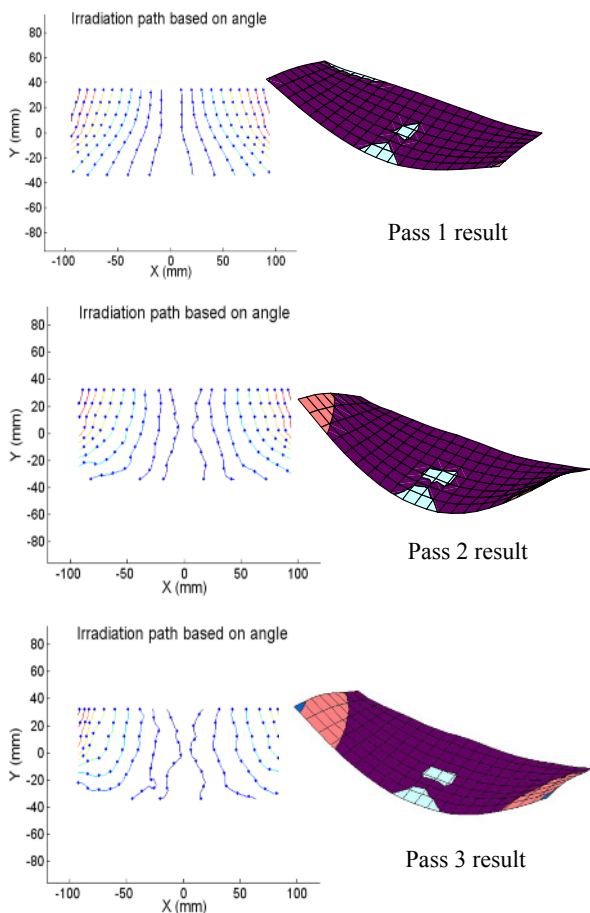


Fig. 3. Evolution of laser formed part and the predicted scan strategy over the first 3 passes, $200\times 80\times 1\text{mm}$ AA5251, 200W , 3mm beam diameter, speed range $40\text{-}90\text{mm/s}$.

The speed range and power were selected to prevent faceting and melting. This produced a component to within $\pm 5\text{mm}$ and a part with very little visible surface effects or witness marks (fig 4).

Though there is no visible evidence of a dwell on the surface a dwell still occurs. This is undesirable as it is an unnecessary added input of heat. However, this is easily preventable. By closing the laser's shutter prior to the end of the movement or increasing the size of the irradiation path to place dwell points off the work piece would solve this problem.

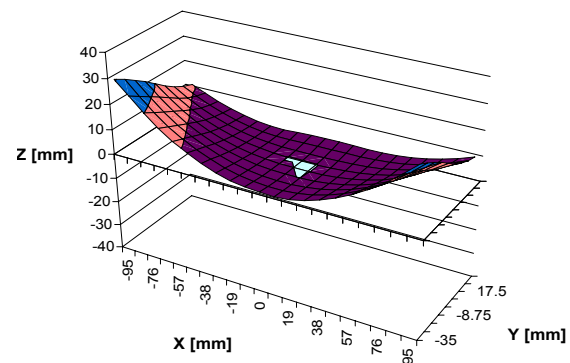
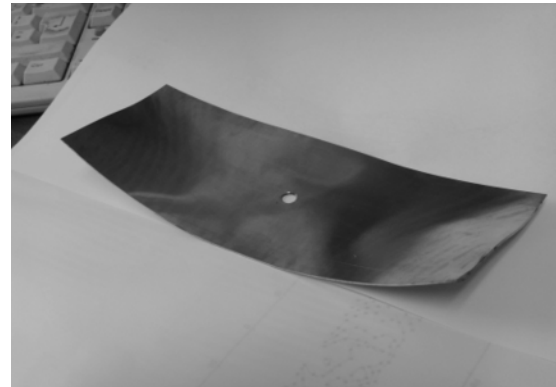


Fig. 4. Final geometry produced. $200\times 80\times 1\text{mm}$ AA5251, 200W , 3mm beam diameter, speed range $40\text{-}90\text{mm/s}$

When scaled up to $400\times 200\text{mm}$ there was a great deal more forming than expected with the first pass producing an over formed part with an error of -2mm and $+12\text{mm}$ (figure 5). This can easily be improved with a reduction in speed. Another reason for over forming was that the part moves into focus as it is formed, which reduced the spot size and increased the fluence on the outer paths. A solution to this would be to start the scan path at the outside and working inwards, the laser then passes over sections that have not yet moved. This will reduce the increase in forming due to moving into focus.

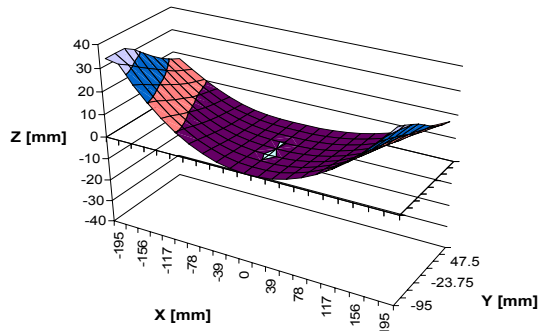
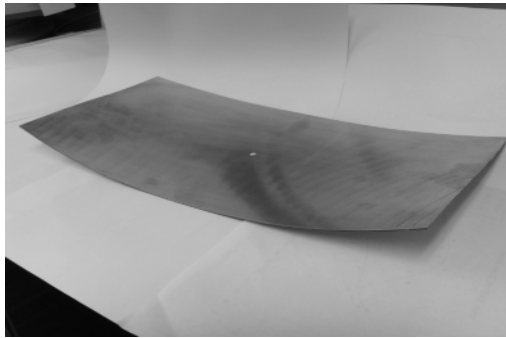


Fig. 5. Final geometry produced. 400x200x1mm AA5251, 200W, 3mm beam diameter, speed range 40-90mm/s

4. Conclusions

- It is possible to predict an irradiation strategy for developable shapes using contours of angle.
- By using an iterative pass-by-pass approach, it has been possible to form a 3D shape in a controlled manner to a reasonable degree of accuracy, taking account of unwanted deformations from program error or material non-uniformity.

- The system can be used for correction distortion with the ability to calculate a scan strategy to form a shape from just about any other shape.
- Size or ratio of a part effects how it reacts to laser forming, further 2D investigation is needed to be able to increase the accuracy of the system.
- Further investigation into speed calibration is needed.
- Although the system is very good at creating accurate shapes, for smaller adjustments more investigation is needed.
- Dwell points add surplus heat that can melt and/or damage the work piece and need to be programmed out.

5. References

- [1] Magee J, Watkins K G, Steen W M, Advances in Laser Forming (1998). *Journal of Laser Applications* 10, 235-246.
- [2] Vollertsen, F. (1994) Mechanisms and Models for Laser Forming, in Proceedings of Laser Assisted Net shape Engineering Conference (LANE 94), Erlangen, Germany.
- [3] Edwardson S P, Watkins KG, Dearden G, Magee J (2001). Generation of 3D Shapes Using a Laser Forming Technique. in Proceedings of ICALEO'2001, Jacksonville, Florida USA.
- [4] Edwardson SP, Watkins KG, Dearden G, French P, Magee J (2003). Strain Gauge Analysis of Laser Forming. *Journal of Laser Applications* 15 225-232.
- [5] Abed E, Edwardson SP, Dearden G, Watkins KG (2005). Closed Loop 3-Dimensional Laser Forming of Developable Surfaces. in IWOTE' 05, Bremen, Germany.
- [6] Edwardson SP, Moore AJ, Abed E, McBride R, French P, Dearden G, Hand DP, Watkins KG, Jones JDC (2004). Iterative 3D Laser Forming of Continuous Surfaces in Proceedings of ICALEO'2004. San Francisco, California.

Fracture Toughness Modifications By Means of CO₂ Laser Beam Surface Processing of a Silicon Nitride Engineering Ceramic

P. P. Shukla and J. Lawrence

Wolfson School of Mechanical and Manufacturing Engineering, Loughborough University, Leicestershire LE11 3TU UK.

Abstract. Surface treatment of an Si₃N₄ engineering ceramic with a CO₂ laser was carried out to identify changes in the fracture toughness (K_{Ic}). A Vickers macro hardness indentation method was adopted to determine the K_{Ic} prior to and after the CO₂ laser treatment. After determination of the surface integrity, crack geometry, crack lengths and the dimensions of the diamond indentations, computational and analytical methods were employed to calculate the K_{Ic} . A decrease in the surface hardness of nearly 7% and of 44% in the resulting crack lengths was found after laser treatment. This inherently led to a 64% increase in the K_{Ic} for the Si₃N₄. This could have occurred due to melting and redistribution of the melt zone which softened the near (top) surface layer forming a degree of oxidation, causing the surface of the engineering ceramic to transform into a new composition.

Keywords: CO₂ laser, Si₃N₄ engineering ceramic, K_{Ic} .

1. Introduction

Because ceramics are hard and brittle, the K_{Ic} is a very important material property as high K_{Ic} implies increased softness and ductility [1-9]. Unlike metals, it is difficult for dislocations to propagate with ceramics which makes them brittle [10-12]. Also, ceramics do not mechanically yield in comparison to metals which leads to a much lower resistance to fracture [10-12]. Ceramics in comparison with metal and metal alloys have a low K_{Ic} ; thus, it is beneficial if the K_{Ic} of ceramics could be increased.

Despite being lengthy, the calculation of K_{Ic} using the experimental values from indentation tests, has been proven to be a consistent technique [3, 4]. Numerous empirical equations are available from previous studies which can be applied to the experimental values [1-4, 13-21], which act as the input parameters for determining the value required.

This study is focused on the use of various empirical equations from the literature combined with the Vickers indentation method to calculate the K_{Ic} of a Si₃N₄

engineering ceramic and observe the effects thereon of the CO₂ laser surface treatment.

2. Experimental Techniques and Analysis

2.1 CO₂ laser treatment

The CO₂ laser treatment was conducted on cold isostatic pressed (CIP) Si₃N₄ with 90% Si₃N₄, 4% yttria, 4% Al₂O₃ and 2% other (unspecified content), (Tensky International Co., Ltd.) in ambient conditions. Each test piece was obtained in blocks of 10 x 10 x 50 mm³. A 1.5 kW CO₂ laser (Everlase S48; Coherent, Ltd.) emitting at a wavelength of 10.6 μm in the continuous wave (CW) mode was used. To obtain an operating window, trials were conducted by varying the power between 50 and 200 W and varying the traverse speed between 100 and 600 mm min⁻¹. From these trials, it was found that 150 W at 600 mm min⁻¹ were the ideal laser parameters to use in terms of achieving a crack-free surface. The stand-off distance between the nozzle and the work-piece was kept to 16 mm in order to obtain a focal spot size of 3 mm. Programming of the laser was conducted using an integrated software which controlled the motion system. A 50 mm line was programmed as a potential beam path using numerical control (NC) programming. This was transferred as a .dxf file.

2.2 Vickers indentation method

A diamond indenter of a specific shape was used to indent the as-received and CO₂ laser treated surface of the Si₃N₄. Around 50 indentation tests were performed on the as-received and laser treated surfaces. The diamond was initially pressed on to the as-received surface of the Si₃N₄ and the load of 5 kg was then released. The indented surface and the resulting crack lengths were measured using the optical microscopy and a co-ordinate measuring

machine. This is a standardized technique to ensure that valid diamond indentation tests were performed [22]. Thereafter, the surface area of the indentation was placed into Equation 1 to calculate the hardness value:

$$HV = 2P \sin [\theta/2] / D^2 = 1.8544P/D^2 \quad (1)$$

where, P is the applied load, D is the average diagonal size of the indentation and θ is the angle between the opposite faces of the diamond indenter.

2.3 Calculation of K_{Ic}

Various equations are available to calculate the K_{Ic} [1-4]. Previous work by Shukla and Lawrence [4] showed that Equation 2 [1, 2] was the most suitable for use in this work. This is given by:

$$K_{Ic} = 0.016 (E/Hv)^{1/2} (P/c^{3/2}) \quad (2)$$

where, P is the load, c is crack length, Hv is the Vickers material hardness value, E is Young's modulus (320 GPa) and 0.016 (materials empirical value) [1, 2]. The hardness obtained from the Vickers indentations test, crack length, and Young's modulus of the Si_3N_4 were the changing input parameters for Equation (2). Young's modulus was increased to 360 GPa when calculating the K_{Ic} of the CO_2 laser treated surface because of the ceramic being anisotropic. Further, the Si_3N_4 underwent a heating resulting from interaction with the CO_2 laser beam, which would, in turn, have led to an increase in the stress and strain ratio from the induced thermal stress. It was therefore proper to increase the Young's modulus for the laser treated samples in order to calculate the K_{Ic} .

3. Results and Discussion

3.1 As-received surface: Hardness, crack lengths and the K_{Ic} .

An average hardness of 1106 Hv for the as-received surface of the Si_3N_4 was determined. The highest value found on the surface of the Si_3N_4 was 1648 Hv and the lowest value was 707 Hv, as shown in Figure 1. This fluctuation is considerable and well outside the expected range of $\pm 10\%$ [23]. This wide fluctuation in the hardness values is not unusual and resulted from surface scarring and pre-existing cracks as a result of the manufacturing process [24].

The crack lengths ranged between 228 to 638 μm with an average of 387 μm , as presented in Figure 2. Crack length has a close relationship with the hardness of a ceramic; high hardness inherently leads to a high level of cracking and materials with low hardness produces smaller sized cracks. This relates directly to the final K_{Ic} value as materials with high hardness will give rise to

long crack lengths which in turn will generate lower K_{Ic} values; materials with low hardness are softer and more ductile and will therefore produce shorter crack lengths through resistance to indentation and in turn produce high K_{Ic} values.

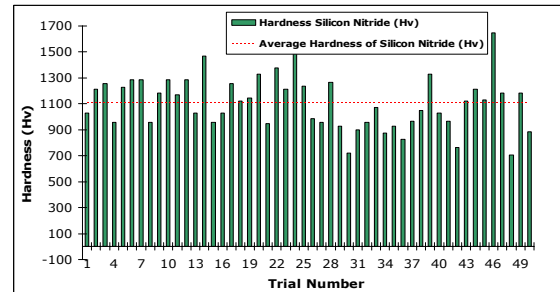


Fig. 1. Hardness of the as-received surface of the Si_3N_4 .

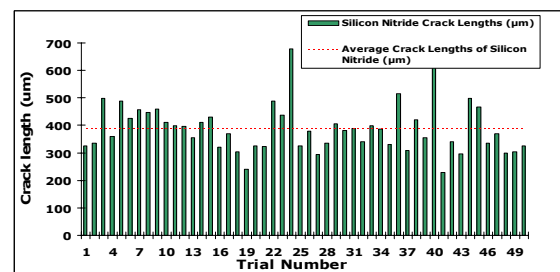


Fig. 2. Crack length as-received surface of the Si_3N_4 ceramic.

The calculated K_{Ic} values ranged between 0.55 and 3.06 $MPa m^{1/2}$ and averaged 1.71 $MPa m^{1/2}$, as can be seen from Figure 3. The crack length and the hardness are the major parameters in influencing the end value of the K_{Ic} . The K_{Ic} values for Si_3N_4 engineering ceramic are given in the literature as ranging between 4 and 8 $MPa m^{1/2}$ [5], but this is the bulk K_{Ic} . For this investigation, the K_{Ic} was calculated specifically for the surface, where impurities such as manufacturing induced macro-cracks and pre-existing surface flaws are present. These impurities considerably reduce the surface strength and the resistance to indentation of the Si_3N_4 . Also, due to the applied indentation load only penetrating to a depth of approximately 75 μm , the strength of the Si_3N_4 at this depth may still be low, so the true hardness value of the Si_3N_4 was not recorded. This is not an issue, however, as in this work the loading conditions were the same for the laser treated Si_3N_4 surface; thus the work and the findings were comparable. In this case, the indentation load was kept constant at 5 kg and the Young's modulus was 320 GPa for the as-received surface.

Figure 4 illustrates an example of a footprint of the diamond indentation at 5 kg with its crack profile and the calculated K_{Ic} value. It was found that for this particular diamond indentation the hardness was 770 Hv, with an indentation size of 110 μm and the crack length of 294 μm - producing a K_{Ic} value of 3.01 $MPa m^{1/2}$. This result was compared with the CO_2 laser treated sample (see

Figure 7), which showed that the diamond indentation was larger in size by 9%. This indicates that the laser surface treatment brought about the softening of the surface of the Si₃N₄.

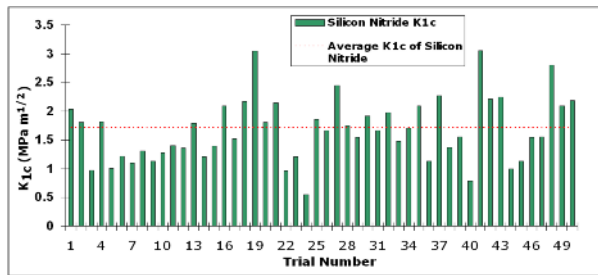


Fig. 3. K_{1c} of the as-received surface of the Si₃N₄.

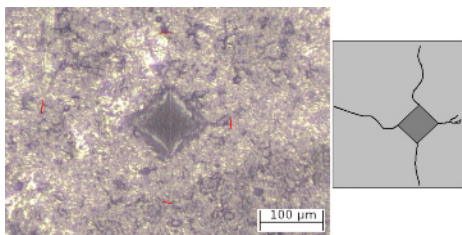


Fig. 4. Microscopic image (left) and the crack profile (right) of the as-received surface of the Si₃N₄ ceramic.

3.2. CO₂ laser treated surface: Hardness, crack lengths and the K_{1c}

The average hardness of the CO₂ laser treated surface was 1028 Hv - a reduction of 7 % from the as-received surface. This reduction in the surface hardness indicated that a softer surface layer was produced by the CO₂ laser treatment, resulting in a surface that would be more resistant to cracking and fracture. The hardness values ranged between 264 and 1449 Hv, as shown in Figure 5. It is evident from Figure 5 that the fluctuation in the hardness values was large. The reason for this was due to the surface containing an oxide layer of around 123 μm thickness (see Figure 7) which was somewhat softer and more uneven in comparison to the laser unaffected surface. As such, the diamond indenter penetrated deeper into the surface in some of the regions than in others: which is why the diamond indentation in Figure 7 is not symmetrical in comparison to that of the as-received surface.

Reduction of the surface hardness from the CO₂ laser treatment led to a reduction in the cracks lengths induced by the Vickers diamond indenter to an average of 210 μm . This was 44% lower in comparison to the as-received surface of the Si₃N₄ ceramic. The crack lengths ranged between 135 to 295 μm . The fluctuation from the values in Figure 6 have resulted from the newly formed, uneven oxide layer after the CO₂ laser treatment.

Figure 7 presents an example of a diamond indentation produced and the accompanying crack

geometry. It can be seen from Figure 7 that the diamond indentation was larger than that of the as-received surface (see Figure 4) by about 8 μm . The indentation size measured was 118 μm , with a hardness of 666 Hv and the crack length of 160 μm . Figure 8 is a topographical image of the laser treated surface, showing the profile of the laser treated surface including the newly formed surface layer comprising of surface oxidation along with the heat affected zone (HAZ) and the laser unaffected zone. The new surface was formed from the result of the Si₃N₄ ceramic being exposed to the atmosphere at high temperatures. This would have led to a possible compositional change where the Si₃N₄ was changed to SiO₂. The change in composition of the Si₃N₄ was also confirmed from a previous investigation by Lysenko *et al* [25].

The average K_{1c} of the CO₂ laser treated surface was found to be 4.78 MPa m^{1/2} and ranged between 2.74 and 11.90 MPa m^{1/2}. These values also fluctuate considerably due to the variations found in the hardness and the crack lengths that led to generating an uneven surface profile after the CO₂ laser treatment.

Two other parameters that can influence the K_{1c} of the Si₃N₄ are the indentation load and the Young's modulus. Whereas the indentation load was kept constant in this study, so the effects of this parameter were zero. However, the Young's modulus would also influence the K_{1c} of the Si₃N₄ since an increase in the ratio of stress and strain which in turn increases the Young's modulus value and affects the end K_{1c} value. If the effect of Young's modulus was ignored then the K_{1c} value for the CO₂ laser treated surfaces would be reduced to 6 % on average.

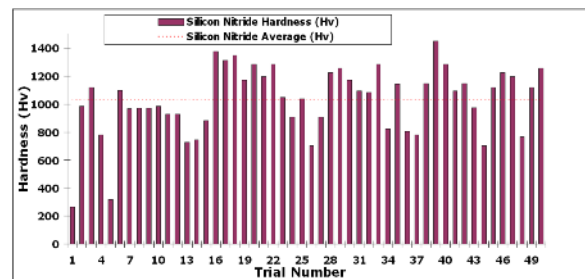


Fig. 5. Hardness of the CO₂ laser treated surface of the Si₃N₄.

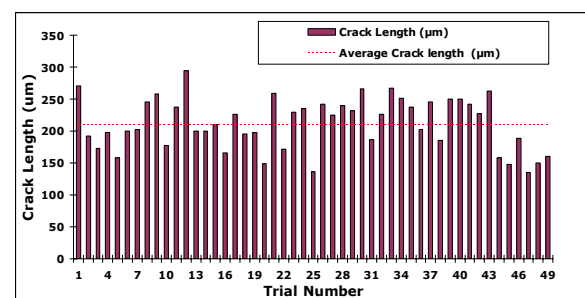


Fig. 6. Crack length of the Vickers indentation test of the CO₂ laser treated Si₃N₄ ceramics.

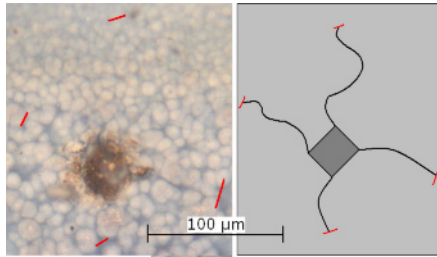


Fig. 7. Microscopic image (left) and the crack profile (right) of the CO₂ laser treated surface of the Si₃N₄ ceramic.

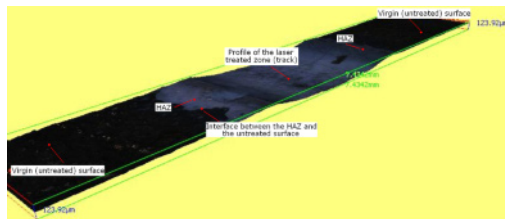


Fig. 8. Surface profile of the CO₂ laser treated Si₃N₄ ceramic.

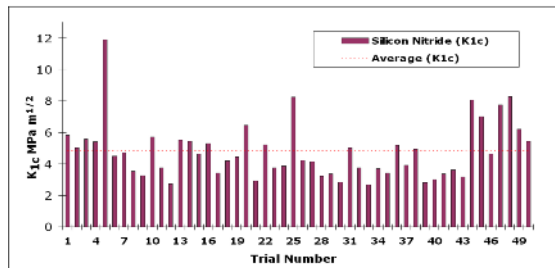


Fig. 9. K_{1c} of the CO₂ laser treated surface of the Si₃N₄ ceramic.

4. Conclusions

K_{1c} of the as-received and CO₂ laser treated surfaces were investigated using the Vickers hardness indentation method and by employing empirical equations for hard, brittle ceramics from the literature. The K_{1c} of the CO₂ laser treated surface compared with the as-received was increased by 64%. This was due to a 7% reduction in hardness and 44% reduction in the crack lengths produced from the CO₂ laser surface treatment. Moreover, the reduction in hardness generated lower cracks during the Vickers indentation tests which indicated that the surface had more resistance to fracture. This occurred through the effect of softening and redistribution of the melt zone which produced a change in the composition of the CO₂ laser treated surface of the Si₃N₄ and induced ductility in comparison to that of the as-received surface. The CO₂ laser treatment of the Si₃N₄ had also formed a new surface layer which comprised of a different composition to that of the laser unaffected surface. The change in composition occurred due to the

Si₃N₄ ceramic being exposed to the atmosphere at high temperatures which modified the top layer of the Si₃N₄ to SiO₂. Further work is being undertaken to fully understand the change in the chemical composition which led to the K_{1c} modification of the CO₂ laser treated Si₃N₄ ceramic.

References

- [1] Ponton CB, Rawlings, (1989), *Materials Science Technology*, 5:865-872.
- [2] Ponton CB, Rawlings, (1989), *Materials Science Technology*, 5:961-976.
- [3] Shukla PP, (2007), MSc by Research thesis, Coventry University: UK.
- [4] Shukla PP, Lawrence J, (2009) *Proceedings of the IMechE Part B*, (in press).
- [5] Richardson DW, (2006), *Modern Ceramic Engineering*, Cambridge: Taylor & Francis Group.
- [6] Liang KM, Orange G, Fantozzi G, (1990) *Journal of Materials Science*, 1990, 25: 207-214.
- [7] Chicot D, (2004), *Materials Science and Technology*, 20:877-884.
- [8] Matsumoto RKL, (1987), *Journal of the American Ceramic Society*, 70:366-368.
- [9] Liang KM, Orange G, Fantozzi G, (1988), *Science Ceramics*, 14:709-714.
- [10] Castaing J, Veysiere P, (1985), *Core Structure Dislocations in Ceramics* Gordon and Breach Science Publishers Inc and OPA Ltd. U.K, 12: 213-227.
- [11] Castaing J, (1995), *Radiation Effects and Defects in Solids* Gordon and Breach Science Publishers Inc and OPA Ltd, S.A, 137: 205-212.
- [12] Lawn BR, Swain MV, (1975) *Journal of Materials Science*, 10:113-122.
- [13] Niihara K, Morena R, Hasselman T, (1982), *Journal of Materials Science Literature*, 1:13-16.
- [14] Evans AG, Charles EA, (1976), *Journal of the American Ceramic Society*, 59(7-8):371-372.
- [15] Evans AG, (1979), *Fracture mechanics applied to brittle materials*. ASTM STP 678, (Ed. S.W. Freiman), Philadelphia: ASTM, pp. 112-135.
- [16] Blendell JE, (1979), PhD thesis, MIT.
- [17] Lawn BR, Evans AG, Marshall DB, (1980), *Journal of the American Ceramic Society*, 63(9-10):574-581.
- [18] Anstis GR, Chanrikul P, Lawn B R, Marshall D B, 1981, *Journal of the American Ceramic Society*, 64:533-538.
- [19] Miranzo P, Moya JS, (1984), *Ceramic International*, 10 (4):147-152.
- [20] Laugier MT, (1985), *Journal of Materials Science Letters*, 4:1539-1541.
- [21] Tanaka K, (1987), *Journal of Materials Science*, 22:1501-1508.
- [22] British Standards, (2005), *Vickers Hardness Test- Part 2- Verification and Calibration of testing Machines*, Metallic Materials - ISO 6507-1.
- [23] McColm I J, 1990, *Ceramic Hardness*, New York: Platinum Press.
- [24] Strakna TJ, Jahanmir S, (1995), *Machining of Advanced Materials*, 208:53-64.
- [25] Lysenko VS, Nazarov AN, Lokshin MM, Kaschieva SB, (1977), *Fiz. Tekh. Poluprovodn*, 1, (11): 2254-2257.

Surface oxygen diffusion hardening of TA2 pure titanium by pulsed Nd:YAG laser under different gas atmosphere

CHEN Changjun¹, ZHANG Min¹, ZAHNG Shichang¹, CHANG Qingming¹, MA Hongyan²

¹ Key Laboratory for Ferrous Metallurgy and Resources Utilization of Ministry of Education, Laser Processing Research Centre, Wuhan University of Science & Technology, Wuhan 430081 P.R. China

² Department of Materials Engineering, Shenyang Institute of Aeronautical Engineering, Shenyang 110034 P.R. China.

Abstract. Titanium and its alloys are widely used in a variety of application in aerospace, automotive, chemical and biomedical industries. High affinity with oxygen limits their use at elevated temperatures. Exposure of titanium and its alloys to any oxygen containing atmosphere at elevated temperatures leads to formation of an oxide layer (OL) on the surface with an oxygen diffusion zone (ODZ) beneath it. TA2 pure titanium was surface treated by laser oxygen diffusion hardening for improving the surface hardness. The present study aims at characterization of the surface oxygen-containing film formed in laser surface oxygen diffusion hardening process by mean of a scanning electron microscope(SEM) and X-ray photoelectron spectroscopy(XPS).The laser formed surface oxygen-containing film is obtained by different gas atmospheres with oxygen, air, N₂, Ar+N₂ and O₂+Ar mixed gas. The hardening film on the TA2 surface has different colours, and has a certain thickness. The surface hardness can be as high as 1200Hv as compared with 310Hv for the as-received TA2 substrate. The findings show clearly that laser surface oxygen diffusion hardening process significantly improves the surface properties of the TA2 pure titanium.

Keywords: Laser oxygen diffusion hardening; TA2 titanium alloy; microstructure; hardness

1. Introduction

Titanium oxide (TiO_x) is a widely used coating material for catalytic, sensors and microelectronic applications due to its exceptionally physical and chemical properties [1]. The two most important crystalline phases of stoichiometric TiO₂ (rutile and anatase) possess high refractive indices, high dielectric constants, high chemical stability and biocompatibility as well as low friction coefficients.

Modification of the titanium surface by Nd:YAG pulsed laser was reported in previous publications[2-9]. It was shown that the surface state of a material is strongly influenced by the laser treatment parameters and experimental conditions. The formation of a thick oxidized layer on the titanium alloy surface by laser treatment can significantly improve the tribological

properties of titanium [7,9]. No reports have been found which discuss the influence of the gas type on the surface harden layer formation.

The aim of this work is to study of the surface oxygen diffusion hardening of titanium in air, oxygen, N₂, Ar+N₂ and Ar+O₂ gas with a pulsed Nd:YAG laser. Samples treated under different gas atmosphere have been obtained and analyzed through several characterization techniques.

2. Experimental work

The flat TA2 pure titanium specimens used in this study were 10mm×8mm×4mm in dimension and were cut from the ingot, mechanically polished with SiC paper to a mirror finish and ultrasonically cleaned in demineralised water and ethanol.

Laser surface oxygen diffusion hardening was performed using a pulsed Nd:YAG laser. The samples were irradiated with a pulsed Nd:YAG laser in protected gas atmosphere using the following processing parameters: pulse rate = 6.0 Hz, pulse duration = 4.0ms, laser spot (defocused) diameter = 2 mm, laser scanning speed = 3 mm/s. These parameters were selected after preliminary trials attempting to obtain oxide films of reasonable quality in terms of thickness and uniformity. During laser processing, a thermal couple was attached to the back of the sample to monitor the temperature variation. The laser processing parameters finally selected are given in Table 1.

Microstructure examinations of the samples were conducted by a scanning electron microscope (SEM) and optical microscope (OM). The surfaces of the laser treated samples were analyzed by XPS. Hardness measurements were carried out on the cross-sections of the polished samples with a Vickers indenter under the indentation load of 100g with a holding time of 15s.

Table 1 Laser processing parameters used in study

Sample No.	1	2	3	4	5
Outpower	120W	120W	120W	120W	120W
gas	O ₂	O ₂ +Ar	O ₂ +N ₂	N ₂	air

(Note : O₂:1L/min, N₂:5L/Min; air: the ambient atmosphere; O₂+N₂ is a mixed gas with oxygen and nitrogen, the gas flow velocity is O₂:1L/min, N₂:5L/min; O₂+Ar is a mixed gas with Ar and O₂, the gas flow velocity is O₂:1L/min, Ar : 5L/min)

3. Results and Discussion

Figure 1 shows the surface appearance of the laser treated samples. The treated samples present different uniform colours depending on the environment gas: dark-green; brown; golden; yellow to green; brown-green. The surface colour is related to the composition of the surface.

Detailed study of the surface of the samples by SEM (see Figure 2) revealed that the spatial distribution of the surface is not really uniform. The most interesting phenomena observed with the present study are the periodic surface structures (PSS). Some have periods at micrometer scale (Figure 2. a2, b2) and some at nanometer scale (Figure 2. d4, e2). The micrometer scale ones are apparently the result of melting and subsequent corrugation due to kinetic pressure. Furthermore, both concentric and radial ripples could be observed (Figure 2 (a, a1, a2, b, b1, b2) at the surface of the craters, with periods ranging from 4 μ m to 10 μ m (Figure 2 a2, b2). The small periodic surface structures obtained at nanometer scale are completely different (Figure 2 d4, e2). The periodicity is about 700nm. All of the phenomena indicate that the ripples originate from the interference of the incident laser beam with the so-called surface waves scattered off imperfections on the alloy surface and running along the surface [2, 3].

Some cracks on all the samples surface can be observed, especially serious for the sample treated under oxygen atmosphere. The large volume ratio of rutile to Ti(1.73) [4, 5], large lattice mismatch and the large difference in the coefficient of thermal expansion between rutile and titanium are considered to be responsible for the spallation of the oxide layer from the substrate [5]. The evolution in surface appearance confirms that the target surface has been heated up to the liquid phase, which may lead to oxygen diffusion from the surface to the layer below it.

A cross-section micrograph of the laser treated samples is shown in Figure 3. By analysis of this figure, the oxide compound (or nitride compound) layers on the surface of the samples are clearly observed. These layers

are comprised of the TiO₂ and TiN (confirmed by XPS). Beneath this layer, a variation is observed in grain structure which is different from that of the substrate. The zone is essentially related to the diffusion of oxygen/nitrogen and/or heating at high temperatures during laser process. Moreover, the TiO₂ scale is not dense when treated under O₂ atmosphere. From Figure 3(c-d), a visible crack can be seen clearly.

High resolution XPS collections of Ti and O binding energy regions for the surface oxygen diffusion hardening TA2 are recorded as shown in Figure 4. The Ti 2p XPS spectrum exhibits two dominant peaks, identified as Ti⁴⁺(TiO₂) 2p_{3/2} at 458.4~458.5eV and Ti⁴⁺(TiO₂) 2p_{1/2} at 463.8~464eV (see Figure 4(a-b)). Figure 4(a-e) shows the O 1S XPS spectra obtained at different atmospheres. The O 1S spectra of the outermost surface of TA2 after laser treatment can be divided into four peaks, a lower binding energy peak near 530eV originating from titanium oxide and three higher binding energy peaks, in the vicinity of 530.2 eV, 531.7 eV and 532.3eV. The results are similar to the observed in TiO₂ in reference [6]. The strongest oxide signal in all the diffractograms corresponds to TiO₂ (solid solution of oxygen within the titanium matrix), which appears in all the cases.

Figure 5 shows the XPS survey scan spectra for the laser treated samples. The dominant signals of the treated samples are C, O and Ti, whereas for the O₂+N₂, N₂ atmosphere treated samples, signals of N are also found. And some small signals (such as 741.75eV) are detected on all the samples.

The hardness measurements through microhardness indentation test revealed that the hardness can be as high as 1200 Hv across section of the samples. The hardness of the top layers of the nitrided sample was higher than those of the oxidation samples. The improved hardness can be assigned to both the surface oxide layer and the diffusion zone, owing to the diffusion of oxygen and nitrogen into the alloys.

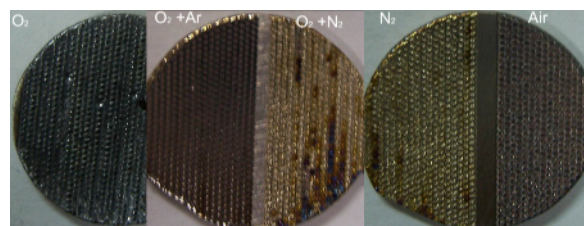


Fig. 1. Surface appearance of the laser treated samples

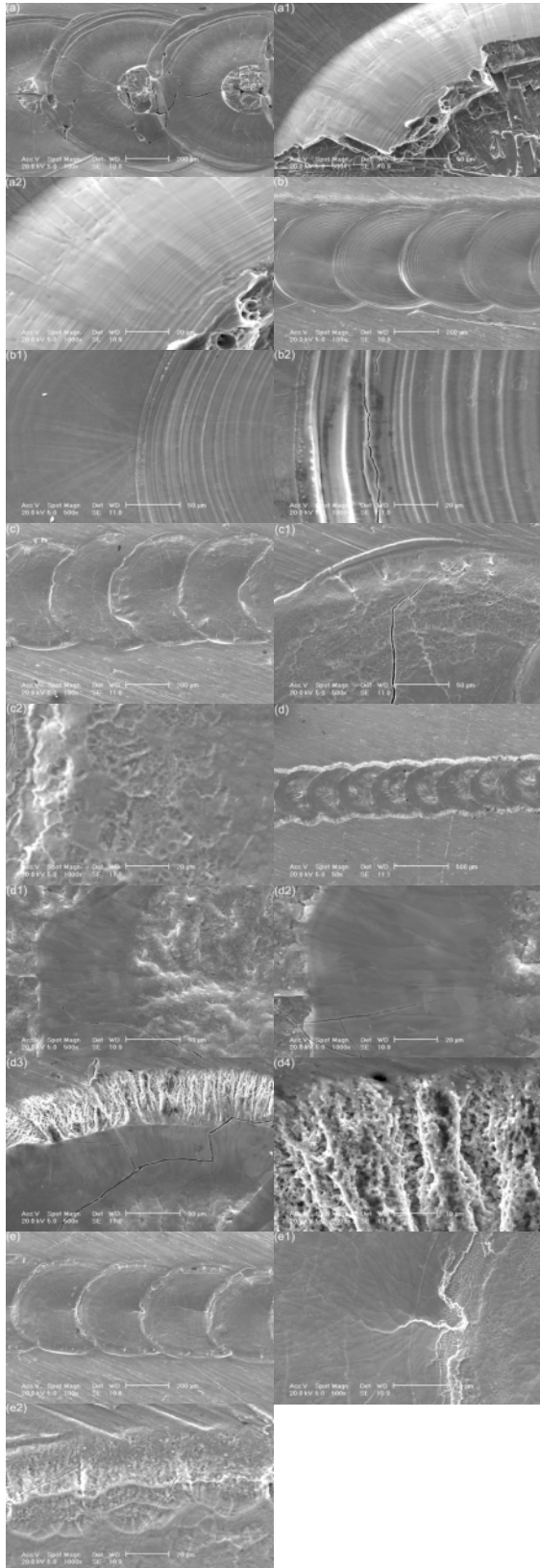


Fig. 2. SEM images of surface morphology of laser oxygen diffusion hardening samples: (a-a2) O₂; (b-b2) O₂+Ar; (c-c2) O₂+N₂; (d-d4)N₂; (e-e2) Air

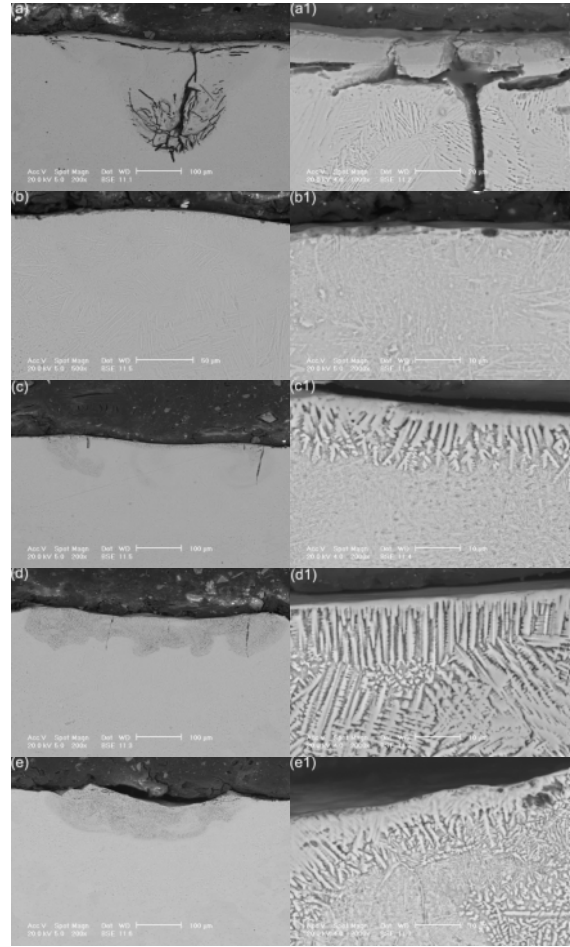


Fig. 3 SEM images of cross-section of laser oxygen diffusion hardening samples for different gases (a,a1) O₂; (b,b1) O₂+Ar; (c,c1) O₂+N₂; (d,d1)N₂; (e,e1) Air (a-e) low magnification, (a1-e1) high magnification

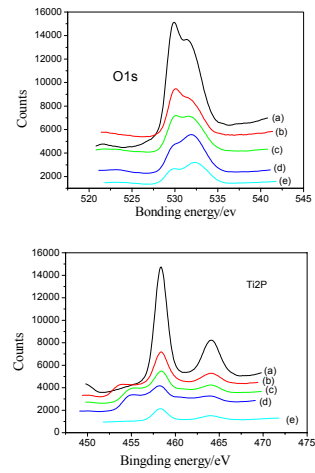


Fig. 4 XPS titanium 2p peaks of a standard TiO₂, Oxygen 1s for the (a) O₂; (b) O₂+Ar; (c) O₂+N₂; (d) N₂; (e) Air

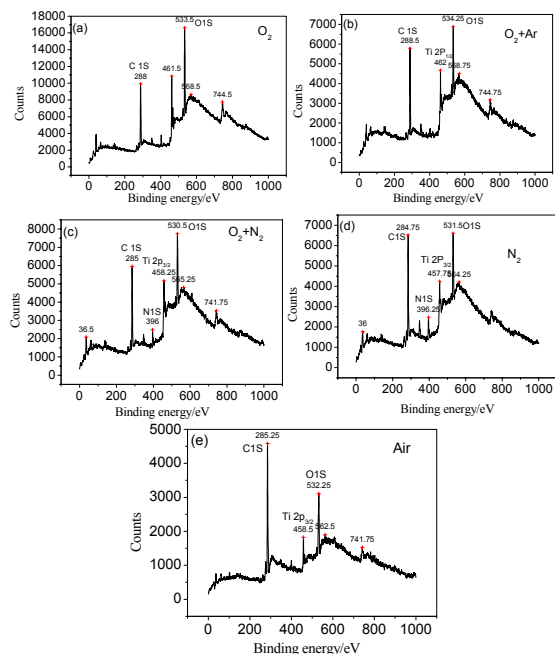


Fig. 5 XPS survey scan spectra of the treated samples

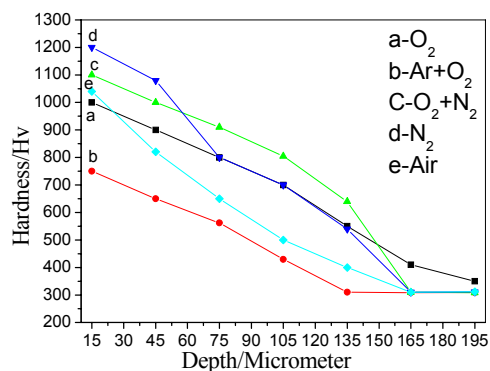


Fig. 6 Hardness profile of laser oxygen hardening TA2 under different gases

4. Conclusions

The surface chemistry of the TA2 titanium treated by laser under different environment gases was investigated by XPS, and the microstructure was observed by SEM.

In the surface oxidation treatment of TA2 with an Nd:YAG laser led to macroscopic colour of the samples. It was observed that the surfaces of these samples were dominated by Ti, C, O elements, in addition of N for the N_2 , N_2+Ar treated atmosphere. A titanium nitride layer was created by the surface of TA2 under N_2 , N_2+Ar gases and TiO_2 layer by O_2 , O_2+Ar and air. TiO_2 existed at the outermost surface layer and was detected for all the treated samples. The surface hardness has been enhanced as high as 1200 HV.

Acknowledgements

This work is financed by Science Foundation of Aeronautics of China with grant no.20095445001.

References

- [1] X. Wang, F. Zhang and Z. Zheng, (2000) Effect of O pressure on the synthesis of titanium oxide film by ion beam enhanced deposition[J]. *Mater. Lett.* 44, 105–109
- [2] A. Pérez del Pino, P. Serra, J. L. Morenza(2002) Coloring of titanium by pulsed laser processing in air[J]. *Thin Solid Films*, Volume 415, Issues 1-2, 1 August, Pages 201-205
- [3] A. Pérez del Pino, J. M. Fernández-Pradas, P. Serra, J. L. Morenza(2004) Coloring of titanium through laser oxidation: comparative study with anodizing[J]. *Surface and Coatings Technology*, Volume 187, Issue 1, 1 October, Pages 106-112
- [4] Jinlong Li, Mingren Sun, Xinxin Ma(2006) Structural characterization of titanium oxide layers prepared by plasma based ion implantation with oxygen on Ti6Al4V alloy[J]. *Applied Surface Science*, Volume 252, Issue 20, 15 August, Pages 7503-7508
- [5] L. Lavissee, J.M. Jouvard, L. Imhoff, O. Heintz, J. Korntheuer, C. Langlade, S. Bourgeois, M.C. Marco de Lucas(2007) Pulsed laser growth and characterization of thin films on titanium substrates[J]. *Applied Surface Science*, Volume 253, Issue 19, 31 July, Pages 8226-8230
- [6] L. Lavissee, J.M. Jouvard, L. Imhoff, O. Heintz, J. Korntheuer, C. Langlade, S. Bourgeois, M.C. Marco de Lucas(2007) Pulsed laser growth and characterization of thin films on titanium substrates[J]. *Applied Surface Science*, Volume 253, Issue 19, 31 July, Pages 8226-8230
- [7] M.C.Marco De Lucas, L.Lavissee, G.Pill. (2008) Microstructure and tribological study of Nd:YAG laser treated titanium plates[J]. *Tribology International*, Volume 41, 985-991
- [8] L. Lavissee, D. Grevey, C. Langlade, B. Vannes(2002) The early stage of the laser-induced oxidation of titanium substrates[J]. *Applied Surface Science*, Volume 186, Issues 1-4, 28 January, Pages 150-155
- [9] CHEN Changjun, ZHANG Min, CAHNG Qingming, ZHANG Shichang, MA Hongyan(2010) The effect of laser-induced oxygen-diffusion hardening on the surface structure and scratch resistance of commercially pure Ti[J]. *Int. J. Surface Science and Engineering*, Vol.4, No.X, In press

Investigation on the Key Techniques of Confined Medium and Coating Layer for Laser Shock Processing on Aeroengine Blade

Zhigang Che, Shuili Gong, Shikun Zou, Ziwen Cao, Qunxing Fei
National Key Laboratory of Science and Technology on Power Beam Processes, Beijing Aeronautical Manufacturing Technology Research Institute (BAMTRI), Beijing 100024, China

Abstract. Laser shock processing (LSP) is an advanced technology of surface treatment, which can remarkably extend fatigue life and improve corrosion resistance of aeroengine blades. Some key techniques are investigated through LSP on aeroengine blades in this paper. The Nd:YAG laser is used with pulse energy about 50 J. Flowing deionized water spouted on the double sides of blade is applied in this study. The methods of removing folds on aluminum foil (as coating layer) are discussed relating with laser energy and pasting modes of Al foil. The measures of improving processing effect related with coating layer are studied. The mode of spouting water near blade root is investigated. The spouting water and Al foil on the rear of blade as protected mediums are explained for improving the treatment effect of LSP. The abating of pockmark on the surface of Al foil after LSP is researched. All the results of experiment and analysis in this paper are beneficial to improving the efficiency and effect of LSP on aeroengine blades.

Keywords: Laser shock processing; Aeroengine Blade; Coating Layer; Fold; Pockmark

1. Introduction

The aeroengine blades endure the loadings of tension, bending and vibration during high velocity rotating and scoured by strong airstream. And the work conditions are very harsh. The blades, especially the ones sited at compressor inlet-end or front fan, are easily impacted by foreign object damage (FOD), such as gravels or birds. This case can make engine void and cause accidents. The fundamental reasons are the formation of deformation, crack and gap at the local of the forward and backward borders of blades, which cause stress concentration or become the failure source and threaten the safety and use of blades. It is the important means of improving the fatigue performance through importing compressive residual stress into the surface of blades [1].

The technique of LSP is suitable for the structure of thin walled and complex profile, such as engine blades. It is flexible for hole, groove and curve surfaces. The depth of compressive residual stress for LSP is larger than the one induced by shot peening. It is beneficial to improving fatigue performance [2]. However there is less studies

about coating layer and confined medium of LSP on aeroengine blades, which are important using this technique on blades. The key techniques, including the folds or bubbles on the surface of Al foil, the mode of pasting, the mode of spouting and preventing the bulging of Al foil and the pockmark of jointing surface, are investigated relating with treatment effect using Al foil as coating layer and flowing deionized water as confined medium.

2. Principle of LSP

The principle of LSP is shown in Fig.1. The surface of target is plastered with a coating layer (also called sacrificial layer, normal organic paint or metallic foil, such as tape, zinc or aluminum) after polishing [3]. The laser with high peak value power ($>1 \text{ GW/cm}^2$) and short duration (nano second level) irradiates on the surface of coating layer traveling transparent confined medium (water or glass) by focusing lens. The coating layer absorbs the laser energy, explodes and forms plasma in very short time. The plasma is restrained by confined medium during expanding and products high pressure shock wave [4]. When the peak value of stress wave is beyond the HEL (Hugoniot Elastic Limit) of the target for a suitable time, the dense and stable dislocations (or twin crystal) are formed. The surface strain hardening is produced at the same time. The elastic deformation energy with shock wave is greater than or equal to the plastic and yielding deformation energy of material. The compressive residual stress is generated on the surface and in material due to the plastic deformation layer restraining the resuming of the elastic deformation energy. The existence of compressive residual stress alters the distribution of stress field and improves the fatigue performance of material surface. So the technique of LSP can evidently improve the performance of corrosion and fatigue resistance [5,6]. The heat effect can be ignored due to the existence of coating layer and the

very short time of interaction and protecting the target from thermal damage. The confined medium is used to enhance the pressure of shock wave and prolong the action time.

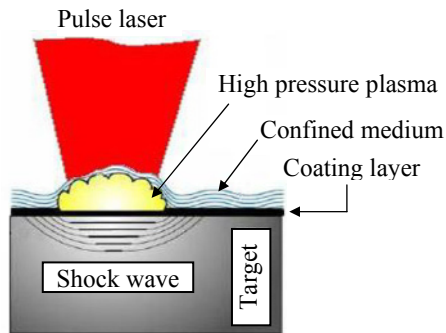


Fig. 1. Scheme of LSP

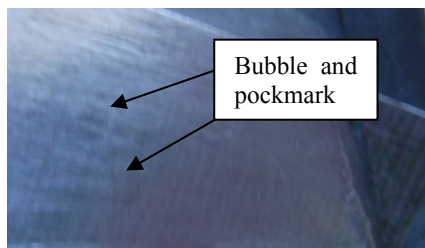
The Nd:YAG laser of BAMTRI is used for the experiment with pulse energy about 50 J, pulse duration 30 ns and wavelength 1064 nm. The flowing deionized water with 1-2 mm thickness is used on the double sides of blades as the confined medium. The Al foil is chosen as the coating layer with 0.1-0.2 mm (easy to be pasted and removed and no pollution comparing with paint). The diameter of spot size is 4-5 mm with laser intensity 8 GW/cm².

3. Results and discussions

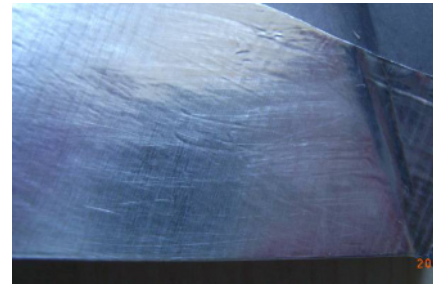
3.1 The eliminating of folds and bubbles on Al foil surface

The folds or bubbles on the Al foil surface could emerge due to tactless or unskilled operating, which are not even and smooth for the coating layer as shown in Fig.2a. The existence of these flaws not only influences the shocked effect but also causes the damage of the surfaces or edges of blade illustrated in Fig.3. The surface smoothness and gloss of Al foil before LSP are required. There are two methods to eliminate the folds and bubbles for smoothness seen in Fig.2b, which are rolled using the special tool for LSP or pasting it again respectively.

The BAMTRI has established the perfect process and the criterion for LSP on blades.



(a)



(b)

Fig. 2. Blade surface coated with Al foil, (a) with flaws; (b) no flaws

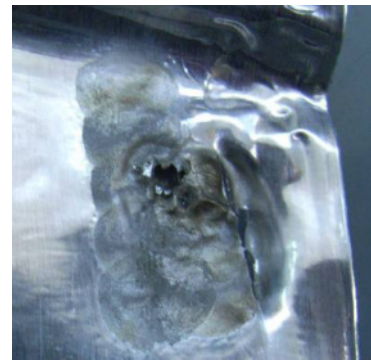


Fig. 3. The shocked Al foil surface with flaw.

3.2 Modes of pasting Al foil

The modes of pasting Al foil affect directly the quality of LSP. Even the irrational modes cause the damage of blades during LSP. The initial mode is single Al foil and then two foils of double sides of blade are used as shown in Fig.4. However the mode with two Al foils has two flaws. The one flaw is the small energy has to be used for protecting the blade flanks from damage since the small covering region on the edges with two Al foils and the shocked effect is poor. The other one is normal energy is used for better effect while the flanks of blade are damaged in different degrees seen in Fig.5. The blade flanks are the main positions of the crack initiation and blade fracture, and are the special protected and shocked regions.

Therefore the single Al foil pasted on two sides of blade is used in order to obtain the better shocked effect as shown in Fig.6. This method not only reduces the pasting time and improves the efficiency but also protects the blade flanks and avoids harming blade at higher energy. The same energy is used on the double sides of blade, which guarantees the shock effect on the flanks and surfaces.



Fig. 4. LSP of double sides of blade with two Al foils



Fig. 5. Injured flank of blade due to rupturing Al foil

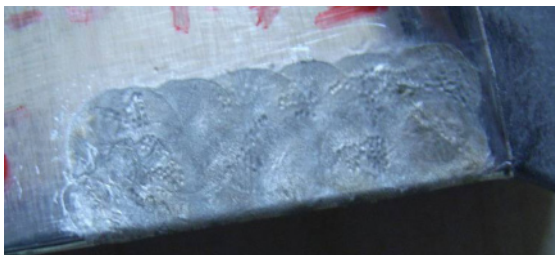


Fig. 6. Single Al foil pasted on two sides of blade

3.3 Mode of inclined spouting

The mode of inclined spouting is used on the surfaces of blade in order to obtain the smooth and uniform confined layer for the distort surface, especially the curve surface around root of blade. The related tools and technique ensure the smooth, gentle and uniform thickness flowing water and avoid the interference between water and laser.

3.4 Flowing water used on the rear blade for abating the bulging foil

If the material is thin walled structure and no measure is taken on the rear of the target at the same time, the spallation will happen seen in Fig.7 due to the propagation of intense stress wave and its reflecting when

some materials are treated by laser under appropriate parameters. Even if the parameters are adjusted, the bulging Al foil still can be seen to some extent in Fig.8 on the rear surface of shocked blade.



Fig. 7. Spallation on the rear of target

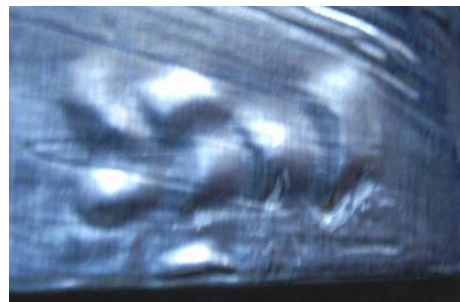


Fig. 8. Bulging on the rear of blade after shocking

In order to ensure the shocked quality and improve the effect, the flowing water is scoured on the rear surface of blade during LSP. The rear appearance of Al foil after LSP is shown in Fig.9, where no bulging on the Al foil comparing with Fig.8. Since the flowing water on the rear surface of blade is imported and the impedance of water is larger than the one of air, the reflection of shockwave is weakened between Al foil and blade. The distribution of state is illustrated in Fig.10 after changed process of LSP.

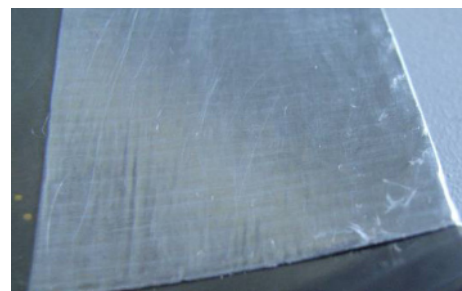




Fig. 9. The smooth and even surface of Al foil after scouring water on the rear surface of blade during LSP

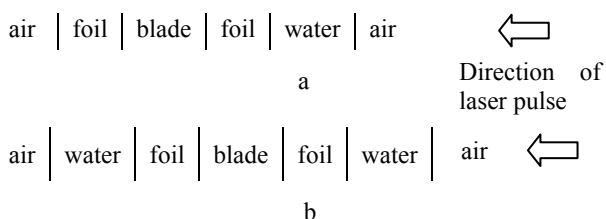


Fig. 10. Distribution of state (a) before modification; (b) after modification.

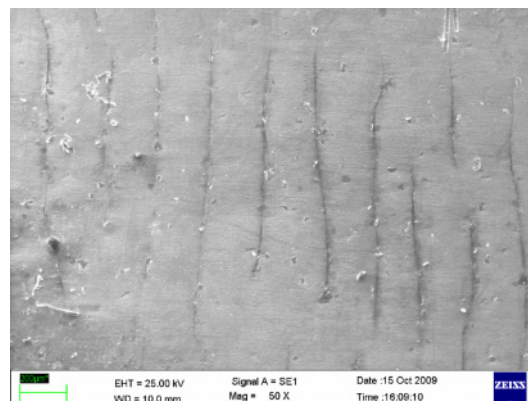
3.5 The abating of pockmark

The pockmarks on the jointing surfaces between Al foil and blade emerge due to the difference of the selected parameters and the mode of uncovering Al foil as seen in Fig.11a. These pockmarks can be also seen on the blade surface shown in Fig.11b, which will affect the roughness of blade surface.

The generation and size of pockmarks relate with laser energy and its distribution and the uncovering mode of Al foil through experiment analysis and observation. In order to abate or eliminate the adverse effect from pockmarks on blade, the lower limit value should be used on the premise of ensuring the shocked energy and effect; and the operation should strictly follow the instructions of BAMTRI about the uncovering foil.



a



b

Fig. 11. Pockmarks (a) on the surface of Al foil; (b) on the surface of blade

4. Conclusion

The experiment analysis is discussed about the key techniques during LSP on engine blades. The important factors of affecting impacting effect related with coating layer and confined medium, including the folds or bubbles on the Al foil surface, the pasting mode, the spouting mode of flowing water as confined medium, the bulging of Al foil and the pockmark of jointing surface, are systematically investigated. All the factors can influence the effect of LSP on blades. The improvement measures given in this paper could effectively protect the blades at the same time improving the quality of LSP

References

- [1] Wang J, Zou SK and Tan YS, (2005) Application of laser shock processing on turbine engines. *Applied Laser*, 25(1):32-34
- [2] King A, Evans AD, Withers PJ, (2005) The effect of fatigue of residual peening stresses in aerospace components. *Materials Science Forum*, 490(491): 340-345
- [3] Zhang W, Yao YL, (2001) Modelling and simulation improvement in laser shock processing. *Proc. of ICALAO, Section A*: 59-68
- [4] Wang YN, Kysar JW, Yao YL, (2008) Analytical solution of anisotropic plastic deformation induced by micro-scale laser shock peening. *Mechanics of Materials*, 40:100-114
- [5] Fairand BP, Wilcox BA, Gallagher WJ, et al. (1972) Laser shock-induced microstructural and mechanical property changes in 7075 aluminum. *J. Appl. Phys*, 43:3893
- [6] Zhang YK, Ye YX et al., (2004) *The technology of laser machining*. Chemical Industry Press

Improvement of Corrosion Performance of HVOF MMC Coatings by Laser Surface Treatment

M. Rakhes, E. Koroleva, Z. Liu

Corrosion and Protection Centre, School of Materials, The University of Manchester, Manchester, M60 1QD, UK

Abstract. Thermal spray coatings are characterised as splat-structures consisting of stackings of lamellae grains with numerous defects, such as inter-connected porosity and oxide inclusions along the splats interlayer boundaries. The existence of such defects significantly increases their corrosion susceptibility in aqueous solutions. In order to improve corrosion performance of T800 (Co-Mo-Cr-Si), and T800-based WC HVOF-sprayed coatings, laser surface modification was carried out using a high-power diode laser to eliminate/reduce of the microstructural defects of the coatings by precise control of treatment depth with or without melting. Characterization of the laser-modified surfaces was conducted, in terms of microstructural morphology, chemical composition and phase analysis. Corrosion behaviors of the coatings before and after laser treatment were evaluated using electrochemical impedance spectroscopy (EIS) and immersion tests. The results indicated that the corrosion resistance of the HVOF coatings can be improved as a result of laser densification of the coatings by elimination of discrete splat-structure and porosity. However, the improvement of resistance to microgalvanic corrosion between the WC and Co-matrix after laser treatment can be limited depending on the extent of melting occurred to the WC within the coatings.

Keywords: HVOF, WC-Co, MMC, Corrosion, Laser.

1. Introduction

High-velocity oxy-fuel (HVOF) sprayed Co-based WC metal matrix composite (MMC) coatings have been widely used for extending the lifetime of critical components in various industrial applications. When it is used in erosion-corrosion environment, corrosion can be a key factor in accentuating material loss [1]. These coatings have been described as highly susceptible to corrosion in aqueous solution, due to inherent characteristics of HVOF coatings causing complex microgalvanic and interfacial mechanisms. The dominating mechanisms were considered as [2]: 1) the difference of electrochemical potentials between the coating constituents providing a driving force for localized corrosion by a mechanism of microgalvanic corrosion; 2) the interface between the WC and the metal matrix may represent a physical microcrevice, providing another driving force for localized attack by classic mechanisms of differential

aeration; 3) the existence of inter-connected porosity and lamellar grain, splat-structures with oxide inclusions at interlayer boundaries resulting in another major concern to the failure of the coatings due to corrosion penetration into the interlayer and eventually de-bonding of the coatings. Although corrosion resistance could be improved using Ni or Ni-Cr instead of Co as a binder alloy or adding Cr_3C_2 , the mechanical properties can be deteriorated consequently. Therefore, post-treatment of HVOF sprayed WC-based MMC coatings has been considered as a potential way of improving corrosion resistance without sacrificing mechanical performance. Among various post-treatments of thermal-sprayed MMC coatings, laser surface treatment has been reported to be capable of removing some of the detrimental microstructural defects by precise control of treatment depth with or without melting [3,4]. Liu *et al* [3] show the improvement of corrosion and wear resistance of laser-treated HVOF Inconel 625- and WC-based coatings, by removal of discrete splat-structures, porosity and micro-crevice as well as the reduction of micro-galvanic activity. Recently, Zhang *et al* [4] report the potential benefits of laser treatment (causing partially melting) of HVOF WC-24% Cr_3C_2 -6%Ni coatings for improved tribological and electrochemical properties, as a result of decreasing the size and number of porosities, and compact interface achieved by laser treatment. Up to now, there has been no work reported on laser surface treatment of Co-based WC HVOF coatings.

This work aims to investigate the corrosion performance of HVOF sprayed T800 and T800-based WC coatings, and to correlate microstructural characteristics of various coatings with variation of WC contents to their corrosion performance before and after laser treatment.

2. Experimental Procedure

In this work the substrate was AISI 316L stainless steel in thickness of 10 mm. Four HVOF coatings, in thickness of

approximately 230 μm on the substrate included T800 (Co–17.5Cr–28.5Mo–3.4Si, wt. %), T800-21WC, T800-43WC and T800-68WC (wt.%).

A Laserline 1.5 kW diode laser, with a rectangular beam size of 2.5 mm \times 3.5 mm, having a uniform intensity distribution and mixed wavelengths of 808 and 940 nm, was used. The samples were treated in a hermetic box purged by argon to reduce/eliminate oxidation in laser processes. In order to achieve melting of the coatings with minimum dilution and crack-free, the laser power was set between 450 W and 550 W, with the scanning velocity of 3 mm/s and overlap ratio of 30%.

The coatings were characterized by field emission gun scanning electron microscopy (FEG-SEM) with energy dispersive X-ray (EDX) analysis, and X-ray diffractometry (XRD), in terms of microstructural morphology, chemical composition and phases.

Corrosion behaviours of the coatings were evaluated by electrochemical impedance spectroscopy (EIS) in 0.5 M H_2SO_4 solution. The EIS was performed at open circuit potential in the frequency range of 30000 Hz to 0.005 Hz, with an amplitude of 10 mV. In addition to the EIS, immersion tests were also carried out in 3 M H_2SO_4 solution at room temperature for 72 h.

3. Results and discussion

3.1 Coating characteristics

The HVOF coatings, as shown in Figure 3.1, consisted of lamellae grains with microstructural defects, such as inter-connected porosity and splats interlayer boundaries. The splat interlayer boundaries became less pronounced with increasing the content of WC. After the laser treatments, both T800 and T800-21WC coating layers were partially melted with the melt depth of $\sim 100 \mu\text{m}$. T800-43WC and T800-68WC coating layers were melted completely reaching the interface at the coating/substrate, leading to the formation of fusion bond instead of mechanical interlocking bonding mechanism for typical HVOF coatings. T800 coating exhibited dendritic structures with complete removal of porosity and splat boundaries, while for the other three coatings with WC, the laser treatment only resulted in the fully melting of the T800 matrix along with the partial melting of the WC. This led to the formation of new phases via diffusion between the Co-matrix and WC. From Figure 1 it was evident that the higher the content of WC, the more WC remained un-melted. This can be further confirmed from the XRD analysis as shown in Figure 2. For T800 coating, the laser treatment resulted in formation of a new phase of Co_2Si as well as the increased amount of the hard Laves phase of $\text{Co}_3\text{Mo}_2\text{Si}$. For the coatings containing WC, the laser treatment reduced the amount of WC and Co phases, by forming new phases of $\text{W}_2\text{Co}_4\text{C}$,

and $\text{Co}_{0.9}\text{W}_{0.1}$, due to the interdiffusion and interaction between the WC and Co-matrix.

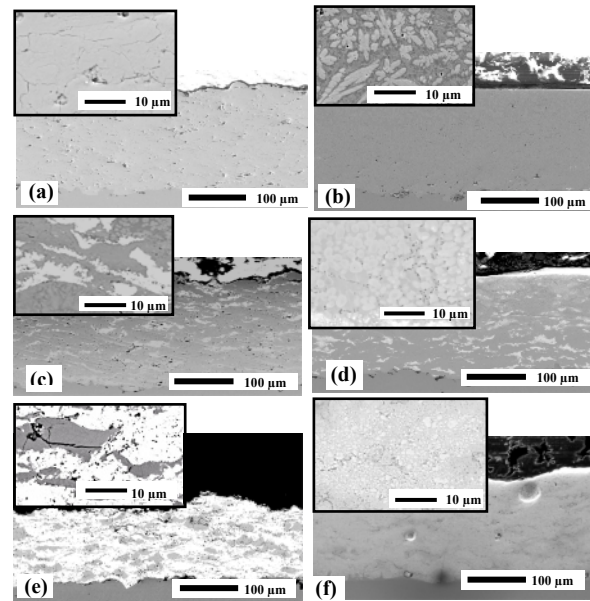


Fig. 1. SEM micrographs of HVOF coatings before and laser treatments (a) and (b) T800, (c) and (d) T800-21WC, (e) and (f) T800-68WC.

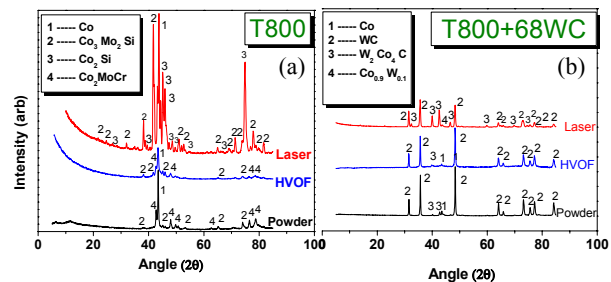


Fig. 2. XRD spectra of T800 (a) and T800-68WC (b) coatings before and after laser treatments.

3.2 Electrochemical impedance spectroscopy

Figure 3 shows the Nyquist plots of EIS spectra of various coatings with and without laser treatment after immersion time of 12 h in 0.5 M H_2SO_4 solution. For EIS data simulation, an equivalent circuit model was proposed in Figure 3.4, which was found to fit all the coatings. In this model, R_s is resistance of the solution; R_p is the resistance of the coating that is directly linked to the coating defects like porosity and microcracks; CPE_p is constant phase element that is used as a substitute for the capacitor to fit more accurately the impedance data; R_{ct} is charge transfer resistance and CPE_{dl} is associated with capacitor behaviour of double layer. The corrosion resistance of the coatings can be evaluated by R_{ct} . The

higher the value of R_{ct} , the less easily the charges transferred through the electrolyte/substrate interface and the higher the resistance to the corrosion is. Tables 1 and 2 summarise the electrochemical parameters using the circuit described in Figure 4.

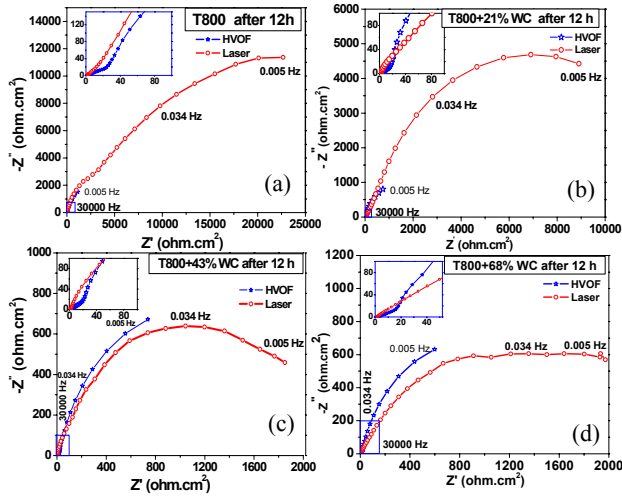


Fig. 3. Impedance spectra of various coatings before and after laser treatment, (a) T800, (b) T800-21WC, (c) T800-43WC and (d) T800-68WC.

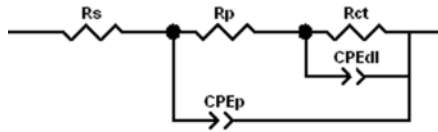


Fig. 4. Equivalent circuit.

Table 3.1 shows that the values of R_{ct} for all the HVOF coatings were in the range of 10200 and 2400 $\Omega \cdot \text{cm}^2$, and decreased with the addition of WC. This might be associated with several reasons. Firstly, the addition of WC increased the surface area of the T800 coating matrix by introduction of numerous interfaces between the matrix and carbides. Such interfaces can be subjected to dissolution governed by galvanic corrosion and form inter-connected channels which are responsible for the electrolyte penetration through the coating causing more corrosion in the coating and at the coating/steel interface. Secondly, the values of R_p decreased with increasing the content of WC, indicating the increased porosity with WC. These inter-connected porosities provided channels allowing the electrolyte to penetrate through the coatings to reach the interfaces at the coating/steel, leading to galvanic corrosion on the steel substrate. Thirdly, for all the coatings, the splat-boundaries that might be decorated by oxide inclusions could be the common sites for initiation of localised corrosion [5]. As described earlier, the splat-boundaries became less pronounced with increasing the content of WC. It was believed that the overall corrosion resistance of the coatings could be

considered as a combined effect. The addition of WC significantly reduced the values of R_{ct} by the first two mechanisms dominating the corrosion process, but increasing the content of WC did not affect the R_{ct} significantly due to the third mechanism contributing to the overall process of corrosion.

Table 1. Electrochemical parameters obtained from EIS spectra of HVOF coatings.

Electrochemical Parameters	HVOF			
	T800	T800-21WC	T800-43WC	T800-68WC
R_s ($\Omega \cdot \text{cm}^2$)	2.2	1.7	1.9	1.8
R_p ($\Omega \cdot \text{cm}^2$)	46	29	33	24
R_{ct} ($\Omega \cdot \text{cm}^2$)	10200	3750	2400	2600
CPE_p (mF cm^{-2})	38	6.1	6.4	7.6
CPE_{dl} (mF cm^{-2})	4.4	6.6	8.5	11.2
n_p	0.64	0.63	0.64	0.65
n_{dl}	1	1	1	1

Table 2. Electrochemical parameters obtained from EIS spectra of laser-treated coatings.

Electrochemical Parameters	Laser Treated			
	T800	T800-21WC	T800-43WC	T800-68WC
R_s ($\Omega \cdot \text{cm}^2$)	1.5	1.0	1.8	1.6
R_p ($\Omega \cdot \text{cm}^2$)	8427	200	370	63
R_{ct} ($\Omega \cdot \text{cm}^2$)	17617	15100	1800	2500
CPE_p (mF cm^{-2})	0.1	0.2	0.8	0.3
CPE_{dl} (mF cm^{-2})	0.8	0.4	1.2	0.65
n_p	0.69	0.77	0.84	0.77
n_{dl}	1	0.7	0.65	0.55

After laser treatments, the values of R_{ct} for T800 coating were increased from 10200 to 17617 $\Omega \cdot \text{cm}^2$, indicating an improved corrosion resistance of the coating. It was also evident from Figure 3.5, that the corrosion attacks of the HVOF coating as well as the attack at the interface of coating/substrate was much severer than that of the laser-treated. For T800-21WC coating, the laser treatment increased the values of R_{ct} from 3750 to 15100, representing a significant improvement of corrosion resistance of the coating due to the formation of new phase of $\text{W}_2\text{Co}_4\text{C}$ at the interface of WC/T800 matrix to reduce the micro-galvanic activity. With increasing the content of WC, more WC grains remained un-melted in the coating after laser treatment. Therefore, the reduction of micro-galvanic activity between the two phases became less effective. As a result, the laser treatment for T800-43WC and T800-68WC coatings presented no improvement of corrosion resistance, in the consideration of R_{ct} .

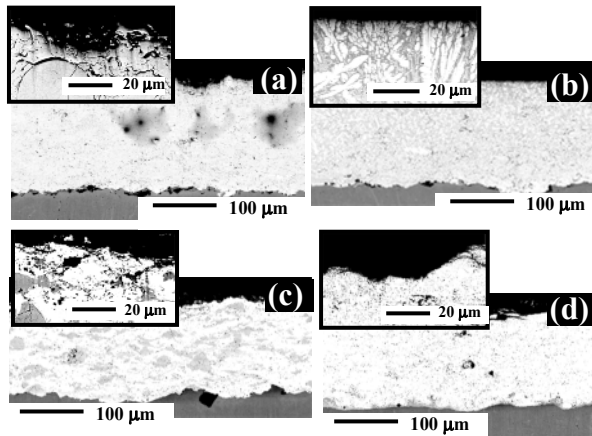


Fig. 5. SEM micrographs of the cross sections of T800 before (a) and after (b) laser, T800+68WC before (c) and after (d) laser treatment after 12h immersion in 0.5 M H_2SO_4 solution.

3.3 Immersion test

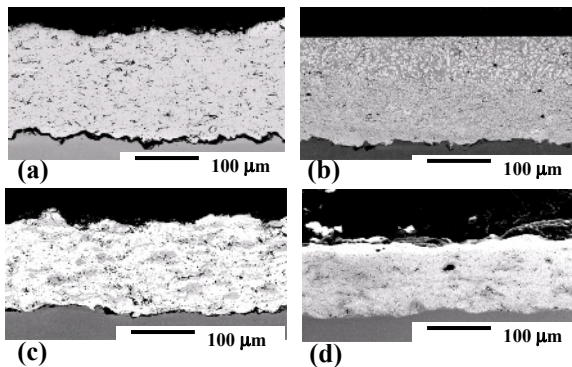


Fig. 6. SEM cross-section images of T800 before (a) and after (b) laser treatment, T800-68WC before (c) and after (d) laser treatment after Immersion of 72 h in 3 M H_2SO_4 solution.

In order to investigate the effects of the reduction of porosity after laser treatment on the corrosion behaviour of various coatings, immersion tests in 3 M H_2SO_4 solution for 72 h were conducted. The results showed that all the HVOF coatings, especially T800 coating, showed clear corrosion attack occurred at the interface of coating/steel substrate, while the laser-treated coatings did not show any corrosion at the interface due to the elimination/reduction of the inter-connected porosity. The reduction of the porosity for all the coatings can be also reflected by the dramatically increased values of R_p after laser treatments for all the coatings.

4. Conclusions

Laser surface treatment of HVOF sprayed Co-based WC MMC coatings significantly reduced the microstructural defects such as porosity and splat-boundaries. Laser surface treatment also resulted in the formation of new phases due to the interdiffusion and interaction between the WC and Co-matrix. EIS analysis and immersion tests along with the SEM examination of corrosion morphology confirmed that the densification of the coatings by laser treatment prevented the electrolyte penetration and subsequent corrosion attack of the steel substrate. EIS analysis further indicated that corrosion resistance of the laser-treated T800 and T800-21WC coatings were significantly improved due to the progression of micro-galvanic corrosion between the WC and Co-matrix. However, for the T800-43WC and T800-68WC coatings, the laser treatment under the current processing conditions did not produce sufficient melting of the WC to reduce the microgalvanic activity. Investigation of further melting with minimum dilution of the coatings is on the way for further improved corrosion resistance.

References

- [1] Souza, V.A.D., and Neville, A., *Corrosion and Synergy in a WC-Co-Cr HVOF Thermal Spray Coatings - Understanding Their role in Erosion-Corrosion Degradation*, Wear, 2005, 259, p.171.
- [2] Neville, A. and Hodgkiess, T., *Towards Novel Ceramic Base Coatings for Corrosion Wear Applications*, British Corrosion Journal, 1999, 34, p 262-266.
- [3] Liu, Z., et al., *Improving corrosion and wear performance of HVOF-sprayed Inconel 625 and WC-Inconel 625 coatings by high power diode laser treatments*. Surface and Coatings Technology, 2007. 201(16-17): p. 7149-7158.
- [4] Zhang, SH, et al., Influence of CO_2 laser heat treatment on surface properties, electrochemical and tribological performance of HVOF sprayed WC-24%Cr3C2-6%Ni coating, materials Chemistry and Physics, 2010, 119, p. 458-464
- [5] N. Ahmed, M.S. Bakare, D.G. McCartney, K.T. Voisey *The effects of microstructural features on the performance gap in corrosion resistance between bulk and HVOF sprayed Inconel 625*, Surface and Coatings Technology, 2010, 204, p. 2294-2301.

Numerical and Experimental Studies on the Laser Melting of Steel Plate Surfaces

I.A. Roberts¹, C.J. Wang¹, K.A. Kibble¹, M. Stanford¹ and D.J. Mynors¹

¹Department of Engineering and Technology, University of Wolverhampton, Telford, TF2 9NT, United Kingdom

Abstract. The direct impingement of laser on the surface of a platform occurs during additive layer manufacturing especially for the first layer of powder coating. As a result, thermal stresses develop due to high temperature gradients in a thin layer of the plate surface, which can result in undesired surface deformation of the steel platform used. This study investigates the residual stress profiles on a hot-rolled AISI 1015 steel plate produced by direct laser application. A three-dimensional finite element simulation model is developed which considers the laser heating process as a sequentially coupled thermal elasto-plastic problem. Experiments using optical laser scanning microscopy to obtain surface topography of the melted surface are also presented showing reasonable agreement with the simulation results. The influence of the plate thickness on the stress-depth distribution is presented.

Keywords: Laser Melting, Surface Topography, Hardening

1. Introduction

Laser processing is an invaluable tool used in manufacturing. The heating characteristics of lasers have been employed in many forming, sintering and melting processes as utilized in additive layer manufacturing (ALM). Physical processes including welding, hardening, alloying, cladding and bending can be effected by laser irradiation [1, 2]. These laser processes are associated with characteristic thermal cycles in small, highly localized regions on the surface of a workpiece. The thermal cycles result in physical and microstructural changes [3], which can have a number of undesirable effects on the accuracy of the finished components.

The transient temperature distribution in the irradiated material is a vital element for understanding the physical processes that occur. Yáñez *et al.* [3] have studied the temperature distribution during laser heating of steel using both analytical and finite element models. The models used were limited to constant material properties. Wang *et al.* [4] developed a finite element model for simulating the temperature field in a line scan laser hardening of C45 steel using temperature dependent material properties. In addition to non-linearities introduced by temperature dependent properties, the laser

scanning movement adds asymmetry to the problem; hence there is need for three-dimensional modelling. Chiang and Chen [1] studied the changes in microstructure with depth of H13 steel as a result of the laser melting of its surface. Selvan *et al.* [5] carried out experimental and analytical studies on CO₂-laser treated En18 (medium carbon steel) and showed that quenching occurred at the scanned surface which resulted in a local increase in the hardness to about 950HV at the surface. The hardness decreased with depth to 250HV which is the material's original hardness value.

In this paper, a three-dimensional finite element model is developed to model the temperature and residual stress fields generated during the laser melting of the surface of a hot-rolled steel platform over a raster area. The aim is to provide a basis for comparison in a future study involving the addition and melting of powder layers to understand the contribution to the overall stress state and distortion in built parts. The model incorporates temperature dependent thermal, mechanical properties and latent heat during phase transitions.

2. Simulation Model

During laser melting of a metal surface, complex phenomena such as temperature dependence of material properties and laser absorption occur in very short time periods; hence, knowledge of the temperature field in and around the melt region is essential for modelling for the laser heating process.

According to Shi *et al* [6], in order to simplify the calculation, the fundamental mode (TEM₀₀) Gaussian laser irradiance distribution can be replaced by a modified expression to calculate the average heat flux density as follows:

$$q = \frac{1}{A} \int_S IdA = \alpha \frac{1}{\pi R^2} \int_0^R \frac{2P}{\pi R^2} e^{-2r^2/R^2} 2\pi r dr \quad (1.1)$$

Where q is heat flux, P is power, R is spot radius, and α is the absorptance.

The variation of absorptance of materials is an important property that limits the amount of laser energy that is delivered into the material. The absorptance value from previous studies varies from the optical/radiative absorptance to the calorimetric absorptance and is known to depend on factors such as temperature, nature of surface, and wavelength of laser [7]. For this study, the calorimetric absorptance of steel as reported by Bertolotti [8] is used: 0.2 for the solid material and 0.1 for the molten material.

The temperature field can be represented as a quasi-steady state problem for the moving heat source using Fourier's heat transfer equation:

$$\rho \left(\frac{\partial H}{\partial t} \right) = \nabla \cdot (k \nabla T) + \dot{q} \quad (1.2)$$

According to the specific problem additional terms must be included to reflect the particular loads and boundary conditions:

Preheat temperature: $T = T_o$

Surface convection: $(-k \nabla T) \cdot \hat{n} = h(T - T_o)$

Where ρ is density, k is thermal conductivity, H is enthalpy and h is convection coefficient.

The stress field can be modelled by determining the elastic component of the total strain [9]:

$$\varepsilon = \varepsilon_{el} + \varepsilon_{ie} + \varepsilon_{th} \quad (1.3)$$

The thermal strain component depends on the expansion coefficient, while the inelastic strain component depends on the stress deviation, strain hardening parameter and the temperature.

The stress field components are derived thus [10]:

$$\{\sigma\} = [D] \{\varepsilon - \varepsilon_{ie} - \varepsilon_{th}\} \quad (1.4)$$

Where $[D]$ is the stress-strain matrix.

2.1 Material Modelling

The temperature-dependent physical and mechanical properties of hot-rolled AISI 1015 have been taken from [11, 12]. Hardness tests conducted for the material gave a value of 143 HV corresponding to an ultimate tensile strength of 400 MPa and yield strength of 255 MPa. For temperatures close to and above the melting point, the material loses all of its stiffness. To resolve numerical difficulties posed by zero matrices, very small values were used for the elastic and Engesser moduli and yield stress.

2.2 Finite Element Model

The laser heating of a 1 mm × 2 mm area on a 5 mm × 5 mm plate having a thickness of 1mm was modelled

using ANSYS Mechanical, for which the general thermal and elasto-plastic algorithms have been described [10]. The solidification process is modelled as a linear isotropic hardening problem using the von Mises yield criterion and an associative flow rule.

The finite element mesh consists of 8-node brick elements for solving the temperature and structural field problems respectively. The same mesh was used for both field analyses. Because the laser beam has a size of 100 μm, the element size had to be very small, in this case 25 μm × 25 μm. Refined mesh was used in regions exposed to the laser scanning, which become coarser away from the scanned zone as shown in Fig. 1.

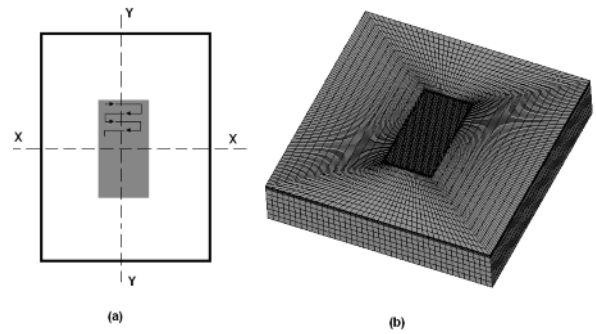


Fig. 1. Scanning pattern and finite element model

The movement of the heat source was considered to occur in discrete timesteps, irradiating a region equivalent to the size of the beam for a time period determined by the beam diameter and speed of travel [13]. The cooling down time was taken as 600 s. The solidification process was modelled as a coupled thermal-structural field problem. The heat generated by plastic deformation of the material is negligible compared to the heat input of the laser beam [6]. Therefore, the problem is modelled as a sequential coupled field problem, using the transient temperature loads of the thermal field analysis as input for the structural model [14]. To prevent rigid body movement, a zero displacement boundary condition is applied to one side of the plate model.

3. Experimental Set Up

An EOS M270 [15] machine with a continuous wave Nd:YAG laser of wavelength, $\lambda = 1.06 \mu\text{m}$ and an output power reaching 200 W, having a non-expanded beam size of about 100 μm was used to achieve laser melting. Stress-relieved test pieces with overhanging 5 mm × 5 mm × 1 mm cantilever platforms shown in Fig. 2 were machined from hot-rolled steel blanks.

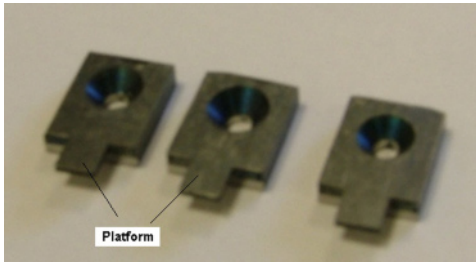


Fig. 2. Test samples

A central region $1\text{ mm} \times 2\text{ mm}$ mapped from a CAD model was laser scanned on the platform surface. Typical process parameters for building TiAl_6V_4 parts were used for the experiment – the laser power and speed were set to 195 W and 1200 mm/s respectively with no overlaps specified. The raster scanning method (see Fig. 1) as used with most laser prototyping systems was used.

The topography experiment involved capturing the surface state of the platform area before and after the laser scanning using an Olympus Confocal Laser Scanning (OLS3000) microscope [16]. The platform surface was divided into cells of $480\text{ }\mu\text{m} \times 640\text{ }\mu\text{m}$. A series of images taken at intervals were then knitted to form a 1024×768 pixel surface topography image of a $4800\text{ }\mu\text{m} \times 5120\text{ }\mu\text{m}$. Vertical displacements for specified divisions along the designated paths X - X and Y - Y [see Fig. 1(a)] were obtained as the difference between the primary height profiles before and after laser melting using the OLS3000 surface roughness analysis tool. Due to visually evident splattering of molten material in the scanned zone, the displacement changes are measured for the regions outside the scanned zone. The entire process was repeated with three samples for which the average values were obtained.

4. Results and Discussion

Pilot studies were conducted with the simulation model. These were validated against the temperature measured experimentally and predicted analytically by [17] for the temperature field. The stress field analysis was validated against an analytical model used by [9].

4.1 Temperature Field Distribution on Steel Platform

The temperature distribution on the steel platform at various times is shown in Fig. 3. The results show that the different spots that make up a surface experience similar thermal cycles and that the heating and cooling cycles experienced by the spots occur within a few milliseconds. These rapid thermal cycles are associated with commensurate thermal stresses.

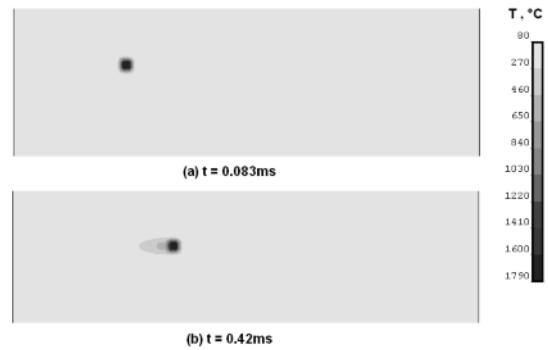


Fig. 3. Temperature field results

4.2 Surface Profilometry (Model Validation)

Fig. 4 compares the surface height profiles for the paths X and Y shown in Fig. 1. It can be seen that the scanned zone forms a concave depression. This is due to the high tensile stresses that are generated at the surface of the plate. The resultant effect is a contraction in the scanned zone which tends to pull the surrounding undisturbed material to a new equilibrium position.

Several factors may have contributed to the discrepancy between the simulation and experimental results, including the absorptance of the material to the laser beam, which depends on a number of factors. In general, the simulation results show good agreement with the experimental results.

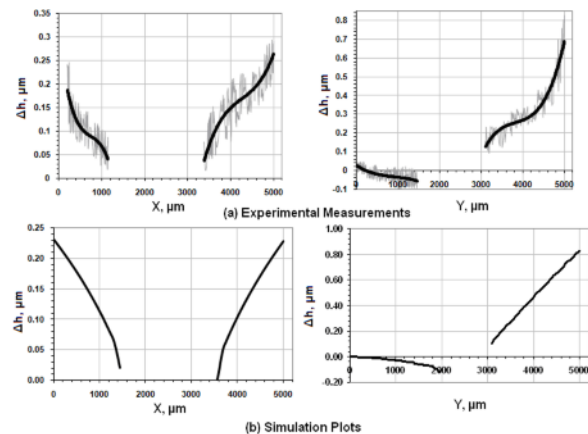


Fig. 4. Comparison between experiment and simulation model

4.3 Stress Field Results

The stress analysis was performed for a $1\text{ mm} \times 1\text{ mm}$ region scanned on a $3\text{ mm} \times 3\text{ mm}$ platform. Results for the transverse and longitudinal stresses are presented in Fig. 5. The longitudinal stresses are taken in the direction of travel of the laser while the transverse stresses are taken in the perpendicular direction.

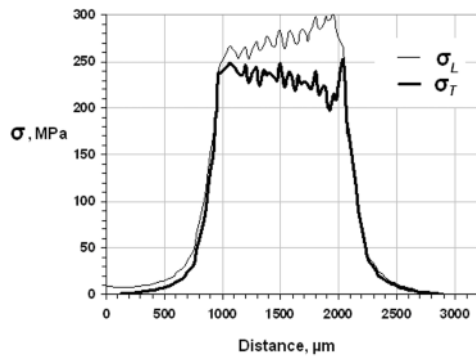


Fig. 5. Residual stress distribution

It can be seen that the longitudinal stresses are greater than the transverse stresses across the scanned zone.

4.4 Stress-Depth Profile

Grum and Sturm [18] studied the change in the residual stress states in the melt zone and were able to determine the depth of the hardened zone from this information. Fig. 6. shows that after laser melting, the residual stresses on the surface of the plate are tensile in nature, these however transform to compressive stresses with depth.

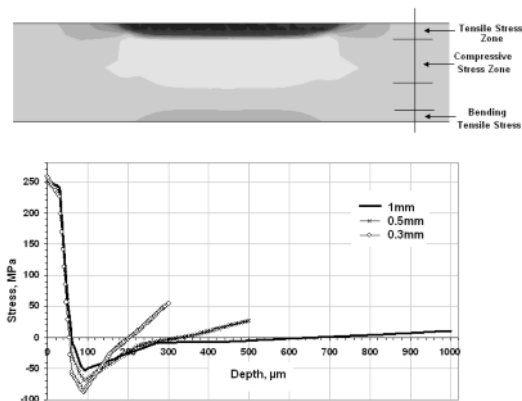


Fig. 6. Stress-depth profile

It can be seen from Fig. 6. that the depth at which the residual stress is zero is the same for all thickness cases analysed. The emergence of secondary tensile stresses towards the bottom of the plate is due to the deformation of its free end. This can result in accuracy issues if a thin platform is to be used for building metal parts.

5. Conclusions

A three-dimensional finite element model has been used to study the direct laser melting of a steel platform surface. The model has successfully predicted the temperature and stress fields associated with the process. After laser melting, tensile residual stresses develop on

the surface which transform to compressive residual stresses with depth. Tensile stresses disappear at about the same distance in all platform thickness cases analysed. The platform thickness did not affect the magnitude of surface residual stresses but had an effect on the stress distribution with depth. Secondary tensile stresses emerge beyond the region of compressive stresses due to the distortion of the platform. These distortions could cause part accuracy for the conditions used in this work. The stress-depth profile can provide a robust means of determining the hardened zone depth.

References

- [1] Chiang K-A and Chen Y-C, (2005) Laser surface hardening of H13 steel in the melt case. *Materials Letters*, 59: p.1919-1923.
- [2] Zhang P, Guo B, Shan D-B, and Ji Z, (2007) FE simulation of laser curve bending of sheet metals. *Journal of Materials Processing Technology*, 184: p.157-162.
- [3] Yáñez A, Álvarez JC, López AJ, Nicolás G, Pérez JA, Ramil A, and Saavedra E, (2002) Modelling of temperature evolution on metals during laser hardening process. *Applied Surface Science*, 186: p.611-616.
- [4] Wang XF, Lu XD, Chen GN, Hu SG, and Su YP, (2006) Research on the temperature field in laser hardening. *Optics & Laser Technology*, 38: p.8-13.
- [5] Selvan JS, Subramanian K, and Nath AK, (1999) Effect of laser surface hardening on En18 (AISI 5135) steel. *Journal of Materials Processing Technology*, 91: p.29-36.
- [6] Shi Y, Shen H, Yao Z, and Hu J, (2007) Temperature gradient mechanism in laser forming of thin plates. *Optics & Laser Technology*, 39: p.858-863.
- [7] Taylor CM, (2004) Direct Laser Sintering of Stainless Steel: Thermal Experiments and Numerical Modelling. Ph.D Thesis, University of Leeds.
- [8] Bertolotti M, (1983) Physical Processes in Laser-Materials Interactions. Plenum Press,
- [9] Masubuchi K, (1980) Analysis of Welded Structures. Vol. 33. Pergamon Press,
- [10] ANSYS10.0: ANSYS Release 10.0 Documentation (2007)
- [11] USDD, (1998) Military Handbook - MIL-HDBK-5H: Metallic Materials and Elements for Aerospace Vehicle Structures. U.S. Department of Defence,
- [12] Mills KC, (2002) Recommended Values of Thermophysical Properties for Selected Commercial Alloys. Woodhead Publishing, 320
- [13] Dai K and Shaw L, (2005) Finite element analysis of the effect of volume shrinkage during laser densification *Acta Materialia*, 53: p.4743-4754.
- [14] Dai K and Shaw L, (2004) Thermal and mechanical finite element modeling of laser forming from metal and ceramic powders. *Acta Materialia*, 52: p.69-80.
- [15] Electrical Optical Systems: EOS M250Xtended, M270 Basic Operation Manual (2005)
- [16] Olympus: Confocal Laser Scanning Microscope - LEXT OLS3000/3100 User's Manual (2008)
- [17] Yilbas BS, Sami M, and Shuja SZ, (1998) Laser-induced thermal stresses on steel surface. *Optics and Lasers in Engineering*, 30: p.25-37.
- [18] Grum J and Sturm R, (1998) Influence of laser surface melt-hardening conditions on residual stresses in thin plates. *Surface and Coatings Technology*, 100-101: p.455-458.

Analysis of temperature distribution during fibre laser surface treatment of a zirconia engineering ceramic

P. P. Shukla and J. Lawrence

Wolfson School of Mechanical and Manufacturing Engineering, Loughborough University, Leicestershire, LE11 3TU, UK.

Abstract. The thermal effects of fibre laser surface treatment of a ZrO₂ engineering ceramic were studied using finite element analysis (FEA). Temperature increases on the surface and in the bulk of the ZrO₂ during fibre laser processing were measured. FEA was then used to model the flow and distribution of the radiated heat resulting from the fibre laser surface treatment. Data obtained from a thermogravimetry-differential scanning calorimetry (TG-DSC) analysis and the FEA model predictions was used to map the phase transformations in the ZrO₂ resulting from fibre laser surface treatment. The mapping revealed that the fibre laser surface treatment generally resulted in a phase transformation of the ZrO₂ from the M state to a mixture of T+C during fibre laser irradiation and from T+C to T followed by the M state during solidification.

Keywords: Fibre laser, ZrO₂ engineering ceramic, finite element analysis (FEA), phase transformation.

1. Introduction

The study of laser interaction with materials, in particular engineering ceramics, is a complex process due to the multiparameter nature of laser materials processing: effect of laser power density, traverse speed, instantaneous heating and ablation; and the properties of the engineering ceramic: mechanical properties and thermal characteristics. To analyse such events thermal analysis by means of an experimental study and by employing computation means are useful methods of investigating the laser-ceramic surface and bulk interactions. This research focuses on investigating the thermal distribution in a fibre laser surface treated ZrO₂ engineering ceramic by means of experimental and finite element analysis (FEA). Thereafter the thermal data is used for determining any changes within the ceramic such as phase transformations by correlating the findings with data obtained from thermo, gravimetric- differential scanning calorimetry (TG-DSC) analysis.

The positioning and mounting of thermocouples within a sample to measure temperatures during laser processing is ideal for recording temperature changes in

the bulk; it is not suitable for measuring surface temperatures so pyrometers or contact-less devices are also employed [1, 2]. Temperature measurement during the laser surface treatment is important as this can be used as input parameter into computational models for studying features such as deformation during the thermal exposure, as well as for generating thermal heat maps and tracking heat distribution.

Several previous investigations have demonstrated the use of FEA for investigating the residual stress and thermal distribution of various laser processing techniques with conventional metals and alloys [3-13]. In contrast, very little work has been published detailing FEA modelling of the laser surface treatment of engineering ceramics.

A considerable amount of research has been conducted with regards to the phase transformation of ZrO₂ ceramics [2, 14-24], which occur when the ceramic is exposed to increasing/decreasing or changing temperatures [14, 18, 19]. With respect to the changing temperature being introduced during fibre laser surface treatment it is important to understand the thermal effects of the laser radiation upon the crystal phases of the ZrO₂ ceramics.

2. Experimental Techniques and Analysis

2.1 Fibre laser treatment

The material used in this work was cold isostatic pressed (CIP) ZrO₂ with 95% ZrO₂ and 5% yttria (Tensky International Company, Ltd.). Each test piece was obtained in a block of 50 x 10 x 10 mm³. The experiments were conducted in ambient conditions. A 200 W fibre laser (SP-200c-002; SPI, Ltd.) was employed which emitted a continuous wave (CW) mode beam at a wavelength of 1.075 μm. The processing gas used was Ar and was supplied at a flow rate of 25 l/min. To obtain an

operating window, trials were conducted at a fixed spot size of 3 mm and by varying the power between 25 and 200 W, and varying the traverse speed between 25 and 500 mm/min. From these trials it was found that 125 W at 100 mm/min were the ideal laser parameter to use in terms of achieving a crack-free surface.

2.2 Temperature measurements

The surface processing temperature of the ZrO_2 was measured using a portable infra-red thermometer (Cyclops 100 B; Land Instruments International, Ltd.). The device was positioned 1 m away from the processing area. The infra-red thermometer was aligned with the work-piece by means of a He-Ne beam. Temperature measurements were taken from five different areas on the surface of the ZrO_2 . To produce consistency in the temperature readings, an average of the temperature measurements was taken after making five repeated readings on identical samples in order.

The bulk temperature measurement was measured using precision fine wire (0.20 mm diameter by 152 mm in length), R-type, thermocouples, capable of reading up to 2300°C (P13R; Omega Instruments, Ltd.) and were precisely mounted at various positions within the bulk of the sample. Each of the thermocouples was connected to a digital temperature reader (N9002; Thermo-meter, Comark, Ltd.). Three holes of 3 mm diameter were drilled into the ceramic samples using an ultrasonic drilling method, after which the tips of the thermocouples were mounted into the holes at 3, 6 and 8 mm from the surface (see Figure 1). To assure firm fixation, the holes were filled with organic filler that was stable during high temperature processing. Measurements were taken in three different passes of the fibre laser beam.

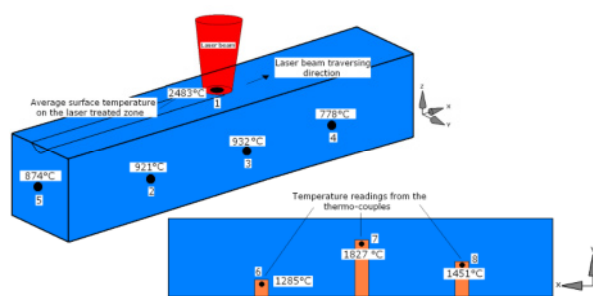


Fig. 1. Schematic representation of the ZrO_2 ceramic samples showing the positions of the thermocouples and (a) the surface temperature measurements and (b) the temperatures measured in the bulk during fibre laser surface treatment.

2.3 Finite element analysis (FEA)

A FEA model was constructed using Unigraphics; NX 5.0, Nastran design and simulation software. The component part was first designed to comprise a 3 mm diameter blind hole with a depth of 100 μm , equivalent to the footprint of the fibre laser beam. The depth of 100 μm

was assigned to the blind hole as it was found from previous investigation that the average material removal of the laser beam the ZrO_2 was about 100 μm deep [25]. The FEA was constructed in six distinct stages. Stage 1 involved component part design and selection of the correct solver (thermal). Stage 2 involved assigning the mechanical/ thermal properties of the ZrO_2 engineering ceramic. Constraints of 25°C were placed on the sample in two positions in Stage 3. A thermal load of 4527.77 Wmm^2 along with 90% absorption and 0.40 emissivity were also assigned to the model in Stage 4. Stage 5 involved three-dimensional meshing of the sample. Last, post processing, results and thermal simulation of the model were carried out in Stage 6.

2.4 Thermogravimetry-differential scanning calorimetry (TG-DSC) analysis

TG-DSC analysis (1500 DSC; Stanton Redcroft, Ltd.) was conducted on the as-received and fibre laser treated ZrO_2 samples. The average surface area of the samples was approximately 2 mm^2 and the mass was 29.45 mg. The samples were placed into an Al_2O_3 crucible and N_2 was used as a purge gas at 50 ml/min. Once in place, the samples were heated up to 1500°C at a rate of 10°C/min to measure the mass flow as the temperature increased. The samples were then cooled to ambient temperature at the same rate using the same parameters to measure the mass flow as the temperature reduced. The heat flow through the as-received and fibre laser treated samples was recorded for any changes during the heating and cooling cycles and is shown in Figure 2. From this recording it was then possible to identify specific phase events that occur in the ZrO_2 during heating at what temperature these events take place.

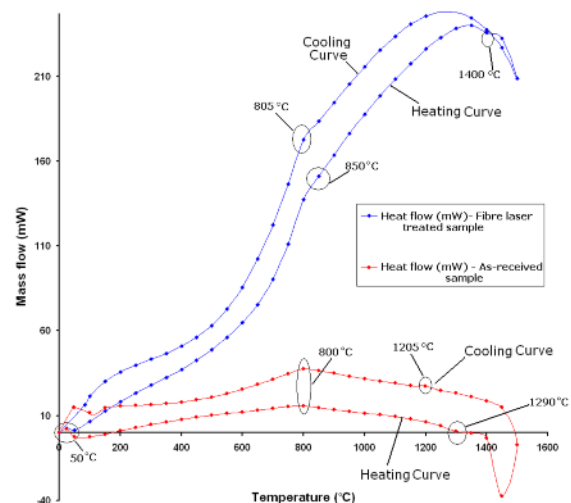


Fig. 2. TG-DSC curves for the as-received and fibre laser treated ZrO_2 ceramic samples.

3. Results and Discussion

3.1 Finite element analysis (FEA) model validation

The average temperatures found on the surface after five passes of the fibre laser beam are presented in Figure 1(a). At the laser-ceramic interface the surface temperature was found to be 2483°C. This result is in good agreement with that of a previous investigation by Shukla and Lawrence [25], where it was found that fibre laser surface treatment of ZrO₂ resulted in some degree of melting of the top (near) surface layer. Interestingly, the temperature readings would be expected to be stable throughout a plane, but this was not the case as up to 16% difference in temperatures between Positions 2 to 3 and 4 to 5 was observed. The difference between the two results may have occurred due to temperature measuring errors. Still, the experimental surface temperature measurements agree with those of the FEA model with a +10% accuracy. Further modification to the temperature measurement settings would improve the consistency in obtaining more accurate temperature readings.

The average temperatures measured within the bulk of the ZrO₂ after five readings are shown in Figure 1(b). These measured temperatures also agree with the bulk temperatures predicted by the FEA model. At 3 mm below the surface the temperature was up to 2035°C. The FEA by comparison gave a temperature of over 1900°C, and agreement of just over 7%. The temperature in Position 8 (see Figure 1) was found to be 1451°C which in comparison to the FEM was 79°C lower, indicating an accuracy of 5.5%. Finally, at Position 6 the temperature recorded was 1285°C, while the temperature predicted by the FEA model was 245°C lower, a difference of 19%. It is clear that the bulk material temperatures measured experimentally were slightly lower than those produced from the FEA model. This may have resulted due to three known factors: (a) heat loss through the 3 mm holes drilled into the sample; (b) lack of contact of the thermocouples to the material surface and (c) the thermocouple response time. Such aspects were not taken into account by the FEA model and so the FEA results will always be higher.

3.2 Temperature mapping

By taking into account the surface temperature at the laser-ceramic interface a thermal snap-shot at various positions was created with the FEA model for the incident fibre laser beam, as shown in Figure 2 and Figure 3. The FEA model illustrates the surface and the bulk heat distribution as the motion of the CW fibre laser beam is frozen in the centre of the ZrO₂ sample. The total time to cover the length of the of the sample was 30 s at a traverse speed of 100 mm/min. This means that a distance of 1.66 mm/s would be covered.

The difference between the experimental model and the computational FEA model was up to 5%, particularly for the temperature predictions over the length of the surface. The bulk readings for the two models were also in good agreement. Even so, consideration should be given to the accuracy of the infra-red thermometer used for measuring the temperatures experimentally ($\pm 10\%$), as well as the distance of 1 m from which the temperature measurements were taken; for this distance will change as the fibre laser beam traverses away from the focused infra-red beam of the thermometer. This would naturally result in some fluctuation in the measured surface temperatures.

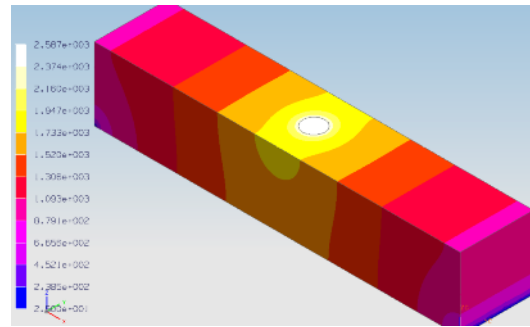


Fig. 3. FEA model of the heat distribution in the ZrO₂ for a fibre laser beam focused in the centre of the sample.

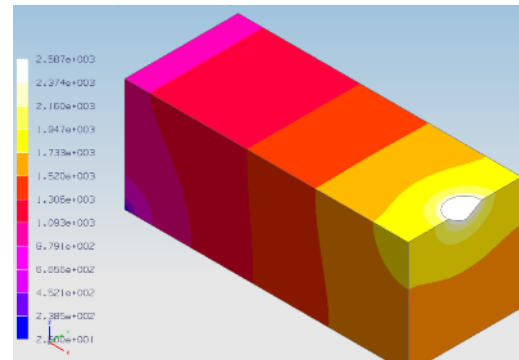


Fig. 4. FEA model of the cross-sectional heat distribution in the ZrO₂ for a fibre laser beam focused at the edge of the sample.

3.3 Phase changes

The TG-DSC analysis is given in Figure 2. The heating curve for the as-received ZrO₂ surface shows an exothermic peak at 50°C and a corresponding reduction in mass flow of 8 mW, indicating a possible release of moisture. At 800°C the small peak observed suggests a possible phase change where the mixture of M+T could have occurred. At 1290°C a further change in the curve indicated a phase transformation of M-T. The mass flow reduced as the sample reached 1500°C during the heating cycle. During the cooling process mass flow was much higher and similar effects took place to that of the heating curve. At 1205°C the curve showed an additional peak

which may have occurred due to the change in the phase transformation from the T to the T+M phase.

The curve produced by the fibre laser treated ZrO₂ sample was somewhat different to that of the as-received sample as more heat will have flowed through the bulk due to air blocks or cavities within the as-received sample, which would in turn cause a decline in the mass flow. During the heating cycle the curve produced for the fibre laser treated ZrO₂ showed changes at 850°C, which mark the beginning of the M+T phase change. At 1400°C the curve showed a minor change, indicating that the T transformation had fully occurred. This is different to the effect of the as-received sample and that of previous findings [25]. A possible cause of this would be due to the ceramic changing its composition after the fibre laser treatment; hence the observed increase in mass flow. During the cooling cycle there were no changes to be seen until 805°C, this is a sign that the ZrO₂ had transformed back to the M state. The TG-DSC analysis only investigated changes up to 1500°C. Since the temperatures measured experimentally and predicted from the FEA model were much higher, we can only surmise the effects beyond 1500°C.

From observing the temperature distribution obtained experimentally and from the FEA model (see Figures 1, 2 and 3) it can be seen that the distribution of heat varies in different positions on the ZrO₂ ceramic as the fibre laser beam is frozen in one position on the sample in order to investigate the heat distribution. From this one can see that the rapid surface and bulk heating occurs followed by the rapid cooling effect taking place where the ZrO₂ is transformed from M → M+T → T → T+C during heating. It is then instantaneously transformed back from T+C → T → T+M → M.

4. Conclusions

The thermal effects of the fibre laser surface treatment of a ZrO₂ engineering ceramic were modelled using finite element analysis (FEA). From both surface and bulk temperature measurements the distribution of temperature over the length and the depth of a ZrO₂ engineering ceramic sample during fibre laser surface treatment was also presented and the FEA model was verified with an overall accuracy of +10%. This is consistent over estimate of temperature by the FEA model may have resulted due to: (a) heat loss through the 3 mm holes drilled into the sample; (b) lack of contact of the thermocouples to the material surface and (c) the thermocouple response time. Such aspects were not taken in account by the FEA model and so the FEA results will always be higher.

Data obtained from a thermogravimetry-differential scanning calorimetry (TG-DSC) analysis and the FEA model predictions was used to map the phase transformations in the ZrO₂ resulting from fibre laser surface treatment. The mapping revealed that the fibre

laser surface treatment generally resulted in a phase transformation of the ZrO₂ from the M state to a mixture of T+C during fibre laser irradiation and from T+C to T followed by the M state during solidification. Variation between the TG-DSC curves for the as-received and fibre laser treated ZrO₂ indicated that there was some level of chemical change within the fibre laser treated ZrO₂ sample that allowed more mass flow to take place.

The FEA model will be expanded further through the addition of parameters such as time, speed and power density which when correlation with one another will produce a complete three-dimensional model of the fibre laser surface processing of the ZrO₂ engineering ceramic.

References

- [1] Zhang Z, Modest MF, (1998), *Journal of Heat Transfer*, 120:322-327.
- [2] Ignatiev MB, Smurov I, Flamant G, Senchenko VN, (1996), *Journal of Applied Surface Science*, 96-98: 505-512.
- [3] Braisted W, Brockman R, (1998), *International Journal of Fatigue*, 21: 719-724.
- [4] Hu Y, Yao Z, Hu J, (2006) *Surface and Coatings Technology*, 21:1426-1435.
- [5] Ocan JL, Morales M, Molpeceres C, Torres J, (2004), *Applied Surface Science*, 238:224-248.
- [6] Chen H, Kysar JW, Lawrence YY, (2004) *Journal of Applied Mechanics*, 71: 713-723.
- [7] Kim MJ, (2005), *Applied Mathematical Modelling*, 29:938-954.
- [8] Shiomi M, Abe F, Osakada K, (1998), *International Journal of Machine Tools and Manufacture*, 39:237-252.
- [9] Carmingnani C, Meres R, Toselli G, (1999), *Computer Methods in Applied Mechanics and Engineering*, 179:197-214.
- [10] Spina R, Tricarico L, Basile G, Sibilano T, (2007), *Journal of Material Processing Technology*, 191:215-219.
- [11] Yilbas BS, Arif AFM, Abdul Aleem BJ, (2009), *Optics & Laser Technology*, 41:760-768.
- [12] Zain-UI-Abdein M, Nélias D, Jullien JF, Deloison D, (2008), *International Journal of Material Forming*, 1:1063-1066.
- [13] Naeem UD, Ejaz M, Hammouda M, (2009), *Journal of Mechanical Science and Technology*, 23:1118-113.
- [14] Garvie RC, Hannink RH, Pascoe RT, (1965) *Journal of Physics and Chemistry*, 69:1238-1243.
- [15] Porter DL, Heuer AH, (1977), *Journal of the American Ceramic Society*, 60:183.
- [16] Meriani S, (1982), *Thermo-chemica Acta*, 58:253-25.
- [17] Zhou Y, Ge QL, Lei TC, (1990), *Physics Letters*, 16:349-354.
- [18] Sato T, Ohtaki S, Shimada M, (1985), *Journal of Material Science*, 20:1466-1470.
- [19] Haraguchi K, Sugano N, Nishi T, Miki H, Oka K, Yoshikawa H, (2001), *The Journal of Bone & Joint Surgery*, 83:996-1000.
- [20] Shackelford JF, Doremus HR, (2008), *Ceramic and Glass Materials*, New York: Springer.
- [21] Richardson DW, (2006) *Modern Ceramic Engineering*, Cambridge: Taylor & Francis Group.
- [22] Huang X, Zakurdaev A, Wang D, (2008), *Journal of Material Science*, 43:2631-2641.
- [23] Lee WL, Rainforth WM, (1994), *Ceramic Microstructures*, London: Chapman & Hall.
- [24] Holand W, Beall G, (2002) *Glass-Ceramic Technology*, New York: The American Ceramic Society.
- [25] Shukla PP, Lawrence J, (2009) *Proceedings of the IMechE Part B*, (in press).

WC Nano powder cold planting via laser shock peening onto aluminium/magnesium alloy surfaces

Minlin Zhong*, Liang Lv, Changsheng Dong, Renjie Zhu, Hongjun Zhang, Wenjin Liu
Key Laboratory for Advanced Materials Processing Technology Ministry of Education, Department of Mechanical Engineering, Tsinghua University, Beijing 100084, P. R. Chin

* corresponding author: zhml@tsinghua.edu.cn, Tel: +86-10-62772993, Fax: +86-10-62773862

Abstract. We have developed a novel process for hardfacing aluminium/magnesium alloys: nano powder cold planting via laser shock peening (NPCP/LSP). The pre-coated nano powders are planted into the near surface layer by the GPa pressure induced by a laser shock peening process. This paper reports our recent work on WC NPCP/LSP onto aluminium/magnesium alloys, focusing on the combination of nano powders with the substrate, the interface bond between the nano particles and the matrix, and also the significant improvement on the surface hardness, wear resistance, and tribological properties.

Keywords: nano powder planting, aluminium/magnesium alloys, laser shock peening, interface bond, microstructure, wear resistance

1. Introduction

Nowadays, aluminium and magnesium alloys are extensively used light alloys in many industries like aerospace, transportation and shipping as structural materials due to their lightness, high strength weight ratio and good corrosion resistance. This can reduce the material/energy consumed and recycle the materials for environment protection [1]. However, the surface hardness and wear resistance of aluminium and magnesium alloys are usually poor, which limits their service lifetime for applications. There are some available processes being capable of improving the surface properties of the light alloys, such as plasma spraying, micro-arc oxidation, laser cladding and laser alloying, as well as a variety of heat treatments. These processes are mostly thermal processes, which normally involve a high temperature melting pool. Aluminium and magnesium alloys usually contain some lower-melting-point elements. In such a thermal process with relatively high temperature, defects frequently occur, such as the melting loss of lower-melting-point elements, porosity, cracking and surface deterioration [2]. Combining the unique characteristics of nano powders and laser shock peening, we have developed a novel process: nano powder cold planting via laser shock peening with pre-coated nano

powders (refer to NPCP/LSP) onto light metal surfaces [4]. The nano powders are planted into the near surface layer of the light metal alloys by very high pressure (up to Giga or even tens of Giga Pascal) induced by the laser shock peening process. Light alloy surfaces can be dramatically enhanced by the combined strengthening of the nano powders and also the laser shock peening process. This is not a thermal process which can effectively avoid the shortcomings associated with a thermal process. The unique features of the nano-powders can be integrated into the near surface layer of the light alloys with good combination. This paper reports our continuous research on NPCP/LSP, focussing on the confirmation of nano powders planted onto the light alloy surface, the combination of nano powders with the substrate, the interface bond between the nano particles and the matrix. The paper also reports about the significant improvement in surface hardness, wear resistance, and tribological properties by NPCP/LSP process. An analytical model was proposed to discuss the comprehensive strengthening mechanism by NPCP/LSP.

2. Experimental Procedures

The experiments were performed on a LSP system that consists of a Q-switch pulsed Nd:YAG laser, a CNC controlled working table and some accessories. The maximum energy of the laser is 50 J/pulse, pulse width is 30 ns, beam diameter is 6-9 mm and thus the powder density is 1.0-6.0 GW/cm². Black paint or aluminum film was used as absorptive layers. Either flowing water or K9 glass was used as restraint layer. Fig 1 shows the diagrammatic sketch of the NPCP/LSP process. The nano powder used in the experiments is WC nano powder with average diameter about 100 nm. The substrate materials used were 5A06 (AlMgMn) aluminum alloy and AZ31 (MgAlZnMn) magnesium alloy.

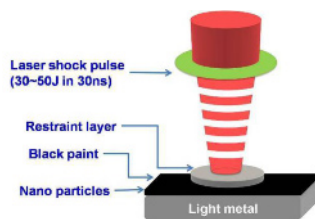


Fig. 1. Diagrammatic sketch of NPCP/LSP process

After NPCP/LSP experiments, the as-processed samples were cleaned by an ultrasonic wave device, cut by a linear cutting machine and then observed with a scanning electronic microscope-SEM (QUANTA 200 FEG) for surface morphology. The composition analysis was analyzed by energy diffraction spectrum-EDS. Transmission electronic microscopy-TEM was used for phase identification and interface observation. Vickers hardness was tested to verify the impacts of nano-particle cold enhancing by shock peening. Each sample was measured at 16 points for hardness to calculate the average hardness.

3. Results and Discussion

3.1 Confirmation on nano particles planting

Figure 2 shows some SEM backscattering surface morphologies of aluminium and magnesium alloys after NPCP/LSP. In these SEM backscattering images, the lighter coloured particles are the heavy element W. The grey or dark areas are the aluminium or magnesium alloy substrate composed of lighter elements. These figures indicate that the WC nano powders have been combined into the aluminium/magnesium surface layer by the NPCP/LSP process. The WC nano powders still remain in the aluminium surface layer after the rigid post ultrasonic cleaning process. These WC nano powders are believed to be forced to penetrate into the near surface layer under the extremely high pressure induced by the laser shock peening process. The penetrated layer thickness is about $5\ \mu\text{m}$ as seen from Figure 2b. EDS analysis indicates that about 7 at% of WC nano-particles have been planted into the aluminium surface layer. X-ray diffraction result of the NPCP/LSP processed aluminium sample, it demonstrates that the as-processed sample shows an additional WC phase except of its original Al phase. This WC phase is introduced by the NPCP/LSP process.

Figure 3 shows some TEM images of aluminium alloy surface planted with WC nano powder by laser shock peening process. Some particles in nano dimension present within the aluminium substrate. Local electron-beam diffraction confirms these particles are WC. Figure 3a shows a TEM dark-field photograph where two WC nano particles can be clearly seen with a good combination to the aluminium alloy substrate. Figures 3b

and c show bright-field photographs of the two WC nano particles corresponding to the particles in Figure 3a. Figure 3d is a corresponding electron-beam diffraction image. These images prove the planting of the WC nano particles into the interior of the aluminium alloy substrate. Figure 3e shows an electron beam diffraction image of the aluminium alloy substrate after NPCP/LSP process.

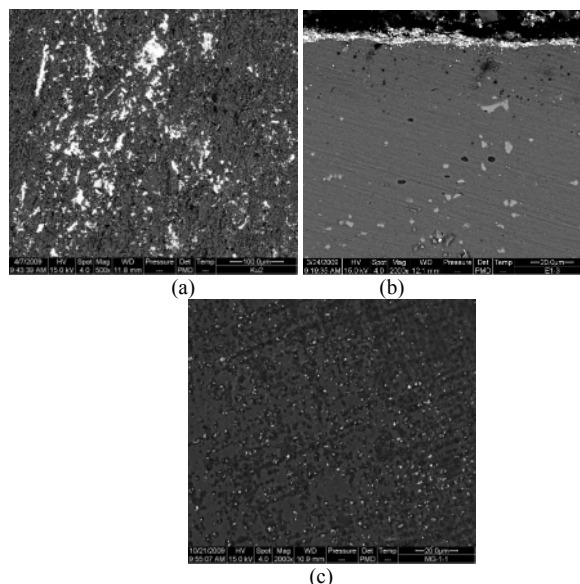


Fig. 2. SEM backscattering images of NPCP/LSP processed aluminium (a) (b) and magnesium (c) alloy samples

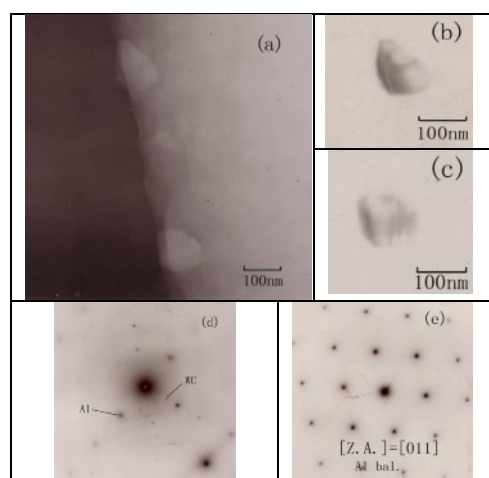


Fig. 3. TEM observation of the as-peened aluminium alloy with WC nanoparticles

Fig 4 shows two TEM images of the interface between the WC nano particles and the aluminium matrix. The WC nano particles remain their regular shape with good combination to the matrix. It can be deduced that there exists a good interface bond between the WC nano particles and the aluminium matrix. The WC nano particles are obviously not just put on the surface but are planted into the interior layer of the surface with good interface bond.

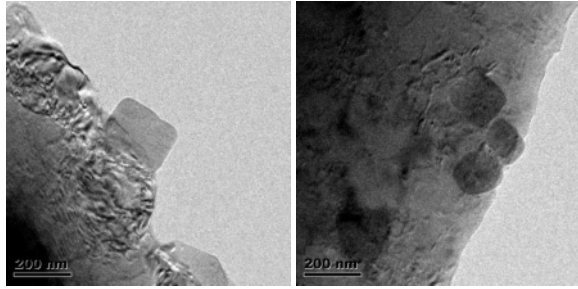


Fig 4. TEM morphology of combination between WC particles and aluminum substrate

3.2 Hardness and wear resistance analyses

Figure 5 shows comparatively the average surface hardness ($HV_{0.05}$) of aluminum and magnesium alloy samples in four processing conditions: the alloy substrate with no treatment, the substrate with pre-coated nano powder, the substrate processed by direct laser shock peening and the substrate processed by laser shock peening with pre-coated WC nano powder-NPCP/LSP.

The surface hardness of the untreated 5A06 aluminium alloy is $HV_{0.05}$ 34. It is changed slightly to $HV_{0.05}$ 38 after being coated with a layer of WC nano powder without a strong bond. After laser shock peening process, the hardness is increased to $HV_{0.05}$ 48, which is an increase of about 41% due to the strengthening of laser shock peening itself. Combined with pre-coated nano powder and laser shock peening (nano powder cold planting via laser shock peening), the surface hardness has increased to $HV_{0.05}$ 55, i.e. a 62% increase in hardness compared to the aluminium substrate and an increase of 15% compared to the LSP strengthened aluminium. This is a significant improvement as for the hardfacing of light alloys. The magnesium alloy has a similar hardness increase the nano powder cold planting by laser shock peening process. The above results also confirm that the pre-coated WC nano powders in NPCP/LSP enhance the strengthening impact by the LSP process.

Ball-on-flat wear tests were performed on samples in above four processing conditions in an UMT-3V test machine. Figure 6 shows the relative wear resistance of the samples in four conditions. Compared to the original aluminium alloy with no treatment, the wear resistance of the samples with pre-coated WC nano powders, direct laser shock peening and NPCP/LSP are respectively 1.5 times, 3.19 times and 5.14 times. The WC nano powder cold planting via laser shock peening process can significantly increase the wear resistance of the aluminium alloy. The wear resistance of the NPCP/LSP processed sample is obviously improved (over 60%) even compared with that by the laser shock peening itself. This again confirms that the pre-coated WC nano powders in NPCP/LSP enhance the strengthening impact by the LSP process.

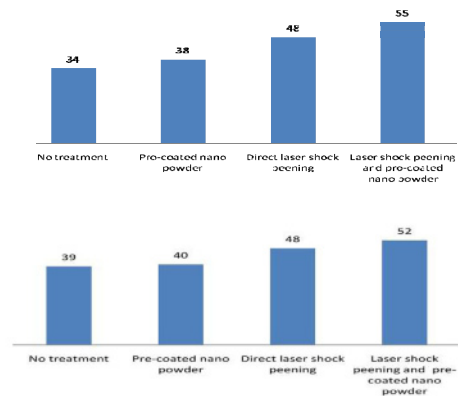


Fig 5. Average surface $HV_{0.05}$ hardness of aluminum (up) and magnesium samples (down) and in four conditions

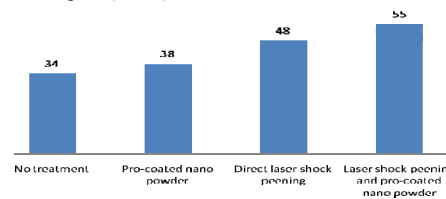


Fig 6. The relative wear resistance of the aluminium sample in four conditions

Figure 7 shows the comparison between the friction coefficients of samples in four conditions under the same wear testing environment. The average friction coefficient of sample with pre-coated nano WC powders decreases by about 9% compared to the sample with no treatment. The sample processed with only laser shock peening process has no obvious improvement in friction coefficient. The sample processed with both pre-coated nano-powder and laser shock peening-NPCP/LSP shows the lowest average friction coefficient, reducing approximately 14% when compared with the untreated sample. This indicates a significant improvement in terms of tribological property.

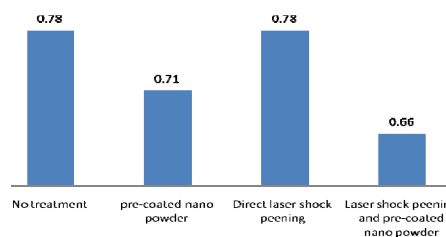


Fig 7. Average friction coefficient values in different treatments

The significant improvement in wear resistance and tribological property of the sample by WC nano powder cold planting via laser shock peening process can be attributed to two aspects, the effect induced by the laser shock peening and the special characteristics accompanying with nano powders. Laser shock peening, producing a shock wave with very high pressure, can form plastic deformation along with dense dislocation

structure and residual compressive stress in the surface layer. Thus, it can increase the hardness, wear resistance, fatigue resistance, fretting fatigue resistance and other performance, which has been reported by many researches. We hereby analyze mainly the impact by the planted WC nano particles with good interface bond to the matrix. The nano-material itself has good comprehensive properties on strength, hardness, plasticity and toughness, contributing to very good tribological properties, far superior to the traditional materials. Nano metal particles applied in coating material can improve wear-resistant, corrosion resistance and high temperature properties. Adding nano metal powders into lubricant oil can effectively reduce friction and wear, and can also effectively repair the worn surface [5]. We proposed a simple analytical model (Fig. 8) to discuss the unique tribological property by the nano powder cold planting via laser shock peening process.

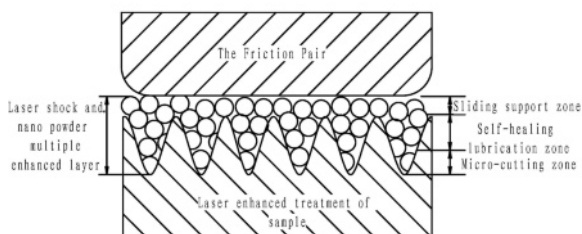


Fig 8. A simple analytical model for analyzing the unique tribological property by nano powder cold planting via laser shock peening

Considering the nano particles as spheres, we can then divide the near surface area with nano particle planting into three regions with different friction and wear mechanisms, which refer to "sliding support zone" as outer layer, "self-healing lubrication zone" as middle layer and "micro-cutting zone" as inner layer as in Figure 8. They correspond also to different friction stages and wear processes. At the initial stage of the friction process, the nano particles on outer layers between the friction pairs mainly form the "sliding support zone". The nano particles act as "micro-rolling" elements and switch the normal sliding friction into rolling friction, thus reducing the friction coefficient and frictional resistance. With the continuation of the friction and wear process, the "sliding support zone" wears out and the "self-healing lubrication zone" works as the surface layer. The surface micro texture, structured by the original surface roughness of the alloy surface and by the laser shock peening process, plays an important role by reducing the friction coefficient and frictional resistance due to the reduction of friction-contact-area. The nano particles with a good bond with the substrate function as hard particles for micro-cutting, polishing the surface of the friction pairs. At the same time, the nano particles filled in the pits

between micro bumps as storage rooms, still act as "micro-rolling" elements to change the sliding friction into rolling friction. In the third stage of the friction and wear process, the micro bumps are gradually polished, no longer acting as storage room for nano particles. More and more hard particles get exposed, micro-cutting and micro-polishing becomes the major form in the friction and wear process. Therefore, the as-planted nano particles, with good bond to the matrix, play unique functions for excellent wear resistance and tribological property.

4. Conclusion

A novel process nano powder cold planting via laser shock peening- NPCP/LSP was developed, by which WC nano particles are successfully planted into the near surface layer of aluminum and magnesium alloys by laser shock peening with pre-coated nano powders. The nano powders show good combination with the surface of light alloy substrates. TEM analyses confirm good interface bond between the planted WC nano particles and the matrix.

WC nano cold planting via laser shock peening can significantly improve the surface hardness, wear resistance and the tribological properties of the as-processed light alloy surface. Nano particles dramatically enhance the strengthening impacts by laser shock peening. An analytical model was proposed to analyze the comprehensive strengthening mechanism induced by the nano powder planting via laser shock peening.

Acknowledgement

The authors thank The National Natural Science Foundation of China for funding under grant number 50735001.

References

- [1] Su Xuechang. Reinforce of Aluminum alloy. *Light Alloy Fabrication Technology*. 1996, 24(9): 2-5
- [2] Zhi Z, Lijun W, Yue W, et al. Numerical and experimental investigation on temperature distribution of the discontinuous welding. *Computational Materials Science*. 2009 (44): 1153-1162
- [3] Tian Hua, Xue Wenbin, Li Xijin, et al. Tribological performance of micro-arc oxidation coatings on 15sic_p/2024 aluminum matrix composites. *Journal of the Chinese Ceramic Society*. 2008, 36(5): 636-641
- [4] Renjie Zhu, Minlin Zhong, Liang Lv, Changsheng Dong, Wenjin Liu, Nano WC powder cold enhancing of light metal surface by laser shock peening process, *Proceedings of ICALEO'2009*, Orlando, FL, USA, Nov. 2-5, 2009, 262-269
- [5] L Rapoport, V Leshehinsky, M Lvovsky, et al. Friction and wear of powdered composites impregnated with WS2 inorganic fullerent-like nanoportieles [J]. *Wear*, 2002, 252:518-527.

Femtosecond laser induced two-photon polymerization of dielectric-loaded surface plasmon-polariton nanowaveguides

Yan Li, Zhaopei Liu, Haibo Cui, Hong Yang, Qihuang Gong
State Key Laboratory for Mesoscopic Physics, Department of Physics, Peking University, Beijing, 100871, China
li@pku.edu.cn

Abstract. Dielectric-loaded surface plasmon-polariton waveguides have been fabricated on gold film by femtosecond laser induced two-photon polymerization. Due to the high-index-contrast between the dielectric and air, these waveguides present strong lateral confinement and low edge-scattering and bend loss. The leakage radiation microscopy shows that the nanowaveguides with optimal transverse dimensions around 250 nm are single-mode with strong mode confinement at excitation wavelength of 830 nm.

Keywords: two-photon polymerization, femtosecond laser, nanofabrication, nanowaveguide

1. Introduction

Femtosecond laser induced two-photon polymerization (TPP) has been utilized to fabricate various three dimensional (3D) structures with sub-diffraction-limit feature-sizes [1,2]. When the near-infrared pulses are tightly focused into a UV curable resin such as SCR500, a highly localized chemical reaction results in an organic crosslinking, i.e. the material is transformed from the liquid into the solid state. Since the process of multiphoton absorption depends nonlinearly on the light intensity, the interaction region is limited to the focal volume, while outside of the focus the material stays unchanged. Therefore, the feature size can be much smaller than the wavelength. In addition, by moving the focus in three directions, arbitrary 3D structures beyond the diffraction limit can be created [3-8].

Recently, TPP has been applied to the polymerization of the dielectric-loaded surface plasmon-polaritons waveguides (DLSPWs) comprised of dielectric ridges deposited on a smooth gold film [9-11]. Due to the high-index-contrast between the dielectric and the air, DLSPWs present stronger lateral confinement, lower edge-scattering and bend losses. Furthermore, the chemical and optical characteristics of dielectrics such as dye-doped polymers can be easily modified to develop active plasmonic components.

Up to now, the feature sizes of the DLSPWs fabricated by TPP have still been on the microscale. At the transmission windows of optical communication, ~830 nm, all the reported single-mode DLSPWs at nanoscale were produced by electron-beam lithography.

In this paper, we systematically investigated the polymerization of 3D nanostructures via TPP with femtosecond laser pulses at a wavelength of 830 nm and found approaches to reduce the feature-size to ~20 nm, to compensate for the shrinkage and tapering, and to determine the minimum spacing of suspended nanorods, which enabled us to fabricate nanoscale single-mode DLSPWs for the excitation wavelength of 830 nm. The mode effective index, confinement, and propagation length of DLSPWs are calculated by the effective-index method. The optimal transverse dimensions for single-mode guiding, i.e., ridge height and width, are selected by the trade-off between the confinement and the loss. The SPP guiding of the DLSPWs is characterized by leakage radiation microscopy.

2. Experiment

In our experiment, the commercial resin SCR500 from JSR without special treatment was sandwiched between two soda-lime glass slides of 150 μm thickness each. The distance between the two slides was set by a spacer to ~100 μm . The laser beam was focused by the microscope objective (100 \times , 1.35N.A.) through the lower glass slide and the SCR500 onto the bottom surface of the upper slide. This surface was coated with the gold film and the surface plasmon-polaritons (SPP) structures were generated on it. The laser beam was from a Ti:Sapphire femtosecond oscillator (Mira900, Coherent: central wavelength at 830 nm, pulse duration of 140 fs, repetition rate at 76 MHz). In the TPP process, both the power of the incident beam and the scan velocity of focus (~12 mW at the velocity of >60 $\mu\text{m}/\text{s}$) were close to the

thresholds of polymerization in order to reduce the feature size and the influence of the laser beam reflected by the gold film. In addition, structures were written several times to ensure smooth and well-defined surfaces. After exposure, the sample was developed in ethanol to remove unexposed resin.

3. Results and discussion

To ensure the high performance of the nanodevices, reduction of feature size, compensation for shrinkage and stretching, and determination of the minimum spacing were systematically investigated.

Due to the weak intensity of the outer part of the laser focus, there was a lower-degree polymerized zone at the outer portion of each polymerized structure, which was always washed out during development. However, when two structures came close enough, the lower-degree polymerized zone around one structure would react with the zone around the other structure. The overlapped region was re-exposed by the laser focus' outer part whose intensity was high enough to convert the lower-degree polymerized material into the higher-degree polymerized form but unable to induce higher-degree polymerization direct from the unexposed liquid resin. Therefore, the lower-degree polymerized zone was re-polymerized and became strong enough to survive the development. It was obvious that the closer the spacing, the stronger the re-polymerization. By controlling laser power and laser focus scan speed, we polymerized suspended nanorods between two large anchor supports with sub-25 nm feature-size. Figure 1 shows a suspended nanorod with feature size of ~ 50 nm. Based on re-polymerization, the feature-size was further reduced to ~ 15 nm, which is very beneficial to nanofabrication with ultra-high spatial resolution.

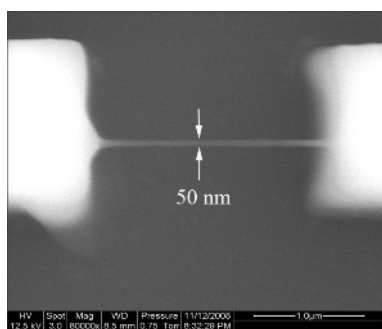


Fig. 1. A suspended nanorod with feature size of ~ 50 nm.

Because the solid phase had a higher mass density than the liquid phase, the polymer shrank during the polymerization process. When the unpolymerized resin was rinsed out, in order to obtain freestanding structures, a strong capillary force developed during the final evaporative drying, resulting in further shrinkage. The

distortion of polymerized structures during the whole fabrication process needs to be studied to accurately fabricate structures with high resolution. The width-dependent shrinkage rates of suspended nanorods fabricated by two-photon photopolymerization have been measured. However, it is still difficult to directly measure the length-dependent strain rates of suspended nanorods because the actual lengths are determined by the distance between the two supports.

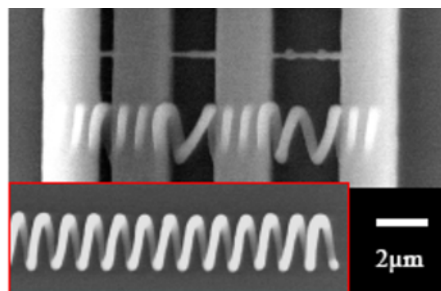


Fig. 2. The fabricated structures shrank after polymerization and rinsing, but the suspended nanorods were also stretched by measuring the distance changes of the originally periodical points added on the nanorods. The pitch changes of microsprings also demonstrate the shrinkage of the supports and the stretching between supports. The pitch was designed to be $1 \mu\text{m}$. The inset shows the reference microspring adhered to the substrate.

We proposed a method to measure the shrinkage and the extension rate by marking the nanostructure with periodical points and measuring the separation changes after the polymerization. It was found that the suspended nanorods were stretched due to the shrinkage of their supports. The shrinkage of the supports was also demonstrated by the pitch change of the microsprings existing on or between the supports as shown in Fig. 2. Using this technique, the shrinkage of the polymerized cuboids was analyzed by the changes in the separation between points on the top surfaces. This shrinkage increased with the increasing height of the cuboids.

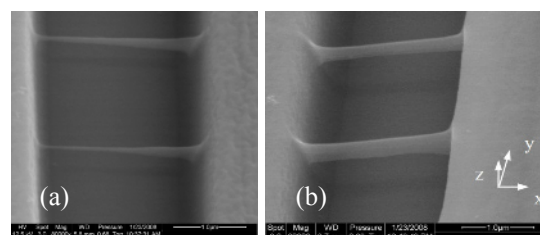


Fig. 3. (a) The suspended nanorods thickened in the scanning direction. The lateral widths of the thin and the thick ends are about 50 and 150 nm. The longitudinal widths in the z direction vary from 200 to 550 nm. (b) Bidirectional scanning method to overcome the size difference.

Suspended nanorods near the substrate gradually thickened in the scanning direction when the scanning speed was faster than $60 \mu\text{m/s}$. For a $2 \mu\text{m}$ long suspended

nanorod, the lateral widths of the thin and the thick ends were about 50 and 150 nm respectively, as shown in Fig. 3. In our experiment, the scanning speed was relatively high. When the scanning speed was fast enough, the width was so small that the change induced by the radical and the thermal transports should be taken into account. After laser irradiation, some radicals propagated outwards and at the same time part of the generated heat also transport outwards. When the focal spot was scanned, the polymerization at the new site was initiated by both the laser irradiation and the inflow of the radicals and the heat from the previous sites. Therefore, the rods thickened in the scanning direction. It was obvious that the size increase would saturate because the radical and thermal transports in the vicinity contributed most to the thickening while those from far away faded away. A bidirectional scanning technique was proposed to effectively eliminate the size difference, resulting in uniform suspended nanorods of 100 nm in width and 2 μm in length. The lateral widths of the two nanorods in Fig. 3(b) were about 140 and 160 nm, and the longitudinal thicknesses in the middle part were 360 and 510 nm, respectively.

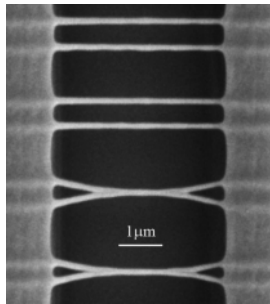


Fig. 4. Four nanorod pairs with length of 4 μm and width of ~ 200 nm. The spacings are 650, 600, 550, 500 nm from top to bottom, respectively.

The minimum spacing between suspended nanorods was not only dependent on the feature sizes, but also limited by the inevitable stiction problem that resulted from the capillary, electrostatic, van der Waals forces during fabrication and the developing process. When the suspended nanorods were close enough, surface tension pulled the nanostructure towards each other as the liquid was dried. The structure might adhere permanently. The minimum spacing was found to be determined by the stiction and could be predicted based on a theoretical model calculating the adhesion length [12], which was in good agreement with the experimental results for suspended nanorods with feature-size around 200 nm. Figure 4 shows the image of four nanorod pairs with length of $\sim 4 \mu\text{m}$ and width of ~ 200 nm. The spacings are $\sim 650, 600, 550, 500$ nm from top to bottom, respectively. It can be clearly seen that the nanorods adhered to each other when the spacing was smaller than 550 nm.

The DLSPWs were designed by the effective-index method (EIM) and then fabricated by TPP. Figure 5

shows the AFM image of four polymerized ridge nanowaveguides on the gold film. Their widths are $\sim 230, 250, 320$ and 350 nm while heights are 170–190 nm.

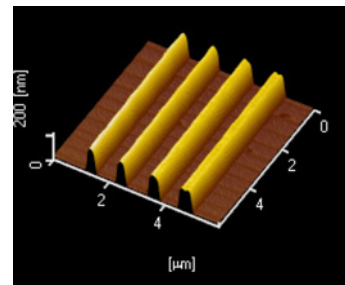


Fig. 5. AFM image of four polymerized ridge nanowaveguides on the gold film with heights of 170–190 nm.

The SPP guiding of the DLSPWs was characterized by the leakage radiation microscopy (LRM). Figure 6(a) shows the optical microscope image of a straight DLSPW with a semicircular SPP launching structure. This waveguide had the optimal width ($w \sim 250$ nm) for height $t \sim 200$ nm. To characterize DLSPW in LRM, a CW 830 nm polarized laser beam was focused onto the semicircular polymer ridge whose center was located at the beginning port of the straight polymer ridge. SPPs at the gold-air interface were launched by the semicircular ridge, and then focused into the straight ridge to excite DLSPW modes. The leakage radiations of DLSPW modes were collected by an oil immersion objective (100 \times , 1.35N.A.). The images of sample and Fourier planes were captured to calculate the propagation length and the mode effective index.

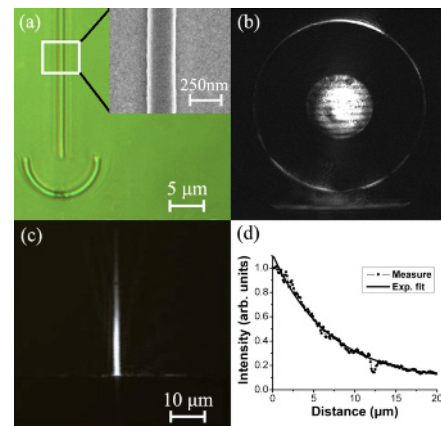


Fig. 6. (a) Optical microscope image of a straight DLSPW with a semicircular SPP launching structure. The inset is the SEM image within the white frame. (b) The LRM image at Fourier plane without beam block. The bright line at the bottom is DLSPW mode. (c) The image of object plane when only DLSPW mode was retained. (d) Exponential fit of the intensity along the core of waveguide in (c).

The Fourier plane image without beam block is showed in Fig.6 (b). The bright circular spot at the center comes from the transmitted light, and the bright ring is the leakage radiations from the SPPs. The signature of DLSPPW mode appeared as a long line in the horizontal direction at the bottom of Fig.6 (b).

For a better signal-to-noise ratio, we blocked the excitation laser spot at the intermediate image plane of the sample to remove the directly transmitted light and the scattered light of semicircular ridge, and then blocked the central zone and the bright ring of Fourier plane to remove the rest of the transmitted light and the gold-air SPPs. Fig.6 (c) is the corresponding image acquired at the final image plane of sample showing the DLSPPW mode propagating along the waveguide with strong mode confinement. The intensity distribution across the waveguide confirmed that this DLSPPW mode indeed was single-mode as expected by EIM calculation. By exponentially fitting the intensity along the core of waveguide in Fig.6 (d), the propagation length can be obtained as $8.2\pm 0.5\ \mu\text{m}$. The effective index of DLSPPW mode was $\sim 1.22\pm 0.03$. Both the results of the propagation length and the mode effective index were in good agreement with the theoretical values.

4. Conclusion

In conclusion, we have investigated the polymerization of 3D nanostructures via TPP with femtosecond laser pulses to find the way to reduce the feature-size to $\sim 20\ \text{nm}$, to compensate for the shrinkage and tapering, and to determine the minimum spacing of suspended nanorods, which enable us to fabricate high quality DLSPPWs on gold film. Leakage radiation microscopy shows that the nanowaveguides with optimal transverse dimensions around $250\ \text{nm}$ are single-mode with strong mode confinement at excitation wavelength of $830\ \text{nm}$.

References

- [1] Kawata S, Sun HB, Tanaka T, Takada K, (2001) Finer features for functional microdevices *Nature* **412**: 697-698
- [2] Maruo S, Fourkas JT, (2008) Recent progress in multiphoton microfabrication *Laser & Photon. Rev.* **2**: 100-111
- [3] Seet KK, Juodkazis S, Jarutis V, Misawa H, (2006) Feature-size reduction of photopolymerized structures by femtosecond optical curing of SU-8 *Appl. Phys. Lett.* **89**: 024106
- [4] Tan DF, Li Y, Qi FJ, Yang H, Gong QH, Dong XZ, Duan XM, (2007) Reduction in feature size of two-photon polymerization using SCR500 *Appl. Phys. Lett.* **90**: 071106
- [5] Li LJ, Gattass RR, Gershgoren E, Hwang H, Fourkas JT, (2009) Achieving $\lambda/20$ resolution by one-color initiation and deactivation of polymerization *Science* **324** 910-3
- [6] Park S, Lim T, Yang D, Cho N, Lee K, (2006) Fabrication of a bunch of sub-30-nm nanofibers inside microchannels using photopolymerization via a long exposure technique *Appl. Phys. Lett.* **89**: 173133
- [7] Li Y, Qi FJ, Yang H, Gong QH, Dong XZ, Duan XM, (2008) Nonuniform shrinkage and stretching of polymerized nanostructures fabricated by two-photon photopolymerization *Nanotechnology* **19**: 055303
- [8] Li Y, Cui HB, Qi FJ, Yang H, Gong QH, (2008) Uniform suspended nanorods fabricated by bidirectional scanning via two-photon photopolymerization *Nanotechnology* **19**: 373504
- [9] Kiyan R, Reinhardt C, Passinger S, Stepanov AL, Hohenau A, Krenn JR, Chichkov BN, (2007) Rapid prototyping of optical components for surface plasmon polaritons, *Opt. Express*, **15**: 4205-4215
- [10] Reinhardt C, Kiyan R, Passinger S, Stepanov AL, Ostendorf A, Chichkov BN, (2007) Rapid laser prototyping of plasmonic components, *Appl. Phys. A*, **89**:321-325
- [11] Luo H, Li Y, Cui HB, Yang H, Gong QH, (2009) Dielectric-loaded surface plasmon-polariton nanowaveguides fabricated by two-photon polymerization, *Appl. Phys. A*, **97**: 709-712
- [12] Wu DM, Fang N, Sun C, Zhang X, (2006) Stiction problems in releasing of 3D microstructures and its solution. *Sensors and Actuators A* **128**: 109-115

Real-time control of polarization in ultra-short pulse laser micro-processing

O. J. Allegre¹, W. Perrie¹, K. Bauchert², D. Liu¹, S. P. Edwardson¹, G. Dearden¹ and K. G. Watkins¹

¹ Laser Group, Department of Engineering, University of Liverpool, Liverpool, L69 3GQ, UK

² Boulder Nonlinear Systems, Inc., Lafayette CO 80026, USA

Abstract. The use of a fast-response, transmissive, ferroelectric liquid-crystal device for real-time control of the polarization direction of a femtosecond laser beam, and the benefits on various aspects of ultra-short pulse micro-processing, are discussed. Several configurations have been used for driving the polarization in real-time. Following successful testing of these applications, real-time polarization control has emerged as a flexible toolbox for the laser processing engineer. Microscopic investigation of the produced features revealed the significant improvement in process quality.

Keywords: Ultra-short pulse laser, Polarization, Micro-drilling.

1. Introduction

The past decade has seen the development of ultra-short pulse lasers, with processes based on femtosecond and picosecond pulse durations becoming increasingly widespread. Thanks to the ultra-short timescale on which laser energy is coupled to the material, high precision sub-micron machining of metals has been achieved with very little thermal damage [1, 2]. Industrial applications include the very precise drilling of holes for fuel-injection nozzles in the automotive industry [2, 3]. The key parameters influencing the laser-machining process quality are the pulse duration, wavelength, peak power, beam quality and polarization [4-6].

The influence of polarization on micro-machining has been experimentally demonstrated in [6-10], showing that drilling high-aspect-ratio (depth/diameter) microscopic holes in metal with linear polarized ultra-short-pulse lasers produces anisotropic profiles. This is due to the higher reflectivity of the *s*-polarized radiation, relative to the *p*-polarized radiation [7]. As the hole develops through the material, the *p*-polarized radiation is more readily absorbed in the sidewalls, whereas the *s*-polarized radiation tends to be reflected down to the base of the hole. This results in a distorted hole when the beam reaches the exit side. The simplest way to reduce these distortions is to use a circular polarized beam, which removes the differential in reflectivity during drilling. In some cases however, the remaining distortions associated with circular polarization are not satisfactory [6]. Another

technique, referred to as *polarization trepanning*, consists of rotating the linear polarization during drilling to further improve the hole quality [7, 10]. The trepanning optic developed in [8] produced holes of remarkable quality using this technique. However, these methods involve mechanical rotation of optical components and could be adversely affected by vibrations and prone to mechanical failure, leading to potentially expensive maintenance. An alternative laser-specific polarization switching method is detailed in [5]. It is based on an intra-cavity polarization chopper wheel synchronized to the laser pulse train. However, this method requires the laser cavity to be re-designed and therefore cannot be easily applied to existing laser systems.

In this paper, we propose a flexible method for rapidly switching the linear polarization of a laser beam between two orthogonal directions during micro-machining, using a fast-response liquid-crystal polarization rotator. As a proof of principle, helical drilling tests were performed on stainless steel using various polarization configurations. The early experimental results using a femtosecond laser system show a small, but consistent improvement of the micro-drilling quality compared to linear or circular polarization configurations.

2. Experiment

2.1 Experimental setup

The experimental setup is shown in Fig. 1. The output from a femtosecond laser system (Clarke-MXR CPA2010, with a minimum pulse width of 160fs, 775nm central wavelength, 1mJ maximum pulse energy, 1kHz repetition rate and vertical linear polarization) is attenuated by a half-wave-plate and a glan laser polarizer. The resulting horizontally polarized beam is incident on a transmissive, ferroelectric, liquid-crystal polarization rotator developed by Boulder Nonlinear Systems, Inc.

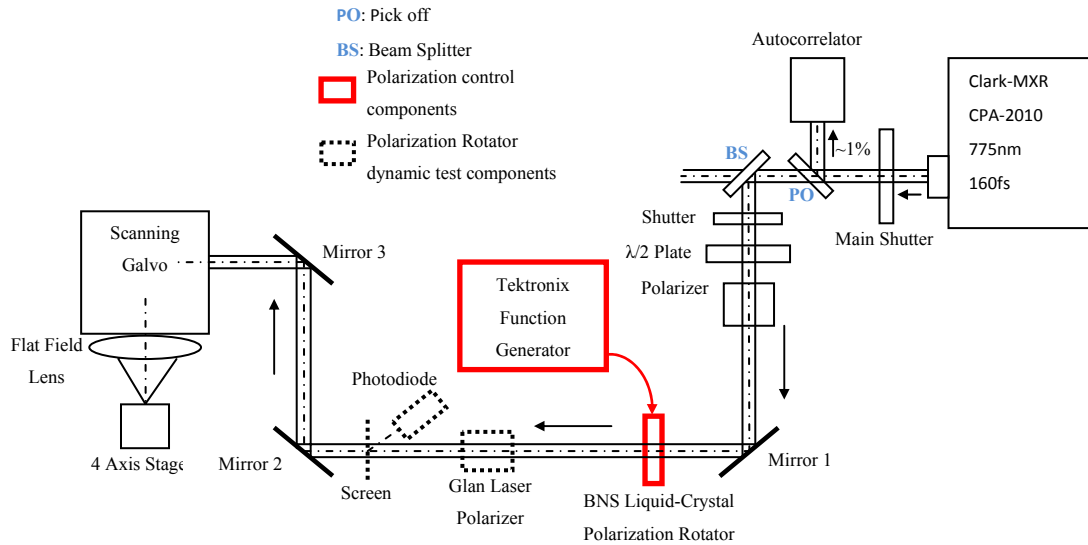


Fig. 1. Helical drilling experimental setup showing how the liquid-crystal polarization rotator was used. For the drilling tests, the dashed components were removed. This setup is a modified version of the one used in [11].

(MS Series). The liquid-crystal polarization rotator offers a switching speed of up to 20kHz between two orthogonal output states, with a response time of typically less than 100 μ s. This device behaves like a zero-order half-wave retarder mounted in a mechanical rotation stage. Varying the electric field applied to the device is equivalent to rotating the mechanical stage. The polarization rotator is driven by a programmable waveform from a function generator (Tektronix). After reflection on Mirrors 2 and 3, the beam enters the 10mm aperture of a scanning galvo system with a flat field lens ($f = 100$ mm), driven by a programmable PC interface board. Samples are mounted on a precision 4-axis (x , y , z , θ) motion control system (Aerotech) allowing accurate positioning of the sample at the laser focus.

2.2 Test strategy

In helical drilling, the laser beam performs a circular movement with a defined diameter on the surface of the work piece. As material is removed by each pulse, the beam works its way through the material on a helical path. The parameters influencing the geometry of the machined hole include the diameter of the circular beam path, the ablation spot size and the polarization [6].

Series of helical drilling tests were performed on 380 μ m thick stainless steel samples. Circular beam paths with diameters of 55, 65 and 70 μ m were programmed on the scanning galvo. A pulse energy value of 75 μ J was used, corresponding to a fluence of 20J/cm². This produced ablation spot diameters of typically around 60 μ m. As the fluence was much higher than the ablation threshold (around 0.1J/cm² for steel), some melting occurred at the entrance of the holes, but the overall drilling time per hole was reduced to below 60s. The test

strategy consisted of using the various polarization modes available with the liquid-crystal polarization rotator, varying the operating parameters to improve the circularity and reduce the taper of the micro-holes. Linear and circular polarized beams were used first to provide comparative data for subsequent tests. The experimental configuration of the setup for each test is summarized in Table 1.

3. Results and discussion

The helical drilling tests produced tapered holes with an entrance opening diameter of typically around 110 μ m corresponding to a programmed circular beam path of 65 μ m in diameter and a pulse energy of 75 μ J. The entrance of the holes showed no dependence on polarization, but was slightly elliptical in shape due to the ellipticity of the incident laser beam profile. On the exit side, the shape and taper of the holes varied with polarization, with a typical half-angle side-wall taper ranging between 4 $^\circ$ and 5 $^\circ$. A summary of the test results as well as SEM images of the exit holes for the various polarization modes are shown in Table 1.

3.1 Scanner-synchronized polarization switching

In *polarization trepanning*, the direction of linear polarization rotates synchronously to the beam motion around the hole so that it is always oriented in the same way with regard to the wall [6]. This is normally achieved by placing a wave-plate in the optical path and mechanically rotating it synchronously with the beam. In order to obtain a similar effect, our liquid-crystal polarization rotator was synchronized with the scanning

galvo head. As only two orthogonal directions of polarization were available, this test produced an approximation of *polarization trepanning* by maintaining the direction of polarization as close as possible to a *p*-polarization during helical drilling. Our experimental results are described in Table 1. The quality of holes drilled using this method was limited by only having two directions of polarization. However, optical *polarization trepanning* in this way may prove useful when drilling geometric shapes, such as square- and cross-shaped holes or cutting linear grooves, where the polarization direction can be best optimized.

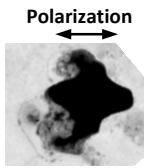
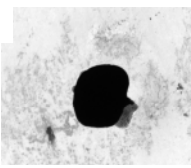
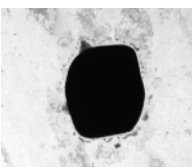
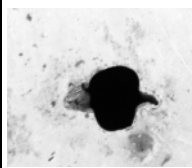
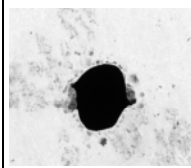
3.2 Laser-synchronized polarization switching

In this mode, the polarization rotator was synchronized with the kHz femtosecond-pulse-train from the laser. Our

helical drilling tests showed reduced distortions in the shape of the exit holes compared to linear polarization (see Table 1). This was due to the averaging of reflectivity during drilling. This averaging effect occurred because the polarization rotator was not synchronized with the scanning galvo in this case. The averaging effect is discussed further in section 3.3.

We also used the laser-synchronized polarization switching mode to test the response time of the liquid-crystal device, by placing a Glan Laser Polarizer behind it. Thus, a rotation in polarization direction was translated into a modulation of the amplitude transmitted through the polarizer. The resulting beam amplitude was measured with a photodiode (see dashed components in Fig. 1). This confirmed that the response time of the polarization rotator was less than 0.5ms (manufacturing specification: 0.1ms). In our laser system, the time lapse

Table 1. Description and results of helical drilling tests on a 380 μ m-thick stainless steel plate, including qualitative comparison of the exit holes (775nm, 240fs pulses, 1kHz repetition rate, pulse energy: 75 μ J).

	Linear polarization	Circular polarization	Scanner-synchronized polarization switching	Laser-synchronized polarization switching	Un-synchronized polarization switching
Configuration of the setup	Polarization rotator removed. The linear polarized laser beam is used to drill the sample.	Polarization rotator removed. A quarter-wave plate is inserted into the beam path to produce circular polarization.	Polarization rotator driven with a 10Hz square wave synchronized with the galvo scanner.	Polarization rotator driven with a 100Hz square wave synchronized with the laser pulse-train.	Polarization rotator driven with a 10Hz square wave, not synchronized with the laser or the galvo scanner.
Aim of test	Provide comparative data for subsequent tests.	Provide comparative data for subsequent tests.	Reduce the variability in reflectivity during drilling. This configuration is similar to polarization trepanning.	Provide accurate control of the polarization state of each femtosecond pulse.	Reduce the polarization induced distortions thanks to averaging effects.
SEM images of the holes exit aperture					
Qualitative comparison	Elliptical exit hole shape, showing the distortions typically associated with linear polarization, as described in [7].	Exit hole less elliptical than linear polarization. Low levels of distortion on the hole walls.	Increase in size of exit aperture compared to circular polarization. Small levels of distortion on the hole walls are still present.	Shape of the hole improved compared to linear polarization. No improvements when compared to circular polarization.	Increase in size of exit aperture compared to circular polarization. Low levels of distortion on the hole walls.

between each femtosecond pulse is 1ms (1 kHz repetition rate). The response time of the liquid-crystal device was therefore sufficient to provide accurate control over the polarization direction of each individual pulse. The interesting aspect of this polarization mode is that it enables dynamic pulse-to-pulse amplitude control for surface machining of periodic structures. Experiments using this technique (in preparation) will be published elsewhere.

3.3 Un-synchronized polarization switching

During helical drilling, the laser beam rotates about the central axis of the hole. When the polarization rotator is not synchronized with the scanner system, a given coordinate in the circular beam path will see the polarization direction vary over time. The resulting value for the reflectivity of the laser beam at this coordinate will vary accordingly. This leads to an averaging effect which tends to reduce the distortions in the exit shape of the hole [7].

The synchronizing signals linked to the polarization rotator were removed, allowing these averaging effects to take place. Our helical drilling tests showed reduced distortions in the shape of the exit holes compared to the other polarization modes (see Table 1). However, these averaging effects should also have occurred in the laser-synchronized polarization mode described in section 3.2. The difference in machining quality between these two cases is thought to be due to a difference in the polarization switching frequencies. Future work will determine the optimum ratio between polarization switching frequency and beam scanning speed to maximize the averaging effects and improve the machining quality.

4. Conclusions

A method for dynamically switching the polarization direction of a femtosecond laser beam with a fast-response, transmissive, ferroelectric liquid-crystal device has been presented. Helical drilling of high-aspect-ratio micro-holes in a steel plate was tested, using the various polarization driving modes available, such as scanner-synchronized, laser-synchronized and un-synchronized polarization switching. Microscopic investigation of the resulting features revealed improvements in the machining quality. A profitable line of future experimental work could be testing different geometries, aspect-ratios and materials to confirm these preliminary findings.

To our knowledge, this is the first time *polarization trepanning* has been achieved using a solid-state device for micro-machining. The liquid-crystal polarization rotator is found to provide more flexibility than the wave-plate elements it replaces, thanks to its tolerance to optical miss-alignment. Since it is a solid-state device, it

provides polarization rotation without any undesirable mechanical motion, associated vibrational problems and reducing maintenance downtime. However, the liquid-crystal device is not without some operational constraints. For example its angular rotation range, limited to 90° and its requirement for a dc-balanced, 50% duty-cycle periodic driving voltage. As a result, the device is limited to machining periodic structures, or axi-symmetric features.

Although the machining quality often associated with high-precision trepan drilling heads has not been achieved, the fast-response liquid-crystal polarization rotator presented here could emerge as a flexible alternative, providing an improved machining quality to existing micro-machining systems.

Acknowledgements

The authors gratefully acknowledge the support of the EPSRC and the kind help from Mr. Kipp Bauchert, Boulder Nonlinear Systems, Inc., who provided the liquid-crystal polarization rotator used in this research.

References

- [1] F. Dausinger, "Machining of metals with ultrashort laser pulses: from fundamental investigations to industrial applications", Proc. SPIE 5777, 840-845 (2005).
- [2] D. Breitling, A. Ruf, F. Dausinger, "Fundamental aspects in machining of metals with short and ultrashort laser pulses", Proc. SPIE 5339, 49-63 (2004).
- [3] T. Otani, L. Herbst, M. Heglin, S. V. Govorkov, A. O. Wiessner, "Microdrilling and micromachining with diode-pumped solid-state lasers", Appl. Phys. A 79, 1335-1339 (2004).
- [4] P. S. Banks, M. D. Feit, A. M. Rubenchik, B. C. Stuart, M. D. Perry, "Material effects in ultra-short pulse laser drilling of metals", Appl. Phys. A 69, S377-S380 (1999).
- [5] S. Hahne, B. F. Johnston, M. J. Withford, "Pulse-to-pulse polarization-switching method for high-repetition-rate lasers", Appl. Opt. 46, 954-958 (2007).
- [6] C. Föhl, F. Dausinger, "High precision deep drilling with ultrashort pulses", Proc. SPIE 5063, 346-351 (2003).
- [7] S. Nolte, C. Momma, G. Kamlage, A. Ostendorf, C. Fallnich, F. von Alvensleben, H. Welling, "Polarization effects in ultrashort-pulse laser drilling", Appl. Phys. A 68, 563-567 (1999).
- [8] C. Föhl, D. Breitling, F. Dausinger, "Precise drilling of steel with ultrashort pulsed solid-state lasers", Proc. SPIE 5121 271-279 (2003).
- [9] C. Föhl, D. Breitling, F. Dausinger, "Influences on hole quality in high precision drilling of steel with ultra-short pulsed laser systems", Proc. ICALAO (2002).
- [10] H. K. Tönshoff, C. Momma, A. Ostendorf, S. Nolte, G. Kamlage, "Microdrilling of metals with ultrashort laser pulses", J. Laser Applications 12, 23-27 (2000).
- [11] Z. Kuang, et al., "Fast parallel diffractive multi-beam femtosecond laser surface micro-structuring", Appl. Surf. Sci. (2009), doi:10.1016/j.apsusc.2009.02.043.

Laser Inertial Fusion-based Energy (LIFE) - Developing Manufacturing Technology for low cost and high volume fusion fuel is critical to our future energy needs.

K. Carlisle and R. R. Miles

Lawrence Livermore National Laboratory, P.O. Box 808, Livermore, CA 94551

Abstract. Sustainably providing for the world's energy needs is one of the most urgent – and difficult – challenges facing today's society. Worldwide electric power demand is expected to double from its current level of about two trillion watts (TW) to four TW by 2030 and could reach eight to ten TW by 2100. As many as 10,000 new one-gigawatt (GW) power plants will be needed to keep up with this demand. Yet fossil-fuel supplies, such as coal and natural gas, are limited, and the environmental effects of that many additional fossil-fuel plants could be devastating. Conventional nuclear power could provide clean energy, but poses waste-disposal and proliferation concerns. All available energy options have limitations and liabilities, so revolutionary responses must be pursued in parallel with evolutionary ones. The Laser Inertial Fusion Energy concept, or LIFE, is one such revolutionary response.

Today, researchers at the Lawrence Livermore National Laboratory are close to demonstrating the scientific basis required to make LIFE a reality. The capability of lasers to create the conditions required for ignition and thermonuclear burn in the laboratory with inertial confinement fusion (ICF) is expected to be demonstrated on the National Ignition Facility (NIF) located in the U.S. during fiscal years 2010 or 2011. With the appropriate research, development and engineering program, LIFE power plants could begin to provide electricity to U.S. consumers within 20 years and could provide a very significant fraction of U.S. and international electricity demand by 2050. See Figure 1.

At the heart of the LIFE power plant is a fuel capsule containing a tiny amount of solid deuterium-tritium (DT) which is compressed to high density by lasers, and then a short-pulse laser beam delivers energy to ignite the compressed core until a fusion reaction is initiated – analogous to a sparkplug in an internal combustion engine. The fission reaction produces thermal energy for electricity generation. The fuel capsule consists of a spherical shell with an internal layer of foam that retains the DT within its pores. The capsule is attached to the hohlraum, which converts laser light into x-ray energy to compress the DT, and a cone that injects energy directly to the center of the imploding capsule to hasten the fusion reaction. The fuel capsule components shown in Figure 2 would be fabricated in a central factory and then assembled at the LIFE power plant. Fuel capsules would be injected into the target chamber at a rate of 10 to 20 targets per second. The current fuel capsule fabrication techniques are unsuitable for low-cost, high throughput. For ICF fusion energy to be cost-competitive with other forms of energy, the high-precision fuel capsules must be manufactured in quantities of about 1.73 million per day per plant and at unit costs of less than \$0.25 USD.

The challenge is to develop inexpensive processes that can be used to meet the specified tolerances of the fuel capsule. The fuel capsule must be made to micrometer tolerances to attain a stable contraction of the fusion fuel. The fuel must align to the laser centroid to within 50 μm . Manufacturing methods such as injection moulding or the development of new processes based on chemical engineering mass-production principles are examples. The greatest probability of success lies with a simple fuel capsule design using a minimal number of parts and materials that accommodate the component fabrication and assembly operations. The final fuel capsule design will be the result of an optimization effort in which all factors are weighed and new solutions are explored to improve the overall target cycle.

This paper outlines the requirements, the current state-of-the-art and research plan for several aspects of the fuel capsule fabrication. A fuel manufacturing R&D is being planned with a goal of demonstrating the unit processes needed for a prototype LIFE power plant. R&D efforts will be conducted in collaboration with industrial partners.

Keywords: laser inertial fusion energy, LIFE, inertial confinement fusion, hohlraum, fuel capsule, foam shells, microencapsulation, diamond CVD, projection micro-stereolithography, holographic nanolithography, electro-phoretic deposition, microballoons

1. Introduction

At the heart of the LIFE system is a tiny amount of solid deuterium-tritium (DT), which is compressed by an intense laser energy pulse until a fusion reaction is initiated. The fusion reaction creates a neutron flux sufficient to cause a fission reaction in pellets flowing through the surrounding chamber walls. The fission reaction produces thermal energy for electricity generation. The fuel capsule that houses the DT consists of a spherical capsule with an internal layer of foam that retains the DT within its pores. The capsule is attached to the hohlraum, which converts laser light into x-ray energy to compress the DT, and a cone that injects energy directly in the center of the imploding capsule to hasten

the fusion reaction. The fuel capsules are injected into the target chamber at a rate of 13 to 20 targets per second.

The challenge is to develop high-volume low-cost manufacturing processes to meet the specified tolerances of the LIFE fuel capsule. The greatest probability of success lies with simple target designs using a minimal number of parts and materials that accommodate the component fabrication and assembly operations.

Is there potential to develop existing commercial high-throughput manufacturing methods for the small ultra-high precision needed for the LIFE fuel capsules and/or the development of new processes based on chemical engineering mass-production principles? The challenge in both cases is to determine whether or not inexpensive processes can be used to meet the specified tolerances of the LIFE fuel capsule. The greatest probability of success lies with simple target operations. This paper outlines the requirements, current state-of-the-art and research plan for several aspects of the fuel capsule fabrication and assembly. A significant research and development program is required to ultimately produce the LIFE fuel capsule to the desired specifications, costs, and production volumes.

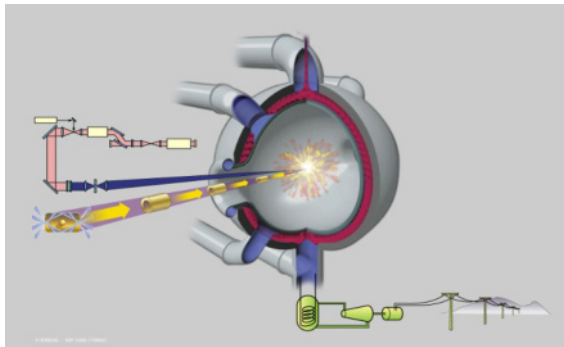


Fig. 1. The LIFE reactor.

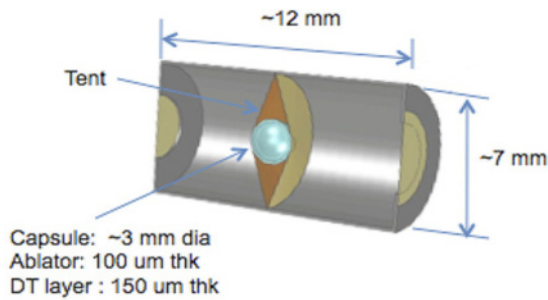


Fig. 2. Fuel Capsule.

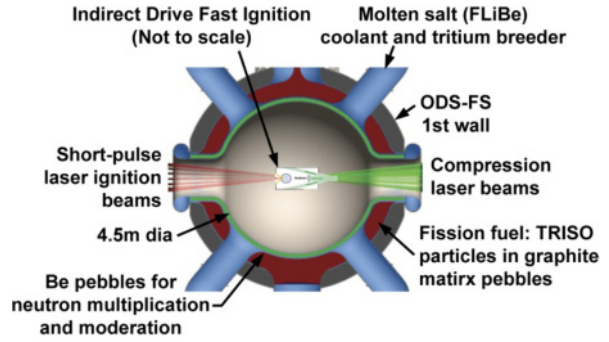


Fig. 3. Life Reactor.

2. LIFE Fuel Capsule Specification

There are a number of potential designs under consideration all of which are made from three basic sub elements shown in Figure 4. together with their dimensional specifications. The final design will be influenced by the developing manufacturing processes to meet performance and cost goals.

3. Fuel Capsule Fabrication

The primary objective of the fabrication effort is to meet the cost, throughput and design specification requirements of the LIFE fuel capsule. Unlike capsules built to date, the LIFE capsule is not a research product but is a key component in a commercial enterprise and must be cost competitive in the consumer market.

A prudent research plan will pursue multiple paths simultaneously. There are many methods available for fabricating each of the major components of the fuel capsule, the hohlraum/cone, the capsule and the foam. Some of the possible fabrication options for each of these components are shown in Figure 5.

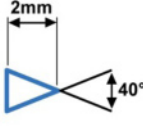

Cone	Capsule (Shell)	Hohlraum (Cylinder)
 <p>Roughness: 0.2μm rms Thickness: 20–500μm</p>	<p>Max Dia: 3mm Min Dia: 2mm Total: \pm 10μm</p>  <p>Roundness: \pm 10μm Roughness: <100nm rms Thickness: 200μm \pm 5μm</p>	<p>Max: 20mm Min: 10mm Total: \pm 20μm</p> <p>Inside dimension</p> <p>57% of ID</p> <p>Max: 10mm ID Min: 5mm ID Total: \pm 10μm</p> <p>Roundness: \pm 4μm Roughness: 0.2 μm rms Thickness: 20–500μm \pm 3μm</p>
Material: Lead, gold	Material: Beryllium, diamond, PE	Material: Lead, gold, tantalum, uranium, bismuth & polymers

Fig. 4. Basic components of the fuel capsule.

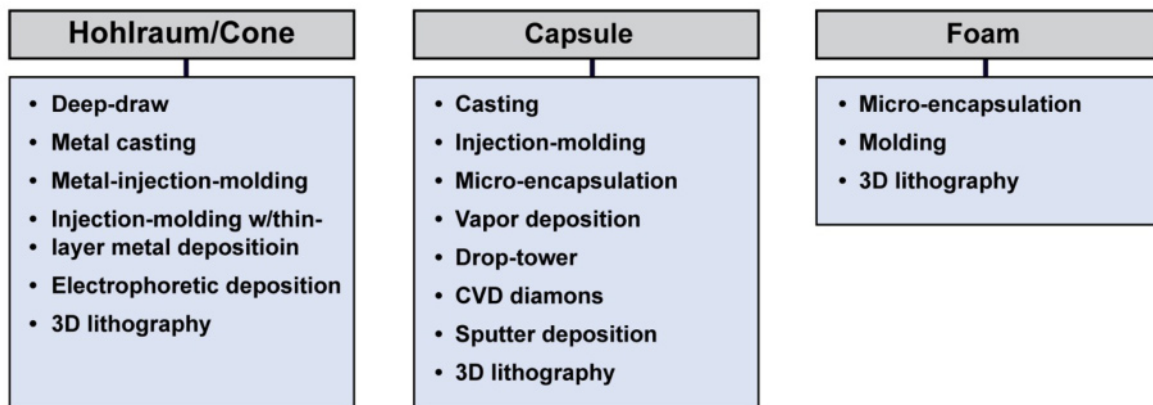


Fig. 5. Possible fabrication processes.

3.1 Metal Working

3.1.1 Description

Metal working technology covers a wide range of process technologies. Examples are:

1. Hohlraum and cones can be deep drawn around tooling which conforms to the desired shape
2. Metal capsules can be cast or formed into hemispheres which are then joined to make the spherical capsules.
3. Metal joint techniques such as brazing or welding can be considered for joining parts of the hohlraum and cone.

3.1.2 Material considerations

Current materials under consideration for the hohlraum/cone fabrication include gold, tantalum, lead, uranium, mercury, and bismuth, amongst which gold and lead are the two top candidates for metal-working because of their good formability/workability at relatively low homogenous temperatures. Elemental lead, in

particular, has unique advantages over other materials systems because it is cost-effective, and amenable to large deformation processes such as cryogenic mechanical properties must be taken into account when selecting hohlraum/cone materials because they could be operated at low temperatures.

Key research issues:

1. Scale-down of the current metal-working technologies for extremely small components.
2. Characterize the mechanical properties of hohlraum materials at micro- and nano-scale.

3.2 Description of Micro Injection Molding

Micro-injection molding is one of the promising methods that could allow the production of large quantities of high precision fuel capsules for the LIFE application at low costs. The technique is a special case of injection molding that is widely used in industry. This high-throughput, low-cost technology permits a high degree of process automation and allows one to produce complex precision parts from plastics, ceramics, and metals.

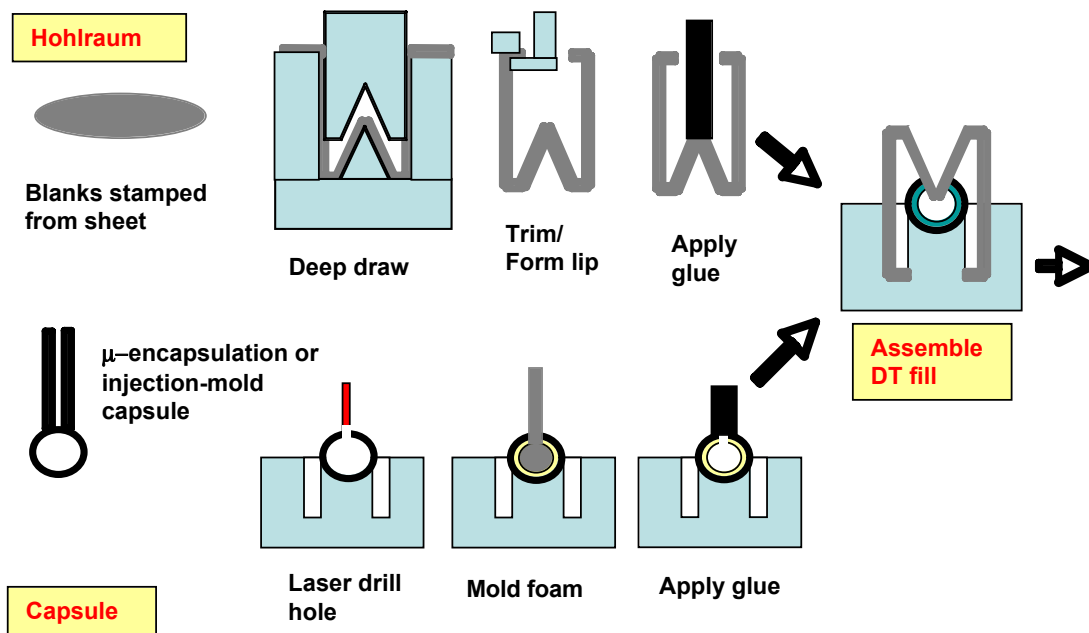


Fig. 6. Example fuel capsule fabrication process.

3.2.1 Current state of the art

The smallest feature is ≤ 200 nm, roughness 50-nm Ra depending on the mold, highest pin aspect ratio at 2000 μm high and 115 μm width, suitable for nearly all materials. Thermoplastics and thermoplastic elastomers, elastomers and duromers are under development.

The capsule could be made from nearly all thermoplastics including polyethylene (PE). Hollow capsules can be realized by gas-assisted injection molding. At present, it cannot be said if this technique would be capable of delivering the required capsule wall thickness and homogeneity (peak-to-valley roughness $\sim 1\%$ of the wall thickness, or < 1 micron for a 100-micron-thick ablator), as the fabrication of such high-precision mm-sized shells has not been demonstrated yet. Another issue is the formation of a seam around the shell, which is the consequence of the two-part mold required for this process. Using a high-precision mold, one could expect a 5-micron-wide and 5-micron-high seam. Simulations need to be performed to address the effect of such a 2D line defect on fuel capsule performance.

In principle, the hohlraum (cylinders) structure could also be formed by injection molding using an organic binder highly filled with a high-Z metal powder using metal injection molding, followed by de-binding and sintering. Although the parts typically shrink 15 to 20 percent during de-binding and sintering, tolerances as low as 0.3% of the nominal dimension can be achieved. However, this technique has not yet been demonstrated for lead, which is our preferred hohlraum material. In conclusion, metal injection molding might be an interesting alternative to the fabrication of the hohlraum

by cold working (swaging, deep drawing) or casting, specifically in the case of high melting point and/or brittle materials such as tungsten.

3.2.2 Research needs include:

1. Develop micro-injection molding processes for improved precision.
2. Perform simulations to assess the effect of a seam around the shell/capsule on target performance.
3. Develop a high-density plastic precursor (nanographite or nano-diamond doped plastic) for the ablator application.
4. Develop a micro-injection molding process for lead hohlraums.

3.2.3 Conclusion

Micro injection molding is a promising method that could allow the production of large quantities of high-precision targets for the LIFE application at low costs. It is a high-throughput, low-cost technology that permits a high degree of process automation and potentially could be used to produce large quantities of both components of a LIFE fuel capsule—the low-Z capsule as well as the high-Z hohlraum. However, at present, it cannot be said whether or not the required precision can be achieved.

3.3 Micro-encapsulation

3.3.1 Description

Micro-encapsulation is the general term given to the basic technique currently used at LLNL in the fabrication of hollow spherical shells. A triple orifice generator is used,

consisting of a concentric nozzle dispensing two immiscible liquids (see Figure 7). The inner liquid (oil 1) forms the inner void of a hollow shell, while the middle liquid (R/F) contains the precursor materials to form the shell wall. The outermost liquid is used to strip the droplet off of the tip of the nozzle into a collection tube. After formation of the compound droplet, the shell wall is cured into a solid, and finally the liquid is extracted from the inside of the shell. For foam shells, an additional step is used to prepare a solid density plastic permeation barrier on the outside of the shell.

A two-layer capsule is required for the LIFE fuel capsule. Using this process, the outer layer is a solid polymer with a wall thickness of 200 μm . The inner layer is a low density ($\leq 30 \text{ mg/cc}$) open cell polymer foam layer with a thickness of 250 μm . Since a large hole for the cone is needed in the capsule, there is the opportunity to manufacture either layer first.

Droplet Generator Process

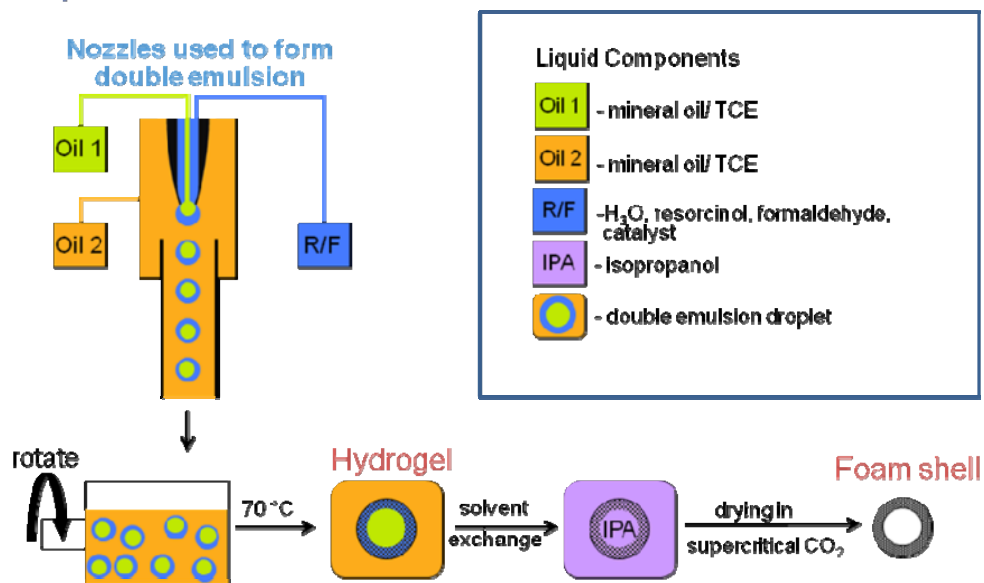


Fig. 7. The Droplet Generator used in the microencapsulation of shell.

The potential approaches and relevant steps are summarized as follows:

Foam Shell Option I (inside-out)

- Droplet generation using microencapsulation of oil/water/oil or water/oil/water systems
- GDP coat or mold overcoat

Foam Shell Option II (outside-in); two approaches

- Spin coat interior of shell
- Grow foam from interior surface of shell

Foam Shell Option III (inside-out)

- Form foam film on sacrificial substrate
- Vacuum form foam shell
- GDP coat or mold overcoat
- Alternative: direct molding of foam shell

Foam Shell Option IV (outside-in)

- Produce capsule shell and bore cone insert hole
- Insert inflatable/deflatable spherical mold into shell
- Form foam film in gap between mold and shell

3.3.2 Current state of the art

Currently, for thin ($\sim 15\text{-}\mu\text{m}$ wall thickness) microencapsulated shells, the diameter variation is $\pm 20 \mu\text{m}$, which is higher than required for LIFE. Other specifications can easily be met. The roundness is $1 \mu\text{m}$ for 2-mm-diameter capsules, the wall variation is $<1\%$ avg. The surface roughness meets or is under the required specification (20 nm rms).

There is less experience for the thick (200- μm wall thickness) microencapsulated shells than for thin walls. Some thick shells have been made, and we are in the process of characterizing those batches. For these shells,

there are two major challenges: wall uniformity and vacuoles.

3.3.3 Research needs

For foam shells with a solid GDP overcoat:

1. Optimizing the foam material for strength and density
2. Optimize the GDP coating parameters for fast coating rate and smooth surface

For solid shells to address the high cost of producing thick capsule shells:

1. Microencapsulated thick-walled shells will cost much less than vapor-phase deposited GDP shells
2. Improve the encapsulation process by optimize the concentration and molecular weight of the polystyrene, which influences the viscosity of the compound droplet wall
3. Determine the maximum thickness that could be made without exceeding the wall uniformity specification
4. Develop dielectrophoresis (DEP) forces generated by electric fields to further improve the wall uniformity. There is an ongoing collaboration between the University of Rochester and General Atomics to work on this.

3.3.4 Conclusion

Microencapsulation has great potential but requires major research to reduce cost and improve productivity. Quality is an issue currently requiring 100% automated optical inspection system to measure the diameter, wall thickness, and wall thickness uniformity of each shell at a speed sufficient so that a small number of these systems

could measure and reject shells in real-time for a commercial power plant design.

3.4 Diamond Plasma-Assisted Chemical Vapor Deposition

Besides beryllium and plastic, diamond has a unique combination of physical properties that makes it a very promising capsule material. Furthermore, diamond is chemically extremely inert, which allows one to apply very aggressive processing and cleaning procedures; finally, synthetic diamond is an environmentally friendly material that, despite diamond's reputation as an expensive material, can be produced cost-efficiently.

3.4.1 Description of the diamond CVD process

In a joint research project, LLNL and the Fraunhofer Institute for Applied Solid State Physics in Freiburg, Germany, succeeded in developing an environmentally safe and cost-efficient batch process that allows one to produce large quantities of ultra-high precision diamond shells (see Figure 8). The fabrication of diamond capsules is a multi-step process that involves a microwave plasma-assisted chemical vapor deposition (PACVD) process to deposit a thickness of 100 μm on silicon mandrels followed by polishing, micro-fabrication of holes using a laser, and removing of the silicon mandrel by an etch process (see Figure 9).

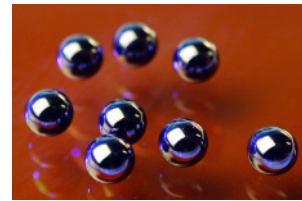


Fig. 8. Diamond shells.

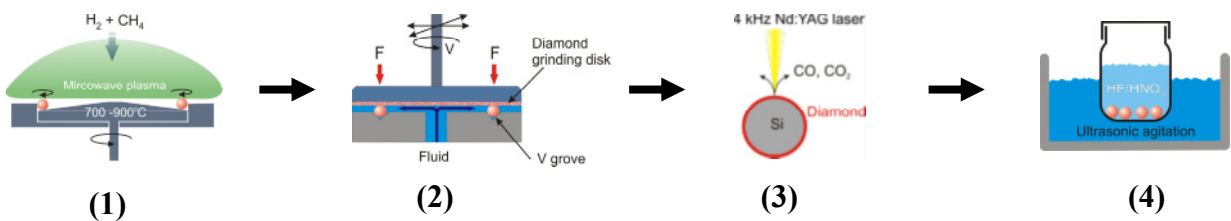


Fig. 9. Fabrication of diamond capsules is a multi-step process that involves the following steps: 1) microwave-assisted chemical vapor deposition, 2) ultra-high precision polishing, 3) Nd:YAG laser hole machining, and 4) ultrasonically assisted wet etch.

3.4.2 Current state of the art

Using this process, diamond shells that meet all the stringent requirements of the LIFE application have successfully been made. However, the production costs

must be lowered considerably. Currently, the most cost-intensive process step of the fabrication of diamond shells is the diamond PACVD process. For the ablator application, nano-crystalline diamond (NCD) is preferred

over coarse-grained material. Without changing the current technology, the diamond deposition costs can be lowered by running larger batches.

3.4.3 Research Needs

In the case of diamond shells, the research will be focused on reducing the costs rather than improving the quality, which is already more than sufficient. Specifically, the following research areas need to be addressed:

1. Demonstration that scaling-up of the current technology can be done without jeopardizing the quality of the diamond shells
2. Increasing the deposition rate by a factor of two without degrading the material quality
3. Developing more efficient, high-throughput seeding techniques while maintaining the high nucleation density currently achieved (e.g., using colloidal solutions of diamond nano-particles)
4. The development of thick ultra-smooth NCD films to avoid polishing (RMS surface roughness less than 100 nm)
5. Exploration of the potential benefits of the hot-filament CVD (HFCVD) diamond process (thick ultra-smooth NCD, larger deposition area, larger batches)

Specifically, the development of thick ultra-smooth (mirror finish) NCD films needs to be pushed forward to avoid polishing. The deposition of smooth, thick NCD films on planar substrates via hot-filament CVD (currently PACVD is used in the fabrication of diamond ablator shells) has already been demonstrated. In a second step, this technique needs to be transferred from planar substrates to spherical substrates.

3.4.4 Conclusion

In conclusion, the fabrication of ultrahigh precision diamond shells has already been demonstrated. Lowering of the production costs could be achieved by a combination of scaling up the current technology and using higher deposition rates as well as lower-cost deposition equipment. The development of more efficient high-throughput seeding techniques and of ultra-smooth NCD films on spherical substrates will be required. Finally, the hot-filament CVD diamond process has the potential to further lower the production cost by running much larger batches.

4. Fuel Capsule Assembly

4.1 Description

A major design objective for LIFE fuel capsules is to reduce the number of component parts. A manufacturing

process capable of producing a one piece design is very desirable and may be possible in the distant future. For the near future, we have identified three basic component groups that form the fuel capsule: 1) hohlraum (cylinders), 2) capsules (shells) and 3) cones. Our assembly procedures to date have been developed around NIF targets, which are a much more complicated design, driven by research needs. The concept is the same, but the number of component parts is greater and more demanding than perceived for the LIFE fuel capsule. We have progressed from a manual assembly to a much needed semi-automated process and only produce two assemblies per day, which meet our current needs. Experience has shown that design to aid assembly is essential, requiring the parts to be robust for automated handling, requiring precision for self-aligning, clean room environment and quality control. Figures 10 and 11 show basic examples of bonding and self-alignment.

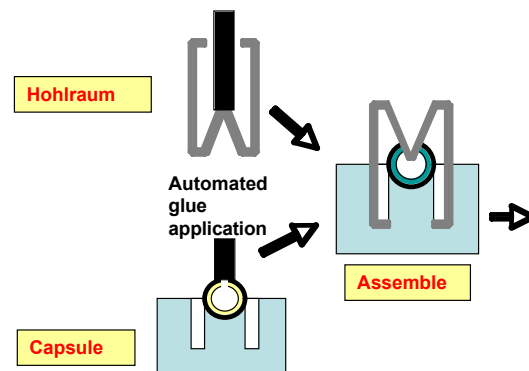


Fig. 10. Pictorial of assembly and glue operation.

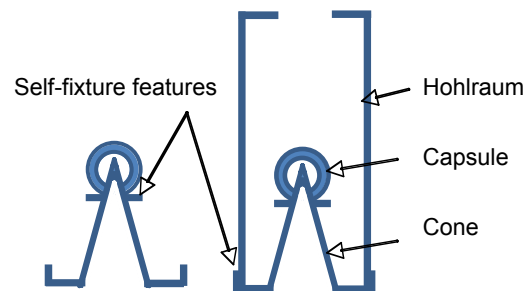


Fig. 11. Self-featured assembly.

4.2 Material Considerations

Materials to be joined are expected to be lead for the hohlraum and polymers of some variety for the capsule and foam components. The capsule could also consist of a low Z material such as beryllium or diamond. Joint materials are most likely to be polymeric glues, although metallic bonding procedures such as welding or soldering could be used for metallic parts.

4.3 Research needs

Principal research needs include the ability to handle delicate parts and to locate them accurately in a fixture. Location accuracies will result from dimensional tolerances of the part, the fixture and any allowance required for sliding fits if needed. Research needs for fixturing include:

- Design and build high-accuracy, compliant fixturing to relax part location accuracies to <10 μm and fixture alignment accuracies to <5 μm
- Determine techniques to mate “upside down” hohlraum to capsule (or visa-versa) through vacuum hold or other techniques
- Fully automated assembly to meet the throughput and cost objectives for the targets
- Automatic part bonding methods must be investigated

5. Emerging Fabrication Technologies

There are several emerging micro- and nano-fabrication technologies that may significantly contribute to LIFE fuel capsule fabrication. They may have impact on all major fabrication challenges including hohlraums, capsules, and foam geometries. Three of these technologies, Projection Microstereolithography, Electro-phoretic Deposition, and the Hollow Jet Instability Method are briefly discussed in the following sections.

5.1 Projection Microstereolithography

5.1.1 Process description

Projection Microstereolithography (P μ SL) with a Digital Micromirror Device (DMD) or Liquid Crystal on Silicon (LCoS) display (see Figure 12) is capable of fabricating complex three-dimensional microstructures in a bottom-up, layer-by-layer fashion. Resolution in these systems is limited to one-half of the wavelength of the incident light because they can only transmit the propagating components emanating from the source.

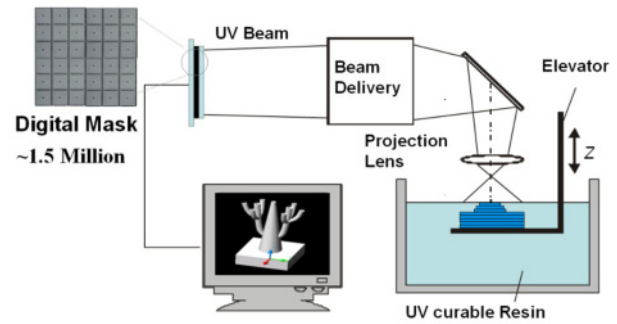


Fig. 12. Schematic of baseline P μ SL system.

5.1.2 Superlens

Recently, work by Pendry has predicted that a so-called “superlens” can amplify the evanescent waves, thus restoring the image that exists below the diffraction limit. This enhancement of evanescent waves by surface plasmons in silver films was first reported by Fang (LLNL collaborator) and co-workers. They also showed the first demonstration of a silver film superlens by imaging features onto photoresist at $\sim 1/6\lambda$. To utilize this near-field effect in a P μ SL system, it must be converted to a far-field phenomenon. The amplified evanescent waves can be converted into a propagating field by using thin-film silver grating-type structures. Further development of this far-field concept for integration into a P μ SL system will allow for rapid direct writing of three-dimensional nanostructures below the diffraction limit. To date, superlens’ have only been utilized for imaging purposes.

5.1.3 Digital holographic nanolithography

Holographic nanolithography has emerged as a method of three-dimensional volumetric nanofabrication (see Figure 13). This can also be integrated with the P μ SL system for fuel capsule fabrication. This method can create designed features and aperiodic micro- and nano-structures by interfering light from multiple DMD or LCoS devices in the resin bath. This will allow a variety of porous structures and materials to be fabricated and point features to be intentionally positioned. The digital dynamic masks can be exploited to project a computed three-dimensional hologram into liquid polymers for fabrication of highly interconnected functionally graded density materials with 10s - 100s of nanometer precision. It should be possible to achieve meso-scale (>1 μm) components while maintaining quarter-wavelength resolution of 70 - 100 nm.

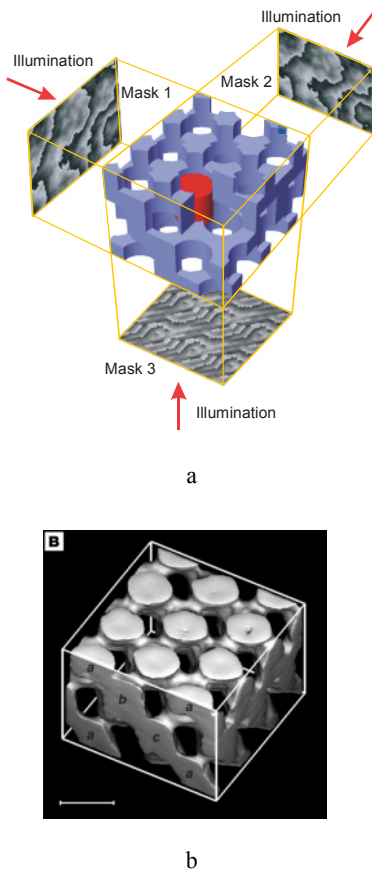


Fig. 13. Synthetic holographic nanolithography reproduces (b) complex 3D crystallographic orders in a single snapshot; proof-of-principle demonstration by Campbell *et al.*

5.1.4 Research Needs

1. What limits resolution of the system (with and without a superlens) and what is the best achievable resolution?
2. Impact of metal and ceramic particles in resin. What materials are feasible? Is sintering required and what is the effect on the final geometry?
3. Holographic nanolithography has never been attempted in this configuration. How deep a structure can be fabricated with one hologram?
4. What limits the throughput/speed of the system?
5. Modeling efforts will be required to compliment experiments and answer some research questions.

5.2 Electrophoretic Deposition

5.2.1 Process description

Electrophoretic deposition (EPD) is a directed particle assembly method that utilizes electric fields to deposit charged nanoparticles from a solution onto a substrate. EPD requires the deposition substrate to act as one electrode to attract oppositely charged particles from the solution (see Figure 14). This can be achieved on non-

metal parts by coating the surface with a thin metal layer (order 100 nm thick). The part is then submerged in a conductive solution (solvent or aqueous) containing suspended nanoparticles of the desired coating material. The nanoparticle charge and size as well as the electric field strength determine the deposition rate and eventual coating thickness. These parameters can be controlled to provide precise coating thicknesses and the packing structure of the deposited particles. The coating is then stabilized through drying and/or sintering. This approach is proposed for coating a pre-fabricated polymer (or similar material) hohlraum with a 20- μm -thick metal layer.

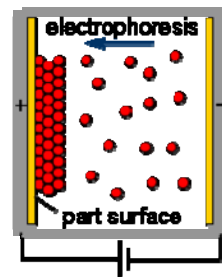


Fig. 14. Schematic of the electrophoretic deposition process.

5.2.2 Current state of the art

EPD has been used with a wide range of nanoparticles including oxides, metals, polymers, semiconductors, and even diamond. The process can currently be used to synthesize cylindrical and other net-shape mm-scale parts, density and composition-gradient coatings and materials. Coatings can be as thick as a few millimeters. The surface roughness is dependent on the particle size and other deposition parameters. The process is primarily used to deposit ceramic coatings on metals, but several groups have demonstrated electrophoretic deposition of colloidal gold. Researchers at LLNL demonstrated electrophoretic deposition of multilayer colloidal gold films using 30- to 80-nm precursor material.

5.2.3 Research needs

1. Materials compatibility and deposition parameters will need to be determined based on the selected material for the hohlraum part and desired coating.
2. Process modeling will be necessary to ensure uniform coating thickness around the non-planar hohlraum shape. Corners and edges will generate electric field gradients, which will increase particle-particle interactions during deposition. These interactions can be eliminated by altering field magnitudes based on the process model.
3. Drying and sintering of the proposed material must be analyzed as a function of thickness and deposition parameters. Optimized conditions will eliminate cracking and peeling due to internal stresses.

5.3 Hollow Jet Instability Method

5.3.1 Process description

The fabrication of high-quality amorphous metal microballoons with uniform shell thickness, low surface roughness, and high sphericity can be accomplished by exploiting the natural instability of a hollow liquid jet under free fall. It is well known that a falling liquid jet is naturally unstable with respect to “break up” into droplets. Under controlled conditions, spherical droplets with a narrow size distribution are formed when oscillations of the jet diameter grow with distance along the path of fall. Lee, Kendall, and Johnson were able to produce uniform distributions of solid metallic glass spheres by allowing such droplets of Au-based metallic glass-forming liquid to solidify during free fall in a drop tower. When the liquid droplets crystallize during fall, the sphere surfaces are rough and non-uniform due to the discontinuous nature of liquid-crystal phase transition, which involves discontinuous changes in molar volume, enthalpy, etc. By contrast, when the cooling rate of the droplet during fall is sufficient to bypass crystallization, the under-cooled liquid reaches the glass transition without crystallizing, and metallic glass spheres are formed. These spheres were found to exhibit extremely smooth surfaces (see Figure 15) with roughness in the range of nms.

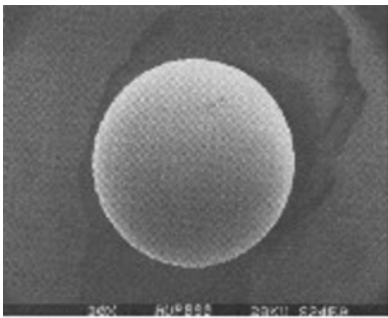


Fig. 15. A metallic glass microballoon of diameter ~ 1 mm and wall thickness of about $20\ \mu\text{m}$.

The Au-based glass forming alloys used in the early work were relatively poor glass formers with critical casting thicknesses of the order of 1 mm or less. The critical casting thickness reflects the minimum cooling rate required to bypass the crystallization of the alloy and therefore reflects the “processability” of the alloys. Since the early work on microballoons, the Caltech group and other groups worldwide have developed several families of glass forming alloys with critical casting thicknesses ranging up to cms. These highly processable alloys would be better suited to the production of glassy spheres and microballoons in a drop tower set-up. For LIFE capsules, it may be desirable, for example to fabricate microballoons from alloys containing metals that have low cross sections for neutron absorption. For example, Be and Zr are two such metals.

6. Conclusion

A fuel manufacturing R&D facility is being planned with a goal of demonstrating the unit processes needed for a prototype LIFE power plant. R&D efforts will be conducted in collaboration with industrial partners.

Acknowledgements

This work was performed under the auspices of the U.S. Department of Energy by Lawrence Livermore National Laboratory under Contract DE-AC52-07NA27344.

Initial Strategies for 3D RAP Processing of Optical Surfaces Based on a Temperature Adaptation Approach

M. Castelli¹, R. Jourdain¹, G. McMeeking¹, P. Morantz¹, P. Shore¹, D. Proscia², P. Subrahmanyam²

¹ Cranfield University, Precision Engineering Centre, Cranfield, MK43 0AL, United Kingdom

² RAP Industries, 46535 Fremont Blvd, Fremont, CA 94538, United States of America

Abstract. The new Reactive Atom Plasma (RAP) facility Helios 1200 at Cranfield Precision Engineering Centre (UK) has a unique material removal rate and proven nanometre level repeatability. Thus, it incorporates high potential capability for ultra-precise, cost-effective figuring of large specular surfaces. In this paper, experimental results concerning substrate temperature and time dependence of the removal rate are presented, these constituting a fundamental part for an in-process temperature adaptation required to “steer” material etching. In particular, the etching process is believed to follow an Arrhenius’ type law and the removal rate is assessed in the range of 20-105 °C. The plume footprint is characterised to allow classical de-convolution methods (Lucy-Richardson, Van Cittert) to be later investigated to compute initial dwell-time maps and tool-path algorithms for free form figuring. Attempts to implement the process through thermal effects compensation techniques are presented. Those experimental results are analyzed and discussed. Characterisation of pre- and post-processed substrates is performed using phase-shift interferometry for shape assessment and white light interferometry for surface topography measurement. rms-Roughness of 3-4 nm results after neutral removal rasterings on synthetic fused silica substrates over a 70x200 mm area, with depths ranging from 100 to 200 nm.

Keywords: RAP, atmospheric pressure, plasma torch, removal rate, roughness, low thermal expansion glass, ultra-precision surfaces, figuring.

1. Introduction

Helios 1200 was conceived for the figuring of metre square sized optical components which are required for Extreme Ultraviolet Lithography, very large telescopes and fusion facilities. Fabricated by RAP Inc. for the figure correction of 1.2 m diameter mirror surfaces, its submicron accuracy motion is ensured by computer numerical control system (Fanuc 30i series). It integrates dedicated software and has a double skin structure to increase machine safety. It has three axes of motion with the component moving along the YY direction while scanned by the plasma torch travelling in the XZ plane (see Fig. 1). An argon Inductively Coupled Plasma “cold”

torch constitutes the etching source at atmospheric pressure. Reduced heat propagation is secured by a conic brass nozzle which cools down the plasma jet and controls its flow distribution. The etching beam is assessed as near Gaussian footprint measured as 10 mm full width at half maximum (FWHM). Further details of the machine specifications can be found in [3].

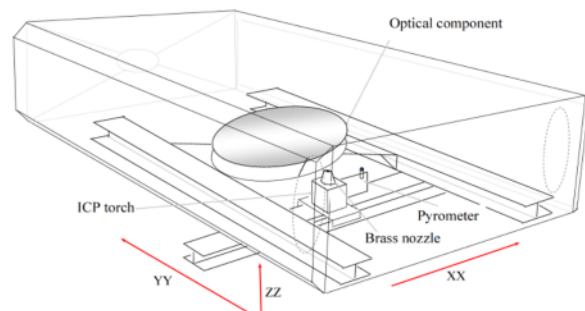


Fig. 1. Machine motion configuration.

RAP technology has already been proven [1] to be deterministic at nanometre level and to achieve higher removal rates than competing processes, such as polishing, magnetorheological finishing and Ion Beam Figuring (IBF).

The work presented in this article confirms the validity of the RAP process for the case of the new torch. Furthermore, it also introduces a new approach aimed at gaining control of the removal rate with respect to substrate exposure time and temperature [1] - [2].

Consequently, results of initial attempts to produce a neutral removal are showed and discussed. The achievement of this task is a fundamental prelude to a complete figuring process control.

Finally, the roughness of processed substrates was also assessed and its evolution is reported and compared with polishing performances.

Both form and roughness measurements were carried out, using a monochromatic Twyman-Green and white light coherence probe interferometers respectively.

2. Experiments, results and discussion

For the whole series of experiments the processing conditions are:

- RF generator forwarded power 1000 W.
- RF generator frequency 39 MHz
- Standoff distance between samples and torch nozzle 7.5 mm.
- Temperature and humidity controlled room.
- SF₆/Ar 4% gas mixture.
- Purposely tuned pyrometer emissivity.

All tests carried out during these experiments were performed on ULE or Fused Silica (grade Q1) substrates.

2.1 Process characterisation

To assess the material removal rate capability of the new torch, etching of both spots and trenches was carried out. Fig. 2 shows the material removal of the static plasma beam for increasing dwell time on ULE disks. In the graph, the etching rate follows a steep trend, reaching a removal of about 0.5 mm³ over an area of 531 mm² within few seconds. The non linearity is ascribed to heat affecting the rate of chemical reaction.

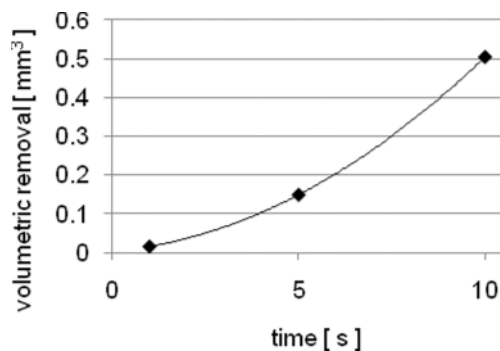


Fig. 2. Volumetric material removal rate of static etching.

More characteristic for the processing of optical surfaces is raster-type etching. Therefore removal depth as a function of the travel speed was assessed both on ULE and Fused Silica samples (see Fig. 3). Their sizes are, respectively, 200x200x25 mm and 200x200x27 mm.

Each trench was etched on a surface having a start temperature of 20 °C. This set of experiments is used,

together with the Gaussian trench width (10 mm FWHM), as characterisation for the plume “Tool” footprint of the process. In fact, unlike Ion Beam Figuring [4], [5], “spot-tests” can be considered unsuitable for RAP to describe the properties of the beam function in dynamic mode. This is due to differences in heat transfer. In particular, non-linearity has to be expected and implemented in deconvolution calculations for the derivation of velocity maps and tool-path algorithms. Under this aspect, two de-convolution methods, Lucy-Richardson and Van Cittert, are currently being investigated.

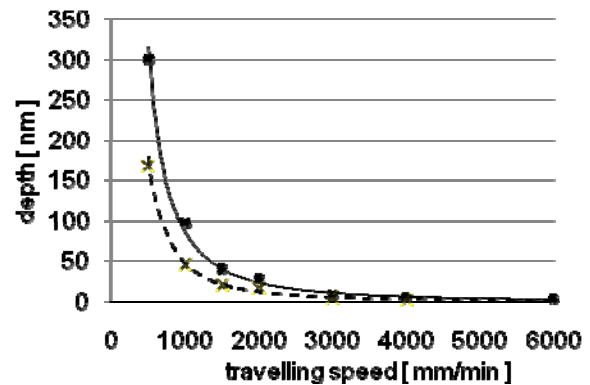


Fig. 3. Removal depth versus torch travel speed for ULE (solid line) and SiO₂ (dash line).

High etching rates and non linear trends are attributed to the increase of the substrate temperature and heat propagation within the material during the plasma process. A deeper understanding of the removal rate – temperature relationship is a key task for the implementation of an in-process adaptation by unleashing the etching rate-temperature-time “loop”.

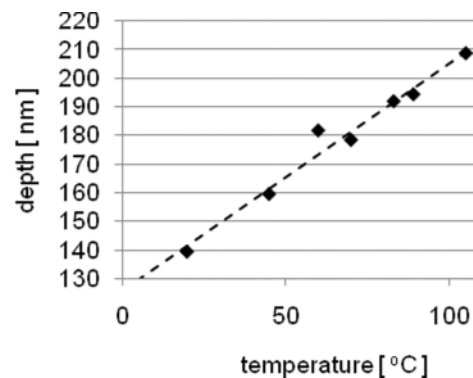


Fig. 4. Substrate temperature dependence of etching depth for static beam.

In this context, a first row of tests was carried out in static mode on ULE disks (diameter: 50mm, thickness: 5mm).

After uniform pre-heating, the surface was etched by the torch dwelling for one second. The temperature previous to etching was recorded with thermocouples on the backside of the samples, ensuring contact through thermal paste. The procedure was repeated for a series of temperature values (see Fig. 4).

On the basis of a similar principle, experiments on thermal effects in dynamic mode were performed. The machine was equipped with a pyrometer positioned along the X-axis and aligned with the nozzle centre (see Fig. 1). This makes non-contact thermal measurements of sample front surfaces possible.

First of all, 200x200x25 mm ULE samples were heated locally by rastering in argon-only plasma mode. Then single trench etching at 4000 mm/min was performed by introducing the reactive gas SF₆ into the argon plasma torch. The surface temperature was recorded by the pyrometer an instant before torch traverse. Etch depth increase with temperature was observed (see Fig. 5).

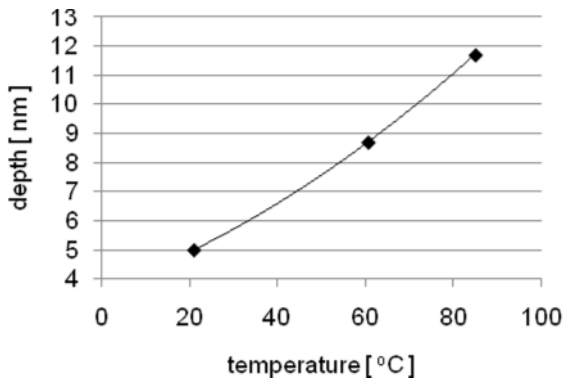


Fig. 5. Substrate temperature dependence of etching depth in dynamic mode. Traverse speed: 4000 mm/min.

A significant difference emerges from a direct comparison of the results of static and dynamic etching mode within the 20°-80°C temperature range (see Fig. 4 and 5). An increase in etching depth of 100% is observed for the dynamic case, versus 37% for the high temperature spots. This discrepancy can be explained by the relatively long dwell time (1 sec) in the stationary mode.

The trend of etching depth versus temperature in the dynamic mode emulates a rastering process. This trend was used as knowledge platform for the next stage of this study.

2.2 Neutral removal and temperature control

Neutral removal achievement was based on surface temperature assessment which allows travel speed tuning.

Two different strategies were pursued. Both serpentine and alternated rasterings (see Fig. 6) were carried out with and without travelling speed tuning based on surface temperature measurement. Optical materials with low thermal conductivity were selected: ULE and fused silica. In future work, this technique will suit the surface figure correction with regard to machine motion design.

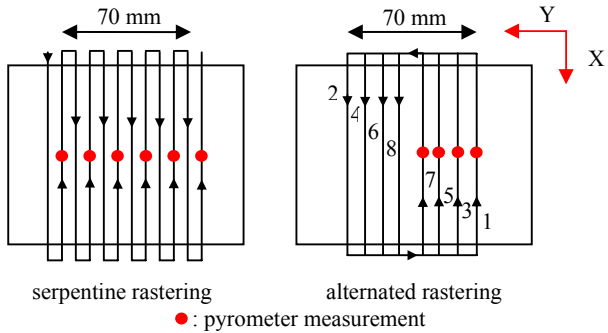


Fig. 6. Tool-paths.

Results of a serpentine tool-path are presented (see Fig. 7). Mean cross section profiles of a 200x70mm processed area is plotted. A brass mask was used to define a clear reference area required for interferometry measurement purposes. The dash line corresponds to a rastering performed at constant velocity (4000 mm/min along X, shifting the pitch by 2 mm along Y). The solid line shows how the thermal monitoring improved the initial results. Only the first travelling speed was 4000 mm/min then each further velocity was computed according to surface temperature which was acquired in flight by the pyrometer. This instrument is located 15cm away (along X) from the plasma plume on one side only. Therefore the temperature measurement was acquired every two passes.

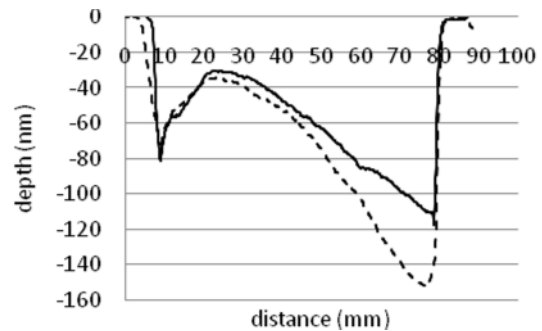


Fig. 7. Profiles resulting from serpentine rastering with (continuous line) and without (dash line) temperature control.

The outcome of alternated rastering is illustrated in Fig. 8. Unlike previous tool-path algorithms, plume shifting along the Y axis did not follow a direct 2mm increment.

Here the algorithm took advantage of the entire area and consequently heat transfer is spread symmetrically (see Fig. 6 for details). Surface temperatures were measured and exploited to adjust the velocity. Solid and dash line represent mean cross-sections for both tuned and non-controlled alternated etching (see Fig. 8). Peak-to-valley fluctuation is reduced by 50% over the 70 mm.

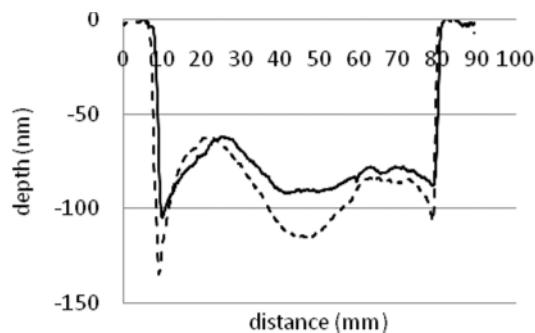


Fig. 8. Profiles resulting from alternated rastering with (solid line) and without (dash line) temperature control.

The method analyzed in this section has produced visible improvements for the realization of a consistent amount of removal over a defined area. Residual non uniformity of the etching process is, however, to be noticed for both types of rastering. In the case of the alternated passes, the higher degree of homogeneity can be explained in terms of enhanced heat diffusion. Possible causes for the limitations seen so far could be identified in further unexplored temperature effects and non regularities of plasma flow.

2.3 Roughness assessment

All surface topographies were assessed with a Taylor Hobson CCI 6000 using a Nikon 50X magnification lens (measurement area: 360x360 μm , optical resolution: 0.4 μm). The plotted curves (see Fig. 9) represent the average of two parallel rows of 24 measurements, with 5 mm spacing along the Y direction.

Polished fused silica substrate was characterized (1.6 nm S_q) then the serpentine scanning described in 2.2 (4000 mm/min, 2 mm pitch) was applied. Post-process measurements are performed both after surface IPA flash cleaning and using a Baikalex emulsion containing 20 nm Al_2O_3 particles. Etching depth was measured in the range of 150–200 nm across the 70mm distance and mean S_q value is below 2.5nm.

3. Conclusions

The work presented in this article demonstrates the removal rate potential of Helios 1200, making it an ideal candidate for large optics figuring.

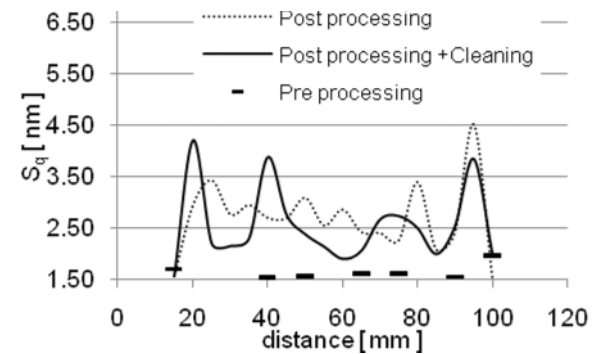


Fig. 9. Roughness evolution across 70 mm area, processed with a serpentine rastering.

Work in progress is aimed at consolidating the described techniques and eliminating possible non-uniformities, thus increasing RAP ultra-precision finishing quality.

Minor increase in surface roughness results from SF_6 plasma etching; this could be simply improved by rapid polishing procedures.

Acknowledgements

SiO_2 samples were kindly supplied by Schott GE. Project funds are acknowledged from EPSRC for the Cranfield IMRC and RCUK for the Basic Technologies Translation Grant Program.

References

- [1] Fanara C, Shore P, Nicholls JR, Lyford N, Kelley J, Carr J, Sommer P, (2006) A New Reactive Atom Plasma Technology (RAPT) for Precision Machining: the Etching of ULE[®] Surfaces. *Advanced Engineering Materials* 8 (10): 933–939.
- [2] Fanara C, O'Brien W, Shore P, Nicholls JR, Sommer R, (2007) Reactive Atom Plasma Technology (RAP[®]) etching of ULE[®] and SiC optics. TPW, 5th Technological Plasmas Workshop, Belfast.
- [3] Jourdain R, Shore P, Proscia D, Subrahmanyam P, (2009) Novel Plasma Surface Figuring Facility Designed for Effective Production of Large Scale Optical Surfaces. JEOS conference, Munich.
- [4] Allen LN, Roming HW, (1990) Demonstration of an ion figuring process. *Advanced Optical Manufacturing and Testing* – Proceeding of SPIE 1333: 22–33.
- [5] Hänsel T, Frost F, Nickel A, Schindler A, (2007) Ultra-precision Surface Finishing by Ion Beam Techniques. *Vakuum in Forschung und Praxis* 5 (19): 24–30.

Wireless & Powerless Laser Welding Monitoring System

Giuseppe D'Angelo

Fiat Research Centre - Process Research Dept. - Strada Torino 50, 10043 - Orbassano, Italy

Abstract. For quality assurance in the manufacture of automotive parts, the integrity of the laser-beam welds joining steel parts must be monitored. A considerable number of on-line inspection systems have been developed to improve weld quality. Traditional monitoring systems in industrial plants use through wired systems, using communication cables and sensors. These systems suffer from two main drawbacks: a) the sensor cables are easily damaged and this conflicts with the need for easy installation and retrofitting into industrial plants, b) the installation and maintenance of sensor cables is much more expensive than the cost of the sensors themselves. Integration of electronics, sensors and wireless communications has prompted monitoring practitioners to consider alternatives that reduce wiring costs, make connections not previously feasible, and retrofit more measurement points cost effectively as well. This paper presents a prototype sensing device to achieve wireless and powerless operation for implementing a monitoring laser welding system. The weld monitor is designed to be simple, low cost and able to withstand a harsh manufacturing environment.

Keywords: wireless communication, energy harvesting, laser welding

1. Introduction

Laser welding technology is widely used in different industrial contexts. It is applied in the automotive industries, for instance, to the welding of car roofs, base plates, using high-speed welding, structural parts, (including car doors and bodies) and the welding of transmission control gears. Nevertheless, the quality of the weld is critical for a successful application. On-line inspection systems have been developed for enabling the level of productivity and quality unattainable under human or machine control to improve while giving considerable resource savings, reduced unproductive time in the run-up of machines and timely recognizing process deviations. The function of the weld monitor is based on the collection of the photonic emission directly from the weld pool and the conversion, by suitable transducers, of these emissions to an electrical signal which can be analyzed by computer software. A selection of detectable optical emissions (Fig 1) which can be used as process signal are: a) reflected laser, originated from the amount of the laser source radiation which is not absorbed by the material, b) process radiation by metal vapour and

plasma. Since the signals contain information about the beam-material interaction, welding defects can be detected during the process and recorded for each single work piece [1-9].

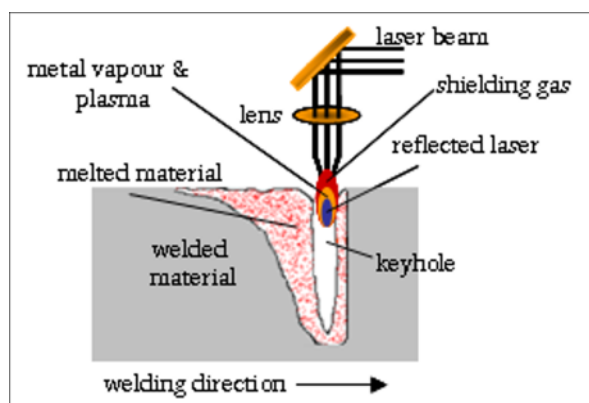


Fig. 1. Radiation emission during laser welding

All the monitoring systems are realized through wired systems, formed by sensors and communication cables (Fig. 2).

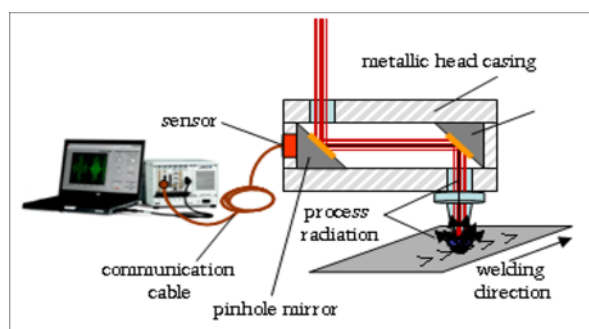


Fig. 2. Laser process monitoring system

The wired configuration presents two main drawbacks: a) the communication cables are easily damaged and This conflicts with the need for easy installation and retrofitting, b) the installation and maintenance of the

sensors cables is much more expensive than the cost of the sensor itself. In order to tackle these drawbacks, a wireless and powerless sensing apparatus, able to work independently inside the optical head, has been designed and this is described. The paper is organised as follows: in Section 1.2, the design of a low power communication module for transmitting through the metallic optical head casing is presented. Section 1.3 describes the energy harvesting module. Finally, section 1.4 shows the test results on the apparatus.

2. Communication module

Fig. 3 shows the schematic view of the optical head with the communication module inside, powered by the energy harvesting module. The communication module, in response to the sensor output (voltage signal), generates electromagnetic pulses able to pass through the optical head casing, to deliver the signal to the data acquisition terminal.

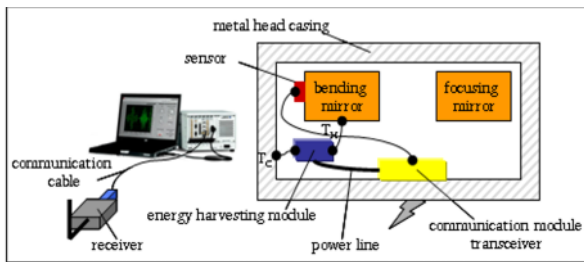


Fig. 3. Wireless and powerless monitoring system

No signal cables pass through the optical head casing. The communication module antenna is in direct contact with the inner surface of the optical head casing. The metal wall is used as the media to transmit data outside the optical head. The energy harvesting module (described in the next sections) drives the communication module, making the sensing apparatus completely self-sustaining. In order to design the energy harvesting module correctly, the special transmission path needs to be analyzed in detail to obtain the estimated power consumption. Let's start from the Maxwell equations in differential form:

$$\begin{aligned} \nabla \cdot \vec{B} &= 0 & \nabla \cdot (\epsilon \vec{E}) &= \rho \\ \nabla \times \vec{E} + \frac{\partial \vec{B}}{\partial t} &= 0 & \nabla \times \vec{H} - \frac{\partial (\epsilon \vec{E})}{\partial t} &= \vec{j} \end{aligned}$$

and let's define the potential vector \vec{A} and the potential scalar ϕ :

$$\vec{B} = \nabla \times \vec{A} \quad \vec{E} + \frac{\partial \vec{A}}{\partial t} = -\nabla \phi$$

By Lorenz gauge [10-14], the following equations are obtained:

$$\begin{aligned} \nabla^2 \phi - \frac{1}{\gamma^2} \frac{\partial^2 \phi}{\partial t^2} &= -\frac{\rho}{\epsilon} \\ \nabla^2 \vec{A} - \frac{1}{\gamma^2} \frac{\partial^2 \vec{A}}{\partial t^2} &= -\mu \vec{j} \end{aligned}$$

The last equation is a time-dependent partial differential equation (PDE). By calculating the differential terms on both sides of the equation, the dissipation term $\mu \vec{j}$ can be determined. This term indicates the power dissipated during signal delivery and the transceiver power consumption of the EM pulse communication module can be estimated. The power consumption value is the main input for correctly designing the energy harvesting module.

3. Self-powered generator design

The self-power generator consists of a thermoelectric module [15-20] which, employing the Seebeck effect, converts heat energy to electricity. In this case, the temperature gradient, which is created between the mirror hit by the laser beam and the surface of the optical head, is responsible for the electric power generation. A typical thermoelectric generator (TEG) consists of an array of Bismuth Telluride semiconductor pellets that have been "doped" so that one type of charge carrier, either positive or negative, carries the majority of current (Fig. 4).

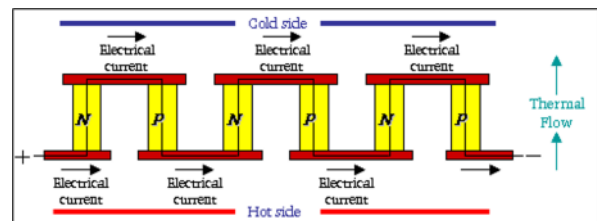


Fig. 4. Thermoelectric module

The pairs of P/N pellets are configured so that they are connected electrically in series, but thermally in parallel. Metalized ceramic substrates provide the platform for the pellets and the small conductive tabs that connect them. The pellets, tabs and substrates thus form a layered configuration. When a temperature gradient is created across the thermoelectric device, a DC voltage develops across the terminals. When a load is properly connected, electrical current flows. The parameters which

exhaustively characterize the thermoelectric generator are the open circuit voltage V_{oc} (Volts) and the matched load voltage V (Volts), the internal resistance R_i (Ohms), the power at matched load P_{wr} (Watts) and the efficiency at matched load.

4. Experiments

The communication module and the energy harvesting device, after having been assembled, were separately tested. This section presents the preliminary results of the testing activity.

4.1 Communication module

This is based on nRF905 single-chip radio transceiver produced by Nordic Semiconductor. The transceiver consists of a fully integrated frequency synthesiser, receiver chain with demodulator, a power amplifier, a crystal oscillator and a modulator. It is based on GFSK modulation. The transmitted data rate (Manchester-encoder embedded) is 100kbps. Current consumption is very low, in transmit only 11mA at an output power of -10dBm, and in receive mode 12.5mA. With the supply voltage at 1.9V, the power consumption is about 25mW. Experiments have been conducted both to verify the transmission effectiveness through the metal and to compare the sensor signal transmitted by wire and wireless. For these preliminary tests, the sensor placed behind the mirror has been connected by wire to the communication module and placed inside a metal box with walls having the same thicknesses as the optical head casing (Fig. 5).

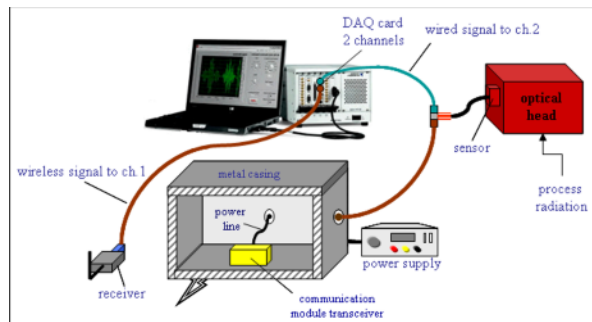


Fig. 5. Communication module test case

The external PC, by a dual-channels DAQ card, will contemporarily acquire the same signal, one from the sensor and transmitted by wire (blue line) and the second (brown line) wireless sent to the receiver connected to the PC. During the welding test, the data sampling was set at 10 kHz, consequently the signal can be delivered by EM pulse of 0.1 msec width. Fig. 6 shows the signals transmitted by wire (blue) and wireless (red) passing through the metal casing, with the receiver placed at

50cm from the metal casing. The wireless signal is a little bit lower than one transmitted by wire and is affected by low noise. The receiver has then been moved away from the metal box. For the different distance, the signal amplitude has been calculated and the signal to noise ratio has also been evaluated. Up to a distance of 2 meters, the signal can be correctly transmitted, without losing the signal information.

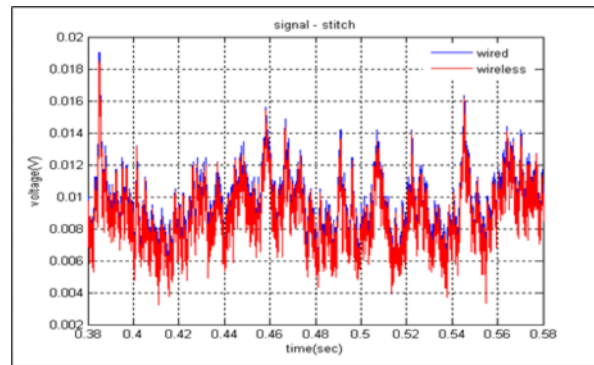


Fig. 6. Detected signals

4.2 Energy harvesting module

It is based on HV56 eTEG™ module, produced by Nextreme. Fig. 7 shows the relationship between ΔT (K), V_{oc} (voltage open circuit) (V) and power output (mW).

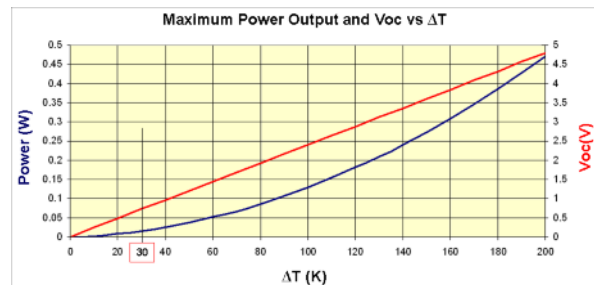


Fig. 7. Maximum power output and V_{oc} vs ΔT

To achieve data transfer from sensors inside a closed metal box to an outside data centre, it was found that the transmission through the metal casing needs at least a supply voltage of 2 V, with a current of 15 mA and a power of 30 mW. In order to get these values, two different solutions have been implemented. The first solution involves the use of 3xHV56 eTEGs connected in series, capable of generating 44.3 mW @ 1.023V and 43.3 mA, coupled to the IC boost converter TPS61201 produced by Texas Instruments, for generating 34.6 mW @ 3.3 V. The complete module measures 12.1mm x 3.3 mm x 0.6 mm. The second solution uses 4 x HV56 eTEGs mounted on a common substrate and wired together in series, capable of generating 46.2 mW @ 2.25 V and 23 mA. This solution does not use the boost

converter because the parameter values for the transmission are met. The complete module measures 8 mm x 8 mm x 1 mm. The second solution was preferred to the first one, because it can be easily mounted and generates a higher power level.

Experiments have been carried out to accurately determine the open circuit voltage, V_{oc} , and short circuit current line for a fix ΔT . The following steps have been followed:

- the open circuit voltage of the TEG has been measured,
- a resistor of 23.6ohms across the leads from the TEG, has been added,
- the heat into the system has been readjusted, until the original target ΔT of 30⁰C has been re-established (the ΔT drops when the resistor is added),
- the voltage drop across the resistor has been measured,
- a line on a plot of V and I from the V_{oc} to the I_{sc} , has been projected. Maximum power is found at 1/2 V_{oc} and 1/2 I_{sc} on this line.

Both the measured power and open circuit voltage are a little bit lower than the expected ones: 43 mW instead of 46.2 mW and 2 Volts instead of 2.25 Volts. These lower values are not significant, because they enable the data to be correctly transmitted through the metal casing.

5. Conclusions

A wireless and powerless sensing module consisting of a communication module and a thermoelectric self-powered generator has been developed. Testing the feasibility of achieving data transfer from sensors inside a closed metal box to an outside data centre has established that data transmission through the metal casing does not require any signal cable or power line connection. The proposed power mining technique uses the temperature gradient to generate sufficient power for enabling the sensor node. A special means of wireless signal transfer is reported in this study. Unlike the usual concept, where the wireless communication is through the air; this study demonstrated that wireless signal transfer through a metal casing is possible. Using an EM pulse, the signal can be transmitted from the inner location of the optical head to the outer wall for data acquisition.

References

- [1] Chen, H. B., Li, L., Brookfield, D. J., Williams, K., and Steen, W. M. (1991). Laser process monitoring with dual wavelength sensors. In: Proc. ICALEO 91, San Jose, CA. Orlando, FL: Laser Institute of America, SPIE 1722, pp. 113-122.

- [2] G. D'Angelo, G. Pasquettaz, A. Terreno (2007). Laser process monitoring at FIAT group. In: Proc. EALA 07 - Bad Nauheim/Frankfurt, Germany, 30/31 January 2007.
- [3] C. Alippi, G. D'Angelo, V. Piuri et al (2003). Composite techniques for quality analysis in automotive laser welding. CIMSA 2003 – Lugano, Switzerland, 29-31 July 2003.
- [4] G. D'Angelo, G. Pasquettaz, A. Terreno (2006). Improving the analysis of laser welding process by the reassigned time-frequency representations. In: Proc. ICALEO 06, Scottsdale, AZ.
- [5] G. D'Angelo, A. Terreno (2007). Wireless laser welding monitoring for automotive application. In: Proc. ICALEO 07, Orlando, FL.
- [6] P. G. Sanders, J. S. Keske, G. Kornecki, and K. H. Leong. Real-time Monitoring of Laser Beam Welding Using Infrared Weld Emissions. Technology Development Division Argonne National Laboratory Argonne, IL 60439 USA
- [7] Bagger, C., Miyamoto, I., Olsen, F., and Maruo, H. (1991). On-line control of the CO2 laser welding process. In: Beam Technology Conference Proceedings, Karlsruhe, Germany, March 13-14, DVS-Berichte 135, pp. 1-6.
- [8] Olsen, F. O., Jørgensen, H., Bagger, C., Kristensen, T., and Gregersen, O. (1992). Recent investigations in sensorics for adaptive control of laser cutting and welding. In: Proc. LAMP2, Nagoka, Japan: High Temperature Society of Japan, pp. 405-414.
- [9] Chang, D.U. (1994). Monitoring laser weld quality in real time. *Indust. Laser Rev.* 15-16, November
- [10] A. Ancona, V. Spagnolo, P.M. Lugara and M. Ferrara, (2001). Optical sensor for real-time monitoring of CO2 laser welding process, *Applied Optics*, Vol. 40 (33), pp. 6019-25
- [11] Chari, M.V.K. (1987). Electromagnetic field computation of open boundary problem by a semi-analytic approach. *IEEE Transactions on Magnetics* 1987, 23, 3566-3568.
- [12] F. De Flaviis, M. G. Noro, R.E. Diaz, G. Franceschetti, N. G. Alexopoulos, (1998). A Time-Domain Vector Potential Formulation for the Solution of Electromagnetic Problems. *IEEE Microwave and Guided Wave Letters*, Vol. 8, No. 9,
- [13] "Time domain vector potential formulation for the solution of electromagnetic problems," in *IEEE AP-S Int. Symp.*, Montreal, Canada, July 1997.
- [14] G. Franceschetti (1983). *Campi Elettromagnetici*. Ed. Boringhieri
- [15] G. Franceschetti, I. Pinto (1980). Volterra series solution of Maxwell equation in non-linear media.
- [16] Ali Muhtaroglu, et Al., (2008). Integration of thermoelectrics and photovoltaics as auxiliary power sources in mobile computing applications. *Journal of Power Sources* 177 (2008) 239-246
- [17] L. Mateu, C. Codrea, N. Lucas, M. Pollak and Peter Spies (2006). *Energy Harvesting for Wireless Communication Systems Using Thermogenerators*.
- [18] A. Muhtaroglu, A. von Jouanne (2006)- *Proceedings of the Sixth International Workshop on Micro and Nanotechnology for Power Generation and Energy Conversion Applications (PowerMEMS 2006)*.
- [19] A. Muhtaroglu, A. Yokochi, A. von Jouanne, (2007). *J. Micromech. Microeng.* 171767-1772.
- [20] A. Muhtaroglu, A. Yokochi, A. von Jouanne, (2007). A sustainable power architecture for mobile computing systems, *J. Power Sources*
- [21] European Commission: European cooperation on the field of scientific and technical research (1999): "Digital mobile radio towards future generation systems", Final report, Bruxelles.

System Design for Laser Assisted Milling of Complex Parts

Wu X F, Wang Y, Zhang H Z

School of Mechatronics Engineering, Harbin Institute of Technology, Harbin, China

Abstract. Laser assisted milling (LAML) is a potential method for machining difficult-to-machine materials such as superalloys and ceramics. Several LAML experiments have showed the feasibility of the method and advantages including good surface finish, decreased cutting force and tool wear, and no large microcrack zones. While several studies have been made of machined features, including faces, grooves and chamfers, few attempts have been made to study the laser-assisted milling of complex parts due to the restraints of the machining systems. In this paper, a machining setup is designed to meet the LAML requirements. The material removal temperature is the key parameter influencing machining results, so to help establishing the system a finite element model is developed to simulate the temperature distribution in the workpiece when subject to a traversing laser heating source. A NC codes automatic transcoding algorithm is proposed for continuous LAML of the workpiece. VERICUT software is used to simulate the NC machining process in order to verify the feasibility of the system and the LAML process function that can be achieved.

Keywords: laser assisted milling, finite element analysis, heat transfer, LAML device

1. Introduction

Laser assisted machining (LAM) is an effective method for machining difficult-to-machine materials such as ceramics. It uses a high power laser to locally heat a workpiece prior to material removal with a traditional cutting tool. At elevated temperatures, the mechanical properties change, with yield strength decreasing and the material deformation behavior changing from brittle to ductile, thus reducing tool wear, improving surface finish and increasing material removal rates. The feasibility of the method and its advantages have been proved through the application of LAM to various ceramics [1-3] and difficult-to-machine metals [4]. Laser assisted milling (LAML) is also a potential machining method with the ability of machining planes and grooves of difficult-to-machine materials. The feasibility of laser assisted milling was first shown by König on stellite 6[5]. Shen[6] developed a finite element model to simulate the temperature and stress fields during LAML of silicon nitride. Tian [7] developed a transient, three-dimensional thermal model for laser assisted milling and successfully conducted experiments on silicon nitride ceramic and

Inconel 718. Yang[8,9] demonstrated the and feasibility of milling silicon nitride ceramics with laser assistance. Applying a laser in micro-milling is helpful in reducing the yield strength of the workpiece and improving machine tool system stiffness. Özel [10] applied pulsed laser assistance in micromilling for die/mould manufacturing. Melkote [11] developed a novel laser assisted micro-milling machine to enable the creation of freeform, three-dimensional, micro-scale features in hard materials. Experiments were carried out on the hardened A2 tool steel workpiece.

Since there is no dedicated laser assisted milling system, only the feasibility of the laser assisted milling process has been tested, via milling simple features such as grooves and plane. This paper attempts to design a simple and practical experimental system to achieve continuous LAML. In order to achieve this, a three-dimensional FEA model of transient heat transfer is developed for a Si_3N_4 workpiece to investigate the temperature distribution characteristics, and the NC code generation method for the system is presented.

2. Thermal modeling for laser assisted milling

In the process of laser assisted machining, it is extremely important to maintain the material removal temperature within a proper range in order to complete the processing and obtaining good final quality, especially with ceramic workpieces. Thermal analysis can help to select the operating parameters and provide suggestions for the establishment of the system.

The thermal model for temperature distribution in a ceramic workpiece during LAML is based on a 3-D transient heat conduction analysis of a moving Gaussian heat source applied to the workpiece surface. The heat transfer model of a workpiece heated by laser for LAML is illustrated in Fig. 1. The Si_3N_4 workpiece is fixed on the insulated table, the bottom surface is considered adiabatic. The set boundary conditions account for laser heat flux, convection and radiation at different workpiece surfaces. The convection condition is determined by free

convection, and radiation exchange between the workpiece surfaces and surroundings is assumed to be from a small surface to a large enclosure. At the material removal zone, thermal energy generated by the material deformation and tool-workpiece friction is difficult to model. In general, the heat generation from machining is much less than the energy input from the laser [9] and is neglected in the model.

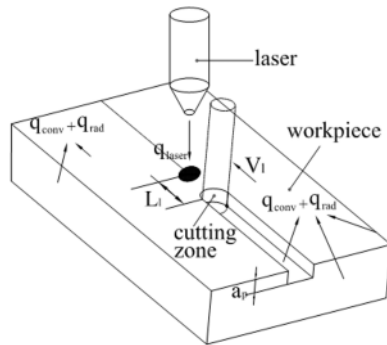


Fig. 1. Schematic of heat transfer for LAM

The Finite Element method is used to discretize the governing equation. Temperature-dependent thermophysical properties are used and updated at each step. The workpiece is 50mm×50mm×15mm. The system is symmetrical about a vertical plane that passes through the laser spot center and cutting path so a half model is used and the mesh is refined within the range of laser spot and the depth of cut. The cutting speed is determined by the interval time of one load step. The element birth and death method is used to simulate the material removed by the tool and the removal elements deactivated by multiplying their conductivity by a severe reduction factor. The initial workpiece temperature is set to 25°C, the absorptivity of workpiece is 0.83 and the free convection coefficient is assumed to be 10 W/m°C.

A contour plot of the temperature distribution on workpiece after the laser spot has moved 25 mm is shown in Fig.2 for the case of 300W laser power, 4 mm laser beam diameter, 3 mm laser-tool lead, 3 mm milling tool diameter and 1 mm/s laser moving speed. The surface, heated by laser spot, conducts energy to the interior of workpiece and the temperature drops rapidly at any point as the laser moves away. The temperature beneath the laser spot is very high and the gradient of temperatures around the laser spot is very large due to the high intensity of the laser power and the low conductivity of silicon nitride. The temperature decreases with increasing distance from laser spot center. A simple criterion to ensure the smooth process of cutting is to keep the temperature at the farthest point of the removal zone away from the laser spot above the softening temperature.

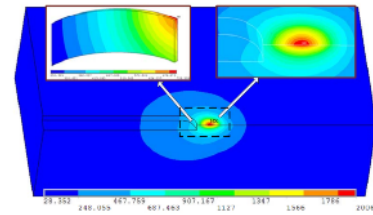


Fig. 2. Temperature distribution in the workpiece

Many theoretical and experimental studies show that, of all the operating parameters, laser power has the most significant impact on the workpiece temperature. Laser traverse speed also influences the amount of energy deposited per unit time. Increasing laser power and decreasing laser traverse speed could increase the material removal temperature while causing a high temperature gradient. Another important parameter in LAM is the lead distance between laser beam and cutting tool. As the lead distance increases, the time for the absorbed energy to be conducted into the workpiece increases, which causes a significant temperature drop on the surface. Therefore, the cutting area should be as close as possible to the laser spot, provided that the distance is high enough to prevent the tool body from being directly affected by the laser. The results showed that the temperature decreases away from the spot center for the Gaussian distribution, so the diameter of the cutter should be limited to a range less than the diameter of the laser beam. Laser beam diameter which has the largest effect on temperature gradient should not be small.

Generally, a preheating cycle is an effective way to elevate the material temperature above the softening temperature before machining to reduce the amount of chipping on the tool for LAM. However, it would take a long time to reach the required temperature by local laser heating and this would cause overheating on the top surface near the laser beam center and workpiece damage. It is difficult to achieve softening temperature without damage using existing laser systems with Gaussian beam characteristics and power limitations. Therefore, it is necessary to apply another heat source to elevate the workpiece to a certain temperature and then increase from there to softening temperature by laser heating prior to material removal. A high-temperature electric ceramic heater, whose surface temperature could reach about 1000°C was considered as the heat source. The heater was fixed on the top surface of the workpiece, and the heat energy transferred within the workpiece through thermal conduction. After heating for a period of time, the heater was moved away and the machining process started.

In the thermal model, the heater is determined to be a constant temperature boundary for the top surface nodes. The material removal temperatures histories predicted with the above conditions are shown in Fig. 3.

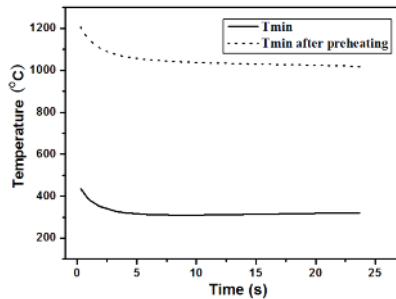


Fig. 3. Predicted minimum temperature histories for different conditions

3. Establishment of experimental system

From the above thermal model analysis and laser assisted milling requirements, a continuous processing system should have the following characteristics: (1) the laser spot must be located ahead of the tool during the whole process, exactly at the material to be removed; (2) the tool location should be as close as possible to the laser spot without being irradiated by the laser and the tool diameter should be less than the diameter of laser beam; (3) the laser incident area should be only within areas on the processing path to prevent collateral damage.

For single-direction path machining, the relative position of tool and laser spot does not need to change, but for complex path machining, positioning represents a challenge, since the laser spot may not be able to irradiate the next location to be machined. There are two ways to overcome this: change the location of the incident laser or change the direction of tool path. For the first approach, the laser should be able to be positioned at any point around the milling tool, this needs a complex optical system or laser head mobile system which may cause equipment interference. The second way can be achieved by appending a rotational axis to alter the relative direction of machining, making the machining path coincide with the laser spot trajectory, which is convenient and practical to realize.

The designed experimental system for LAML is shown in Fig.4. The device is mounted on a three-axis conventional CNC milling machine. A rotary table is fixed on the milling table and the rotary center must be concentric with the spindle. A 2D worktable is installed on the rotary table. The rotary table only changes the direction of machining; a 2D,x-y worktable and the z axis of the milling machine are the axes required for a 3D milling operation. A 300W continuous wave Nd:YAG laser system is used to generate the laser beam in front of a mill tool, which is delivered through a fibre optic and focused on the workpiece surface at an angle of about 60°. A laser head fixture which can be used to adjust the relative position between laser and workpiece is fixed on the milling head. During milling, the laser beam does not move, while the workpiece translates with the worktable and rotates with the rotary table to change the relative

position of the move direction and laser incidence. Therefore, the relative positions of laser spot and cutting edge remain the same during milling. The control of the laser shutter is integrated into the NC system to ensure the synchronization of the two subsystems during LAML.

With the addition of a special rotational worktable, NC codes are different from conventional. Because the relative position of the cutting tool and working table has

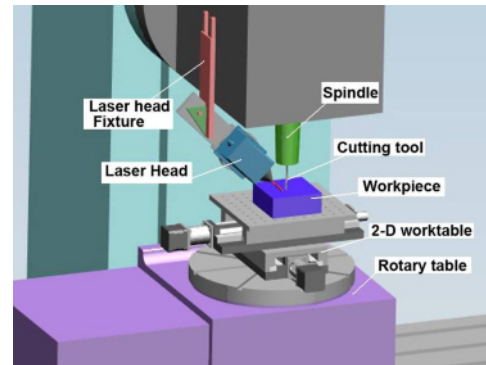


Fig. 4. Experimental system for Laser-Assisted Milling

not changed while rotating, three-dimensional movement of the G-codes does not need to change and the only difference is to increase the rotation axis G-codes. A sketch of the G-code programming is shown in Fig. 5. OXY is the absolute coordinate system for the milling machine and processing path is A→B→C. A line through the laser and milling tool centerlines is parallel to the x-axis of OXY. When processing from the A point, the laser needs to heat along the path A→B, so the target value of the rotation is θ_1 . After processing to the B point, the destination of line BC is parallel to the OX-axis, The absolute angle value is $-\theta_2$ in the case of using the absolute coordinates. As a result, the value of the computed angle between the x-axis of the coordinate system and the original tool path is considered as the coordinate values of the forth axes. When machining free curves, straight-line segments were used to approximate the desired path and the rotation angle between the line segments were obtained from the above method.

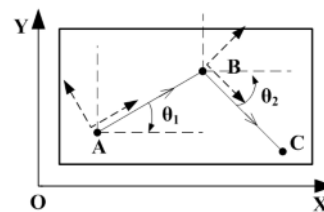


Fig. 5. The sketch of the G-code programming

Vericut is a software which is able to verify a G-code program and simulate CNC machining. It is used here to verify the feasibility of the device and G-code programs. The rectangular workpiece is 50mm×50mm×15mm, tool

diameter is 3mm, laser beam diameter is 4mm and the tool-lead distance is 2mm. Multi-line and free-curve machining paths were simulated and the machining result is shown in Fig.6. Simulation results indicate that the processing path overlapped the laser scan path for the straight-line machining. But the laser spot is outside the machining region while rotating due to the certain distance between the laser head and milling tool. Consequently, the laser should close when the rotating table works. The laser shutter controlled by the NC system could be used to prevent the laser from irradiating the workpiece. From the result of machining a free curve, the path of laser scan and processing does not completely coincide, especially when the radius of curvature is small. The laser spot obviously deviates from the machining path which may cause damage to the workpiece. The impact of the laser on the workpiece will be analyzed in future studies.

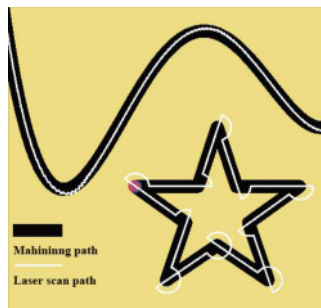


Fig. 6. Simulated laser scan and machining path

Since the laser has to close for a short time while rotating and the laser is unable to scan the entire machining path, the material removal temperature is not stable during processing. The machining path and the minimum temperature histories of the material removal zone are shown in Fig. 7. The temperatures decreases clearly in the rotation point. However, the basic processing requirements can be met.

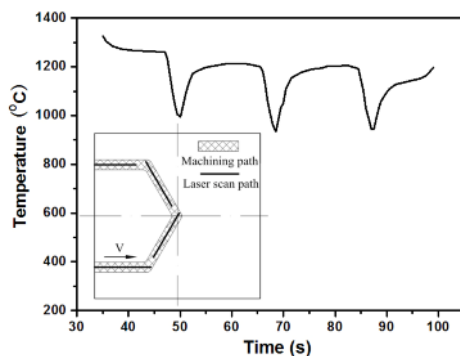


Fig. 7. Machining path and the minimum temperature histories of the material removal zone

4. Conclusion

A transient, three-dimensional thermal model for LAML of silicon nitride ceramic has been developed. The transient temperature distribution in the workpiece and the characteristics of the material removal in the process of LAML were investigated. Material removal at or above the softening temperature, which is suitable for machining, can be achieved by the whole surface preheating method. Based on the temperature field simulation and the characteristic of LAML, a laser assisted milling system for continuous machining was designed and a G-codes generation method for the LAML system presented. The laser path and machining path simulated by the vericut software and the minimum temperature histories showed the correctness of the G-codes and the feasibility of the system.

The machining experiments and the behavior of silicon nitride subjected to the laser for LAML will be investigated in the continuing work.

References

- [1] Rozzi JC, Pfefferkorn FE, Shin YC, et al, (2000) Experimental Evaluation of the Laser Assisted Machining of Silicon Nitride Ceramics. *Journal of Manufacturing Science and Engineering*. 122(4): 666-670
- [2] Rebro PA, Shin YC, Incropera FP, (2002) Laser-Assisted Machining of Reaction Sintered Mullite Ceramics. *Journal of Manufacturing Science and Engineering*. 124(4): 875-885
- [3] Pfefferkorn FE, Shin YC, Tian Y, et al, (2004) Laser-assisted machining of magnesia-partially-stabilized zirconia. *Journal of Manufacturing Science and Engineering*. 126(1): 42-51
- [4] Anderson M, Patwa R, Shin YC, (2006) Laser-assisted machining of Inconel 718 with an economic analysis. *International Journal of Machine Tools and Manufacture*. 46(14): 1879-1891
- [5] Konig W, Zaboklicki A K, (1993) Laser-assisted hot machining of ceramics and composite materials. *International Conference on Machining of Advanced Materials*, NIST Special Publication, Gaithersburg, MD. 847:455-463
- [6] Shen X, Liu W J, Lei S, (2005) Three-dimensional thermal analysis for Laser assisted milling of silicon nitride ceramics using FEA. Orlando, FL, United States: American Society of Mechanical Engineers, New York, NY 10016-5990, United States
- [7] Tian Y, Wu B, Anderson M, et al, (2008) Laser-Assisted Milling of Silicon Nitride Ceramics and Inconel 718. *Journal of Manufacturing Science and Engineering*. 130(3): 31013-31019
- [8] Yang B, Lei S, (2008) Laser-Assisted Milling of silicon nitride ceramic: a machinability study. *Int. J. Mechatronics and Manufacturing Systems*, 1(1):116-130
- [9] Yang B, Shen X, Lei S, (2009) Mechanisms of edge chipping in laser-assisted milling of silicon nitride ceramics. *International Journal of Machine Tools and Manufacture*. 49(3-4): 344-350
- [10] Ozel T, Pfefferkorn F, (2007) Pulsed laser assisted micromilling for die/mold manufacturing. Atlanta, GA, United States: American Society of Mechanical Engineers, New York, NY 10016-5990, United States
- [11] Melkote S, Kumar M, Hashimoto F, et al, (2009) Laser assisted micro-milling of hard-to-machine materials. *CIRP Annals - Manufacturing Technology*. 58(1): 45-48

Direct Laser Writing System of Mask for Integrated Photonics Devices

S.Messaoud¹, A.Allam¹, F.Siserir¹, Y.Bouceta¹, T. Kerdja¹, D.Ouadjaout², T.Touam¹

¹ Centre de développement des technologies avancées, Cite 20 Août 1956, 16303 Baba Hassan, Algiers, Algeria

² Unité de développement de la technologie du silicium, 2 Boulevard Frantz Fanon, Algiers, Algeria

Abstract. In this work a developed experimental setup for the direct laser writing (DLW) system of a photolithography mask for integrated photonics devices will be described. The DLW system is mainly composed of a pulsed Nd:YAG laser source, beam handling system, (X-Y) table, PC computer, CCD camera and TV monitor. The synchronization between the laser source and the (X-Y) table is achieved by a NI Instruments and LabVIEW based program. The experimental micromachining results from some samples of continuous writing lines obtained by removal of chromium deposited on glass substrates will be presented and discussed.

Keywords: Nd:YAG laser, laser writing, laser ablation, mask, photonics devices

1 Introduction

Recently direct laser writing (DLW) systems have received a great deal of attention compared to conventional photolithography or e-beam lithography [1, 2]; it has excellent features such as high speed, small structures with a high quality border, flexibility and low cost manufacture. The most important application of DLW is mask fabrication of photonics circuits which require feature resolutions of a few micrometers, with channel lengths of at least several centimeters [3, 4]. The required pattern is made by direct laser ablation which consists of the removal of thin metallic layers (such as chromium films) from glass substrates [5, 6]. Laser ablation of chromium films using Nd:YAG lasers has also been reported in the literature by Abe [7], where they mainly studied the quality of chromium film removal. Siegel et al. [8] investigated the removal mechanism of a chromium film on quartz, and compared the measured removal rate with the result of numerical calculations.

In this work we used a DLW system based on laser ablation process [9]. Our experimental setup consisted of a Q-switched pulsed Nd:YAG laser source operating at second harmonic generation with a round tophat profile. The optical system included a beam expander, a dichroic mirror and a microscope objective [10, 11]. Both a CCD camera and TV monitor were used to control the writing process. A motorized (X-Y) stage was used to move the

mask depending on the required pattern. A LabVIEW based program and NI instruments were used for synchronization [11, 12]. To reduce the vibration of the DLW system an optical table with granite based supports was used. In this first part of our work the developed experimental setup for DLW system will be fully described. The results from some samples of continuous writing lines obtained by removal of thin chromium layers [10] deposited on glass substrates will be presented and discussed.

2 Experimental setup

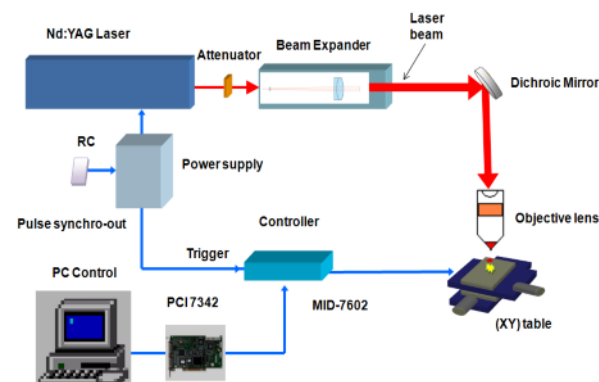


Fig. 1. Experimental Setup

The experimental setup used is shown in Figure 1. A YG980 Q-switched pulsed Nd:YAG laser source operating at $0.532 \mu\text{m}$ was used to generate the continuous lines in chromium films. The laser had a maximum output energy of 300 mJ/pulse, 8 ns pulse duration and 20 Hz maximum repetition rate. The output laser beam diameter was 10 mm. The laser pulse energy was attenuated by adjusting of delay time between flash lamp and Q-switch from $210 \mu\text{s}$ to $320 \mu\text{s}$. The optical system was constituted by an adjustable 5×1 beam expander which was used for reducing both the beam

divergence and the laser power density. The laser ablation of the chrome on the glass was achieved using a dichroic mirror that deflected the laser beam vertically to pass through the objective lens with a working distance d_f of 15 mm and Numerical Aperture of 0.1. The focalization of the spot beam was performed manually by varying the objective-substrate distance. The total travel length was fixed at 300 mm; this single axis stage was motorized by a stepper motor (24V/1A) to move the substrate in the perpendicular direction to the laser beam. Rotation speed was 200 steps per revolution, with a linear resolution of 20 μm per step. The stepping motor was controlled by a computer through the NI PCI-7342 card that used two axis NI MID-7602 stepper motor power drives. The synchronization between the laser source and the stage was performed by a LabVIEW based program. The front panel of the user interface is depicted in Figure 2.

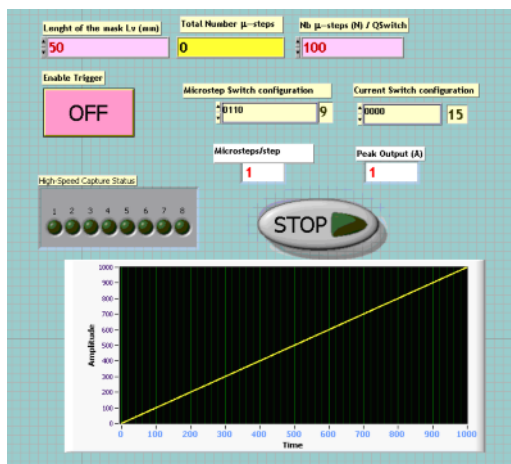


Fig. 2. User interface of the experimental setup

The output synchronization Q-switch signal coming from the YG 980E Nd: YAG laser was applied to the MID-7602 input trigger to move the stage. The trigger signal is shown in Figure 3.

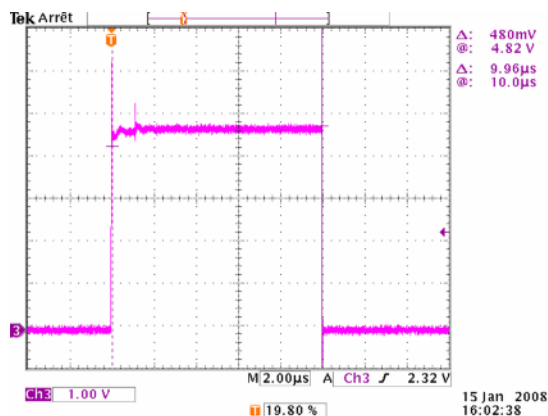


Fig. 3. TTL Synchronization Q-switch signal

The chromium layers were deposited onto glass substrates by using evaporation vacuum deposition technique [10, 13]. A Scanning Electron microscope (SEM: JEOL JSM-6360LV) was used to measure the different chromium deposited layers. The thickness of the layers was estimated to be ~ 250 nm as shown in Figure 4. A Zeiss Optical microscope Imager A1m was used to determine the shapes and sizes of the continuous writing lines. Tektronix TDS 3000 Oscilloscope, Gentec ED-100 and ED-200 joule meters were used to measure the pulse energy laser.

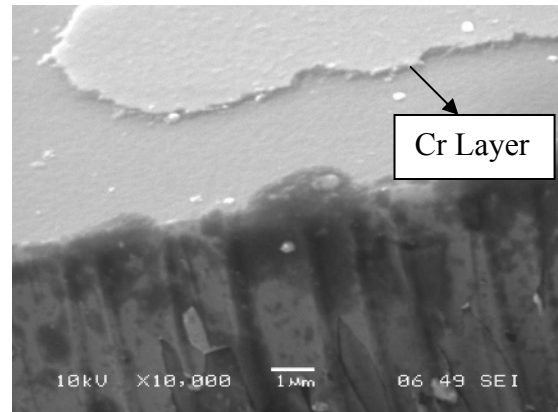


Fig. 4. SEM picture of chromium layer

3 Results and discussion

The chromium layers were fully ablated in a single shot at low energy using the 0.532 μm radiation. The absorbed energy in the chromium was around 40 % for different power and was almost completely transmitted by the glass substrate (92% transmission). Figure 5 shows the continuous writing line which is generated by the DLW system with the following writing parameters: 500 μJ laser pulse energy, 20 Hz repetition rate and 20 μm linear stage steps. The continuous writing lines were analyzed and measured using the optical microscope. The width of the measured continuous writing lines was in the range of between 55.08 and 62.88 μm .

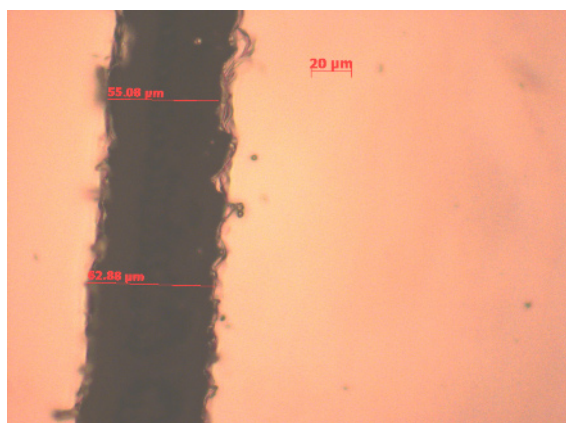


Fig. 5. Microscope picture of continuous writing line

From the experimental result shown in Figure 5, a non-uniformity of the line border can be observed. This is due to the natural round shape of the laser beam ($60\ \mu\text{m}$ spot size) and the step size of the linear stage ($20\ \mu\text{m}$ step resolution).

The non-uniformity profile can be reduced by operating the stepper motor in micro-stepping mode, whereby decreasing the step size of the linear stage. In this case however the laser energy is not optimized. The non-uniformity of the line border can be eliminated by using a square tophat profile with a linear stage step less or equal than the square spot size. This means that the laser pulse energy is optimized. The laser repetition rate does not affect the overlap rate but can change the removing process time. Our limitation of the laser working frequency to a few kHz was due to the mechanical characteristics of the stepper stage.

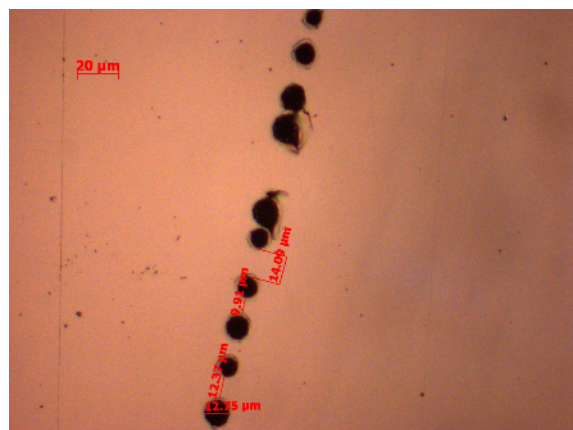


Fig. 6. Microscope picture of ablated holes

High resolution features were achieved by using the objectives lens with a working distance of $10\ \text{mm}$ and a numerical aperture of 0.2 . Figure 6 shows the ablated holes in the chromium layer with different diameters. The

above observation indicates that when the diameter of the ablated holes is less than the linear stage step ($20\ \mu\text{m}$) the overlap rate of the laser spot is 0% . The discrepancy in the distance between the ablated holes is essentially due to the shot-by-shot fluctuation of the laser and / or the instability of the stepping device.

4 Conclusion

This work has successfully demonstrated the feasibility of the developed DLW system, which is based on NI instruments and Lab-VIEW program, for micromachining and micro fabrication applications.

The DLW of the continuous writing lines in thin film removal process it is necessary to use a short pulse laser with high wavelength pulse laser absorption and square tophat laser beam profile in order to optimize the pulse energy.

We have also noticed that laser frequency has no effect on the overlap rate.

To ensure a higher overlap rate in the round tophat profile, the stepper motor power drive needs to be operating in micro-stepping mode operation. The different writing parameters used in our system allowed us to select the laser source features and the stage characteristics to build better DLW system for future investigation.

Acknowledgments

We are grateful to M. Hamiçi, Y. Hamoum, B. Guedaour, Y. Belaroussi and F. Haed for their experimental help and useful discussion.

5 References

- [1] P.Rai-choudhury, Handbook of Microlithography, Micromachining & Microfabrication, London: IEE, 1997, 11-251 pp.
- [2] K.Venkatakrishnan, K.Venkatakrishnan, B.K.A.Ngoi, P.Stanley, L.EN.Lim, B.Tan, N.R.Sivakumar (2002) Laser writing techniques for photomask fabrication using a femtosecond laser, *Appl. Phys.A* 74, 493-496
- [3] D.Day and M.Gu (2006) Femtosecond fabricated photomasks for fabrication of microfluidic devices, *Optical Society of America*, Vol 14, N° 22, 10753-10758.
- [4] Y.Liao, J.Xu, Y.Cheng, Z.Xu, K.Sugioka and K.Midorikawa (2009) Electro-optic integration of embedded electrodes and waveguides in LiNbO_3 with femtosecond laser, in Proceedings of LAMP2009, Kobe, Japan.
- [5] S.Kopac, J.Pirs, J.Mozina (1995) Optodynamic analysis of direct laser writing of graduation lines, *Appl. Phys.A* 62, 77-82.
- [6] S.M.Metev, V.P.Veiko, Laser-Assisted Microtechnology, Berlin: Springer, 1998.

- [7] C.Abe, (1990) Machine Tool Series: Laser Processing, Taiga Press, 135-142
- [8] J.Siegel, K.Ettrich, E.Welsch, E.Matthias (1997) UV-laser ablation of ductile and brittle metal films”, Appl. Phys, A64, 213-218.
- [9] S.Messaoud, A.Allam, F.Siserir, Y.Boucetta, T.Kerdja, D.Ouadjaout (2009) Q-Switched Nd:YAG laser micro-machining system, in Proceedings of LAMP2009, Kobe, Japan.
- [10] F.Siserir, S.Messaoud, A.Allam, Y.Boucetta, , T.Kerdja, D.Ouadjaout, T.Touam (2009) Optique de mise en forme d’un faisceau laser Nd:YAG pour l’écriture directe, in Proceedings of SENALAP2009, Ouargla, Algeria.
- [11] S.Messaoud, A.Allam, F.Siserir, Y.Boucetta, , T.Kerdja & D.Ouadjaout (2008) Q-Switched Nd:YAG laser micro-machining system,in Proceedings of LAPAMS2008, Algiers, Algeria,111-114.
- [12] GaryW.Johnson, Labview Graphical Programing, Montreal: Mc Graw Hill, 1997
- [13] D.M.Mattox, Handbook of physical vapor deposition (PVD) processing, NJ, Noyes publication, 1998.

Direct Laser Welding for Al- Li Alloy Plate without the Cleaning of Surface Film

Kai C, Wuxiong Y, Rongshi X

Institute of Laser Technology, Beijing University of Technology, Beijing 100124, China

Abstract. It is well known that the oxide film on the surface of Al-Li alloys has to be cleaned before welding in order to achieve welds without pores. However it is hard work and may cause pollution if chemical cleaning is used. This paper reports on experiments in which a plate of Al-Li alloy was not treated in any way as a precondition of laser welding. A DC035 CW CO₂ laser system, in the TEM00 mode, with an output up to 3500 W was employed and an experimental study was conducted on porosity control during the welding of 1420 Al-Li alloy by a dual- beam laser. The experimental results show that the influence from the right (upper) surface oxide film on the porosity in the weld is bigger than that from backside one when the laser welding is in the form of a beam on the surface of a plate. However the porosity from the backside oxide film has a distinct connection with the formation of the inverse weld when butt joint laser welding is used. Optimized laser welding techniques have been achieved from experiments with the aim of decreasing the porosity in the weld and increasing the weld qualities. The tensile strength of laser welding joint was also tested in the experiments. The data indicate that the average value of tensile strength of the joints can be up to 336.1 MPa which is equal to 87.5% value of substrate alloy

Keywords: Laser welding; Dual-beam; Al-Li alloy; Porosity; Tensile strength

1. Introduction

Al-Li alloys have a low density (2.47–2.50g/cm³), high specific strength and rigidity, eximious properties in low temperature, excellent corrosion resistance and superplasticity when compared with general Al alloys. When 1% of Li element by weight is added into the Al base, the density will reduce by 3% and the elasticity will rise of 6%. If general Al alloys are used instead of Al-Li alloys, a 10-15% reduction in structure mass and a 15-20% increment in rigidity will be gained. Now they are widely used in the parts manufactured for aircraft and space applications [1,2].

However, in the welds of Al-Li alloys, there is a tendency for bigger welding pores to occur than in other alloys because of the active Lithium element in the substrate [3-5]. The melting of the loose oxide film formed on the surface of the alloys creates conditions for

the pores in welds and results in reducing the qualities and the properties of the welded joints. The common way, now, for solving the problem is to use various treatments for removing the surface film of Al-Li plate before welding. These include mechanical milling and chemical cleaning with organic solvents. Generally speaking, 0.2-0.3 mm in thickness of the surface has to be removed in order to ensure the elimination of the pores[6-8].

Although satisfactory weld qualities of Al-Li alloys can be achieved using these process, pollution results from the use of organic solvents and a waste of the alloy materials occurs with milling.

In this study, a special dual-beam laser welding technique was used in the experiments and the beams acted directly on the 1420 Al-Li alloy plates without any pretreatment before welding. The control of the weld porosity and its influence on the properties of the joint were explored.

2. Experimental equipment and material

2.1 Experimental equipment

A DC035 CW CO₂ laser, in the TEM00 mode, with output up to 3500 W was employed in the experiments. The technical data of the laser were: beam diameter $\phi=17\text{mm}$ and beam parameter product $Kf=3.7\text{mm}\cdot\text{mrad}$. A parabolic copper mirror with focal distance of $F=300\text{mm}$ and a focal spot diameter $D=0.2684\text{mm}$ was used for welding.

A schematic diagram of the dual-beam laser principle is shown in Fig. 1. A laser beam from the resonator is first separated into two beams by reflection mirror 1 and mirror 2 and then they are focused separately by focal mirrors 3 and 4. The locations of the two focuses on the surface of plate and the distance between them could be easily adjusted by changing the angles of two mirrors.

The distribution of laser power density and the shapes of two focal spots are displayed in Fig.2.

2.1.1 Experimental material

The experiment material was 1420 Al-Li alloy and its chemical composition is shown in Table 1. The size of the sample was 100x50x1.9mm. The samples were cleaned by acetone solution before the experiments.

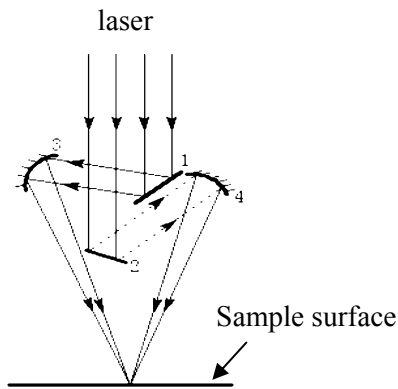


Fig. 1. Scheme of dual beam laser system (1- reflection mirror., 2- reflection mirror, 3- focal mirror, 4- focal mirror)

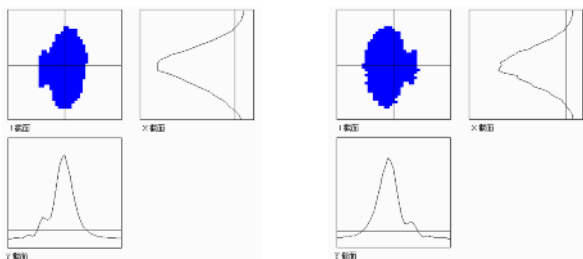


Fig. 2. Distribution of the laser power density of twin focuses

Table 1. Chemical composition of 1420 alloy (wt%)

	Mg	Li	Zr	Mn	Si	Al
1420	4.9-5.5	1.8-2.1	0.08-0.15	0.2	<0.25	bal

Table 2. Statistics of porosity amount in the welds

Sample	Number with different diameter (d/μm) pores			Diameter of biggest pore /μm	Average area of weld /μm ²	Porosity / %
	d<100	100<d<200	200>d			
1	12	5	1	364	4506923	0.080
2	5	4	0	118	4710852	0.011
3	14	5	0	161	4690677	0.076

Note: 1-Originalal rolling plate surface; 2-Right surface with 0.05mm grinded off in thickness; 3-Reverse surface with 0.05mm grinded off

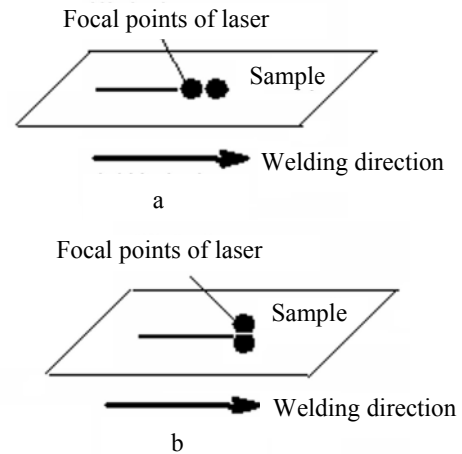


Fig. 3. Arrangement of double focuses

Fig. 3 shows the different arrangements of both focuses in the experiments. Fig 3a shows that the central line of the two focuses is the same as the direction of welding but in Fig. 3b, it is vertical.

3. Results and discussion

3.1 Influence of surface film on porosity

In order to investigate the influence of oxide-film on the right(upper) and reverse(lower) surfaces on the porosity in the weld of 1420 Al-Li alloy under the condition of laser penetration welding, the arrangement of double focuses (Fig.3b) was used in the experiments. (In this way, the pores arising from laser welding of 5083 Al alloy were controlled in a previous study[9]). At the same time, the samples of 1420 Al-Li alloy were divided into three types, the plate surface with the case from its original rolling, the right surface with 0.05mm ground in thickness only and the reverse surface with 0.05mm ground. The samples were cleaned by acetone solution before laser welding. The welding parameters were laser power of 2.5kW, defocused distance of 0 mm, welding velocity of 3m/min, the line of two focuses was

perpendicular to the direction of welding, the distance between focuses was 0.4mm.

Six cross-sections were obtained from every experimental weld and they were observed by an OLYMPUS-PMG3 optics microscope. The porosity of the welds, the diameter of pores and weld areas were measured and the data are listed in Table 2. The data, from Table 2, show that there are some pores with different size and ball-shape in all welds and the lowest porosity occurs in the case of moving oxide-film from Table 2 shows there are some pores with different size and ball-shapes in all welds and the lowest porosity occurs in the moving oxide-film with the right surface. When the cross-sections were examined, it was found that most pores were formed near the fusing-line of the welds on the original surface. The formation of these kinds of pores closely corresponds with the solubility of hydrogen in aluminium alloy in both solid state and liquid one.

It is obvious from Table 2 that the influence of the pores in the weld from the film of right surface is much higher than that of the reverse surface. The polish of the oxide film acted on directly by the laser beam effectively counteracts the source of hydrogen in welds and the full penetration processing could make the oxide-film on the reverse surface evaporate from the welding pool. In this case, welds with low porosity and reduced size of pores could be achieved. However, the polish of the oxide-film on the reverse surface has not the same function. This is because a part of the oxide-film on the right surface could melt into the molten pool although most of it would be vaporized under the laser irradiation.

3.2 Porosity in bead on plate special dual-beam laser welding

The setting of dual-beam is shown in Fig. 3a. The line of two focuses is parallel with the direction of welding with a separation distance of 1mm. The defocused distance for the former(front) one was 20mm and 0 mm for the latter(back) and the nip angle between the two beams 22 deg. In the welding process, the front defocused laser beam impacted the surface of metal plate and made it melt and the oxide-film gasify and evaporate. Then, the back laser focused on the already melted areas and deep penetration laser welding was achieved. At same time, the efficiency of the laser welding was increased owing to the higher absorptivity of the metal surface to the laser by the front laser preheating the surface.

The pores on the longitudinal section of weld with a length of 20mm are shown in Fig 4. There are only a few single pores apparent on it. This means that extremely low porosity has occurred.

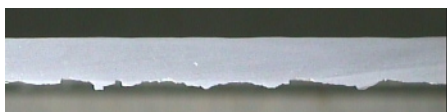


Fig. 4. Porosity on the longitudinal section of weld

3.3 Porosity in butt joint special dual-beam laser welding

The next experiment was the dual-beam laser welding of a butt joint of 1420 alloy. Two laser welding processes were used in tests. For process one, the parameters were just same with former experiment and the only difference for process two was that a single laser of power 1.7kW, defocused distance 20mm and welding speed 3.5m/min, was used on the butt joint position of the inverse surface first. This was immediately followed by the dual-beam laser welding.

3.3.1 Porosity in the welds of butt joint

The experiment data indicated that the samples with the two laser welding processes had full penetrated and both welds forming of right surface were all right. For weld forming on the inverse surface and the porosity, the outcomes were quite different for the two processes. For laser process two, from Fig 5, the weld formed is smooth and there are only a few pores in weld and for laser process one, not only is the inverse weld badly formed but also there are more pores in the weld as shown in Fig. 6. To compare with the two processes, it was very obvious that low porosity could be made and the size of pores could become smaller at the same time when laser process two was adopted in the experiments.

However, why the situations are so different for laser process one when it was used in the two cases of beam on plate and butt joint. This is because the affecting factors become complex in butt joint process such as the presence of gap and the quality of fitting for two butt plates.

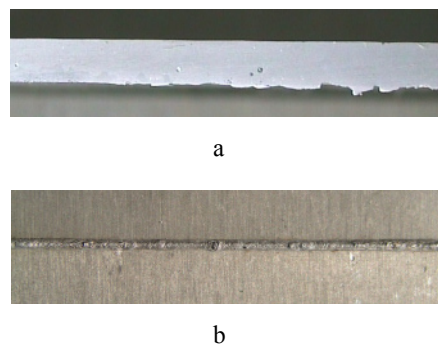


Fig. 5. Porosity (a) and inverse form (b) of weld by welding process two

Due to the fitting interval between butt plates could influence the stability of welding process and cause the bad weld forming with lots of burres and unsmooth surface on inverse surface. In such a welding process, a part of oxide-film at inverse surface would be melted into fused bath and surrounding gas be taken into the bath also. As a result of it, a lot of pores were produced in liquid bath and remain in the weld. For laser process two, before laser penetration welding, the oxide-film on the inverse surface of the butt plates has been cleaned by

laser remelting, so the porosity is reduced and welding quality is improved.

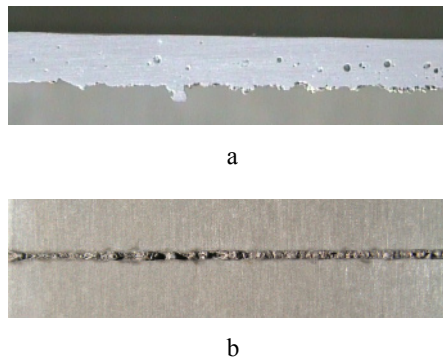


Fig. 6. Porosity (a) and inverse form (b) of weld by welding process one

3.3.2 Tensile strength of butt joints

Fig.7 is shows the tensile strength of the butt joints with the two kinds of dual-beam laser welding processes for 1420 Al-Li alloy. The data show that the average strength for laser process two is 336.1MPa, equivalent to 87.5% of that of base metal(383.7MPa), because of the effective control of pores in the welds. But for laser process one, the average strength is only 236.6MPa, 61.6%of base metal. The main reason is that pores in weld reduce the capacity for carrying stress because of the loss in cross-sectional area of the welds.

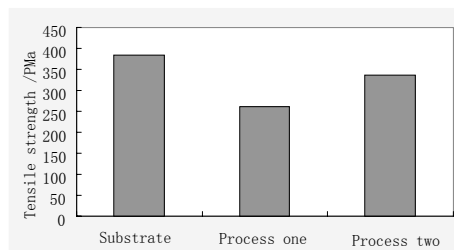


Fig. 7. Tensile test value of 1420 alloy welded joints

4. Conclusion

For the methods described for the laser welding of 1420 Al-Li alloy, in which the alloy plate was not treated in any way before welding, the following conclusions have been reached:

- 1) For bead on plate experiment using the special dual-beam laser welding arrangement, the affect on reducing porosity from the oxide-film on the right (upper) surface is much higher than that on the reverse (lower) surface.
- 2) For butt joint welding, the pores display higher sensitivity to the oxide-film of the reverse surface and have a direct relation with quality of the weld forming on reverse surface.
- 3) Adopting the two step procedure of laser welding, at first to clean the oxide-film off the reverse surface by a single laser beam and then using the special dual-beam laser welding for penetration of the butt joint, the occurrence of pores is reduced and the strength of the weld is improved, achieveing an average tensile strength up to 87.5% of the base metal.

References

- [1] Qiu Huizhong. Al-Li Alloys and Their Manufacturing Techniques for Aerospace Products Outside China[J]. Aerospace Materials & Technology, 1998,(4):39-43, in Chinese
- [2] Ren Jialie, WU Aiping. Jointing of Advanced Materials [M]. Beijing: Press of Mechanical Industry, 2000:39-74, in Chinese
- [3] Pickens J.R. Review: Recent developments in the weld-ability of lithium containing aluminum alloys[J]. Journal of Materials Science, 1990, 25: 3035-3047
- [4] Ellis M B D. Fusion welding of aluminium-lithium alloys [J].Welding & Metal Fabrication, 1996, 64(2):55-60
- [5] Xiao Rongshi, Yang Wuxiong, Chen Kai. Porosity characterization in laser welds of Al-Li alloy1420 Applied Laser [J]. 2007, 27 (1): 13-16
- [6] Twardowska A, Kusinki J. Laser welding of Al-Li-Mg-Zr alloy. Proc. SPIE Vol. 4238 (2000), 180-185
- [7] Wang Wei, Xu Guangyin, Duan Aiqing et al. Po-rosity Formation Mechanism in Laser Welding 1420 Al-Li alloy [J]. Transactions of the China Welding Institu-tion. 2005,26(11):59-62
- [8] Xiao Rongshi, Yang Wuxiong, Chen Kai. Nd:YAG laser welding of 1420 aluminum lithium alloy[J]. Chinese Journal of Laser, 2007, Vol. 34 Suppl.
- [9] Kai Chen, Rongshi Xiao, Rui Huang, Xudong Zhao, Song Zhang. Study on the pore control of 5083 Al alloy by dual-beam laser welding. Proceeding of PICALO 2008, 556-560 Beijing , People's Republic of China.

Characteristics of keyhole and molten pool during laser welding of TC4 Ti-alloy

Duan Aiqin^{1*}, Chen Li¹

¹ National Key Laboratory of Science and Technology on Power Beam Processes, BAMTRI, Beijing, China

* duan_aiqin@tom.com

Abstract. In this paper, the characteristics of keyhole and molten pool during laser welding of TC4 have been studied through measuring its images. The study shows that the size of keyholes in all processes almost keep constant. This means that there is a quite steady absorption for laser energy in all welding processes of TC4, and this stability almost is not affected by welding parameters. Because of this steady energy input, the steady molten pool would be formed in all quasi-stationary processes, and it is verified by images of molten pool at different time. The results at different heat input clearly show that the area of different temperature rises with the increase of the heat input. The length of molten pool also increases with the heat input. But the heat input has less influence on the width than others.

Keywords: laser welding, keyhole, molten pool, Ti-alloy

1. Introduction

The use of laser welding in aeronautic industry has increased significantly in the recent years. This increased use is driven by aeroplane designs requiring a reduction in weight, offering performance increases in the final product. Except for manufacture technology, the use of light alloy, such as Ti-alloy and Al-alloy, also has increased greatly for the same objectives. Laser welding is widely used in joining of thin light alloy component, and distortion is one of the most difficult problem,

especially for large structures. It is known that reducing of heat input is the best way to solve this problem, but performances of the final joint also must be considered. For laser welding, it is related not only heat input, but dynamic characteristics of keyhole and molten pool as well. And the characteristics of molten pool almost decide the features of the final joint. The geometry, temperature field and thermal cycle are key factors for formation of a weld. The main objective controlling welding parameters is to limit these features of the molten pool. Many studies have been made about keyhole and molten pool during laser welding of various metals. The main methods can be divided two kinds, modeling or measuring^[1-14]. In this paper, the main characteristics of keyhole and molten pool were measured and analysed during laser welding of TC4 Ti-alloy.

2. Experimental Setup and Material

In this study, the welded material was TC4 Ti-alloy with thickness of 1.5mm. Its characteristics, such as low – density, highly strength and highly corrosion-resistant, make it widely use in aerospace to reduce the weight. Its main chemical composition is given in Table 1.

The laser used was a 4kW YAG laser. The images of

Table 1 Chemical composition of TC4 (w%)

Element	Al	V	Fe	N	H	O	Ti
(wt%)	6.27~6.32	4.15-4.19	0.18-0.2	0.012-0.014	0.0041	0.18-0.19	others

Table 2 Thermal parameters of TC4

Melting temperature	Boiling temperature	Thermal conductivity λ ($J/(m \cdot s \cdot K)$)	viscosity coefficient μ ($kg/(m \cdot s)$)	Surface tension coefficient γ (N/m)
1700°C	3287°C	24.86297	0.00291943	1.64113717

welding process were captured by an Phantom V4.1 high-speed camera with the optical filters. All experiments yield a penetration weld with the Ar shielding gas. All selected welding parameters close to the real thing ,so that practical welding processes can be observed and the results can benefit for industry application.

3. Results and Discussion

During laser welding process, there are three main parameters, that is the keyhole, molten pool and vapor/plasma. The incident beam is absorbed by keyhole, then the molten pool is formed by thermal conduction. Because of this, the laser keyhole is of prime importance in all cases involving penetration welding.

3.1 The characteristics of the keyhole during YAG laser welding of TC4

Dynamic behavior of the keyhole is observed with the high-speed camera for different welding speeds, the incident laser power and spot diameter being kept constant at 2000W and 0.4mm respectively. The images of dynamic processes of the keyhole for welding speed of 2.5m/min are given in Fig. 1. It can be found that the sizes of keyholes in all processes, from $t=0\text{ms}$ to $t=8.1\text{ms}$, keep constant. This result indicates that there is a quite steady absorption for laser energy in all welding processes of TC4. More results for different welding speeds also show that this stability almost is not affected by welding parameters. This mainly is related with thermal physical parameters of TC4(see in table 2), especially small thermal conductivity above melting temperature. This performance makes temperature and vaporization of the keyhole keep relative stability.

The processes for different welding speeds are observed, as shown in Fig. 2. The results show that although the stability of the keyhole almost is not affected by welding parameters, the shape and depth is related with welding parameter, especially surface diameter of keyhole and penetrating depth.

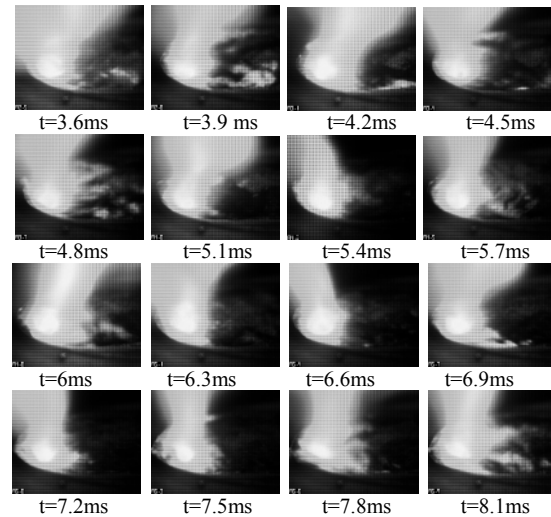
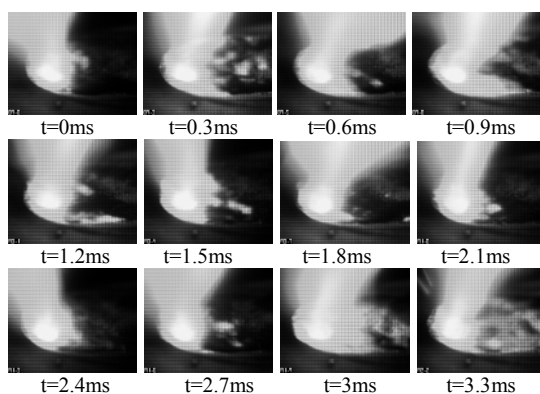


Fig. 1 Images of dynamic processes of the keyhole for welding speed of 2.5m/min

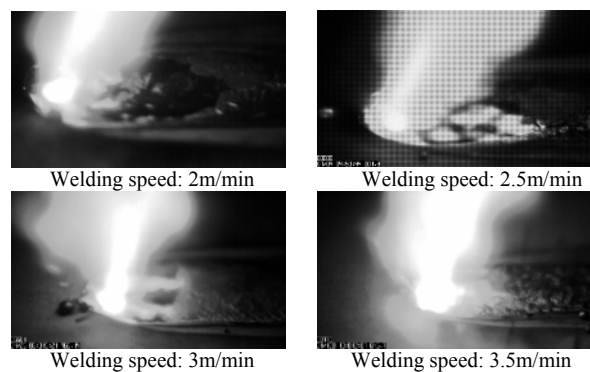
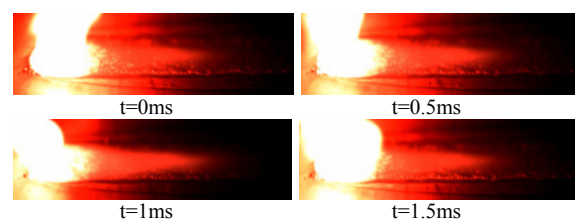


Fig. 2 The typical images of the keyhole for different welding speeds during laser welding of TC4

3.2 The characteristics of the molten pool during YAG laser welding of TC4

From the results on the keyhole, it can be known that there is a steady absorption of incident beam during laser welding of TC4. Because of this steady energy input, the steady molten pool would be formed in all quasi-stationary processes, and it is verified by images observed by high-speed camera. The Images of the molten pool from $t=0\text{ms}$ to $t=10\text{ms}$,for welding speed of 2.5m/min, are given in Fig. 3. It is apparent that the sizes of the molten pool at different time are almost the same.



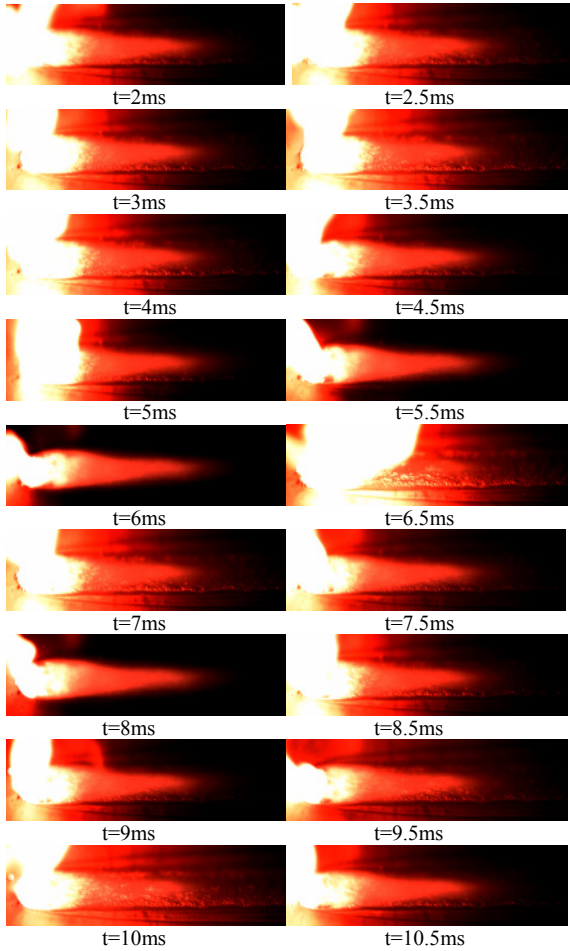


Fig. 3 Images of the molten pool at different time during a welding process (V=2.5m/min)

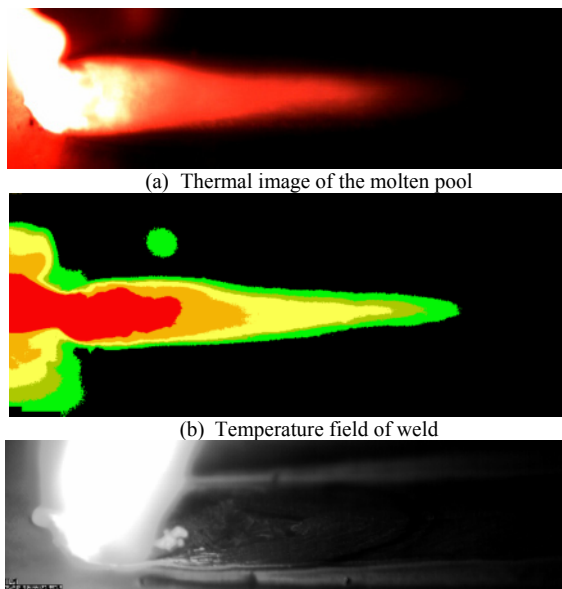


Fig. 4 The typical images of the molten pool

Measured a clear image of the molten pool for above process(see Fig. 4(a)), it can be found that in this welding condition, it is about 8.6mm in length and 2.2mm in width. From the shape of the molten pool shown in Fig. 4(c), the liquid-solid interface and heat-affected zone on the weld surface can be seen clearly. The thermal cycle is measured by the rapid thermocouple, shown in Fig. 5 It can be found that the heating velocity is very quick and the time dropping from the highest to 800°C is about 1000ms.

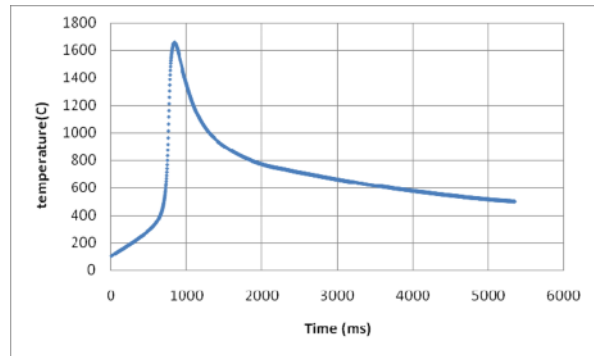


Fig. 5 The typical thermal cycle during laser welding of TC4

3.3 The influence of welding parameters on the characteristics of the molten pool

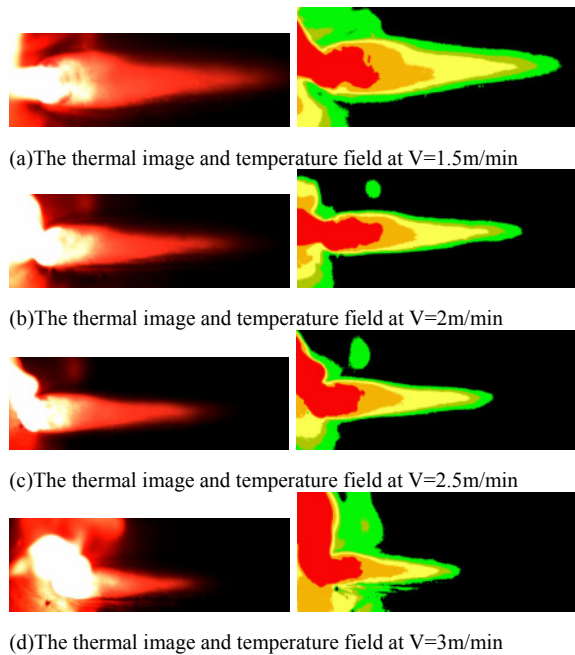


Fig. 6 The thermal images and temperature field at different welding speed

During laser welding, the geometry of the molten pool largely depends on the keyhole, heat input (J/mm) and welding speed. Experiments were designed to keep laser power constant and only to change welding speed. The

features of the molten pool and the temperature field are measured when heat input changes from 80J/mm to 40J/mm, that is welding speed changing from 1.5m/min to 3m/min. All images of the molten pool at different parameters are given in Fig. 6, including thermal images and related temperature field images. It is clearly shown that the areas of different temperature rise with the increase of the heat input. The length of the molten pool also increases with the heat input. The heat input has less influence on the width than others.

Conclusions

For YAG laser welding of TC4, under these welding conditions, some conclusions about characteristics of the keyhole and molten pool are as follows:

(a) The study about keyhole shows that the sizes of the keyholes in all processes keep constant. This means that there is a quite steady absorption for laser energy in all welding process of TC4, and this stability almost is not affected by welding parameters.

(b) Because of this steady energy input, the steady molten pool would be formed in all quasi-stationary processes, and it is verified by images of molten pool at different time. For welding process with speed of 2.5m/min, the length of the molten pool is about 8.6mm and the width is about 2.2mm. The thermal cycle shows that the heating velocity is very quick and the time dropping from the highest to 800°C is about 1000ms.

(c) The results at different heat input clearly show that the areas of different temperature rise with the increase of the heat input. The length of the molten pool also increases with the heat input. But the heat input has less influence on the width than others.

References

- [1] Joerg Beersiek. A CMOS camera as a tool for process analysis not only for laser beam welding. In: Congress Proceedings ICALEO,2001,212~220
- [2] Akira Matsunawa. Dynamics of keyhole and molten pool in high power laser welding. Journal of laser applications. 1998, 10(6):247-254
- [3] F.Coste, F.Janin, M.Hamadou, R.Fabro. Deep penetration laser welding with Nd:YAG lasers combination up to 11kW laser power. In: Congress Proceedings ICALEO, 2002.
- [4] Naito Yasuaki. Penetration Characteristics in YAG Laser and TIG Arc Hybrid Welding, and Arc and Plasma/Plume Behavior during Welding. In: 溶接学会论文集, 2006, 24(1): 32~38
- [5] S.Palanco et al. Spectroscopic diagnostics on CW-laser welding plasmas of aluminum alloys. Spectrochimica Acta Part B, 2001,56:651~659
- [6] Duhamel, R.V., Banas, C.M. Laser Welding of Steels and Nickel Alloys. Laser in Materials Processing., 1983, 209.
- [7] Duan A Q, Chen L. Dynamic behavior of plasma in CO2 laser welding of stainless steel. Transactions of the China Welding Institution, 2005,26(11):17-20. (in Chinese)
- [8] Duan A Q, Chen L. Molten pool and temperature field in CO2 laser welding. China Welding, 2006,15(1): 30-33.
- [9] Kawahito Yousuke. Visualization of interaction between laser beam and YAG-laser -induced plume. In proceedings of the ICALEO'2005 Conference, p920.
- [10] Remy Fabbro. Analysis of the various melt pool hydrodynamic regimes observed during CW Nd:YAG deep penetration laser welding. In proceedings of the ICALEO'2007 Conference, Orlando,USA, Oct.29.
- [11] Remy Fabbro. Experimental study of the humping process during Nd:YAG CW laser welding. In proceedings of the ICALEO'2007 Conference, Orlando,USA, Oct.29.
- [12] Remy Fabbro(2005). Study of keyhole behavior for full penetration Nd:YAG CW laser welding, J.Phys.D:Appl.Phys.38,1881-1887.
- [13] Remy Fabbro(2006). Experimental study of the dynamical coupling between the induced vapor plume and the melt pool for Nd:YAG laser welding.,J.Phys. D:App.Phys.39,394-440.
- [14] Remy Fabbro(2008). Characteristic melting pool hydrodynamic behaviors for CW Nd-YAG deep penetration laser welding. In proceedings of the ICALEO'2008 Conference, Beijing, China.

Typical Joint Defects in Laser Welding of Aluminium-Lithium Alloy

J Yang^{1,2}, S Gang², X Li¹, Li Chen², F Xu²

¹ College of Material Science and Engineering, Beijing University of Technology, Beijing, China

² National Key Laboratory of Science and Technology on Power Beam Processes, BAMTRI, Beijing, China

Abstract. Welding trials of autogenous laser welding, laser welding with filling wire and laser-MIG arc hybrid welding have been carried out. The characteristics, cause and controlling methods of joint defects were analyzed by optic microscope, X-ray detection and numerical simulation. The results indicated that the common defects were imperfect shape and porosity inside the weld. The characteristics of weld surface defects varied during different welding processes; porosity was also different in shape and formation during full penetration welding and incomplete penetration welding. All the defects mentioned above could be controlled or avoided by optimizing the welding process procedures.

Keywords: aluminium-lithium alloy, laser welding, defect

1. Introduction

The development of aeronautical manufacturing places higher requirements for strength and weight reduction on materials, including aluminum-lithium alloy due to its high specific strength, stiffness, fracture toughness and fatigue strength^[1,2]. In past decades, Al-Li alloy has been rapidly developed and is widely used in military and civil aircraft and rocket fuselages, fuel tanks, cockpits. It has become an important aerospace structural material. For these alloys, laser welding technology is increasingly receiving widespread attention and is also being considered for wider applications in the aero industry because of its advantages of high energy density, low distortion and high productivity among others.

Use of laser welding of Al-Li alloy in welded structures and products has broad application prospects. However, because the Mg, Li and other chemical elements in Al-Li alloy are extremely active, the surface forms a high melting point oxide film, which can easily cause porosity. In addition, the low boiling point, high flowability, reflecting rate and thermal conductivity of aluminum alloy are prone to cause various defects^[3-6]. To solve these problems, characteristics of joint defects in Al-Li alloy autogenous laser welding, laser welding with filler wire and laser-MIG hybrid welding were studied, their causes and mechanism were analyzed and control methods were introduced.

2. Material and Equipment

The parent metal used in this work was 3 mm thick Al-Li alloy 5A90 with moderate strength, low density, and good corrosion resistance. The filler wire was ER5356 with diameter of 1.2mm.

A YAG laser with a laser processing head of 150 mm focal length, and a pulse MIG equipment with push - pull wire feeder were used in welding system.

As defined, d is the wire extension, α is the wire feed angle, DLA is the distance between focal point and wire tip. The optimal fixed parameters selected were: $\alpha = 60^\circ$ and $d = 8$ mm.

3. Result and Discussion

3.1 The Characteristics of Laser Welded Joints

With the optimum process parameters, good shape joints can be obtained in autogenous laser welding, laser welding with filler wire and laser-arc hybrid welding.

Because of the special physical nature of Al-Li alloy and the characteristics of autogenous laser welding, as with other aluminum alloys, the joint formation was poor. The surface shows uneven "fish-scale patterns", inconsistent weld width, weld toes present irregular wave types and slight depressions and undercuts can be seen from the cross-section morphology of the weld (Figure 1-a).

There is also an obvious and uneven "fish-scale pattern" on the weld surface in laser welding with filler wire. The filling wire supplements the burnt metal during the welding process, and though the surface is not entirely smooth, the phenomena of depression and undercut occurring in laser welding is effectively improved (Fig. 1b).

Since the introduction of an arc as a heat resource supplement in laser-arc hybrid welding, the size of the molten pool is much larger than that in autogenous laser welding. The seam surface is smooth except for some

inconspicuous molten pool flow lines, the weld width is consistent, because of adequate melting, full backfilling and an even spreading of the solidification process is apparent. The weld cross-section shows that the transition on the surface of the weld and base material is uniform, the weld width is increased, and at the same time the necessary penetration depth can be guaranteed. The phenomena of depression and undercut are significantly improved (Figure 1- c).

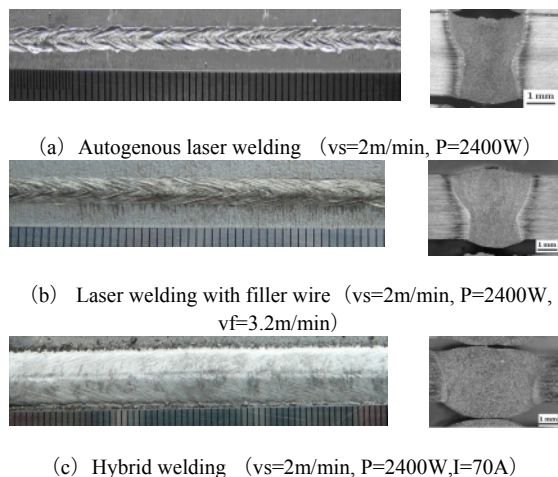


Fig. 1. Characteristics of weld joints using different welding ways

3.2 The External Defects of Joints

3.2.1 Defects in Autogenous Laser Welding

The forming defects of penetration welds are mainly poor uniformity, depression and undercut (Figure 1-a). At the lower melting point and boiling point, the defects of depression and burn through are easily formed owing to the violent eruption force of a large amount of metal vapor in the keyhole and the burnt metal during the autogenous laser penetration welding process.

Meanwhile, the low density, high thermal conductivity and liquid fluidity of Al-Li alloy, high welding speed and cooling speed during laser welding, and instability "churn" of the keyhole and pool, will all cause, to a certain extent, an uneven weld surface.

In addition, the narrow radiated area, less molten metal, and poor liquid metal backfilling ability, coupled with high cooling weld speed result in a part of the parent metal which had melted but cannot be covered completely by molten metal, therefore, the undercut forms.

3.2.2 Defects in Laser Welding with Filler Wire

If the welding process parameters are not suitable, then welding beading, excessive penetration, undercut, surface pores and other weld defects will be produced in laser welding with filler wire.

While the DLA is zero or negative, that is, the wire tip is in the center or behind the laser focal spot, the weld has discontinuities (Figure 2-a), and welding beading will sometimes occur severely (Figure 2-b). If the laser is blocked by the wire tip and it irradiates the wire directly, most of the energy cannot reach the parent material and is used to melt the wire and thereby a transition to large droplets occurs.

As shown in Figure 2-c, the surface pores are mainly due to partial wire feed and improper protection on the weld surface. Pre-wire feed way is usually used, if wire is placed in the back-end bath, it cannot be fully melted, the defects of "wire heap" and undercut are easily formed, and "wire stay" phenomenon will come out in severe cases (Figure 2-d). When the heat input is too high or the wire feed rate is comparatively low, serious depressions are produced, as shown in Figure 2-e. If the welding heat input is too low, it will generate the defects of weld reinforcement, and incomplete penetration (Figure 2-f). These defects can be avoided by process parameters optimization.

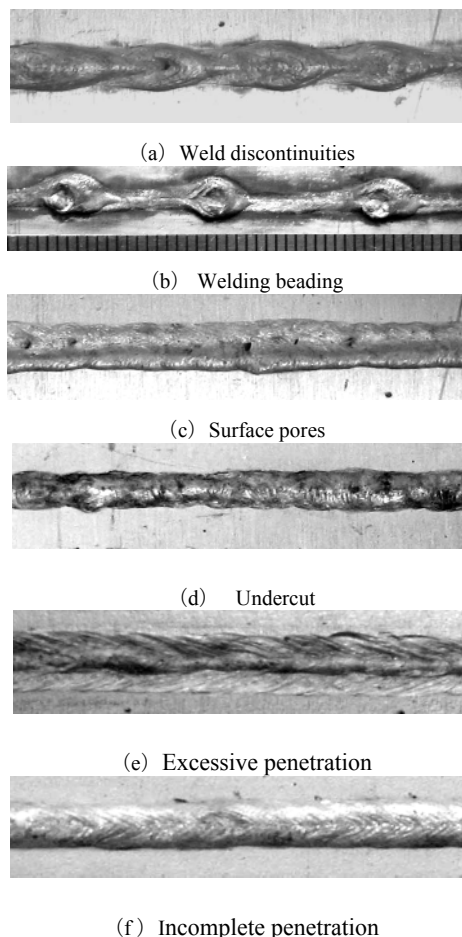
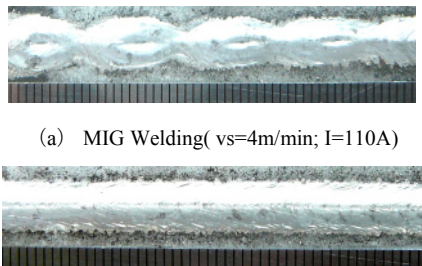


Fig. 2. Defects of weld surface in laser welding with filler wire

3.2.3 Defects in Laser Hybrid Welding

When MIG welding speed reached 4m/min, the weld is not continuous, which is caused by the arc drift phenomenon, as shown in Figure 3-a. The stability is greatly increased during hybrid welding due to the guidance of the laser (Figure 3-b).

This is an inevitable result due to the interaction of combined heat sources of the laser and arc. On one hand, the laser absorption rate is enhanced by the preheating of the arc; on the other hand, under the guidance of the laser, the arc can reach the deep keyhole. In addition, the weld width is slightly smaller than that of MIG, mainly because the plasma provides a conductive path for the arc to reduce the arc column resistance so that the arc is compressed.



(a) MIG Welding(vs=4m/min; I=110A)
(b) Hybrid Welding (vs=4m/min; P=2200W; I=110A)

Fig. 3. Morphology of weld in high speed

When the hybrid welding speed is up to 5 m/min, the defects of hump, uneven weld width and hot-melt cracks occur as shown in Figure 4.

Hump is caused by arc instability which results from a higher welding speed. Serious depression and hot cracking are produced under the condition of higher heat input. In addition, the defect as shown in Figure 3-a is prone to appear when the wire extension is too much. These defects can also be eliminated by process optimization as in laser welding with filler wire.



(vs=5m/min; P=3000W; I=190A)

Fig. 4. Defects morphology of weld in high-speed welding

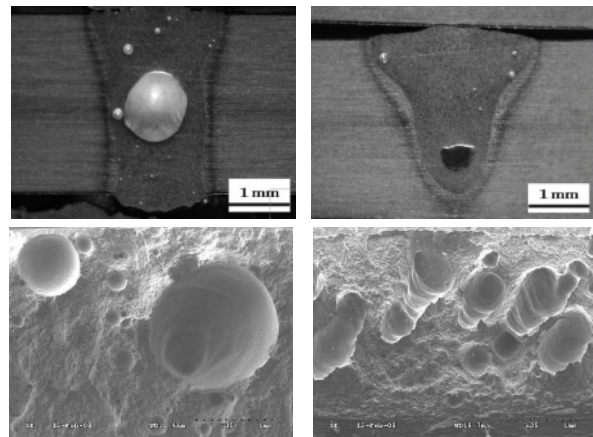
3.3 The Internal Defects of Joints

Compared with conventional aluminum alloy, Al-Li alloy has more pores during laser welding owing to the activity of the Li, as well as the surface layers formed in high-temperature processing, which contain the compounds of Li₂O, LiOH, Li₂CO₃ and LiN that can easily adsorb water from the surrounding environment to

increase the porosity. The pores can be divided into "metallurgical-type" pores and "keyhole-type" pores.

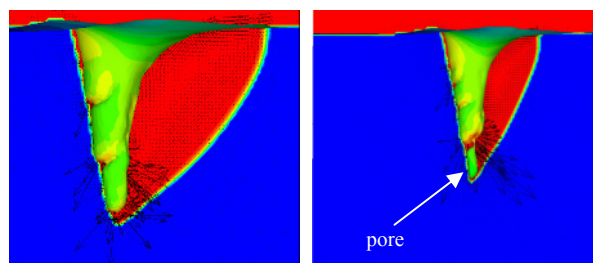
There are two types of "metallurgical type" pores. One is the crystallization layer pore, of smaller size; the other is due to the deposition of supersaturated hydrogen in the pool, gathering and growing until finally it is too late for it to escape during the cooling process so it forms large pores. "Metallurgical type" pores are generally characterized by the process of: nucleation - grow up - go up - stranded - formation, Their macro appearance is a relatively regular circle shape and smooth wall, as shown in Figure 5-a. The pool is deep and narrow in laser penetration welding, pores are "shelved" with the movement of the pool during the float process, so these pores are randomly distributed within the joints. The emergence of these holes is caused by deficient surface treatment, resulting in increased hydrogen absorption.

According to the result of simulation, "keyhole-type" pores are due to the shielding gas or metal vapor engulfed in the keyhole and covered by liquid metal resulting from the instability "stirred up" of the keyhole during the welding process (Figure 6). These pores are basically characterized by a series of big size blow-holes, irregular shape and "step"-shaped marks on the wall, as shown in Figure 5-b. Most of pores occur when the penetration is inadequate or unstable. In general, a large number of pores are gathered at the waist or in the middle seam.



(a) Metallurgical-type pores (b) Keyhole-type pores

Fig. 5. Porosity in laser welding



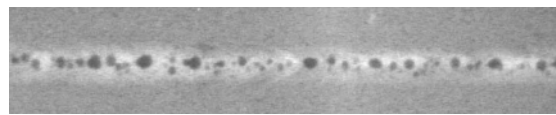
a) Speed trend of pool (b) Keyhole is cut

Fig. 6. The formation of "keyhole-type" pore

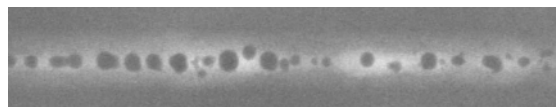
In the Al-Li alloy autogenous laser welding and laser welding with filler wire, if surface treatment is not properly carried out, any number of "metallurgical-type" pores will appear in the weld. A series of "keyhole-type" pores will be found in the weld center when the penetration is inadequate, as shown in Figure 7-a and 7-b.

In the laser hybrid welding process, pores are mainly "metallurgical-type", the sizes are large when the surface treatment is deficient. If the weld penetration is inadequate, "keyhole-type" pores will rarely be formed in the weld center, shown in Figure 7-c.

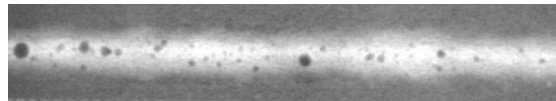
For the Al-Li alloy autogenous laser welding, laser welding with filler wire and laser-hybrid welding, the porosity can be controlled or eliminated by a strict alkaline wash + pickling + drying way to remove the surface oxide film completely before welding, and welding within 24h after surface treatment for full penetration, as shown in Figure 7-d to Figure 7-f.



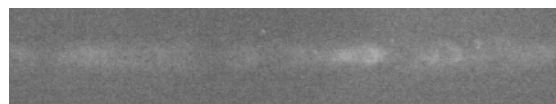
(a) Laser incomplete penetration welding ($V_s=3\text{m/min}$, $P=2000\text{W}$)



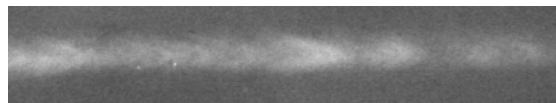
(b) Incomplete penetration welding with filler wire ($V_s=1.5\text{m/min}$, $P=1900\text{W}$, $V_f=2\text{m/min}$)



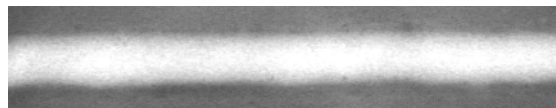
(c) Hybrid incomplete penetration welding ($V_s=2\text{m/min}$, $P=1800\text{W}$, $I=110\text{A}$)



(d) Laser penetration welding ($V_s=2\text{m/min}$, $P=2100\text{W}$)



(e) Penetration welding with filler wire ($V_s=2\text{m/min}$, $P=2400\text{W}$, $V_f=2\text{m/min}$)



(f) Hybrid penetration welding ($V_s=2\text{m/min}$, $P=1800\text{W}$, $I=130\text{A}$)

Fig. 7. X-ray inspection photos of Al-Li alloy laser-welded joint

4. Conclusion

1. The typical defects of Al-Li alloy laser-welded joints are mainly embodied in external poor shape and internal porosity.
2. The excessive penetration, undercut and uneven hill-shaped distribution "fish-scale pattern" surface are the main features of the external forming defects in autogenous laser welding.
3. The "beads chain" like weld surface, surface pores, depression and undercut are the common external forming defects in laser welding with filler wire.
4. In laser-arc hybrid welding process, the external forming defects are mainly uneven bead width as well as penetration depth, humping and hot cracks.
5. The external forming defects are mainly due to improper welding procedures, which can be optimized to control or eliminate the effects effectively.
6. The internal defects are mainly "metallurgical-type" pores and "keyhole-type" pores. A good shape and almost no pores in the weld can be achieved through a rigorous pre-weld surface treatment, and to achieve full-penetration welding.

References

- [1] Rioja RJ. Fabrication methods to manufacture isotropic Al-Li alloys and products for space and aerospace applications [J]. *Materials Science and Engineering*, 1998. A257 :100~107
- [2] Pan Su. Aluminum-lithium alloy development and process characteristics [J]. *Aerospace process*, 1994. (5): 40~45
- [3] Ren Jialie, Wu Aiping. *Advanced materials connection* [M]. China Machine Press, 2000: 39~74
- [4] Fei Xu, Li Chen, Shuili Gong, et al. Effects of Welding Current on Laser-MIG hybrid welding of Al-Li Alloy [J]. *Hot working technology*, 2009, 38 (7): 103~105.
- [5] Matsunawa A. Dynamics of keyhole and molten pool in laser welding [J]. *Journal of Laser Applications*, 1999, 10(6): 247-254.
- [6] Soderstrom E. and Mendez P. Humping mechanism present in high speed welding [J]. *Science and Technology of Welding and Joining*, 2006, 11(5): 572-579.